ARO 40058.1-PH CF

1999

Nonlinear Guided Waves and Their Applications

Technical Digest

1–3 September 1999

Palais des Congrès
Dijon, France

Postconference Edition

20001122 139

OSA®
Optical Society of America

Sponsored by
Optical Society of America

REPORT DOCUMENTATION PAGE

Form Approved
OMB NO. 0704-0188

Public Reporting burden for this collection of information is estimated to average 1 hour per response, including the time for reviewing instructions, searching existing data sources, gathering and maintaining the data needed, and completing and reviewing the collection of information. Send comment regarding this burden estimates or any other aspect of this collection of information, including suggestions for reducingthis burden, to Washington Headquarters Services, Directorate for information Operations and Reports, 1215 Jefferson Davis Highway, Suite 1204, Arlington, VA 22202-4302, and to the Office of Management and Budget, Paperwork Reduction Project (07040188,) Washington, DC 20503.

1. AGENCY USE ONLY (Leave Blank)	2. REPORT DATE	3. REPORT TYPE AND DATES COVERED
	July 13, 2000	Final 07/01/99 – 06/30/00

4. TITLE AND SUBTITLE
Organization of the 1999 Nonlinear Guided Waves and Their Applications Topical Meeting

5. FUNDING NUMBERS
DAAD19-99-1-0232

6. AUTHOR(S)
John A. Thorner

7. PERFORMING ORGANIZATION NAME(S) AND ADDRESS(ES)
Optical Society of America
2010 Massachusetts Ave., NW
Washington DC 20036

8. PERFORMING ORGANIZATION REPORT NUMBER

9. SPONSORING / MONITORING AGENCY NAME(S) AND ADDRESS(ES)
U. S. Army Research Office
P.O. Box 12211
Research Triangle Park, NC 27709-2211

10. SPONSORING / MONITORING AGENCY REPORT NUMBER
ARO 40058.1-PH-CF

11. SUPPLEMENTARY NOTES
The views, opinions and/or findings contained in this report are those of the author(s) and shouldnot be construed as an official Department of the Army position, policy or decision, unless so designated by other documentation.

12 a. DISTRIBUTION / AVAILABILITY STATEMENT
Approved for public release; distribution unlimited.

12 b. DISTRIBUTION CODE

13. ABSTRACT (Maximum 200 words)

The general purpose of the meeting was to bring together researchers in all aspects of nonlinear optics in guidewave and self-guided geometries. The meeting covered the range from theory to experiments, and from fundamentals to applications. Development of new ideas and novel techniques in the areas of materials, fabrication, devices, applications, and nonlinear theory were particularly emphasized. This meeting provided a forum for the discussion of nonlinear waveguide and soliton phenomena from theoretical, material, device and applications perspectives; identified nonlinear effects in optical communications and switching systems, and understand the opportunities and challenges that arise from them; improved the interaction between device and applications, communities, particularly in the areas of optical communications, optical switching, and waveguide frequency conversion; encouraged development of novel structures, materials, and devices with enhanced nonlinear functionality; addressed effects such as intrinsic localization in various nonlinear environments such as waveguide arrays, resonators, periodic structures and photorefractive materials, and the novel phenomena based on them; identified nonlinear phenomena in waveguide amplifiers, lasers, and effects in amplified systems; highlighted the similarities and differences between nonlinear effects in conservative and dissipative systems.

14. SUBJECT TERMS

15. NUMBER OF PAGES

16. PRICE CODE

17. SECURITY CLASSIFICATION OR REPORT	18. SECURITY CLASSIFICATION ON THIS PAGE	19. SECURITY CLASSIFICATION OF ABSTRACT	20. LIMITATION OF ABSTRACT
UNCLASSIFIED	UNCLASSIFIED	UNCLASSIFIED	UL

Articles in this publication may be cited in other publications. To facilitate access to the original publication source, the following form for the citation is suggested:

Name of Author(s), "Title of Paper," in *Nonlinear Guided Waves and Their Applications*, OSA Technical Digest (Optical Society of America, Washington DC, 1998), pp. xx-xx.

Optical Society of America

ISBN

Conference Edition	1-55752-578-1
Postconference Edition	1-55752-587-0
1999 Technical Digest Series	1-55752-584-6

Library of Congress Catalogue Card Number

Conference Edition	98-83001
Postconference Edition	99-63510

Copyright © 1999, Optical Society of America

Individual readers of this digest and libraries acting for them are permitted to make fair use of the material in it, such as to copy an article for use in teaching or research, without payment of fee, provided that such copies are not sold. Copying for sale is subject to payment of copying fees. The code 1-55752-584-6/99/$15.00 gives the per-article copying fee for each copy of the article made beyond the free copying permitted under Sections 107 and 108 of the U.S. Copyright Law. The fee should be paid through the Copyright Clearance Center, Inc., 21 Congress Street, Salem, MA 01970.

Permission is granted to quote excerpts from articles in this digest in scientific works with the customary acknowledgment of the source, including the author's name and the name of the digest, page, year, and name of the Society. Reproduction of figures and tables is likewise permitted in other articles and books provided that the same information is printed with them and notification is given to the Optical Society of America. In addition, the Optical Society may require that permission also be obtained from one of the authors. Address inquiries and notices to Director of Publications, Optical Society of America, 2010 Massachusetts Avenue, NW, Washington, DC 20036-1023. In the case of articles whose authors are employees of the United States Government or its contractors or grantees, the Optical Society of America recognizes the right of the United States Government to retain a nonexclusive, royalty free license to use the author's copyrighted article for United States Government purposes.

Printed in the U.S.A.

Contents

Agenda v

WA	Spatio-Temporal and Transverse Effects	1
WB	Nonlinear Effects in Fibers	23
WC	Localized Structures in Optical Cavities	43
WD	Poster Session 1	57
WE	Quadratic and Discrete Solitons	193
ThA	Dispersion Management 1	213
ThB	Nonlinear Periodic Media	233
ThC	Frequency Conversion and Cascaded Nonlinearity	247
ThD	Poster Session 2	261
ThE	Vectoral Solitons and Incoherent Solitons	395
FA	Materials and Characterization	421
FB	Parametric Effects	441
FC	Frequency Conversion in Glasses versus Crystals	461
FD	Dispersion Management 2	475

Key to Authors and Presiders 491

Technical Program Committee

General Chairs:
David J. Richardson, *Univ. of Southampton, UK*
Stefan Wabnitz, *Univ. de la Bourgogne, Dijon, France*

Program Chairs:
J. Stewart Aitchison, *Univ. of Glasgow, UK*
Falk Lederer, *Univ. of Jena, Germany*
Mordechai Segev, *Princeton Univ., USA*

Category 1: Nonlinear Fiber Effects and Temporal Solitons
Y. Kodama, *Ohio State Univ., Columbus, USA, Chair*
G. Agrawal, *Univ. of Rochester, USA*
P. Mamyshev, *Tyco Submarine Systems, USA*
T. Georges, *CNET, Lannion, France*
W. Forysiak, *Aston Univ., UK*

Category 2: Spatial Solitons and Transverse Effects
Yu. Kivshar, *Australian National Univ., Canberra, Australia, Chair*
Y. Silberberg, *Weizmann Inst., Rehovot, Israel*
L. Torner, *Universität Polit. Catalunya, Barcelona, Spain*
W. Torruellas, *Washington State Univ., Pullman, USA*

Category 3: Nonlinear Periodic Structures and Cavities
L. Lugiato, *Univ. of Milan, Italy, Chair*
S. Trillo, *Univ. of Ferrara, Italy*
J. R. Tredicce, *Univ. of Nice, France*
M. de Sterke, *Univ. of Sydney, Australia*
P. St. J. Russell, *Univ. of Bath, UK*

Category 4: Frequency Conversion and Switching
A. Barthélémy, *Univ. of Limoges, France, Chair*
M. Asobe, *NTT, Japan*
P.G. Kazansky, *Univ. of Southampton, UK*
P. Di Trapani, *Univ. of Milan, Italy*

Category 5: Materials and Fabrication
A. Villeneuve, *Univ. of Laval, Quebec, Canada, Chair*
W. Sohler, *Univ. Paderborn, Germany*
T. Kaino, *Tohoku Univ., Japan*
F. Laurell, *Royal Inst. of Tech., Sweden*
P. LiKamWa, *Univ. of Central Florida, USA*

*Gregory Magel, *Texas Instruments Inc., USA*

**OSA Technical Council Representative*

Agenda

■ Tuesday
■ 31 August 1999

Foyer-Bar

16.00–18.00
Registration Open

Palais des Congrés

18.00–20.00
Welcoming Reception

■ Wednesday
■ 1 September 1999

Foyer-Bar

07.00–17.00
Registration Open

Salle Morey–St-Denis

07.55–08.00
Opening Remarks
David J. Richardson, *Univ. of Southampton, UK* and Stefan Wabnitz, *Univ. de la Bourgogne, Dijon, France*

08.00–10.00
WA ■ Spatio-Temporal and Transverse Effects
Govind Agrawal, *University of Rochester, USA, Presider*

08.00 (Invited)
WA1 ■ Generation of optical spatio-temporal solitons, X. Liu, L.J. Qian, F.W. Wise, *Cornell Univ., USA.* We report the experimental observation of spatio-temporal solitons. Femtosecond pulses in a quadratic medium evolve to constant and compressed beam size and pulse duration. **(p. 2)**

08.30
WA2 ■ Spatio-temporal solitary waves in a self-defocusing AlGaAs slab waveguide, Nicolas Bélanger, Alain Villeneuve, *COPL, Univ. Laval, Canada;* J. Stewart Aitchison, *Univ. Glasgow, UK.* We report the observation of a spatio-temporal solitonlike wave. In our experiments, we used coupled bright temporal and dark spatial solitary wave. **(p. 5)**

08.45
WA3 ■ Competing neck and snake instabilities of vector Kerr and type I quadratic solitons, Dmitry V. Skryabin, William J. Firth, *Univ. Strathclyde, UK.* We demonstrate dynamical competition between neck and snake instabilities of spatial solitons in normally dispersive χ^2 and χ^3 media. This competition originates either from the presence of internal soliton modes or from the second phase symmetry and results in spatial and/or polarization symmetry breaking. **(p. 8)**

09.00
WA4 ■ Observation of hybrid stripe-needle screening soliton interaction, Eugenio DelRe, *Fondazione Ugo Bordoni, Italy;* Stefano Trillo, *Univ. Ferrara, Italy;* Mordechai Segev, *Princeton Univ., USA.* We investigate experimentally the interaction of a one-dimensional and a two-dimensional photorefractive screening spatial soliton, observing phase-dependent warping, and particlelike collisions. **(p. 11)**

09.15
WA5 ■ Pair generation of (2+1) dimensional dark spatial ring solitons, M.M. Méndez-Otero, S. Chávez-Cerda, M.D. Iturbe-Castillo, *INAOE, Mexico.* We report the generation of dark spatial ring solitons using an amplitude jump. An even number of collapsing and divergent ring solitons are generated simultaneously. **(p. 14)**

09.30
WA6 ■ Transverse structures in cavity-less parametric amplifier, W. Chinaglia, S. Minardi, S. Sapone, G. Coppo, P. Di Trapani, *Univ. Insubria, Italy;* A. Berzanskis, G. Valiulis, *Univ. Vilnius, Lithuania;* K. Staliunas, *PTB braunschweig, Germany.* Large-beam transverse structures in saturated parametric amplification is demonstrated for a cavity-less configuration. Possibility of image digitalization and processing is pointed out. **(p. 16)**

09.45
WA7 ■ Pulse propagation and soliton formation using optical rectification, U. Peschel, K. Bubke, D.C. Hutchings, J.S. Aitchison, *Univ. Glasgow, UK.* We model the interaction of optical and microwave pulses due to optical rectification. We demonstrate that mutual bound states of both waves exist. **(p. 19)**

Foyer-Bar

10.00–10.30
Coffee Break

Salle Morey–St-Denis

10.30–12.00
WB ■ Nonlinear Effects in Fibers

David J. Richardson, *University of Southampton, UK, Presider*

10.30
WB1 ■ Coupled core and cladding stimulated Brillouin scattering in single-mode optical fibers, Isabelle Bongrand, Antonio Picozzi, Eric Picholle, Carlos Montes, *CNRS, France.* A coherent model for longitudinal and transverse Brillouin scattering in fibers describes their coupling, in good agreement with experiments in a long-fiber ring resonator. **(p. 24)**

10.45
WB2 ■ Four-wave mixing of femtosecond pump-probe pulses in optical fibers, Gilbert Boyer, *Ecole Polytechnique-ENSTA, France;* Bjorn Hall, Dan Anderson, Mietek Lisak, Magnus Karlsson, *Chalmers Univ. of Technology, Sweden;* Anders Berntson, *Ericsson Telecom AB, Sweden.* A new physical feature involving a large spectral jump is found, experimentally and numerically, for femtosecond pump-probe pulses near the zero-dispersion wavelength. **(p. 27)**

11.00
WB3 ■ Modulational instability in optical fibers with polarization-mode dispersion, F.Kh. Abdullaev, *Uzbek Academy of Sciences, Uzbekistan;* J. Garnier, *Ecole Polytechnique, France;* E. Seve, S. Wabnitz, *Univ. Bourgogne, France.* Random polarization-mode dispersion leads to a substantial extension of the modulational instability domain in both the normal and anomalous dispersion regime of fibers. **(p. 30)**

11.15
WB4 ■ Optimized design of a fiber-based pulse compressor for gain-switched DFB laser pulses at 1.5 microns, L.P. Barry, *Dublin City Univ., Ireland;* B.C. Thomsen, J.M. Dudley, J.D. Harvey, *Univ. Auckland, New Zealand.* The design of a fiber-based pulse compressor for gain-switched laser pulses is optimized using a technique based on frequency-resolved optical gating. **(p. 33)**

11.30
WB5 ■ Observation of isotropic polarization modulational instability in spun fibers, Pascal Kockaert, Marc Haelterman, *Univ. Libre de Bruxelles, Belgium.* Performing an experiment of polarization modulational instability in the normal dispersion regime, we show the possibility of achieving effective isotropy in an optical spun fiber. **(p. 36)**

11.45
WB6 ■ Fiber-optical parametric amplifier with 120-nm bandwidth, M.-C. Ho, M.E. Marhic, Y. Akasaka, F.S. Yang, L.G. Kazovsky, *Stanford Univ., USA.* We have measured gain in excess of 12 dB over a 120-nm bandwidth for a fiber-optical parametric amplifier made from a 20-m high-nonlinearity fiber and an 11W pulsed pump. **(p. 39)**

12.00–13.30
Lunch

Salle Morey–St-Denis

13.30–15.00
WC ■ Localized Structures in Optical Cavities

J.R. Tredicce, *University of Nice, France, Presider*

13.30 (Invited)
WC1 ■ Spatial solitons in a single-mirror feedback system, B. Schaepers, M. Feldmann, T. Ackemann, W. Lange, *Univ. Muenster, Germany.* Spatial solitons and their interaction are investigated experimentally and theoretically in a bistable single-mirror feedback system. **(p. 44)**

14.00 (Invited)
WC2 ■ Two-dimensional vectorial localized structures in optical cavities, P. Colet, R. Gallego, E. Hernandez-Garcia, M. Hoyuelos, M. San Miguel, M. Santagiustina, *Univ. Illes Balears, Spain;* G.L. Oppo, *Univ. Strathclyde, UK.* The existence and dynamics of different types of polarized localized structures is discussed in broadarea lasers, Kerr resonators, and type II degenerate optical parametric oscillators. **(p. 47)**

14.30
WC3 ■ Interaction of cavity solitons in degenerate optical parametric oscillators, Dmitry V. Skryabin, William J. Firth, *Univ. Strathclyde, UK.* Numerical studies together with asymptotic and spectral analysis establish regimes where soliton pairs in degenerate optical parametric oscillators fuse, repel, or form bound states. A novel bound state stabilized by coupled internal oscillations is predicted. **(p. 50)**

14.45
WC4 ■ Spatial structures and their control in injection-locked broadarea VCSELs, T. Ackemann, *IMEDEA, Spain, CNRS, France and Univ. Muenster, Germany;* S. Barland, *IMEDEA, Spain and CNRS, France;* M. Cara, M. Giudici, S. Balle, *IMEDEA, Spain.* We demonstrate tilted wave emission and hexagons in broadarea vertical-cavity surface-emitting lasers (VCSELs) locked to a master oscillator and explore the possibility of cavity solitons. **(p. 53)**

Foyer-Bar

15.00–16.30
WD ■ Poster Session 1/ Refreshment Break

WD1 ■ Quadratic bright solitons: counterpropagating scheme, Kazimir Y. Kolossovski, Alexander V. Buryak, Rowland A. Sammut, *Univ. College, Australian Defence Force Academy, Australia.* We analyze stability and optimal conditions for generation of quadratic bright solitons in a counterpropagating configuration. **(p. 58)**

WD2 ■ Steering of discrete solitons, Hagai Eisenberg, Yaron Silberberg, *Weizmann Institute of Science, Israel;* Roberto Morandotti, Ulf Peschel, J. Stewart Aitchison, *Univ. Glasgow, UK.* We experimentally investigate the propagation of solitons in waveguide arrays. We found the dynamical properties to be considerably modified by the discrete nature of the structure. **(p. 61)**

WD3 ■ Solitons due to double resonance wave mixing in quadratic nonlinear media, Alexander V. Buryak, Isaac Towers, Rowland A. Sammut, *Univ. College, Australian Defence Force Academy, Australia;* Boris A. Malomed, *Tel Aviv Univ., Israel.* We investigate the existence and stability properties of three-wave solitons due to double resonance (type I plus type II) parametric interaction in quadratic nonlinear media. Among other findings we present a novel family of stable quasi-solitons. **(p. 64)**

WD4 ■ Collapse suppression via parametric wave mixing, Victoria V. Steblina, Alexander V. Buryak, Rowland A. Sammut, *Australian Defence Force Academy, Australia;* Yuri S. Kivshar, *Australian National Univ., Australia.* We demonstrate that even a weak parametric coupling between a fundamental beam and its third harmonic can suppress catastrophic collapse in a bulk cubic (Kerr) nonlinear optical medium. **(p. 67)**

WD5 ■ Asymmetric incoherent solitons, Wieslaw Królikowski, Nail N. Akhmediev, *Australian National Univ., Australia;* Natalia M. Litchinitser, Govind P. Agrawal, *Univ. Rochester, USA.* Media with slow saturable nonlinearity can support spatial solitons, which are asymmetric in shape and are composed of only a finite number of modes of the self-induced waveguide. **(p. 70)**

WD6 ■ Do stable multihump solitons exist?, Elena A. Ostrovskaya, Yuri S. Kivshar, *Australian National Univ., Australia;* Dmitry V. Skryabin, William J. Firth, *Univ. Strathclyde, Scotland.* Stability analysis of multihump optical solitons in saturable media is presented. It is shown that, in contrast with common beliefs, multihump solitons can be stable. **(p. 73)**

WD7 ■ Self-trapping of necklace beams in self-focusing Kerr media, Marin Soljacic, Suzanne Sears, Mordechai Segev, *Princeton Univ., USA.* We believe we present the first (2+1)D beams that exhibit stable self-trapping in a system described by the cubic self-focusing (2+1)D Nonlinear Schrodinger Equation. An analytical framework we developed allows us to predict and control dynamics of such beams, so we can design shapes that are essentially stationary for very large distances. **(p. 76)**

WD8 ■ Coherence and incoherence in multisoliton complexes, Andrey A. Sukhorukov, Nail N. Akhmediev, *Australian National Univ., Australia.* We obtain a general N-soliton solution of M coupled NLSE, describing propagation of multisoliton complexes and their collisions. Coherent and incoherent internal interactions are studied. **(p. 79)**

WD9 ■ Two-color multistep cascading and parametric soliton-induced waveguides, Solomon Saltiel, *Univ. Sofia, Bulgaria;* Andrey A. Sukhorukov, Yuri S. Kivshar, *Australian National Univ., Australia.* We introduce the concept of two-color multistep cascading in quadratic optical media. We demonstrate creation of parametric waveguides by spatial solitons and describe their properties. **(p. 82)**

WD10 ■ Solitary waves in quadratically nonlinear media with loss and gain, S. Darmanyan, L. Crasovan, F. Lederer, *Friedrich Schiller Univ. Jena, Germany.* We report the existence of double-hump bright localized waves in nonconservative quadratic media. Numerics reveal a fair robust behavior of these waves. **(p. 85)**

WD11 ■ Dark spatial solitonlike structures induced by low-power upconverted photobleaching of dye-doped polymer film, Aaron Wilkosz, *Nichols Research Corp., USA;* Sergey Sarkisov, *Alabama A&M Univ., USA.* Theoretical and experimental results are reported on the evolution of a Gaussian beam within a waveguide slab into a structure similar to a dark spatial soliton. **(p. 88)**

WD12 ■ Guiding light by incoherent dark solitons, Zhigang Chen, *San Francisco State Univ., USA;* Mordechai Segev, *Technion-Israel Institute of Technology, Israel and Princeton Univ., USA;* Demetrios N. Christodoulides, *Lehigh Univ., USA;* Robert S. Feigelson, *Stanford Univ., USA.* We believe we report the first experimental demonstration of optical guidance of coherent light beams using incoherent light. Such guidance is made possible by generating self-trapped incoherent dark beams—incoherent dark solitons. **(p. 91)**

WD13 ■ Towards soliton emission in GaAs/AlGaAs multiple quantum well asymmetric waveguide structures below half the bandgap, Patrick Dumais, Alain Villeneuve, *COPL, Univ. Laval, Canada;* A. Saher-Helmy, J. Stewart Aitchison, *Univ. Glasgow, UK;* Lars Friedrich, Russell A. Fuerst, George I. Stegeman, *CREOL, Univ. Central Florida, USA.* We have observed an intensity-dependent translation of a beam guided in a strip-loaded AlGaAs multiple quantum well waveguide with an asymmetric nonlinear cladding. **(p. 94)**

WD14 ■ Quadratic soliton interactions in a bulk medium, Anatoly P. Sukhorukov, Dmitry A. Chuprakov, Xin Lu, *Moscow State Univ., Russia.* We believe the relative displacement of FF and SH beams of spiraling and scattering parametric solitons was first discovered. Cascaded soliton spiraling was investigated numerically. **(p. 97)**

WD15 ■ Optical needles: ultranarrow Maxwell's spatial solitons in Kerr media, N.N. Rosanov, V.E. Semenov, N.V. Vyssotina, *Vavilov State Optical Institute, Russia.* Spatial solitons are found in Kerr media as solutions of a full set of Maxwell's equations. Their width is less than wavelength for sufficient beam power. **(p. 100)**

WD16 ■ Formation and interaction of adaptive waveguides using photorefractive screening solitons, Juergen Petter, Carsten Weilnau, Cornelia Denz, *Darmstadt Univ. of Technology, Germany.* Photorefractive solitons provide an attractive possibility for adaptive waveguiding and all-optical beam steering. To realize complex waveguide structures, the time-resolved examination of the development of their interaction is indispensable. **(p. 103)**

WD17 ■ Stimulated Rayleigh wing scattering in soliton propagation, R. Barille, J.P. Bourdin, G. Rivoire, *Univ. Angers, France.* We show that the spectral observations of soliton propagation at the output of a waveguide are due to the stimulated Rayleigh wing scattering mainly produced in cascade process. **(p. 106)**

WD18 ■ Quasi-periodic quadratic solitons in Fibonacci QPM gratings, Yuri Kivshar, *Australian National Univ., Australia;* Ole Bang, Carl Balslev Clausen, Peter L. Christiansen, *Technical Univ. of Denmark, Denmark.* We analyze nonlinear wave propagation and cascaded self-focusing due to second-harmonic generation in Fibonacci optical superlattices and introduce the novel quasiperiodic soliton. **(p. 109)**

WD19 ■ A unified approach to self-trapped partially coherent beams in logarithmically nonlinear media, Wieslaw Królikowski, D. Edmundson, *Australian National Univ., Australia;* Ole Bang, *Technical Univ. of Denmark, Denmark.* We investigate the propagation of a partially coherent beam in a logarithmically nonlinear medium using the evolution equation for the mutual coherence function. Depending on the detuning between the effective diffraction radius and the nonlinearity the beam either oscillates or forms stationary incoherent soliton. **(p. 112)**

WD20 ■ Theoretical demonstration of beam scanning using time-dependent solitary wave interactions in a $Bi_{12}TiO_3$ photorefractive crystal, A.D. Boardman, P. Bontemps, *Univ. Salford, UK.* The operation of a photorefractive scanning device, based on the time-dependent interaction of two (1D+1) solitary beams, is investigated numerically and analytically. **(p. 115)**

WD21 ■ Collapse dynamics of multidimensional coupled waves, Luc Bergé, *Commissariat à l'Energie Atomique, France;* O. Bang, W. Krolikowski, *Australian National Univ., Australia;* J. Juul Rasmussen, *Risø National Laboratory, Denmark.* Different interaction regimes between two coupled waves in focusing Kerr media are identified. Four-wave mixing and walk-off are shown to alter significantly their self-focusing dynamics. **(p. 118)**

WD22 ■ Transverse instability of coupled dark–bright solitons, Z.H. Musslimani, A. Nepomnyashchy, *Technion-Israel Institute of Technology, Israel;* M. Segev, *Princeton Univ., USA;* Y.S. Kivshar, *Australian National Univ., Australia.* We investigate the transverse instability of two-component (1+1)D vector (Manakov-like) solitons in three-dimensional saturable nonlinear media, in relation to recent experiments with incoherently coupled photorefractive soliton pairs. We show that both the nonlinearity saturation and the interaction between the vector constituents can lead to strong suppression of the soliton instability. **(p. 121)**

WD23 ■ Solitary waves formation in liquid crystalline waveguides, Miroslaw A. Karpierz, Waldemar K. Bajdecki, Andrzej W. Domanski, Marek Sierakowski, Tomasz R. Wolinski, *Warsaw Univ. of Technology, Poland.* The stable solitary waves governed by the orientation nonlinearity in nematic liquid crystalline waveguide have been analyzed theoretically and observed experimentally for light power of 30 mW. **(p. 124)**

WD24 ■ Engineered discrete breathers, C. Balslev Clausen, Yu. B. Gaididei, P.L. Christiansen, *Technical Univ. of Denmark, Denmark;* L. Torner, *Univ. Politecnica de Catalunya, Spain.* We show that engineered quasi-phase-matched samples with transverse patterns can generate a latticelike dynamical system, which support stable breathers. **(p. 127)**

WD25 ■ Transition towards dynamical parametric solitary waves, Antonio Picozzi, Marc Haelterman, *Univ. Libre de Bruxelles, Belgium.* We present a novel transition towards a dynamical parametric solitary wave through an original extension of the Kolmogorov–Petrovskii–Piskunov conjecture. **(p. 130)**

WD26 ■ Gateless computing using N–Manakov solitons, Suzanne M. Sears, Ken Steiglitz, Mordechai Segev, Marin Soljacic, *Princeton Univ., USA;* Mariusz Jakubowski, *Microsoft Corp., USA;* Richard Squier, *Georgetown Univ., USA.* We find explicit solutions for two soliton collisions in the N–Manakov system and discuss how such collisions could be used to possibly implement gateless computing. **(p. 133)**

WD27 ■ Multistep cascading spatial solitons, Tristram J. Alexander, Yuri S. Kivshar, *Australian National Univ., Australia;* Solomon Saltiel, *Univ. Sofia, Bulgaria.* We introduce a novel class of parametric spatial optical solitons supported simultaneously by two second-order nonlinear cascading processes, second-harmonic generation, and sum-frequency mixing. **(p. 136)**

WD28 ■ Magneto optical cavity multistability and polarized dissipative solitons: dissitons, N.N. Rosanov, D.V. Liseev, *Vavilov State Optical Institute, Russia;* A.D. Boardman, M. Xie, *Univ. Salford, UK.* A theory of multistability, modulation instability, and polarized dissipative spatial solitons in a wide-aperture driven cavity with planar magneto optical nonlinear waveguide is presented. **(p. 139)**

WD29 ■ Experimental observation of optical patterns in multiple well microcavities, I. Ganne, G. Slekys, I. Sagnes, R. Kuszelewicz, *France Telecom–CNET, France.* Patterns have been observed for the first time to our knowledge in GaAlAs/MQW vertical-cavity microresonators. We show and discuss how cavity resonance fluctuations affect the mechanism of pattern selection. **(p. 142)**

WD30 ■ Emission of coupled vortex beams from nonlinear VCSEL arrays, J. Scheuer, Y. Yadin, Y. Gross, M. Orenstein, *Technion, Israel.* Novel emission of coherently coupled vortex beams from nonlinear vertical-cavity surface-emitting laser (VCSEL) arrays was measured and analyzed. Coupled beams with a variety of vortex and "amplitude" charges were exhibited. **(p. 145)**

WD31 ■ Self-organized light pixels in semiconductor microresonators for optical information processing, M. Brambilla, T. Maggipinto, I. Perrini, *Univ. Politecnico di Bari, Italy;* L.A. Lugiato, L. Spinelli, G. Tissoni, *Univ. Insubria, Italy.* We describe models for semiconductor broadarea microresonators, where self-organized light peaks can be realized and exploited for all-optical signal treatment. We discuss some effects linked to experiments on such devices. **(p. 148)**

WD32 ■ Donutlike patterns in intracavity second harmonic generation, Ruman Iliew, Pey-Schuan Jian, William E. Torruellas, *Washington State Univ., USA;* Falk Lederer, *Friedrich Schiller Univ., Germany.* We demonstrate experimentally the formation of donutlike patterns in intracavity second-harmonic generation with powers in excess of 5 Watts allowing the optical manipulation of mesoscopic particles. **(p. 151)**

WD33 ■ Instability and multistability of cavity solitons in optical parametric oscillators, Dmitry Skryabin, *Strathclyde Univ., UK.* It is demonstrated that Hopf instability of cavity solitons in optical parametric oscillators can be directly linked with internal modes of free propagating quadratic solitons. Results on multistability and complex instability induced spatio-temporal dynamics of the single- and multihump cavity solitons are also presented. **(p. 154)**

WD34 ■ Stability of cavity solitons in parametric downconversion, C. Etrich, D. Michaelis, F. Lederer, *Friedrich Schiller Univ. Jena, Germany.* We identified stable and unstable branches of cavity solitons in the degenerate parametric oscillator. Unstable cavity solitons may decay into oscillating structures. **(p. 157)**

WD35 ■ On existence of gap solitons, E. Alfimov, *Lukin's Institute of Physical Problems, Russia;* V.V. Konotop, *Univ. Madeira, Portugal.* We study the existence of gap solitons as periodic in time and localized in space solutions of the nonlinear wave equation with periodic coefficients. **(p. 160)**

WD36 ■ Evaporative cooling of a soliton gas, Soeren Rutz, Fedor Mitschke, *Univ. Rostock, Germany.* In numerical simulations of a synchronously driven fiber ring resonator, an optical soliton gas is transformed into a soliton crystal by evaporative cooling. **(p. 163)**

WD37 ■ Nonlinear intermode interference in $LiNbO_3$ planar optical waveguides, Yury Larionov, Vladymir Shandarov, Stanislav Shandarov, *State Univ. of Control Systems and Radioelectronics, Russia.* The theoretical and experimental nonlinear interference of collinear guided modes of photorefractive optical waveguide in $LiNbO_3$ in conditions of significant spatial self-action of light beams was made. **(p. 165)**

WD38 ■ Curvature dynamics and fronts in the optical parametric oscillator, J.N. Kutz, *Univ. Washington, USA;* T. Erneux, M. Haelterman, *Free Univ. of Brussels, Belgium;* S. Trillo, *Univ. Ferrara, Italy.* For positive signal detuning, topological solitons of the optical parametric oscillator are shown to be stable with the front curvature governed by the heat equation. **(p. 168)**

WD39 ■ Excitation and interactions of gap quadratic solitons, Sergey V. Polyakov, Anatoly P. Sukhorukov, *CREOL, Univ. Central Florida, USA.* Gap soliton train generation under input cw FF signal in quadratically nonlinear gratings is first numerically investigated. Collisions of slow and immobile solitons are considered. **(p. 171)**

WD40 ■ Optical velocity control of parametric gap solitons, Michele De Sario, Claudio Conti, Gaetano Assanto, *Terza Univ. of Rome and National Institute for the Physics of Matter, Italy.* The velocity of solitons excited by fundamental frequency pulses in Bragg reflectors with quadratic nonlinearity can be controlled by a small coherent second-harmonic seed. **(p. 174)**

WD41 ■ Optical gap solitons in nonresonant quadratic media, Takeshi Iizuka, *Ehime Univ., Japan;* Yuri S. Kivshar, *Australian National Univ., Australia.* We derive a novel physical model for gap solitons in quadratic Bragg grating in which the optical rectification plays an important role. **(p. 177)**

WD42 ■ Formation and switching of multilobed patterns in ring-shaped complex nonlinear media, J. Scheuer, D. Arbel, M. Orenstein, *Technion, Israel.* Formation of spatial patterns with increasing complexity within a complex nonlinear medium was modeled. The predictions were verified experimentally with patterns emitted from ring-shaped VCSELs. **(p. 180)**

WD43 ■ Polarization-locked vector solitons in a fiber laser, J.M. Soto-Crespo, *C.S.I.C., Spain;* N.N. Akhmediev, *Australian National Univ., Australia;* B.C. Collings, W.H. Knox, *Bell Laboratories, Lucent Technologies and Princeton Univ., USA;* S.T. Cundiff, *Univ. Colorado and NIST–Boulder, USA;* K. Bergman, *Princeton Univ., USA.* Stable polarization-locked temporal vector solitons are found in a saturable absorber mode-locked fiber laser with weak cavity birefringence. **(p. 183)**

WD44 ■ Multiple-soliton states in a passively mode-locked Ti:sapphire laser, M.J. Lederer, B. Luther-Davies, H.H. Tan, C. Jagadish, N.N. Akhmediev, *Australian National Univ., Australia;* J.M. Soto-Crespo, *C.S.I.C., Spain.* Multiple-pulse operation of a passively mode-locked Ti:sapphire soliton laser is considered. The mechanisms involved in the transition between and formation of multiple soliton states are analyzed. **(p. 186)**

WD45 ■ Cavity-less oscillator through second-harmonic generation in backward quasi-phase-matching, Claudio Conti, Gaetano Assanto, *Terza Univ. Rome and National Institute for the Physics of Matter, Italy;* Stefano Trillo, *Univ. Ferrara, Italy.* Nonlinear feedback via second-harmonic generation can enhance the gain of an optical amplifier, up to oscillation. **(p. 189)**

Salle Morey–St-Denis

16.30–18.45

WE ■ Quadratic and Discrete Solitons

Falk Lederer, *University of Jena, Germany, Presider*

16.30 (Invited)

WE1 ■ Vortex dynamics in quadratic nonlinear media, Lluís Torner, D.V. Petrov, J.P. Torres, G. Molina, J. Martorell, R. Vilaseca, *Univ. Politecnica de Catalunya, Spain;* J.M. Soto-Crespo, *C.S.I.C, Spain.* A review of the recent progress in the dynamics of optical vortices in quadratic nonlinear media, including their impact to spatial soliton systems, is presented. **(p. 194)**

17.00

WE2 ■ Observation of quadratic spatial solitons in PPLN, B. Bourliaguet, V. Couderc, A. Barthélémy, *Univ. Limoges CNRS, France;* G.W. Ross, P.G.R. Smith, D.C. Hanna, *Univ. Southampton, UK;* C. De Angelis, *Univ. Brescia, Italy.* We believe we report the first observation of quadratic-spatial-solitons in periodically poled lithium niobate, designed for second-harmonic generation. Solitary wave propagation was observed over more than six diffraction lengths. **(p. 197)**

17.15 (Invited)

WE3 ■ Second-harmonic generation in waveguides induced by photorefractive spatial solitons, Song Lan, Charalambos Anastassiou, *Princeton Univ., USA;* Ming-feng Shih, *National Taiwan Univ., Taiwan;* Greg Mizell, *VLOC, II-VI Inc., USA;* J.A. Giordmaine, *Princeton Univ. and NEC Research Institute, USA;* Zhigang Chen, *San Francisco State Univ., USA;* John Martin, *Deltronic Crystal Industries, USA;* Mordechai Segev, *Princeton Univ., USA and Technion, Israel.* We propose and demonstrate experimentally second-harmonic generation in waveguides induced by photorefractive solitons, and show that the conversion efficiency is improved considerably. **(p. 200)**

17.45

WE4 ■ Cantor set fractals from solitons, Marin Soljacic, Suzanne Sears, Mordechai Segev, Dmitriy Krylov, Keren Bergman, *Princeton Univ., USA.* We describe a general principle for generating fractals in physical systems that can support solitons. We illustrate this by numerically constructing Cantor set fractals in (1+1)D cubic self-focusing NLSE. To our knowledge, these are the first fractals proposed in optics. **(p. 203)**

18.00 (Invited)
WE5 ■ First experimental observation of optical Bloch-oscillations, U. Peschel, R. Morandotti, J.S. Aitchison, *Univ. Glasgow, UK;* H. Eisenberg, Y. Silberberg, *Weizman Institute of Science, Israel.* We believe we report the first experimental observation of Bloch-oscillations in waveguide arrays. The action of the focusing nonlinearity leads to symmetry breaking and power-induced beam spreading. **(p. 206)**

18.30
WE6 ■ New families of discrete solitons in quadratic waveguide arrays, A. Kobyakov, S. Darmanyan, T. Pertsch, F. Lederer, *Friedrich Schiller Univ. Jena, Germany.* We discover novel types of localized modes in quadratically nonlinear discrete systems, derive stability criteria, and estimate required powers in a lithium niobate waveguide array. **(p. 209)**

■ Thursday
■ 2 September 1999

Foyer-Bar

07.30–17.00
Registration Open

Salle Morey–St-Denis

08.00–10.00
ThA ■ Dispersion Management 1
Stefan Wabnitz, *Université de la Bourgogne, Dijon, France, Presider*

08.00 (Invited)
ThA1 ■ Pulse-overlapped dispersion-managed data transmission and intrachannel four-wave mixing, P.V. Mamyshev, N.A. Mamysheva, *Bell Laboratories–Lucent Technologies, USA.* We show that strong overlap of adjacent pulses in dispersion-managed RZ transmission reduces pulse-to-pulse interaction and the timing jitter. The limiting factor for this 'pulse-overlapped' transmission is the amplitude fluctuations induced by four-wave mixing between spectral components within a single channel. **(p. 214)**

08.30
ThA2 ■ 160-Gbit/s soliton transmission in a densely-dispersion-managed fiber in the presence of variable dispersion and polarization-mode dispersion, T. Hirooka, T. Nakada, A. Liang, *Osaka Univ., Japan;* A. Hasegawa, *Kochi Univ. of Technology and NTT Science and Core Technology Laboratory Group, Japan.* Soliton transmission at 160 Gbit/s over 2,500 km is numerically demonstrated using a dispersion flattened densely-dispersion-managed fiber with variable dispersion. **(p. 217)**

08.45
ThA3 ■ Dispersion maps with optimized amplifier placement for wavelength-division multiplexing, Brian S. Marks, William L. Kath, *Northwestern Univ., USA;* Tian-Shiang Yang, *National Cheng Kung Univ., Taiwan;* Sergei K. Turitsyn, *Aston Univ., UK.* We obtain amplifier placements in two-step dispersion maps that minimize dispersive radiation in different wavelength channels. Configurations appropriate for Bragg grating dispersion compensators are described. **(p. 220)**

09.00
ThA4 ■ Timing jitter of a strongly-dispersion-managed soliton in a WDM system, Hiroto Sugahara, Akihiro Maruta, *Osaka Univ., Japan.* Collision-induced timing jitter in a wavelength-division multiplexed (WDM) system is theoretically studied for a strongly-dispersion-managed line. We also propose an optimal path averaged dispersion by means of minimizing the timing jitter induced both by collision in WDM and amplifier noise. **(p. 223)**

09.15
ThA5 ■ Efficient reduction of interactions in dispersion-managed links through in-line filtering and synchronous intensity modulation, Erwan Pincemin, Frederic Neddam, Oliver Leclerc, *Alcatel Corporate Research Center, France.* The impact of combined use of in-line filtering and synchronous intensity modulation on interactions is investigated in a 40-Gbit/s dispersion-managed link. Numerical results confirm analytical predictions and show that interactions are efficiently suppressed. **(p. 226)**

09.30 (Invited)
ThA6 ■ Towards N x 40 Gbit/s transoceanic regenerated systems, O. Leclerc, P. Brindel, D. Rouvillain, E. Princemin, B. Dany, E. Desurvire, *Alcatel Corporate Research Center, France;* C. Duchet, E. Boucherez, S. Bouchoule, *Opto+, France.* Error-free 40-Gbit/s regenerated transmission over more than 20,000 km is demonstrated using new InP Mach–Zehnder modulator with wavelength-division compatibility, in good agreement with numerical simulations. This is a first step towards N x 40-Gbit/s transoceanic system demonstration. **(p. 229)**

Foyer-Bar
10.00–10.30
Coffee Break

Salle Morey–St-Denis

10.30–12.00
ThB ■ Nonlinear Periodic Media
Neil G. Broderick, *University of Southampton, UK, Presider*

10.30 (Invited)
ThB1 ■ Quantum and nonlinear optics in a photonic bandgap, Sajeev John, *Univ. Toronto, Canada.* Photonic bandgap (PBG) materials are a new class of dielectric materials, which exhibit a complete three-dimensional gap to electromagnetic wave propagation. The new effects such as light localization, inhibited spontaneous emission, and nonlinear wave propagation predicted to occur in these materials, as well as their consequences, are described. **(p. 234)**

11.00
ThB2 ■ Laue soliton in photonic crystal, B.I. Mantsyzov, *Moscow State Univ., Russia.* The theory of nonlinear dynamic two-wave Bragg diffraction of coherent short pulse in resonantly absorbing multidimensional photonic crystal is developed. A novel type of soliton has been found in the case of Laue geometry of diffraction. **(p. 235)**

11.15
ThB3 ■ The spectral characteristics of nonlinear pulse compression in an integrated Bragg waveguide filter, P. Millar, N.G.R. Broderick, D.J. Richardson, J.S. Aitchison, R. De la Rue, T. Krauss, *Univ. Glasgow, UK.* We present measurements of nonlinear pulse compression from 400 ps to 80 ps and the spectral broadening associated with soliton formation inside an integrated Bragg filter. **(p. 238)**

11.30
ThB4 ■ Soliton pulse compression in chalcogenide fiber Bragg gratings, G. Lenz, B.J. Eggleton, M.E. Lines, R.E. Slusher, *Lucent Technologies, Bell Labs, USA;* N.M. Litchinitser, *Univ. Rochester, USA;* J.S. Sanghera, I.D. Aggarwal, *Naval Research Laboratory, USA.* We propose chalcogenide fiber Bragg gratings for picosecond pulse compression as well as pulse train generation. The large nonlinearity and dispersion allow a small versatile device. **(p. 241)**

11.45
ThB5 ■ Femtosecond second-harmonic and sum-frequency generation near the photonic band edge in one-dimension periodic media, A.V. Balakin, V.A. Bushuev, N.I. Koroteev, B.I. Mantsyzov, I.A. Ozheredov, A.P. Shkurinov, *Moscow State Univ., Russia;* D. Boucher, P. Masselin, *Univ. Littoral, France.* Results of femtosecond second-harmonic and sum-frequency generation in multilayer structure for different GVD parameters and various states of polarization of incoming beam are discussed. **(p. 244)**

12.00–13.30
Lunch

Salle Morey–St-Denis

13.30–15.00
ThC ■ Frequency Conversion and Cascaded Nonlinearity
Alain Villeneuve, *University of Laval, Canada, Presider*

13.30 (Invited)
ThC1 ■ Frequency conversion and switching in birefringent fibers, G. Millot, E. Seve, S. Wabnitz, *Univ. Bourgogne, France;* S. Trillo, *Fondazione Ugo Bordoni and Univ. Ferrara, Italy.* Experiments show that cross-phase-modulation instability induced by a small signal wave leads to strong frequency conversion and switching in a normally dispersive high-birefringence optical fiber. **(p. 248)**

14.00 (Invited)
ThC2 ■ Nondegenerate four-wave mixing in DFB lasers and its applications, H. Kuwatsuka, *Fujitsu Laboratories Ltd., Japan.* The wavelength conversion and the phase-conjugate wave generation have been realized by nondegenerate four-wave mixing in distributed feedback (DFB) lasers. **(p. 251)**

14.30
ThC3 ■ Wavelength shifting through cascaded second-order processes in a lithium-niobate channel waveguide, I. Cristiani, L. Tartara, M. Rini, G.P. Banfi, V. Degiorgio, *Univ. Pavia, Italy.* We have performed a wavelength-shifting experiment by using a cascaded second-order process in a 58-mm-long Ti-diffused lithium-niobate channel waveguide. Efficient wavelength conversion is obtained in the 1100-nm spectral range. **(p. 254)**

14.45
ThC4 ■ High-energy femtosecond pulse compression using the cascade nonlinearity, X. Liu, L.J. Qian, F.W. Wise, *Cornell Univ., USA.* 100-microjoule pulses are efficiently compressed from 120 fs to 45 fs using cascade nonlinearities. Scaling to higher energies and compression ratios will be possible. **(p. 257)**

Foyer-Bar

15.00–16.30
ThD ■ Poster Session 2/ Refreshment Break

ThD1 ■ Upper limit of power for stationary pulse train generation in modulational-instability fiber laser with intracavity Fabry–Perot filter, E.V. Vanin, *Ericsson Telecom AB, Sweden;* S.Helmfrid, *Industrial Microelectronics Center, Sweden.* We theoretically investigated the dynamics of modulational-instability fiber lasers with intracavity Fabry–Perot filter and found an upper power limit for stationary pulse train generation. **(p. 262)**

ThD2 ■ Demonstration of new optical regeneration scheme for dispersion-managed solitons in dense WDM systems, Bruno Dany, Patrick Brindel, Olivier Leclerc, Emmanuel Desurvire, *Alcatel Corporate Research Centre, France.* We demonstrate compatibility between new black box optical regenerator and soliton dispersion management for dense-wavelength-division multiplexed (WDM) systems with 16 x 40 Gbit/s transoceanic application. **(p. 265)**

ThD3 ■ Variational analysis of non-return-to-zero pulse propagation in optical transmission line, Akihiro Maruta, *Osaka Univ., Japan.* We give an analysis of non-return-to-zero pulse propagation in an optical transmission line by means of the variational method with a properly chosen ansatz for the pulse. It can describe pulse propagation in a dispersion-managed transmission line. **(p. 268)**

ThD4 ■ Soliton interactions in moderate-strength dispersion-managed systems, A.M. Niculae, W. Forysiak, N.J. Doran, *Aston Univ., UK.* Soliton interaction in moderate-strength dispersion-managed systems is studied. The collapse distance is maximized by symmetrizing the pulse dynamics via optimum positioning of the amplifier. **(p. 271)**

ThD5 ■ Noise suppression in SOA transmission lines, Christian Knöll, Michael Gölles, Falk Lederer, *Friedrich Schiller Univ. Jena, Germany.* Stable propagation of high-bit-rate RZ signals can be achieved by properly combining a semiconductor optical amplifier (SOA) with a saturable absorber. Experiments have confirmed the predictions. **(p. 274)**

ThD6 ■ Experimental observation of a new chirped continuous pulse-train soliton solution to the Maxwell–Bloch equations, Shihadeh Saadeh, Gregory J. Salamo, *Univ. of Arkansas, USA.* Chirped continuous pulse-train solutions to the Maxwell–Bloch equations have been observed, experimentally, numerically, and analytically. **(p. 277)**

ThD7 ■ Cross-polarization mixing of a laser beam and a spectrum of light in a single-mode optical fiber, K.S. Chiang, K.P. Lor, *City Univ. of Hong Kong, Hong Kong.* We demonstrate a new cross-polarization four-wave mixing process in a single-mode optical fiber with a pulsed dye laser as the pump source. **(p. 280)**

ThD8 ■ Standard perturbative analysis of zero-average dispersion management, C. Paré, V. Roy, F. Lesage, P. Mathieu, P.-A. Bélanger, *Univ. Laval, Canada.* A coupled-field description is used for the analysis of zero-average dispersion management. A straightforward perturbative treatment is shown to lead to a nonlinear integral equation for the spectral distribution of the pulse. This extends previous work and allows an accurate determination of the critical map strength parameter. **(p. 283)**

ThD9 ■ Slow dynamics of dispersion-managed solitons, Anders Berntson, *Ericsson Telecom AB, Sweden;* Dan Anderson, Mietek Lisak, *Chalmers Univ. of Technology, Sweden;* Boris Malomed, *Tel Aviv Univ., Israel.* We show that strong dispersion management prevents optical pulses, deviating from the soliton shape, from shedding dispersive waves. **(p. 286)**

ThD10 ■ Propagation of an optical pulse in a fiber link with random dispersion management, Boris Malomed, *Tel Aviv Univ., Israel;* Anders Berntson, *Ericsson Telecom AB, Sweden.* Real-world communication networks consist of fibers with randomly varying lengths. Soliton propagation in two models of a dispersion-managed communication line with randomly varying lengths of the fiber segments is studied in this work analytically and numerically. **(p. 289)**

ThD11 ■ Criterion for an oscillatory instability of multiparameter solitons, Dmitry Skryabin, *Strathclyde Univ., UK.* Criteria for the oscillatory and novel stationary instabilities of multiparameter solitons are obtained using a general form of the asymptotic approach to the stability problem. **(p. 292)**

ThD12 ■ 40-Gbit/s standard fiber transmission for a range of input pulse widths, D.S. Govan, P. Harper, S.B. Alleston, N.J. Doran, *Aston Univ., UK.* The effect of varying the pulse width in a 40-Gibt/s dispersion-managed transmission line is investigated numerically. **(p. 295)**

ThD13 ■ Complete characterization of THz periodic pulse trains generated from nonlinear processes in optical fibers, J.M. Dudley, *Univ. Auckland, New Zealand;* M.D. Thomson, *Johann Wolfgang Goethe Univ., Germany;* F. Gutty, S. Pitois, P. Grelu, G. Millot, *CNRS, France.* We show how an adapted frequency-resolved optical gating measurement technique allows complete intensity and phase characterization of THz pulse trains generated in optical fibers. **(p. 298)**

ThD14 ■ Symmetries, chirp-free points and bistability in dispersion-managed fiber lines, S.K. Turitsyn, J.H.B. Nijhof, V.K. Mezentsev, N.J. Doran, *Aston Univ., UK.* Using an elementary symmetry analysis we show that in dispersion-compensated systems where a "lossless" model is valid, a chirp-free point is at the center of map symmetry, if the periodic solution is unique. We also present an example when effect of bistability occurs. **(p. 301)**

ThD15 ■ Cross-phase-induced pulse splitting—the optical axe, Lukas Helczynski, Bjorn Hall, Dan Anderson, Mietek Lisak, *Chalmers Univ. of Technology, Sweden;* Anders Bernstson, *Ericsson Telecom AB, Sweden;* Mats Desaix, *Univ. Boras, Sweden.* A new phenomenon—pulse splitting by induced cross phase modulation in a pump-probe configuration in a defocusing Kerr medium is analyzed analytically and numerically. **(p. 304)**

ThD16 ■ Modulation instability in long amplified links with dispersion compensation, E. Ciaramella, M. Tamburrini, *Fondazione Ugo Bordoni, Italy.* In typical conventional fiber links with dispersion compensation, modulation instability features are far different than in uniform links, and can give much lower system impairments. **(p. 307)**

ThD17 ■ Dynamics of dispersion-managed solitons in optical communication lines with random parameters, F.Kh. Abdullaev, B.B. Baizakov, *Uzbek Academy of Sciences, Uzbekistan.* Disintegration of a soliton propagating in dispersion-managed optical communication line with randomly varying dispersion magnitudes of spans and span lengths is shown to occur. Soliton decay length is calculated for both types of modulation. **(p. 310)**

ThD18 ■ Dispersion-managed solitons and the inverse scattering transform, J.H.B. Nijohf, S.K. Turitsyn, N.J. Doran, *Aston Univ., UK.* We apply the inverse scattering transform method to dispersion-managed (DM) solitons, and find how symmetries of the DM soliton imply symmetries of the scattering data. **(p. 313)**

ThD19 ■ Transmission characteristics of optical fiber solitons in a dispersion-slope compensated system, Joji Maeda, Hiromitsu Ogawa, Nobumitsu Umezawa, *Science Univ. of Tokyo, Japan.* We numerically study transmission characteristics of a 50-Gbit/s soliton transmission system using dispersion-slope compensation. It is predicted that the compensation within 0.4 times third-order dispersion length would greatly improve the transmission performance. **(p. 316)**

ThD20 ■ Theoretical and numerical methods for dispersion-managed solitons, Vincent Cautaerts, Akihiro Maruta, Yuji Kodama, *Osaka Univ., Japan.* We present comparative results of different methods for calculating the pulse shape, width, and energy of dispersion-managed solitons. The applicability of those methods, depending on the dispersion map parameters, will be exposed. **(p. 319)**

ThD21 ■ Modulational instability in fiber transmission lines, M. Gölles, S. Darmanyan, G. Onishchukov, A. Shipulin, V. Lokhnygin, F. Lederer, *Friedrich Schiller Univ. Jena, Germany.* Modulational instability of cw solutions in fiber systems with cascaded semiconductor optical amplifiers is studied. SOA and filter characteristics appreciably affect the instability behavior. **(p. 322)**

ThD22 ■ Propagation and breakup of prechirped N-soliton pulses in anomalous optical fibers, D. Krylov, L. Leng, K. Bergman, *Princeton Univ., USA;* J.C. Bronski, *Univ. Illinois–Urbana, USA;* J.N. Kutz, *Univ. Washington, USA.* Strongly prechirped N-soliton pulses are shown numerically and experimentally to break up into an ordered train of fundamental solitons, imposing limits on chirped pulse propagation. **(p. 325)**

ThD23 ■ 10-Gbit/s OTDM to 4 x 2.5 Gbit/s WDM conversion using an SOA-NOLM, Bragg gratings, and a supercontinuum pulse source, D.M. Ryan, N.J. Doran, *Aston Univ., UK.* A 10-Gbit/s time-division multiplexed datastream is converted to four separate wavelength 2.5-Gbit/s channels using an SOA-NOLM. The clock pulses are obtained using serial Bragg gratings and a supercontinuum source. **(p. 328)**

ThD24 ■ Photorefractive grating assisted directional coupler, Ewa Weinert-Raczka, Robert Iwanow, *Technical Univ. of Szczecin, Poland.* Asymmetric directional coupler controlled by thin photorefractive grating based on Franz–Keldysh effect in AlGaAs/GaAs quantum wells as switching and demultiplexing element with memory is analyzed. **(p. 331)**

ThD25 ■ Engineering competing quadratic and qubic nonlinearities, Ole Bang, Carl Balslev Clausen, Peter L. Christiansen, *Technical Univ. of Denmark, Denmark;* Lluis Torner, *Univ. Politecnica de Catalunya, Spain.* Weak modulation of a quasi-phase-matching (QPM) grating opens possibilities for engineering both the quadratic nonlinearity and the Kerr nonlinearity induced by QPM. **(p. 334)**

ThD26 ■ Derivative quadratic nonlinearity and cascaded solitons in quasi-phase-matched waveguide systems, A.M. Kamchatnov, V.M. Agranovitch, *Russian Academy of Sciences, Russia;* M. Neviére, *Laboratorie d'Optique electromagnetique, France;* A.D. Boardman, *Univ. Salford, UK.* The quasi-phase-matching technique implementation in the waveguide geometry with a thin periodically modulated quadratically nonlinear layer placed on the surface of the waveguide is considered theoretically. **(p. 337)**

ThD27 ■ KDV solitons on GaAs transmission lines due to the intrinsic second-order nonlinearity, K. Bubke, U. Peschel, D.C. Hutchings, *Univ. Glasgow, UK.* Soliton development in GaAs electrical transmission lines due to second-order nonlinearities is investigated. The theoretical analysis leads to a Korteweg-de Vries equation. **(p. 339)**

ThD28 ■ Spontaneous formation of symbiotic solitary wave attractors in backward quadratic interaction and parametric oscillators, A. Picozzi, Marc Haelterman, *Univ. Libre de Bruxelles, Belgium;* C. Montes, *CNRS, France.* The amplifier and cavity configurations exhibit the formation of parametric solitary waves. An energy localization phenomenon through a zero-velocity solitary wave is presented. **(p. 342)**

ThD29 ■ All-optical modulation in second-order nonlinear directional couplers by second-harmonic generation, Uwe Hempelmann, *Univ. Paderborn, Germany.* Based on the principle of seeded down-conversion, all-optical modulation by a weak control signal via type I second-harmonic generation in second-order nonlinear directional couplers is demonstrated theoretically. **(p. 345)**

ThD30 ■ Modeling the effects of loss and fabrication error for second-harmonic generation in semiconductor waveguides, F.A. Katsriku, B.M.A. Rahman, K.T.V. Grattan, *City Univ., UK.* An accurate numerical method is presented for modeling of second-harmonic generation in semiconductor waveguides after considering loss and domain fabrication error. **(p. 348)**

ThD31 ■ The study of nonideal implementation and noise effects on quasi-phase-matched parametric interactions in optical waveguides, Ching-Fuh Lin, Hsu-Feng Chou, Yue-Wen Hong, *National Taiwan Univ., Taiwan.* The nonideal implementations of waveguide and noise of the pumping wave are found to have substantial influences on the quasi-phase-matched parametric interactions in optical waveguides. **(p. 351)**

ThD32 ■ Finite-difference beam propagation methods for modeling quasi-phase-matched second-order nonlinear interaction in waveguide, Ching-Fuh Lin, Hsu-Feng Chou, Shing Mou, *National Taiwan Univ., Taiwan.* Two iterative finite-difference beam propagation methods are proposed to model quasi-phase-matched second-order nonlinear interaction in waveguide. Comparisons with already published methods show their superiority. **(p. 354)**

ThD33 ■ Wavelength conversion from 1.3 micrometer to 1.5 micrometer using Raman-assisted three-wave mixing in a single-mode optical fiber, T. Sylvestre, H. Maillotte, E. Lantz, *Univ. Franche-Comte, France;* P. Tchofo Dinda, A.B. Moubissi, *Univ. Bourgogne, France.* We demonstrate wavelength conversion from 1.32 to 1.52 micrometer, by Raman-assisted three-wave mixing of a 1.413-micrometer pump with a 1.32-micrometer signal in an optical fiber. **(p. 357)**

ThD34 ■ Simultaneous second- and third-harmonic generation in layered media and related phenomena, V.V. Konotop, *Univ. Madeira, Portugal;* V. Kuzmiak, *Czech Academy of Sciences, Czech Republic.* Using geometry of layered media, conditions for simultaneous second- and third-harmonic generation can be provided. In particular, fractional frequency conversion in such media is possible. **(p. 360)**

ThD35 ■ A new class of optical solitary waves: embedded solitons, Alan R. Champneys, *Univ. Bristol, UK;* Boris A. Malomed, *Tel Aviv Univ., Israel.* Existence and application of quiescent and moving isolated solitons embedded into the continuous spectrum in fiber and planar second-harmonic-generating waveguides with gratings. **(p. 362)**

ThD36 ■ Phase-matched second-harmonic generation in composite planar waveguide, M. Alshikh Khalil, G. Vitrant, *LEMO-ENSERG, France;* P. Raimond, P.A. Chollet, F. Kajzar, *CEA-(LETI-Technologies Avancées), France.* We report on the fabrication, and characterization, of composite planar waveguide using ion-exchanged glass and nonlinear poled polymer for frequency doubling. Phase-matching is obtained by using modal dispersion between TM_0 fundamental and TM_2 harmonic wavelength. **(p. 365)**

ThD37 ■ Photochromic properties of PMMA-DR1 functionalized polymer films: evidence of reversible trapped molecular states, Guy Vitrant, Amparo Rodriguez, Xavier Grégoire, Nadege Bodin, *LEMO-ENSERG, France;* P.A. Chollet, F. Kajzar, *CEA/LETI, France.* We report on photoinduced refractive index and absorption anisotropies in thin films of PMMA-DR1. We have obtained a photoinduced memory effect and experimental evidence of physical mechanisms of photoisomerization process. **(p. 368)**

ThD38 ■ Chalcogenide glass films for nonlinear optics, S. Spälter, G. Lenz, H.Y. Hwang, J. Zimmermann, S.-W. Cheong, T. Katsufuji, M.E. Lines, R.E. Slusher, *Lucent Technologies, Bell Labs, USA.* We are fabricating highly nonlinear single-mode chalcogenide glass waveguides for nonlinear optics experiments and switching applications at the communication wavelength 1.55 microns. **(p. 371)**

ThD39 ■ Waveguide writing in As_2S_3 glasses by a train of femtosecond laser pulses, T. Cardinal, M. Couzi, J.L. Brunéel, *Univ. Bordeaux I, France;* O.M. Efimov, L.B. Glebov, K.A. Richardson, E. Van Stryland, G.I. Stegeman, *CREOL, Univ. Central Florida, USA;* S.H. Park, *Yonsei Univ., South Korea.* Waveguide writing using femtosecond pulses at 850 nm in As_2S_3 glass is reported. The refractive-index variation and the photodarkening observed in the photoinduced structure were attributed to chemical changes. **(p. 374)**

ThD40 ■ Evidence of structural orientations in poled niobium borophosphate bulk glass, V. Nazabal, E. Fargin, G. Le Flem, *ICMCB CNRS, France;* T. Buffeteau, B. Desbat, *ICMCB, Univ. Bordeaux, France.* The second-harmonic generation efficiency of a niobium borophosphate poled glass is measured. Infrared structural characterizations of the poled glass evidenced the breakdown of isotropy. **(p. 377)**

ThD41 ■ Optimizing the conversion efficiency for the Cerenkov second-harmonic generation in planar optical waveguides, Libor Kotacka, Hugo J.W.M. Hoekstra, *LDG Univ. Twente, The Netherlands;* Jiri Ctyroky, *IREE, The Netherlands.* The position of the maximum of the conversion efficiency and its continuous tuning to a desired wavelength for three and four layered waveguides has been investigated. **(p. 380)**

ThD42 ■ Asynchronous optical logic, K.J. Blow, *Aston Univ., UK;* A.J. Poustie, R.J. Manning, *BT Labs, UK.* We discuss optical logic when the data stream is not synchronized to a local clock. We show how to generate a packet synchronization pulse. **(p. 383)**

ThD43 ■ An easy approach for estimating absorption loss in organic thin sold films, Yu Shen, Shen Yuquan, Chen Yingli, Cao Zhuangqi, Edward YB Pun, *Institute of Photographic Chemistry, China.* An UV-VIS-NIR spectroscopic method for determination of optical loss in organic/polymeric films has been suggested. The optical losses of two polyimide polymers with push-pull azobenzene chromophore attached were examined by this method and the data calibrated by convertional optical methods. **(p. 386)**

ThD44 ■ Spinning light bullets in second-harmonic-generating media, Yefim Bakman, Boris Malomed, *Tel Aviv Univ., Israel.* Solutions to a three-dimensional model with the quadratic nonlinearity are found, by means of variational approximation and direct simulations, in the form of fully localized vortex solitons. Consideration of the linearized equations suggests that the solitons are stable. **(p. 389)**

ThD45 ■ Stable solitons in quadratic waveguides with losses and gain, Lucian-Cornel Crasovan, Dumitru Mihalache, Dumitru Mizilu, *National Institute of Physics and Nuclear Engineering, Romania;* Boris Malomed, *Tel Aviv Univ., Israel;* Falk Lederer, *Friedrich-Schiller-Univ., Germany.* A model of a second-harmonic-generating waveguide with linear gain and filtering is proposed, in which fully stable pulses exist, the background instability being suppressed by an extra parallel-coupled lossy core. **(p. 392)**

Salle Morey–St-Denis

16.30–18.45

ThE ■ Vectoral Solitons and Incoherent Solitons

Yuri Kivshar, *Australian National University, Australia, Presider*

16.30 (Invited)

ThE1 ■ New physics and applications of Kerr spatial solitons in AlGaAs waveguides, George I. Stegeman, Lars Friedrich, *CREOL, Univ. Central Florida, USA;* Patsy Millar, J. Stewart Aitchison, *Univ. Glasgow, UK;* Nail N. Akhmediev, *Australian National Univ., Australia.* Experiments in AlGaAs slab waveguides investigating the polarization dynamics of spatial vector solitons and employing spatial solitons as reconfigurable interconnects will be presented. **(p. 396)**

17.00

ThE2 ■ Four-wave mixing of vector solitons, C. Anastassiou, M. Segev, J.A. Giordmaine, S. Lan, K. Steiglitz, *Princeton Univ., USA;* M. Mitchell, *Lucent Technologies, USA;* M.F. Shih, *National Taiwan Univ., Taiwan.* We study theoretically and experimentally collisions between vector (Manakov-like) solitons. We demonstrate energy switching between solitons at large collision angles, for which scalar solitons pass through each other practically unaffected. **(p. 399)**

17.15

ThE3 ■ Applied magneto-optic soliton dynamics based upon TM and TE TM driven system, A.D. Boardman, M. Xie, *Univ. Salford, UK.* Novel effects based upon a magneto-optic influence on spatial solitons are analyzed. The general framework is given and schemes for structure optimization are found. **(p. 402)**

17.30

ThE4 ■ Incoherent solitons—properties and collisions, N. Akhmediev, A. Ankiewicz, A. Snyder, W. Królikowski, G. McCarthy, B. Luther-Davies, *Australian National Univ., Australia.* We study the formation and interaction of partially coherent solitons in slow nonlinear media. Our theoretical predictions are confirmed in experiments with photorefractive screening solitons. **(p. 405)**

17.45

ThE5 ■ "Cooling" of spatially incoherent light beams using interactions with incoherent and coherent solitons, Tamer H. Coskun, Alexandra G. Grandpierre, Demetrios N. Christodoulides, *Lehigh Univ., USA;* Mordechai Segev, *Technion-Israel Institute of Technology, Israel and Princeton Univ., USA.* We show that the spatial coherence of a partially incoherent beam can be greatly enhanced through its interaction with an incoherent or coherent spatial dark soliton. **(p. 408)**

18.00

ThE6 ■ Two-dimensional incoherent light beams in Kerr media, Ole Bang, *Technical Univ. of Denmark, Denmark;* D. Edmundson, Wieslaw Królikowski, *Australian National Univ., Australia.* We show that incoherent beams are unstable and may collapse in bulk Kerr media. The internal dynamics of collapsing and diffracting incoherent beams is illustrated. **(p. 411)**

18.15

ThE7 ■ "Phase memory" effects and incoherent dark Y-soliton splitting, Tamer H. Coskun, Demetrios N. Christodoulides, *Lehigh Univ., USA;* Zhigang Chen, *San Francisco State Univ., USA;* Mordechai Segev, *Technion-Israel Institute of Technology, Israel and Princeton Univ., USA.* The effects of incoherence on the evolution of incoherent dark soliton doublets are investigated both theoretically and experimentally. We show that the dynamics of these incoherent self-trapped entities are associated with strong "phase-memory" effects, which are otherwise absent in the linear regime. **(p. 414)**

18.30

ThE8 ■ Fixing solitonic waveguides in photorefractive strontium barium niobate, Matthew Klotz, Mike Crosser, Gregory J. Salamo, *Univ. Arkansas, USA;* Mordechai Segev, *Princeton Univ., USA.* Two-dimensional solitonic optical waveguides and *y*-junctions have been formed in a strontium barium niobate crystal. The waveguides are 10–20 microns in diameter and propagate unpolarized light with little loss. **(p. 417)**

Chateau de Marsannay

19.30–23.00

Conference Banquet
(separate registration required)

■ Friday
■ 3 September 1999

Foyer-Bar

07.30–17.00
Registration Open

Salle Morey–St-Denis

08.00–10.00
FA ■ Materials and Characterization
J. Stewart Aitchison, *University of Glasgow, UK, Presider*

08.00 (Invited)
FA1 ■ Frequency conversion and parametric processes in form birefringent semiconductor heterostructures, V. Berger, *THOMSON CSF, France;* G. Leo, *Univ. "Roma Tre", Italy.* We discuss the feasibility of a parametric oscillator integrated on a GaAs chip, after reviewing the recent frequency conversion experiments using form birefringence in GaAs/oxidized-AlAs waveguides. **(p. 422)**

08.30
FA2 ■ Determination of nonresonant optical nonlinearities in undisordered and disordered semiconductor superlattices, D.C. Hutchings, *Univ. Glasgow, UK.* A band-structure algorithm is developed for semiconductor superlattices specifically formulated for determining nonlinear optical coefficients including the effects of disordering. The modulation of the second-order optical susceptibility tensor elements are addressed. **(p. 425)**

08.45
FA3 ■ Ultrafast excitonic saturable absorption at 1.55 μm in heavy-ion irradiated quantum well vertical cavity, J. Mangeney, J.L. Oudar, J.C. Harmand, C. Mériadec, G. Patriarche, G. Aubin, *France Telecom, France;* N. Stelmakh, J.M. Lourtioz, *Univ. Paris-Sud, France.* We describe an ultrafast saturable absorber InGaAs/InAlAs multiple quantum well vertical-cavity device operating at 10 GHz, suitable for all-optical regeneration in a wavelength-division multiplexed context. **(p. 428)**

09.00
FA4 ■ Dispersion-scan method for the measurement of nonlinear refraction and absorption of waveguides, E. Lopez-Lago, F. Louradour, A. Barthélémy, *IRCOM, France.* The spectral analysis, after self-phase modulation, of short pulses with variable linear chirp is used for a simple and accurate measurement of Kerr nonlinearity. **(p. 431)**

09.15 (Invited)
FA5 ■ Wide bandwidth 1.5 μm and 1.3 μm wavelength conversion in periodically-poled waveguides, M.-H. Chou, K. Parameswaran, M.M. Fejer, *Stanford Univ., USA;* I. Brener, *Bell Labs, USA.* Near-generate difference frequency mixing in periodically-poled lithium niobate waveguides is demonstrated for signal processing functions such as wavelenth conversion and spectral inversion. Efficient mixing is obtained for simple and for cascaded operation at pump powers in the range of 100 mW. **(p. 434)**

09.45
FA6 ■ Giant two-wave mixing in a photorefractive planar waveguide fabricated with He^+ implanted $BaTiO_3$, Pierre Mathey, Alexandre Dazzi, Pierre Lompré, Pierre Jullien, *Univ. Bourgogne, France;* Paul Moretti, *Univ. Claude Bernard Lyon 1, France;* Daniel Rytz, *Edelsteine/Edelmetalle GmbH, Germany.* The highest known value of gain (58 cm^{-1}) in a photorefractive waveguide is obtained from measurements conducted in function of the grating vector orientation. **(p. 437)**

Foyer-Bar
10.00–10.30
Coffee Break

Salle Morey–St-Denis

10.30–12.00
FB ■ Parametric Effects
L. Lugiato, *University of Milan, Italy, Presider*

10.30
FB1 ■ Competition between convection and chromatic dispersion in an all-fiber synchronously driven bistable ring resonator, Stephane Coen, Philippe Emplit, Marc Haelterman, Mustapha Tlidi, *Univ. Libre de Bruxelles, Belgium.* An analytical and experimental study of a synchronously driven fiber cavity reveals the key role of convection and chromatic dispersion in optical bistability. **(p. 442)**

10.45
FB2 ■ Dynamical quadratic cavity solitons, D. Michaelis, C. Etrich, U. Peschel, F. Lederer, *Friedrich Schiller Univ. Jena, Germany.* Spatial symmetry breaking of a polarization front in vectorial second-harmonic generation leads to the formation of novel kinds of breathing and running cavity solitons. **(p. 445)**

11.00
FB3 ■ Raman-assisted parametric generation of non-phase-matched waves in normally dispersive optical fibers, E. Seve, G. Millot, P. Tchofo-Dinda, *Univ. Bourgogne, France;* T. Sylvestre, H. Maillotte, E. Lantz, *Univ. Franche-Comté, France.* We demonstrate generation of non-phase-matched idler waves by three-wave mixing interaction of a pump with an anti-Stokes signal in normally dispersive fibers. **(p. 448)**

11.15
FB4 ■ Second-harmonic generation and localized modes in multilayered structures, Andrey A. Sukhorukov, Yuri S. Kivshar, *Australian National Univ., Australia;* Ole Bang, *Technical Univ. of Denmark, Denmark.* We study second-harmonic generation at nonlinear interfaces embedded in linear medium. Two-color modes localized at a single interface are found, and profiles of gap solitons in multilayer structures are determined. **(p. 451)**

11.30
FB5 ■ Generation and characterization of 0.6 THz polarization domain wall trains in a spun fiber, F. Gutty, S. Pitois, P. Grelu, G. Millot, *Univ. Bourgogne, France;* M.D. Thomson, *Johann Wolfgang Goethe Univ., Germany;* J.M. Dudley, *Univ. Auckland, New Zealand.* We report the experimental generation and characterization via frequency-resolved optical gating of periodic trains of polarization domain walls in an ultralow birefringence spun fiber. **(p. 454)**

11.45
FB6 ■ Surface-emitting THz difference-frequency generation in GaAs-based waveguides, Yu. H. Avetisyan, *Yerevan State Univ., Armenia.* It was shown that THz difference-frequency generation emitted by the GaAs-based planar waveguide propagates in the normal direction to the surface of the waveguide due to its birefringence. **(p. 457)**

12.00–13.30
Lunch

Salle Morey–St-Denis

13.30–15.00
FC ■ Frequency Conversion in Glasses versus Crystals
P. G. Kazansky, *University of Southampton, UK, Presider*

13.30 (Invited)
FC1 ■ Quasi-phase-matched parametric fluorescence in poled silica fibers, G. Bonfrate, V. Pruneri, P.G. Kazansky, *Southampton Univ., UK;* P.R. Tapster, J.G. Rarity, *DERA Malvern, UK.* We believe we report the first observation of parametric fluorescence from a periodically poled silica fiber. The achieved pair-photon production rate resulted in >100 MHz at 1532 nm for 300 mW of pump power at 766 nm. **(p. 462)**

14.00 (Invited)
FC2 ■ Parametric mid-infrared generation in periodically poled Ti:$LiNbO_3$ waveguides, D. Hofmann, H. Herrmann, G. Schreiber, C. Haase, W. Grundkötter, R. Ricken, W. Sohler, *Univ. Paderborn, Germany.* Difference-frequency generation of highest conversion efficiency (105 %/W), pulsed optical parametric fluorescence and cw optical parametric oscillation of lowest threshold (about 7 mW coupled) are reported. **(p. 465)**

14.30
FC3 ■ Near-infrared cascaded difference-frequency generation in periodically poled Ti:$LiNbO_3$ waveguides, G. Schreiber, D. Hofmann, W. Grundkötter, R. Ricken, W. Sohler, *Univ. Paderborn, Germany.* –14 dB conversion efficiency has been achieved in a difference-frequency generation experiment using two successive second-order processes in an 80-mm-long periodically poled waveguide. **(p. 468)**

14.45
FC4 ■ Blue upconversion in Tm^{3+}-Yb^{3+}-phosphosilicate rib waveguide generated by a cw pump at 980 nm, M.V.D. Vermelho, J.S. Aitchison, *Univ. Glasgow, UK.* Infrared to blue upconversion generation at 476 nm with 25 mW of delivered cw pump power was observed. Optimization of this glass system points towards considerable improvement of the measured conversion efficiency. **(p. 471)**

Foyer-Bar
15.00–15.30
Refreshment Break

Salle Morey–St-Denis

15.30–17.00
FD ■ Dispersion Management 2
Wladek Forysick, *Aston University, UK, Presider*

15.30 (Invited)
FD1 ■ Distributed amplification of optical solitons, G.P. Agrawal, Z.M. Liao, T. Lakoba, *Univ. Rochester, USA.* The issue of lumped versus distributed amplification is revisited. With a proper optimization of dopant density, the use of distributed amplification together with dispersion management can permit large spacing between pumping stations at even relatively high bit rates. **(p. 476)**

16.00
FD2 ■ Experimental investigation of soliton transmission over high-strength dispersion-managed transmission lines, S.B. Alleston, P. Harper, D. Govan, I. Bennion, N.J. Doran, *Aston Univ., UK.* We demonstrate experimentally transmission of data over high-strength dispersion maps using dispersion-managed soliton techniques. We determine the limiting factors, and several interesting features. **(p. 479)**

16.15
FD3 ■ Reduced interaction between π-shifted dispersion-managed solitons, C. Paré, P.-A. Bélanger, S. Larochelle, *Univ. Laval, Canada.* The interaction between two dispersion-managed solitons is known to be independent of their relative phase when the pulses are sufficiently far apart. This work shows that the dynamics of the interacting pulses is different when they are brought close to each other and this is interpreted as being due to the existence of an antisymmetric dispersion-managed soliton. **(p. 482)**

16.30
FD4 ■ Energy, frequency, and time fluctuations reduction of DMS through synchronous amplitude modulation only, Fabien Merlaud, *France Telecom, France;* Thierry Georges, *Algety Telecom, France.* Numerical evidences are given that nontypical propagation regimes of dispersion-managed solitons exist where the use of amplitude modulators only is sufficient to achieve an active control on amplitude, frequency, and time fluctuations. **(p. 485)**

16.45
FD5 ■ Tuning of in-line filter position for dispersion-managed soliton transmission, A. Tonello, A.D. Capobianco, *Univ. Padova, Italy;* S. Wabnitz, *Univ. Bourgogne, France;* S.K. Turitsyn, *Aston Univ., UK.* We optimize the positioning of filters in dispersion-managed transmissions. Stabilization of both soliton energy fluctuations and interactions are achieved with filters at optimal positions. **(p. 488)**

Salle Morey–St-Denis

19.00–20.30
Postdeadline Paper Presentations

Nonlinear Guided Waves and Their Applications

Spatio-Temporal and Transverse Effects

Wednesday, 1 September 1999

Govind Agrawal, University of Rochester, USA
Presider

WA
08.00-10.00
Salle Morey—St-Denis

Generation of Optical Spatiotemporal Solitons

X. Liu, L. J. Qian, and F. W. Wise

Department of Applied Physics
212 Clark Hall
Cornell University
Ithaca, New York 14853
tel: (607) 255-1184
fax: (607) 255-7658

Solitons have been studied in many areas of science over the last two decades. Multi-dimensional solitons include stationary waves that are confined in two transverse spatial dimensions as well as spatio-temporal solitons (STS). STS are theoretically unstable in third-order nonlinear media, but solutions can be stabilized if the nonlinearity is saturable.

Recently, there has been a resurgence of interest in the effective third-order nonlinearity that arises from the cascading of second-order processes. The nonlinearity saturates with increasing intensity, so quadratic media possess the properties required for STS formation. Stationary spatial solitons have been generated in one [1] and two [2] transverse spatial dimensions *via* the cascade nonlinearity, as have temporal solitons [3]. However, STS in either quadratic or cubic nonlinear media have not been reported.

Here we show experimentally that STS can be produced in a quadratic medium. Self-focussing and nonlinear phase shift balance the effects of diffraction and dispersion, respectively, to produce a soliton in one transverse spatial dimension and time.

Experiments were performed with a 1-cm-long $LiIO_3$ crystal cut for type-I phase-matching. Pulses of duration 120 fs and energy up to 1 mJ at a wavelength of 795 nm are produced by a Ti:sapphire regenerative amplifier. The pulses traverse gratings and lenses that create large negative dispersion in one transverse direction (x), while focussing the beam in the other (y). With the crystal oriented to produce a self-focussing nonlinearity, the output pulse duration and beam profile depend strongly on intensity. When the intensity reaches a threshold value, the output pulse begins to narrow temporally and the beam waist simultaneously decreases. Typical intensity autocorrelations and beam profiles are shown in Figure 1 for intensities near and well-above threshold. The corresponding results obtained by numerical solution of the coupled wave equations are also shown, and agree reasonably well with the experiments. The second-harmonic beam-size also decreases dramatically with intensity, which confirms the mutual trapping of the fundamental and harmonic beams.

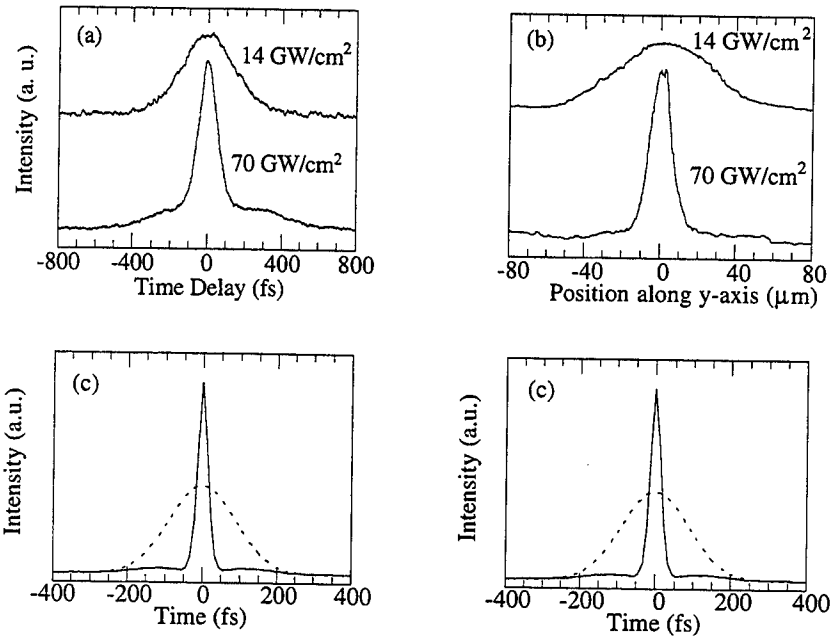


Figure 1. Intensity autocorrelations (a) and beam profiles (b) of output pulses generated with the indicated intensities. Calculations of the corresponding intensities and beam profiles are shown in (c) and (d).

Similar trends are observed over wide ranges of phase-mismatch and intensity. Measurements made with $\Delta kL = -80\pi$ and $\Delta kL = -240\pi$ (Figure 2, next page) exemplify these trends. The pulse duration decreases from ~400 fs to ~80 fs, and the beam waist is reduced by a factor of 12 compared to the ordinary diffracting beam, in good agreement with calculations.

In conclusion, we have generated stable spatiotemporal solitons in a quadratic nonlinear medium. The fundamental and harmonic pulses trap each other spatially and temporally, overcoming the effects of diffraction and group-velocity dispersion. The results presented here open the way to studies of the interactions of spatiotemporal solitons. We expect that spatiotemporal solitons will find numerous applications in science and technology in the future.

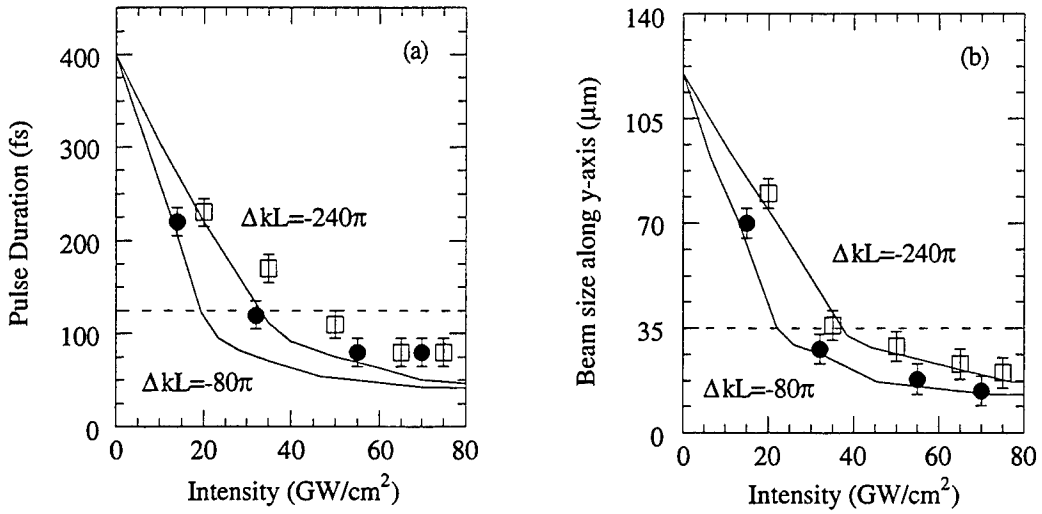


Figure 2. Dependence of output pulse duration (a) and beam size (b) on incident intensity for the indicated values of phase mismatch. Symbols are measured points and solid lines are the results of calculations. The pulse duration and beam size incident on the crystal are indicated by the dashed lines.

References

1. R. Schiek, Y. Baek, and G. I. Stegeman, *Phys. Rev. E* **53**, 1138 (1996).
2. W. E. Torruellas, Z. Wang, D. J. Hagan, E. W. VanStryland, G. Stegeman, L. Torner, and C. R. Menyuk, *Phys. Rev. Lett.* **74**, 5036 (1995).
3. P. Di Trapani, D. Caironi, G. Valiulis, A. Dubietis, R. Danielus, and A. Piskarskas, *Phys. Rev. Lett.* **81**, 570 (1998).

Spatio-temporal solitary waves in a self-defocusing AlGaAs slab waveguide

Nicolas Bélanger, Alain Villeneuve
Centre d'optique photonique et laser, département de physique, pavillon Alexandre-Vachon,
Université Laval,
Cité Universitaire (Qc), G1K 7P4 Canada
nbelange@phy.ulaval.ca, avillene@phy.ulaval.ca

J. Stewart Aitchison
Department of Electronics and Electrical Engineering, University of Glasgow, G12 8QQ UK
jsa@elec.gla.ac.uk

Solitons can be bright or dark [1], temporal or spatial. Until now, several possibilities have been observed (for a review see Ref.2). Bi-dimensional dark[3,4] and bright[5] spatial solitonic waves have also been reported. Here we present the first observation, to our knowledge, of a spatio-temporal soliton-like wave in a Kerr medium.

We used an AlGaAs slab waveguide which guiding layers consists of four 20-nm GaAs quantum wells separated by 200-nm $Al_{0.2}Ga_{0.8}As$ barriers. This guiding layer is bounded by a 4-µm-thick lower layer cladding and a 1.0-µm-thick uplper cladding of $Al_{0.25}Ga_{0.75}As$. At wavelengths (around 820 nm) just below the band gap (750 nm), the nonlinearity of AlGaAs is self-defocusing and the dispersion is normal[2]. The sign product of the dispersion and of the nonlinearity implies a bright pulse in time. However, the diffraction acts in the spatial dimension as an anomalous dispersion leading to a dark spatial soliton.

The propagation of a pulsed beam in this waveguide is describe by a particular case of the bi-dimentional Nonlinear Schrödinger equation that corresponds, if we ignore the losses, to the u-4 equation (also called ϕ-4) which is known to be non-integrable[6]. However, we have already shown by numerical simulations that a solitary wave can propagate in this waveguide over several dispersion and Rayeigh lengths[2]. The linear loss and, particularly, the two-photon absorption are not negligible. Hence, the propagation of the pulse in the slab waveguide is governed by the following differential equation:

$$\frac{\partial V(x,z,t)}{\partial z} = \frac{i}{2\beta_0}\frac{\partial^2 V(x,z,t)}{\partial x^2} - i\frac{\beta_2}{2}\frac{\partial^2 V(x,z,t)}{\partial t^2} + \left(ik_0 n_2 - \frac{\alpha_2}{2}\right)\frac{|V(x,z,t)|^2}{h_{eff}}V(x,z,t) - \frac{\alpha_0}{2}V(x,z,t)$$

The pulse (V) propagates along z, t is the local time of the pulse that moves with it, and x is the unguided transverse dimension. β_0 is the guided wave number ($=n_{eff}k_0$ where n_{eff} is the effective index and $k_0=2\pi/\lambda$), β_2 is the dispersion parameter in s^2/m (positive for normal dispersion), h_{eff} is the effective thickness of the slab, n_2 is the nonlinear Kerr parameter in m^2/W (negative when self-defocusing), α_2 stands for the two-photon absorption, and α_o represents the weak linear loss. Note that in this equation the pulse's envelope (V) is expressed in $\sqrt{W/m}$.

In order to observe temporal soliton-like pulses, 190 fsec (dispersion length[7] = 1.0 mm) pulses from a mode-locked Ti:Sapphire laser (82 MHz) were used. The pulses were hyperbolic secant and were slightly chirped as shown by the time-bandwidth product (TBWP) $\Delta\nu\Delta t=0.38$ corresponding to a RMS TBWP=1.2. To observe the dark spatial soliton the input beam was shaped by a cylindrical telescope and a π phase jump produced by a phase mask placed between the 10X microscope-objective and the input facet of the 2.04 mm long slab waveguide. The Rayleigh length is of the order of 10µm. Therefore, a soliton regime can be self established in both temporal and spatial dimensions.

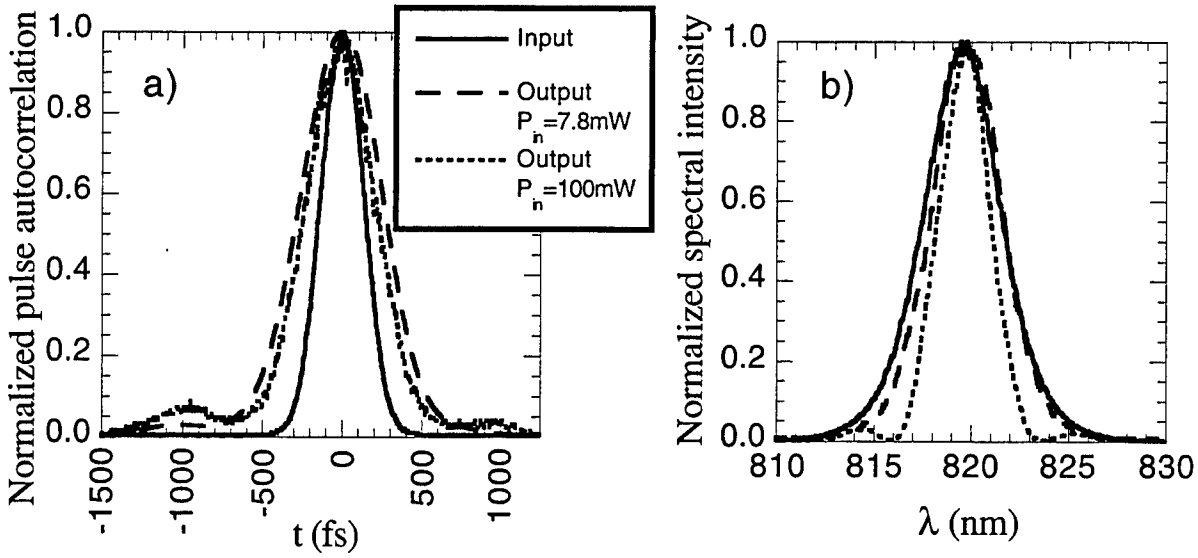


Fig. 1: a) Normalized autocorrelation and b) spectrum of the output pulse at low power (thin dashed line) and at high power (dotted line) compared to the input (full line).

Figure 1 depicts the pulse autocorrelation and the spectrum getting narrower with increasing input power. Notice that the output autocorrelation is always broader than the input contrary to the output spectrum that becomes narrower at high power. This narrowing of the spectrum is due to the soliton effect that shifts the pulse in the soliton family to compensate for the pulse broadening induced by the two-photon absorption[2]. This interplay between the time and the frequency domains makes the RMS TBWP decrease from 2.97 at low intensity to a minimal value of 2.48 at high intensity. The recovery of the TBWP, a signature of a soliton, is more significant for the $\Delta\nu\Delta t$ that diminishes from 0.64 to 0.43. The two-photon absorption and non-solitonic radiations are responsible for the wings on the autocorrelation and on the spectrum that prevent the recovery of the initial RMS TBWP.

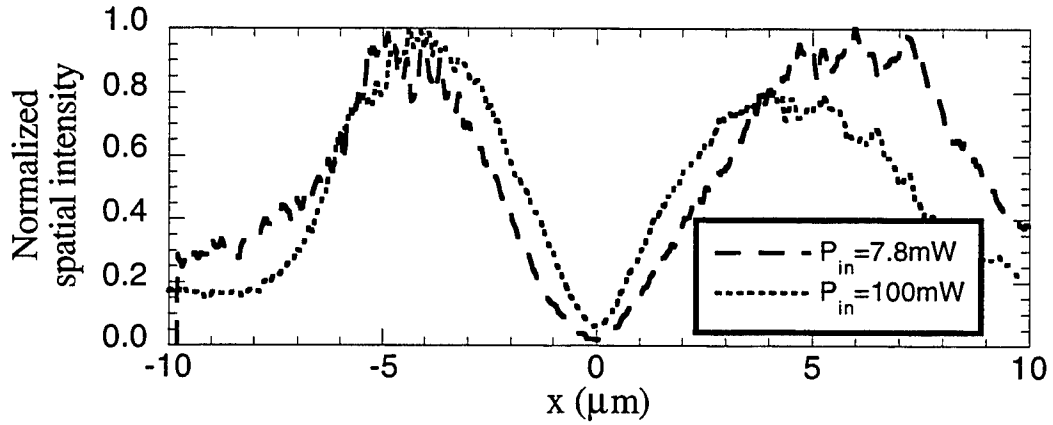


Fig.2: Normalized output spatial profile at low power (thin dashed line) and at the high power (dotted line).

In Fig. 2 we see the output beam profile with a typical dip of a dark soliton. This dip is produced by the diffraction along the waveguide of the input beam that has passes through the phase mask. By increasing the input power this dip becomes narrower, which is an indication that a solitonic effect occurs. The whole beam also gets narrower with increasing power, most probably due to a thermal self-focusing nonlinearity. As we can see on Fig.3 the dip narrows monotonously for increasing power, while the whole beam (finite background) first broadens at low power before getting narrower for higher power. Moreover, the width of the whole beam

always decreases slower than the width of the dip. This implies that at low power the self-defocusing Kerr type nonlinearity is stronger than the self-focusing thermal nonlinearity. At higher power, the thermal nonlinearity slowly dominates the self-defocusing Kerr type nonlinearity and reduces the beam width. The Kerr type nonlinearity is local and is mostly effective at the beginning of the waveguide before the pulse's has been greatly reduce by the tow-photon absorption. Indeed at the highest power levels used the transmission is reduced to 12% of the low power value. The heat produced at the beginning of the waveguide spreads further in the waveguide and enhances the thermal nonlinearity. This may explains why the whole beam narrows at high power, but still requires a solitonic effect to explain the dynamic of the dip. The high repetition rate of our laser, which causes the thermal effect, simply creates a potential well, as does the finite width of the background, where evolves the dark solitary wave.

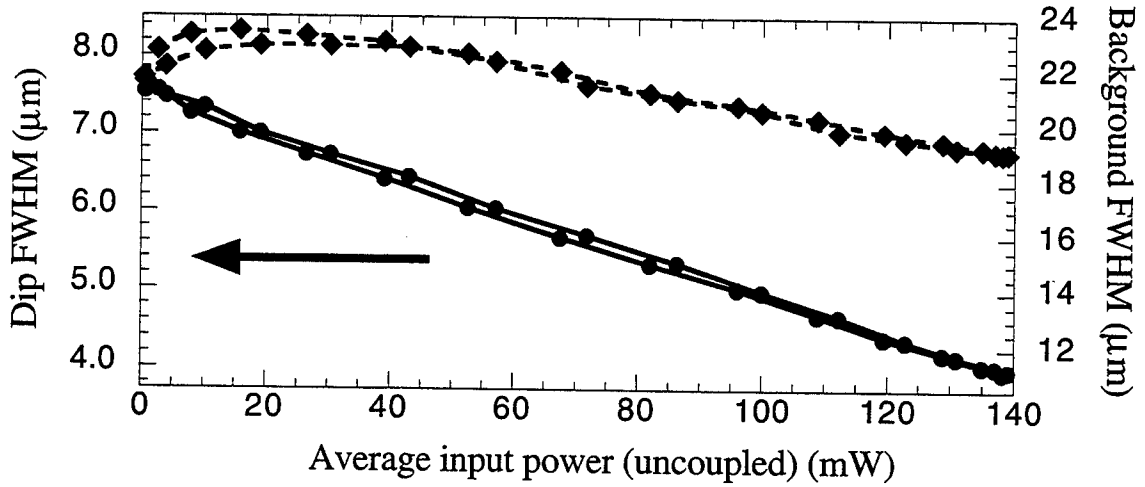


Fig.3: Output Full Width Half Maximum (FWHM) of the dip (full line with circles) compare to the FWHM of its finite background (dashed line with diamonds). The two vertical axes are proportional to each other.

In conclusion, we have observed a compensation of the dispersion and of the diffraction by a self-defocusing nonlinearity at high power even in the presence of two-photon absorption. This is the first experimental observation of a spatio-temporal soliton-like wave in a Kerr type medium. Also, the output spatial profile is narrower at high power than forseen due to another nonlinear effect that is self-focusing (probably a thermal nonlinearity).

REFERENCES

[1] for example, see G. P. Agrawal, Nonlinear Fiber Optics (Academic, New York, 1989).
[2] N. Bélanger, A. Villeneuve, J. S. Aitchison, J. Opt. Soc. Am B **14**, 3003 (1997).
[3] G. R. Allan, S. R. Skinner, D. R. Andersen, and A. L. Smirl, Opt. Lett. **16**, 156 (1991).
[4] G. A. Swartzlander, Jr., D. R. Andersen, J. J. Regan, H. Yin, and A. E. Kaplan, Phys. Rev. Lett. **66**, 1583 (1991).
[5] for example, see V. Tikhonenko, J. Christou, and B. Luther-Daves, J. Opt. Soc. Am. B **12**, 2046 (1995).
[6] W.-H. Steeb, N. Euler, Nonlinear evolution equations and PainLevé test (Wold Scientific, New Jersey, 1988).
[7] We use the definition of the dispersion length that corresponds to a broadening of the RMS temporal width by a factor equals to the square root of 2, as it is the case for a gaussian pulse.

Competing neck and snake instabilities of vector Kerr and type-I quadratic solitons.

Dmitry V. Skryabin and William J. Firth
Department of Physics and Applied Physics, John Anderson Building,
University of Strathclyde, 107 Rottenrow, Glasgow, G4 0NG, UK
fax: 44 141 5522891 phone: 44 141 5523354 dmitry@phys.strath.ac.uk

Introduction. Solitary waves may exhibit MI (modulational instability) if they are localized in some dimensions but extended in one or more others [1]. From a formal point of view the problem of the solitary wave MI can be considered as a continuation of the soliton spectrum at zero modulational frequency Ω into the region $\Omega \neq 0$ [1].

In the our recent work [3] we considered GVD (group velocity dispersion) induced MI of spatial solitons supported by the nondegenerate three-wave mixing in a $\chi^{(2)}$ medium (type-II geometry). It was shown that presence of an additional symmetry in the differential phase leads to the appearance of the novel neutral soliton modes at $\Omega = 0$, which give a new branch of the neck MI in media with normal GVD. It was found that the novel instability strongly dominates the usual snake MI throughout the region of soliton existence. Because of this dominance, physical mechanisms responsible for the relative strength of the neck and snake instabilities are hidden in the type-II geometry. The internal modes of the quadratic solitons also produce MI branches, but in the type-II geometry they have been found suppressed by the MI linked with the differential phase [3].

Here we study MI of the incoherently coupled vector-Kerr and type-I quadratic solitons. The former problem has two phase symmetries. In spite of the fact that the symmetries are the same as in type-II model, the MI induced dynamics of solitons in the Kerr medium is more rich. In particular we show that the relative strength of the nonlinear cross-coupling governs the competition between neck and snake MIs in such a way that either of them can be dominating.

The studies of MI of type-I quadratic solitons have been recently reported by several group of authors [2,4–7]. However the role of the internal modes, which $\chi^{(2)}$ solitons are known to have [8], has not been examined. As it will be demonstrated below these modes are responsible for an appearence of the novel branch of the neck MI, which competes and dominates over the standard snake MI over the region of negnetive wavevector mismatches.

Vector Kerr solitons. The evolution of two suitably scaled slowly varying incoherently coupled wave envelopes E_1 and E_2 in a weakly nonlinear, dispersive and diffractive medium is governed by the following equations

$$i\partial_z E_1 + \alpha_1 \vec{\nabla}_\perp^2 E_1 + \gamma_1 \partial_t^2 E_1 + (|E_1|^2 + \beta |E_2|^2) E_1 = 0, \quad (1)$$
$$i\partial_z E_2 + \alpha_2 \vec{\nabla}_\perp^2 E_2 + \gamma_2 \partial_t^2 E_2 + (|E_2|^2 + \beta |E_1|^2) E_2 = 0,$$

where $\vec{\nabla}_\perp = \vec{i}\partial_x + \vec{j}\partial_y$. (z) and (x, y) are, respectively, scaled longitudinal and transverse coordinates and t is the scaled retarded time. Diffraction parameters $\alpha_{1,2}$ are positive while GVD parameters $\gamma_{1,2}$ can have either sign. Rescaling x, y, t once more one can always choose α_1/α_2 and $|\gamma_1|/|\gamma_2|$ to be any convenient constants. The parameter β measures the relative strength of cross-phase modulation compare to self-phase modulation. The nonlinearity was chosen to be self-focusing because below we are interested in the dynamics of bright solitary waves.

Eqs. (1) describe a variety of physical situations but we will focus here on their application to propagation of electro-magnetic waves. Using a circular polarization basis to describe propagation of the quasimonochromatic waves in isotropic dielectric materials leads to Eqs. (1), where, in such a case, E_1 and E_2 are envelopes of the left- and right- polarized components. The diffraction and GVD parameters can be taken as $\alpha_{1,2} = 0.5$, $\gamma_{1,2} = \gamma = \pm 0.5$, and $\beta = 1 + \chi^{(3)}_{xyyx}/\chi^{(3)}_{xxyy}$, where $\chi^{(3)}_{ijkl}$ is the nonlinear susceptibility tensor. For example, $\beta = 2$ for the nonresonant electronic nonlinearity and $\beta = 7$ for the nonlinearity due to molecular orientation.

While MI of circular polarised solitons is perfectly analogous to the MI of solitons in the single NLS equation [1], linearly and elleptically polarised solitons show novel dynamics. For the sake of simplicity below we focus on the case of the linearly polarized one-dimensional solitons, $E_{1,2}(x) = e^{i\kappa z}\sqrt{\frac{2\kappa}{1+\beta}}\, sech\sqrt{2\kappa}x$, which covers the most important features of the MI induced dynamics.

We have found numerically three branches of soliton spectrum which are linked with the translational symmetry ($x \to x_0$), and with symmetries in the absolute ϕ and differential ψ phases,

$$(E_1, E_2) \to (E_1 e^{i\phi + i\psi}, E_2 e^{i\phi - i\psi}).$$

Assuming that $\Omega^2 \ll 1$ we also derived the analytical expressions for MI growth rates λ:

$$\lambda_x^2 = -\frac{4}{3}\Omega^2\gamma\kappa, \ \lambda_\varphi{}^2 = 4\Omega^2\gamma\kappa, \ \lambda_\psi{}^2 = 2\Omega^2\gamma\kappa f(\beta).$$

Here $f(\beta) = (\int sechx\, g(x,\beta)\, dx)^{-1}$ and function g obeys to $(\partial_x^2 - 1 + 2\frac{3-\beta}{1+\beta} sech^2 x)g = sechx$. Physically $\beta > 1$ and $f(\beta)$ is always positive in this region.

The λ_ϕ^2 eigenvalues and associated neutral mode $(E_1, E_2)^T$ are linked to the symmetry in the absolute

phase ϕ and have their analogies in the spectral problem for solitons in single NLS. The ${\lambda_\psi}^2$ eigenvalue and associated neutral mode $(E_1, -E_2)^T$ are attributed to the symmetry in the differential phase ψ. This branch of the discrete spectrum generates instability for normal GVD ($\gamma < 0$). Thus, the asymptotic analysis indicates that for $\gamma < 0$ neck MI due to a symmetry in the differential phase and snake MI (λ_x^2) due to the translational symmetry coexist.

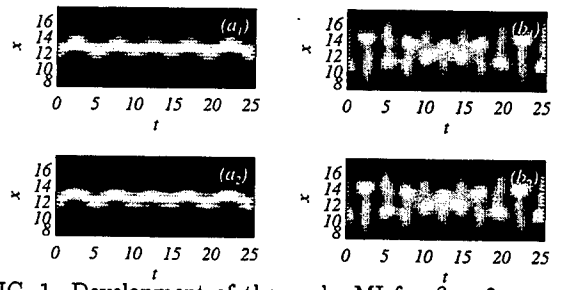


FIG. 1. Development of the snake MI for $\beta = 2$, $\kappa = 1$, $\delta = 0$, $\gamma = -0.5$. ($a_{1,2}$) $|E_{1,2}|$ for $z = 12$; ($b_{1,2}$) $|E_{1,2}|$ for $z = 14.7$.

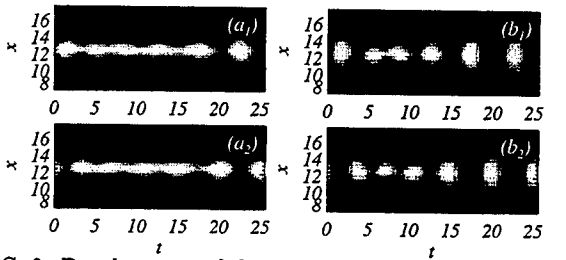


FIG. 2. Development of the anti-phase neck MI for $\beta = 7$, $\kappa = 1$, $\delta = 0$, $\gamma = -0.5$. ($a_{1,2}$) $|E_{1,2}|$ for $z = 8.4$; ($b_{1,2}$) $|E_{1,2}|$ for $z = 10.2$.

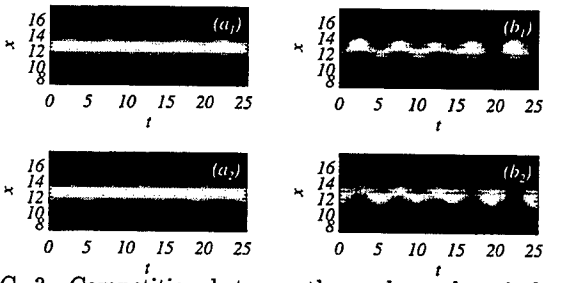


FIG. 3. Competition between the snake and anti-phase neck MIs: $\beta = 3.47$, $\kappa = 1$, $\delta = 0$, $\gamma = -0.5$. ($a_{1,2}$) $|E_{1,2}|$ for $z = 9$; ($b_{1,2}$) $|E_{1,2}|$ for $z = 12$

We have found that the snake MI dominates the anti-phase neck for $1 < \beta < \beta_{sn}$ and vice versa for $\beta > \beta_{sn} \simeq 3.47$. Typical simulation results are presented in Fig. 1,2,3. For $\beta < \beta_{sn}$ we observed in-phase snaking of the stripe along the temporal dimension, see Fig. 1. For $\beta > \beta_{sn}$ the soliton stripe breaks in such a way as to form the interleaved intensity peaks of E_1 and E_2, see Fig. 2, as expected when the out of phase neck MI is dominant. The spatio-temporal patterns formed at the initial stage of MI finally spread because of the unbalanced action of the normal GVD and self-focusing nonlinearity. For $\beta \simeq \beta_{sn}$ we observed competition between the neck and snake MIs, see Fig. 3. In Fig. 3 (b_1), (b_2) one can clearly see that at the intermediate stage of MI the typical in-phase snake pattern is superimposed on the anti-phase neck pattern.

The rescaled instability growth rate λ as function of the modulational frequency Ω can be related to physical units using the formulae:

$$\lambda_{ph} = \frac{\lambda}{4kw^2\kappa}, \; \Omega_{ph}^2 = \frac{\gamma\Omega^2}{2k''w^2\kappa}.$$

Here λ_{ph} and Ω_{ph} are the instability growth rate and modulational frequency in physical units, k is the wave vector, w is the beam width, $k'' = \partial_\omega^2 k$. κ and γ are the same parameters which have been used throughout the text. For example for radiation at $1\mu m$ propagating in an AlGaAs planar waveguide $k'' \simeq -10^{-23}s^2/m$ [10] and for typical soliton transverse size $w \simeq 50\mu m$ [11] we get $\lambda_{ph} \simeq \lambda/(\kappa \cdot 5cm)$ and $\Omega_{ph}^2 \simeq \Omega^2/(\kappa \cdot 10^{-25}s^2)$. For experiments with fused silica at wavelength $830nm$, see second from Refs. [9], $k'' \simeq -10^{-26}s^2/m$ and $\Omega_{ph}^2 \simeq \Omega^2/(\kappa \cdot 10^{-28}s^2)$.

Quadratic solitons. Interaction of the slowly varying envelopes of the first (E_1) and second (E_2) harmonics under the type-I phase matching conditions can be described by the following rescaled equations:

$$i\partial_z E_1 + \frac{1}{2}\partial_x^2 E_1 + \gamma_1 \partial_\tau^2 E_1 + E_1^* E_2 = 0, \qquad (2)$$
$$i\partial_z E_2 + \frac{1}{4}\partial_x^2 E_2 + \gamma_2 \partial_\tau^2 E_2 + \frac{1}{2}E_1^2 = \beta E_2,$$

where β is the wave-vector mismatch and γ_m are GVD coefficients. Eqs. (2) with suppressed temporal derivatives have a famous family of soliton solutions $E_m = A_m(x)e^{im(\kappa z+\phi)}$, $m = 1, 2$. It has been demonstrated that for the normal GVD these solitons are snake unstable [2,4,5] and for the anomalous GVD they are neck unstable [2,5–7]. However analyzes presented in [4–7] were biased by the traditional focus on MI branches linked with the phase, $E_m \to E_m e^{im\phi}$, and translational symmetries [1,2] and the role played by the internal modes was largely ignored. Though breaf comments given in [1,4] could be a guideline for the more detail investigation of this problem.

Key to the presented here results is that the traditional formula for the neck instability growth rate in the low frequency limit

$$\lambda^2 \simeq \frac{2\Omega^2}{\partial_\kappa Q} \int dx(\gamma_1 A_1^2 + 4\gamma_2 A_2^2) \qquad (3)$$

fails, if point $\partial_\kappa Q = 0$ is close enough. This is because an asymptotic method behind this formula does not work

and should be modified. The proper modification gives the quadratic equation for λ^2

$$\lambda^2\left(\frac{1}{2}\partial_\kappa Q+\lambda^2 M\right)=\Omega^2\int dx(\gamma_1 A_1^2+4\gamma_2 A_2^2), \quad (4)$$

where $M>0$ is the soliton mass, see, e.g. [12]. At $\Omega=0$ Eq. (4) describes eigenvalues of the doubly degenerate neutral mode and of the two internal modes. The previously reported calculations for the snake MI [2,4,5] remain correct throughout the eintire region of the soliton existence, because no spatially asymmetric modes exist inside the gap of the continuous spectrum for $\Omega=0$.

Providing that $\gamma_m<0$ and $\partial_\kappa Q>0$, the neck MI starts to grow from

$$\Omega_c^2=(\partial_\kappa Q)^2\left[16M\int dx(\gamma_1 A_1^2+4\gamma_2 A_2^2)\right]^{-1}.$$

At $\Omega=\Omega_c$ two pair of the stable internal modes collide and give onset to the MI with complex conjugated eigenvalues. Because these modes are even functions of x this instability is the neck one and it coexists with the snake MI. The novel neck MI is dominating over the standard snake MI for any $\beta<0$. The snake MI becomes dominating one only for $\beta>0$ and in the cascading limit $\beta\gg 1$ the neck MI complitely disappears.

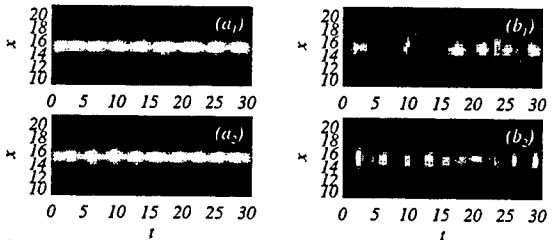


FIG. 4. Competition between neck and snake instabilities. Snake instability is suppressed. $\kappa=1$, $\beta=-1$, $\gamma_1=\gamma_2=-0.5$. $(a_{1,2})$ $|E_{1,2}|$ at $z=10$, $(b_{1,2})$ $|E_{1,2}|$ at $z=15$

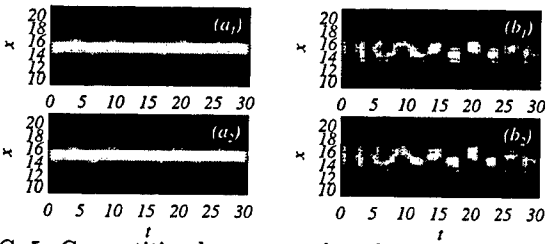


FIG. 5. Competition between neck and snake instabilities. Neck and snake instabilities have approximatly equal growth rates. $\kappa=1$, $\beta=0$, $\gamma_1=\gamma_2=-0.5$. $(a_{1,2})$ $|E_{1,2}|$ at $z=10$, $(b_{1,2})$ $|E_{1,2}|$ at $z=15$

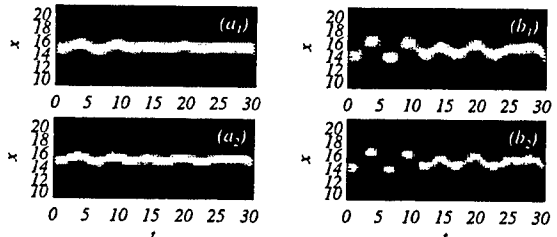


FIG. 6. Competition between neck and snake instabilities. Neck instability is suppressed. $\kappa=1$, $\beta=5$, $\gamma_1=\gamma_2=-0.5$. $(a_{1,2})$ $|E_{1,2}|$ at $z=10$, $(b_{1,2})$ $|E_{1,2}|$ at $z=12$

Summary. We have shown coexistent and competing neck and snake instabilities of spatial solitons in normally dispersive $\chi^{(2)}$ and $\chi^{(3)}$ media. In a $\chi^{(3)}$ medium this coexistence comes into play when the vector nature of the electromagnetic waves, resulting in the extra phase symmetry, is taken into account and in a $\chi^{(2)}$ medium it originates form the presence of the internal soliton modes. In particularly, we found that in a $\chi^{(3)}$ medium with normal GVD the snake MI induced spatial symmetry breaking in the transverse plane changes to the neck MI induced polarization symmetry breaking when the relative strength of the cross-phase modulation exceeds a certain threshold value.

[1] V.E. Zakharov and A.M. Rubenchik, Sov. Phys. JETP **38**, 494 (1974).
[2] A.A. Kanashov and A.M. Rubenchik, Physica D **4**, 122 (1981).
[3] D.V. Skryabin and W.J. Firth, Phys. Rev. Lett. **81**, 3379 (1998).
[4] A. De Rossi *et al.*, Opt. Lett. **22**, 868 (1997).
[5] A. De Rossi *et al.*, Phys. Rev. E **56**, R4959 (1997).
[6] D.V. Skryabin and W.J. Firth, Opt. Commun. **148**, 79 (1998).
[7] D.-M. Baboiu and G.I. Stegeman, Opt. Lett. **23**, 31 (1998); Opt. & Quant. Electr. **30**, 937 (1998).
[8] C. Etrich *et al.*, Phys. Rev. E **54**, 4321 (1996).
[9] J.K. Ranka *et al.*, Phys. Rev. Lett. **77**, 3783 (1996); A.A. Zozulya *et al.*, Phys. Rev. Lett. **82**, 1430 (1999).
[10] N. Belanger *et al.*, J. Opt. Soc. Am. B **14**, 3003 (1997).
[11] J.S. Aitchison *et al.*, J. Opt. Soc. Am. B **14**, 3032 (1997).
[12] O. Bang *et al.*, Phys. Rev. E **58**, 5057 (1998).

Observation of hybrid stripe-needle screening soliton interaction

Eugenio DelRe
Fondazione Ugo Bordoni, Via B.Castiglione 59, 00142 Roma, Italy
edelre@fub.it

Stefano Trillo
Dipartimento di Ingegneria, University of Ferrara, Via Saragat 1, 44100 Ferrara, Italy
edelre@fub.it

Mordechai Segev
Electrical Engineering Department, Princeton University, NJ 08544, USA
segev@ee.Princeton.EDU

Amongst the characterizing elements of solitons in nature, perhaps the most intriguing and important are their collisional properties, so much so that the actual operational definition of soliton pulses is largely dependent on the rigidity, upon collision, of the nonlinearly trapped confined wave-perturbations. Experiments in many diverse fields of Physics have tested this remarkable property, and today we might state that for real situations, self-trapped perturbations can behave much like particles. Although initial investigation in soliton physics was limited essentially to one-dimensional systems (1+1D), recent experimental endeavors in Optics have allowed the accessible observation of two dimensional (2+1D) self-trapped perturbations in photorefractive, quadratic, and Kerr-saturable media [1]. This circumstance spurns us to undertake the investigation of a basic, yet hereto unaddressed, issue of general import to soliton phenomenology: what happens when solitons of the same continuos medium, of approximately the same nonlinear nature, but of different dimensionality, collide and interact?

We perform our experiments with optical spatial solitons in a biased centrosymmetric photorefractive sample of potassium-lithium-tantalate-niobate (KLTN) [2]. In these crystals, through the so-called screening nonlinearity, we have previously observed 1+1D spatial stripe solitons and 2+1D spatial needle solitons [3]. In the noncentrosymmetric screening configuration, interaction and collision of solitons has been previously investigated in diverse situations [4]. Individually, these manifestations, i.e. nondiffracting micron-size stationary optical beams, are characterized by a soliton existence curve, that is a combined set of system parameters, namely the ratio between the beam peak intensity I_o and the background illumination I_b , the beam size Δx (intensity full-width-half-maximum, FWHM), applied external voltage V, and the crystal temperature T, that allows for their stable formation. For stripe solitons this set of parameters can actually be approximately predicted in the standard photorefractive model, whereas for needle structures no clear theoretically understanding is yet agreed upon, although experiments suggest that this curve actually does exist. Thus, in a single photorefractive sample, we can fix independently the soliton parameters of two beams so as to give rise simultaneously to a stripe and a needle particle. Since observations indicate that the two curves are far from coincident except for regions of low nonlinear saturation, simultaneous observation of the two events requires two beams of generally different size and peak intensity, since I_b and V are forcibly in common. The experimental apparatus is similar to those typically employed for the observation of screening photorefractive solitons. The zero-cut 3.7 $^{(x)}$ x 4.6 $^{(y)}$ x 2.4 $^{(z)}$ mm sample is kept at a constant temperature T slightly above its ferroelectric phase-transition ($T_c \approx 10°C$), so as to exhibit relevant quadratic electro-optic response. The two beams leading to stripe and needle self-trapping, polarized parallel to the direction of the externally applied field, are obtained from two independent lasers (one Argon ion laser at λ=514nm and one

doubled CW Nd:YAG laser at λ=532nm) for incoherent collisions, whereas the same Argon ion laser is split into the two diffracting beams for coherent interaction investigation. In both cases I_b is obtained from the Argon ion laser, and is polarized orthogonal to the soliton beams. Photographs of input and output intensity distribution are made by imaging the input and output facets of the sample onto a CCD camera.

In order to find the "working point" of the hybrid system, we simultaneously launch the two beams at zero mutual angle, $\alpha\cong 0°$, but far enough so as to not lead to interaction. For a given V (electrodes are on the x facets of the sample) and I_b, we fix the stripe peak intensity I_s and needle peak intensity I_n so as to observe soliton propagation. Simultaneous formation is obtained for $V\cong 1.4kV$, $\Delta x_n\cong 12\mu m$, $\Delta x_s\cong 10\mu m$, and intensity ratios $u_n=(I_n/I_b)^{1/2}\cong 2.2$, $u_s=(I_s/I_b)^{1/2}\cong 1.6$ (neglecting the difference in photorefractive response at the two frequencies). Furthermore, the sample has effective quadratic electro-optic coefficient $g_{eff}\cong 0.12 m^2C^{-4}$, $n\cong 2.4$, is operated at $T\cong 21°C$ (dielectric constant $\varepsilon_r\cong 8900$) in the paraelectric phase.

Having found the working point, we send forth the two beams at an angle α so as to intersect within the sample. In Fig.1 we show typical results in two cases, one for $\alpha\cong 2.0°$ and another for $\alpha\cong 1.3°$. In the first case, the needle and slab solitons maintain their self-trapped characteristics after the collision, whereas in the second case, for the smaller angle, the output beams are appreciably distorted. In particular the slab beam in proximity of the needle (along the y axis) is destabilized, breaking its slab symmetry, whereas the needle is elongated in the y direction, losing its circular-symmetry (symmetry and structure exchange from one particle to the other). Discernible distortion was observed for values of $\alpha<1.5°$. For values of $\alpha>1.5°$ the self-trapped structure survives the interaction. Thus, for such scattering conditions, the pulses behave as solitons. Parallel, but close propagation in this configuration did not lead to strong beam distortion.

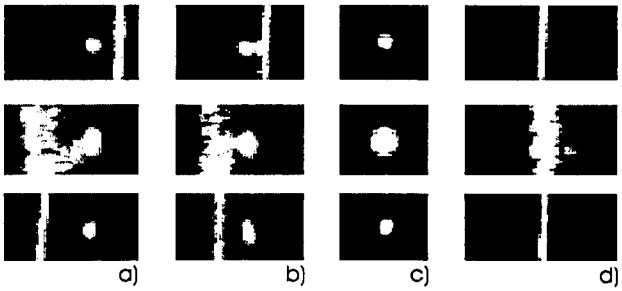


Fig.1: Hybrid soliton collisions: (a) "non-interacting" case for α=2.0°; (b) "interacting" case for α=1.3°; (c) single needle soliton; (d) single slab soliton.

Next we investigate the somewhat richer phenomenology related to mutually coherent beams. We check the approximate input relative phase by observing the fringe pattern the two beams form with the background beam, simply by introducing at the output, before the CCD camera, a 45° oriented polarizer. Results are shown in Fig.2, where the two beams are launched at $\alpha\cong 0°$ and at a peak to peak distance of approximately 20μm. For a relative phase $\phi\cong\pi$, the beams repel, whereas they attract for a zero phase condition $\phi\cong 0$. Note, however, that in this case appreciable beam distortion is observed, both for the stripe structure and for the needle structure.

The theoretical interpretation of this phenomenology is rather intricate, if not altogether impossible at present. In fact, as mentioned, the very interaction that supports circular-symmetric trapping in photorefractives is still not understood. We may, however, draw insight from results as to behavior of other, less complicated soliton supporting nonlinearities. Clearly the different dimensionality of the two particles poses a number of theoretical and modeling riddles. One thing can be interpreted: the presence (and eventually value) of the critical α that allows soliton behavior. In a "linear perspective", the two solitons can be viewed as "self-induced-waveguides". The stripe soliton can be seen, once formed, as a self-induced slab-waveguide, whereas the needle soliton a typical optical fiber waveguide. In such a simplified picture, light can pass from one soliton to the other, seeding interaction, when the relative scattering angle α is comparable to the angular aperture θ_c of the single "waveguides". We can phenomenologically identify θ_c with the equivalent (complementary) critical angle defined by the

relationship $\cos(\theta_c)\cong(n-\Delta n)/n$, where $\Delta n\cong(1/2)n^3 g_{eff}\varepsilon_0^2(\varepsilon_r-1)^2(V/L)^2(u^2/(1+u^2))^2$, where ε_0 is the vacuum dielectric constant, L is the distance between the electrodes (L=3.7mm) and $u=u_s$ for slab solitons, and $u=u_n$ for needle solitons. This approach only roughly estimates the single soliton waveguide saturation and guiding characteristics (even more roughly for the optical needle) [4]. In our conditions we obtain $\theta_c\cong1°$ for the slab structure, $\theta_c\cong1.2°$ for the needle. We expect to observe significant soliton coupling for $\alpha\approx\theta_c$, as is indeed the case. For parallel coherent interaction we show in Fig.3 the soliton interaction simulated by the generalized 2D-NLS equation with a local saturable nonlinearity, manifesting phenomena which is qualitatively similar to that reported in Fig.2.

Finally, for the parallel propagating case, we are observing the nonlinear equivalent of a very interesting phenomena, first described by Marcuse in 1989: directional coupling from a fiber to an infinite slab [5]. Although this theory is clearly linear, it does have a very unique ingredient: coupling amongst structures of *different* dimensionality, and it may be that in finding an interaction potential concepts developed in this paper are helpful. Furthermore, the same structures can actually be used to investigate the linear phenomena predicted by the author, coupling a non-photorefractively active infra-red beam, for example,

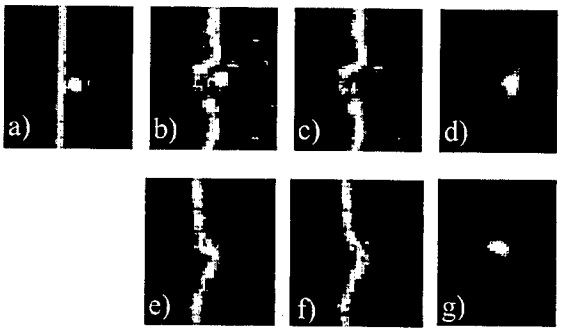


Fig.2: Coherent soliton interaction for parallel propagating stripe and needle solitons. a) input b) $\phi=\pi$ repulsive case c) output with needle beam temporarily blocked d) output needle with stripe temporarily blocked e) $\phi=0$ attractive case f) output with needle beam temporarily blocked g) output needle with stripe temporarily blocked.

at telecommunication wavelengths (λ=1.3-1.5μm), into the needle guiding structure, obtaining a versatile soliton based equivalent of the fiber-surface plasmon sensors, much like we realized in a previous experiment a soliton based directional coupler.

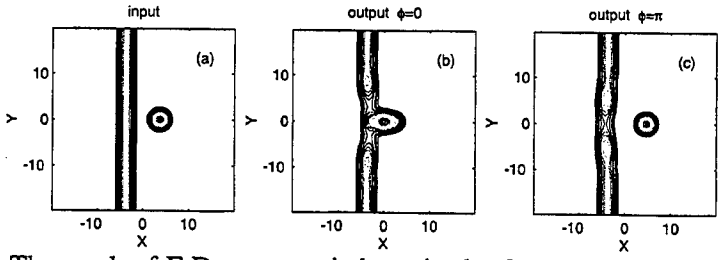


Fig.3: Stripe-needle soliton interaction simulated by the generalized 2D-NLS equation with a local saturable nonlinearity: (a) input condition; (b) output pattern for in-phase interaction; (c) output pattern for out-of-phase interaction. Here the input intensity ratio of the stripe and needle solitons are u_s=1.3 and u_n=2, respectively, and the output patterns correspond to a propagation distance of about twenty diffraction lengths.

The work of E.D. was carried out in the framework of an agreement between Fondazione Ugo Bordoni and the Italian Communication Administration.

[1] For a comprehensive overview, see the Special Issue on Spatial Solitons, *Opt.Quant.Electron.* **30**, 499-954 (1998).

[2] A.Agranat, R.Hofmeister, and A.Yariv, *Opt.Lett.* **17**, 713 (1992).

[3] E.DelRe, B.Crosignani, M.Tamburrini, M.Segev, M.Mitchell, E.Refaeli, and A.Agranat, *Opt.Lett.* **23**, 421 (1998); E.DelRe, M.Tamburrini, M.Segev, E.Refaeli, and A.Agranat, *Appl.Phys.Lett.* **73**, 16 (1998).

[4] M.Shih, Z.Chen, M.Segev, T.Coskun, D.Christodoulides, *Appl.Phys.Lett.* **69**, 4151 (1996); H.Meng, G.Salamo, M.Shih, and M.Segev, *Opt.Lett.* **22**, 448 (1997); A.Mamaev, M.Saffman, and A.Zozulya, *J.Opt.Soc.Am.B* **15**, 2079 (1998).

[5] D.Marcuse, *J.Light.Tech.* **7**, 122 (1989).

Pair generation of (2+1)-Dimensional dark spatial ring solitons

M. M. Méndez-Otero, S. Chávez-Cerda, M. D. Iturbe-Castillo
Photonics and Physical Optics, INAOE, Apdo. Postal 51/216 Puebla, Pue. 72000, México
diturbe@inaoep.mx, sabino@inaoep.mx

It is well known that propagation of (1+1)-dimensional dark soliton stripes in self-defocusing media suffer from transverse instabilities that can lead to the formation of optical vortices. These dark spatial solitons in (2+1) dimensions, has been shown that are stable structures [1, 2]. A different type of (2+1)-D dark solitons with circular symmetry were studied theoretically by Kivshar and Yang [3]. In that work, ring structures with initial amplitude of hyperbolic tangent were investigated analytically and numerically and found that they were robust to perturbations. Experiments to study ring solitons were implemented by placing an opaque circle at the input of the nonlinear medium [4].

In this paper we report the generation of two dimensional dark spatial solitons using an initial condition similar to the (1+1)-D case for generation of dark soliton pairs. As in the (1+1) case, these gray solitons have a travelling wave component in opposite directions, creating a collapsing ring dark soliton and a divergent soliton. We performed the experiments in photorefractive media with a DC external electric field. We also analysed numerically the formation and evolution of the dark rings finding a very good agreement using a model with a nonlinear Schrödinger equation (NLSE) with Kerr-type nonlinearity. Further propagation shows that the ring dark solitons formed in this manner are not stable.

The experiments were made using a He-Ne laser beam at λ = 632.8 nm and an amplitude mask with opaque rings with different radii and widths on a glass substrate. The medium used was a 5x2x9 mm Photorefractive BTO crystal. Typical results are shown in figure 1, where a ring of 46 μm of width and a radius of 40 μm was used. In 1(a) we show the input distribution on the crystals, and in 1(b) the output without external field. And in 1(c) the output for 10 kV/cm applied external field, respectively. When the external field is applied, two dark rings are generated after the 9 mm of propagation in the crystal. The inner dark ring is more defined than the outer one. The external field was applied along the 2 mm transverse dimension, corresponding to the horizontal direction in the images.

For a broader initial dark ring, more pairs of dark soliton rings are generated with different degree of darkness, being darker those in the middle of the output distribution.

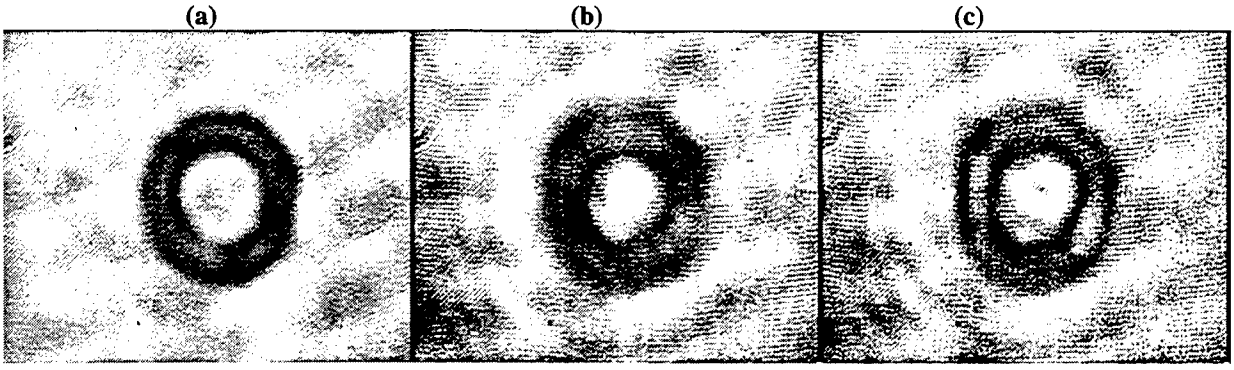


Figure 1. Generation of two ring dark soltions using an intial ring of 46 μm with a inner diameter of 80.μm (a) Input; b) ouput and c) output with 10 kV/cm applied external field.

We investigated the generation and propagation of the (2+1)-D rings we used the NLSE

$$-i\frac{\partial u}{\partial \xi}+\frac{1}{4}\nabla^2 u-\eta|u|^2 u=0$$

where the longitudinal coordinate ξ is normalised to the diffraction length, ∇^2 is the normalised transverse Laplacian and η is a parameter which carries the information of the nonlinearity strength. The function $u(x, y, \xi)$ is normalised such that at onset of propagation its maximum value is one. Our numerical results agreed very well with the experiment, despite the nonlinearity was assumed Kerr-type. Instead of showing this, we would like to present a very intriguing behavior of the solitons formed with equal phases at each side of the amplitude dip. For the initial condition of an annular amplitude dip with radius $R = 6$, width $w = 1$ and $\eta = -18$. We found that, contrary to what occurs for hyperbolic tangent ring dark solitons, they are not stable on propagation. Results of numerical simulations are shown in figure 2 where we observe that soliton pairs are formed. On propagation, the inner rings travel towards the center (collapsing) while the outer is diverging.

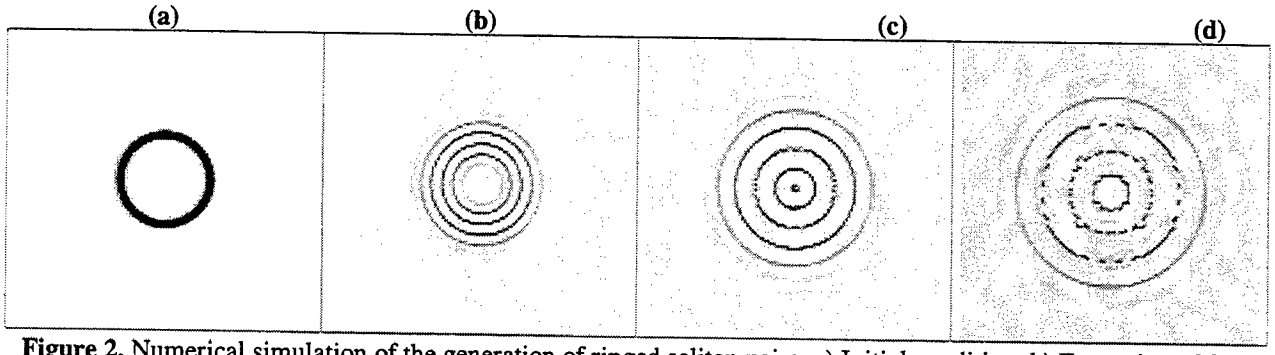


Figure 2. Numerical simulation of the generation of ringed soliton pairs. a) Initial condition. b) Formation of four ring dark solitons, those at the middle are darker than the central and outer ones. c) Appearance of the transverse instability in one of the ring dark solitons. d) Break up into vortices pairs.

We have observed that the darker ring is subject to transverse instabilities as the (1+1)-dimensional solitons do. We remark that the neighbor rings do not break up but until later stages of propagation, this possibly induced by the splitting one. The rings split into vortices pairs as was expected. Changing the diameter or the width of the ring produces similar results approximately at the same propagation distance. By changing the widths, as mentioned above, a different number of rings are produced.

In conclusion we have shown the possibility of generation of ring dark solitons using an annular initial condition. The solitons generated this way are not stable and break up into vortices pairs.

[1] A. W. Snyder, L. Polodian and D. J. Mitchell, Opt. Lett. **17**, 789 (1992).
[2] G. A. Swartzlander, Jr. And C. T. Law, Phys. Rev. Lett. **69**, 2503 (1992).
[3] Y. S. Kivshar and X. Yang, Phys. Rev E **50**, R40 (1994).
[4] S. A. Baluschev, I. Dreischuh, S. Velchev, S. Dinev and O. Marazov. Phys. Rev. E **52**, 5517 (1995).

Transverse structures in cavity-less parametric amplifier

W. Chinaglia, S. Minardi, S. Sapone, G. Coppo, and P. Di Trapani
Department of Sciences, University of Insubria, Como, Italy
(ditrapan@fis.unico.it)

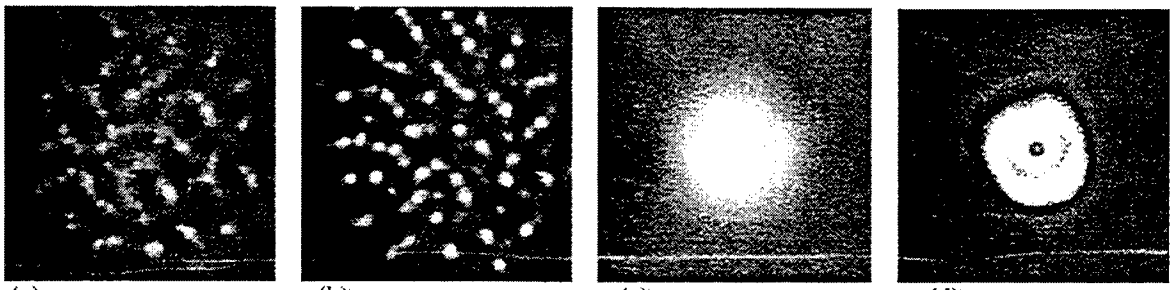
A. Berzanskis, G. Valiulis
Department of Quantum Electronics, University of Vilnius, Lithuania

K. Staliunas
PTB, Braunschweig, Germany

The single-pass (or traveling-wave, or cavity-less) parametric amplifier is a good candidate for achieving the generation and the ultrafast control of transverse structures of large complexity for image processing, switching, addressing, parallel beam processing and several other applications. In fact, the absence of any feedback mechanism and the fast electronic nonlinearity make the device response time very short (i. e. in the sub-ps regime, the limit being given by the gvm of the interacting waves); moreover, the large parametric gain (up to 10^8) allows the use of very weak signals for controlling the structure formation in intense laser beams.

In this work we propose a *reportage* on our preliminary results on the generation and control of the large-beam transverse structures occurring in a cavity-less parametric amplifier (a 30mm LBO crystal in noncritical phase matching), pumped by single 1.5ps 527nm laser pulses and operated in regime of strong pump depletion. The phase matching was so that the gain is peaked at the collinear direction, in linear regime.

Fig. 1

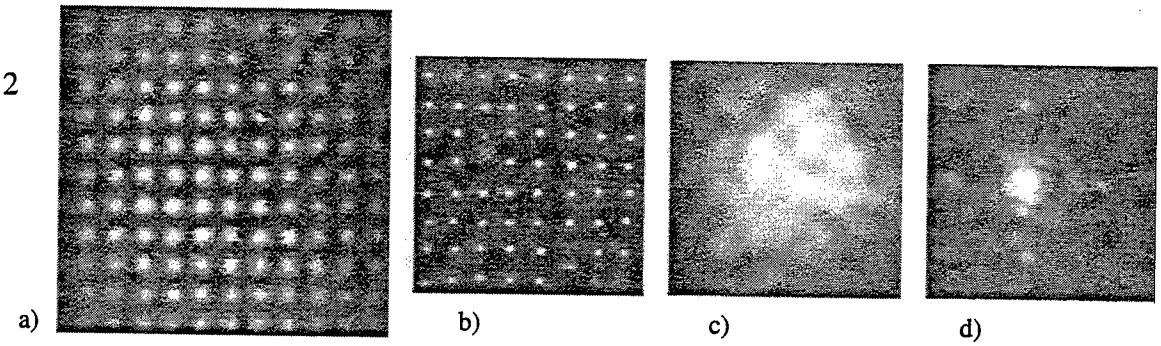


(a) (b) (c) (d)

Figure 1a shows the near-field pattern-like structure occurring on the signal-beam (as well as on the depleted pump) when the input *pump is a 1mm gaussian beam* and the amplification is *seeded by the quantum noise*. The result seems to indicate the occurrence of a (short range) honeycomb-like structure, similar to those previously observed in resonators. We like to say that, in the present scheme, the spatial frequency of the structure is too low (i. e. the angular spectrum too narrow) to introduce sufficient correlation in the whole beam for the given aperture. This could justify the local character of the observed structure. Work is in progress to overcome this limitation, as well as to obtain a suitable interpretation the observed phenomenon (the absence of any feedback means that pattern is not originated by a sort of bistability). Preliminary investigation, however, seems to indicate that the symmetry of the structure is originated by the cascaded quadratic nonlinearity, whilst its breaking into a given realization is controlled by the defect distribution in the crystal. *Figure 1b* shows the structure obtained when *a plane-wave quasi-monochromatic seed*, 10^5 times weaker than the pump pulse, is launched to the crystal synchronous with the pump pulse, whose intensity was slightly reduced. Beside the sharp increase in the contrast, this seeding gives rise to mutually trapped signal and pump beams, sitting on the bonds of a honeycomb-like structure very similar to that originated from quantum-noise amplification. Moreover, this plane-wave seeding should have the effect of locking the phases of the

different portions of the beam. This increase in "coherence" is evident in *Figures 1c and 1d*, where the far-field signal intensity distributions are reported for the quantum-noise and plane-wave seeding, respectively. Note the 3 peaks in the rings of the signal angular spectrum that, together with the 3 other peaks in the idler wave (not seen by our detector), are consistent with the observed honeycomb-like structure.

Fig. 2



In the following part of the work we investigate the structures *obtained when a square-lattice intensity modulation is superimposed to the gaussian pump beam.* The effect is achieved by simply placing a slide with modulated transmission on the pump-beam path. The slide has a $\sin^2$ modulation with 100 μm periodicity, 100% contrast (leading to) 25% transmission. *Figure 2a* shows the *low-intensity pump-beam* profile at the crystal exit when the slide was placed at the crystal input face. *Figure 2b* shows the output signal-beam profile obtained at high pump intensity (total conversion efficiency 40%) from *parametric amplification of the quantum noise.* Both the output signal and pump (not shown) appeared to be formed by a well ordered lattice of mutually trapped solitary-like beams, of about 20 μm diameter. Measurements of the divergence of the single beams composing the lattice lead to $M^2=1$ for the beam-quality parameter. Therefore the process here described represents a very simple method to achieve the generation of high-power spatially quasi-coherent beams of tunable radiation. Quasi-coherent means that the phases of the different beams are randomly distributed, since the amplification is seeded by the noise. However, this would not be a problem for all those application in which parallel beam processing is required. In order to achieve the phase locking among the different beams we repeated the experiment by seeding the amplifier with *a plane-wave quasi-monochromatic seed*, 10^5 times weaker than the pump. The near field profiles are not distinguishable by those in Fig. 2b. The impact of the external seeding on the whole-beam coherence is evident in the results shown in *Figures 2c and 2d*, where the *far-field signal intensity distributions are reported without and with seeding, respectively.*

Fig. 3

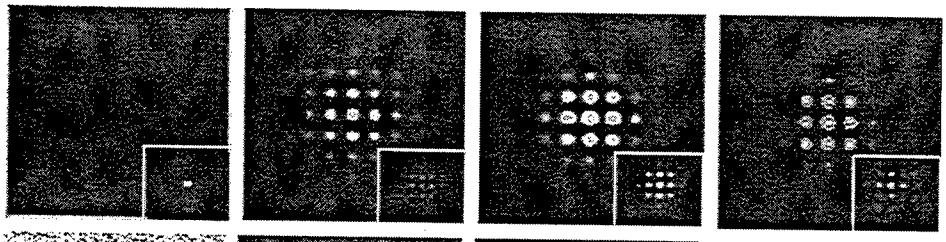
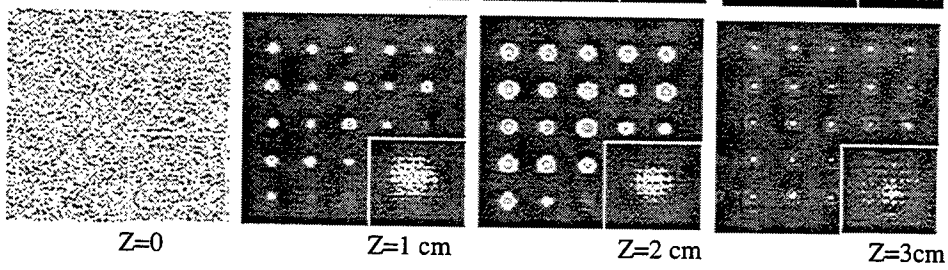
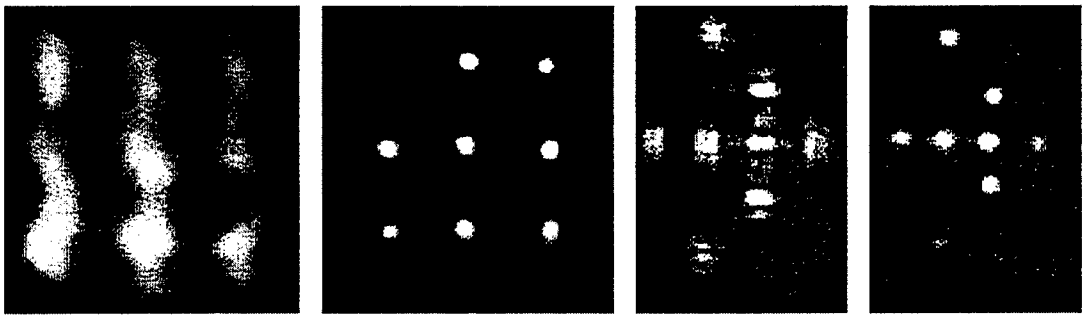


Fig. 4



The sequences in *Figure 4* sows the results of the numerical calculations concerning the evolution of the signal beam profile inside the crystal, for the case of quantum noise amplification. The evolution of the angular spectrum is shown in the inset. The dynamics indicates that in the linear regime of amplification the signal underlies a sort of spatial mode-locking forced by the trasverse gain modulation, leading to the formation of single coherent beams. These beams finally forms the spatial solitons in the final part of the crystal, where gain saturation occurs. *Figure 3* shows the analogous evolution for the case of the plane-seeding wave.

Fig. 5



a) b) c) d)

The next point we like to address concerns the capability of this modulated-pump system of being used as a method for recovering high contrast pictures from eventually defocused images. To this end we placed *the grid-slide 8 cm before* the crystal input face. *Figure 5a* shows the resulting *low-intensity* pump profile as measured at the crystal input face. In spite of the very low contrast, the nonlinear process is still capable of reconstructing the soliton-like lattice, as evident in the high-intensity *output signal-beam* profile shown in *Figure 5b*. Note that not only the contrast is increased but also the spatial resolution. In fact the area of each generated soliton is about 2 order of magnitude smaller than that of the single input beams in the grid. A question which spontaneously arises concerns the capability of the system of processing more complex images. To this end we first verified that each soliton may be switched off independently by suitably darkening the corresponding cell in the slide. *Figure 5c* shows the *low-intensity pump* profile at the crystal exit when an arrow was "drawn" on the slide. *Figure 5d* shows the corresponding *signal profile* at high pump intensity, with the high contrast perfectly recovered. Also in this case the reconstructed image remained virtually unchanged when modifying the input-slide position by several cm along the pump-beam path.

Work is in progress to achieve the control of the excited solitary beams by means of weak external seeding signal beams, launched to the desired positions together with a uniformly modulated pump. In this case the pump intensity have to be set just below the threshold for spontaneous soliton formation from quantum noise amplification. Preliminary measurements indicate that the modulation in the pump beam helps in stabilizing the position of the excited solitons respect to the wandering of the pump or of the writing-signal beams, a quite important issue if the possibility of coupling the solitons with a fiber bundle in on-field application is considered.

Pulse Propagation and Soliton Formation using Optical Rectification

U.Peschel, K.Bubke, D.C.Hutchings and J.S.Aitchison

University of Glasgow, Glasgow G12 8QQ, UK,
Tel.:44 141 3305230, Fax: 44 141 3304907, E-Mail: kbubke@elec.gla.ac.uk

It is well known that in the presence of quadratic nonlinearities not only does frequency doubling occur but a static electric field is also generated. In early experiments it was shown that a laser pulse propagating through a non-centrosymmetric crystal gives rise to the formation of a voltage pulse [1]. It was realized that the generated dc-field may not only be an elegant tool for detecting the optical wave, but may also be the source of coherent THz radiation. Here we demonstrate that the refractive effects on the optical pulse are considerable. They may give rise to the formation of temporal solitons composing of bound states of the optical and microwave fields.

Unfortunately there is no theory available to link the optical and the microwave propagation in a resonant geometry although those waveguiding structures are well known as e.g. electro-optic modulators. A typical example realized in AlGaAs is shown in Fig.1. Optical guiding is achieved by a high index layer, where lateral confinement is provided by a rib etched into the cladding. The microwave field spreads between the metal electrode on top and the doped substrate. Here we assume monomode operation and the optical field to be polarized in Y-direction (TE) and the microwave to be mainly polarised in X-direction. (TM). To derive the basic set of evolution equations we start in Fourier space. In case of weak nonlinearities the mode amplitudes $u(z,\omega)$ evolve in the z-direction according to [2]

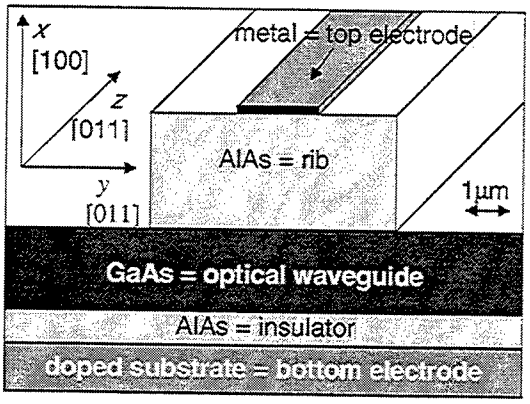


Fig.1 Structure under investigation

$$\left[\frac{d}{dz} - i\beta(\omega)\right] u(z,\omega) = \frac{i\omega}{p_0} \int dx \int dy \left(\vec{E}^0\right)^* \bullet \vec{P}, \tag{1}$$

where p_0 is the guided mode power. It is assumed that the field structure of the respective guided modes $\vec{E}^0$ is not affected by the action of the weak nonlinearly induced polarization $\vec{P}^{\omega}$. Provided that the structure is not phase matched with the second harmonic the field evolution takes place in two distinct spectral domains: one centered around the optical frequency ω_0 and the other around $\omega=0$. An expansion of the propagation constant $\beta(\omega)$ around these points and a subsequent Fourier back transformation results in two evolution equations for the slowly varying envelope of the optical pulse and for the microwave fields.

$$\left[i\frac{\partial}{\partial z} + \frac{1}{v_{opt}}\frac{\partial}{\partial t} - \frac{D_{opt}}{2}\frac{\partial^2}{\partial t^2}\right] u_{opt}(z,t) = \frac{1}{p_0}\left(i\omega_{opt} - \frac{\partial}{\partial t}\right) \int dx \int dy \left(\vec{E}_{opt}^0\right)^* \bullet \vec{P}_{opt} \tag{2}$$

$$\left[\frac{\partial}{\partial z} + \frac{1}{v_{mic}}\frac{\partial}{\partial t} - \frac{T_{mic}}{6}\frac{\partial^3}{\partial t^3}\right] u_{mic}(z,t) = -\frac{1}{p_0}\frac{\partial}{\partial t} \int dx \int dy \vec{E}_{mic}^0 \bullet \vec{P}_{mic} \tag{3}$$

Here we have neglected all losses and have dropped the expansion after the first dispersive term. Further we have assumed that the field structures remain unchanged in the respective frequency domains and that the propagation constant obeys the symmetry relation $\beta(-\omega)=-\beta(\omega)^*$ resulting in a suppression of all even

terms in the expansion around ω=0. In what follows we express the nonlinear polarization by the respective fields, while taking into account the growth [100] and cleaving [01 $\bar{1}$] directions of the fcc-lattice and as well as the polarization of the respective fields. We end up with the following set of equations

$$\left[\frac{\partial}{\partial z}+\frac{1}{v_{\mathrm{opt}}}\frac{\partial}{\partial t}+i\frac{D_{\mathrm{opt}}}{2}\frac{\partial^2}{\partial t^2}+2i\omega_{\mathrm{opt}}\chi_{\mathrm{eff}}U_{\mathrm{mic}}\right]U_{\mathrm{opt}}=2\chi_{\mathrm{eff}}\frac{\partial}{\partial t}\left[U_{\mathrm{mic}}U_{\mathrm{opt}}\right] \tag{4}$$

$$\left[\frac{\partial}{\partial z}+\frac{1}{v_{\mathrm{mic}}}\frac{\partial}{\partial t}-\frac{T_{\mathrm{mic}}}{6}\frac{\partial^3}{\partial t^3}\right]U_{\mathrm{mic}}=\chi_{\mathrm{eff}}\frac{\partial}{\partial t}\left|U_{\mathrm{opt}}\right|^2, \tag{5}$$

where we have scaled the optical field U_{opt} with the guided power p_0 and the microwave field U_{mic} with the electrical power $p_{\mathrm{el}}=p_0/2$. The nonlinear interaction is mediated by the overlap integral

$$\chi_{\mathrm{eff}}=\frac{\varepsilon_0}{2p_0\sqrt{p_{\mathrm{el}}}}\int dx\int dy\;\chi_{123}\left(E^0_{\mathrm{opt}\,y}\right)^2E^0_{\mathrm{mic}\,x}$$

In case of the structure depicted in Fig.1 and for χ_{123}=200pm/V [3] it amounts to $\chi_{\mathrm{eff}}=8.3*10^{-14}\,\mathrm{s\,m^{-1}W^{-1/2}}$. While the internal structure of eq.(4) is quite common in optics, eq.(5) is closer to a KdV equation. Energy exchange is driven by the time derivatives rather than by the nonlinearly induced polarization itself as it is for usual frequency conversion. We find an additional term in (4), which describes the electro-optic modulation of the optical field by the generated dc-voltage, but does not give rise to an energy exchange.

A simulation of an optical pulse injected into the structure depicted in Fig.2 shows, that two microwave pulses with opposite phases are generated close to the input facet. One "ghost pulse" travels with the velocity of the microwave, while the other one - the "image pulse" - stays with the optical pulse in a stationary state. Both are almost the exact image of the optical power distribution. The reason for this behavior is the huge velocity difference between both waves. In our case the group refractive indices differ by about 1. Consequently the group velocity difference is by far the dominant term in eq.(5). In the stationary limit eq.(5) can be integrated once and the resulting microwave field can be approximated by

$$U_{\mathrm{mic}}\approx\frac{\chi_{\mathrm{eff}}\left|U_{\mathrm{opt}}\right|^2}{\frac{1}{v_{\mathrm{mic}}}-\frac{1}{v_{\mathrm{opt}}}} \tag{6}$$

resulting in an exact image of the optical pulse.

If reinserted into eq.(4) we end up with an effective cubic nonlinearity due to the electro optical effect. Its strength is given by

$$\gamma=\frac{2\omega_{\mathrm{opt}}\,\chi^2_{\mathrm{eff}}}{\frac{1}{v_{\mathrm{opt}}}-\frac{1}{v_{\mathrm{mic}}}} \tag{7}$$

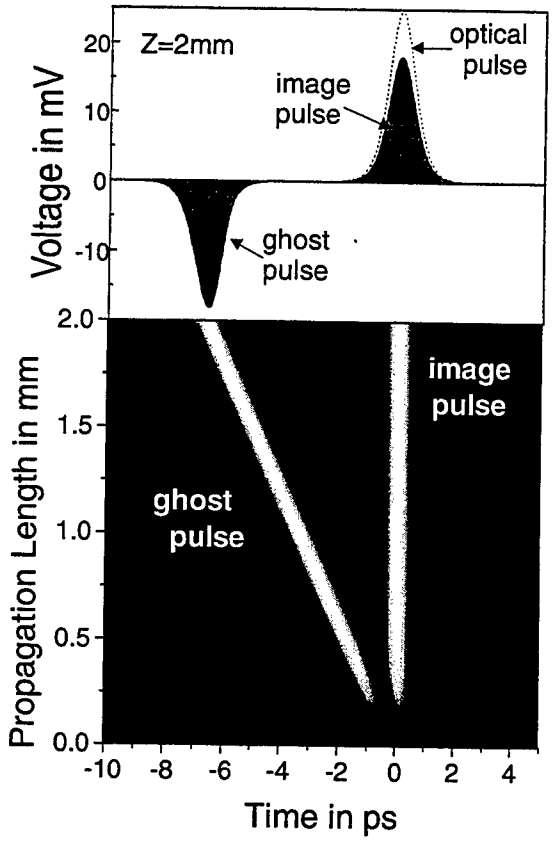


Fig.2 Generation of microwave pulses in the geometry depicted in Fig.1 (parameters of the optical pulse: duration: 1ps, peak power: 100W, λ=1.5μm, injected at t=0, parameters of the structure: impedance: $54\Omega, T_{mic} = 1.1*10^{-35}\,s^3m^{-1}$, $D_{opt} = 2.02*10^{-23}\,s^2m^{-1}$, n_{opt}^{group} - $n_{mic}^{group}=1$, $\chi_{eff} = 8.3*10^{-14}\,s\,m^{-1}W^{-1/2}$)

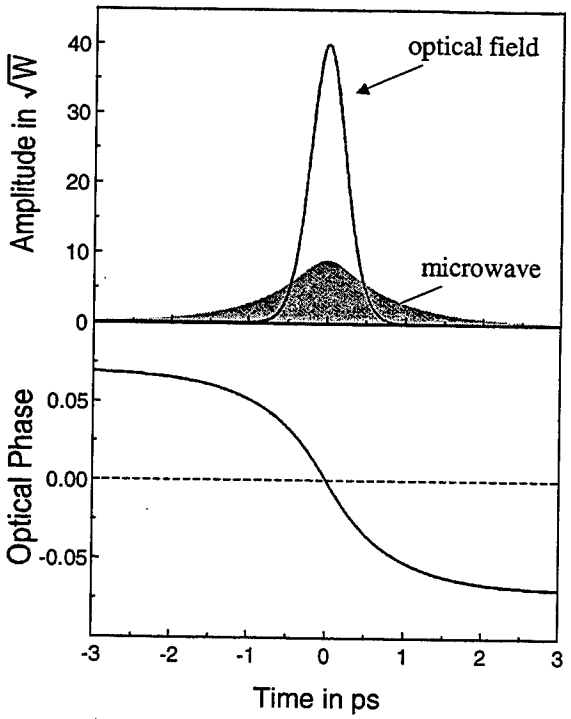


Fig.3 Soliton with a propagation constant in z-direction of 1.675mm^{-1} (parameters as given in Fig.2, except $n_{opt}^{group} - n_{mic}^{group} = -0.001$)

and amounts to $\gamma = -5.2*10^{-3}\,m^{-1}W^{-1}$ in case of our sample. This is still three orders of magnitude smaller than values obtained from intrinsic cubic nonlinearities. However, it can be easily enhanced by matching the respective group velocities as it is done in conventional electro-optic modulators. The effective index of microwave modes can be adjusted in a wide range by either pattering the metal electrodes or by covering the structure with high index materials, which are available for microwave frequencies [4].

At least in this Nonlinear Schrödinger Equation limit we expect to find stable light pulses or solitons, provided that the sign of the velocity difference is chosen properly. A more detailed analysis reveals that even the whole set of equations (4) and (5) supports soliton solutions (see Fig.3). The optical field in these mutually bound states shows a nontrivial phase dynamics. It is real valued only if the energy exchange term in (4) can be neglected compared to the electro optic coefficient. In this case the solitons known from second harmonic generation are reproduced, although the dynamics which led to their formation are entirely different.

[1] M.Bass, P.A.Franken, J.F.Ward, and G.Weinreich, Phys.Rev.Lett. 9, 446 (1962).
[2] M.Börner, R.Müller, R.Schiek, and G.Trommer, *Elements of Integrated Optics*, (Teubner, Stuttgart, 1990) (in German).
[3] T.Y.Chang, N. van Tran, C.K.N.Patel, Appl.Phys.Lett.**13**, 357 (1968).
[4] R.G.Walker, IEEE Journ.Quant.Electron.**27**, 654 (1991).

Nonlinear Guided Waves and Their Applications

Nonlinear Effects in Fibers

Wednesday, 1 September 1999

David J. Richardson, University of Southampton, UK
Presider

WB
10.30-12.00
Salle Morey—St-Denis

COUPLED CORE AND CLADDING STIMULATED BRILLOUIN SCATTERING IN SINGLE-MODE OPTICAL FIBERS

I. BONGRAND, A. PICOZZI, E. PICHOLLE and C. MONTES

C.N.R.S., Laboratoire de Physique de la Matière Condensée,
Université de Nice - Sophia Antipolis, Parc Valrose, 06108 Nice cedex, France
tél. (+33) 492 076 780 fax : (+33) 492 076 754 e-mail : name@naxos.UNICE.fr

Besides their obvious industrial interest, single-mode optical fibers are ideal tools for fundamental studies of the dynamics of nonlinear interactions between light and matter, made easy by the high optical flux and the very long interaction lengths achieved in such media. Moreover, they are usually considered as fairly unidimensional, which is a key feature in the stability of nonlinear optical structures, such as NLS solitons. Nevertheless, it should be kept in mind that their finite numerical aperture sometimes allow unusual phase-matching conditions and call for more complex approximations to account for the observed dynamics in fiber devices.

Here, we are interested in the electrostrictive interaction between light and matter, namely the stimulated Brillouin scattering (SBS). Implicitly, SBS usually refers to the 1D approximation, where a forward propagating "pump" wave creates both a backward propagating ($\theta = \pi$) "Brillouin" wave and a ultra-high frequency (tens of GHz) forward ($\theta = 0$) longitudinal acoustic wave. For coherent enough pump beams, it is the dominant nonlinear effect in fibers, and its very rich dynamics, which includes solitonic, chaotic, and bistable behaviours in resonators, is now fully understood in the frame of a coherent (*i.e.* phase-sensitive) 3-wave model, accounting for the optical Kerr effect.[1]

Nevertheless, the Brillouin process can also couple the pump wave with *transverse* acoustic waves propagating mostly in the fiber cladding ($\theta \approx \pi/2$); from now on we will denote this geometry as cladding Brillouin scattering (CBS). The whole body of the fiber then constitutes an acoustic resonator, yielding a discrete set of resonant frequencies typically in the 10^7-10^9 Hz range,[2,3] and the scattered optical wave ($\theta <$ NA) propagates together with the pump. In the spontaneous regime, for low enough optical intensities, CBS is known as guided-acoustic-wave Brillouin scattering (GAWBS) and a major limitation to quantum optics experiments in fibers.[4] At higher level, it has recently become clear that CBS-induced phase modulations introduced an important slow electrostrictive contribution to the nonlinear index n_2, of the same order than the fast Kerr contribution in the near infrared,[5,6] and that this so-called "long-range interaction" is a key cause of jitter in solitonic optical telecommunications.[2] We pointed out in a previous work[7] its analogy with stimulated Raman scattering during the propagation of short optical pulses, where CBS induces a small self-frequency-shift. CBS has also been shown to affect in various ways the dynamics of fiber lasers.[8,9]

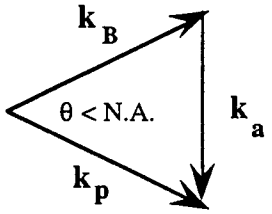


Figure 1 : copropagative phase-matching

Here, we are interested in the coupling between both Brillouin process, SBS and CBS, in single-mode fiber resonators. Our basic device (Fig. 2) is a cw pumped (argon-ion pump laser @ 514.5 nm) fiber resonator of length L with a low Brillouin feedback ($R \approx 1\%$) and an intracavity isolator avoiding pump recoupling. If SBS alone is considered, the dynamics of the interaction depends on a single parameter, namely the overall gain $G = g_{SBS} I_p L$ for a given R : whenever $R < 15$ %, a regular Hopf bifurcation separates a cw "SBS mirror" regime from a stable pulsed regime at lower G.[10] On the other hand, the spontaneous noise f_n (the CBS seed) would increase linearly with L. In a previous paper, we reported observation of high-order modes (typ. 10 FSR), related to transverse acoustic resonances, in the transition region between the stable cw and pulsed regimes of a L = 80 m device, where the transients are long enough to be sensitive to any perturbation.[1]

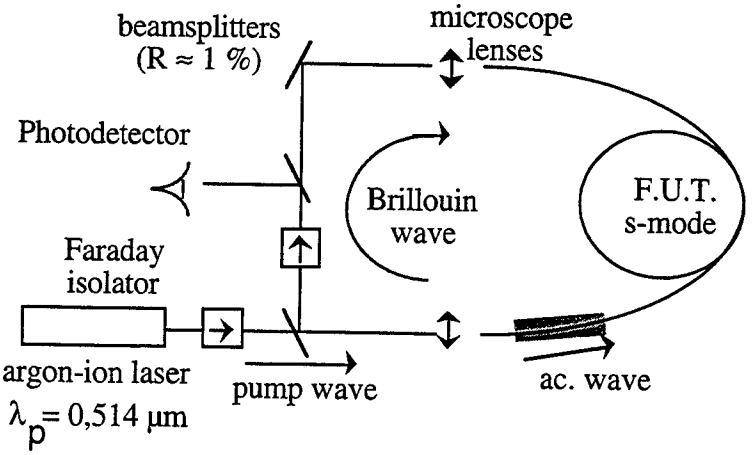


Figure. 2 : Experimental setup

No influence of those transverse acoustic modes have been reported on shorter devices. For L = 150 m, this CBS instability appears to be developed enough to prevent the establishment of any stable pulsed regime : instead of the smooth pulses previously observed, we obtain rather unstable trains of pulses, with imperfect mode-locking (larger width) and strong intrapulse modulation (Fig. 3). The transition region is fully unstable, and even the "mirror" region presents a very poor stability in this configuration. This influence, through CBS, of the fiber length on the stability of SBS fiber lasers has been observed at various λ_p, and configurations as thoroughly discussed in ref. 1

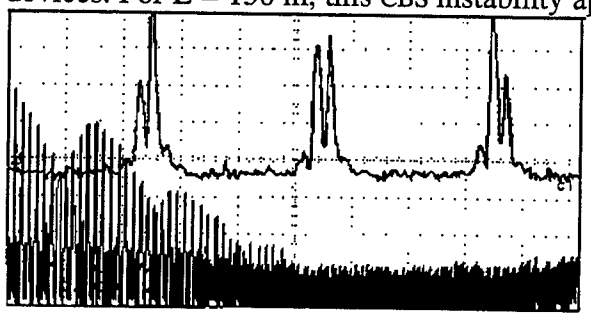


Figure 3 : Modulated Brillouin pulses and FFT (experimental).

We have developed a coherent model for CBS, which accounts for the transverse acoustic modal structure of the fiber, analyzed in some details in previous works;[2,4] we describe locally each mode of frequency Ω_n, damping γ_n, and amplitude q_n through a standard forced harmonic oscillator equation :

$$\left[\partial_{tt} + 2\,\gamma_n\,\partial_t + \Omega_n^2 \right] q_n = 2\,\Omega_n\,\kappa_n^{str.} \left| E \right|^2 + f_n(z, t) \qquad (1)$$

This model is fully compatible with the usual 3-wave model of SBS, which describes the coupling of a pump wave E_p (ω_p) to a backscattered wave E_s (ω_s), though a longitudinal acoustic wave E_a ($\omega_a = \omega_p - \omega_s$). It is customary to neglect the acoustic longitudinal propagation (of velocity $c_s << c$), its dynamics being described though :

$$\left[\partial_t + \gamma_a \right] E_a = \kappa_{SBS}\,E_p\,E_s^* + f_a(z, t) \qquad (2)$$

A poorer overlap between optical and acoustical waves yields a much lower gain in the CBS case ($g_{CBS} \approx 10^{-2}\, g_{SBS}$). Accounting for the optical Kerr effect but neglecting the dispersion, we obtain for the Brillouin envelope :

$$\left[\partial_t - \frac{c}{n} \partial_z + \gamma_e \right] E_B = \kappa_{SBS}\, E_p\, E_a^* + i \left\{ \Sigma_n\, W_n\, X_n + \kappa_{kerr} \left(2\, I_p + I_B\right) \right\} E_B \qquad (3)$$

and a similar expression for the pump wave. Even with this very simplified model, we obtained a fair qualitative agreement between the numerical simulations and the experiment. No stable regime is ever achieved but, for long computation times (up to 5000 roundtrips), an asymptotic evolutive train of modulated pulses is obtained (Fig. 4). Although we neglected several modes of comparable efficiency, the discrepancy remains well within the uncertainty over the estimation of the CBS mode width γ_n.

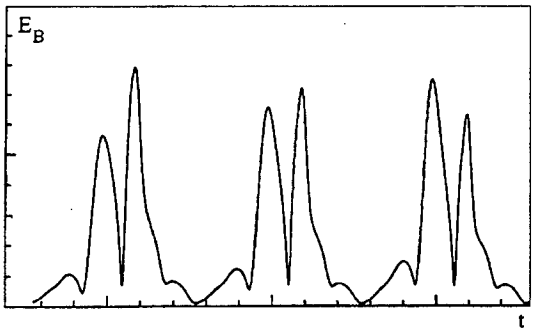


Figure 4: Numerical simulation of the 4 wave problem (CBS + SBS + Kerr)

The CBS characteristic length is of the same order than the Kerr length, and, as could be expected from earlier Kerr studies,[11] more complex structures were obtained for higher $\kappa^{st.}$ but could not be correlated to the experiment, and chaotic behaviours appeared for $\kappa^{st.} > 10\, \kappa^{Kerr}$.

We will also present new experimental results about CBS-induced cross-amplitude modulation when a secondary cw-laser beam is launched in the resonator, with an arbitrary wavelength and an intensity too low to stimulate Brillouin scattering by itself. The agreement between the new model of these electrostrictive interactions presented here, bypassing the usual one-dimensional approximation in single-mode fibers, and various experiments in Brillouin fiber ring resonators is satisfactory. From this, it can be inferred that the coherent dynamics of CBS and SBS are very similar, and thus that CBS might become a major limitation to high bit/rate telecommunication systems, once its instability threshold is attained (typically in the THz range).

1 C. Montes, D. Bahloul, I. Bongrand, J. Botineau, G. Cheval, A. Mamhoud, E. Picholle, and A. Picozzi, to appear in J. Opt. Soc. Am. B, **16**, june 1999.

2 E.M. Dianov, A.V. Luchnikov, A.N. Pilipetskii and A.N. Starodumov, Opt. Lett. **15**, 6, p 314 (1990);

3 A.J. Poustie, J. Opt. Soc. Am. B., **10**, 4, p 691 (1993);

4 R.M. Shelby, M.D. Levenson, and P.W. Bayer, Phys. Rev. B, **31**, p 5244 (1985).

5 E.L. Buckland and R.W. Boyd, Opt. Lett. **22**, 10, p. 676 (1997).

6 D. Le Quang, Y. Jaouën, M. Zimmerli and P. Gallion, IEEE Photonics. Tech. Lett., **8**, 3, p. 414 (1996);

7 I. Bongrand, A. Picozzi and E. Picholle, Electron. Lett., **34**, 1769-1770 (1998).

8 A.B. Grunidin, D.J. Richardson, and D.N. Payne, Electron. Lett., **29**, 21, p. 1860 (1993).

9 A.N. Pilipetskii, E.A. Golovchenko, and C.R. Menyuk, Opt. Lett., **20**, 8, p. 907 (1995).

10 C. Montes, A. Mamhoud and E.Picholle, Phys. Rev. A, **49**, 2, p. 1344 (1994).

11 D. Yu, Weiping Lu and R.G. Harrison, Phys. Rev. A, **49**, R24 (1994).

Four-wave mixing of femtosecond pump-probe pulses in optical fibers

Gilbert Boyer
Laboratoire d'Optique Appliquée, Centre de l'Yvette, 91761 PALAISEAU cedex, France
boyer@enstay.ensta.fr

Bjorn Hall, Dan Anderson and Mietek Lisak
Dept. of Electromagnetics, Chalmers University of Technology, S-412 96 Goteborg, Sweden
bjorn.hall@elmagn.chalmers.se, elfda@elmagn.chalmers.se, elfml@elmagn.chalmers.se

Magnus Karlsson
Dept. of Microelectronics, Chalmers University of Technology, S-412 96 Goteborg, Sweden
magnus@elm.chalmers.se

Anders Berntson
Ericsson Telecom AB, S-126 25 Stockholm, Sweden
Anders.Berntson@etx.ericsson.se

Introduction The nonlinear propagation of a pump-probe pulse pair in an optical fiber has been extensively studied both experimentally, numerically and theoretically. In particular, it has been shown that the probe can attain a spectral shift under the influence of cross-phase modulation (XPM) from the pump, an effect having important applications in e. g. optical switching and demultiplexing.

Propagation of femto-second pump-probe pulse pairs near the zero-dispersion wavelength of a fiber, gives rise to new effects. In earlier work, spectral splitting of a single pulse propagating near the zero-dispersion wavelength was observed [1]. For moderate pump powers, the pump causes a gradual spectral shift of the probe-pulse, due to XPM [2]. However, for sufficiently high pump-powers, we have discovered that this continuous spectral shifting is replaced by a new physical feature involving a large spectral jump, with substantial parametric amplification of the new signal. The physical mechanism behind this feature is four-wave mixing (FWM). Phase-matching for this process is greatly simplified by the high peak-power and large spectral width inherent in femto-second pulse-propagation. On the other hand, group-velocity matching emerges as an equally important factor to be fulfilled for efficient power-conversion from the pump to the probe.

Experiments We synthesized the pump-probe pair by spectrally filtering an initial, spectrally broad pulse. The laser-source was a Kerr-lens mode-locked femto-second Cr^{4+}:forsterite laser, previously described in [3]. After filtering, the pulses were of around 200 fs in duration, with a peak-power of up to 670 W for the pump and 1–5 W for the probe. The probe-wavelength could be tuned between 1260–1330 nm, while the pump was fixed at 1260 nm to maximize pump-power. The pump-probe pair was coupled into a 15 m long standard single-mode fiber and the output-spectra were recorded on a spectrometer.

A typical result is presented in figure 1. For increasing but relatively low power, the probe is spectrally shifted by cross-phase modulation in the conventional way. However, above a certain pump-power threshold, a new signal rapidly builds up at a much longer wavelength. In fact, this results in a much increased spectral shift, along with a parametric amplification of the probe.

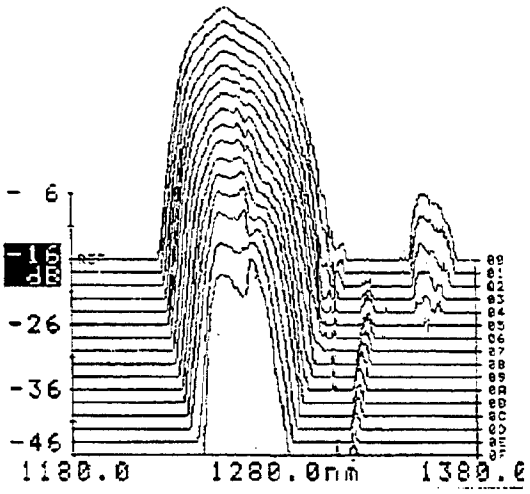


Figure 1: Experimental demonstration of frequency-jump.

Simulations We have simulated the propagation of the pump-probe pulse pair using the nonlinear Schrödinger equation:

$$i\frac{\partial A}{\partial z} = \frac{\beta_2}{2}\frac{\partial^2 A}{\partial t^2} + \frac{i\beta_3}{6}\frac{\partial^3 A}{\partial t^3} - \kappa|A|^2 A$$

where we have included dispersion up to third order but neglected stimulated Raman-scattering and self-steepening. The equation was solved numerically using the split-step Fourier-method. By solving one single NLSE for the entire spectral and temporal domain of interest, no assumptions need to be made regarding phase-matching, group-velocity matching and pulse walk-off. Typical results are presented in figure 2. As can be seen, the agreement with experimental data was good.

By varying the pump-amplitude, time-delay and relative phase between the pump and the probe, the origin of the frequency-jump could be determined. For low pump-intensities, only the XPM-induced spectral shift is observed. This shift is insensitive to the phase, but very dependent on the time-delay between the pulses in terms of size and direction (red or blue). For a FWM-process, on the other hand, the time-delay is only important in terms of interaction length, while the relative phase is a very important parameter. By analyzing the behaviour of the frequency-jump when we varied the time-delay and the phase, we could conclude that the jump is indeed caused by a FWM-process. Apart from this, it was noted that the new signal always was group-velocity matched with the peak wavelength of the pump.

Theoretical studies FWM is usually studied in terms of four coupled equations; one for each frequency taking part in the process [4]. One is then forced to assume that the spectra do not overlap. When using femto-second pulses, with their much larger spectral width, this assumption is no longer valid, and the pulse dynamics must rather be regarded as a redistribution of energy within a quasi-continuous spectrum, formed by simultaneous as well as cascaded FWM-processes.

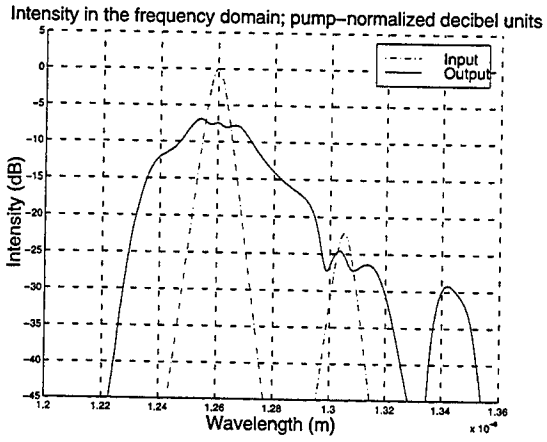


Figure 2: Numerical simulation of the frequency-jump, showing fiber input and output

Some qualitative understanding of the dynamics can still be obtained from the results for longer pulses. For degenerated FWM, optimum phase-matching can be achieved if the pump is slightly shifted from the zero-dispersion wavelength. This makes it reasonable to assume that the most important FWM-process in our case is a degenerated process with the probe serving as a "pseudo-pump", while the jump-frequency wave and the original pump-wave are playing the parts of Stokes and anti-Stokes waves respectively. In this situation, one of the sidebands is much larger than the pseudo-pump and the other sideband. By analyzing the resulting system with respect to phase- and group-velocity matching we infer that the probe pulse must indeed have a wavelength close to the zero-dispersion wavelength. The pseudo-pump is also boosted by contributions from the spectral broadening of the pump, analogous to the case of spectral splitting [1]. We infer that the process is more efficient when the second- and third-order dispersion terms are such that the low-frequency band of the splitted spectrum appears at the jump-frequency. A theoretical model is presently being developed to describe the main features of the FWM process responsible for the appearance of the new signal at the jump-frequency.

Conclusions The present experimental and numerical results demonstrate a new phenomenon of spectral shifting of a weak signal pulse by FWM involving a high-intensity femtosecond pump-pulse close to the zero-dispersion wavelength. Simulations of the nonlinear Schrödinger equation including third order dispersion give good agreement with the experimental results.

References

[1] V. P. Yanovsky and F. W. Wise, Opt. Lett. **19**, 19, 1547 (1994)

[2] G. R. Boyer, M. A. Franco, M. Lachgar, B. Grèzes-Besset and A. Alexandrou, J. Opt. Soc. Am. B, **11**, 8, 1453 (1994)

[3] G. R. Boyer, G. Kononovitch, Optics Comm. **133**, 205 (1997)

[4] Y. Chen, J. Opt. Soc. Am. B, **6**, 11, 1986 (1989)

Modulational instability in optical fibers with polarization mode dispersion

F. Kh. Abdullaev
Physical-Technical Institute of the Uzbek Academy of Sciences,
G. Mavlyanov str. 2-b, 700084, Tashkent, Uzbekistan
J. Garnier
Centre de Mathématiques Appliquées, Ecole Polytechnique, 91128 Palaiseau Cedex, France
E. Seve and S. Wabnitz
Laboratoire de Physique de l'Université de Bourgogne,
avenue Alain Savary , B.P. 47 870, 21078 Dijon Cedex, France

As is well known, the interplay between optical Kerr effect and chromatic dispersion leads to the phenomenon of modulational instability (MI) of light waves [1]. Such instability, also called Benjamin-Feir instability, occurs in different physical environments : plasmas, fluids, solid-state lattices, electrical circuits and nonlinear optics. MI leads to the breakup of a cw or quasi-cw beam into a train of ultrashort pulses and it can be used to generate a train of soliton-like pulses [2]. MI also sets a fundamental nonlinear limiting factor in the transmission of dense wavelength-division multiplexed signals in long-distance fiber links.

All these results were obtained by deterministic models. In realistic fiber transmission links, the chromatic dispersion, nonlinearity and birefringence are not constant but can fluctuate stochastically around a constant value. In this work we will study MI in fibers with random birefringence. In the model we adopted to treat random birefringence, the orientation of the principal axes is taken as constant but their magnitude varies randomly with distance. This simplified model has the advantage of leading to exact solutions for the linear stability analysis of plane waves. The evolution of the polarized fields in randomly birefringent fibers is ruled by a modified vector nonlinear Schrödinger system with a random group velocity mismatch or polarization mode dispersion (PMD) between the two modes [3-4]

$$iu_z + i\Delta(z)u_t + \beta u_{tt} + \left(|u|^2 + \alpha\,|v|^2\right) u = 0, \tag{1}$$

$$iv_z - i\Delta(z)v_t + \beta v_{tt} + \left(|v|^2 + \alpha\,|u|^2\right) v = 0. \tag{2}$$

Here standard dimensionless variables are used. The group velocity dispersion coefficient β is equal to 1 or -1, for the anomalous and normal dispersion regime, respectively. $\Delta(z)$ is the sum of a constant term Δ_0, and a white Gaussian-distributed noise

$$\langle\Delta(z)\rangle = \Delta_0, \quad \langle(\Delta(z) - \Delta_0)(\Delta(z') - \Delta_0)\rangle = 2\sigma^2\delta(z - z'). \tag{3}$$

The standard linear stability analysis of MI consists in perturbing the stationary solution of the nonlinear Schrödinger equations [1]. In our notation, we write a perturbed plane wave as

$$u(z,t) = (A + u_1(z,t))e^{i\left(A^2+\alpha B^2\right)z}, v(z,t) = (B + v_1(z,t))e^{i\left(B^2+\alpha A^2\right)z}. \tag{4}$$

One obtains a linear system of equations for u_1 and v_1 ; using the complex representation, $u_1 = \bar{c}+i\bar{d}$, $v_1 = \bar{e} + i\bar{f}$ and performing the Fourier transform $c = \int \bar{c}e^{-i\omega t}d\omega$, we obtain a differential system $\frac{dq}{dz} = Q(z)q$ with $q = (c, d, e, f)^t$. This ODE system describes the evolution of the amplitude of the perturbation along the fiber. The eigenvalues of the associated matrix Q give the MI gain. Unlike the deterministic case, the perturbation matrix is no longer constant but varies randomly with distance. The study of the first moments of the perturbations is not sufficient to determine stability

in the random case. Indeed, the MI gain for the average values of the perturbation coefficients is simply reduced, owing to the presence of random phases of the kind $\exp(\pm i\omega\sigma\int_0^z \Delta(y)dy)$ that multiply the coefficients c, d, e, and f, so that their expectation values decay exponentially along the fiber. It is therefore necessary to consider the moments of the moduli $|c|^2$, $|d|^2$, $|e|^2$ and $|c|^2$. By applying the Furutzu-Novikov formulae [5], one obtains a 16-dimensional differential system $\frac{dr}{dx} = Rr$ where r is a row vector whose elements are $\langle|c|^2\rangle$, $\langle|d|^2\rangle$, $\langle|e|^2\rangle$, $\langle|f|^2\rangle$, and the real and imaginary parts of $\langle c^*d\rangle$, $\langle c^*e\rangle$, $\langle c^*f\rangle$, $\langle d^*e\rangle$, $\langle d^*f\rangle$ and $\langle e^*f\rangle$, while R is a 16×16 dimensional matrix. Simple analytical formulae for the MI gain can be found for $\sigma \ll 1$ or $\sigma \gg 1$. In the general case, the MI gain can be evaluated by computing the eigenvalues of the stability matrix R through a numeric manipulation package. The left part of figure 1 shows MI gain curves for the anomalous dispersion ($\beta = 1$) case, different average PMDs and standard deviations σ. When the average PMD is zero, the MI region is enhanced so that all frequencies are unstable as soon as $\sigma^2 > 0$. Nevertheless, the MI peak gain is reduced with respect to the deterministic case. We find that the MI gain peak is equal to $2(1+\alpha)A^2$ when $\sigma = 0$, and it decays to $2A^2$ as σ goes to infinity.

Consider now the case $\Delta_0 > 0$. When $\Delta_0 < \alpha A^2$, MI is present for all sideband frequencies, but the peak gain is reduced and converges to $2|\omega|\sqrt{2A^2 - \omega^2}$ (which is the MI gain corresponding to the case $\alpha = 0$). Finally, if $\Delta_0 > \alpha A^2$ and $\sigma = 0$, the MI gain consists of a first peak at low frequencies and a second peak which lies close to Δ_0. When taking into account PMD fluctuations, the second peak is strongly reduced and ultimately it disappears for large σ, while the first peak converges to $2|\omega|\sqrt{2A^2 - \omega^2}$.

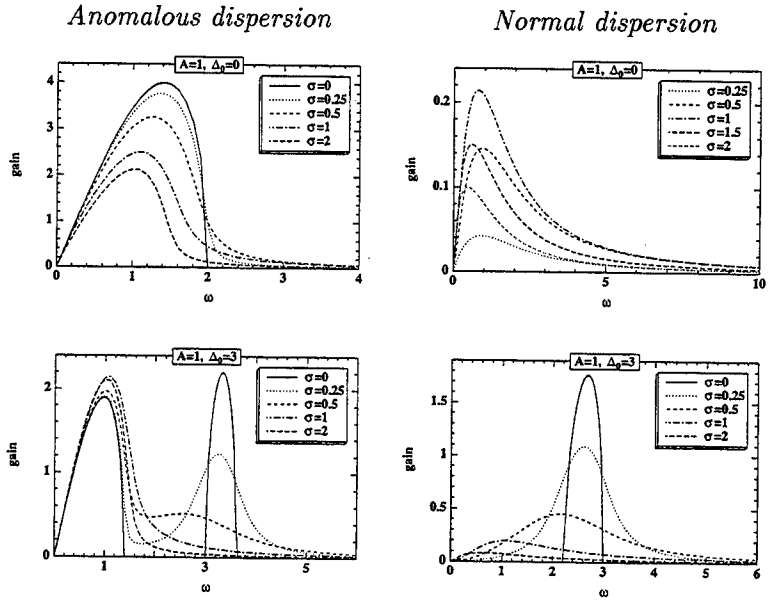


Figure 1: *MI gain vs frequency for anomalous ($\beta = 1$) and normal dispersion ($\beta = -1$), $\alpha = 1$ and different average PMD Δ_0 and standard deviation σ.*

The right part of figure 1 displays the gains in the normal dispersion ($\beta = -1$) case. Whenever the PMD between the fields is identically zero (i.e. $\Delta_0 = 0, \sigma = 0$), there is no MI in the normal dispersion [1]. Nevertheless, if the group velocities are randomly mismatched (i.e., $\sigma > 0$), one finds that MI is present, and even that all frequencies are unstable! With increasing σ, the MI peak gain first grows larger, then it reaches a maximum for some particular σ_0 which depends on α, but not on the power A^2. For $\alpha = 1$, one finds that $\sigma_0 = 0.85$. For deviations larger than σ_0, the gain

decays to zero. When $\Delta_0 \neq 0$, deterministic MI occurs for frequencies between $\sqrt{\Delta_0^2 - 2(1+\alpha)A^2}$ and $\sqrt{\Delta_0^2 - 2(1-\alpha)A^2}$. Whenever the PMD fluctuations increase, all frequencies are unstable but the peak gain decays to zero. For large σ, one gets the same behavior as for $\Delta_0 = 0$, whatever Δ_0.

Above mentioned results were obtained by means of the linear stability analysis of Eqs(1-2). To check the validity of the results we performed the numerical experiments by directly solving the system (1-2) with a randomly varying PMD $\Delta(z)$. The simulations were done using the split-step Fourier method. The discrete value of the deviation σ is $\sigma_{dis} = \sigma/\sqrt{dz}$, where dz is the z step. The initial condition was $u_1, v_1 = \varepsilon \exp(-i\omega t) + \varepsilon \exp(i\omega t)$, with $\varepsilon = 10^{-4}$. The number of points in the time domain was 256 and the z step is a small fraction of the propagation length ($dz = L/200$). The value of Δ was randomly changed after each step since we have considered a white Gaussian-distributed noise.

The results of the numerical simulations in the *anomalous* and *normal* dispersion regimes are presented in the left and right part of Fig. 2, respectively. In both cases, the analytic stability analysis (solid curves) predicts the extension of the spectral width of the MI gain, which leads to instability for all frequencies of modulations. These predictions are well confirmed by the numerical simulations in all cases (stars) : note the quantitative agreement with the numerically calculated MI gain values.

The PMD induced extension of MI to a broad range of wavelengths around the pumps both in the normal and anomalous dispersion regime, that we discovered in this work, may have interesting implications to the stability of fiber transmissions, in particular when operating close to the zero dispersion wavelength or whenever dispersion compensation techniques are employed.

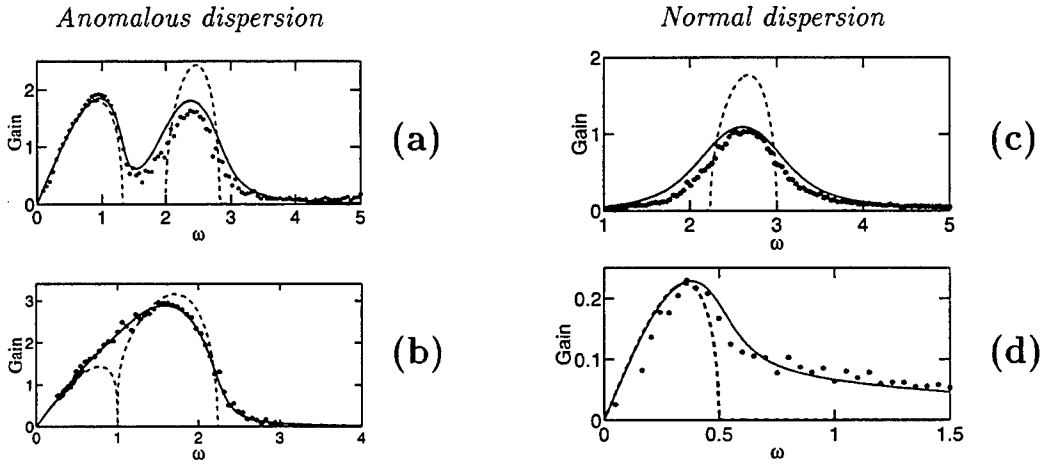


Figure 2: *Gain curves for $\beta = 1$ (a, b) and $\beta = -1$ (c, d). $A = 1$ and $\sigma = 0.25$ for both cases. Δ_0 2 (a), 1 (b), 3 (c) and 0.5 (d). The stars represents the MI gain obtained with the simulation of system (1-2), the solid curve is from linear stability analysis ; the dashed curve is the deterministic gain curve (i.e., with $\sigma = 0$).*

References

[1] G.P. Agrawal, Nonlinear fiber Optics, 2nd Edition, 1995 and references therein.
[2] G. Millot, E. Seve, S. Wabnitz et M. Haelterman, J. Opt. Soc. Am. B., 15, 1266 (1998)
[3] Yu. S. Kivshar and V. V. Konotop, Sov. J. Quantum Electron. **20**, 1495 (1990).
[4] T. I. Lakoba and D. J. Kaup, Phys. Rev. E **56**, 6147 (1997).
[5] E. A. Novikov, Sov. Phys. JETP **20**, 1290 (1965) [Zh. Eksp. Teor. Fiz. **47**, 1919 (1964)].

Optimized design of a fiber-based pulse compressor for gain-switched DFB laser pulses at 1.5 μm

L. P. Barry
School of Electronic Engineering, Dublin City University, Dublin 9, Ireland.
barryl@eeng.dcu.ie

B. C. Thomsen, J. M. Dudley and J. D. Harvey
Department of Physics, University of Auckland, Private Bag 92019 Auckland, New Zealand
bct@phy.auckland.ac.nz, j.dudley@auckland.ac.nz, j.harvey@auckland.ac.nz

The development of future Terabit all-optical communication systems exploiting Optical Time Division Multiplexing (OTDM) will require stable laser sources around 1.55 μm producing transform-limited sub-picosecond pulses [1]. A simple and reliable technique for pulse generation around 1.55 μm is the gain-switching of semiconductor laser diodes. Although the pulses generated using this technique are usually heavily chirped, and have durations exceeding 10 ps, it has been shown that near-transform limited sub-picosecond pulses can be obtained after fiber-based pulse compression [2]. Although many different fiber-based compression schemes have been proposed [3-5], the design of such compressors is usually only approximate. Typically, a simple model of the gain-switched pulses assuming symmetric gaussian profiles with a linear chirp is used to determine initial approximate lengths for the fiber used in the pulse compressor. This is then followed by trial-and-error length optimization to obtain the best experimental compression [2].

It is clear that the generation of transform-limited sub-picosecond pulses from gain-switched lasers would be greatly simplified if the design of fiber pulse compressors could be performed in a systematic manner without *a priori* assumptions about the nature of the initial pulse characteristics, or the time-consuming process of trial-and-error optimization. In this paper we report a systematic approach to fiber compressor design based on the complete intensity and phase characterization of the initial gain-switched laser pulses using the technique of frequency-resolved optical gating (FROG) [6]. The complete characterization of the electric field of the laser pulses allows the precise design of a fiber pulse compressor using numerical simulations based on the nonlinear Schrödinger equation (NLSE). We have recently demonstrated the utility of FROG for gain-switched pulse characterization, and suggested its use in compressor design [7], and in the paper we present experimental verification of the use of FROG for this purpose. We report results showing the compression of initially-chirped 10 ps pulses to near chirp-free 800 fs pulses.

Figure 1 shows the experimental set up for pulse generation and compression. The laser source was a distributed feedback (DFB) laser with an operating wavelength of 1538 nm, a threshold current of 24 mA, and a 10 GHz modulation bandwidth. The laser was biased below threshold at 5 mA, and gain-switched at a repetition rate of 500 MHz using electrical pulses from a step recovery diode. The electrical pulses had a duration of 80 ps and an amplitude of 13 V. The intensity and phase of the DFB laser pulses were characterized using spectral and autocorrelation measurements, as well as a second-harmonic generation FROG set-up [6].

The gain-switched pulses are compressed in a two-stage fiber compressor. Firstly, dispersion compensating fiber (DCF) compensates for the linear part of the intrinsic negative chirp on the DFB laser pulses to generate near-transform-limited pulses with average power around 140 μW. Secondly, these pulses are amplified in an erbium doped fiber amplifier (EDFA) to an average power level of around 7 mW and injected into a nonlinear compression stage containing both dispersion shifted fiber (DSF) and standard single mode fiber (SMF). The propagation in the DSF is governed by the interplay of self-phase modulation and a small normal dispersion. This leads to temporal and spectral broadening, and the development of a large positive chirp across the pulse center. The large

chirp developed in the DSF is then compensated in the SMF leading to a chirp-free compressed output pulse. We note that this method of nonlinear compression is advantageous when compared to soliton compression schemes as it does not require a threshold input intensity, and leads to comparable levels of compression with only modest levels of pre-amplification. To optimize the compressor, NLSE simulations were used to propagate the fully characterized initial DFB pulses through various lengths of DCF, DSF and SMF in order to determine the lengths required to obtain the shortest possible output pulse with the minimum amount of low amplitude pedestal structure.

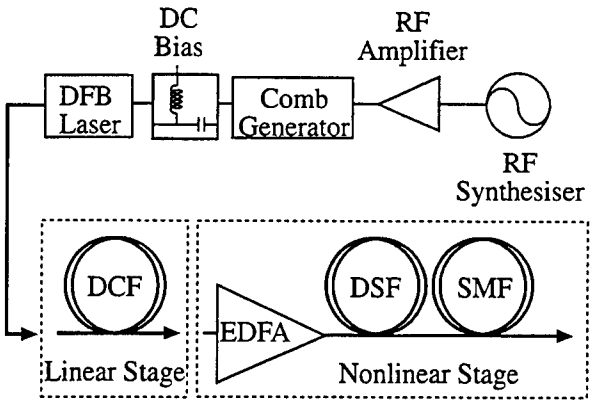


Figure 1. Experimental set-up used for pulse generation and compression.

Figure 2 presents NLSE simulation results showing the optimal evolution of the initially chirped DFB pulses. The optimum fiber lengths were found to be: 75 m of DCF (D =-102.5 ps/nm/km, γ = 2 $W^{-1}km^{-1}$), 1.3 km of DSF (D =-0.6 ps/nm/km, γ = 2.3 $W^{-1}km^{-1}$) and 80 m of SMF (D =16.0 ps/nm/km, γ = 1.1 $W^{-1}km^{-1}$). The parameters D and γ in each case are the fiber dispersion and nonlinearity parameters respectively. The effect of the 6 m long EDFA was also included in the simulations but at the amplification levels in our experiments, its effect on the pulse duration and chirp characteristics was found to be negligible.

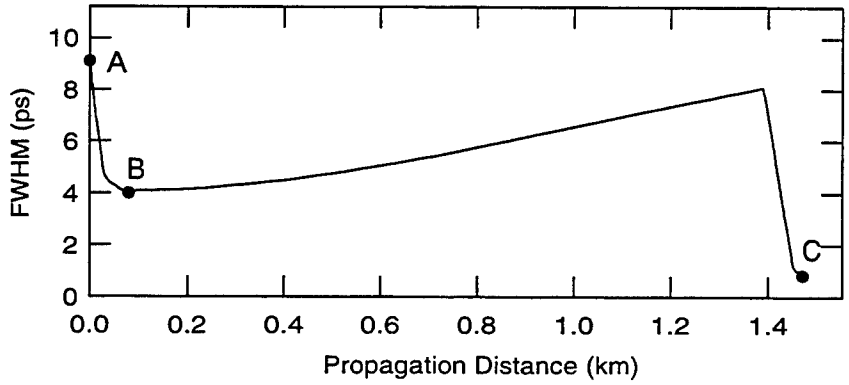


Figure 2. Evolution of pulse FWHM in the pulse compressor. Point A corresponds to the input pulse while B and C correspond to the outputs of the DCF and SMF respectively.

With the compressor designed according to the simulation results, FROG measurements were used to measure the intensity and chirp of pulses at three different points in the compressor in order to verify the accuracy of the numerical design procedure. These results are shown in Figure 3. Figure 3(a) shows the initially chirped pulse from the DFB with a FWHM $\approx$ 9 ps. The pulse in Figure 3(b) was measured after linear compression in the DCF, and it is clear that the chirp is significantly reduced, and the pulse is compressed by around a factor of 2 with a FWHM $\approx$ 4.5 ps. The solid and dashed

lines in Figure 3(c) show the intensity and chirp of the pulse after the nonlinear compression stage. This stage results in a further factor of 6 compression with the final output pulse having a FWHM ≈ 800 fs. It is important to note that these output pulses are essentially chirp-free across the pulse center. The residual pedestal structure is due to uncompensated nonlinear chirp. To illustrate the accuracy of our numerical design procedure, the circles in Figure 3(c) show the expected output pulses obtained from the NLSE propagation of the input pulse through the compressor. It is clear that there is excellent agreement.

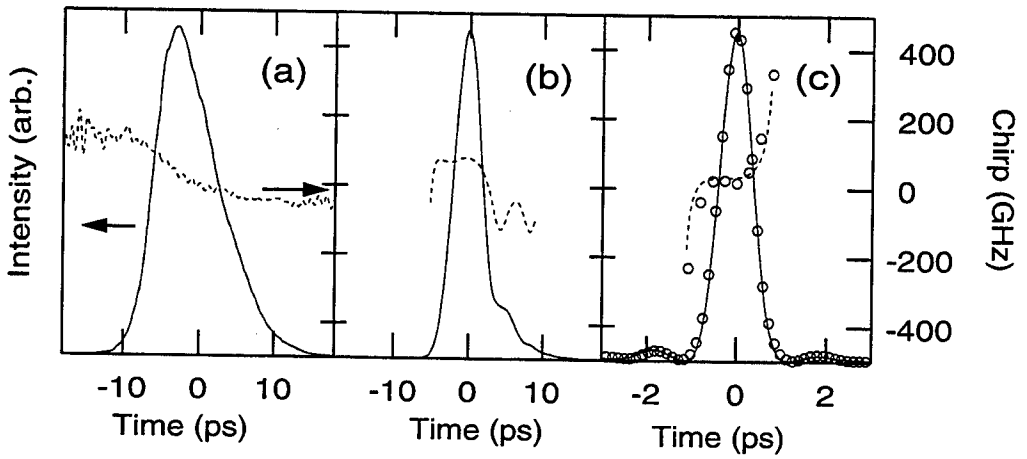


Figure 3. Intensity (solid line, left axis) and chirp (dashed line, right axis) of (a) initial DFB pulse, (b) pulse after the linear stage in DCF, and (c) pulse after the nonlinear stage in DSF and SMF The circles in (c) show the expected pulse characteristics from the NLSE simulations. The chirp is only plotted over regions of significant intensity.

In conclusion, we have shown that the complete intensity and phase characterization of DFB laser pulses using FROG allows the precise optimization of a multi-stage fiber pulse compressor via NLSE simulations. We have presented experimental results using a compressor design optimized for high compression factors and minimal pedestal structure in order to obtain output pulses suitable for telecommunications applications. From initially chirped 9 ps pulses generated from a DFB laser, we obtain chirp-free 800 fs pulses. We expect that this method of compressor design will find wide application in optimizing other forms of pulse compressor based on fiber Bragg gratings, fiber loop mirrors or dispersion decreasing fiber.

References

[1] S. Kawanishi, IEEE J. Quant. Electron. **35**, 2064-2079 (1998).
[2] L. Chusseau and C. Kasmierski, IEEE Photon. Technol. Lett. **6**, 24-26 (1994).
[3] I.Y. Khrushchev, I.H. White, and R.V. Penty, Electron. Lett. **34**, 1009-1010 (1998).
[4] B. Satorius, C. Bornholdt, O. Brox., M. Mohrle, P. Brindel, O. Leclerc, and E. Desurvire, Electron. Lett. **34**, 2344-2345 (1998).
[5] M. D. Pelusi, Y. Matsui and A. Suzuki, Electron. Lett. **35**, 61-63 (1999).
[6] K. W Delong, R. Trebino, J. Hunter and W. E. White, JOSA B **11**, 2206-2215 (1994).
[7] L. P. Barry, B. C. Thomsen, J. M. Dudley and J. D. Harvey, IEEE Photon. Technol. Lett. **10**, 935-937 (1998).

Observation of isotropic polarization modulational instability in spun fibers

Pascal Kockaert and Marc Haelterman

Service d'Optique et d'Acoustique, Université Libre de Bruxelles, CP 194/5
50 Av. F. D. Roosevelt, B-1050 Brussels, Belgium
Pascal.Kockaert@ulb.ac.be, Marc.Haelterman@ulb.ac.be

Modulational instability (MI) in optical fibers is a spontaneous four wave mixing process in which phase-matching is automatically achieved through the compensation of chromatic dispersion by Kerr nonlinearity. Self-phase modulation in silica results from a positive Kerr effect and can therefore be compensated only in the anomalous dispersion regime. However, if the polarization of light is taken into account, cross-phase modulation enters into play allowing MI to appear in the normal dispersion regime. In this case, MI is called Polarization MI (PMI) because it alters the state of polarization. The existence of MI in the normal dispersion regime was predicted by Berkhoer and Zakharov (BZ) [1] as early as in 1970 but has never been, up to now, the object of a direct experimental demonstration. The main experimental obstacle was to satisfy the basic assumption of isotropy of the Kerr medium. However, as shown by Wabnitz [2], PMI can also occur in birefringent fibers, but in this case birefringence plays an essential role in the phase matching condition, leading to physical behaviors that can be very different from those predicted in the framework of BZ's theory (PMI due only to dispersion and nonlinearity). Several experiments [3, 4] in birefringent fibers have indeed confirmed that birefringence in the phase matching condition induces different behaviors between light polarized along the fast and the slow axis. Recently, several attempts have been performed in order to confirm BZ's theory by means of other physical systems such as the bimodal fiber proposed by Millot *et al.* [5].

We performed the first observation of BZ's predictions using a specially designed (spun) fiber having a residual birefringence of less than 10^{-8}, which makes the fiber effectively isotropic because this birefringence is so low that it is negligible against the Kerr nonlinearity at readily accessible optical powers. The experimental setup consists essentially in a Nd:YAG laser emitting pulses (230 ps, 1064 nm) which are injected in the spun fiber. This fiber has a total length of 50 m and is wounded with a radius of curvature of 25 cm so that the induced birefringence is negligible ($< 10^{-8}$). Before the injection, various wave plates allow to control the input state of polarization, while a quarter wave plate and a polarizer at the output of the fiber allow for the selection of one polarization component before the spectral measurement.

Using this setup, we have checked all BZ's predictions about PMI. The most remarkable result is the verification that PMI appears with the same gain for all orientations of the linear input state of polarization [see Fig. 1(a)]. This result proves that residual birefringence has negligible effects on the four-wave-

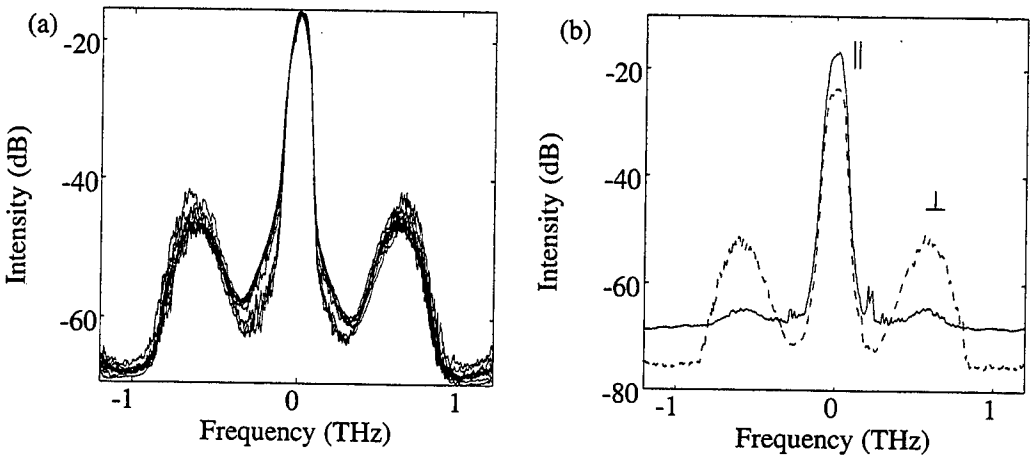


Figure 1: Spectra recorded at the fiber output for an input peak power of 120 W. (a) Total power spectra recorded for an input linear polarization angle varying by steps of 10° over 90°. (b) Power spectra in the polarizations parallel (||) and orthogonal (⊥) to that of the pump.

mixing process underlying PMI. The fiber can therefore be considered as being isotropic.

This result is confirmed by the analysis of both polarizations at the output of the fiber. Fig. 1(b) shows that the sidebands appear in the polarization orthogonal to the pump. The small depolarization (about 1% in intensity) is already present before the injection of light in the fiber and is due to the imperfections of the polarizing components. In accordance with the theory, we verified that the PMI gain, $G_{\mathrm{PMI}} \propto 1-2\sqrt{1-3/4q^2}$, decreases when the ellipticity (q) of the polarization state increases. Fig. 2(a) shows this evolution. We see, in particular, that the PMI gain vanishes for a circular polarization state.

In addition to these spectral measurements, we have recorded an autocorrelation trace of the output signal [see Fig. 2(b)], which is in excellent agreement with the theory [see Fig. 2(c)]. We are currently planning the measurement of the temporal pulse profiles by means of a phase and amplitude retrieval technique. We expect from these measurements the observation of polarization domain-wall structures that are reminiscent of the fundamental vector soliton associated with PMI, i.e., the so-called polarization-domain wall soliton.

All these results show that we obtained effective isotropy in a spun fiber over a distance as long as 50 m, which suggests that this fiber is suitable for the study of other phenomena requiring an isotropic Kerr media, like the polarization domain-wall solitons [6], the rotating elliptically polarized bright soliton [7] and the vector soliton bound states [8], as well as their applications in the field of data transmission and all-optical signal processing in fiber.

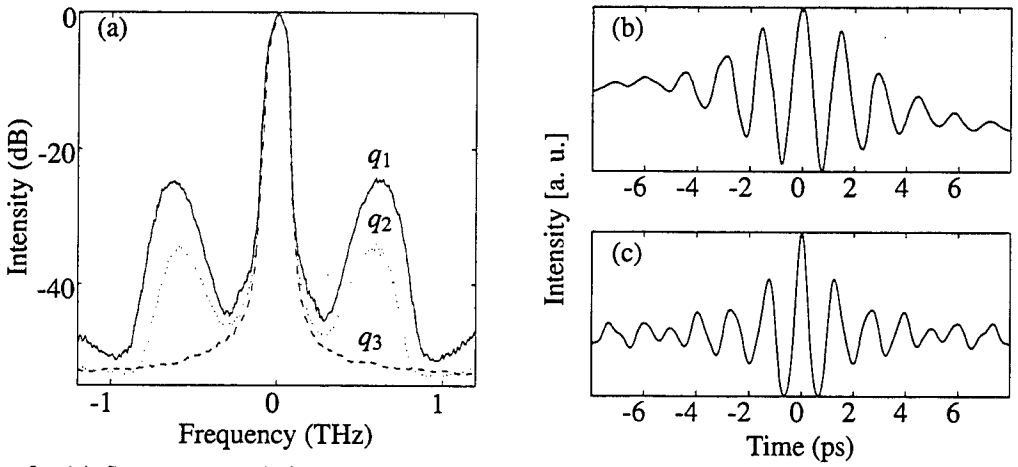


Figure 2: (a) Spectra recorded at the output of the fiber when the ellipticity (q) is increased ($q_1 = 0$, $q_2 \approx 0.4$, $q_3 = 1$). (b) Experimental and (c) theoretical autocorrelation traces. In all cases, the input peak power is of 120 W.

References

[1] A. L. Berkhoer and V. E. Zakharov, *Sov.Phys. JETP* **31**, 486 (1970).

[2] S. Wabnitz, Phys. Rev. A **38**, 2018 (1988).

[3] P. Tchofo Dinda, G. Millot, E. Seve and M. Haelterman, *Opt. Lett.* **21**, 1640 (1996).

[4] S. G. Murdoch, R. Leonhart and J. D. Harvey, *Opt. Lett.* **20**, 866 (1995).

[5] G. Millot, S. Pitois, P. Tchofo Dinda and M. Haelterman, Opt. Lett. **22**, 1686 (1997).

[6] M. Haelterman and A. P. Sheppard, *Phys. Rev. E* **49**, 3389 (1994).

[7] M. Haelterman and A. P. Sheppard, *Phys. Rev. E* **49**, 3376 (1994); Y. Silberberg and Y. Barad, *Opt. Lett.* **20**, 246 (1995).

[8] P. Kockaert and M. Haelterman, J. Opt. Soc. Am. B , (In press) (1999).

Fiber optical parametric amplifier with 120 nm bandwidth

M.-C. Ho, M. E. Marhic, Y. Akasaka[a], F. S. Yang, and L. G. Kazovsky
Department of Electrical Engineering, Stanford University
203 Durand Bldg. MC9515, Stanford, CA 94305
Phone: 650-723-1382, Fax: 650-723-9251, E-mail: mcho@wdm.stanford.edu
[a]on leave from Furukawa Electric Co., Ltd., JAPAN

INTRODUCTION

Several techniques have recently been studied for making optical amplifiers with bandwidths exceeding the 35 nm available with conventional EDFA's. They include: dual-band silica EDFA's[1]; tellurite EDFA's[2], possibly assisted by Raman gain; Raman amplifiers with multiple pumps[3]. We have shown that fiber optical parametric amplifiers (OPA's) can in principle exhibit gain over several hundred nanometers, if they are made from high-nonlinearity fibers, and use a few Watts of pump power[4]. In a previous experiment with a conventional dispersion-shifted fiber (DSF), we measured gain over a 35 nm bandwidth, limited by an EDFA used for the measurement[4]. Here we report on measurements performed on a fiber OPA made from a high-nonlinearity fiber, with 11W pump power. We have measured gain in excess of 12 dB over a 120 nm bandwidth (limited by the signal lasers available); to our knowledge this is the largest bandwidth obtained to date with a fiber amplifier of any kind.

With this wide bandwidth, the Raman gain due to the pump may not be negligible; therefore, we have also performed a separate measurement of the Raman gain to ascertain whether it played a role in our measurements.

EXP#1 – OPA GAIN MEASUREMENT

The gain medium used in this demonstration is a high-nonlinearity fiber (NLF) provided by Furukawa Electric. The parameters of this NLF are: zero dispersion wavelength λ_0 = 1540 nm, dispersion slope D_λ = 0.031 ps nm^{-2}km^{-1}, nonlinear coefficient γ = 18 km^{-1}W^{-1}, fiber length L = 40 m, and $\beta_4 = -1.5\times10^{-55}$ s^{4}m^{-1}. The nonlinear coefficient of this NLF is nine times that of DSF, while the dispersion slope is smaller than half of DSF's. Both characteristics make this fiber suitable for wideband amplification. Theory predicts net gain over 200 nm.

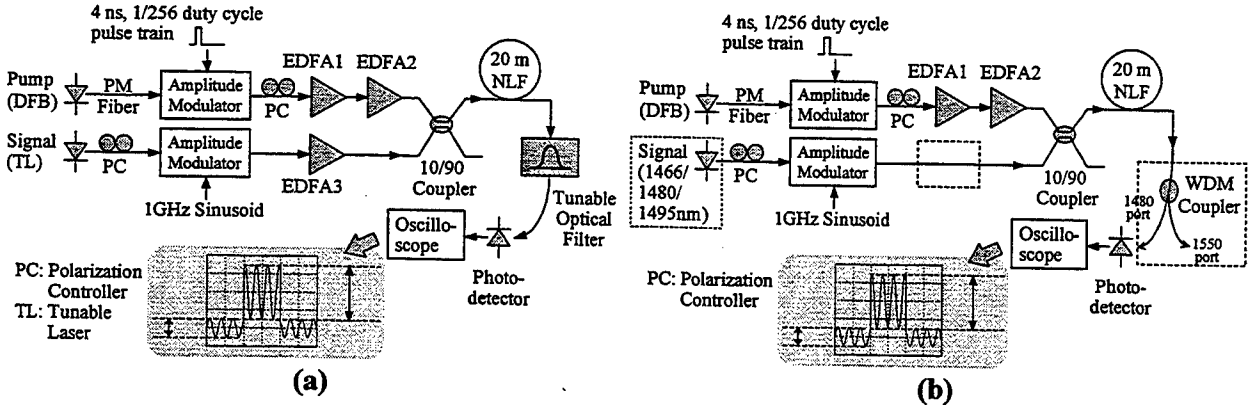


Figure 1: Experimental Setup for measuring OPA gain (a) from 1535nm to 1587nm; (b) at 1466, 1480, and 1495 nm. Differences are enclosed in dashed lines.

Two experimental setups used for this pulsed OPA demonstration are shown in Figure 1 (a) and (b). For wavelengths from 1535nm to 1587nm, Figure 1(a) is used. In this setup, a DFB laser with λ_p = 1542 nm is used as the pump. The pump is modulated by a train of 4 ns square pulses with duty cycle of 1/256, using a Mach-Zehnder modulator. This provides a high peak pump power of 11W at the output of EDFA2. A tunable laser (TL) generates the signal, which is externally modulated at 1GHz to allow AC gain measurements. EDFA3 is used to compensate the loss due to the Mach-Zehnder modulator and the 10/90 coupler. The signal power at the input of the NLF is approximately 0 dBm. Tunable optical filters in series are used to extract the signal and suppress the pump at the output of the NLF. The gain is measured by comparing the AC amplitude of the signal during the 'on' and 'off' portions of the pump pulses, as shown at the bottom of Figure 1(a). The range of measurement is mainly limited by the tuning range of the available tunable filter.

The setup used to measure OPA gain at three discrete wavelengths - 1466, 1480, and 1495 nm is shown in Figure 1(b). It is similar to Figure 1(a) except for the filter in use, and the absence of EDFA3. The filter in the second setup is a WDM coupler normally used to separate EDFA 1480 nm pump from signal. EDFA3 is removed because EDFA absorbs signal around 1480 nm rather than amplify it. Fortunately, the three discrete laser sources have enough power to compensate the loss due to the Mach-Zehnder modulator and the 10/90 coupler. The input signal power to NLF is again maintained around 0 dBm.

EXP#2 – RAMAN GAIN MEASUREMENT

To estimate Raman gain in this nonlinear fiber, the following experiment is conducted. The experimental setup is shown in Figure 2. The Raman gain was measured under cw conditions, by using a low power pump. In this manner the OPA gain was confined to a small bandwidth near the pump, and the Raman gain could be measured very clearly. A 1.9 km NLF, from which the 20 m NLF is cut, is used as the gain medium. Furukawa High Power Pumping Unit (HPU) is used as the pumping source. HPU consists of five pumping diodes, but only two 1480 nm diodes are used in this experiment. The wavelength is chosen to be far away (~60 nm separation) from λ_0, so that OPA gain is negligible in this measurement. The two diodes are polarization-combined to avoid polarization-dependent gain. However, a polarization controller is still inserted in the signal path to ensure maximum gain is obtained. The input power to NLF is 107 mW after subtracting connector and splice loss. The net gain is measured by comparing the output signal power in the optical spectrum analyzer, with and without pumping signal.

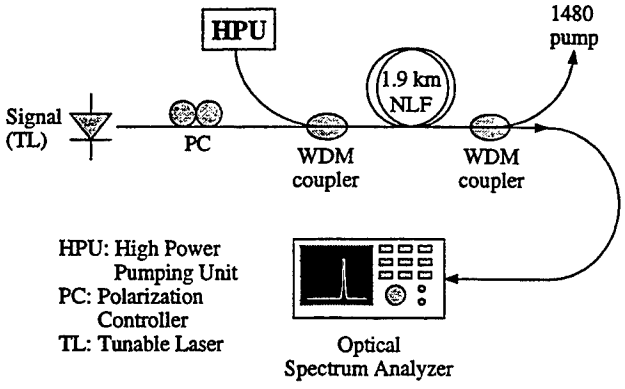


Figure 2: Experimental Setup for measuring Raman gain in NLF.

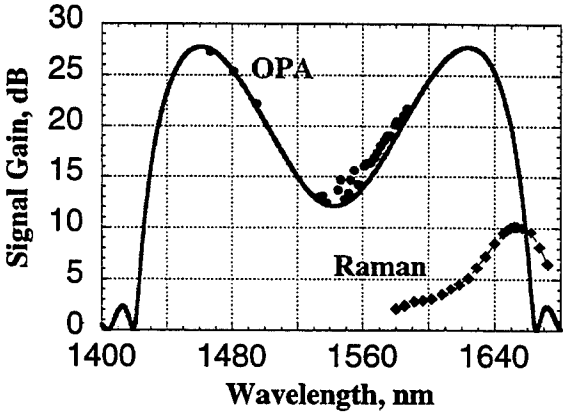


Figure 3: Results of exp#1 and exp#2.

RESULTS AND DISCUSSIONS

The results of the pulsed OPA demonstration are shown in Figure 3. The solid line is a theoretical plot, and the dots are experimental data. From the plot, we see that the experimental results match well with the theoretical curve, except for points near the pump wavelength. This is because filtering out pump power as well as EDFA ASE is difficult in that region. The Raman gain curve obtained in exp#2 is converted to parameters equivalent to those used in exp#1, i.e. 1542 nm pump wavelength, 11 W pump power, and 20 m NLF. In this manner we have the Raman gain as if we had measured it under the same conditions as the OPA gain. The result is plotted in the same figure as OPA gain. The diamond dots are experimental results, while the dashed line is a curve fit to smoothly connect data points. From Figure 3, we see that the Raman gain peak is 17.5 dB smaller than the OPA gain peak, and offset from it by 30 nm. This implies that within the measurement range (1535-1587nm), the Raman gain, which is less than 2.5 dB, is negligible compared to the OPA gain, larger than 12 dB. A similar conclusion holds for our OPA gain measurements at 1466, 1480, and 1495 nm. Hence, the 120 nm gain bandwidth that we have measured is entirely attributable to OPA gain.

CONCLUSION

We have measured gain in excess of 12 dB over 120 nm, for a fiber OPA with a theoretical bandwidth of about 200 nm. This work confirms that fiber OPA's may provide a means for making very broadband amplifiers (as well as wavelength converters) for future optical communication systems.

REFERENCES

[1] Y. Sun et al., "A Gain-Flattened Ultra Wide Band EDFA for High Capacity WDM Optical Communications Systems," ECOC'98 pp. 53-54.

[2] M. Yamada et al, "Gain-Flattened Tellurite-Based EDFA with a Flat Amplification Bandwidth of 76nm," OFC'98 PD pp. 71-74.

[3] K. Rottwitt and H.D. Kidorf, "A 92 nm Bandwidth Raman Amplifier", OFC'98 PD pp. 61-64.

[4] M.E. Marhic et al., ""Broadband Fiber Optical Parametric Amplifiers," Optics Letters, 21, pp. 573-575, 1996.

Nonlinear Guided Waves and Their Applications

Localized Structures in Optical Cavities

Wednesday, 1 September 1999

J.R. Tredicce, University of Nice, France
Presider

WC
13.30-15.00
Salle Morey—St-Denis

Spatial solitons in a single-mirror feedback system

B. Schäpers, M. Feldmann, T. Ackemann and W. Lange

Institut für Angewandte Physik, Universität Münster, Corrensstraße 2/4, D-48149 Münster, Germany, Tel.: +49-251-83-33553, Fax: +49-251-83-33513, E-mail: ackeman@uni-muenster.de

Two-dimensional spatially localized structures are intriguing objects in self-organizing nonlinear systems and provide new insights into the process of pattern formation. Therefore they found considerable attention during the last years also in the context of optics [1, 2, 3, 4, 5], where they are often referred to as spatial solitons (SS). They might turn out to be the key for new methods of all-optical information coding and processing. We demonstrate the existence of spatial solitons in a single–mirror feedback system based on sodium vapor as a nonlinear medium and provide quantitative characterization of their properties. Special focus is on the interaction of multiple spatial solitons.

In our experimental setup, an enlarged and spatially filtered cw dye laser beam tuned several GHz above the sodium D_1–line is injected into a cell containing sodium vapor. 99% of the transmitted power is fed back into the sodium cell by a plane mirror at distance d behind the vapor. By means of a CCD camera we observe the near field intensity distribution of the transmitted light (Fig. 1). A small area photodetector monitors the transmission in the beam center.

The input beam is circularly polarized. Optical pumping between the Zeeman sublevels of the sodium ground state creates an orientation which in turn changes the complex susceptibility of the vapor. If an external magnetic field is applied, we can create a bistable response of the system to the power of the input beam (Fig. 2). The low transmission branch has no distinct large amplitude structures. At the switch-up point bright spots appear spontaneously in the beam profile (Fig. 3a). They are not densely packed as in a periodic (hexagonal) lattice but

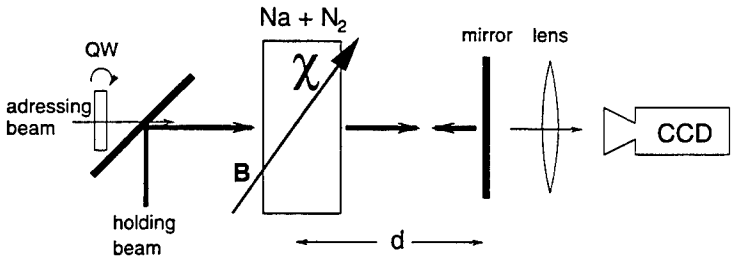


Figure 1: Schematic view of setup. Beam radius of holding beam $w_0 \approx 1.5$ mm, of addressing beam 0.1 to 0.2 mm ($1/e^2$-point of intensity). The polarization of the adressing beam can be changed by a quarter waveplate.

might form clusters which however do not have an apparent symmetry. These facts hint already at their solitary origin.

In the bistable region single spots can be ignited by injecting an incoherent second laser beam of smaller width and the same circular polarization as the holding beam. The SS remain stable when the second beam is switched off. By changing the sign of the circular polarization of the second beam we can make use of the polarization properties of the light–matter interaction and use the second beam to erase the SS. This provides a very robust and phase-insensitive way of control. A detailed analysis of the switching behaviour reveals critical slowing down of the switching time for small intensities of the second laser beam (lower trace in Fig. 2).

Optical structures in general and self-guided waves in particular are stabilized by an interplay of nonlinearity and diffraction. Since these features are separated in space in the system under study, their effect can be investigated separately: By changing the position of the imaging lens the variation of the intensity profile during the free space propagation from the vapor cell to the mirror and back can be examined. It turns out that the incoming laser-field experiences a local phase retardation inside the sodium vapor and thus is focused during its propagation. We conclude that the SS are stabilized by a self-lensing effect.

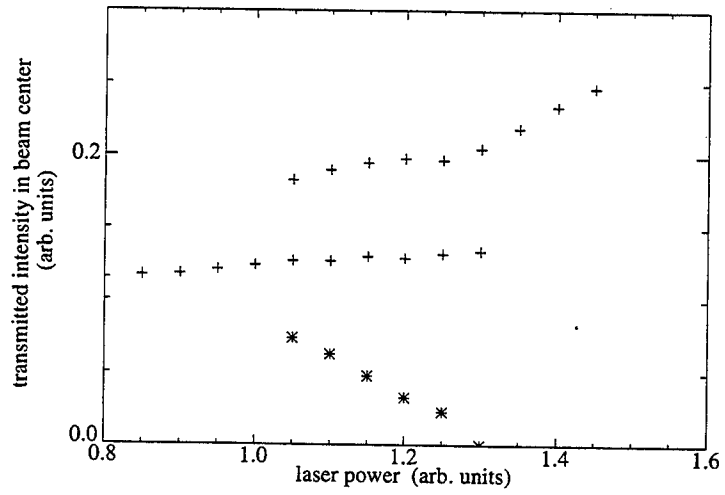


Figure 2: The crosses denote the transmission of the sodium cell in beam center in dependence of the power of the holding beam. The stars denote the power necessary to ignite a SS in dependence of the input power of the holding beam.

The intensity profile of a SS reentering the vapor cell consists of an intense central spot which is surrounded by several diffraction fringes. The latter influence the interaction of spatial solitons: For a given number of spatial solitons only a few stable configurations are observed in the experiment. Especially for two constituents, there is only a discrete set of distances between them. Similar behavior is found for clusters of solitary excitations in gas discharges and reaction diffusion systems [6].

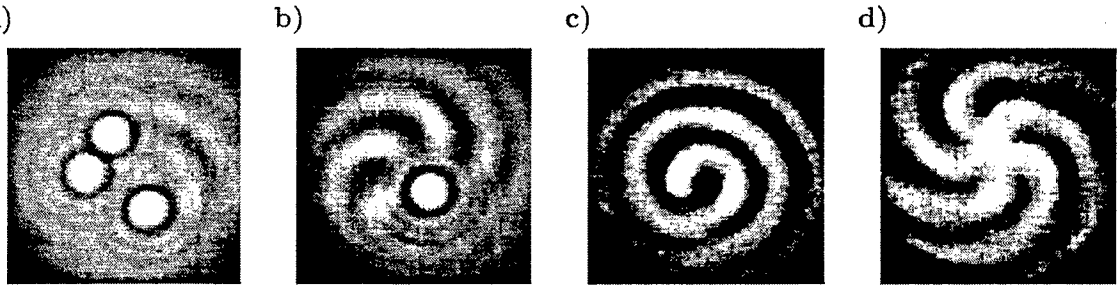


Figure 3: Typical near field intensity distributions displaying spatial solitons and spirals.

Numerical and analytical calculations reveal that these spatial solitons appear in a region where the homogeneous solution is bistable due to a light–shift induced level crossing of the Zeeman ground states of the sodium atom [7]. The spatial solitons and the existence of a discrete set of stable mutual distances can be reproduced in numerical simulations of the microscopic model. The simulations indicate that the excitation is no longer localized, i.e. a whole hexagonal lattice appears, if the intensity on the first diffraction fringe is high enough to excite further spatial solitons. The SS can therefore interpreted to be the building block of the emerging periodic pattern.

For slightly modified experimental parameters, the linear stability analysis predicts a complicated situation involving instability regions of focusing and defocusing length scales as well as a Hopf bifurcation. The experiments in this region show a spiraling pattern and the interaction of spirals with spatial solitons (Fig. 3b-d).

References

[1] N. N. Rozanov, Proc. SPIE **1840**, 130 (1991).

[2] W. J. Firth and A. J. Scroggie, Phys. Rev. Lett. **76**, 1623 (1996).

[3] M. Kreuzer, A. Schreiber, and B. Thüring, Mol. Cryst. Liq. Cryst. **282**, 91 (1996).

[4] V. B. Taranenko, K. Staliunas, and C. O. Weiss, Phys. Rev. A **56**, 1582 (1997).

[5] M. Brambilla *et al.*, Phys. Rev. Lett. **79**, 2042 (1997).

[6] C. P. Schenk, P. Schütz, M. Bode, and H.-G. Purwins, Phys. Rev. E **57**, 6480 (1998).

[7] T. Ackemann, A. Heuer, Y. A. Logvin, and W. Lange, Phys. Rev. A **56**, 2321 (1997).

Two dimensional vectorial localized structures in optical cavities

P. Colet[1], R. Gallego[1], E. Hernández-García[1], M. Hoyuelos[1], G.L. Oppo[2], M. San Miguel[1], and M. Santagiustina [1]

[1] *Instituto Mediterráneo de Estudios Avanzados, IMEDEA (CSIC-UIB), Universitat Illes Balears, E-07071 Palma de Mallorca, Spain.*

Tel: +34 971 173229, Fax: +34 971 173426, e-mail: maxi@imedea.uib.es, http://www.imedea.uib.es/PhysDept/

[2] *Department of Physics, University of Strathclyde, Glasgow G4 0NG, Scotland, U.K.*

Localized structures in lasers and in optical cavities containing nonlinear optical materials are being intensively studied [1–4] because of two main reasons. On the one hand complex spatio-temporal dynamics is often dominated by these particle-like objects. Secondly, the ability to control, create and erase these objects opens the way to new technological developments, including parallel information processing. We are here concerned with two dimensional localized objects in the transverse plane of an optical cavity. Generally speaking they are named cavity solitons and they can take the form of vortices or bright or dark dissipative spatial solitons.

Most studies of localized structures in optical systems consider light with a fixed polarization. However, the vectorial degree of freedom of light leads to a very interesting phenomenology associated with a space and time dependent polarization [5]. Such degree of freedom is also relevant from the point of view of information encoding and processing. We address here the question of new types of localized structures emerging from polarization nonlinear dynamics.

A visualization of vectorial localized structures can be given in terms of isolated zeroes or peaks of either of the two independent polarization components of the electric field. Situations of hole-hole, peak-hole or peak-peak in a given polarization background can be envisaged. A proper classification [6] of these objects depends on the reference states preferred by a particular system. We consider here three different systems which give relevant examples of possible vectorial localized structures and of their dynamics.

Broad Area Lasers

The interaction of the two polarization components of light in rotationally symmetric large aperture lasers can be described, close to threshold, by the Vector Complex Ginzburg Landau Equation (VCGLE) [7]. The VCGLE can be written as coupled equations for the two circularly polarized components $A_\pm$ of the slowly varying part of the vector complex field:

$$\partial_t A_\pm = A_\pm + (1+i\alpha)\nabla^2 A_\pm - (1+i\beta)(|A_\pm|^2 + \gamma|A_\mp|^2)A_\pm. \tag{1}$$

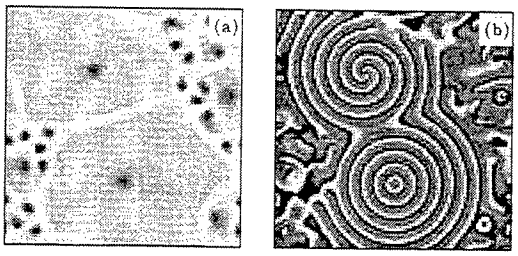


FIG. 1. Frozen field configuration: (a) $|A_+|^2$, (b) ϕ_g ($\gamma = 0.1$, $\alpha = 0.2$, and $\beta = 2$).

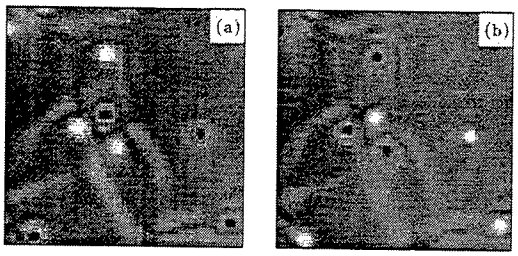


FIG. 2. Instantaneous configuration for $\gamma = 0.8$. (a) $|A_+|^2$, (b) $|A_-|^2$. Bright (dark) spots correspond to maximum (minimum) intensity.

The parameters α and β are associated with the strength of diffraction and detuning respectively and the condition $1+\alpha\beta > 1$ is always satisfied. For the coupling parameter $\gamma < 1$, as considered here, homogeneous linearly polarized solutions in an arbitrary direction are preferred. In this background it is natural to look for localized structures of vortex type as isolated zeros of A_+ and/or A_- [4]. Charges $n_\pm$ are associated with the change of the phases $\phi_\pm$ of $A_\pm$ around those zeroes. We call *vectorial defect* a zero that is present in both components of the field at the same point. A vectorial defect can be of *argument* type ($n_+ = n_- = 1$)

or of *director* type ($n_+ = -n_- = 1$). They are identified, respectively, by a two-armed spiral or a target pattern of the global phase $\phi_g = \phi_+ + \phi_-$ (Fig. 1). A *mixed defect* is a zero present only in one component of the field. Vectorial defects are stable in a range of parameters. Within this range they freeze the dynamics creating exclusion islands with mixed defects concentrated at their borders. Vectorial defects loose their stability either by an unbinding of the zeroes of the two fields or by an instability of the phase spirals. This leads to a dynamical state in which $A_\pm$ are highly anticorrelated. This state is dominated by mixed defects characterized as a localized bound state of a zero of one component and a peak of the opposite circularly polarized component. These localized objects move on a linearly polarized background (Fig. 2).

Vectorial self-defocusing Kerr Resonators

Consider a ring cavity filled with an isotropic Kerr medium and driven by an external linearly polarized input field. This can be described by coupled driven and damped Non Linear Schrödinger Equations for the two circularly polarized components $A_\pm$ of the slowly varying part of the vector complex field. In a mean field approximation they become [5]

$$\partial A_\pm = -(1 - i\theta)A_\pm + ia\nabla^2 A_\pm + A_0 - i[\alpha|A_\pm|^2 + (\alpha + \beta)|A_\mp|^2]A_\pm, \tag{2}$$

where A_0 is the input field, and θ is the cavity detuning. A stripe pattern orthogonally polarized to the input field occurs close to threshold. For higher values of A_0 the system prefers either of two equivalent homogeneous states which are close to circularly polarized states. Polarized localized structures are here visualized as a hole of A_+ (A_-) in the background of a circularly positive (negative) polarized state together with a peak of A_- (A_+) (Figs. 3 and 4) . These structures are related to domain walls separating the two equivalent homogeneous circularly polarized states. They are stable for $A_{0,m} < A_0 < A_{0,M}$ within the range in which homogeneous states are stable. For $A_0 < A_{0,m}$ a circular spot of one polarization, in the background of the opposite one, grows and leads to a labirynthine pattern. For $A_{0,M} < A_0$ the system, after switching-on A_0, evolves in a self-similar way to a final homogeneous state. The situation is reminiscent of what has been described for vectorial intracavity Second Harmonic Generation [3].

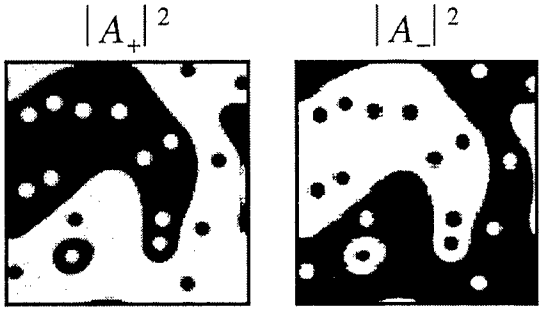


FIG. 3. Field intensities $|A_\pm|^2$ in the range of existence of localized structures $A_{0,m} < A_0 < A_{0,M}$.

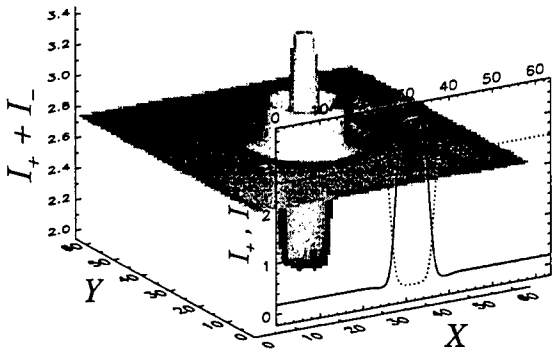


FIG. 4. Total field intensity ($|A_+|^2 + |A_-|^2$) of a localized structure and transverse profile of the intensities $|A_+|^2$ (solid line) and $|A_-|^2$ (dotted line).

Type II Degenerate Optical Parametric Oscillator

A Type II degenerate OPO, for which the pump is not resonant with the cavity, can be described by the following equations for the signal A_x and the idler A_y. These are two orthogonally and linearly polarized complex fields.

$$\partial_t A_x = -(1 + i\Delta)A_x + ia\nabla^2 A_x + \mu A_y^* + \sigma|A_y|^2 A_x \tag{3}$$

$$\partial_t A_y = -(1 + i\Delta)A_y + ia\nabla^2 A_y + \mu A_x^* + \sigma|A_x|^2 A_y \tag{4}$$

The parametric coupling coefficient μ and the nonlinear coupling coefficient σ depend on phase mismatch and they are generally complex. We consider a situation of negative detuning $\Delta < 0$ for which preferred

states are traveling waves of A_x and A_y in an arbitrary direction, with the same amplitude and frequency but with opposite phase and wavenumber. Localized structures occur in this background as isolated zeroes of the two fields A_x and A_y. Due to the parametric coupling these defects occur simultaneously for the two fields (Fig. 5) and with opposite charge, $n_1 = \pm 1$ and $n_2 = \mp 1$, for each field. Note that they do not correspond to isolated zeroes of the circularly polarized components of the vector field. These localized structures are spontaneously formed when switching-on the pump field. After a transient dynamics, in absence of walk-off [8], they are stable and their number is conserved for very long times (Fig. 6). One of these objects can be isolated and stabilized by choosing a beam size smaller than the wavelength of the traveling wave selected in the background. These structures are spontaneously formed vectorial dark spatial solitons of a different nature than the bright structures discussed for degenerate Type I OPO [2] or the dark structures for non-degenerate Type I OPO [9]. They are also different from the dark solitons which can be stabilized in a degenerate Type I OPO by imposing the structure in the pump beam [10] or by the walk-off [11].

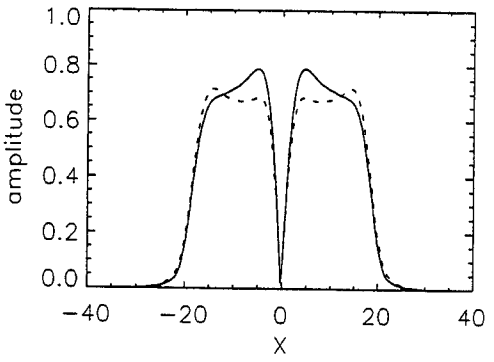


FIG. 5. Transverse amplitude profile (solid line $|A_x|$, dotted line $|A_y|$ across the center of a vectorial dark soliton at perfect phase-matching ($\mu = 1.5, \sigma = -1.5$, other parameters $\Delta = -0.2, a = 2$).

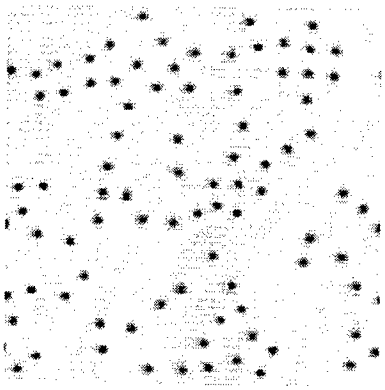


FIG. 6. Instantaneous configuration of $|A_x|$; dark spots correspond to minimum intensity ($\Delta = -0.25$, $a = 1$, other parameters as in fig. 5).

[1] N. N. Rosanov, *Progress in Optics* **35**, 1 (1996); M. Tlidi, P. Mandel and R. Lefever, *Phys. Rev. Lett.* **73**, 640 (1994); W. Firth and A.J. Scroggie, *Phys. Rev. Lett.* **76**, 1623 (1996); A. Schreiber, B. Thuring, M. Kreuzer, and T. Tschudi, *Opt. Comm.* **136**, 415 (1997); L. Spinelli, G. Tissoni, M. Brambilla, F. Prati, and L. Lugiato, *Phys. Rev.A* **58**, 2542 (1998); C. Etrich, U. Peschel, and F. Lederer, *Phys. Rev. Lett.* **79**, 2454 (1997); C. O. Weiss, M. Vaupel, K. Staliunas, G. Slekys, and V. B. Taranenko, *Appl. Phys. B* **68**, 151 (1999) and references therein.

[2] K. Staliunas and J. V. Sânchez-Morcillo, *Phys. Rev. A* **57**, 1454 (1998); G.L. Oppo, A.J. Scroggie, and W.J. Firth, *Journal of Optics B: Quantum Semiclass. Opt.* **1**, 133 (1999); M. Le Berre, D. Leduc, E. Ressayre, and A. Tallet, *Journal of Optics B: Quantum Semiclass. Opt.* **1**, 153 (1999).

[3] U. Peschel, D. Michaelis, C. Etrich and F. Lederer *Phys. Rev. E* **58**, R2745 (1998).

[4] E. Hernández-García, M. Hoyuelos, P. Colet, R. Montagne, and M. San Miguel, *Int. J. Bif. and Chaos* (1999).

[5] M. Hoyuelos, P. Colet, M. San Miguel, and D. Walgraef *Phys. Rev. E* **58**, 2992 (1998) and references therein.

[6] L.M. Pismen, *Physica D* **73**, 244 (1994).

[7] M. San Miguel, *Phys. Rev. Lett.* **75**, 425 (1995); A. Amengual, E. Hernández-García, R. Montagne, and M. San Miguel, *Phys. Rev. Lett.* **78**, 4379 (1997).

[8] G. Izús, M. Santagiustina, M. San Miguel, and P. Colet, *J. Opt. Soc. Am.*, to be published in the Special Issue on Optical Parametric Processes, Devices, and Applications, September 1999.

[9] V. J. Sánchez-Morcillo, E. Roldán, G. J. de Valcárcel, and K. Staliunas, *Phys. Rev A* **56**, 3237 (1997).

[10] G-L Oppo, A.J. Scroggie, and W.J. Firth, EQEC98 Technical Digest, paper QFA2, Glasgow (1998).

[11] M. Santagiustina, P. Colet, M. San Miguel, and D. Walgraef, *Opt. Lett.* **23**, 1167 (1998).

Interaction of cavity solitons in degenerate optical parametric oscillators.

Dmitry V. Skryabin and William J. Firth
Department of Physics and Applied Physics, John Anderson Building, University of Strathclyde, 107 Rottenrow, Glasgow, G4 0NG, UK
fax: 44 141 5522891 phone: 44 141 5523354 dmitry@phys.strath.ac.uk

Many nonlinear media can support soliton-like structures when contained in a driven optical cavity [1–4]. We will refer to such structures as *cavity solitons* (CS). In quadratic nonlinear media CS have recently been predicted in both optical parametric oscillator (OPO) [3] and second harmonic generation [4] configurations. Although experimental observation of $\chi^{(2)}$-CS remains a challenge, impressive bistability results [5] demonstrate the required level of nonlinearity and thus pave the way towards this goal.

The large values of effective $\chi^{(2)}$ accessible in artificially phase-matched materials in combination with their practically instantaneous response are important advantages of using quadratic nonlinearity for implementation of CS for all-optical processing of information. They thus represent an interesting alternative to the CS which can be created in cavities with dispersive-absorptive [1],and resonant electron-hole [2] types of nonlinearities. In all such schemes high CS density is desirable and therefore understanding of their interaction is a practically important problem which is still largely open. In this Letter we focus on the interactions of CS found in the below-threshold regime of a degenerate doubly resonant OPO, under conditions where the signal field has three coexistent plane-wave states [3].

Assuming phase-matching, a plane-wave input field, and ignoring walk-off, the mean-field OPO equations can be presented in the following dimensionless form [3]

$$\begin{aligned} -i\partial_t E_1 &= (\alpha_1\partial_x^2 + \delta_1 + i\gamma_1)E_1 + (E_2+\mu)E_1^*, \\ -i\partial_t E_2 &= (\alpha_2\partial_x^2 + \delta_2 + i\gamma_2)E_2 + E_1^2/2, \end{aligned} \qquad (1)$$

Here E_1 and $(E_2+\mu)$ are the signal and pump fields, respectively, at frequencies ω and 2ω (we use μ as a measure of the pump strength). The slow time t is scaled so that γ_m (proportional to the cavity damping rates) and δ_m (to the detunings from its resonances) are of order unity. Here and below $m = 1, 2$.

This system can describe either diffractive or dispersive effects. We consider x a dimensionless transverse coordinate, and so set $\alpha_m = 1/m$. For this case, existence of CS for $\delta_m < 0$ was numerically demonstrated [3] for $\mu_L < \mu < \mu_R$, where $\mu_L = |\gamma_1\delta_2 + \gamma_2\delta_1|/\sqrt{\delta_2^2+\gamma_2^2}$, and $\mu_R = \sqrt{\delta_1^2+\gamma_1^2}$ is the OPO threshold. Within this range two different non-trivial homogeneous solutions ($E_m \neq 0$, $\partial_x E_m = 0$) coexist with the trivial one ($E_m = 0$), and the CS are sech-like localized states on the zero background.

We start our analysis by applying a perturbative method [6] to the problem of CS interaction. We seek solutions of Eqs. (1) in the form

$$\begin{aligned} &E_m(x,t) = A_m(x-x_A) + B_m(x-x_B) + \\ &\epsilon(a_m(x-x_A, x_B, t) + b_m(x-x_B, x_A, t)) + O(\epsilon^2), \end{aligned} \qquad (2)$$

where $A_m(x-x_A)$ and $B_m(x-x_B)$ are CS centred on $x_{A,B}$. Note that Eqs. (1) are invariant with respect to a π phase flip of the signal field, so that A and B can be either in-phase or out-of-phase CS. We assume $0 < \epsilon \ll 1$, and that the perturbation functions a_m, b_m are negligible except close to x_A, x_B respectively. We further assume that $x_{A,B}$ vary on the slow time scale $\tau = \epsilon t$ and that $d = |x_A - x_B|$ is large enough that the overlap functions $\mathcal{I}_1 = A_2B_1^* + B_2A_1^*$ and $\mathcal{I}_2 = A_1B_1$ are of order ϵ.

Substituting ansatz (2) into Eqs. (1) and truncating $O(\epsilon^2)$ terms we obtain two analogous systems of equations for a_m and b_m, the former expressible in the form:

$$(\hat{\mathcal{L}}_A - \partial_t)\vec{a} = -(\partial_\tau x_A)\vec{\xi}_A + \vec{\mathcal{I}}/\epsilon, \qquad (3)$$

Here $\vec{a} = (Rea_1, Rea_2, Ima_1, Ima_2)^T$; operator $\hat{\mathcal{L}}_A$ is the linearization of Eqs. (1) around the soliton A_m; $\vec{\xi}_A = \partial_x(ReA_1, ReA_2, ImA_1, ImA_2)^T$ is the neutral eigenmode of $\hat{\mathcal{L}}_A$ associated with translational symmetry, $\hat{\mathcal{L}}_A\vec{\xi}_A = 0$; and $\vec{\mathcal{I}} = (-Im\mathcal{I}_1, -Im\mathcal{I}_2, Re\mathcal{I}_1, Re\mathcal{I}_2)^T$ controls the interaction of the two CS.

The solution of Eq. (3) should in general be expressed as a superposition of the eigenmodes of $\hat{\mathcal{L}}_A$ with time dependent coefficients, because the CS interaction will couple to them all. However, apart from the above-mentioned neutral eigenmodes, the only analytic knowledge about the eigensystems of $\hat{\mathcal{L}}_A$ and $\hat{\mathcal{L}}_B$ is that they have two bands of continuum modes with eigenvalues λ lying on $Re\lambda = -\gamma_m$, i.e. that all extended eigenmodes are damped. We have obtained their full eigensystems numerically, using finite-differences, over wide ranges of all relevant parameters. We find that for sufficiently large dissipation all cavity solitons are stable throughout the entire region of their existence. A Hopf bifurcation can occur as photon lifetime is increased, but we will not consider here any parameter regions where isolated CS are unstable. With oscillatory eigenmodes absent or well damped, only the neutral mode is easily excited by external perturbations, and so we meantime neglect all other modes. This enables us to obtain semi-analytic results on CS interactions.

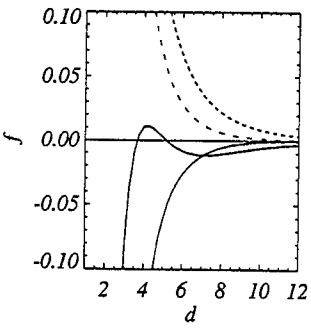


FIG. 1. Plots of the CS velocity function f vs d. Full (dashed) lines correspond to in-phase (out-of-phase) solitons and thin (thick) lines correspond to $\mu = 1.6(1.9)$. Other parameters are $\delta_2 = -4.0$, $\delta_1 = -1.8$, $\gamma_1 = 1$, $\gamma_2 = 0.8$.

To exclude secularly growing solutions the right-hand side of Eq. (3) must be orthogonal to the neutral eigenmode of $\hat{\mathcal{L}}_A^\dagger$ (which we calculated numerically). This solvability condition, together with that for the B soliton, defines a function f which governs the dynamical evolution of the distance d between the soliton centers:

$$\partial_t d = f(d). \tag{4}$$

We computed f for both in-phase and out-of-phase interacting CS, for many parameter values. Typical examples are plotted in Fig. 1. Regions where f is negative (positive) correspond to CS attraction (repulsion). Zeros of $f(d)$ thus mark stationary *bound states* of CS pairs, which are stable if $\partial_d f < 0$ where $f = 0$.

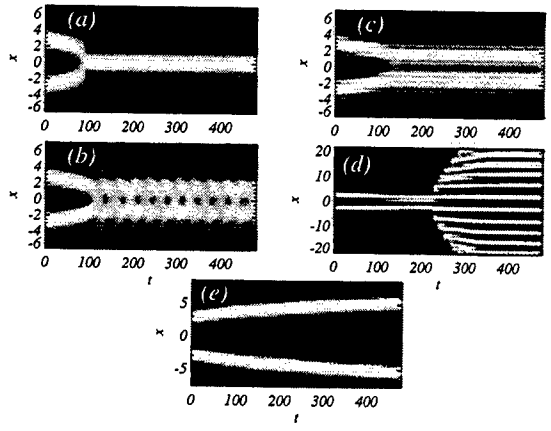


FIG. 2. Interaction dynamics of $\chi^{(2)}$ cavity solitons [8]. At different values of pump parameter μ, in-phase CS: (a) merge, $\mu = 1.6$; (b) form oscillatory bound state, $\mu = 1.8$; (c) form stable stationary bound state, $\mu = 1.9$; (d) generate a pattern *via* a switching wave, $\mu = 2$. Out-of-phase solitons repel, e.g. at $\mu = 2$, (e). Other parameters as for Fig. 1.

We find that this equation gives generally correct predictions of the inter-soliton forces, in particular that in-phase CS attract and out-of-phase CS repel. Both repulsion and attraction become stronger as μ increases, presumably because the signal component (E_1) of the CS becomes less localized as μ approaches plane-wave threshold at μ_R. A similar effect can be envisaged in other CS models. For in-phase CS the function f can develop pairs of zeros, see Fig. 1. This predicts birth of new pairs of CS bound states, one stable and one unstable.

In Fig. 2 we present simulation results showing different interaction scenarios for two CS initially separated by about three soliton widths. The interaction of *in-phase* solitons gives a rich variety of phenomena. For small μ mutual attraction results in fusion of two solitons into one (Fig. 2(a)). Gradually increasing μ we first observe formation of a stable oscillatory bound state (Fig. 2(b)), then of a stationary bound state (Fig. 2(c)) which is stable (the radiation visible in Fig. 2(c) decays, albeit slowly). Note that the equilibrium separation in Fig. 2(c) is predicted quite well by the appropriate zero of $f(d)$ in Fig. 1, even though these CS are close enough to endanger the assumptions of our perturbation method. Stationary two-hump solitary states have been found previously [3] as solutions of an approximate equation derived from Eqs. (1), but no analysis of soliton interactions was performed. Close to the upper boundary of CS existence the interaction of two solitons excites a global pattern (Fig. 2(d)). As predicted by Eq. (4), *out-of-phase* CS repel each other throughout the entire region of their existence - contrast Fig. 2(e) with Fig. 2(d), which corresponds to the same value of μ.

Now we will describe numerical results of the interaction of CS where weakly-damped oscillatory modes strongly influence the soliton interactions. Oscillating solitons generally radiate energy, which can become trapped between neighbouring solitons, exerting a radiation force which may lead to formation of a bound state. An effect of this kind has been reported for solitons in models with a weak global dissipation [7]. We investigated a quite different situation, where linear waves escaping from the soliton are strongly damped. Here strong interaction between the solitons is due, not to radiation modes, but to proto-Hopf modes, and thus has novel aspects.

The effect is strong providing that two conditions are satisfied. First, and crucially, the corresponding eigenmodes must have tails with well pronounced and weakly decaying oscillatory structure, see Fig. 3(a). Second, as might be expected, the oscillatory mode should be weakly damped (see Fig. 3(b)), i.e. the CS is close to a Hopf instability. If both conditions hold, then, even if the global damping due to the γ_m is strong, a CS acts as a guide for waves weakly damped in both space and time. If a second CS is close enough, these guided waves can couple and reinforce each other. Fig. 3(c, d) illustrates the dynamics of two interacting CS having eigenmodes shown in Fig. 3(a). Note that the separation of the interacting solitons in Fig. 3(c) is much greater than their width. Comparison with Fig. 3(b) clearly indicates that the undamped pulsations shown in Fig. 3(d) originate

from coupling and mutual reinforcement of the oscillatory modes of the two solitons. A further interesting point is that we find these dynamic bound states also for *out-of-phase* solitons, balancing the repulsion induced by their neutral-mode interaction.

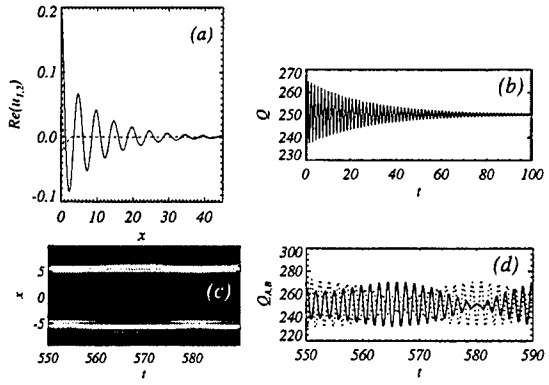


FIG. 3. Dynamic interaction of CS for $\mu = 2$, $\delta_1 = -3$, $\delta_2 = -12$, $\gamma_1 = 0.3$, $\gamma_2 = 1$, for which the CS has a mode with eigenvalue pair $\lambda \simeq -0.03 \pm i4.14$: (a) Spatial structure of the eigenmode, $Re(u_1)$ - full lines, $Re(u_2)$ -dashed lines; (b) Temporal evolution of signal energy $Q = \int dx|E_1|^2$ for slightly perturbed single soliton, showing damped oscillation; (c) Spatio-temporal evolution [8] of $|E_1|$ (time window much later than in (b)), showing dynamic bound state; (d) Temporal evolution of signal energies of the two CS in (c), in the same time window, showing rapid undamped oscillations and slow energy exchange between the two solitons.

In summary, we have presented the analytical and numerical study of the interaction of cavity solitons in a degenerate OPO and identified distinct static and dynamic binding mechanisms.

[1] N.N. Rosanov, Progress in Optics **35**, 1 (1996); M. Tlidi, P. Mandel, and R. Lefever, Phys. Rev. Lett. **73**, 640 (1994); W.J. Firth and A.J. Scroggie, Phys. Rev. Lett. **76**, 1623. For a recent review of CS, see W.J. Firth and G.K. Harkness, Asian J. Phys. **7**, 665 (1998).

[2] M. Brambilla, L.A. Lugiato, F. Prati, L. Spinelli, and W.J. Firth, Phys. Rev. Lett. **79**, 2042 (1997); D. Michaelis, U. Peschel, and F. Lederer, Phys. Rev. A **56**, R3366 (1997).

[3] K. Staliunas and V.J. Sánchez-Morcillo, Opt. Commun. **139**, 306 (1997); S. Longhi, Phys. Scripta **56**, 611 (1997); S. Trillo and M. Haelterman, Opt. Lett. **23**, 1514 (1998).

[4] C. Etrich, U. Peschel, and F. Lederer, Phys. Rev. Lett. **79**, 2454 (1997); S. Longhi, Opt. Lett. **23**, 346 (1998).

[5] C. Richy, K.I. Petsas, E. Giacobino, C. Fabre, and L. Lugiato, J. Opt. Soc. Am. B **12**, 456 (1995); A.G. White, J. Mlynek, and S. Schiller, Europhys. Lett. **35**, 425 (1996).

[6] Various versions of this method can be found, e.g., in: K. A. Gorshkov and L. A. Ostrovsky, Physica D **3**, 428 (1981); S. Longhi, Phys. Rev. E **55**, 1060 (1997).

[7] B.A. Malomed, Phys. Rev. E **47**, 2874 (1993).

[8] Only the central third of the computational window in x is shown in Figs. 2(a)-(c),(e), 3(c).

Spatial structures and their control in injection locked broad-area VCSELs

T. Ackemann[1,2,3], S. Barland[1,2], M. Cara[2], M. Giudici[2], S. Balle[2]

[1]*Dept. de Física Interdisciplinar, Instituto Mediterráneo de Estudios Avanzados, IMEDEA (CSIC-UIB), E-07071 Palma de Mallorca, Spain*

[2] *Institut Non Linéaire de Nice, UMR 6618 CNRS-UNSA, 1361 Route des Lucioles, F-06560 Valbonne, France*

[3]*Permanent address: Institut für Angewandte Physik, Universität Münster, Corrensstraße 2/4, D-48149 Münster, Germany, Tel.: +49-251-83-33553, Fax: +49-251-83-33513, E-mail: ackeman@uni-muenster.de*

The existence of localized, soliton-like excitations (cavity solitons) in the transverse cross-section of nonlinear optical systems has attracted a lot of attention in the last years [1, 2, 3] and experimental proof was given in an electro-optical system [4], dye lasers with saturable absorber [5] and sodium vapor [6]. Recent work predicts the possibility of cavity solitons in semiconductor microcavities [7]. Their demonstration might enable new forms of all-optical information coding and processing with the speed, compactness and robustness of a semiconductor device.

We set up an experiment to study this in vertical-cavity surface emitting lasers (VCSEL) which are biased electrically around threshold (Fig. 1a). Injecting a homogeneous holding beam in the VCSEL should create a bistable response of the slave in dependence of the injection level [7]. A second addressing beam is used to manipulate locally the spatial structure in the bistable interval.

The investigated devices are based on three InGaAs/GaAs quantum wells in a λ-cavity emitting in the 960 to 990 nm region [8]. The emission takes place through the anti-reflection coated substrate (bottom emitter). The p-side is soldered on a diamond heat spreader for heat sinking. The active region is circular with a diameter of 38 μm. An oxide layer close to the active region provides the current confinement and optical confinement.

The output of a high power edge emitter is stabilized by feedback from a grating and injected into the VCSEL via two mode matching lenses. The injection level is controlled with an acoustooptical modulator, the polarization chosen to coincide with the axis of the dominant polarization mode of the solitary VCSEL. The near and far field of the output of the VCSEL, respectively the reflected master, are observed with two CCD cameras. The spectra are monitored with a scanning Fabry-Perot interferometer and a monochromator.

Injection locking and an amplification of the reflected beam is achieved in a rather broad region to the blue side of the longitudinal resonance (Fig. 2g). The amplification is highest around the lasing frequency of the solitary VCSEL. The emission shows distinct contributions on a ring in Fourier space which contracts if the detuning is reduced. A log-log plot of the

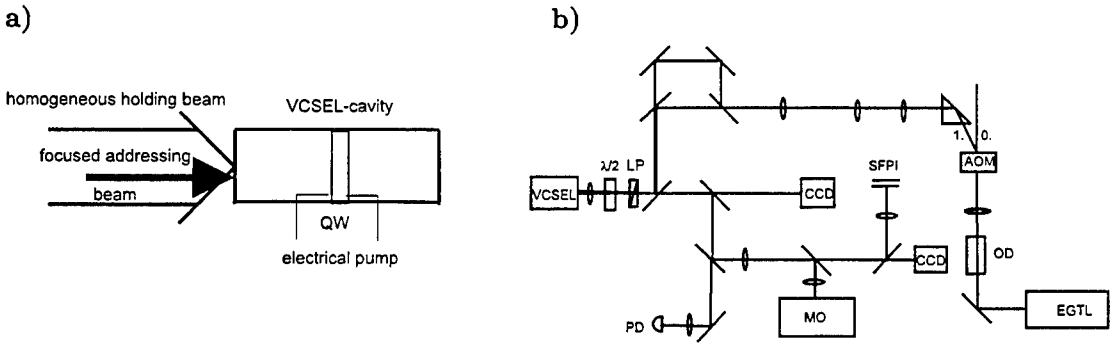


Figure 1: a) Schematic view of setup, QW quantum well. b) Experimental setup: EGTL external grating tunable laser, OD optical diode, AOM acoustooptical modulator, $\lambda/2$ half-waveplate, LP linear polarizer, SFPI scanning Fabry-Perot interferometer, MO monochromator.

magnitude of this transverse wavevector in dependence of the detuning yields a scaling exponent between 0.43 and 0.54. An exponent of 0.5 is expected for the emission of tilted waves in a plano-planar resonator [7]. In the near field we observe – starting from high detuning – rings (Fig. 2a), which become increasingly modulated (Fig. 2b) until true symmetry breaking sets in (Fig. 2c). In this region the patterns are hexagons. Moving closer to the resonance the patterns are increasingly irregular, have a coarser scale and contract towards one side of the laser (Fig. 2d, e, f).

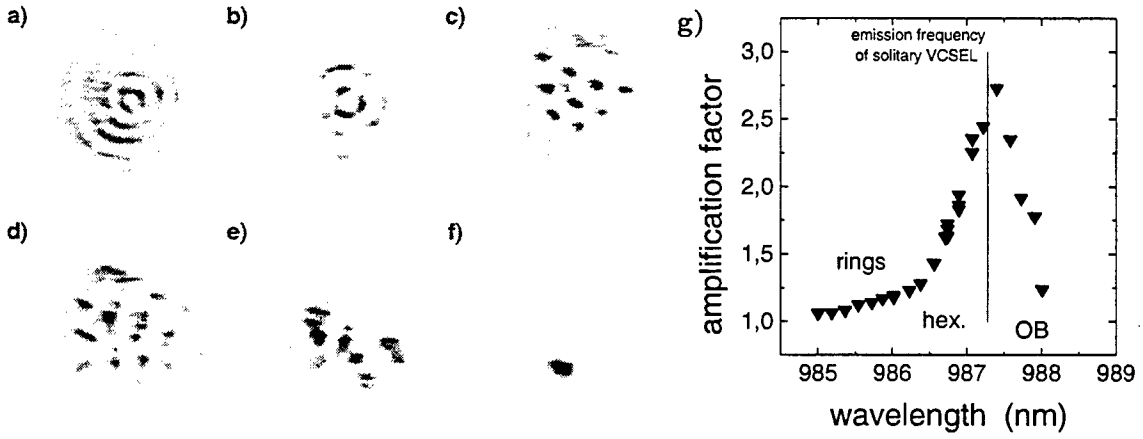


Figure 2: a)-f) typical near field patterns. The detuning with respect to the longitudinal resonance of the cavity decreases from a) to f). g) amplification of injected power in dependence on the detuning.

Biasing the slave above threshold we can achieve a bistable response to the external injection (Fig. 3a). The low-and high transmission branches correspond to the emission of one, respectively two, spots. We can induce the switch up of the second spot by an injection of a second addressing beam. After the perturbation is removed the system remains in the high

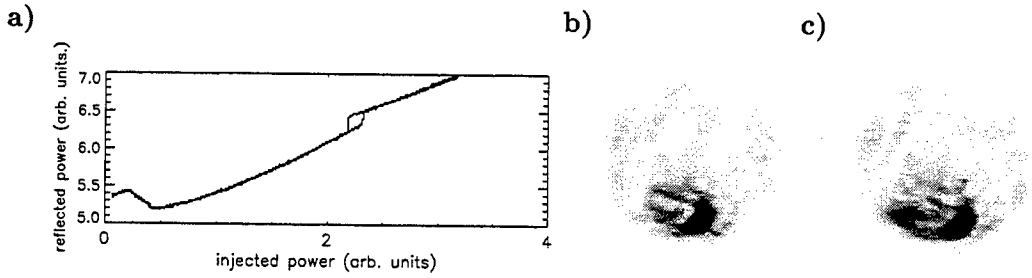


Figure 3: a) Bistable characteristic of injection locked laser. Near field structure in b) low and c) high emission state.

transmission branch.

To conclude we demonstrated the emission of tilted waves and hexagonal patterns in an injection locked VCSEL. These are prerequisites for stable cavity solitons which can be placed at an arbitrary point in the cross section of the laser. In the region most favorable for cavity solitons further investigations will be carried out with devices of improved homogeneity.

The authors are grateful to the group of K. J. Ebeling, University of Ulm, for supplying the devices.

References

[1] N. N. Rozanov, Proc. SPIE **1840**, 130 (1991).

[2] M. Tlidi, P. Mandel, and R. Lefever, Phys. Rev. Lett. **73**, 640 (1994).

[3] W. J. Firth and A. J. Scroggie, Phys. Rev. Lett. **76**, 1623 (1996).

[4] M. Kreuzer, A. Schreiber, and B. Thüring, Mol. Cryst. Liq. Cryst. **282**, 91 (1996).

[5] V. B. Taranenko, K. Staliunas, and C. O. Weiss, Phys. Rev. A **56**, 1582 (1997).

[6] B. Schäpers, T. Ackemann, and W. Lange, in *Patterns in nonlinear optical systems* (Pueblo Acantilado, Alicante, Spain, 1998), pp. PII–6.

[7] M. Brambilla *et al.*, Phys. Rev. Lett. **79**, 2042 (1997).

[8] M. Grabherr *et al.*, IEEE Photon. Tech. Lett. **10**, 1061 (1998).

Nonlinear Guided Waves and Their Applications

Poster Session 1

Wednesday, 1 September 1999

WD
15.00-16.30
Foyer-Bar

Quadratic bright solitons: counterpropagating scheme

Kazimir Y. Kolossovski, Alexander V. Buryak, Rowland A. Sammut

School of Mathematics and Statistics, University College, Australian Defence Force Academy, Canberra 2600, Australia
k-kolossovski@adfa.edu.au ph:+61 2 6268-8433 fax: +61 2 6268-8886

Self-guided optical beams (or spatial solitons) have attracted significant research interest because they offer the possibility of all-optical switching and controlling light by light (see, e.g., [1]). During the last few years it has been realised that quadratic nonlinearity is particularly attractive for potential practical realizations of all-optical switching, not only supporting stable solitons both in planar waveguides and bulk media, but also providing ultra-fast electronic nonlinear response (see, e.g., [2]). The advantages of quadratic nonlinear materials are hampered in part by difficulties with obtaining close phase-velocity matching between interacting waves. One of the most effective ways to achieve such a matching is the use of so-called quasi-phase-matching (QPM) technique, where large wave-vector mismatch between interacting waves is compensated by periodic alternation of the sign of effective $\chi^{(2)}$ coefficient. This technique has been known since 1962, Ref. [3], but only in the last decade has technological progress put the QPM technique in the front line of modern nonlinear optics [4]. In spite of all the theoretical and experimental progress achieved in the field of quadratic solitons, only solitons formed by waves with the same direction of propagation have been analysed so far (conventional *co-propagating* configuration; see, e.g., [2,5]). In a few works the advantages and implications of QPM technique to this type of solitons have been analysed specifically [6]. However, a parametric interaction between counterpropagating quasi-phase-matched waves in quadratic $[\chi^{(2)}]$ media is also possible. Corresponding analysis made for non-soliton (plane wave interaction) case [7] revealed certain advantages of a counterpropagating interaction system in comparison with conventional copropagating strategies. Moreover, recently a very similar so-called *backward* QPM configuration has been investigated experimentally (see [8] for details). Here we investigate the QPM counterpropagating scheme, searching for bright solitons and investigating their stability.

We consider the interaction between four optical waves in a slab waveguide with appropriate nonlinear grating. Two forward-propagating waves, the fundamental at frequency ω and with the wave number k_ω and the second harmonic $(2\omega, k_{2\omega})$, are coupled with two backward-propagating ones, the fundamental $(\omega, -k_\omega)$ and the second harmonic $(2\omega, -k_{2\omega})$ [see Fig. 1, (a)]. Spatial modulation of nonlinear susceptibility along a crystal can be described in terms of square-wave function $d(z)$ [see Fig. 1, (b)]. In this case the only nonzero matrix elements of the Fourier transform of $d(z)$ are given by: $d_l = -2i/(\pi l)$, where $l = 2m-1$, $m = \pm 1, \pm 2, \pm 3\ldots$ Following the method developed in Ref. [6] we can derive the corresponding normalised system of equations which has the following dimensionless form:

$$\begin{aligned}
i\frac{\partial E_\omega^+}{\partial z} + \frac{\partial^2 E_\omega^+}{\partial x^2} - \alpha_+ E_\omega^+ + A_{2\omega} E_\omega^{-*} &= 0,\\
-i\frac{\partial E_\omega^-}{\partial z} + \frac{\partial^2 E_\omega^-}{\partial x^2} - \alpha_- E_\omega^- + A_{2\omega} E_\omega^{+*} &= 0,\\
i\sigma\frac{\partial E_{2\omega}^+}{\partial z} + \frac{\partial^2 E_{2\omega}^+}{\partial x^2} - \sigma\beta_+ E_{2\omega}^+ + A_\omega^+ E_\omega^- &= 0,\\
-i\sigma\frac{\partial E_{2\omega}^-}{\partial z} + \frac{\partial^2 E_{2\omega}^-}{\partial x^2} - \sigma\beta_- E_{2\omega}^- + A_\omega^- E_\omega^+ &= 0,
\end{aligned} \tag{1}$$

where $A_{2\omega} \equiv (d_{-l}E_{2\omega}^+ + d_l E_{2\omega}^-)$, $A_\omega^+ \equiv 2d_l E_\omega^+$, $A_\omega^- \equiv 2d_{-l}E_\omega^-$, $\beta_+ \equiv \alpha_+ - \alpha_- + \delta$, $\beta_- \equiv \alpha_- - \alpha_+ + \delta$; $E_\omega^\pm(x,z), E_{2\omega}^\pm(x,z)$ are the envelopes of the fundamental wave and its second harmonic, respectively, sign "+" ("−") corresponds to the forward (backward) propagating wave; x is the transverse coordinate normalised on the width of the beam r_0; z is the propagation distance which is normalised on the diffraction length $z_d = k_{2\omega}r_0^2$; parameters α_+ and α_- are nonlinear induced propagation constant shifts of the fundamental waves. Other two system parameters, $\sigma \equiv k_{2\omega}/k_\omega = 2$ and $\delta \equiv (2\pi l/L - k_{2\omega})z_d$ (where L is the period of the nonlinear grating and l is the order of QPM), are defined by the particular experimental setup. Note, that in contrast to Ref. [6] we have omitted all effective cubic terms in Eqs. (1). This is well justified for lower order QPM (for $l < 15$) because in this case the cubic terms would become noticeable only when light intensity exceeds the damage threshold for the typical nonlinear crystal.

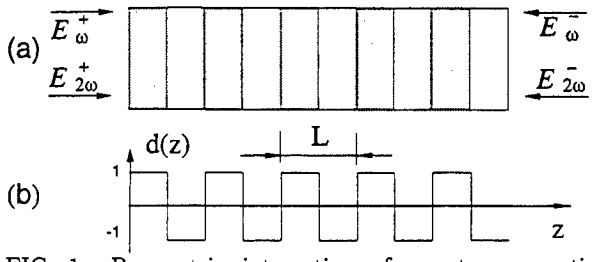


FIG. 1. Parametric interaction of counterpropagating waves. (a) Nonlinear grating is used to couple forward- ("+") and backward-propagating ("−") waves; (b) square-wave function $d(z)$ approximates the periodic modulation of the effective second order nonlinear susceptibility coefficient.

The system (1) has the following family of power-like integrals of motion, which are important for our analysis.

$$Q(p_1,p_2) = \int_{-\infty}^{+\infty}\{2p_1|E_\omega^+|^2 + 2p_2|E_\omega^-|^2 + \\ +\sigma(p_1-p_2)(|E_{2\omega}^+|^2 - |E_{2\omega}^-|^2)\}\,dx, \quad (2)$$

where p_1, p_2 are any real numbers. Using the asymptotic expansion technique and the method based on integrals of motion (see Ref. [9]) one can demonstrate that the stability threshold for the fundamental family of stationary localised solutions of the system (1) is given as:

$$\frac{\partial(Q_1,Q_2)}{\partial(\alpha_+,\alpha_-)} = \frac{\partial Q_1}{\partial\alpha_+}\frac{\partial Q_2}{\partial\alpha_-} - \frac{\partial Q_1}{\partial\alpha_-}\frac{\partial Q_2}{\partial\alpha_+} = 0, \quad (3)$$

where Q_1, Q_2 are any two linearly independent invariants from the family (2), calculated for the fundamental stationary solitons, e.g. $Q_1 = Q(1,0)$ and $Q_2 = Q(0,1)$. More elaborate analysis shows that for the instability domains either of the two following conditions is satisfied in the vicinity of stability/instability boundaries:

$$\frac{\partial Q_1}{\partial\alpha_+}\left(\frac{\partial Q_1}{\partial\alpha_+}\frac{\partial Q_2}{\partial\alpha_-} - \frac{\partial Q_1}{\partial\alpha_-}\frac{\partial Q_2}{\partial\alpha_+}\right) < 0, \\ \frac{\partial Q_2}{\partial\alpha_-}\left(\frac{\partial Q_1}{\partial\alpha_+}\frac{\partial Q_2}{\partial\alpha_-} - \frac{\partial Q_1}{\partial\alpha_-}\frac{\partial Q_2}{\partial\alpha_+}\right) < 0. \quad (4)$$

At $\alpha_+ = \alpha_-$, $\delta = \sigma\alpha_+/2$ the system (1) has an exact analytical stationary localised solution in the form of $E_{\omega,s}^{\pm}(x) = 3\alpha_+/[4|d_l|\cosh^2(\sqrt{\alpha_+}x/2)]$, $E_{2\omega,s}^{\pm}(x) = \mp iE_{\omega,s}^{\pm}(x)$. For other values of the parameters, analytical expressions cannot be found and numerics should be used. For the numerical analysis it is more convenient to renormalise the system (1) reducing the number of parameters. As a result we obtain the system

$$i\frac{\partial V^+}{\partial Z} + \frac{\partial^2 V^+}{\partial X^2} - V^+ + (W^+ + W^-)V^{-*} = 0, \\ -i\frac{\partial V^-}{\partial Z} + \frac{\partial^2 V^-}{\partial X^2} - \gamma V^- + (W^+ + W^-)V^{+*} = 0, \\ i\sigma\frac{\partial W^+}{\partial Z} + \frac{\partial^2 W^+}{\partial X^2} - \sigma\beta_W^+ W^+ + 2V^+V^- = 0, \quad (5) \\ -i\sigma\frac{\partial W^-}{\partial Z} + \frac{\partial^2 W^-}{\partial X^2} - \sigma\beta_W^- W^- + 2V^+V^- = 0,$$

where $\beta_W^+ \equiv 1-\gamma+\alpha$, $\beta_W^- \equiv \gamma-1+\alpha$. The connection between Eqs. (1) and Eqs. (5) is given by scaling $E_\omega^\pm = \alpha_+ V^\pm/|d_l|$, $E_{2\omega}^\pm = \mp i\alpha_+ W^\pm/|d_l|$, $x = X/\sqrt{\alpha_+}$, $z = Z/\alpha_+$. The new system (5) has only two parameters, defined as $\gamma \equiv \alpha_-/\alpha_+$, $\alpha \equiv \delta/\alpha_+$. Stationary solitons of the system (5) can be found numerically, e.g., by relaxation technique, for all $\gamma > 0$, $\beta_W^\pm > 0$. Some examples of stationary solitons of the system (5) are shown in Fig. 2.

Criteria (3), (4) can be rederived for the system (5), and then used to calculate the boundary of stability area in the (α,γ) plane. However, when values of the parameters α and γ are close to the boundary of soliton existence (e.g. when $\gamma \ll 1$), solutions become weakly localised and it is difficult to calculate Q_1 and Q_2 accurately by conventional numerical methods. Thus we use the tangential transformation of transverse soliton coordinate $X = \tan\pi\tilde{X}$ as was suggested in Ref. [10]. Using this map we can cover the infinite interval in X $(-\infty < X < \infty)$ by a finite one in $\tilde{X}$ $(-1/2 < \tilde{X} < 1/2)$ and calculate the invariants very accurately.

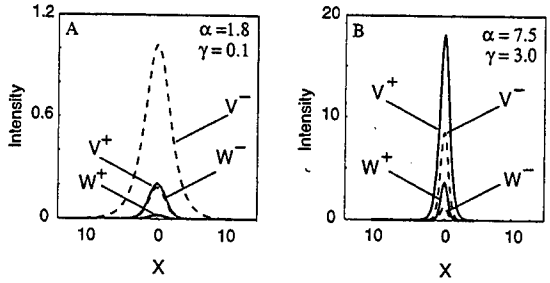


FIG. 2. Examples of stationary solitons due to counter-propagating QPM configuration. Profiles are calculated for the system (5). Solid curves correspond to the forward set of waves, dashed lines - to the backward-propagating ones.

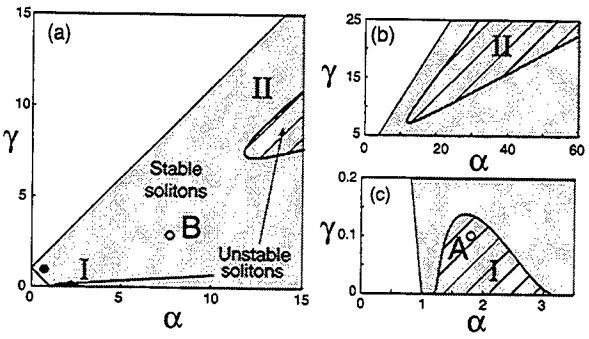


FIG. 3. (a) Existence (shaded) and stability (dashed) domains for the stationary solitons of system (5). Solid curves are defined by the stability threshold condition (3); (b), (c) enlarged plots of the unstable regions I and II. Soliton profiles calculated for the points A and B are shown in Fig. 2. Filled circle corresponds to the exact solution (see text).

To confirm the validity of the stability results given by Eqs. (3) and (4) we analyse numerically an eigenvalue/eigenvector problem corresponding to Eqs. (5) linearised about stationary solitons of interest. In all analysed cases the theoretically predicted stability/instability properties were confirmed numerically. However, we should note that the theoretical approach which we use does not describe so-called *oscillatory* instabilities (see, e.g., [11]) and, although we have not detected such instabilities numerically, further analysis is necessary to completely rule out their possibility. The stability/instability domains given by criteria (3) and (4) are shown in Fig. 3. Note, that the system (1) is invariant under the transformation $z \to -z$, $E_\omega^\pm \to E_\omega^\mp$, $E_{2\omega}^\pm \to E_{2\omega}^\mp$, and $\alpha_\pm \to \alpha_\mp$. Using this symmetry one can derive that if the boundary of the first instability domain is given by $\gamma = \gamma_{\rm I}(\alpha)$, then the boundary of the second domain can be written in a parametric form as $\alpha_{\rm II} = \alpha/\gamma_{\rm I}(\alpha)$, $\gamma_{\rm II} = 1/\gamma_{\rm I}(\alpha)$.

Direct numerical modelling of Eqs. (5) confirms the results of our stability analysis. Two examples of propa-

gation of unstable solitons are presented in Fig. 4.

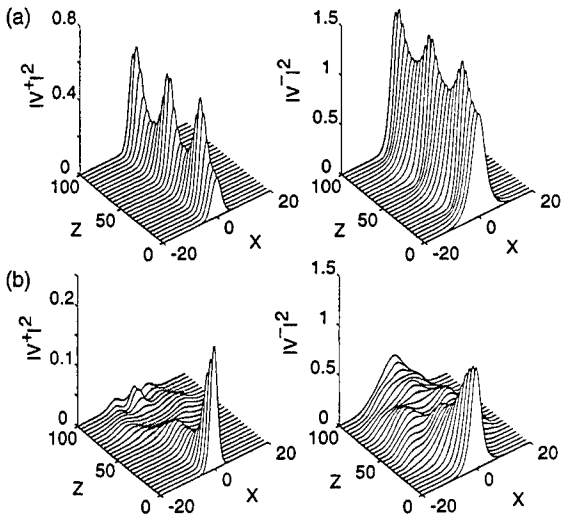


FIG. 4. Examples of unstable propagation of a slightly perturbed stationary soliton shown in Fig. 2, A. Two typical kinds of instability correspond to slightly increased, (a), and reduced, (b), soliton amplitudes. Unstable soliton with a slightly increased amplitude is clearly evolving to some stable state with an excited internal mode (see, e.g., [12]).

Optical power required for generation of counterpropagating solitons of a given beam width can be estimated by the method proposed in Ref. [13]. After defining the soliton width R_s as the maximum width at the half-maximum of the the second harmonic amplitude $E^+_{2\omega}$ the conditional minimum $\tilde{Q}_{min}$ of the total power functional $\tilde{Q}(\alpha,\gamma) = R_s^{3/2}\int_{-\infty}^{+\infty}\{|V^+|^2+|V^-|+2\sigma|W^+|^2+2\sigma|W^-|^2\}\,dX$ has to be found. Then minimal power density I_{min} can be calculated as:

$$I_{min} = \tilde{Q}_{min}\frac{L_{eff}}{4\pi\chi^2_{bulk}r_0^4|d_l|^2}, \qquad (6)$$

where nonlinear coefficient $\chi_{bulk} = (\omega^2/c^2)(2/c\epsilon_0 n)^{1/2}\chi^{(2)}$ is expressed in $W^{-1/2}cm^{-1}$, $\chi^{(2)}$ is the effective element of the second order susceptibility tensor, L_{eff} is the width of a waveguide. For the first order QPM, i.e. $l = 1$, and the values from Ref. [5]: $r_0 = 20\mu m$, $\lambda = 2\pi c/\omega \simeq 1.064\mu m$, refractive index $n \simeq 1.79$, $\chi^{(2)} \approx 6pm/V$ and a waveguide with effective width L_{eff} about $1\mu m$, we obtain $I_{min} \approx 2.8\ W/\mu m$ ($\tilde{Q}_{min} \approx 103$ at $\alpha = 3.15, \gamma = 1.00$). Our analysis shows that the point of optimal generation is in the domain of stability and corresponds to $V^+ = V^-$ and $W^+ = W^-$, i.e., one can generate the whole four-wave soliton using only two seeded forward-propagating waves at one end of a crystal and a mirror on the other [the use of mirror will also halve the generation threshold (6)]. Thus the solitons due to counterpropagating QPM, in principle, require less optical power for an experimental observation in comparison with conventional quadratic solitons, for which the corresponding value is $I_{min} \approx 3.4\ W/\mu m$ (see Ref. [13]).

In practice lowering the generation threshold requires a very short (sub-micron) grating period to arrange for lower order QPM. This was not the case for the experiments [8] where the grating period was about $3\mu m$ and QPM order was high. However, experimental progress in quantum well technology (see, e.g., [14]) may make lower order counterpropagating QPM experimentally possible in the near future.

In conclusion, we have demonstrated the existence of solitons due to counterpropagating QPM in quadratic media. We obtained an analytic criterion for the stability threshold for these solitons and found a substantial region of stability with only two small regions of unstable solitons. We also discussed the conditions for experimental observation of these novel solitons.

[1] M. Segev and G. I. Stegeman, Physics Today **51**, No. 8, 42 (1998), and references therein.

[2] G. I. Stegeman, D. J. Hagan, and L. Torner, J. Opt. Quantum Electron. **28**, 1691 (1996).

[3] J. A. Armstrong, N. Bloembergen, J. Ducuing, P. S. Pershan, Phys. Rev. **127**, 1918 (1962).

[4] M. M. Fejer, G. A. Magel, D. H. Jundt, R. L. Byer, IEEE J. Quant. Electron. **28**, 2631 (1992); G. M. Miller, R. G. Batchko, W. M. Tulloch, D. R. Weise, M. M. Fejer, R.L. Byer, Opt. Lett. **22**, 1834 (1997).

[5] W. E. Torruellas, Z. Wang, D. J. Hagan, E. W. Van Stryland, G. I. Stegeman, L. Torner, C. R. Menyuk, Phys. Rev. Lett. **74**, 5036 (1995); V. V. Steblina, Yu. S. Kivshar, A. V. Buryak, Opt. Lett. **23**, 156 (1998); B. Costantini, C. De Angelis, A. Barthelemy, B. Bourliaguet, V. Kermene, Opt. Lett. **23**, 424 (1998).

[6] C. B. Clausen, O. Bang, Yu. Kivshar, Phys. Rev. Lett. **78**, 4749 (1997); M. Cha, Opt. Lett. **23**, 250 (1998); C. B. Clausen, L. Torner, Opt. Lett., **24**, 7 (1999).

[7] Y. J. Ding, J. B. Khurgin, Opt. Lett. **21**, 1445 (1996); G. D. Landry, T. A. Maldonado, Appl. Opt. **37**, 7809 (1998).

[8] J. B. Kang, Y. J. Ding, W. K. Burns, J. S. Melinger, Opt. Lett., **22**, 862 (1997); X. Gu, R. Y. Korotkov, Y. J. Ding, J. U. Kang, J. B. Khurgin, J. Opt. Soc. Am. B, **15**, 1561 (1998).

[9] A. V. Buryak, Y. Kivshar, S. Trillo, Phys. Rev. Lett. **77**, 5210 (1996).

[10] S. J. Hewlett, F. Ladouceur, J. Lightwave Tech. **13**, 375 (1995).

[11] I. V. Barashenkov, D. E. Pelenovsky, and E. V. Zemlyanaya, Phys. Rev. Lett. **80**, 5117 (1998); A. De Rossi, C. Conti, and S. Trillo, Phys. Rev. Lett. **81**, 85 (1998).

[12] Yu. S. Kivshar, D. E. Pelenovsky, T. Cretegny, and M. Peyrard, Phys. Rev. Lett. **80**, 5032 (1998).

[13] A. V. Buryak, Yu. S. Kivshar, S. Trillo, J. Opt. Soc. Am. B **14**, 3110 (1997).

[14] O. A. Aktsipertov, P. V. Elyutin, E. V. Malinnikova, E. D. Mishina, A. N. Rubtsov, W. de Jong, and Th. Raising, Physics-Doklady, **42**, 340 (1997); R. C. Tu, Y. K. Su, and S. T. Chou, J. of Appl. Phys., **85**, 2398 (1999).

Steering of Discrete Solitons

Hagai Eisenberg and Yaron Silberberg
Department of physics of complex systems
Weizmann Institute of Science, Rehovot 76100, Israel
feisen@wis.weizmann.ac.il, feyaron@wis.weizmann.ac.il

Roberto Morandotti, Ulf Peschel and J. Stewart Aitchison
Department of Electronics and Electrical Engineering
University of Glasgow, Glasgow G128QQ, Scotland

Optical solitons can be formed in the presence of the optical Kerr effect. They have been demonstrated in the past, both in the time domain as stable light pulses [1], and in space, as self-guided beams in a slab waveguide [2]. Recently, there is a growing interest in discrete spatial solitons. These solitons share a few properties with spatial solitons and differ in others. They were proposed as candidates for all-optical switching devices. One advantage over traditional solitons is the waveguide structure they are formed in, enabling easy in-coupling and collection of their light. The formation of discrete solitons in a structure of optical waveguide array was demonstrated recently [3]. In this experiment, light is coupled into one ridge waveguide of an array. As the light propagates, linear coupling between neighboring waveguides broadens the light distribution in a process that is called discrete diffraction. After propagating for about four coupling lengths, the light is distributed among some 35 waveguides. Increasing the light intensity, such that the Kerr effect becomes significant, results in confinement of the light around the input waveguide. This confined distribution which propagates along the waveguide without a change of profile is a discrete soliton.

As was already mentioned, discrete solitons share some properties with spatial solitons. One example is the possibility to have solitons advancing at an angle to the waveguides direction. In the continuous analogue, because of rotational symmetry, this is rather obvious. Surprisingly, it is possible in the discrete case as well. A discrete soliton which is launched with a gradient of the field phase across the initial distribution, will hop sideward while propagating in the array. The deviation from the continuous case appears at higher powers, where the soliton may be locked to the initial waveguides and the transverse motion is prevented [4]. This effect leads to power dependant steering.

We report here the demonstration of power steering. We used 100-200fs pulses with an in-coupled peak power of about 1kW at a wavelength of 1.53μm. The waveguide array pattern was etched on top of an AlGaAs slab waveguide. The wavelength was chosen to be such that two-photon absorption processes are minimized. An elliptically shaped beam was injected into the center of a 41 waveguide array, 6mm long. By controlling the angle of incidence in which the beam was coupled, we were able to induce the required phase gradient. The output facet was imaged onto an infrared camera and sampled and analyzed in a computer.

We present the results of such an experiment in figure 1. The output profile of the light coming out of the array is drawn as a function of the induced angle inside the sample. If the soliton was free to move sideways as in the continuous case, a straight diagonal line would have been formed, representing a linear relation between the output central location and the input angle. We observed this kind of behavior for other, low energy beams propagating in the array. As this high energy soliton is discrete, it has enough power to lock on the input waveguide and to resist the induced steering. Only a sufficient tilt can release the soliton so it can propagate at an angle to the waveguides direction.

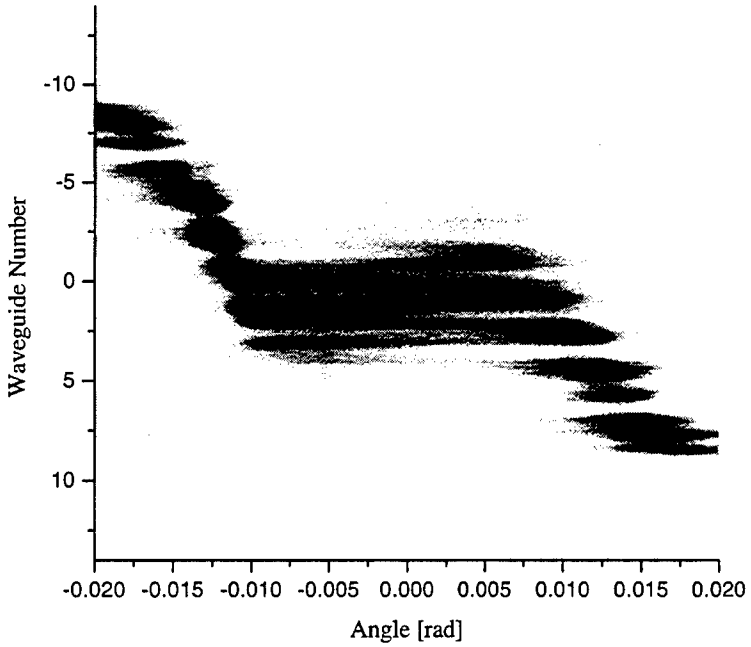


Fig. 1: Output distribution of a discrete soliton as a function of the input angle.

Power induced locking is a result of a discreteness induced lateral potential for discrete solitons across the array. This potential is known from solid state physics and is called the Peierls-Nabarro potential [5]. Another result of this potential is that a discrete soliton centered on a waveguide (mode A), has the minimal Hamiltonian as compared with a soliton centered in between two adjacent waveguides (mode B) which has the maximal Hamiltonian. Therefore, mode A is stable and is harder to steer than mode B, which is unstable.

We observed an effect that is directly related to the presence of this potential. The input position of a beam with no phase gradient was scanned laterally by moving the array sample on a piezo-driven stage. The output profile as a function of the scanning input position is sketched in figure 2. The waveguides periodicity is 9μm and such a cycle is clear in the results. Position zero matches the case for launching mode A, while at -4.5μm and 4.5μm, mode B is launched. At other positions we observed a very large transversal shifts of the output beams, amplifying small deviations of the input beam position from the symmetric input conditions. An input change as small as 3μm, without any initially induced angle, resulted in an output deviation of about 30μm. These deviations are a clear difference from the continuum case where translational invariance exists and hence, small changes in the input position have small effects. The sensitivity to small changes of the output distribution around mode A is obviously smaller than the rapid sweep around mode B, because of the difference in their stability.

In conclusion, we observed two effects, which are unique to discrete spatial solitons. These are discrete soliton power locking and induced steering due to the presence of the Peierls-Nabarro potential. They appear because of the lack of rotational and translational symmetries in the array structure, respectively. Techniques for controlling the position where solitons emerge out of a waveguide may be useful for ultrafast optical switches.

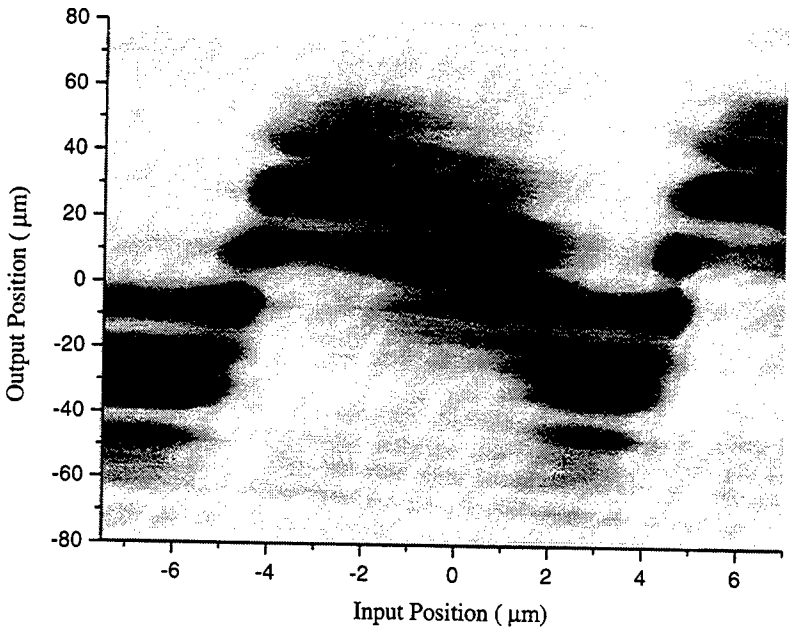


Fig. 2: Output distribution of a discrete soliton as a function of lateral input position.

References

[1] L.F. Mollenauer, R.H. Stolen and J.P. Gordon, Phys. Rev. Lett. **45**, 1095 (1980).

[2] A. Barthelemy, S. Maneuf and C. Froehly, Opt. Commun. **55**, 201 (1985). J.S. Aitchison, Y. Silberberg, A.M. Weiner, D.E. Leaird, M.K. Oliver, J.L. Jackel, E.M. Vogel and P.W.E. Smith, J. Opt. Soc. Am. B **8**, 1290 (1990). J.S. Aitchison, K. Al-Hemyari, C.N. Ironside, R.S. Grant and W. Sibbett, Electron. Lett. **28**, 1879 (1992).

[3] H.S. Eisenberg, Y. Silberberg, R. Morandotti, A.R. Boyd and J.S. Aitchison, Phys. Rev. Lett. **81**, 3383 (1998).

[4] A.B. Aceves, C. De Angelis, T. Peschel, R. Muschall, F. Lederer, S. Trillo and S. Wabnitz, Phys. Rev. E **53**, 1172 (1996).

[5] W. Królikowski and Y. Kivshar, J. Opt. Soc. Am. B **13**, 876 (1996).

Solitons due to double resonance wave mixing in quadratic nonlinear media

Alexander V. Buryak, Isaac Towers, and Rowland A. Sammut

School of Mathematics and Statistics, Australian Defence Force Academy, Canberra, ACT 2600, Australia
a-buryak@adfa.edu.au ph: +61 2 6268-8464 fax: +61 2 6268-8886

Boris A. Malomed

Department of Interdisciplinary Studies, Faculty of Engineering, Tel Aviv University, Tel Aviv 69978, Israel
malomed@eng.tau.ac.il ph: +972-3-6406413 fax: +972-3-6410189

Analysis of mixing between waves at different carrier frequencies is a fundamental problem of nonlinear optics [1]. In an optical medium without a centre of symmetry, the lowest-order nonlinear response is quadratic, leading to three-photon interactions. Resonant parametric mixing among three waves at different carrier frequencies occurs when the resonance condition $\omega_3 = \omega_1 + \omega_2$ is satisfied. A particular case of this three-wave interaction, is known as type II second-harmonic generation (SHG), for which the frequencies are degenerate (i.e., $\omega_1 = \omega_2$), but the polarisations of the fields are different. In a more degenerate case (when the two waves at the fundamental frequency are identical), such a resonant interaction reduces to two-wave mixing or type I SHG.

Solitary waves due to single resonance (type I or type II) SHG have been extensively investigated in the literature recently (see, e.g., [2] for type I SHG solitons and [3,4] for type II SHG solitons). Usually, the type II interaction is considered in anisotropic birefringent models. The analysis of the natural type I - type II mix for a model with two polarization components of the fundamental harmonic in an *isotropic* medium with no birefringence was developed too [5].

More complex cases of double (or multi) resonance wave mixing in quadratic media have not received much attention because of serious difficulties of their experimental realisation by traditional birefringence-based wave-vector matching schemes. (We are only aware of one work: very recently solitons due to double resonance wave mixing involving fundamental, second, and third harmonics have been considered [6].) However, the experimental situation has changed recently as a result of rapid progress in the quasi-phase matching (QPM) technique (see, e.g., [7]), where large wave-vector mismatch between interacting waves is compensated by periodic reversal of the sign of the effective χ^2 nonlinearity. QPM technique not only leads to high values of effective χ^2 coefficients, but may also allow more than one parametric mixing resonance (in different QPM orders) to be achieved. Thus an important question arises: will double (or multi) resonance wave mixing in quadratic media bring any novel features for solitons in comparison to single resonance two-wave (type I) or three-wave (type II) interaction processes? In this paper we analyse this question for the example of double resonance (combined type I and type II) three wave interaction.

The derivation of equations describing double resonance $\chi^{(2)}$ interaction is quite similar to one described in Ref. [4] and is not presented here. The resulting normalised equations have the form

$$\begin{aligned} i\frac{\partial v}{\partial z} + \nabla_\perp^2 v - \beta v + wv^* + \chi wu^* &= 0, \\ i\frac{\partial u}{\partial z} + \nabla_\perp^2 u - (\beta + \Delta k_1 - \Delta k_2)u + \chi wv^* &= 0, \\ 2i\frac{\partial w}{\partial z} + \nabla_\perp^2 w - (4\beta + 2\Delta k_1)w + \frac{v^2}{2} + \chi uv &= 0, \end{aligned} \tag{1}$$

where v and u are fundamental harmonic components of orthogonal polarisations, w is the second harmonic component, z is the propagation distance normalised in diffraction length units, $\nabla_\perp^2 = \partial^2/\partial x^2$ for (1+1)-dimensional case which we investigate in this work, $\Delta k_1 \equiv 2k_1 - k_3$ and $\Delta k_2 \equiv k_1 + k_2 - k_3$ are wave-vector mismatches for type I and type II SHG respectively, the parameter χ measures the relative strength of second order nonlinear susceptibility coefficients responsible for type I and type II interactions, and β is the nonlinear induced shift to the propagation constant.

Similar to type I SHG soliton equations the system (1) has only one power (Manley-Rowe) invariant:

$$Q = \int_{-\infty}^{+\infty} (4|w|^2 + |v|^2 + |u|^2)dx. \tag{2}$$

Not surprisingly the stability criterion for the fundamental family of solitons of the system (1) can be derived in a similar way and has the same form as for type I SHG self-guided beams: $\partial Q/\partial\beta > 0$, for stable solitons. In the case of type II SHG equations considered in Ref. [4,8], there is an extra integral of motion (power imbalance) and the stability criterion has a significantly more complicated form.

When one or both wave-vector mismatch parameters are large, Eqs. (1) may be reduced to a certain version of the model of *competing nonlinearities* [9]. For example, if $|\Delta k_2| \gg 1$ and $|\Delta k_1| \sim 1$, then the second equation of the system (1) can be approximated by an algebraic relation $u \approx -\chi wv^*/\Delta k_2$ which, in turn, helps to eliminate u from other equations of the system (1). However, in this and other limits, which are usually called *cascading limits*, the values of coefficients in the resulting equations

differ significantly from the values for which a full-scale analysis has been conducted in the literature.

To reduce the number of parameters of the system (1) it can be rescaled further. There are two alternative ways of doing this. In the first variant of the rescaling we use the transformation $d = \beta D$ (where $d = v, u, w$ and $D = V, U, W$), $z = Z/\beta$, and $x = X/\sqrt{|\beta|}$, which leads to the system:

$$\begin{aligned} i\frac{\partial V}{\partial Z} + s\frac{\partial^2 V}{\partial X^2} - V + WV^* + \chi WU^* &= 0, \\ i\frac{\partial U}{\partial Z} + s\frac{\partial^2 U}{\partial X^2} - \gamma U + \chi WV^* &= 0, \\ 2i\frac{\partial W}{\partial Z} + s\frac{\partial^2 W}{\partial X^2} - \alpha W + \frac{V^2}{2} + \chi UV &= 0, \end{aligned} \tag{3}$$

where $s \equiv \mathrm{sign}(\beta)$, $\alpha \equiv 4 + 2\Delta k_1/\beta$, and $\gamma \equiv 1 + (\Delta k_1 - \Delta k_2)/\beta$.

For the case of bright solitons $\beta > 0$ so that we can put $s = +1$ and have only three parameters left in Eqs. (3). Because of this small number of parameters and because of the rectangular shape of the soliton existence area ($\alpha > 0$, $\gamma > 0$) the system (3) is the best suited for numerical analysis. However this (α, γ) representation is not the most appropriate for detection of multistability. For this purpose we need to use another type of rescaling: $d = |\Delta k_1|\tilde{D}$ (where $d = v, u, w$ and $\tilde{D} = \tilde{V}, \tilde{U}, \tilde{W}$), $z = \tilde{Z}/|\Delta k_1|$, and $x = \tilde{X}/\sqrt{|\Delta k_1|}$, which allows us to obtain the system:

$$\begin{aligned} i\frac{\partial \tilde{V}}{\partial \tilde{Z}} + \frac{\partial^2 \tilde{V}}{\partial \tilde{X}^2} - \tilde{\beta}\tilde{V} + \tilde{W}\tilde{V}^* + \chi\tilde{W}\tilde{U}^* &= 0, \\ i\frac{\partial \tilde{U}}{\partial \tilde{Z}} + \frac{\partial^2 \tilde{U}}{\partial \tilde{X}^2} - (\tilde{\beta} + \Delta)\tilde{U} + \chi\tilde{W}\tilde{V}^* &= 0, \\ 2i\frac{\partial \tilde{W}}{\partial \tilde{Z}} + \frac{\partial^2 \tilde{W}}{\partial \tilde{X}^2} - (4\tilde{\beta} + 2r)\tilde{W} + \frac{V^2}{2} + \chi UV &= 0, \end{aligned} \tag{4}$$

where $\tilde{\beta} \equiv \beta/|\Delta k_1|$, $\Delta \equiv (\Delta k_1 - \Delta k_2)/|\Delta k_1|$, and $r \equiv \mathrm{sign}(\Delta k_1)$. In this normalisation three cases ($r = +1, 0, -1$) have to be analysed separately. However, if the solitons of Eqs. (3) are known, the solitons (and their integral characteristics) of Eqs. (4) can be obtained by simple rescaling transformations. Thus, below we mainly concentrate on the analysis of Eqs. (3).

It is easy to show that Eqs. (3) have two families of exact soliton solutions

$$v = a\,\mathrm{sech}^2(\frac{x}{2});\; u = b\,\mathrm{sech}^2(\frac{x}{2});\; w = c\,\mathrm{sech}^2(\frac{x}{2}), \tag{5}$$

where $a^2 = [9(1 + 4\chi^2) \pm 9\sqrt{1 + 4\chi^2}]/[4\chi^2(1 + 4\chi^2)]$, $c = 3a^2/(9 - 4\chi^2 a^2)$, and $b = 2\chi ac/3$, which exist for $\alpha = \gamma = 1$. The other way to obtain more analytical information about solitons of Eqs. (3) is to apply the variational approach (VA), see, e.g., [5,10,11]. To avoid excessive complexity of analysis we use the simple form of trial functions ("ansatz") which comply with the linear asymptotics of Eqs. (3): $v = v_0 \exp(-|x|)$, $u = u_0 \exp(-\sqrt{\gamma}|x|)$, and $w = w_0 \exp(-\sqrt{\alpha}|x|)$. Note the difference between this type of ansatz and those used earlier based on sech [10] or Gaussian [11] functions.

Although the formal range of applicability of such variational trial functions is limited to $\alpha \sim \gamma \sim 1$, we found that usually it gives qualitatively correct predictions in a much broader parameter range. For example, for the well-studied case of type II SHG soliton equations of Ref. [8], this version of VA has easily detected soliton multistability. The final result of variational analysis related to Eqs. (3) is given by:

$$\begin{aligned} w_0 &= -(\sqrt{\gamma}K_1 \pm \sqrt{\gamma K_1^2 + 4K_2^2\sqrt{\gamma}})/(2K_2^2), \\ v_0^2 &= 2w_0\sqrt{\alpha}/(K_1 + 2K_2^2 w_0/\sqrt{\gamma}), \\ u_0 &= K_2 v_0 w_0/\sqrt{\gamma}, \end{aligned} \tag{6}$$

where $K_1 = 1/(2 + \sqrt{\alpha})$, $K_2 = \chi/(1 + \sqrt{\alpha} + \sqrt{\gamma})$. This result again shows the existence of two distinct soliton families for all $\alpha > 0$, $\gamma > 0$.

Numerical analysis (based on the relaxation technique) has confirmed VA predictions of the existence of two soliton families. However, direct propagation of solitons of the "upper" family [plus sign in Eqs. (6)] demonstrates that all of them are unstable. Solitons of the "lower" family can be either stable or unstable according to some renormalised version of the criterion $\partial Q/\partial\beta > 0$. Although the region of existence of stable solitons is very substantial (see Fig. 1), neither variational nor numerical analysis could find soliton multistability, i.e. for any fixed value of soliton power at most one stable soliton solution may exist. This conclusion cannot be made from Fig. 1 itself, but is very easy to obtain by plotting stability/instability boundary for Eqs. (4) on $(\tilde{\beta}, \Delta)$ parameter plane (see, e.g., Fig. 2). Multistability may occur only if the boundary curve crosses a line of constant Δ at more than one point. We could never find a situation when this happens. At first glance the absence of multistability looks strange, because although multistability does not occur for solitons due to type I SHG, it does occur for type II SHG solitons [8]. However, there is an important difference between our model and the type II SHG model. In the latter case there are two *independent* power-like invariants and two related β parameters (in contrast to just one in our model). We can conclude that the increase of the number of $\beta's$ rather than simple increase of system's complexity leads to multistability effects in purely $\chi^{(2)}$ media. Also we note that for the double resonance model, solitons can become unstable when both wave-vector mismatches Δk_1 and Δk_2 are positive whereas all single resonance $\chi^{(2)}$ solitons are stable for any non-negative wave-vector mismatches.

The other important difference between our system and the single resonance $\chi^{(2)}$ systems is the presence of *quasisolitons* (see, e.g., [12] for the definition and examples). In general, quasisolitons are weakly radiative quasistationary solitary waves. They can be stable in the

sense that weak perturbations added to them do not grow exponentially fast, but, in principle, even stable quasisolitons always radiate and decay at $z \to \infty$. We found that quasisolitons exist for large negative values of the parameter γ. Quasisolitons are stable and are attractors for a range of initial conditions for Eqs. (3) at $\alpha \ll 1$, when the amplitude of U-component and the radiation rate are small (see Fig. 3). At larger values of α ($\alpha \sim 1$), oscillations in U-component tails become very large and quasisolitons eventually become unstable. The existence of two families of stable solitons/quasisolitons for double resonance $\chi^{(2)}$ systems may be potentially important for switching applications based on spatial solitons.

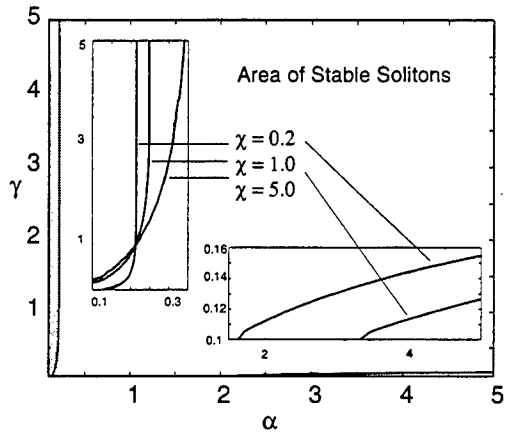


FIG. 1. Stability/instability domains for the fundamental solitons of Eqs. (3) in (α, γ) plane at $\chi = 0.2$. Inserts show blow-ups of the soliton stability boundaries at three characteristic values of the parameter χ.

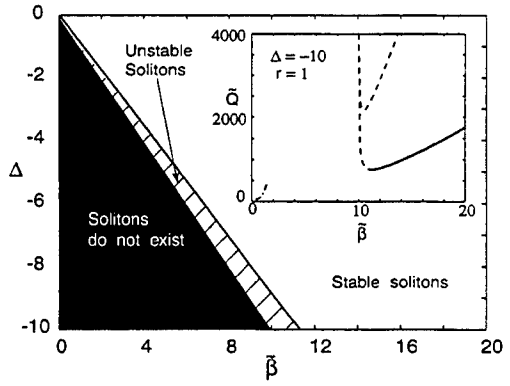


FIG. 2. Stability/instability domains ploted for the fundamental solitons of Eqs. (4) in $(\tilde{\beta}, \Delta)$ plane at $\chi = 0.2$ and $r = 1$. Insert shows a typical $\tilde{Q}$ versus $\tilde{\beta}$ dependence for soliton/quasisoliton families of Eqs. (4) with $\tilde{Q}$ defined similarly to Eq. (2). In the insert solid curve represents stable soliton family, dashed curves – unstable soliton families, and dashed-dotted curve – quasisolitons. (For quasisolitons $\tilde{Q}$ is calculated on a finite interval around localised soliton core.)

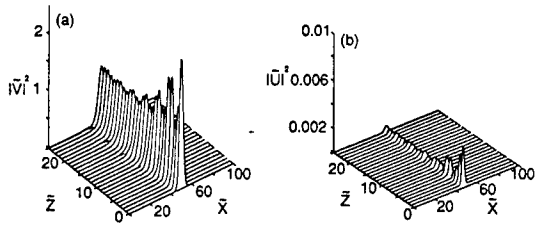


FIG. 3. An example of stable quasisoliton generation. Eqs. (4) are modelled with the initial conditions $\tilde{V} = 1.5 \exp(-x^2/a^2)$, $a \approx 3.55$, $\tilde{U} = \tilde{W} = 0$ for $\Delta = -10$, $r = +1$ and $\chi = 1.0$.

In conclusion, we have analysed a system describing double resonance (type-I plus type-II) wave mixing in quadratic nonlinear media. We found that double resonance interactions allow the existence of stable solitons in a broad parameter range. However no conventional soliton multistability has been detected. Our results show that for quadratic media soliton multistablity phenomena are more usual for the systems with two Manley-Rowe invariants. Finally, we have shown that double resonance interactions can lead to stable quasisolitons and to multistablity in the sense of the coexistence of two stable soliton/quasisoliton families. This may be potentially important for soliton-based optical switching.

[1] J. A. Armstrong, N. Bloembergen, J. Ducuing, and P. S. Pershan, Phys. Rev. E, **6**, 1918 (1962).

[2] A. V. Buryak and Yu. S. Kivshar, Phys. Lett. A **197**, 407 (1995); D. E. Pelinovsky, A. V. Buryak and Yu. S. Kivshar, Phys. Rev. Lett. **75**, 591 (1995).

[3] H. T. Tran, Opt. Commun., **118**, 581 (1995); D. Anderson, M. Lisak, and B.A. Malomed, Opt. Commun. **126**, 251 (1996).

[4] A. V. Buryak, Yu. S. Kivshar, and S. Trillo, J. Opt. Soc. of Am. B, **14**, 3110, (1997).

[5] A. D. Boardman, P. Bontemps, and K. Xie, Opt. and Quant. Electron., **30**, 891, (1998)

[6] Yu. S. Kivshar, T. J. Alexander, and S. Solomon, Opt. Lett., 1999 (in press).

[7] M. M. Fejer, G. A. Magel, D. H. Jundt, and R. L. Byer, IEEE J. Quant. Electron., **28**, 2631 (1992); G. D. Miller, R. G. Batchko, W. M. Tulloch, D. R. Weise, M. M. Fejer, and R. L. Byer, Opt. Lett., **22**, 1834, (1997).

[8] A. V. Buryak, Yu. S. Kivshar, and S. Trillo, Phys. Rev. Lett., **78**, 3286, (1997); U. Peschel, C. Etrich, F. Lederer, and B.A. Malomed, Phys. Rev. E **55**, 7704 (1997).

[9] A. V. Buryak, Yu. S. Kivshar, and S. Trillo, Opt. Lett. **20**, 1961 (1995); O. Bang, Yu. S. Kivshar, A. V. Buryak, A. De Rossi, and S. Trillo , Phys. Rev. E, **58**, 5057 (1998).

[10] W.C.K. Mak, B.A. Malomed, and P.L. Chu, Phys. Rev. E **58**, 6708 (1998).

[11] V. V. Steblina, Yu. S. Kivshar, M. Lisak, and B. A. Malomed, Opt. Comm., **118**, 345 (1995).

[12] P. K. A. Wai, H. H. Chen, Y. C. Lee, **41**, 426 (1990); D.J. Kaup, T.I. Lakoba, and B A. Malomed, J. Opt. Soc. Am. B **14**, 1199 (1997); V. E. Zakharov and E. A. Kuznetsov, JETP, **86**, 1035 (1998).

Collapse suppression via parametric wave mixing

Victoria V. Steblina, Alexander V. Buryak, and Rowland A. Sammut,

School of Mathematics and Statistics, University College
Australian Defence Force Academy, Canberra ACT 2600 Australia
Phone: 61-2-62688464, Fax: 61-2-62688886, Email: v-steblina@adfa.edu.au, a-buryak@adfa.edu.au, r-sammut@adfa.edu.au

Yuri S. Kivshar

Optical Sciences Centre, Research School of Physical Sciences and Engineering
Australian National University, Canberra ACT 0200 Australia
Phone: 61-2-62493081, Fax: 61-2-62495184, Email: ysk124@rsphy1.anu.edu.au

Very soon after the first paper reporting the idea of optical self-focusing [1] was published, it was realised that a balance between beam diffraction and positive (self-focusing) nonlinearity corresponds to *unstable states* [2]. From the physical point of view, the instability means that all beams with power P below the critical value P_{cr} of the self-trapped state diffract, whereas all beams with higher power ($P > P_{cr}$) experience a catastrophic *collapse* – the beam width tends to zero and its amplitude grows to infinity at some finite propagation distance. This theoretical prediction is based on the rigourous analysis [3] of the *paraxial approximation* model of the (2+1)-dimensional beam propagation in Kerr media, which is described by the Nonlinear Schrödinger (NLS) equation. Because of this catastrophic singularity, the NLS equation is now believed to be an incomplete model for (2+1)-dimensional beam self-trapping and different types of physical effects (such as saturation, nonlocal response, dissipation, vectorial corrections, etc.) have been analysed to describe its validity limits. Comprehensive analysis of different mechanisms of the collapse arrest or suppression have been recently overviewed in Refs. [4,5].

The majority of the mechanisms for collapse suppression discussed so far are based on some perturbations to NLS equation derivation procedure (e.g., nonparaxiality, vectorial corrections) or special assumptions about the properties of the nonlinear medium (e.g., nonlocal response, nonlinearity saturation, etc). However, one of the most crucial effects has been missed so far in all those studies. Indeed, the conventional multiple-scale asymptotic derivation of the effective equation for an envelope of a monochromatic wave (see, e.g., [6]) neglects any coupling with higher order harmonics which are, in fact, always excited in a nonlinear medium. In sharp contrast to previous beliefs, we have shown that even a far-detuned parametric coupling of the fundamental beam to its third-harmonic field can produce an effective mechanism for collapse suppression.

To introduce the model, we follow the derivation procedure presented in Refs. [7] assuming that the fundamental ($\omega_1 = \omega$, k_1) and the third-harmonic ($\omega_2 = 3\omega$, k_2) beams have the same linear polarisation and interact resonantly. The normalised system of coupled equations describing such an interaction can be written in the following form

$$i\frac{\partial u}{\partial z} + \nabla_\perp^2 u - u + \left(\frac{1}{9}|u|^2 + 2|w|^2\right)u + \frac{1}{3}u^{*2}w = 0,$$
$$i\sigma\frac{\partial w}{\partial z} + \nabla_\perp^2 w - \alpha w + (9|w|^2 + 2|u|^2)w + \frac{1}{9}u^3 = 0, \quad (1)$$

where u and w are envelopes of the fundamental and third harmonic beams, respectively, $\nabla_\perp^2 \equiv \partial^2/\partial x^2 + \partial^2/\partial y^2$, z is the propagation distance, α is the renormalised nonlinear induced propagation constant (which is also dependent on the quality of wave-vector matching between the harmonics: $\alpha = 9$ corresponds to the exact matching) and, for the spatial beam evolution, $\sigma = 3$. Radially symmetric stationary beams are described by real functions, $u(r)$ and $w(r)$, where $r \equiv \sqrt{x^2 + y^2}$, defined as localised solutions of slightly modified Eqs. (1) [with the $z-$derivatives omitted and $\nabla_\perp^2 \equiv d^2/dr^2 + (1/r)d/dr$]. These localised solutions depend only on a single dimensionless parameter α.

We follow the analysis of Ref. [7], and first obtain the structure of the soliton families of Eqs. (1). Analysis of asymptotics of stationary radially symmetric solutions of Eqs. (1) shows that radiationless bright solitons with exponentially decaying tails can exist only for $\alpha > 0$. Using a direct analogy with the theory of $\chi^{(2)}$ solitons, first we investigate the solitary waves of the so-called cascading limit when $|\alpha| \gg 1$. In this limit $w \approx u^3/(9\alpha)$, and Eqs. (1) become the cubic-quintic NLS equation which supports a familiar class of fundamental solitons of a simple bell-shape. This asymptotic solution has been used as a starting point in the search for families of stationary solitons, which we find with the help of a numerical relaxation technique. To characterise different families of these solitons we use the normalised total power

$$P_{\rm tot} = \iint_{-\infty}^{\infty} (|u|^2 + 3\sigma|w|^2)\, dx\, dy, \quad (2)$$

which is one of the conserved quantities of the dynamical

system (1)

In the right part of the central diagram of Fig 1 we show the normalised total power, $P_{\rm tot}$, vs. the normalised mismatch parameter α, for different types of two-wave localised solutions of the system (1). The most important class of two-wave bright solitons is described by a family of localised solutions for coupled fundamental and third harmonic fields The distribution of power between the two components varies from being predominantly in the third harmonic, for smaller α, to being predominantly in the fundamental, at larger values of α, i.e. in the cascading limit

A simple analysis shows that the family of two-frequency solitary waves bifurcates from the one-frequency solution for the third harmonic, which exists for all $\alpha > 0$ and represents scalar Kerr solitons This family of one-frequency solitary waves is characterised by the normalised power, $P_{\rm tot} = const \approx 11.70$, and it is described by the standard (2+1)-dimensional cubic NLS equation which follows from the second equation of the system (1) at $u = 0$ It is clear that this type of solitary wave is possible only due to the self-phase modulation effect taken into account for the third harmonic. Because an analytic form of this one-frequency soliton is unknown, numerical (or approximate variational) methods should be used to find the position of the bifurcation point, where two new families of two wave solitons appear Variational analysis based on the use of simple exponential trial functions gives $\alpha_{bif}^{(var)} = 105.83$ which agrees reasonably well with the numerical result $\alpha_{bif}^{(num)} = 104.16$. Two representatives of this fundamental family of two-frequency solitary waves are shown as the plots A and B in Fig 1.

Stability of one-wave and two-wave solitons described above is an intriguing issue. *Our analysis demonstrated that all two wave solitons of the bifurcated branch are unstable* Note, that one-wave w-component solitons, for which $\partial P_{\rm tot}/\partial\alpha = 0$, are also unstable due to the usual critical collapse instability of a single NLS equation [8].

The third family of localised solutions shown in Fig. 1 includes the simplest self similar solution, which was earlier discussed by Hayata *et. al.* [9]. This solution is marked by a filled point G in Fig 1. It exists only at $\alpha = 1$ having the following form

$$u_s(x,y) = a\, f(r)\ , \quad w_s(x,y) = b f(r), \qquad (3)$$

where the parameters a and b can be found with a procedure described in Ref. [7] and $f(r)$ is a radially symmetric stationary solution of the (2+1) dimensional NLS equation.

Similar to the (1+1)-dimensional case [7], the self-similar solution of the model (1) and the asymptotic solution of the cascading limit, $\alpha \gg 1$, do not belong to the same family Moreover, varying continuously the effective mismatch parameter α along this family of localised solutions shows that this class of solitary waves corresponds to *multi-hump solitary waves*, as is shown in the plot C The point $\alpha = 1$ is special: it separates two subfamilies of solitons with different numbers of humps in third harmonic. Thus, even though it is a one-hump solution itself, the self-similar soliton at $\alpha = 1$ belongs to a higher order soliton family. It is not surprising that all solutions of this family are also unstable, a conclusion which we have verified by direct numerical simulations. Unfortunately, in Ref. [9], only solitons corresponding to our unstable solution (3) have been analysed and thus parametric collapse stabilisation has not been achieved. Note that the diagram presented in Fig. 1 does not show all possible soliton families, but only those containing the solitons of simple one-hump shape. Other (higher-order) soliton families also exist and they will be analysed elsewhere.

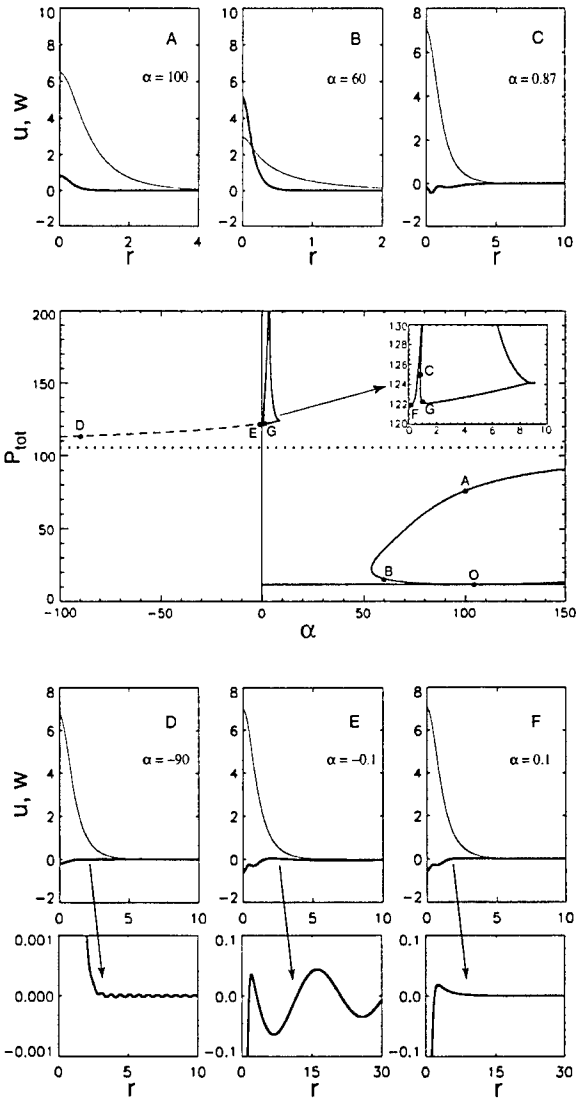


FIG. 1. Bifurcation diagram for localised solutions of Eqs. (1). Examples of quasisolitons and solitons are shown above and below the main diagram, including blow up plots of tails of the third-harmonic component. Point G represents the self-similar solution (3); O is the bifurcation point.

The physical explanation of observed collapse instability of *all* stationary solitons of Eqs. (1) is the following: at large positive values of α (cascading limit) the third harmonic adds additional self-focussing described by an effective *positive quintic nonlinearity*, which can only accelerate the collapse. Qualitatively this effect does not change even for small positive values of α.

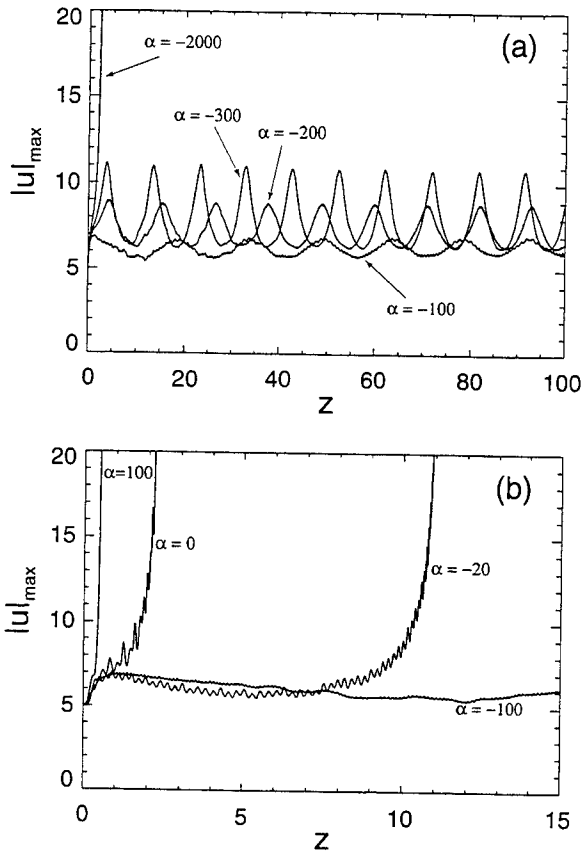


FIG. 2. Examples of the evolution of maximum amplitude of the fundamental harmonic component for the initial condition $u = 5.0\exp[-1.39(x^2+y^2)/2]$, $w = 0$ at different values of the parameter α.

On the other hand, the similar physical argumentation suggests that the large *negative* α (i.e for large negative mismatch parameter $\Delta \sim 3k_1 - k_2$) the situation should be opposite and cascading mechanism could provide stabilisation via effective negative quintic nonlinearity. The problem is that such a stabilisation cannot lead to formation of a stable *stationary* soliton because of unavoidable resonance with linear waves (see, e.g., Ref. [10] for a relevant discussion). However, only the third-harmonic component is in resonance and may radiate. The intensity of this radiation can be estimated [10] and is exponentially small for large values of α. Thus we can expect the existence of a family of weakly radiative (quasi-stable) solitons. (For a discussion about this class of solitons, which are also called *quasisolitons* see, e.g., Ref. [11].) Numerical analysis has indeed detected a family of quasisolitons at *all negative values of* α. This family continuously transforms into a family of conventional stationary solitons as α changes its sign to become positive. The corresponding dependence is presented in the left part of the main diagram of Fig. 1. Note, that because of nondecaying oscillatory tails in third-harmonic component (see the plots D and E in Fig. 1) we have to modify the definition of $P_{\rm tot}$ for the family of quasisolitons calculating power only for the soliton core. Our analysis confirms that quasisolitons are quasistable provided $|\alpha| \gg 1$.

The existence of robust quasisolitons is an indication of a possibility of the collapse arrest. Indeed our numerical modelling demonstrates that if we start from a single Gaussian beam of the fundamental harmonic, then at large negative values of α the collapse can be suppressed for very long propagation distances (see Fig. 2).

Thus we reveal an effective physical mechanism for collapse suppression in a nonlinear Kerr medium based on parametric wave mixing and generation of a weak third-harmonic wave. We also demonstrate that even a far-detuned coupling between the fundamental beam and its generated harmonic field (for, e.g., $\alpha \sim 10^2$) creates an effective mechanism of radiative losses that suppresses the collapsing beam dynamics. We believe that this finding opens a new direction of research of the beam stabilisation and stability in a bulk medium under the action of different types of parametric wave interactions.

[1] R. Y. Chiao, E. Garmire, and C. H. Townes, Phys. Rev. Lett. **13**, 479 (1964).

[2] P. L. Kelly, Phys. Rev. Lett. **15**, 1005 (1965).

[3] K. Rypdal and J. J. Rasmussen, Phys. Scripta, **40**, 192 (1989).

[4] L. Berge, Phys. Rep. **303**, 259 (1998).

[5] Yu. S. Kivshar and D. E. Pelinovsky, *"Self-focussing and transverse instabilities of solitary waves"*, Phys. Rep. (1999) in press.

[6] See, e.g., A. Jeffrey and T. Kawahara, "Asymptotic Methods in Nonlinear Wave Theory" (Pitman, Boston, 1982), Chap. 3.

[7] R. A. Sammut, A. V. Buryak, and Yu. S. Kivshar, Opt. Lett. **22**, 1385 (1997); J. Opt. Soc. Am. B **15**, 1488 (1998).

[8] E. A. Kuznetsov, A. M. Rubenchik, and V. E. Zakharov, Phys. Rep. **142**, 103 (1986).

[9] K. Hayata, Y. Uehira, and M. Koshiba, Phys. Rev. A **51**, 1549 (1995).

[10] A. V. Buryak, Phys. Rev. E **52**, 1156 (1995).

[11] V. E. Zakharov and E. A. Kuznetsov, JETP, **86**, 1035 (1998).

Asymmetric incoherent solitons

Wiesław Królikowski[†], **Nail N. Akhmediev**[††]
Natalia M. Litchinitser[*] and **Govind P. Agrawal**[*]

[†]Australian Photonics CRC, Laser Physics Centre, Research School of Physical Science and Engineering, The Australian National University, Canberra ACT 0200, Australia
wzk111@rsphysse.anu.edu.au

[††] Australian Photonics CRC, Optical Sciences Centre, Research School of Physical Science and Engineering, The Australian National University, Canberra ACT 0200, Australia
nna124@rsphysse.anu.edu.au

[*]The Institute of Optics and Rochester Theory Center of Optical Science and Engineering, University of Rochester, Rochester, NY 14627 USA
natasha@optics.rochester.edu and gpa@optics.rochester.edu

Incoherent spatial solitons have attracted considerable attention recently [1], especially after the first experimental observation of partially incoherent solitons (PCS) was made by Mitchell *et al.* [2]. The notion of spatially and temporally incoherent solitons was introduced by Hasegawa in a series of papers [3], both for plasma waves and for nonlinear pulses in multimode fibers. However, the generation of incoherent solitons in optical fibers requires unrealistically high pulse energies. Photorefractive materials are probably the most suitable medium for experimental studies of incoherent solitons since they generally exhibit very strong nonlinear effects at extremely low optical powers [4].

Photorefractive materials usually have saturable nonlinearity. For the special case of the logarithmic nonlinearity which is an approximation of the saturable nonlinearity, the symmetric solutions can be written in an analytic form [1]. The description of optical beams in nonlinear media in terms of a self-induced multimode waveguide has been especially fruitful. This idea has been used for incoherent solitons [1]. In this point of view, stationary soliton propagation is governed by a proper combination of various mutually incoherent linear modes of the self-induced waveguide. On the other hand, this approach has provided so far only symmetric solutions [1]. The diffraction-less ray-optics limit for treating spatial incoherent solitons has been proposed in Ref. [5]. This approach is accurate when the size of the PCS is much larger than the optical wavelength. In terms of a multimode waveguide, this limit is valid when the number of modes goes to infinity, so that the soliton becomes completely incoherent. It has been shown, in this limit, that solitons of arbitrary shape may exist. However, the question of existence of asymmetric solitons in media with saturable nonlinearity when the number of modes is finite is not obvious.

Propagation of a partially coherent beam in nonlinear media can be represented by a set of equations for the mutually incoherent components constituting the beam [1]. For a beam consisting of N such components, the corresponding equations have the following form in case of saturable nonlinearity:

$$i\frac{\partial \psi_i}{\partial z} + \frac{1}{2}\frac{\partial^2 \psi_i}{\partial x^2} + \frac{\alpha\, I}{1 + I/I_0}\psi_i = 0, \qquad (1)$$

where ψ_i denotes the amplitude of i-th component of the beam ($i = 1, 2, \ldots$), α represents the strength of nonlinearity, I_0 is the saturation parameter, x and z denote dimensionless transverse and propagation coordinates, respectively, and

$$I = \sum_{i=1}^{N} |\psi_i|^2 \tag{2}$$

is the total intensity created by all incoherent components of the light beam. The specific form $(1 + I/I_0)^{-1}$ of the saturation of nonlinearity used in Eq. (1) holds, for instance, for a homogeneously broadened two-level system and biased photorefractive crystals; other functional forms should also exhibit similar qualitative behavior. The nonlinear medium is assumed to have slow response compared with the time scale over which the phases of the individual components change, so that the change of the refractive index is determined by the total intensity given by Eq. (2). It can be shown that the width of the spatial coherence function depends on the number of components included in the sum appearing in Eq. (2). For this reason, we refer to the beam with finite N as "partially coherent."

We are interested in PCS solutions of Eq. (1) when N is finite and a relatively small number. Such solutions correspond to stationary waveguides self-induced by their own modes. However, the self-consistency condition, represented by Eq. (2), requires these solutions to be multi-soliton complexes, which are nonlinear superposition of fundamental solitons propagating in parallel and thus creating the waveguide. This complementary view is important for a physical understanding of the PCS. Stationary solutions of Eq. (1) can be written in the form

$$\psi_i(x, z) = u_i(x) \exp(i\lambda_i z), \tag{3}$$

with real functions $u_i(x)$ and real eigenvalues λ_i. Then the set of Eqs. (1) reduces to a set of ordinary differential equations of the form

$$\frac{\partial^2 u_i}{\partial x^2} + 2\alpha \left(\frac{\sum_{j=1}^{N} u_j^2}{1 + \sum_{j=1}^{N} u_j^2/I_0} \right) u_i = 2\lambda_i u_i. \tag{4}$$

Physically, λ_i is the propagation constant associated with the mode profile $u_i(x)$.

Equation (4) can be solved numerically using either a shooting or an iteration technique. In the latter case, we first find the modes of a given (zero-oder approximation) waveguide, vary the amplitudes of different modes to modify the refractive index profile, and then use the self-consistency condition (2). Repeating these steps results in a convergence to a stationary beam profile. Using this iterative approach, we have found the intensity profiles of several different PCSs and their constituent linear modes. In our simulations, the propagation distance z is normalized to the diffraction length and we choose $\alpha = 2$ and $I_0 = 2$ in Eq. (1). In turns out that, in the case $N = 2$, the numerical procedure converges only to a symmetric solution, similar to those presented in previous works [1]. However, when $N > 2$ simulations result in both symmetric and asymmetric solutions. We should note that asymmetric solutions are generic and appear on the same basis as symmetric ones.

We should stress again, that in the case of a single NLSE or two coupled NLSE with constant coefficients stationary asymmetric solutions do not exist. The one-soliton (N = 1) solution is symmetric, and all higher-order solitons are non-stationary solutions of the NLSE. In fact, it appears that only a coupled set of NLS's with $N > 2$ admit stationary asymmetric solutions. Similar phenomenon happens in multi-core nonlinear fiber couplers [6]. Only when the number of fibers is higher than 2, asymmetric solutions appear (see Fig.3 of [6]). This happens only in the case of nonintegrable models. When the equations are integrable (Manakov model) asymmetric solutions exist even when $N = 2$. This difference is still mysterious and has to be explained. The integrable model is unique in a sense that solitons in it do not have binding energy. They can be located at any distance from each other and this distance does not change with propagation. Hence, asymmetric solution consisting of two unequal solitons when $N = 2$ appears naturally. If the model is non-integrable, binding energy is nonzero and two solitons cannot stay at fixed distance from each other. They will oscillate around their common "center of mass". Hence, stationary asymmetric solution cannot exist.

When $N = 3$, three-soliton asymmetric solution can become stationary again. It might happen that binding energy between three solitons at certain conditions reduces to zero. This requires specific soliton amplitudes and relative distances. In this case they may propagate parallel to each other. We have found several numerical examples of asymmetric solutions and checked that they are indeed stable solutions of Eq. (1) in the sense that they do not change their shape during propagation inside the nonlinear media. However, the shape of the PCS changes appreciably after collisions. Moreover, collisions transform stationary solutions into non-stationary beams which change their shape periodically. This means that binding energy also changes after collisions.

Natalia M. Litchinitser thanks Aileen S. Andrew Foundation for a postdoctoral fellowship.

1. D. N. Christodoulides, T. H. Coskun, R. I. Joseph, Opt. Lett., **22**, 1080 (1997); D. N. Christodoulides, T. H. Coskun, M. Mitchell and M. Segev, Phys. Rev. Lett., **80**, 2310 (1998).

2. M. Mitchell, Z. Chen, M. Shih and M. Segev Phys. Rev. Lett., **77**, 490 (1996).

3. A. Hasegawa, Phys. Fluids, **18**, 77 (1975); Phys. Fluids, **20**, 2155 (1977); Opt. Lett., **5**, 416 (1980).

4. G. Duree, J. L. Shultz, G. Salamo, M. Segev, A. Yariv, B. Crosignani, P. Di Porto, E. Sharp, and R. R. Neurgaonkar, Phys. Rev. Lett. **71**, 533 (1993); M. D. Iturbe-Castillo, P. A. Marques Aguliar, J. J. Sanches-Mondragon, and V. Vysloukh, Appl. Phys. Lett. **64**, 408 (1994); A. V. Mamaev, M. Saffman, D. Z. Anderson, and A. A. Zozulya, Phys. Rev. A **54**, 870 (1996).

5. A. W. Snyder, D. J. Mitchell, Phys. Rev. Lett., **80**, 1422 (1998).

6. Akhmediev N. N. and Buryak A. V., *JOSA B*, **11**, 804 (1994).

Do stable multi-hump solitons exist?

Elena A. Ostrovskaya[1], Yuri S. Kivshar[1], Dmitry V. Skryabin[2], and William J. Firth[2]

[1] *Australian Photonics Cooperative Research Centre, Optical Sciences Centre, Research School of Physical Sciences and Engineering, The Australian National University, Canberra ACT 0200, Australia*

[2] *Department of Physics and Applied Physics, University of Strathclyde, Glasgow, G4 0NG, Scotland*

Self-guided optical beams, or *spatial optical solitons*, are the building blocks of all-optical switching devices where light itself guides and steers light without fabricated waveguides[1]. In the simplest case, a spatial soliton is created by one beam of a certain polarization and frequency, and it can be viewed as a self-trapped mode of an effective waveguide it induces in a medium[2]. When a spatial soliton is composed of two (or more) modes of the induced waveguide[3], its structure becomes rather complicated, and the soliton intensity profile may display several peaks. Such solitary waves are usually referred to as *multi-hump solitons*; they have been found for various nonlinear models of coupled fields.

In realistic (nonintegrable) physical models, solitary waves can become unstable demonstrating self-focusing, decay, or a nonlinearity-driven transition to a stable state, if the latter exists[4]. All these scenarios of soliton evolution are initiated by exponentially growing perturbations and they are attributed to *linear instability*. It is usually believed that *all types* of multi-hump solitary waves *are linearly unstable*, except for the special case of neutrally stable solitons in the integrable Manakov model. On the contrary, recent experimental results[5] indicate the possibility of observing *stationary structures* resembling multi-hump solitary waves. This naturally poses a question: *Were those observations only possible because of short propagation distance and a small instability growth rate?* Here we present the results of a linear stability analysis indicating that stable multi-hump solitons do exist.

In the experiments[5], spatial multi-hump solitary waves were generated by incoherent interaction of two optical beams in a biased photorefractive crystal. The corresponding model has been derived by Christodoulides *et al.*[6], and it is described by a system of two coupled nonlinear equations for the normalized beam envelopes, $u(x,z)$ and $w(x,z)$, which for the purpose of our current analysis can be written in the following form[7]:

$$\begin{aligned} i\frac{\partial u}{\partial z} + \frac{1}{2}\frac{\partial^2 u}{\partial x^2} + \frac{u(|u|^2+|w|^2)}{1+s(|u|^2+|w|^2)} - u = 0, \\ i\frac{\partial w}{\partial z} + \frac{1}{2}\frac{\partial^2 w}{\partial x^2} + \frac{w(|u|^2+|w|^2)}{1+s(|u|^2+|w|^2)} - \lambda w = 0, \end{aligned} \qquad (1)$$

where the transverse, x, and propagation, z, coordinates are measured in the units of $(L_d/k)^{1/2}$ and L_d, respectively, L_d is a diffraction length, and k is the wavevector in the medium. The parameter λ is a ratio of the nonlinear propagation constants, and s is an effective *saturation parameter*. For $s \to 0$, the system (1) reduces to the integrable *Manakov equations*.

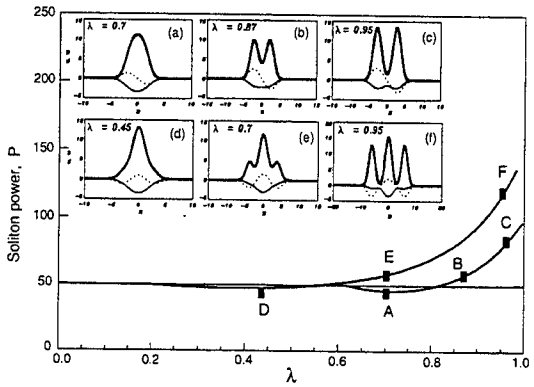


Fig. 1. Soliton bifurcation diagram for $s = 0.8$. Horizontal line - branch of the fundamental $u-$soliton. A-B-C - branch of $|0,1\rangle$ solitons. D-E-F - branch of $|0,2\rangle$ solitons. Inset: Transverse profiles of u- (thin), w- (dashed) fields, and total intensity (thick), shown for marked points.

We look for stationary, z-independent, solutions of Eqs. (1) with both components $u(x)$ and $w(x)$ real and vanishing as $|x| \to \infty$. Different types of such two-component localized solutions, existing for $0 < \{\lambda, s\} < 1$, can be characterized by the total power, $P(\lambda,s) = P_u + P_w$, where the partial powers, $P_u = \int_{-\infty}^{\infty} |u|^2 dx$ and $P_w = \int_{-\infty}^{\infty} |w|^2 dx$, are integrals of motion. If one of the components is small, i.e. $w/u \sim \varepsilon$, Eqs. (1) become decoupled and, in the leading order, the equation for the u-component has a solution $u_0(x)$ in the form of a fundamental, *sech*-like, soliton with no nodes. The second equation can then be considered as an eigenvalue problem for the "modes" $w_n(x)$ of a waveguide created by the soliton $u_0(x)$ with the effective refractive index profile $u_0^2(x)/[1+su_0^2(x)]$. Parameter s determines the total number of guided modes and the cut-off value for each mode, $\lambda_n(s)$. Therefore, a two-component *vector* soliton (u_0, w_n) consists of a fundamental soliton and an nth-order mode of the waveguide it induces in the medium. Henceforward we denote such a composite solitary wave by its "state vector": $|0,n\rangle$.

On the $P(\lambda)$ diagram (for fixed s), continuous

branches representing $|0,n\rangle$ solitons emerge at the points of bifurcations $\lambda_n(s)$ of one-component solitons (see Fig. 1). It is noteworthy that the first-order mode is in fact *the lowest possible mode of the waveguide* induced by the fundamental soliton $u_0(x)$. This is because the state $|0,0\rangle$, node-less in both components, can exist only in the degenerate case $\lambda = 1$, when Eqs. (1) have a family of equal-width solutions $u_0 = A(x)\sin\theta$ and $w_0 = A(x)\cos\theta$, with arbitrary θ, and amplitude A satisfying the scalar equation, $dA/dx = \pm s^{-1}[\log(1+sA^2) - s(1-s)A^2]^{1/2}$.

Additionally, indefinitely many families of vector solitons $|m,n\rangle$, where $m \neq n \neq 0$, can be formed as *bound states* of phase-locked $|0,n\rangle$ solitons[8]. Although such states do contribute to the rich variety of the multi-hump solitons existing in our model, we exclude them from our present consideration.

Families of vector solitons can be found by numerical relaxation technique. Some results of our calculations are presented in Fig. 1, for $|0,1\rangle$ and $|0,2\rangle$ solitons found at $s = 0.8$. Observing the modification of soliton profiles with changing λ (see inset in Fig. 1), one can see that the modal description of two-component solitons is valid only near bifurcation points. For $\lambda \gg \lambda_n$, the amplitude of an initially small w-component *grows* and the soliton-induced waveguide deforms. *It is this purely nonlinear effect that gives rise to the existence of multi-hump solitons.* In particular, two- and three-hump solitons are members of the soliton families $|0,1\rangle$ (branch A-B-C) and $|0,2\rangle$ (branch D-E-F) originating at different bifurcation points. At $\lambda \sim \lambda_n(s)$, while the w-component remains small, all $|0,n\rangle$ solitons are *single-humped*, as shown in Figs. 1(a,d). As the amplitude of w grows with increasing λ, the total intensity profile, $I(x) = u_0^2(x) + w_n^2(x)$, develops $(n+1)$ humps [see Figs. 1(b,e)], and at sufficiently large λ the u-component itself becomes *multi-humped* [Figs. 1(c,f)]. The separation distance between the soliton humps tends to infinity as $\lambda \to 1$.

To analyze the linear stability of multi-hump solitons, we seek solutions of Eqs. (1) in the form of weakly perturbed solitary waves: $u(x,z) = u_0(x) + \varepsilon[F_u(x,z) + iG_u(x,z)]$ and $w(x,z) = w_n(x) + \varepsilon[F_w(x,z) + iG_w(x,z)]$, where $\varepsilon \ll 1$. Setting $F_{u,w} \sim f_{u,w}(x)e^{\beta z}$, $G_{u,w} \sim g_{u,w}(x)e^{\beta z}$, one can obtain the following eigenvalue problem (EVP)

$$\hat{\mathcal{L}}_1\hat{\mathcal{L}}_0\vec{g} = -\Lambda\vec{g}, \qquad \hat{\mathcal{L}}_0\hat{\mathcal{L}}_1\vec{f} = -\Lambda\vec{f}. \tag{2}$$

Here $\vec{g} \equiv (g_u, g_w)^T$, $\vec{f} \equiv (f_u, f_w)^T$, $\Lambda = \beta^2$, and

$$\hat{\mathcal{L}}_{0,1} = \begin{pmatrix} -\frac{1}{2}\frac{d^2}{dx^2} + 1 - a_{0,1} & b_{0,1} \\ b_{0,1} & -\frac{1}{2}\frac{d^2}{dx^2} + \lambda - c_{0,1} \end{pmatrix},$$

where $a_0 = c_0 = I/(1+sI)$, $b_0 = 0$, $a_1 = a_0 + 2u_0^2/(1+sI)^2$, $c_1 = c_0 + 2w_n^2/(1+sI)^2$, and $b_1 = -2u_0w_n/(1+sI)^2$.

Because $\hat{\mathcal{L}}_1\hat{\mathcal{L}}_0$ and $\hat{\mathcal{L}}_0\hat{\mathcal{L}}_1$ are adjoint operators with identical spectra, we can consider the spectrum of only one of these operators, e.g. $\hat{\mathcal{L}}_1\hat{\mathcal{L}}_0$. Considering the complex Λ-plane, it is straightforward to show that $\Lambda \in (-\infty, -\lambda^2)$ is a continuum part of the spectrum with unbounded eigenfunctions. Stable bounded eigenmodes of the discrete spectrum (the so-called *soliton internal modes*[9]) can have eigenvalues only inside the gap, $-\lambda^2 < \Lambda < 0$. The presence of either positive or complex Λ implies soliton instability, because in this case there always exists at least one eigenvalue of the soliton spectrum with $\mathrm{Re}\beta > 0$.

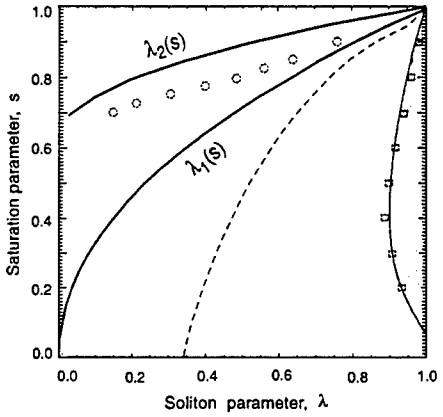


Fig. 2. Existence and stability domains for two- and three-hump solitons. Shown are the existence thresholds $\lambda_1(s)$ and $\lambda_2(s)$ for the $|0,1\rangle$ and $|0,2\rangle$ soliton families. Dashed - the line where $|0,1\rangle$ solitons become two-humped. Shaded - analytically obtained instability domain for two-hump solitons. Squares and circles- numerically obtained instability thresholds for $|0,1\rangle$ and $|0,2\rangle$ solitons, respectively.

Numerical solution of the EVP (2) shows that both $|0,1\rangle$ and $|0,2\rangle$ types of solitary wave solutions *can be stable in a certain region of their existence domain*, see Fig. 2. In the case of $|0,1\rangle$ solitons, the appearance of the instability is related to the fact that close to the curve where the total intensity I becomes two-humped [dashed line in Fig. 2], a pair of internal modes split from the continuum into the gap. As λ grows, the corresponding, purely imaginary, eigenvalues $\beta = \pm i\sqrt{|\Lambda(\lambda)|}$ tend to zero, and at a certain critical value $\lambda = \lambda_{\mathrm{cr}}(s)$, they coincide at $\beta = 0$. At this point, an eigenmode with positive eigenvalue Λ emerges, thus generating linear instability (see Fig. 3) with the instability growth rate $\beta = \sqrt{\Lambda(\lambda)}$. For $|0,2\rangle$ solutions, the dynamics of internal modes can not be related in any obvious way

with a change in the spatial solitary profiles, nevertheless the scenario of the instability development is similar to that for two-hump solitons. The dependence of β on λ, for $|0,1\rangle$ and $|0,2\rangle$ soliton families giving rise to two- and three-hump solitary waves, is shown in Fig. 3 for $s = 0.3$ and $s = 0.8$, respectively. A decline in the instability growth rate as $\lambda \to 1$ (see Fig. 3) is caused by the fact that, in this limit, all multi-hump solitons decompose into a number of the neutrally stable $|0,0\rangle$ solitons separated by infinitely growing distance.

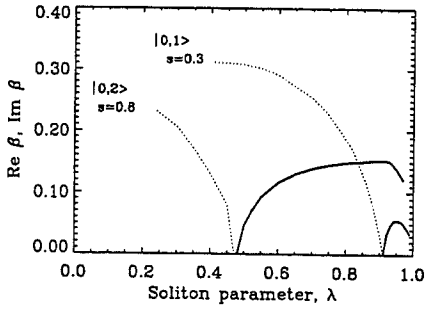


Fig. 3. Instability eigenvalues vs. λ for $|0,1\rangle$ and $|0,2\rangle$ solitons; dashed line - Imβ, bold line - Reβ.

With the aid of analytical asymptotic technique[10], it is possible to show that a perturbation mode with small but positive eigenvalue, and therefore the linear instability of a general localized solution (u, w), appears if the functional $J(u, w)$, defined as

$$J = \frac{P_u}{2s}\frac{\partial P_w}{\partial \lambda} - \frac{P_w}{2s}\frac{\partial P_u}{\partial \lambda} + \frac{\partial P_u}{\partial s}\frac{\partial P_w}{\partial \lambda} - \frac{\partial P_w}{\partial s}\frac{\partial P_u}{\partial \lambda}, \tag{3}$$

changes its sign. The threshold condition $J = 0$ is, in fact, the Vakhitov-Kolokolov stability criterion[11], generalized for the case of two-parameter vector solitons. In this case, it does not necessarily give a threshold of leading instability and the presence of other instabilities (which are not associated with the condition $J = 0$ and can have stronger growth rates) is still possible.

For two-hump solitons, we have been able to locate the critical curve in (λ, s)-plane corresponding to the condition $J = 0$. Superimposing this curve onto the numerically calculated values $\lambda_{cr}(s)$, we have found a remarkable agreement between the numerical and analytical instability thresholds, as shown in Fig. 2. *This gives us the first example of the generalized Vakhitov-Kolokolov criterion for the instability threshold of vector multi-hump solitary waves.* For the whole family of $|0,2\rangle$ solutions, including three-hump solitons, it appears that $J \neq 0$ throughout the entire existence region. Thus, appearance of instability of three-hump solutions is not associated with the change of the sign of the functional J.

To make a link between our stability analysis and experiment, we note that for the experiment[5] the diffraction length is defined as $L_d = 2/sb$ and nonlinearity of the medium (SBN:60 crystal) is characterised by the parameter $b = kr_{\text{eff}}n_b^2E_0$, where r_{eff} is the effective electro-optic coefficient (= 280 pm/V), n_b is the background refractive index (= 2.3), and E_0 is the applied electric field ($\approx$ 2x10^5 V/m). For strong saturation we have $s \sim 1$ and $L_d \approx 0.2$mm. Now, the characteristic instability length z_{cr} can be defined through the maximum growth rate $\beta_{\max}$ and, as a result, for two-hump solitons at $s = 0.3$ we obtain $z_{cr} \approx 12.18$ mm. These estimates indicate that the instability, if it exists, could be detected for two-hump solitons within the experimental setup of Ref.[5] and therefore *stable two-hump solitons* have been indeed observed.

1. M. Segev and G.I. Stegeman, Phys. Today **51**, 42 (1998).
2. R.Y. Chiao, E. Garmire, and C.H. Townes, Phys. Rev. Lett. **13**, 479 (1964).
3. A.W. Snyder, S.J. Hewlett, and D.J. Mitchell, Phys. Rev. Lett. **72**, 1012 (1994).
4. See, e.g., D.E. Pelinovsky, V.V. Afanasjev, and Yu. S. Kivshar, Phys. Rev. E **53**, 1940 (1996).
5. M. Mitchell, M. Segev, and D.N. Christodoulides, Phys. Rev. Lett. **80**, 4657 (1998).
6. D.N. Christodoulides *et al.*, Appl. Phys. Lett. **68**, 1763 (1996).
7. E.A. Ostrovskaya and Yu.S. Kivshar, Opt. Lett. **23**, 1268 (1998).
8. E.A. Ostrovskaya and Yu.S. Kivshar, J. Opt. B: Quantum Semiclass. Opt. **1**, 77, (1999).
9. Yu.S. Kivshar *et al.*, Phys. Rev. Lett. **80**, 5032 (1998).
10. A.V. Buryak, Yu.S. Kivshar, and S. Trillo, Phys. Rev. Lett. **77**, 5210 (1996).
11. M.G. Vakhitov and A.A. Kolokolov, Sov. Radiophys. **16**, 783 (1973).

Self-trapping of Necklace Beams in Self-Focusing Kerr Media

Marin Soljačić, Suzanne Sears, and Mordechai Segev
Princeton University, Princeton, NJ 08544
Tel: ++1-609-258-1949
Fax: ++1-609-258-1954
soljacic@princeton.edu
smsears@princeton.edu
segev@ee.princeton.edu

Solitons of the cubic Nonlinear Schrödinger Equation (NLSE) are probably the most studied solitons in nature. One of the reasons is the mathematical elegance and simplicity of this equation. But another more important reason is the vast number of physical systems that can be described by this equation. Single polarization envelope waves propagating in isotropic materials, when only the lowest order nonlinearity matters most often obey this equation. In optics, the cubic NLSE models temporal solitons in optical fibers, and low intensity solitons of all dimensions in any centrosymmetric media. Outside of optics, this equation often models envelope solitons in deep sea water, plasma, etc. Needless to say, physics of bright solitons that live in higher dimensions is much more interesting than the physics of solitons in (1+1)D. However, it was previously thought that all bright (2+1)D solitons of the cubic NLSE are unstable, and that they disintegrate within a few diffraction lengths (L_D). Here, we present numerical simulations demonstrating the existence of what is to the best of our knowledge the first ever described (2+1)D self-trapped family of stable bright beams in the (2+1)D cubic NLSE [1]. Furthermore, we obtain analytical solutions for some of our beams. Some additional analytical results enable us to predict and control the dynamics of the radius of any of our beams, so we know how to make beams which are almost stationary for very large distances, $\mathcal{O}(50L_D)$.

The normalized self-focusing (2+1)D cubic NLSE is given by:

$$i\frac{\partial\psi}{\partial z}+\frac{1}{2}\{\frac{\partial^2\psi}{\partial x^2}+\frac{\partial^2\psi}{\partial y^2}\}+|\psi|^2\psi=0, \tag{1}$$

where z is the direction of propagation, and x and y are the dimensions transverse to the direction of propagation. Cyllindrically symmetric solitons of Eq.(1) of all orders collapse or diffract after a few diffraction lengths (L_D). But, ignoring the 3^{rd} term in Eq.(1) reduces it to the (1+1)D cubic NLSE, whose solitons are known to be stable; therefore, one can construct solutions of Eq.(1) which are solitons of the (1+1)D cubic NLSE in x and z, and that are uniform in y. However, these solutions suffer from Modulational Instability (MI); small perturbations of large wavelengths in y grow on top of the pulses as the pulses propagate, and the pulses eventually breaks up. One can arrest MI by modulating the ψ sinusoidally in the y direction. This works if the period of the modulation is smaller than the smallest wavelength that would grow on top of the comparable pulse that is uniform in y. Such solitons have been demonstrated experimentally [2] and they indeed exhibit stable self-trapping. Nevertheless, such a soliton is not completely satisfactory because no experimental beam can be infinite in y, so instabilities occur at the y ends of the pulse; furthermore, most physically interesting properties of such a pulse are really those of a (1+1)D creature. This brings about an interesting question: can one construct **stable** (2+1)D structures, based on a topology similar to that of the intensity-modulated (1+1)D beam, in nonlinear Kerr media after all?

Encouraged by Ref. 2, we take a pulse which is initially sinusoidally modulated in y and self-trapped in x, and wrap it around its own tail to form a ring like in Fig. 1. We make sure that the

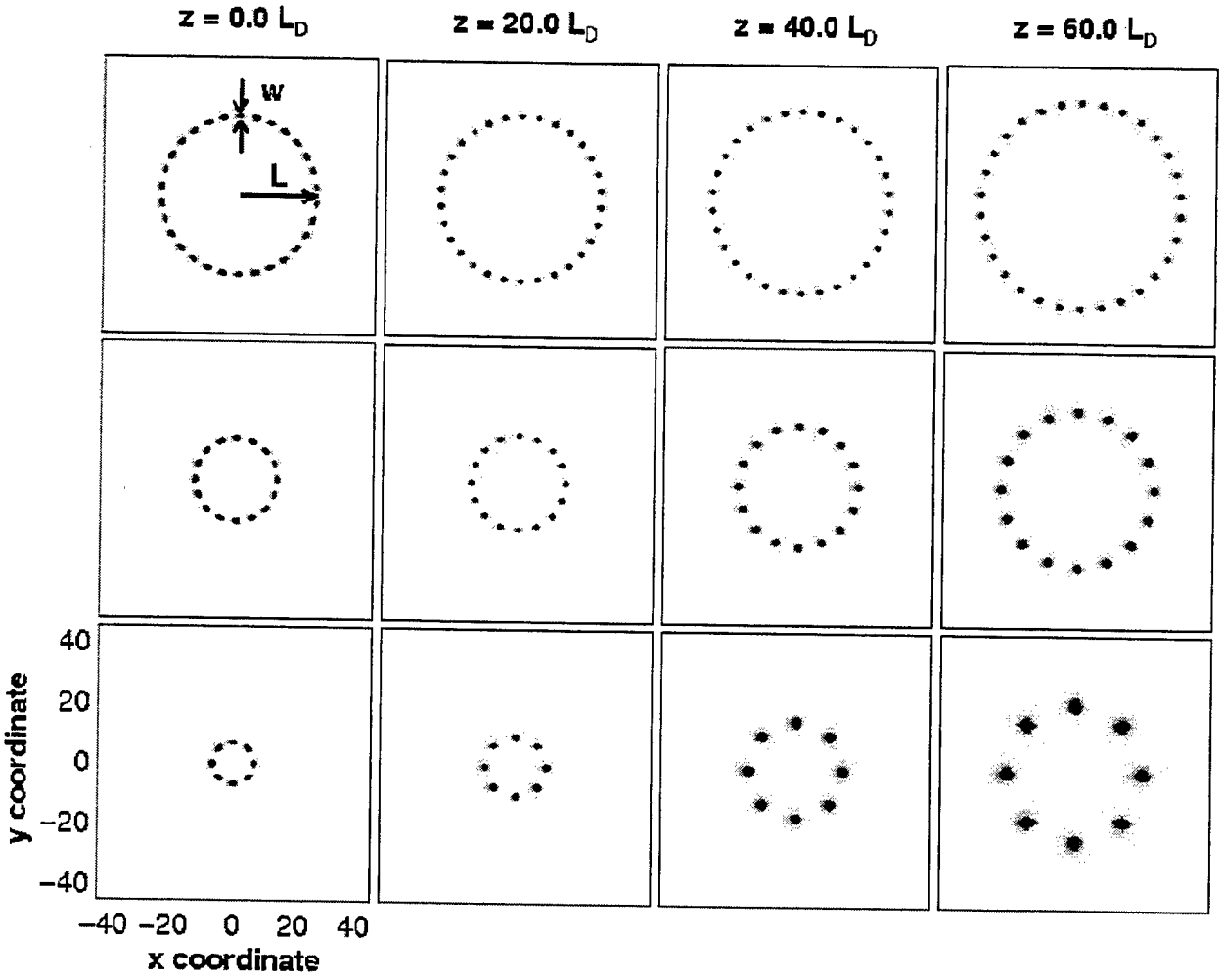


Figure 1: Examples of evolution of necklace-ring beams. The input shape for all the plots was $\psi(r,\theta,z=0) = \alpha * sech((r-L)/w) * cos(\Omega\theta)$, where r is the radial, and θ is the azimuthal variable; $\Omega = 15$, $\Omega = 8$, and $\Omega = 4$ in first, second and third rows, respectively. In all the cases $\alpha = 1$, $w = 1$, and $L/\Omega = 1.707$. The axes are the same for all plots. Dark color indicates high intensity. In all figures in this paper, constrast is enhanced for better clarity.

width of the pulse w is much smaller than its radius L. We call such pulses to be Necklace beams. Since the (1+1)D structure of Ref. 2 was stable, one does not expect the small amount of curvature to cause instability in Necklace beams. In fact, Necklace beams proved to be stable in our numerical simulations for $\mathcal{O}(100L_D)$. Furthermore, we find that they remain stable even under fairly large perturbations ($\sim 5\%$) in the initial widths or powers, and in the presence of random noise (e.g., we have injected up to 1% of the total power of white noise in the Fourier space every L_D.) In addition, we have tested the stability of Necklace beams under azimuthally-asymmetric variations in input conditions. We launched the input shapes of Fig. 1 but with a $\sim 2\%$ ellipticity, and found that these imperfect rings also exhibit stable self-trapping, yet they do not evolve into a circular shape. We thus conclude that, at least for small azimuthal perturbations, the necklace beam is stable, but its circular shape is not an "attractor".

Depending on the initial parameters, Necklace beams can grow or shrink with the propagation distance, e.g. last row of Fig. 1. This dynamics does not destabilize our pulses because of the existence of a rescaling property of the (2+1)D cubic NLSE which does not change the total power

in the pulse. Nevertheless, by adding an appropriate phase front, (i.e. multiplying the whole pulse with $e^{i\alpha r}$, where r is the radial distance from the center, and α is an appropriate constant,) one can have significant control over the dynamics of Necklace beams; their dynamics can even be stopped for very long distances: $\mathcal{O}(50L_D)$. Such a phase front is trivial to apply experimentally; a simple lens will do the job to a good approximation. For comparison, please note that if there was not for the nonlinear effects, our pulses would diffract within $\mathcal{O}(1L_D)$, like shown in Fig. 2.

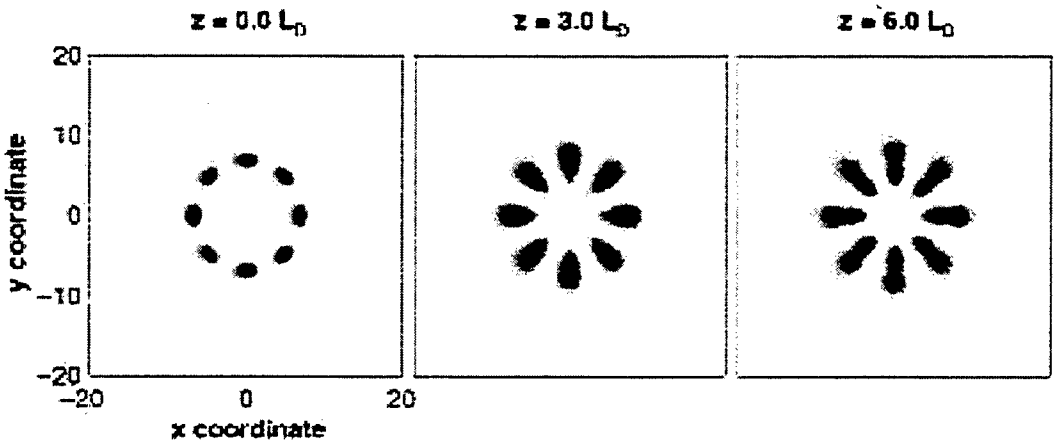


Figure 2: Evolution of the same initial shape as in the third row of Fig. 1, with nonlinearity set to zero. The beam diffracts within $\mathcal{O}(1L_D)$.

Finally, using the variational method, we found excellent approximate analytical solutions for the necklace shapes, as a function of the propagation distance, in a certain regime of necklace parameters. Using this solution, one can understand and predict the dynamics of a necklace shape, and can also understand analytically what happens with the dynamics of a necklace when an arbitrary phase front is applied to it. This approximate solution works best when the thickness of the necklace is much smaller than its radius, and when the scale of azimuthal modulation is much smaller than the thickness of the necklace. Nevertheless, one would also like to understand the dynamics of the necklaces that do not fall into this particular regime of parameters. We used another analytical approach in order to predict dynamics of a necklace of an arbitrary initial shape, even if this shape is not the equilibrium necklace shape. Although this approach tells us nothing about the true necklace shape as the necklace propagates, it gives us a pretty good analytical prediction for the necklace radius as a function of the propagation distance. Furthermore, this approach also allows us to predict what happens with the dynamics of the necklace radius once an arbitrary phase front is applied to it. We checked that the two analytical approaches agree in the appropriate limit.

In conclusion, we have demonstrated the first bright (2+1)D self-trapped stable creatures in the (2+1)D cubic NLSE [1]; we got analytical solutions in some regimes of the parameters, and found a good way of predicting and controling the dynamics of the radius of an arbitrary necklace. The analytical framework we developed tells us how to design necklaces which are essentially stationary for very long distances: $\mathcal{O}(50L_D)$. Our discovery is important because of the generality of the cubic NLSE which describes very many nonlinear wave systems in nature.

References

[1]. For some of these results see: M. Soljačić, S. Sears and M. Segev, Phys. Rev Lett. **81**, 4851 (1998).
[2]. A. Barthelemy, S. Maneuf and C. Froehly, Opt. Comm. **55**, 201 (1985).

Coherence and Incoherence in Multi-Soliton Complexes

Andrey A. Sukhorukov and Nail N. Akhmediev
Optical Sciences Centre, Research School of Physical Sciences and Engineering, The Australian National University, Canberra ACT 0200, Australia
Phone: (61) 6249 2430, Fax: (61) 6249 5184, E-mail: ans124@rsphysse.anu.edu.au

One of the most noted discoveries of modern soliton science is that solitons can be excited by an incandescent light bulb instead of a high power laser source [1]. This produces "incoherent solitons" [1–3]; they can exist in photorefractive materials which require amazingly low powers to observe highly nonlinear phenomena [4–6]. It is also remarkable that, in certain conditions, incoherent solitons in photorefractive materials can be studied using coupled nonlinear Schrödinger equations (NLSE) [3,7].

In general, coupled nonlinear Schrödinger equations (NLSE) can be applied to various phenomena. These include incoherent solitons in photo-refractive materials, plasma waves in random phase approximation [8], multicomponent Bose-Einstein condensate [9] and self-confinement of multimode optical pulses in a glass fiber [10]. Therefore its solutions are of great interest for theoretical physicists. In special cases these equations are found to be integrable [11]. Then, in analogy with single (scalar) NLSE (when the number of equations, M, is 1) [12] and the Manakov case [13] ($M = 2$), the total solution consists of a finite number (N) of solitons and small amplitude radiation waves. The former is defined by the discrete spectrum of linear (L, A) operators [12,13] and the latter is defined by the continuous spectrum. Most applications deal with the soliton part of the solution as it contains the most important features of the problem. Moreover, a localized superposition of fundamental solitons can be called "multisoliton complex". An incoherent soliton is a particular example of a multisoliton complex [14].

The cases $M = 1, 2$ have been extensively discussed in the literature [12,13]. On the other hand, results for general M are scarce. The linear (L, A) operators are important elements for the inverse scattering technique, which can be considered as a basis for integrability of M coupled NLSEs. Moreover, it has been shown [15] that N-soliton solutions of M coupled NLSE can be found using a simple technique which is an extension of the theory of reflectionless potentials [16]. In recent works [14,17] cases when each component has only one fundamental soliton have been considered. It was demonstrated that, in this configuration, the formation of stationary complexes may be observed, and corresponding solutions for $M = N \leq 4$ were presented in explicit form [17].

So far, only the case of complete mutual incoherence of the fundamental solitons has been considered. In this case the multisoliton complex can also be viewed as a self-induced multimode waveguide [14]. The general case, where fundamental solitons in the multisoliton complex interact both coherently and incoherently, has not been analyzed. Such interactions may be observed if N is larger than M, so that each component has not less than one fundamental soliton. In general, each fundamental soliton can be "spread out" among several components. We will refer to this effect as mixed "polarization" of fundamental solitons. However, in order to capture distinctive features of coherent and incoherent soliton interactions, we will focus on a special case which is important for incoherent solitons. Specifically, we consider a situation where all the fundamental soliton polarizations are mutually parallel or orthogonal, and thus are conserved in collisions [14]. Due to the symmetry of the NLSE with respect to rotations in functional space, hereafter we assume that each fundamental soliton is polarized in one component only. It is for this case that we present new explicit N-soliton solutions of M coupled NLSEs, and we discuss the new physics which it brings into the theory.

We consider propagation of an incoherent self-trapped beam in a slow Kerr-like medium and write the set of coupled NLSEs in the form [3,7,14]:

$$i\frac{\partial \psi_m}{\partial z} + \frac{1}{2}\frac{\partial^2 \psi_m}{\partial x^2} + \delta n(I)\psi_m = 0, \qquad (1)$$

where ψ_m denotes the m-th component of the beam, z is the coordinate along the direction of propagation, x is the transverse coordinate, and $\delta n(I) = \sum_{m=1}^{M} \alpha_m |\psi_m|^2$ is the change in refractive index profile created by all incoherent components of the light beam, where the α_m (> 0) are the coefficients representing the strength of the nonlinearity, and M is the number of components.

Solutions in the form of multisoliton complexes of Eq. (1) and their collisions can be obtained using the formalism of [15,18] with some refinements. First, we introduce functions $u_j(x, z)$ as solutions of the following set of equations:

$$\sum_{m=1}^{N} D_{jm} u_m = -e_j. \qquad (2)$$

where N is a total number of fundamental solitons, $e_j = \chi_j \exp\left(k_j \bar{x}_j + i k_j^2 \bar{z}_j/2\right)$, $\bar{x}_j = x - x_j$ and $\bar{z}_j = z - z_j$ are shifted coordinates, and χ_j are arbitrary coefficients. The values x_j and z_j characterize the initial positions of fundamental solitons, but the actual beam trajectories may not follow the specified points due to mutual interactions between fundamental solitons. Each fundamental soliton is characterized by an eigenvalue $k_j = r_j + i\mu_j$. Its real part, r_j, determines the amplitude of the fundamental soliton, while the imaginary part, $\mu_j = \tan\theta_j$,

accounts for the soliton velocity (i.e. motion in transverse direction). Here θ_j is the angle of the fundamental soliton propagation relative to the z axis.

To distinguish coherent and incoherent contributions to the multi-soliton complex, we use variables n_j, which represent the number of the component where the j-th soliton is located. Thus, two fundamental solitons with $n_j = n_m$ are coherent, and they are incoherent otherwise. Now we can write the expression for the matrix D:

$$D_{jm} = \frac{e_j e_m^*}{k_j + k_m^*} + \begin{cases} 1/(k_j + k_m^*), & n_j = n_m, \\ 0, & n_j \neq n_m. \end{cases} \quad (3)$$

Finally, the N-soliton solution of the original Eq. (1) can be obtained by adding up of all the u_j corresponding to a given component number m:

$$\psi_m = \sum_{j;\, n_j = m} u_j / \sqrt{\alpha_m}.$$

Note that the number of terms in the sum is exactly the number of fundamental solitons polarized in this component, viz. N_m, and the total N is $\sum_{m=1}^{M} N_m$.

One of the features of this approach is that coherent fundamental solitons are "split" among all the u_j functions for a given component. However, when obtaining analytical solutions in explicit form, it is possible to separate fundamental solitons by combining terms with corresponding propagation constants. Consequently, we write the exact solutions for a different set of functions $\widetilde{u}_j$, with each of them containing one fundamental soliton (at distances where coherent interactions are small). These are combined into the original functions in the following way: $\psi_m = \sum_{j;\, n_j = m} \widetilde{u}_j / \sqrt{\alpha_m}$.

The coefficients χ_j are arbitrary, and we can choose particular values for them:

$$\chi_j = \prod_{m;\, n_m \neq n_j} \sqrt{b_{jm}},$$

where $b_{jm} = (k_j + k_m^*)/(k_j - k_m)$, and the square root value is taken on the branch with positive real part. This step significantly simplifies further analysis, as the resulting solution will acquire a highly symmetric form.

Finally, the explicit expressions for solutions can be found as sums over specific permutations:

$$\widetilde{u}_j = \frac{e^{i\gamma_j}}{U} \sum_{\{1,\ldots,j-1,j+1,\ldots,N\} \to L} C_L^j F_L^j(x,z), \quad (4)$$

$$U = \sum_{\{1,\ldots,N\} \to L} C_L F_L(x,z).$$

Here L denotes four sets of indices (L_1, L_2, L_3, L_4). The summation is performed over all combinations in which the given set of soliton numbers (for example, $\{1, \ldots, N\}$) can be split among all the L_j. When performing permutations, L_1, L_2 are only filled with numbers of mutually coherent solitons (thus the number of elements in these sets is the same).

The functions in (4) are determined for each realization of the permutation L:

$$F_L(x,z) = \cos(S_g)\cos(S_f)\cosh(S_b) - \sin(S_g)\sin(S_f)\sinh(S_b),$$
$$F_L^j(x,z) = \cos(S_g + S_g^j)\cos(S_f)\cosh(S_b + S_b^j) - \sin(S_g + S_g^j)\sin(S_f)\sinh(S_b + S_b^j).$$

Note that the F functions are written in the simplest form in terms of trigonometric and hyperbolic functions, due to the specific choice of coefficients χ_j. The new variables are found as sums performed over the L_j sets: $S_g = \sum_{j \in L_1} \gamma_j - \sum_{j \in L_2} \gamma_j$, $S_b = \sum_{j \in L_3} \beta_j - \sum_{j \in L_4} \beta_j$. Here the real variables β_j and γ_j are determined as $\beta_j + i\gamma_j = k_j \bar{x}_j + i k_j^2 \bar{z}_j / 2$. All the other parameters do not depend on coordinates (x, z), and are expressed in terms of the wave numbers k_j and shifts in positions $(x_j,\ z_j)$ of the N fundamental solitons. As the total solution has translational symmetry, one of the shifts can be fixed, and the number of independent parameters controlling the multisoliton complex is $2N - 1$.

If an incoherent soliton consists only of orthogonally polarized fundamental solitons ($n_j \equiv j$, $N \equiv M$), and all are propagating in the same direction, then its transverse intensity profile remains stationary [17]. In this particular case, the general expressions can be simplified: $C_L = T$, $C_L^j = 2 r_j \chi_j T$, $T = \prod_{j \in L_3;\, m \in L_4} |b_{jm}|$, $F_L = \cosh(S_b)$, $F_L^j = \cosh(S_b^j)$.

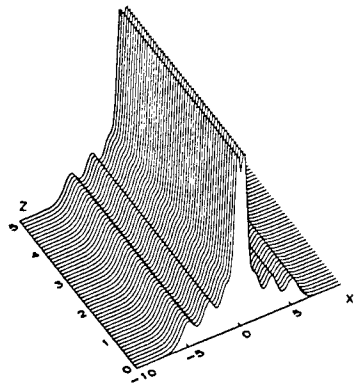


FIG. 1. Stationary propagation of an incoherent soliton consisting of eight completely incoherent fundamental solitons (polarized in different components).

Now we present numerical examples to illustrate these results. An example of a stationary incoherent soliton consisting of eight components ($N = M = 8$) is shown in Fig. 1. The profiles of the constituent fundamental solitons, and their superposition as a whole, are determined by the wave numbers and relative shifts along the

x axis. In this configuration, the shifts in propagation direction, z_j, correspond to arbitrary phase changes of different components, but these do not influence the evolution due to the incoherent nature of the inter-component interactions.

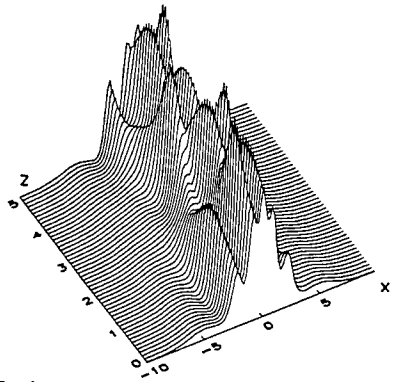


FIG. 2. Evolution of an incoherent soliton with multi-scale periodic "beating" due to internal coherent interactions (8 fundamental solitons in 5 components).

On the other hand, if $N > M$, two or more of the fundamental solitons are polarized in the same components, and thus interact coherently. If the inclination angles of the fundamental solitons are all the same, the beam will remain localized upon propagation. Such a multi-soliton complex is an incoherent soliton with an intensity profile which evolves periodically or quasi-periodically, as shown in Fig. 2. These oscillations, appearing due to internal coherent intra-component interactions, are a general feature of incoherent solitons, and can be eliminated only in specific cases, as discussed earlier. It follows that spatial "beating" always accompanies the interaction of fundamental solitons of a single NLSE, which agrees with previous studies [19].

Our explicit solution (4) also describes collisions of incoherent solitons. As mentioned earlier, the polarizations of the fundamental solitons are preserved in collisions (provided they are orthogonal or parallel), and thus the degree of internal coherence doesn't change. However, the shifts of the fundamental soliton trajectories differ, and this results in the incoherent solitons changing their shapes. These transformations can be seen clearly in Fig. 3.

The shift of j-th fundamental soliton along the x axis due to collisions can be calculated by taking appropriate limits in Eq. (4):

$$\delta x_j = \frac{1}{r_j} \sum_m \pm \begin{cases} 2\ln(|b_{jm}|), & n_j = n_m, \\ \ln(|b_{jm}|), & n_j \neq n_m. \end{cases}$$

Here the summation involves the fundamental solitons which feature in the collisions. The "+" sign corresponds to the case when colliding soliton number m comes from the right (i.e. has larger x coordinate before the impact), and the "−" sign when from the left. This is a generalization of the expressions found in [17].

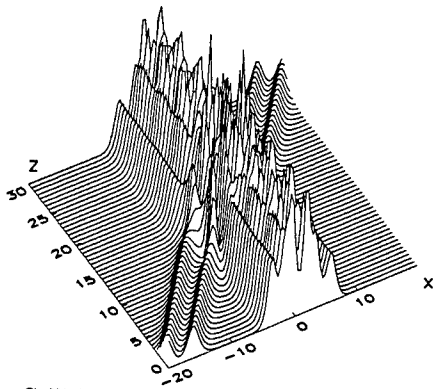


FIG. 3. Collision of a completely incoherent soliton (consisting of two orthogonally polarized fundamental solitons) and an incoherent soliton with internal coherent contributions (6 fundamental solitons in 5 components).

The authors are part of the Australian Photonics CRC. We are grateful to Dr. Ankiewicz for critical reading of this manuscript.

[1] M. Mitchell and M. Segev, Nature (London) 387, 880 (1997).
[2] M. Mitchell, Z. Chen, M. Shih, and M. Segev, Phys. Rev. Lett. **77**, 490 (1996).
[3] M. I. Carvalho, T. H. Coskun, D. N. Christodoulides, M. Mitchell, and M. Segev, Phys. Rev. E **59**, 1193 (1999).
[4] G. Duree *et al*, Phys. Rev. Lett. **71**, 533 (1993);
[5] A. A. Zozulya, D. Z. Anderson, A. V. Mamaev, and M. Saffman, Europhys. Lett. **36**, 419 (1996).
[6] M. D. Iturbe-Castillo *et al*, Appl. Phys. Lett. **64**, 408 (1994)
[7] V. Kutuzov, V. M. Petnikova, V. V. Shuvalov, and V. A. Vysloukh, Phys. Rev. E **57**, 6056 (1998).
[8] A. Hasegawa, Physics of Fluids **20**, 2155 (1977).
[9] E. P. Bashkin and A. V. Vagov, Phys. Rev. B **56**, 6207 (1997).
[10] A. Hasegawa, Opt. Lett. **5**, 416 (1980).
[11] V. G. Makhan'kov and O. K. Pashaev, Teor. Mat. Fiz. **53**, 55 (1982) [Theor. Math. Phys. **53**, 979 (1982)].
[12] V. E. Zakharov and A. B. Shabat, Zh. Eksp. Teor. Fiz. **61**, 118 (1971) [Sov. Phys. JETP **34**, 62 (1971)].
[13] C. B. Manakov, Zh. Teor. Eksp. Fiz. **65**, 505 (1973) [Sov. Phys. JETP **38**, 248 (1974)].
[14] N. N. Akhmediev, W. Królikowski, and A. W. Snyder, Phys. Rev. Lett. **81**, 4632 (1998).
[15] Y. Nogami and C. S. Warke, Phys. Lett. **59A**, 251 (1976).
[16] I. Kay and H. E. Moses, J. Appl. Phys. **27**, 1503 (1956).
[17] A. Ankiewicz, W. Królikowski, and N. N. Akhmediev, Phys. Rev. E (to be published in May, 1999).
[18] C. S. Gardner, J. M. Greene, M. D. Kruskal, and R. M. Miura, Comm. Pure Appl. Math. **27**, 97 (1974).
[19] N. Akhmediev and A. Ankiewicz, *Solitons, nonlinear pulses and beams* (Chapman & Hall, 1997).

Two-Color Multistep Cascading and Parametric Soliton-Induced Waveguides

Solomon Saltiel[1], Andrey A. Sukhorukov[2], and Yuri S. Kivshar[2]

[1] *Quantum Electronics Department, Faculty of Physics, University of Sofia, Sofia 1164, Bulgaria*
[2] *Australian Photonics Cooperative Research Centre, Research School of Physical Sciences and Engineering Optical Sciences Center, Australian National University, Canberra ACT 0200, Australia*
Phone: (61) 6249 2430, Fax: (61) 6249 5184, E-mail: ans124@rsphysse.anu.edu.au

Recent progress in the study of cascading effects in optical materials with quadratic (second-order or $\chi^{(2)}$) nonlinear response has offered a broad spectrum of new opportunities for all-optical processing, optical communications, and optical solitons [1,2]. Most of the studies of cascading effects employ parametric wave mixing processes with a single phase-matching and, as a result, two-step cascading. For example, the two-step cascading associated with type I second-harmonic generation (SHG) includes the generation of the second harmonic ($\omega + \omega = 2\omega$) followed by reconstruction of the fundamental wave through down-conversion frequency mixing (DFM) process ($2\omega - \omega = \omega$). These two processes are governed by one phase-matched interaction and they differ only in the direction of power conversion.

The idea to explore more than one simultaneous nearly phase-matched processes, or *double-phase-matched (DFM) wave interactions*, became attractive only recently [3], for the purposes of all-optical transistor, enhanced nonlinearity-induced phase shift, and polarization switching. More recently, it was shown [4] that multistep cascading can be achieved by two second-order nonlinear cascading processes, SHG and sum-frequency mixing (SFM), and these two processes can also support a novel class of multi-color parametric solitons [5].

Then, the important question is: *Can we find parametric processes which involve only two frequencies but allow to get all advantages of multistep cascading ?* In this Letter, we answer positively this question introducing the concept of *two-color multistep cascading*. In particular, using one of the processes of the two-color multistep cascading, we show how to introduce and explore the concept of light guiding light for quadratic spatial solitons, that has been analyzed earlier for nonresonant nonlinearities and Kerr-like spatial solitary waves [6] but seemed impossible for parametric interactions.

To introduce more than one parametric process involving only two frequencies, we consider waves with different polarization. We denote two orthogonal polarization components of the fundamental wave (ω) as A and B, and two orthogonal polarization of the second harmonic (2ω), as S and T. Then, for an example, a simple multistep cascading process consists of the following steps. First, the fundamental wave A generates the second-harmonic wave S via type I SHG process. Then, by down-conversion SA-B, the orthogonal fundamental wave is generated. At last, the initial fundamental wave is reconstructed by the processes SB-A or AB-S, SA-A. The two principal second-order processes AA-S and AB-S correspond to *two different components* of the nonlinear second-order (or $\chi^{(2)}$) susceptibility tensor, thus introducing additional degrees of freedom into the parametric processes. There exist different types of multistep cascading processes. The principal processes are: (a) (AA-S, AB-S), as described above; (b) (AA-S, AB-T), and (c) (AA-S, BB-S).

To demonstrate some of the unique properties of the multistep cascading, we discuss here how it can be employed for light-guiding-light effects and soliton-induced waveguides in quadratic media. For this purpose, we consider the principal DPM process (c) in the planar slab-waveguide geometry. Using the slowly varying envelope approximation with the assumption of zero absorption of all interacting waves, we obtain

$$
\begin{aligned}
&2ik_1\frac{\partial A}{\partial z} + \frac{\partial^2 A}{\partial x^2} + \chi_1 S A^* e^{-i\Delta k_1 z} = 0,\\
&2ik_1\frac{\partial B}{\partial z} + \frac{\partial^2 B}{\partial x^2} + \chi_2 S B^* e^{-i\Delta k_2 z} = 0,\\
&4ik_1\frac{\partial S}{\partial z} + \frac{\partial^2 S}{\partial x^2} + 2\chi_1 A^2 e^{i\Delta k_1 z} + 2\chi_2 B^2 e^{i\Delta k_2 z} = 0,
\end{aligned}
\tag{1}
$$

where $\chi_{1,2} = 2k_1\sigma_{1,2}$, and the nonlinear coupling coefficients σ_k are proportional to the elements of the second-order susceptibility tensor. In Eq. (1), A and B are two orthogonal polarization components of the fundamental wave, S is the second-harmonic wave, Δk_1 and Δk_2 are the corresponding wave-vector mismatch parameters.

To simplify the system (1), we look for stationary solutions and introduce the normalized envelopes u, v, and w according to the following relations, $A = \gamma_1 u \exp(i\beta z - \frac{i}{2}\Delta k_1 z)$, $B = \gamma_2 v \exp(i\beta z - \frac{i}{2}\Delta k_2 z)$, and $S = \gamma_3 w \exp(2i\beta)$, where $\gamma_1^{-1} = 2\chi_1 x_0^2$, $\gamma_2^{-1} = 2x_0^2(\chi_1\chi_2)^{1/2}$ and $\gamma_3^{-1} = \chi_1 x_0^2$, and the longitudinal and transverse coordinates are measured in the units of $z_0 = (\beta - \Delta k_1/2)^{-1}$ and $x_0 = (z_0/2k_1)^{1/2}$, respectively. As a result, we finally obtain the system of coupled normalized equations,

$$
\begin{aligned}
&i\frac{\partial u}{\partial z}+\frac{\partial^2 u}{\partial x^2}-u+u^*w=0,\\
&i\frac{\partial v}{\partial z}+\frac{\partial^2 v}{\partial x^2}-\alpha_1 v+\chi v^*w=0,\\
&2i\frac{\partial w}{\partial z}+\frac{\partial^2 w}{\partial x^2}-\alpha w+\frac{1}{2}(u^2+v^2)=0.
\end{aligned}
\tag{2}
$$

where $\chi \equiv (\chi_2/\chi_1)$, $\alpha_1 = (\beta - \Delta k_2/2)(\beta - \Delta k_1/2)^{-1}$, and $\alpha = 4\beta(\beta - \Delta k_1/2)^{-1}$.

First of all, we notice that for $v = 0$ (or, similarly, $u = 0$), the dimensionless model (2) coincides with the corresponding model for two-step cascading due to type I SHG discussed earlier [1,2], and its stationary solutions are defined by the system of equations for real u and w,

$$
\begin{aligned}
&\frac{d^2u}{dx^2}-u+u^*w=0,\\
&\frac{d^2w}{dx^2}-\alpha w+\frac{1}{2}u^2=0,
\end{aligned}
\tag{3}
$$

that possesses a one-parameter family of two-wave localized solutions (u_0, w_0) found earlier numerically for any $\alpha \neq 1$, and also known analytically for $\alpha = 1$: $u_0(x) = (3/\sqrt{2})\mathrm{sech}^2(x/2) = \sqrt{2}w_0(x)$ (see Ref. [2]).

Then, the equation for real orthogonally polarized fundamental wave v can be treated as an eigenvalue problem for an effective waveguide created by the second-harmonic field $w_0(x)$,

$$
\frac{d^2v}{dx^2}+[\chi w_0(x)-\alpha_1]v=0. \tag{4}
$$

Therefore, an additional parametric process allows *to create an effective waveguide* for the orthogonal polarization, the waveguide induced in a quadratic medium by a two-wave spatial soliton. However, this type of waveguides is different from what has been studied for Kerr-like solitons because it is *coupled parametrically* to the guided modes and, as a result, the physical picture of the guided modes is valid, rigorously speaking, only in the case of stationary phase-matched beams. As a result, the stability of the corresponding waveguide and localized modes of the orthogonal polarization it guides is a key issue. In particular, the waveguide itself (i.e. two-wave parametric soliton) becomes unstable for $\alpha < \alpha_{cr} \approx 0.2$ [7].

In order to find all possible guided modes of the parametric waveguide created by a two-wave quadratic soliton, we have to solve Eq. (4) where the solution $w_0(x)$ is known numerically only. These solutions have been also described by the variational method [8], but the different types of the variational ansatz used do not provide a good agreement for the soliton profiles for all x. For our eigenvalue problem (4), the function $w_0(x)$ defines the number and parameters of the guided modes and, in order to obtain accurate results, it should be calculated as close as possible to the exact solution found numerically.

To resolve this difficulty, below we suggest a novel 'almost exact' approximation that *would allow to solve analytically many of the problems involving quadratic solitons*, including the eigenvalue problem (4). First, we notice that from the exact results at $\alpha = 1$ and the asymptotic results for large α, $w \approx (1/2\alpha)u^2$, it follows that the second-harmonic field $w_0(x)$ of Eqs. (3) remains almost self-similar for $\alpha \geq 1$. Thus, we are looking for the second-harmonic field in the form $w_0(x) = w_m\,\mathrm{sech}^2(x/p)$, where w_m and p are unknown yet parameters. The solution for $u_0(x)$ should be consistent with this choice of the shape for the second harmonic, and it is defined by the linear equation of the system (3). Therefore, we can take u in the form of the lowest guided mode, $u_0(x) = u_m\,\mathrm{sech}^p(x/p)$, that corresponds to an effective waveguide $w_0(x)$. By matching the asymptotics of these trial functions with those defined directly from Eqs. (3) at small and large x, we obtain the following solution,

$$
u_0(x) = u_m\mathrm{sech}^p(x/p), \quad w_0(x) = w_m\mathrm{sech}^2(x/p), \tag{5}
$$

where

$$
u_m^2 = \frac{\alpha w_m^2}{(w_m-1)}, \quad \alpha = \frac{4(w_m-1)^3}{(2-w_m)}, \quad p = \frac{1}{(w_m-1)}, \tag{6}
$$

i.e. all the parameters are functions of α. For $\alpha_{cr} < \alpha < \infty$, the SH amplitude varies in the region $1.3 < w_m < 2$, so that all the terms in Eq. (6) remain positive.

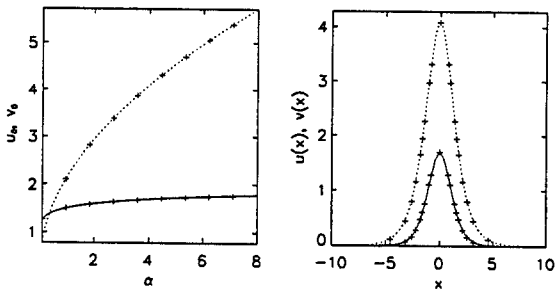


FIG. 1. Comparison between the numerical (continuous lines) and analytical (crosses) solutions for two-wave parametric solitons: (a) Maximum amplitudes of the fundamental (dotted) and second (solid) harmonics; (b) Two-wave soliton profile at $\alpha = 4$.

It is really amazing that the analytical solution (5), (6) provides *an excellent approximation* for the profiles of the two-wave solitons found numerically. Figures 1(a,b) show a comparison between the maximum amplitudes of the fundamental and second harmonics and selected profiles (at $\alpha = 4$), respectively. As a matter of fact, the numerical and analytical curves on these plots are not distinguishable. For $\alpha < 1$, the SH profile changes, but

in the region $\alpha_{cr} < \alpha$ approximate solution (5), (6) is still very close to the exact one: the relative error is less than 1%, for the amplitudes, and it does not exceed 3%, for the power components. That is why we define the analytical solution given by Eqs. (5), (6) as 'almost exact'. Details of the derivation, as well as the analysis of the case $\alpha < 1$ will be presented elsewhere [9].

Now, the eigenvalue problem (4) can be readily solved analytically. The eigenmode cutoff is defined by the matching parameter α_1 that takes one of the following discrete values, $\alpha_1^{(n)} = (s-n)^2/p^2$, where $s = -(1/2) + [(1/4) + w_m \chi p^2]^{1/2}$. The number n defines the mode order ($n = 0, 1, \ldots$), and the localized solutions are possible provided $n < s$. The profiles of the guided modes are found analytically as

$$v_n(x) = W \mathrm{sech}^{s-n}(x/p) H(-n, 2s-n+1, s-n+1, \zeta),$$

where $\zeta = \frac{1}{2}[1 - \tanh(x/p)]$, and H is the hypergeometric function.

According to these results, the maximum number of the guided modes can be observed for smaller values of α. Figures 2(a,b) show the dependence of the mode cutoff values $\alpha_1^{(n)}$ vs. α, at fixed χ, and vs. the coupling parameter χ, at fixed α, respectively. For the case $\chi = 1$, the dependence has a simple form: $\alpha_1^{(n)} = [1 - n(w_m - 1)]^2$.

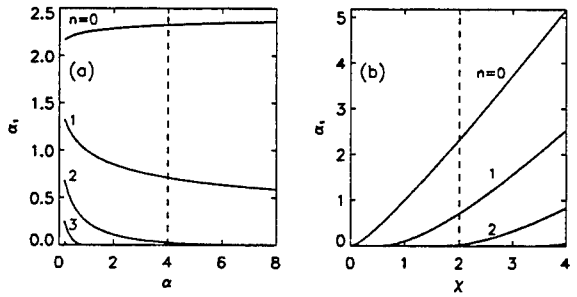


FIG. 2. Cutoff eigenvalues $\alpha_1^{(n)}$ of the guided modes shown as (a) functions of α at $\chi = 2$, and (b) functions of χ at $\alpha = 4$. Dashed lines correspond to the intersection of the plots in the parameter space (α, χ).

Because a two-wave soliton creates an induced waveguide parametrically coupled to the mode of the orthogonal polarization it guides, the dynamics of the guided modes *may differ drastically* from that of conventional waveguides based on the Kerr-type nonlinearities. In particular, the mode can be unstable being amplified due to parametric interaction with the waveguide.

For a practical realization of the DPM processes and light-guiding-light effects described above, we mention two general methods. *The first method* is based on the use of *two commensurable periods* of the quasi-phase-matched (QPM) periodic grating. Indeed, to achieve DPM, we can employ the first-order QPM for one parametric process, and the third-order QPM, for the other parametric process. Taking, as an example, the parameters for $LiNbO_3$ and AA-S ($xx-z$) and BB-S ($zz-z$) processes, we find [11] two points for DPM at about 0.89 μm and 1.25 μm. This means that a single QPM grating can provide simultaneous phase-matching for two parametric processes. For this configuration, we obtain $\chi \approx 1.92$ or, by interchanging the polarization components, $\chi \approx 0.52$. *The second method* to achieve the conditions of DPM processes is based on the idea of *quasi-periodic QPM grating*. As has been recently shown experimentally [12], Fibonacci optical super-lattices can provide an effective way to achieve quasi-phase-matching at *several incommensurable periods* allowing multi-frequency harmonic generation for the same type of the super-lattice QPM structure.

[1] For a comprehensive overview of cascading, see G. Stegeman, D.J. Hagan, and L. Torner, Opt. Quantum Electron. **28**, 1691 (1996).

[2] For an overview of quadratic spatial solitons, see L. Torner, in: *Beam Shaping and Control with Nonlinear Optics*, F. Kajzer and R. Reinisch, Eds. (Plenum, New York, 1998), p. 229; Yu.S. Kivshar, In: *Advanced Photonics with Second-Order Optically Nonlinear Processes*, A.D. Boardman, L. Pavlov, and S. Tanev, Eds. (Kluwer, Dordretch, 1998), p. 451.

[3] See, e.g, G. Assanto, I. Torelli, and S. Trillo, Opt. Lett. **19**, 1720 (1994); A.D. Boardman, P. Bontemps, and K. Xie, Opt. Quantum Electron. **30**, 891 (1998).

[4] K. Koynov and S. Saltiel, Opt. Commun. **152**, 96 (1998).

[5] Yu.S. Kivshar, T. Alexander, and S. Saltiel, Opt. Lett. **24** (1999) May 15.

[6] M. Segev and G. Stegeman, Phys. Today **51**, 42 (1998); A.W. Snyder and F. Ladouceur, Optics & Photonics News **10**, No. 2, 35 (1999).

[7] D.E. Pelinovsky, A.V. Buryak, and Yu.S. Kivshar, Phys. Rev. Lett. **75**, 591 (1995).

[8] V.V. Steblina *et al.*, Opt. Commun. **118**, 345 (1995); A.D. Boardman *et al.*, Phys. Rev. A **52**, 4099 (1995); V.M. Agranovich *et al.*, Phys. Rev. B **53**, 15451 (1996).

[9] A.A. Sukhorukov, to be published.

[10] For an example of the nonlinear theory of soliton-induced waveguides, see E.A. Ostrovskaya and Yu.S. Kivshar, Opt. Lett. **23**, 1268 (1998).

[11] V.G. Dmitriev, G.G. Gurzadyan, and D.N. Nikogosyan, *Handbook of Nonlinear Optical Crystals* (Springer, Berlin, 1997).

[12] S. Zhu *et al.*, Phys. Rev. Lett. **78**, 2752 (1997); S. Zhu, Y. Zhu, and Y. Qin, Science **278**, 843 (1997).

Solitary waves in quadratically nonlinear media with loss and gain

S. Darmanyan, L. Crasovan, and F. Lederer

Institute of Solid State Theory and Theoretical Optics, Friedrich-Schiller Universität Jena,
Max-Wien-Platz 1, 07743 Jena, Germany
Tel.: +(49) 3641 947170, Fax: +(49) 3641 947162

It is now widely accepted that optical media with a quadratic, or $\chi^{(2)}$, nonlinearity exhibit interesting phenomena which can be exploited in all-optical signal processing (see [1,2] and references therein). In particular, different types of dichromatic solitary waves (mutually locked fundamental field (FF) and second harmonic (SH)) in conservative quadratic media have been identified and their potential use for signal routing and steering has been discussed [3,4]. In particular, double-hump solitary waves not existing in the Schrödinger limit have been identified and their stability behavior and decay scenarios have been discussed [5-7].

Recently taking loss and gain effects into account it was shown that rather stable dichromatic shock-like [8] and bright solitary [9] waves may exist in a quadratic environment. In this contribution we identify double-hump solitons in dissipative quadratic media and numerically prove their robustness.

The system of equations describing pulse/beam propagation in a quadratically nonlinear medium with loss and gain has the form:

$$iA_x + D_1 A_{ss} + 2A^* B + i\gamma_1 A = 0 \tag{1a}$$

$$iB_x + kB + D_2 B_{ss} + A^2 + i\gamma_2 B = 0 \tag{1b}$$

where x is the propagation distance, s the transverse coordinate in the spatial or the retarded time in the temporal case, A and B are normalized envelopes of first and second harmonics, k is the phase mismatch, $\gamma_{1,2}$ are linear gain or loss coefficients, $D_{1,2} = D'_{1,2} + iD''_{1,2}$ are complex valued

coefficients, where $D_{1,2}^{'}$ account for dispersion/diffraction and $D_{1,2}^{''}$ for bandwidth-limited amplification or filtering.

We have found that the system (1) has a double-hump chirped bright solitary wave solution

$$A = a\sinh(\lambda s)[\cosh(\lambda s)]^{-2+i\varepsilon}\, e^{i(Qx+\varphi_1)}, \quad B = b[\cosh(\lambda s)]^{-2+2i\varepsilon}\, e^{2i(Qx+\varphi_2)}, \tag{2}$$

where the amplitudes and the relative phase are given by

$$a^4 = 4b^2\lambda^4|D_2|^2(4\varepsilon^4+13\varepsilon^2+9), \quad b^2 = \lambda^4|D_1|^2(\varepsilon^4+13\varepsilon^2+36)/4, \tag{3}$$

$$\tan(\varphi_2-2\varphi_1) = (6-\varepsilon^2-5d_1\varepsilon)/(d_1(6-\varepsilon^2)+5\varepsilon), \tag{4}$$

the chirp parameter ε is a solution of the fourth order algedraic equation

$$2(d_1+d_2)(\varepsilon^4-20\varepsilon^2+9)+15(d_1d_2-1)(\varepsilon^3-3\varepsilon)=0 \tag{5}$$

The widths and wave vectors are

$$\lambda^2 = \gamma_1/D_1^{''}(\varepsilon^2+2\varepsilon d_1-1), \quad Q = \lambda^2 D_1^{''}[d_1(\varepsilon^2-1)-2\varepsilon], \tag{6}$$

where we have introduced $d_{1,2} = D_{1,2}^{'}/D_{1,2}^{''}$. This exact solution exist if the constraints

$$2\gamma_1 D_2^{''}(1-\varepsilon d_2) = \gamma_2 D_1^{''}(\varepsilon^2+2\varepsilon d_1-1), \quad k = 2\lambda^2\left[(1-\varepsilon^2)D_1^{'}+2\varepsilon D_1^{''}+D_2^{'}+\varepsilon D_2^{''}\right] \tag{7}$$

are satisfied. The first constraint ensures the balance between gain and loss which is necessary for solutions to exist. An analysis of the constraints reveals that solutions exist in different domains of parameter space. Both the shapes and the phases of the double hump solution (2) are shown in Fig.1. We note a nonzero relative phase shift in the center of pulses which is described by formula (4). The stability of the solitary wave solution was numerically checked. The evolution of the FF component is displayed in Fig.2. In the parameter domain chosen the solitary wave propagates rather stable. The anticipated onset of the background instability is observed for large propagation distances.

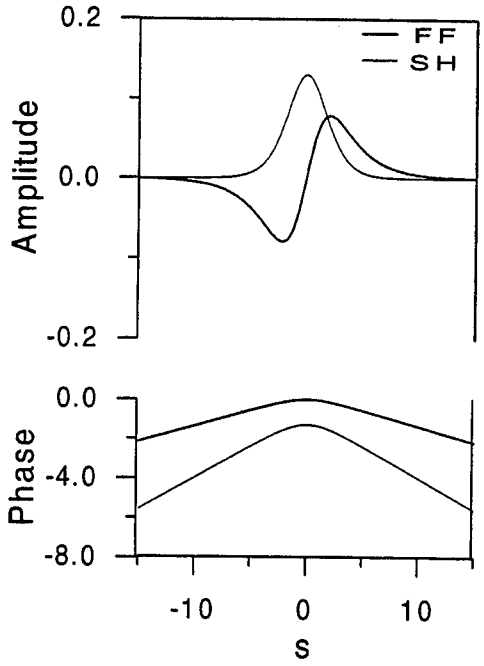


Fig.1 Amplitude and phase profiles of the solution (2), parameters: $\gamma_1 = 0.07$, $\gamma_2 = -0.05$, $d_1 = d_2 = -2$, $D_1^{''} = -0.5$, $D_2^{''} = -0.25$, $k = -0.06$, resulting in: $\varepsilon = 1.03$, $\lambda = 0.18$, $a = 0.16$, b=0.13, $\varphi_1 = 0$, $\tan(\varphi_2) = -3.25$.

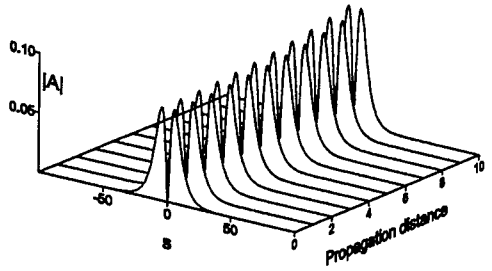


Fig.2 Evolution of the FF of the solution (2). The SH fields exhibit a similar behavior. Parameters are as in Fig.1.

References

1. G. Stegeman, D. Hagan, and L. Torner, Opt. Quantum. Electron. **28** 1691 (1996).
2. A. Kobyakov and F. Lederer, Phys. Rev. A **54** 3455 (1996).
3. C. Menyuk, R. Schiek, and L. Torner, J. Opt. Soc. Am. B **11** 2434 (1994).
4. A. Buryak and Yu. Kivshar, Phys. Rev. A **51** 41 (1995).
5. D. Mihalache, F. Lederer, D. Mazilu, and L.-C. Crasovan, Opt. Eng. **35** 1616 (1996).
6. M. Haelterman, S. Trillo, and P. Ferro, Opt. Lett. **22** 84 (1997).
7. C. Etrich, U. Peschel, F. Lederer, D. Mihalache, and D. Mazilu, Opt. Quantum. Electron. **230** 881 (1998).
8. S. Darmanyan, A. Kamchatnov; and F. Lederer, Phys. Rev. E **58** R4120 (1998).
9. L. Crasovan, B. Malomed, D. Mihalache, and F.Lederer, Phys. Rev. E **59** (1999) (in press).

Dark Spatial Soliton Like Structures Induced by Low-Power Upconverted Photobleaching of Dye-Doped Polymer Film

Aaron Wilkosz, Nichols Research Corporation, 4040 S. Memorial Parkway, Huntsville, Alabama 35815, wilkosza@nichols.com

Sergey Sarkisov, Alabama A&M University, Normal, Alabama 35762, sergei@caos.aamu.edu

INTRODUCTION

The study of dark spatial solitons spans more than a decade [1]. Dark spatial solitons were found to guide light beams through various media such as liquids with defocussing Kerr effect [2,3], or photorefreactive crystals [4]. Their operation is based on the following principles. A (1+1)-dimensional dark spatial soliton (the optical fields vary in only one transverse direction and the longitudinal direction) results from nonlinear propagation of a light beam with π-step phase jump across its axis. The soliton induces a refractive index pattern in the medium where the near-axis region has high index and thus works as a guide for a relatively weak probe beam propagating along the main beam. By changing the intensity and the phase profile of the main beam one can alter the refractive index pattern and thus perform steering, splitting or combining the probe beam. This paper presents theoretical and experimental data and discusses a theoretical model developed to study optical beam splitting induced by photobleaching a dye-doped polymeric waveguide, where instant refractive index reaction to light intensity redistribution is replaced by permanent index decrease associated with dye photobleaching.

MODEL THEORY

The index response to an optical field amplitude E is given by the rate equation

$$\frac{\partial\,\tilde{n}(E)}{\partial t} = -C\frac{|E|^2}{2}(\tilde{n}(E) - \tilde{n}_s) \qquad (1)$$

for $\tilde{n} = 0$ at $t = 0$, where $\tilde{n}(E)$ is the electric field dependent component of the refractive index $\tilde{n}(E) = n(E) - n_0$, where n_0 is the initial unperturbed refractive index; E is the electrical component of a TE mode propagating in a single mode slab waveguide; C is the efficiency of light induced index modification; and $\tilde{n}_s$ is the saturation index change. Equation (1) applies to nonstationary and nonuniform optical fields. According to experimental data the absorption coefficient and dependent on it propagation loss rate remain constant. The light propagation in a single mode slab waveguide is given by a two dimensional nonlinear Schrödinger type equation

$$-2i\beta\frac{\partial E}{\partial x} + \frac{\partial^2 E}{\partial y^2} - i\gamma\beta E + \frac{\beta^2\tilde{n}(E)}{n_0} = 0 \qquad (2)$$

where x and y are coordinates in the plane of the waveguide along and across the propagation direction respectively; β is the mode wave number; and γ is the propagation loss factor. The light beam injected into the waveguide was assumed to have a uniform phase plane wavefront and a Gaussian profile of the optical field given by $E = E_0 \exp(-y^2/2\sigma^2)$ at $x = 0$, where E_0 is the beam amplitude, and σ is the beam width. Equations 1 and 2 were solved numerically with two different methods: the split step Fast Fourier Transform (FTF), and the three-layer finite difference method, which is similar to the Crank-Nicholson scheme.

RESULTS

Figure 1 shows results obtained from numerical simulations of light with π-step phase jump across its axis propagating in the waveguide at various times after the light was launched. The time scale shown in Figure 1 is based on a normalized time parameter given by $\tau = t/CIE_0l^2/n_0$. One can see apparent primary beam splitting into two secondary beams with separation between them growing in time. This process can be understood qualitatively in terms of light escaping out of bleached regions with low refractive index to unbleached regions with high index of refraction.

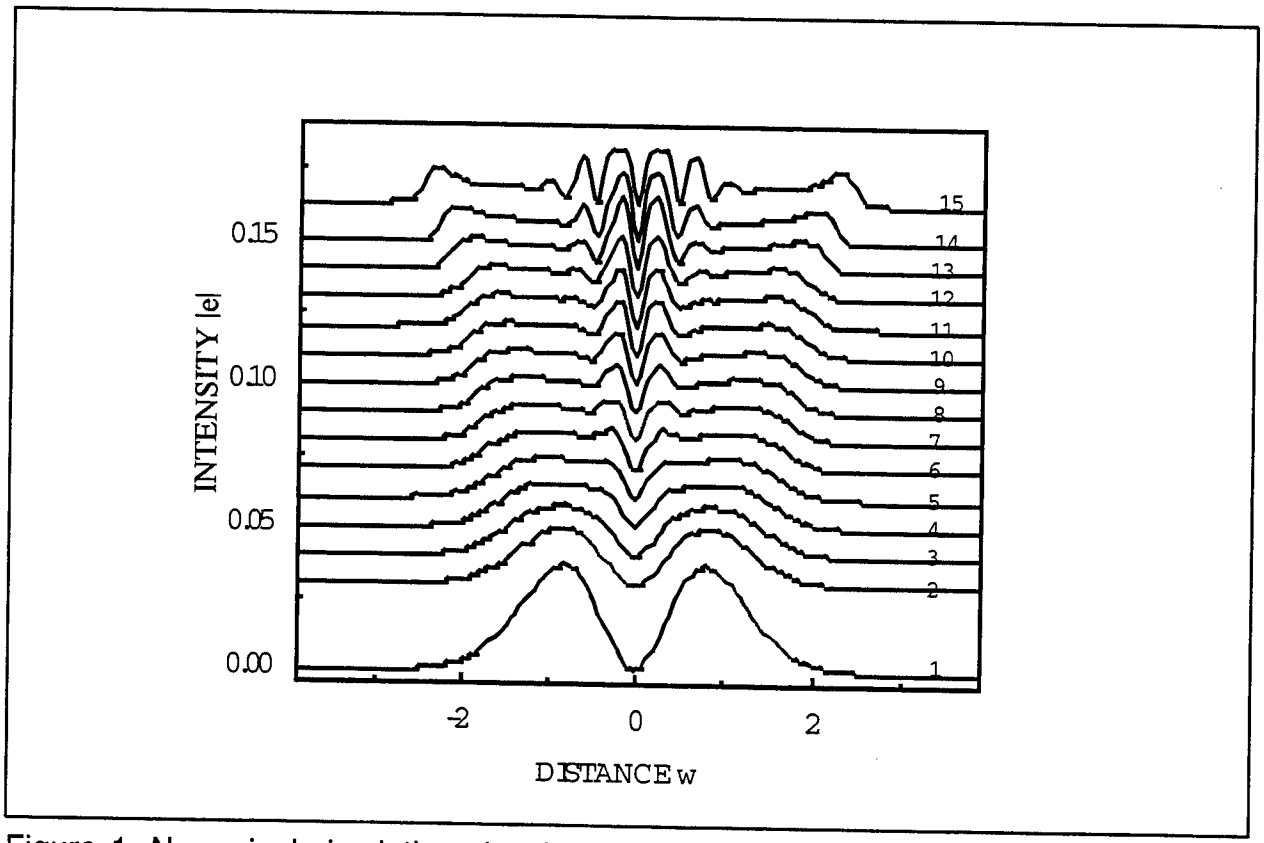


Figure 1. Numerical simulation showing the evolution of the transverse profile of the main beam at (1) the coupling point and at normalized distance $u=6.5\times10^5$ from the coupling point for (2) $\tau=0$, (3) $\tau=0.1$, (4) $\tau=0.2$, (5) $\tau=0.3$, (6) $\tau=0.4$, (7) $\tau=0.5$, (8) $\tau=0.6$, (9) $\tau= 0.7$, (10) $\tau=0.8$, (11) $\tau=0.9$, (12) $\tau=1.0$, (13) $\tau=1.5$, (14) $\tau=2.0$, (15) $\tau=3.0$.

The experimental waveguide was fabricated by spin-coating preoxidized silicon wafer with SiO_2 layer with a thickness of 1.5 μm and a refractive index of 1.46. The coat was made of poly(methyl methacrylate) (PMMA) solution in chlorobenzene doped with the dye 4-(Dicyanomethylene)-2-methyl-6-(p-dimethylaminostyryl)4H-pyran (DCM) and spin coated. This produced a dual mode slab waveguide with thickness of 1.2 μm and a refractive index of 1.496 at 633 nm. The Gaussian beam width of 0.35 mm from a He-Ne cw laser (633 nm) with TE polarization was injected into the waveguide using a prism coupler. Figure 2 shows the transverse intensity profiles of experimental results taken at different times. The features of the branch structures are similar to those predicted by the computer model. The appearance of the two central branches in Figure 2 coincides with simulation results shown in Figure 1. In conclusion, optical branching has been modeled and experimentally observed with very close agreement between theory and experiment.

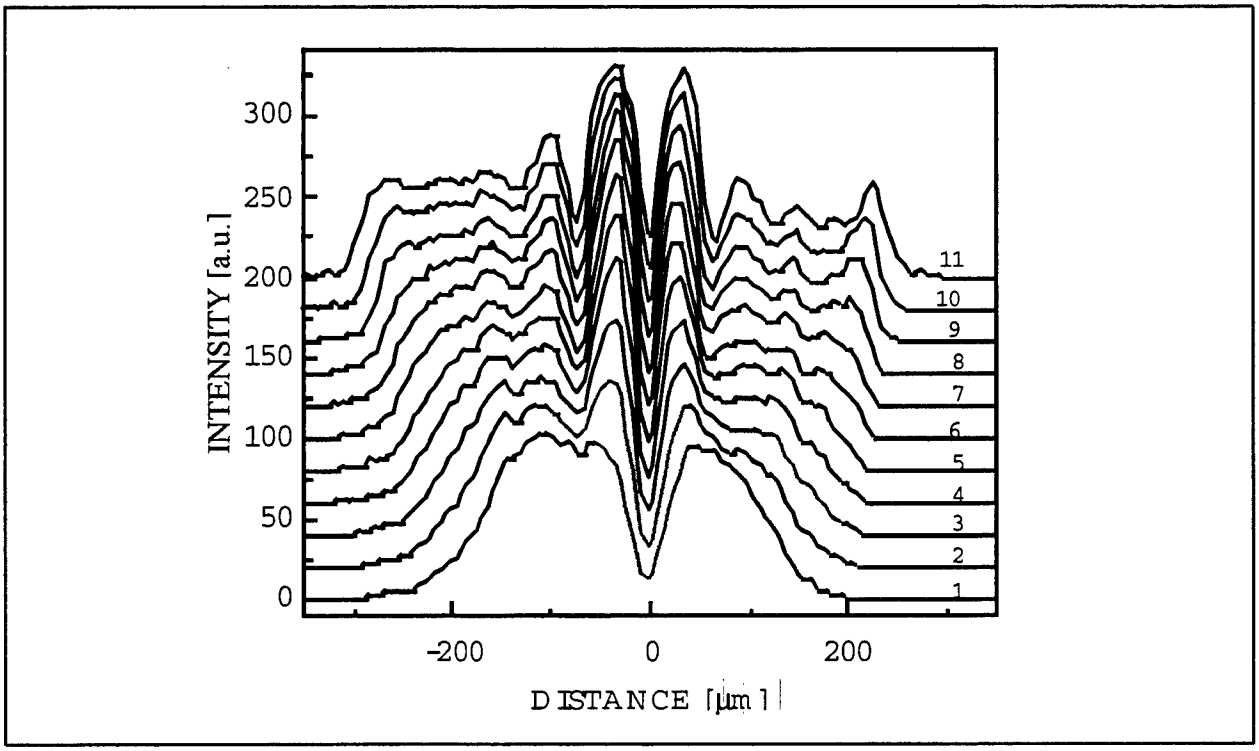


Figure 2. Experimental measurements showing the evolution of the transverse profile of the main beam at a distance of 27 mm from the coupling point for (1) t=10 s, (2) t=32 s, (3) t=60 s, (4) t=90 s, (5) t=120 s, (6) t=168 s, (7) t=180 s, (8) t=260 s, (9) t=330 s, (10) t=420 s, and (11) t=540 s.

REFERENCES

1. Yu. S. Kivshar, IEEE J. Quantum Electron. 29 (1993) 250.
2. B. Luther-Davies, X. Yang, Opt. Lett. Vol. 17 (1992) 496, 1755.
3. C. Bosshard, P.V. Mamyshev, G.I. Steegeman, Opt. Lett. 19 (1994) 90.
4. G. Duree, M. Morin, G. Salamo, M. Segev, A. Yariv, B. Crosignani, P. DiPorto, E. Sharp, Phys. Rev. Lett. 74 (1995) 1978.

Guiding Light by Incoherent Dark Solitons

Zhigang Chen
Dept. of Physics and Astronomy, San Francisco State University, San Francisco, CA 94123
(415) 338-3876 Fax: (415) 338-2178 Email: zchen@stars.sfsu.edu
Mordechai Segev
Physics Department, Technion – Israel Institute of Technology, and
Electrical Engineering Dept., Princeton University, Princeton, NJ 08544
Demetrios N. Christodoulides
Dept. of Electrical Eng. and Computer Science, Lehigh University, Bethlehem, PA 18015
Robert S. Feigelson
Center for Materials Research, Stanford University, Stanford CA 94305

Recently, optical spatial solitons have been highly touted and tested for applications in optical interconnects, optical communications, and other areas. In this report, we demonstrate experimentally optical guidance of light beams using incoherent light. Such guidance is made possible by generating partially spatially incoherent self-trapped dark beams (dark incoherent solitons) in a non-instantaneous nonlinear medium. The incoherent solitons induce 1-D and 2-D waveguides that can guide other intense coherent light beams. In the 1-D case, we demonstrate single and Y-junction planar induced-waveguides, whereas in the 2-D case, we show circular induced-waveguides. These experiments introduce the possibility of controlling high-power laser beams with low-power incoherent light sources such as Light Emitting Diodes or light bulbs.

For decades, solitons have been exclusively considered to be coherent entities, and optical solitons have been studied only with intense coherent light beams. Nature, however, is full of incoherent radiation sources. Can incoherent light also form a soliton and thus induce a waveguide? This intriguing and challenging question has recently motivated several experiments [1, 2] on self-trapping of incoherent light. By now, a series of experimental and theoretical [3, 4] studies has clearly demonstrated that incoherent spatial solitons are indeed possible in slow responding nonlinear media such as biased photorefractives. It is now understood that an incoherent bright soliton can have many modes populating in its induced waveguide [3], whereas an incoherent dark soliton results from a combination of radiation modes and bound states [4]. In either case, the light-induced variation of the refractive index forms a waveguide structure in the self-trapped region. Such an induced waveguide allows optical guidance of other beams that may be coherent or incoherent. When the nonlinearity employed is of the photorefractive type, these guided beams can be very intense if they are at a less-photosensitive wavelength. In this particular case, even a weak incoherent light beam can guide a strong coherent laser beam.

In our experiments, we first convert a coherent beam from an argon ion laser (λ=514 nm) into a quasi-monochromatic spatially incoherent light source by passing it through a rotating diffuser [1, 2]. The laser beam is focused by a lens onto the diffuser, and the scattered light from the diffuser is collected by another lens. The rotating diffuser provides random phase fluctuations, thus turning the beam into partially spatially incoherent. The spatial degree of coherence of this beam is revealed by the average size of the speckles borne on it. One can actually trace the temporally varying speckles with a fast camera, or, as we do here, monitor the beam when the diffuser is stationary. We then launch the speckled beam onto a phase or an amplitude mask, and redirect the reflected dark beam onto the input face of a photorefractive crystal in a way similar to that previously followed in generating coherent dark screening solitons [5, 6]. The photorefractive crystal used here is a 12-mm-long SBN grown at Stanford using the Bridgeman method. We first generate a 1-D incoherent dark stripe from a phase mask.

By providing an appropriate bias field, we obtain self-trapping of the incoherent dark stripe. We then launch a cylindrically focused probe beam from a red HeNe laser (λ=633 nm) into the incoherent dark soliton to test its waveguide properties. Figure 1 shows typical experimental results. The incoherent dark soliton is 18 μm (FWHM) wide, generated at a bias field of 950 V/cm. This beam has a coherence length (estimated from the average speckle size) of 15 μm away from the dark stripe. In the absence of nonlinearity, the probe beam diffracts from 20 μm (Fig. 1a) to 68 μm (Fig. 1b) after liner propagation through the crystal. Once the dark incoherent soliton has formed, guidance of the probe beam is observed (Fig. 1c). For the above experimental parameters, about 80% of the input power of the probe beam are guided into the output of the waveguide channel induced by the incoherent dark soliton.

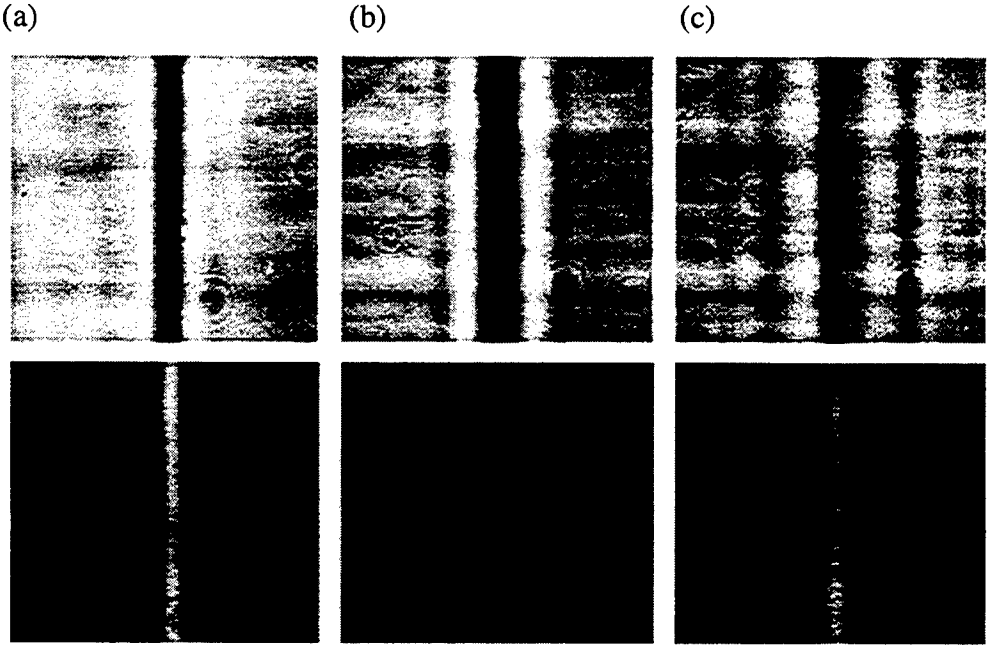


Fig.1: Photographs showing guidance of a probe beam (bottom) by an incoherent dark soliton (top) initiated from a phase mask. (a) input, (b) output with linear diffraction, and (c) output with nonlinearity.

Next we generate a dark stripe from an amplitude mask. Such an amplitude mask can be a simple mirror crossed by a fine wire. This in turn provides the "even" input conditions (because the phase across the beam is uniform) necessary to excite the Y-junction dark soliton pair. Y-splitting of dark incoherent solitons was recently studied in Ref. [7]. Here we show that such a dark incoherent soliton Y-splitting also induces an Y-junction waveguide capable of guiding other light beams. We perform experiments similar to that depicted in Fig. 1, except that we replace the phase mask with an amplitude mask. Figure 2 depicts the generation of Y-junction incoherent dark solitons as well as the guidance of the probe beam by the Y-junction (beam-splitting) induced waveguide. As expected, when the coherence of the dark beam decreases, the grayness of the soliton pair increases. Interestingly enough, however, the spacing of the two incoherent gray solitons at the crystal output face remains nearly the same. This is due to a special "phase memory" effect as discussed in [7]. Thus, the structure of the beam-splitting waveguides remains almost the same when the Y-splitting is created by either incoherent or coherent dark solitons.

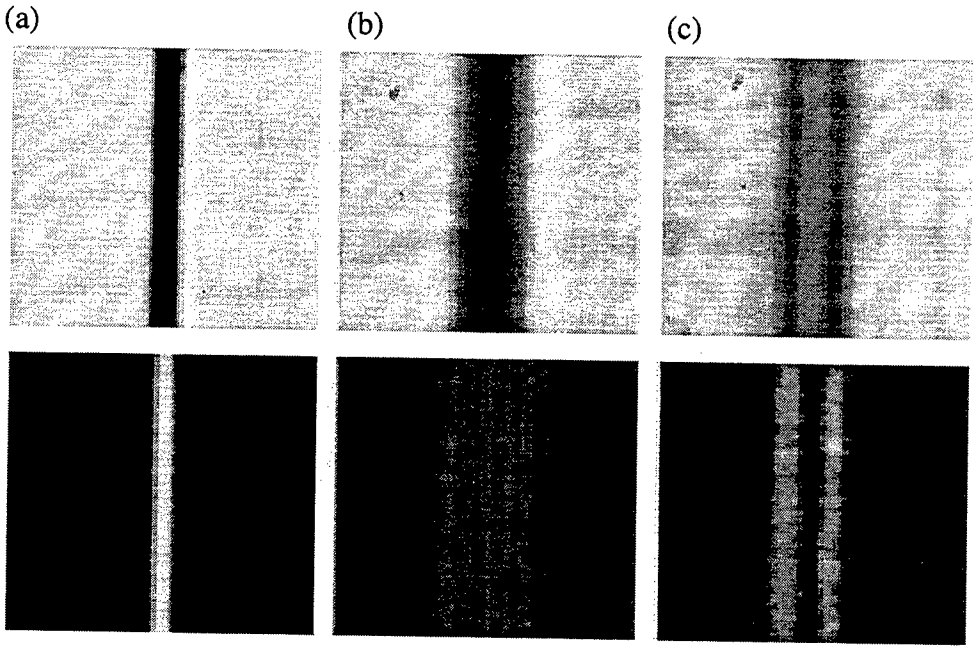


Fig.2: Photographs showing guidance of a probe beam (bottom) by an incoherent Y-junction dark soliton pair (top) initiated from an amplitude mask. (a) input, (b) output with linear diffraction, and (c) output with nonlinearity.

Finally, we replace the amplitude mask with a helicoidal phase mask [6]. A 2-D fiber-like waveguide induced by a self-trapped incoherent optical vortex (a 2-D incoherent dark soliton) is also observed. Although we have employed a quasi-monochromatic spatially incoherent light source, our experiments suggest that spatial solitons formed from "fully" (temporally and spatially) incoherent light sources (e.g., incoherent white light) can also induce waveguides capable of guiding other coherent and incoherent beams.

This research is supported by Research Corp., ARO, AFOSR and NSF.

[1] M. Mitchell, Z. Chen, M. Shih, and M. Segev, Phys. Rev. Lett. **77**, 490 (1996); M. Mitchell and M. Segev, Nature **387**, 880 (1997).
[2] Z. Chen, M. Mitchell, M. Segev, T.H. Coskun and D.N. Christodoulides, Science **280**, 889 (1998).
[3] D. N. Christodoulides, T. Coskun, M. Mitchell, and M. Segev, Phys. Rev. Lett. **78**, 646 (1997); M. Mitchell, M. Segev, T. Coskun and D. N. Christodoulides, Phys. Rev. Lett. **79**, 4990 (1997); D. N. Christodoulides, T. H. Coskun, M. Mitchell, and M. Segev, Phys. Rev. Lett. **80**, 2310 (1998); A. W. Snyder and D. J. Mitchell, Phys. Rev. Lett. **80**, 1422 (1998); V. V. Shkunov and D. Z. Anderson, Phys. Rev. Lett. **81**, 2683 (1998).
[4] D. N. Christodoulides, T. Coskun, M. Mitchell, Z. Chen and M. Segev, Phys. Rev. Lett. **80**, 5113 (1998).
[5] Z. Chen, M. Mitchell, M. Shih, M. Segev, M. Garrett and G. Valley, Opt. Lett. **21**, 629 (1996); Opt. Lett. **21**, 716 (1996); Z. Chen, M. Segev, S. R. Singh, T.H. Coskun and D.N. Christodoulides, J. Opt. Soc. Am. B **14**, 1407 (1997).
[6] Z. Chen, M. Shih, M. Segev, D. W. Wilson, R. E. Muller and P. D. Maker, Opt. Lett. **22**, 1751 (1997).
[7] T. H. Coskun, D. N. Christodoulides, Z. Chen, M. Mitchell and M. Segev, Phys. Rev. E, Rapid Comm. May (1999).

Towards soliton emission in GaAs/AlGaAs multi-quantum-well asymmetric waveguide structures below half the bandgap

Patrick Dumais, Alain Villeneuve
Pavillon Vachon, Université Laval, Cité Universitaire, Québec, Canada G1K 7P4
pdumais@phy.ulaval.ca, avillene@phy.ulaval.ca

A. Saher-Helmy, J. Stewart Aitchison
Department of Electronics and Electrical Engineering, University of Glasgow, Glasgow, G12 8QQ, United Kingdom
a.saher@elec.gla.ac.uk, S.Aitchison@elec.gla.ac.uk

Lars Friedrich, Russell A. Fuerst, George I. Stegeman
CREOL, P. O. Box 162700, 4000 Central Florida Blvd, Orlando, FL 32816-2700
lars@soliton.creol.ucf.edu, Russell.Fuerst@uniphase.com, george@creol.ucf.edu

We report here the first experimental evidence of nonlinear beam displacement in a strip-loaded GaAs/AlGaAs multi-quantum-well (MQW) waveguide with an asymmetric nonlinear cladding. An intensity-dependent spatial displacement of ~ 2 μm was observed for the guided mode at a wavelength of 1.55 μm. The detailed theoretical and numerical analysis of this phenomenon is described in [1]. This device is closely related to a soliton coupler, a device proposed by Heatley, Wright, and Stegeman [2], where a nonlinear cladding region between two waveguides induces an exchange of power between the waveguides for a given intensity. The present device, which we call a soliton-emitting waveguide, is a single-waveguide version of the soliton coupler. As is described in [1], this device emits a spatial soliton in the nonlinear cladding region for a given input intensity. It is perhaps important to note that until now, there was no suitable material with which to build such a device that would function using an ultrafast (i. e. non-resonant) nonlinearity.

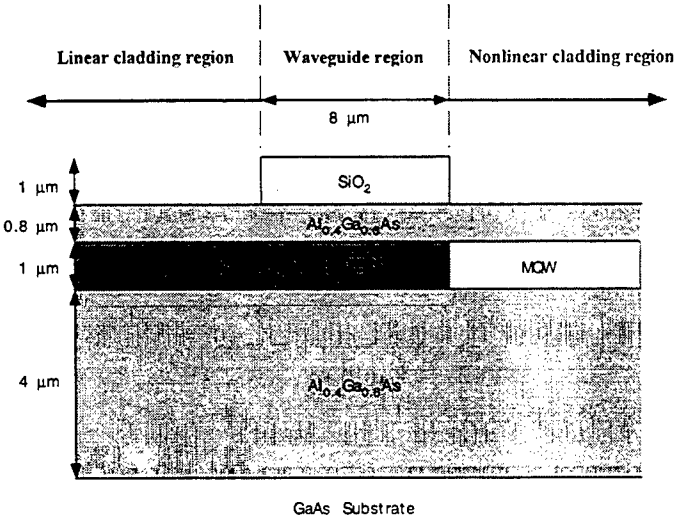


Fig. 1: Waveguide and device structures.

The device is based on a single-mode waveguide at 1.55 μm wavelength. This wavelength is below half the band gap of the MQW waveguide material, so that the guided mode suffers little or no two-photon absorption. The wafer structure was grown on a SI GaAs substrate as can be seen in Fig. 1. The MQW region consists of 76 periods of 2.8 nm GaAs wells with 10 nm $Al_{0.4}Ga_{0.6}As$ barriers. The waveguide is defined by strip-loading the structure with 200 nm of SiO_2. In addition, the MQWs of the waveguide

together with one of the cladding regions are selectively disordered as illustrated in Fig. 1. The MQW structure yields a higher nonlinear coefficient n_2 than the equivalent bulk composition from the quantum confinement and bandgap shift effects [3]. Disordering the structure thus lowers its nonlinear coefficient. Disordered MQWs were reported to have up to 64 % reduction in their n_2 nonlinear coefficient [4]. Therefore, after the intermixing process we are left in essence with a linear waveguide having one nonlinear cladding region. Disordering is achieved through an impurity-free vacancy disordering technique [4], where dielectric caps are used during rapid thermal annealing to control the out-diffusion of Ga from the semiconductor. The Ga out-diffusion has a substantial impact on the interdiffusion rates of Al and Ga across the MQW heterostructures. The samples presented here used SiO_2 and SiO_2:P to enhance and inhibit intermixing respectively. Standard photolithography was used for patterning the dielectric caps and hence tailoring the waveguide nonlinear profile.

In the low-power regime, the entire waveguide can be regarded as linear, and the guided mode propagates as the fundamental mode of the strip-loaded waveguide. At higher powers, however, the right-hand nonlinear cladding region, as seen in Figure 1, would exhibit an induced Kerr nonlinearity, which increases the refractive index with regard to the waveguide region. At a sufficiently high power densities, the nonlinear refractive index change can compensate the linear index step defining the waveguide, effectively eliminating the index boundary on one side. When the mode power exceeds this threshold power, the light propagating in the waveguide can escape in the nonlinear cladding region and would stabilize in the form of a spatial soliton, propagating at an angle with regard to the waveguide.

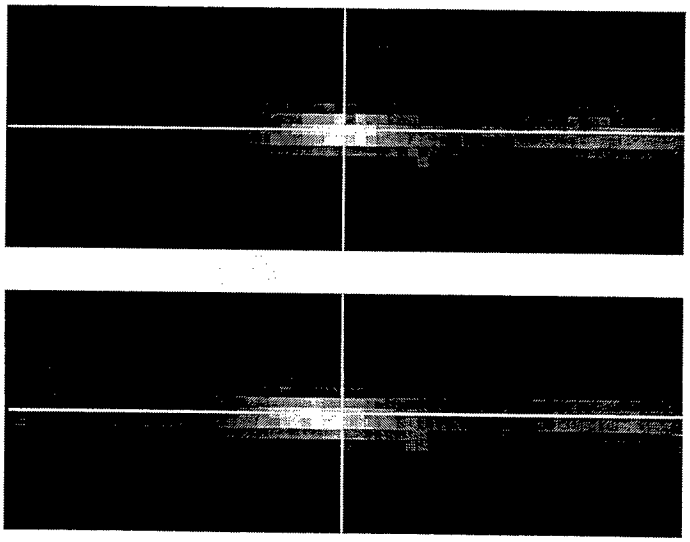


Fig. 2: Images of the device output at low (top) and high (bottom) input power. The crosshairs indicate the position of the center of the beam at low power.

A LBO-based OPG-OPA system pumped by a Q-switched, frequency-doubled YAG laser was used for testing the samples described above. The output pulses had energies of the order of 10 microjoules, with pulse width of 20 ps, at a repetition rate of 10 Hz and a wavelength of 1560 nm. A 40x microscope was used objective to couple-in a collimated beam of 2.5 mm diameter, which produces a 1.6 μm spot. The corresponding Rayleigh length for this setup is ~ 5 μm. The waveguide was 3 mm long, and the mode size of the waveguide was 10 x 0.8 μm. The optimal overlap integral between the mode and the circular input beam would be ~ 0.3. The fluence at the focal point was sufficiently large to induce optical damage within the waveguide material. The beam had to be not optimally coupled into the waveguide to avoid optical-induced damage. Considering the overlap integral and reflection losses, the maximum coupled peak power would be 25 kW, corresponding to a peak intensity of 200 GW/cm^2, which is the upper limit for this setup.

For these conditions we have observed an intensity-dependent lateral shift of 2 _m, for a mode width of 10 _m. In Figure 2, we have illustrated the images from the output face of the device, the top image corresponding to a low input intensity, and the bottom image corresponding to a high input intensity. These images are normalized to each of their peak intensity. It can be seen from the fixed crosshair that the lateral position of the high intensity output, at bottom, shifts to the left of the crosshair, which is placed on the center of the low intensity image, at top. In Figure 3, we have the corresponding intensity profiles of these output which quantify the displacement.

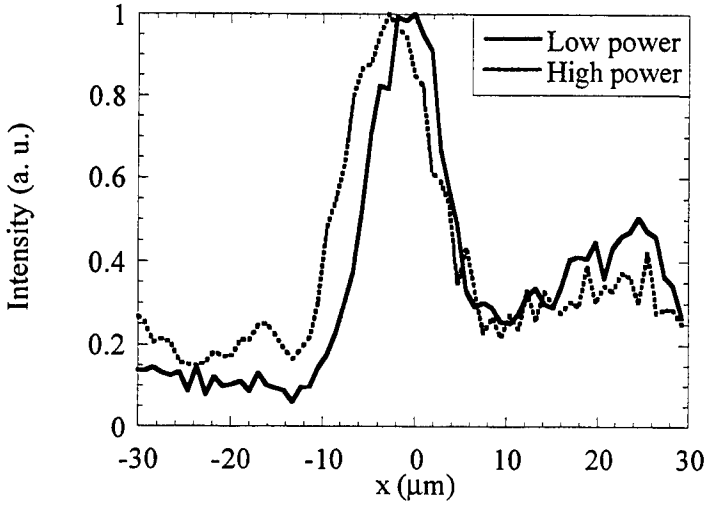


Fig. 3: Beam profiles at the device output face at low and high power. These correspond to the images seen in Figure 2.

Although the simulations in [1] were made with realistic parameters, including linear and nonlinear losses, the locality of the disordering process and tolerance on waveguide dimensions, there are additional factors that we now have to consider. First, there was an angular difference of 1 mrad between the waveguides and the nonlinear pattern for this sample, resulting in a 3 μm translation the intermixing patterns with regard to the waveguides. This is due to the limited accuracy of optical lithography. The misalignment results in the waveguide linear/nonlinear interface moving into the guiding region as the beam propagates. Moreover, the intermixing of the MQW structure induces linear refractive index change in the sample. The refractive index of the intermixed regions would thus increase for the TM mode of the slab [5]. This would increase the index step at the linear/nonlinear interface, thus increasing the threshold switching power. Our recent simulations that take these factors into account are in agreement with the experimental results observed here. We will present these recent simulations.

In conclusion, we have observed an intensity-dependent spatial displacement of a guided beam in a strip loaded asymmetric waveguide. The results are consistent with our numerical models. The device has the potential of providing the first soliton emission-based, ultrafast all-optical switch.

References:

[1] P. Dumais, A. Villeneuve, A. Saher Helmy, J. S. Aitchison, Opt. Express **2**, 455-461 (1998).
[2] D. R. Heatley, E. M. Wright, and G. I. Stegeman, Appl. Phys. Lett. **53**, 172-174 (1988).
[3] C. C. Yang, A. Villeneuve, G. I. Stegeman et al., IEEE J. Quantum Electron. **29**, 2934-2939 (1993).
[4] C. J. Hamilton, J. H. Marsh, D. C. Hutchings, J. S. Aitchison, G. T. Kennedy and W. Sibbett, Appl. Phys. Lett. **68**, 3078-3080 (1996).
[5] Y Suzuki, H. Iwamura, T Miyazawa, A. Wakatsuki, O Mikami, J. Quant. Electron. **32**, 1922 (1996).

Quadratic soliton interactions in a bulk medium

Anatoly P. Sukhorukov, Dmitry A. Chuprakov and Xin Lu
Moscow State University, Vorobjevy Gory, Moscow, 117234 Russia
aps@nls.phys.msu.su, chup@nls.phys.msu.su, lu@nls.phys.msu.su

The perspective of all-optical switching and controlling light by light made a study of soliton interactions more exciting [1]. It is remarkable that interacting spatial solitons can be considered as particles [2,3]. Interactions of (1+1)-D quadratic solitons were studied numerically in [4,5] and (2+1)-D solitons in [6-8]. In the case of nonplanar interactions of (2+1) spatial solitons, one can observe spiraling of optical beams [6-9]. In this report we demonstrate the new features of quadratic soliton interactions: spiraling of cascaded solitons, relative displacement of FF and SH beams into interacting parametric solitons and inhomogeneous phase mismatching between inclined beams.

The slowly varying complex amplitudes of the fundamental wave A_1 and second harmonic A_2 obey the coupled equations:

$$\frac{\partial A_1}{\partial z} \pm iD_1\Delta_\perp A_1 \pm i\gamma A_1^* A_2 e^{-i\Delta kz} = 0, \qquad \frac{\partial A_2}{\partial z} \pm iD_2\Delta_\perp A_2 \pm i\gamma A_1^2 e^{i\Delta kz} = 0, \tag{1}$$

where z is the propagation distance, D_i are the diffraction coefficients, $\Delta_\perp = \partial^2/\partial x^2 + \partial^2/\partial y^2$ (x and y are transverse coordinates), γ is the nonlinear coefficient, $\Delta k = k_2 - 2k_1$ is the mismatch.

We investigate nonplanar interaction of two spatial parametric solitons (Fig. 1). The incident FF and SH beam axes lie in the parallel planes d apart and oppositely inclined to z direction by the angle θ.

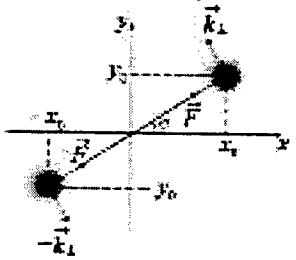


Fig.1: The cross section of solitons.

The nonplanar collisions of quadratic solitons have been investigated theoretically recently [6-8]. In this report we consider two-colour beams spiraling both with seeded and first non-seeded SH beams.
In the case that only FF beams are launched into a crystal, there are two stages of soliton spiraling (Fig. 2, the upper row).

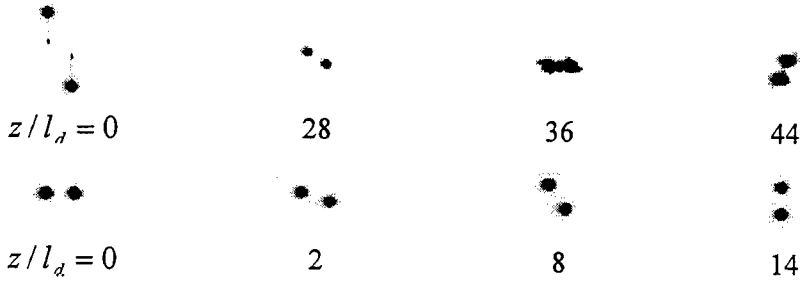


Fig.2. Sequential positions of solitons at different distances for soliton spiraling (the upper row) with cascaded nonlinearity ($\gamma A_1(0) = 15$ $\theta = 0.3$, $\Delta k l_d = 0.125$) and (the lower row) phase-matching ($\gamma A_1(0) = 8.45$, $\gamma A_2(0) = 8.15$, $\theta = 0.33$).

In the first stage of propagation, the soliton trapping with cascaded nonlinearity takes place. The beams are so distant from each other that their attraction is very weak to the point of minimal separation at $z = 36 l_d$. Next becomes strong soliton interaction and the beams are curled into a spiral. After distance of length about $\Delta z = 8 l_d$, the soliton pair is turned through 90 degrees.

The second stage of soliton spiraling have been examined on a basis of the effective particle approach in [6-8]. A system of equations for the soliton center coordinates can be derived using integrals of motion such as the energy invariant, the vector of momentum and Hamiltonian for interacting beams. They are evident from Eqs. 1. We develop a soliton-particle model by variation of Lagrangian

$$J_3 = \iint dxdy\left[2D_1|\nabla_\perp A_1|^2 + D_2|\nabla_\perp A_2|^2 - \Delta k|A_2|^2 - \gamma(A_1^2 A_2^* + A_1^{*2} A_2)\right]. \quad (2)$$

For weak interplay of solitons, the complex envelopes can be represented in the following form

$$A_j = B_j(x \pm x_{0j}, y \pm y_{0j}) \exp\left\{\pm ik_j\left[(x \pm x_{0j})\theta_x + (y \pm y_{0j})\theta_y\right] - iq_\perp z + i\Phi_j\right\}. \quad (3)$$

Here B_j is the soliton envelope as the exact solution of Eqs (1), $j = 1,2$, $q_\perp$ is the nonlinear shift of the propagation constant, $q_2 = 2q_1 - \Delta k$, x_{0j}, y_{0j} are the transverse coordinates of the FF and SH beams, $\theta_x = dx_{0j}/dz$, $\theta_y = dy_{0j}/dz$ are the angles of beam inclination or components of soliton transverse velocity, Φ_j is the phase shift of wave, $d = 2r_0$ is the separation between soliton centers.

Although the positions of FF and SH beams of parametric soliton are not coincide to one another due to interaction, for simplicity assume that $x_{01} = x_{02} = x_0$ and $y_{01} = y_{02} = y_0$. Then substituting of Eqs. (3) into Eq. (2), we represent Lagrangian as $L = W - T$, where $T = 2k_1 P_{sol}(\dot{x}_0^2 + \dot{y}_0^2)$ is the kinetic energy of moving soliton, $P_{sol} = \iint\left[B_1^2(x,y) \pm B_2^2(x,y)\right]dxdy$ is the total power of soliton. The potential energy of interacting soliton equals to

$$W = -4\gamma \iint\left(B_{11}^2 B_{22}\cos\phi_1 + 2B_{11}B_{12}B_{21}\cos\phi_2\right)dx\,dy. \quad (4)$$

Here $B_{j1} = B_j(x - x_0, y - y_0)$, $B_{j2} = B_j(x + x_0, y + y_0)$, $\phi_1 = 4k_1(x\dot{x}_0 + y\dot{y}_0) + 2\Delta\Phi$, $\phi_2 = 2k_1(x\dot{x}_0 + y\dot{y}_0) + \Delta\Phi$, $\Delta\Phi = \Phi_{11} - \Phi_{12}$. Note that the present approach takes into account the inhomogeneous distribution of phase mismatch $\phi_{1,2}$ between the separated oppositely inclined solitons. This effect proportional to spatial soliton tilt lowers a force of soliton interaction. The corresponding terms do not included in the ordinary consideration [6-8].

Minimizing Lagrangian $L = W - T$, we derive the system of dynamic equations for spatial separation between soliton centers in the form

$$\frac{d^2x_0}{dz^2} = -\frac{1}{m}\frac{\partial W}{\partial r_0}\cos\varphi, \qquad \frac{d^2y_0}{dz^2} = -\frac{1}{m}\frac{\partial W}{\partial r_0}\sin\varphi. \quad (5)$$

Here we introduce the effective soliton mass as $m = 4k_1 P_{sol}$ and the polar coordinates (r_0, φ). According to Eqs. (5), solitons behave similar to classical particles.

The results of direct numerical simulation of soliton spiraling with phase match are shown in Fig. 2, the lower row. The dependence of the spiral angle on the distance between solitons was obtained both by direct
numerical solutions of Eqs. (1) and by calculations in the frame of the effective particle theory based on Eqs. (5).

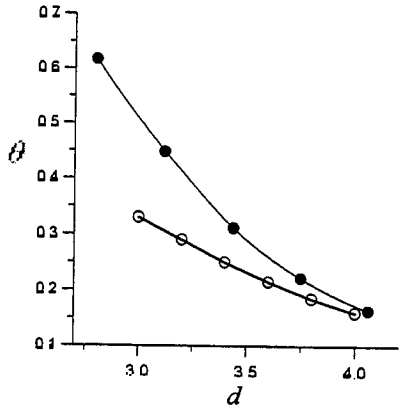


Fig. 3: The soliton spiral angle θ versus the separation between solitons d. The data were obtained from direct numerical simulations (open circles) and calculations of overlap integral (filled circles).

Close examination of soliton interaction process shows that FF and SH beams of quadratic soliton are slightly displaced relative to each other (Fig. 3).

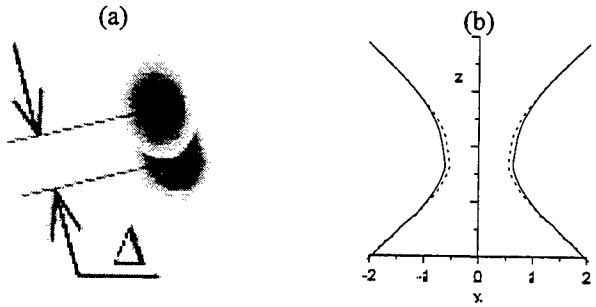


Fig. 3: The FF and SH beams relative displacement due to interaction of quadratic solitons: (a) the displacement in spiraling soliton is $\Delta \approx 0.1$ for $d = 3$, $\theta = 0.33$ and (b) the trajectories at soliton scattering for fundamental beam (solid line) and second harmonic (dashed line) with maximum $\Delta \approx 0.1$ for the input parameters $d = 6$, $\theta = 1$.

Such an effect means that a force acting on FF part of the soliton differs from one on second harmonic. We observed first this new phenomena on numerical simulation of soliton spiraling and scattering. The closer are solitons, the greater is the beam displacement Δ.

This research was supported by INTAS, RFBR and FUR.

REFERENCES:

1. G. I. Stegeman, D. J. Hagan, and L. Torner, J. Opt. and Quantum Electon. **28**, 1691 (1996).
2. K. A. Gorshkov and L. A. Ostrovsky, Physica D **3**, 428 (1981).
3. V. I. Karpman and V. V. Solov'ev, Physica D **3**, 487 (1981).
4. D. M. Baboiu and G. I. Stegeman, J. Opt. Soc. Am. B **14**, 3143 (1997).
5. C. Etrich, U. Peschel, F. Ledere, and B. Malomed, Phys. Rev. A **52**, R3444 (1995).
6. V. V. Steblina, Yu. S. Kivshar, and A. V. Buryak, Opt. Lett. **23**, 156 (1998).
7. X. Lu., A. P. Sukhorukov, and D. A. Chuprakov, Izv. RAN. Ser. Phys. **62**, 2319 (1998).
8. A. V. Buryak, and V. V. Steblina, J. Opt. Soc. Am. B **16**, 245 (1999).
9. M. Shin, M. Segev, and G. Salamo, Phys. Rev. Lett. **78**, 2551 (1997).

Nonlinear guided waves and their applications

Optical needles: ultra-narrow Maxwell's spatial solitons in Kerr media

N.N.Rosanov, V.E.Semenov, N.V.Vyssotina
Institute for Laser Physics, Vavilov State Optical Institute,
12 Birzhevaya liniya, St. Petersburg, 199034 Russia
Phone 7 812 3281093, Fax 7 812 3285891
rosanov@ilph.spb.su

The limiting levels of light energy concentration can be achieved by shortening of laser pulses (femto- and attosecond range) and by transverse squeezing of beams (sub-micrometer sizes). The latter approach can be realized in media with nonlinearity of refractive index of self-focusing type.

The main theoretical investigations of the fundamental phenomenon of self-focusing and self-trapping [1,2] were performed in approximation of slowly varying envelope (paraxial equation) [3,4]. In Kerr medium this theory predicts collapse of the beam into a point, if the beam power exceeds the critical power of self-focusing P_0. However, paraxial equation is not applicable to the case of beams with transverse size less than the light wavelength. In the vicinity of the nonlinear focus it is necessary to solve the full set of Maxwell's equations taking into account complex polarization structure of radiation. Few such attempts are known (see [4] and references therein), but they are applicable to unrealistic (transversely one-dimensional) geometry or to special types of beams with cylindrically symmetric intensity distribution, which are unstable.

The goal of this report is to demonstrate that regimes of spatial solitons, or radiation self-trapping, with nontrivial polarization structure exist in transparent media with Kerr nonlinearity, if the beam power is larger than the critical power of self-focusing. A special case of these solitons, the "optical needles" characterized by width less than the radiation wavelength exists when the beam power is large enough.

The initial equations are the Maxwell's equations for monochromatic radiation with frequency ω in a medium with Kerr nonlinearity, when nonlinear part of the electric displacement $\mathbf{D}_{nl}$ is cubic in the electric field $\mathbf{E}$:

$$\mathbf{D}_{nl} = A(\mathbf{E}\cdot\mathbf{E}^*)\mathbf{E} + \frac{B}{2}(\mathbf{E}\cdot\mathbf{E})\mathbf{E}^*. \qquad (1)$$

For the sake of simplicity we assume $B = 0$ which is valid for striction mechanism of nonlinearity in fluids. Then it is possible to introduce a nonlinear electric permittivity $\varepsilon = \varepsilon_0 + \varepsilon_2|\mathbf{E}|^2$, where coefficient of nonlinearity $\varepsilon_2 > 0$. We assume also that magnetic permeability $\mu = 1$. The fields with multiple frequencies (e.g., 3ω) are small because synchronism conditions are not fulfilled for them. To take into account a vector nature of the electromagnetic field, it is convenient to introduce, instead of electric $\mathbf{E}$ and magnetic $\mathbf{H}$ fields, the vector $\mathbf{\Pi}$ and scalar ϕ potentials, so that

$$\mathbf{H} = -\frac{i\omega}{c}\,\mathrm{rot}\,\mathbf{\Pi}, \quad \mathbf{E} = -\mathrm{grad}\,\phi + \frac{\omega^2}{c^2}\mathbf{\Pi}. \qquad (2)$$

After choice of the scalar potential $\phi = -\frac{1}{\varepsilon}\,\mathrm{div}\,\mathbf{\Pi}$, we get the following equation for the vector potential

$$\Delta\mathbf{\Pi} + \frac{\varepsilon\omega^2}{c^2}\mathbf{\Pi} - \mathrm{grad}\ln\varepsilon\cdot\mathrm{div}\,\mathbf{\Pi} = 0. \qquad (3)$$

Then the electric field $\mathbf{E} = \frac{1}{\varepsilon} \operatorname{rot} \operatorname{rot} \mathbf{\Pi}$. Next we assume that the field dependence on the longitudinal coordinate z is exponential: $\mathbf{\Pi}(x, y, z) = \mathbf{\Pi}(x, y) \exp(i\gamma z)$, where γ is a real propagation constant. The Maxwell's equations admit solution with the potential longitudinal component $\Pi_z = 0$. The final form of equations for the potential transverse components is

$$\Delta_\perp \Pi_x - \gamma^2 \Pi_x + \frac{\varepsilon\omega^2}{c^2}\Pi_x - \frac{\partial(\ln\varepsilon)}{\partial x}\left(\frac{\partial \Pi_x}{\partial x} + \frac{\partial \Pi_y}{\partial y}\right) = 0,$$
$$\Delta_\perp \Pi_y - \gamma^2 \Pi_y + \frac{\varepsilon\omega^2}{c^2}\Pi_y - \frac{\partial(\ln\varepsilon)}{\partial y}\left(\frac{\partial \Pi_x}{\partial x} + \frac{\partial \Pi_y}{\partial y}\right) = 0. \qquad (4)$$

Here $\Delta_\perp = \partial^2/\partial x^2 + \partial^2/\partial y^2$ is the transverse Laplacian. The radiation power P is determined as the integral over transverse section of time averaged z-component of Pointing vector. After scaling of the variables we use dimensionless coordinates ($\mathbf{r} \to k\mathbf{r}$, $k = (\omega/c)\sqrt{\varepsilon_0}$), power ($P \to P/P_0$), propagation constant ($\gamma \to \gamma/k$) and assume $\varepsilon = 1 + |\mathbf{E}|^2$.

Approximate analytical solution of Eqs. (4) can be given for high power P, if we neglect the small terms with derivatives of . It follows from this solution that there is a discrete set of regimes of self-trapping with different critical power. The fundamental spatial soliton has a minimum critical power and therefore seems to be most stable. Its field structure is universal, only its scales vary with variation of power. Its width decreases with the power, and arbitrary narrow spatial solitons ("optical needles") exist if the ratio P/P_0 is large enough.

In numerical solution of Eqs. (4) we use iterative procedure for matching of transverse distributions of the potential, electric field, and dielectric permittivity. Results of the numerical solution are given in Figs. 1-3. They correlate well with the approximate analytics.

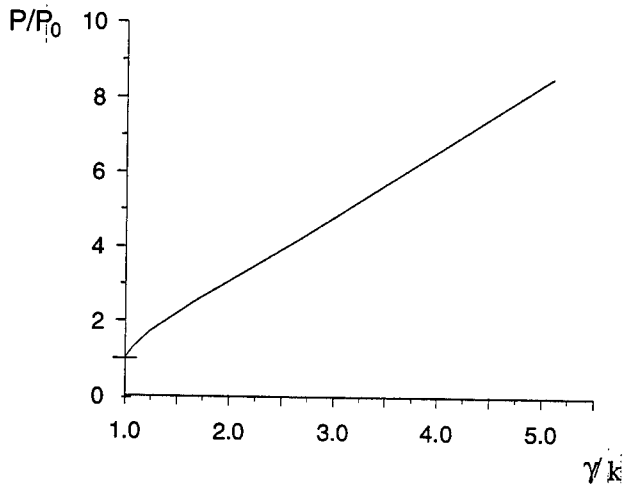


Fig. 1. Radiation power P versus propagation constant γ in the regime of steady state self-focusing in Kerr medium. Power is scaled on the critical power of self-focusing in the parabolic approximation P_0, and propagation constant γ is scaled on the radiation wavenumber in a linear medium k.

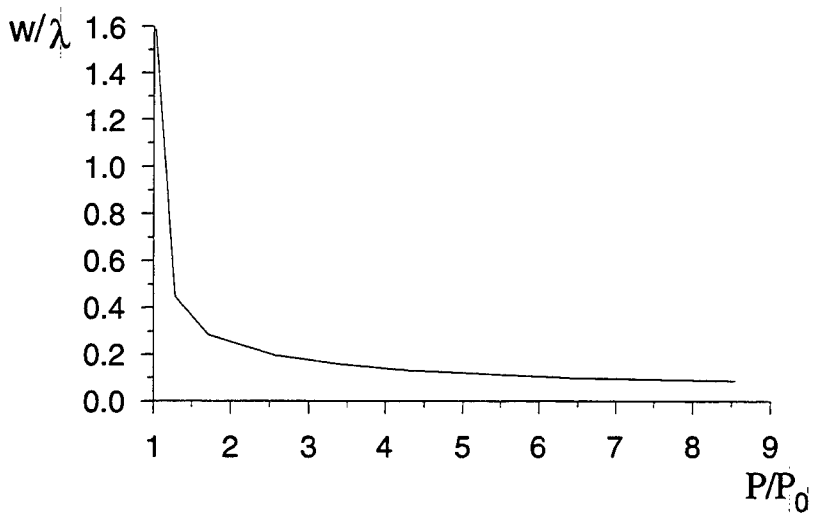


Fig. 2. Effective width of the beam w versus radiation power P in the regime of steady state self-focusing. Width is scaled on radiation wavelength in the linear medium λ, and power is scaled on the critical power of self-focusing in the parabolic approximation P_0.

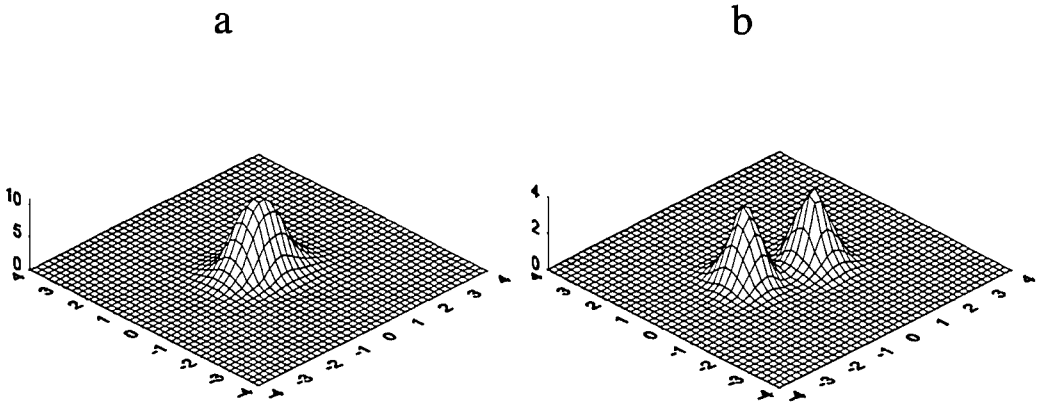


Fig. 3. Transverse profiles of radiation intensity in the regime of the "optical needles": (a) intensity of the field transverse component $I_\perp = |E_x|^2 + |E_y^2|$; (b) intensity of the longitudinal component $I_{||} = |E_z|^2$; the total power

In conclusion, we have found for the first time solutions of the full system of the Maxwell's equations corresponding to nontrivial polarization structure of radiation in a medium with Kerr nonlinearity. The spatial soliton field structure depends on the soliton power. For high power a universal field structure is formed where only scales depend on power. Extremely narrow (with width less than radiation wavelength) spatial solitons, or "optical needles", can be formed for sufficiently high soliton power.

References

1. G.A.Askaryan. Sov. Phys. JETP **42**, 1567, 1962.
2. R.Y.Chiao, E.Garmire, C.H.Townes. Phys. Rev. Lett. **13**, 479, 1964.
3. J.H.Marburger. Prog. Quant. Electron. **4**, 35, 1975.
4. S.N.Vlasov, V.I.Talanov. Wave self-focusing. Inst. Appl. Phys., Nizhnii Novgorod, 1997 (in Russian).

Formation and interaction of adaptive waveguides using photorefractive screening solitons

Jürgen Petter, Carsten Weilnau, Cornelia Denz
Institute of Applied Physics, Darmstadt University of Technology
Hochschulstr. 6, D-64289 Darmstadt, Germany
Juergen.Petter@physik.tu-darmstadt.de

Photorefractive screening solitons have attracted a lot of interest in the last years, because they can be created with very low laser power using a biasing DC electric field and a background illumination. Their anisotropic potential makes them unique among the different types of spatial optical solitons, like Kerr- or quadratic solitons [1-4]. Due to this anisotropy a lot of different interaction scenarios between them can be realized, as fusion [5, 6], creation [7], annihilation [8], rotation [9] and spiraling [10] of spatial solitons. These effects, combined with the simplicity of their generation, makes them very promising for waveguide applications, as e.g. all-optical switching, adaptive interconnects and logic operations [11-14].

Due to their anisotropic potential, different interaction scenarios between photorefractive (PR) solitons in the direction parallel (x-direction) and perpendicular (y-direction) to the applied electric field can be found. While these solitons always attract when aligned in y-plane, repulsion and attraction can appear in the plane parallel to the external electric field (x-plane), depending on their initial separation. This provides the possibility of realizing different waveguide interconnections, as eg. 2-to-1 coupling or waveguide separation depending on the plane of incidence. Furthermore 2-to-3 or 3-to-1 coupling devices can be realized using coherent solitons [7, 8].

These interaction effects have been described mostly in steady-state situations. However temporal effects become important when investigating the formation and interaction of 2D spatial solitons. Furthermore, resolving the temporal development is a suitable way to obtain a complete insight in spatial soliton physics, which is a necessity to gain control over the soliton interaction for waveguide applications. Here we focus on the anomalous anisotropic [15, 9] dynamical behaviour of the interaction of incoherent PR screening solitons when they are launched into the crystal under skewed geometry. These initial conditions lead to a mutual winding of the solitons and strong interaction in the noncentral potential they create. In terms of application the mutual winding of the solitons can be used to realize a device to swap positions of waveguides or to guide one beam to a different position by a second one (all-optical switch).

The interaction of mutually incoherent spatial solitons was investigated experimentally in a standard configuration [7-9]. A Cerium-doped Strontium Barium Niobate (SBN) crystal with a size of $13.5 \times 5 \times 5$ mm^3 ($a \times b \times c$) was biased with a DC voltage of $2-3$ kV applied along its polar c-axis. Two circular beams derived from a frequency-doubled Nd:YAG laser ($\lambda = 532$ nm) were directed by a system of mirrors and beam splitters on the entrance face (x, y) of the crystal. The relative angle of the interacting beams could be precisely adjusted by the external mirrors. The beams had Gaussian diameters of $\approx 15\mu$m, an intensity of 3μW, and were polarized along the x-axis, to make use of the large r_{33} electrooptic coefficient. The process of screening of the photorefractive space charge field is determined by the degree of saturation I_{sat}, which is defined as the ratio of the soliton peak intensity I_s to the background illumination I_b. To control the degree of saturation, the crystal was illuminated by a wide beam derived from a white light source. The power of the background illumination was set to such a level that the degree of saturation was approximately equal to $I_b/I_s \approx 2$ for all beams. The input and output light intensity distributions were recorded

with CCD cameras.

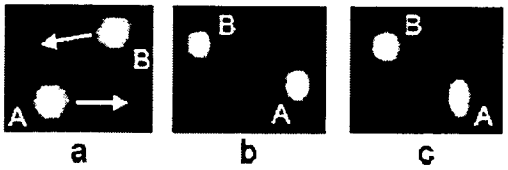


Figure 1: Stationary state representation of spiraling of an incoherent soliton pair. (a) Beams at the entrance face of the crystal, indicating the direction of relative skewing of both beams, (b) at the exit face without interaction and (c) during spiraling due to the interaction when the external field is operating. The direction of the electric field is horizontal.

Fig. 1 shows a typical scenario of two solitons propagating in a PR medium in the steady state. Fig. 1(a) shows the entrance face of the crystal and Fig. 1(b und c) the exit face of the crystal without and with interaction of the two beams, respectively. When comparing the pictures (b) and (c) it seems that the solitons almost do not interact except a slight mutual rotation of only a few degree. Another interpretation of the situation can state a mutual rotation of the written waveguides of almost 2π.

When this situation is resolved in time, the insight into the interaction behaviour becomes much more transparent. Fig. 2 shows a temporally resolved series of the interaction of two PR solitons. Here, the second beam (B) is launched into the crystal when the first beam (A) already propagates in its steady state. In the first seconds the second soliton (B) forms at its launching position (fig. 2.2). Subsequently, both beams break up into different spatial components (fig. 2.3), until they reappear in a clockwise rotated position (fig. 2.6). During this stage, power exchange takes place between the two beams. Then beam B rotates counterclockwise around beam A, and reaches its steady state position (fig. 2.7-12). Note that the solitons turn around each other in an elliptical orbit, as it was found in [10]. The reason for the change in the rotation direction can be found in the anisotropic potential structure which provides regions of attraction as well as of repulsion
Another possibility to investigate the interaction of two solitons in detail is a spatial shift of the initial x-coordinate of one beam with respect to the other, while all other conditions are kept unchanged. In this case the length of mutual interaction of the two solitons in the PR material can be varied. In our experiments the beams were separated about $\approx$ 10 μm in y direction, and we changed the distance in x direction from -30 to 30 μm. We found that after a counterclockwise rotation of the beams of about $\approx 90°$ the solitons start to exchange energy at a initial distance of the beams of $\approx$ 5 μm. When the beams are launched in a plane vertical to the electric field (distance in x-direction = 0 μm) the beam fuse to a single soliton at the exit face of the crystal. When shifting the initial beam position further and thus increasing the relative distance, the beams separate again with changed positions and the counterclockwise rotation proceeds about another $\approx 80°$. At a relative initial distance of more than 30 μm the beams do not interact any longer and propagate undisturbed.

In conclusion, temporally and spatially resolving the behaviour of soliton interaction may explain steady-state results of the interaction in a different light and gives a detailed insight into the complex interaction scenarios that take place during soliton propagation. This knowledge is an essential point to gain control of the interaction of solitons and will lead to a variety of practical applications in adaptive waveguiding. The realization of different adaptive waveguide interconnects,

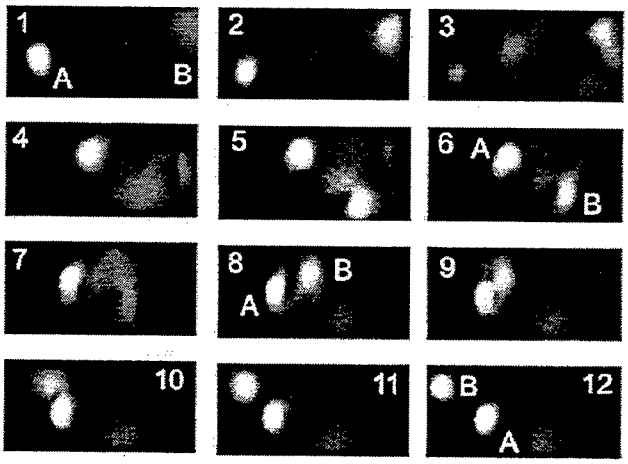


Figure 2: Time-resolved complex rotation of a soliton pair. The sequence starts when a second beam is launched to a steady-state soliton. The time interval between consecutive frames is 0.36 s.

as 2-to-1 and 3-to-2 coupler, waveguide interchanging devices and all-optical switches is presently under investigation. The authors acknowledge kind support by Prof. Dr. T. Tschudi.

1. M.D. Iturbe-Castillo, P.A. Marquez-Aguilar, J.J. Sanchez-Mondragon, S. Stepanov, V. Vysloukh, Appl. Phys. Lett. **64**, 408 (1994).
2. M. Segev, G.C. Valley, B. Crosignani, P. DiPorto, A. Yariv, Phys. Rev. Lett. **73**, 3211 (1994); D. N. Christodoulides, M. I. Carvalho, J. Opt. Soc. Am. B **12**, 1628 (1995).
3. M. Shih, M. Segev, G.C. Valley, G. Salamo, B. Crosignani, P. DiPorto, Electron. Lett. **31**, 826 (1995).
4. A. A. Zozulya, D. Z. Anderson, A. V. Mamaev, M. Saffman, Europhys. Lett. **36**, 419 (1996).
5. M. F. Shih, M. Segev, Opt. Lett. **21**, 1538(1996).
6. M. F. Shih, M. Segev, G. Salamo, Appl. Phys. Lett. **69**, 4151 (1996).
7. W. Krôlikowski, S. A. Holmstrom, Opt. Lett. **22**, 369 (1997).
8. W. Królikowski, B. Luther-Davies, C. Denz, T. Tschudi, Opt. Lett. **23**, 97 (1998).
9. W. Królikowski, M. Saffman, B. Luther-Davies, C. Denz, Phys. Rev. Lett. **80**, 3240 (1998).
10. M. F. Shih, M. Segev, G. Salamo, Phys. Rev. Lett. **78**, 2551 (1997).
11. T.-T. Shi, S. Chi, Opt. Lett. **15**, 1123 (1990); R. McLeod, K. Wagner, S. Blair, Phys. Rev. A **52**, 3254 (1995); P. D. Miller, N. N. Akhmediev, Phys. Rev. E **53**, 4098 (1996).
12. B. Luther-Davies, X. Yang, Opt. Lett. **17**, 498 (1992); B. Luther-Davies, X. Yang, W. Krolikowski, Int. J. Nonlin. Opt. Mat. **2**, 339 (1993).
13. W. J. Firth, A. J. Scroggie, Phys. Rev. Lett. **76**, 1623 (1996); M. Brambilla, L.A. Lugiato, M. Stefani, Europhys. Lett. **34**, 109 (1996).
14. R. de la Fuente, A. Barthelemy, C. Froehly, Opt. Lett. **16**, 793 (1991).
15. A. A. Zozulya and D. Z. Anderson, Phys. Rev. A **51**, 1520 (1995).

Stimulated Rayleigh wing scattering in soliton propagation

R. Barille, J.P Bourdin, and G. Rivoire

Laboratory of Optical Properties of Materials and Applications
University of Angers, 4, Bd Lavoisier, BP. 2018
49016 Angers Cedex
Tel : (33) 02-41-73-54-18, Fax : (33) 02-41-73-53-30
Email : barille@univ-angers.fr

The recent spectral observations of a light beam propagated in a waveguide filled with CS2 have shown than the phase modulation is not the only phenomenon explaining the spectral broadening[1]. The stimulated Rayleigh wing scattering (SRWS) has to be taken into account. This assumption has been permitted by the comparison with recent observations of SRWS in another guided propagation configuration due to Bessel beam excitation in bulk medium[2 - 3]. We show that in guided propagation the SRWS is mainly produced in cascade processes characterized by the presence of Stokes/anti-Stokes couplings. We analyse the intrication of these modulation and SRWS in the soliton propagation for different spatial sizes of the input beam.

In bulk medium the SRWS is produced with a Bessel beam [2]. The Bessel beam can be considered as a superposition of planes waves, the wave vectors of which form a cone. The interaction domain in the material is confined to a narrow and long line along the cone axis[4]. The configuration allows the separation of non linear effects. The results show at the threshold either a sharp Stokes line with frequency shift Ω = 2.5 cm^{-1} or 7 cm^{-1} or a double structure consisting of the two sharp Stokes lines. Above the SRWS threshold a large Stokes spectrum appears composed of several lines without anti-Stokes components.

The interpretation of these results is based on the role played by four photon processes coupling two exciting photons, one Stokes and one anti-Stokes scattered photons. The proccess is efficient near the wave vector matching condition, favourized by guided propagation. In the condition of Bessel beam experiments the Stokes line becomes exciting line for a new scattering four photon process.

In the case of a planar waveguide near the soliton threshold, a spatial soliton is obtained when the input power is : $Ps = \frac{2 n_o d}{n_2 y_{in} k^2}$ where d is the thickness of the waveguide and y_{in} the size of the input beam. The soliton intensity Is and the SRWS threshold I_T are of the same order in our experimental conditions. But contrary to Is, I_T is independent of the dimension y_{in}.

Thus the study of the influence of y_{in} on the output spectra will give informations on the role of SRWS in the soliton propagation.

The output spectra have been observed for different values of the input power P around the soliton power *Ps* in the case of a TM input beam (fig. 1).

Just above the soliton power (P/Ps ≈ 1.2 to 1.4) all the spectra are broadened. However, their shapes differ stongly according to the values of y_{in}.

- for small y_{in} (40 μm, 80 μm) - ie for large values of Is - a dip is observed at the laser wavelength. The intensity is maximum at the red end of the spectrum. Anti-Stokes wings are present.
- for small y_{in} (110 μm), anti-Stokes wings are absent. The intensity of the Stokes lines decrease from the laser wavelength to the red end of the spectrum. This spectral behaviour presents a good reproducibility.

These observations - together with those made at larger values of P - support the idea that the phase modulation process dominates in small size solitons, while the four photon SRWS process dominates in large size solitons. The choice of the spatial size of the soliton can thus help to control the role of SRWS in the soliton formation.

1. D. Wang, R. Barille, and G. Rivoire, JOSA B, 15(1), (1998), 181.
2. S.Sogomonian, R. Barille, and G. Rivoire, Opt. Comm., 157, 182, (1998).
3. R. Barille, S.Sogomonian, and G. Rivoire, (accepted for publications in JOSA B)
4. J.Durnin, J.J. Miceli, Jr., and J.H.Eberly Phys.Rev.Lett.58, (1987), 1499.

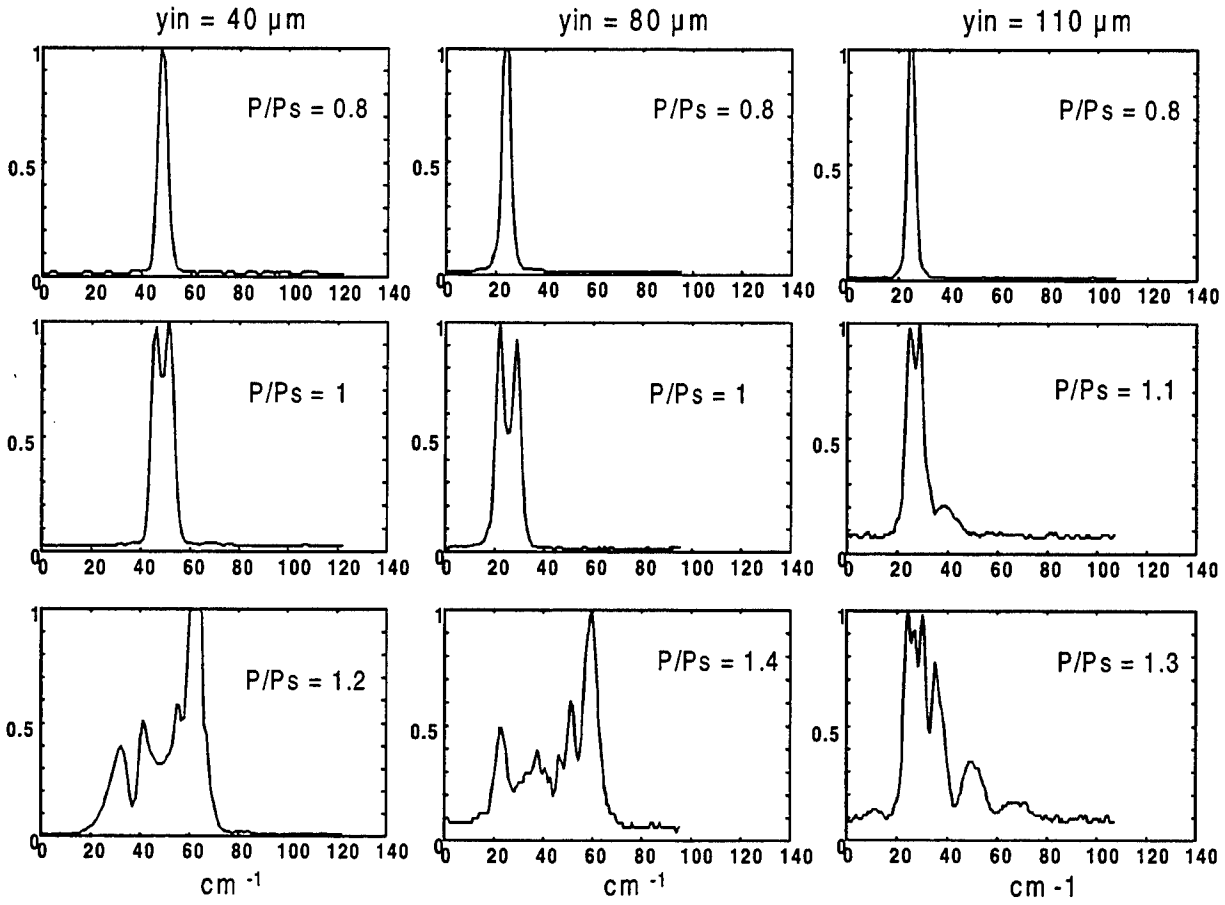


Fig. 1. Spectral broadening for different input beam size

Quasiperiodic quadratic solitons in Fibonacci QPM gratings

Yuri Kivshar

Optical Sciences Centre, Research School of Physical Sciences and Engineering, Australian National University, Canberra ACT 0200, Australia.
Tel.: (+61-2) 6249 3081; Fax: (+61-2) 6249 5184; email: ysk124@rsphysse.anu.edu.au

Ole Bang, Carl Balslev Clausen, and Peter L. Christiansen

Department of Mathematical Modelling, Technical University of Denmark, Anker Engelundsvej 1, DK-2800 Lyngby, Denmark
Tel.: (+45) 45 25 30 92; Fax: (+45) 45 93 12 35; E-mail: plc@imm.dtu.dk

Recently reported experimental results on multi-color harmonic generation in quasiperiodic superlattices [1,2] allow the possibility of simultaneous phase-matching of different frequencies. Those results also open a door to a novel class of problems involving the propagation and dynamics of spatial optical solitons supported by parametric wave mixing. In this paper we consider second-harmonic generation (SHG) and nonlinear beam propagation in *Fibbonacci optical superlattices*, and demonstrate numerically the possibility of spatial self-trapping of quasiperiodic waves whose envelope amplitude varies quasiperiodically, while still maintaining a stable, well-defined spatially localised structure, *a quasiperiodic envelope soliton.*

We consider the interaction of a fundamental wave (FW) with the frequency ω and its second harmonic (SH) in a layered slab waveguide with quadratic (or $\chi^{(2)}$) nonlinear response. Assuming the nonlinear susceptibility to be modulated and the nonlinearity to be of the same order as diffraction, we write the dynamical equations in a general form

$$\begin{aligned} i\frac{\partial w}{\partial z} + \frac{1}{2}\frac{\partial^2 w}{\partial x^2} + d(z)w^* v e^{-i\beta z} = 0, \\ i\frac{\partial v}{\partial z} + \frac{1}{4}\frac{\partial^2 v}{\partial x^2} + d(z)w^2 e^{i\beta z} = 0, \end{aligned} \tag{1}$$

where $w(x,z)$ and $v(x,z)$ are the slowly varying envelopes of the FW and its SH, respectively. The parameter $\beta = \Delta k|k_\omega|x_0^2$ is proportional to the phase mismatch $\Delta k = 2k_\omega - k_{2\omega}$, k_ω and $k_{2\omega}$ being the wave numbers at the two frequencies. The transverse coordinate x is measured in units of the input beam width x_0, and the propagation distance z, in units of the diffraction length $l_d = x_0^2|k_\omega|$. The spatial modulation of the nonlinear susceptibility $\chi^{(2)}$ is described by the quasi-phase-matching (QPM) grating function $d(z)$. In the context of SHG the QPM technique is known as an effective way to achieve phase matching, and it has been studied intensively (see Ref. [3] for a review).

Here, we consider a QPM grating produced by a quasiperiodic nonlinear optical superlattice. Quasiperiodic optical superlattices, one-dimensional analogs of quasicrystals [4], are usually designed to study the effect of Anderson localisation in the linear regime of light propagation. For QPM gratings, the nonlinear quasiperiodic superlattice of $LiTaO_3$, in which two antiparallel ferro-electric domains are arranged in a Fibbonacci sequence, was recently fabricated by Zhu *et al.* [1], who measured multi-colour SHG with energy conversion efficiency of $\sim 5\% - 20\%$. This quasiperiodic optical superlattice in $LiTaO_3$ can also be used for efficient direct third harmonic generation [2].

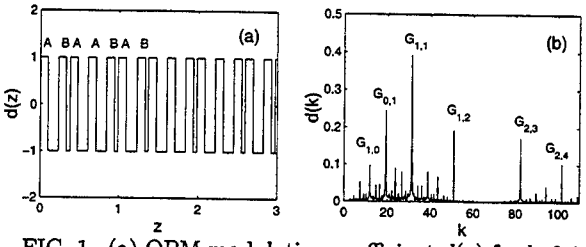


FIG. 1. (a) QPM modulation coefficient $d(z)$ for l=0.1 and η=0.34 with the building blocks A and B. (b) Numerically calculated Fourier spectrum of $d(z)$ with the analytically predicted position of the four largest peaks.

The quasiperiodic QPM gratings we consider have two building blocks A and B of the length l_A and l_B, respectively, which are ordered in a Fibonacci sequence, as shown in Fig. 1(a). Each block has a domain of length l_{A_1}=l (l_{B_1}=l) with d=+1 and a domain of length l_{A_2}=$l(1+\eta)$ (l_{B_2}=$l(1-\tau\eta)$) with d=-1. In the case of $\chi^{(2)}$ nonlinear QPM superlattices this corresponds to positive and negative ferro-electric domains, respectively. The specific details of this type of Fibbonacci optical superlattices can be found elsewhere (see, e.g., Ref. [1] and references therein). For our simulations presented below we have chosen η=$2(\tau-1)/(1+\tau^2)$=0.34, where τ=$(1+\sqrt{5})/2$ is the so-called *golden ratio.* This means that the ratio of length scales is also the golden ratio, l_A/l_B=τ. Furthermore, we have chosen l=0.1.

The modulation coefficient $d(z)$, which varies between +1 and −1 according to the Fibonacci sequence, can be expanded in a Fourier series

$$d(z) = \sum_{m,n} d_{m,n} e^{iG_{m,n}z}, \tag{2}$$

where the wavenumber components are

$$G_{m,n} = 2\pi D^{-1}(m + n\tau), \qquad (3)$$

and $D=\tau l_A + l_B=0.52$ for the chosen parameter values. Hence the Fourier spectrum is composed of sums and differences of the basic wavenumbers $k_1=2\pi/D$ and $k_2=2\pi\tau/D$. These components fill the whole Fourier space densely, since k_1 and k_2 are incommensurate. Figure 1 shows a part of the grating function $d(z)$ and its corresponding numerically calculated Fourier spectrum $G_{m,n}$. The lowest-order "Fibonacci modes" are clearly the most intense. From Eq. (3) and the numerically found spectrum we identify the six most intense modes presented in Table 1. The corresponding $G_{m,n}$ is in good agreement with Eq. (3).

m	1	0	1	2	1	2
n	1	1	2	3	0	4
$G_{m,n}$	31.42	19.42	50.83	82.25	12.00	101.66

TABLE 1. The numerically found six most intense Fibonacci modes $G_{m,n}$.

To analyse the beam propagation and SHG in a quasiperiodic QPM grating, one could apply the averaging theory developed for regular periodic QPM gratings [5]. This theory is applicable to the case of *rapidly varying* QPM structures, such as those designed and analysed in Ref. [1], where the domain length corresponds to $l < 0.01$. To lowest order this approach always yields a system of averaged equations with constant mean-value coefficients, which does not allow to describe oscillations of the beam amplitude and phase. However, here we wish to go beyond the averaged equations and consider the rapid large-amplitude variations of the envelope functions. This can be done analytically for periodic QPM gratings [5]. For the quasiperiodic gratings we consider here we have to resolve to numerical simulations.

Thus we have solved Eqs. (1) numerically with a second-order split-step routine, in which the linear part is solved with the fast-Fourier-transform (FFT) method and the nonlinear part, with a fourth-order Runge-Kutta scheme. The step-length is adapting to the local domain length of the QPM grating. At the input of the crystal we excite only the fundamental beam (corresponding to unseeded SHG) with a Gaussian profile,

$$w(x,0) = A_w\, e^{-x^2/10}, \quad v(x,0) = 0. \qquad (4)$$

As an example, we consider the quasiperiodic QPM grating with matching to the peak at $G_{2,3}$, i.e., $\beta=G_{2,3}=82.25$. First, we study the small-amplitude limit when a weak fundamental beam is injected with a low amplitude $A_w=0.25$. Figures 2(a,b) show contour plots of the evolution of the FW and its SH in this effectively linear regime. As is clearly seem from Fig. 2(b) the SH is excited, but both beams eventually diffract.

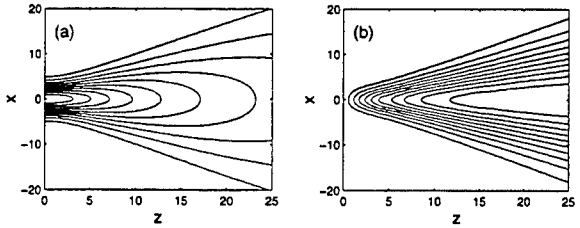


FIG. 2. (a) Diffraction of a weak FW beam with amplitude $A_w=0.25$ for $\beta = 82.25$. (b) Corresponding SH component.

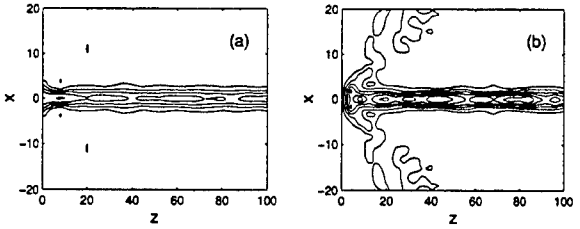


FIG. 3. Excitation of quasiperiodic soliton by a FW beam with amplitude $A_w=5$ for $\beta=82.25$. (a) FW component, (b) SH component.

When the amplitude of the input beam exceeds a certain threshold, self-focusing should be observed for both the FW and its SH. Figures 3(a,b) show an example of the evolution of a strong input FW beam with the amplitude $A_w=5$, and its corresponding SH. Again the SH component is generated, but now the nonlinearity is so strong that it leads to self-focusing and mutual self-trapping of the two fields, resulting in a spatially localized two-component solitary wave, despite the continuous scattering of the quasiperiodic QPM grating.

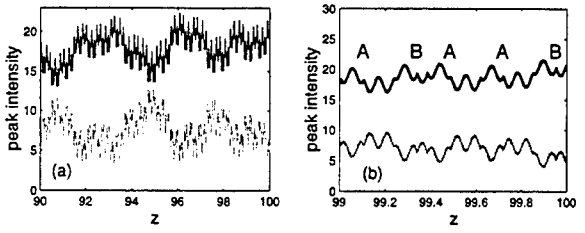


FIG. 4. Amplitude oscillations of the quasiperiodic soliton excited in Fig. 3. (a),(b) Close-ups of the peak intensity $|w(z,0)|^2$ of the FW (black) and $|v(0,z)|^2$ of the SH (grey). The Fibonacci building blocks A and B are indicated in (b) with d=1 in grey regions, and d=-1 in white regions.

It is important to notice that the formed two-component self-trapped beam is quasiperiodic itself. After an initial transient its amplitude oscillates in phase with the quasiperiodic QPM modulation $d(z)$. This is illustrated in Fig. 4, where we show in more detail the peak intensities of both the components in an asymptotic regime of the evolution.

Since the oscillations shown in Fig. 4 are in phase with the oscillations of $d(z)$, their spectra should be similar.

This is confirmed by Fig. 5, which gives the spectrum of the peak intensity $|w(z,0)|^2$ of the FW. Superimposed on this spectrum is the positions of Fibonacci peaks $G_{m,n}$ of $d(z)$. Note that the Fibonacci peak at k=82.25 is suppressed (or reduced) because the identical mismatch β down-converts it to the dc-component. Sum and difference wavenumbers between β and $G_{m,n}$ appear, which are generated by the nonlinearity. For example, the component at k=62.8 is the difference between β=82.25 and $G_{0,1}$=19.42.

Our numerical results show that such quasiperiodic solitons can be generated for a broad range of the phase-mismatch β. The amplitude and width of the solitons depend on the effective mismatch, which is the separation between β and the nearest strong peak $G_{m,n}$ in the Fibbonacci QPM grating spectrum. Thus, low-amplitude broad solitons are excited for β-values in between peaks, whereas high-amplitude narrow solitons are excited when β is close to a strong peak, as shown in Fig. 3.

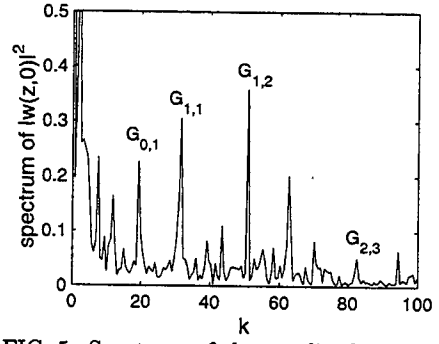


FIG. 5. Spectrum of the amplitude oscillations of the FW component of the quasiperiodic soliton, calculated from z=90 to 100 in Fig. 4(a). The peaks correspond to the Fibonacci peaks $G_{m,n}$ in $d(z)$ and sum and difference thereof with the mismatch β=82.25.

The existence of spatially localized self-trapped states in nonlinear quasiperiodic media should not depend on the particular kind of nonlinearity. The dependence on β observed here for the $\chi^{(2)}$ gratings is simply due to the fact that the "real" strength of the quadratic nonlinearity is inversely proportional to the phase-mismatch. In fact, it is well-known that for large values of the mismatch parameter β the quadratic nonlinearity becomes effectively cubic [6]. Thus, our findings are directly applicable to nonlinear optical superlattices in cubic (or $\chi^{(3)}$) nonlinear media.

To analyse in more detail the transition between the linear (diffraction) and nonlinear (self-trapping) regimes, we show in Fig. 6 the dependence of the beam amplitude at the output of a crystal of length L=100, on the amplitude of the FW input beam. This dependence clearly illustrates how the generation of a localized state depends on the strength of the nonlinearity, i.e. a quasiperiodic soliton is generated only for sufficiently high amplitudes.

This is of course a general phenomenon also observed in many nonlinear isotropic media. However, here the self-trapping occurs for quasiperiodic waves, and it is preserved in the quasiperiodic variations of the amplitude of both components.

Numerical simulations for other cases reveal the basic properties of the quasiperiodic self-trapping: Spatial solitons are formed in Fibonacci quadratic nonlinear slab waveguides above a certain power threshold, and such solitons are always *quasiperiodic*, i.e. they exhibit large-amplitude oscillations along z, which are composed of mixing of the two incommensurate Fibonacci wavenumbers. The amplitude and width of these solitons depend on the difference between the phase-mismatch parameter β and the nearest peak $G_{m,n}$ in the Fibonacci spectrum. When the domain length is sufficiently small, the effect of the amplitude oscillations become small, and the dynamics can be described by averaged equations similar to those derived for periodic QPM gratings [5].

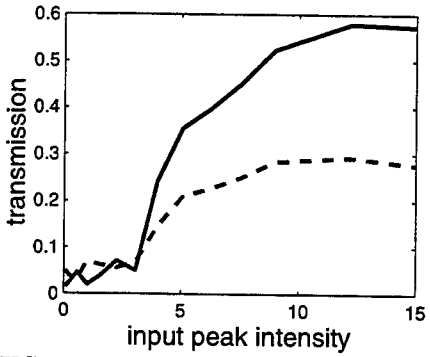


FIG. 6. Transmission $|w(L,0)/w(0,0)|^2$ of the FW (solid) and $|v(L,0)/w(0,0)|^2$ of the SH (dashed) vs. the input intensity $|w(0,0)|^2$ of the FW. Crystal length: L=100. Phase-mismatch: β=82.25.

The authors acknowledge support from the Danish Technical Research Council (Talent Grant no. 9800400), the Danish Natural Science Research Council (Grant no. 9600852), the Australian Photonics Cooperative Research Centre.

[1] S. Zhu, Y. Zhu, Y. Qin, H. Wang, C. Ge, and N. Ming, Phys. Rev. Lett. **78**, 26752 (1997).
[2] S. Zhu, Y. Zhu, and N. Ming, Science **278**, 843 (1997).
[3] M.M. Fejer, G.A. Magel, D.H. Jundt, and R.L. Byer, IEEE J. Quantum Electron. **28**, 2631 (1992).
[4] D. Schechtman, I. Blech, D. Gratias, and J.W. Cahn, Phys. Rev. Lett. **53**, 1951 (1984).
[5] C. Balslev Clausen, O. Bang, and Yu.S. Kivshar, Phys. Rev. Lett. **78**, 4749 (1997).
[6] See, e.g., Yu.S. Kivshar, In: *Adavanced Photonics with Second-order Optically Nonlinear Processes*, Eds. A.D. Boardman *et al.* (Kluwer, Amsterdam, 1999), p. 451.

A unified approach to self-trapped partially coherent beams in logarithmically nonlinear media

Wiesław Królikowski[1], Darran Edmundson[2], and Ole Bang[3]

[1] *Australian Photonics Cooperative Research Centre, Laser Physics Centre, Research School of Physical Science and Engineering, The Australian National University, Canberra ACT 0200, Australia*

[2] *Australian Photonics Cooperative Research Centre, Optical Science Centre, Research School of Physical Science and Engineering, The Australian National University, Canberra ACT 0200, Australia*

[3] *Department of Mathematical Modelling, Technical University of Denmark, Building 305/321, DK-2800 Lyngby, Denmark*

The subject of incoherent (or partially coherent) spatial solitons has attracted lots of attention recently [1–12]. The light beam generated by the incoherent light source exhibits some level of randomness of phase between any two points. Additionally, its intensity has a speckle structure which prevents the "standard" uniform self-focusing observed in instantenous nonlinear media as the beam tends to form filaments. It turns out, however, that self-focusing and soliton formation are still possible provided the nonlinear medium is inertial and responds much slower than the time scale characterizing the random phase variation.

Typically few different approaches are used in the description of partially coherent beams in a slow nonlinear medium. The coherent density method is based on representation of the beam as a superposition of mutually incoherent components [3,4]. In case of stationary soliton propagation solution can be found using a multimode decomposition of the field [9,8]. Finally, in the diffractionless limit, the geometric optics approach can be also used [11,12].

However, the most natural way of treating the partially coherent beam is to use the mutual coherence function [13]. Here we show that the evolution equation for the coherence function in a logarithmically nonlinear medium has an exact analytical solution for partially coherent beams. We find conditions for the formation of stationary solitons and show that they are only a special case of a much larger class of periodic solitons.

The properties of the partially coherent beam with the amplitude $\psi(\vec{r})$ are described by the mutual coherence function $\Gamma(\vec{r}_1,\vec{r}_2)$ defined as:

$$\Gamma(\vec{r}_1,\vec{r}_2)=\langle\psi(\vec{r}_1)\psi^*(\vec{r}_2)\rangle \tag{1}$$

where $\vec{r}=(x,y)$ and brackets denote temporal or ensemble averaging. In particular, the time averaged intensity is obtained as $I(\vec{r})=\Gamma(\vec{r},\vec{r})$. We take the refractive index change δn to be a logarithmic function of the average intensity $\delta n(I)=n_2\ln I$.

It can be shown that $\Gamma(\vec{r}_1,\vec{r}_2)$ satisfies the following differential equation (see also [12,14,15])

$$i\frac{\partial\Gamma_{12}}{\partial z}+\nabla_{\vec{R}}\cdot\nabla_{\vec{p}}\Gamma_{12}+n_2\ln\left(\frac{\Gamma_{11}}{\Gamma_{22}}\right)\Gamma_{12}=0. \tag{2}$$

where $\vec{R}=(\vec{r}_1+\vec{r}_2)/2$, $\vec{p}=\vec{r}_1-\vec{r}_2$ and Γ_{ij}=$\Gamma(\vec{r}_i,\vec{r}_j)$, i,j=(1,2).

We assume that the incident beam possesses Gaussian statistics

$$\Gamma(\vec{r}_1,\vec{r}_2,z=0)=\exp\left(-\frac{r_1^2+r_2^2}{2\rho_0^2}-\frac{|\vec{r}_1-\vec{r}_2|^2}{r_c^2}\right), \tag{3}$$

where ρ_0 and r_c denote the initial diameter and coherence radius of the beam, respectively.

We will look for solutions to Eq. (2) using the Gaussian anzatz

$$\Gamma(\vec{R},\vec{p},z)=$$
$$A(z)\exp\left(-\frac{R^2}{\rho^2(z)}-\frac{p^2}{\sigma^2(z)}+i\vec{R}\cdot\vec{p}\mu(z)\right), \tag{4}$$

where $A(z)$ and $\mu(z)$ represent the amplitude and phase variation of the coherence function, and $\rho(z)$ and $\sigma(z)$ its diameter and coherence radius, respectively. Inserting Eq.(4) into Eq. (2) we obtain the equation describing the dynamics of the width $\rho(z)$ of a partially coherent beam (with Gaussian statistics) in a logarithmic nonlinear medium

$$\frac{d^2\rho}{dz^2}-\frac{4}{\rho^3}\frac{\rho_0^2}{\sigma_0^2}+\frac{2n_2}{\rho}=0, \tag{5}$$

where the effective coherence radius $1/\sigma_0^2=1/r_c^2+1/(4\rho_0^2)$. Clearly, the dynamics is determined by a competition between free spreading and nonlinearity. Choosing the initial condition such that $(d\rho/dz)(z=0)$=0, and integrating Eq. (5) once, we find that the evolution of $\rho(z)$ is described by Newton's equation for an effective particle,

$$(d\rho/dz)^2+P(\rho)=0, \tag{6}$$

moving in the potential $P(\rho)$, which is given by

$$P(\rho)=\frac{4}{\sigma_0^2}\left(\frac{\rho_0^2}{\rho^2}-1\right)+4n_2\ln\left(\frac{\rho}{\rho_0}\right). \tag{7}$$

This asymmetric potential is depicted in Fig. 1.

Stationary soliton solutions with constant beam width (corresponding to the effective particle being located at the bottom of the potential well) are formed at zero detuning

$$\Delta\equiv n_2-\frac{2}{\sigma_0^2}=n_2-\frac{2}{r_c^2}-\frac{1}{2\rho_0^2}=0. \tag{8}$$

Physically, this condition means that soliton existence requires the nonlinearity-induced focusing to compensate for beam spreading due to both diffraction and incoherence. The diameter of the stationary partially coherent soliton is given by $\rho_0^2 = (2n_2 - 4/r_c^2)^{-1}$. For perfectly coherent beams, i.e. for r_c=∞, we recover the known solution for coherent solitons in logarithmically nonlinear media [16,17]. On the other hand, it is also clear that a soliton cannot exist if the coherence radius of the input beam is lower than $\sqrt{2/n_2}$. This reproduces the earlier results obtained by using both a coherent density approach [4] and modal decomposition [9] - and it indicates that all of these theoretical descriptions of the beam are equivalent.

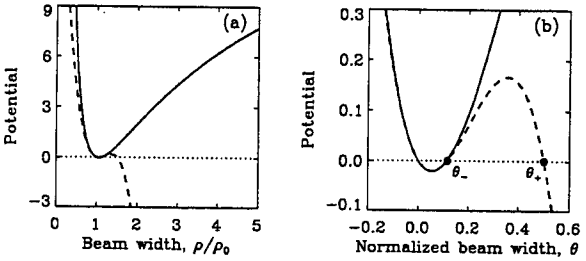


FIG. 1. (a) Potential $P(\rho)$ (solid) and its third order Taylor expansion $P_3(\rho)$ (dashed) for an initial coherence radius of σ_0=1 and a focusing logarithmic nonlinear medium with n_2=1.8. (b) Zoom $P(\theta)$ and $P_3(\theta)$ near the bottom of the potential, with θ=ρ/ρ_0 1.

For nonzero detuning, $\Delta \neq 0$, the beam diameter (as well as the coherence radius) will undergo periodic oscillations [12], corresponding to the effective particle oscillating in the bottom of the potential well. We can find an approximate analytical expression for these oscillating solutions when the detuning is small. In this case $\rho(z)$ will remain close to the initial value ρ_0 and can be expressed in terms of the Jacobi elliptic sn-function [18].

$$\rho(z) = \rho_0[1 + \theta_- \mathrm{sn}^2(\frac{\sqrt{\theta_+ \alpha_2}}{\rho_0} z; m)], \quad m = \frac{\theta_-}{\theta_+}. \qquad (9)$$

Here $\alpha_2 = n_2/3 - 4/\sigma_0^2$ while $\theta_- \approx -\Delta/n_2$ and $\theta_+ \approx 3/5$. Thus the beam width will oscillate between ρ_0 and another value, where the potential is negative. For positive detuning the nonlinear self-focusing dominates and the beam width decreases initially, i.e. it oscillates between ρ_0 and a somewhat lower value. For negative detuning the diffraction dominates and the beam width increases initially, i.e. it oscillates between ρ_0 and a somewhat larger value.

The analysis presented above can easily be extended to the case of elliptical beams. If ρ_{x0} and ρ_{y0} are the initial beam diameters along the x- and y-axes, respectively, and r_{cx}, r_{cy} are the corresponding initial coherence radii then, the dynamics of the beam radii can be described by the following equations:

$$\frac{d^2\rho_x}{dz^2} - \frac{4}{\rho_x^3}\frac{\rho_{x0}^2}{\sigma_{x0}^2} + \frac{2n_2}{\rho_x} = 0$$
$$\frac{d^2\rho_y}{dz^2} - \frac{4}{\rho_y^3}\frac{\rho_{y0}}{\sigma_{y0}^2} + \frac{2n_2}{\rho_y} = 0, \qquad (10)$$

where

$$\frac{1}{\sigma_{x0}^2} = \frac{1}{r_{cx}^2} + \frac{1}{4\rho_{x0}^2}, \quad \frac{1}{\sigma_{y0}^2} = \frac{1}{r_{cy}^2} + \frac{1}{4\rho_{y0}^2}. \qquad (11)$$

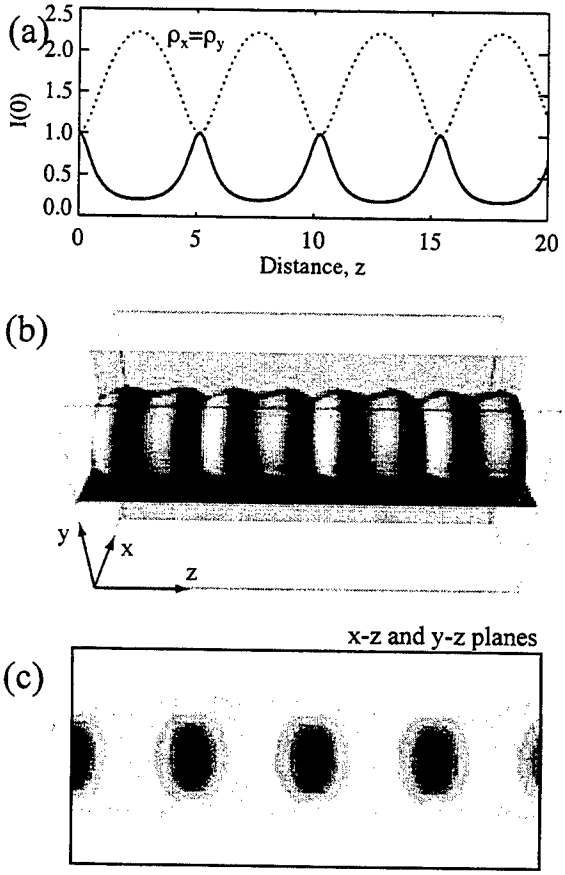


FIG. 2. Nonstationary propagation of a cylindrical partially coherent beam in a logarithmic nonlinear medium. (a) beam diameter (dotted) and peak intensity (solid) as a function of the propagation distance; (b) 3-dimensional view of the beam with an intensity isosurface at 10% of the peak value; (c) longitudinal crossection of the beam.

It is evident from Eqs. (10) that the dynamics along both principal axes are completely uncoupled. In general, a partially coherent Gaussian beam of elliptical shape propagating in a logarithmic nonlinear medium will experience periodic oscillations along both axes. Further, an elliptically shaped stationary soliton can be formed if the coherence parameters of the beam and its diameters are given by the following relations:

$$\rho_{x0}^{-2} = 2n_2 - 4/r_{cx}^2 \quad \rho_{y0}^{-2} = 2n_2 - 4/r_{cy}^2 \qquad (12)$$

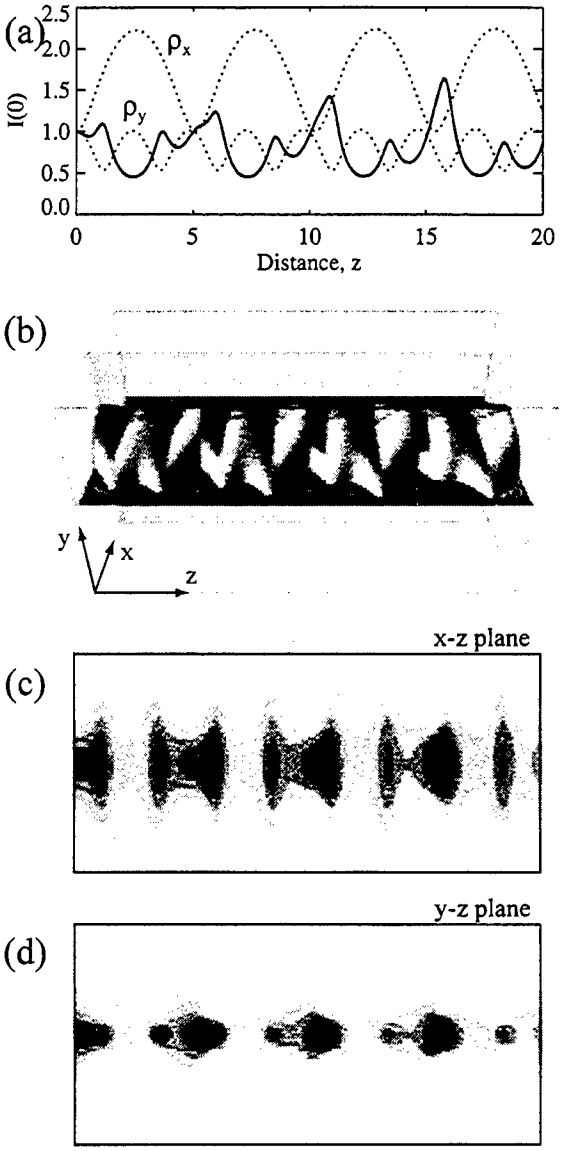


FIG. 3. Nonstationary propagation of an elliptical partially coherent beam in a logarithmic nonlinear medium. (a) beam radii (dotted) and peak intensity (solid) as a function of propagation distance; (b) 3-dimensional view of the beam; (c-d) longitudinal crossections of the beam.

In Fig. 2 and Fig. 3 we show the nonstationary propagation of two partially coherent beams. In Fig. 2, the initial parameters are chosen such that $\rho_{x0} = \rho_{y0} = 1.0$, $r_{cx} = r_{cy} = 1.15$, and $n_2 = 1$. In the top graph we plot the beam radii (dotted lines) as well as the peak intensity of the beam (solid line) as functions of the propagation distance. To emphasize the 3-dimensional nature of the beam, Fig. 2(b) shows an isosurface of the beam intensity (thresholded at 10% of the peak value) along with two orthogonal cut planes whose intensity is displayed in Fig. 2(c). In this particular case, the circularly symmetric beam exhibits periodic contractions and expansions during propagation.

Fig. 3 shows the nonstationary propagation of an elliptical partially coherent beam. The initial conditions are the same as in Fig. 2 with the exception of the y-axis coherence whose value is changed to $r_{cy} = 2.3$. Here the principal beam radii oscillate with incommensurate periods and the peak intensity exhibits quasi-periodic oscillations. The complexity of the overall intensity distribution is shown in Figs. 3 (b)-(d) where now the two orthogonal cut planes display differing intensity patterns.

In conclusion, we have presented a rigorous analysis of the propagation of partially coherent beams with Gaussian statistics in a logarithmically nonlinear medium. Our approach is based on the evolution of the mutual coherence function and captures simultaneously the dynamics of the beam diameter as well as its coherence properties.

[1] M. Mitchell *et al.*, Phys. Rev. Lett. **77**, 490 (1996).
[2] M. Mitchell and M. Segev, Nature **387**, 880 (1997).
[3] D.N. Christodoulides *et al.*, Phys. Rev. Lett. **78**, 646 (1997).
[4] D.N. Christodoulides, T.H. Coskun, and R.I. Joseph, Opt. Lett. **22**, 1080 (1997).
[5] M. Mitchell, *et al.*, Phys. Rev. Lett. **79**, 4990 (1997).
[6] M. Mitchell, M. Segev, and D.N. Christodoulides, Phys. Rev. Lett. **80**, 4657 (1998).
[7] V.A. Vysloukh *et al.*, Sov. J. Quantum Electron. **27**, 843 (1997).
[8] N.Akhmediev, W.Królikowski, A.Snyder, Phys. Rev. Lett. **80**, (1998).
[9] D.N. Christodoulides, *et al.*, Phys. Rev. Lett. **80**, 2310 (1998).
[10] M.I. Carvalho, *et al.*, Phys. Rev. E **59** 1193, (1999).
[11] A.W. Snyder, D.J. Mitchell, Phys. Rev. Lett. **80**, 1422 (1998).
[12] V.V. Shkunov, and D.Z. Anderson, Phys. Rev. Lett. **81**, 2683 (1998).
[13] L. Mandel and E.Wolf *Optical coherence and quantum optics*, (Cambridge University Press, Cambridge, 1995).
[14] G.A. Pasmanik, Sov. Phys. JETP **39**, 243 (1974).
[15] V.A. Aleshkevich, S.S. Lebedev, and A.N. Matveev, Sov. J. Quantum Electron. **11**, 647 (1981).
[16] I. Bialynicki-Birula and J. Mycielski, Phys. Scripta **20**, 539 (1979).
[17] A. Snyder and J. Mitchell, Opt. Lett. **22**, 16 (1997).
[18] M. Abramowitz, and I.A. Stegun, *Handbook of mathematical functions*, (Dover, New York, 1970)

Theoretical Demonstration of Beam Scanning Using Time-Dependent Solitary Wave Interactions in a $Bi_{12}TiO_3$ Photorefractive Crystal

A.D.Boardman and P.Bontemps
Photonics and Nonlinear Science Group
Physics Department
University of Salford
Salford M54WT
United-Kingdom

Introduction

In the past few years, spatial optical solitons at low (μW) power levels have been observed in photorefractive crystals [1]. Spatial solitons are light beams in nonlinear optical materials for which any possibility of diffraction has been eliminated by material nonlinearity. In the case of photorefractive crystals, the nonlinearity is due to a reversible variation of the refractive index induced by the spatial variation of the optical intensity. Originally, this effect was interpreted as an 'optical damage' of the crystal, provoked by the beam.
This mechanism, compared to other nonlinear effects such as Kerr nonlinearity, is very slow. This is often seen as a major drawback of this effect, although ways to compensate the slow response time by increasing the beam power have been proposed. As shown in this paper, slow soliton formation or, more precisely, the solitary wave formation, can be used in a constructive manner to develop a time-dependent scanning device. Finally, another important property of photorefractive solitary waves is their stability in bulk crystal, (2D+1) configurations. This property, common to all non-Kerr solitary waves such as quadratic $\chi^{(2)}$ nonlinearity, promises an exciting extension to higher-dimensions beyond the work presented here.

Mathematical development

Unlike many numerical/theoretical publications in this field where the beam is assumed to evolve in a steady-state configuration, the approach taken here includes the time dependence in the wave equation. Using the -Kukhutarev-Vinetskii model- in the case of an electromagnetic wave propagating along z and diffracting only along the ferroelectric c axis, denoted x, it is possible to derive an expression for the time dependent space charge field E [2]. Assuming that the time dependent process of charge generation and recombinaison evolves on a time scale negligible to the current distribution time scale [3], the space charge field E is given by [2,4]

$$E = E_0 \exp\left(-\frac{e\mu}{\varepsilon_0\varepsilon_r}\frac{n_0}{I_0}It\right) + \left[1-\exp\left(-\frac{e\mu}{\varepsilon_0\varepsilon_r}\frac{n_0}{I_0}It\right)\right]\left[\left(E_{ext}+E_{ph}\right)\frac{I_d}{I} - \frac{\kappa_B}{Ie}T\frac{\partial I}{\partial x}\right] \qquad (1)$$

where E is the electric field applied to the crystal and E_0 is the initial (time=0) field
E_{ph} and E_{ext} are, respectively, the photovoltaic and external applied fields.
I is the intensity of the beam and I_d the dark irradiance.
e is the charge of the electron
ε_0 and ε_r are, respectively, the electric permittivity of vacuum and the dielectric tensor
μ and κ_b are, respectively, the electric mobility and the Boltzman constant
T and t are, respectively, the temperature and the time

On the other hand, the evolution of the optical beam U(x,z,t) can be obtained using Maxwell's equations and assuming that U(x,z,t) is a slowly varying function, a nonlinear Schrodinger type equation is found where the nonlinear coefficient is directly proportional to the refractive index change caused by the beam.

This is the well-known Pockels effect. Using (1) and renormalising the optical field amplitude $U(x,z,t) \rightarrow \frac{U(x,z,t)}{\sqrt{I_d}}$, the time-dependent refractive index change in the case of an incoherent interaction between two optical beams V(x,z,t) and W(x,z,t) is

$$(\Delta n)_V = -\frac{1}{2} n^3 r_{eff} E = \left[1 - \frac{1}{N^2} - \exp\left(-\frac{I_d\left(1+\gamma\left(|V|^2+|W|^2\right)\right)}{\Sigma} t\right)\right] \frac{N^2}{\gamma} \frac{1}{1+\gamma\left(|V|^2+|W|^2\right)} + \frac{|V|^2}{1+\gamma\left(|V|^2+|W|^2\right)} - \frac{N^2}{\gamma} \exp\left(-\frac{I_d\left(1+\gamma\left(|V|^2+|W|^2\right)\right)}{\Sigma} t\right) \quad (2)$$

where $(\Delta n)_V$ should be understood as the refractive index change caused by the optical beam V(x,z,t). Similar expression $(\Delta n)_W$ is found for the second beam involved in the interaction, W(x,z,t).

Note that the other variables appearing in equation (2) are

n and r_{eff} respectively the refractive index and electro-optic coefficient of the crystal,

$N^2 = \frac{k^2 n^2 r_{eff} x_0^2 \left(E_{ext} + E_{ph}\right)}{2}$; $D = \frac{k^2 n^2 r_{eff} x_0 \kappa_B T}{2e}$: the diffusion coefficient

$\Sigma = \frac{\varepsilon_0 \varepsilon_r I_0}{e\mu n_0}$ and γ, the saturation parameter

Numerical experiments

As seen from (2), the response time of the photorefractive materials clearly depends on the intensity of the optical beam. This property can be used in an interesting way to design time-dependent switches as illustrated in this publication. Let imagine the idealised configuration represented on figure 1 where two beams carrying different input powers are launched in a $Bi_{12}TiO_{20}$ photorefractive crystal.

This is a stable configuration because beams with rather different intensities are always simultaneously allowed in a photorefractive medium because it, in essence, behaves as a saturable medium. In other terms, the system is bistable and the low and high intensity beams used in figure 1 are *steady-state* (t=∞) solitary waves belonging respectively to the low and high branches of the bistability diagram. It is clear that for each configuration, i.e. value of the saturation parameter γ, a new set of two localised solutions must be found.

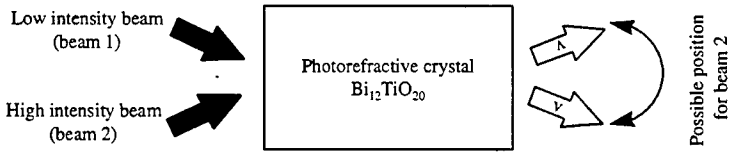


Figure 1. Schematic represention of the time-dependent switch

The evolution of the beam interaction with time can be easily qualitatively understood. During the first few seconds, both beams evolve linearly. After a short while, the higher beam reaches its steady state whereas the lower beam is still linear; here no interaction occurs. When the lower beam reaches its steady state, interference occurs and the beams, in this particular configuration, repel.

These predictions can be verified in figure 2 where a numerical simulation of the time dependent interaction is represented. The data used in figure 2 are as follows : $Bi_{12}TiO_{20}$ photorefractive crystal, n=2.25, N=1, γ=0.4 and the diffusion coefficient D is neglected in agreement with [2].

The wavelength is λ=850nm and an initial separation of 90μm is chosen. The initial velocity of the beams is 0.3, a larger value would make the beams cross each other in the steady state regime. The use of the device as a time-dependent switch is illustrated on figure 3 where the output position of the 'stronger' beam (i.e. beam 2 on figure 1) is seen to be strongly dependent on time.

It is interesting to note that the lowest beam has a peak power to dark irradiance ratio r (i.e. normalised amplitude) of 1.78 and therefore the time to reach its steady state is $2T_e$ where $T_e = \frac{\Sigma}{Id} \approx 10s$ for $Bi_{12}TiO_{20}$ [2]. Similarly, the high intensity beam has a response time of less than a second (r=18.5). Such response times are obviously too long for applications such as optical switching but are typical for photorefractive crystals and the design can be used for scanning purposes. Faster response times (μs-ns) can be obtained, as it will be illustrated in the presentation. These numerical results can be confirm by means of an adiabatic perturbation approach where, using a beam splitting method, the perturbation term for the beam V, for example, is found to be

$$P_V = \left[(\Delta n)_W + \left(\frac{1+|W|^2}{1+\gamma|W|^2} \right) \right] W \qquad (3)$$

Figure 4 shows the comparison between the beam trajectories found analytically (line) and numerically (circles) for three different times (t=0, 7 and 50s).

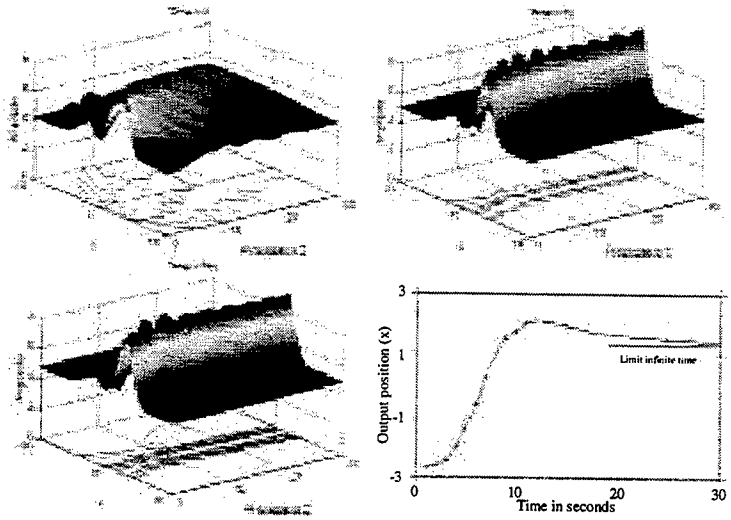


Figure 2. Snapshots of the interaction at different times. Scale: x=20mm, z=9mm. **Figure 3.** Output position (x=30) of the high intensity beam versus time.

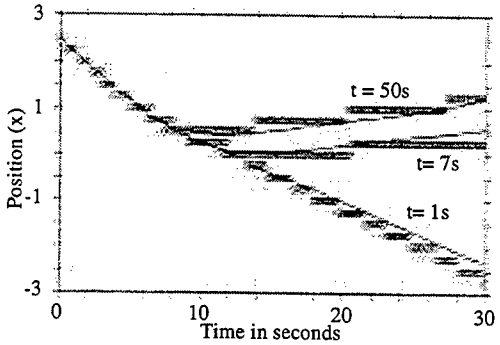


Figure 4. Beam trajectories found analytically (line) and numerically (circles) at different times t.

Conclusion

In this publication, the operation of a time-dependent switch or scanning device, based on the dependence of the crystal response time to the intensity of the optical beams has been shown numerically. An analytical approach based on the adiabatic perturbation method confirms the numerical predictions. Results for a large range of possible devices in (1D+1) will be given as well as preliminary results for the higher dimensions (2D+1) where exciting possibilities are expected.

References

1. G.C.Duree, J.L.Shultz, G.J.Salamo, M.Segev, A.Yariv, B.Crosignani, P.D.Porto, E.J.Sharp and R.R.Neurgaonkar, "Observation of self-trapping of an optical beam due to the photorefractive effect", Phys. Rev. Lett. **71**, 533, 1993.
2. N.Fressengeas, J.Maufoy and G.Kugel, "Temporal behavior of bidimensional photorefractive bright spatial solitons", Phys. Rev. E **54**, 6866, 1996
3. P.Yeh, "Introduction to Photorefractive Nonlinear Optics", Wiley, New-York 1993.
4. A.A.Zozulya and D.Z.Anderson, "Nonstationary self-focusing in photorefractive media", Opt. Lett. **20**, 837, 1995.

Collapse dynamics of multidimensional coupled waves

Luc Bergé

Commissariat à l'Energie Atomique, CEA/Bruyères-le-Châtel, B.P. 12, 91680 Bruyères-le-Châtel, France.

Tel : (+33) 1. 69.26.73.76. Fax : (+33) 1. 69.26.71.06. e-mail : berge@bruyeres.cea.fr

Summary

For a focusing Kerr medium, the process of light self-trapping is basically described by a (1+1)-dimensional nonlinear Schrödinger equation (NLS), whose solutions relax to robust sech-shaped solitons when optical beams only undergo anomalous group-velocity dispersion (GVD). Recent developments based on this model rapidly increased due to the possibility of making two wave components couple nonlinearly and propagate as mutually-trapped solitons.[1–3] However, these solitons were only recently detected in experiments,[2] partly because of the difficulty in overcoming parametric four-wave mixing (FWM) processes which become relevant when the two orthogonal polarizations are not incoherently coupled. Besides FWM, the components moreover undergo linear convection, often termed as "walk-off", which can be either attached to the half-difference of their group velocity in birefringent media,[3] or connected with the angle between the transverse and carrier wave vectors in, e.g., biased photorefractive crystals.[4] In this scope, only one-dimensional dispersion was considered, whereas multi-dimensionality of the model, including diffraction in the transverse plane, can strongly affect the propagation of coupled waves. It is indeed well-known that NLS solutions can spread out or self-focus until collapse when transverse diffraction is no longer disregarded, which leads to deal with (D+1)-dimensional NLS equations with a number of spatio-temporal dimensions, D, at least equal to two.[5] Even if the collapse singularity is ultimately arrested by saturation mechanisms, the dynamics preceding it is important and justifies to study the self-focusing of nonlinear waves when FWM and walk-off cannot be ignored. Therefore, in this contribution, we first review the interaction regimes characterizing two incoherently-coupled NLS waves, which can be classified into four distinct categories. Then, the influence of FWM and walk-off is investigated, with emphasis on their potential modifications of the power threshold for collapse when D=2. By means of analytical estimates and numerical verifications, we indeed show that FWM can contribute to self-focusing by lowering this threshold, whereas walk-off acts against the collapse.

We consider the slowly-varying envelopes $u_1(\vec{r}, z)$ and $u_2(\vec{r}, z)$ of two waves copropagating along the z-axis of a Kerr medium. Here $\vec{r}$ refers to the vector of a generalized D-dimensional transverse diffraction plane, which can also

include a retarded time variable when anomalous GVD is retained. The waves are assumed to undergo walk-off and FWM and their interaction is described by the generic model[2-4,6]

$$i(\partial_z + \vec{\delta}_n \cdot \vec{\nabla}_\perp)u_n - \beta_n u_n + \vec{\nabla}_\perp^2 u_n + (|u_n|^2 + A|u_{3-n}|^2)u_n + Bu_{3-n}^2 u_n^* = 0, \quad n = 1, 2, \tag{1}$$

where $*$ means complex conjugate, $\vec{\delta}_1 = -\vec{\delta}_2 = \vec{\delta}$ and $\beta_1 = -\beta_2 = \beta$. In Eq.(1), standard notations have been used. In particular, the second term describes walk-off effects, such as linear spatial convection or a group-velocity difference due to GVD. The third term accounts for the mismatch in wave numbers between both components and the last term represents the contribution of FWM. The constants A and B are positive and they measure the strength of the nonlinear coupling between the two waves. Their values are determined by the symmetry of the medium and by the interaction geometry. In isotropic media, they satisfy $A + B$=1 when u_1 and u_2 represent two orthogonal polarizations of a vector field (as, e.g., A=2B=2/3 in birefringent fibers[3]), while they are linked by A=2B=2 for two copropagating beams with scalar amplitudes u_1 and u_2. For Eq.(1) the total power $P = P_1 + P_2 = \int (|u_1|^2 + |u_2|^2) d\vec{r}$ is always conserved, and it keeps invariant each individual power $P_n \equiv \int |u_n|^2 d\vec{r}$ when $B = 0$ only. Equations (1) also conserve the Hamiltonian integral related to the complete system. Furthermore, we can derive a virial identity describing the evolution of the total mean square radius of both waves along z. This relation governs the second-order z-derivative of the integral $\mathcal{I}(z) \equiv \frac{1}{P} \int |\vec{r} - \langle \vec{r} \rangle|^2 \sum_{n=1}^{2} |u_n|^2 d\vec{r}$, which involves the total center of mass $\langle \vec{r} \rangle \equiv P^{-1} \int \vec{r} \sum_{n=1}^{2} |u_n|^2 d\vec{r}$. After employing a straightforward procedure,[7] the virial identity yields the main properties in the wave dynamics: it allows us to predict either the full diffraction, or the total self-focusing (collapse) of both waves, in the basic configuration for which there is neither walk-off ($\delta_n = 0$) nor FWM ($B = 0$). For Gaussian beams being well-separated initially, such waves are shown to undergo different evolutions by mutual coupling. Following their incident power and mutual separation, they can indeed disperse independently of each other, or fuse and disperse as a whole entity. At high power levels, they can alternatively fuse into a single collapsing structure, or self-focus individually if the power in each component exceeds the collapse threshold of isolated Gaussians.

Next, we identify the roles of FWM ($B \neq 0$) and walk-off ($\delta_n \neq 0$), separately.

For FWM alone ($\delta_n = 0$), virial arguments determine a critical power for collapse in the form $P > 2P_c/(1+A+B)$, where $P_c \simeq 11.7$ denotes the critical power for self-focusing of one NLS wave.[5] Confronted with direct numerical simulations, this condition is shown to apply with a reasonably-good agreement to Gaussian beams with equal powers and small mismatch parameter β. Thus, in the limit $\beta \to 0$, the FMW terms lower the power threshold for collapse

and thereby strengthens the self-focusing dynamics, compared with the case of incoherently-coupled waves ($B = 0$). Non-zero values of β, however, are shown to slightly affect this property and increase to some extent the threshold power for collapse.

When considering walk-off alone ($B = 0$), the virial theory gives a critical power for self-focusing, which grows up with the walk-off length δ. The main influence of walk-off is thus to delay, even arrest the collapse. It manifests by acting on the centroids of the waves and by detrapping them. We show that walk-off indeed competes with the collapse by modifying the trajectories of both components in the transverse plane. The wave centroids, initially located at the origin, are then shifted from 0 and further fuse again at this point, where collapse occurs. Reversely, when the two waves contain enough power for promoting individual collapses, walk-off can make them separate from each other and collapse on their own center of mass, far away from the origin. In the diffraction regime excluding the collapse, the two components can either undergo one or more crossings before decaying into noise, or continue to walk off away from each other while they both decouple and disperse. All these behaviors are explained through simple analytical descriptions.

---

1. S.V. Manakov, *Sov. Phys. JETP* **38**, 248 (1974).

2. J.U. Kang, G.I. Stegeman, J.S. Aitchison and N. Akhmediev, *Phys. Rev. Lett.* **76**, 3699 (1996).

3. C.R. Menyuk, *Opt. Lett.* **12**, 614 (1987); *J. Opt. Soc. Am. B* **5**, 392 (1988).

4. D.N. Christodoulides, T.H. Coskum, M. Mitchell and M. Segev, *Phys. Rev. Lett.* **78**, 646 (1997).

5. J.J. Rasmussen and K. Rypdal, *Physica Scripta* **33**, 481, (1986).

6. C.R. Menyuk, *IEEE J. Quantum Electron.* **QE-23**, 174 (1987); D.N. Christodoulides and R.I. Joseph, *Opt. Lett.* **13**, 53 (1988).

7. C.J. McKinstrie and D.A. Russel, *Phys. Rev. Lett.* **61**, 2929 (1988); L. Bergé, *Phys. Rev. E* **58**, 6606 (1998); O. Bang, L. Bergé and J. Juul Rasmussen, *Phys. Rev. E* **59**, 4600 (1999).

Transverse Instability of Coupled Dark-Bright Solitons

Z. H. Musslimani, M. Segev, A. Nepomnyashchy and Y. S. Kivshar

Vector solitons are solitons that consist of two (or more) components that mutually self-trap in a nonlinear medium. They were first suggested by Manakov [1] in the context of the Kerr nonlinearity, which leads to two cubic Non-Linear Schrödinger Equations (NLSEs) coupled through the nonlinear terms. These vector solitons were in a $(1+1)D$ configuration, that is, one direction of self-trapping and one direction of propagation. Because it is very well established that both bright and dark scalar Kerr solitons (solutions of a single cubic NLSE) are unstable in a higher dimension [2,3], the commonly held belief was that vector solitons are not observable in a higher dimension either. In other words, if a vector soliton is narrow in the x-direction, uniform in y and is propagating along z, it suffers from instabilities in y that break the soliton and destroy it. As a result, attempts to observe vector solitons were limited to temporal solitons in birefringent fibers [4] and to spatial solitons in planar waveguides [5] , both inherently $(1+1)D$ systems. Following the discovery of photorefractive spatial solitons, vector (Manakov-like) solitons were suggested also in photorefractive media, in several forms. In contradistinction with the Kerr nonlinearity, the photorefractive nonlinearity is saturable [6]. One of these forms of vector solitons is of particular interest, because it applies to any non-instanteneous nonlinearity and allows more than two vector components: vector solitons based on mutual incoherence between the various constituents [7]. Indeed, observations of two-component vector pairs in three realizations: bright-bright, dark-dark and dark-bright coupled pairs, followed soon thereafter [8]. However, unlike all earlier experiments with vector solitons [4,5], these of [8] were in a $3D$ (bulk) nonlinear media, in sharp contrast with the early belief that transverse instability necessarily leads to destruction of $(1+1)D$ vector solitons in $3D$ nonlinear media. Furthermore, a very recent paper has reported the observation of multi-mode vector solitons, also employing the photorefractive saturable nonlinearity [9]. These experimental observations raise a basic important question: Can saturation arrest the transverse instability of solitons in a higher dimension [10]. For scalar (one component) solitons, the answer lies in [2] for bright solitons, and in [11] for dark solitons, but for vector solitons (of any type, including Manakov solitons [1]), the issue of transverse instability of solitons in a higher dimension has never been addressed.

In this paper, we investigate the transverse instability of $(1+1)D$ dark-bright vector soliton in three dimensional nonlinear media. We find that for saturable media, it is the nonlinearity saturation which leads to the suppression of the transverse instability. Furthermore, surprisingly, in the low intensity limit, i.e., Manakov limit, the nonlinear mode coupling leads to a strong transverse stabilization, that is, even in the absence of saturation. In other words, the transverse instability of a single dark soliton in bulk Kerr media is suppressed solely due to the presence of a bright component. Moreover, the suppression of the transverse instability is enhanced when the amplitude of the bright component is increased. This is valid for transverse perturbations on scale larger than that of the soliton, which is the scale at which transverse instabilities occur for all $(1+1)D$ solitons. We start from the normalized equations [7]

$$i\frac{\partial U}{\partial z}+\frac{1}{2}\nabla^2 U-\frac{\gamma U}{1+|U|^2+|V|^2}=0\,, \tag{1}$$

$$i\frac{\partial V}{\partial z}+\frac{1}{2}\nabla^2 V-\frac{\gamma V}{1+|U|^2+|V|^2}=0\,, \tag{2}$$

where U, V are the envelopes of the two interacting beams, $\gamma=\beta(1+\rho)$ and ρ is the total intensity at infinity. β is a constant proportional to the space-charge field at "infinity", and $\nabla^2=\partial^2/\partial x^2+\partial^2/\partial y^2$ is the transverse Laplacian. Equations (1) and (2) describe two coupled beams in a saturable optical medium with a refractive index change proportional to $1/(1+|U|^2+|V|^2)$. Such an interaction can form *vector solitons* that consist of two (or more) components mutually self-trapped in a nonlinear medium. In the small-intensity (Kerr) limit, the governing equations describe the so-called *Manakov solitons* [1]. Consider the transverse instability of the dark-bright soliton pair. We look for the stationary solutions in the form of bright, $U_0(z,x,y)=u(x)e^{i\mu z}$, and dark, $V_0(z,x,y)=v(x)e^{i\nu z}$, components defined by the boundary conditions $u(\pm\infty)\to 0$ and $v(\pm\infty)\to\pm\sqrt{\rho}$, respectively. Following a standard multi-scale perturbation expansions we identify, in the long wave limit, two instability modes. First mode is related to the scalar case obtained in [2]. In this case, the perturbation frequency ω is expressed to leading order in q (perturbation wave number) as

$$\omega^2=-\frac{P}{(dP/d\mu)}, \tag{3}$$

where P is the soliton power, $P=\int_{-\infty}^{+\infty}|u|^2dx$. The second instability mode gives

$$\omega^2=\frac{\int_{-\infty}^{+\infty}[u_x^2(x)+v_x^2(x)]dx}{\mathcal{P}+2\rho\lim\limits_{x\to\infty}[v^2(x)\Gamma(x)-x]}, \tag{4}$$

where $\mathcal{P}$ is the complimentary power defined as $\mathcal{P}=\int_{-\infty}^{+\infty}dx[u^2(x)+v^2(x)-\rho]$ and $\Gamma(x)$ is defined by the relation $d\Gamma(x)/dx=1/v^2(x)$. In a particular case (saturable media) discussed in Ref. [7], we can use an approximate analytic solution, $u(x)=\sqrt{r}\,\mathrm{sech}[(\beta\delta)^{1/2}x]$ and $v(x)=\sqrt{\rho}\tanh[(\beta\delta)^{1/2}x]$, where $\delta\equiv(r-\rho)/(1+\rho)<0$; $|\delta|\ll 1$ and the propagation constants are $\mu\simeq-\beta(1-\delta/2)$ and $\nu=-\beta$. In this case, the condition (3) does not lead to instability because $dP/d\mu<0$. However, applying the second condition (4), we obtain the instability growth rate $\omega^2=\beta\delta(r+2\rho)/3(r-2\rho)$. For the experimental parameters from Ref. [8], we find $\beta\simeq 0.566$, and show this result in the figure for different values of δ.

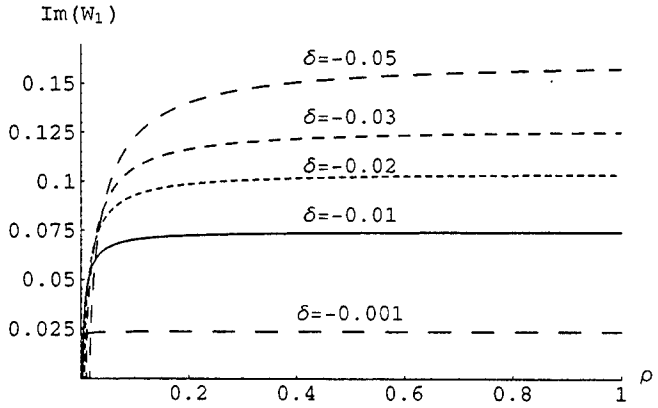


FIG. 1. Growth rate of the transverse instability of a dark-bright soliton pair for different values of δ.

Another important example is the dark-bright Manakov solitons [12]. In this case, the bright and dark components are given by the expressions [12]: $u(x) = \sqrt{1-a^2}\mathrm{sech}(a\,x)$ and $v(x) = \tanh(a\,x)$ with the propagation constant $\mu = -(1-a^2/2)$ where a $(a^2 < 1)$ characterizes the amplitude of the bright component for the normalised background. Again, condition (3) does not lead to any instability because $dP/d\mu < 0$. However, from Eq. (4) we obtain

$$\omega^2 = -\frac{a^2(3-a^2)}{3(a^2+1)}. \tag{5}$$

When $a = 1$, i.e., a single dark soliton, then we retrieve the result of [3], $\omega^2 = -1/3$. Moreover, the result (5) indicates *an unexpected feature* of the dark-bright soliton pairs: *a bright component, embedded in a defocusing media, leads to an effective suppression of the transverse instability of a dark soliton.* This instability suppression results *solely* from the presence of the bright component and becomes stronger as we increase the bright soliton intensity. Finally, we also analyse the transverse instability of bright-bright and dark-dark coupled soliton pairs and map the problem to the scalar case if the nonlinearity is isotropic.

---

[1] S. V. Manakov, Sov. Phys. JETP **38**, 248 (1974).

[2] V. E. Zakharov and A. M. Rubenchik, Sov. Phys. JETP **38**, 494 (1974).

[3] E. A. Kuznetsov and S. K. Turitsyn, Sov. Phys. JETP **76**, 1583 (1988).

[4] Y. Barad and Y. Silberberg, Phys. Rev. Lett. **78**, 3290 (1997).

[5] J. U. Kang, G. I. Stegeman, J. S. Aitchison and N. Akhmediev, Phys. Rev. Lett. **76**, 3699 (1996).

[6] M. Segev, G. C. Valley, B. Crosignani, P. DiPorto and A. Yariv, Phys. Rev. Lett. **73**, 3211 (1994); D. N. Christodoulides and M. I. Carvalho, J. Opt. Soc. Am. B **12**, 1628, (1995).

[7] D. N. Christodoulides, S. R. Singh, M. I. Carvalho and M. Segev, Appl. Phys. Lett. **68**, 1763 (1996).

[8] Z. Chen, M. Segev, T. Coskun and D. N. Christodoulides, Opt. Lett. **21**, 1436, 1821 (1996); Z. Chen et al., J. Opt. Soc. Am. B **14**, 3066 (1997).

[9] M. Mitchell, M. Segev and D. N. Christodoulides, Phys. Rev. Lett. **80** 4657 (1998).

[10] In this paper we deal with an isotropic saturable nonlinear medium, and do not attempt to resolve the debate between the claim of A.V. Mamaev et al., Phys. Rev. A **54**, 870 (1996), that in photorefractives (which are inherently anisotropic) such solitons are highly transversely unstable, which is contradicted by experiments of K. Kos et al., Phys. Rev. E **53**, R4330 (1996), Z. Chen et al., J. Opt. Soc. Am. B **14**, 1407 (1997) and others, and by the theoretical work of E. Infeld and T. Lenkowska-Czerwinska, Phys. Rev. E **55**, 6101 (1997). All these papers show that the development of the instability is suppressed provided the input beam is close to a soliton in parameter space.

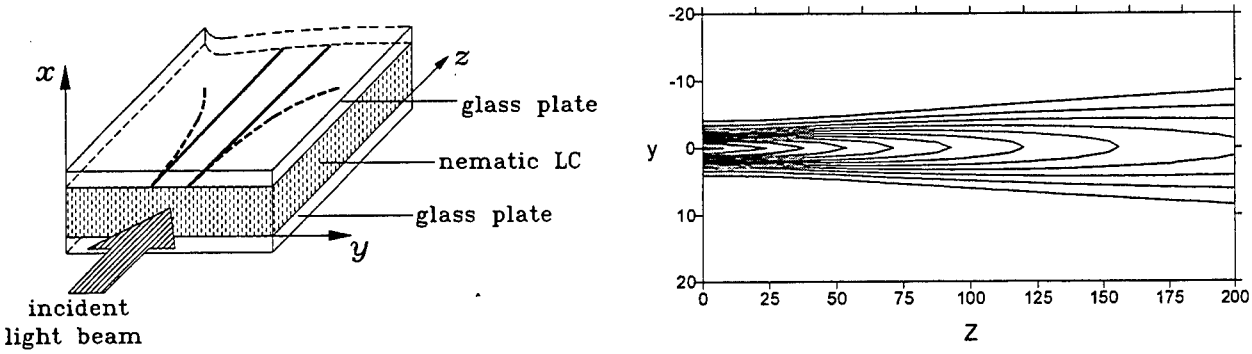
[11] B. Luther-Davies, J. Christou, V. Tikhonenko and Yu. S. Kivshar, J. Opt. Soc. Am. B **14**, 3045 (1997).

[12] A.P. Sheppard and Yu.S. Kivshar, Phys. Rev. E **55**, 4773 (1997).

Solitary waves formation in liquid crystalline waveguides

Mirosaw A. Karpierz, Waldemar K. Bajdecki,
Andrzej W. Domaski, Marek Sierakowski, Tomasz R. Woliski
Faculty of Physics, Warsaw University of Technology, Koszykowa 75, 00-662 Warszawa, Poland
tel: (4822)6607660, fax: (4822)6282171, e-mail:karpierz@if.pw.edu.pl

Liquid crystals are very important materials in numerous technical applications. In the nematic phase, the correlation among liquid crystalline molecules is very strong because of the high anisotropy as well as the collective behavior of the molecules. This is responsible for the fact that liquid crystal molecules can easily reorient even with a very low applied field. The molecular reorientation due to interactions with the electric field of the light wave changes the local birefringence axis of liquid crystal and it is the basis of the optical orientational nonlinearity [1,2]. The orientational nonlinearity in liquid crystalline waveguides leads to numerous effects not observed in another types of nonlinearity. Among others there are obtained the threshold and optical bistable effects resulting in nonlinear refractive index changes, strong dependence on light polarisation as well as possibility of controlling the nonlinearity by external electric or magnetic fields. Theoretically analyzed unique properties of liquid crystalline nonlinear waveguides have been also confirmed in recently reported experiments with liquid crystalline waveguides [3-6].



(a) (b)

Fig.1. (a) Schematic drawing of liquid crystalline planar waveguides and (b) theoretical simulation of the light beam propagation in the linear regime. Units in figure (b) are measured in microns

In this paper the detailed analysis of the self-focusing effect in a planar waveguide filled with homeotropically aligned nematic liquid crystal (see Fig.1) is presented. Initially, the electromagnetic field with both TM polarization (with E_x component of the electric field) and TE polarization (with E_y component of the electric field) are taken into account. As a result in nonlinear regime the liquid crystal molecules are forced to reorient in the xy plane and consequently the electric permittivity tensor has the form:

$$\varepsilon = \begin{pmatrix} \varepsilon_\perp + \Delta\varepsilon\cos^2\theta & \Delta\varepsilon\sin\theta\cos\theta & 0 \\ \Delta\varepsilon\sin\theta\cos\theta & \varepsilon_\perp + \Delta\varepsilon\sin^2\theta & 0 \\ 0 & 0 & \varepsilon_\perp \end{pmatrix}, \qquad (1)$$

where $\varepsilon_\perp$ is an ordinary electric permittivity, $\Delta\varepsilon$ is an optical anisotropy and θ is an orientation angle of the liquid crystalline molecules director measured according to the *x* axis. The TE-like field is assumed to be much weaker than the TM-like field. Therefore, the reorientation of the liquid crystal and obtained

electric permittivity changes are small enough to use a small nonlinearity approximation, i.e. to use an electric field in the form:

$$E_x = A(y,z)\psi(x)\exp(i\omega t - ik_0 N_x z), \tag{2}$$

$$E_y = B(y,z)\varphi(x)\exp(i\omega t - ik_0 N_y z), \tag{3}$$

where $\psi\exp(i\omega t\text{-}ik_0N_xz)$ and $\varphi\exp(i\omega t\text{-}ik_0N_yz)$ are modes of the planar waveguide with homeotropically aligned liquid crystal (for θ=0). Then the slowly varying complex amplitudes A and B fulfil equations:

$$\left[\kappa_1 + \frac{1}{2k_0N_y}\frac{\partial^2}{\partial y^2} - i\frac{\partial}{\partial z}\right]B = -\kappa_{12}A\exp\left(-ik_0\left(N_x - N_y\right)z\right), \tag{4}$$

$$\left[-\kappa_2 + \frac{1}{2k_0N_x}\frac{\partial^2}{\partial y^2} - i\frac{\partial}{\partial z}\right]A = -\kappa_{12}B\exp\left(ik_0\left(N_x - N_y\right)z\right), \tag{5}$$

where nonlinear coefficients are defined as follows: $\kappa_1 = k_0\Delta\varepsilon\int\sin^2\theta\varphi^2dx\big/2N_y\int\varphi^2dx$, $\kappa_2 = k_0N_x\Delta\varepsilon\int\sin^2\theta\psi^2dx\big/2\varepsilon_{\|}\int\psi^2dx$, and $\kappa_{12} = k_0\Delta\varepsilon\int\sin\theta\cos\theta\varphi\psi dx\big/2N_y\int\varphi^2dx$. The reorientation angle θ is calculated from the Euler-Lagrange equation for the nematic liquid crystals in the form [5]:

$$\frac{d^2\theta}{dx^2} + \frac{\varepsilon_0\Delta\varepsilon}{4K}\left[2|AB|\varphi\psi\cos\Delta\alpha\cos 2\theta + \left(|B\varphi|^2 - |A\psi|^2\right)\sin 2\theta\right] = 0, \tag{6}$$

where $\Delta\alpha$ is a phase difference between E_x and E_y field components and K is an elastic constant in the one-elastic constant approximation (with assumption of equal energies for splay and bend deformations). Additionally, the solution of equation (6) for strong anchoring conditions and homeotropical alignment requires fulfilling the boundary conditions for the orientation angle: $\theta(0)=\theta(d)=0$.

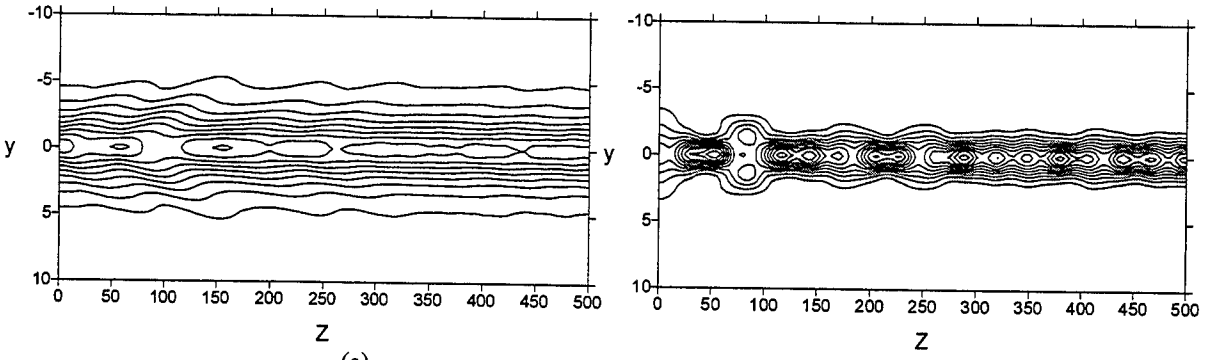
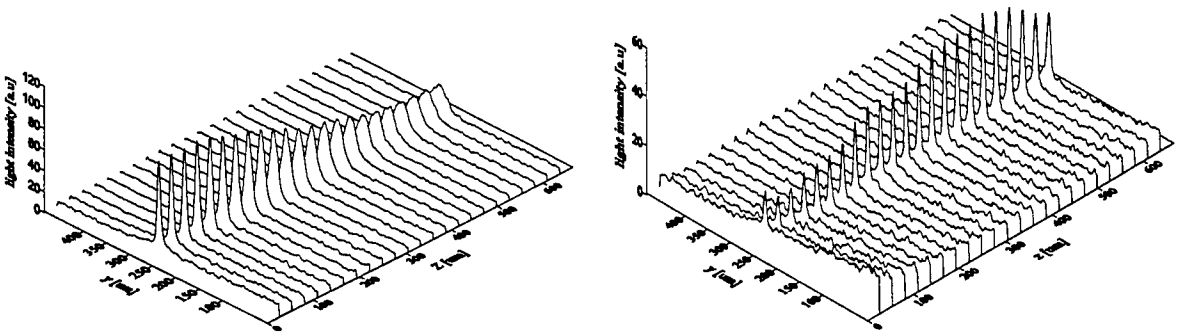


Fig.2. Theoretical simulation of nonlinear propagation of the light beam (a) with the TM polarization and (b) with the TE polarization. Units are measured in microns

The set of equations (1-6) have been solved numerically to simulate the propagation of the light beam in a waveguide with *4-trans-4'-n-hexyl-cyclohexyl-isothiocyanatobenzene* (6CHBT) nematic liquid crystal film with the thickness d=10μm surrounded by glass plates. At the input the light beam with the width $\sigma\approx$10μm was assumed and with both polarization amplitudes ratio $(A(y=0)/B(y=0))^2$=20. In the linear limit, i.e. without reorientation of the liquid crystal molecules the light beam diffracts as it is shown in figure 1(b). However, for larger values of light power at the input, the reorientation is induced and the nonlinearity causes focusing of the light beam. Finally, for high enough input light power (approximately

$P \approx 30$ mW) the light in the planar waveguide forms the beam with constant cross-section shape. This spatial soliton creation is shown in Fig.2. Note, that in the equation (5) the nonlinear coefficient κ_2 is responsible for the defocusing of the light beam but their influence is compensated by the coupling term connected with the coefficient κ_{12}.

The self-focusing phenomena in liquid crystalline waveguide have been also obtained experimentally [6]. The figure 3 presents experimental results measured by the CCD camera placed at the top of the planar waveguide. Therefore, the intensity distribution of the scattered light shown in fig.3 represents the shape of the TE-like electromagnetic field.



(a) (b)

Fig.3. The cross section distribution of the light intensity of the laser beam guided in nonlinear liquid crystalline waveguide for (a) low intensities and (b) for 30 mW of light power at wavelength λ=842nm. Experimental results were obtained for the 6CHBT liquid crystal waveguide with a thickness d=10μm.

In conclusions, the nematic liquid crystals allow to obtain the auto-collimated light beam for relatively low power (in our experiment $P \approx 30$ mW). In the proposed theoretical model the self-focusing is caused by the nonlinear coupling between TM-like and TE-like fields. The experimental results are in perfect agreement wit the theoretical analysis.

This work was partially supported by the Polish Committee of Scientific Research (KBN) under the grant No. 8T11D 01915.

REFERENCES

1. I.C. Khoo and S.T. Wu, *Optics and Nonlinear Optics of Liquid Crystals*, World Scientific Publishing Co Ltd., Singapore, New Jersey, London, Hongkong 1993.
2. T.R. Wolinski, M.A. Karpierz, *Optica Applicata* **24**, 265 (1994).
3. M.Warenghem, J.F. Hennit, G. Abbate, *Opt. Express* **2**, 483 (1998)
4. G. Abbate, L. De Stefano, and E. Santamato, *J.Opt.Soc.Am.* ***B*** **13**, 536 (1996)
5. M.A. Karpierz, T.R. Wolinski, M. Swillo, *Mol. Cryst. Liq. Cryst.* **282**, 365 (1996).
6. M.A. Karpierz, M.Sierakowski, M. Swillo, T.R. Wolinski, *Mol. Cryst. Liq. Cryst.* **320**, 157 (1998).

Engineered discrete breathers

C. Balslev Clausen, Yu. B. Gaididei, and P. L. Christiansen
Department of Mathematical Modelling, Technical University of Denmark, DK-2800 Lyngby
cbc@imm.dtu.dk, yg@imm.dtu.dk, plc@imm.dtu.dk

L. Torner
Laboratory of Photonics, Department of Signal Theory and Communications, Universitat Politecnica de Catalunya, Barcelona, ES 08034, Spain
torner@tsc.upc.es

The potential of QPM extends far beyond the efficient phase matching of a single wave-mixing process which takes place in a sample with a regular, periodic grating. More complicated grating patterns can be fabricated which results in media with unusual properties that can thus be engineered in a controllable fashion. This has been explored in a variety of devices that are based on creative grating designs. We have considered an array of *narrow* grating stripes as indicated in figure 1. Each stripe is composed of gratings with a narrow width, in the sense that the gratings are confined in the transverse direction to a width which is less than the beam width. Experimental setups usually require tightly focused beams with widths of $10 \sim 20$ μm. Grating stripes with these widths can be implemented with the current state of the art lithographic QPM technology[1], but even smaller grating widths might be more challenging. There have so far not been attempts to fabricate such narrow gratings, so the feasibility is an open question and only an experimental trial can give the answer. In practice, it can be anticipated that inhomogeneities appear along the interfaces between grating stripes and grating-free regions[2].

Our aim is to make a construction with a *lattice-like nature*, in which each grating stripe plays the role of a *site* in the lattice. If the lattice features prevail, the beam evolution should essentially be governed by a discrete system, in close analogy to the beam evolution in an array of weakly coupled quadratic nonlinear waveguides[3]. Our investigation is based on numerical simulations of beam evolution in the grating structure of figure 1. Averaging in the longitudinal direction over one coherence length we find at the lowest order, that the dynamics of the scaled envelopes of a fundamental beam (A_1) and a second harmonic beam (A_2) are governed by[4, 5]

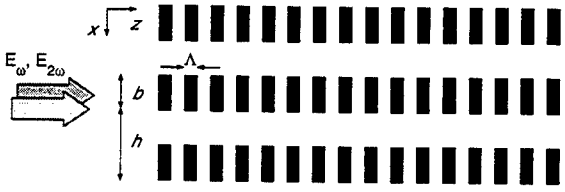


Figure 1: Schematic top-view of grating design of QPM structure.

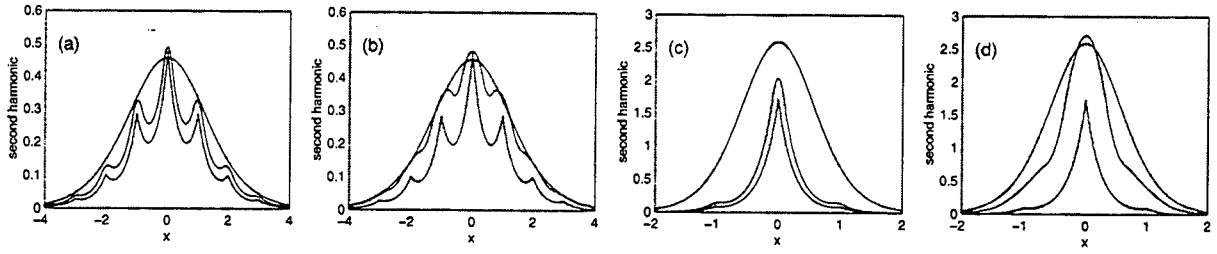


Figure 2: Second harmonic part of stationary localized modes (solid lines) with $\beta = 1$ and $h = 1$. Superimposed are profiles of continuous solitons with $b = h$ (dotted lines) and discrete solitons with $b = 0$ (dashed lines). The shaded areas indicate the regions where $g(s) = 1$, i.e. the nonlinear regions. (a) b=0.3, $q = 0.25$, (b) b=0.7, $q = 0.25$, (c) b=0.2, $q = 1.5$, (d) b=0.7, $q = 1.5$.

$$
\begin{aligned}
i\frac{\partial A_1}{\partial z} + \frac{1}{2}\frac{\partial^2 A_1}{\partial x^2} + \frac{1}{b}\sum_n g(x - x_n)A_1^* A_2 = 0, \\
i\frac{\partial A_2}{\partial z} + \frac{1}{4}\frac{\partial^2 A_2}{\partial x^2} - \beta A_2 + \frac{1}{b}\sum_n g(x - x_n)A_1^2 = 0,
\end{aligned}
\tag{1}
$$

where β is the residual phase mismatch. For convenience, the envelopes have been scaled with the width, b, of the grating lines. The comb-like transverse grating structure is composed of a sequence of "hat-functions", $g(x - x_n)$, which are each centered on $x_n = nh$, $g(x) = H(x - b/2) - H(x + b/2)$, where $H(x)$ is Heaviside's function and h is the separation of the grating lines. following the method of Ref. [7], the system can be reduced to a set of discrete equations in the limit $b \to 0$,

$$
\begin{aligned}
i\frac{\mathrm{d}B_n}{\mathrm{d}z} + \frac{1}{2h^2}(B_{n+1} + B_{n-1} - 2B_n) + \frac{1}{h}B_n^* D_n = 0, \\
i\frac{\mathrm{d}D_n}{\mathrm{d}z} + \frac{1}{4h^2}(D_{n+1} + D_{n-1} - 2D_n) - \beta D_n + \frac{1}{h}B_n^2 = 0,
\end{aligned}
\tag{2}
$$

B_n and D_n are the amplitudes on the n'th site of the fundamental and second harmonic, respectively. In deriving eqs. (2) we have assumed that the beam amplitudes are small. We expect that as b is increased from zero, the QPM structure will interpolate between a fully discrete system ($b = 0$) to a continuous medium ($b = h$), and refer to the structure as a quasi-lattice. In order to expose the interpolating character of the quasi-lattice we have numerically found the localized, stationary modes of the structure, i.e. we have inserted $A_1 = A(x)\exp(iqz)$ and $A_2 = B(x)\exp(i2qz)$ in eqs. (1) and solved the resulting boundary value problem. In figure 2 we plot the amplitude $B(x)$ of the numerically found stationary modes with $h = 1$, $\beta = 1$ and two different values of b and q. The corresponding profiles of the solitons in the limits $b = 0$ (discrete) and $b = h$ (continuous) are superimposed on the plots as dashed and dotted lines, respectively. It should be clear that with small b the stationary modes resemble the discrete soliton, while with large b they resemble the continuous solitons. Also, we note that with large amplitudes (q large) a relatively small value of b is required in order to obtain a good resemblance with the discrete solitons.

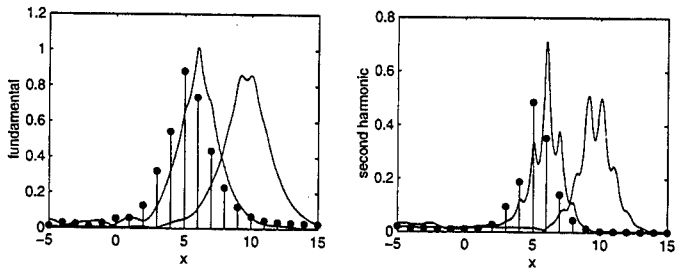


Figure 3: Output at $z = 30$. Stemplot (bullets on sticks) are results from discrete eqs. (2) and lines are from eqs. (1) with $b = 0.25$ (solid lines) and $b = 0.5$ (dashed lines). $\beta = 1$, $h = 1$. Input position and velocity is $x_0 = -10$ and $v = 0.5$, respectively. (a) Fundamental and (b) second harmonic.

We have made a careful numerical study solving eqs. (1) with a variety of initial conditions and parameter values. We give here an example where the simple discrete system (2) predicts correctly the behavior of the beam dynamics in the original system. A mode with an initial phase tilt $v = 0.5$ is launched with an initial position $x_0 = -10$, and the output position at $z = 30$ is shown in figure 3. The result from the discrete system (2), which are marked with bullets, show that the mode has been slowed down by the discreteness and is positioned at $x = 5$. The results from numerical simulations of eqs. (1) with $b = 0.25$ show that the mode moves in the quasi-lattice in agreement with (2), while the results with $b = 0.5$ show that the mode moves in agreement with the translational symmetry of a continuous system. Still, reminescent features of discreteness are visible in appearance of the profiles of the freely moving mode. We have here studied the simplest possible grating design with discrete features. However it should be remarked that more involved layouts can be envisioned with possible unique properties. For example, different lattices that each quasi phase match a particular wavelength may be interleaved to form a complex multi-wavelength discrete system. Inclusion of chirped, tilted, or dislocated gratings[8] in the region between the lattice sites could provide *novel classes of nonlinear couplings* between lattice sites. Furthermore, a lattice with competing nonlinearities may be constructed by exploiting the Kerr-like effects which are inherent to the QPM technique[4]. We are most grateful to M. M. Fejer for important discussions and remarks.

References

[1] L. E. Myers *et al*, Opt. Lett. **21**, 591 (1996); B. Widiyatmoko *et al*, Opt. Lett. **24**, 315 (1999); G. Imeshev *et al*, Opt. Lett. **23**, 673 (1998).

[2] M. J. Missey *et al*, Opt. Lett. **23**, 664 (1998); Y. Tomita *et al*, Appl. Phys. Lett. **66**, 1484 (1995); K. Eda *et al*, Appl. Phys. Lett. **66**, 827 (1995).

[3] T. Peschel, U. Peschel and F. Lederer, Phys. Rev. E **57**, 1127 (1998).

[4] C. Balslev Clausen, O. Bang, and Yu. S. Kivshar, Phys. Rev. Lett. **78**, 4749 (1997).

[5] L. Torner and G. I. Stegeman, J. Opt. Soc. Am. B **14**, 3127 (1997).

[6] C. Balslev Clausen, J. P. Torres, and L. Torner, Phys. Lett. A **249**, 455 (1998); A. A. Sukhorukov, Yu. S. Kivshar, and O. Bang, (unpublished).

[7] Yu. B. Gaididei *et al*, Phys. Rev. E **55**, R13365 (1997).

[8] C. Balslev Clausen and L. Torner, Phys. Rev. Lett. **81**, 790 (1998); Opt. Lett. **24**, 7 (1999).

Transition towards dynamical parametric solitary waves

Antonio Picozzi and Marc Haelterman
Service d'Optique et d'Acoustique, Université Libre de Bruxelles
50 Avenue F. D. Roosevelt, C.P. 194/5, B-1050 Brussels, Belgium

Parametric solitary waves result from a balance between energy exchanges and group velocity differences between waves interacting through a parametric process. Apart from the group velocity differences, dispersion effects on the interacting waves have been systematically ignored in previous theoretical studies of parametric solitary waves [1–4]. This omission is usually justified by the fact that the nonlinear effects take place over a length that is much shorter than the characteristic dispersion length of the interacting waves. We show here that this standard criterion is not valid and that even very weak dispersion can drastically alter the parametric solitary waves dynamics. In particular, we show that dispersion induces a dynamical transition of the parametric solitary waves that results in the formation of moving periodic patterns across their field envelopes.

The periodic patterns consist of arrays of phase defects whose amplitude profiles result from a balance between dispersion and nonlinearity in a way similar to what happens in symbiotic quadratic solitary waves [5]. The symbiotic solitary waves consist of another type of nonlinear waves sustained by a parametric interaction. They result from a balance between dispersion and nonlinearity in the absence of net energy exchanges and thus do not require walk-off, unlike parametric solitary waves. Both bright and dark optical symbiotic solitary waves have been predicted theoretically [5]. The new class of solitary wave that results from the dynamical transition can therefore be viewed as exhibiting a hybrid parametric and symbiotic nature : the envelope resulting from net parametric energy exchanges and walk-off is modulated by a moving periodic array of symbiotic dark solitons resulting from a balance between dispersion and nonlinearity. The originating dynamical transition is described analytically through an extension of the Kolmogorov-Petrovskii-Piskunov (KPP) conjecture.

We consider the degenerate phase-matched three-wave parametric interaction that couples a fundamental wave and its second harmonic in a quadratic nonlinear optical crystal. The slowly varying amplitude envelopes u_1 and u_2 of the signal and pump waves of frequencies ω_1 and $\omega_2 = 2\omega_1$ are ruled by the following equations:

$$\frac{\partial u_1}{\partial t} - \frac{\partial u_1}{\partial x} + \mu_1 u_1 = u_2 u_1^* - i\beta_1 \frac{\partial^2 u_1}{\partial x^2}\,, \qquad \text{(1a)}$$

$$\frac{\partial u_2}{\partial t} + \frac{\partial u_2}{\partial x} + \mu_2 u_2 = -2u_1^2 - i\beta_2 \frac{\partial^2 u_2}{\partial x^2}\,, \qquad \text{(1b)}$$

where x and t are respectively the longitudinal space coordinate and the time in a reference frame traveling at the average velocity $(v_1 + v_2)/2$. We normalize the fields amplitudes u_i, the time t, the space variable x and the damping rate γ_i to the constant pump amplitude e_0 at the input of the crystal and to the parametric coupling constant σ, i.e., $u_i/e_0 \to u_i$; $t\sigma e_0 \to t$; $\gamma_i(\sigma e_0)^{-1} \to \mu_i$; $x\sigma e_0/\delta \to x$, where $\delta = (v_1 - v_2)/2$. β_i are the dispersion coefficients at frequency ω_i, for simplicity we assume in the following that $\beta = \beta_2 = \beta_1$ and $v_1 > v_2$.

In the absence of dispersion effects ($\beta = 0$), Eq. (1) has been extensively studied in the literature and analytical solitary waves solutions have been derived in the form of a sech-shaped envelope for the signal wave and a tanh-shaped envelope for the pump wave [1, 2]. Our scope here is to study the influence of dispersion on this solitary wave. To this end we numerically solve Eq. (1) with $\beta \neq 0$ and with

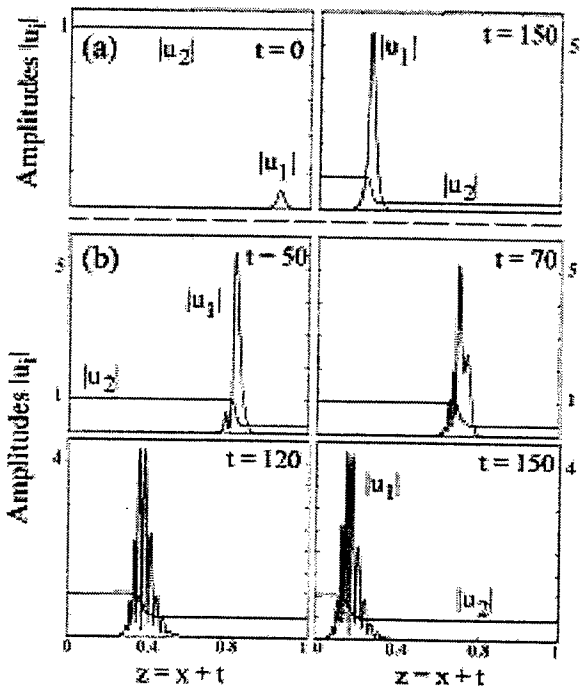


Figure 1: Evolution along the propagation of the interacting amplitudes $u_{1,2}$ in the co-moving reference frame of the signal wave. (a) Classical parametric solitary wave. (b) Dynamical solitary wave.

an initial condition given by a constant pump wave and a sech profile for the signal wave. The amplitude envelopes are shown in Fig. 1 in the reference frame traveling at the signal group velocity defined by $z = x + t, \tau = t$.

As evidenced in Fig. 1, for a small value of the dispersion parameter, the dispersion has no significant effects on the solitary wave profile. In particular, the expected envelope reshaping induced by dispersion is almost invisible. The scenario changes completely for a slightly larger value of the dispersion parameter as illustrated in Fig. 1(b). We see that dispersion is responsible for the formation of a dynamical periodic pattern in the solitary wave envelope. A detailed analysis shows that the pattern is generated from the drift of π-phase shifts that appear periodically in the leading front of the signal pulse. The drift of the phase defects can be easily explained physically from the fact that these phase defects constitute symbiotic solitary waves of the dark type that propagate at the group velocity of the signal wave that is smaller than the velocity of the solitary wave (note that due to the energy transfer from the pump, the solitary wave envelope is superluminous for the case $v_1 > v_2$ assumed here).

We described this dynamical transition through an original extension of the KPP conjecture which proved powerful in nonlinear diffusion problems and dynamical pattern selection [6, 7]. We generalize here the approach to include the description of the dynamical transition. The KPP approach consists in describing the properties of fronts propagating into un unstable state from a linear analysis of the leading edge of the front profile. The general solutions to the linearized Eq. (1) in a reference frame ($\xi = x + Vt$, $\tau = t$) traveling at the velocity of the solitary wave V has the form

$$u_1(\xi, \tau) = \int_C \widetilde{u_1}(k)\ \exp[\gamma(k) - kV]\tau\ \exp(k\xi)\, dk, \tag{2}$$

where $\widetilde{u_1}(k)$ is obtained from the initial condition by inverting the expansion Eq. (2). Since we study the influence of dispersion on the profile of the parametric solitary wave that is characterized by a sech shape, we take as initial condition of the linearized problem the corresponding exponential front, $u_1(\xi, \tau = 0) = \exp(k_0\xi)$. The function $\widetilde{u_1}(k)$ then possesses a pole on the real axis in $k = k_0$. On the other hand, the function $f(k) = \gamma(k) - kV$ has a saddle points k_s. The integral Eq. (2) can be easily evaluated by choosing the contour C as depicted in Fig. 2. The long term behavior of integral (2) is then ruled by the competing contributions of the pole and the saddle point. The signal amplitude takes the form:

$$u_1(\xi, \tau) \propto I_{pol} + I_{sad}, \tag{3}$$

where I_{pol} is given by the residue

$$I_{pol} \propto \exp\big[(\gamma(k_0) - k_0 V)\tau\big]\ \exp(k_0\xi) \tag{4}$$

while I_{sad} is the saddle point contribution:

$$I_{sad} \propto \widetilde{u_1}(k_s)\ \exp\big[(\gamma(k_s) - k_s V)\tau\big]\ \exp(k_s\xi). \tag{5}$$

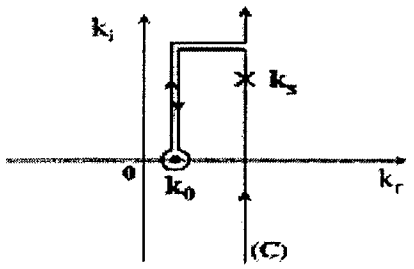


Figure 2: Contour (C) in the complex k plane.

The long term behavior of the solution will then be dominated by the pole or the saddle depending on the relative value of $\mathrm{Re}[f(k)]$ in k_0 and k_s. This condition provides an analytical expression of the critical value of the dispersion parameter β for which the system bifurcates from the well-known continuous family of parametric solitary waves towards the dynamical solitary wave. Indeed, when the saddle point dominates, the exponential leading front of the signal amplitude [Eq. (5)] has a real part that describes the envelope solitary wave and an imaginary part that describes the array of kinks that modulates this envelope. The periodicity of the kink array has been determined analytically following the description of Ref. [7].

Note that when the initial conditions do not include an exponential front for the signal wave, the pole k_0 no longer exists and the saddle point is isolated in the above analysis. Consequently, according to the KPP conjecture, dynamical solitary waves are unconditionally formed, even for arbitrarily small dispersion values. This has been verified numerically by means of gaussian signal envelopes in the initial conditions. This result indicates that the dynamical solitary wave constitutes a robust attractor of the system, which should make its experimental observation easy. Note however that, as β increases, the dispersion effect becomes dominant with respect to the walk-off effect, which unavoidably leads to the modulational instability [4]. Therefore, in order to avoid this problem in practice we suggest a quasi-phase-matched backward configuration [8] for the experimental observation of the dynamical parametric solitary waves. In this situation the simulation reported in Fig. 1(b) corresponds to realistic experimental conditions, for which, one may envisage the observation of the dynamical solitary waves in single pass configuration.

In summary, by means of an original extension of the KPP approach to front propagation into unstable states, we described analytically the dynamical transition that affects parametric solitary waves owing to the effects of dispersion on their constituent interacting waves. We can reasonably expect in a near future the experimental observation of the dynamical solitary wave in the context of nonlinear optics thanks to the recent progress made on quasi-phase-matched quadratic materials.

[1] J.A. Armstrong, S.S. Jha, and N.S. Shiren, IEEE J. Quant. Elect. **QE-6**, 123 (1970); D.J. Kaup, A. Reiman and A. Bers, Rev. Mod. Phys., **51**, 275 (1979); E. Picholle *et al.*, Phys. Rev. Lett., **66**, 1454 (1991); C. Montes, *et al.*, Phys. Rev. E, **55**, 1086 (1997).

[2] A. Picozzi and M. Haelterman, Opt. Lett., **23** 1808 (1998); Phys. Rev. E, **59** 3749 (1999).

[3] A. Picozzi and M. Haelterman, Europhys. Lett., **45**, 463 (1999).

[4] S. Trillo, Opt. Lett., **21**, 1111 (1996).

[5] for a review, see G.I. Stegeman, D.J. Hagan and L. Torner, Opt. Quant. Elect., **28**, 1691 (1996).

[6] V.G. Kolmogorov, I.G. Petrovskii and N.S. Piskunov, Bull. Moscow State University, Math. and Mechanics **1**, 1 (1937).

[7] G. Dee and W. van Saarloos, Phys. Rev. Lett., **60**, 2641 (1988); M. Santagiustina *et al.*, Opt. Lett., **23**, 1167 (1998).

[8] J.U. Kang *et al.*,, Opt. Lett., **22**, 862 (1997).

Gateless Computing using N-Manakov Solitons

Suzanne M. Sears, Ken Steiglitz, Mordechai Segev and Marin Soljačić
Princeton University, Princeton, NJ 08544
smsears@princeton.edu, ken@cs.princeton.edu, segev@ee.princeton.edu, soljacic@princeton.edu
Mariusz H. Jakubowski
Microsoft Corporation, Redmond, WA
Richard Squier
Georgetown University, Washington DC 20057

Despite the fantastic rate at which silicon-based technologies have been progressing, there are several fundamental limitations which suggest that this progress cannot continue without bound. Even within the next decade or two these factors may start to become a real hindrance, and so interest in alternative technologies, such as quantum and DNA computing, has been growing. Here we describe results which suggest that collisions of N-Manakov vector solitons can be used as a new medium for information processing and computation. N-Manakov like solitons can be found in optics [6]. Such an environment could support the new concept of gateless computing where there are no actual fabricated gates anywhere, but all general computing tasks are performed using soliton collisions.

It is well known that solitons behave like particles in many ways, and that (at least in integrable systems) solitons can collide with one another without energy being lost to radiation. It is therefore tempting to visualize computation with solitons as in early proposals for particle machines. One problem is that many sorts of solitons are actually too robust and information cannot be transferred in collisions. In general, there exist some finite number of parameters with which one can fully describe a soliton collision. We define the parameters which can be altered by collisions to be the "state" of the soliton (see [1]). In order for information to be exchanged during such collisions, it is necessary that the resultant state of each soliton depend on the initial state of the other soliton. Not all solitons interact in this manner. For example, in Kerr media, a soliton remains intact after a collision, but the parameters are not altered in any way such that one can determine any useful information about the other soliton. This is not at all the case for vector solitons. The (1+1)D N-Manakov system is described by the N coupled equations,

$$i\vec{q}_t + \vec{q}_{xx} + 2|\vec{q}|^2\vec{q} = 0 \tag{1}$$

where $\vec{q}(x,t)$ is an N component complex vector describing the evolution of the solution. A complex-valued state for solitons in 2-Manakov was defined in [2], where it was shown that collisions are described by explicit linear fractional transformations of that state, using the new two soliton solutions in [3]. We will show that the N-Manakov system can also be described in this way and offers significantly greater freedom and flexibility than the 2-Manakov system for computation.

To illustrate these ideas, we briefly review one model for encoding a bit and performing a NOT operation in the 2-Manakov system described in [2]. In this system, the state of each soliton , ρ , is defined to be the ratio of the first component of the soliton over the second component. This is a single complex number, containing information about the energy distribution and relative phase between the components. A soliton followed by its inverse, $-\frac{1}{\rho^*}$, is called an inverse pair. Any 2-Manakov soliton colliding sequentially with the members of an inverse pair will remain unchanged by the collision, the second soliton undoing any changes caused by the first. For example, a soliton with all of its energy in the first component (hereafter referred to as (A)) and a soliton with all of its energy in the second component (B) form one such inverse pair. To encode data, a "1" bit is represented by the sequence (AB) and a "0" bit by (BA). A NOT operator is then constructed by composing a sequence of four solitons which collide with the inverse pair and reverse their states.

Thus, (AB) would be changed to (BA) and vice-versa. That energy can be interchanged in this manner is a remarkable result in itself and follows from the findings in [3]. Jakubowski et al. also demonstrate that other physical quantities, such as relative phase, can be used to encode information. For example, in a 2-Manakov system that describes two orthogonally-polarized optical fields, such a NOT gate converts right circularly polarized light into left circularly polarized light. In either case, the NOT operator acts on an inverse pair, and thus both operator and data solitons are reusable in further calculations.

In general, for any N, it can be readily verified that one set of solutions to Eq.(1) is:

$$\vec{q}(x,t) = \frac{1}{2}\vec{a}e^{-\frac{R}{2}+i\eta_I} sech(\eta_R + \frac{R}{2}) \tag{2}$$

where $\eta = k(x+ikt), e^R = \frac{|\vec{a}|^2}{k+k^*}, \vec{a}^{T*}\vec{a} = 1$, and $\vec{a}$ and k are arbitrary complex parameters. Conservation of energy and momentum require that the parameter k remain unchanged by collisions. Thus collisions between two such N-Manakov solitons may be described fully by changes in the complex vector $\vec{a}$ for each soliton. We note that Eq. (1) is symmetric under rotations of the SU(N) group, meaning, if $\vec{q}(x,t)$ is a solution of Eq. (1), then so is $\vec{v}(x,t) = \hat{A}\vec{q}(x,t)$ provided $\hat{A}^{T*} = \hat{A}^{-1}$. This implies that collisions of two N-Manakov solitons of the form Eq.(2) may be reduced to collisions between two 2-Manakov solitons, because it is always possible to rotate to a basis in which only the first two components of the $\vec{a}$ vectors are non-zero. Since explicit asymptotic solutions to collisions of 2-Manakov solitons of this form have already been found, we can solve the N-Manakov problem by simply transforming to a 2-Manakov problem, solving it, and transforming back. Thus, state transformations of these N-Manakov solitons are completely understood.

The N-Manakov system provides a medium for logic that is more versatile than 2-Manakov, and offers the possibility of implementing Turing-universal computation (a significant open problem). Each soliton has 2N-1 real parameters that can be controlled via collisions. Clearly many possible methods of encoding data in solitons exist, but a reasonable number of bits which can be encoded per soliton is O(N).

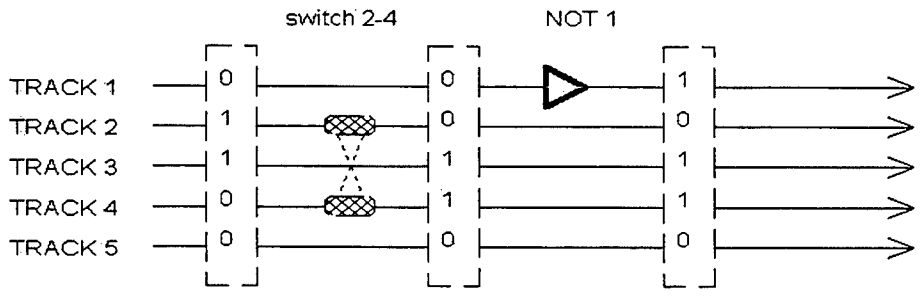


Figure 1: Diagrammatic representation of one way data and operators can be organized in an N-Manakov system.

The data encoding described above for the 2-Manakov system can be used also in the N-Manakov system, but with greater flexibility. The same principles that were used to create a NOT switch in 2-Manakov can now be used to switch data between "tracks". Suppose any soliton contains all of its energy in only the *i*th component (we will represent this state by the *i*th letter of the alphabet). We then pair the components in "tracks", i.e. the 1st and 2nd components are track 1, the 3rd and 4th track 2, and so on (see Fig.1). A simple data sequence like [1 0] (a 1 on the 1st track and a 0 on the 2nd track) would be encoded as the four soliton sequence (ABDC). Then, with a little bit of

rearrangement, the construct above can be used as a switch. In our example it would take (ABDC) (CDBA) and we would now have [0 1] (a 1 on the 2nd track and a 0 on the 1st). Note that only the two tracks of choice are exchanged and that the other tracks remain oblivious to the event. The advantage of using N-Manakov solitons over 2-Manakov solitons is clear: in the 2-Manakov system, only 1 data track would be allowed.

One particularly nice aspect of such a representation is that every data bit is an inverse pair. Thus, all operators are unchanged by the interactions, and both operator and data solitons are reusable. The discovery of designs for other controlled reversible operators, such as the Fredkin-Toffoli gate [4], together with sufficiently flexible routing operations, would lead to a system capable of universal computation.

Soliton computation is naturally suited to the idea of reconfigurable computing. In the conventional scheme, some logic architecture is permanently laid out on a chip, and data is routed to gates where computations are performed. This means that certain computational structures are inherent to the machine; for example, the number of bits used to represent numbers and the accuracy of arithmetic computations. In a soliton computer, there would be no real distinction between data and operators: all would be solitons. The input could determine how the computation would be performed, and the machine would "reconfigure" itself for every computation. This merging of hardware and software has been shown to lead to linear-time pipelined arithmetic algorithms in an abstract particle model [5].

In summary, using SU(N) transformations, we are able to describe explicitly state transformations occurring due to collisions of N-Manakov solitons in the form of Eq.(2). We show that this makes it possible to switch data between "tracks" and possibly make general logical operators. If a universal computer could be simulated in the N-Manakov system, it would open some potentially exciting alternatives to standard models of computation.

References

[1] M. H. Jakubowski, K. Steiglitz, and R. Squier. *Physical Review E*, **56**, 1997.

[2] M. H. Jakubowski, K. Steiglitz, and R. Squier. *Physical Review E*, **58**, 1998.

[3] R. Radhakrishnan, M. Lakshmanan, and J. Hietarinta. *Physical Review E*, **56**, 1997.

[4] E. Fredkin and T. Toffoli. *International Journal of Theoretical Physics*, **21**, 1982.

[5] R. Squier and K. Steiglitz. *Complex Systems*, **10**, 1996.

[6] The easiest way to construct an N-Manakov system in Optics is based on mutual incoherence between the vector components. This requires a non-instantaneous nonlinearity, and the relative phase between every pair of the vector components should fluctuate much faster than the response time of the medium, so that the interference terms do not give rise to a change in the index – they average out on the time scale of the medium's response. This idea was first suggested by D. N. Christodoulides, S. R. Singh, M. I. Carvalho and M. Segev, Appl. Phys. Lett., **68**, 1763 (1996), and first demonstrated by Z. Chen, M. Segev, T. Coskun and D. N. Christodoulides, Opt. Lett., **21**, 1436 (1996) with photorefractive spatial solitons. Unknowingly, it was also used to eliminate the four-wave-mixing terms in the first experiment of 2-Manakov solitons, by J. U. Kang, G. I. Stegeman, J. S. Aitchison and N. Akhmediev, Phys. Rev. Lett., **76**, 3699 (1996), in semiconductor waveguides which possess a non-instantaneous Kerr nonlinearity. Another way to realize N-Manakov also relies on having a non-instantaneous nonlinearity: to have each vector component at a slightly different optical frequency, where the smallest frequency difference between components much exceeds the inverse of the response time of the medium. This idea was utilized by M. Shalaby, and A. J. Barthelemy, IEEE J. Quant. Elect., **28**, 2736 (1992) to demonstrate dark-bright spatial vector solitons.

Multistep cascading spatial solitons

Tristram J. Alexander and Yuri S. Kivshar

Optical Sciences Center, Research School of Physical Sciences and Engineering
Australian National University, Canberra ACT 0200, Australia.
Tel.: (+61-2) 6249 2042; Fax: (+61-2) 6249 5184; email: tja124@rsphysse.anu.edu.au

Solomon Saltiel

Faculty of Physics, University of Sofia, Sofia 1164, Bulgaria

As is known, optical cascaded nonlinearities due to parametric wave mixing can lead to a large nonlinear phase shift and spatial solitary waves, resembling those for a Kerr medium [1]. However, solitary waves supported by cascaded nonlinearities demonstrate much richer dynamics due to nonintegrability of governing nonlinear equations and, unlike solitons of the Kerr nonlinearity, the quadratic solitons can become unstable in a certain parameter region [2].

In this contribution we introduce *a novel class of parametric spatial solitons* supported simultaneously by two nonlinear quadratic (or $\chi^{(2)}$) optical processes: second-harmonic generation (SHG) and sum-frequency mixing (SFM). As has been recently shown by Koynov and Saltiel [3] for continuous waves, under the condition that the two wave-mixing processes are nearly phase matched, the presence of multistep cascading leads to a four fold reduction of the input intensity required to achieve a large nonlinear phase shift. Here, we demonstrate that the multistep cascading can lead to *a new type of parametric solitons*. Introducing a third wave generated via a SFM process, we find that it can alter both the general properties and stability of the two-wave $\chi^{(2)}$ spatial solitons. Moreover, we reveal the existence of a new type of the so-called *quasi-soliton*, that appear for a negative mismatch of the SFM process.

To introduce the model of multistep cascading, we consider the fundamental beam with frequency ω entering a noncentrosymmetric nonlinear medium with a $\chi^{(2)}$ response. As a first step, the second-harmonic wave with frequency 2ω is generated via the SHG process. As a second step, we expect the generation of higher order harmonics due to SFM, for example, a third harmonic ($\omega + 2\omega = 3\omega$) or even fourth harmonic ($2\omega + 2\omega = 4\omega$) [4]. When both such processes are nearly phase matched, they can lead, via down-conversion, to a large nonlinear phase shift of the fundamental wave [3]. Additionally, as we demonstrate in this paper, the multistep cascading can support *a novel type of three-wave spatial solitary waves* in a diffractive $\chi^{(2)}$ nonlinear medium, *multistep cascading solitons*.

We start our analysis with the reduced equations derived in the slowly varying envelope approximation with the assumption of zero absorption of all interacting waves (see, e.g., Ref. [3]). Introducing the effect of diffraction in a slab waveguide geometry, we obtain

$$
\begin{aligned}
&2ik_1\frac{\partial A_1}{\partial z} + \frac{\partial^2 A_1}{\partial x^2} + \chi_1 A_3 A_2^* e^{-i\Delta k_3 z} + \\
&\qquad\qquad \chi_2 A_2 A_1^* e^{-i\Delta k_2 z} = 0, \\
&4ik_1\frac{\partial A_2}{\partial z} + \frac{\partial^2 A_2}{\partial x^2} + \chi_4 A_3 A_1^* e^{-i\Delta k_3 z} + \chi_5 A_1^2 e^{i\Delta k_2 z} = 0, \\
&6ik_1\frac{\partial A_3}{\partial z} + \frac{\partial^2 A_3}{\partial x^2} + \chi_3 A_2 A_1 e^{i\Delta k_3 z} = 0,
\end{aligned}
\tag{1}
$$

where $\chi_{1,2} = 2k_1\sigma_{1,2}$, $\chi_3 = 6k_1\sigma_3$, and $\chi_{4,5} = 4k_1\sigma_{4,5}$, and the nonlinear coupling coefficients σ_k are proportional to the elements of the second-order susceptibility tensor which we assume to satisfy the following relations (no dispersion), $\sigma_3 = 3\sigma_1$, $\sigma_2 = \sigma_5$, and $\sigma_4 = 2\sigma_1$.

In Eqs. (1), A_1,A_2 and A_3 are the complex electric field envelopes of the fundamental harmonic (FH), SH, and the third harmonic (TH), respectively, $\Delta k_2 = 2k_1 - k_2$ is the wavevector mismatch for the SHG process, and $\Delta k_3 = k_1 + k_2 - k_3$ is the wavevector mismatch for the SFM process. The subscripts '1' denote the FH wave, the subscripts '2' denote the SH wave, and the subscripts '3', the TH wave. Following the technique earlier employed in Refs. [5], we look for stationary solutions of Eq. (1) and introduce the normalised envelope $w(z,x)$, $v(z,x)$, and $u(z,x)$ according to the relations,

$$
\begin{aligned}
&A_1 = \frac{\sqrt{2}\beta k_1}{\sqrt{\chi_2\chi_5}} e^{i\beta z} w, \quad A_2 = \frac{2\beta k_1}{\chi_2} e^{2i\beta z + i\Delta k_2 z} v, \\
&A_3 = \frac{\sqrt{2\chi_2}\beta k_1}{\chi_1\sqrt{\chi_5}} e^{3i\beta z + i\Delta k z} u,
\end{aligned}
\tag{2}
$$

where $\Delta k \equiv \Delta k_2 + \Delta k_3$. Renormalising the variables as $z \to z/\beta$ and $x \to x/\sqrt{2\beta k_1}$, we finally obtain a system of coupled equations,

$$
\begin{aligned}
&i\frac{\partial w}{\partial z} + \frac{\partial^2 w}{\partial x^2} - w + w^* v + v^* u = 0, \\
&2i\frac{\partial v}{\partial z} + \frac{\partial^2 v}{\partial x^2} - \alpha v + \frac{1}{2} w^2 + w^* u = 0, \\
&3i\frac{\partial u}{\partial z} + \frac{\partial^2 u}{\partial x^2} - \alpha_1 u + \chi v w = 0,
\end{aligned}
\tag{3}
$$

where $\alpha = 2(2\beta + \Delta k_2)/\beta$ and $\alpha_1 = 3(3\beta + \Delta k)/\beta$ are two dimensionless parameters that characterise the nonlinear phase matching between the parametrically interacting waves. Dimensionless material parameter $\chi \equiv \chi_1\chi_3/\chi_2^2 = 9(\sigma_1/\sigma_2)^2$ depends on the type of phase matching, and it can take different values of order of one. For example, when both SHG and SFM are due to quasi-phase matching (QPM), we have $\sigma_j = (2/\pi m)(\pi/\lambda_1 n_1)\chi^{(2)}[\omega; (4-j)\omega; -(3-j)\omega]$, where $j = 1, 2$. Then, for the first-order ($m = 1$) QPM processes (see, e.g., Ref. [6]), we have $\sigma_1 = \sigma_2$, and therefore $\chi = 9$. When SFM is due to the third-order QPM process (see, e.g., Ref. [7]), we should take $\sigma_1 = \sigma_2/3$, and therefore $\chi = 1$. At last, when SFM is the fifth-order QPM process, we have $\sigma_1 = \sigma_2/5$ and $\chi = 9/25$.

Dimensionless equations (3) present a fundamental model for three-wave multistep cascading solitons in the absence of walk-off. Additionally to the type I SHG solitons (see, e.g., Refs [5]), the multistep cascading solitons involve the phase-matched SFM interaction ($\omega + 2\omega = 3\omega$) that generates a third harmonic wave. If this latter process is not phase-matched, we should consider α_1 as a large parameter, and then look for solutions of Eq. (3) in the form of an asymptotic series in α_1. Substituting $w = w_0 + \varepsilon w_1 + \ldots$, $v = v_0 + \varepsilon v_1 + \ldots$ and $u = \varepsilon u_1$, where $\varepsilon \equiv \alpha_1^{-1}$, we find $u_1 \approx \chi v w$, and Eqs. (3) reduce to the model,

$$\begin{aligned} i\frac{\partial w}{\partial z} + \frac{\partial^2 w}{\partial x^2} - w + w^* v + \varepsilon\chi|v|^2 w = 0, \\ 2i\frac{\partial v}{\partial z} + \frac{\partial^2 v}{\partial x^2} - \alpha v + \frac{w^2}{2} + \varepsilon\chi|w|^2 v = 0. \end{aligned} \tag{4}$$

In the limit $\varepsilon \to 0$, Eqs. (4) coincide with the model of two-wave solitons analysed in Refs. [5].

For smaller α_1, the system (3) cannot be reduced to Eq. (4), and its two-parameter family of localised solutions consists of three mutually coupled waves. It is interesting to note that, similar to the case of nondegenerate three-wave mixing [8], Eqs. (3) possess an exact solution. To find it, we make a substitution $w = w_0 \operatorname{sech}^2(\eta x)$, $v = v_0 \operatorname{sech}^2(\eta x)$ and $u = u_0 \operatorname{sech}^2(\eta x)$, and obtain unknown parameters from the following algebraic equations $w_0^2 = 9v_0/(3 + 4\chi v_0)$, $4\chi v_0^2 + 6v_0 = 9$, $u_0 = \frac{2}{3}\chi w_0 v_0$ valid for $\eta = \frac{1}{2}$ and $\alpha = \alpha_1 = 1$. These equations have two solutions corresponding to *positive* and *negative* values of the amplitude. This indicates a possibility of multivalued solutions, even within the class of exact solutions.

In a general case, three-wave solitons of Eqs. (3) can be found only numerically. Figures 1(a) and 1(b) present two examples of solitary waves for different sets of the mismatch parameters α and α_1. When $\alpha_1 \gg 1$ [see Fig. 1(a)], which corresponds to an unmatched SFM process, the amplitude of the third harmonic is small, and it vanishes for $\alpha_1 \to \infty$ according to the asymptotic solution of Eq. (4) discussed above.

To summarise different types of three-wave solitary waves, in Fig. 2 we plot the dependence of the total soliton power defined as

$$P = \int_{-\infty}^{+\infty} dx \left(|w|^2 + 4|v|^2 + \frac{9}{\chi}|u|^2 \right), \tag{5}$$

on the mismatch parameter α_1, for fixed $\alpha = 1$. It is clearly seen that for some values of α_1 (including the exact solution at $\alpha_1 = 1$ shown by two filled circles), there exist *two different branches* of three-wave solitary waves, and only one of those branches approaches, for large values of α_1, a family of two-wave solitons of the cascading limit (Fig. 2, dashed). The slope of the branches changes from negative (for small α_1) to positive (for large α_1), indicating a possible change of the soliton stability. However, the soliton stability should be defined in terms of physical parameters, and in the case of two-parameter solitons as we have here, the stability threshold is determined by a certain integral determinant condition, similar to that first derived for the three-wave mixing problem [9].

Ratios of the maximum amplitudes of the soliton components for the three-wave solitons of the lower branch

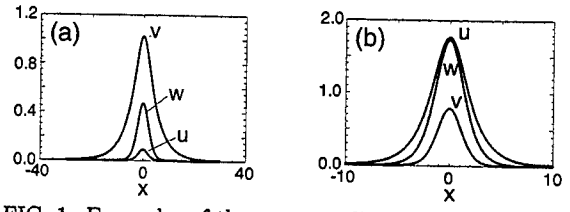


FIG. 1. Examples of three-wave solitary waves of Eqs. (3) for (a) $\alpha = 0.05$, $\alpha_1 = 5$, and (b) $\alpha = 5$, $\alpha_1 = 0.35$.

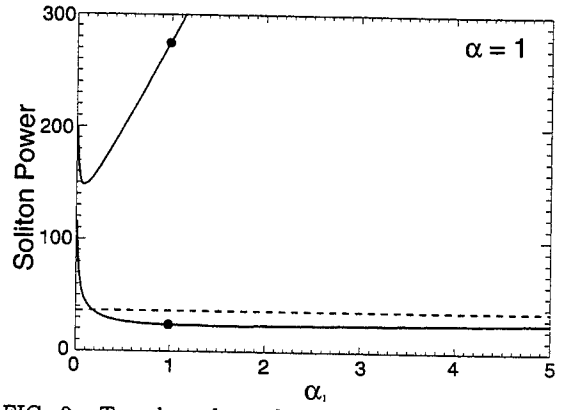


FIG. 2. Two branches of multistep cascading solitons shown as the total soliton power P vs. α_1 for $\alpha = 1$ and $\chi = 1$. Filled circles show the analytical solutions. The lower branch approaches a family of two-wave quadratic solitons (for $\alpha_1 \to \infty$) shown by a dashed line.

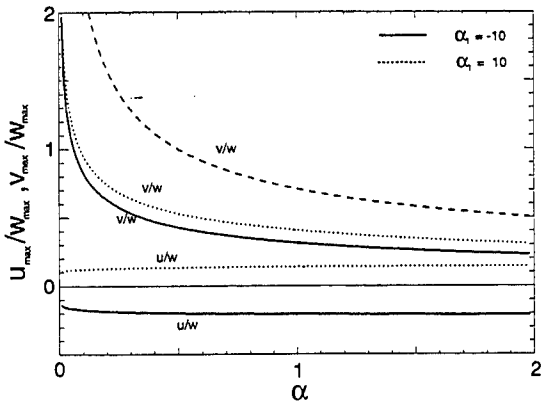


FIG. 3. Peak intensity ratios for the family of three-wave solitary waves ($\chi = 1$) at $\alpha_1 = -10$ (solid), $\alpha_1 = 10$ (doted). Upper dashed curve shows the asymptotic limit of large α_1 corresponding to the two-wave quadratic solitons.

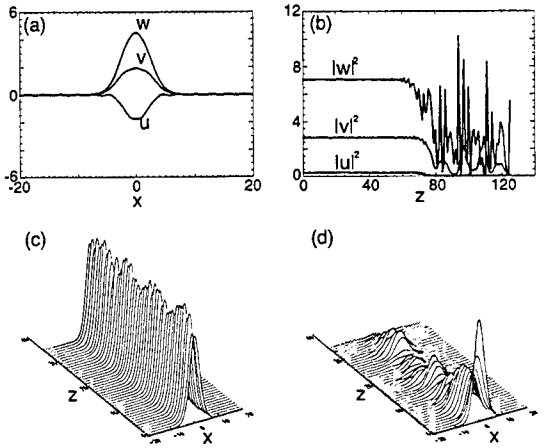


FIG. 4. Examples of (a) a three-wave quasi-soliton ($\alpha = 1$, $\alpha_1 = -5$) and (b) its instability-induced long-term evolution shown for the peak intensities ($\alpha = 1$, $\alpha_1 = -10$). (c,d) Evolution of the fundamental harmonic of a two-wave soliton owing to an unseeded unmatched SFM process with $\alpha_1 = +8$ and $\alpha_1 = -8$, respectively.

in the model (3) are presented in Fig. 3, where the upper dashed curve is the asymptotic limit of two-wave solitons for $\alpha_1 \to \infty$. Soliton solutions of the second (upper) branch in Fig. 2 correspond to large values of the total power and they have been verified numerically to be unstable.

The analysis of the asymptotics for Eqs. (3) suggests that localised solutions should not occur for $\alpha_1 < 0$. However, we reveal the existence of an extended class of relatively robust localised solutions which we classify as 'quasi-solitons' [10], solitary waves with small-amplitude oscillating tails. In principle, such solitons are known in one-component models (see, e.g., Ref. [11]) but here the nonvanishing tails appear only due to a resonance with the third-harmonic field [see Fig. 4(a)]. Such solitons are expected to be weakly unstable, and this is indeed demonstrated in Fig. 4(b) for rather long propagation distances.

Existence of quasi-solitons for any value of negative phase-matching with a higher-order harmonic field indicates that all two-wave quadratic solitons *can become unstable* due to an additional SFM process. This is confirmed in Figs. 4(c,d) where we present the results of numerical simulations of the dynamics of an initially launched two-wave soliton for two cases, positive and negative phase-matching of a SFM process. For $\alpha_1 > 0$ [see Fig. 4(c)], a small harmonic ($v_{\max} \approx 0.1$) is generated and the initial two-component beam converges to a three-wave soliton. In contrast, for $\alpha_1 < 0$ [see Fig. 4(d)], the input beam decays rapidly into radiation and diffracting harmonic fields.

In conclusion, we have investigated, analytically and numerically, multistep cascading and nonlinear beam propagation in a diffractive optical medium and introduced a novel type of three-wave parametric spatial optical solitons, multistep cascading solitons. The detailed analysis of the soliton stability, the effect of walk-off, higher-dimensional and spatio-temporal effects are possible directions of the future research.

The authors are indebted to K. Koynov, R. Schiek, and E. Kuznetsov for useful discussions. The work has been partially supported by the Australian Photonics Cooperative Research Centre.

[1] For an overview, see G. Stegeman, D.J. Hagan, and L. Torner, Opt. Quantum Electron. **28**, 1691 (1996); Yu.S. Kivshar, In: *Advanced Photonics with Second-Order Optically Nonlinear Processes*, Eds. A.D. Boardman *et al.* (Kluwer, Amsterdam, 1998), p. 451.

[2] D.E. Pelinovsky, A.V. Buryak, and Yu.S. Kivshar, Phys. Rev. Lett. **75**, 591 (1995).

[3] K. Koynov and S. Saltiel, Opt. Commun. **152**, 96 (1998).

[4] See, e.g., S. Akhmanov, A. Dubovik, S. Saltiel, I. Tomov, and V. Tunkin, JETP Lett. **20**, 117 (1974).

[5] A.V. Buryak and Yu.S. Kivshar, Opt. Lett. **20**, 1612 (1994); Phys. Lett. A **197**, 407 (1995).

[6] O. Pfister, J.S. Wells, L. Hollberg, L. Zink, D.A. Van Baak, M.D. Levenson, and W.R. Basenberg, Opt. Lett. **22**, 1211 (1997).

[7] P. Baldi, C.G. Trevino-Palacios, G.I. Stegeman, M.P. De Micheli, D.B. Ostrowsky, D. Delacourt, and M. Papuchon, Electron. Lett. **31**, 1350 (1995).

[8] B.A. Malomed, D. Anderson, and M. Lisak, Opt. Commun. **126**, 251 (1996).

[9] A.V. Buryak, Yu.S. Kivshar, and S. Trillo, Phys. Rev. Lett. **77**, 5210 (1996).

[10] V.E. Zakharov and E.A. Kuznetsov, Zh. Eksp. Teor. Fiz. **113**, 1892 (1998) [JETP **86**, 1035 (1998)].

[11] See, e.g., V.I. Karpman, Phys. Lett. A **193**, 355 (1994).

Magneto-optic cavity multistability and polarized dissipative solitons: dissitons

N.N.Rosanov and D.V.Liseev
Institute for Laser Physics, Vavilov State Optical Institute,
12 Birzhevaya liniya, St. Petersburg, 199034 Russia
rosanov@ilph.spb.su

A.D.Boardman and M.Xie
Photonics and Nonlinear Science Group
University of Salford, Salford, UK
A.D.Boardman@physics.salford.ac.uk

We consider regimes of a transversely distributed cavity, which is filled with a planar magneto-optic nonlinear waveguide and is driven by an external coherent radiation. Even without a cavity, nonlinear magneto-optic planar waveguides are promising for applications because of adequate combination of nonlinear optical and polarization magneto-optic effects and of feasibility of integration with lasers, detectors and so on; a theory of magneto-optic spatial solitons in such the waveguides was given in [1]. On the other hand, classical cavity bistability [2] and scalar spatial solitons in wide-aperture driven cavities [3-5] demonstrate the rich potential of these dissipative schemes. The goal of this report is a study of the schemes that combine the advantages of the two approaches and thus are promising for applications in optical information processing. The governing equations for the electric field envelopes $\psi_{1,2}$, corresponding to two circular polarisations inside the cavity filled with a medium with Kerr nonlinearity, in the mean-field approximation are

$$\frac{\partial \psi_2}{\partial t} - i\frac{\partial^2 \psi_2}{\partial x^2} - 2i\alpha(|\psi_2|^2 + \mu|\psi_1|^2)\psi_1 - iQ\psi_2 + \varsigma_2\psi_2 - E_{i,2} = 0.$$

$$\frac{\partial \psi_1}{\partial t} - i\frac{\partial^2 \psi_1}{\partial x^2} - 2i\alpha(|\psi_1|^2 + \mu|\psi_2|^2)\psi_1 + iQ\psi_1 + \varsigma_1\psi_1 - E_{i,1} = 0,$$

Here t is dimensionless time, x is a dimensionless transverse coordinate, parameter $\alpha = 1$ or -1 for self-focusing or self-defocusing media. The parameter $\mu = 2$ for electronic nonlinearity, the value Q is the magneto-optic parameter, complex values $\zeta_{1,2}$ describe losses and detunings for the two polarizations, and $E_{i1,2}$ are dimensionless envelopes of external radiation with corresponding polarization. By scaling of time $Qt \to t$, coordinate $Q^{1/2}x \to x$, and so on, it is possible to assume $Q = 1$. In what follows we assume that frequencies of the external radiation for the two polarizations coincide ($\zeta_1 = \zeta_2$), that intensities of these external waves are equal ($E_{i,1} = E_{i,2}$), and $\alpha = 1$.

Intensities of steady-state homogeneous wave are determined from two coupled cubic algebraic equations. Thus there are from one to nine solutions. An interesting feature of the dependencies of intensities $I_{1,2} = |E_{1,2}|^2$ on intensity of external plane wave $I_i = |E_i|^2$ is appearance of closed loops.

Our next step is a linear stability analysis, when time-dependent transversely homogeneous small perturbations are introduced. The analysis indicates that, depending on parameters, there are mono-, bi- and multistability. It is important to distinguish the two types of loss of stability. First, if at the boundary of

stability we have a real root, and it changes its sign when we cross the boundary. This is a saddle-node bifurcation corresponding to edges of branches of intensity dependence $I_{1,2}(I_i)$. More interesting is the case when there is a pair of complex-conjugated roots with nonzero imaginary part, and real part changes its sign crossing the boundary. In this case (a Hopf bifurcation) creation of stable periodic regime near unstable stationary regime is possible. By direct solution of the governing equations we demonstrate such the periodic regimes and transient to them. Note that we have here a generalized bistability (coexistence of stationary and periodic regimes).

In more the general case the perturbations depend on the transverse coordinate x (modulation instability). Because the problem is linear for small perturbations, it is possible to use a Fourier transform with coordinate dependence of the elementary perturbation of the form $\exp(\pm i\kappa x)$, where κ is the perturbation spatial frequency. The time dependence of the elementary perturbation is $\exp(\gamma t)$ where $\gamma = \gamma(\kappa)$ is the complex perturbation increment. Typically, modulation instability ($\mathrm{Re}\,\gamma > 0$) occurs for all the branches of the dependence of $I_{1,2} = |E_{1,2}|^2$ on the intensity of external plane wave $I_i = |E_i|^2$ with one exception of the lower branch, which is stable against any small perturbations ($\mathrm{Re}\,\gamma < 0$). Perturbations grow only in some finite range of the spatial frequencies, $\kappa_{min} < \kappa < \kappa_{max}$, $\kappa_{min} > 0$. Therefore, it is possible to suppress modulation instability by spatial filtering inside the cavity. The dependence $\gamma(\kappa)$ was calculated for some sets of parameters. Direct solution of the governing equations under conditions of modulation instability shows the following transverse patterns of radiation.

First, for large enough intensity of the external radiation, when the lower branch does not exist, typical are spatio-temporal field distributions with deep modulation that seem to be chaotic.

Second, within the wide range of intensity of the external radiation close to the range of coexistence of the lower and one of other branches (with modulation instability), the localized structures arise - the polarized dissipative solitons, or *dissitons*. For them, the transverse profiles of real and imaginary parts of the envelope have a bell-like shape on the constant background corresponding to the lower branch of homogeneous distributions. One of corresponding intensity profiles is given in Fig. 1. The *dissiton* nature is the same as for scalar *dissitons*, or "*diffractive autosolitons*" [3-5]. They are similar to the special type of the scalar *dissitons*, when one of the branches of homogeneous distributions exhibits modulation instability; this type of *dissitons* was first studied in [6,7] and later in [8]. The polarized *dissitons* exist even in a small range of intensities where the only homogeneous distribution is the lower branch (no "classical" bistability); the possibility of such situation for the scalar *dissitons* was pointed out in [9].

In conclusion, we have proposed for the first time a theory of a wide-aperture cavity filled with a planar magneto-optic waveguide with Kerr nonlinearity, driven by a coherent radiation (plane wave). For transversely homogeneous field distributions we have found conditions of mono-, bi- and multistability (up to nine solutions for fixed parameters of the scheme). Corresponding dependence of output intensities on intensity of incident wave includes closed loops (*isolas*). With a change of the scheme parameters, bifurcations occur, including Hopf bifurcation, when loss of stability of the steady-state regimes is accompanied by appearing of regimes periodic in time. In this case generalized bistability (coexistence of steady-state and periodic regimes) takes place.

Optical patterns under conditions of modulation instability have been studied. The most important results concern to the polarized localized dissipative structures of radiation, or polarized (magneto-optic) *dissitons*. They are characterized by an extremely wide range of existence, which, in combination with hard (threshold-like) type of excitation and such an additional degree of freedom as polarisation, gives promise for various applications for optical information processing.

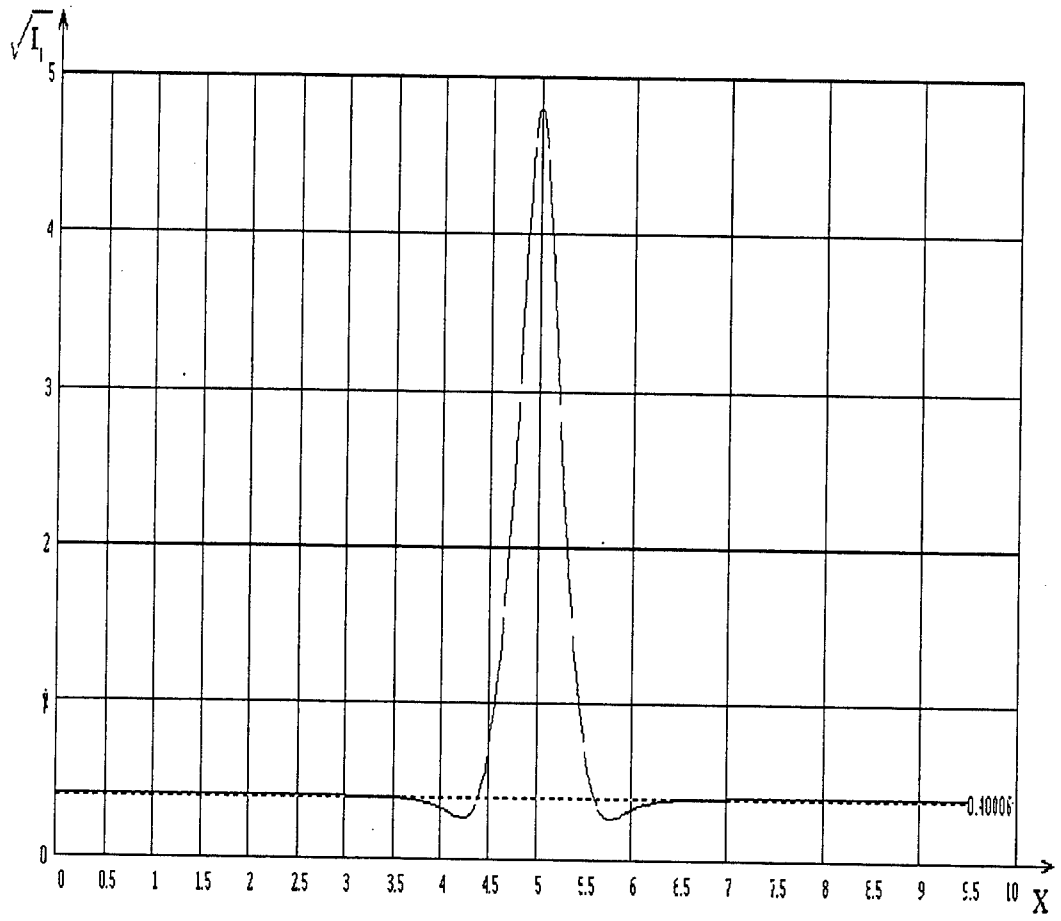


Fig. 1. Transverse profile of amplitude $|\psi_1|$ for the dissiton.

References

[1] A.D.Boardman, K.Xie. JOSA B **14**, 3102, 1997.
[2] H.M.Gibbs. Optical bistability – Controlling light with light (Acad. Press, Orlando), 1985.
[3] N.N.Rosanov, G.V.Khodova. Opt.&Spectr. **65**, 449, 1988.
[4] N.N.Rosanov, A.V.Fedorov, G.V.Khodova. Phys. Status Solidi b **150**, 545, 1988.
[5] N.N.Rosanov. Progress in Optics **35**, 1, 1996.
[6] N.N.Rosanov, G.V.Khodova. Opt.&Spectr. **72**, 1403, 1992.
[7] S.V.Fedorov, G.V.Khodova, N.N.Rosanov. Proc. SPIE **1840**, 208, 1992.
[8] M.Tlidi, P.Mandel, R Lefever. Phys. Rev. Lett. **73**, 640, 1994.
[9] N.N.Rosanov, G.V.Khodova. JOSA B **7**, 1057, 1990.

Experimental observation of optical patterns in multi quantum well microcavities

I. Ganne, G. Slekys, I. Sagnes, and R. Kuszelewicz

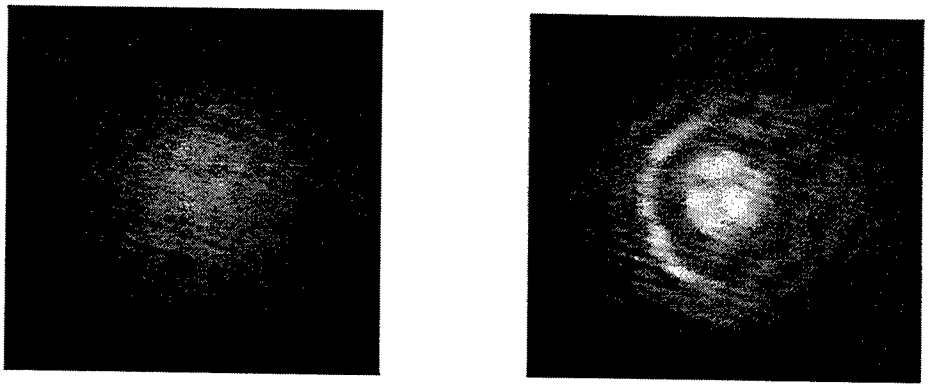
CNET- Laboratoire de Bagneux - B.P. 107
92225 Bagneux cedex – France
Tel : (33) 1 42 31 75 11
Fax : (33) 1 42 53 49 30
e-mail isabelle.ganne@cnet.francetelecom.fr

Summary :

There has been in the last decade an increasing development in the field of Transverse Nonlinear Optics (TNO), mostly because the interplay of nonlinear light propagation with transverse mechanisms such as light diffraction or transverse diffusion of excited lead to self-organization. Recently, systems including a nonlinear resonator have been a subject for intense and fruitful theoretical work. If originally, only the transverse homogeneous response of plane resonators was considered[1], the extension to the full account of transverse diffractive and eventually diffusive mechanisms, has introduced the ingredients necessary to a thorough description of patterns and localized (or solitonic) states[2,3]. In this approach, the cavity appears as a constitutive element of the complex mechanisms interacting within the system, in providing a feedback mechanism and thereby an additional contribution for stabilizing solitonic features[4,5].

Self-organizing properties of the optical response of resonators naturally point to applications in all-optical information processing domains, through the ability to form controlled arrays of optical information bits[6]. Moreover, it proposes quite innovative processing schemes including reconfigurable arrays and operative modes of the cellular automaton type. Recent modeling schemes have introduced direct gap semiconductors as candidate materials for realizing the active part of a nonlinear microresonator[7]. Indeed, III-V semiconductors display either purely dispersive or mixed absorptive-dispersive type of saturating nonlinearities. Moreover, due to their characteristic lifetime, at the nanosecond scale, semiconductor-based systems can serve high bit-rate processing. Stable localized states i.e. cavity solitons (CS) may exist, owing their existence to the destabilization by Modulational Instabilities (MI) of some section of the homogeneous lower or upper branches of the S-shaped transmission characteristic curve. In this respect, the defocusing case can yield the particular situation where the lower branch is unstable while the upper branch remains stable.

We report on the first experimental observation of such patterns in a passive resonator whose structure consists of a back mirror made of 23.5 pairs of a $Ga_{0.9}Al_{0.1}As/AlAs$ alternation of quarter-wave layers, a $3/2\lambda$-thick nonlinear layer including 18 GaAs wells of 100 Å thickness separated by 100 Å-thick $Ga_{0.7}Al_{0.3}As$ barriers, and finally a front mirror comprizing 17 pairs of the same alternation as for the front mirror. The whole structure is grown by Metal-Organic Vapor Phase Epitaxy (MOVPE). The sample characterizes by its short-range thickness fluctuations and long-range uniformity fluctuations.



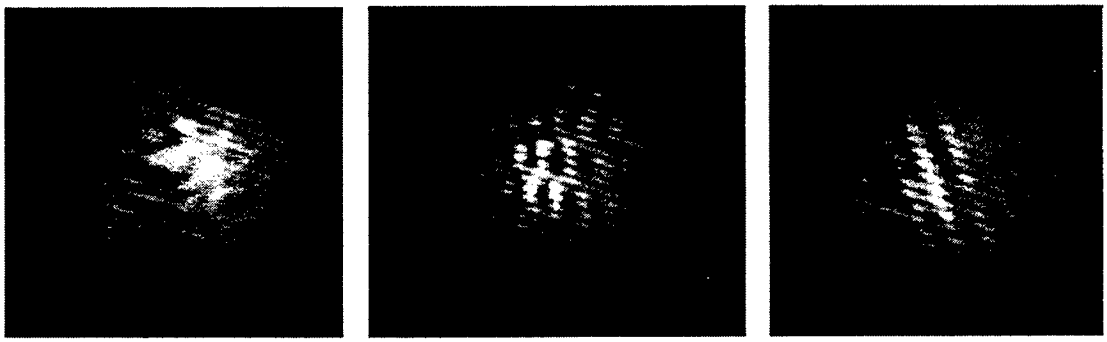
(a) (b)

Fig. 1 : Patterns observed in the reflective mode on a GaAlAs/GaAs MQW microcavity. (a) Modulational instability of the low excitation branch (high reflectivity) gives rise to a quasi-hexagonal pattern. As intensity increases (b), spatial switching occurs bringing the central part solely into a high excitation (low reflectivity) state.

The sample was excited in a regime corresponding to almost a purely dispersive saturable defocusing nonlinearity[8] in the Urbach's tail of absorption. The intensity level of rectangular optical incident pulses allowed to set the system at arbitrary positions with respect to the switching point. We were able to observe the bistable regime and evidenced spatial switching in the reflective mode (fig.1b). Then the beam split radially into two parts : a central part above threshold with lower reflected intensity, and a peripheral part still below. The two parts are connected by a switching front followed by damped diffraction oscillations of the intensity. Below threshold patterns could be observed at arbitrary low intensities (fig.1a) and seemed to owe their existence to a modulational instability of the high reflectivity branch. Surprisingly, when changing the intensity, no observable transition between an homogeneous and a patterned response could be detected. However, the transition was observed from an homogeneous response at larger wavelength detunings, to disordered and then regular patterns as the detuning was decreased. The contrast and regularity increased accordingly.

Due to the high finesse of these microresonators, thickness fluctuations, even at the scale of a single atomic layer, are influencing pattern formation. Various shapes of patterns have been observed,

depending on the position of the excitation beam on the sample, and revealing the symmetry of underlying fluctuations or defects. Figure 2 shows a series of patterns as different as random, hexagonal or stripe-like.



(a) (b) (c)

Fig. 2 : Various patterns obtained at different locations on the sample. Underlying spatial fluctuations of the sample properties induced (a) randomly distributed, (b) hexagon-like, or (c) stripe-like patterns.

In general one can consider two major contributions to the rise of patterns when the right domain of parameters is reached : field boundary conditions and fluctuations of the structure thickness. Their action is translated in the reciprocal space by specific selection rules. Here, in the absence of observable MI threshold, boundaries do not introduce strong conditions. Conversely, transverse fluctuations of cavity resonance are imposing their own. They act as an additional criterion for pattern selection by defining spatial scales and symmetries. Similarly, the role of internal material defects are found to be an important additional mechanism of the patterning process.

REFERENCES

[1] J.H. Marburger and F.S. Felber, Phys. Rev. A, **17**, 335 (1978) ; R. Kuszelewicz, J.-L.Oudar, J.C. Michel, and R. Azoulay, Appl. Phys. Lett., **53**, 22, 2138, (1988).
[2] L. Lugiato, M. Brambilla, and A. Gatti, Advances in Atomic, Molecular, and Optical Physics, **40** (1999)
[3] M. Tlidi, P. Mandel, and R. Lefever, Phys. Rev. Lett., **73**, 640 (1994)
[4] G. Slekys, K. Staliunas, and C. Weiss, Opt. Com., **149**, 113, (1998)
[5] C.O Weiss, ESPRIT LTR Project PASS Report (1997).
[6] W.J. Firth and A.C. Scroggie, Phys. Rev. Lett. **76**, 1623 (1996)
[7] M. Brambilla, L.A. Lugiato, F. Prati, L. Spinelli, and W.J. Firth, Phys. Rev. Lett. **79**, 2042 (1997)
[8] C. Etrich, U. Peschel, and F. Lederer, Phys. Rev. Lett. **79**, 2454 (1997)

Emission of coupled vortex beams from nonlinear VCSEL arrays

J. Scheuer, Y. Yadin, Y. Gross and M. Orenstein

Department of Electrical Engineering, Technion, Haifa 32000, Israel

Tel. 972-4-8294696, Fax. 972-4-8323041, E-mail: meiro@ee.technion.ac.il

Arrays of coherently coupled VCSELs were exhibited [1]. The VCSEL, which combines a nonlinear medium with a two dimensional optical resonator, enables the formation of complex optical field patterns. We present experimentally and theoretically coupled VCSEL arrays with novel emission patterns, in which each element is emitting an optical field vortex (or several vortices [3]). The nonlinearity of the laser oscillators enabled the locking of the emission from all the laser elements to form a single complex supermode of the array. This complex transverse pattern has a larger information content than the regular supermodes – namely the vortices "charge". The variety of supermodes exhibited by the vortex emitting arrays (compared to the regular supermodes) may contribute significantly to interconnection and free space optical information distribution [2].

We examined the transverse intensity patterns emerging from coherent arrays of proton implanted, medium area VCSELs (10-20μm in diameter each). The active layer consisted of three 8nm $In_{0.2}Ga_{0.8}As$ wells, emitting at ~0.95μm and the array was prepared by the mirror patterning method [1]. The near-field (NF), far-field (FF), spectral intensity patterns were examined at room temperature under pulsed operation.

At low injection current – the arrays of coupled VCSELs emitted only the regular anti-phase supermodes which have a lower loss relative to the in-phase supermodes (due to their zero amplitude in the interlaser spacing). Cyclic arrays of an odd number of lasers could not emit an odd number of anti-phase lobs due to phase frustration. When the threshold current was reached in these structures, the array emitted an even number of anti-phase lobs, either by merging the emission of 2 adjacent lasers, or by a double lobe splitting the emission of one of the lasers[4].

When the injection current was increased, all the lasers in the array simultaneously switched to an identical pattern consisting of a single "black" optical vortex (Figs. 1-3), or a combination of several black vortices (to be presented at the meeting [3]).

Thus the VCSELs arrays were emitting an overall optical field made of a multiple vortices array - each with absolute spin "charge 1" (Figs. 1-3). For this emission - each laser element of the array was carrying two independent "charge" types: 1. It's amplitude sign relative to the neighboring lasers (either in-phase or anti-phase), and 2. The vortex "spin" (±1). The interplay of the two charges enabled the VCSEL arrays to exhibit a rich variety of complex supermodes.

The vortex spin and the relative amplitude signs of the lasers were determined experimentally by measuring the NF, FF and NF interference patterns. The vortices spins were determined by the NF interference pattern (e.g. Fig. 2). The image of the NF pattern and a plane wave were brought to interference. Due to the phase shift in the vortex, constructive interference on one side of the vortex became destructive on the other side, and one interference fringe disappeared. The direction of the disappearance depends on the sign of the spin. Fig. 2 shows the disappearance of

an interference fringe in each of the two vortices, in the same direction (the fringe exists on the upper side of the vortex and disappears on the lower side). This pattern is therefore an emission of two coupled vortices having the same spin.

The "amplitude sign" of the optical field emitted by each laser was determined by examining the FF pattern. The FF pattern of two identical sources is the same as the FF of one source multiplied by a sine (for anti-phase locking) or a cosine (for in-phase locking). If the sources are not identical, as in the case of opposite spin values, the FF pattern is more complex, but still clearly distinguishes between the in-phase and anti-phase locking. We calculated the FF distributions (see figures) and compared them to the experimental findings to resolve the amplitude signs.

For linear VCSEL arrays – two types of locked vortices configurations were observed: 1. Anti-phase supermode, similar to the regular supermode observed previously. The spins in this supermode were identical (Fig. 2) 2. In-phase combination, with alternating spins (figure not presented here).

Cyclic VCSEL arrays with an even number of lasers (Fig. 3b) exhibited the anti-phase supermode, with identical spins for all vortices. The coupled multi-vortices emission exhibited an odd number of "black" beams (Figs. 3a, 3c), which were locked in-phase, and with identical spins. However – the NF distribution is much more complicated than could be seen at first glance. This kind of locking essentially generates an optical vortex with an opposite spin in each interlaser spacing. For example, the array shown in fig. 5c consists of 5 vortices of spin 1 in the middle of each lob, 5 vortices of spin –1 in each interlaser spacing, and an additional vortex of spin 1 in the center of the array. The total number of vortices is 11, with a net charge of +1. The vortex in the interlaser spacing is accompanied by a zero amplitude value, which is responsible for this mode to experience small losses.

Complex and rich combinations of coupled vortices beams emerged from medium size VCSELs arrays. In the presentation we will discuss the generation and coupling of vortex arrays in VCSEL nonlinear resonators, the selection rules for the exhibited supermodes, and the vortex charge conservation as a tool for tailoring desired far-field patterns.

REFERENCES

[1] M. Orenstein et al, Appl. Phys. Lett. 58, 804 (1996)
[2] M. Orenstein et al, LEOS 1990, Boston MA, paper SDL1.2/MKK2
[3] The emission of multiple vortices from a single VCSEL: J. Scheuer et al, Non Linear Optics 98' Princeville, Kawai, Hawaii, paper ThC13, pp. 361.
[4] T. Fishman et al, Opt. Lett. 21, 600 (1996).

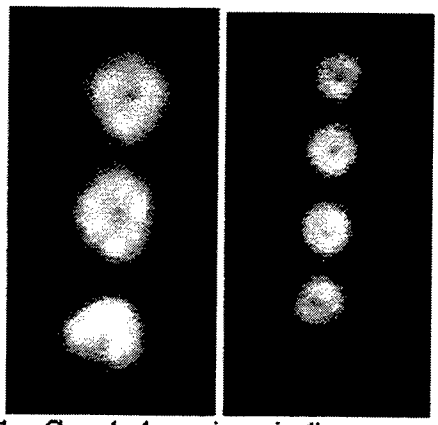


Figure 1 - Coupled vortices in linear arrays

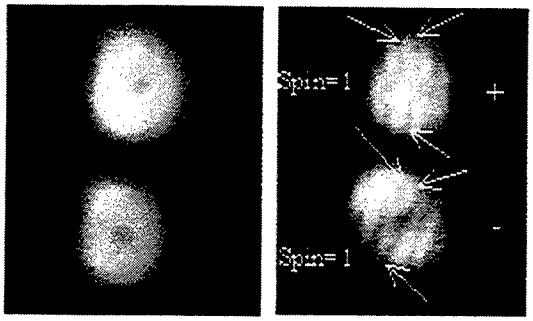


Figure 2 - anti-phase coupled vortices with identical spin - NF and interference pattern

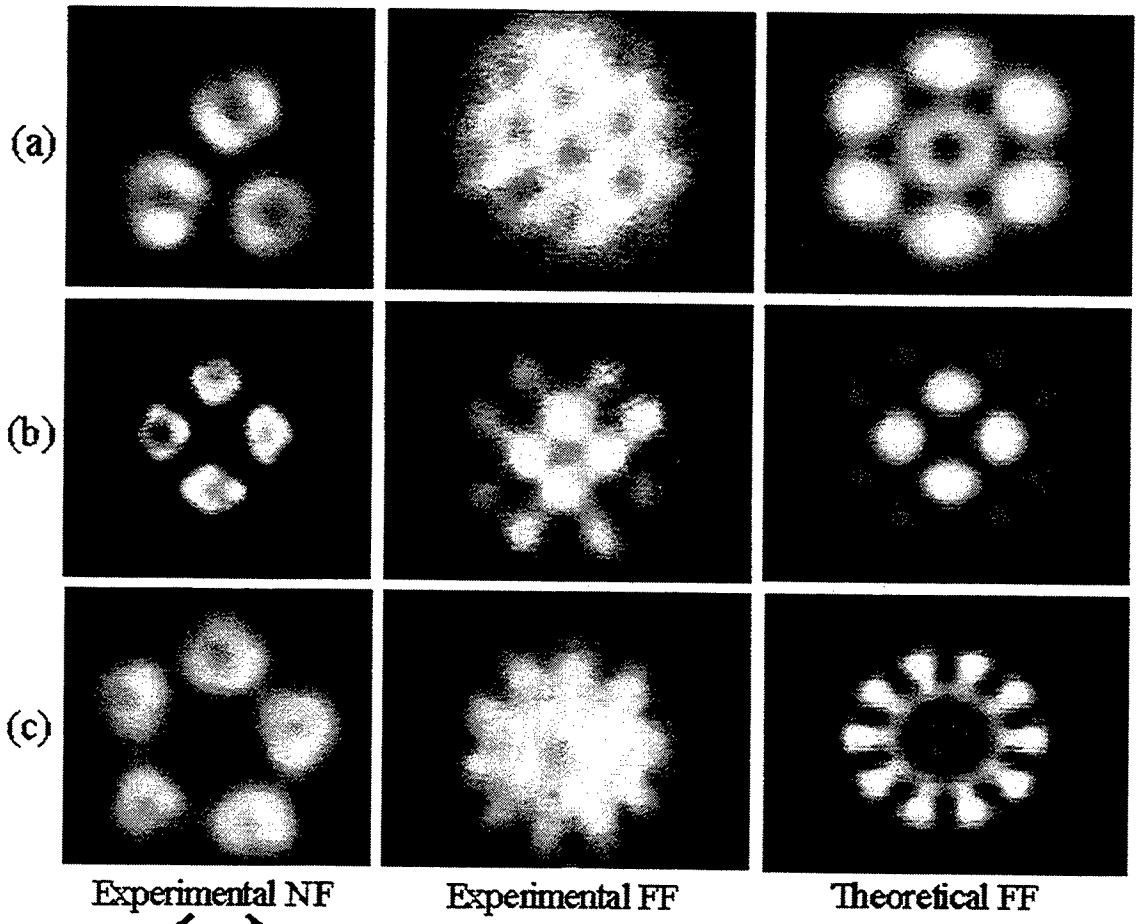


Figure 3 – vortices from cyclic coupled VCSELs. (a), (c) - 3,5 elements in-phase. (b) 4 elements – anti phase. Injection currents ~ 130-150mA.

Self-organized light pixels in semiconductor microresonators for optical information processing

M. Brambilla, T. Maggipinto and I. Perrini
INFM e Dipartimento Interateneo di Fisica, Università e Politecnico di Bari,
Via E.Orabona 4, 70126 Bari, ITALY. Fax +39-080-5442434
brambilla@fisica.uniba.it, t.maggipinto@fisica.uniba.it

L. A. Lugiato, L. Spinelli, G. Tissoni
INFM e Dipartimento di Scienze Chimiche, Fisiche e Naturali, Università dell'Insubria,
Via Lucini 3, 22100 Como, ITALY.
luigi.lugiato@mi.infn.it, lorenzo.spinelli@mi.infn.it, giovanna.lia.tissoni@mi.infn.it

The ever increasing level of integration between light and electronics in information processing devices has recently benefitted from the microscale architecturing of semiconductor-based optical resonators. These have been widely implemented in order to realize light pixels which can in turn be the entity where the light signal is treated in an all-optical manner (amplification, commutation, see e.g. [1]), or interfaced to a micro-electronic circuitry stage for a hybrid processing of the signal (see e.g. [2]). By means of various etching techniques, arrays of vertical microresonators can be obtained, each of them being separately addressed by an external beam (or electrical current). While this approach has certainly exploited interesting features, there remain some problems concerning all-optical information treatment, linked e.g. to the accuracy needed in interfacing the addressing beam and/or the readout stage, or to the rigidity of the array with respect to reconfigurability, signal fan-in and fan-out, channel commutation.

To this point, recent theoretical works ([3,4] and references quoted therein) predicted the stability of self-organized light peaks in broad area nonlinear resonators, which can be regarded as the result of a localization of a global morphogenic process occurring in the transverse profile of the coherent field emitted by such classes of resonators in presence of a modulational instability. The onset of pattern forming instabilities is strictly related to the coupling of diffractive and nonlinear phenomena in the light propagation process through the resonator, the feedback action of reflectors causing the structure to become self-sustained at regime and appear as a stationary modulation of the field profile. Experimental evidences have been provided about such light peaks (which are commonly called Cavity Solitons (CS)) demonstrated experimentally in liquid crystal light valves [5] and in lasers with saturable absorbers [6].

A significant progress towards application of the CS as a light pixel, has been set by the prediction of stable CS in microresonators based on a MQW GaAs/GaAlAs nonlinear layer [7,8]. CS appear stable for sizeable parametric domains and injected field intensities which fall within experimental feasibility, and can be found both in regimes of pure carrier photogeneration , and in presence of an electrical injection of carriers. An important feature is the stability of the CS even in presence of well known anti-patterning medium characters, as carrier diffusion and self-defocusing nonlinearity (see also [9]) which is the typical response of a MQW device when the injection occurs on the red side of the excitonic resonance.

We obtained recently a significant progress in the theoretical description of these phenomena by formulating and analyzing a microscopic model which provides a much improved description of the optical nonlinearities in such microresonators. This approach applies, for the moment, to the case of bulk semiconductor media, this being a simpler device to grow in highly homogenous broad area samples, by means of epitaxial techniques [10].

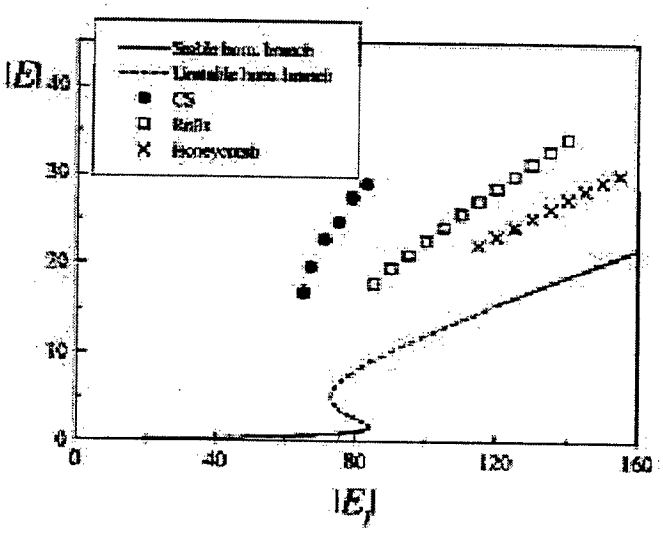


Fig. 1: The stationary curve for the intracavity field versus the input field in a bulk microresonator: the full line plots the homogeneous field intensity, the dashed portion thereof indicates the regime of injection where a modulational instability leads to pattern formation. Different symbols indicate the branch of different stable patterns obtained in the numerics.

The two key features of the cavity soliton, which makes it an appealing bit-wise unit to encode and treat information, are the self-confinement and its mobility in the transverse section of the resonator. The first feature makes it possible to excite a soliton at a precise location of the device's section by shining a narrow pulse which can then be turned off. The self-sustaining feedback action of the resonator lets the CS live for an indefinite time in principle. Iterating the procedure, any number of pulses can excite an equivalent number of CS in different locations, provided that the CS at regime do not exceed a certain density which our models allow to interpret intuitively. The tolerance requirements on the pulse intensity, phase and duration are quite relaxed, due to the stability of the CS.

The second feature is intrinsic in the diffractive-nonlinear confinement of the CS, at difference from what happens in arrays of microresonators [11] where the etched material confines the radiation. As it appears from simulations, CS shift quite robustly across the transverse section of the device, following phase or intensity gradients of the input beam. This not only means that we can bring bits to a controlled interaction, by acting on the external field profile, but also that the maxima of the profile are stable locations for CS, which are thus "trapped" against e.g. noise-induced Brownian motion. CS can be arranged in arrays which are in principle easily reconfigured, provided one can control the position of the maxima in the input field profile.

On the basis of these fundamental properties of CS we have developed a theoretical/numerical investigation of the applicative aspects of these flexible pixels, contemplating schemes for signal amplification and commutation via CS, all-optical logic gates and processing [12].

Since the aforementioned predictions, an intense experimental activity was initiated within the framework of an ESPRIT European Programs and our theoretical activity has been focused towards the modelistic inclusion of the main features characterizing these devices on a more realistic point of view. Among the more significant issues, we have studied the role of Gaussian and super-Gaussian beam in influencing the appearance of patterns and changing the stability scenario of CS, another mainstream of activity was the analysis of the effect of the slow carrier dynamics in the pattern and soliton dynamics, and

an attentive investigation was performed about the relevance of the microcavity resonance fluctuations due to layer inhomogeneities, which are intrinsic in MOVPE growth of devices which have been obtained and studied at CNET Labs in Bagneux. We have evidences that the present experimental observations at CNET and PTB (Braunshcweig) are compatible with the prediction of our models, although a reliable validation is still on its way.

References

1. W. F. Sharfin and M. Dagenais, Appl. Phys. Lett. **48**, 321 (1986).
2. Dong-Su Kim, J. Chris Dries, Milind R. Gokhale and Stephen R. Forrest, IEEE J. Quantum Electron. **33**, 1407 (1997).
3. W. J. Firth and A. J. Scroggie, Phys. Rev. Lett. **76**, 1623 (1996).
4. M. Brambilla, L. A. Lugiato and M. Stefani, Europhys. Lett. **34**, 109 (1996).
5. A. Schreiber, B. Thuring, M. Kreuzer and T. Tschudi, Opt. Commun. **136**, 415 (1997).
6. V. B. Taranenko, K. Staliunas and C. O. Weiss, Phys. Rev. A **56**, 1582 (1997).
7. M. Brambilla, L. A. Lugiato, F. Prati, L. Spinelli and W. J. Firth, Phys. Rev. Lett. **79**, 2042 (1997).
8. L. Spinelli, G. Tissoni, M. Brambilla, F. Prati and L. A. Lugiato, Phys. Rev. A **58**, 2542 (1998).
9. D. Michaelis, U. Peschel and F. Lederer, Phys. Rev. A **56**, R3366 (1997).
10. G. Tissoni, L. Spinelli, M. Brambilla, I. Perrini, T. Maggipinto and L. A. Lugiato, *Cavity solitons in bulk semiconductor microcavities. I. Microscopic model and modulational instabilities; II. Dynamical properties and control*, submitted for publication to J. Opt. Soc. Am. B (1999).
11. T. Rivera, F. R. Ladan, A. Izrael, R. Azoulay, R. Kuszelewicz and J. L. Oudar, Appl. Phys. Lett. 64, 869 (1994).
12. L. Spinelli and M. Brambilla, *Signal amplification by means of cavity solitons in semiconductor microcavities*, in press on European Phys. J. D (1999).

Donut like Patterns in Intracavity Second Harmonic generation

Rumen Iliew, Pey-Schuan Jian, William E. Torruellas
Department of Physics, Washington State University
Pullman, WA 99164-2814
Tel.: 1-509-335 4671
Email: williamt@wsu.edu

Falk Lederer
Friedrich-Schiller-Universitaet, Institute of Solid-State Theory and Theoretical Optics,
Max-Wien-Platz 1, O7743 Jena, Germany

Summary

Because of the recent advances in high-power diode lasers producing in certain cases over 50 Watts of CW power, solid state lasers have seen a renaissance. Achieving optimum efficiencies in spectral regions where no solid state laser material is known to operate and controlling the patterns produced by the laser system with nonlinear optical elements offers an array of new opportunities for nonlinear guided waves applications. We present here an example of such an application aimed at optically manipulating gas bubbles in out of space experiments.

Due to the large absorption present in the near and mid-infrared in most liquids and in particular water, in order to manipulate large particles and bubbles we are forced to operate in the visible portion of the spectrum. Our experience has shown that laser beams at for example 1064nm produce thermal turbulence in most liquids making the optical stabilization of particles and bubbles and as a result their manipulation literally impossible under normal laboratory conditions.

Furthermore, to the best of our knowledge, no diode laser or solid state laser is known to directly emit in the blue-green region of the spectrum with CW powers in excess of 1 Watt. As a result we have implemented an intracavity frequency-doubling scheme producing a "donut-like" laser pattern with over 5 Watts of CW power at 532nm near the absorption minimum of water.

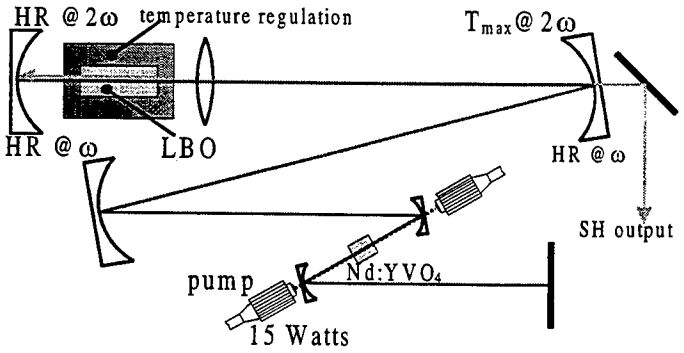


Figure 1: Intracavity frequency doubling geometry. The laser crystal is Neodymium doped Yttrium-Vanadate ($Nd:YVO_4$) and the frequency doubling crystal is a 2cm long, temperature tuned Lithium-TriBorate (LBO). We have modified an existing commercial laser to demonstrate that mode control is achievable in intracavity frequency doubling with an all-solid-state-laser-system.

A natural question then arises: *How can we produce a "donut-like" mode pattern at 532 nm maintaining an optimum operation for the laser?* The answer is relatively simple. Introducing intracavity losses has shown to be futile because of the large intracavity optical powers involved in the near IR. With intracavity powers in excess of 200 Watts we have been able to melt for example thin metal wires. Extra cavity mode converters would add an additional degree of complexity in the system. We have thus chosen to obtain mode control with the intracavity second harmonic element.

With our setup we have been able to produce a series of "donut-like" laser beam patterns with powers at 532nm in excess of 5 Watts.

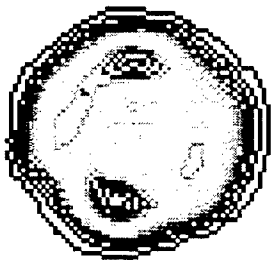


Figure 2: Mode pattern generated by our intracavity SHG system.

The above figures show our experimental setup and one of the mode patterns we have obtained with our intracavity frequency doubled laser. Note the two-fold symmetry in the laser pattern, indicative of the interference between the TEM_{00} mode and the TEM_{02}* mode. We have obtained similar patterns with a four-fold symmetry, verifying that the cavity geometry allows us to chose higher order modes with azimuthal symmetry.



Figure 3: Single and multiple bubble trapping with our laser

We have been able to trap single and multiple bubbles with our setup. The above two figures show the intense scattering from air bubbles when they are trapped, in other words when buoyancy is counteracted by optical radiation pressure with a laser beam coming from the top of the figures.

We will present simple models based on mode expansions allowing qualitative and almost-quantitative estimates of the efficiency of intracavity frequency doubling. These models point to the physical mechanisms involved in the pattern generation we have observed.

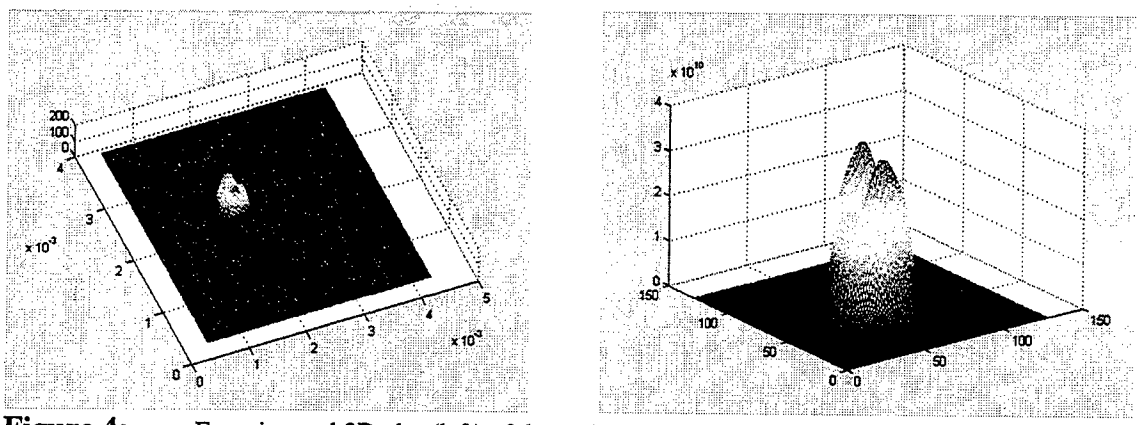


Figure 4: Experimetnal 3D plot (left) of the optical and theoretical prediction (right) figure above.

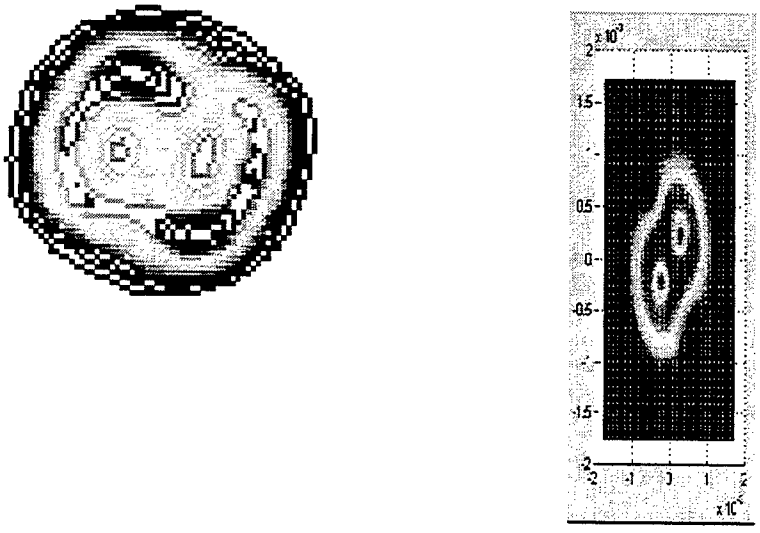


Figure 5: Experimental pattern (left) and theoretical prediction (right)

We have been able to predict and demonstrate more complex optical patterns with higher degrees of symmetry. The above figure shows for example what we call the "8 pattern".

Instability and multistability of cavity solitons in optical parametric oscillators.

Dmitry V. Skryabin
Department of Physics and Applied Physics, John Anderson Building, University of Strathclyde, 107 Rottenrow, Glasgow, G4 0NG, UK
fax: 44 141 5522891 phone: 44 141 5523354 dmitry@phys.strath.ac.uk

Cavity solitons (CS) supported by the quadratic nonlinearity have recently been predicted in both optical parametric oscillator (OPO) [1] and second harmonic generation [2] configurations. The large values of the effective $\chi^{(2)}$ accessible in artificially phase-matched materials and the instantaneous electronic response are important practical advantages of using CS in the $\chi^{(2)}$-cavity in future all-optical schemes of the information processing.

Experimental observation of $\chi^{(2)}$-CS remains a challenge. However, an intensive work of the last years in the direction to achieve an efficient frequency conversion in the semiconductor microcavities, ongoing wave of the experimental results on transverse instabilities and recent observations of the plane wave bistability [5] in the quadratically nonlinear cavities pave the way towards this goal. Thereby, stability of $\chi^{(2)}$-CS becomes an interesting and important problem not only from fundamental but also from practical points of view.

Quadraticaly nonlinear media also support solitons propagating free in a bulk [7]. An important point is that the soliton instabilities in free propagation schemes are *convective* ones, i.e. perturbations grow with propagation, therefore even if a soliton is actually unstable in a particular range of parameters, the stable trapping still can be observed over the short length of a nonlinear sample. Contrary, in the most of the cavity schemes stability and instability are *absolute* ones, i.e. perturbations decay or grow in time at a fixed spatial point, therefore unstable CS transform into some other stable solutions on the time scale of the characteristic cavity photon life time. Thus CS stability with respect to the small disturbances is an essential prerequisite for their experimental observation.

One of the main objectives of this work is to study CS instabilities in the doubly resonant degenerate OPO starting from *a limit situation when CS formally become free propagating solitons.* The latter ones are known to possess so called *internal* modes causing longlived pulsations of the soliton width [8] and playing the crucial role in its *convective* instability [9]. We will show below that dynamics of the $\chi^{(2)}$ solitons in a cavity significantly underlined by the fact of the presence of these internal modes. Such a look at the problem allows to make certain predictions about stability of other dissipative localised structures which have their conservative counterparts.

We start from the dimensionless mean-field equations for OPO given in Ref. [1] and describing the interaction of the signal and pump envelopes. It can be shown that these equations can be presented in the 'quasi-Hamiltonian' form

$$(\partial_t + \gamma_m)E_m = i\frac{\delta H}{\delta E_m^*},\ m = 1,2, \qquad (1)$$

where H is the following functional: $H = \int dx[-\alpha_1|\partial_x E_1|^2 - \alpha_2|\partial_x E_2|^2 + \delta_1|E_1|^2 + \delta_2|E_2|^2 + \frac{1}{2}(E_1^2E_2^* + \mu E_1^2 + c.c.)]$ and $\alpha_m = 1/m$. Here E_1 and $(E_2 + \mu)$ are the signal and pump fields, respectively, at frequencies ω and 2ω. μ characterizes strength of the external pump field and without restriction of generality can be assumed positive. t is the time describing evolution of the envelopes on the scale of the cavity photon life-time. γ_m and δ_m characterize, respectively, cavity losses and detunings from its resonances.

Among the variety of the bright and dark localized structures observed in the numerical modelings of OPO we choose the bright CS seating on zero background field [1], as more relevant for the practical implementation. It was numerically demonstrated that a continuous family of the solitary solutions exists within the following range of the pump values $\mu_L < \mu < \mu_R$ providing that $\delta_m < 0$, here $\mu_R = \sqrt{\delta_1^2 + \gamma_1^2}$ and $\mu_L = |\gamma_1\delta_2 + \gamma_2\delta_1|/\sqrt{\delta_2^2 + \gamma_2^2}$.

The exact analytical expressions for the single-hump upper- (u) and low- (l) branch CS can be found for $\gamma_2 = 0$ and $\delta_1 = \delta_2 - \mu\cos 2\phi^{u,l}$, where $2\phi^l = arcsin(\gamma_1/\mu)$ and $\phi^u = \pi/2 - \phi^l$, then $A_m^{u,l} = 1.5|\delta_2|sech^2[|\delta_2|x/2]\ \exp(im\phi^{u,l})$, where $A_m(x) = E_m(x,t)$. Thus CS become progressively narrower for the larger $|\delta_m|$. Numerically build graphs of the energy of the signal field vs pump for two different parameter sets are presented in Fig. 1 and typical transverse profiles in Fig. 2. One can see that close to the μ_R upper branch of the single-hump CS bifurcates back into a sequence of the higher order multi-hump CS. While the existence of the single- and two-hump branches was numerically demonstrated before [1] their link with each other and with the higher-order solitons as well as the analytic expressions for A_m are novel features. Note, that for $\gamma_2 = 0$ stationary problem for the CS transverse profiles formally reduces to the equivalent problem for the free propagating solitons, thus CS can be considered as their continuations.

Now we turn our attention to the main problem we want to address here, i.e. to the stability of CS families with respect to the small perturbations. We seek solutions of the Eqs. (1) in the form $A_m(x) + \varepsilon(U_m(x,t) + iW_m(x,t))$. Here $\varepsilon \ll 1$ and U_m, W_m are real perturbations. After the standard linearization and substitutions $U_m = u_m(x)e^{\lambda t}$, $W_m = w_m(x)e^{\lambda t}$ we derive an eigenvalue problem (EVP) $\lambda\vec{\xi} = \hat{\mathcal{L}}\vec{\xi}$, where $\vec{\xi} = (w_1, w_2, u_1, u_2)^T$ and

$\hat{\mathcal{L}}$ is the linearisation of (1) near a soliton. The discrete spectrum of the nonselfadjoint operator $\hat{\mathcal{L}}$ has been found numerically using second-order finite differences.

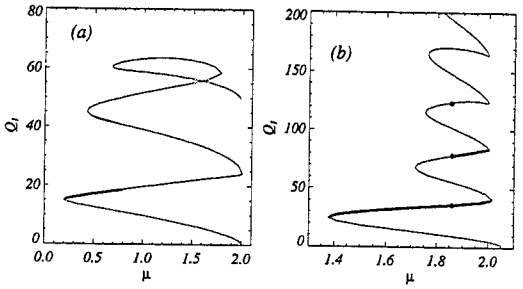


FIG. 1. Energy of the soliton signal field, $Q_1 = \int dx|A_1|^2$, vs pump μ. (a) $\gamma_{1,2} = 0.1$, $\delta_{1,2} = -2$; (b) $\gamma_1 = 1$, $\gamma_2 = 0.8$, $\delta_1 = -1.8$, $\delta_2 = -4$. Bold and thin lines mark, respectively, stable and unstable solitons.

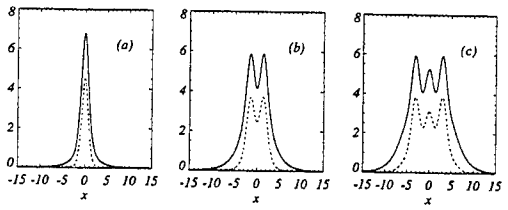


FIG. 2. Transverse profiles of $|A_1|$ (full lines) and $|A_2|$ (dashed lines) for single-, two- and three-hump solitons marked by rohmds in Fig. 1(b).

We start the discussion of the stability properties focusing on the single-hump CS. To understand an origin of their instability we consider a limit situation when Eqs. (1) become Hamiltonian, i.e. $\gamma_m = 0$. It appears that CS do exist under these conditions. However, they are still very different from $\chi^{(2)}$ solitons in the free propagation geometry [7–9]. This is because the total energy $\int dx(|E_1|^2 + 2|E_2|^2)$ is not a conserved quantity. It becomes conserved and CS become equivalent to the free propagating solitons only when pump photons are not injected into a cavity any more, i.e. $\mu = 0$. Then, in accord with Noether's theorem, Eqs. (1) acquire the phase symmetry, $E_m \to E_m e^{im\phi}$, which generates the eigenmode $\vec{\xi}_0 = (ReA_1, 2ReA_2, -ImA_1, -2ImA_2)^T$ with double zero eigenvalues, $\hat{\mathcal{L}}\vec{\xi}_0 = 0$. Note that considering an all-fiber ring cavity the limit $\mu \to 0$, $\gamma_m \to 0$ corresponds to the lossless fiber loop supporting solitons due to the balanced action of the nonlinearity and group velocity dispersion. For $\gamma_m = 0$ the left existence boundary of the CS is $\mu = \mu_L = 0$. Once we deviate μ from the zero moving along the low soliton branch a pair of zero eigenvalues associated with $\vec{\xi}_0$ split and move along the real axis, $Im\lambda = 0$, of the $(Re\lambda, Im\lambda)$-plane in the opposite directions, see the dashed lines in Fig. 3 (a). Thus, the low branch is unstable. Contrary, moving along the upper soliton branch we have found that the eigenvalues move in the opposite directions along the imaginary axis, $Re\lambda = 0$. Thus the upper soliton branch remains stable at least for small μ. However at some $\mu = \mu_{HH}$ these imaginary eigenvalues meet the pair of other eigenvalues which are the direct continuation of the eigenvalues corresponding to the *internal* eigenmodes of the free propagating quadratic solitons [8]. This collision gives onset to the Hamiltonian-Hopf instability of the CS, see full lines in Fig. 3(a). The situation when the free propagating solitons are themselves unstable will not be considered here.

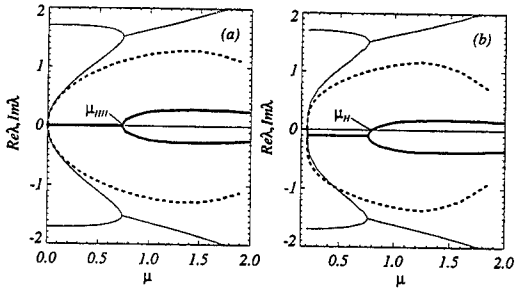


FIG. 3. Real (bold lines) and imaginary (thin lines) parts of the eigenvalues governing stability of the upper (full lines) and low (dashed lines) branches of the single-hump solitons vs pump μ for $\delta_{1,2} = -2$. (a) $\gamma_{1,2} = 0$, (b) $\gamma_{1,2} = 0.1$.

Introducing linear losses, which are unavoidable in a real cavity, and keeping them equal for the both harmonics one will find that the bifurcation diagram simply becomes shifted down along the axis $Im\lambda = 0$ by the value equal to γ_m, see Fig. 3(b). This fact can also be deduced from the explicit form of $\hat{\mathcal{L}}$. Non-Hamiltonian corrections transform Hamiltonian-Hopf bifurcation into the standard Hopf bifurcation ($\mu_{HH} \to \mu_H$), see Fig. 3 (b), well known for the dissipative systems. Considering stability of the multi-hump CS it has been found that they are Hopf unstable if losses are small enough. However, the large dissipation has stabilizing effect and coexistent stable single- and two-hump CS have been found, see Fig. 1(b).

To study dynamics of the unstable CS an extensive series of the numerical simulations has been performed. Inside the instability region, but close to the critical boundary, a stable attractor in form of an oscillating CS has been found, see Fig. 4(a),(b). Deeper inside the instability region we have observed two scenarios of the soliton destruction. For some intermediate region of μ the growing amplitude of the oscillations leads to the switching into the trivial solution, see Fig. 4(c),(d). For μ close enough to μ_R the pulsating soliton easily excites a chaotic pattern which quikly fills the entire computational window, see Fig. 4(e),(f).

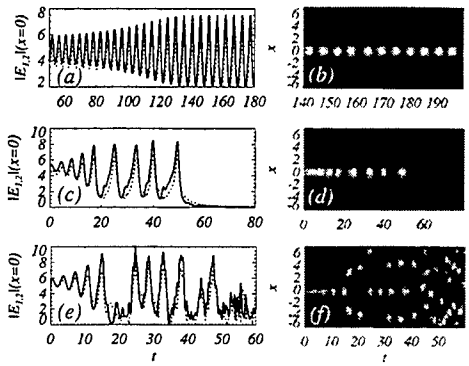


FIG. 4. Dynamics of the upper-branch single-hump soliton in the region of its Hopf instability. (a) Stable pulsations, $\mu = 0.8$; (b) Switching into stable trivial solution, $\mu = 1$; (c) Switching into the regime of spatio-temporal chaos, $\mu = 1.5$. Other parameters as for Fig. 1(a). Full/doted lines in Figs. (a), (c), (e) mark, respectively, $|E_1(t)|$ and $|E_2(t)|$ at $x = 0$. Figs. (b), (d), (f) show $|E_1(x,t)|$.

A possible interpretation of the last scenario is that the radiation escaping from the oscillating soliton along its tails, which are weakly damped when μ is close to μ_R, locally produces the parametric gain greater than μ_R thus making the background unstable and a chaotic pattern existing near the upper branch of the homogeneous solution is excited. Initialising Eqs. (1) with the homogeneous solutions results in the similar chaotic pattern. Two spatially localized periodic attractors have been found taking multi-hump CS as initial conditions. One of them corresponds to the Hopf unstable two-hump CS, see Fig. 5(a), and another one to the Hopf-unstable three- or four-hump CS, see Fig. 5(b). The dynamical regimes shown in Figs. 4, 5 also serve as attractors for a wide range of the experimentally relevant initial conditions in the form of the gaussian pulses of the pump radiation with suitable width, height and duration.

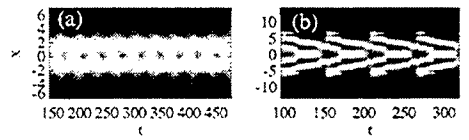


FIG. 5. Spatio-temporal evolution of $|E_1|$ resulting from the Hopf instability of the two-hump (a) and four-hump (b) solitons. (a) $\mu = 1.8$, (b) $\mu = 1.9$. Other parameters as for Fig. 1(b).

Considering extension of our results to other externally driven nonlinear optical cavities and generally to other dissipative systems we have to say that assuming that in the absence of the external driving and losses a model has solitary solutions one can expect similar bifurcation scenarios. One of the reasons for this is that an external pump always breaks the phase symmetry associated with the energy conservation and losses destroy Hamiltonian structure in a manner similar to the described in the present context. However this symmetry breaking is sufficient only for an appearence of the stable upper and unstable low CS branches, but it is not sufficient for the Hopf instability of the upper branch. Another important ingredient, which practically guaranties this instability, is a presence of the *internal* soliton modes in the limit when pump and loss are negligible. These modes have already been demonstrated for large variety of models describing free propagating optical solitons, see e.g. [8,10], and admitting their cavity generalizations. Let us point out, that recently reported oscillating bright [4] and dark [3] localized structures in dissipative models with saturable or quintic-qubic nonlinearities echo complex internal dynamics of their counterparts in the free propagation schemes [10,11]. From the other hand Hopf instability of the bright solitary waves found in the one-dimensional cubic NLS equation with loss and driving [6] can not be linked with internal or unstable modes of the NLS soliton because neither of them exist. In such a case instabilities may appear due to non-Hamiltonian and/or non-conservative corrections resulting in the splitting of additional eigenmodes from the continuum.

In summary: Stability, multistability and instability of the single- and multi-hump cavity solitons in the degenerate optical parametric oscillators have been examined by means of the linear stability analysis and numerical simulation of the dynamical and stationary equations. It is demonstrated that Hopf instability leading to the complex spatially localized dynamics originates from the presence of the internal modes of the free propagating quadratic solitons.

[1] K. Staliunas and V.J. Sánchez-Morcillo, Opt. Commun. **139**, 306 (1997); S. Longhi, Phys. Scripta **56**, 611 (1997); S. Trillo and M. Haelterman, Opt. Lett. **23**, 1514 (1998).
[2] C. Etrich *et al.*, Phys. Rev. Lett. **79**, 2454 (1997).
[3] D. Michaelis *et al.*, Opt. Lett. **23**, 1814 (1998).
[4] R.J. Deissler and H.R. Brand, Phys. Rev. Lett. **72**, 478 (1994); T. Kapitula and B. Sandstede, J. Opt. Soc. Am. B **15**, 2757 (1998); A.G. Vladimirov *et al.*, J. Opt. B **1**, 101 (1999).
[5] C. Richy *et al.*, J. Opt. Soc. Am. B **12**, 456 (1995).
[6] K. Nozaki and N. Bekki, Physica D **21**, 381 (1986); M. Bondila *et al.*, Physica D **87**, 314 (1995).
[7] W.E. Torruelas *et al.*, Phys. Rev. Lett. **74**, 5036 (1995).
[8] C. Etrich *et al.*, Phys. Rev. E **54**, 4321 (1996).
[9] D.E. Pelinovsky *et al.*, Phys. Rev. Lett. **75**, 591 (1995).
[10] Y.S. Kivshar *et al.*, Phys. Rev. Lett. **80**, 5032 (1998).
[11] I.V. Barashenkov and E.Y. Panova, Physica D **69**, 114 (1993).

Stability of cavity solitons in parametric down-conversion

C. Etrich, D. Michaelis, and F. Lederer

Institut für Festkörpertheorie und Theoretische Optik
Friedrich-Schiller-Universität Jena
Max-Wien-Platz 1, 07743 Jena, Germany

Localized structures or cavity solitons in resonators with a nonlinear response attracted some interest recently [1]. One of the basic and most intensively studied configurations is the degenerate parametric oscillator where two types of cavity solitons were shown to exist [2]. The aim here is to show where in parameter space (two-dimensional) cavity solitons exist, to demonstrate the existence of higher order structures and to perform a linear stability analysis.

Considering a Fabry-Perot resonator with a quadratically nonlinear medium the mean field equations of the optical parametric oscillator for the transmitted fields A and B of the fundamental and second harmonics are

$$i\frac{\partial A}{\partial T}+\frac{\partial^2 A}{\partial X^2}+\frac{\partial^2 A}{\partial Y^2}+(\Delta_1+i)A+A^*B=0\,,$$
$$i\frac{\partial B}{\partial T}+\alpha\left(\frac{\partial^2 B}{\partial X^2}+\frac{\partial^2 B}{\partial Y^2}\right)+(\Delta_2+i\gamma)B+A^2=E\,, \qquad (1)$$

where T denotes the time, X and Y the transverse coordinates, Δ_1 and Δ_2 are the detunings of the fields from the corresponding resonances, γ is the ratio of the photon lifetimes and α half the ratio of the refractive indices corresponding to the fundamental and second harmonics. We assume $\alpha = 1/2$ which is a reasonable approximation for realistic configurations. The input field of the second harmonic is E.

The homogeneous steady state or plane wave solutions of Eqs.(1) and their stability behaviour with respect to homogeneous perturbations are well known (see for example [3]). Equating the derivatives in Eqs.(1) to zero the moduli of the fields of the plane wave solutions are

$$A_0=0\,,\quad |B_0|^2=\frac{E^2}{\Delta_2^2+\gamma^2}\,, \qquad (2)$$

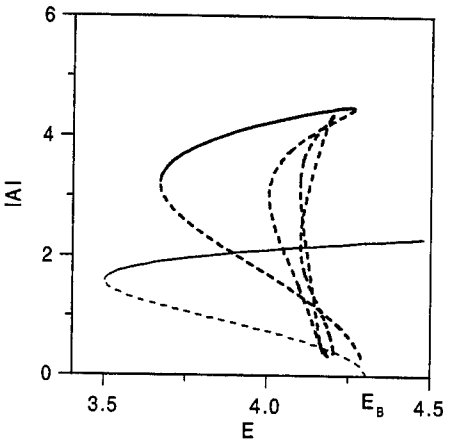


Figure 1: Bifurcation diagram displaying branches of plane wave solutions (thin lines) and cavity solitons (bold lines) for $\Delta_1 = -1$, $\Delta_2 = -3$ and $\gamma = 0.5$. Solid lines refer to stable (homogeneously stable for plane wave solutions) and dashed lines to unstable solutions.

$$|A_0|^2=\Delta_1\Delta_2-\gamma\pm\sqrt{E^2-(\gamma\Delta_1+\Delta_2)^2}\,,$$
$$|B_0|^2=\Delta_2+1\,. \qquad (3)$$

The solution of Eq. (3) is doubly degenerate with phase difference π [4] and the stationary critical points can be derived from this equation. At $E_B = \sqrt{(\Delta_1^2+1)(\Delta_2^2+\gamma^2)}$ this solution bifurcates from the branch of solutions of Eq. (2), that is supercritically if $\Delta_1\Delta_2-\gamma<0$ and subcritically if $\Delta_1\Delta_2-\gamma>0$. In the subcritical case Eq. (3) describes two branches

of solutions with a limit point at $E_L = |\gamma\Delta_1 + \Delta_2|$ where the solution with the upper sign in Eq. (3) stabilizes. We refer to the branch of solutions of Eq. (2) as trivial solution and to the branches of solutions of Eq. (3) as nontrivial lower (negative sign) and upper branches (positive sign). For $\Delta_1\Delta_2 < 0$ which is not considered here the bifurcation is always supercritical. In this case the branch of Eq. (3) can destabilize via a Hopf bifurcation.

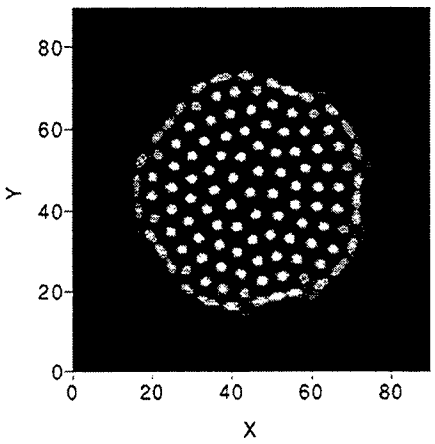


Figure 2: Decay of a higher order cavity soliton (fundamental) into a pattern with a fivefold symmetry for $\Delta_1 = -1$, $\Delta_2 = -3$, $\gamma = 0.5$ and $E = 4.17$.

Cavity solitons are calculated as rotationally symmetric stationary solutions of Eq. (1). They are localized solutions on a plane wave background and were found for $\Delta_1\Delta_2 > 0$. To determine the stability of cavity solitons we separate Eqs. (1) into real and imaginary parts $A = A_r + iA_i$, $B = B_r + iB_i$, substitute $A_{r0,i0}(R) + \delta A_{r,i}(R)\exp(im\phi)\exp(\lambda T)$, $B_{r0,i0}(R) + \delta B_{r,i}(R)\exp(im\phi)\exp(\lambda T)$ where $A_0(R) = A_{r0}(R) + iA_{i0}(R)$, $B_0(R) = B_{r0}(R) + iB_{i0}(R)$ is a localized structure and linearize with respect to the deviations. This leads to a one-dimensional eigenvalue problem in terms of $\delta A_{r,i}(R)$, $\delta B_{r,i}(R)$ for λ which can be solved numerically for the different values of m.

For negative detunings and $\Delta_1\Delta_2 > \gamma$ there is a branch of cavity solitons emanating subcritically from the bifurcation point E_B (Fig. 1), i.e., they are on a trivial plane wave background. The cavity solitons stabilize at a limit point. If the nontrivial upper branch is modulationally unstable, i.e. with respect to spatially inhomogeneous perturbations more and

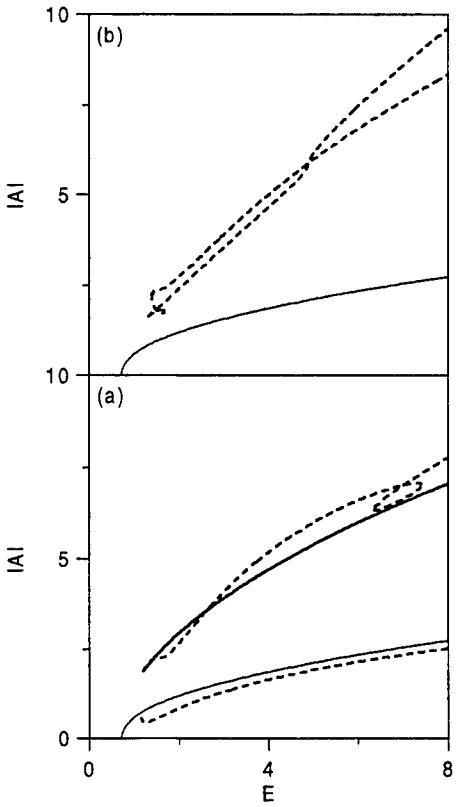


Figure 3: Bifurcation diagrams displaying branches of plane wave solutions (thin lines) and cavity solitons (bold lines) for $\Delta_1 = 1$, $\Delta_2 = 0$ and $\gamma = 0.5$. Solid lines refer to stable (homogeneously stable for plane wave solutions) and dashed lines to unstable solutions.

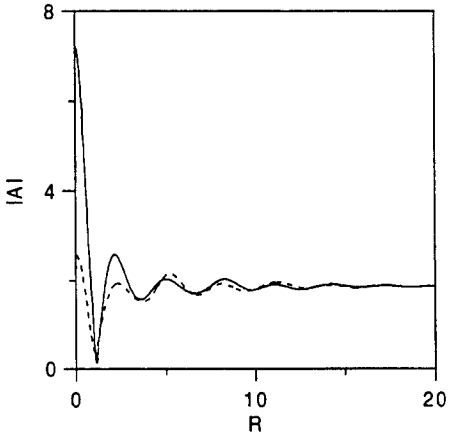


Figure 4: Oscillating cavity soliton for $\Delta_1 = 1$, $\Delta_2 = 0$, $\gamma = 0.5$ and $E = 4$ (maximum solid, minimum dashed).

more limit points develop leading to higher order cavity solitons (Fig. 1). They seem not to stabilize again rather being unstable through $\lambda > 0$ with increasing values of m going to higher order cavity solitons. An example for $m = 5$ is displayed in Fig. 2 where eventually a pattern of cavity solitons with a fivefold symmetry develops.

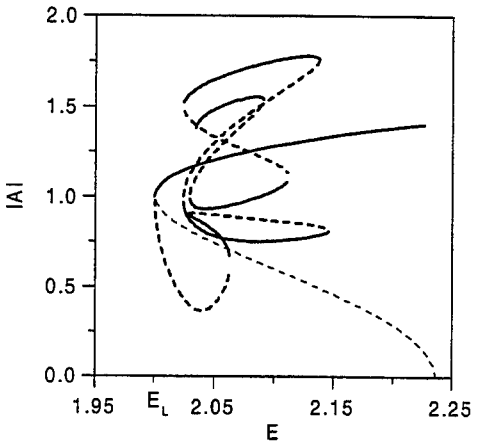


Figure 5: Bifurcation diagram displaying branches of plane wave solutions (thin lines) and cavity solitons (bold lines) for $\Delta_1 = 1$, $\Delta_2 = 1.5$ and $\gamma = 0.5$. Solid lines refer to stable and dashed lines to unstable solutions.

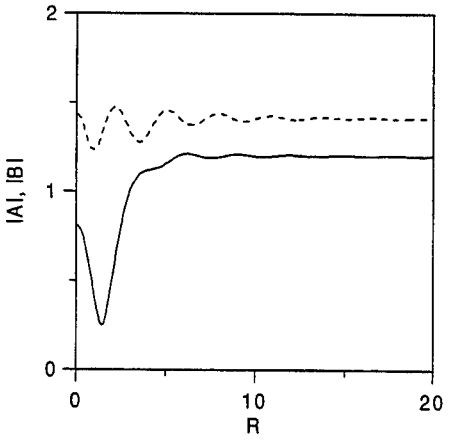


Figure 6: Cavity soliton on the first stable branch of Fig. 5 for $E = 2.05$ (fundamental solid, second harmonic dashed).

For positive detunings two cases were considered. In either case the cavity solitons have a nontrivial plane wave background which is due the trivial branch being modulationally unstable for $E < E_B$. In Fig. 3 the modulational instability terminates on the nontrivial branch. From this point we have cavity solitons emanating subcritically. The branch seems to extend to infinity. This is also true for the other branches which we identified (Fig. 3). Since they are not emanating from a plane wave solution they must be connected by limit points. We found one stable branch of cavity solitons (Fig. 3a). In Fig. 3b there is no entirely stable branch. One branch of cavity solitons is unstable with a real $\lambda > 0$ for $m = 3$ and a pair of complex conjugate λ with $\mathrm{Re}\lambda > 0$. Using the radial version of Eqs. (1) we could confirm numerically the existence of oscillating cavity solitons (Fig. 4). Propagating these oscillating cavity solitons (starting for instance from an unperturbed unstable stationary cavity soliton) by means of a two-dimensional beam propagation method, for smaller values of E the oscillating cavity solitons decay developing a pattern with a threefold symmetry. For higher values of the control parameter E these oscillations seem to be stable as far as numerics can tell.

In Fig. 5 the upper nontrivial branch is stable and there are cavity solitons emanating from the limit point E_L. They stabilize at a limit point and there are alternating stable and unstable branches of cavity solitons displaying multistability. These cavity solitons may be regarded as another type not indentified in [2]. They are hole-like structures (Fig. 6).

To sum up we identified stable and unstable cavity solitons on a stable plane wave background. The unstable structures may decay developping symmetric patterns or oscillating cavity solitons which are remarkably pronounced. For positive detunings multistability of cavity solitons is possible.

References

[1] D. Michaelis, U. Peschel, and F. Lederer, Phys. Rev. A **56**, R3366 (1997); M. Brambilla, L.A. Lugiato, F. Prati, L. Spinelli, W.J. Firth, Phys. Rev. Lett. **79**, 2042 (1997); C. Etrich, U. Peschel, and F. Lederer, Phys. Rev. Lett. **79**, 2454 (1997).

[2] K. Staliunas and V.J. Sánchez-Morcillo, Opt. Commun. **139**, 306 (1997); K. Staliunas and V.J. Sánchez-Morcillo, Phys. Rev. A **57**, 1454 (1998).

[3] L.A. Lugiato, C. Oldano, C. Fabre, E. Giacobino, and R.J. Horowicz, Il Nuovo Cimento **10D**, 959 (1988).

[4] S. Trillo, M. Haelterman, and A. Sheppard, Opt. Lett. **22**, 970 (1997).

On existence of gap solitons.

E. Alfimov
F.V.Lukin's Institute of Physical Problems, Zelenograd, Moscow, 103460, Russia.

V. V. Konotop
Department of Physics and Center of Mathematical Sciences, University of Madeira, Praça do Município, Funchal, P-9000, Portugal

Although gap solitons, since their discovery by Chen and Mills [1] attracted a great deal of attention, mathematical aspects of their existence have not been addressed, so far. This problem is naturally related to the role of high harmonics in the gap soliton evolution especially in the cases when there are no small parameters in the problem. Namely the high harmonics may play a prominent role in destruction of the gap solitons. One can easily predict the respective mechanism. A stop gap prevents dissipation of the energy of a wave packet at the carrier wave frequency. At the same time the nonlinearity results in higher harmonic generation. In a generic situation these new harmonics do not fall into stop gaps and hence represnt a channel of the energy transmission from the localized mode to quasi-linear (i.e. delocalized) modes. This rises a natural question: Is the gap soliton indeed a mathematical object (i. e. periodic in time and localized in space solution of the nonlinear wave equation with periodic coefficients)? If not, then what is the role of higher harmonics in the gap soliton evolution? In the present work we address to these questions. In particular, we develop an approach allowing one to take into account the contribution of higher harmonics (up to any order) to the gap soliton evolution. Next, we study in detail the field evolution in the approximation of only one principal harmonic and estimate numerically the contribution of higher harmonics. We show that shock waves appear on the tails of envelope solitons. Finally, we report the results of direct numerical simulation of gap soliton evolution on the basis of nonlinear wave equation (rather than of the equation appearing in the parabolic approximation).

We start with the one-dimensional equation for the TE field in a general form

$$\frac{\partial^2 E}{\partial x^2} \quad \frac{1}{c^2}\frac{\partial^2 D}{\partial t^2} = 0 \tag{1}$$

where $D = \varepsilon(x)E + 4\pi P$ is the induction and P is the polarization which consists of linear and nonlinear components: $P = P_l + P_{nl}$. We write down them in the form

$$P_l = \varepsilon(x) \int \chi^{(1)}(\omega_1)\tilde{E}(x,\omega_1)e^{\ i\omega_1 t}d\omega_1 \tag{2}$$

$$P_{nl} = \chi(x) \iiint \chi^{(3)}(\omega_1,\omega_2,\omega_3)\tilde{E}(x,\omega_1)\tilde{E}(x,\omega_2)\tilde{E}(x,\omega_3)e^{\ i(\omega_1+\omega_2+\omega_3)t}d\omega_1 d\omega_2 d\omega_3 \tag{3}$$

where $\tilde{E}(x,\omega)$ is the Fourier transform of the electric field:

$$E(x,t) = \frac{1}{2\pi}\int_{\infty}^{\infty} e^{i\omega t}\tilde{E}(x,\omega)\,d\omega.$$

Our approach is based on possibility of expansion of a periodic solution in a Fourier series. In a particular case of "even"solution one has

$$\tilde{E}(x,\omega_1) = \frac{1}{2}\sum_{n=1}^{\infty} E_{2n\ 1}(x)[\delta(\omega_1 \quad \Omega_{2n\ 1}) + \delta(\omega_1 + \Omega_{2n\ 1})] \tag{4}$$

where the coefficients of the Fourier expansion solve the equation

$$\frac{d^2 E_{2m\ 1}}{dx^2} + \gamma_{2m\ 1}\varepsilon(x)E_{2m\ 1} + 4\pi\Omega^2_{2m\ 1}\Phi_{2m\ 1}(E_1, E_3, ...) = 0 \tag{5}$$

with $\gamma_{2m\ 1} = \Omega_{2m\ 1}\left(1 + 4\pi\chi^{(1)}(\Omega_{2m\ 1})\right)$,

$$\Phi_{2m\ 1}(E_1, E_3, ...) = \sum_{m_1,m_2,m_3} \chi(\Omega_{2m\ 1}; \Omega_{2m_1\ 1}, \Omega_{2m_2\ 1}, \Omega_{2m_3\ 1}) E_{2m_1+1} E_{2m_2+1} E_{2m_3+1} \tag{6}$$

and

$$\chi(\Omega, \Omega_1, \Omega_2, \Omega_3) = \frac{1}{2\pi}\chi(\Omega_1, \Omega_2, \Omega_3)\int_0^{2\pi} \cos(\Omega t)\cos(\Omega_1 t)\cos(\Omega_2 t)\cos(\Omega_3 t)\, dt \tag{7}$$

being the nonlinear susceptibility describing contribution of processes of four wave mixing.

It can be shown that the most favorable situation for the gap soliton existence occurs when the Kerr type medium does not have material dispersion. To simplify mathematics we represnt the results for this particular case. The proof of nonexistence of the gap soliton solutions as mathematical objects is based on the fact that if not all the fequencies $(2n+1)\omega$ belong to stop gaps, then imposing zero boundary conditions on (5) and matching condition at $x = 0$ results on overdetermined system of equations for the constants of integration. The fact that in a generic case not all friquencies belong to stop gaps follows from the Fedoryuk theorem determining distribution of stop gaps at large values of the wave vectors [2].

For purposes of numerical study of the gap soliton structure we use the multimode approximation which is the trancation of (5) at some $m = M$, i.e. on the assumption that all harmonics at $n > M$ have zero amplitude. Then there are two quantities to be computed: (i) the convergence of the procedure at $M \to \infty$ and (ii) the matching condition at $x = 0$ for the third and higher harmonics (subject to supposition that the carrier wave satisfies all the assumptions).

Considering the soliton dynamics we discuss two physical reasons for the gap soliton decay. First the presence of non-localized harmonics allows one to suppose that the gap soliton "death" can be caused by emission of some radiation which propagates outward along x axis and results in breaking of localization and, at last, in decay of the GSE. Another scenario is consistent with breaking of continuity of solutions of the nonlinear wave equation which can be rewritten in the form

$$\frac{\partial^2 A(x,E)}{\partial t^2} = \frac{\partial^2 E}{\partial x^2} \tag{8}$$

with

$$A(x,E) = \varepsilon(x)E + E^3 \tag{9}$$

It is well known that (8) can describe shock wave formation. We study the characteristics of Eq. (8) numerically and show that indeed there exist characteristics which cross each other in some point where the field becomes not uniquely defined. At this moment *gradient catastrophe* occurs and both partial derivatives of E become infinite. Since this moment the lowest order approximation to the nonlinear wave equation (1) is not valid any more and additional terms (corresponding to dissipation, higher dispersion, etc.) should be taken into account.

The predictions of the theory developed are verified by means of the direct numerical simulations of the nonlinear wave equation with the periodic dielectric permittivity. It is

confirmed, in particular, that only one of the gap edges there exists long-leaving solitonic solution (this situation corresponds to the slow envelope solitons described by de Sterke and Sipe [3]). We indeed observe that the detuning towards the center of the gap results in a rapid destructuion of gap solitons. The distruction has two different origins depending on the frequency detuning towards the stop gap. At small values of the frequency detuning gap solitons dissappear due to radiation, i.e. energy transfer to higher harmonics. Another scenario is found for the case of strong detuding. Then discontinuity of the solution obtained withing the framework of M-mode approximation, which can be associated with the gradient catastrophe. Moments of the gradient catastrophe for various initial data are computed numerically.

Supported of FEDER and Program PRAXIS XXI, grant N^0 PRAXIS/2/2.1/FIS/176/94 and of the NATO Linkage Grant N^0 OUTR.LG960298 is acknowledged.

References

[1] W. Chen and D. L. Mills, Phys. Rev. Lett. **58**, 160 (1987).

[2] M. V. Fedoryuk *Asymptotical methods for linear ordinary differential equations* (Moscow, Nauka, 1983) [In Russian]

[3] C. M. de Sterke and J. E. Sipe, Phys. Rev. A **38**, 5149 (1988); **39**, 5163 (1989).

Evaporative cooling of a soliton gas

Soeren Rutz and Fedor Mitschke

Fachbereich Physik, Universität Rostock

18051 Rostock, Germany

Tel.: +49 - 381 498-1648, Fax.: +49 - 381 498-1650

email: soeren.rutz@physik.uni-rostock.de

It is well known and widely accepted by now that soliton pulses are the most promising 'bits' for information-carrying optical fiber due to their stability and particle-like behavior. This stability allows a wide variety of perturbations and manipulations. Solitons can be attenuated and amplified again, get filtered, can collide with other solitons etc. without being destroyed.

It is also well known that nonlinear feedback systems provide an enormous wealth of nontrivial dynamic behavior. This applies not just to optics, but to many other fields in nature and technology as well. Here we deal with a combination of soliton propagation and nonlinear feedback system. The complex processes encountered may contribute fresh insights into soliton dynamics.

We consider an optical ring resonator mainly consisting of a length of single-mode optical fiber. The resonator is driven with a train of picosecond pulses from a modelocked laser source. The repetition time of the drive pulses is brought into synchronism with the resonator round trip time. The resulting interplay of linear (dispersive) and nonlinear (Kerr) distortion of the pulses with the repetitive interference at the input port has been shown previously to give rise to many interesting phenomena, among them the formation of a turbulent ensemble of solitons which has been called a soliton gas[1].

It also has recently been shown that a reduction in the power of the drive pulses leads to a transition to a different state of the soliton ensemble in which the solitons sit on a regular lattice[2,3]. In keeping with the thermodynamic analogy, this may be called a soliton crystal.

A phase transition from fluid to solid is normally obtained by reducing the temperature i.e. reducing the influx of thermal energy. One might thus speculate that the drive pulse energy is the equivalent of a heat source. Resonator losses would then represent a heat sink, and the system operates in a balanced state of energy flow, if far from thermal equilibrium. It might then be possible to reduce the fluid to the solid state not by reducing the heat input, but by increasing the heat output. We ventured to determine whether just that could be done by some optical means more elegant than simply increasing losses.

The hottest particles in a gas have the highest velocity. In the soliton gas, solitons with the highest relative velocity (referred to the center-of-mass of the ensemble) must have optical frequencies that are most off center. Application of a selective filter should then allow to cool the soliton gas. This is the equivalent to evaporative cooling which is well known to be equally effective for a Bose-Einstein condensate and for a hot cup of coffee.

In numerical simulations we demonstrate the effect of a filter in cooling the soliton gas such that the phase transition is reached without reduction of the energy flow into the system.

---

1. A. Schwache and F. Mitschke, Phys. Rev. E **55,** 7720 (1997).

2. B. Malomed, A. Schwache, and F. Mitschke, Fiber and Integrated Optics **17,** 267 (1998).

3. F. Mitschke, I. Halama, and A. Schwache, Chaos, Solitons and Fractals **10,** 913 (1999).

Nonlinear intermode interference in $LiNbO_3$ planar optical waveguides

Yury Larionov, Stanislav Shandarov, and Vladymir Shandarov
Department of Electronic Devices,
State University of Control Systems and Radioelectronics,
40 Lenin Avenue, Tomsk 634050, Russia
ylar@ed.rts.tusur.ru

Optical waveguide structures allow to light beams for some interaction effects having no analogs in bulk media. These are, for example, interactions of guided modes with the same polarization but with different mode indices. The one of such effects is the longitudinal intermode interference of light beams. It was observed and studied in planar glass waveguides and in Ti - diffused $LiNbO_3$ waveguide. In this work we investigate and discuss some features of such an effect in a case of the spatial self - action of light beams due to the photorefractive effect in Fe - doped $LiNbO_3$ planar optical waveguide.

The strong photorefractive nonlinearity of $LiNbO_3$ doped by suitable impurity originates the formation of light - induced negative lens under light beam influence. In a waveguide with nonuniform distribution of an active dopant near its surface the photovoltaic constant β, the photoconductivity σ_{ph}, and the dark conductivity σ_d are considerably changed over waveguide depth. It results in the significant difference of the temporal characteristics of the space - charge electric field for different guided modes. Thus, the parameters of light - induced lenses may differ for these modes as well. It is the main reason to distinctions of an intermode interference in the nonlinear case when compared with the linear one.

In analysis the optical field in a waveguide was described by the expression $E_{opt}(x,z,t)=A(x,z)\exp(ikz-iwt)$+c.c. In the paraxial approximation the slowly varying amplitude, $A(x,z)$ is determined by the parabolic equation

$$\left(\frac{\partial}{\partial z}-\frac{i}{2k}\frac{\partial^2}{\partial x^2}\right)A(x,z)=\frac{i\,k\,\Delta n}{n_{eff}}A(x,z)\,, \tag{1}$$

where Δn is the nonlinear change of the refractive index, n_{eff} is the effective refractive index, and k is the optical wave number in the material, $k=2\pi n_{eff}/\lambda$, where λ is the wavelength. In lithium niobate Δn is related to the light intensity $I(x,z) = |A(x,z)|^2$ by [1]

$$\Delta n(x,z)=-\frac{1}{2}n_{eff}^3\,r_{33}\,\beta_{33}I(x,z)\left[\sigma_d+\sigma_{ph}\cdot I(x,z)\right]^{-1}, \tag{2}$$

where r_{33} is electrooptic constant, β_{33} is photovoltaic constant. If the value of σ_d within the waveguide sagnificantly exceeds the σ_{ph} value then the term related to σ_{ph} can be neglected. Thus the equation 2 can be rewritten as

$$\Delta n(x,z)=-\frac{1}{2}n_{eff}^3\frac{r_{33}\,\beta_{33}}{\sigma_d}|A(x,z)|^2\,. \tag{3}$$

Put in the consideration the parameter $\delta=-0.5\,n_{eff}^3\frac{r_{33}\beta_{33}}{\sigma_d}$. As it was mentioned above, the values of β, σ_{ph}, σ_d are changed over the waveguide depth and different guided modes are characterized by their own δ value. The ratio of δ_m/δ_{m-1} where m is a mode order can reach the values up to 10.

To get a distribution of light field at intermode interference the parameters of real waveguide sample on $LiNbO_3$ must be used. For numerical calculations the following values of r_{33}, β_{33} and σ_d for TE_3 mode was taken from [2]:
$\sigma_d = 1.24 \times 10^{-9}\ \Omega^{-1}m^{-1}$,
$\beta_{33} = (0.7–1.1) \times 10^{-10}$ A/W,
$r_{33} = 3.3 \times 10^{-11}$ m/V.
For this waveguide formed by the Ti diffusion in a doped sample of X cut $LiNbO_3$:Fe (0.03% by weight), the effective refractive indices of TE modes at the light wavelength λ=0.63 μm were n_0^*=2.213, n_1^*=2.206, and n_2^*=2.204.

Using such parameters, we evaluated δ value as $\delta \sim 1.6 \cdot 10^{-5}$ mm²/W. It corresponds to nonlinear change of refractive index $\Delta n = -1 \cdot 10^{-4}$ that is obtained at the light intensity $I(x,z)$=6.25 W/ mm². We consider in the input area of a waveguide the focused light beam of a Gaussian shape with the magnitude $\sqrt{I(x,z)}$ and the dimension close to its waist. Replacing in Eq.1 Δn with the Eq.3 and making a numerical calculation of Eq.1 with given values of all parameters, the distribution of light field along the waveguide mode path can be obtained. A sum of light fields of two guided modes gives a picture represented in Fig.1a. This distribution was calculated for TE_1 and TE_2 modes with initial aperture a=20 μm and with effective refractive indices of n_1^*=2.206 and n_2^*=2.204. The following values of δ were taken: $\delta = -1 \cdot 10^{-5}$ mm²/W for TE_1 mode and $\delta = -5 \cdot 10^{-5}$ mm²/W for TE_2 mode. If the values of nonlinearity for neighbouring waveguide modes will be equel to each other ($\delta_1 = \delta_2$), we obtain usual interference picture (Fig.1b).

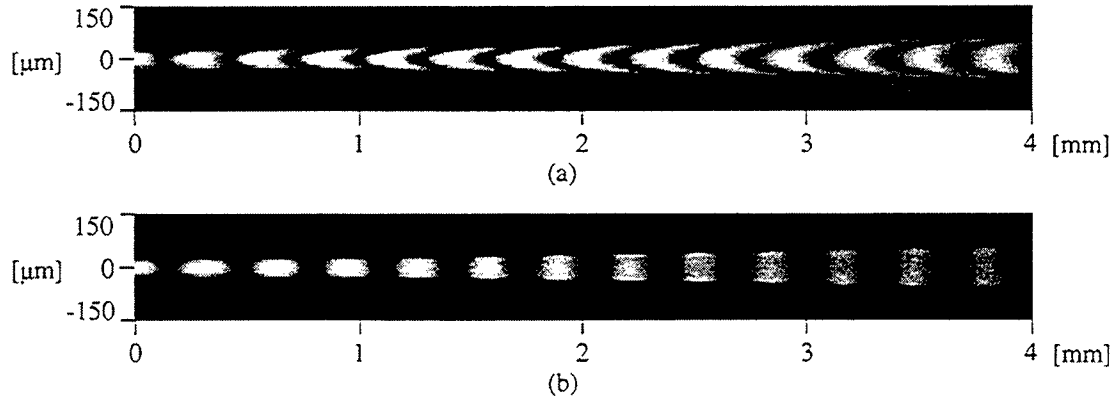


Fig.1: Numerically calculated interference images in waveguide mode track

In experiments we used the $LiNbO_3$ waveguide with characteristics similar to discussed above. The sample tested was formed upon a Z-cut wafer of $LiNbO_3$ in two steps. The dimensions of the wafer were 16x20x3 mm along X, Y and Z axes of a crystal. The first step included the titanium indiffusion from Ti film ~40 nm thick at a temperature of 1000° C in an air atmosphere. In the second step the photorefractive properties of this waveguide were enhanced through the additional Fe-diffusion from a Fe film ~50 nm thick at the same diffusion conditions. Because this sample was formed in X cut wafer, not in z-cut as was supposed in calculations, all experiments on the intermode interference were performed using guided TM modes.

The photorefractive properties of the waveguide were tested at the same wavelength in two-beam coupling scheme. It has been found, that the dark conductivity of a crystal within waveguide region considerebly exceeded its photoconductivity for light intenisity 1 W/cm^2. The dark decay of a photorefractive grating formed by TM_0 modes was ~1 s and it increased considerably for such gratings formed by TM modes of higher order. Such a behavior of a dark decay time is the result of the nonuniform Fe distribution by the waveguide depth. The defocusing capability of this sample was also observed.

The experimental setup is shown in Fig.2. The light beam of He-Ne laser (L) was collimated by a collimator (C). Then it was focused by cylindrical lens (CL) with focal length of 100 mm. The focused beam was coupled in the waveguide (W) by the prism element (PE). The position of a light beam waist within the waveguide could be changed by a variation of a distance between a lens (CL) and prism-coupling element. The image of a light beam track within the waveguide was inspected visually with an optical microscope (M).

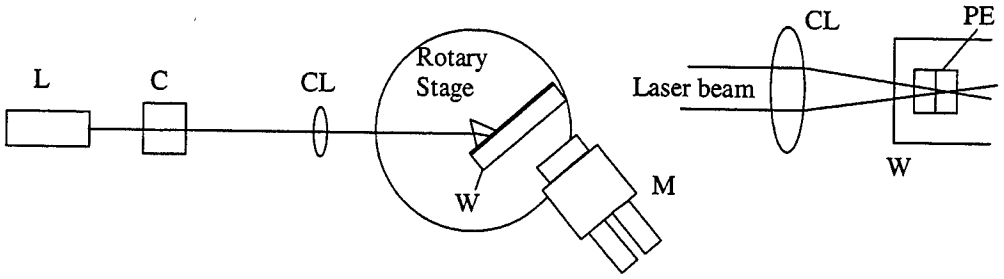


Fig.2: Experimental setup for observation of nonlinear intermode interference

The next effects were observed at light excitation within waveguide and beam waist position in the in-coupling region. First, the light beam divergence in the waveguide plane considerably increased from the initial up to some steady-state value for the time period of ~1 s for TM_0 mode. Second, simultaneous excitation of two neighbouring TM modes could be observed for the single exciting light beam. Such effect took place only at using in experimental setup the focusing lens with focal lenth of less than 100 mm. In a case when two TM modes were excited in the waveguide simultaneously we observed the interference image like that represented in the Fig.1a. The shapes of the interference fringes were almost identical for the experiment and calculation. Pictures of such type were observed in steady state on each of TM modes.

In conclusion, we experimentally observed the nonlinear interference of collinear guided modes of photorefractive optical waveguide in $LiNbO_3$ in conditions of significant spatial self - action of light beams. The numerical simulations show the good accordance between theoretical predictions and experimental results. This effect may be useful for the measurements of nonlinear parameters of optical waveguides and for some applications in photonic elements.

1. V. Shandarov, S. Shandarov, SPIE Vol. 2969, 158
2. G. Glazov, I. Itkin, V. Shandarov, E. Shandarov, and S. Shandarov, J. Opt. Soc. Am. B 7(1990), 2279

Curvature Dynamics and Fronts in the Optical Parametric Oscillator

J. N. Kutz

Department of Applied Mathematics, University of Washington, Seattle, Washington 98105
kutz@amath.washington.edu

T. Erneux

Optique Nonlinéaire Théorique, Université Libre de Bruxelles, CP 231, Bruxelles 1050, Belgium

S. Trillo

Dipartimento di Ingegneria, University of Ferrara, Via Saragat 1, 44100, Ferrara, Italy

M. Haelterman

Service d'Optique et Acoustique, Université Libre de Bruxelles, CP 194/5, B-1050 Bruxelles, Belgium

Frequency conversion via optical parametric oscillation in nonlinear $\chi^{(2)}$ materials is a well-known phenomena whose effects were demonstrated at the inception of the study of nonlinear optics. However, only through recent efforts has this frequency conversion mechanism allowed optical parametric oscillators (OPOs) to be regarded as promising sources of broadly tunable coherent radiation [1]. As a consequence, much research has been devoted towards theoretical and computational studies of the nontrivial spatial structures which arise in the transverse electric field due to the parametric interactions between signal and pump fields in the presence of diffraction. These electric field structures, or patterns, arise in 1D, 2D, and 3D geometries and are a hallmark feature of a broader class of spatially extended nonlinear systems driven from equilibrium (see [3] and references therein). We present the first analytic verification of the stability of front structures (topological solitons) of the optical parametric oscillator when driven beyond equilibrium. Front solutions are shown to be exponentially stable with *any* perturbation to the ideal system simply acting to shift the center position of the front through a translational invariance. Although the stability results are derived for 1D, it can be applied to the 2D case for which it is shown that the front curvature is governed by the heat equation. Thus only stripes can be supported in the long time behavior provided we are below threshold for any Turing instabilities. These analytic results, which support previous numerical observations [3, 4, 5, 6, 7], are crucial in determining whether topological solitons can be observed experimentally in the increasingly important and rapidly developing field of $\chi^{(2)}$ OPO systems.

We consider the mean-field model of a degenerate optical parametric oscillator where the dimensionless signal (U) and pump (V) field envelopes at the fundamental and second harmonic are governed by [3]:

$$U_t = \frac{i}{2}U_{xx} + VU^* - (1 + i\Delta_1)U + F_u \tag{1a}$$

$$V_t = \frac{i}{2}\rho V_{xx} - U^2 - (\alpha + i\Delta_2)V + S + F_v \tag{1b}$$

where t is time, x is the spatial transverse coordinate, Δ_1 and Δ_2 are the cavity detuning parameters, ρ is the diffraction ratio between signal and pump fields, α is the pump-to-signal loss ratio, S represents the pumping term, and F_u (F_v) $\ll 1$ are physically realizable perturbations to the signal (pump) field.

The onset of instability of the uniform solution $U = 0$ and $V = S/(\alpha + i\Delta_2)$ can be explored using an order parameter approach [2]. In particular, by utilizing an iterative procedure and orthogonality conditions, we find the long-time evolution to be governed by the Fisher-Kolmogorov equation [8]:

$$\phi_\tau - \phi_{\zeta\zeta} + \phi^3 - 2\gamma\phi = F\,. \tag{2}$$

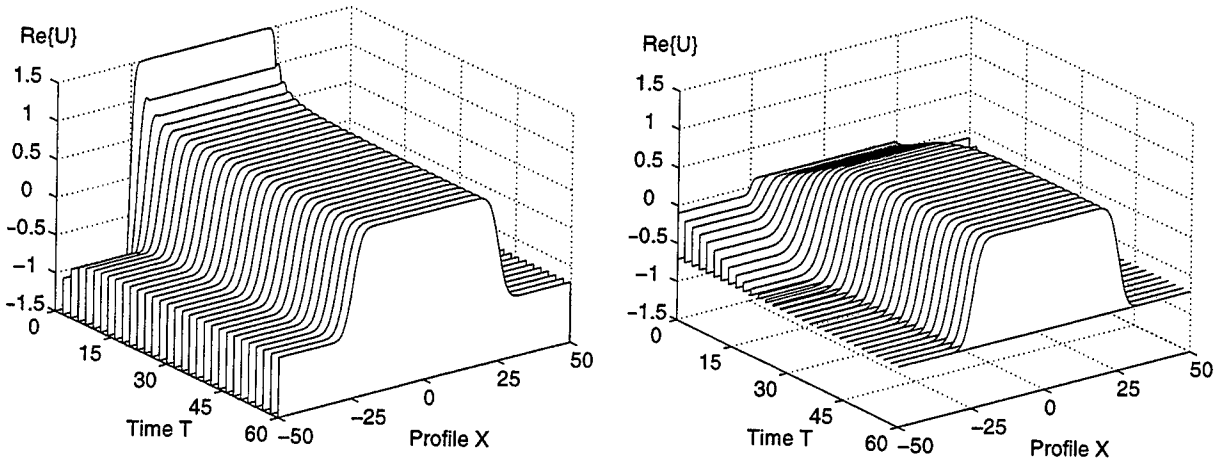


Figure 1: Numerical solution to Eq. (1) in 1-D depicting the formation of the steady-state front solution of the signal field. Here we have taken $\Delta_1 = 1$, $\Delta_2 = 1$, $\rho = 0.5$, and $S = S_c + 0.5$ and demonstrated stability of the front starting with two arbitrary initial conditions.

Here $u = ((\alpha^2 + \Delta_2^2)/(\alpha - \Delta_1\Delta_2))^{1/2}\phi$, $\xi = (\Delta_1/2)^{1/2}\zeta$, and $2\gamma = C(1 + \Delta_1^2) > 0$ so that $C = 1$, and we have a supercritical bifurcation. The perturbation $F = F(F_u, F_v)$ incorporates perturbations to both the signal and pump fields explicitly. We note that this equation supports front solutions when $\Delta_1 = O(1) > 0$ and $\alpha - \Delta_1\Delta_2 = O(1) > 0$:

For $F = 0$, we find a front (kink) steady-state solution whose linear stability can be determined exactly. Specifically, we find the front solution to be neutrally stable due to a translational invariance. However, small perturbations decay exponentially to the steady-state. Thus, arbitrary initial conditions settle quickly to a steady-state solution with a decay rate which is in good agreement with the linearized theory (see Fig. 1). We note that a split-step, pseudo-spectral algorithm with periodic boundary conditions was utilized in solving Eq. (1) so that pairs of fronts arise in the simulations.

To explore the front curvature dynamics, we consider an initial front which is nearly uniform in a single variable. We then seek a front solution of Eq. (2) of the form $\phi(\tau, \zeta, \eta) = \phi(\tau, z)$ where $z \equiv \zeta - \zeta^0(\tau, \eta)$ is a coordinate attached to the front and ζ^0 is the position of the front which is now a function of τ and slowly varying in η. Here the variable η arises from our perturbation $F = \phi_{\eta\eta}$ where η is the second transverse variable. With the boundary conditions $\phi(\tau, \pm\infty, \eta) = \pm\sqrt{2\gamma}$, we obtain the solution

$$\phi = \sqrt{2\gamma}\tanh\left(\sqrt{\frac{\gamma}{1 + (\zeta_\eta^0)^2}}z\right) \tag{3}$$

provided that the position of the front satisfies the heat equation given by

$$\zeta_\tau^0 = \zeta_{\eta\eta}^0 . \tag{4}$$

Equation (4) suggests that the evolution of the front curvature is purely diffusive. Indeed, the predicted $\sqrt{\tau}$ law for the curvature decay can be verified numerically by solving Eq. (1). The diffusive behavior of the front explains the progressive evolution to straight and steady fronts shown in Fig. 2. As a result of the periodic boundaries, only an even number of stripes are capable of being supported, whereas for no flux boundary conditions an odd number of fronts may arise. The actual number is determined by the initial conditions.

To summarize, the first analytic proof that front solutions for $\Delta_1 > 0$ are exponentially stable above threshold is given. Physical perturbations to the 1D OPO system which do not preserve

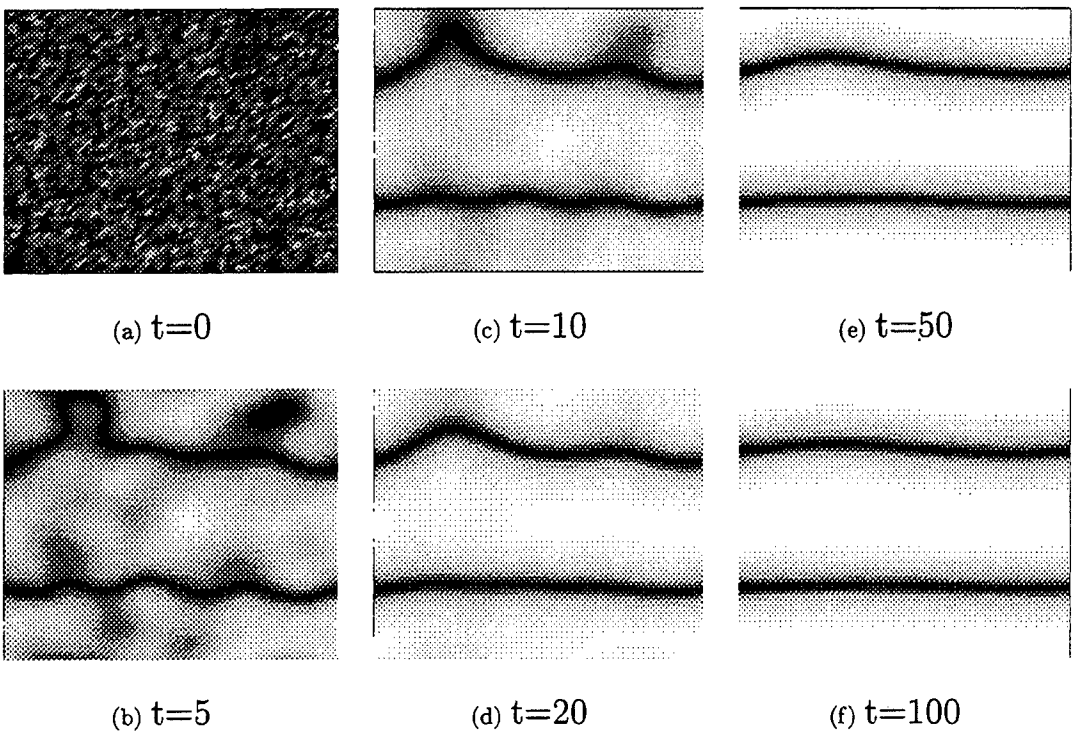


Figure 2: Numerical solution to Eq. (1) depicting the formation of a uniform solution to the signal field intensity with two stripes (fronts). We begin initially with white-noise and notice that the complicated structures slowly straighten out and form the uniform state with the straight fronts depicted at time t=100. The grid size is $x, y \in [-20, 20]$

certain symmetries simply give rise to a drift in the front position. This does not, however, effect the underlying stability of the fronts. These results have important implications for the 2D problem. In particular, the curvature of a front is governed by a heat equation so that the only stable structures supported must be stripes. These results, which are verified via numerical simulations, suggest that fronts are indeed observable in experimental OPO systems.

References

[1] See, for instance, the special issue on Optical Parametric Oscillation and Amplification, J. Opt. Soc. Am. B **10**, 2147 (1993); and Optical Parametric Devices, J. Opt. Soc. Am. B **12**, 2083 (1995).

[2] M. C. Cross and P. C. Hohenberg, Rev. Mod. Phys. **65**, 851 (1993).

[3] S. Trillo, M. Haelterman, and A. Sheppard, Opt. Lett. **22**, 970 (1997).

[4] S. Longhi, Phys. Scripta **56**, 611 (1997).

[5] M. Tidli, P. Mandel, and R. Lefever, Phys. Rev. Lett. **81** 979 (1998).

[6] See, for example, M. Santagiustina, P. Colet, M. San Miguel and D. Walgraef, Opt. Lett. **23**, 1167 (1998).

[7] K. Staliunas and V. J. Sánchez-Morcillo, Phys. Rev. A, **57**, 1454 (1998).

[8] G. T. Dee and W. Van Sarloos, Phys. Rev. Lett. **60**, 2641 (1988).

Excitation and Interactions of Gap Quadratic Solitons

Sergey V. Polyakov
CREOL, University of Central Florida
4000 Central Florida Blvd., Orlando, FL 32816-2700, USA
(407)-823-6944
serge@creol.ucf.edu

Anatoly P. Sukhorukov
Physics Department, Moscow State University
Vorobiovy Gory, Moscow, 119899, Russia
(+7-095)-939-1662
aps@nls.phys.msu.su

Interaction of the 1-st and 2-nd harmonics in Bragg gratings with quadratic nonlinearity can support parametric gap solitons [1-6]. The properties of slow and immobile gap solitons are apprehensible at present [1-5]. The study of gap soliton trapping and interaction was begun recently [5,6].

Here we discuss numerical simulation of nonlinear tunneling of optical coupled harmonics in quadratic gratings, slow and immobile gap quadratic soliton trapping and interactions. For envelopes of two harmonics $B_{1,2}$ one writes:

$$\frac{\partial B_1}{\partial t} = iD_1 \frac{\partial^2 B_1}{\partial z^2} - i\Theta_1 B_1 + i\beta_1 B_1^* B_2,$$

$$\frac{\partial B_2}{\partial t} = iD_2 \frac{\partial^2 B_2}{\partial z^2} - i\Theta_2 B_2 + i\beta_2 B_1^2, \qquad (1)$$

where t is the time, z is the propagation coordinate, D_j ($D_1 D_2 > 0$) are the dispersion coefficients of gratings at cutoff frequencies $\omega_{c,j}$, β_j describe quadratic nonlinearity, terms $\theta_j = \omega_j - \omega_{c,j}$ express frequency detunings; $j = 1,2$. The set (1) has been solved numerically with different boundary conditions. The evolution of CW input impulses consisted of FF and SH is of interest. We simulated the effect of CW wave splitting into train of slightly-oscillating slow gap quadratic solitons. The variations of SH input intensity don't critically affect soliton formation. Moreover, it is possible to generate slow gap soliton series by irradiating the system with the FF wave only (Fig. 1).

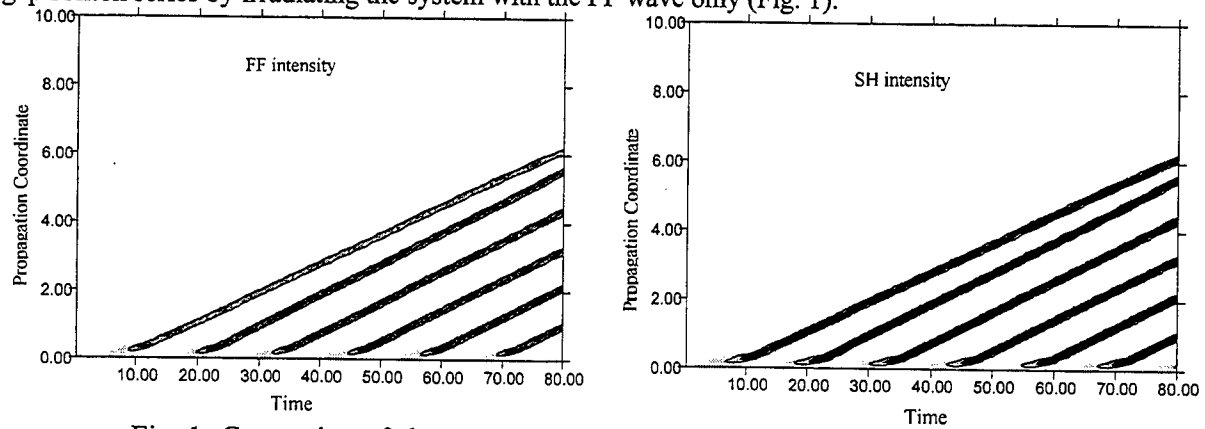


Fig. 1: Generation of slow gap quadratic soliton train by input cw FF signal.

Generated SH accumulates near the crystal edge, then starts to interact with FF pulse and forms a train of gap solitons. This effect is very important for the experiments in the future.

The interactions between two parametric $sech^2$ solitons, injected into the medium from the bound were simulated (Fig. 2a). At the first stage two solitons without phase mismatch propagate almost in a parallel way, but end up with fusing. In a contrary, same solitons with $\pi/2$ phase shift with respect to FF propagate through the gratings without interaction. A collision of slow and immobile soliton (Fig. 2b) leads to distracting of immobile state.

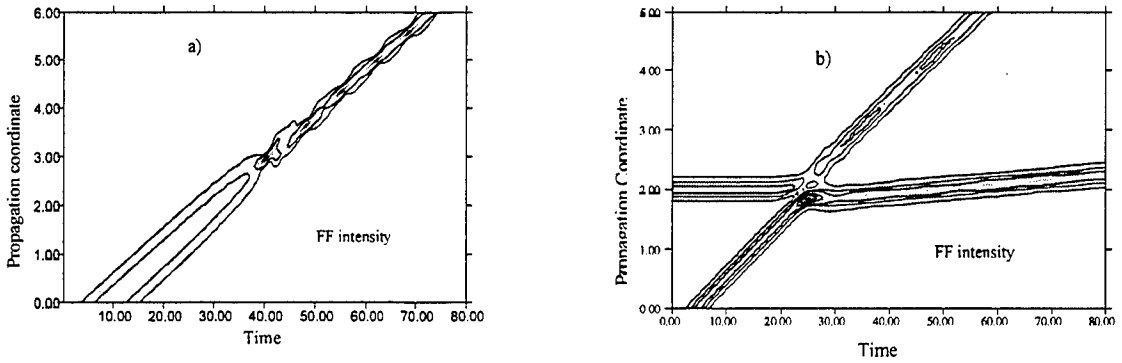


Fig. 2: Collisions of two parametric slow solitons in-phase (a) and slow – immobile solitons (b).

The fusion effect allows to decrease the peak intensity of input $sech^2$ solitons and obtain non-propagating underthreshold impulses, while the pair of these can fuse and generate propagating signal. This regime was observed in numerical simulations. The fusion occurs near the entrance of the system.

The set of equations (1) is known to have the following integrals of motion: $I_1 = \int\sum|B_j|^2 dz$,

$I_2 = \int\sum B_j\left(\partial B_j^*/\partial z\right)dz$, and

$I_3 = \int\left[2D_1\left|\frac{\partial B_1}{\partial z}\right|^2 + D_2\left|\frac{\partial B_2}{\partial z}\right|^2 - \beta B_1^2 B_2^* - \beta B_1^{2*} B_2 + 2\Theta_1|B_1|^2 + \Theta_2|B_2|^2\right]dz$. Notice, that I_3 could become negative for powerful immobile waves, which guarantees localization. For slow impulses I_3 possesses additional positive term. Obviously, the condition of self-trapping remains the same, so we should modify I_3, with the help of other integrals: I_1 and I_2. For the case of equal phase velocity ($D_1 = 2D_2$), we obtain: $\tilde{I}_3 = I_3 - D_1|I_2|^2/2I_1$. This modification is useful for evolution prediction of a slow signal. Similar approach can be applied to inclined spatial solitons. The same modification could be made for qubic nonlinearity [5].

This research was supported by INTAS, NSF, RFBR and FUR.

REFERENCES:

1. Yu. S. Kivshar, Phys. Rev. E. **51,** 1613 (1995).
2. C. Conti, S. Trillo, and G. Assanto, Phys. Rev. Lett. **78**, 2341 (1997); Phys. Rev. E **57**, R1251 (1998).

3. T. Peschel, U. Peschel, F. Lederer, and B. A. Malomed, Phys. Rev. E **55**, 4730 (1997).
4. C. Conti, A. De Rossi, and S. Trillo, Opt. Lett. **23**, 1265 (1998).
5. S. V. Polyakov, A. P. Sukhorukov // Bull. Russ. Acad. Sci. Phys. **62**, 1849 (1998).
6. C. Conti, G. Assanto, and S. Trillo, Phys. Rev. E **59**, 2467 (1999).

Optical velocity control of parametric gap solitons

Michele De Sario, Claudio Conti and Gaetano Assanto

Department of Electronic Engineering, Terza University of Rome
and National Institute for the Physics of Matter, INFM – RM3 Division
Via della Vasca Navale 84, 00146 Roma, Italy
Tel. +3906 55177028; Fax +3906 5579078; E-mail: Assanto@ele.uniroma3.it

It has been demonstrated theoretically and experimentally [1-2] in Bragg gratings written in fibers with Kerr nonlinearity that the propagation of nondispersive bell-shaped pulses or gap solitons (GS) is possible at frequencies within the photonic band-gap (PBG) originated by the periodicity. Given the interest recently devoted to optical media with quadratic nonlinearities, we investigated the case of a Bragg grating in a structure yielding efficient second harmonic generation (SHG). Various theoretical papers [3-5] have demonstrated that, in this case, GS still exist as two colors (or "parametric") solitary waves formed by a fundamental frequency (FF) wave and its second harmonic (SH). They travel in the structure locked together at a velocity V much lower than the linear group velocity.

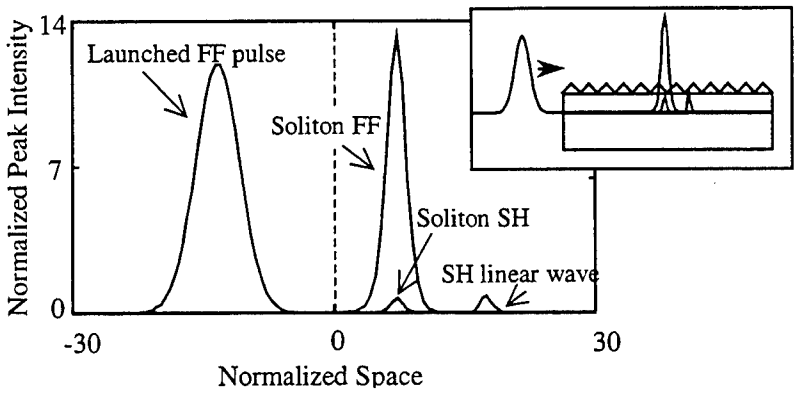


Fig.1. Snapshot of the process of excitation of a parametric gap soliton, by launching an FF input pulse (space=0 is the interface with the Bragg grating). For space>0 the FF locks to the SH to form the forward moving two-color GS, and the SH linear wave freely propagates to the end.

As in the Kerr case, such simultaneous propagation takes place even if the FF is within the PBG, with the SH in or out its own band-gap. In this communication we will focus our attention on the latter case (i.e. a "singly resonant structure"), and numerically investigate the generation of gap solitons trying to establish a link between the excitation process and the velocity of the generated nondispersive two-colors pulse. In order to study numerically the non-trivial boundary value problem modelling this system, we developed an algorithm for the integration of the hyperbolic system of PDEs resulting from the Maxwell equations [6] and based on a pseudo-spectral approach with Chebichev polynomials. [8]

The nearly Bragg-resonant counterpropagating FF fields $u_1^{\pm}$ coupled with the SH fields $u_2^{\pm}$ are described by the four normalized equations [7]

$$\pm i\frac{\partial u_1^{\pm}}{\partial \xi}+i\frac{\partial u_1^{\pm}}{\partial \tau}+\delta_1 u_1^{\pm}+u_1^{\mp}+u_2^{\pm}(u_1^{\pm})^{*}=0, \qquad \pm i\frac{\partial u_2^{\pm}}{\partial \xi}+i\frac{1}{v}\frac{\partial u_2^{\pm}}{\partial \tau}+\delta_2 u_2^{\pm}+\frac{(u_1^{\pm})^2}{2}=0$$

where ξ ($|\xi| \le L/2$, L is the length of the Bragg grating) and τ ($\tau \ge 0$) normalized space and time coordinates. The fields' evolution depends on three normalized parameters: the detuning from FF Bragg resonance δ_1 (FF inside the PBG for $|\delta_1|<1$), the SHG wavevector mismatch δ_2, and the linear group velocity ratio v. Hereafter, in order to consider a typical situation, we will assume $\delta_1 = -0.9$, $\delta_2 = 5$, and v=0.5. Launching an FF gaussian pulse $u_1^+(-L/2,\tau) = G_1^+ \exp(-\tau^2/W^2)$, with G_1^+ and W normalized pulse amplitude and width, respectively, and the bounds $u_{1,2}^-(L/2,\tau) = 0$ (no input from the other side of the structure), the SH generated inside the grating is partially reflected, partially locked with the FF to form a forward moving two-color GS, and partially transmitted as a linear wave which freely propagates in the singly resonant grating (Fig.1). [6] Although in a previous publication [7] we showed that the velocity of the generated nonlinear wave does not change appreciably by varying G_1^+, the theoretical analysis revealed the existence of solitons with different V for the same parameters. Hereby we numerically demonstrate that overlapping a small SH gaussian pulse $u_2^+(-L/2,\tau) = G_2^+ \exp(i\Delta\varphi)\exp(-\tau^2/W^2)$ to the FF input pulse can give rise to solitons with different velocities and shapes depending on the SH amplitude G_2^+ and on the relative phase $\Delta\varphi$ between the two harmonic fields. *Notice that the employed input peak intensity of the SH pulse $|G_2^+|^2$ is about two order of magnitude smaller than the FF's.* As a representative result, we choose $G_1^+ = \sqrt{12}, W = 5$, (these parameters correspond to a realistic input FF pulse of 100ps duration and peak intensities of the order of 100MW/cm^2 for a typical Bragg grating in a $KNbO_3$ waveguide) and vary G_2^+ for different values of $\Delta\varphi$. As a rule of thumb, more intense solitary waves travel faster; so one could expect that by increasing the input SH amplitude the velocity of the excited soliton increases as well. However, in this case the locking between the generated SH and the FF in the GS formation plays an important role: when $\Delta\varphi = \pi$ it is favoured and, indeed, V increases with G_2^+; conversely, when $\Delta\varphi = 0$ the opposite happens (Fig.2).

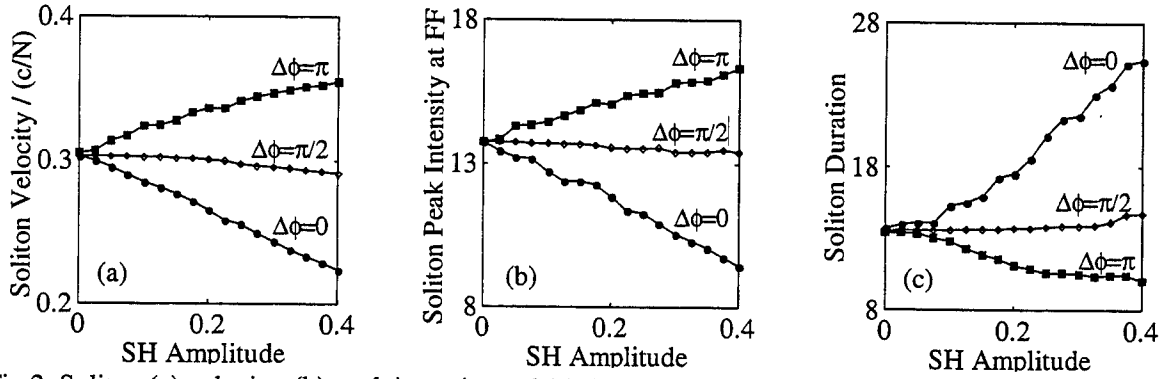


Fig.2. Soliton (a) velocity, (b) peak intensity and (c) duration vs. SH amplitude for three values of phase.

While the energy of the FF component of the soliton is about the same in all cases, what changes is the amount of SH locked with the FF and the GS width. When $\Delta\varphi = \pi$ the peak intensities at FF and SH ($|u_1^+|^2+|u_1^-|^2$ and $|u_2^+|^2+|u_2^-|^2$) and V increases with the amplitude of the input control pulse, while the duration (calculated at the 10% of the peak value) decreases. On the contrary, when $\Delta\varphi = 0$ an increase in SH amplitude makes solitons longer, with lower peak intensity and group velocity. Similar results were obtained for different values of $\delta_{1,2}$ and SH amplitudes G_2^+.

The previous analysis suggests the possibility of controlling V by varying the relative phase $\Delta\varphi$ between the two harmonics, given a sufficient amount of SH seed at the input. For example, for $G_2^+ = 0.3$, and varying $\Delta\varphi$ from $-\pi$ to π, we calculated velocity, peak intensity and duration of the solitons (Fig. 3.). Consistently with the previous analysis, V exhibits a minimum when $\Delta\varphi = 0$ and maxima when $\Delta\varphi = \pm\pi$. It is interesting to note that, by acting on $\Delta\varphi$, a range of values can be obtained wider than by varying the SH amplitude. Moreover this range is determined by the amplitude of the SH control pulse.

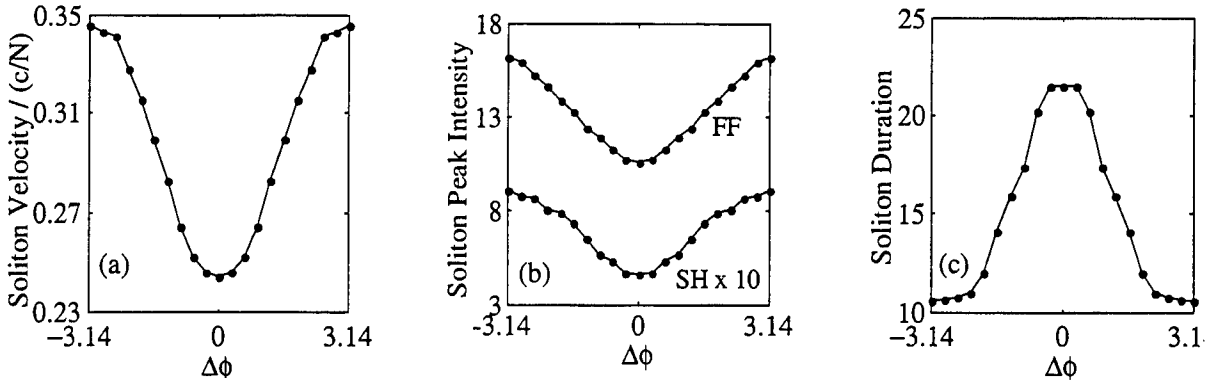


Fig. 3. Soliton (a) velocity, (b) peak intensity at FF and SH, and (c) duration vs. relative phase when $G_2^+ = 0.3$.

In summary, we investigated the possibility of controlling the velocity of parametric gap solitons using a small coherent second harmonic seed. Potential applications in switching devices, delay lines and optically-controlled memories are envisaged in the framework of all-optical communication systems.

References

[1] C. M. De Sterke and J. E. Sipe, in *Progress in Optics XXXIII*, edited by E. Wolf (Elsevier, Amsterdam, 1994), Chap. III.

[2] B.J. Eggleton *et al.*, Phys. Rev. Lett. **76**, 1627 (1996).

[3] C. Conti, S. Trillo, and G. Assanto, Phys. Rev. Lett. **78**, 2341 (1997).

[4] H. He and P. D. Drummond, Phys. Rev. Lett. **78**, 4311 (1997).

[5] T. Peschel, U. Peschel, F. Lederer, and B. A. Malomed, Phys. Rev. E **55**, 4730 (1997).

[6] C. Conti, G. Assanto, S. Trillo, Opt. Express **3**, 389 (1998).

[7] C. Conti, G. Assanto, S. Trillo, Phys. Rev. E **59**, 2467 (1998).

[8] C. Canuto, M. Hussaini, A. Quaternoni, and T. A. Zang, *Spectral Methods in Fluid Dynamics*, Springer Verlag, New York, 1988.

Optical Gap Solitons in Nonresonant Quadratic Media

Takeshi Iizuka[1,2] and Yuri S. Kivshar[2]

[1] *Department of Physics, Faculty of Science, Ehime University,790-8577,Matsuyama Japan*
TEL (+81)89-927-9584, FAX (+81)89-927-9580
[2] *Optical Sciences Centre, Australian National University, Canberra ACT 0200, Australia*
TEL (+61)2-6249-3081, FAX(+61)2-6249-5184

It has been shown that quadratic nonlinearities can support spatial optical solitons[1] and also different types of gap solitons 4in periodic Bragg gratings with a quadratic [or $\chi^{(2)}$] nonlinear response[2]. Importantly, when an input electromagnetic wave $\mathbf{E}$ at frequency ω is launched into a noncentrosymmetric material, it generates also a quasi-static electric field (or *dc field*) at frequency zero. This effect is known as *optical rectification*[3]. Recently Bosshard *et al.* have shown[4] that the combined processes of optical rectification and the linear electro-optic effect lead to an *additional, nonresonant* contribution into an effective nonlinear refractive index of noncentrosymmetric materials due to cascading processes.

The effect of optical rectification is *usually neglected* in the theory of quadratic solitons because the equation for the dc field can be integrated explicitly, leading to a nonresonant contribution into the effective cubic nonlinearity of the nonlinear Schrödinger (NLS) equation[5]. However, for the propagation of spatio-temporal multi-dimensional optical pulses in nonresonant quadratic media, such a reduction is no longer possible and, as a result,the multi-dimensional NLS equation becomes coupled to a dc field[6], similarly to the integrable case of the Dawey-Stewartson equation[7].

In the present paper we shall show that the dc wave plays an important role in quadratically nonlinear optical gratings. We consider propagations of light in a periodic medium with a quadratic $\chi^{(2)}$ nonlinear response. Let us start from Maxwell's equation,

$$c^2\nabla^2 E - \frac{\partial^2}{\partial t^2}\left[\hat{\epsilon}(z, i\partial_t) + \chi^{(2)}E\right]E = 0, \tag{1}$$

where ∇^2 stands for the Laplacian, c is the speed of light in vacuum, E is the x-element of the electric field, $\boldsymbol{E} = E(z,t)\boldsymbol{e_x}$, and the quadratic nonlinearty is represented by a tensor element $\chi^{(2)} = \boldsymbol{\chi^{(2)}_{xxx}}$. We assume that $\hat{\epsilon}(z,\omega)$ is a periodic function of z, so it can be presented in a general form as a Fourier series, $\hat{\epsilon}(z,\omega) = \epsilon(\omega)\left(1 + \sum_{j=1}^{\infty}\epsilon_j e^{2ikz} + \sum_{j=1}^{\infty}\epsilon_j^* e^{-2ikz}\right)$, where $d = \pi/k$ is the period of the Bragg-grating structure. Deriving the couple-mode equations below, we assume the case of a *shallow grating*, i.e. that the condition $\epsilon_j \ll 1$ holds. For a periodic structure, the Bragg reflection leads to a strong interaction between the forward and backward waves at the Bragg wavenumber $k_B \approx k$. Therefore, we consider the asymptotic expansion for the electric field in the form,

$$\begin{aligned} En = &\left(E_+ e^{ikz} + E_- e^{-ikz}\right)e^{-i\omega t} + \text{c.c.} \\ &+ E^{(0,0)} + E^{(0,2)}e^{2ikz} + E^{(0,-2)}e^{-2ikz} + \left(E^{(2,0)} + E^{(2,2)}e^{2ikz} + E^{(2,-2)}e^{-2ikz}\right)e^{-2i\omega t} + \text{c.c.}, \end{aligned} \tag{2}$$

where $E_\pm = E_\pm(z,t)$ are slowly varying envelopes of the forward(+) and bakward(-) waves. The frequency ω satisfies the dispersion relation for linear waves, $c^2k^2 = \omega^2\epsilon(\omega)$. Slowly varying functions $E^{(n,m)} = E^{(n,m)}(z,t)$ are defined as nonlinear amplitudes of the (n,m)-order harmonics $e^{-in\omega t}e^{imkz}$.

We introduce a small parameter ε so that we assume $E_\pm \sim O(\varepsilon)$, $\partial E_\pm/\partial t \sim \partial E_\pm/\partial z \sim O(\varepsilon^3)$ and $\epsilon_j \sim O(\varepsilon^2)$. Then, substituting the expansion (2) into Eq. (1), we compare the

terms of the same order in front of the coefficients $e^{-in\omega t}e^{imkz}$. At the orders $(2,0)$, $(2,\pm 2)$ and $(0,\pm 2)$ we respectively obtain,

$$E^{(2,0)} = -\frac{2\chi^{(2)}}{\epsilon(2\omega)}E_+E_- \quad E^{(2,\pm 2)} = -\frac{\chi^{(2)}}{[\epsilon(\omega)-\epsilon(2\omega)]}E_\pm^2, \quad E^{(0,\pm 2)} = -\frac{\chi^{(2)}}{2c^2k^2}\frac{\partial^2}{\partial t^2}\left(E_\pm^* E_\mp\right),$$

where we have assumed condition for the non-resonant interaction, i.e. $\epsilon(\omega) \neq \epsilon(2\omega)$. Note that $E^{(2,0)}$ and $E^{(2,\pm 2)}$ are of $O(\varepsilon^2)$ and $E^{(0,\pm 2)}$ is of $O(\varepsilon^6)$.

At the orders $(1,\pm 1)$ and $(0,0)$ we obtained a system of coupled nonlinear equations,

$$i\left(\frac{\partial}{\partial t} + v_g\frac{\partial}{\partial z}\right)E_+ + \kappa E_- + \left(A|E_+|^2 + B|E_-|^2 + CE^{(0,0)}\right)E_+ = 0, \tag{3}$$

$$i\left(\frac{\partial}{\partial t} - v_g\frac{\partial}{\partial z}\right)E_- + \kappa^* E_+ + \left(B|E_+|^2 + A|E_-|^2 + CE^{(0,0)}\right)E_- = 0, \tag{4}$$

$$\left(\frac{\partial^2}{\partial z^2} - \frac{1}{v_0^2}\frac{\partial^2}{\partial t^2}\right)E^{(0,0)} + D\frac{\partial^2}{\partial t^2}\left(|E_+|^2 + |E_-|^2\right) = 0, \tag{5}$$

where $v_g(\omega) = d\omega/dk$, $v_0 = v_g(0)$, $\kappa = \omega^2\epsilon(\omega)\epsilon_1 f^{-1}(\omega)$, $A = 2(\chi^{(2)})^2\omega^4\{f(\omega)[c^2k^2 - \omega^2\epsilon(2\omega)]\}^{-1}$, $B = -4(\chi^{(2)})^2\omega^2[f(\omega)\epsilon(2\omega)]^{-1}$, $C = 2\omega^2\chi^{(2)}f^{-1}(\omega)$, and $D = -2\chi^{(2)}/c^2$ with $f(\omega) \equiv [\omega^2\epsilon(\omega)]'$. System (3)-(5) describes the interaction between the forward and backward waves coupled to a dc wave induced via the rectification effect.

Important issue is a link between our new model (3)-(5) and the previous studies of gap solitons in a periodic media with a nonlinear quadratic resonance. In spite of the fact that the dc wave $E^{(0,0)}$ itself is of *a higher order*($\sim \varepsilon^2$) in comparison with the main waves, it becomes coupled to the fields E_+ and E_- *in the main order*. As a result, the model (3)-(5) reduces to a particular form of the conventional model of $\chi^{(2)}$ gap solitons[2] valid for a nonresonant limit of a large mismatch.

Next, we look for spatially localized solutions of Eqs. (3)-(5) for *bright gap solitons* in the form,

$$E_+ = \Delta^{-1/2}f(\zeta)e^{i[\theta_1(\zeta)-\Omega t+g/2]}, \qquad E_- = \Delta^{1/2}f(\zeta)e^{i[\theta_2(\zeta)-\Omega t-g/2]}. \tag{6}$$

where $\zeta = z - Vt$; functions $f(\zeta)$ and $\theta_{1,2}(\zeta)$, and the parameters Ω, V, Δ are assumed to be real and $\kappa = |\kappa|e^{ig}$. Substitution the ansatz (6) into Eq. (5) gives, $E^{(0,0)}(\zeta) = -v_0^2V^2D(v_0^2 - V^2)^{-2}\left(\Delta + \Delta^{-1}\right)f^2(\zeta)$, and therefore the contribution of the dc field should vanish at $V = 0$. We must set the parameter Δ as $\sqrt{(v_g - V)/(v_g + V)}$, and then obtain a system of coupled ODEs for f, $\theta_- \equiv \theta_1 - \theta_2$ and $\theta_+ \equiv \theta_1 + \theta_2$. We obtain a solution

$$f(\zeta) = \left\{\frac{\mp(4\mu/\delta)[1 - (\nu/2\mu)^2]}{\cosh(\zeta\sqrt{4\mu^2 - \nu^2}) \mp (\nu/2\mu)}\right\}^{1/2},$$

where the $\pm$ stands for the $\delta > 0$ and $\delta < 0$, respectively. θ_1 and θ_2 are obtained as

$$\theta_- = \theta_1 - \theta_2 = -2\tan^{-1}\left\{\sqrt{\frac{2\mu - \nu}{2\mu + \nu}}\ \tanh^{\mp 1}\ \frac{\sqrt{4\mu^2 - \nu^2}}{2}\zeta\right)^{\mp 1}\right\}, \tag{7}$$

$$\theta_+ = \theta_1 + \theta_2 = -\frac{\nu V}{v_q}\zeta \pm \frac{4\eta v_g}{\delta}\tan^{-1}\left[\sqrt{\frac{2\mu \pm \nu}{2\mu \mp \nu}}\tanh\ \frac{\sqrt{4\mu^2 - \nu^2}}{2}\zeta\right)\right] + C_\pm, \tag{8}$$

where $C_{\pm}$ are integration constants. Constants μ, ν, δ, and η are defined as $\mu = |\kappa|/(v_g^2 - V^2)^{1/2}$, $\nu = -(2v_g\Omega)/(v_g^2 - V^2)$, $\delta = -2(v_g^2 - V^2)^{-1/2}\left(\frac{(v_g^2+V^2)}{(v_g^2-V^2)}\tilde{A} + \tilde{B}\right)$, and $\eta = -4(v_g^2 - V^2)^{-3/2}v_g V\tilde{A}$, respectively, with $\tilde{A} = A - \frac{V^2v_0^2CD}{(v_0^2-V^2)}$ and $\tilde{B} = B - \frac{V^2v_0^2CD}{(v_0^2-V^2)}$.

The solution obtained from Eq. (7) describes a two-parameter family of gap solitons, spatially localized waves in the Bragg gratings, which are similar to the gap solitons of the conventional couple-mode theory. Actually, by an renormalization we can demonstrate that the solution is essentially the same as that earlier obtained[8].

The recent stability analysis of the conventional gap solitons[9] revealed the existence of two types of instabilities, *oscillatory* and *translational*. The most important, translational instability appears for large V, so that the induced dc field is expected to have a strong effect on the soliton stability. However, the detailed discussion of the stability is beyond the scope of the present study.

Our new model (3)-(5) is a Hamiltonian system which means that it has an conserved quantity which correspond to the energy. Other than the energy the we can derive 3 integrals of motion, which correspond to the field momentum, the total number of the forward and backward waves, and an independently conserved number of the dc waves. Therefore, in a sharp contrast to the conventional coupled-mode theory of gap solitons, the model (3)-(5) possesses one additional integral of motion, and it has no analogy with other soliton-bearing nonintegrable models where the soliton stability has been investigated so far.

In conclusion, we have demonstrated the importance of optical rectification effect in the theory of quadratic gratings. We have derived, for the first time to our knowledge, a novel model of the coupled-mode theory for optical gap solitons that describes a coupling of the forward and backward modes to an induced dc field, and we have found the analytical solutions forn solitons.

References

1. For an overview, see L. Torner, In : *Beam Shaping and Control with Nonlinear Optics*, F. Kajzar and R. Reinisch, Eds. (Plenum, New York, 1998), p. 229.

2. Yu.S. Kivshar, Phys. Rev. E **51**, 1613 (1995); Yu.S. Kivshar *et al.*, Int. J. Mod. Phys. **9**, 2963 (1995); C. Conti, S. Trillo, and G. Assanto, Phys. Rev. Lett. **78**, 2341 (1997); Opt. Lett. **22**, 445 (1997); T. Peschel, U. Peschel, F. Lederer, and B. Malomed, Phys. Rev. E **55**,4730 (1997); H. He and P.D. Drummond, Phys. Rev. Lett. **78**, 4311 (1997); C. Conti, G. Asanto, and S. Trillo, Opt. Lett. **22**, 1350 (1997); A. Arraf and C.M. de Sterke, Phys. Rev. E **58**, 7951 (1998).

3. M. Bass, P.A. Franken, J.F. Ward, and G. Weinreich, Phys. Rev. Lett. **9**, 446 (1962).

4. C. Bosshard, R. Spreiter, M. Zgonik, and P. Günther, Phys. Rev. Lett. **74**, 2816 (1995).

5. A.G. Kalocsai and J.W. Haus, Phys. Rev. A **49**, 574 (1994).

6. M.J. Ablowitz, G. Biondini, and S. Blair, Phys. Lett. A **236**, 520 (1997).

7. See, e.g., M. Boiti, J.J. Leon, L. Martina, and F. Pempinelli, Phys. Lett. A **132**, 432 (1988).

8. A.B. Aceves and S. Wabnitz, Phys. Lett. A **141**, 37 (1989); D.N. Christodoulides and R.I. Joseph, Phys. Rev. Lett. **62**, 1746 (1989).

9. I.V. Barashenkov, D.E. Pelinovsky, and E.V. Zemlyanaya, Phys. Rev. Lett. **80**, 5117 (1998); A. De Rossi, C. Conti, and S. Trillo, Phys. Rev. Lett. **81**, 85 (1998).

Formation and Switching of multilobed Patterns in Ring Shaped Complex Nonlinear Optical Oscillators

J. Scheuer, D. Arbel and M. Orenstein
Department of Electrical Engineering, Technion, Haifa 32000, Israel
Tel. 972-4-8294696, Fax. 972-4-8323041, E-mail: meiro@ee.technion.ac.il

The formation of a variety of stable complex transverse light patterns in nonlinear optical cavities was studied both in one and two dimensions [1-3]. A laser, which is based on a nonlinear resonator, can emit spontaneously some of these patterns [3,4]. A ring shaped laser is a special case of a two dimensional structure that imposes periodic boundary conditions in the azimuthal coordinate and therefore may emit interesting and complex patterns. Vertical cavity surface emitting lasers (VCSELs) are unique within the family of semiconductor lasers by having a 2-dimensional resonator and may serve as an ideal tool for the exploration and exploitation of complex electrical fields. Previous research on pattern formation in nonlinear active cavities [5-7] explained the on-switching of higher order lasing modes and of complex patterns by the gain-loss balance modified by the gain saturation (spatial hole burning). Here we show that the switching of patterns is caused mainly by a dynamic effect - the Modulation Instability (MI) of the self consistent field patterns and present the threshold conditions for the formation of the patterns.

We modeled the evolution of the electrical field in the semiconductor laser medium using the 1D wave equation which is applicable for large enough ring shaped lasers. The paraxial wave equation, which is valid for the VCSEL geometry, is written for the electrical field:

$$\frac{\partial E}{\partial z} - \frac{i}{2k_0 n_0}\frac{\partial^2 E}{\partial x^2} - ik_0 n_2 \cdot |E|^2 E = \frac{1}{2}[g_0 - \alpha_{tot}]\cdot E - \frac{k_0 n_2}{R}\cdot |E|^2 E \qquad (1)$$

where k_0 is the wave number, n_0 – the linear index of refraction, R – the anti-guiding factor and α_{tot} – the loses. g_0 is the unsaturated gain defined as $g_0(N_p) = \Gamma\alpha\cdot(N_p - N_0)$ where Γ is the confinement factor, α - the differential gain, N_p – the carrier density due to the pump and N_0 – the carrier density for transparency. n_2 the effective nonlinear refraction index is given by $n_2 = \frac{R\cdot g_0}{2k_0 I_{sat}}$, where I_{sat} is the saturation energy - $I_{sat} = h\nu/(\Gamma\alpha\tau_{sp})$.

For simplicity we introduce the following variables - $x'=k_0x$, $z'=k_0z/2n_0$ and $E(x,z) = \sqrt{1/n_0 n_2}\cdot A(x',z')$. Substituting them into (1) and dropping the primes, yields the normalized field equation:

$$\frac{\partial A}{\partial z} - i\frac{\partial^2 A}{\partial x^2} - 2i|A|^2 A = \gamma\cdot A - \frac{2}{R}|A|^2 A \qquad \text{where } \gamma = n_0 R\cdot(g_0 - \alpha_{tot})/k_0 \qquad (2)$$

Equation (2) has soliton like solutions [9] but also uniform Tilted Wave (TW) solutions, $A = A_0 e^{i(kx-\eta z)}$:

$$|A_0| = \sqrt{\frac{R}{2}};\quad k = \frac{2\pi}{L}\cdot n;\quad \eta = k^2 - R;\quad n = 0,1,2...$$

L is the ring's perimeter. The quantization of k is caused by the cyclic boundary conditions imposed by the ring geometry. In order to explore the existence range of each solution we analyzed its stability to small spatial harmonic perturbation. When the examining the n^{th}

order solution, a field component (noise) with a spatial frequency k+Ω will experience exponential growth if it is larger than k and lower than a certain frequency k_{max}:

$$k < k + \Omega < \sqrt{k^2 + 2\gamma R} \qquad (3)$$

The MI range depends on the pumping, the laser parameters and the specific steady state solution. For a given net gain (γ), higher order solutions have smaller MI range and are therefore more stable. Pattern switching will occur when the positive MI gain curve of the actually lasing pattern could excite the next order solution, which is (for the same pump rate) stable. From the perturbation analysis we can derive a threshold gain for the lasing of the $(n+1)^{th}$ solution:

$$\gamma = \frac{2\pi^2}{R \cdot L^2}(2n+1) \qquad (4)$$

Thus, a necessary condition for achieving thresholds for the higher multiple soliton solutions is R>0, satisfied by all semiconductor lasers, however may be not satisfied for other types of lasers. Further more, the threshold gains are smaller for larger rings and thus the appearance of complex pattern will require lower injection currents in larger lasers. The ring shaped VCSEL has, therefore, many threshold currents. The first one is the conventional uniform field lasing threshold (corresponds to net gain γ=0) The other threshold levels, derived from the MI consideration and not from gain-loss balance, correspond to the thresholds of the emergence of multiple lobed emission.

Another two important conclusions that rise from the perturbation analysis are: 1) The MI mechanism is unidirectional in the sense that it enables energy transfer only from lower order solutions to higher order solutions. This explains the increase of spatial frequency of the formed patterns with the pumping parameter. 2) A TW solution is unstable to perturbation of it's complex conjugate TW (solution n is basically unstable in the presence of solution –n). The lasing of the n^{th} TW solution excites its complex conjugate and as a result a standing wave azimuthal pattern would emerge. Again this explanation is stemming from the fundamental phenomena of the MI and does not require any inhomogeneities and imperfections that are conventionally used to explain this counter rotating wave coupling.

Figure 1 shows BPM simulation of Eq. (1) when the current is below the second (n=1) threshold. The perturbed electric field reached a uniform steady state distribution and in Fig. 2 - the BPM simulation above the third (n=2) threshold evolved into four-lobed solution.

All the above predictions were tested and verified experimentally. The near-field intensity pattern emerging from a proton implanted ring shaped VCSELs (20-40μm in diameter) with three 8nm $In_{0.2}Ga_{0.8}As$ QW, emitting at ~0.95 μm [8] were monitored. The near-field patterns were examined at room temperature under pulsed operation.

A uniform near-field was registered until the injected current was increased to ~1.5 times the threshold current. Then the pattern switched to an azimuthal standing pattern. As the current was increased, the number of light lobes increased, but not monotonically – probably due to defects and the inhomogeneous nature of the laser.

Fig. 3 shows the near-field intensity pattern of 40μm and 28μm diameter lasers at various currents.

The semi-analytical solutions of eq. (1) based on the perturbation analysis will be presented and compared with the experimentally measured near-fields and the BPM simulation results. It should be emphasized that the theory presented here is in principle valid for every semiconductor laser structure with cylindrical symmetry (disks, coupled rings etc.) [3]. The pattern selection mechanism shown here is, therefore, a general rule that applies for every cylindrical symmetric problem.

REFERENCES

[1] W. J. Firth et al, Europhys. Lett. 26 (1994) 521.

[2] G. D'Alessandro et al Phys. Rev. A46 (1992) 537.

[3] L. Djaloshinski and M. Orenstein, Opt. Lett., **23** (1998) 364.

[4] E. Pampaloni et al, Europhys. Lett. 24 (1993) 647.

[5] H. Adachihara, O. Hess, E. Abraham, P. Ru and J.V. Moloney, J. Opt. Soc. Am B. **10**, 658 (1993).

[6] J. R. Maricante and G. P. Agrawal, IEEE J. Quantum Electron. **32**, 590 (1996).

[7] J. Scheuer and M. Orenstein, Non Linear Optics 98' Princeville, Kawai, Hawaii, paper ThC13, pp. 361.

[8] M. Orenstein et al, Appl. Phys. Lett. 56 (1990) 2384.

[9] D. Arbel, J. Scheuer and M. Orenstein, Non Linear Optics 98' Princeville, Kawai, Hawaii, paper ThC4, pp. 334.

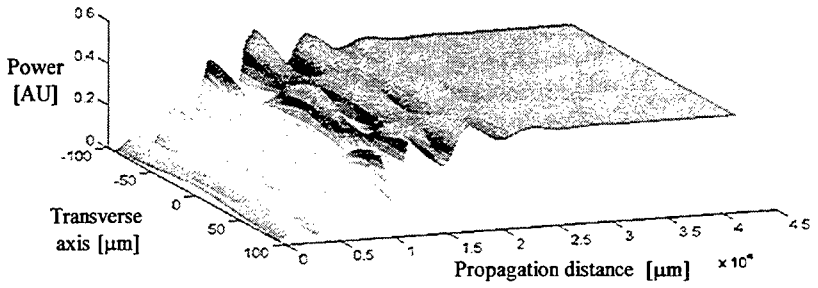


Figure 1 – Stability for current below the second threshold, I_{sat}=20, I=185, g_0=0.01004, α_{tot}=0.01

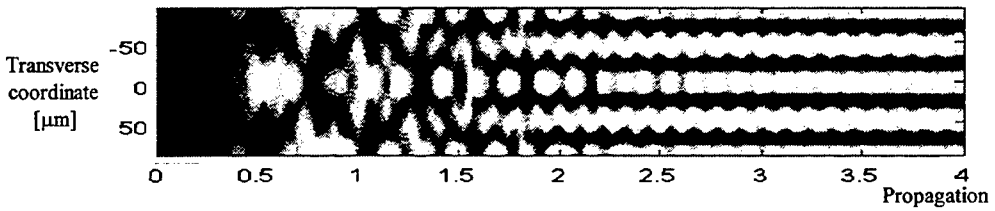


Figure 2 – Stability at current above second threshold

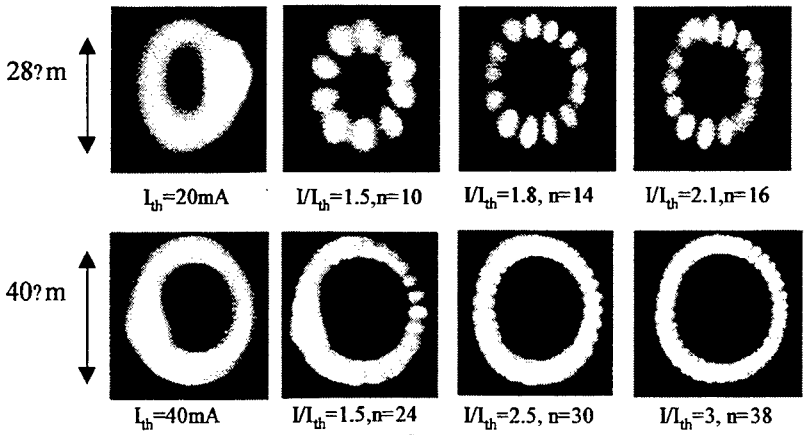


Figure 3 – Ring VCSEL near-field patterns - experimental results

POLARIZATION-LOCKED VECTOR SOLITONS IN A FIBER LASER

J. M. Soto-Crespo
Instituto de Óptica, C.S.I.C., Serrano 121, 28006 Madrid, Spain
jsoto@soliton.optica.csic.es

N. N. Akhmediev
APCRC, Optical Science Centre, RSPhysSE, ANU, Canberra ACT 0200, Australia
nna124@rsphysse.anu.edu.au

B. C. Collings
Bell Laboratories, Lucent Technologies, Holmdel, NJ 07733 (current address)
Electrical Engineering Department, Princeton University, Princeton, NJ 08544, USA
collings@lucent.com

S. T. Cundiff
JILA, University of Colorado and National Institute of Standards and Technology,
Boulder, CO 80309-0440, USA
cundiffs@jila.colorado.edu

K. Bergman
Department of Electrical Engineering, Princeton University, Princeton, NJ 08544, USA
bergman@EE.Princeton.EDU

W. H. Knox
Bell Laboratories, Lucent Technologies, Holmdel, NJ 07733, USA
wknox@lucent.com

The vectorial nature of light is often ignored in the discussions of optical solitons because typically it does not drastically alter the behavior of solitons. When a soliton propagates in homogeneously birefringent fiber polarization effects have to be taken into account [1,2]. In some systems such as long-haul transmission, polarization effects need to be considered even in the case of random birefringence [3]. On the other hand, when the soliton propagates in the randomly birefringent fiber, it maintains the shape and the same state of polarization accross the pulse [3]. Passively mode-locked fiber lasers [4,5] are unique sources of ultrashort optical pulses for telecommunications and other applications. The pulses which they generate can typically be viewed as solitons independent of the method of the passive mode-locking. The vectorial nature of these pulses becomes important if birefringent elements are included in the cavity [6]. Moreover, the presence of both birefringence and gain/loss in the system can give rise to new phenomena.

Phase locking of the two orthogonal polarization components of a soliton, due to nonlinear coupling overcoming the linear beating in a weakly birefringent, lossless fiber, has been theoretically predicted [7,8]. It has been shown that in addition to "scalar" solitons with a single polarization component along the fast or slow axis, there are vector soliton solutions which are elliptically polarized and bifurcate from the branch of the fast axis soliton. We note that these solitons are single solitons distributed between the two axes in contrast to vector solitons found in Refs. [9–11], which are, in effect, two soliton solutions [12]. In this sense, elliptically polarized solitons are ground state nonlinear modes of the birefringent fiber although they require some threshold energy for their existence. The evolution of the state of polarization of solitons in a weakly birefringent fiber has been studied experimentally [13]. The total state of polarization of a soliton has been found to evolve as a unit and that solitons polarized along the fast axis are unstable. Also, the evolution of the state of polarization of solitons in a homogeneous birefringent fiber is mapped onto periodic orbits on the Poincaré sphere in accordance with the approximation of average profile [14]. However, stationary elliptically polarized solitons have not been observed experimentally. Placing the birefringent fiber inside a cavity removes many of the difficulties which plagued prior experiments. The laser is a self-regulated system and it generates high-energy pulses defined by the parameters of the cavity, including the value of birefringence. Hence the pulses should be the nonlinear modes of this combined system. Polarization locking effects have been experimentally discovered by Cundiff, Collings and Knox [6] in a laser with weakly birefringent fiber in the cavity. They found that at certain values of the parameters, the two polarization components of the pulse were locked in phase. These pulses which are stationary elliptically polarized soliton were called "polarization locked vector solitons" (PLVS) [17].

In this work, we investigate the state of polarization of pulses in a mode locked fiber laser with linearly birefringent fiber inside the cavity. Earlier [15] we found that such laser systems reveal a multiplicity of various phenomena related to the soliton generation with two polarization components. Here we are interested only in elliptically polarized solitons. These are formed in the laser as a result of the balance between nonlinearity, birefringence and dispersion on the one hand and gain and loss on the other. We observe that essentially the former balance determines the soliton profile and the relation between its polarization components. The latter balance primarily fixes the energy of the soliton, selecting one from the whole family of elliptically polarized solutions of the conservative case. This whole family is investigated in our experiment by externally changing the average linear birefringence, which is determined by a sequence of three pieces of birefringent fiber with variable angles between their principal axes. We used the model described in Ref. [15] with some modifications:

$$i\phi_z + \gamma\phi + \frac{D}{2}\phi_{tt} + |\phi|^2\phi + A|\psi|^2\phi + B\psi^2\phi^* = i[g(Q_1) - \delta_l - \delta_s(|\phi|^2)]\phi + i\beta\phi_{tt},$$
$$i\psi_z - \gamma\psi + \frac{D}{2}\psi_{tt} + |\psi|^2\psi + A|\phi|^2\psi + B\phi^2\psi^* = i[g(Q_2) - \delta_l - \delta_s(|\psi|^2)]\psi + i\beta\psi_{tt}, \quad (1)$$

where z is normalized to the cavity length Z_0, $t = [T-(z/(V_g Z_0)]/T_0$, $(T_0 = \sqrt{Z_O|\beta_2|})$, β_2 is the intracavity group velocity dispersion, ψ and ϕ are the normalized envelopes of the two optical field components, γ is the half-difference between the propagation constants of these two components, $D = \beta_2/|\beta_2|$ $(= -1$ in our case) , A is the cross-phase modulation coefficient, B is the coefficient of the energy-exchange term (four-wave-mixing), β represents the spectral filtering or bandwidth limited gain ($\beta > 0$). $g(Q_i)$ is the gain in the cavity, which depends on the energy, $Q_1 = \int_{-\infty}^{\infty}(|\phi|^2)\,dt$, $Q_2 = \int_{-\infty}^{\infty}(|\psi|^2)\,dt$, δ_l is the linear loss term and δ_s represents the loss due of the semiconductor saturable absorber.

The gain term, $g(Q_i)$, in (1) describes an active medium with a recovery time much longer than the round-trip time of the cavity and therefore does not depend explicitly on t. It describes depletion of the gain medium and depends on the partial pulse energy $g(Q_i) = \frac{g_0}{1+Q_i/E_L}$, where g_0 is the small signal gain and E_L is the saturation energy. The absorption of the saturable absorber is described by the rate equation: $\frac{\partial\delta_s}{\partial t} = -\frac{\delta_s-\delta_0}{T_1} - \frac{|\Upsilon|^2}{E_A}\delta_s$, where T_1 is the recovery time of the saturable absorber, δ_0 is the loss in absence of pulses, Υ refers to ψ or ϕ, and E_A is the saturation energy of the absorber.

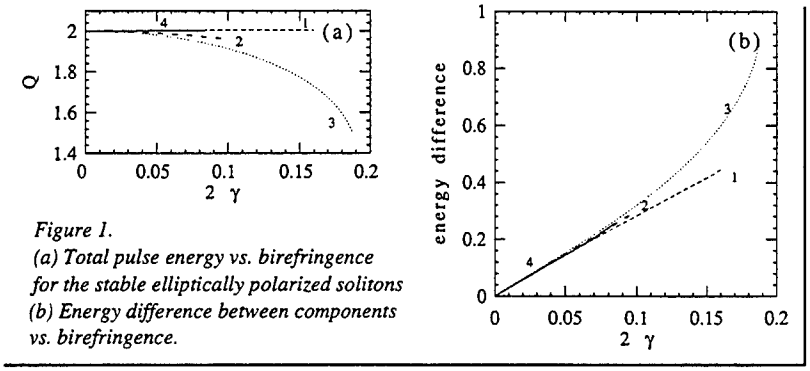


Figure 1.
(a) Total pulse energy vs. birefringence for the stable elliptically polarized solitons
(b) Energy difference between components vs. birefringence.

Figure 2. Comparison between the energy difference vs birefringence for the solutions of the conservative case (solid circles) and our laser system with gain and loss using the anisotropic (continuous line) and isotropic (dotted line) models with the proper gain to keep Q constant.

We numerically seek elliptically polarized solitons following the method described in Ref. [19]. We start with $\gamma = 0$, and find the numerical soliton solution for this case. Then using this solution as an initial condition, we increase the birefringence until the solution converges. Above a certain value of the birefringence the polarization does not lock. For $\gamma = 0$, we always find a stable solution with both amplitude components equal and $\pi/2$ radians out of phase. The energy Q for this solution depends on the gain/loss parameters. Different values for this set of parameters can produce the same solution. Fig.1 shows (a) Q versus birefringence and (b) energy difference versus birefringence, for four values of the gain/loss parameters. Namely $(E,\delta_0,T_1,E_A,\beta,g_o)$ are: (1) (0.5,0.12,0.5,0.4,0.02,0.327); (2) (0.4,0.07,0.5,0.04,0.04,0.145); (3) (0.5,0.08,0.3, 0.018, 0.1, 0.137); (4) (0.5,0.08,0.5,0.04,0.02,0.115). The other parameters are common: $\delta_l = 0.01$, $A = 2/3$, and $B = 1/3$. This choice of parameters produces the same stable circularly polarized pulselike solution

with $Q = 2$ for $\gamma = 0$. The isotropy of the gain/loss has been introduced into equations (1) numerically, by simply evaluating the gain/loss terms uniformly along all possible directions. The procedure is equivalent to the randomization of the anisotropy in the location of erbium atoms in a glass host matrix. The gain and loss are locally anisotropic but isotropic in average.

In Fig.1, when γ increases, the two components of the solution diverge. The gain/loss terms influence them differently depending on the values of the parameters. The energy (Q) decreases with γ and the functions $Q(\gamma)$ are different for the four sets of parameters even if for all $Q(0) = 2$. The energy distribution between the components also changes with γ but differently in the four cases. The main difference between the curves is that each has a different upper limit, implying that the solution loses its stability at different values of γ. This means that the gain/loss terms play a crucial role in the stability of these solutions.

In the laser system, the nonconservative terms are small and serve mainly to fix the soliton amplitude. The rest of the soliton parameters are determined by the conservative terms: nonlinearity, dispersion and the birefringence. This suggests that the comparison with the conservative case [7,8] should be done on the following basis. In the case of the above cited Hamiltonian system (i.e. that described by the l.h.s of Eqs.1 set to zero), the elliptically polarized solitons comprise a one-parameter family of solutions. The parameter of the family is the propagation constant q. The energy Q, the energy ratio and any other pulse characteristics depend on this parameter. On the other hand, because of the scaling properties of this Hamiltonian system, if we fix the energy, then the energy ratio will depend on γ. Let us recall that $Q/\sqrt{\gamma}$ depends exclusively on q/γ (see Fig.1(b) in Ref. [8]). In the experiment, the pulse energy does not significantly depend on γ, providing the basis for comparison with those solutions found in Refs. [7,8].

As stated above, the pulse energy Q is not experimentally observed to depend on γ while the remainder of the laser parameters are fixed. In the simulations, we fix the value of Q by varying the small signal gain (g_o), while fixing the rest of parameters. The gain must be increased only slightly with increasing γ in order to obtain an elliptically polarized soliton of constant energy. Fig.2 shows the energy difference versus γ for solutions with $Q = 2$. The solid line corresponds to the anisotropic case and the dotted line to the isotropic model described above. As we can see, the only difference between the anisotropic and isotropic case is that the isotropic case keeps the elliptically polarized soliton stable over a larger interval of γ. The filled circles correspond to the conservative solutions obtained in Refs. [7,8]. The agreement of these three curves is excellent. The similarities among the solutions are not only in the energy difference between components but also in the rest of the pulse characteristics.

The work of J.M.S.C. was supported by the Dirección General de Enseñanza Superior under contract PB96-0819. K. Bergman and B. Collings acknowledge support form the Office of Naval Research Grant N00014-96-0773 and the National Science Foundation Grant ECS-9502491.

---

[1] Menyuk C. R. *IEEE J. Quant. Electron.*, **QE–25**, 2674 (1989).
[2] Blow K. J., Doran N. J. and Wood D. *Opt. Lett.*, **12**,202 (1987).
[3] Evangelides S. G., Mollenauer L. F., Gordon J. P. and Bergano N. S., *J. Lightwave Technol.*, **10**, 28 (1992).
[4] I. N. Duling, Opt. Lett. **16,** 539 (1991); C.-J. Chen, P. K. A. Wai, and C. R. Menyuk, Opt. Lett. **19,** 198 (1994); H. A. Haus, J. G. Fujimoto, and E. P. Ippen, JOSA B **8**, 2068 (1991); F. X. Kärtner and U. Keller, Opt. Lett. **20**, 16 (1995).
[5] B.C. Collings, K. Bergman, S.T. Cundiff, S. Tsuda, N. Kutz, J.E. Cunningham, W.Y. Jan and W.H. Knox, IEEE J. of Sel. Top. Quant. Electr. **3**, (1997).
[6] S. T. Cundiff, B. C. Collings and W. H. Knox, *Optics Express*, **1**, 12 (1997).
[7] N. Akhmediev, A. Buryak, J. M. Soto-Crespo, *Optics Comm.*, **112**, 278 (1994).
[8] N. Akhmediev, A. Buryak, J.M.Soto-Crespo, Andersen D. R., *JOSA B*, **12**, 434 (1995).
[9] D. N. Christodoulides, and R. I. Joseph, Opt. Lett. **13**, 53 (1988).
[10] M. V. Tratnik and J. E. Sipe, Phys. Rev. A **38**, 2001, (1988).
[11] N. N. Akhmediev *et al.*, Sov. Tech. Phys. Lett. **15**, 587 (1989).
[12] N. Akhmediev and A. Ankiewicz, Solitons, nonlinear pulses and beams, Chapman & Hall, London, 1997.
[13] Y. Barad and Y. Silberberg, Phys. Rev. Lett. **78**, 3290 (1997).
[14] N. N. Akhmediev and J. M. Soto - Crespo, *Phys. Rev. E*, **49**, 5742 (1994).
[15] N. N. Akhmediev,J. M. Soto-Crespo,S. T. Cundiff, B. C. Collings and W. H. Knox, Opt.Lett. **23**,852 (1998).
[16] S. T. Cundiff, B. C. Collings, N. N. Akhmediev, J. M. Soto-Crespo, W. H. Knox, paper presented at Nonlinear Optics'98, Princeville, Kauai, Hawaii, paper TuB3.
[17] S. T. Cundiff, B. C. Collings, N. N. Akhmediev, J. M. Soto-Crespo, K. Bergman, W. H. Knox, "Observation of polarization-locked vector solitons in optical fiber", PRL, **82**, May, 17-th (1999).
[18] N. Akhmediev, A. Ankiewicz, M. Lederer, B. Luther-Davies, Opt. Lett. **23** 1998.
[19] J. M. Soto-Crespo, N. N. Akhmediev and V. V. Afanasjev, JOSA B **13**, 1439 (1996)

Multiple-soliton States in a passively mode-locked Ti:sapphire Laser

M. J. Lederer, B. Luther-Davies

Laser Physics Centre, Research School of Physical Sciences and Engineering, The Australian National University, Canberra, 0200 ACT, Australia

MJL111@rsphysse.anu.edu.au, ph.: 61-2-62490694, fax: 61-2-62490029

H. H. Tan, C. Jagadish

Electronic Materials Engineering, Research School of Physical Sciences and Engineering, The Australian National University, Canberra, 0200 ACT, Australia

N. N. Akhmediev

Optical Sciences Centre, Research School of Physical Sciences and Engineering, The Australian National University, Canberra, 0200 ACT, Australia

J. M. Soto-Crespo

Instituto de Optica, C.S.I.C., Serrano 121, 28006 Madrid, Spain

1. Introduction

Multi-pulse operation of soliton lasers has been reported sporadically over the last decade. The break-up of single pulses into double or multiple pulses was observed in both Kerr-lens mode-locked (KLM) [1] and semiconductor saturable absorber mirror (SESAM) [2] mode-locked solid-state lasers when the pump power was increased. The pulse spacings were irregular in these cases. The appearance of regularly spaced multiple pulses within a laser cavity is of significance to the production of GHz repetition rate soliton pulse sources for optical fiber communications. Recent advances in this area have led to a refinement of harmonic mode-locking in both Er-doped fiber lasers [3] as well as Cr:YAG bulk lasers [4]. In our experiments we have used a SESAM to induce soliton mode-locking in a Ti:sapphire laser. By decreasing the negative dispersion or increasing the small signal gain we observed transition to multiple pulse operation with the separation between pulses not reproducible. Apart from far separated pulse pairs, triplets and quadruplets we could also generate closely spaced multiple pulse states which could possess various relative inter-pulse phase relationships. We explain our observations within the framework of the generalized complex Ginzburg-Landau equation (GCGLE) as the master equation of the laser. Conditions for the stability of single as well as multiple solitons are given and the mechanisms responsible for the transitions between pulse states are explained. Results from numerical simulations of the GCGLE are in good agreement with the various double pulse states observed experimentally. The regions for existence of single and multiple pulses in the parameter space of dispersion and small signal gain are given. The simulations also show that there are regions wherein the laser operates in permanent nonequilibrium, also in agreement with the experiments. We believe that the mechanisms concerning the switching between soliton states identified in this work are general and valid for all soliton lasers.

2. Experiment

A schematic of the standard femtosecond cavity used in the experiments is shown in Fig. 1. The SESAMs had their absorption recovery times tailored using ion-implantation [5] which resulted in recovery times $\tau<1$ ps (see inset). The typical reflectivity modulation from the SESAMs was $dR<0.5\%$. Mode-locking was self-starting with the SESAMs present whilst it could not be initiated without, indicating negligible KLM due to gain-guiding effects.

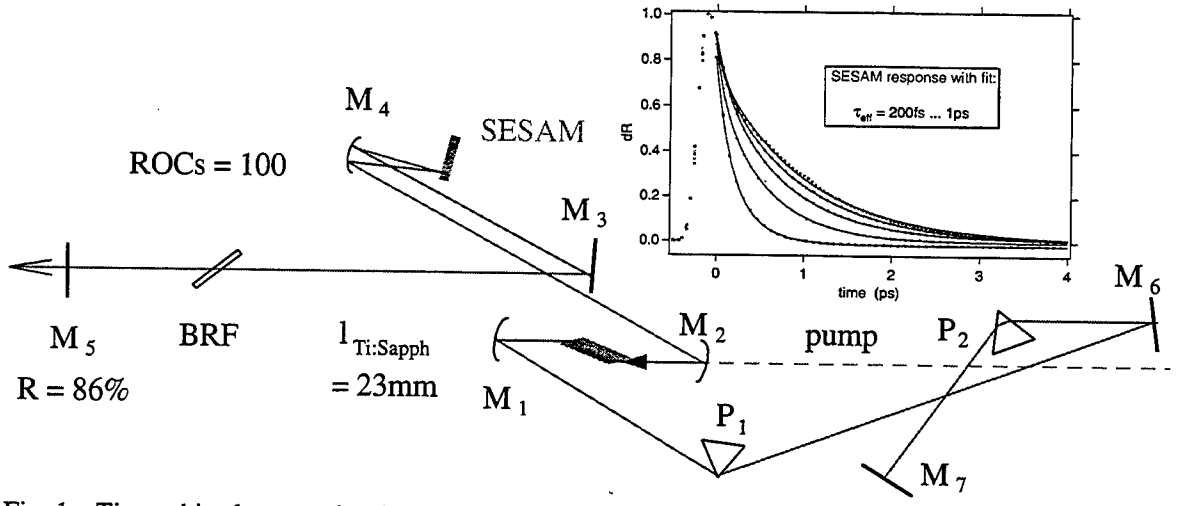


Fig. 1: Ti:sapphire laser cavity. M's mirrors, R reflectivity, P's prisms, BRF birefringent tuning filter, ROC radius of curvature. The inset shows the response of various SESAMs.

Starting from single-pulse operation, decreasing the negative dispersion in the cavity through insertion of P_2 (or increasing the small signal gain) led to the appearance of double pulses. Fig. 2 shows some examples of the observed autocorrelation and averaged spectra. Further decrease in dispersion resulted in a transition to triple pulses and finally, depending on the small signal gain, in irregular chaos-like behaviour followed by the generation of chirped ps-pulses after crossing to positive dispersion. Increasing the dispersion reversed this trend, generally with hysteresis.

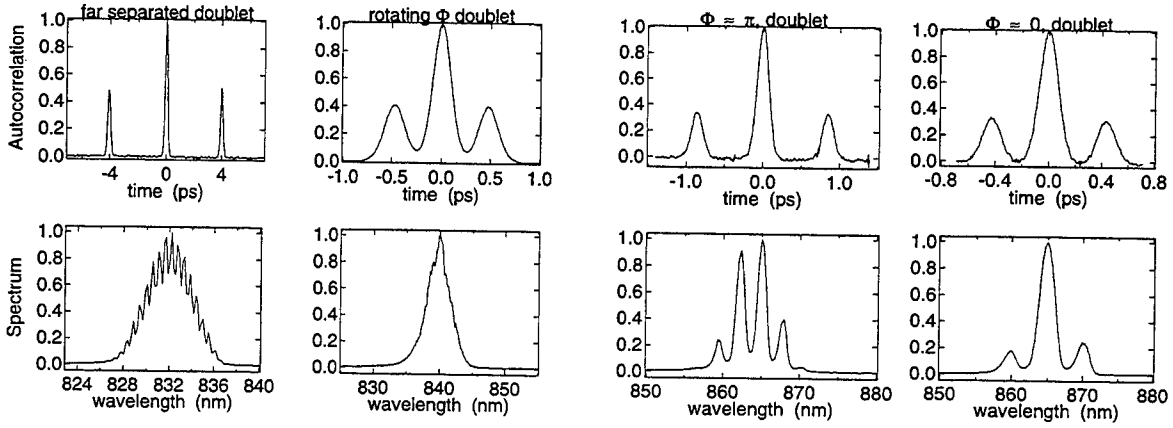


Fig. 2: Example traces of autocorrelation and averaged spectra of double pulses. Far separated as well as closely spaced doublets are shown which have their relative phase either rotating, or closer to ≈ 0 or $\approx \pi$. The two far separated solitons do not interact coherently nor through the absorption recovery tail.

3. Theory

We have used the GCGLE as master equation to analyse the multi-pulse behaviour of the laser. Fig. 3 shows the modulation background line g - l_0 - q_0 obtained from a numerical simulation of the GCGLE. Here, g is the saturated laser gain, l_0 is the linear loss and q_0 is the maximum amplitude modulation of the SESAM. The inset shows the energy balance for the laser in equilibrium with δ and α being the energy losses due to the filter and the absorber respectively; l_c is the loss experienced by the dispersive continuum and ε is a margin that depends on the absorber recovery time τ ($\varepsilon \to 0$ for $\tau \to 0$). Fig. 3 illustrates that the stability of a single soliton is impaired only if the modulation background line approaches or crosses zero (depending on ε), i. e. if the total dynamic losses exceed the maximum possible SESAM modulation, $[\alpha_1 + \delta_1 + \varepsilon]_{Q1} \geq q_0$. Then, the continuum shed by the soliton can grow and a second stable and well separated soliton is formed if $[\alpha_1 + \delta_1]_{Q1} > [\alpha_2 + \delta_2]_{Q2}$. A further decrease in dispersion β_2 causes the appearance of a third soliton and so forth. On the other hand, increasing the dispersion switches back to a single soliton with hysteresis. This is despite the fact that the laser apparently switches to a state with higher loss. A stability analysis shows that this switch occurs when $\Delta\delta < -\Delta\alpha$, i. e. a change in the filter loss, for instance due to an energy imbalance, is outweighed by the negative change in the absorber loss.

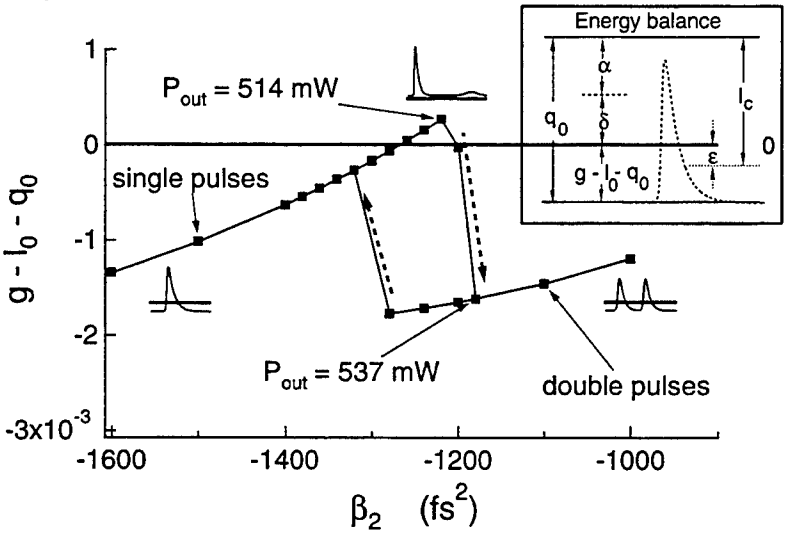


Fig. 3: Modulation background line obtained from a simulation of the GCGLE. The inset shows the graphical representation of the energy balance in the laser. The symbols are explained in the text.

Further simulations have confirmed the existence of closely spaced pulses and the possibility of operation with permanent nonequilibrium in the framework of the GCGLE, both in reasonable agreement with the experiment, and have identified the regions of existence of single and multiple pulses.

[1]C. Spielmann, P. F. Curley, T. Brabec, and F. Krausz, *IEEE J. of Quantum Electr.*, **QE-30**, 1100, 1994
[2]J. Aus der Au, D. Kopf, F. Morier-Genoud, M. Moser, and U. Keller, *Opt. Lett.*, **22**, 307, 1997
[3]B. C. Collings, K. Bergmann, and W. H. Knox, *Opt. Lett.*, **23**, 123, 1998
[4]B. C. Collings, K. Bergmann, and W. H. Knox, *Opt. Lett.*, **22**, 1098, 1997
[5]M. J. Lederer, B. Luther-Davies, H. H. Tan, and C. Jagadish, *IEEE J. Quantum Electron.*, **QE-34**, 2150, 1998

Cavity-less oscillator through second harmonic generation in backward quasi-phase-matching

Claudio Conti and Gaetano Assanto

Department of Electronic Engineering, Terza University of Rome and
National Institute for the Physics of Matter, INFM-RM3 Division
Via della Vasca Navale 84, 00146 Rome, Italy
Tel. +3906 55177028; Fax +3906 5579078; E-mail: Assanto@ele.uniroma3.it

Stefano Trillo

Dipartimento di Ingegneria, Università di Ferrara
Via Saragat 1, 44100 Ferrara, Italy

Feedback in the presence of a nonlinear response can lead to optical hysteresis and bistability (OB) in numerous configurations.[1] OB and limiting have also been predicted through backward second-harmonic generation (B-SHG) via short-period or higher order quasi-phase matching (QPM) gratings, and the development of reliable technologies for QPM in ferroelectrics has recently lead to the demonstration of backward second harmonic generation (B-SHG) in Lithium Niobate.[2-3] Hereby we consider the nonlinear feedback provided by B-SHG in the presence of gain at the input fundamental frequency (FF). The presence of nonlinear phase-mismatch in B-SHG can introduce feedback via successive up- and down-conversion processes, thereby forming a nonlinearly induced resonator in an otherwise reflection-less structure and leading to a strong enhancement of the effective amplification. Such phenomenology is investigated numerically. In this Communication we refer to the realistic case of $LiNbO_3$ waveguides realized by Titanium indiffusion or proton exchange in crystals doped with Erbium ions in order to exhibit amplification of several dB at (FF) 1.55μm.[4] Defining e_1 and e_2 as the counterpropagating FF and SH slowly-varying field envelopes, normalized such that their square-moduli are powers, $v_{g1,2}$ the corresponding group velocities and Δk the SHG wavevector mismatch (including the QPM momentum), the model of a backward second harmonic generator with FF gain can be cast in the form:[5-6]

$$\begin{aligned} \frac{\partial e_1}{\partial z}+\frac{1}{v_{g1}}\frac{\partial e_1}{\partial t}&=\kappa e_1^* e_2+\frac{\gamma_1}{2}e_1 \\ \frac{\partial e_2}{\partial z}-\frac{1}{v_{g2}}\frac{\partial e_2}{\partial t}&=\kappa e_1^2-i\Delta k e_2 \end{aligned} \qquad (1)$$

Our results refer to single mode waveguides at 1.55μm with 1st-order QPM, equivalent cross section S_{EFF}=47 μm^2, nonlinear strength $\kappa\sqrt{S_{EFF}}=6\times10^{-4}$ $W^{-1/2}$, (effective) propagation length L=3cm. We consider the case of a single FF input (i.e. $e_2(z=L,t)=0$) with power $P_{in}^{FF}=|e_1(0,t)|^2$, and evaluate the transmitted FF power $P_{out}^{FF}=|e_1(L,t)|^2$, the reflected SH power $P_{out}^{SH}=|e_2(0,t)|^2$, the transmittance $T^{FF}=P_{out}^{FF}/P_{in}^{FF}$ and the trans-reflectance is $R^{SH}=P_{out}^{SH}/P_{in}^{FF}$. Focusing on the stationary behavior ($\partial_t=0$), in the absence of gain these are multivalued functions which can be described by Jacobian elliptic functions. Each state of the system is characterized by a certain number of humps in the distribution of the fields (see Figure 1). These humps can be interpreted as photon loops, where FF photons are up-converted to SH, travel backward until they are down converted to FF. The number of photon loops identifies the longitudinal mode of a nonlinear resonator with feedback provided by the B-SHG, and determines the output power at both harmonics. Such description in terms of photon loops is convenient when FF gain is included, because the amplification can be enhanced by the re-circulation of energy (i.e. photons) in a "loop". Figure 2a displays the outputs versus gain for various excitations. The dashed lines are real exponentials corresponding to FF transmission in the absence of nonlinearity.

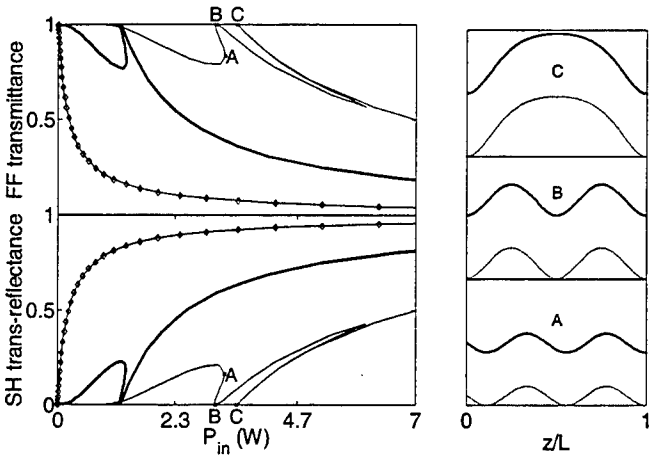


Figure 1: Stationary response of the system in absence of gain when: $\Delta kL=2$ (diamonds), $\Delta kL=12$ (thick line), $\Delta kL=20$ (thin line). The fields profile (a.u., thick line: FF $|e_1|^2$, thin line: SH $|e_2|^2$) are also shown to illustrate the concept of photon loop.

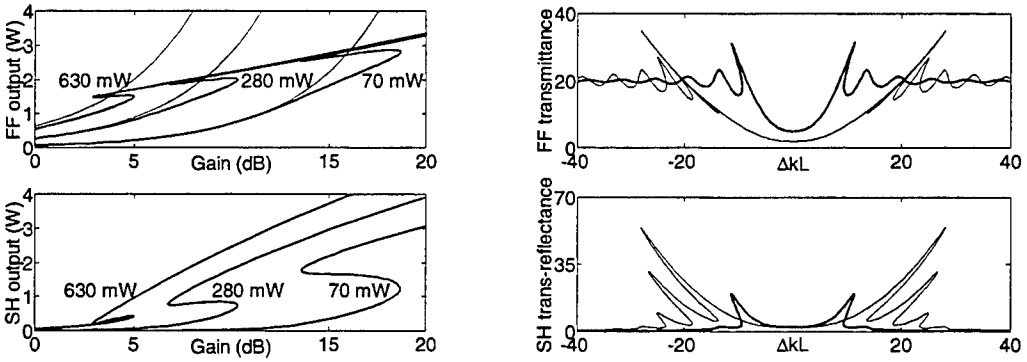


Figure 2: Response of the system in the presence of gain: a) vs gain for different input powers (the exponentials are the response in absence of nonlinearity); b) vs nonlinear mismatch, with 13dB gain, when Pin=70mW (thick line) and Pin=280mW (thin line).

In specific intervals the B-SHG (solid lines) enhances the resulting amplification: SHG acts as a loss for the FF until, for large enough gain, the system switches from zero to one photon-loop and the SH output power becomes comparable to that transmitted at FF. In the example in Fig. 2 the system has only two states (zero and one photon-loop) independent on gain, due to the low Δk. Figure 2b shows the spectral response (symmetric around the origin as expected from equations (1)), for given excitation and gain. A range of enhanced gain is apparent between the regions of high mismatches where neither SHG nor nonlinear-resonator are in effect, and the region of satisfactory phase-matching where the power is substantially up-converted. Clearly, a slight phase-mismatch is needed to allow the formation of photon-loops.

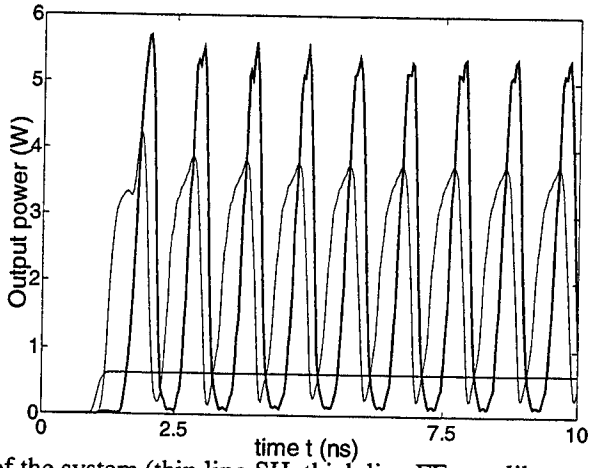


Figure 3 Self-pulsing of the system (thin line SH, thick line FF, steplike waveform FF input; here $\Delta kL=12$ and the gain is 8.7dB)

Moreover, the maximum number of photon loops in the system is strictly related to Δk and determines the multi-valued behavior visible in Fig. 2b. Notice that the highest-output state corresponds to a single photon-loop, such that all the available length (i.e. waveguide volume) can contribute to the enhancement of gain. Finally, in the non-stationary regime, integrating Eqs. (1) with a pseudo-spectral approach, we found that the system exhibits three different temporal regimes in response to an asymptotically constant FF excitation. For a relatively low gain, the structure behaves like the conservative one, settling down (after a transient) to the lowest branch of the multistable output characteristic (see Fig. 2). When the gain increases (for a fixed input intensity) the system begins to exhibit a robust self-pulsing as shown in Fig. 3 (for typical values of the parameters). The mean value of the oscillatory output (after the transient) equals that obtained from the stationary analysis. Such behavior suggests the periodic creation and annihilation of an unstable photon-loop. This self-pulsing destabilizes at much larger gains, eventually giving rise to the chaotic emission of temporal bursts, even in the absence of an SH seed as employed in [6]. A detailed temporal stability analysis will be carried out in order to underline the relevant dynamics. In conclusion, we propose a novel application of a parametric nonlinearity in the presence of gain in a nonlinear periodic medium: a cavity-less parametric oscillator with outputs at FF and SH. The phenomenon, described in terms of photon-loops through up-and-down conversion in backward SHG, could open the way to an entirely new generation of oscillating devices in ferroelectric materials subject to periodic domain orientation. An experimental demonstration is envisaged in the near future.

References

[1] *Optical Bistability III*, edited by H. M. Gibbs, P. Mandel, N. Peyghambarian, and S.D. Smith, Springer-Verlag, New York, 1986.

[2] U. Kang, Y. J. Ding, W. K. Burns, and J. S. Melinger, Opt. Lett. **22**, 862 (1997).

[3] X. Gu, R. Y. Korotkov, Y. J. Ding., J. U. Kang, and J. B. Khurgin, J. Opt. Soc. Am. B **15**, 1561 (1998).

[4] I. Baumann, R. Brinkmann, M. Dinad, W. Sohler, and S. Westenhoofer, J. Quantum. Electron. **32**, 1695 (1996).

[5] M. Matsumoto, and K. Tanaka, J. Quantum. Electron. **31**, 700 (1995).

[6] G. D'Alessandro, P. St. J. Russel, and A. A. Wheeler, Phys. Rev. A **55**,3211 (1997).

Nonlinear Guided Waves and Their Applications

Quadratic and Discrete Solitons

Wednesday, 1 September 1999

Falk Lederer, University of Jena, Germany
Presider

WE
16.30-18.45
Salle Morey—St-Denis

Vortex Dynamics in Quadratic Nonlinear Media

L. Torner, D. V. Petrov, J. P. Torres, G. Molina, J. Martorell, R. Vilaseca
Universitat Politecnica de Catalunya, Gran Capitan UPC-D3, ES 08034 Barcelona, Spain

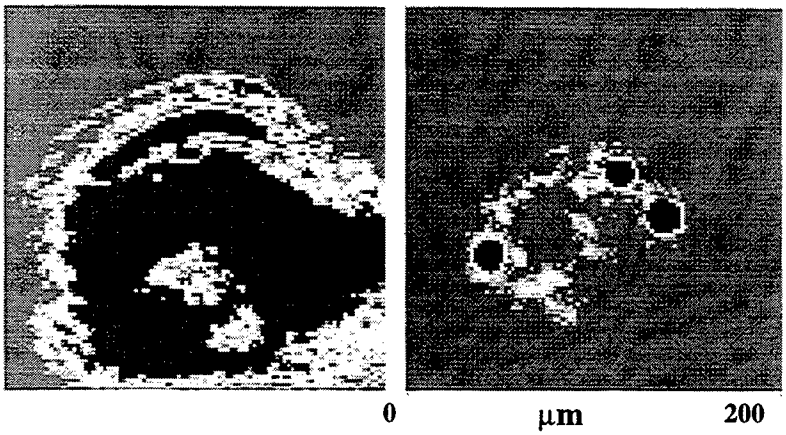
J.M. Soto-Crespo
Instituto de Optica, C.S.I.C., ES 28006 Madrid, Spain

Singular light beams, that contain topological wave front dislocations, are ubiquitous entities that display fascinating properties with widespread important applications.[1–3] Screw dislocations, or vortices, are a common dislocation type. They are spiral phase-ramps around a singularity where the phase of the wave is undefined and its amplitude vanishes. The order of the screw dislocation multiplied by its sign is referred to as the winding number, or topological charge of the dislocation.

Vortices appear spontaneously in several settings, including in speckle-fields, in optical cavities and in the doughnut laser modes, and otherwise they can be generated with phase masks, or with astigmatic optical components. Vortices also form by self-wave front modulation in nonlinear optical media.[4,5] In this context, parametric wave mixing of multiple waves propagating in quadratic nonlinear media constitutes a fascinating scenario. Charge-doubling in second-harmonic generation schemes,[6,7] and sum- and difference-charge arithmetic operations in three-wave mixing processes,[8] have been demonstrated with moderate light intensities and wide pump beams. Spontaneous vortex pair nucleation in seeded up-conversion schemes,[9] and vortex excitation in parametric amplification from quantum noise,[10] constitute two additional examples of the phenomena that have been discovered and observed recently. The spontaneous nucleation of multiple vortex twins whose subsequent explosion under appropriate conditions yields quasi-aligned patterns of single-charge vortices in walking parametric wave mixing has been also recently predicted numerically.[11]

With intense, tightly focused beams the so-called cascading effects offer a new rich variety of phenomena.[12] Cascading modifies drastically the dynamics of the beam evolution, in particular by yielding the formation of optical solitons. In this regime, pump beams containing optical vortices nested exhibit azimuthal modulational instability (AMI).[13] On theoretical grounds, the self-breaking of the beams is mediated by the AMI of the flat top of higher-order, ring-shaped bright vortex solitary-wave solutions of the evolution equations.[14–16] As a consequence, the light beams self-break inside the crystal into sets of stable, bright spatial solitons, a phenomenon that has been observed recently in up-conversion second-harmonic generation schemes in bulk potassium titanyl phosphate cut for type II phase-matching at $\lambda = 1.064$ μm.[17] The far-field evolution of the solitons is critically impacted by the orbital angular momentum carried by the light signals due to the presence of the vortices. Such a phenomenon defines the principle of operation of a new class of optical devices that can potentially process information by mixing topological wave front charges and producing certain patterns of bright spatial solitons spots.[18–19]

In this paper, a review of the progress in the above mentioned topics will be presented, with emphasis on latest theoretical predictions open for experimental exploration.



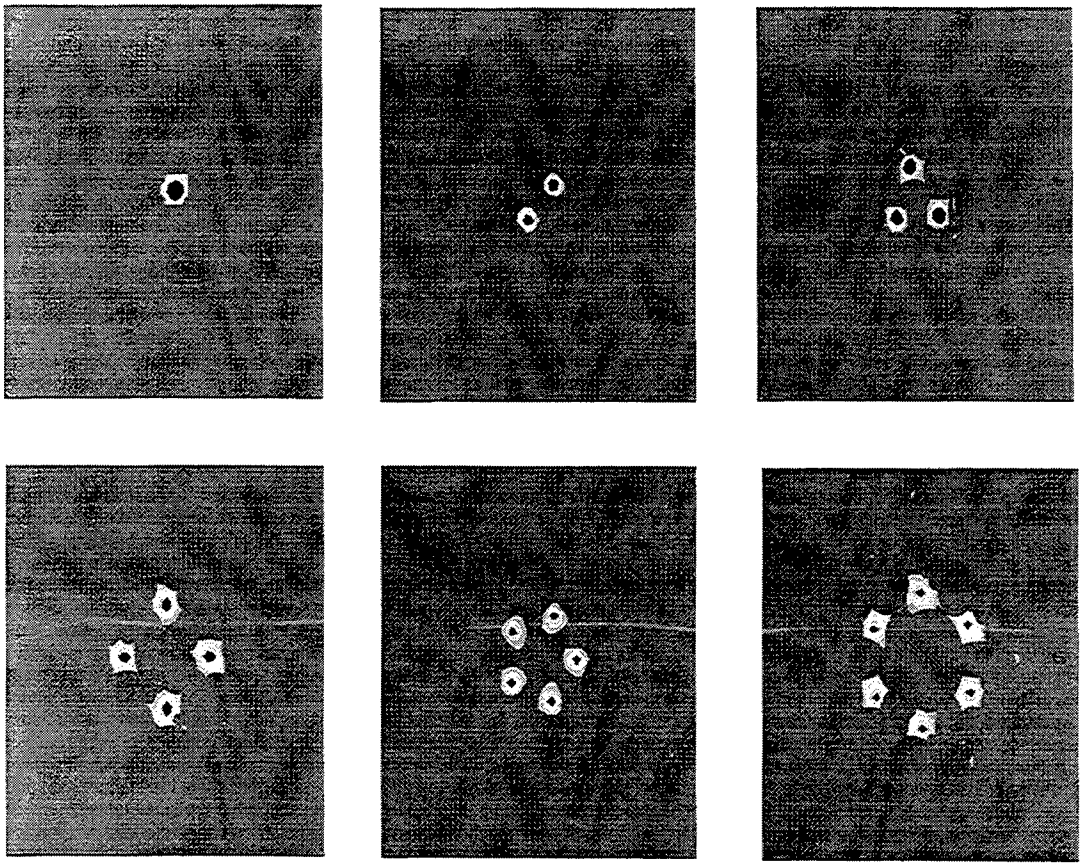


Figure Caption : Above: experimentally observed SH light pattern output of the KTP crystal for low and high fundamental input powers. Below: output soliton pattern predicted numerically for different combinations of the topological charges of the input signals.

REFERENCES

1. J. F. Nye and M. V. Berry, Proc. R. Soc. London A **336**, 165 (1974).
2. A. Ashkin, J. M. Dziedzic, and T. Yamane, Nature **330**, 769 (1987); M. Padgett and L. Allen, Phys. World **10**, 35 (1997).
3. G. Indebetouw, J. Mod. Opt. **40**, 73 (1993); B. Luther-Davies, J. Christou, V. Tikhonenko, and Y. S. Kivshar, J. Opt. Soc. Am. B **14**, 3045 (1997); D. Rozas, C. T. Law, and G. A. Swartzlander, J. Opt. Soc. Am. B **14**, 3055 (1997); Y. S. Kivshar and B. Luther-Davies, Phys. Rep. **298**, 81 (1998).
4. T. Ackemann, E. Kriege, and W. Lange, Opt. Commun. **115**, 339 (1995).
5. A. V. Ilyenkov, A. I. Khiznyak, L. V. Kreminskaya, M. S. Soskin, and M. V. Vasnetsov, Appl. Phys. B **62**, 471 (1996).
6. I. V. Basistiy, V. Y. Bazhenov, M. S. Soskin, and M. V. Vasnetsov, Opt. Commun. **103**, 422 (1993).
7. K. Dholakia, N. B. Simpson, M. J. Padgett, and L. Allen, Phys. Rev. A **54**, 3742 (1996); J. Courtial, K. Dholakia, L. Allen, and M. J. Padgett, Phys. Rev. A **56**, 4193 (1997).
8. A. Berzanskis, A. Matijosius, A. Piskarskas, V. Smilgevicius, and A. Stabinis, Opt. Commun. **140**, 273 (1997); **150**, 372 (1998).
9. D. V. Petrov and L. Torner, Phys. Rev. E **58**, 7903 (1998); D. V. Petrov, G. Molina-Terriza, and L. Torner, Opt. Commun. **162**, 357 (1999).
10. P. D. Trapani, A. Berzanskis, S. Minardi, S. Sapone, W. Chinaglia, Phys. Rev. Lett. **81**, 5133 (1998).
11. G. Molina-Terriza, L. Torner, and D.V. Petrov, "Vortex streets in walking parametric wave mixing," Opt. Lett. (1999). In press.
12. For a review see G. I. Stegeman, D. J. Hagan, and L. Torner, Opt. Quantum Electron. **28**, 1691 (1996).
13. L. Torner and D. V. Petrov, Electron. Lett. **33**, 608 (1997); D. V. Petrov and L. Torner, Opt. Quantum Electron. **29**, 1037 (1997).
14. W. J. Firth and D. V. Skryabin, Phys. Rev. Lett. **79**, 2450 (1997); D. V. Skryabin and W. J. Firth, Phys. Rev. E **58**, R1252 and 3916 (1998).
15. J. P. Torres, J. M. Soto-Crespo, L. Torner, and D. V. Petrov, J. Opt. Soc. Am. B **15**, 625 (1998); Opt. Commun. **149**, 77 (1998).
16. G. Molina-Terriza, J. P. Torres, L. Torner, and J.M. Soto-Crespo, Opt. Commun. **158**, 170 (1998).
17. D.V. Petrov, L. Torner, J. Martorell, R. Vilaseca, J. P. Torres, and C. Cojocaru, Opt. Lett. **23**, 1444 (1998).
18. L. Torner and D. V. Petrov, J. Opt. Soc. Am. B **14**, 2017 (1997).
19. L. Torner, J. P. Torres, D.V. Petrov, and J.M. Soto-Crespo, Opt. Quantum Electron. **30**, 809 (1998).

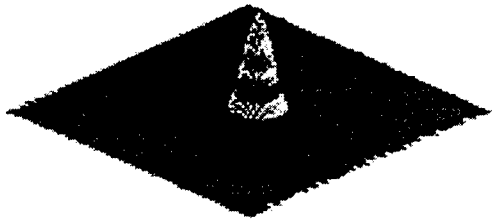
Observation of quadratic spatial solitons in periodically poled lithium niobate

B. Bourliaguet, , V. Couderc, A. Barthélémy,
I.R.C.O.M., Faculté des Sciences, Université de Limoges/CNRS,
123 ave. A. Thomas, 87060 Limoges, France
Tel : +33 555457256, fax : +33 555457514, abarth@ircom.unilim.fr

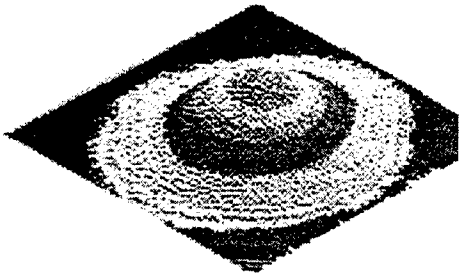
G.W. Ross, P.G.R. Smith, D.C. Hanna,
Optoelectronics Research Centre, University of Southampton,
Southampton SO17 1BJ, United Kingdom
Tel : +44 1703 593144, fax :+44 1703 593142, gwr@orc.soton.ac.uk

C. De Angelis
Istituto Nazionale per la Fisica della Materia,
Dipartimento di Elettronica per l'Automazione, Universita' di Brescia,
ViaBranze 38, 25123 Brescia, Italy
Tel: +39 498277697 , Fax: +39 498277699, deangeli@dei.unipd.it

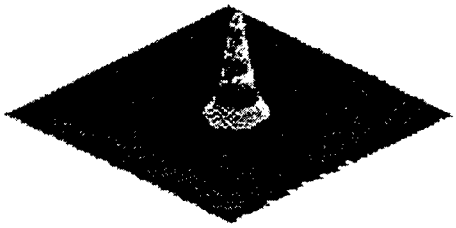
In the last years, second order nonlinear effects have attracted a great deal of interest in the scientific community; in particular solitons sustained by second order nonlinearity have been extensively studied after the first experimental demonstration of soliton propagation in a KTP crystal [1].
Until now, however, the intensity required to obtain self-trapping of a beam of about 20 microns radius remained of the order of 10 GW/cm^2. This has been due to the lack of nonlinear crystals which combine the attributes of a large nonlinearity and phase-matching capability at experimentally convenient wavelengths. However, the technique of quasi-phase matching (QPM) offers a simple and attractive solution [2,3]. The technology is particularly mature with regard to lithium niobate whose material properties may be readily customised in PPLN [4,5].
Although spatial solitary waves in PPLN have been predicted theoretically and simulated numerically [6,7], this paper reports their first experimental observation and characterization.
The PPLN in our experiments was fabricated using the electric-field poling technique. The grating had a period of 6.58 microns which was designed for QPM frequency doubling of 1064nm. The crystal was mounted in a temperature-controlled oven. The experiments were carried out using a Q-switched mode-locked Nd :YAG laser which delivered 45 ps (FWHMI) pulses of up to 10 mJ energy at 1064nm. The input beam was focused onto the entrance face of the uncoated PPLN sample to a spot of 22 μm diameter (FWHMI). The beam had a Gaussian transverse profile and was polarised parallel to the c-axis of the PPLN to access the material's largest quadratic nonlinear coefficient, d_{33}. The 14.5 mm propagation distance through the PPLN crystal represented, for the fundamental wave, approximately 6.5 diffraction lengths of the Gaussian input beam.
Initial measurements were made with the PPLN crystal tuned to almost perfect SHG phase-matching (T_{pm}=162°C). For sufficiently high fundamental input powers, a significant reduction of both the fundamental and the second harmonic output beam diameters was clearly observed. Figure 1 shows the measured beam profiles of the fundamental comparing (a) the input, (b) the output at low input intensity and (c) the output at high input intensity (above the threshold for soliton waveguiding).



a)



b)



c)

Figure 1 : Experimental beam profiles to outline the observed self-trapping: input pattern (a); output pattern in the low intensity regime (diffraction dominates) (b); output pattern at high intensity showing a 2D Spatial Solitary Wave (c)

The output beam width versus the input intensity for an input of 22μm full width at half maximum in intensity is shown in Figure 2. It can be seen that the fundamental wave begins to self-focus at moderate intensities (0.4 GW/cm^2) and becomes self-trapped for intensities greater than 1.35 GW/cm^2. The experiments were repeated for different phase-matching situations by examining QSS for a range of temperatures between 140 and 170°C. This temperature range allowed us to vary the ΔkL product from +20π to -10π ($\Delta k = k_{2\omega} - 2k_{\omega}$). Results are shown in Figure 3, where the output fundamental spot diameter is plotted versus temperature for four values of the input intensity.

The data clearly confirm that the stronger self-focusing is obtained close to perfect phase-matching. The self-focusing strength decreases smoothly when temperature decreases, i.e. going toward larger positive phase-mismatch. On the contrary, when going on the negative side of the phase-mismatch (i.e. increasing the temperature) the focusing evolves abruptly and quickly disappears. From Figure 3 one can see that for an intensity of 1.9 GW/cm^2, QSS propagation can be maintained over a broad range of positive phase-mismatches, and may even be observed when the phase mismatch is slightly negative. For a fixed temperature in the range $T<T_{pm}$, the variation of the output spot-size with respect to the input intensity was qualitatively similar to that shown on Figure 2. For $T>T_{pm}$ (negative phase-mismatch) the behaviour can be seen to be rather more complex. When the input power is increased, for a fixed detuning in temperature, the fundamental field first undergoes a self-defocusing effect that broadens the output pattern. On increasing the intensity still further the field evolution turns self-focusing until soliton propagation is reached. The trends are consistent with similar observations reported for QSS in KTP [1]. Numerical integration of the 2D+1 coupled wave equations was carried out using an implicit finite difference scheme. The results of our computations modelling are in optimum agreement with the experimental observations. The intensities chosen to get theoretical curves that are comparable in shape with the experimental data are about one half of their experimental counterparts, due to the fact that simulations assumed a continous radiation on the contrary to experiments carried with short pulses and time integrated recording of the spatial beam profile.

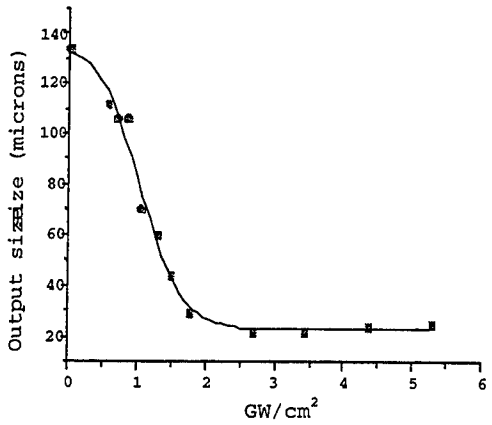


Figure 2: Dependence of the output beam diameter versus the input intensity.

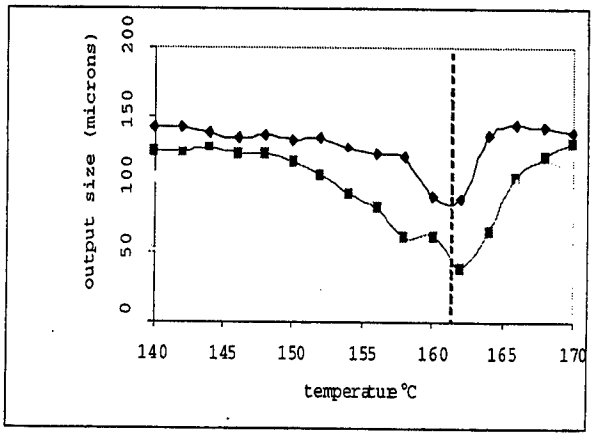


Figure 3: Dependence of the output beam width with respect to temperature variations for internal input intensity of 0.35 GW/cm^2 (diamond), 0.7 GW/cm^2 (square), 1.3 GW/cm^2 (triangle) 1.9 GW/cm^2 (cross). Perfect phase matching is at 161.5°C.

In conclusion we have observed spatial soliton formation using cascaded second order nonlinearities in PPLN. The PPLN crystal was designed and fabricated for QPM frequency doubling of 1064 nm, and quadratic spatial solitons were propagated over more than six diffraction lengths. The results confirm that PPLN is one of the most promising materials for all-optical processing using quadratic nonlinearities.

The authors aknowledge the financial support of the European Commission in the frame of the ESPRIT Open LTR research program.

References :

[1] W. E. Torruellas, Z. Wang, D. J. Hagan, E. W. VanStryland, G. I. Stegeman, L. Torner, and C. R. Menyuk, *Phys. Rev. Lett.*, **74**, 5036 (1995).
[2] L. Torner, and G. I. Stegeman, *Journal of the Optical Society of America B*, **14**, 3127 (1997).
[3] C. B. Clausen, and L. Torner, *Optics Letters*, **24**, 7 (1999).
[4] M. M. Fejer, G. A. Magel, *Journal of Quantum Electronics*, Vol. 28, 1992, pp. 2631-2654.
[5] P. Vidakovic, D.J. Lovering, J.A. Levenson, J. Webjorn, P.J. Russel, *Optics Letters*, **22**, 277 (1997).
[6] C. B. Clausen, O. Bang, and Y. S. Kivshar, *Phys. Rev. Lett.*, **78**, 4749, (1997).
[7] L. Torner ; " Spatial solitons in quadratic nonlinear media" in Beam Shaping and Control with Nonlinear Optics, Kazjar and Reinisch Edit.,Plenum Press, New York, 1998, p. 236.

Second Harmonic Generation in Waveguides Induced by Photorefractive Spatial Solitons

Song Lan, Ming-feng Shih[*], Greg Mizell[+], Joeseph Giordmaine[#], Zhigang Chen[**], Charalambos Anastassiou, John Martin[++] and Mordechai Segev[##]

Department of Electrical Engineering, Princeton University, Princeton, NJ 08544

The most unique application proposed for photorefractive solitons is to utilize the waveguides induced by them for nonlinear frequency conversion.[1] Photorefractive solitons induce 2D waveguides,[2] that are "fixable" (can be permanently impressed into the crystalline lattice),[3] and are wavelength-sensitive in the sense that a waveguide can be induced by very weak soliton and guide in it an intense beam of a non-sensitive wavelength.[4] Because these waveguides are induced by "real-time" solitons, they offer another important property: a large degree of tuning of all waveguide parameters. Thus, a waveguide can be induced by very weak soliton and guide in it two (or three) intense beams of longer wavelengths, which interact via $\chi^{(2)}$. Phase matching can be achieved with crystalline birefringence or by periodic poling. Because solitons can be launched at a broad range of angles (with respect to the crystalline axes), wavelength tunability can be achieved by simply rotating the crystal and launching a soliton at a new direction. Finally, the propagation constants of the guided modes in the waveguides are also tunable by varying the intensity ratio, allowing tuning with no mechanical movements. **We demonstrate all of that theoretically and experimentally.**

We use a photorefractive $KNbO_3$ crystal, and launch all beams along **b**-axis. Phase-matching occurs between **a**-polarized 982nm and **c**-polarized 491nm beams, in which the waveguide-related electro-optic coefficient is r_{13}. First we measure the SHG conversion efficiency in the bulk $KNbO_3$ crystal. We launch a 15mW, 22μm (FWHM) circular ~982-nm **a**-polarized cw beam. We obtain phase-matching at λ=982.6-nm, and output power at λ=491.3-nm of 350nW, with a conversion efficiency of 0.15%/W.

Then we pursue an active method, in which a separate beam is used to build the soliton. We use a 488-nm **c**-polarized laser beam to generate the soliton and a uniform 488nm **a**-polarized beam as the background illumination. We focus the 488-nm beam to a 9μm x 9μm input spot (Fig. 1a) with an intensity ratio of 15. At the output the beam diffracts to a 103μmx118 μm (Fig. 1b). When we apply a voltage of 2,600 volts, the beam self-traps into a 6μmx10μm output (Fig. 1c). Then we launch the 982-nm **a**-polarized beam into this soliton- induced waveguide. At the input, the IR beam is 22μm x 22μm FWHM (Fig. 1d). With 2,600 volts applied and after the soliton has formed, the 982-nm beam is guided by the induced waveguide and attains an output of 24μm x 36μm (Fig. 1f). Fig. 2 displays the temporal

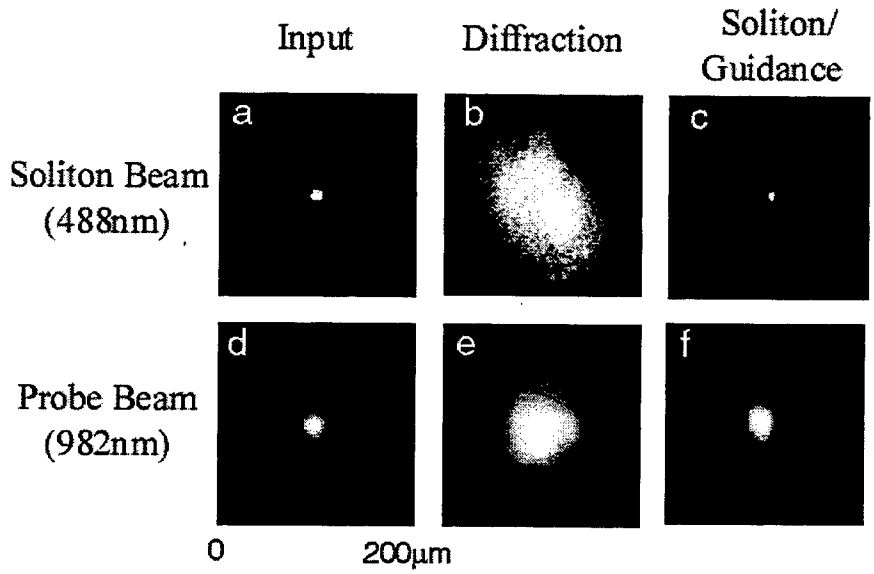


Figure 1: Experimental results with the active method. (a) The input 488-nm beam; (b) The output 488-nm beam without voltage; (c) The output 488-nm soliton; (d) The input 982-nm beam; (e) The output 982-nm beam without voltage; (f) The output 982-nm beam guided by the soliton.

response of the output SH power during soliton formation after the voltage is turned on. When we just apply the voltage (t=0), the SH power is very low, because the field across the crystal changes the refractive indices, taking the process out of phase matching. As the space charge field builds up, it forms the waveguide and traps the fundamental and SH beams, and also establishes phase matching. At steady state, the SH output power stays at 2240nW, with a conversion efficiency of 0.996%/W, 6.4 times higher than that in a bulk hase-matched crystal.

In our case the SH is at a photorefractively-active wavelength, so one can use the SH beam to generate a soliton to guide itself and the fundamental beam. This is a fully passive method. Experimentally, we use the cw IR beam as an input (Fig. 3a). Through SHG, a 57μmx61μm FWHM spot of 491-nm light emerges at the output (Fig. 3d), with a 350nW power. Then we apply a voltage of 2,600

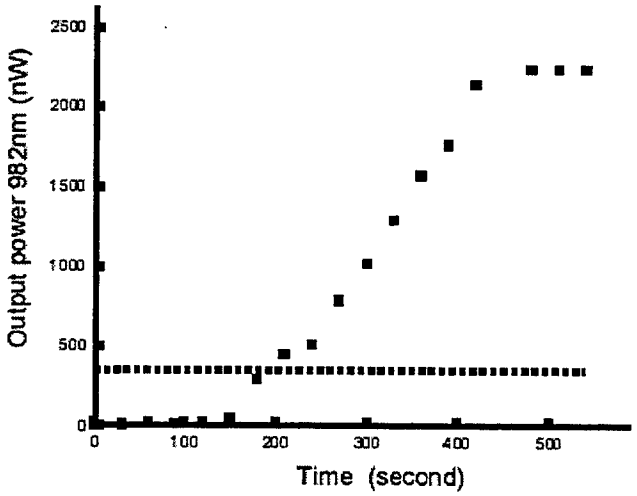


Figure 2 Temporal response of the SH power after the voltage is turned on (dotted). The dashed line is the SH power in a bulk crystal without voltage.

volts. As the waveguide forms, the SH output width shrinks very quickly and reaches its minimum size 10μmx13μm (Fig. 3c). The size of the output fundamental beam is 25μmx38μm under guidance (Fig. 3e). At this moment, the SH output power is 810nW: 2.3 times of the SH power in a bulk crystal.

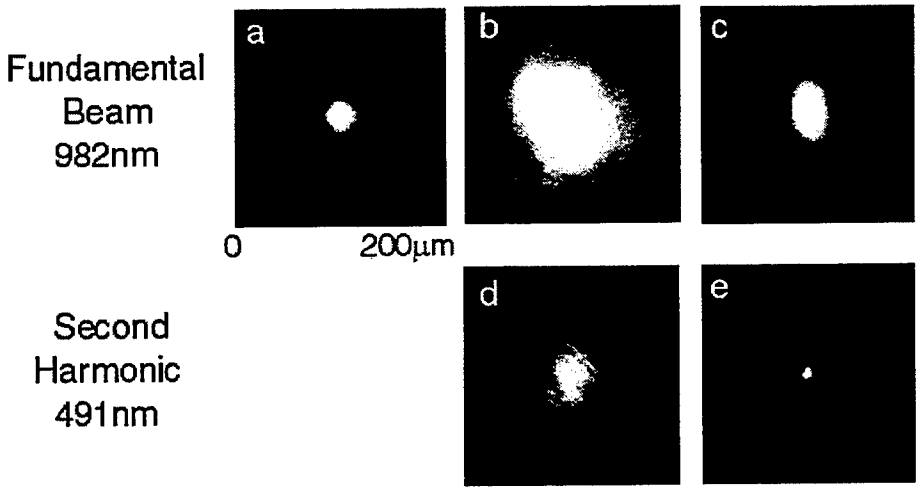


Figure 3 Experimental results with the passive method. (a) The input fundamental beam; (b) The output fundamental beam without voltage; (c) The output fundamental beam a few seconds after the voltage is on; (d) The output SH beam without voltage ; (e) the output of the SH beam a few seconds after the voltage is on.

To summarize, we have demonstrated SHG in soliton-induced waveguides, in both active and passive methods and observed an improvement of the conversion efficiency in both. We expect much higher improvement with a longer crystal and a narrower soliton: an 8μm guided beam in a 1cm long crystal will give a 425 improvement factor. Frequency conversion in soliton-induced waveguides offers a broad range of wavelength tunability by launching the soliton and the SHG in a range of phase-matchable crystalline orientations, as done with plane waves in a bulk crystal. Such tunability is non-existent with "conventional" fabricated waveguides. This research at Princeton University was supported by the US Army Research Office.

* Present address: Dept. of Physics, National Taiwan Univeristy, Taipei, Taiwan 10764
+ VLOC, II-VI Inc., New Port Richey, FL 34655
# Also at NEC Research Insititute, Princeton, NJ 08540
** Present address: Dept. of Physics and Astronomy, San Francisco State University, San Francisco, CA 94132
++Deltronic Crystal Industries, Dover, NJ 07801
Current address: Physics department, Technion, Haifa 32000, Israel Phone: (972)4-829-3926 FAX: (972)4-823-5107

References

1. M. Segev, M. Shih, and G. Valley, J. Opt. Soc. Am. B, **13**, 706, (1996).
2. M. Segev, B. Crosignani, A. Yariv and B. Fischer, Phys. Rev. Lett. **68**, 923 (1992).
3. M. Klotz, H. Meng, G. J. Salamo, M. Segev, and S. R. Montgomery, Opt. Lett. 24, 77 (1999)
4. S. Lan, M. Shih, and M. Segev, Opt. Lett. **20**, 1467 (1997).

Cantor Set Fractals from Solitons

Marin Soljačić, Suzanne Sears, Mordechai Segev, Dmitriy Krylov, and Keren Bergman
Princeton University, Princeton, NJ 08544
Tel: ++1-609-258-1949; Fax: ++1-609-258-1954

Solitons are general non-linear phenomena, appearing in a myriad of nonlinear wave systems in nature. Many of these systems support self-similar solitons, where a simple scaling relation exists for their sizes and intensities that maps all the solitons onto each other. Self-similar solitons occur when the underlying equation describing the system does not have any natural scale. A good example of such a system is the cubic nonlinear Schrödinger equation (NLSE):

$$i\frac{\partial\psi}{\partial z} + \frac{1}{2}\nabla_T^2\psi + |\psi|^2\psi = 0, \tag{1}$$

where z is the direction of propagation, and ∇_T^2 is the laplacian in the directions transverse to the direction of propagation, (or else the second order time derivative.) This equation describes optical temporal envelope solitons in fibers, optical spatial Kerr solitons, envelope solitons in plasma, deep sea water waves, etc.

Unlike the cubic NLSE, most wave equations describing physical systems do have natural scales. Nevertheless, these scales are often invisible over a wide parameter range of solitons. As long as all the solitons of interest are in one of the regions of parameters where all the natural scales built into the underlying equation are invisible, these solitons are almost perfectly self-similar to one another. For example, the saturable NLSE, which describes, e.g., (1+1)D photorefractive screening solitons and spatial solitons in atomic vapor:

$$i\frac{\partial\psi}{\partial z} + \frac{1}{2}\nabla_T^2\psi + \frac{|\psi|^2\psi}{1+|\psi|^2} = 0, \tag{2}$$

has a natural scale given by the factor 1 in the denominator of the nonlinear term. However, solitons that satisfy $|\psi|^2 \ll 1$ over the whole soliton profile are all self-similar to each other since the Eq.(2) reduces to Eq.(1) in that case. Similarly, for Eq.(2), one can show that if most of the energy of all solitons in a given system is contained in the regions where $|\psi|^2 \gg 1$, the intensity profiles of the solitons are all self-similar to each other. (In the deep saturation regime, the difference between the intensity profiles is minute and appears only in the margins of the beam, where $|\psi|^2 \leq 1$.)

If solitons of a wave equation that are all self-similar to each other are present simultaneously in a physical system, then the system supports self-similarity. This self-similarity property is translated into a fractal structure, if, in addition, a group of solitons on ever smaller scales exists within each soliton on a larger scale, such that the same generic structure (in this case, of solitons) is repeated on an ever decreasing scale.

In the cases of Eq.(1) and Eq.(2), this can be done by starting with a localized pulse whose dimensions are such that its nonlinear cohesive forces are much stronger than its tendency to diffract or disperse. (This is in contradistinction with a "conventional" soliton pulse, in which the self-acting exactly balances the diffraction.) In our simulations of the (1+1)D cubic self-focusing NLSE, such a pulse (or a beam in space) naturally breaks up into a few smaller solitons. In systems with considerable noise this breakup occurs due to modulational instability, whereas in systems with little noise, it occurs due to the dynamics-driven breakup. For examples, see the second row of Fig. 1, in which no noise was present; in the cases presented in Fig. 1, all the products of the first breakups are of the same sizes for each case, although this might not be easy to achieve in a typical experiment.

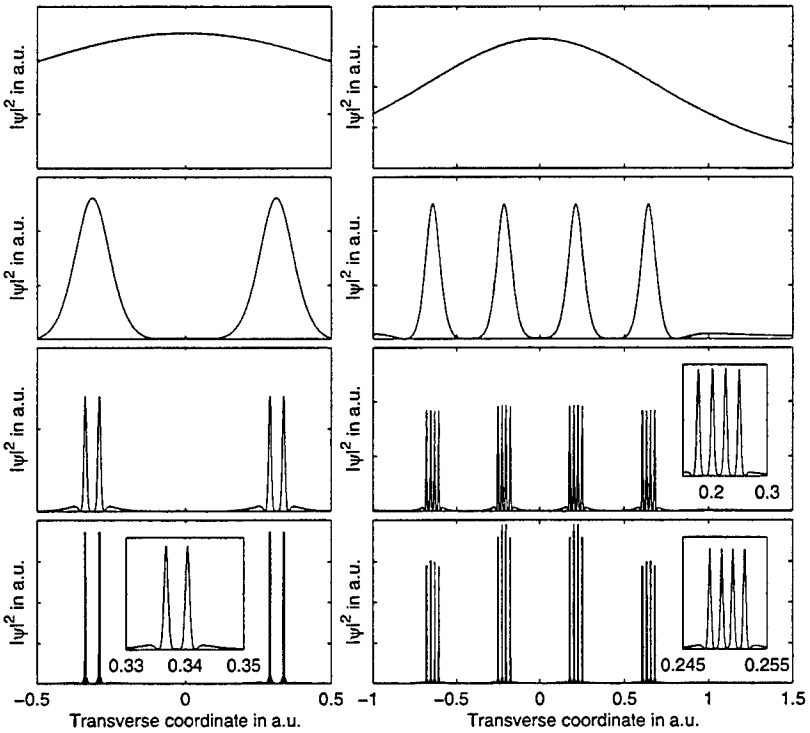


Figure 1: The two columns of the figure represent Cantor set fractal generation for two particular cases in the (1+1)D cubic self-focusing NLSE. In each case, we started with a sech-shaped pulse that was significantly higher than the soliton of the same width, as seen is the first row of the figure. The pulses started breaking up, as seen in the second row of the figure. When pulses looked as they appear in the second row, we abruptly significantly decreased the diffraction coefficients in the underlying equations, thereby inducing the second stage of the breakup, as seen in the third row of the figure. When pulses looked as they appear in the third row, we decreased the diffraction coefficient abruptly again, which resulted in the final stage of the breakup as seen in the fourth row of the figure. In some cases, the pulses were too tiny to see at the given magnification, so the insets in the plots show magnified details of their corresponding plots.

We can build on this idea in order to describe a general principle of creating fractals in any solitonic system [1,2]. Once the original pulse broke up into smaller solitons, one alters the "daughter-solitons" in such a way so that their self-acting is much stronger than the diffraction tendencies. This can be done either by altering the intensity of the pulses abruptly, or by changing the magnitude of the nonlinearity, or else by changing the diffraction (or dispersion) coefficient abruptly. It is important that the change in the equation is abrupt, so that the change forces the breakup of every "daughter-soliton" into even smaller pulses (beams); an adiabatic change does not cause the required breakup. Consequently, each of the pulses undergoes a self-similar breakup. This process can be repeated, in principle, an infinite number of times, thereby creating a fractal structure. Of course, care must be taken to ensure that the system always operates in the regimes of parameters where all its underlying natural scales are indeed invisible. For some examples of fractal generation processes, please see Fig. 1.

We emphasize another characteristic of the particular fractals we present in Fig. 1. Namely, all fractals we are aware of in physical systems in nature are statistical fractals; that is, they look the same on all scales of magnification only statistically. The principle we described will generically result in a statistical fractal also, especially in the presence of noise. However, as shown in Fig. 2, our principle also allows us to create exact fractals. This is achieved when the initial stage (when properly rescaled) can be mapped on each of the final products almost exactly, and this rescaling factor is almost the same for each of the final products. This particular exact fractal is called Cantor

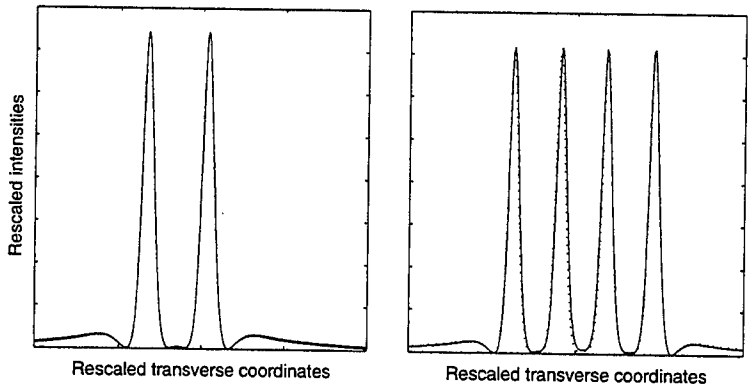


Figure 2: This illustrates the fact that the fractals we generated in Figure 1 are indeed exact. We took the shapes of the second row of Figure 1, shifted the shapes, rescaled them with the right factors, and superimposed them on the insets of the last row of Figure 1. The doted-lines represent the rescaled versions of the shapes of the second row of Figure 1, while the full-lines represent the shapes of the insets of the last row of Figure 1. The overlap in the left plot is so excellent that the two curves can hardly be distinguished.

Set fractal. Mathematically, a Cantor set can be generated in the following manner: one starts with a line, divides it into three equal parts, deletes the middle part, and repeats the procedure on each of the two remaining smaller lines, and then repeats this procedure recursively an infinite number of times. Of course, there is nothing special about dividing line into three equal parts. Instead, one could divide it into any number of arbitrarily sized parts and delete some of them; one would be left with what is called the motif of this particular Cantor set. Then, one would take this motif and apply it (properly rescaled) on each of the remaining lines, and continue the procedure recursively. Clearly, the full width half maxima of the solitons in the successive stages of Fig. 1 obey exactly the process of generating a Cantor set. The example in Fig. 1 can be designed with physical parameters of Spatial Kerr Solitons, or, perhaps even more promising, with the parameters of Temporal Kerr Solitons in fibers. To our knowledge, these are the first Exact fractals ever proposed in any physical system (outside of math) in nature.

Since the fractals of the kind we propose are always described by a known wave equation, the principle we propose yields one of very few fractal systems in nature for which one can actually write down and study all the dynamical equations describing it. (Recall that most other natural fractals rely on mean field theories and other statistical or Monte-Carlo approaches). At the same time, one can perform accurate experiments that can feed back into the theory. In contrast, for most fractal systems studied experimentally the equations describing the fractal creation are unknown, and most fractal systems studied mathematically are not associated with any physical system. This gives additional importance to the principle we described: besides proposing the first fractal system in optics, we suggest a way to experimentally and theoretically study fractals in almost any system in nature that supports solitons. In addition, the procedure we described allows one to create exact fractals (as opposed to most common statistical fractals) in some clean physical systems with suitable dynamical properties. Finally, we note that we are currently pursuing experiments to verify the described ideas using temporal fiber solitons.

References

[1] The first paper suggesting these ideas will be given by M. Soljačić, M. Segev and C. R. Menyuk, *Self-similarity and Fractals driven by soliton dynamics*, at the QELS'99 Conference, paper QWF5.
[2] A paper by M. Soljačić, M. Segev and C. R. Menyuk, *Fractals From Solitons*, has been recently submitted to PRL.

First Experimental Observation of Optical Bloch-Oscillations

U.Peschel R. Morandotti, and J. S. Aitchison
University of Glasgow, Glasgow G12 8QQ, UK,
Tel.:44 141 3305230, Fax: 44 141 3304907, E-Mail: morandot@elec.gla.ac.uk

H. Eisenberg and Y. Silberberg
The Weizmann Institute of Science, 76100 Rehovot, Israel

Waveguide arrays are well known as basic components of high power semiconductor lasers or as promising candidates for ultra fast signal processing. Solitons can exist in this discrete environment [1], but their dynamical behavior is modified considerably. Inhomogenities add a further degree of freedom to the beam evolution. In a slab waveguide the high index regions attract the field. However the dynamics in inhomogeneous arrays are different. If the effective indices of the individual waveguides differ by a constant amount the field does not constantly move towards the higher indices, but oscillates around the initial guide [2]. These so-called Bloch-oscillations are found in other discrete systems as e.g. semiconductor super lattices.

Here we use arrays of AlGaAs waveguides to demonstrate the occurrence of Bloch-oscillations. Besides the test of the linear properties this material system enables us to investigate the influence of a nonlinearity on the field evolution. The sample under investigation consisted of 25 ridge waveguides. It was etched 1.2μm deep on top of an AlGaAs slab waveguide composed by a guiding layer of $Al_{0.18}Ga_{0.82}As$, 1.5μm thick, sandwiched between two layers of $Al_{0.24}Ga_{0.76}As$. These upper and lower claddings were 1.5μm and 4.0 μm thick, respectively. To obtain a linear increase of the effective index the rib width was varied from 2 to 3.4μm, corresponding to an index difference of $\delta n = 1.275 * 10^{-4}$ between adjacent guides. To ensure constant coupling the spacing between the guides was also varied from 6.6 down to 3.3μm (see Fig.1). Finally the sample was cleaved into pieces of different length varying from 3 to 18mm to allow for an insight into the field evolution.

To measure the optical response of the sample we used 180 fs long pulses at a wavelength of λ=1.53 μm, which is well below half the band gap resulting in the suppression of two photon absorption. We used an elliptically shaped input beam with a width varying from 3 to 20 μm. The image of the output field was recorded with an infrared camera.

Numerical simulations were performed using coupled mode theory. Under ideal conditions (cw without losses) the system can be modeled with the following set of equations

$$i\frac{da_n}{dz} + \delta\beta\, n\, a_n + \gamma|a_n|^2 a_n + C(a_{n-1} + a_{n+1}) = 0$$

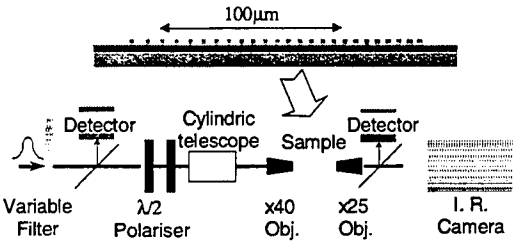


Fig.1 Experimental set-up

where a_n accounts for the amplitudes of the individual guides. In our case the wavenumber difference between adjacent guides amounts to $\delta\beta=520m^{-1}$ and the coupling constant was about $C=1240m^{-1}$. The nonlinear coefficient was determined to be $\gamma=6m^{-1}W^{-1}$. Although linear losses (2dB/cm) were present and although the transient behavior influences the field evolution the qualitative behavior was not effected.

Fig.2 shows the field evolution for a narrow input beam (3μm), which excited the central waveguide only. In the low power case (see

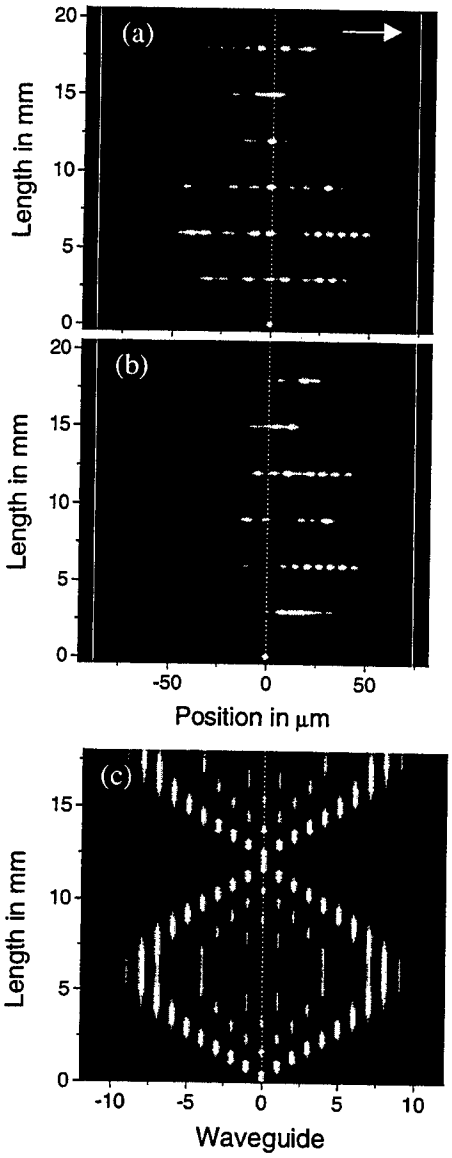


Fig.2 Field evolution for the excitation of the central waveguide (dotted line: input guide, bold line: array boundaries, arrow: direction of growing potential).
a) experimental data for low power,
b) experimental data for high power,
c) simulation of the linear field evolution

Fig.2a and c) the field first spreads into both directions as it does in an homogenous array. The action of the linear potential results in a subsequent refocusing of the beam.

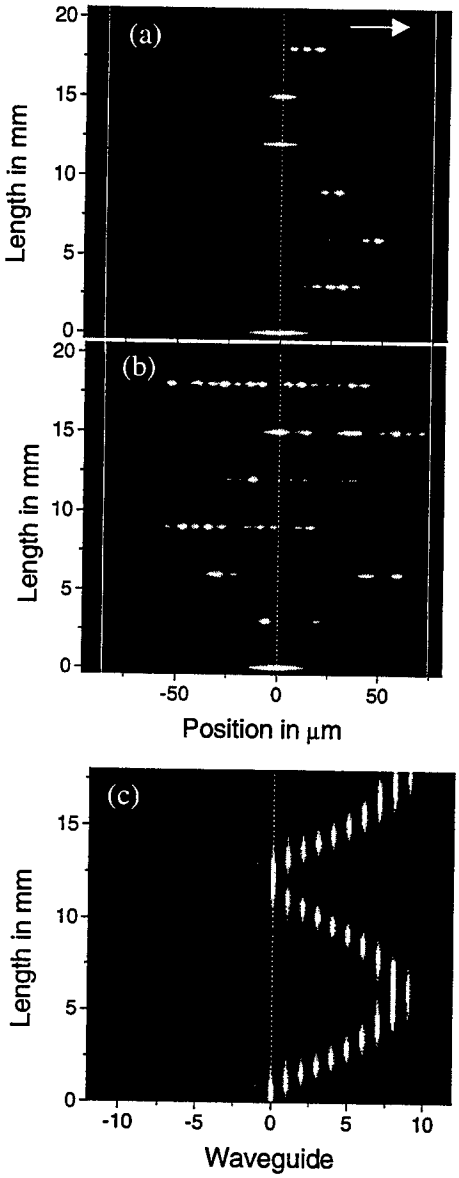


Fig.3 Field evolution for a broad incident beam (20μm ≈ 2 guides) centered on the central guide (dotted line: guide of excitation, bold line: array boundaries, arrow: direction of growing potential).
a) experimental data for low power,
b) experimental data for high power,
c) simulation of the linear field evolution

Consequently a periodic breathing or Bloch-oscillations are observed. The main reason for this somehow unexpected behavior is the

discreteness of the system. In contrast to a continuous system the linear eigenmodes of the array with a linear index gradient have a limited extension and equally spaced discrete propagation constants - the so-called Wannier-Stark-ladder. Hence after a certain propagation length (in our case 12mm) every initial distribution is recovered because the phase differences between the modes have reached multiples of 2π. In between a considerable spreading may occur which is defined by the extension of the linear modes of the array. But in the linear case the power distribution stays symmetric all the time, where adjacent waveguides on the low/high index side have opposite/equal phases. For increased power levels these phase relations are disturbed resulting in symmetry breaking and incomplete recovery (see Fig.2b).

In case of a wider beam and for still low power levels (see Fig.3 a and c and 4) the field evolution is still periodic, but almost no spreading occurs. Because several guides are excited the field at the low index side is eliminated due to destructive interference and the beam keeps confined. As far as the boundaries of the array are not touched this behavior is the same for any input condition (compare Fig.3a and 4). Again the action of the nonlinearity (see Fig.3b) disturbs the phase relations, which are vital for the confinement of the beam. Now the field starts to spread due to the action of the focusing nonlinearity. These strong power induced changes of the field distribution (see Fig.5) might be useful for signal steering and switching applications. In contrast to previously proposed switching schemes an initial beam tilt is not required to a sharp beam scanning.

In conclusions we investigated an array of coupled waveguides with linearly increasing wavenumbers. We observed a periodic motion of the low power field similar to Bloch-oscillations known from e.g. semiconductor physics. The field evolution is very sensitive to the beam width. Any action of the focusing Kerr nonlinearity disturbs this behavior. In particular a previously confined beam starts to spread.

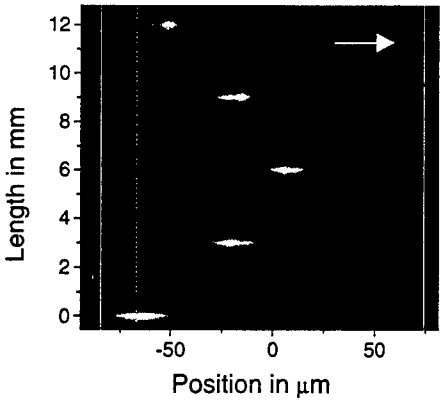


Fig.4 Experimentally determined field evolution for a broad incident beam (20µm ≈ 2 guides) centered around the 8th waveguide counted from the central guide (dotted line: guide of excitation, bold line: array boundaries, arrow: direction of growing potential).

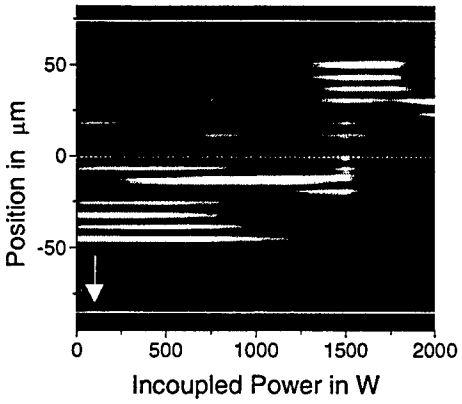


Fig.5 Output field distribution of a 9mm long sample for varying input power levels (same parameters as Fig.3).

[1] H.S.Eisenberg, Y.Silberberg, R.Morandotti, A.R.Boyd, and J.S.Aitchison, Phys.Rev.Lett. 81, 3383 (1998).

[2] U.Peschel, T.Pertsch, and F.Lederer, Opt.Lett. 23, 1701 (1998).

New families of discrete solitons in $\chi^{(2)}$ waveguide arrays

A. Kobyakov[1], S. Darmanyan[1,2], T. Pertsch[3], and F. Lederer[1]

[1] *Institute of Solid State Physics and Theoretical Optics, Friedrich-Schiller-Universität Jena, Max-Wien-Platz 1, 07743 Jena, Germany*
tel. +49 3641 947 170, fax +49 3641 947 162, e-mail: pfl@uni-jena.de
[2] *Institute of Spectroscopy, Russian Academy of Sciences, 142092 Troitsk, Russia*
[3] *Fraunhofer-Institut für Angewandte Optik und Feinmechanik, Schillerstr. 1, 07745 Jena, Germany*

More than ten years ago it was realized that an array of nearest-neighbor coupled guides can support localized structures [1]. Nonlinear waveguide arrays on AlGaAs basis have been recently fabricated and localized modes, or discrete solitons (DSs), have been experimentally observed [2]. There are various ideas to exploit DSs for all-optical applications [3]. For instance, one can take advantage of the ability of a relatively wide DS to move across the array provided that the initial excitation exhibits a small phase gradient. The collision between a moving and a trapped DSs can be exploited to steer the output position of the DS. Alternatively, beam steering may be achieved either by a local change of the linear coupling or by a varying coupling strength across the whole array [3]. However, for the very realization of switching concepts it is important to minimize the operating power and the operation complexity. Besides the high peak power required due to the weak nonresonant cubic nonlinearity another difficulty in above mentioned schemes is that all-optical phase control is difficult to achieve.

It is now commonly believed that switching operations exploiting a quadratic ($\chi^{(2)}$) nonlinearity may require less power [4]. In this respect, established fabrication technologies for $LiNbO_3$ waveguide configurations feed the anticipation that the implementation of quadratic nonlinear arrays is feasible. Intensity-dependent switching in Ti:$LiNbO_3$ coupled channel waveguides has been already performed experimentally [5]. The extention of a recently suggested switching strategy that relies on the exploitation of the *controllable DS's instability* [6] toward a *quadratic nonlinearity* could result in potentially more efficient all-optical operations. However, the $\chi^{(2)}$ DSs found previously [7] occurred to be either always (un)stable or transforming into long-living oscillatory states.

In this contribution we identify new families of quadratic DSs and prove that these DSs possess peculiar stability properties that can be exploited for digital applications.

The propagation of the fundamental wave (FW) a_n and the second harmonic (SH) b_n in the nth waveguide of the array is described by a set of dimensionless difference-differential equations [7]

$$\begin{aligned} &i da_n/dz + c_a(a_{n-1} + a_{n+1}) + 2\gamma a_n^* b_n = 0, \\ &i db_n/dz + c_b(b_{n-1} + b_{n+1}) + \beta b_n + \gamma a_n^2 = 0, \end{aligned} \qquad (1)$$

where the normalized amplitudes a_n, b_n are related to the square root of the maximum SH guided power $B_{\max}$ as $a_n = \sqrt{2}A_n/B_{\max}$, $b_n = B_n \exp(-i\Delta k z)/B_{\max}$; $c_{a,b} = \pi L_0/2L_{A,B}$ and $\gamma = \omega d_{\text{eff}} L_0 B_{\max} \Psi/\sqrt{2\epsilon_0 c^3 n_\omega^2 n_{2\omega}}$ characterize the linear ($L_{A,B}$ - half-beat length) and nonlinear coupling, respectively, n_ω and $n_{2\omega}$ are the effective indices of the guided modes, L_0 is some characteristic length, e.g. the waveguide length, used for normalization $Z = zL_0$, $\beta = -\Delta k L_0$ denotes the normalized wave vector mismatch, where $\Delta k = 2k_\omega - k_{2\omega}$, and Ψ stands for the nonlinear overlap integral of the guided modes. Then the product $(B_{\max}\Psi)^2$ is an effective intensity.

In what follows we are interested in stationary solutions to (1) in the form $a_n = a u_n \exp(ikz)$, $b_n = b v_n \exp(i2kz)$. Assuming a strong localization of the initial excitation u_n, v_n we find a family of *discrete domain walls*

$$\begin{aligned} u_n &\approx (..., 1, 1, 1, u_1, u_2, u_3, u_4, 0, 0, 0, ...), \\ v_n &\approx (..., 1, 1, 1, v_1, v_2, v_3, v_4, 0, 0, 0, ...), \end{aligned} \qquad (2)$$

where the peak FW and SH amplitudes are related by $a^2 = b(2k - 2c_b - \beta)/\gamma > 0$ and the nonlinear dispersion relation reads as $k = 2(\gamma b + c_a)$. The nontrivial amplitudes u_j, v_j ($j = 1..4$) can be expressed in terms of the ratios between linear coupling and nonlinearity

$$x = c_a/(2\gamma b), \quad y = c_b/(4\gamma b - \beta) \qquad (3)$$

being likewise inverse proportional to the degree of localization and are supposed to be small, viz. $|x|, |y| \ll 1$. Calculated with second-order accuracy with respect to x and y the excitations u_j, v_j have the following form

$$\begin{aligned} &u_1 = 1 - x^2/4 - 3xy/4, \quad v_1 = 1 - x^2/2 - xy/2, \\ &u_2 = 1 + (x+y)/2 - 3x^2/8 + (1-\nu)xy/(2-\nu) - 3y^2/8, \\ &v_2 = 1 + x - x^2/2 + xy/2, \\ &u_3 = x - 3x^2/2 + 3xy/2, \quad v_3 = y + x^2 - \nu xy/(2-\nu), \\ &u_4 = x^2, \quad v_4 = y^2, \end{aligned} \qquad (4)$$

where $\nu = \beta/(2\gamma b)$ is an effective mismatch.

A propagation of the discrete domain wall (2),(4) is shown in Fig. 1a. We have also found that two domain walls of opposite polarity may form a bound state

(Fig. 1b). Such a quasirectangular, or Π-DS, can be viewed as a discrete plane wave $u_n = v_n = 1$ sandwiched between two fronts. The existence of domain wall solutions and their respective bound states is a consequence of the discreteness and has no analogs in continuous $\chi^{(2)}$ media.

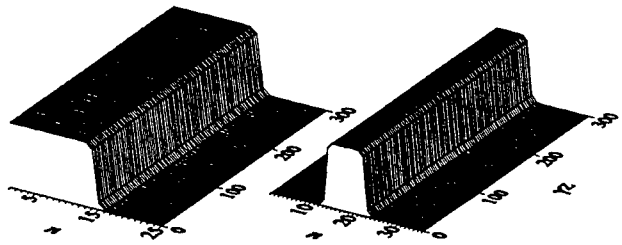


FIG. 1. Propagation of a discrete domain wall and a Π-DS in a $\chi^{(2)}$ waveguide array. Parameters: $b = -1$, $\beta = -2\gamma$, $c_a = 2c_b = 0.2\gamma$. The amplitude of the FW component is shown, while the SH component has a similar form.

To study the stability of Π-DSs we split the solution into three parts: the weakly excited guides, the transition (front) regions, and the "plane wave". We assume that the weakly excited part, being in fact a linear system, is stable. Thus it is left to derive criteria for the front instability (FI) as well as the modulational instability (MI) of the "plane wave". Later we will confirm the validity of this approach by direct numerical integration of (1).

First we identify regions of FI. We impose a complex perturbation $\delta_j^{a,b}(z) = \delta_{jR}^{a,b} + i\delta_{jI}^{a,b}$ on each nontrivially excited waveguide, insert the perturbed profiles into (1) and solve the linearized eigenvalue problem for the real-valued components of the perturbation vector $\vec{\delta}(z)$ (for details of the stability analysis of two-component localized modes see [6]). To study MI we substitute the perturbed in-phase plane wave solutions $a_n = (a + \rho_n(z))\exp(ikz)$, $b_n = (b + \mu_n(z))\exp(2ikz)$ into (1). The subsequent linearization and separation of real and imaginary parts yields a fourth-order eigenvalue problem [7]. For $x > 0$ (zero phase of the SH) both FI and MI occurs. However, for $x < 0$ (π phase of the SH) the domain of FI and MI do not overlap. For small β the FI domain typically lies inside the MI domain.

We found explicit MI criteria for nonlinear plane waves and Π-DSs from the approximate analytical solution of the corresponding eigenvalue problem to be $x > 0$ and

$$x < 0, \quad \nu < \nu_{MI} \approx 2\left[3 + \sqrt{s(2+s)}\right]x + 2, \qquad (5)$$

where $s = c_a/c_b$. A negative nonlinearity γ ($x < 0$) can be mimicked by a π-phase shift of the SH. The maximum MI gain near the stability boundaries occurs for an out-of-phase perturbation.

Hence, two types of short-term instability, viz. Π-DS's decay due to MI and front spreading due to FI can be distinguished. Both types of instability are controllable by varying $\hat{x}$ (i.e. the nonlinearity γ) near the respective boundary. Typically, MI gain exceeds FI gain near the boundary. Hence, the controlled Π-DS decay due to MI requires less power and is more appropriate for all-optical applications. It is a genuine feature of the $\chi^{(2)}$ nonlinearity that the onset of MI can be controlled by power. As can be inferred from (3,4) Π-DSs do also exist in the cascading limit ($|\beta| \gg 1$), i.e. they may be observed in strongly phase mismatched quadratic as well as in cubic arrays. However, only the weaker FI can be induced by power variation. The passage of the other instability boundary $x = 0$ is phase-controlled, i.e. requires to revert the sign of b.

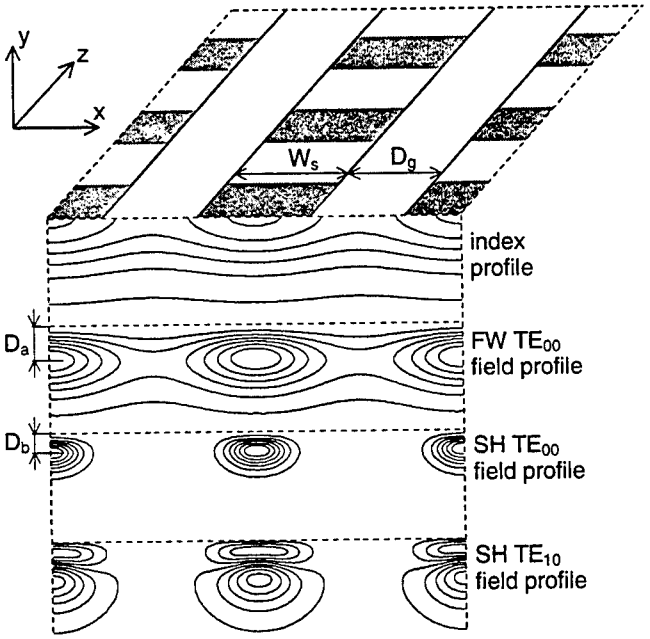


FIG. 2. Scheme of a QPM $LiNbO_3$ waveguide array with the index profile induced by indiffusion of Ti stripes of width $W_s = 10\mu$m and separation $D_g = 20\mu$m. The calculated field profiles of the TE_{00}^{ω}, $TE_{00}^{2\omega}$, and $TE_{10}^{2\omega}$ modes show strong coupling for the FW and negligible coupling for the SH.

The Π-DSs discussed above can be observed in an array of waveguides fabricated by titanium indiffusion into a $LiNbO_3$ substrate (Fig. 2). To estimate the required powers we have taken parameters from an established fabrication process [5]. The titanium-diffusion process itself and the induced increase in the refractive index was modeled with effective diffusion depths in X and Y direction being $D_X = 10$ μm and $D_Y = 5$ μm, respectively. We used a vectorial finite-element method (FEM) to calculate mode profiles, propagation constants, coupling coefficients, and overlap integrals for the FW and SH modes. To exploit the highest nonlinear tensor component d_{33} we considered a $TE_{00}^{\omega} \leftrightarrow TE_{00}^{2\omega}$ interaction in a first order quasi-phase-matched (QPM) waveguide. A peculiarity of the geometry used is that strong coupling of guided modes

in adjacent waveguides can only be achieved for the FW ($c_b \to 0$). Because of the slower evanescent decay of the field the modes sink deeper into the substrate for a longer wavelength ($D_a > D_b$ in Fig. 2), which leads to a weaker transverse confinement and therefore stronger coupling of the FW modes.

Versatile power-controlled switching requires that Π-DSs can be excited by a finite, homogeneous beam $a_n = a$, $b_n = b$. Propagation of a Π-DS in this case is shown in Fig. 3. A rectangular initial exciation which corresponds to a stable Π-DS maintains its form over large distances (Fig. 3a). A transition to a modulationally unstable Π-DS ($a_n = 1.05 \to a_n = 0.9$) drastically change the evolution of the whole mode by evoking strong oscillations of the intensity in the initially excited waveguides. Subsequently, the mode becomes delocalized and spreads over the whole array (Fig. 3b). The SH component has a similar structure, however, it is subject to less pronounced changes for the lack of coupling.

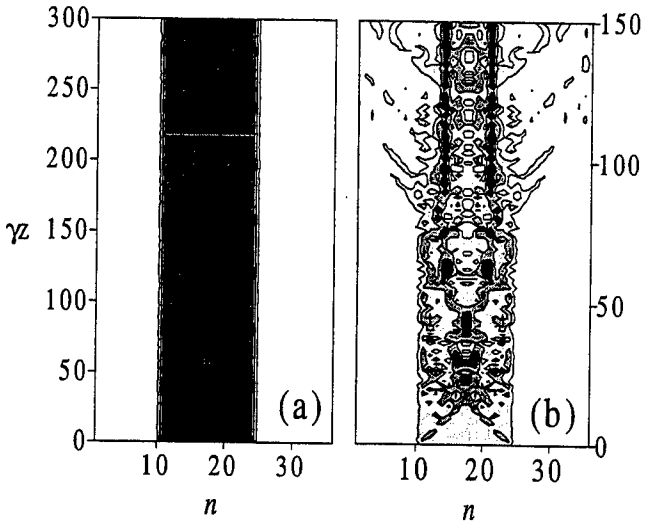


FIG. 3. Propagation of the FW amplitude of a "rectangular" excitation comprising N=14 waveguides in a waveguide array with the decoupled SH (c_b=0, Fig. 2), $b = -1$, $\beta = -2\gamma$: (a) $c_a = 0.22\gamma$, (b) $c_a = 0.3\gamma$.

To estimate power levels required to observe a transition from a stable to an unstable Π-DSs we have assumed a Z=6.5 cm long $LiNbO_3$ waveguide array with $D_g = 17.1$ μm that corresponds to a FW half-beat length L_A=10.5 mm. Then the corresponding overlap integral amounts to $\Psi = 7.25 \times 10^4$ m^{-1}. For γz=20, where a mode destabilization can be observed (Fig. 3b), we get $|A|^2 \approx |B|^2 \approx 100$ W with $d_{\text{eff}} = 31.8 \times (2/\pi)$ pm/V for λ=1.32 μm. The required grating period for first-order QPM is then $\Lambda = 14.4$ μm.

Another peculiarity of the array considered is that the higher order SH mode $TE_{10}^{2\omega}$ (Fig. 2) can come into play. This situation has been studied for a single waveguide in [8]. Here the corresponding overlap integral compares to that of the primary process ($\tilde{\Psi} \approx 0.7\Psi$). However, the QPM grating compensates only partially for the mismatch in $TE_{00}^{\omega} \leftrightarrow TE_{10}^{2\omega}$ process ($\tilde{\beta} \approx -3\beta$). Thus the secondary process remains moderately phase mismatched and acts as an additional perturbation for the launched Π-DS. In Fig. 4 all fields involved are displayed. Even in this case the stable Π-DS survives and propagates quite robustly. The weak secondary SH field, which is not present at the input, exhibits small oscillations (Fig. 4).

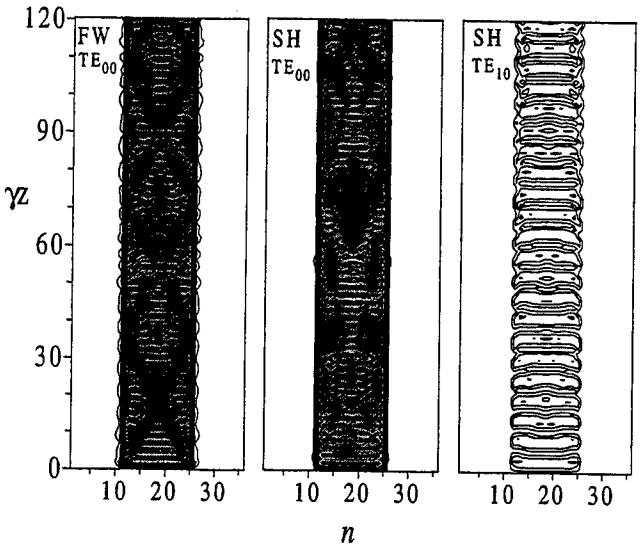


FIG. 4. Propagation of a Π-DS shown in Fig. 3a. accounting for an additional mode mixing process $TE_{00}^{\omega} \leftrightarrow TE_{10}^{2\omega}$.

In conclusion the existence of novel optical frontlike and quasirectangular modes in discrete systems with quadratic nonlinearity has been proved. Parameters of a typical waveguide array made from Ti:$LiNbO_3$ are calculated.

[1] D. N. Cristodoulides and R. I. Joseph, Opt. Lett. **13**, 794 (1988).

[2] H. Eisenberg *et al.*, Phys. Rev. Lett. **81**, 3383 (1998).

[3] A. B. Aceves *et al.*, Phys. Rev. E **53**, 1172 (1996); O. Bang and P. D. Miller, Opt. Lett. **21**, 1105 (1996); W. Krolikowski and Y. S. Kivshar, J. Opt. Soc. Am. B **13**, 876 (1996); T. Peschel, R. Muschall, and F. Lederer, Opt. Commun. **136**, 16 (1997).

[4] G. I. Stegeman, D. J. Hagan, and L. Torner, Opt. Quantum Electron. **28**, 1691 (1996).

[5] R. Schiek, Y. Baek, and G. I. Stegeman, J. Opt. Soc. Am. B **15**, 2255 (1998).

[6] S. Darmanyan *et al.*, Phys. Rev. E **57**, 3520 (1998).

[7] S. Darmanyan, A. Kobyakov, and F. Lederer, Phys. Rev. E **57**, 2344 (1998).

[8] C. G. Treviño-Palacios *et al.*, Appl. Phys. Lett. **67**, 170 (1998).

Nonlinear Guided Waves and Their Applications

Dispersion Management 1

Thursday, 2 September 1999

Stefan Wabnitz, Université de la Bourgogne, France
Presider

ThA
08.00-10.00
Salle Morey—St-Denis

Pulse-overlapped dispersion-managed data transmission and intra-channel four-wave mixing.

P. V. Mamyshev and N. A. Mamysheva
Bell Laboratories - Lucent Technologies, Holmdel, NJ 07733
pavel@bell-labs.com

Introduction

Nonlinear pulse-to-pulse interaction is one of the main limiting factors in high-bit-rate transmission systems. The fiber nonlinearity shifts the frequencies of the interacting pulses which, in turn, results in timing jitter and intersymbol interference. The important parameter which determines the strength of the interaction is the ratio τ/T, where τ is the pulse width (FWHM) and T is the spacing between adjacent pulses (1/T is the transmission bit rate). To avoid interaction-induced penalties in classical soliton transmission systems, the pulses should not overlap significantly with each other: τ/T should be less than 0.2- 0.3 [1]. Similarly, for the case of dispersion-managed (D- M) soliton systems, when the pulse width oscillates with the distance, the current thinking suggests that the maximally stretched pulse should be (considerably) less than T (see, for example, [2,3]). In this paper, we describe a new type of transmission with reduced pulse-to- pulse interaction - the 'pulse-overlapped dispersion- managed transmission' (it can be soliton or non-soliton). We also classify the dispersion-managed systems and determine the influence of the pulse-to-pulse interaction on different types of D-M systems.

XPM-induced pulse-to pulse interaction.

Nonlinear interaction between adjacent pulses in dispersion-managed systems can be described in terms of the cross-phase modulation (XPM) effect since the interacting pulses are highly chirped when they start to overlap with each other. XPM shifts the leading pulse to the 'red' spectral region, and the trailing pulse - to the 'blue' spectral region. Figure 1 shows the XPM-induced frequency shift as a function of the τ/T parameter. One can see that the interaction is very small when τ/T is smaller than 0.4, i.e. when the pulses barely overlap, which is a well-known fact from the classical soliton and classical D-M soliton theory. The new and unexpected conclusion is that the interaction is also

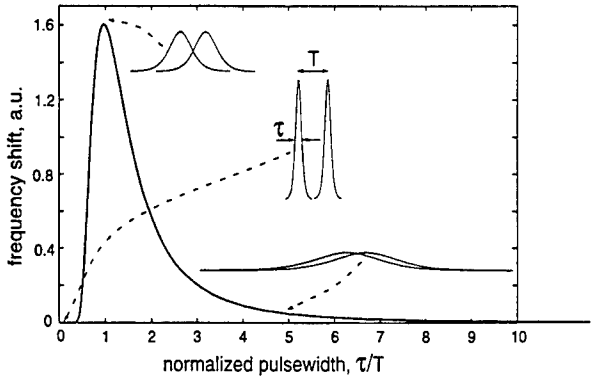


Figure 1. XPM-induced frequency shift of two interacting gaussian pulses as a function of the pulse width normalized to the pulse separation. Pulse energy is constant.

very small when the pulses overlap nearly completely ($\tau/T \gg 1$), and the strongest interaction occurs when the pulses are partially overlapped ($\tau/T \approx 1$). The reason for such an interesting behavior is as follows. The XPM-induced frequency shift per unit distance is proportional to the *time derivative* of the interacting pulse's intensity: $\frac{d\omega(t)}{dz} = 2\frac{2\pi}{\lambda} n_2 \frac{dI(t)}{dt}$. When $\tau/T \ll 1$ the slope is the highest, but the pulse overlap is small, so the interaction is weak. When $\tau/T \approx 1$ the

pulses begin to overlap and the pulse derivative is still high in the overlapping region. That results in a very strong interaction. For the case of nearly complete overlap ($\tau/T >> 1$), there are two reasons for a weak interaction. First, the pulse derivative reduces with the pulse broadening. Secondly, the sign of the derivative changes across the region of overlap so that the net effect tends to be canceled out. The described effect of reduction of pulse-to-pulse interaction provides

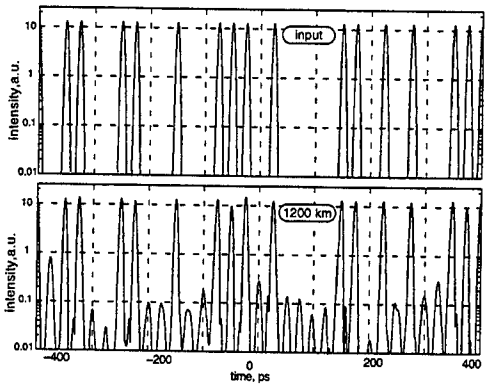


Figure 2. Input and output signals of pulse- overlapped D-M transmission shown on a logarithmic scale. Average signal power is 6 dbm.

the basis for the 'pulse-overlapped D-M' transmission systems. In such a system, the minimum unchirped pulse width τ_{min} is smaller that the bit slot T . At the same time, the length of the dispersion map (or the dispersion compensation period) is much greater than the local dispersive length of the pulses, $L_{map} >> L_d$, where $L_d = \frac{\pi c}{2\ ln2\ \lambda^2} \frac{\tau_{min}^2}{|D|}$ and D is the fiber's dispersion. As a result, the pulse width breathes over a wide range, so that the maximum pulse width is much greater than the bit slot: $\tau_{max}/T >> 1$. Under these conditions, the pulses spend only a small fraction (approximately τ_{max}/T) of the total transmission distance in the strong interaction regime (when τ is around T), so that the interaction is greatly reduced. As an example of such a transmission, consider a 40 Gbit/s D-M soliton system with τ_{min} =5 ps based on standard and dispersion compensating fibers. The dispersion map length equals the amplifier spacing, ≈80 km. In this system, the pulse width oscillates from 5 ps to τ_{max} which is more than 700 ps, while the bit slot is only 25 ps. It means that the pulses are strongly overlapped during most of the transmission. As a result the XPM-induced pulse-to-pulse interaction is reduced, which manifests itself in a small timing jitter at the output of the transmission (see fig.2). The eye diagram of the output signal is clearly open, which shows the capability of the pulse-overlapped D-M transmission. The described theory explains the success of the recent experiments on high-bit-rate RZ transmission with strong dispersion management [4,5].

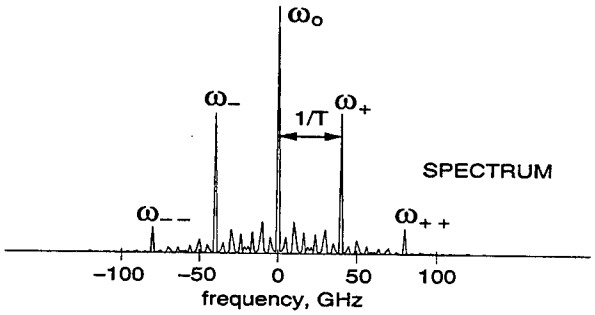


Figure 3. Spectrum of the data shown on Fig.2.

Intra-channel four-wave mixing.

The next question is: what limits the maximum error-free distance of the pulse-overlapped transmission? By looking closely at the output signal shown on Fig.2 on a logarithmic scale, one can see some amplitude jitter in the 'ones', and small 'ghost' pulses beginning to appear in the 'zeros'. This effect becomes more pronounced at longer distances. The interesting fact is that these 'ghost' pulses are not the usual dispersive waves, they appear exactly in the middle of the 'zero' slots. We explain this effect as a consequence of a special case of four-wave mixing

(FWM) between spectral components in a single channel. The spectrum of an RZ data stream at a bit rate of 1/T contains strong components separated by 1/T from each other (see fig.3), and these components play an important role in the FWM process. The following processes can generate light at the carrier frequency ω_0 : $\omega_+ + \omega_- \rightarrow 2\omega_0$, $2\omega_+ - \omega_{++} \rightarrow \omega_0$, $2\omega_- - \omega_{--} \rightarrow \omega_0$. The phase mismatch for these processes is $\Delta k = 2\pi D\lambda^2/(T^2 c)$. We will illustrate the 'intra channel' FWM effect in an example of the first of the above mentioned processes. One can define the

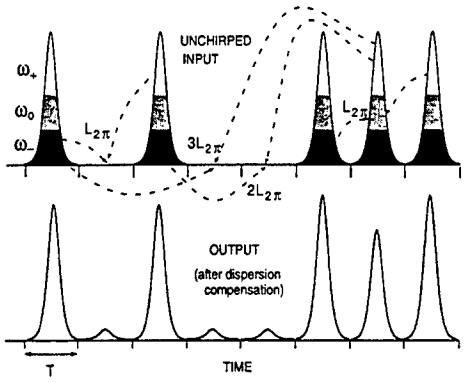


Figure 4. Qualitative description of the 'ghost' pulse generation in 'zeros' and of the amplitude jitter in 'ones'. See text.

FWM coherence length as $L_{2\pi} = 2\pi/\Delta k$. When the pulses are unchirped, all the spectral components are in phase. Qualitatively, in the time domain, this means the spectral components overlap in time and 'sit' on top of each other within the pulses (see fig.4). When the pulses start to propagate in the D-M system, the dispersion broadens and chirps the pulses: the 'blue' spectral components propagate faster than the 'red' ones (for D>0). After an *integral number* of coherence lengths $L_{2\pi}$ the 'blue' components ω_+ of one pulse meet (collide) with the 'red' components ω_- of another pulse exactly in the middle of a bit slot (this slot could be a 'zero' or 'one'). Note that this stems from the fact that, as we mentioned above, the separation of the spectral components under consideration and the temporal separation between the pulses are related to each other. As a result, the FWM process generates a field at ω_0 in the middle of the bit slots. If the slot is a 'zero', it means the generation of a 'ghost' pulse. In the case of slots with 'ones', the interference between the 'ones' and the FWM-generated field leads to the amplitude jitter (see fig.4). Another source of an amplitude jitter in 'ones' is the energy transfer from 'ones' to the 'ghost' pulses through the described FWM process.

Conclusions.

In conclusion, we determined three main regimes of XPM-induced interaction of (chirped) pulses. The strongest interaction occurs in the regime with partially overlapped pulses ($\tau/T \approx 1$), while the interaction is weak in the regimes of non-overlapped pulses ($\tau/T << 1$) and nearly completely overlapped pulses ($\tau/T >> 1$). Based on these results, we can determine three regimes of dispersion-managed data transmission and predict their behavior. In the first, 'non-pulse-overlapped', regime, adjacent pulses barely overlap during most of the transmission, so that the pulse interaction is not a problem in this case. In the 'partially-pulse-overlapped' regime, the adjacent pulses spend a considerable portion of the transmission being partially overlapped ($\tau(z)$ being around T). Cross-phase modulation causes the frequency and timing jitter in this case. In the third, 'pulse-overlapped', regime, the adjacent pulses are almost completely overlapped with each other during most of the transmission. The XPM-induced pulse-to-pulse interaction is greatly reduced in this case in comparison with the previous one. The main limiting factor for this regime of transmission is the amplitude fluctuations and 'ghost' pulse generation caused by the described above intra-channel four-wave mixing.

References

[1] J. P. Gordon, Opt. Lett, 8, 596 (1983).
[2] T.Yu, E. A. Golovchenko, A. N. Pilipetskii, and C. R. Menyuk, Opt. Lett., 22, 793 (1997).
[3] M. Matsumoto and H. A. Haus, IEEE Phot. Techn. Letters, 9, 785 (1997).
[4] D. Le Guen et al, OFC-99, postdeadline paper PD-4.
[5] G. Raybon, B. Mikkelsen, R.-J. Essiambre, J. E. Johnson, K. Dreyer and L. Nelson, "100 Gbit/s single-channel transmission over 200 km True Wave fiber and 160 km of conventional fiber using semiconductor pulse source and demultiplexer", submitted to ECOC-99.

160 Gb/s soliton transmission in a densely dispersion-managed fiber in the presence of variable dispersion and polarization-mode dispersion

T. Hirooka[1], T. Nakada[1], A. Liang[1] and A. Hasegawa[2]

[1] Graduate School of Engineering, Osaka University
2-1 Yamada-oka, Suita, Osaka 565-0871, Japan
Phone: +81-6-6879-7728, Fax: +81-6-6879-7688
E-mail: hirooka@comf5.comm.eng.osaka-u.ac.jp

[2] Kochi Unversity of Technology
and NTT Science and Core Technology Laboratory Group

One of the major limitations on transmission speed per single-channel in dispersion-managed soliton (DMS) systems is soliton interactions between neighboring pulses induced by large pulse breathing within one dispersion-management period [1]. To overcome this limitation, densely dispersion-managed soliton (DDMS) system was recently proposed, and it is numerically demonstrated that 80 Gb/s soliton transmission over 9,000 km may be possible without any active controls [2].

For further increase of bit-rate per single-channel up to 160 Gb/s, however, it is indispensable to assess the impact of dispersion slope and polarization mode dispersion (PMD), which may deteriorate transmission characteristic significantly in such ultra high-speed transmission. Furthermore, one should assume large variation of group-velocity dispersion (GVD) for practical dispersion flattened fibers.

In dispersion-managed systems schematically shown in Fig. 1, soliton interaction between neighboring pulses can be minimized by satisfying the condition $S \sim 1.6$ in a lossless case [1], where S is defined as $S = |\beta_1 z_1 - \beta_2 z_2|/t_s$ and t_s is FWHM of DMS when it is transform-limited. Given the amplifier spacing z_a and the value of both anomalous and normal dispersion, this condition is satisfied by a proper choice of the number of DM period n within one amplification period ($n = z_a/(z_1 + z_2)$). For instance, when $z_a = 40$ km, $d_1 = 2.5$ ps/nm/km and $d_2 = -2.49$ ps/nm/km, n becomes 20. Fig. 2 shows dependence of collision distance on n (and corresponding S). The interaction forces become stronger for $n > 20$ ($n < 20$), since the stationary pulse approach to sech solitons [3,4] (the pulse width oscillates too much.).

Based on this observation, it is expected that even when fiber GVD varies owing to the fabrication of dispersion flattening, soliton interaction may be minimized by arranging dispersion profile such that it satisfies the condition $S = 1.6$. As one approach, given a pair of fibers having anomalous and normal dispersion d_1 and d_2 respectively, the length of each section z_1 and z_2 may be determined so that S becomes 1.6 and the average dispersion is constant along the line. Fig. 3 shows an example of dispersion profile based on this method, where we assume fibers having Gaussian distribution in GVD with the average of 0 and the variance of 3.0, and total average dispersion is kept 0.005 ps/nm/km. Propagation of DDMS in this line is shown in Fig. 4. Transmission characteristic may further be improved by connecting fibers in descending

value of GVD [5]. Fig. 5 shows the arrangement of dispersion profile based on this using the same pieces of fibers as in Fig. 3. In Fig. 6, propagation of a DMS in this profile is plotted, where we note that solitons suffer less from fluctuation of amplitude in this arrangement.

To test bit-error rate, we performed numerical simulations of transmission of 32 bit sequence of 160 Gb/s on the dispersion map shown in Fig. 5. We assumed fibers having loss of 0.2 dB/km, a Kerr nonlinearity of 2.3 $W^{-1}km^{-1}$, PMD of 0.1 $ps/\sqrt{km}$, and residual dispersion slope of 0.005 $ps/nm^2/km$. Amplifiers are assumed to have noise figure of 5.0 dB. To reduce soliton interaction, in-line optical filters with a bandwidth of 1,800 GHz are inserted at every amplifier location (45 km interval). Fig. 7 shows the received eye diagram at 2,500 km. This result demonstrates successful transmission on a terrestrial scale.

In summary, we have investigated feasibility of ultra-fast single-channel soliton transmission in a densely dispersion-managed fiber. Thanks to a large tolerance of DMS to random distribution of GVD, 160 Gb/s single-channel soliton transmission is possible on a terrestrial scale by reducing dispersion slope down to minimum and by proper arrangement of dispersion profile.

References

[1] T. Yu, E.A. Golovchenko, A.N. Pilipetskii, and C.R. Menyuk, *Opt. Lett.* **22,** 793 (1997).
[2] A. Liang, H. Toda, and A. Hasegawa, "High speed soliton transmission in dense periodical fibers," submitted to *Opt. Lett.*
[3] A. Hasegawa and Y. Kodama, *Opt. Lett.* **16,** 1385 (1991).
[4] T. Okamawari, Y. Ueda, A. Maruta, Y. Kodama, and A. Hasegawa, *Electron. Lett.* **33,** 1063 (1997).
[5] R. Ohhira, A. Hasegawa, and Y. Kodama, *Opt. Lett.* **20,** 701 (1995).

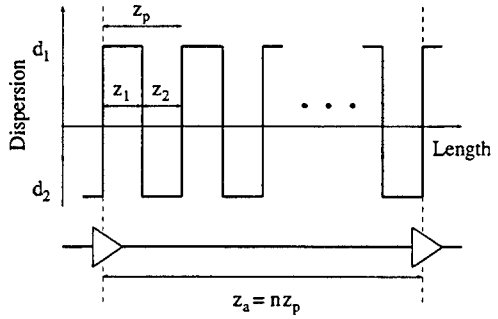


Fig. 1. Densely dispersion-managed system.

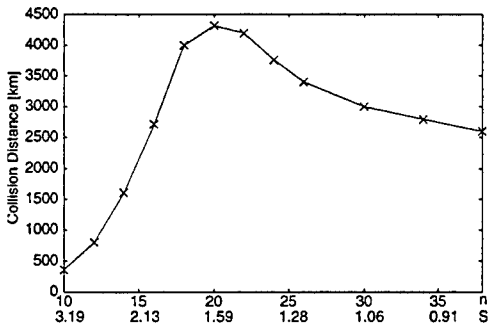


Fig. 2. Dependence of collision distance on n (and corresponding S parameter). A pair of DMS, whose pulse width is 2 ps, are initially separated by 6.25 ps.

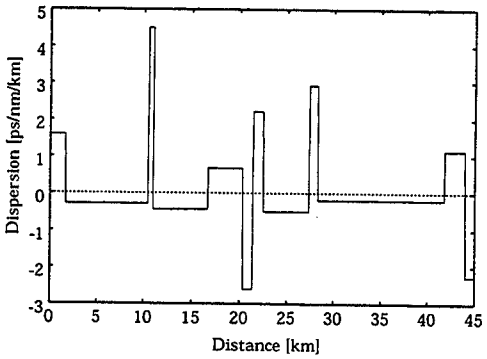


Fig. 3. A model of dispersion profile.

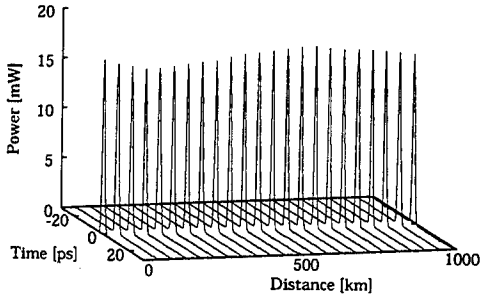


Fig. 4. Propagation of DDMS in the profile shown in Fig. 3.

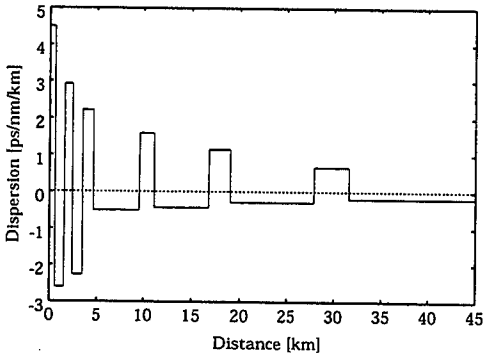


Fig. 5. Dispersion profile revised from Fig. 3.

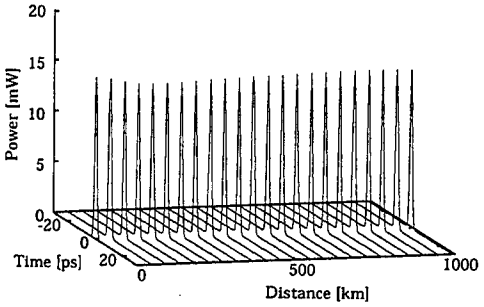


Fig. 6. Propagation of DDMS in the profile shown in Fig. 5.

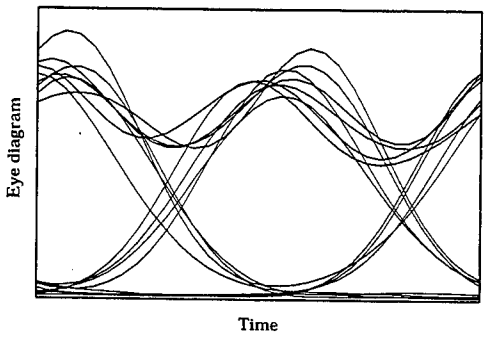


Fig. 7. Received eye diagram at 2,500 km obtained from numerical simulation.

Dispersion maps with optimized amplifier placement for wavelength-division-multiplexing

Brian S. Marks and William L. Kath

Department of Engineering Sciences and Applied Mathematics, 2145 Sheridan Road, Northwestern University, Evanston, Illinois 60208, USA, Tel: 1-847-491-3345, FAX: 1-847-491-2178, {bsm,kath}@nwu.edu

Tian-Shiang Yang

Department of Mechanical Engineering, National Cheng Kung University, Tainan, Taiwan 701, tsyang@mail.ncku.edu.tw

Sergei K. Turitsyn

Photonics Research Group, Department of Electronic Engineering and Applied Physics, Aston University, Aston Triangle, Birmingham B4 7ET, UK, s.k.turitsyn@aston.ac.uk

1. Introduction

Dispersion management has proven to be an effective way of reducing detrimental effects, such as four-wave mixing and Gordon-Haus timing jitter, in long-haul RZ transmission. Recently, much work has been done on optimization of simple two-step dispersion maps for use with single-channel and wavelength-division-multiplexed (WDM) transmission[1–3]. It has been discovered that by properly locating the amplifier in the map, one can substantially improve system performance[1,2]. Optimization of WDM systems involves many practical constraints and is a rather complicated issue that requires long-term, time-consuming numerical simulations. As a result, analytical results can be extremely useful.

In this paper, we extend previous work in which a multiple-scale averaging method was used to obtain so-called 'magic' dispersion maps that simultaneously reduce dispersive radiation in multiple channels by determining an optimal launch point for unchirped pulses that is independent of carrier frequency[5,4]. This means that the detrimental effect of the dispersion slope in WDM systems can be reduced, not with expensive per-channel compensation, but rather by using proper system design. Numerical simulations have confirmed that minimized energy shedding from the input signal into radiation can be achieved. In Ref. 5, the only case considered was the one in which an amplifier is deployed at the same location as a change in dispersion in a two-step map. In the present paper, we extend the results of Ref. 5 and consider the location of the amplifier to be at an arbitrary point in the dispersion map. This new degree of freedom can be advantageously used for additional system performance optimization. The result of this extra parameter is an interesting class of dispersion maps in which one fiber segment can be reduced to infinitesimal length (i.e., a point device). This compensation scheme can be realized in practice by the use of a fiber Bragg grating which effectively imparts a large aggregate dispersion.

Here we present the main theoretical results and numerical simulations that demonstrate the effectiveness of these 'magic' maps for reducing transient behavior in the pulse evolution. In our numerical simulations, systems with different group velocity dispersion parameters do appear to have nearly the same chirp-free locations in the case of these magic configurations, as the theory predicts.

2. Finding Magic Maps

Optical pulse propagation in a system with dispersion management and amplification is described by the nonlinear Schrödinger equation (NLS) with distance-dependent dispersion and nonlinear coefficients,

$$iu_z + d(z)u_{tt} + c(z)|u|^2u = 0 \tag{1}$$

where

$$d(z) = \frac{L\lambda_0^2}{4\pi c\tau_0^2} D(z) \tag{2}$$

$$c(z) = \left(\frac{L\lambda_0^2|\langle D\rangle|}{2\pi c\tau_0^2}\right)\left(\frac{G\ln G}{G-1}\right)e^{-\alpha Lz}. \tag{3}$$

In Eq. (3), $c(z)$ is specified for $0 < z < 1$, and is taken to be periodic such that $c(z+1) = c(z)$. The piecewise constant function $D(z)$ specifies the dispersions and lengths of the fiber segments in the dispersion map (see Fig. 1), and the path-average dispersion is given by $|\langle D \rangle|$. The length of the map is given by L, and we assume one amplifier per map period. The power $|u|^2$ has been scaled by the characteristic value $P_0 = \lambda_0^2 |\langle D \rangle| / 2\pi c \tau_0^2 \gamma$. Other parameters are λ_0, the operating wavelength; c, the speed of light; α, the dB/km fiber loss; γ, the fiber's nonlinear coefficient; and τ_0, a characteristic time. The amplifier gain $G = \exp(\alpha L)$. Note that we have scaled z by the length of a map so that $z = 0, 1, 2, \ldots$ correspond to the locations of the amplifiers.

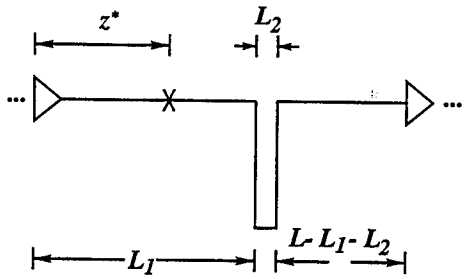


Fig. 1. One period of a dispersion map between two amplifiers. The piece-wise constant dispersion values are given by D_1—D_2—D_1. The 'X' denotes the launch point, and the '▷' denotes an amplifier.

We consider (as shown in Fig. 1) a two-step dispersion map offset relative to the amplifiers consisting of dispersions D_1—D_2—D_1. Thus,

$$D(z) = \begin{cases} D_1, & 0 < zL < L_1 \\ D_2, & L_1 < zL < L_1 + L_2 \\ D_1, & L_1 + L_2 < zL < L \end{cases} \tag{4}$$

We assume D_1 and the path-average dispersion $\langle D \rangle$ are given. The second dispersion, D_2, can then be determined in terms of these quantities.

Formulas similar to those given in Ref. 5 allow calculation of the chirp-free points as a function of the various parameters. 'Magic' maps are found by requiring the chirp-free points z^* to be independent of group velocity dispersion. The configuration of the fiber segments can then be described by the following set of equations.

For $0 < z^* < L_1/L$, we have

$$\frac{L_1}{L} = \frac{1}{\alpha L} \ln \left\{ \left(\frac{\alpha L}{1 - \alpha L z^*} \right) \left(\frac{G}{G-1} \right) \times \left(\frac{1 - e^{-\alpha L_2}}{\alpha L_2} \right) \right\}. \tag{5}$$

For $L_1/L < z^* < (L_1 + L_2)/L$, we have, implicitly,

$$\left[\left(\frac{1 - \alpha L z^*}{\alpha L} \right) \frac{L_2}{L} + z^* \right] e^{\alpha L_1} - \frac{L_1}{L} e^{\alpha L_1} = \left[\frac{G}{(G-1) \ln G} \right] \left(1 - e^{-\alpha L_2} \right). \tag{6}$$

Finally, for the case $(L_1 + L_2)/L < z^* < 1$, we have

$$\frac{L_1}{L} = \frac{1}{\alpha L} \ln \left\{ \left(\frac{\alpha L}{1 + \alpha L - \alpha L z^*} \right) \left(\frac{G}{G-1} \right) \times \left(\frac{1 - e^{-\alpha L_2}}{\alpha L_2} \right) \right\}. \tag{7}$$

Combining the results from these three equations describes all possible configurations of two-step magic maps for given values of α and L. Note that it makes sense to only consider cases in which $L_1 \in (0, L)$ and $L_2 \in (0, L - L_1)$. We plot these curves for α=0.2 dB/km and L=60 km in Fig. 2.

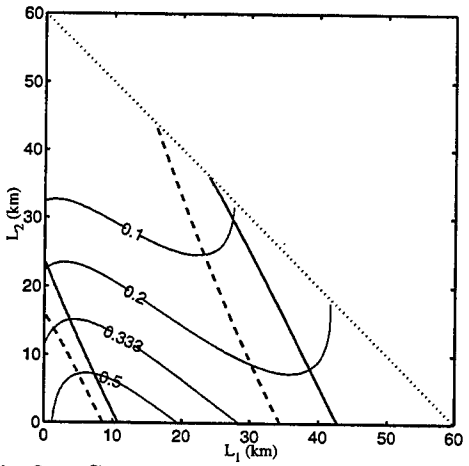


Fig. 2. Curves indicating configuration of magic maps. These are generated assuming a loss of α=0.2 dB/km and L=60 km. The solid line denotes the magic maps corresponding to the launch point z^*=42.7879 km, and the dashed line corresponds to the launch point z^*=8.5829 km.

There are several points worth noting in Fig. 2. Firstly, the curves intersecting the line $L_2 = L - L_1$ join continuously with those intersecting the L_2-axis (the identities of L_1 and L_2 are interchanged between the two cases, however).

Secondly, there are two configurations for each value of the launch point z^* for which L_2 vanishes. For one of these configurations, the launch point appears within the long fiber segment. This is useful in that, in an existing system that does not employ dispersion management (such as one using standard single-mode fiber), a dispersion-compensating fiber grating can be placed as specified in the above configuration. An RZ signal then launched at the chirp-free point would reduce energy shedding into radiation while making use of WDM, because the launch point is the same for all channels. The lighter contours shown in Fig. 2 correspond to the power enhancement provided by the map as determined in the multiple-scale averaging.[5,4] These are given for initially 12 ps FWHM sech pulses and $|\langle D\rangle|$=0.16 ps/nm·km and D_1=1.6 ps/nm·km.

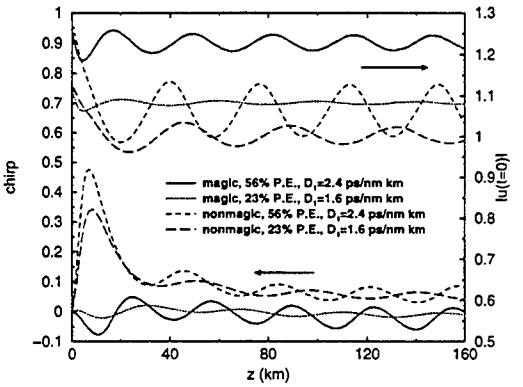


Fig. 3. Plots of the stroboscopic chirp and peak amplitude for numerical simulations of pulse evolution in a magic map using two different values of the GVD parameter.

In Fig. 3, we show the result of a full numerical simulation using such a dispersion map for two channels near the central operating wavelength λ_0=1550 nm. The figure shows the evolution of the chirp and peak amplitude of a single pulse once per map period (stroboscopically). The solid and dotted curves correspond to a 'magic' configuration in which L_2=10 m with L=60 km. For comparison, the short-dashed and long-dashed curves correspond to a (non-'magic') configuration in which the compensator is placed directly before the amplifier and the launch point is the midpoint between the amplifiers. The solid and short-dashed curves are for D_1=2.4 ps/nm·km while the dotted and long-dashed curves are for D_1=1.6 ps/nm·km. The path-average dispersion is $|\langle D\rangle|$=0.16 ps/nm·km. In this simulation, we assumed initially 12 ps FHWM sech pulses. The total propagation distance in Fig. 3 is 160×60 km = 9600 km. Note that oscillations in the amplitude are significantly reduced in the case of the 'magic' configuration simultaneously for both channels. This demonstrates the advantage for WDM transmission.

In conclusion, we have identified a class of advantageous two-step dispersion maps (with arbitrary location of the amplifier within the map) that simultaneously minimizes dispersive radiation in many channels for WDM. The specific choice of amplifier placement can lead to two-step maps in which the dispersion compensator acts as a point device. This dispersion map configuration is appropriate for the use of in-line fiber Bragg gratings in massive WDM.

References

1. S. B. Alleston, *et al.*, Post Deadline presentation, PD3-1, OFC'99, San Diego, USA.
2. T. Yu, *et al.*, IEEE Photon. Tech. Lett. **11** (1), 75-77.
3. N. S. Bergano, *et al.*, Post Deadline presentation, PD12-1, OFC'98, San Jose, USA.
4. T.-S. Yang, W. L. Kath, and S. K. Turitsyn, "The multiple-scale averaging and dynamics of dispersion-managed optical solitons," J. Eng. Math., to appear.
5. T.-S. Yang, W. L. Kath, and S. K. Turitsyn, Opt. Lett. **23** (8) 597.

Timing jitter of a strongly dispersion managed soliton in a wavelength-division-multiplexed system

Hiroto Sugahara and Akihiro Maruta

Graduate School of Engineering, Osaka University, 2-1 Yamada-oka, Suita, Osaka 565-0871, Japan.
Phone: +81-6-6879-7728, Fax: +81-6-6879-7688, E-Mail: sugawara@comf5.comm.eng.osaka-u.ac.jp

Wavelength-division-multiplexed (WDM) optical soliton transmission system is one of the most promising candidates for a transoceanic and high bit rate communication in the next generation. The most serious problem in such a system is the collision induced frequency shift[1] which results in undesirable timing jitter of the signal pulse.

Recently, several analyses of timing jitter for a strongly dispersion managed soliton in a WDM system were performed in Refs.[2-5]. In such a system, the collision induced residual frequency shift, that is, the shift of the frequency separations of the colliding pulses measured at before and after a complete collision process, can be reduced as compared with traditional soliton in a constant dispersion line[2-4]. However, due to a long overlapping distance of colliding pulses, a collision induced position shift which is directly arising from the collision and a residual frequency shift induced by an incomplete collision cause dominant timing shift for a narrow channel spacing in such a system[5]. On the other hand, dispersion management is also effective for reducing Gordon-Haus (GH) jitter[6-8] that induced by interaction between signal and amplifier noise. In this paper, we analyze the collision induced timing shift in a two-channel WDM system with a practical dispersion map and propose an optimal path averaged dispersion (PAD) of the map with respect to the minimum timing jitter induced both by collision and amplifier noise. We also comment a timing jitter for a multi-channel WDM system and discuss the maximum number of channels.

The variational analysis[9] with Gaussian ansatz[10] for the pulse is used below. In a dispersion managed line, since a group velocity of a pulse depends on fiber dispersion and pulse's carrier frequency, a pulse zigzags in a frame moving with averaged group velocity and many collisions occur throughout a collision process. Therefore in such a system having a long overlapping distance, a collision induced position shift and residual frequency shift by an incomplete collision may give dominant contribution for timing shift especially for small PAD and/or narrow channel spacing. On the other hand, GH jitter becomes large as increasing PAD[8]. This predicts that a system may have an optimal PAD which gives the minimum timing jitter.

As a simple but practical example, we consider a two-step dispersion managed line composed by two equal length fibers, that is, standard telecommunication fiber (STF) with dispersion $17 + D_{ave}$[ps/nm/km] and reversed dispersion fiber (RDF) with $-17+D_{ave}$[ps/nm/km] are concatenated with this order[11]. Here D_{ave} represents the PAD of the line. We take the period of dispersion management $z_d = 40$[km], which equals to the period of lumped amplifier compensating 0.2[dB/km] fiber loss. Since the timing shift induced by the frequency shift depends on the pulse energy, we fix its initial value to 0.1[pJ].

We first analyze a single channel case and obtain particular parameters of initial pulse, for which the solution is periodic with the period z_d. Using the stable periodic solution, we then analyze a WDM case and calculate the timing shift. Figure 1 shows the timing shift af-

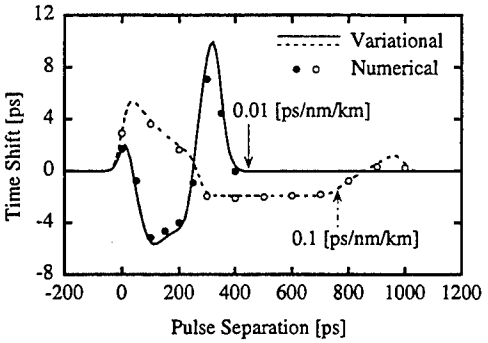


Figure 1: Timing shift after 9[Mm] propagation.

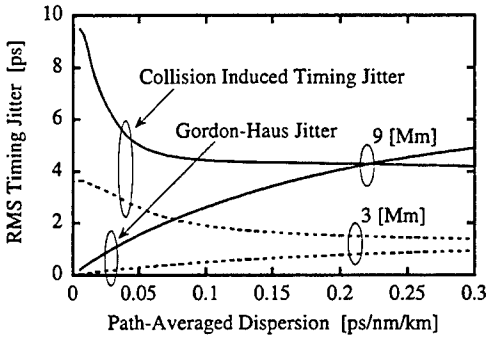


Figure 2: RMS timing jitter versus PAD after 3 and 9[Mm] propagation.

ter 9[Mm] propagation versus initial separation (t_{sep}[ps]) of pulses in different channels with channel spacing $\Delta\lambda = 0.8$[nm]. The solid and dashed line represent the case with $D_{ave} = 0.01$ and 0.1[ps/nm/km], respectively. Circles are obtained by direct numerical simulations of nonlinear Schrödinger equation (NLSE). For small initial pulse separation, the colliding pulse are initially close to each other and there remains a large frequency shift after collision process is completed.

Using this numerically obtained timing shift as a function of initial pulse separation $\delta t(t_{sep})$, we can obtain a total timing shift between neighboring pulses (the interval between them is k times bit slot t_s) Δt_k for a certain bit stream $b_n = 0$ or 1 (n :integer) with[12]

$$\Delta t_k = \sum_{n=-\infty}^{\infty} (b_{n+k} - b_n)\delta t(t_{sep,0} + nt_s), \quad (1)$$

where $t_{sep,0}$ is the initial separation of interchannel pulses which can take $0 \leq t_{sep,0} < t_s$. Using sufficient patterns of bit stream, we obtain the root-mean-square (RMS) timing shifts with

$$\langle(\Delta t)^2\rangle = 2^{-k}\sum_{k=1}^{\infty}\langle(\Delta t_k)^2\rangle. \quad (2)$$

Figure 2 shows the root-mean-square timing jitter versus PAD for 20[Gbit/s/channel] after 3 and 9[Mm] propagation. Here we take $t_{sep,0} = 25$[ps] for $t_s = 50$[ps], i.e. pulses in one channel are allocated at the center of pulses in another channel. We have also calculated other cases of $t_{sep,0}$ and confirmed that the RMS timing jitter has almost no dependency on $t_{sep,0}$. As predicted previously, the collision induced timing jitter becomes large as decreasing the PAD.

Since the collision induced timing jitter and GH jitter are independent process and their probability density functions are both Gaussian, we can evaluate the total variance of jitter by summing up both variances. Since average of those jitters are zero, the variances equal to RMS timing jitter which have been shown in Fig.2. Here we estimate the bit-error-rate (BER) by[13]

$$\mathrm{BER} = \mathrm{erfc}\left[\frac{t_{FWHM}}{\sqrt{2\sigma^2}}\sqrt{\frac{\ln(A/A_{th})^2}{\ln 2}}\right], \quad (3)$$

where $(A_{th}/A)^2$ represents the ratio between threshold power and peak power and σ^2 is the total variance. Figure 3 shows the BER and the FWHM width at a receiver versus the PAD after 9[Mm] propagation. While BER degrades for an extremely small or large PAD, the safe region of the PAD which gives error free 9[Mm] propagation is obtained for $0.03 < D_{ave} < 0.13$[ps/nm/km]. We also find that the improvement of BER for $D_{ave} > 0.2$[ps/nm/km]. It is because the FWHM width is large in such a region. However it cause large pulse-pulse interaction and we may not use this region.

We here comment on a timing jitter for a multi-channel WDM system. Assuming that only

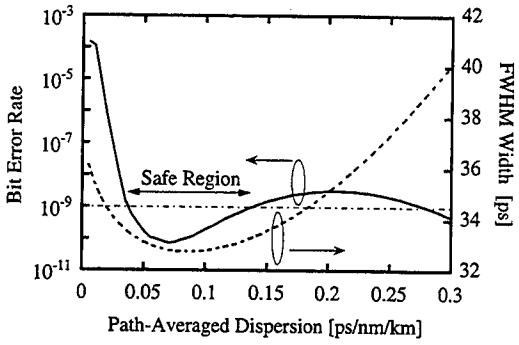


Figure 3: BER and FWHM width after 9[Mm] propagation.

cross-phase modulation contributes to the timing shift, the shift in one channel is the sum of the shifts independently caused by the other channels. Therefore the relative timing shift for channel j can be expressed as,

$$\Delta t_k^j = \sum_{i=1, i\neq j}^{N} \Delta t_k^{ji}, \qquad (4)$$

where N is the total number of channels and Δt_k^{ji} represents the timing shift of channel j caused by channel i, which has been given in Eq.(1). We here also assume only a binary (i.e. two channel) collision. Since $b_{n+k} - b_n$ in Eq.(1) is independent in each channel, all the cross-products in right-hand-side of Eq.(4) has no correlation. Therefore, the total variance of collision induced timing jitter equals to the sum of the variances resulting from the other channels. This has been obtained also for constant dispersion and weak dispersion managed case[12].

Using Eqs.(4) and (2), we obtain the total timing jitter for the three-channel WDM system with adjacent channel spacing $\Delta\lambda = 0.8$[nm] and $D_{ave} = 0.07$[ps/nm/km]. For the central (outside) channel, $\langle(\Delta t)^2\rangle = 41.34$[ps^2] (22.00[ps^2]), that is almost the same with the sum of the previously obtained variances for two-channel case ; i.e., $\langle(\Delta t)^2\rangle = 20.70$[ps^2] for $\Delta\lambda = 0.8$[nm] and $\langle(\Delta t)^2\rangle = 1.30$[ps^2] for $\Delta\lambda = 1.6$[nm]. Since BER $> 10^{-9}$ for the central channel, we can not achieve error-free-transmission for three-channel WDM. The timing jitter can be reduced for smaller pulse energy. For 0.05[pJ] which is sufficient to keep SN ratio, the total timing jitter for a central channel after 9[Mm] transmission is less than 5[ps] by using an optimal PAD (shown as the safe region in Fig.3) and the BER is much smaller than 10^{-9}.

In conclusion, we have analyzed the collision induced timing shift in a two-channel WDM system with a practical dispersion map and proposed an optimal PAD of the map. We have also discussed a timing jitter for a multi-channel WDM system. Ultra-long massive WDM soliton transmission may be realized by using an optimally designed dispersion management.

References

[1] L. F. Mollenauer, S. G. Evangelides, and J. P. Gordon, J. Lightwave Technol., **9**, 362 (1991).

[2] T. Hirooka and A. Hasegawa, Opt. Lett., **23**, 768 (1998).

[3] H. Sugahara, T. Inoue, A. Maruta, and Y. Kodama, Electron. Lett., **34**, 902 (1998).

[4] H. Sugahara, A. Maruta, and Y. Kodama, Opt. Lett., **24**, 145 (1999).

[5] D. J. Kaup, B. A. Malomed, and J. Yang, Opt. Lett., **23**, 1600 (1998).

[6] J. P. Gordon and H. A.Haus, Opt. Lett., **11**, 665 (1986).

[7] M. Suzuki, I. Morita, N. Edagawa, S. Yamamoto, H. Taga, and S. Akiba, Electron. Lett., **31**, 2027 (1995).

[8] T. Okamawari, A. Maruta, and Y. Kodama, Opt. Commun., **149**, 261 (1998).

[9] D. Anderson, Phys.Rev.A, **27**, 3135 (1983).

[10] N. J. Smith, F. M. Knox, N. J. Doran, K. J. Blow, and I. Bennion, Electron. Lett., **32**, 54 (1996).

[11] M. Murakami, T. Matsuda, and T. Imai, Electron. Lett., **35**, 488 (1999).

[12] M. J. Ablowitz, G. Biondini, S. Chakravarty, and R. L. Horne, Opt. Commun., **150**, 305 (1998).

[13] L. F. Mollenauer, P. V. Mamyshev, and M. J. Neubelt, Opt. Lett., **19**, 704 (1994).

Efficient reduction of interactions in dispersion-managed links through in-line filtering and synchronous intensity modulation

Erwan Pincemin, Frederic Neddam and Olivier Leclerc

Alcatel Corporate Research Center, Route de Nozay, 91460 Marcoussis, France
Tel: (33) 1 69 63 10 08
Fax: (33) 1 69 63 18 65
E-mail: Erwan.Pincemin@alcatel.fr

Introduction

Dispersion-managed (DM) solitons have recently demonstrated their potential in high-capacity terrestrial and transoceanic systems at 10-20Gbit/s line-rate /1-2/. An expected development to further increase system capacity is the introduction of 40Gbit/s granularity. However, analytical descriptions of DM soliton propagation based upon Lagrangian formalism have shown that, at that line-rate, interactions between adjacent pulses appear to be a major limitation /3-4/, hence forbidding a potential use of the 40Gbit/s granularity in long-haul transmission systems.

In this paper, after incorporating both in-line filtering and synchronous intensity modulation (IM) in the aforementioned analytical model /3-4/, we investigate the impact of combined use of in-line filtering and IM on interactions in a transoceanic 40Gbit/s dispersion-managed system. Numerical simulations have also been computed as a matter of comparison with the analytical model.

Modeling interactions with in-line filtering and IM.

Propagation of a pulse $u(z,t)=\sqrt{a(z)}q(z,t)$ in a line with dispersion $D(z)$ and energy evolution $a(z)$ with distance z is described by the non-linear Schrödinger equation (NLSE) :

$$i\frac{\partial q}{\partial z}+\frac{1}{2}D(z)\frac{\partial^2 q}{\partial t^2}+a(z)q^2q^*=0$$

In order to reduce the number of parameters and for sake of clarity, adjacent solitons are supposed to have the same energy, temporal pulse width and chirp during propagation. By a proper choice of time and frequency origin, the normalized field of the pulses is modeled by :

$$q(z,t)=\sqrt{B}\,\exp\left[-(1+ib)\frac{(t\mp\alpha)^2}{2W^2}+i\phi\mp i\omega t\right]$$

where the subscripts + and – are related to the position and frequency shift of the first and second pulse, respectively. The temporal pulse width W and chirp parameter b are related to the parameters γ and C by :

$$W^2=1+\gamma^2C^2 \qquad\qquad b=-\gamma C$$

where γ is equal to twice the square of the quadratic bandwidth and C corresponds to a non-linear extension of the cumulative dispersion. The pulse energy evolution with propagation distance z is expressed by :

$$a(z)E=a(z)\int_{-\infty}^{+\infty}qq^*\,dt=a(z)BW\sqrt{\pi}$$

In the model, lumped filtering is characterized by a Gaussian transfer function $T_f(\omega)=\exp(-\beta_2\omega^2)$ /5/. Parameters β_2 and k_f (filtering strength) are related by:

$$k_f=\frac{2\beta_2\gamma_o}{Z_f}\ \ with\ \ \beta_2=\frac{2ln(2)}{4\pi^2\Delta\nu_f^2}$$

where $\Delta\nu_f$ is the filter bandwidth, Z_f the filtering period and γ_o the value of γ at the end of the dispersion map.

Lumped IM is defined by its temporal response $T_m(t)=1-a_m\cos^2(\omega_m t)$ where IM depth a_m, modulation frequency ω_m and regeneration periodicity Z_m are related to intensity modulation strength k_m through the expression:

$$k_m = 2\frac{\omega_m^2}{Z_m} a_m \gamma_o$$

Along the propagation, the pulse parameters follow:

$$\alpha_z' = -D\omega + k_f \omega C - \frac{k_m}{\gamma_0}\alpha\left(\frac{1}{\gamma_0} + \gamma C^2\right)$$

$$\omega_z' = \frac{aKE}{2\sqrt{\pi}}\frac{\alpha}{W^3}\exp\left(-\frac{\alpha^2}{W^2}\right) - k_f\omega - k_m\alpha C$$

$$\gamma_z' = \frac{2a\gamma CE}{\sqrt{2\pi W^3}}\left[1+\frac{K}{2\sqrt{2}}\left(1-\frac{2\alpha^2}{W^2}\right)\exp\left(-\frac{\alpha^2}{W^2}\right)\right] - k_f\gamma + k_m\left(\frac{1}{\gamma_0}+\gamma C^2\right)$$

$$C_z' = D + \left(C^2 - \frac{1}{\gamma^2}\right)\frac{aE}{\sqrt{2\pi W^3}}\left[1+\frac{K}{2\sqrt{2}}\left(1-\frac{2\alpha^2}{W^2}\right)\exp\left(-\frac{\alpha^2}{W^2}\right)\right] - 2\frac{k_m}{\gamma_0^2}C$$

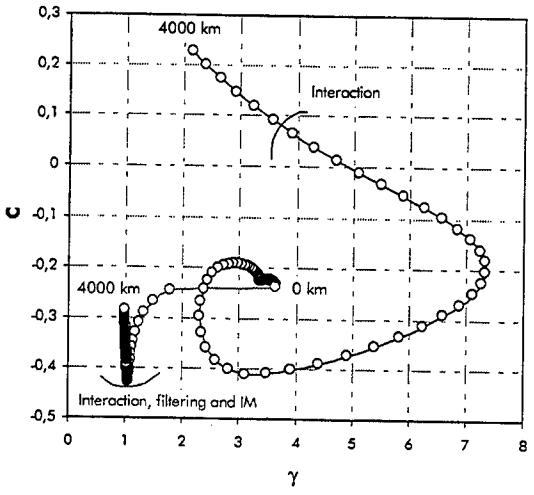
where γ_o and C_o are values of γ and C, respectively, at the end of the dispersion map. K is equal to 2 for pulses of same polarization state.

Impact of combined use of in-line filtering and IM on interactions

We consider a dispersion-managed link made of an arrangement of 20.5km of anomalous dispersion fiber (D=+2ps/nm/km) and 19.5km of normal dispersion fiber (D=-2ps/nm/km), yielding a dispersion compensation ratio of 95%. The fiber span is followed by a filter, an intensity modulator and an amplifier of gain G compensating for the losses (fiber, filter and modulator). We now investigate the propagation of two co-polarized Gaussian pulses of 0.08pJ energy, temporally spaced by 25ps (bit duration at 40Gbit/s) in the aforementioned system.

Figure 1 shows the (γ,C) parameters evolution with distance with and without in-line filtering and IM (i.e. k_m=k_f=0, k_m=k_f=0.73, respectively) in a 4000km transmission line (100 unit cells). Launching conditions are given by the fixed point /3/ found in absence of interactions, filtering and IM and are defined by γ=3.654 and C=-0.238 resulting in initial temporal pulsewidth and prechirp of 11.54ps and–18.68ps/nm, respectively.

Fig 1: Phase diagram of the propagation in the plan (γ,C) for 100 unit cells

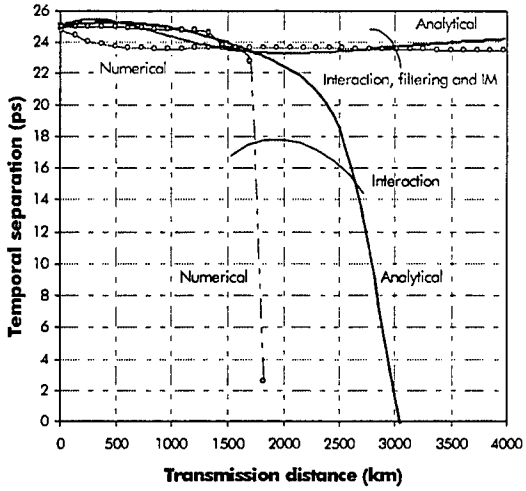


It is seen from Fig.1 that without in-line filtering and IM, pulse propagation is rapidly affected by interaction with adjacent pulse, resulting in a destabilization of the propagation. On the contrary, when filtering and IM are incorporated, pulses reach a stable propagation regime and are no longer affected by interaction. Note that the fixed point reached with filtering and IM is slightly different from that found without in-line control techniques.

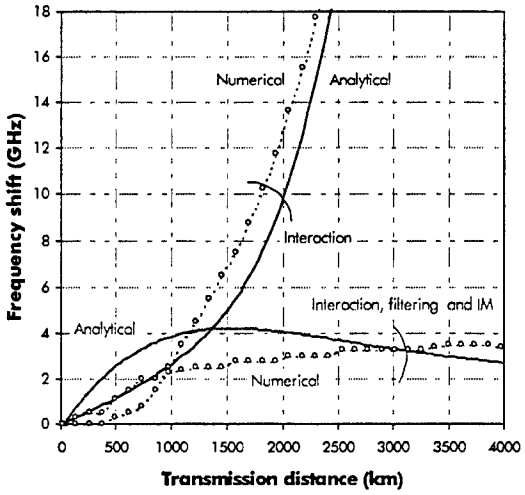
Figure 2a shows the evolution of the temporal separation between the two pulses as a function of distance with and without filtering and IM. This evolution is analytically predicted using the previously described model and numerically assessed by simulations based on the resolution of the NLSE with the split-step Fourier method.

Fig 2: (a) Evolution of temporal separation between the two pulses as a function of transmission distance

(b) Evolution of frequency shift of pulses as a function of transmission distance



(a)



(b)

In absence of filters and IM, the temporal separation of the pulses is found to decrease with propagation distance, as an illustration of the effect of interactions. Similar evolutions are predicted using either analytical or numerical model except for the collision distance (3000 and 1700km, respectively). The difference is attributed to the incomplete modeling of interaction for very closely spaced pulses in the analytical model. When in-line filtering and IM are incorporated in the link, the temporal separation decreases with distance but its value stabilizes near 24ps after 1500km, demonstrating the efficient control provided by the association of in-line filtering and IM on interactions. Note the good agreement between analytical and numerical predictions, validating the analytical model.

Figure 2b shows the evolution of the pulse frequency shift as a function of distance with and without filtering and IM as predicted analytically or numerically. It is seen from figure 2b that without in-line control, pulse frequency shift is an ever-increasing function of distance. When filtering and IM are added, the frequency shift still increases with distance but reaches a 3GHz asymptotic value after 3000km, as predicted both analytically and numerically.

Conclusion

In this paper, we have incorporated both filtering and synchronous modulation in the analytical model of DM soliton propagation and validated it through numerical simulations. We also demonstrate both analytically and numerically the efficiency of combined use of in-line filtering and synchronous intensity modulation in limiting the detrimental effects of pulse-to-pulse interaction in 40Gbit/s dispersion-managed long-haul systems. These results are of very high interest for the design of very high capacity transoceanic systems.

References

/1/ D.LeGuen, S.DelBurgo, M.L.Moulinard, D.Grot, M.Henry, F.Favre, and T.Georges, "Narrow-band 1.02Tbit/s (51x20Gbit/s) soliton DWDM transmission over 1000km of standard fiber with 100km amplifier spans", OFC'99, PD4.

/2/ O.Gautheron, J.B.Leroy, P.Marnier, "320Gbit/s (32x10Gbit/s) transmission over 6150km with a 50GHz wavelength spacing", OFC'99, WJ3.

/3/ T.Georges, "Soliton interaction in dispersion-managed links", JOSA B, 1998, **15**, pp 1553-1560.

/4/ M.Matsumoto, "Analysis of interaction between stretched pulses propagating in dispersion-managed fibers", IEEE Photon. Technol. Lett., **10**, pp 373-375.

/5/ F.Merlaud and T.Georges., "Influence of filtering on jitter and amplitude fluctuations for dispersion-managed solitons", ECOC'98, pp 497-498.

Towards Nx40Gbit/s transoceanic regenerated systems

O.Leclerc, P.Brindel, D.Rouvillain, E.Pincemin,
B.Dany, E.Desurvire, C.Duchet*, E.Boucherez* and S.Bouchoule*
Alcatel Corporate Research Center (*Opto+), Route de Nozay 91460 Marcoussis, France
Olivier.Leclerc@alcatel.fr

The first response to the demand for capacity in transoceanic transmission systems is the technique of wavelength-division-multiplexing (WDM), which allows a substantial increase in system capacity without constraints in the terminal's electronics bandwidth. Considering next the transmission format in transoceanic applications (6-12Mm distances), one of the main advantage of RZ-soliton over linear-NRZ is the possibility to use substantially higher line rates such as 10, 20 or 40 Gbit/s with possibly longer amplifier spacing (60-200 km). However, two main impairments of long-haul soliton transmission, i.e. the Gordon-Haus and the WDM-collision timing jitter, ultimately require in-line control in the frequency and/or time domain. Among these is "3R" optical regeneration based on synchronous modulation (SM). The principle makes possible unlimited-distance propagation [1]. More specifically, intensity modulation (IM) combined with narrowband filtering suppresses timing jitter and blocks noise accumulation [1], while pure phase modulation (PM) reduces jitter without suppressing noise [2]. Actually, efficient jitter/noise control was shown to require both IM and PM [3].

Because "3R" regeneration potentially addresses the terabit/s submarine system market, the current challenge is to further increase the capacity. A key requirement is that it could operate at 40Gbit/s, both for WDM granularity and SONET/SDH layer considerations; 40Gbit/s granularity minimizes the number of WDM channels to transmit (hence, of parallel in-line modulators), which reduces both system complexity and cost. In order to further reduce the number of regenerators in WDM systems, simultaneous regeneration of WDM channels in a single modulator is also possible [4]. This last solution points towards a potential superiority of 'optical' over 'electronic' regeneration. It has been studied through various numerical simulations [4], and experimentally implemented at 20Gbit/s [5-6].

Up to now, only single-channel 40Gbit/s experiments have been demonstrated [7-9] but Nx40Gbit/s WDM upgrade of such systems could be rapidly requested. For that, it is required to operate optical regenerators with adequate specifications. It should first operate at 40GHz and provide both IM and PM with independent control of their depths. Practical device implementation in WDM systems will require long-term stability as well as polarization insensitivity, hence excluding the use of $LiNbO_3$ materials [7]. Simultaneous WDM implementation (multiple channels passing through a single regenerator), should require immunity to crosstalk and wavelength insensitivity, excluding electro-absorption modulators [8].

Recently, we have reported a newly developed 40GHz InP Mach-Zehnder (MZ) modulator meeting these requirements. It combines both polarization and wavelength-independence and provides adjustable IM/PM response through a dual-electrode, push-pull configuration [9]. Figure 1 shows an ESM picture of the modulator (top left) and the schematic of a dual-electrode Mach-Zehnder modulator (bottom left) along with two graphs showing polarization and wavelength-insensitive response of the modulator.

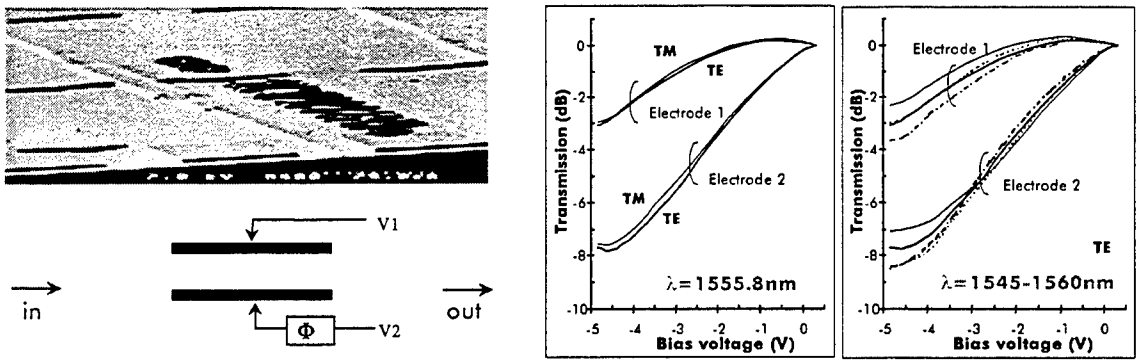


Figure 1 : ESM picture (top left) and schematic of dual-electrode Mach-Zehnder modulator (bottom left) along with transmission vs. bias voltage graphs for TE/TM polarization modes of input light at 1555.8nm (middle) and for 1545-1560nm wavelengths with TE polarization mode (right).

This component was also found immune from WDM crosstalk [9], which makes it amenable to simultaneous regeneration of WDM channels. In order to validate its properties, this new modulator was inserted into a recirculating loop and made it possible to demonstrate a single-channel regenerated transmission at 40Gbit/s over more than 20,000km. In addition, asymptotic stabilization of bit-error-rate (BER) at low levels ($<10^{-12}$) over transmission distance was experimentally shown for the first time through Q-factor measurements.

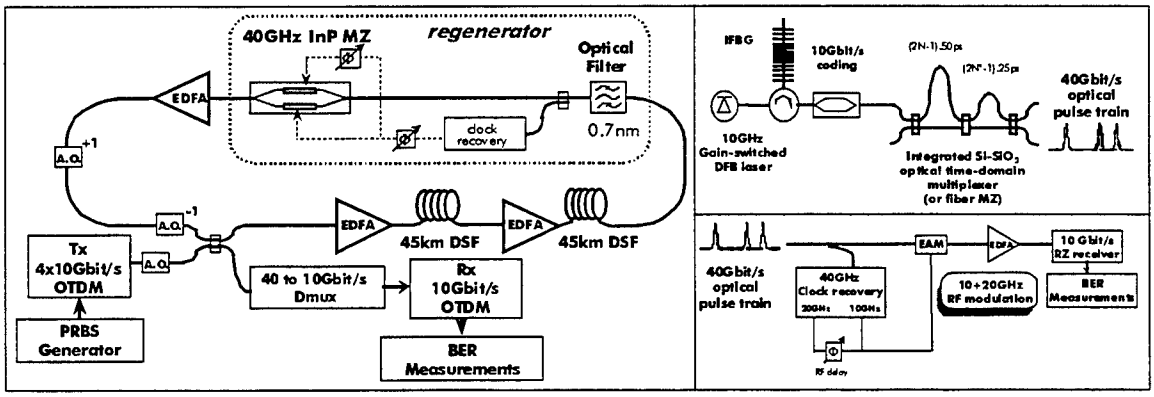


Figure 2: Experimental Q-factor vs. transmission distance with single-electrode (open circles) and push-pull (full squares) configurations. Insets shows 10Mm eye diagrams at 40Gbit/s and 10Gbit/s monitored on 45GHz photodiode before and after time-domain demultiplexing.

Figure 2 shows the 40Gbit/s experimental recirculating loop along with emitter/receiver experimental setup. Pulses at 10GHz repetition rate (20ps width) generated from a gain-switched DFB laser at 1555.75nm are first compressed to 6ps through a 30ps/nm, in-fiber Bragg grating. The output is then modulated by a 10Gbit/s, 2^7-1 PRBS sequence before time-interleaving through an integrated Si-SiO_2 double-MZ multiplexer, yielding a single-polarization 40Gbit/s signal. The loop consists of two 45km-long spans (0.24dB/km loss) and three 1480nm-pumped EDFAs ($NF=2n_{sp}/\eta_{in}=7dB$). The span dispersion is D=0.15ps/(nm·km), corresponding to a mean soliton power of 5±1dBm at the EDFA output. The RF clock, which is locally recovered at 40GHz through a Q=300 filter, is split with independent phase adjustments to drive the MZ in either single-electrode or push-pull operation. An optical bandpass filter of 0.7nm optimized width is inserted before the MZ for further jitter/noise control [1]. Bit-error-rate (BER) measurements are made at 10Gbit/s after demultiplexing through a PI electro-absorption modulator electrically driven by 20 and 10GHz RF sines, yielding a temporal switching window of 17ps. Error-counting is made by random sampling of the four 10Gbit/s tributaries. The evolution of amplitude Q-factor with distance was measured when operating the modulator in push-pull mode, which permits to

adjust the effective PM. For the optimum operating point, corresponding insertion loss and IM depth are measured to be 16.3dB and 7.2dB, respectively.

With these experimental system parameters, we have computed numerical simulations of this 40Gbit/s regenerated transmission experiment using the vector nonlinear Schrödinger equation with temporal and spectral resolution of 0.391ps/78MHz, resp. We took into account both 10 to 40Gbit/s OTDM and 40 to 10Gbit/s demultiplexing and incorporated polarization effects occurring in recirculating loops such as signal repolarization [10] and its effect when associated to fiber PMD. Theoretical Q-factors result from the concatenation of 3 runs with random noise/polarization seeds. Like in the experiment, the performance is set by the minima of amplitude and timing Qs between the four 10Gbit/s tributaries.

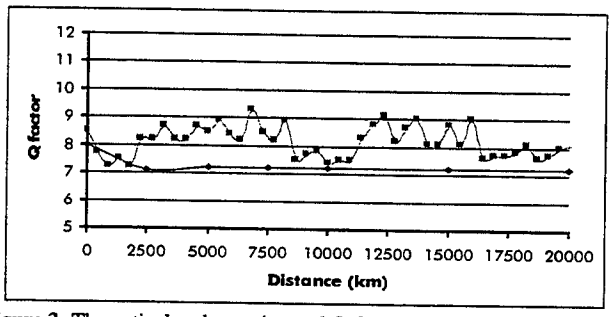


Figure 3: Theoretical and experimental Q-factor vs. transmission distance

Figure 3 shows both experimental measurements and numerical predictions of Q-factors with distance. Experimental Q-factors (smooth curve) are seen to rapidly reach an asymptotic value of 7.2 (BER<10^{-12}), thus demonstrating the efficiency of 3R regeneration; these measurements represent the first experimental confirmation of this type of evolution. Theoretical Q-factors (broken curve) also evolves towards an asymptotic value near 8 at 20Mm. Note the good agreement between experimental and numerically estimated values of Q-factors, confirming the possibility to model and predict SM systems performance. The slight difference among theses values can be explained by the incomplete estimation of full noise/polarization statistics in the simulations.

Optical 3R regeneration is a attractive candidate for achieving Terabit/s capacity over transoceanic distances with 40Gbit/s WDM granularity. In order to experimentally assess its potential, we have developed a new type of 40GHz, polarization-insensitive and wavelength-independent regenerator, and demonstrated an 40Gbit/s error-free transmission over more than 20,000km without measuring any signal degradation. Immunity to WDM crosstalk was also observed [9], showing the potential of this component for simultaneous WDM regeneration. Further improvement of the regenerator characteristics (modulator insertion loss, filtering) associated with numerical optimization of the system configuration (dispersion map, channel spacing) should, in the near future, lead to the first experimental investigation of Nx40Gbit/s regenerated transmission.

References

[1] M.Nakazawa, E.Yamada, H.Kubota and K.Suzuki, Electron. Lett., Vol.27, n°14, pp.1270-1272 (1991).
[2] N.J.Smith, K.J.Blow, W.J.Firth and K.Smith, Optics Commun., n°102, pp.324-328 (1993).
[3] O.Leclerc, P.Brindel, C.Duchet, M.Goix, E. Maunand and E.Desurvire, Electron. Lett., Vol.34, n°10, pp.1011-1013 (1998).
[4] O.Leclerc, E.Desurvire and O.Audouin, Optical Fiber Technol., Vol.3, n°2, pp.97-117 (1997).
[5] M. Nakazawa, K. Suzuki, H. Kubota, A. Sahara, and E. Yamada, Electron. Lett. 34, 104 (1998).
[6] O.Leclerc, P.Prindel, S.Bigo, E.Brun-Maunand and E.Desurvire, Electronics Letters, Vol.34, n°2, pp.199-201 (1998).
[7] K.Suzuki, H.Kubota, A.Sahara and M.Nakazawa, Electron. Lett., Vol.34, n°1, pp.98-100 (1998).
[8] G.Aubin, T.Montalant, J.Moulu, F.Pirio, J.-B.Thomine and F.Devaux, , Electron. Lett., Vol.32, n°24, pp.2188-2189 (1996).
[9] O.Leclerc, P.Brindel, D.Rouvillain, E.Pincemin, B.Dany, E.Desurvire, C.Duchet, E.Boucherez and S.Bouchoule, Postdeadline paper 35, Proc. of Optical Fiber Communications, OFC'99 (1999).
[10] C.R.Menyuck, D.Wand and A.N.Pilipetskii, Proc. of European Conference on Optical Communications, ECOC'97, Edinburgh, Vol.3, p.275 (1997).

Nonlinear Guided Waves and Their Applications

Nonlinear Periodic Media

Thursday, 2 September 1999

Neil G. Broderick, University of Southampton, UK
Presider

ThB
10.30-12.00
Salle Morey—St-Denis

Quantum and Nonlinear Optics in a Photonic Band Gap

Sajeev John
Department of Physics
University of Toronto
Toronto, Ontario
Canada M5S 1A7

SUMMARY

Photonic band gap (PBG) materials are a new class of dielectric materials which exhibit a complete three-dimensional gap to electromagnetic wave propagation. These materials facilitate two novel and fundamental optical principles, namely (i) the coherent localization of light and (ii) the control and inhibition of spontaneous emission of light from atoms and molecules. The simultaneous realization of these two effects leads to a variety of theoretical predictions for novel quantum and nonlinear optical effects involving photons and atoms within a PBG. These include photon-atom bound states, non-Markovian band edge lasing effects, collective atomic switching, and coherently controlled, phase sensitive single-atom optical memory. Although the photonic band gap is impervious to linear electromagnetic wave propagation, it is quite rich in nonlinear wave propagation phenomena. These take the form of classical and quantum gap solitons. I review these effects, their possible experimental realization, as well recent progress in the microfabrication of 3-d PBG materials on the optical scale using self-assembly methods.

Laue Soliton in Photonic Crystal

B. I. Mantsyzov

Physics Department, Moscow State University, Moscow 119899, Russia
E-mail: mants@genphys.phys.msu.su ; Fax: 7(095) 939-1489

Light-matter interaction in photonic crystals has been at the heart of scientific interest and research in the last years [1]. The photonic crystals (PC) are one-, two-, or three-dimensional structures with a periodically modulated dielectric function, and what is more, the period of modulation is about optical wavelength. In the case of linear interaction and a weak periodicity, a light propagation in PC is similar to x-ray diffraction in traditional crystal [2]. Specific distinctions of electromagnetic field dynamics in PC are displayed when a nonlinearity of light-matter interaction is taken into account. First of all, this is the existence of a novel kind of nonlinear solitary waves which are propagated at Bragg frequency within the linear forbidden gap band of the periodic medium, so called gap solitons. It has been shown before that gap solitons and oscillating gap solitary waves appear in periodic structures with coherent resonant, Kerr, and quadratic types of nonlinearity [3]. These waves are formed by two counterpropagating coupled Bragg modes in one-dimensional (1D) PC. The progress in technology allows now to fabricate a multidimensional PC [1]. In comparison with the studies of linear and nonlinear light diffraction in 1D PC which were the subject of variety of theoretical and experimental studies, the nonlinear field dynamics in multidimensional PC still remain an uncovered area in the optics of PC. Several recently investigations exhibited a laser action from optically pumped dye-molecules in solution filled in air-rods of 2D PC [4] and second harmonic generation in 3D colloidal PC [5].

Here we study theoretically the dynamics of formation and propagation of nonlinear solitary waves in the general case of two-wave Bragg diffraction problem in multidimensional resonant photonic crystals. The vector Bragg condition for the wave vectors of the incident and diffracted waves and the reciprocal lattice vector is to be satisfied in this case. The equations of two-wave nonlinear dynamic diffraction have been derived from the semiclassical Maxwell-Bloch equations describing the coherent light-matter interaction under Bragg condition. By means of analytical and numerical integration of the equations we investigated the process of formation and propagation of Bragg solitary waves for the different geometric schemes of diffraction. It has been shown that nonlinear solitary waves appear both in the case of Bragg geometry of diffraction like gap solitons and in the case of Laue geometry of diffraction like, so called, two-wave Laue solitons of self-induced transparency. The Laue soliton propagates in the direction of the normal to reciprocal lattice vector. The numerical simulation of diffraction process has given the possibility to study the wave dynamics in a finite medium under different boundary conditions.

The periodically distributed clusters containing resonant two-level atoms in our model form three-dimensional PC. The period of the lattice is about wave length λ and the cluster size is assumed to be less than λ. Corresponding reciprocal lattice of the crystal is also three-dimensional, but if two diffracted wave vectors $\vec{k}_{0,h}$ and reciprocal lattice vector $\vec{H}$ exact satisfy the Bragg condition $\vec{k}_h = \vec{k}_0 + \vec{H}$, we are able to replace three-dimensional problem of diffraction by two-dimensional problem using two-wave approximation and taking into account only two strong Bragg modes $E_{o,h}(\vec{r},t)$ of quasimonochromatic field $E(\vec{r},t)$ within the structure

$$E(\vec{r},t) = \frac{1}{2}[E_0(\vec{r},t)\exp(i\vec{k}_0\vec{r} - i\omega t) + E_h(\vec{r},t)\exp(i\vec{k}_h\vec{r} - i\omega t)] + \text{c.c.}$$

To describe the coherent interaction of light with resonant two-level medium the semiclassical approach has been used. Generalizing the Maxwell-Bloch equations of diffraction problem for 1D structure [3] we have derived the following main equations of nonlinear two-wave dynamic Bragg diffraction in resonant 3D photonic crystals:

$$
\begin{aligned}
&c\frac{\partial\Omega_0(\vec{r},t)}{\partial\vec{k}_0}+\frac{\partial\Omega_0(\vec{r},t)}{\partial t}=\tau_c^{-2}P(\vec{r},t),\\
&c\frac{\partial\Omega_h(\vec{r},t)}{\partial\vec{k}_h}+\frac{\partial\Omega_h(\vec{r},t)}{\partial t}=\tau_c^{-2}P(\vec{r},t),\\
&\frac{\partial P(\vec{r},t)}{\partial t}=n(\vec{r},t)\left[\Omega_0(\vec{r},t)+\Omega_h(\vec{r},t)\right],\\
&\frac{\partial n(\vec{r},t)}{\partial t}=-\mathrm{Re}\left\{P^*(\vec{r},t)\left[\Omega_0(\vec{r},t)+\Omega_h(\vec{r},t)\right]\right\},
\end{aligned}
\qquad (1)
$$

where the directional derivative is given by $\frac{\partial\Omega}{\partial\vec{k}}=(grad\,\Omega)\cdot\frac{\vec{k}}{|\vec{k}|}$, $\Omega_{0,h}=2(\mu/\hbar)E_{0,h}$, $E_{0,h}$ are the slowly-varying envelope of complex electric field amplitudes of the incident and diffracted waves, P is the dimensionless characteristic of complex atomic polarization, n is the inverse population of atoms, cooperative time is given by $\tau_c^{\,2}=8\pi T_1/3c\rho\lambda^2$, ρ is the density of resonant atoms, μ is the matrix element of the projection of the transition dipole moment, c is the light velocity.

Analytical and numerical solutions of Eqs. (1) describing the spatial-temporal dynamics of field and atomic inverse population for different schemes of diffraction geometry are studied in this paper. Figure 1 shows the Laue scheme of diffraction. The incident field does not feel the total Bragg reflection near the boundary, because there is not the Bragg band gap for a field propagating in the x-direction. Two diffracted modes are coupled due to reflection on the crystallographic planes within the structure. We have obtained exact expression for novel kind of coupled-mode soliton: Laue soliton. Computer simulation allows to investigate the process of Laue soliton formation from incident field, and furthermore, the possibility of arising of so called "0-field". This field consists of two coupled diffracted modes with opposite singes of amplitudes, so the sum of the mode amplitudes is equal to zero. As a result, the total 0-field with large partial mode amplitudes propagates through the resonant structure like linear field without nonlinear interaction with two-level atoms.

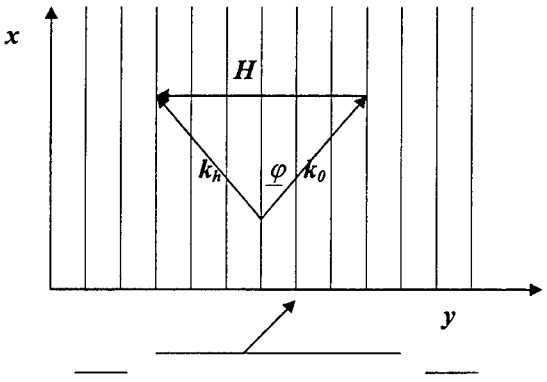


Fig.1. The Laue scheme of diffraction on crystallographic planes of photonic crystal.

Let the symmetrical diffraction scheme be realized, and fields are homogeneous with respect to the y coordinate $\partial\Omega_{0,h}/\partial y=0$.

Then Eqs. (1) has two different solutions. The first one is realized if field sum $\Omega=\Omega_0+\Omega_h$ is not equal to zero but the difference is zero

$\Omega^-=\Omega_0-\Omega_h=0,\quad \Omega=\theta_t\neq 0.$

It means that amplitudes of two modes are equal each other and we obtain the following solutions for both waves:

$$\Omega_0=\Omega_h=\frac{1}{2}\Omega=\frac{1}{\tau}\,\mathrm{sech}\left(\frac{t-x/v}{\tau}\right).$$

This is two-wave Laue soliton, or Laue 2π-pulse, which propagates at the velocity $v=\dfrac{c\cos\varphi}{1+2\tau^2/\tau_c^{\,2}}$ coupling two diffracted modes with equal amplitudes. Another case is realized when the field sum is zero but the difference is not equal to zero:

$\Omega=\Omega_0+\Omega_h=0,\quad \theta=0,\quad \Omega^-=\Omega_0-\Omega_h\neq 0,$

hence

$\Omega_0=-\Omega_h,\quad \theta=0,\quad v=c\cos\varphi.$

We have called this linear solution "0-field" because it is characterized by the sum of fields $\Omega = 0$. Propagating through the structure, it does not interact with resonant atoms ($\theta=0$), even if the amplitude of each diffracted mode is rather large.

Figure 2 illustrates the result of numerical simulation of nonlinear Laue diffraction of the incident pulse in finite photon crystal when pulse amplitude $\Omega_0'=2\ 10^{13}\ s^{-1}$, pulse duration $\tau_0=0.3\tau_c$, $\tau_c=3\ 10^{-13}$ s, and angle of diffraction $\varphi=30^0$. The Laue soliton and 0-field are formed within the structure. Their parameters (the sign and the value of mode amplitudes, velocity and duration) agree with analytical results. Fast 0-field outstrips the slow Laue soliton and does not excite resonant atoms.

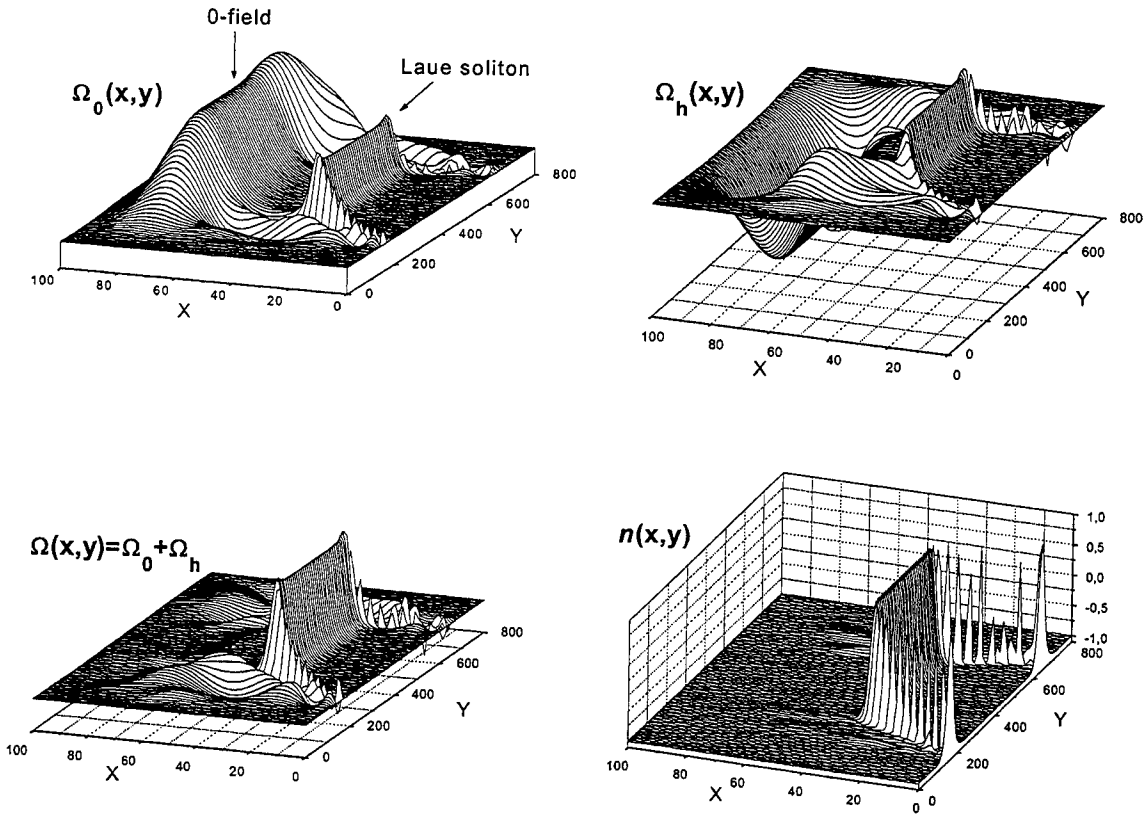


Fig. 2. The Laue soliton and 0-field pulse. Spatial distribution of two diffracted modes of field and inverse population of atoms in the structure.

The developed theory of nonlinear two-wave Bragg diffraction of coherent light in a resonant multidimensional photonic crystal allows to predict a number of novel kinds of nonlinear solitary waves: the Laue soliton, propagating and standing gap solitary waves, as well linear 0-field waves . These phenomena could be observed experimentally , for instance, in an opal photonic crystal with embedded dye molecules [6] or in a structure of air-rods filled with dye solution [4].

This work was supported by the RFBR (98-02-17544) and by the Russian Universities Foundation.

1. *Photonic Band Gap Materials,* edited by C. M. Soukoulis, Kluwer Academic, Dordrecht, 1996.
2. R. W. James, *The optical principles of the diffraction of X-rays*, G.Bell and Sons, London, 1948.
3. B. I. Mantsyzov and R. N. Kuzmin, Sov. Phys JETP **64**, 37 (1986); W. Chen and D. L. Mills, Phys. Rev. Lett. **58,** 160 (1987); C. Conti, S. Trillo, and G. Assanto, Phys. Rev. Lett. **78,** 2341 (1997)
4. K. Inoue, M. Sasada, J. Kawamata, K. Sakoda, and J. Haus, IQEC'98 Technical Digast , 47 (1998).
5. J. Martorell, R. Vilaseca, and R. Corbalan, Phys. Rev. A **55**, 4520 (1997).
6. W. L. Vos, R. Sprik, A. Lagendijk, G. H. Wegdam, A. van Blaaderen, and A. Imhof, in [1] p.107.

The spectral characteristics of nonlinear pulse compression in an integrated Bragg waveguide filter.

P.Millar*, N.G.R. Broderick, D.J. Richardson,University of Southampton, Optoelectronics Research Centre, Department of Physics and Astronomy,Southampton, SO17 1BJ, UK.,Phone: +44 (0)1703 593144, Fax: +44 (0)1703 593142Email: ngb@orc.soton.ac.uk. **J.S. Aitchison, R. De la Rue, T. Krauss**University of Glasgow, Department of Electrical and Electronic Engineering, Oakfield Avenue, Glasgow,G12 8QQ, UK.Phone: +44 (0)141 3306126, email: p.millar@elec.gla.ac.uk. *(permanent address: University of Glasgow, Department of Electrical and Electronic Engineering, Oakfield Avenue, Glasgow,G12 8QQ, UK.)

Introduction

Interest in optical devices based on the properties of nonlinear Bragg gratings has steadily increased in recent years as potential applications within future optical network systems become more apparent. Suggested device applications include optical pulse filtering, shaping, multiplexing, power limiting and all-optical switching. Nonlinear propagation effects in periodic structures have been experimentally explored in many material systems including colloidal crystals[1], InSb planar devices[2], optical fibers[3-5], MQW material[6] and more recently, by our group, in bulk AlGaAs[7].

To date the emphasis in both experimental and theoretical studies of nonlinear Bragg gratings has concentrated on the temporal characteristics of pulses travelling within such periodic structures[1-9]. As a result, no information regarding the spectral evolution of pulse propagation in Bragg filters has been reported, despite the fact that knowledge of the spectral shape of the propagating pulse is essential in order to understand the pulse formation process leading to, for example, nonlinear pulse compression. Therefore, in this paper, we aim to redress this imbalance by presenting experimental nonlinear spectral broadening results obtained using a Bragg grating written in an integrated AlGaAs waveguide. The nonlinear spectral broadening achieved in this device was associated with the compression of a pulse from 400 ps to 80 ps. The data presented shows that in the nonlinear regime; interesting features appear in the output spectrum of a pulse tuned initially to lie within the grating stopband.

Fabrication

A high quality AlGaAs wafer was used to fabricate the integrated grating filters. The wafer was grown by molecular beam expitaxy and had the following structure. The lower cladding layer was 4 μm thick and contained 24% Al, the guiding layer was 1.5 μm thick and contained 18% Al and finally the upper cladding layer was 1 μm thick containing 18% Al. AlGaAs was chosen as the device material as the fabrication technology is well developed. In addition, AlGaAs has an enhanced nonresonant nonlinearity when operating at a wavelength below the half-band gap region, which can be tailored to lie within the 1.55 μm low loss telecommunications window. At this wavelength the detrimental effects of two- and three- photon absorption can minimised through wafer design. The nonlinear refractive index was measured to be ~ 1.5 x 10^{-13} cm^2/W which is 3 orders of magnitude greater than that of silica. Therefore the peak powers required to observe nonlinear effects in this material are considerably lower than for comparable structures in optical fibres. In addition, AlGaAs waveguides provide good optical power confinement over long interaction lengths with sufficient power handling capabilities to perform this type of nonlinear experiment. For example in this experiment upto 1.2 kW of power (660 W launched) was steered into the guides without optical damage occurring. Furthermore, the high nonlinearity of the AlGaAs guides allow a high rep rate sources to be used which enabled spectral measurements to be made with ease. Fig.1 is a schematic of the waveguide filter. The grating filters were based on a weak grating on a strip-loaded waveguide, to minimise excess scattering losses. A one step electron beam lithography process was used to define the grating and the ridge guides simultaneously. Gratings, 8 mm long were written on 1 cm long single moded waveguides, 5 μm wide. A grating period of 235 nm was selected to position the grating stopband around the maximum power range of the laser at ~ 1533 nm.. The waveguides were etched using Reactive ion etch down to a depth of 0.9 μm. Due to reactive ion etching lag the grating etch depth was approximately 0.3 μm, resulting in an effective index modulation of ~4.4×10^{-4}.

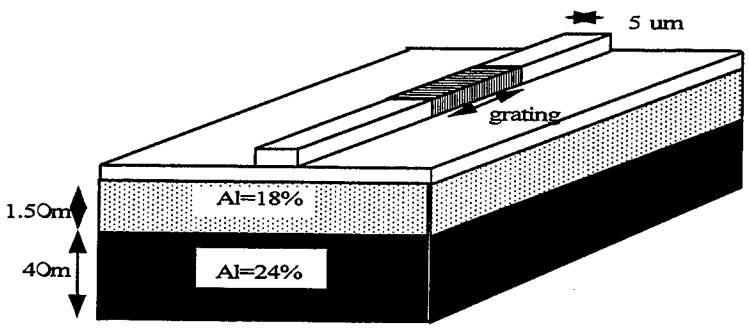


Figure 1: Schematic of the integrated Bragg waveguide filter.

Experimental Set-up

We used light pulses from an externally modulated DFB laser, amplified by a large mode area erbium doped fibre amplifier cascade which generated linearly polarised 415 ps (spectral bandwidth of ~ 3GHz), rectangular shaped pulses with a repetition rate of 100 kHz. The wavelength range of this laser system was 1.52-1.56 μm. The pulses were coupled into and out of the waveguides using an endfire rig with x40 objective lenses. The output pulse was incident alternatively, via an optical fibre, onto a high resolution commercial spectrum analyser and fast optical detector/sampling scope, which had a temporal resolution of 50 ps. Hence both the spectral and temporal characteristics of the transmitted pulse were measured. The average input power was monitored before the input coupling lens, using a pyroelectric meter and the pulse peak power calculated using measurements from a fast photodiode and oscilloscope. A lambda/2 plate before the input lens was used to control the input polarisation. The peak input power launched into the guides was estimated to be 50% of the peak power from the laser.

Experimental results

The grating transmission spectrum is shown in fig. 2. The maximum reflectivity was ~ 99%.The width of the stopband was ~ 0.2 nm. The grating spectrum appears in this figure to be asymmetric this is partly due to the fact that it was measured using the amplified spontaneous emission from the amplifier stage. Fig. 2 also shows the transmitted pulse spectrum of a pulse tuned to lie at the centre of the gap at 1533.873 nm, for a low input peak power of 60 W (light launched into guide). The input pulse width was 415 ps. A comparison was made between the input pulse spectrum and the transmitted pulse spectrum. No change in the spectral shape of the pulse was observed in the linear regime. The incident power was then increased to 385 W. Fig. 3 (a) shows the high power output pulse spectrum superimposed on the gratings transmission spectrum. Figure 3 (b) shows the temporal shape of the output pulse for input peak powers of 60 W, 200 W and 350 W. Comparing fig. 2 to fig. 3 (a) it is obvious that significant pulse shaping and spectral broadening occurs at high powers. Figure 3(b), shows that the pulse was compressed from 400 ps to 80 ps at high input powers, confirming that spectral broadening does occur as the transformed limited pulse has been compressed by a factor of 5. To confirm that the nonlinear spectral broadening was due to the grating itself, we repeated the experiment again with a pulse tuned to lie outside the grating stopband, on the long wavelength side, at 1534.429 nm. We found that no significant spectral broadening occurred at high input powers and the pulses temporal width increased slightly from 415 ps in the linear regime to 420 ps in the nonlinear regime. As shown in fig.3 (a), the output pulse spectrum is doubly peak with one peak at the centre wavelength and another shifted to the short wavelength side. Also, a considerable amount of power is now outwith the grating stopband. The temporal characteristics of this transmitted pulse also had a 2 peak characteristic with a delay of 250 ps between each peak.

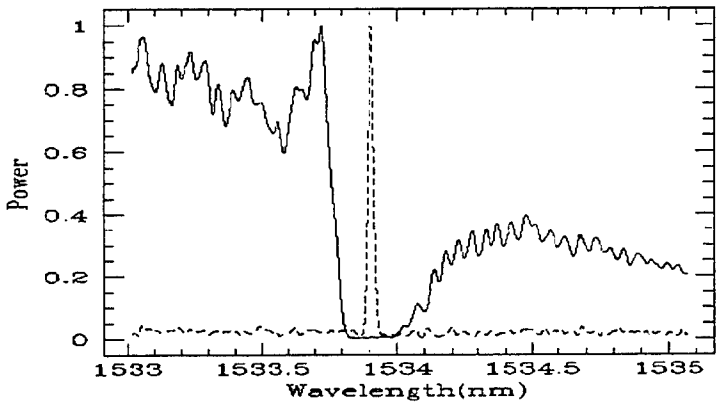


Figure 2: Grating transmission spectrum (solid line) and output spectral pulse shape in linear regime.

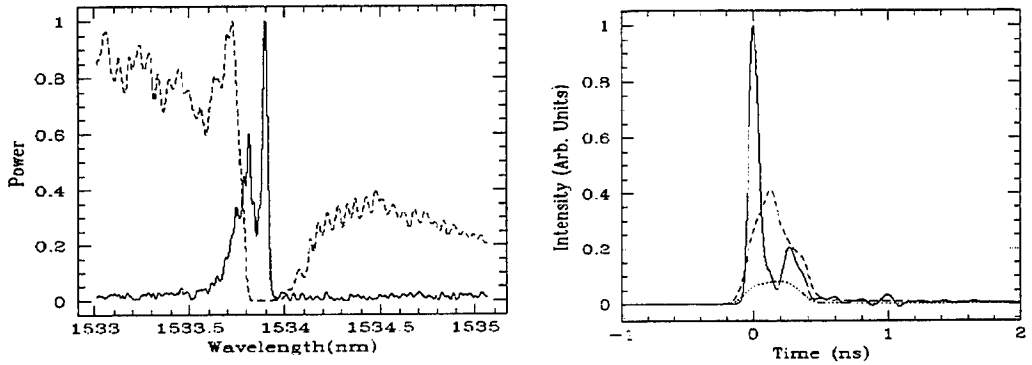


Figure 3(a) :Graph showing the output spectral pulse shape (solid line) for high input peak power of 385 W and the gratings spectrum. b) Transmitted temporal pulse shape for input power of 350 W (solid line), 200 W (long dashed line) and for an input power of 60 W (short dashed line).

Conclusion

We presented spectral measurements which demonstrate that nonlinear spectral broadening, due to pulse compression, within an AlGaAs Bragg filter is asymmetric in nature with the majority of the broadening occurring on the short wavelength side of the stopband. At high input peak powers several distinct peaks appeared in the transmitted pulse spectrum and temporal pulse shape. We are currently modeling the system and have so far obtained qualitative agreement with the experimental results and expect to obtain better agreement in the near future.

References

1. C.J. Herbert, W.S. Capinski and M.S. Malcuit, Opt. Lett., **17**,1037 (1992).
2. J.E. Ehrlich, G. Assanto and G.I. Stegeman, Appl. Phy. Lett., **56**, 602 (1989).
3. N.G.R. Broderick, D. Tavener, D.J. Richardson, M. Ibsen and R. I. Laming, Phy. Rev. Lett., **79**, 4566 (1997).
4. B.J. Egglington, R..E. Slusher, C.M.de Sterke, P.A. Krug and J.E. Sipe, Phy. Rev. Lett.,**76**,1627 (1996).
5. D. Taverner, N.G.R. Broderick, D.J. Richardson, M. Ibsen and R.I. Laming, Opt. Lett., **23**, 328 (1998).
6. D. Campi, C. Coriasso, A. Stano, L. Faustni, C. Cacciatore, C. Rigo and G. Meneghini, App. Phy. Lett., **72**, 537 (1998).
7. P.Millar, J.S.Aitchison, N.G.R. Broderick, D.J. Richardson, Opt. Lett. (to be published May 1999).
8. H.G. Winful and J.H. Marburger and E. Garmire, Appl. Phy. Lett., **35**, 379 (1979).
9. H.G. Winful, Appl. Phy. Lett., **46**, 527 (1985).

Soliton pulse compression in chalcogenide fiber Bragg gratings

G. Lenz, B. J. Eggleton, M. E. Lines and R. E. Slusher
Lucent Technologies, Bell Labs, 700 Mountain Ave., Murray Hill, NJ 07974
glenz@lucent.com, egg@lucent.com, mlines@lucent.com, res@lucent.com
N. M. Litchinitser
The institute of Optics, University of Rochester, Rochester, NY 14627
natasha@optics.rochester.edu
J. S. Sanghera and I. D. Aggarwal
Naval Research Laboratory,4555 Overlook Ave., Washington, DC 20375
sanghera@ccf.nrl.navy.mil, ishaggar@ccf.nrl.navy.mil

Optical time division multiplexing at high speeds (> 40 Gbit/s) is currently of great relevance to the next generation of optical communication systems. This requires ultrafast all-optical components such as short pulse sources. As an example we will consider optical pulse compressors and high repetition rate pulse train generators. Recently, it was shown that decreasing the dispersion adiabatically along the propagation path of a soliton in optical fiber is equivalent to adding gain to the propagation medium. If this effective gain is applied adiabatically, the optical soliton will follow and self-adjust by reducing its pulsewidth and remaining a fundamental soliton [1, 2]. Using standard fiber as the propagation medium has two drawbacks: 1) producing a fiber with a prescribed dispersion map may require specialty fiber and/or splicing fibers with different dispersive characteristics. 2) The typical lengths of fiber required for compression are large due to the small magnitude of the quadratic dispersion in optical fiber. On the other hand, fiber Bragg gratings (FBG's) have none of these constraints; virtually arbitrary grating profiles (and therefore corresponding dispersion maps) can be made and because of the very large dispersion close to the optical band edge of the grating, very small devices are possible. This reduction in size requires the scaling down of the peak power or equivalently an increase in the Kerr nonlinearity of the fiber. Chalcogenide fibers and FBG's with Kerr nonlinearity almost 100 times that of silica (corresponding to a reduction of 100 times in peak power) have been demonstrated [3]. In this paper we will present theory and numerical simulations of FBG-based pulse compressors in chalcogenide fibers. These devices can also be operated as pulse train generators (depending on their input). We will also present measurements of even larger Kerr nonlinearity of a number of additional different chalcogenide materials and discuss their suitability for this application.

The condition for the fundamental soliton in an optical fiber (solution of the nonlinear Schrödinger equation (NLSE)) is written as follows:

$$E\frac{\pi n_2}{\lambda A_{eff}}\frac{\tau}{\beta_2}=1 \qquad (1)$$

where E is the pulse energy, n_2 the nonlinear index, λ the wavelength, A_{eff} the effective mode area, τ the pulsewidth and β_2 the quadratic dispersion at the center wavelength. If the dispersion is decreased slowly enough and in the absence of radiative loss, the soliton may self-adjust by decreasing its pulsewidth τ such that condition (1) is maintained. This turns out to be also true if A_{eff} decreases or n_2 increases adiabatically (or any combination of the above). In FBG's optical solitons are known as Bragg solitons and have been studied theoretically as well as experimentally [4]. In an apodized FBG the quadratic dispersion is given by [5]:

$$\beta_2 = -\left(\frac{n}{c}\right)^2 \frac{1}{\delta} \frac{(\kappa/\delta)^2}{\left[1-(\kappa/\delta)^2\right]^{3/2}} \tag{2}$$

where κ is the coupling constant and is related to the bandwidth of the stop band, δ is the frequency detuning relative to the center of the stop band, n is the average effective refractive index and c the speed of light. Typical numbers yield a dispersion of a few ps^2/cm (or approximately 5 orders of magnitude larger than standard fiber). By going to a non-uniform FBG (i.e., one in which either κ or δ or both vary along the propagation direction in the grating) we can get a monotonically increasing or decreasing dispersion. An adiabatic decrease in dispersion requires [6]

$$\frac{2|\beta_2(0)L|}{\tau^2 \ln[\beta_2(0)/\beta_2(L)]} > 1 \tag{3}$$

When this adiabatic condition is satisfied the input soliton will evolve into a soliton shorter by the factor $\beta_2(0)/\beta_2(L)$. Here $\beta_2(0)$ and $\beta_2(L)$ are the dispersion at the input and output of the FBG (i.e., at $z = 0$ and $z = L$) and L is the grating length. Figure 1 shows a numerical simulation of a 10 ps soliton being compressed by a factor of 4 in a 100 cm long grating. For a grating fabricated in standard fiber, assuming A_{eff} = 20 μm^2 and $n_2 = 2.3\times10^{-16}$ cm^2/W, the launched soliton peak power would need to be ~1.2 kW, whereas with a chalcogenide FBG the required peak power would be less than 1W.

When the launched field into such a device is a beat signal of amplitude A_0 created from two CW lasers and given by,

$$A_0 \sin(\pi \Delta \nu t) \tag{4}$$

the resulting output is a soliton pulse train at a repetition rate of $\Delta\nu$ (the frequency separation between the CW laser lines)[7]. Figure 2 shows the 40 GHz sinusoidal input intensity and the pulse train output consisting of 2.6 ps solitons. This numerical example required a 70 cm apodized FBG with a launch peak power of ~ 1.4 kW. In both of these cases the coupling constant κ was varied linearly along the grating resulting in an adiabatically decreasing dispersion (for a more detailed theoretical investigation see [6, 7]). The result is a compact (~ 1 m long) all-fiber compressor which requires ~ 1 kW of peak power . To make this device useful for more modest peak power would require a medium with a larger nonlinear coefficient (n_2/A_{eff}) such as a chalcogenide FBG which would require peak powers of less than 1W.

Recently, we have embarked on a systematic study of the Kerr nonlinearity in chalcogenide glasses. The goal of this study is to optimize these glasses for a maximum n_2 at a wavelength of 1.55 μm, while keeping the nonlinear absorption to a minimum. To this end bulk glass samples were produced and Z-scan measurements [8] were performed using a tunable, high-energy, femtosecond source. Measurements of both n_2 and the two-photon absorption were performed at a number of wavelengths around 1.55 μm. Our theoretical model predicts the possibility of n_2 of ~ 1000 times that of silica. Initial experimental results on bulk As_2Se_3 indicate n_2 ~ 500 times silica at a wavelength of 1.55 μm and this material may be produced in fiber form. We are currently investigating the photosensitivity properties of this and other chalcogenide glasses, allowing the fabrication of FBG's (FBG's in As_2S_3 fiber were demonstrated in [3]). Using these numbers and accounting for the smaller A_{eff} in these high linear refractive index materials, the

peak powers may be scaled down to the ~ 1 W level, as mentioned earlier. Further details and experimental as well as theoretical results of this material study will be reported.

In summary, chalcogenide FBG's are promising devices for nonlinear picosecond pulse compression and pulse train generation. These devices are short, versatile all-fiber devices requiring low peak powers.

References

[1] S. V. Chernikov, and P. V. Mamyshev, "Femtosecond soliton propagation in fibers with slowly decreasing dispersion," *J. of Opt. Soc. Am. B*, vol. 8, pp. 1633-1641, 1991.

[2] P. V. Mamyshev, S. V. Chernikov, and E. M. Dianov, "Generation of fundamental soliton trains for high-bit-rate optical fiber communication lines," *IEEE Journal of Quantum Electronics*, vol. 27, pp. 2347-2355, 1991.

[3] M. Asobe, "Nonlinear Optical Properties of Chalcogenide Glass Fibers and Thier Application to All-Optical Switching," *Optical Fiber Technology*, vol. 3, pp. 142-145, 1997.

[4] B. J. Eggleton, R. E. Slusher, C. M. de Sterke, P. A. Krug, and J. E. Sipe, "Bragg Grating Solitons," *Physical Review Letters*, vol. 76, pp. 1627-1630, 1996.

[5] N. M. Litchinitser, B. J. Eggleton, and D. B. Patterson, "Fiber Bragg gratings for dispersion compensation in transmission: theoretical model and design criteria for nearly ideal pulse compression," *Journal of Lightwave Technology*, vol. 15, pp. 1303-1313, 1997.

[6] G. Lenz, and B. J. Eggleton, "Adiabatic Bragg soliton compression in nonuniform grating structures," *J. Opt. Soc. Am. B*, vol. 15, pp. 2979-2985, 1998.

[7] N. M. Litchinitser, G. P. Agrawal, B. J. Eggleton, and G. Lenz, "High-repetition-rate soliton-train generation using fiber Bragg gratings," *Optics Express*, vol. 3, pp. 411-417, 1998.

[8] M. Sheik-Bahae, A. A. Said, T.-H. Wei, D. J. Hagan, and E. W. Van Stryland, "Sensitive Measurement of Optical Nonlinearities Using a Single Beam," *IEEE Journal of Quantum Electronics*, vol. 26, pp. 760-769, 1990.

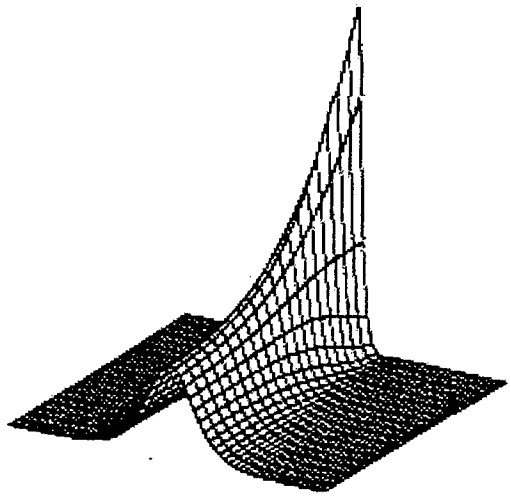


Figure 1: Adiabatic soliton compression in an apodized FBG

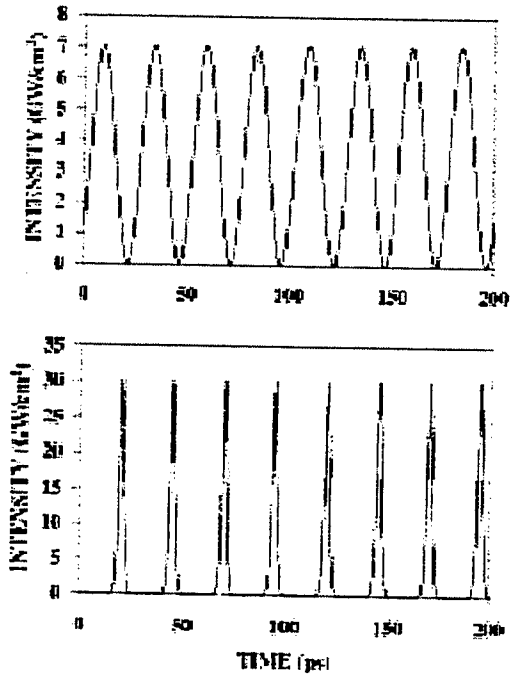


Figure 2: Input beat signal (upper) and resulting output soliton train (lower)

Femtosecond second-harmonic and sum-frequency generation near the photonic band edge in one-dimension periodic media

A.V.Balakin, V.A.Bushuev, N.I.Koroteev, B.I.Mantsyzov, I.A.Ozheredov, A.P.Shkurinov

Physics Department and International Laser Center, M.V.Lomonosov Moscow State University, Moscow, 119899, Russia
E-mail: alex@lasmed.ilc.msu.su

D.Boucher, P.Masselin

Laboratoire de PhysicoChimie de l'Atmosphère, EP 1831 CNRS, MREID, 145 avenue Maurice Schumann, Université du Littoral, 59140, Dunkerque, France
E-mail: masselin@pca3.univ-littoral.fr

During the last years large effort has been devoted to studies of light-matter interaction in an artificial multi-dimensional structures with the periodic modulation of the dielectric function so called photonic crystals (PC) [1, 2]. Fundamental property of PC is an existence of photonic band gaps (PBG) where the propagation of light in the case of linear interaction is forbidden [1]. Despite the appearance of the newest directions of research, such as the possible existence of soliton-like pulse propagation at the Bragg frequency within the PBG [3], the traditional directions of nonlinear optics such as harmonics generation [4], are the subject of particular interest in PC. Recently, it was shown theoretically that the enhancement of the second-harmonic signal in PBG structure can be determined by the increasing of the density of electromagnetic field modes within the structure when the frequency of fundamental field is near the photonic band edge [5]. In [6] we investigated the properties of second-harmonic signal in one-dimensional PBG structure versus the angle of incidence, where the wavelength of the fundamental radiation was fixed near the photonic band edge. We concluded that the enhancement mechanism related with increasing of field energy inside the PBG structure was realized in our experiments.

Here we present and discuss results of experiments on second-harmonic generation (SHG) and sum-frequency generation (SFG) with femtosecond laser pulses. We have measured the efficiency of SHG and SFG processes versus the angle of incidence of p- and s-polarized incoming beam and shown that the shape of the angular distributions is in a good agreement with calculated one from [6]. Moreover, we have shown that the shape of the SH spectra is strongly depended on chirp parameters of the incident femtosecond pulses.

The ZnS/SrF_2 periodical structure used in the experiments consists of 7 pairs of alternate layers of high (ZnS, n_1=2.29) and low (SrF_2, n_2=1.52) refraction index layers. The X-ray diffraction analysis of the structure has shown that the ZnS in the layers is presented mainly in the β-ZnS poly-crystalline form and the SrF_2 structure is the amorphous one. This periodic structure reflects light strongly at the normal incidence in the wavelength range of 745-830 nm.

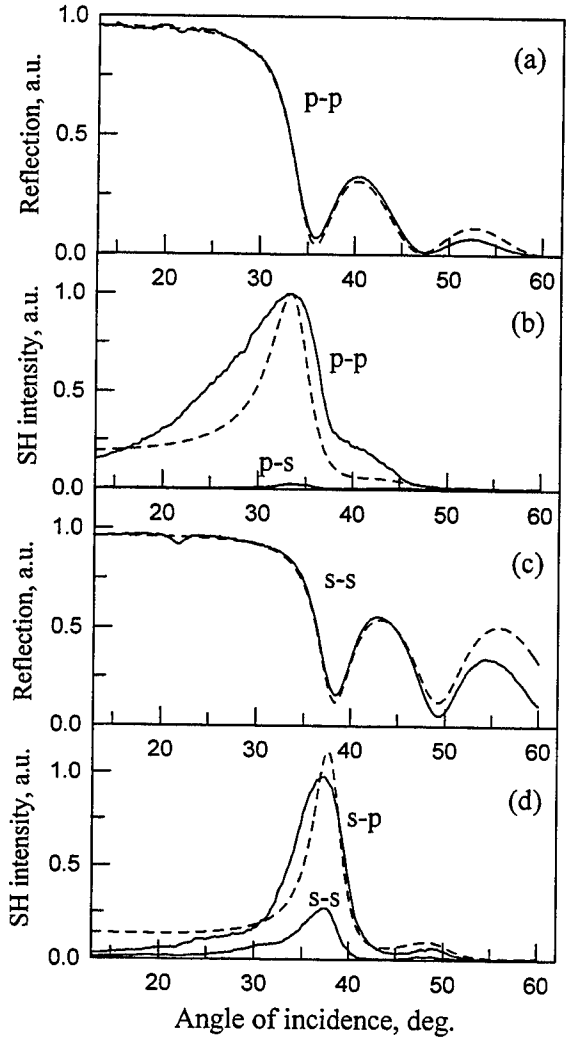


Fig.1. The angular tuning curves of linear Bragg-reflection (a, c) and reflected SH signal (b, d) for different sets of input and output polarizations (p-p, p-s, s-s, s-p). All curves are normalized. The angle is given relatively to the normal to the multilayer structure.

Our experimental setup for SHG was based on Ti:Sapphire laser with a wavelength centered on 780 nm, pulse duration 100 fs, and the pulse repetition rate of 100 MHz. In our experiments on SFG we used setup based on Coherent Inc. femtosecond laser system: Mira-900, regenerative amplifier RegA-9000 and optical parametric amplifier OPA-9400. The PMT and the lock-in-amplifier technique was used for detection of the SH and SF signal. The sample was mounted on the rotary part of the goniometer in order to vary and align incident angles.

Experimental fundamental and SH intensities reflected from the structure as a function of the incident angle are presented in Fig.1 by solid lines. The fundamental wavelength is turned in the PBG for the normal incidence, and the SH frequency is away from either Bragg or absorbing resonance. The dashed curves are calculated from the theory developed in [6].

The linear reflection curves for p- and s-polarized incoming field in the Fig.1 (a, c) exhibit the angular shift of the photonic band edge. There are sharp maxima corresponding to enhancement of SHG in Fig.1 (curves b, d) at the angle of around 33 deg for p-incident polarization

and at the angle of around 37 deg for s-incident polarization. The maxima are localized near the middle of photonic band edge. Moreover, we observed the angular shift of both the SH maximum and the photonic band edge depending on the polarization of incident field also for transmitted signal.

We would like to point out that there is the real enhancement of the SH signal in the PBG structure. The enhancement can be estimated as more than 330 times relative to the single ZnS layer (with the same $d_i = 3\lambda/4n_i$ thickness at $\lambda = 780$ nm) deposited on the same glass substrate.

In conclusion, we have observed the enhancement of second-harmonic and sum-frequency generation with femtosecond laser pulses in one-dimensional photonic crystal near the photonic band edge. The mechanism of enhancement is the increasing of the field on the fundamental frequency within the structure near the band edge. It leads to the strong dependence of the SH and SF signal intensity shapes and the peak positions for different incoming light polarizations on the incident angle.

References

1. E.Yablonovitch, J. of Modern Optics **41**, 173 (1994).

2. "Development and Applications of Photonic Band Gap Materials", ed. by C.M.Bowden, J.P.Dowling, and H.O.Everitt, special issue of J.Opt.Soc.Am. B 10, 279 (1993).

3. B.I Mantsyzov and R.N.Kuz'min, Sov.Phys.JETP **64**, 37 (1986); W.Chen and D.L.Mills, Phys.Rev.Lett. **58**, 160 (1987); C.Conti, S.Trillo, and G.Assanto, Opt.Lett. **22**, 445 (1997).

4. N.Bloembergen and A.J.Sievers, Appl.Phys.Lett. **17**, 483 (1970).

5. M.Scalora, M.J.Bloemer, A. S. Manka, J. P. Dowling, C. M. Bowden, R.Viswanathan, and J.W.Haus, Phys. Rev. **A 56**, 3166 (1997).

6. A.V.Balakin, D.Boucher, V.A.Bushuev, N.I.Koroteev, B.I.Mantsyzov, P.Masselin, I.A.Ozheredov, A.P.Shkurinov, Opt.Lett 1999 (in press).

Nonlinear Guided Waves and Their Applications

Frequency Conversion and Cascaded Nonlinearity

Thursday, 2 September 1999

Alain Villeneuve, University of Laval, Canada
Presider

ThC
13.30-15.00
Salle Morey—St-Denis

Frequency conversion and switching in birefringent fibers

G. Millot, E. Seve, and S. Wabnitz

LPUB, CNRS, 9 Av. A. Savary, BP 47 870, 21078 Dijon, France
millot@jupiter.u-bourgogne.fr, seve@jupiter.u-bourgogne.fr, Stefan.Wabnitz@alcatel.fr

S. Trillo

Fondazione Ugo Bordoni, Via B. Castiglione 59, 00142 Rome and University of Ferrara, Italy
strillo@fub.it

In optical fibers, the interplay of the optical Kerr effect and chromatic dispersion leads to modulational instability (MI) [1]: a continuous wave undergoes a modulation of its amplitude or phase in the presence of quantum noise or a frequency shifted signal wave (induced-MI). MI can be induced into a normally dispersive optical fiber by cross-phase modulation between two copropagating pumps [2]. This CPM-induced MI is also called vector modulational instability. In the temporal domain, induced-MI leads to the break-up of uniform disturbances into modulated structures and can be used to generate soliton-like pulse trains with a high repetition rate fixed by the pump-signal frequency detuning. This process is associated, in the spectral domain, with the frequency conversion of a pump beam into a *cascade* of sidebands.

Another interesting application of vector MI is the frequency conversion of a pump into a *single* sideband pair. In this case, the MI mechanism may be directly viewed in the frequency domain as the parametric interaction of a central-frequency wave with a pair of Stokes and anti-Stokes sidebands. In the first stage of the propagation of the pump wave, and for sufficiently weak input signal the momentum conservation leads to the usual nonlinear phase-matching condition which in turn determines the peak gain modulation frequency. However, for longer fiber lengths, a substantial fraction of pump energy is transferred into the sidebands. This may occur at frequency detunings which may strongly deviate from the usual MI small-signal predictions even for relatively weak (i.e., a few percents of the pump power) input signals. Clearly, a model which takes into account the pump depletion is necessary to describe the strong frequency conversion regime of MI. Such a model was developed for vector MI [3-4] and later succesfully applied for the analysis of experimental results on the strong depleted regime of polarization modulational instability (PMI) in a low-birefringence fiber [5]. This model is based on a three fourier modes truncation of the coupled nonlinear Schrödinger equations (CNLE's) : the resulting system of ODE's describes well the nonlinear evolution of the field in each mode.

In this work we present the observation of strong frequency conversion by vector MI in the normal dispersion regime of a highly birefringent fiber. Modulational instability is induced by mixing a pump beam with a copropagating Stokes signal wave. The pump is polarized at 45° from the birefringence fiber axes and the Stokes signal wave is polarized along the slow axis. The anti-Stokes sideband is parametrically generated from noise on the fast axis.

The experimental setup that we employed for the observation of induced vector MI in a highly birefringent fiber consists of two different laser sources producing nanosecond pulses. With such pulse durations, the two waves can be considered as quasi-cw in comparison with the MI period (hundreds of femtoseconds). The pump pulses were delivered by a cw tunable ring dye laser, pumped by a cw argon laser and amplified by a three-stage dye amplifier. The dye amplifier was pumped by a frequency-doubled, injection-seeded, and Q-switched Nd:YAG laser operating at a repetition rate of 25Hz. Vector MI was induced by a weak signal beam from the Nd:YAG laser that was Raman-shifted in a multiple-pass carbon dioxide cell. The pump and signal pulse widths were

4ns and 2ns, respectively. In all of our experiments, the pump wavelength was tuned around λp=572nm and the signal wavelength was fixed to λs=574.72nm. Pump and signal beams were finally combined by a beam splitter, and focused with a 20x microscope objective in a hi-bi fiber (HB600 Fibercore) of 1.8m. The short length of fiber led to negligible Raman-induced pump depletion. At the fiber output, ligth was analyzed with a spectrometer and with a second-harmonic generation autocorrelator.

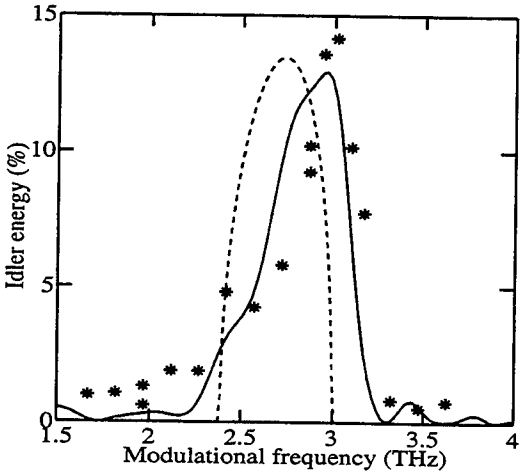


Fig. 1. Comparison between measured (star) and calculated (solid line) generated idler energy vs. signal frequency. The parametric gain (dashed line) is reported with an arbitrary vertical scale.

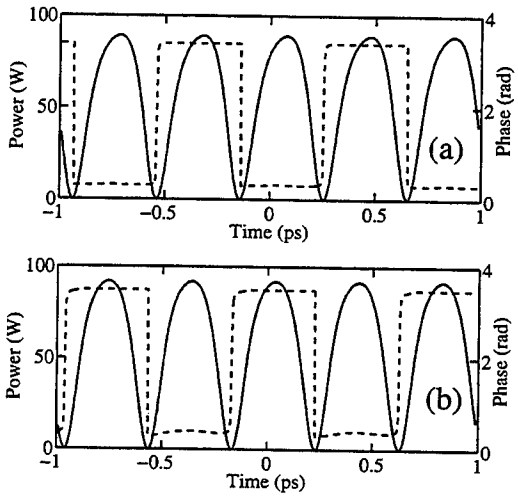


Fig. 2. Theoretical time dependence of output powers (solid curves) and phases (dashed curves) of cw dark soliton trains in the slow (a) and fast (b) fiber axis.

In order to observe the frequency conversion of a single Stokes signal into the conjugated idler, the pump power and pump-signal frequency detuning were carefully chosen such that the unstable frequency band was relatively narrow. Therefore, all the intensities of high-order harmonics were weak, except for the first sideband pair as observed in the experiment. Figure 1 compares the variation of the experimental idler conversion (stars) versus pump signal detuning with the theoretical gain curves obtained from the linear stability analysis (dashed line) and from our three-wave model (solid line). The pump and signal powers are 56W and 6.2W respectively. The idler conversion is maximum (14%) at frequency detuning just above the highest bound of the small-signal gain bandwidth, that is for a initially phase-mismatched process. This experimental data are in good agreement with the three-wave model taking into account the asymetric seed of MI and the pulsed profile of pump and signal waves. The corresponding signal fraction is equal to 24% which corresponds to a total frequency conversion from the pump towards the first sideband pair of 38%. A total energy conversion of about 60% was obtained for a pump (signal) power of 112W (5.9W). We also observed that, for a suitable fiber length, a strong transfer of energy between the pump and the signal-idler sidebands at the fiber output was induced by a small variation of the input signal power.

On the other hand, we shall report on experimental observations of frequency conversion from the pump beam into a cascade of sidebands which, in the time-domain, represent a periodic train of vector dark solitons. The two polarization components of the vector dark soliton train exhibit a cross-trapping that maintains the polarization state of the total field unchanged upon propagation. This interaction was analytically studied with a variational approach [6], whereas the connection between MI and the vector dark soliton was investigated by numerical solutions of the CNLE's as in Fig. 2. Here the pump power is P=112W, the signal power is 2W, and the frequency detuning is 2.5THz. As can be seen, the output temporal profiles of the pulse train generated on both axes are a periodic train of dark solitons. This statement is confirmed by the phase profile of the generated pulse trains which are flat across each pulse, with a π phase change in the dip, which is a characteristic property of

dark solitons. Figure 3 shows the observed spectra at the fiber output for slow and fast axes. The simulations, which take into account the pulsed nature of the beams show a good agreement with the experimental results. An excellent agreement is also obtained between the theoretical and observed auto-correlation traces on each axis (see Fig. 4).

A detailed comparison with earlier results on frequency conversion in a low-birefringence fiber will also be presented.

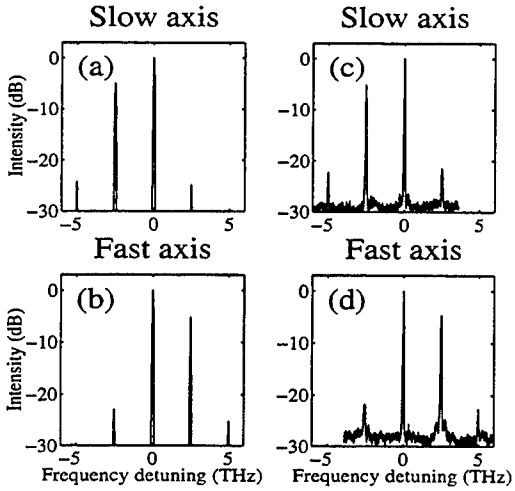


Fig. 3. Theoretical pulse averaged (a)-(b) and experimental (c)-(d) spectra from (top) slow and (bottom) fast axis.

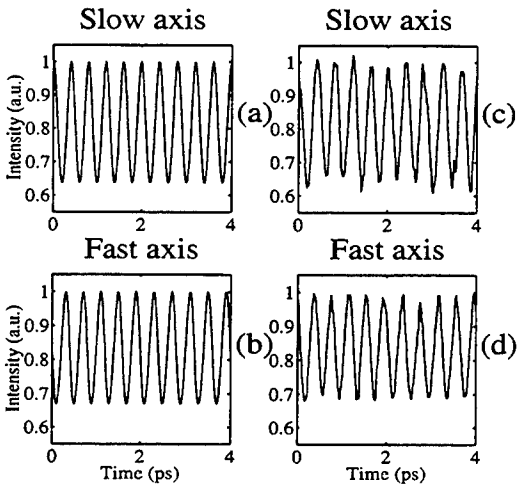


Fig. 4. Theoretical (a)-(b) and experimental (c)-(d) autocorrelation traces from the slow (top) and fast (bottom) fiber axis

References

[1] K. Tai, A. Hasegawa, and A.Tomita, Phys. Rev. Lett. **56**, 135 (1986).
[2] A.L. Berkhoer and V.E. Zakharov, Sov. Phys. JETP **31**, 486 (1970).
[3] G. Cappellini and S. Trillo, Phys. Rev. A **44**, 7509 (1991).
[4] C. De Angelis, M. Santagiustina, and S. Trillo, Opt. Lett. **19**, 335 (1994); Phys. Rev. A **51**, 774 (1995).
[5] G. Millot, E. Seve, S. Wabnitz, and S. Trillo, Phys. Rev. Lett. **80**, 504 (1998); E. Seve, G. Millot, S. Trillo, and S. Wabnitz, J. Opt. Soc. Am. B **15**, 2537 (1998).
[6] Y.S. Kivshar and S.K. Turitsyn, Opt. Lett. **18**, 337 (1993).

Nondegenerate four-wave mixing in DFB lasers and its applications

H. Kuwatsuka
Fujitsu Laboratories Ltd.
Morinosato-Wakamiya 10-1, Atsugi, 243-0197, Japan
Tel: +81-462-50-8249
Fax: +81-462-48-5193
E-mail: hkuwa@flab.fujitsu.co.jp

Nondegenerate four-wave mixing (NDFWM) in semiconductor gain materials has been extensively studied. High speed wavelength converters and phase-conjugate wave converters can be realized using this phenomenon. Semiconductor optical amplifiers (SOAs) are widely used for experiments. A lot of excellent results have been obtained using SOAs [1]. Semiconductor laser diodes (LDs) are another devices in which NDFWM occurs. Because the lasing waves in themselves can be used as the pump beams, we can realize the wavelength converters without external pump sources[2]. In this talk, we introduce our experimental results of NDFWM in distributed feedback (DFB) LDs and an application for the compensation of the chromatic dispersion in optical fibers.

Figure 1 shows the device structure for experiments. We used $\lambda/4$-shifted DFB-LDs. When the wavelengths of the input signal wave and the output conjugate wave are outside the stop-band, the waves do not interact with the corrugation. The LDs function as traveling-wave SOAs for the signal and conjugate waves. Due to the $\lambda/4$-shifted structure, the lasing wave is stable at the middle of the stop-band even if the signal wave is injected. The conjugate is generated by the interaction between the signal wave and the lasing wave traveling toward the same direction with the signal. The conjugate wave generated by the interaction between the signal wave and the lasing wave traveling toward the opposite direction does not grow, because the phase-match condition is not satisfied. Figure 2 a) and b) show the spectra from rear facet of a DFB laser when a signal is put into the front facet. In addition to the lasing wave functioning as pumps and the amplified signals, the third wave is observed, which is the conjugate wave.

The conversion efficiencies from the input signal to the output conjugate are shown in Figure 3. The conversion efficiency increases when the detuning between the pump and the signal decreases. The conversion efficiencies of the positive detuning are always larger than those of the negative detuning. These detuning dependence of the conversion efficiencies are similar to the FWM in SOAs.

The basic mechanisms of NDFWM in LDs are the same with those in SOAs. The carrier density pulsation (CDP) effect, the carrier heating (CH) effect, and the spectral hole burning (SHB) effect contribute to the NDFWM in LDs. The interference of these three effects enhances the conversion efficiencies of the positive detuning and suppresses the efficiencies of the negative detuning.

The differences between the FWM in DFB-LDs and that in SOAs are the clamping of the linear gain and the existence of the lasing-wave traveling toward the opposite direction of the signal. In the DFB-LDs with a κL of nearly 1.25, the saturated gain and the carrier concentration are almost uniform along the

cavity.

Because the linear gain is clamped at a small level, the conversion efficiencies of the DFB lasers are smaller than those of the SOAs. To overcome the small gain, we have proposed and demonstrated the in-line integration of two SOAs and a DFB laser[3]. Because of the increase of the linear gain due to the integration of SOAs and the increase of $\chi^{(3)}$ due to the adoption of compressively strained QWs, a high conversion efficiency of +5 dB at the detuning of 300 GHz has been demonstrated using the structure[3].

A polarization-insensitive phase-conjugate wave converter by using bi-directional FWM in a DFB-LD has been proposed and demonstrated [4]. Figure 4 shows the configuration of the converter. The signal light is insident on an optical circulator followed by a polarization beam splitter (PBS) through which the signal is divided into two orthogonally polarized components. A x-component (counterclockwise), which is the same polarization as that of the DFB-LD, is incident on the first facet of the DFB-LD and converted to a conjugate wave. The polarization state of a y-component (clockwise) is converted to the same polarization with the x-component by using 90° twisted poarization maintaining fiber, and then incident on the second facet of the DFB-LD. The wave is converted to a conjugate wave in the LD. The two converted waves are coupled through the PBS and output from the third port of the optical circulator. When the injection currents in three electrodes are controlled to give the same conversion efficiencies for the x-component and the y-component, polarization-insensitive conversion can be realized.

The chromatic dispersion of optical fibers was compensated by the phase-conjugate wave generator. The signal light was intensity-modulated with a l0 Gbit/s NRZ data stream (PN: 2^{23}-1). At the receiver, the optical signal was amplified and detected by a pin photo-detector after passing through an optical filter with a 1 nm bandwidth. The receiver sensitivity at a bit error rate (BER) of 10^{-9} for back-to-back measurement was -33.4 dBm. The observed power penalty for the generated conjugate was 0.8dB for a signal with 0° polarization. There was little dependence of the penalty on the polarization of the signal. The penalty was mainly due to S/N degradation through the conversion. The BERs before and after l00 km transmission using the phase conjugate generator are shown in Figure 5. In this experiment, the signal was transmitted through the first standard fiber (50 km) with a dispersion of +18.2ps/nm/km before input to the converter. The phase-conjugate wave was then transmitted through the second fiber (50km) with a dispersion of + 17.8 ps/nm/km. The input power into two fibers was set to +3dBm. The waveform distortion was compensated for with a power penalty of 1.1 dB. This penalty can be decreased by increasing the conversion efficiency. Detected eye patterns, given in Figure 6, show good eye-opening and waveform recovery.

In summary, a phase-conjugate wave converter without external pump sources has been realized by using NDFWM in a DFB-LD.

References

[1] F. Girardin, J. Eckner, G. Guekos, R. Dall'Ara, A. Mecozzi, A. D'Ottavi, F. Martelli, S. Scotti and P. Spano, "Low-Noise and very high-efficiency four-wave mixing in 1.5-mm-long semiconductor optical amplifiers," IEEE Photon. Technol. Lett., Vol.9, No.6, pp746-748, 1997

[2] H. Kuwatsuka, H. Shoji, M. Matsuda, and H. Ishikawa, "Nondegenerate four-wave mixing in a long-cavity λ/4-shifted DFB laser using its lasing beam as pump beams, " IEEE J. Quantum Electron. Vol. 33, No. 11, pp2002-2010, 1997

[3] T. Simoyama, H. Kuwatsuka, B. E. Little, M. Matsuda, Y. Kotaki and H. Ishikawa, "High efficiency wavelength conversion using FWM in a DFB laser with SOA integration, " Post deadline paper of ISLC (Nara, Japan, 1998), PD-7

[4] S. Watanabe, H. Kuwatsuka, S. Takeda and H. Ishikawa, "Polarization-insensitive wavelength conversion and phase conjugation using bi-directional forward four-wave mixing in a lasing DFB-LD," Electron. Lett., Vol. 33, No. 4, pp316-317, 1997

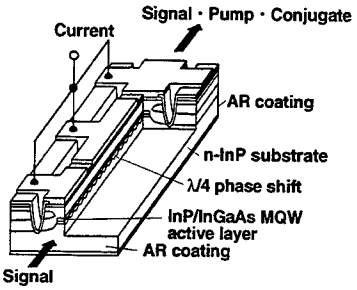


Figure. 1 Device structure of a λ/4-shifted DFB LD for FWM wavelength conversion.

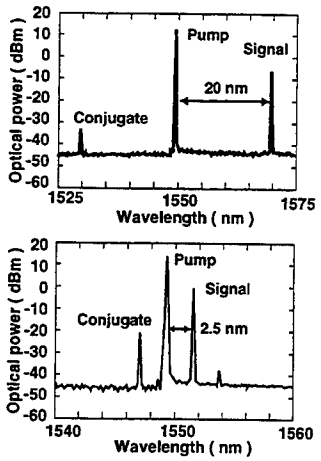


Figure. 2 Spectra from the λ/4-shifted DFB laser with a input signal. a) The case of the detuning of 20 nm. b) The case of the detuning of 2.5 nm.

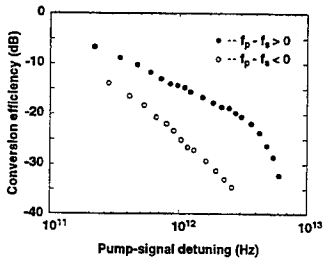


Figure. 3 The conversion efficiency from input signal to the versus pump-signal detuning.

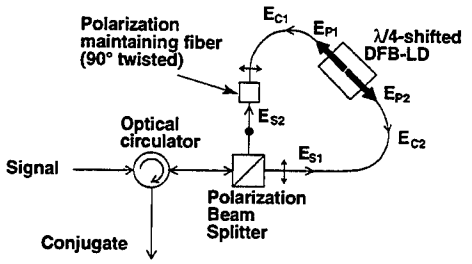


Figure. 4 Configuration of polarization-insensitive phase-conjugate wave generator.

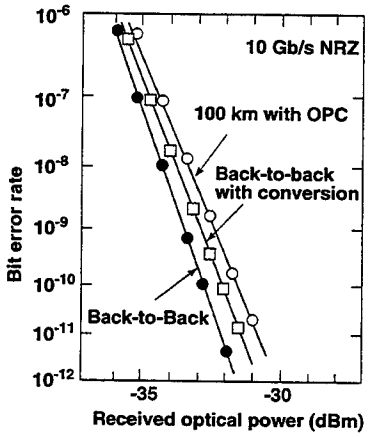


Figure. 5 Bit error rate characteristics of 10 Gbit/s.

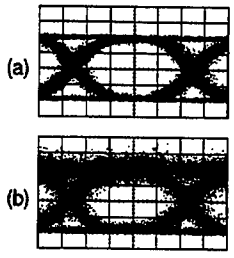


Figure. 6 Detected eye-patterns.a) Before transmission.b) After 100km transmission. Horizontal axis: 20ps/div.

Wavelength shifting through cascaded second-order processes in a lithium-niobate channel waveguide

I. Cristiani, L. Tartara, M. Rini, G. P. Banfi and V. Degiorgio
Istituto Nazionale per la Fisica della Materia and Dipartimento di Elettronica
Università di Pavia, via Ferrata 1, 27100 Pavia, Italy
tel ++39 0382 505221 fax ++39 0382 505221
ilaria@ele.unipv.it

In communications systems an all-optical device capable to frequency shift a signal is essential in order to perform optical routing and space switching, thus allowing the network to be completely transparent to signal format and bit rate [1]. The most investigated methods exploit the nonlinearities of semiconductor optical amplifiers (SOA) [1]. However, it's worth considering alternative techniques based on nonlinear processes of second-order, namely difference-frequency generation (DFG) [2] and cascading of two second-order processes [3,4]. In DFG the pump beam frequency is quite different from that of the signal; this is not convenient from a technological point of view and makes difficult the spatial mode matching in waveguide devices. On the contrary, in the cascaded process a pump field with frequency close to ω_s is used: the second-harmonic (*SH*) of *p*, which is generated in the same crystal, acts as driving field for the parametric interaction [3,4]. Our group recently demonstrated that an efficient wavelength shifting can be attained by a cascading technique with pump intensities as low as a few MW/cm^2 [5]. The efficiency should be markedly improved when going from bulk to waveguide as the optical confinement and modal propagation provide a larger interaction length. Preliminary results are reported in ref. [6].

In this paper we describe a wavelength shifting experiment at wavelengths about 1100 nm based on cascading in a lithium niobate x-cut channel waveguide. The waveguide was manufactured by Pirelli Cables & Systems, Milano, Italy and it is 58 mm long and 6 μm wide. It has excellent optical quality: the estimated linear losses in the infrared amount to 0.2 dB/cm. At 1100 nm, the wavelength used in our experiment, the channel waveguide is nearly monomodal, with an effective mode section around 80 μm^2. The sample is housed in a copper block temperature-controlled to better than 0.1° C. End-fire coupling was used to insert the optical pulses into the guide. Type I phase-matching for second harmonic (*SH*) generation of the pump can be obtained by an appropriate choice of either temperature or wavelength. The pulses *p* and *s* are provided by two BBO-based optical parametric oscillators (OPO), synchronously pumped by the *SH* of the output of a Nd:YAG active-passive mode-locked laser with 10 Hz repetition rate. The OPOs deliver trains of 5 - 6 pulses, each of ≈ 20 ps time duration, separated by 10 ns intervals. The FWHM spectral width of *p* at 1100 nm is 0.3 nm and that of *s* is sligthly larger. The TM polarization of both incident beams is parallel to the x-axis of the crystal. At the output, *SH* is easily discriminated from the IR by using color filters, while the energies of *s* and *f* are separately assessed by employing a monochromator equipped with an S1 photomultiplier and/or a commercial optical spectrum analyzer (ANDO, AQ-6315). We denote by W the energy of a single pulse. From the energy measurements we derive the following quantities: W_p (W_s), the energy the pump (signal) pulse would have at the output in absence of nonlinear conversion, W_{ss}, the energy of the amplified signal pulse at the output, W_f, the energy of the frequency-shifted pulse at the output, and W_{SH}, the energy of the second-harmonic pulse at the output.
We first tested the waveguide for *SH* generation. At fixed pulse energy and temperature, we measured W_{SH} versus λ_p. The results are shown in Fig.1a. The maximum conversion is observed at λ_p = 1103 nm.

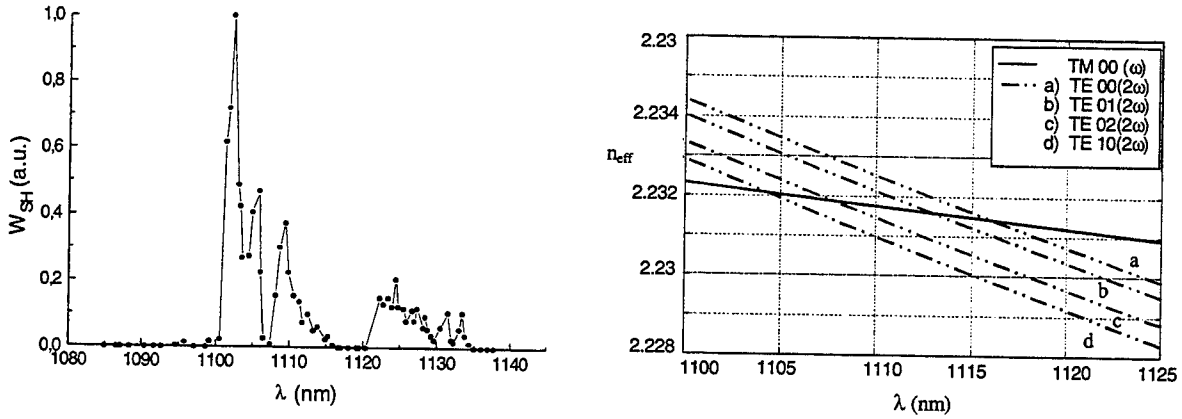


Fig 1.a) Second harmonic vs pump wavelength. b) Effective mode indices of pump and second harmonic vs pump wavelength

The spectral peak structure is due to the interaction of the fundamental mode of *p* (TM00) to the several guided modes of *SH* (TE00, TE01, TE02,TE10) and to the presence of a weakly excited second mode of *p*. In Fig. 1.b are reported the calculated effective mode indices of *p* and *SH* as a function of λ_p; the results appear in good agreement with experiment. The dominant contribution is given by the interaction TM00 (ω) →TE10(2ω) that corresponds to the peak at λ_p = 1103 nm, while the interaction TM00(ω) →TE01(2ω) is not effective as the overlap integral of the spatial modal distributions can be considered as zero. Our calculations suggest that the low power *SH* generated about 1125 nm could be attributed to the interaction of TM01 mode of *p* with the modes of *SH*.

By simultaneously coupling inside the waveguide the pump *p* with $\lambda_p \approx 1103$ nm and the signal *s* with $\lambda_s \approx 1107$ mm a new beam is generated at $\lambda_f \approx 1099$ nm. Although we did not investigate systematically the dependence of η on Δλ, we have data showing no reduction in efficiency when Δλ is increased up to Δλ = 7 nm.

When η becomes appreciable, it is also possible to measure independently the parametric amplification of *s*, defined as $\rho = W_{ss}/W_s$. A plot of both ρ and η versus pump energy is

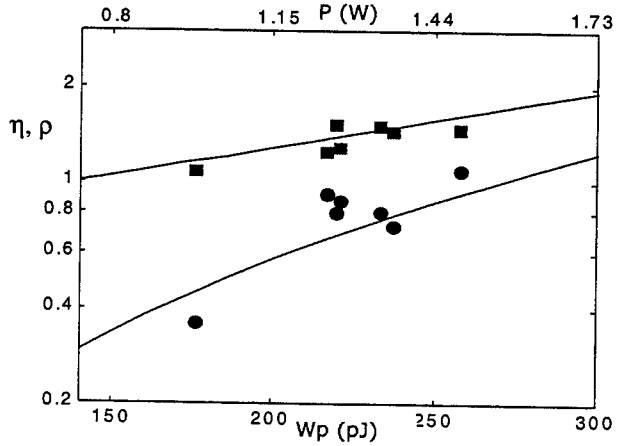


Fig.2 Conversion efficiency η (●) and amplification of signal ρ (■) as a function of W_p

reported in Fig.2. The data have been taken with a signal energy $W_s \approx 10$ pJ. We see that the measured values of ρ and η are fully consistent. One can notice, in particular, that $\eta \approx 1$ is obtained with $W_p \approx 250$ pJ. To compare the data of Fig.2 with the predictions of a simple model dealing with stationary fields we considered the propagation equations for the fields *p*, *s*, *SH* and *f*, by including the overlapping factor between the fundamental modes of *p* and *SH* . The equations have been solved under the following assumptions: monochromatic pump, $\Delta k = 0$ (Δk denotes the mismatch for SH generation: $\Delta k = k_{SH} - 2k_p$), $d_{31} = 4.6$ pm/V, linear losses of the waveguide: 0.2 dB/cm at 1100 nm and 0.4 dB/cm at 550 nm. Spatial overlap integrals of the interacting fields are taken into account. The calculated dependence of η and ρ on the pump power P (the P values are shown on the upper abscissa scale) is given by the solid lines in Fig.2. The trend is fully consistent, but in order to fit quantitatively the calculations to the experimental data, we had to scale down by a factor 5 the experimental pump energy. It should be noted that describing our experimental situation with a stationary model is a crude simplification. In fact, for the 58 mm propagation length in the lithium niobate crystal, we calculate the spectral acceptance for SH generation to be 0.06 nm, which is about 5 times smaller than the spectral width of the pump in the experiment. One can conjecture that the conversion process can use only 1/5 of the pump power. Such a consideration can explain the origin of the scaling factor that was applied in order to fit theory to experiment.

As a conclusion, we have shown that an efficient generation of a wavelength shifted pulse of 20 ps duration can be obtained in a 58-mm LN channel waveguide, at a wavelength around 1100 nm, through a cascaded second-order process by employing a pump pulse of about 250 pJ. A straigthforward improvement to 50 pJ pulse energy (or 1 W pump power) is expected when using transform limited pulses. It should be recalled that the present trend is to use PPLN, where one can benefit at the same time of a considerably larger d_{eff} and of an easy phase-matching at the desired wavelength. The data presented here put on a sounder basis our earlier prediction [5] indicating that, by using a PPLN channel waveguide of good optical quality [7], it should be possible to generate frequency-shifted 10 ps pulses at unit efficiency by using 1 pJ of pump energy (or 0.2 W of pump power).

References

1. S. J. B. Yoo , J. Lightwave Technol.**14**, 955 (1996).
2. C. Q. Xu, H. Okayama, and M. Kawahara, Appl. Phys. Lett. **63**, 3559 (1993). C. Q. Xu, H. Okayama; S.J. B. Yoo , C. Caneau, R. Baht, M. A. Koza, A. Rajhel, and N. Antoniades, Appl. Phys. Lett. **68**, 2609 (1996).
3. H. Tan, G. P. Banfi, and A. Tomaselli, Appl. Phys. Lett. **63**, 2472 (1993).
4. G.I. Stegeman, D.J. Hagan, and L. Torner, Optical and Quantum Electronics **28**,1691 (1996).
5. G. P. Banfi, P. K.Datta, V. Degiorgio, G. Donelli, D. Fortusini, and J. N. Sherwood, Opt. Lett. **23**, 439 (1998).. G. P. Banfi, P. K.Datta, V. Degiorgio, and D. Fortusini, Appl. Phys. Lett. **73**, 136 (1998).
6. C.G Treviño-Palacios, G.I. Stegeman, P. Baldi, and M.P. De Micheli, Electron. Lett. **34**, 2157, 1998.
7. M. A. Arbore and M. M. Fejer , Opt. Lett. **22**, 151 (1997); J. Webjorn, S. Siala, D. W. Nam, R. G. Waarts, and R. J. Lang, IEEE Journ. Quantum. El. **33**, 1673 (1997).

High-Energy Femtosecond Pulse Compression Using the Cascade Nonlinearity

X. Liu, L. Qian, and F.W. Wise

Department of Applied Physics
212 Clark Hall
Cornell University
Ithaca, NY 14853
tel: (607) 255-1184
fax: (607) 255-7658

Pulse compression is a well-established technique for generating optical pulses shorter than those produced directly by lasers or amplifiers. Most commonly, additional bandwidth is generated by self-phase modulation as the pulse propagates nonlinearly in an optical fiber. Compressors based on single-mode fibers are limited to nanojoule pulse energies by higher-order nonlinear effects and ultimately damage to the fiber. Thus, new approaches are needed for compression of the high-energy pulses that are now readily-available from regenerative amplifiers, for example.

One possible approach to this problem was reported by Nisoli *et al.* [1]. These workers achieved large spectral broadening by propagating pulses through a high-pressure noble gas confined in a novel hollow-core waveguide of fused silica. Excellent results were obtained, including compression from 140 to 10 fs. Although the compressed pulse energy is a substantial improvement on that achievable with single-mode fibers, these results do point out a limitation of this approach: the waveguide is lossy. Additional drawbacks include the susceptibility of the waveguide to optical damage, the size and compelxity of the apparatus, and a lack of commercial availability.

Bulk materials can conceivably be used for high-energy pulse compression [2]. As a practical matter, several third-order nonlinear-optical processes occur when high-energy femtosecond-duration pulses interact with a medium. The output beam typically has different frequencies propagating in significantly different directions, and is difficult to control. As a consequence, the use of bulk materials for pulse compression has not found significant use.

Here we show that the effective refractive nonlinearity that arises from the cascading of second-order processes [3] can be exploited for effective pulse compression. We demonstrate pulse compression based on both positive and negative nonlinear phase shifts. In each case 120-fs pulses are compressed by a factor of 3 while maintaining 85% of the input-pulse energy, and higher compression ratios should be possible. Scaling to higher energies will be straightforward, and a practical benefit is that the compressor can consist of simply a frequency-doubling

crystal and a suitably-chosen piece of transparent material.

The phase shift arising from the Kerr nonlinearity is always positive. Therefore, materials with small nonlinear indices are desired for the generation of net negative phase shifts *via* the cascade process. We chose to use a barium metaborate (BBO) crystal 1.7 cm long. Input pulses of duration 120 fs and energy up to 200 μJ at 795 nm were produced by a Ti:sapphire regenerative amplifier. The 6-mm-diameter beam from the regenerative amplifier was compressed to 0.4 mm in one dimension with a cylindrical telescope before passing through the BBO crystal. Typical intensities incident on the crystal were 10 - 80 GW/cm^2.

With phase mismatch $\Delta kL \approx 300\pi$ ($\Delta k = k_{2\omega} - 2k_{\omega}$) the spectrum broadens by a factor of 2 - 3 and develops a multiply-peaked structure due to the negative nonlinear phase shift. Positive group-velocity dispersion (GVD) is required to compensate the negative phase shift, and this greatly simplifies the compressor -- once the optimum dispersion is known, a piece of transparent material can supply the GVD. We used a 1-cm piece of $LiIO_3$, which supplies approximately the desired dispersion. This succeeded in compressing the pulses to 45 fs (Figure 1(a)). The experimental results agree with numerical solutions of the coupled wave equations (Figure 1(b)). In this case the pulse energy is 85% of the input-pulse energy. Most of the loss is due to Fresnel reflections and could be eliminated by anti-reflection coatings on the crystals.

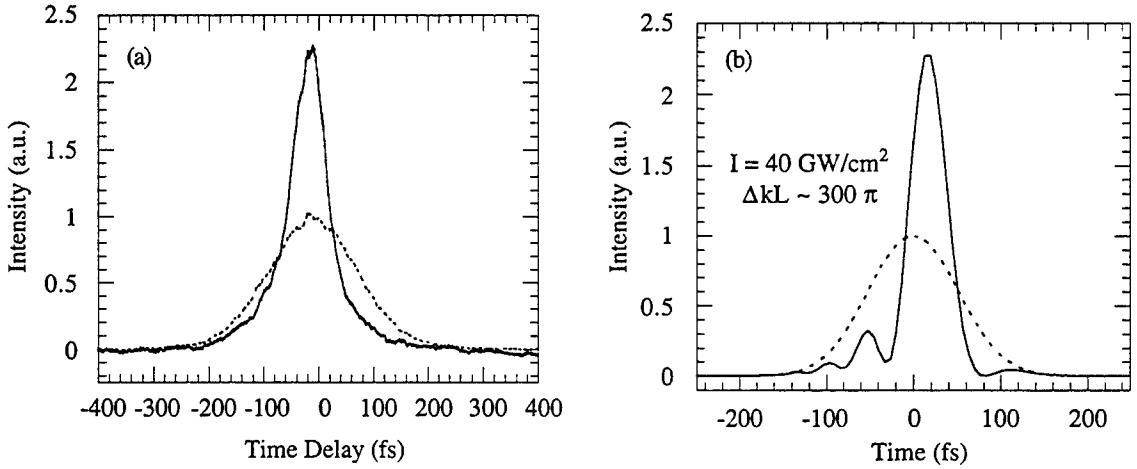


Figure 1. Measured (a) and calculated (b) pulses compressed using negative nonlinear phase shift. The input pulse is indicated by the dashed lines.

A similar compression ratio was achieved using positive nonlinear phase shifts, obtained using a $LiIO_3$ crystal with $\Delta kL \approx -300\pi$. In this case a prism sequence was

used to provide negative GVD, and the compressed pulse energy was reduced owing to 2-photon absorption at the harmonic frequency in $LiIO_3$.

The quadratic compressor based on negative nonlinear phase shifts offers substantial advantages. The compressor is extremely simple, the insertion loss can be well under 10%, and 100-fs pulses can be compressed by a factor of 3 with immediately-available materials. It is reasonable to expect that higher compression ratios will be possible through the use of materials with larger values of $\chi^{(2)}$ than $LiIO_3$ and BBO. To illustrate this point, we performed simulations of pulse compression at 1550 nm, a wavelength for which periodically-poled $LiNbO_3$ is already commercially available. The results (Figure 2) demonstrate a compression ratio of 10 and compressed pulse duration of ~10 fs, obtained with input intensity of less than 10 GW/cm^2.

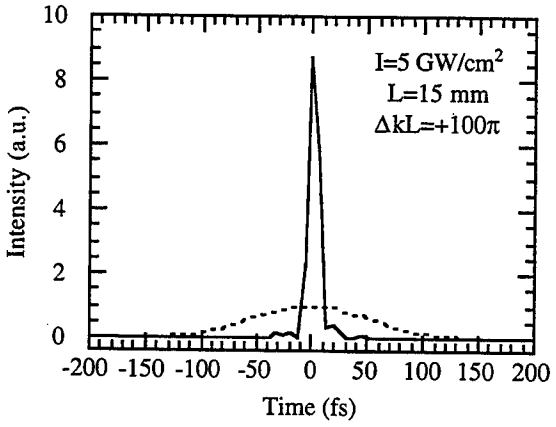


Figure 2. Calculated pulse compression at 1550 nm.

References

1. M. Nisoli, S. De Silvestri, and O. Svelto, *Appl. Phys. Lett.* **68**, 2793 (1996).
2. C. Rolland and P. B. Corkum, *J. Opt. Soc. Am. B* **5**, 641 (1988).
3. H. J. Bakker, P. C. M. Planken, L. Kuipers, and A. Lagendijk, *Phy. Rev. A* **42**, 4085 (1990); R. DeSalvo, D. J. Hagan, M. Sheik-Bahae, G. Stegeman, and H. Vanherzeele, *Opt. Lett.* **17**, 28 (1992).

Nonlinear Guided Waves and Their Applications

Poster Session 2

Thursday, 2 September 1999

ThD
15.00-16.30
Foyer-Bar

Upper limit of power for stationary pulse train generation in modulational-instability fibre laser with intracavity Fabry-Perot filter

E. V. Vanin
Optical Networks Research Laboratories, Ericsson Telecom AB, S-126 25 Stockholm, Sweden
evgeny.vanin@etx.ericsson.se

S. Helmfrid
Industrial Microelectronics Center, Electrum 233, S-164 40 Kista, Sweden
sten.helmfrid@imc.kth.se

High repetition-rate pulsed fibre lasers are very important for future ultra-high-speed communication networks. One of the most promising approaches to fabricate such devices is to take advantage of the effect of modulational instability (MI) in optical fibres [1]. The potential of this method to generate pulse trains up to terahertz repetition rates was demonstrated already in the late 80's [2, 3]. In these experiments the non-linear pulse shaping took place in a fibre externally pumped by a mode-locked laser source. Recently, continuous pulse train generation at more than 100 GHz was demonstrated by Franco *et al.* and Yoshida *et al.* by including a non-linear fibre into the laser cavity [4, 5]. Intracavity pulse shaping reduces the requirement for high pumping power of the device and makes cw pumping feasible. In the experiment by Yoshida *et al.*, a Fabry-Pérot (FP) filter was introduced in the cavity in order to control the repetition rate and reduce the threshold for pulsation. The latter approach is very promising, because the device can be operated with a moderate pump power and the design makes generation of a stationary train of soliton-like transform-limited pulses with a low duty cycle possible. In this paper, we theoretically investigate the dynamics of the MI laser with intracavity FP filter.

The laser ring cavity (see ref. [5]) consists of an amplifying section, a long span of passive fibre, an output coupler, an optical isolator, a band-pass (BP) filter and a FP filter. To model this system, we used the complex Ginzburg-Landau equation [6] in the following form:

$$\frac{\partial A}{\partial z} + id\frac{\partial^2 A}{\partial \tau^2} + i\delta|A|^2 A = \left(\frac{g_0}{1+W/W_{sat}} - \alpha_0\right)A + b\frac{\partial^2 A}{\partial \tau^2}, \qquad (1)$$

where the distance of field propagation z has been normalised to the total cavity length. The coefficient d accounts for the group velocity dispersion, δ for the Kerr nonlinearity, g_0 for the small signal gain, α_0 for the losses and b for the loss dispersion introduced by the BP filter. $W(z) = \int_{\tau}^{\tau+T_R} |A(z,\tau)|^2 d\tau$ is the field energy within a time period corresponding to the free spectral range of the FP filter $T_R = 1/\Delta f_{FP}$, and W_{sat} is the energy saturation parameter of the gain medium.

In our consideration we assume that the FP filter has a high finesse. In combination with optical isolator it results in spectral selection of frequency components that are confined to maximums of the FP-filter transmission. Therefore, the FP filter can be accounted for in the first approximation by considering only solutions with a discrete and equidistant Fourier spectrum. As a result of the spectral filtering, the intensity

profile of the complex field $A(z,\tau)$ will always be periodic with the round-trip time of the FP filter, $|A(z,\tau)|^2 = |A(z,\tau+T_R)|^2$.

To investigate the dynamics of pulse-train formation inside the laser cavity, we numerically solved Eq. (1) by a split-step Fourier method for different frequency detunings between FP- and BP-filter transmission peaks $\Delta f = f_{FP} - f_{BP}$ and for different values of the energy saturation parameter W_{sat}. The laser cavity parameters in our simulations were close to the experiment of Yoshida *et al.* [5]: fibre cavity length is 1.5 km, $d = 1.16\ ps^2$, $\delta = 6.66\ W^{-1}$, $g_0 = 3.45$, $\alpha_0 = 0.23$, $b = 0.25\ ps^2$, and $\Delta f_{FP} = 115GHz$.

First, let us consider the influence of the frequency detuning between the FP and the BP filter on the operation of the laser. The power profile of stationary pulse trains for different frequency detunings is shown in Fig. 1 (a). The laser is operated just above the MI instability threshold when $\Delta f = 0$. The optical pulse train in this case is generated on a cw wave background. When the frequency detuning between the filters increases the contribution of cw background becomes smaller. The optimum configuration is when the centre of BP-filter transmission falls in between FP-filter transmission peaks, i.e. $\Delta f = \Delta f_{FP}/2$. In this case the MI threshold for pulsation takes on its minimum value, and the pulse train is generated without any cw background.

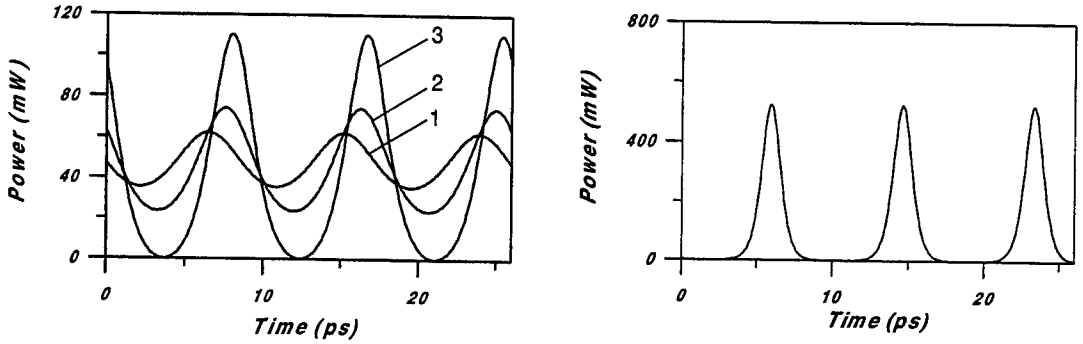


Fig. 1 *Optical power profile of stationary pulse train for (a)* $W_{sat} = 0.03pJ$ *and 1)* $\Delta f = 0$, *2)* $\Delta f = \Delta f_{FP}/4 = 28.75GHz$, *3)* $\Delta f = \Delta f_{FP}/2 = 57.5GHz$; *(b)* $W_{sat} = 0.1pJ$ *and* $\Delta f = 57.5GHz$. *All other laser parameters are defined in the text.*

When the energy saturation parameter is increased the average generated optical power in the cavity also increases. The optical pulses, which form a periodical wave, become shorter and eventually form a train of well separated soliton-like pulses as shown in Fig. 1 (b). The shape of each pulse in this case is well described by the analytical soliton-like solution of Eq. (1), $A(z,\tau) = A_0\,\mathrm{ch}^{-1-i\beta}(\tau/\tau_0)\exp(ihz)$ [6]. Since the group velocity dispersion in the cavity is much higher than the loss dispersion, the pulses presented in Fig. 1 (b) are nearly transform limited.

The fact that the soliton-like pulses show stable propagation inside the laser cavity is actually remarkable. One can see that, in the absence of the FP filter, single soliton-like pulse propagation is not stable, because the zero field background experience positive linear net gain [6]. Any small field perturbation outside the soliton-like pulse will grow when it propagates. In our case, when equidistant spectral filtering is used, pulses form a periodic wave where they interact with each other and suppress any increase of zero field

fluctuations. It follows from this explanation that the pulse train should become unstable when the saturation energy is larger than a certain critical value W_{sat}^{*} and the pulses are very short. Above the critical value, the separation between the pulses is so large compare to the pulsewidth that small field perturbations can grow up before they will be suppressed by bulk soliton-like pulses. In our numerical calculation, the critical value of the saturation energy was $W_{sat}^{*} \approx 0.1pJ$. At this point, the duty cycle of the pulse train reached its minimum value $\tau_{FWHM} / T_R \approx 0.17$. This number gives the theoretical limit for the duty cycle that can be obtained from this laser and shows a good agreement with experimentally obtained data [5].

The results of the numerical simulation that are presented in Fig. 2 demonstrate the presence of a power limit for stationary pulse train generation. In the left plot, $W_{sat} < W_{sat}^{*}$. After a short transient process, the laser field evolves into a stationary train of soliton-like pulses. In the right plot $W_{sat} > W_{sat}^{*}$. Even after a long distance of propagation, the amplitudes and the temporal position of the pulses do not approach any steady state.

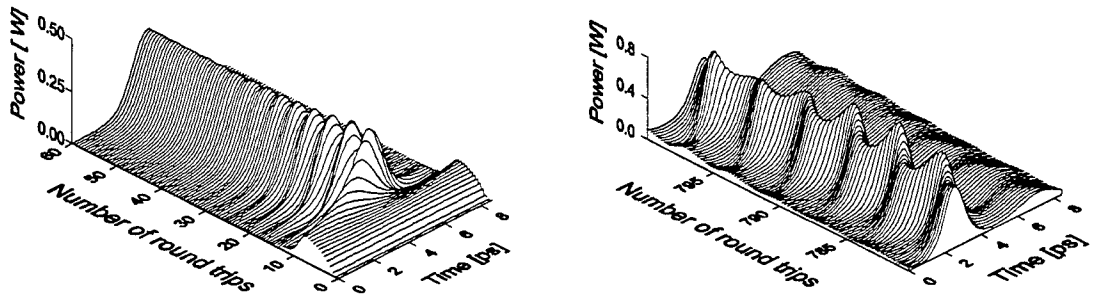


Fig. 2 *Evolution of the intracavity laser field (only one period of the pulse train is shown) for* $W_{sat} = 0.08pJ$ *(left) and* $W_{sat} = 0.15pJ$ *(right). All other laser parameters are the same as on Fig. 1 (b).*

In conclusion, we considered the dynamics of pulse train generation in MI lasers with an intracavity FP filter. We found that the most advantageous alignment of the system is when the BP-filter transmission peak falls in between two adjacent FP-filter transmission peaks. In this case the stationary pulse train is generated without any cw background. The pulses become shorter with increasing power, but the generated pulse train remains stationary only up to some critical value of the power. Above this power level, the pulses show big amplitude and timing jitter. At the critical value, the duty cycle of the pulse train reaches its minimum. The knowledge about the dynamics of the pulse train generation obtained in this work will be very useful in the future development of this type of high-repetition rate fibre lasers.

References

1. A. Hasegawa, Opt. Lett. **9**, 288 (1984)
2. K. Tai, A. Tomota, J. L. Jewell, and A. Hasegawa, Appl. Phys. Lett. **49**, 236 (1986),
3. M. Nakazawa, K. Suzuki, and H. A. Haus, IEEE J. Quantum Electron. **25**, 2036 (1989)
4. P. Franco, F. Fontana, I. Cristiani, M. Midrio, and M. Romagnoli, Opt. Lett. **20**, 2009 (1995)
5. E. Yoshida and M. Nakazawa, Opt. Lett. **22**, 1409 (1997)
6. H. A. Haus, J. G. Fujimoto, and E. P. Ippen, J. Opt. Soc. Am. B **8**, 2068 (1991)

Demonstration of new optical regeneration scheme for dispersion-managed solitons in dense WDM systems

Bruno Dany, Patrick Brindel, Olivier Leclerc and Emmanuel Desurvire

Alcatel Corporate Research Centre,
Route de Nozay, Marcoussis, 91460, France
Bruno.Dany@alcatel.fr, Patrick.Brindel@alcatel.fr, Olivier.Leclerc@alcatel.fr, Emmanuel.Desurvire@alcatel.fr

Ever-increasing capacity needs in long-haul optical communications, particularly in dense and high spectral efficiency WDM systems at 40Gbit/s, require the exploration of novel and high-performance transmission schemes. It is therefore of potential interest to associate two promising technologies such as dispersion management (DM) in soliton propagation /1/ and optical regeneration by synchronous modulation and filtering /2/. However, it is known that filters do not provide efficient amplitude control of DM solitons, as opposed to the "classical" Schrödinger solitons /3/. To remove this limitation, we proposed in /4/ a new "black-box" optical regenerator (BBOR) scheme. The basic idea is to periodically convert the DM soliton into a Schrödinger soliton, the filter recovering its efficiency, then apply soliton regeneration ; upon transmission through the line, the output pulse converts itself back into a DM soliton before it reaches the next regenerator. We have shown the feasibility of a transoceanic 4x40Gbit/s DM soliton transmission system owing to this new regeneration scheme /4/. In this work, we show the compatibility between new BBOR and DM soliton propagation on a 16x40Gbit/s dense-WDM and high-spectral-efficiency transmission system. "Classical" soliton regeneration, as achieved by modulation/filtering of DM solitons, is shown to be comparatively less efficient.

Figure 1a shows the basic BBOR layout. The principle of BBOR is based on the conversion of DM soliton into Schrödinger soliton through propagation in High Dispersion Fibre (HDF)(cf. table 1) with adequate mean power. Then, soliton regeneration by narrow band filtering and intensity modulation is applied. Since narrowband filtering is applied to Schrödinger solitons, it is possible to take full advantage of the filter for stabilisation of amplitude fluctuations. Phase modulation (PM) is first used to reduce timing jitter through propagation in HDF. All simulations take into account realistic component loss, as indicated in the figure. PM/IM depths are set to 80°/8dB.

Figure 1: (a) BBOR layout and (b) transmission line scheme

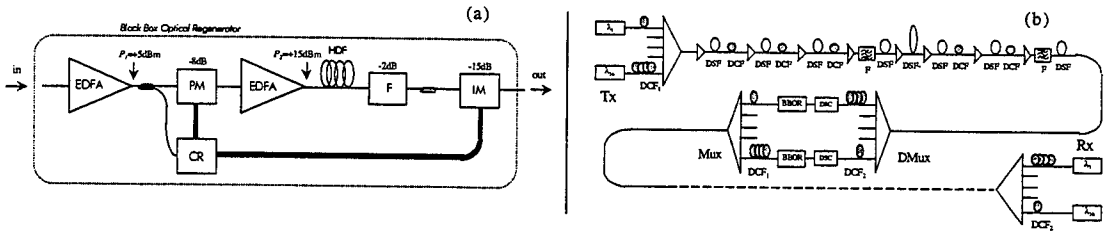


Figure 1b shows the system configuration. The dispersion map is 320km long, corresponding to the regeneration period. The eight DSF+ /DSF- spans are 40km-long while the DCF spans are 1km-long (cf. table 1). The average dispersion and dispersion slope over the dispersion map are, 0.02ps/nm.km and 0.03ps/nm^2.km at λ=1550nm (centre channel 8), respectively. Guiding Fabry-Perot filters are periodically

inserted along the transmission line with 160km periodicity. In order to ensure stable DM propagation, required pre-/post-chirp for each WDM channel is achieved through optimised lengths of DCF_1 and DCF_2. Optical amplifiers are assumed to be flat-gain with 4.5dB noise figure.

Table 1 : Fibres characteristics (D values given at 1550nm)

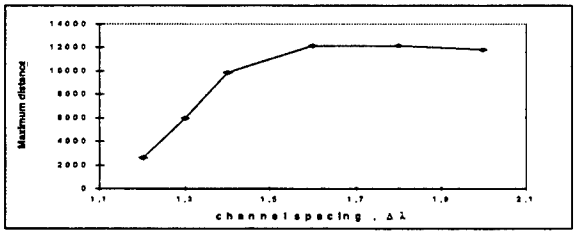
Fibre	D (ps/nm.km)	D' (ps/nm^2.km)	Loss (dB/km)	S_{eff} (μm^2)
DSF+	2.25	0.05	0.2	60
DSF-	-4	-0.06	0.2	40
DCF	-80	-80	0.6	20
HDF	+5	0.05	0.2	60

Every 320km, WDM channels are separately regenerated via a DMux-Mux containing BBORs. In previous work, we showed that the location of the BBORs in the dispersion map is very important to obtain an homogeneous and maximum performance for all WDM channels /4/, resulting, in our system, in individualised DCF_2 and DCF_1 lengths before and after the regenerators. Within the DMux-Mux array, dispersion slope compensation (DSC) is achieved through different fibre spans, matching the cumulative dispersion of each WDM channel to that of channel 8.

Numerical simulations are performed using the scalar non-linear Schrödinger equation. We used 64-bit PRBS sequences with 12.5ps raised-sine. System performance is then evaluated from both timing jitter and amplitude Q-factor measurements on received data, using 3 noise seeds.

We first investigate the 16x40Gbit/s DM soliton system performances and the adequation between BBOR and weak channel spacings compulsory for high spectral efficiency. Centre channel 8 wavelength is set to 1550nm and we proceed to a set of simulations for a channel spacing varying from 1.2nm to 2nm. The optimised EDFA output power is 11dBm (-1dBm/channel). Figure 2 shows the maximum achievable transmission distance (Q=6, BER=10^{-9}) as a function of channel spacing $\Delta\lambda$.

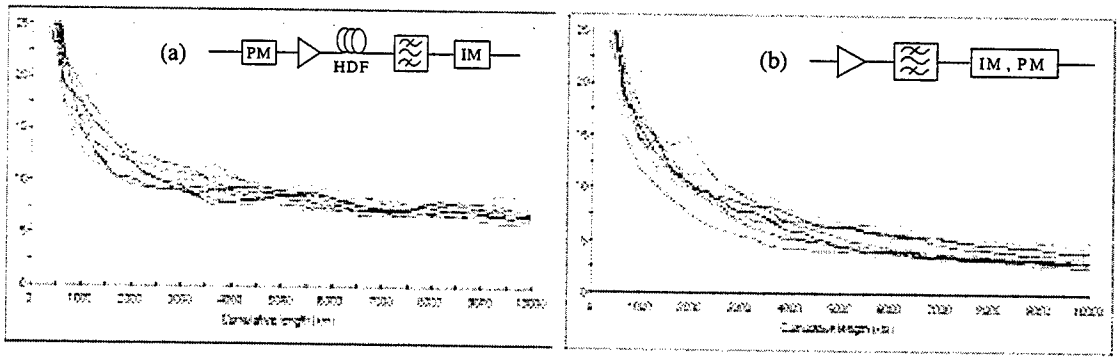
Figure 3: Evolution of the maximum transmission distance (km) vs. channel spacing (nm)



The error-free distance is seen to rapidly decrease for channel spacings smaller than 1.6nm. This can be explained by the increased impairment from nonlinear WDM effects such as XPM and four-wave mixing (FWM), which are enhanced at smaller channel spacing. The slight reduction in transmission distance observed for values of $\Delta\lambda$ greater than 1.6nm is attributed to the effect of dispersion slope. This simulation demonstrates that regeneration through BBORs makes possible a 16x40Gbit/s DM soliton transmission system over transoceanic distances with a channel spacing down to 1.3nm (0.26bit/s/Hz).

Next, we proceed to a comparison between BBOR and "classical" regenerator performances taking as an example a 1.4nm channel spacing. Figure 3 shows the result of this comparison. Q-factor evolution of all 16 channels is represented as a function of DSF transmission distance in both case.

Figure 3: Evolution of Q-factor vs. transmission distance ($\Delta\lambda$=1.4nm) with implementation of (a) BBOR regenerator, (b) "classical" regenerator



When regeneration through BBOR is applied (a), Q-factors are found to slowly decrease with distance, but to reach asymptotic values greater than 6 at 10,000km which is clearly not the case with "classical" regeneration (b) ; indeed, in this case, the error-free achievable distance is limited to less than 3,000km. The stabilisation of Q-factors with distance is clearly due to the efficient control of pulses provided by optical regeneration through BBORs. The only source of degradation of the output signals is observed to be amplitude fluctuations resulting from timing jitter conversion through IM /5/, while timing jitter remains at a stable 0.2ps level at each regenerator output.

In this paper, we have shown that the combination of dispersion management and new "black box" optical regeneration provides dramatic improvement of transmission quality and distance in dense WDM systems. The feasibility of high spectral efficiencies (0.26bit/s/Hz) for 640Gbit/s (16x40Gbit/s) transoceanic systems is demonstrated. The proposed scheme is therefore of great interest for Tbit/s long-haul transmission design.

References:

/1/ N. J. Smith et al.: "Enhanced power solitons in optical fibres with periodic dispersion management", Electron. Lett., 1996, 32, pp. 54.

/2/ M. Nakazawa et al.: "10Gbit/s soliton data transmission over one million kilometres", Electron. Lett., 1991, 27, pp. 1270.

/3/ F.Merlaud, T.Georges: "Influence of filtering on jitter and amplitude fluctuations for dispersion managed solitons", ECOC'98, pp. 497.

/4/ B.Dany et al.: "A transoceanic 4x40Gbit/s system combining dispersion-managed soliton transmission and new black box in-line optical regeneration", Electron. Lett., 1999, 5, pp. 418.

/5/ O.Leclerc et al.: "Assessment of 80Gbit/s (4x20Gbit/s) regenerated WDM soliton transoceanic transmission", Electron. Lett., 1996, 32, pp. 1118.

Variational analysis of non-return-to-zero pulse propagation in optical transmission line

Akihiro Maruta
Graduate School of Engineering, Osaka University
2-1 Yamada-oka, Suita, Osaka 565-0871, Japan
Phone : +81-6-6879-7728, Fax : +81-6-6879-7774, E-mail : maruta@comm.eng.osaka-u.ac.jp

Non-return-to-zero (NRZ) pulse is the most widely used modulation format in optical communication systems. However, the distortion of NRZ pulse due to the group velocity dispersion and the nonlinearity has been theoretically analyzed in few papers[1]. It is an emphatic contrast to many successful experimental and numerical demonstrations([2] and references therein).
Kodama and Wabnitz developed an analytical description of NRZ pulse by means of the WKB approximation of the nonlinear Schrödinger equation[1], but dispersion and nonlinearity of the fiber should be uniform along the transmission line in their analysis. In this paper, we show that the variational method with a properly chosen ansatz provides us with a detailed analysis of NRZ pulse propagation in an optical transmission line. It can be directly applicable for a dispersion-managed line along which the dispersion and/or the nonlinearity change[3],[4]. We also examine the effect of initial frequency chirp for suppressing the pulse distortion.

The pulse propagation in a transmission line having a varying dispersion, nonlinearity, and gain/loss can be described by

$$i\frac{\partial q}{\partial Z} - \frac{d(Z)}{2}\frac{\partial^2 q}{\partial T^2} + s(Z)|q|^2 q = ig(Z)q \ , \quad (1)$$

in normalized units. The normalized quantities, q, T, Z, $d(Z)$, $s(Z)$, and $g(Z)$ express respectively the complex envelope amplitude of electric field E, the retarded time t, the propagation distance z, the group velocity dispersion $k''(z)$, the Kerr nonlinearity $\nu(z)$, and the gain/loss $\gamma(z)$, through $q = E/\sqrt{Q_0}$, $T = t/t_0$, $Z = z/z_{\rm NL}$, $d(Z) = k''(Z)z_{\rm NL}/t_0^2$, $s(Z) = \nu(Z)Q_0 z_{\rm NL}$, and $g(Z) = \gamma(Z)z_{\rm NL}$ with properly fixed time t_0, power Q_0, and nonlinear distance $z_{\rm NL} \equiv 1/(\nu_0 Q_0)$. ν_0 represents a Kerr nonlinearity for normalization and defined by $2\pi n_{20}/(A_{\rm eff0}\lambda)$ with properly fixed nonlinear coefficient of the fiber n_{20}, effective fiber core area $A_{\rm eff0}$, and wavelength of the carrier λ. Using the transformation $q(Z,T) = a(Z)u(Z,T)$, we can rewrite Eq.(1) as

$$i\frac{\partial u}{\partial Z} - \frac{d(Z)}{2}\frac{\partial^2 u}{\partial T^2} + \alpha(Z)|u|^2 u = 0 \ , \quad (2)$$

where $\alpha(Z) = s(Z)a^2(Z)$ and $a(Z) \equiv a(0)$ $\exp\left[\int_0^Z g(Z')dZ'\right]$.

In the Lagrangian variational method[5], a careful choice of proper ansatz for the solution is quite important to ensure the validity of the analysis. We here consider an even NRZ pulse shape. Since the evolution of nonlinear chirp is observed in NRZ pulse propagation[1], we then assume the following solution u in Eq.(2) as a trial function of the variational method,

$$u(Z,T) = \frac{A(Z)}{2}\{\tanh(\tau_+) - \tanh(\tau_-)\}\exp(i\varphi) \ . \quad (3)$$

with

$$\begin{cases} \tau_\pm(Z,T) &= p(Z)\{T \pm T_p(Z)\} \ , \\ \varphi(Z,T) &= \dfrac{E(Z)}{4}T^4 + \dfrac{C(Z)}{2}T^2 + \theta(Z) \ . \end{cases} \quad (4)$$

where $A(Z)$, $p(Z)$, $T_p(Z)$, $E(Z)$, $C(Z)$, and $\theta(Z)$ represent the amplitude, slope of pulse edge, pulse width, nonlinear chirp, linear chirp, and phase respectively. Substituting Eq.(3) into the Lagrangian density of Eq.(2) and applying the variational method, we have

$$\begin{cases} \dfrac{dA}{dZ} &= \dfrac{d(Z)A}{2}\left[C - \dfrac{E}{140p^2}f_A\right], \\ \dfrac{d\tau}{dZ} &= -\dfrac{d(Z)E}{35p^2}f_\tau, \\ \dfrac{dE}{dZ} &= d(Z)\left[320p^6 f_{E_1} + \dfrac{5E^2}{14p^2}f_{E_2} + 4EC\right] \\ & \quad +40\alpha(Z)A^2p^4 f_{E_3}, \\ \dfrac{dC}{dZ} &= d(Z)\left[8p^4 f_{C_1} + \dfrac{E^2}{112p^4}f_{C_2} + C^2\right] \\ & \quad +\alpha(Z)A^2p^2 f_{C_3}, \end{cases} \tag{5}$$

where

$$\begin{cases} f_A(\tau) &= [50f_6(f_0f_2' - 3f_2f_0') \\ & \quad +7f_4(5f_4f_0' - f_0f_4')]/D(\tau), \\ f_\tau(\tau) &= f_0(25f_2f_6 - 7f_4^2)/D(\tau), \\ f_{E_1}(\tau) &= [f_s(f_0f_2' - 2f_2f_0') \\ & \quad +f_s'f_0f_2]/D(\tau), \\ f_{E_2}(\tau) &= [f_6(-3f_0f_2' + 2f_2f_0') \\ & \quad +f_6'f_0f_2]/D(\tau), \\ f_{E_3}(\tau) &= [f_t(f_0f_2' - 5f_2f_0') \\ & \quad +2f_t'f_0f_2]/D(\tau), \\ f_{C_1}(\tau) &= [f_s(3f_4f_0' - f_0f_4') \\ & \quad -2f_s'f_0f_4]/D(\tau), \\ f_{C_2}(\tau) &= [f_6(-f_4f_0' + 3f_0f_4') \\ & \quad -2f_6'f_0f_4]/D(\tau), \\ f_{C_3}(\tau) &= [f_t(9f_4f_0' - f_0f_4') \\ & \quad -4f_t'f_0f_4]/D(\tau), \\ D(\tau) &= f_2(f_0f_4' + f_4f_0') - 2f_2'f_0f_4, \end{cases} \tag{6}$$

with

$$\begin{cases} f_s(\tau) &\equiv 1 + 3\mathrm{cosech}^2\tau(1 - \tau\ \coth\tau), \\ f_t(\tau) &\equiv 4 - 3\coth\tau\{3\tau \\ & \quad +5\coth\tau(1 - \tau\ \coth\tau)\}, \\ f_0(\tau) &\equiv \tau\ \coth\tau - 1, \\ f_2(\tau) &\equiv \tau\ (\pi^2 + \tau^2)\ \coth\tau - (\pi^2 + 3\tau^2), \\ f_4(\tau) &\equiv \tau\ (7\pi^4 + 10\pi^2\tau^2 + 3\tau^4)\ \coth\tau \\ & \quad -(7\pi^4 + 30\pi^2\tau^2 + 15\tau^4), \\ f_6(\tau) &\equiv \tau\ (31\pi^6 + 49\pi^4\tau^2 \\ & \quad +21\pi^2\tau^4 + 3\tau^6)\ \coth\tau \\ & \quad -(31\pi^6 + 147\pi^4\tau^2 \\ & \quad +105\pi^2\tau^4 + 21\tau^6). \end{cases} \tag{7}$$

Here $\mathcal{E} \equiv \int_{-\infty}^{\infty} |u|^2\, dT = A^2 f_0(\tau)/p$ is the total energy of the pulse and a conserved quantity. The function $\tau(Z)$ is defined by $\tau = 2pT_p$. f_i' represents the τ-derivative of f_i , $(i = s, t, 0, 2, 4, 6)$.

Now we examine the validity of the analysis by camparing the results with those obtained by direct numerical simulation of Eq.(1). The system parameters are follows ; fiber dispersion $d(Z) = 0.393$ (-0.05 [ps/(nm·km)]), fiber nonlinearity $s(Z) = 1$ ($n_{20}/A_{\mathrm{eff}0} = 0.4 \times 10^{-9}$ [1/W]), fiber loss $g(Z) = -14.2$ (0.2[dB/km]), carrier wavelength $\lambda = 1.55[\mu\mathrm{m}]$, pulse width $2T_p = 20$ (200[ps] which corresponds to the narrowest pulse in 5 [Gbit/s] system), slope of pulse edge $p = 2$, initial chirp $E = C = 0$ (chirp free), initial peak power $A = 1$ (1 [mW]). amplifier spacing $Z_a = 0.081$ (50[km]). In Figure 1, we compare the waveforms of different pulses observed at 0, 5000, and 10000 [km]. The solid lines are obtained by numerical simulations of Eq.(1) while the dashed ones by the variational method of Eqs.(5). One can see the good agreement between numerical and variational results.

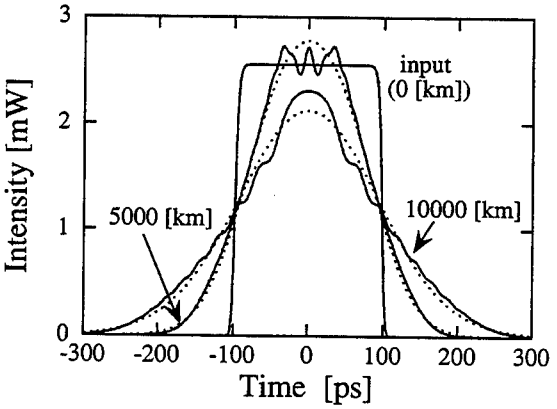


Fig.1 : Comparison of waveforms.

Figure 2 shows the variation of the relative root-mean-square (RMS) pulse widths, $T_{\mathrm{rms}}(z)/T_{\mathrm{rms}}(0)$, along the line. The solid line is obtained by numerical simulations, the filled circles by the variational method, the dashed and dotted lines by analytical expressions, Eq.(6) in [1] and Eq.(26) in [6]. This shows that the variational analysis gives better results than the conventional analysis.

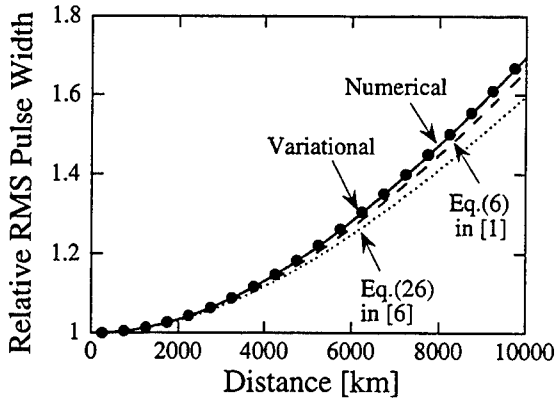


Fig.2 : Variation of the relative RMS pulse widths in a constant dispersion line.

Figure 3 shows the variation of the relative RMS pulse widths in a dispersion-managed line in which $d(Z) = 7.86$ (-1 [ps/(nm·km)]) for 0[km] $< z <$ 40[km] and $d(Z) = -29.475$ (3.75 [ps/(nm·km)]) for 40[km] $< z <$ 50[km] among each amplifier spacing. The average dispersion of this line is the same as the above and the other system parameters are also the same. The solid line is obtained by numerical simulations, while the dotted line by the variational method. This also gives a pretty good agreement between numerical and variational results and shows the applicability of the variational method for analyzing the dispersion-managed line.

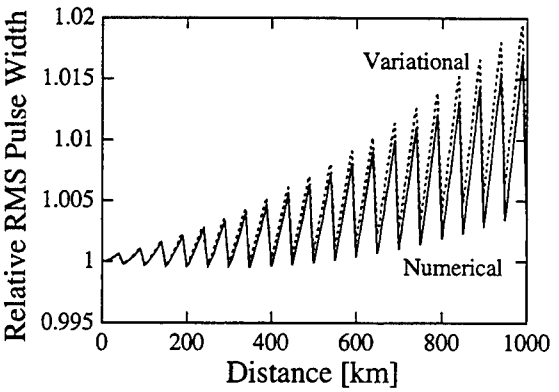


Fig.3 : Variation of the relative RMS pulse widths in a dispersion-managed line.

Proper initial phase modulation is effective to suppress the NRZ pulse broadening[7]. In Figure 4 we campare the variations of the relative RMS pulse widths in the line as the same as that used in Fig.2 for various initial linear chirps, $C = 0, \pm\pi/50$ (0, $\pm$ 0.1 [GHz/ps]). The solid lines and filled circles represent the same in Fig.2.

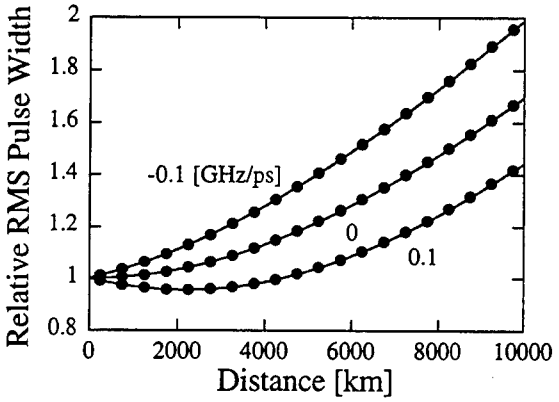


Fig.4 : Variation of the relative RMS pulse widths for various initial linear chirps.

In conclusion, we showed that the NRZ pulse evolution in optical transmission lines can be well explained in the framework of the variational analysis with a properly chosen ansatz for the pulse. This analysis can be easily extended to incorporate perturbation terms and useful to design the optimal line and pulse controller like nonlinear gain[8] or optical filters.

References

[1] Y. Kodama and S. Wabnitz, Opt. Lett. **20**, 2291 (1995).

[2] G. P. Agrawal, *Fiber-Optic Communication Systems*, 2nd ed. (Wiley, New York, 1997).

[3] D. Marcuse, J. Lightwave Technol. **9**, 356 (1991).

[4] E. Lichtman and S. G. Evangelides, Electron. Lett. **30**, 346 (1994).

[5] D. Anderson, Rhys. Rev. A **27**, 3135 (1983).

[6] D. Marcuse, J. Lightwave Technol. **10**, 17 (1992).

[7] Y. Kodama and S. Wabnitz, Electron. Lett. **31**, 1761 (1996).

[8] Y. Kodama, S. Wabnitz, and K. Tanaka, Opt. Lett. **21**, 719 (1996).

Soliton interactions in moderate-strength dispersion managed systems

A. M. Niculae, W. Forysiak, and N.J. Doran
Photonics Research Group, Aston University, Birmingham B4 7ET UK
Tel: +44(0)121 359 3611, Fax: +44(0)121 359 0156, e-mail: W.Forysiak@aston.ac.uk

Dispersion-management offers several advantages for the design of high-speed optical communication systems based on solitons [1]. In particular, the energy of the dispersion managed (DM) soliton can be enhanced by appropriate design of the dispersion map, giving rise to improved performance in systems where timing jitter and signal-to-noise ratio are limiting factors [2]. In addition, for weak dispersion management, the DM soliton interaction is reduced because overlapping portions of the interacting pulse tails are chirped [3]. For stronger dispersion management, however, pulse stretching becomes significant and pulse overlap is substantially increased, leading to strongly increased interaction and reduced collapse distance [4]. Therefore, for practical applications with typical interpulse separations of about five pulse widths, the dispersion management strength is constrained to moderate values below about $S = 4$.

Recently, the DM soliton interaction was studied in simple two-stage dispersion maps to determine the effect of amplifier positioning within the dispersion map [5, 6]. In the theoretical study [5], the collapse distance was shown to depend strongly on the amplifier position and, for the symmetric map considered, a strong correlation between energy enhancement and the DM soliton collapse distance was established. On the other hand, the experimental study [6], which was performed using an asymmetric dispersion map, showed only a weak dependence of the stable DM pulse energy on amplifier position, and yet substantial variations in the error-free distances were observed. In both cases, the dispersion map strength, S, was relatively high ($S \approx 5$ and $S \approx 8$ respectively) giving rise to significant pulse breathing in each case.

In this paper, we analyse numerically the DM soliton interaction for the practically important case of moderate strong dispersion management ($S \leq 4$). We consider three different map configurations corresponding to both symmetric and non-symmetric dispersion maps, made up of varying proportions of anomalous and normal fibre (1:1, 1:9 and 9:1). We show that for these moderate strength maps, the detailed pulse dynamics play the dominant role in determining the collapse distance of DM solitons, irrespective of the dispersion map configuration. In each case, the collapse distance is maximised by locating the amplifier at positions where the pulse evolution is symmetrised within the dispersion map.

To determine the soliton collapse distance we use the variational model presented in Ref. [5]. The evolution equations for the amplitude a_1, width τ_1 chirp μ_1, frequency κ_1, and position ξ_1, of the pulses, are given by,

$$a_1^2\tau_1 = \eta^2 = \text{const.} \tag{1}$$

$$\frac{d\tau_1}{dz} = 2\sigma(z)\tau_1\mu_1 \tag{2}$$

$$\frac{d\mu_1}{dz} = -2\sigma(z)\mu_1^2 + \frac{\sigma(z)}{2\tau_1^4} - \frac{\eta^2 c(z)}{2\sqrt{2}\tau_1^3} + \frac{c(z)\eta^2}{\sqrt{2}\tau_1^3}\left(\frac{4\xi_1^2}{\tau_1^2} - 1\right)\exp\left[-\frac{(2\xi_1^2}{\tau_1^2}\right] \tag{3}$$

$$\frac{d\kappa_1}{dz} = 2\sqrt{2}c(z)\eta^2\frac{\xi_1}{\tau_1^3}\exp\left[-\frac{2\xi_1^2}{\tau_1^2}\right] \tag{4}$$

$$\frac{d\xi_1}{dz} = -\sigma(z)\kappa_1 \tag{5}$$

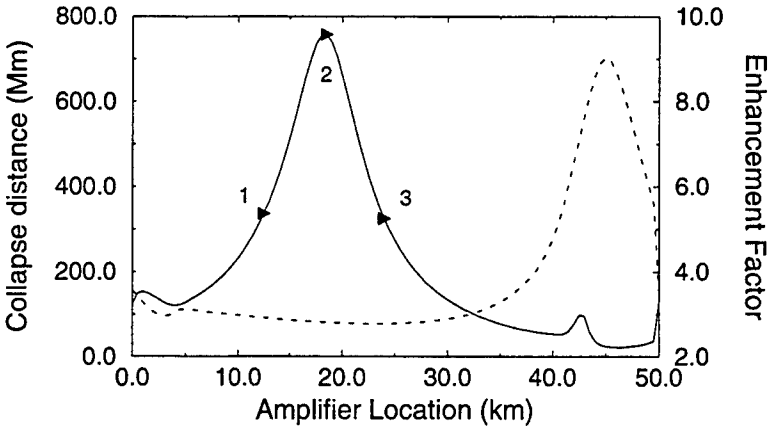


Figure 1: Collapse distance and power enhancement versus amplifier location for $S = 2$ and $L_1 = 5km$. The amplifier position is measured from the start of the normal fibre section.

Here, $\sigma(z)$ and $c(z)$ describe the periodic dispersion map and the gain/loss function, respectively. The energy enhancement factor η^2 is chosen to give periodically stable solutions in the absence of a perturbing puslse. We assume that a pair of interacting pulses are a distance $2\xi_1$ apart such that $a_2 = a_1$, $\tau_2 = \tau_1$, $\mu_2 = \mu_1$, $\kappa_2 = -\kappa_1$ and $\xi_2 = -\xi_1$.

The dispersion managed fibre is made up of alternating lengths, L_1 and L_2, of normal and anomalous dispersion fibre, with dispersion coefficients β_1'' and β_2'' respectively, and characterised by two parameters: the average dispersion, $\beta_a = (\beta_1'' L_1 + \beta_2'' L_2)/(L_1 + L_2)$ and the dispersion map strength, $S = (\beta_2'' L_2 - \beta_1'' L_1)/T_0^2$, where T_0 is the pulse FWHM at its minimum point.

As an example of our calculations, Figure 1 shows the collapse distance as a function of amplifier position for a $L_1 = 45$km, $L_2 = 5km$, $\beta_a = -0.127ps^2/km$ and $S = 2$. The amplifier spacing is $50km$, the fibre loss $0.2dB/km$, and $T_0 = 20ps$. The position of the amplifier, L_a, is measured from the beginning of the section of normal dispersion fibre. Figure 1 shows a strong variation in the collapse distance over the region $L_a = 5 - 30km$, even though the power enhancement factor (shown dashed) remains almost constant. This behaviour can be explained by examining the evolution of the pulse width in this region. Figure 2 shows the pulse dynamics corresponding to points $1-3$ in Fig. 1. It is clear that the greatest collapse distance, achieved when $L_a \approx 18km$, corresponds to the amplifier position which symmetrises the pulse propagation. Thus, the pulses experiencing more asymmetric behaviour also experience greater overlap and consequently stronger interaction.

We have confirmed that the general observations made in Figures 1 and 2 hold true for moderate strength dispersion management, for all three map symmetries. For $S = 2$, the correlation between maximum collapse distance and propagation symmetry is absolutely clear. For $S = 4$, however, the correlation remains good for the asymmetric dispersion maps only, and for the symmetric map, it is necessary to compromise between symmetrising the pulse breathing and minimising the power enhancement to give the greatest collapse distance. For strong dispersion management, $S > 4$, the importance of the pulse breathing symmetry diminishes and power enhancement becomes the dominant factor in determining collapse distance for all map symmetries.

In conclusion, we have shown that for moderate strength dispersion management, the

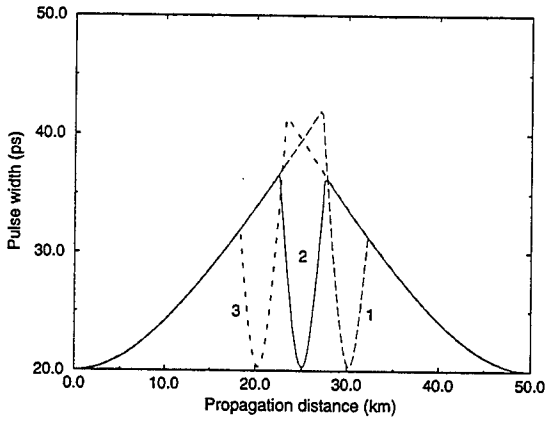


Figure 2: Pulse width versus propagation distance within the map for amplifier positions at $L_a = 12km$, $L_a = 18km$, and $L_a = 24.0km$, corresponding to points $1 - 3$ in Fig. 1

detailed dynamics of the pulse propagation play an important role in determining the soliton interaction, and that the collapse distance is maximised when the pulse breathing is symmetric. The benefit of symmetrising pulsewidth breathing in DM soliton systems has been reported recently [7], and can be achieved by appropriate tailoring of the transmission fibre dispersion, or by the introduction of guiding filters. Here, we have shown that such symmetry can also be achieved by appropriate positioning of the amplifier within the dispersion map.

[1] N. J. Smith, N. J. Doran, W. Forysiak, and F. M. Knox. Soliton transmission using periodic dispersion compensation. *J. Lightwave Technol.*, 15(10):1–15, 1997.

[2] G. M. Carter, J. M. Jacob, C. R. Menyuk, E. A. Golovchenko, and A. N. Pilipetskii. Timing-jitter reduction for a dispersion-managed soliton system: experimental evidence. *Opt. Lett.*, 22(8):513–515, 1997.

[3] T. Okamawari, Y. Ueda, A. Maruta, Y. Kodama, and A. Hasegawa. Interaction between guiding centre solitons in a periodically dispersion compensated optical transmission line. *Electron. Lett.*, 33(12):1063–1065, 1997.

[4] T. Yu, E. A. Golovchenko, A. N. Pilipetskii, and C. R. Menyuk. Dispersion-managed soliton interactions in optical fibers. *Opt. Lett.*, 22(11):793–795, 1997.

[5] M. Matsumoto. Analysis of interaction between stretched pulses propagating in dispersion-managed fibers. *IEEE Photonics Technology Letters*, 10(3):373–375, 1998.

[6] I. S. Penketh, P. Harper, S. B. Alleston, I. Bennion, and N. J. Doran. 10 Gbit/s dispersion managed soliton transmission over 16,5000km in standard fibre by reduction of soliton interaction. *Optics Letters*, 1999. (to be published).

[7] L. F. Mollenauer, P. V. Mamyshev, and J. P. Gordon. Effect of guiding filters on the behavior of dispersion-managed solitons. *Optics Letters*, 24(4):220–222, 1999.

NOISE SUPPRESSION IN SOA TRANSMISSION LINES

C. Knöll, M. Gölles and F. Lederer

Institut für Festköpertheorie und Theoretische Optik, Friedrich-Schiller Universität Jena,
Max-Wien-Platz 1, D-07743 Jena, Germany (pfl@uni-jena.de)

Semiconductor Optical Amplifiers (SOA) are potential candidates for high bit rate optical fiber communication systems at 1300 nm because of their efficiency and compactness. A major drawback is the Amplified Spontaneous Emission (ASE) that has to be reduced in order to further upgrade these systems[1,2]. Saturation of amplification by the signal leads to a net gain for ASE. Introducing a saturable absorber (SA) into the line one can achieve an opposite saturation behaviour where saturated amplification (signal) exceeds the unsaturated gain entailing suppression of ASE. In this contribution we aim at the optimization of such an SOA-SA module for stable, high-bit rate RZ signal transmission in an optical fibber where our studies rely on the well-established model of Agrawal and Olsson[3].

The energy gain of an amplifier (absorber)

$$G_E = \frac{E_O}{E_I} = \int_{-\infty}^{\infty} P(t) e^{h(t)} dt = \frac{E_S}{E_I} \log\left[1 + e^{h_+}\left(e^{E_I/E_S} - 1\right)\right] \tag{1}$$

is providing direct access to its amplification (absorption) properties. Here E_I and E_O are the input and output energy, respectively, E_S is the SOA/SA saturation energy. The quantity h_+ measures the transmission function $h(t)$ before saturation sets in. The energy balance of the transmission line, consisting of a SOA (G_E^a), a SA (G_E^s) and a fiber ($L = e^{\alpha}$), only exhibiting losses, is

$$G = G_E^a \times G_E^s \times L$$

$$G = e^{\alpha} \frac{\nu}{\varepsilon} \log\left\{1 + e^{h_+^s}\left[\left(1 + e^{h_+^a}\varepsilon\right)^{1/\nu} - 1\right]\right\} \tag{2}$$

Dispersion and nonlinearity of the fiber can be neglected because we are operating the system near the zero dispersion wavelength (ZDW) and at low powers. Here ε is the input pulse energy normalized to the saturation energy of the amplifier, ν represents the ratio $\nu = E_s^s / E_s^a$ of the saturation energies of absorber and amplifier, e^{α} marks the fiber losses for one round trip and finally h_+^a (h_+^s) are the SOA (SA) transmission functions before saturation sets in. There are two cases of principal interest, viz. i) $h_+^a = h_0^a$, $h_+^s = h_0^s$ for pulses after a set of zeros and ii) pulses in a regular train. In order to maintain the regularity in the latter situation periodicity of the transmission function is required. This condition permits to numerically determine h_+^a (h_+^s). Introducing T as pulse spacing and τ_R as the recovery time this condition reads as

$$h(t) = h_0 - \left\{h_0 + \log\left[1 - (1 - e^{h_+})e^{-\varepsilon(t)}\right]\right\} \exp\left(-\frac{t}{\tau_R}\right) \tag{3}$$

$$h(t) = h_+ \overset{!}{=} h(t+T) \tag{4}$$

This approximation works well for not too short pulses and recovery times, cases for which more involved models have to be applied [4]. The time dependent energy $\varepsilon(t)$ belongs to the part of the pulse having already entered SOA/SA and is normalized with the saturation energy:

$$\varepsilon(t) = \frac{1}{E_S} \int_{-\infty}^{t} P(t')dt' \tag{5}$$

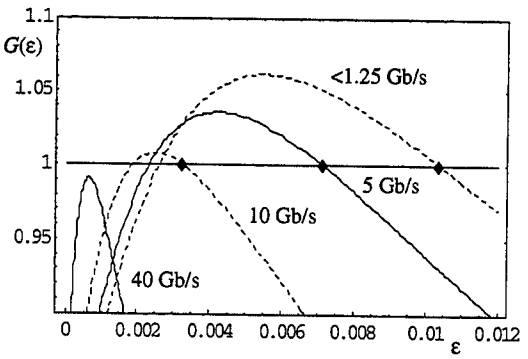


Fig. 1: Dependence of net energy gain on pulse energy for a regular pulse train.
♦ - stable points.

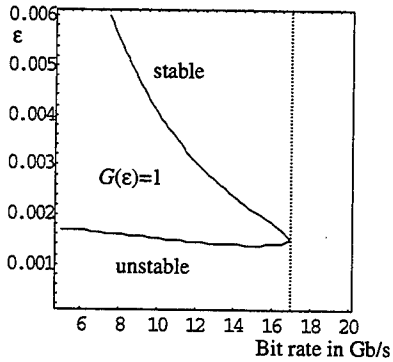


Fig. 2: Bit rate dependent energy of stable and unstable points

In Fig. 1 the energy gain as a function of the normalized input energy is displayed for different bit rates. The fiber losses are chosen to exceed the small signal amplification so ASE is always damped while the signal still experiences net gain. This condition is not met for a 40 Gb/s signal. This result implies that there is a maximum bit rate where net gain can be achieved. Beyond this bit rate the difference between small signal and saturated gain at the amplifier exceeds the small signal absorption. Below this limit there are two points of unit gain, the one at higher energy being stable (♦). Pulses with input energies above the unstable point will converge to stable energies while pulses with too low energy will be damped away. In Fig. 2 the bit rate dependence of the stable points is shown. The dashed line marks the limit above which no stable points exist. Since the location of stable points depends on bit rate one may expect that the pulses will attain discrete energy levels depending on the leading zeros.

The net gain is strongly influenced by the ratio ν of the saturation energies. In Fig. 3 the energy gain is plotted

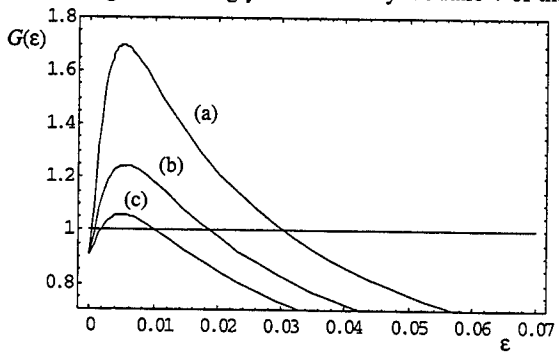


Fig. 3: $G(\varepsilon)$ for $h_0^a = 5$, $h_0^s = -1$, α=-4.1,
(a) ν=0.15, (b) ν=0.20, (c) ν=0.25

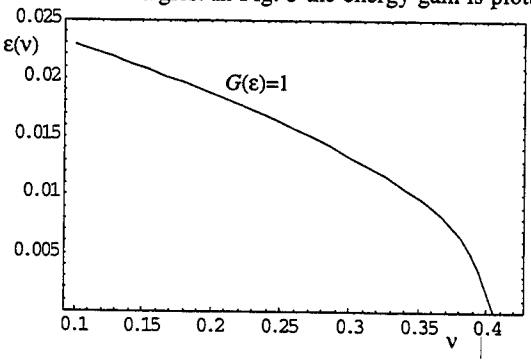


Fig. 4: Dependence of the energy at stable points on the ratio ν of the SAO/SA saturation

for different values v. Only below an definite upper limit a net amplification can be achieved at saturation (see Fig. 4). This limit depends on both the small signal values for amplification and absorption.

In Fig. 5 the joint SOA/SA transmission function for different ratios of the SOA/SA recovery times is shown. The pulses are situated at t = –200ps, 200 ps. Obviously there is no sufficient net gain compared to the background for $\tau_R^s/\tau_R^a = \Delta > 1$, i.e., when the recovery time of the absorber exceeds that of the amplifier. The pulse energy leading to stable pulse propagation depends on Δ (see Fig. 6). Obviously there is a threshold for the recovery time of the absorber. Therefore there is a trade off to be accounted for in fixing the respective recovery times.

The gain function being narrower than the pulse indicates that there will be a considerable pulse shortening. Because of the competition between amplifier and absorber there can be a walk off in either direction, depending on the energy of the pulse. This bi-directional walk off does not occur without SA.

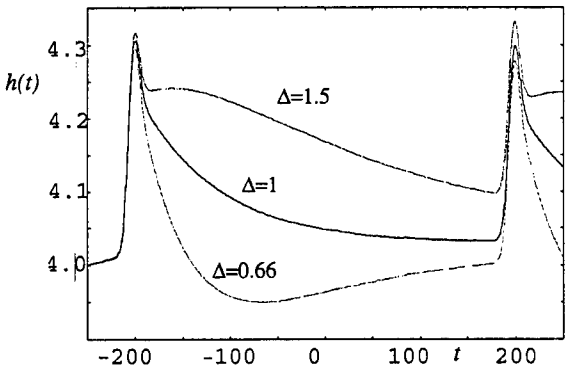


Fig. 5: Joint transmission function for different ratios Δ of the recovery times

ν=0.25, $h_0^a = 5$, $h_0^s = -1$, τ_R^a =100ps,

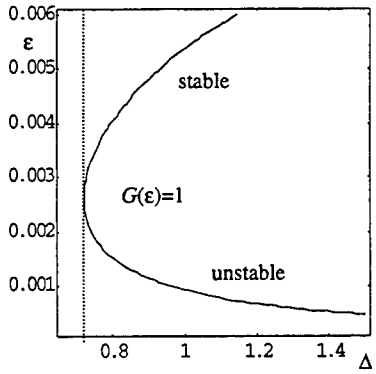


Fig. 6: Energies for stable pulse propagation vs. ratio Δ of the recovery times

Knowing the time derivative of the joint transmission function at the point of maximum peak power t_P one can estimate the direction of the walk off. The sign of the time derivative shows the relative position of maximum amplification and pulse peak:

$$\left.\frac{\partial}{\partial t}\left(h^a(t)+h^s(t)\right)\right|_{t=t_P} = -\frac{P(t_P)e^{h^a(t_P)}}{E_S^a}\left\{1-\frac{1}{\nu}\left[1-\left(1-\frac{1-\exp(-h_+^s)}{(1+\varepsilon\exp h_+^a)^{1/(2\nu)}}\right)^{-1}\right]\right\} \tag{6}$$

$P(t_P)$ is the peak power of the input pulse, E_S^a the saturation energy of the amplifier. Eq. (6) was derived assuming that the walk off per round trip is small compared to the pulse width. For the energy

$$\varepsilon_0 = \left(\left[(\exp(-h_+^s)-1)(1/\nu-1)\right]^{2\nu}-1\right)e^{-h_+^a} \tag{7}$$

the transmission function at $t=t_P$ is at maximum and no walk off will take place. For energies smaller than ε_0 the walk off is positive, at ε_0 the situation is reverted. The actual pulse walk off depends on the preceding bit pattern. In Fig. 7 the bit rate dependence of ε_0 is shown

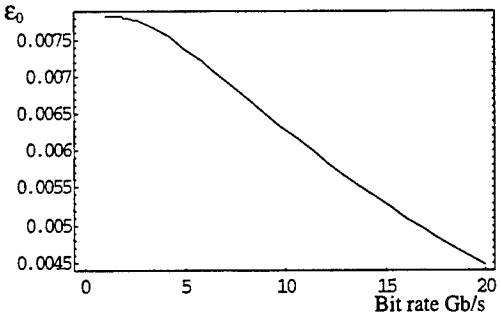


Fig. 7: Bit rate dependence of zero walk off energy ε_0

Because of the connection between phase and transmission function[3] eq. (6) leads to an energy dependent spectral walk off as well. The latter one can be suppressed by applying a filter, which also limits the spectral broadening originating from pulse shortening.

In conclusion, we have shown that an appropriate combination of SOA and SA can be used to achieve net amplification of the signal compared to the ASE. The dependence on the bit rate, the ratio of saturation energies and the input energy was investigated and stable transmission could be predicted. The maximum bit rate depends on the parameters chosen but values higher 10 Gb/s are theoretically possible.

Our recent experiments carried out have shown that the ASE could be suppressed between the pulses as well as in the marks. The existence of bit rate dependent points of stable energy could be qualitatively verified.

1. G. Onishchukov, V.Lokhnygin, A. Shipulin, P.Riedel, Electron. Lett., **34**, 1597 (1998)
2. J.J.E. Reid, L. Cucala, M. Ferreira, M. Settembre, H. Haunstein , R.C.J. Smets Technical Digest of ECOC, 1998, paper WdD01, pp. 567-568
3. G. Agrawal, A. Olsson, IEEE J.Quantum Electron. **QE 25**, 2297 (1989)
4. A. Mecozzi, J. Mørk, J. Opt. Soc. Am. B **14**, 761 (1997)

Experimental Observation of a New Chirped Continuous Pulse-Train Soliton Solution to the Maxwell-Bloch Equations

Shihadeh Saadeh and Gregory J. Salamo
Physics Department. University of Arkansas, Fayetteville, AR 72701
(501) 575-2506
salamo@comp.uark.edu

Coherent propagation of trains of optical pulses through a two-level absorber has been investigated, from a theoretical viewpoint, by many researchers. These investigations have been based on the self-induced transparency (SIT) equations.[1] both with[2-5] and without[6] the assumption of zero relaxation. Recently, theoretical predictions have been supported by experimental observations of the Jacobi elliptic dn solution[7]. In particular, experiments demonstrated the evolution of an arbitrarily shaped input optical pulse train into the analytic shape-preserving Jacobi elliptic pulse train solution to the Maxwell-Bloch equations. A special feature of the solution observed was that the chirp was zero. In this paper we report the demonstration of the evolution of a continuous wave (c.w.) laser beam into a analytic shape-preserving pulse train solution. In this case, the analytic solution is not a Jacobi elliptic function, but rather a sinusoidal function. In our talk, we will present experimental, analytical, and numerical evidence for the existence of this new sinusoidal pulse train solution to the Maxwell-Bloch equations.

The interaction of a plane-wave optical field with an inhomogeneously broadened two-level absorber can be described by two sets of equations that are known as the reduced Maxwell-Bloch equations. For circularly polarized light traveling in the z-direction, the electric field at the position of the atom is:

$$\mathbf{E}(t,z) = E_o(t,z)[e^{i\{\omega t - kz + \phi(t)\}} + c.c.]$$

Where $\phi(t)$, the phase, is a function of time. The instantaneous field frequency may be defined as:

$$\omega(t) = \omega + \frac{d\phi}{dt}$$

The "reduced Maxwell-Bloch equations" in this case are:

$$\frac{\partial u}{\partial t} = -(\Delta\omega - \phi)v - E_2 w\frac{u}{T_2}$$

$$\frac{\partial v}{\partial t} = (\Delta\omega - \phi)u + E_1 w\frac{v}{T_2}$$

$$\frac{\partial w}{\partial t} = -E_1 v + E_2 u\frac{(w+1)}{T_1}$$

$$\partial E_1/\partial z = \alpha/2\pi g(0)\int_{-\infty}^{\infty} v(t,z,\Delta\omega)g(\Delta\omega)\, d\Delta\omega$$

$$\partial E_2/\partial z = -\alpha/2\pi g(0) \int_{-\infty} u(t,z,\Delta\omega) g(\Delta\omega)\, d\Delta\omega$$

where $E_1 = ?\ E_o \cos f$, $E_2 = ?\ E_o \sin f$, T_2' is the relaxation rate of u and v, T_1' is the relaxation rate of w, g(? ?) is the line shape function, and ? ? = ? $_o$ – ?, the difference between the atom resonance frequency and the frequency of the optical field. In this study df (t)/dt is given by:

$$df(t)/dt = f_o \sin dt, \quad \text{or} \quad f(t) = -(f_o/d) \cos dt,$$

where f_o is a constant that determines the amplitude of the phase modulation, i.e., frequency shift from the atom resonance frequency, and d the frequency of the phase modulation.

The experimental apparatus is shown in Figure 1. An Argon laser was used to pump a single-mode fast scanning tunable c.w. dye laser with Rhodamine 6G as the gain medium. The output of the c.w. dye laser was chirped by using an electro-optic crystal. The **chirped c.w.** laser light was directed through a quarter-wave plate to produce (s+) circularly polarized light and focused by a lens (L_1) into the sodium cell, which is housed in an oven inside a magnet. Another lens (L_2) was used between the sodium cell and a detector to image the output laser from the sodium cell onto an aperture (A_1). This was done in order to select only the uniform plane-wave region from the output signal for observation. A third lens (L_3) was used to focus the output from the aperture onto a fast detector. The mode structure of the dye laser was continuously monitored by two Fabry-Perot interferometers.

In this work the frequency of the power amplifier which we used to drive the phase modulator was 31.5 MHz. This frequency is, therefore, the frequency of the phase modulation of our laser light. It dictates the cycle time of the phase modulation to be 1/f = 32 nanosecond. The applied voltage on the phase modulator determines the amplitude of the phase modulation. Then, by applying a magnetic field the laser beam is brought on resonance with the sodium atomic line. The sodium cell was kept at temperature of 190°C which makes al = 5.

Figure 2 shows the input c.w. laser light signal into the sodium cell and the intensity of the laser beam coming through the sodium cell, while a phase modulation of frequency 31.25 MHz and amplitude of 20 MHz is applied to the laser beam. These curves show a modulation in the intensity of the laser beam corresponding to a period of 16 nanoseconds or a frequency of 63 MHz, which is twice the frequency of modulation of the laser beam. The solid line shows the computer simulation intensity of the laser beam after al = 5. Figure 3 (the dotted line) shows the intensity of the laser beam coming through the sodium cell, while a phase modulation of frequency 31.25 MHz and amplitude of 50 MHz is applied to the laser beam. In this case, we observe 4p behavior.

REFERENCES

1. S.L. McCall and E.L. Hahn, Phys. Rev. **183**, 457 (1969).
2. J.H. Eberly, Phys. Rev. Lett. **22**, 720 (1969).
3. M.D. Crisp, Phys. Rev. Lett. **22**, 820 (1969).
4. D. Dialetis, Phys. Rev. A **2**, 10665 (1970).
5. L. Matulic and J.H. Eberly, Phys. Rev. A **6** 822 (1972).
6. M.A. Newbold and G.J. Salamo, Phys. Rev. Lett. **42**, 887 (1979).
7. J. Shultz and G.J. Salamo, Phys. Rev. Lett. **78**, 855 (1997).

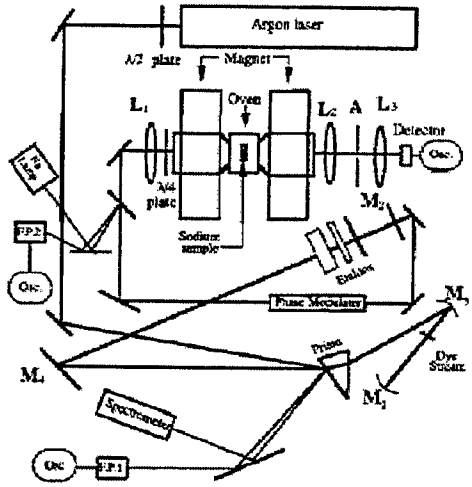


Fig. 1 Apparatus

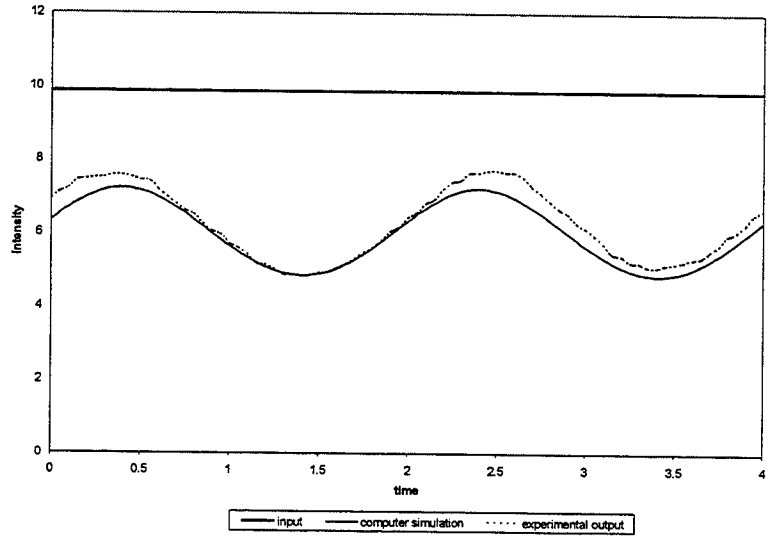


Fig. 2 Soliton formation with low amplitude of the driving frequency corresponding to 2p behavior

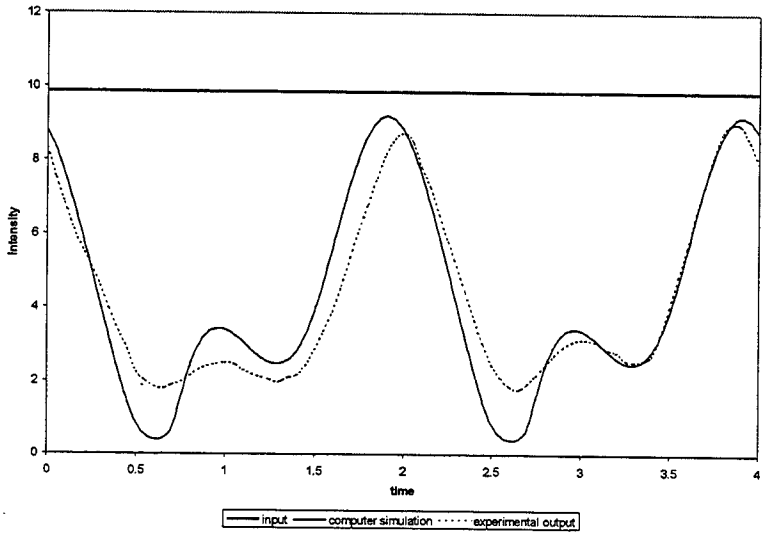


Fig. 3 Soliton formation with larger amplitude of the driving frequency corresponding to 4p behavior

Cross-polarization mixing of a laser beam and a spectrum of light in a single-mode optical fiber

K. S. Chiang and K. P. Lor

Optoelectronics Research Centre/ Department of Electronic Engineering
City University of Hong Kong
83 Tat Chee Avenue, Kowloon, Hong Kong
Tel: (852) 2788 9605
Fax: (852) 2788 7791
E-mail: eeksc@cityu.edu.hk

Being possible sources of cross-talks in wavelength-division-multiplexed (WDM) systems, four-wave-mixing (FWM) processes in single-mode optical fibers have attracted considerable attention.[1-5] Previous studies have been focussed on the generation of new optical frequencies in fibers that are operated near the zero-dispersion frequency or in the anomalous dispersion region. In this paper, we report our study on a new FWM process in a single-mode fiber, which involves the cross-polarization mixing of a laser beam and a spectrum of light. This process could have significant effects on the performance of WDM systems.

Recently, we observed a new FWM process in a birefringent fiber, where a distinct frequency-shifted beam was generated as a result of mixing a laser beam and a spectrum of superfluorescent light.[6] The frequency-shifted beam and the laser beam were found to be always in the two polarized modes of the fiber, respectively.[6] To explain the experiment results, we have analyzed the process of mixing two pump waves at different frequencies, which are launched into the two polarized modes of a birefringent fiber, respectively.[7] We find that two new frequency-shifted beams can indeed be generated and their polarization states are orthogonal to those of the respective pump waves.[7] The frequency shift is proportional to the polarization-mode dispersion in the fiber, and insensitive to the difference between the two pump frequencies.[7,8] This explains why a laser beam can mix with the individual components in a spectrum of light to generate a distinct new frequency,[7] as shown in Fig.1(a).

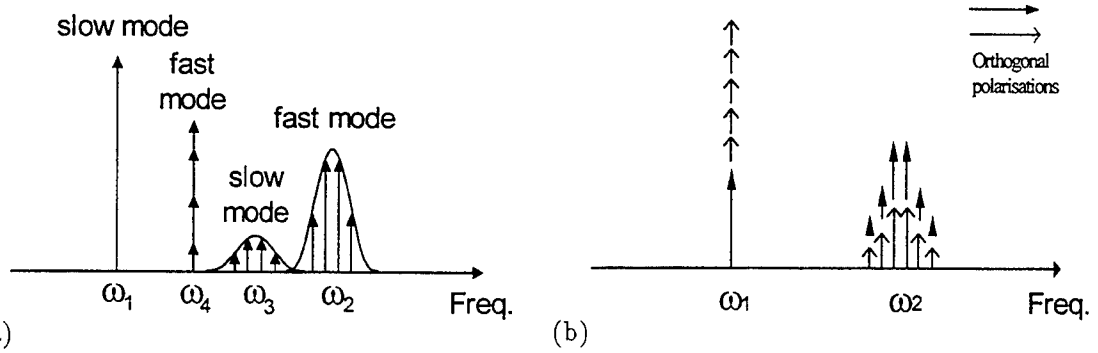


Figure 1: Mixing of a laser beam at ω_1 and a spectrum of light at ω_2 (a) in a birefringent fiber, where new frequency-shifted waves at ω_3 and ω_4 are generated, and (b) in a single-mode fiber, where no new frequencies are generated but the polarization states of the new waves are orthogonal to those of the pump waves.

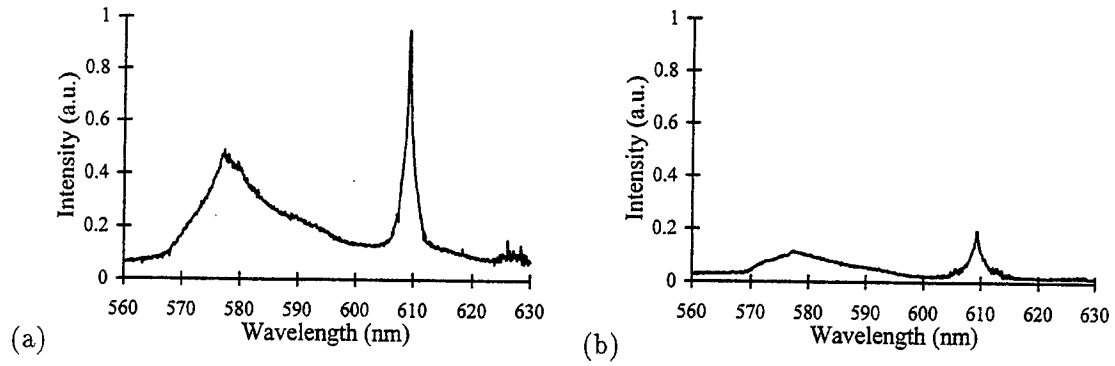


Figure 2: Measured output spectra when the linearly polarized laser beam and the same polarization of the superfluorescent light were launched into the fiber: (a) the analyzer was set at an angle to maximize the laser output from the fiber; (b) the analyzer was rotated by 90° from that in (a) to minimize the laser output from the fiber.

The same process is expected to take place in a single-mode fiber. In an ideal single-mode fiber, there is no polarization-mode dispersion, and, therefore, the frequency shift must be zero. This means that the new waves generated must be at the pump frequencies and their polarization states must be orthogonal to those of the pump waves, as shown in Fig.1(b). As a result, the polarization states of the pump waves are modified by the process. This process is different from the well-known FWM processes, whether due to same-polarization mixing[1,4,5] or cross-polarization mixing,[2,3] that involve the generation of new frequencies. It is also different from the process of cross-phase modulation, which does not involve the generation of new waves.

In our experiments, the light source used was a nitrogen-gas laser pumped dye laser, which generated 3-ns pulses with a peak power up to several hundred watts at a rate up to 20 pulses per second. The dye used was Rhodamin 590, which covered wavelengths from 560 nm to 630 nm. The laser wavelength was set at around 610 nm. At this wavelength, the laser output also contained a broad spectrum (575 - 600 nm) of strong superfluorescent light. The laser beam was linearly polarized, whereas the superfluorescent light was nearly unpolarized. The output light from the laser was launched into a 1-m long single-mode fiber (Fibrecore SM600) with a 10x microscope objective lens. The fiber was laid as straight as possible to reduce bend-induced birefringence. A polarization analyzer was placed at the output end of the fiber and the spectrum of the output light was measured with a spectrometer. We first placed a broadband (400 - 700 nm) polarizer at the input end of the fiber and adjusted its axis to maximize the laser input to the fiber. The analyzer at the output end was then adjusted to maximize the laser output from the fiber. The output spectrum with this setting is shown in Fig.2(a). When the analyzer was rotated by 90°, the laser output from the fiber was minimized, as shown in Fig.2(b). The weak output light shown in Fig.2(b) is due to the residual and induced birefringence in the fiber and the finite extinction ratios of the polarizers. With the present setting, the laser beam and the superfluorescent light launched into the fiber had the same linear polarization state, and no wave mixing should have taken place. We next took away the input polarizer to allow the full unpolarized superfluoresent light to be launched into the fiber together with the laser beam. The output spectra obtained by setting the analyzer at the same angles as those for Figs.2(a) and (b) are shown in Figs.3(a) and (b), respectively. It should be noted that the same vertical scale is used for all the figures shown in Figs.2 and 3, so that the spectra in these figures can be compared on a relative basis. It can be seen that the light spectrum shown in Fig.3(a) is comparable to that shown in Fig.2(a), while the intensity in the spectrum shown in Fig.3(b) is significantly higher than that shown in Fig.2(b). The increase in the intensity of the superfluorescent light shown in Fig.3(b) in relation to Fig.2(b) is, of course, the result of launching the full unpolarized

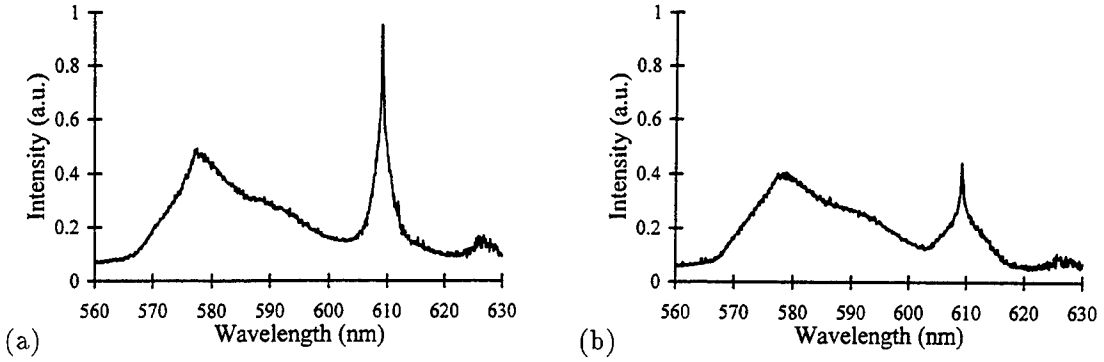


Figure 3: Measured output spectra when the linearly polarized laser beam and the unpolarized superfluorescent light were launched into the fiber: (a) the analyzer was set at the angle as for Fig.2(a); (b) the analyzer was set at the angle as for Fig.2(b).

superfluorescent light into the fiber. The large increase in the intensity at the laser frequency, however, can only be explained by either Raman amplification or the generation of a new wave. To check whether the beam at the laser wavelength shown in Fig.3(b) was produced by Raman amplification of the weak laser beam in Fig.2(b) by the full unpolarized superfluoresent light, we launched the full unpolarized superfluorescent light and the laser beam at a significantly reduced intensity (by adjusting the launching condition) into the fiber. We then adjusted the intensity of the superfluorescent light launched into the fiber by using a variable aperture placed in front of the laser. We found no obvious change in the intensity of the output beam at the laser wavelength when the intensity of the superfluorescent light was changed. This indicates that Raman amplification had negligible effects. We therefore believe that the beam at the laser wavelength shown in Fig.3(b) is the result of the FWM process, as illustrated in Fig.1(b). It can be seen that the linewidth of the laser beam in Fig.3(b) is slightly broadened, compared with that in Fig.2(b). This can be explained by the residual and induced birefringence in the fiber. By comparing Fig.2(a) and Fig.3(a) carefully, we find that the superfluorescent spectrum in Fig.3(a) is slightly stronger than that in Fig.2(a), in agreement with the prediction that the FWM process should also generate a new spectrum that coincides with the original spectrum but has an orthogonal polarization state, as shown in Fig.1(b).

We have demonstrated that a laser beam and a spectrum of light can mix in a single-mode fiber to generate new waves to modify the polarization states of the mixing waves. This FWM process, which can take place in both normal and anomalous dispersion regions, could introduce cross-talks in WDM systems by mixing various channels among themselves or with the amplified spontaneous emissions of erbium-doped fiber amplifiers.

References:

1. M. J. Zeiler, F. DiPasquale, P. Bayvel, and J. E. Midwinter, J. Lightwave Technol. 14 (1996) 1933.
2. N. Shibata, R. P. Braun, and R. G. Waarts, IEEE J. Quantum Electron. QE-23 (1987) 1205.
3. K. Inoue, IEEE J. Quantum Electron. 28 (1992) 883.
4. K. Inoue, J. Lightwave Technol. 11 (1993) 2116.
5. R. W. Tkach, A. R. Chraplyvy, R. Forghieri, A. H. Gnauck, and R. M. Derosier, J. Lightwave Technol. 13 (1995) 841.
6. K. S. Chiang, K. P. Lor, and Y. T. Chow, Opt. Lett. 22 (1997) 510.
7. K. P. Lor and K. S. Chiang, Opt. Commun. 152 (1998) 26.

Standard perturbative analysis of zero-average dispersion management

C. Paré, V. Roy, F. Lesage, P. Mathieu and P.-A. Bélanger

Centre d'Optique, Photonique et Laser (COPL)
Université Laval, Département de Physique
Ste-Foy, Québec, Canada G1K 7P4
FAX: (418) 656-2623
cpare@phy.ulaval.ca, pabelang@phy.ulaval.ca

One of the noteworthy features of the dispersion-managed (DM) soliton is the fact that, in contrast with the conventional NLS soliton, it can sustain stable propagation not only in the anomalous average dispersion regime but also at zero or normal average dispersion [1]. In absence of filtering, the only condition to be satisfied concerns the map strength parameter which should exceed a critical value $S > S_{cr} \approx 3.9$, according to numerical simulations [1]. In this work, we revisit the problem of dispersion management at zero-average dispersion. This regime can be viewed as a frontier for a wavelength-division multiplexing communication system that is expected to operate under both the anomalous and normal dispersion conditions. As such, it deserves a particular attention. Thanks to an appropriate change of variables, we show how a *standard* perturbative analysis allows an extension to the next order of previous results obtained using either a multiple scales analysis [2] or some other kind of averaging [3]. This extension reveals a quasi-invariance property related to the pulse shape at the fiber junction. The analysis also suggests an alternative for the determination of the critical parameter S_{cr}.

We consider a periodic two-step dispersion map consisting of fiber segments of length L_j (j=1,2) and dispersion parameters β_{2j} ($\beta_{21} < 0$, $\beta_{22} > 0$). Assuming zero-average dispersion ($\beta_{21}L_1 = -\beta_{22}L_2$), the propagation in the anomalous (first) and normal (second) fiber segments is described by the nonlinear Schrödinger (NLS) equation:

$$i\frac{\partial U_1}{\partial z_1} + \frac{1}{2}\frac{\partial^2 U_1}{\partial \tau^2} + |U_1|^2 U_1 = 0$$

$$i\frac{\partial U_2}{\partial z_2} - \frac{1}{2}\frac{\partial^2 U_2}{\partial \tau^2} + r\,|U_2|^2 U_2 = 0 \qquad \text{(1 a,b)}$$

The propagation distances $z_j = Z_j/L_{Dj}$ have been scaled to the local dispersion lengths $L_{Dj} = T_o^2/|\beta_{2j}|$, with T_o being a characteristic time scale; this scaling implies $0 < z_j < l$, where $l = L_1/L_{D_1} = L_2/L_{D_2}$. The time τ is in units of T_o and the fields are expressed in conventional NLS soliton units associated with the anomalous fiber. The ratio $r = (\gamma_2 L_2)/(\gamma_1 L_1)$ has been introduced, where $\gamma_{1,2}$ is the nonlinear parameter of the fibers. We restrict the present analysis to the lossless case and also concentrate on the symmetric case $r = 1$.

In the stationary regime here considered, except for a residual uniform nonlinear phase shift θ, the pulse

profile is perfectly reproduced after each period of the map. Moreover, without loss of generality, the field can be considered as real at the midpoint of the anomalous fiber. This implies, according to eqs (1a,b), that the following continuity and periodicity conditions must be satisfied: $U_1(z_1 = 0,\tau) \equiv U_0(\tau)$, $U_1(z_1 = l,\tau) = U_0^*(\tau)$, $U_2(z_2 = 0,\tau) = U_1(z_1 = l,\tau) = U_0^*(\tau)$ and $U_2(z_2 = l,\tau) = \exp(i\theta)\ U_1(z_1 = 0,\tau) = \exp(i\theta)\ U_0(\tau)$.

In the *linear limit* ($\theta = 0$) the fields in each fiber are simply related by $U_2^*(z_2 = z,\tau) = U_1(z_1 = z,\tau)$; we then introduce, with a perturbative treatment in mind, the following substitution:

$$\psi_\pm(z,\tau) \equiv \frac{U_1(z,\tau) \pm U_2^*(z,\tau)}{2} \tag{2}$$

This substitution can be given an alternative interpretation as it is strictly equivalent to a folding of the first half of the map onto the second half, thus evoking a similar technique used for analyzing quantum impurity problems [4].

In the regime of strong dispersion management, the dispersion dominates (*locally*) over the nonlinearity. This suggests a perturbative analysis in terms of a small parameter, e.g. $\varepsilon \approx |U_{0\ \max}|^2$. We then define $\psi_\pm = \sqrt{\varepsilon}\ V_\pm$ and $U_0 = \sqrt{\varepsilon}\ V_0$, with $V_\pm$ and V_0 of order unity. The new fields $V_\pm$ are now coupled over the common domain $0 < z < l$:

$$i\frac{\partial V_\pm}{\partial z} + \frac{1}{2}\frac{\partial^2 V_\pm}{\partial \tau^2} + \varepsilon\left(|V_\mp|^2 V_\mp + 2|V_\pm|^2 V_\mp + V_\pm^2\, V_\mp^*\right) = 0 \tag{3}$$

In this framework, the problem is particularly well suited for a standard perturbative analysis. A regular perturbation expansion of the fields $V_\pm$ and the phase shift θ yields a hierarchy of linear equations that can be easily solved in the spectral domain. As will be shown, a proper consideration of the boundary conditions allows the determination of the fields $U_{1,2}$ anywhere along the map. In particular, one finds, in the spectral domain and in keeping the first two orders of perturbation, the following expression for the field in the middle of the first (anomalous) fiber segment:

$$\tilde{U}_1(z_1 = l/2,\nu) \cong \Phi(\nu) + J(\nu) \tag{4}$$

where the spectral distribution $\Phi(\nu)$, which represents the leading order solution, is given as the solution of the following integral equation:

$$\iint d\nu_1\, d\nu_2 \frac{sin[\,2\pi^2 l\, \nu_1 \nu_2\,]}{2\pi^2 l\, \nu_1 \nu_2}\, \Phi(\nu+\nu_1)\, \Phi(\nu+\nu_2)\, \Phi(\nu+\nu_1+\nu_2) = \lambda\, \Phi(\nu)\ . \tag{5}$$

The eigenvalue λ is directly related to the phase shift θ incurred over one period of the map. Eq.(5) has been obtained elsewhere using either a multiple scales analysis [2] or another averaging method [3]. This

staightforward perturbative analysis allows an extension of the latter work as it easily includes the next order of perturbation which is given here in terms of the function $J(\nu)$:

$$J(\nu) \equiv \frac{l}{2} \iint d\nu_1 d\nu_2 \frac{1-\cos[\,2\pi^2 l \nu_1 \nu_2\,]}{2\pi^2 l \nu_1 \nu_2} \Phi(\nu+\nu_1)\,\Phi(\nu+\nu_2)\,\Phi(\nu+\nu_1+\nu_2) \quad . \qquad (6)$$

As will be discussed, this order of perturbation also shows, in contrast with previous work, the asymmetry observed in numerical simulations when comparing the pulse profile at the midpoint of the two fiber segments. It also reveals an interesting quasi-invariance property of the pulse shape at the fiber junction.

As a check of the accuracy of the present results, Fig. 1 compares the amplitude distribution at the middle of the anomalous fiber, as predicted by eqs (4)-(6), with exact numerical results obtained by solving eq.(1) directly, using the split step Fourier method. The parameters are: $\theta = 0.24$ *rad*, $L_1 = L_2 = 80$ *km*, $\beta_{22} = -\beta_{21} = 10$ ps^2/km. $T_0 = 11.35$ *ps*, implying that a conventional NLS soliton *sech* τ in the anomalous fiber would have a FWHM $= 1.763\ T_0 = 20$ *ps*. The normalized length is then equal to $l = 6.21$. The excellent agreement revealed by Fig.1 demonstrates the accuracy of this perturbative treatment. Further examples will be presented.

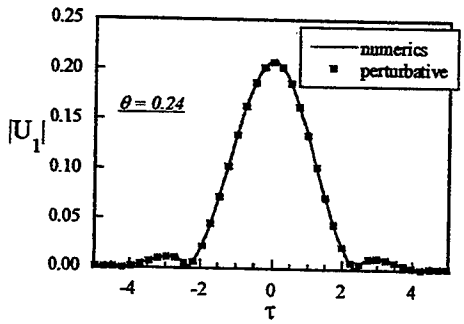


Figure 1. Stationary pulse profile at the midpoint of the anomalous fiber. Comparison between the perturbative analysis (squares) and the exact numerical results (solid line). See text for the system parameters.

This analysis also suggests an alternative (and presumably more accurate) method for determining the value of the critical parameter S_{cr}. As will also be discussed, eq.(5) also admits a solution of odd parity, thus implying the existence of an antisymmetric DM soliton.

References

[1] J.H.B. Nijhof. N.J. Doran, W. Forysiak and A. Bernston, *Electron. Lett.*, **34**, 481 (1998).
[2] M.J. Ablowitz and G. Biondini, *Opt. Lett.*, **23**, 1668 (1998).
[3] S.K. Turitsyn, A.B. Aceves, C.K.R.T. Jones, V. Zharnitsky and V.K. Mezentsev, *Phys. Rev.***E59**, 3843 (1999), and references therein.
[4] I. Affleck and A. Ludwig, *J. Phys.* **A21**, 5375 (1994).

Slow dynamics of dispersion-managed solitons

Anders Berntson
Ericsson Telecom AB, S-126 25 Stockholm, Sweden
Anders.Berntson@etx.ericsson.se

Dan Anderson and Mietek Lisak
Dept of Electromagnetics, Chalmers University of Technology, 412 96 Göteborg, Sweden
elfda@elmagn.chalmers.se, elfml@elmagn.chalmers.se

Boris Malomed
Dept of Interdisciplinary Studies, Faculty of Engineering, Tel Aviv University, Tel Aviv 69978, Israel
malomed@eng.tau.ac.il

Dispersion managed (DM) solitons, or RZ-pulses propagating in a fibre link with periodic dispersion compensation, provides an attractive means for propagating high bit-rate signals over large distances. Compared to standard solitons in fibres with uniform dispersion the power of DM solitons is enhanced [1] and they can propagate at zero and normal path-average dispersion [2,3] resulting in a reduction of the Gordon-Haus timing jitter [4]. Successful propagation of DM solitons have been demonstrated in both single-channel [5] and WDM [6] systems. In this work we investigate the evolution of pulses with shapes deviating from the shape of a DM soliton. We have found that for strong dispersion maps (map strength, $S > 3 - 4$, with S defined as in [3]) these perturbed pulses do not radiate and the pulse dynamics induceed by the perturbation show no sign of decay. The absence of radiation, which is in contrast to the behaviour of standard solitons, is important in communication systems where radiation adds to the noise floor and can cause interaction between subsequent pulses [7].

We have studied a loss-less two-stage map where the dispersion alternates between normal and anomalous. DM solitons (i e pulses that replicate themselves with the period of the disperion map) were calculated numerically using the method of [3]. The DM solitons were first perturbed by applying a chirp. The resulting pulse evolution is illustrated in Fig 1 which shows the chirp as function of the width of the pulse. Fig 1 shows only the slow dynamics, i e the changes from one dispersion period to the next. This is achieved by calculating the chirp and the width at the same point (midpoint of the anomalous fibre segment) in every dispersion period. Each calculation of the chirp and the width generates a point in Fig 1 and points representing subsequent dispersion periods are then joined by a line. (A DM soliton which replicates itself periodically would be represented by a single point in Fig 1). Fig 1a-b show that for low map strength there is a spiraling towards the centre, a process involving radiation and reduction of the slow dynamics. The lower the map strength the closer to the fixpoint in the centre the spiral reaches. For S=0, corresponding to uniform dispersion, the spiral would reach the fixpoint in the centre, meaning that a soliton has emerged. For $S > 0$ (Fig 1) the spiraling is stopped before reaching the fixpoint so the pulse will have some residual dynamics. For strong maps, Fig 1c, no radiation or inward spiraling could be detected (for the sake of clarity single points are plotted in Fig 1c instead of the line joining subsequent points). Although

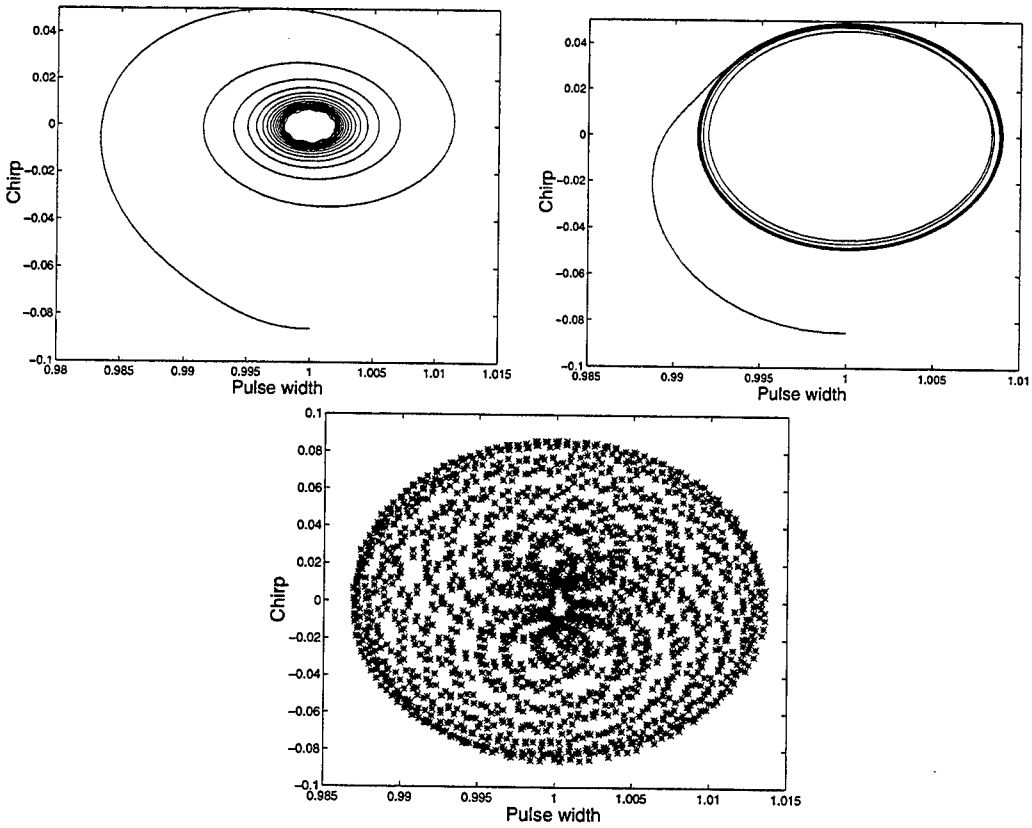


Figure 1: Chirp as function of pulse width for a DM soliton perturbed by a chirp, S=0.75 (top left), S=1.5 (top right) and S=3 (bottom).

many points in Fig 1c end up close to the fixpoint there is no trend that the points approach the fixpoint after longer propagation distance.

We also investigated the evolution of Gaussian pulses, see Fig 2 which shows the same quantities as in Fig 1. The input amplitude, width and chirp were chosen from the corresponding values of the numerically calculated DM soliton. Compared to Fig 1 the starting point in Fig 2 lies closer to the fixpoint. The perturbation also induces more dynamics in this case. However, the main conclusions concerning the radiation and the dynamics remain unchanged.

In conclusion we have shown how the dynamics of optical pulses change gradually from the case of uniform dispersion (S=0) to the case of strong dispersion management. As the map stength is increased the asymptotic pulse dynamics increases but the radiation from the pulse decreases. For strong maps, $S > 3 - 4$, no radiation could be detected.

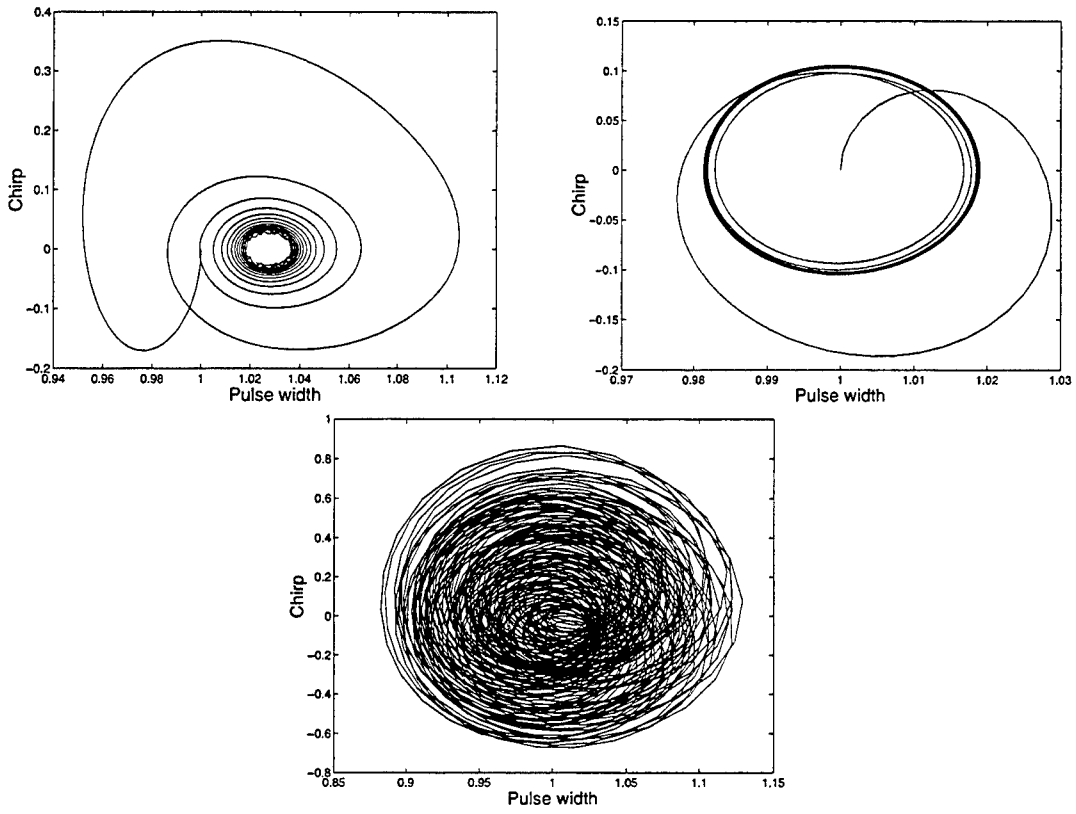


Figure 2: Chirp as function of pulse width for a Gaussian pulses with the same width, chirp and amplitude as the corresponding DM soliton, S=0.75 (top left), S=1.5 (top right) and S=3 (bottom)

[1] N. J. Smith, N. J. Doran, F. M. Knox, and W. Forysiak, Opt. Lett. **21**, 1981, (1996).
[2] J. H. B. Nijhof, N. J. Doran, W. Forysiak, and F. M. Knox, Electron. Lett **33**, 1726, (1997).
[3] A. Berntson, N.J. Doran, W. Forysiak, and J.H.B. Nijhof, Opt. Lett. **23**, 900, (1998).
[4]A. Hasegawa, Y. Kodama, and A. Maruta, Optical Fibre Technology **3**, 197, (1997).
[5] P. Harper, I. S. Penketh, S. B. Alleston, I. Bennion, and N. J. Doran, Electron. Lett. **34**, 1997 (1998).
[6] D. Le Guen et al, Post-deadline papers ECOC'98, 61, (1998). Comm. **149**, 366 (1998).
[7] M. Romagnoli, L. Socci, M. Midrio, P. Franco, and T. Georges, Opt. Lett. **23**, 1182, (1998).

Propagation of an optical pulse in a fibre link with random dispersion management

Boris Malomed
Dept of Interdisciplinary Studies, Faculty of Engineering, Tel Aviv University, Tel Aviv 69978, Israel
email: malomed@eng.tau.ac.il, phone: +972 3 640 6413, fax: +972 3 640 6399

Anders Berntson
Ericsson Telecom AB, S-126 25 Stockholm, Sweden
Anders.Berntson@etx.ericsson.se

Thus far, the work on the use of dispersion management (DM) for pulse transmission in optical-fiber communication networks has been focused on tranmission lines where the dispersion alternates exactly periodically between normal and anomalous. However, real communication systems exist in the form of patchwork webs, which include links with very different lengths. Assuming the distribution of the lengths random, the DM upgrade of the patchwork systems makes it necessary to consider transmission of pulses in the lines subject to *random* DM. Besides its significance for the applications, this issue if also of considerable interest in the context of the soliton propagation in strongly inhomogeneous random media. In this work, semianalytical and direct numerical investigation of the pulse's dynamics in random-DM models is carried out. The semianalytical approach is based on the variational approximation (VA), which has become a widely accepted tool for the theoretical consideration of the DM solitons, demonstrating a fairly good agreement with numerical simulations [1-5]. In this short summary, results obtained by means of VA are presented. Direct simulations produce quite similar results, which will be presented in detail elsewhere. General inferences that are formulated on the basis of the semianalytical results are supported by the direct simulations as well.

Two different models of random DM are considered. In a *two-lengths* model, the lengths $L^{(\pm)}$ of the alternating normal- and anomalous-dispersion pieces are selected randomly from a certain interval independently from each other. In the *one-length* model, equal lengths inside each DM cell, $L^{(+)} \equiv L^{(-)}$, are selected randomly from the same interval. In the former model, the path-average dispersion (PAD) $\overline{\beta}$ is defined for the whole line, while in the latter model $\overline{\beta}$ is PAD inside each cell. The final results turn out to be similar for both models.

The pulse evolition is modelled by the lossless NLS equation. The analysis can be readily extended to include losses and gain, but the first necessary step is to understand fundamental features of random DM in the lossless model. In the case of *strong* DM, the shape of the pulse is well-known to be close to a Gaussian, and, accordingly, VA is based on the Gaussian ansatz

$$u = \tau_0 \sqrt{\frac{P}{\tau_0^2 - 2i\Delta(z)}} \exp\left[-\frac{\tau^2}{\tau_0^2 - 2i\Delta(z)} + i\phi\right] . \tag{1}$$

here $\Delta(z) = \Delta_0 + \int_{z_n}^{z} \beta(z')dz'$ is the accumulated dispersion defined inside the n-th DM cell, Δ_0 and

ϕ being real constants. The width T of the pulse is related to the ansatz's parameters as follows:

$$T(z) = \sqrt{\tau_0^2 + 4\Delta^2(z)/\tau_0^2}. \tag{2}$$

A version of the Gaussian-based VA developed in [5], with normalizations $L^{(-)} + L^{(+)} \equiv 1$, $|\beta_-|\, L^{(-)} = \beta_+ L^{(+)} \equiv 1$, is used here. To remain close to the normalizations, the random lengths $L^{(\mp)}$ are picked up from the interval $0.1 < L^{(\mp)} < 1$ (the minimum length 0.1 is introduced because, in reality, the segment length is not smaller than, say, 20 km), and it is set $|\beta_\pm| \equiv 2$.

Using the technique of VA, one can derive equations for the nonlinearity-induced evolution of the parameters in z: $P\tau_0 \equiv E$ is constant, and $d\tau_0/dz = \sqrt{2}E\tau_0 W^{-3}\Delta(z)$, $d\Delta_0/dz = \overline{\beta} - E(\sqrt{2}W)^{-3}[4\Delta^2(z) - \tau_0^4]$. The changes of the parameters τ_0 and Δ_0 per one DM cell are small, hence they may be calculated as $\delta\tau_0 = \oint (d\tau_0/dz)\, dz$, $\delta\Delta_0 = \oint (d\Delta_0/dz)\, dz$, where $\oint$ is the integral over a cell, and only the rapid variation of $\Delta(z)$ is taken into regard inside the integrals, while τ_0 and Δ_0 are treated as constants. The evolution of the pulse from a cell to a cell is described by a *map*, $\tau_0 \to \tau_0 + \delta\tau_0$, $\Delta_0 \to \Delta_0 + \delta\Delta_0$. After may dispersion periods the evolution of the parameters may be approximated by the differential equations

$$\begin{aligned}
\frac{d\tau_0}{dz} &= \frac{\sqrt{2}E\tau_0^4}{8\left[L^{(-)}+L^{(+)}\right]}\left\{\frac{1}{\sqrt{\tau_0^4+4\Delta_0^2}} + \frac{1}{\sqrt{\tau_0^4+4\left[\Delta_0+2L^{(-)}-2L^{(+)}\right]^2}}\right. \\
&\left. - \frac{2}{\sqrt{\tau_0^4+4\left[\Delta_0+2L^{(-)}\right]^2}}\right\}, \qquad (3) \\
\frac{d\Delta_0}{dz} &= -\overline{\beta} + \frac{\sqrt{2}E\tau_0^3}{8\left[L^{(-)}+L^{(+)}\right]}\left\{\frac{2\Delta_0}{\sqrt{\tau_0^4+4\Delta_0^2}} + \frac{2\left[\Delta_0+2L^{(-)}-2L^{(+)}\right]}{\sqrt{\tau_0^4+4\left[\Delta_0+2L^{(-)}-2L^{(+)}\right]^2}}\right. \\
&- \frac{4\left[\Delta_0+2L^{(-)}\right]}{\sqrt{\tau_0^4+4\left[\Delta_0+2L^{(-)}\right]^2}} - \frac{1}{2}\ln\left(2\Delta_0+\sqrt{\tau_0^4+4\Delta_0^2}\right) \\
&- \frac{1}{2}\ln\left(2\left[\Delta_0+2L^{(-)}-2L^{(+)}\right]+\sqrt{\tau_0^4+4\left[\Delta_0+2L^{(-)}-2L^{(+)}\right]^2}\right) \\
&\left. + \ln\left(2\left[\Delta_0+2L^{(-)}\right]+\sqrt{\tau_0^4+4\left[\Delta_0+2L^{(-)}\right]^2}\right)\right\}. \qquad (4)
\end{aligned}$$

Eqs. (3) and (4) with the randomly varying $L^{(\pm)}$ were numerically integrated in the interval $0 < z < 835$, which corresponds to ≈ 750 DM cells. The most essential characteristic of the pulse propagation at given values of $\overline{\beta}$ and E is the mean width $\overline{T}$, obtained by averaging the width (2) over a DM cell. Note that the difference of $\overline{T}$ from the formal width parameter τ_0 (Eq. (1)) is important, as these two variables are found to evolve in very different ways.

Typical results are displayed in Fig. 1, which pertains to slightly anomalous PAD, $\overline{\beta} = -0.05$, in the two-lengths model. The main part of Fig. 1 shows the case $E = 1$ (tantamount to the physical energy ~ 0.5 pJ, in the typical case). In this case, the pulse demonstrates large-amplitude

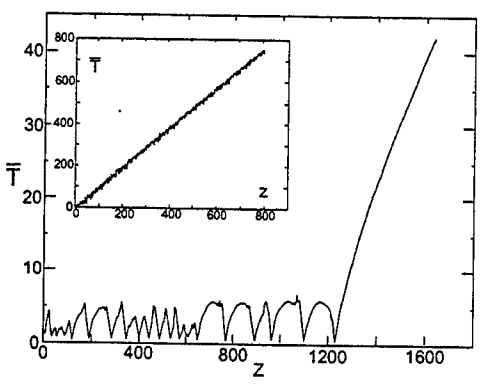


Figure 1: The cell-average width of the pulse vs. the propagation distance in the random-DM model with two independent lengths and $\overline{\beta} = -0.05$. In the main figure, $E = 1$; in the inset, $E = 10$.

random oscillations of its width and shape, but, nevertheless, it remains fairly robust over a finite propagation distance. An irreversible degradation (decay) of the pulse commences at a very large propagation distance, the stable-propagation length being ≈ 1200 average lengths of the DM cell, which implies the real distance to be $> 100,000$ km. However, the same model predicts that, at essentially larger values of the energy, for instance, at $E = 10$ (inset to Fig. 1), the degradation of the pulse commences immediately, hence the pulses with the energy $\gtrsim 5$ pJ are completely unusable. These results are not sensitive to the choice of the initial point, and are nearly the same in the one-length model. They also keep their character in the case of zero or slightly normal PAD (which has recently attracted a great deal of attention [5-9]). The same inferences follow from direct numerical simulations of Eq. (1) (not shown here): the pulse remains stable over a finite but large propagation distance, provided that its energy is small or moderate, but it quickly decays if the energy is too large.

Lastly, it is interesting to note that the qualitative picture of the sudden decay of the pulse after many random oscillations (Fig. 1) strongly resembles what was found earlier in a model with a *periodic* sinusoidal (rather than the usually assumed piecewise constant [1-9]) modulation of the local dispersion coefficient [10,11].

[1] A. Berntson, D. Anderson, M. Lisak, M.L. Quiroga-Teixeiro and M. Karlsson, Opt. Comm. **130**, 153 (1996).
[2] I. Gabitov, E.G. Shapiro and S.K. Turitsyn, Opt. Comm. **134**, 317 (1997).
[3] T.-S. Yang and W.L. Kath, Opt. Lett. **22,** 985 (1997).
[4] M. Matsumoto, Opt. Lett. **22,** 1238 (1997).
[5] T.I. Lakoba, J. Yang, D.K. Kaup, and B.A. Malomed, Opt. Comm. **149**, 366 (1998).
[6] J.H.B. Nijhof, N.J. Doran, W. Forysiak and F.M. Knox, Electr. Lett. **33**, 1726 (1997).
[7] S.K. Turitsyn and E.G. Shapiro, Opt. Lett. **23**, 682 (1998).
[8] J.N. Kutz and S.G. Evangelides, Opt. Lett. **23**, 685 (1998).
[9] A. Berntson, N.J. Doran, W. Forysiak, and J.H.B. Nijhof, Opt. Lett. **23**, 900 (1998).
[10] B.A. Malomed, D.F. Parker and N.F. Smith, Phys. Rev. E **48,** 1418 (1993).
[11] R. Grimshaw, J. He and B.A. Malomed, Physica Scripta **53**, 385 (1996).

Criterion for an oscillatory instability of multiparameter solitons.

Dmitry V. Skryabin
Department of Physics and Applied Physics, John Anderson Building, University of Strathclyde, 107 Rottenrow, Glasgow, G4 0NG, UK
fax: 44 141 5522891 phone: 44 141 5523354 dmitry@phys.strath.ac.uk

Introduction. The problems of soliton stability and instability induced dynamics in nonintegrable Hamiltonian models have paramount importance for understanding of a wide range of nonlinear optical phenomena. Generally, stability of the solitary solutions of the Hamiltonian equations can be lost due to bifurcations involving appearance of a positive eigenvalue (*stationary* instability [1–7]) in the soliton spectrum or a pair of complex conjugate eigenvalues with positive real parts (*oscillatory* instability [6–8]).

A threshold of the stationary instability of the multiparameter solitons is given in many cases by the zero of the determinant of the Jacoby matrix $J_{ij} = \partial_{\kappa_j} Q_i$, where κ_j are the soliton parameters and Q_i are the associated integrals of motions [1–5]. The condition $det(J_{ij}) = 0$ is, in fact, the compatibility condition of the problem arising in the leading (zero) order of the asymptotic solution of the eigenvalue problem governing stability of the soliton [3–5]. To find expressions for the eigenvalues it is necessary to proceed further and solve problems arising in the higher (at least first) orders. Up to now it was done only for the specific class of the model equations having single parameter soliton families [1,3]. Considering stationary bifurcations of the two-parameter solitons the method of the adiabatically varying soliton parameters has been applied in Refs. [4,6], see also discussion below for more details. *No criterion indicating transition to the oscillatory instability has been suggested till now.*

The purposes of this work are to formulate general asymptotic approach to stability of the multi-parameter solitons in Hamiltonian models, to show how it can be used to find expressions for the instability growth rates with an arbitrary accuracy and to demonstrate that under the certain conditions the first order approximation of this approach describes *novel stationary and oscillatory instabilities of the solitons.*

Model and symmetries. We will consider Hamiltonian equations in the general form

$$i\frac{\partial E_n}{\partial z} = \frac{\delta H}{\delta E_n^*},\ n = 1, 2 \dots N, \tag{1}$$

which describes a wide range of physical phenomena related with self-action and interaction of the slowly varying along z wave envelopes in variety of nonlinear media, for physical examples, see, [1,3–8]. Here E_n are the complex fields, z is the propagation direction of the interacting waves, x is the coordinate characterizing dispersion or diffraction, $H = H(\partial_x E_n, E_n, \partial_x E_n^*, E_n^*)$ is the Hamiltonian and * means complex conjugation. We will assume that H is invariant with respect to the set of $(L-1)$ phase transformations:

$$E_n \to E_n \exp(i\gamma_{nl}\phi_l),\ l = 1, 2, \dots (L-1), \tag{2}$$

ϕ_l are the arbitrary real phases and γ_{nl} are some constants. Because H does not depend from x explicitly, Eqs. (1) are invariant with respect to the arbitrary translations along x:

$$E_n(x, z) \to E_n(x - x_0, z). \tag{3}$$

Symmetry properties (2), (3) together with Hamiltonian nature of our problem imply presence of L conserved quantities, which are $(L-1)$ energy invariants

$$Q_l = \int dx \sum_{n=1}^{N} \gamma_{nl}|E_n|^2,\ l = 1, 2, \dots (L-1), \tag{4}$$

and momentum

$$Q_L = \frac{1}{2i}\int dx \sum_{n=1}^{N}(E_n^*\partial_x E_n - E_n\partial_x E_n^*). \tag{5}$$

Solitary solutions of Eqs. (1) can be sought in the form

$$E_n(x, z) = a_n(x - \kappa_L z)\exp(i\sum_{l=1}^{L-1}\gamma_{nl}\kappa_l z), \tag{6}$$

where κ_l are the real parameters characterizing phase velocities and angle of propagation with respect to z axis, and $|a_n| \to 0$ for $x - \kappa_L z \equiv \tau \to \pm\infty$.

Asymptotic stability analysis. To study stability of the solitons we seek solutions of the Eqs. (1) in the form

$$E_n = (a_n(\tau) + \varepsilon_n(\tau, z))\exp(i\sum_{l=1}^{L-1}\gamma_{nl}\kappa_l z), \tag{7}$$

where $\varepsilon_n(\tau, z)$ are the small complex perturbations. Linearizing Eqs. (1) and assuming that $\varepsilon_n(\tau, z) = \xi_n(\tau)e^{\lambda z}$, $\varepsilon_n^*(\tau, z) = \xi_{n+N}(\tau)e^{\lambda z}$ we get the following nonselfadjoint eigenvalue problem (EVP)

$$i\lambda\vec{\xi} = \hat{\mathcal{L}}\vec{\xi}, \tag{8}$$

where $\vec{\xi} = (\xi_1, \dots \xi_N, \xi_{N+1} \dots \xi_{2N})^T$ and $\hat{\mathcal{L}}$ is the linearisation (1) near the soliton.

To solve EVP (8) we will apply the asymptotic approach. This approach relies on the expansion of the

unknown eigenvector $\vec{\xi}$ into an asymptotic series near neutral eigenmodes of the soliton spectrum, i.e. zero-eigenvalue modes. The neutral modes can be generated by the infinitesimal variations of the free parameters of the soliton and thus they always can be presented as explicit functions of the soliton solution. However, as any approximate method, the asymptotic approach has a certain restriction. Namely, it describes only soliton spectrum corresponding to a specific class of the perturbations which in the zero approximation can be expressed as a linear superposition of the neutral eigenmodes. Thus, generally speaking, on the basis of this approach one can get only *sufficient* conditions for soliton instability or, in other words, *necessary* condition for the soliton stability.

By the infinitesimal variations of ϕ_l and x_0 it can be shown that

$$\vec{u}_l = (\gamma_{1l}a_1, \dots \gamma_{Nl}a_N, -\gamma_{1l}a_1^*, \dots -\gamma_{Nl}a_N^*)^T,\ \vec{u}_L = \frac{\partial \vec{a}}{\partial \tau},$$
$$\vec{a} \equiv (a_1, \dots a_N, a_1^*, \dots a_N^*)^T,\ l = 1, \dots (L-1)$$

are neutral modes of $\hat{\mathcal{L}}$, i.e. $\hat{\mathcal{L}}\vec{u}_l = 0$ $(l = 1, \dots L)$. Operator $\hat{\mathcal{L}}$ also has L associated vectors $\vec{U}_l = \partial\vec{a}/\partial\kappa_l$ such that $\hat{\mathcal{L}}\vec{U}_l = -\vec{u}_l,\ l = 1, \dots L$.

It is straightforward to see that any solution of EVP (8) must obey L solvability conditions

$$\langle \vec{w}_l | \lambda \vec{\xi} \rangle = 0,\ l = 1, \dots L, \tag{9}$$

where $\langle \vec{y} | \vec{z} \rangle = \sum_{i=1}^{2N} \int dx y_i^* z_i$ and $\vec{w}_l$ are the neutral modes of the operator $\hat{\mathcal{L}}^\dagger$.

Close to instability threshold it is naturally to assume that $|\lambda| \sim \epsilon \ll 1$. We seek an asymptotic solution of EVP (8) in the following form

$$\vec{\xi} = \sum_{m=0}^{\infty} \epsilon^m \vec{\xi}_m(x),\ \vec{\xi}_0 = \sum_{l=1}^{L} C_l \vec{u}_l \tag{10}$$

where constants C_l and vector-functions $\vec{\xi}_{m>0}$ have to be defined. Here and below $l = 1, 2, \dots L$. Substitution (10) into EVP (8) gives a recurrent system of the equations for $\vec{\xi}_m$

$$\vec{\xi}_{m>0} = \left[\frac{i\lambda}{\epsilon}\hat{\mathcal{L}}^{-1}\right]^m \vec{\xi}_0. \tag{11}$$

Substituting (10), (11) into conditions (9) one will find the homogeneous system of the L linear algebraic equations

$$\lambda^2 \left\langle \vec{w}_l \middle| \sum_{m=0}^{\infty} (-\lambda^2)^m \hat{\mathcal{L}}^{-2m} \sum_{l=1}^{L} C_l \vec{U}_l \right\rangle = 0 \tag{12}$$

for L unknown constants C_l. System (12) has a nontrivial solution providing that the corresponding determinant is equal to zero. This determinant is an infinite-order polynomial with respect to λ^2. Zeros of this polynomial define the spectrum of the solitary wave linked with the chosen class of the perturbations. Thus the equation specifying soliton spectrum is

$$\lambda^{2L} \sum_{j=0}^{\infty} (-\lambda^2)^j D_j = 0, \tag{13}$$

where D_j are the real constants.

To write the explicit expressions for D_j it will be convenient to introduce vectors $\vec{M}_l^{(m)} = (M_{l1}^{(m)} \quad . M_{lL}^{(m)})$, where,

$$M_{ll'}^{(m)} = \langle \vec{w}_l | \hat{\mathcal{L}}^{-2m} \vec{U}_{l'} \rangle,\ m = 0, 1, . \ . \infty$$

Now each D_j can be presented as

$$D_j = \sum_{m_1 + \ . \ m_L = j} \mathcal{D}(\vec{M}_1^{(m_1)}, . \ . \vec{M}_L^{(m_L)}), \tag{14}$$

where $\mathcal{D}(\vec{M}_1^{(m_1)}, \quad . \vec{M}_L^{(m_L)})$ is the determinant of the $L \times L$ matrix consisting from the raws $\vec{M}_l^{(m_l)}$ and sum is taken over all such combinations of $(m_1, . \ . m_L)$ that $\sum_{l=1}^{L} m_l = j \quad M_{ll'}^{(0)}$ can be readily expressed via derivatives of the conserved quantities with respect to the soliton parameters:

$$M_{ll'}^{(0)} = \frac{\partial Q_l}{\partial \kappa_{l'}}, \tag{15}$$

and practical calculation of $M_{ll'}^{(m)}$ for $m > 0$ can be simplified: $M_{ll'}^{(m)} = -\langle \vec{W}_l | \hat{\mathcal{L}}^{(1-2m)} \vec{U}_{l'} \rangle$.

Because $|\lambda|$ was assumed to be small, Eq. (13) has an asymptotic character. Therefore to make it work some additional assumptions must be made about orders of D_j. In the case if these assumptions are satisfied then Eq. (13) describes correctly the soliton spectrum and predicts bifurcations of the soliton. The corresponding eigenvalues can be found using Eq. (13) with any degree of accuracy. For example, let us assume that $D_0 \sim \epsilon^2$ and $D_{j>0} \sim O(1)$. Then, presenting λ^2 as

$$\lambda^2 = \epsilon^2 \sum_{j=0}^{\infty} \zeta_j,\ \zeta_j \sim \epsilon^{2j}, \tag{16}$$

in the first order Eq. (13) gives linear equation for ζ_0,

$$D_0 - \epsilon^2 \zeta_0 D_1 = 0, \tag{17}$$

which indicates threshold of the stationary bifurcation at $D_0 = 0$. Continuing calculations into the next order one obtains

$$\lambda^2 = \frac{D_0}{D_1}\left(1 - \frac{D_0 D_2}{D_1^2} + O(\epsilon^4)\right). \tag{18}$$

If $D_1 \sim \epsilon^2$ then the asymptotic expression (18) fails. To have balanced equation for ζ_0, we must now assume that $D_0 \sim \epsilon^4$. However, in such a case the equation for ζ_0 changes from the linear to the quadratic one:

$$D_0 - \epsilon^2 \zeta_0 D_1 + \epsilon^4 \zeta_0^2 D_2 = 0. \qquad (19)$$

Eq. (19) gives two threshold conditions $D_0 = 0$ and $D_1^2 = 4D_0D_2$, see Fig. 1. The latter condition indicates onset of an oscillatory instability for $D_1^2 < 4D_0D_2$. It is also clear that the point $D_{0,1} = 0$ is a source for the novel stationary instability, see region $D_1^2 > 4D_0D_2$, $D_1 > 0$ in Fig. 1, where the eigenvalue which is positive throughout this region can not be predicted by Eq. (18).

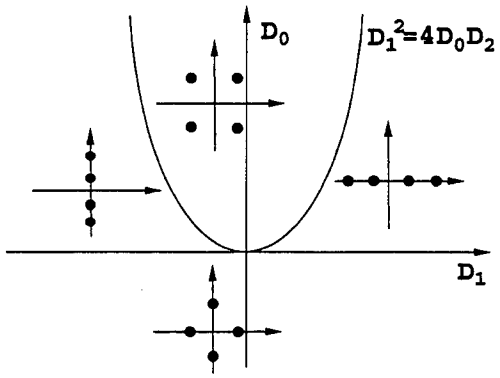


FIG. 1. Soliton bifurcation diagram in the neighbourhood of the point $D_0 = D_1 = 0$ for $D_2 > 0$. Insets show $(Re\lambda, Im\lambda)$-plane with horizontal/vertical axes corresponding to $Re\lambda/Im\lambda$ and dots marking soliton eigenvalues described by Eq. (19).

It is straightforward to see by recurrence that if $D_{j'>0} \sim \epsilon^2$ then, to have balanced equation for ζ_0, we must assume that $D_{j<j'} \sim \epsilon^{2(1+j')}$. Other words asymptotic expansion near the neutral modes can describe soliton spectrum in such regions of the parameter space which are close to the codimension-$(j'+1)$ bifurcation. If $j' = 0$ then only one condition must be satisfied and our asymptotic approach predicts presence of either two purely imaginary or two purely real eigenvalues, which can collide at zero. If $j' = 1$ then two conditions must be satisfied and asymptotic approach predicts presence of two pairs of the eigenvalues which can be real, imaginary or complex. In this situation soliton becomes oscillatory unstable providing that two pairs of imaginary eigenvalues collided. For each further j' two new eigenvalues come into play.

It is instructive now to consider two simplest situations of the one- and two-parameter solitons. For the one parameter solitons: $D_0 = \partial_{\kappa_1} Q_1$, $D_1 = -\langle \vec{W}_1 | \hat{\mathcal{L}}^{-1} \vec{U}_1 \rangle$, $D_2 = -\langle \vec{W}_1 | \hat{\mathcal{L}}^{-3} \vec{U}_1 \rangle$. For the two-parameter solitons:

$$D_0 = \begin{vmatrix} \frac{\partial Q_1}{\partial \kappa_1} & \frac{\partial Q_1}{\partial \kappa_2} \\ \frac{\partial Q_2}{\partial \kappa_1} & \frac{\partial Q_2}{\partial \kappa_2} \end{vmatrix},$$

$$D_1 = \begin{vmatrix} \frac{\partial Q_1}{\partial \kappa_1} & \frac{\partial Q_1}{\partial \kappa_2} \\ M_{21}^{(1)} & M_{22}^{(1)} \end{vmatrix} + \begin{vmatrix} M_{11}^{(1)} & M_{12}^{(1)} \\ \frac{\partial Q_2}{\partial \kappa_1} & \frac{\partial Q_2}{\partial \kappa_2} \end{vmatrix},$$

$$D_2 = \begin{vmatrix} M_{11}^{(1)} & M_{12}^{(1)} \\ M_{21}^{(1)} & M_{22}^{(1)} \end{vmatrix} + \begin{vmatrix} \frac{\partial Q_1}{\partial \kappa_1} & \frac{\partial Q_1}{\partial \kappa_2} \\ M_{21}^{(2)} & M_{22}^{(2)} \end{vmatrix} + \begin{vmatrix} M_{11}^{(2)} & M_{12}^{(2)} \\ \frac{\partial Q_2}{\partial \kappa_1} & \frac{\partial Q_2}{\partial \kappa_2} \end{vmatrix}$$

Comparing the first order approximation for the eigenvalues close to the *stationary* instability threshold, see Eqs (18), and eigenvalues which can be calculated from the effective particle Hamiltonians presented in [4,6] one will discover significant difference in the resulting formulae. Mapping the presented theory to the method used in [4,6], it becomes clear that the results of Refs. [4,6] can be recovered if one will try to calculate λ^2 in order ϵ^2 using ratio C_1/C_2 obtained from the solvability conditions (9) in the order $O(1)$, see Eqs. (7), (10) in [4]

Summary General form of the asymptotic approach to the stability problem of the multi-parameter solitons in Hamiltonian systems has been developed It has been shown that the asymptotic study of the soliton stability reduces to the calculation of a certain sequence of the determinants, where the famous determinant of the matrix consisting from the derivatives of the system invariants with respect to the soliton parameters is just the first in the series. The most important result is that the presented approach gives *criteria for the oscillatory and novel stationary instabilities.*

[1] E.A. Kuznetsov, A.M. Rubenchik, and V.E. Zakharov, Phys. Rep. **142**, 103 (1986).

[2] V.G. Makhankov, Y.P. Rybakov, and V.I. Sanyuk, Usp. Fiz. Nauk **164**, 121 (1994) [Physics-Uspekhi **37**, 113 (1994)].

[3] D.E. Pelinovsky, A.V. Buryak, and Y.S. Kivshar, Phys. Rev. Lett. **75**, 591 (1995); D.E. Pelinovsky, V.V. Afanasjev, and Y.S. Kivshar, Phys. Rev. E **53**, 1940 (1996).

[4] A.V. Buryak, Yu.S. Kivshar, and S. Trillo, Phys. Rev. Lett. **77**, 5210 (1996).

[5] U. Peschel *et al.*, Phys. Rev. E **55**, 7704 (1997); D. Mihalache *et al.*, Phys. Rev. E **55**, R6294 (1997).

[6] A. De Rossi, C. Conti, and S. Trillo, Phys. Rev. Lett. **81**, 85 (1998).

[7] D.V. Skryabin and W.J. Firth, Phys. Rev. E **58**, R1252 (1998).

[8] H.T. Tran *et al.*, Opt. Commun. **93**, 227 (1992); I.V. Barashenkov, D.E. Pelinovsky, and E.V. Zemlyanaya, Phys. Rev. Lett. **80**, 5117 (1998); D. Mihalache, D. Mazilu, and L. Torner, Phys. Rev. Lett. **81**, 4353 (1998).

40Gbit/s standard fibre transmission for a range of input pulse widths

D S Govan, P Harper, S. B. Alleston and N. J. Doran
Photonics Research Group, Aston University
Birmingham B4 7ET
Tel: +44 (0)121 359 3611 ext. 4995
Fax: +44 (0)121 359 0156
email: govands@sun.aston.ac.uk

Dispersion management is increasingly being used for the transmission of data at 40Gbit/s [1,2]. In the case of standard fibre this leads to dispersion map strengths that are well outside the range where stable propagation of dispersion managed solitons has been successful [3]. In this paper we numerically investigate the effect of varying the pulse width in a dispersion map that has been successfully used experimentally to transmit data over more than 1000km of standard fibre. It is found that changing the pulse width does not have a large effect on the total propagation distance, however some improvement in system performance can be gained by optimising the pulse width. The dispersion length of the pulses is also dependent of the pulse width that is used. As the dispersion length is reduced the level of pulse breathing increases and so it becomes more important to take the output near to the point in the dispersion map where the pulses are unchirped. The pulses used in these simulations also demonstrate reduced power when compared to the expected energy of a dispersion managed solitons [6].

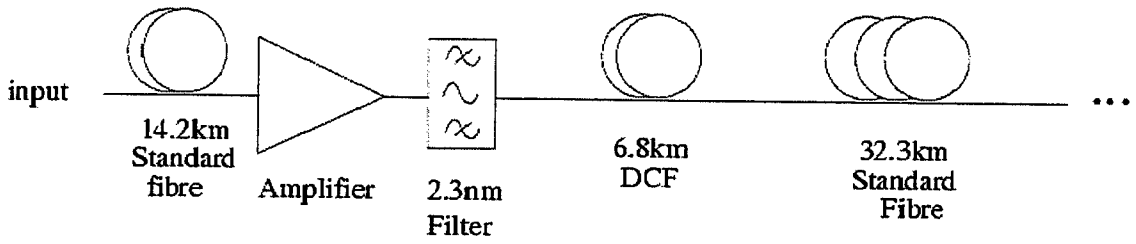


Figure 1: Schematic of the dispersion map used in this model.

The dispersion map used in these simulations is given in figure 1. It consists of 32.3km of standard fibre with dispersion of 16.012ps/(nm km) and third order dispersion of 0.06ps/(nm^{2}km). This fibre was taken to have loss of 0.22dB/km and an effective area of 70.0μm^2 The compensating fibre was of length 6.8km and had dispersion of -76.0ps/(nm km) and third order dispersion of -0.09ps/(nm^{2}km).. The effective area of this fibre was taken to be 30.0μm^2 and it was assumed to have loss of 6.5dB/km. The amplifier gain was ~10dB although it had to be increased for the shorter pulses as more excess gain was required to overcome the loss from the filter, the amplifier was taken to have a noise figure of 4.5dB. The filter had a 2.3nm passband and had a Gaussian profile. It has been found both experimentally and numerically that the optimum position of the compensating fibre, if it is in a single section, is immediately after the amplifier. This maximises the nonlinear effects in the compensating fibre [4,5,6].

Firstly the experiment in reference [2] was modeled using the experimental parameters. The input pulse was Gaussian in shape and had a pulse width of 7.0ps.. The pulse used had energy of 11fJ which is less than the expected energy for a dispersion managed soliton for a map of this strength (S=25). The pulse width used here is greater than would be normally used in a soliton system where a mark to space ratio of at least 1:5 is normally used to limit soliton-soliton interactions. Due to the short dispersion length of the pulses used here (< 1km) the pulse breathing means that the pulses overlap during most of their

propagation. The results of this simulation are given in figure 2. These show that transmission over 1300km is possible with Q values of more than 6 (equivalent to a bit error rate of 10^{-9}). This compares to the experimentally found transmission distance of 1220km

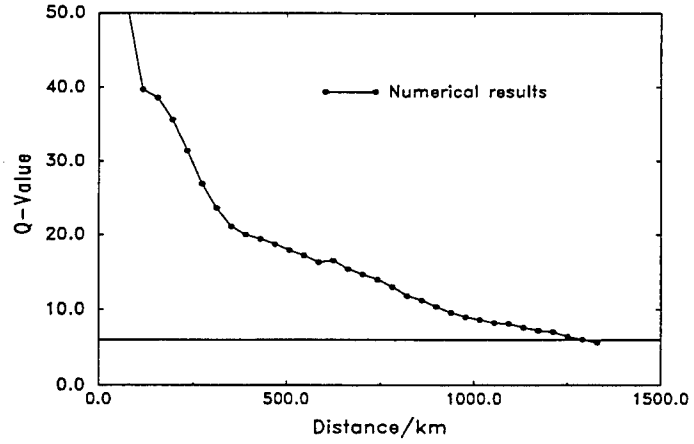


Figure 2. Numerical results for pulse width of 7ps.

The same simulations were also carried out for a range of pulse widths between 2 and 7ps. These results are given in Figure 3. This is equivalent to the dispersion map strength (given by; $S = \frac{L_n\beta_n - L_a\beta_a}{\tau^2}$) varying from 25 to 300. With this wide range of dispersion map strengths it would be expected that the transmission distance would also vary considerably. Figure 3 shows that while there is some variation in total propagation distance it is only 2 or 3 passes through the dispersion map. The change in dispersion map strength would also be expected to considerably change the required pulse energy, however in this case the same pulse energy was used in each simulation. The dispersion map strength is still significant in that it describes the amount of breathing the pulses undergo.

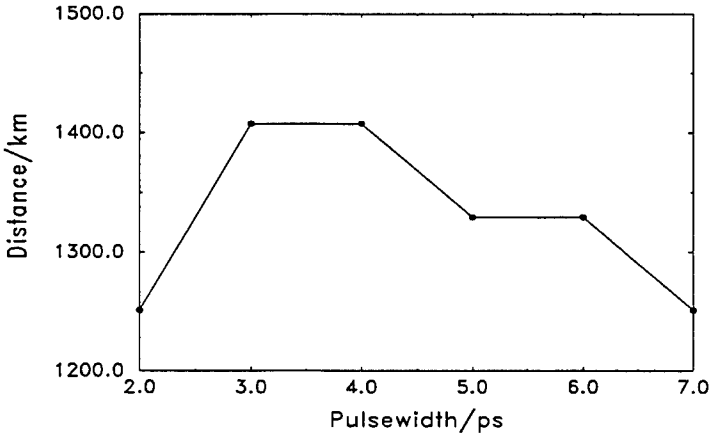


Figure 3. Maximum propagation distance for a range of pulse widths

Figure 4 shows the Q-values around the point in the dispersion map where the pulses are unchirped. It is clear that as the pulses reach the point where they are unchirped the Q-values reach the maximum value. The variation of the Q-value with output position is less for the 7ps pulse than it is for the 2ps pulse. The

reason for this can clearly be seen by comparing the dispersion lengths for the two pulses. A 2ps Gaussian pulse in standard fibre has a dispersion length of 75m while a 7ps pulse has a dispersion length of 900m. The 2ps pulse has broadened to 26ps after propagating through 1km of standard fibre and so has started to interfere with the neighbouring bit, the 7ps pulse has only broadened to 10.5ps in the same length of fibre. It is clear from this that it is less important to take the output at the correct position when broader pulse are used.

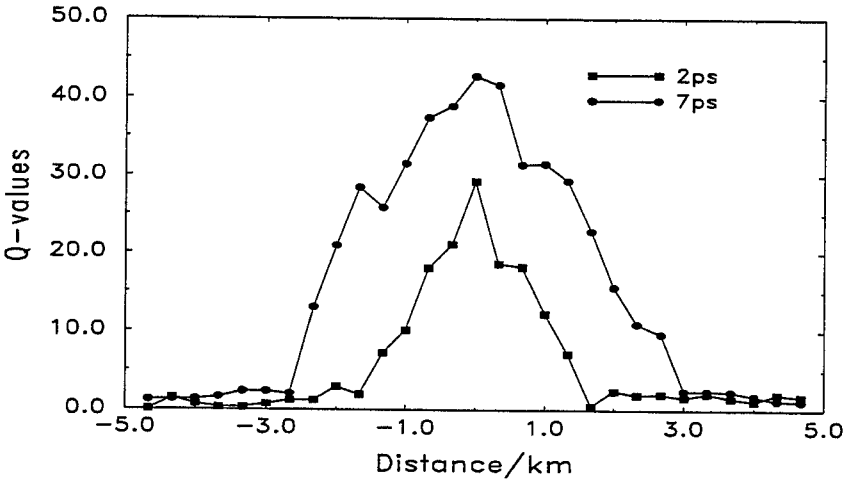


Figure 4. Q-values in the region of the unchirped point for 2ps and 7ps pulses.

In conclusion numerical simulations have been used to examine the effect of varying the pulse width in a dispersion managed standard fibre transmission line operating at 40Gbit/s using RZ pulses. It was found that the total transmission distance is not significantly changed despite the large change in the dispersion map strength. The increased pulse breathing that is observed with shorter pulses means that the output has to be taken closer to the point where the pulses are chirp free when shorter pulse widths are used.

Acknowledgment: This work was supported by the UK Engineering and Physical Sciences Research Council

References:

1. A. Sahara, K. Suzuki, H. Kubota, T. Komukai, E. Yamada, T. Imai, K. Tamura and M. Nakazawa. "Single channel 40Gbit/s soliton transmission field experiment over 1000km in Tokyo metropolitan optical loop network using dispersion compensation". Electron. Lett. 1998. **34.** (22) pp 2154-2155
2. S.B. Alleston, P. Harper, I.S. Penketh, I. Bennion and N.J. Doran. "1220km propagation of 40Gbit/s single channel RZ data over dispersion managed standard (non-dispersion shifted) fibre. OFC 1999. PD3, 1999.
3. J.H.B. Nijhof, N.J. Doran, W. Forysiak and A. Berntson. "Energy enhancement of dispersion managed solitons and WDM" Electron Lett. 1998 **34** (5) pp. 481-482
4. X.Y. Tang "Performance improvement of 10Gbit/s soliton transmission over dispersion managed standard fiber by using the nonlinearity of dispersion compensating fiber. NOC '97, Core and ATM Networks pp25-28
5. D. Bruer, F. Kuppers, A. Mattheus, E.G. Shapiro, I. Gabitov and S.K. Turitsyn. "Symmetrical dispersion compensation for standard-monomode fiber-based communication systems with large amplifier spacing" Opt Lett. 1997 **22** (13) pp 982-984
6. D.S. Govan, W. Forysiak and N.J. Doran "Long-distance 40Gbit/s soliton transmission over standard fiber by use of dispersion management" Opt Lett. 1998. **23** (19) pp 1523-1525

Complete characterisation of THz periodic pulse trains generated from nonlinear processes in optical fibers

J. M. Dudley
Department of Physics, University of Auckland, Private Bag 92019, Auckland, New Zealand
j.dudley@auckland.ac.nz

M. D. Thomson
Physikalisches Institut, Johann Wolfgang Goethe Universitaet, 60054 Frankfurt, Germany
thomson@physik.uni-frankfurt.de

F. Gutty, S. Pitois, P. Grelu, and G. Millot
LPUB, CNRS, 9 Av. A. Savary, BP 47 870, 21078 Dijon, France
gutty@jupiter.u-bourgogne.fr, pitois@jupiter.u-bourgogne.fr, grelu@jupiter.u-bourgogne.fr,
millot@jupiter.u-bourgogne.fr

It is well-known that intense quasi-CW fields injected into optical fibers can evolve into ultrafast periodic pulse trains at THz repetition rates as a result of the interplay between nonlinear and dispersive effects. This was first demonstrated in standard optical fiber in the anomalous dispersion regime via the effect of scalar modulational instability (MI) where a 0.5 THz intensity modulation was observed [1]. For standard fiber in the normal dispersion regime, MI for an incident scalar field is inhibited, but 0.6 THz trains of dark soliton-like pulses have been observed for a dual-frequency input signal as a result of multiple four wave mixing processes [2]. On the other hand, the use of birefringent fibers in the normal dispersion regime has resulted in the observation of the vector form of MI, which has led to the generation of vector dark soliton trains at repetition rates of 2.5 THz [3], and sinusoidal beating signals at repetition rates up to 16 THz [4]. In addition, for propagation in both the normal and anamolous dispersion regimes, THz trains of almost independent solitons can be generated by the adiabatic amplification of a scalar beating signal in a fiber with constant dispersion, or by the propagation of such a signal in a fiber with decreasing dispersion [5].

Aside from their fundamental scientific interest, the generation of THz pulse trains in optical fibers is also of significant applied interest since the development of THz-modulated light sources is an emerging key technology for high capacity optical communications systems and far-infrared spectroscopy [6]. However, a major difficulty with experimental studies of THz pulse trains is that the sub-picosecond temporal structure of the pulse train cannot be directly resolved using photodiodes or streak cameras. Instead, the pulse train characterization is usually performed only indirectly using measurements of the optical spectrum and autocorrelation function [1-4, 6]. As far as the characterisation of sub-picosecond ultrashort pulses is concerned, however, autocorrelation and spectral analysis are now routinely replaced by the technique of frequency-resolved optical gating (FROG) which can provide complete intensity and phase characterization on sub-picosecond timescales [6]. In this paper we show that FROG can also be used to characterize arbitrary periodic pulse trains at THz frequencies. We demonstrate the success of FROG for this purpose by considering the characterization of both bright and dark soliton-like THz pulse trains which have fundamentally different intensity and phase characteristics but which lead to qualitatively similar autocorrelation functions and spectra.

The FROG characterization of an arbitrary ultrashort pulse consists of two steps. The first step is to measure a two dimensional time-frequency spectrogram (or FROG trace) of the pulse, often achieved using a modified second-harmonic generation (SHG) autocorrelator. In this case, the SHG signal which varies as a function of the delay τ between the autocorrelator arms is spectrally resolved to yield a FROG trace which is a function of frequency ω and delay τ. The second step involves applying an iterative algorithm to this FROG trace to retrieve the best estimate of the incident pulse. In versions of the FROG retrieval algorithm developed for ultrashort pulses, it has been considered that successful retrieval requires a FROG trace that is vanishingly small for large values of ω and τ.

However, we show in this report that this is not at all a necessary requirement, and successful retrieval is also possible for functions that are periodic in time, even if they contain a non-zero background everywhere. Although this may seem surprising, it is a natural consequence of the fact that the numerical Fourier transform operations that are used in the retrieval algorithm can be applied equally well on functions that are periodic in time as for ultrashort pulses. Indeed, we have found that existing FROG retrieval algorithms can be adapted for the retrieval of periodic functions by introducing two straightforward modifications: (i) the introduction of a cyclic time-window to ensure that any temporal structure that leaves one edge of the computation window re-enters at the other edge, and (ii) the removal of any filtering effects used for pulsed data to force the edges of the trace to be identically zero. The cyclic time window preserves any periodic structure present in the measured FROG trace, allowing the successful retrieval of periodic intensity and phase structure in the underlying electric field E(t).

To illustrate the FROG characterization of THz pulse trains generated in optical fibers, Figure 1 shows two different pulse trains obtained from numerical simulations of the scalar or vector nonlinear Schrodinger equation. The top curves in Fig. 1 (a)-(c) correspond to a 2.5 THz train of vector dark solitons generated on the slow axis of a birefringent fiber in the normal dispersion regime [3]. Fig. 1(a) shows the pulse train intensity and phase, clearly illustrating the 100% modulation associated with the dark solitons and the π phase difference between adjacent solitons. Fig. 1(b) and (c) show conventional spectrum and autocorrelation function respectively, with the result of the dark soliton train generation being the appearance of a set of discrete spectral components separated by 2.5 THz and an associated temporally-modulated autocorrelation function. The bottom curves in Fig.1 (d)-(e) show the equivalent results obtained for a 0.5 THz pulse train generated in standard fiber in the anomalous dispersion regime at an intermediate stage in the evolution of an initial sinusoidally modulated field into a train of bright solitons.

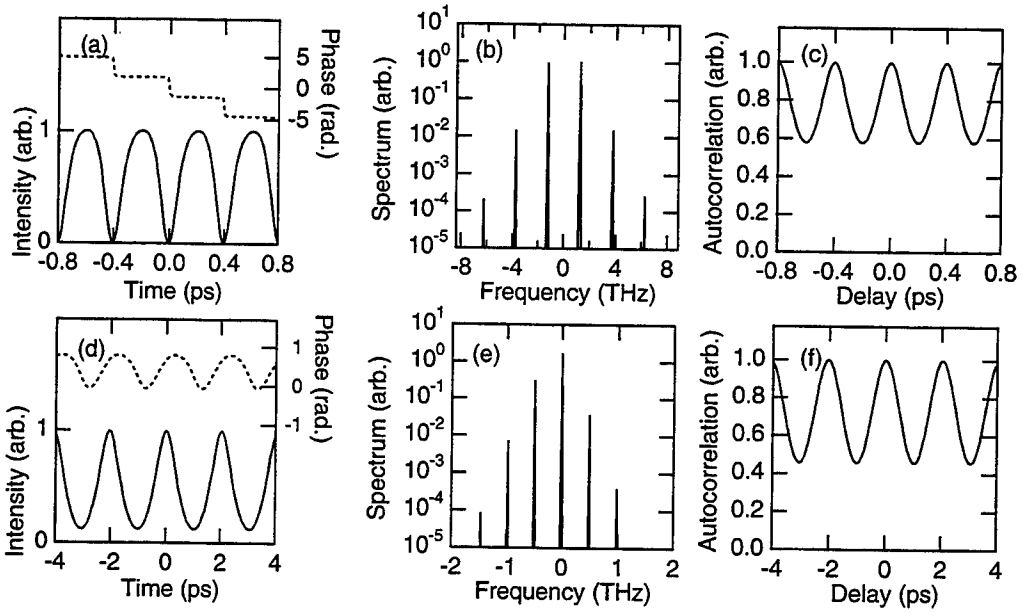


Figure 1. Top (a)-(c): Results for a 2.5 THz dark soliton train in the normal dispersion regime. (a) Intensity (solid line, left axis) and phase (dashed line, right axis), (b) spectrum, and (c) autocorrelation. Bottom (d)-(f): Corresponding results for a 0.5 THz pulse train in the anamalous dispersion regime.

The important feature of the results in Figure 1 is that even though the intensity and phase of the pulse trains in the normal and anamalous dispersion regimes are significantly different, this difference is not clearly manifested in the measurements of the spectrum and autocorrelation

function. Figure 2, however, shows how the use of FROG allows the exact retrieval of the intensity and phase characteristics of the pulse train in both of these cases.

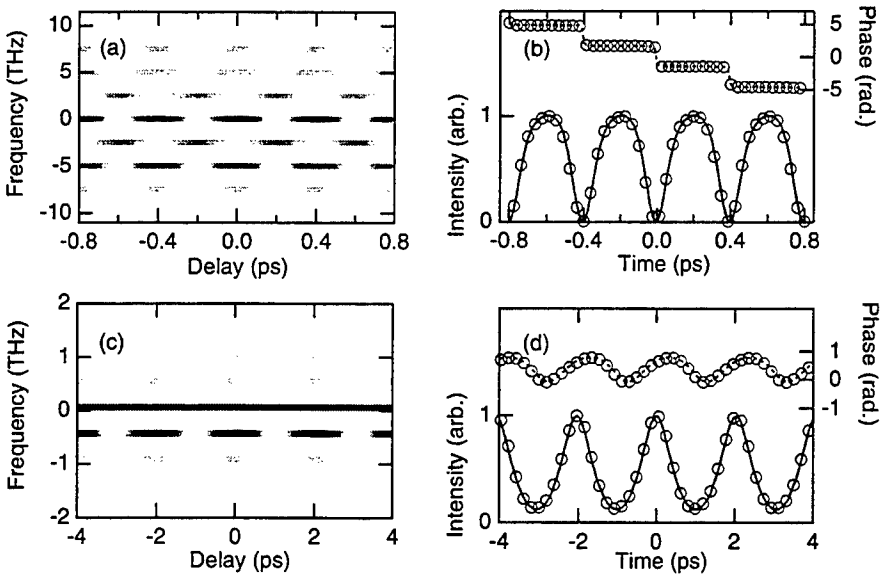


Figure 2: Top: (a)-(b) Results for a 2.5 THz dark soliton train. (a) SHG FROG trace, (b) retrieved intensity and phase (circles) compared with expected results (solid line). Bottom: (c)-(d) Corresponding results for a 0.5 THz pulse train.

The SHG-FROG traces for the 2.5 THz and 0.5 THz pulse trains are shown in Fig. 2 (a) and (c) respectively. The FROG traces contain significantly more information than the separate spectral and autocorrelation measurements because, as well as spectral bands at SHG frequencies corresponding to each component in the fundamental spectrum, they also shows spectral bands at frequencies corresponding to the mixing between these components. This leads to a complex modulation pattern at each SHG frequency component which depends on the exact intensity and phase of the incident pulse train. To simulate experimental conditions, 10% multiplicative noise was added to these FROG traces, and retrieval was then carried out using the adapted FROG algorithm described above. The retrieved intensity and phase are shown as the circles in Fig. 2 (b) and (d) and compared with the corresponding expected intensity and phase from simulations. It is clear that there is excellent agreement.

These results confirm the ability of an adapted-FROG technique to accurately retrieve the intensity and phase of periodic pulse trains at THz frequencies generated in optical fibers. The use of this technique should find wide application in nonlinear fiber optics, and should allow the direct comparison between experiments and theories of THz pulse train generation in fibers.

References

1. K. Tai, A. Hasegawa and A. Tomita, Phys. Rev. Lett. **56**, 135 (1986).
2. P.V. Mamyshev, P.G. Wigley, J. Wilson, C. Bosshard, and G.I. Stegeman, Appl. Phys. Lett. **64**, 3374 (1994).
3. E. Seve, G. Millot and S. Wabnitz, Opt. Lett. **23**, 1829 (1998).
4. S. G. Murdoch, R. Leonhardt and J. D. Harvey, Opt. Commun. **115**, 461 (1995).
5. E. M. Dianov, P. Y. Mamyshev, A. M. Prokhorov and S. V. Chernikov, Opt. Lett. **14**, 1008 (1989).
6. Y. Matsui, M. D. Pelusi, S. Arahira and Y. Ogawa, Electron, Lett. **35**, 472 (1999).

Symmetries, Chirp-Free Points and Bistability in Dispersion Managed Fibre Lines

S. K. Turitsyn, J. H. B. Nijhof, V. K. Mezentsev and N.J.Doran
Photonics Research Group, Aston University,
Aston Triangle, Birmingham, B4 7ET, UK
Phone: +44 121 359 3611
Fax: +44 121 359 0156
E-mail:s.k.turitsyn@aston.ac.uk

Dispersion compensation is a widely applied technique employed in long distance propagation at high data rates removing the effects of dispersion. For purely linear systems it is of no consequence where or how often within the transmission line the compensation is applied (at the start, end or an intermediate point in the system). For systems where there is any degree of nonlinearity this is not the case and the position and frequency of the compensation is a vital consideration. This is particularly so for soliton and RZ transmission format but is also an important consideration for NRZ systems. In this paper we aim to show from elementary symmetry arguments that stable evolution of the signal requires a chirp free point at the mid point of the dispersive sections.

It is now well known from extensive numerical and appropriate analytical models of nonlinear dispersion propagation that ideal periodic pulses can be obtained for a range of strengths of two stage dispersion maps. These solutions are conveniently labelled as solitons since they retain many familiar soliton properties and can be traced back to the 'conventional' solitons in the limit of weak dispersion management. In all cases the observation is that by considering a periodic dispersive structure with two sections of opposite sign of dispersion (with arbitrary different physical lengths) the solution requires that the pulses are unchirped at the mid point in either section. This is a profoundly important observation. It shows that the naïve application of dispersion compensation with initially unchirped source pulses with exact dispersion compensation either periodically or at the end of the system is as far removed from the ideal solution as it is possible to get! The concept of prechirping the source pulses to match the stable chirp needed at the start of the transmission fibre is of course one clear way to deal with this problem. It is worth re-emphasising that if the systems were linear then the initial waveform is immaterial since exact compensation guarantees restortion of whatever waveform is launched. For nonlinear systems this is not the case and only small nonlinearity is sufficient to destroy the perfect reproducability. We consider the fundamental lossless, dispersive nonlinear propagation model [1,2] (which is the limit of the dispersion compensation period L being much larger than the amplification distance Z_a):

$$i\frac{\partial A}{\partial z}+d(z)A_{tt}+\sigma|A|^2A=0, \qquad (1)$$

Here d(z) is the dispersion (see [3] for notations), periodic with the period L. The dispersion-managed soliton solution to Eq. (1) is given (see e.g. [3]) by $A(z,t)=F(z,t,k)\exp(ikz)$ with a periodic function F(z+L,t)=F(z,t). The soliton shape is given by

$$i\frac{\partial F}{\partial z}-kF+d(z)F_{tt}+\sigma|F|^2F=0. \qquad (2)$$

In the most of practical dispersion map, the parameter k (wavenumber or quasi-momentum in terms of the theory of the Bloch functions) completely and uniquely characterizes DM soliton solution of Eq. (1). In practical terms, the parameter k uniquely determines the pulse width and the energy of DM soliton is unambiguously deduced by the pulse width. We do not consider here the degeneracy corresponding to the two branches of the solutions existing in the strong enough map with zero or normal average dispersion and having different energies for the same pulse width [3]. In general, for some maps it could happen that two

stable periodic solutions do exist with the same pulse width (an example will be presented below). However, for most of practical maps we can conclude that it is established on the physical level of accuracy that the parameter k uniquely determines the DM soliton solution of Eq. (2). Based on this statement, we now prove that the chirp-free points in such systems are always located at the points of symmetry of the function d(z), in particular, for the two-step map, in the middle of each fibres. Equation (2) possesses the following symmetry: if $F(z,t,k)$ is a solution of Eq. (2) then $F^*(-z,t,k)$ is also a solution providing that the periodic dispersion map obeys the symmetry condition d(-z)=d(z). Because the function $F(z,t,k)$ describes the DM soliton with the same wavenumber k (and consequently the same pulse width) as $F(-z,t,k)$ it must satisfy condition (extra factors like $\exp(i\alpha)$ are not important due to gauge invariance of Eq. (1)): $F^*(-z,t,k) = F(z,t,k)$. This condition immediately gives that at the origin of any symmetrical map $z = 0, \mathrm{Im}\,F(0,t) = -\mathrm{Im}\,F(0,t) = 0$. Evidently this means that DM soliton uniquely determined by the parameter k, has no chirp at the points of the symmetry of the dispersion map. For two-step map, in particular, such points are always in the middle of the fibre spans for any signal power.

It is already known (see e.g. [2-5] that fitting (even if approximate) of the input signal with the true periodic wave form for a given map can be realized either with prechirping technique [4] using additional fiber or launching the transform-limited pulse at the specific chirp-free points [5]. The appropriate input chirp can be calculated using two basic ordinary differential equations (ODEs) for the RZ signal width and chirp. It is interesting to address the following question: what is the optimal point along the map to launch an input signal with parameters found using this approximate ODEs model ? Is there any difference between launching transform-limited signal at chirp-free point or appropriately chirped pulse at any other point along the dispersion map ? In other words, this is a question about sensitivity of the signal evolution to small deviations of input pulse from the true periodic wave form.

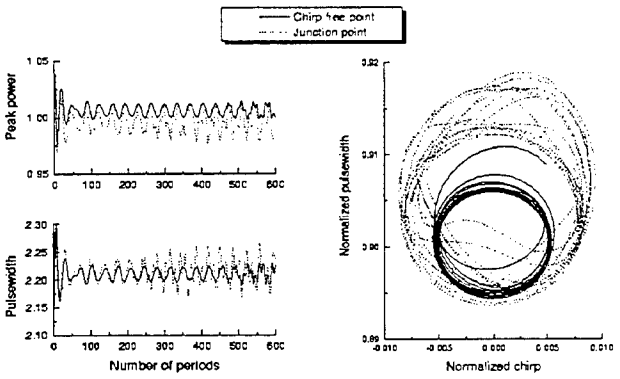


Figure 1. Slow (stroboscopic) evolution of two input Gaussian pulses (with parameters found from ODEs model) launched at chirp-free point (solid lines) and at the junction between fibers (dashed lines).

Fig. 1 shows slow (stroboscopic) evolution of the pulse peak power (top left) and RMS pulse width (bottom left) of the Gaussian pulses with parameters found from the ODEs model, launched either in the chirp-free point (solid lines) or at the junction between two fibers (dashed lines). In the second case pulse

has appropriate chirp. Here d(z) is 5.15 in the first fiber and –4.85 in the second fiber, $\sigma = 1$, other parameters are shown in the figure. The right picture shows the slow (stroboscopical) dynamics as a mapping in the plane pulse width (FWHM), chirp (starting from 30-th section to remove first large amplitude transition trajectories). Input signal launched at chirp-free point during many periods evolves around some circle (DM soliton presents a fixed point in this picture). It is seen that the ODEs approximation of the input signal works much better when the pulse is launched at the chirp-free points. This result has the following qualitative explanation. Near the chirp-free points the changes of the signal parameters are slower compared with a rather fast change near the junction between two fibers. It is natural to expect that the same small initial deviations from periodic solution lead to larger deflections in the corresponding trajectories as it is seen in Fig. 1.

For completeness of the presentation, we point out that developed analysis does not apply to the case of bistability, when two or more stable solutions exist with the same pulse width. There are dispersion maps for which a symmetry breaking occurs, in particular when the dispersion is small near the boundary. For instance, for a dispersion map shown in Fig. 2 with segments of identical lengths and dispersions of -1, -2, -1, 1, 2, and 1, respectively, has two solutions, that are complex conjugate in the midpoints of the fibres. In this case, chirp-free points *are not in the middle of fibers*, even in the lossless case.

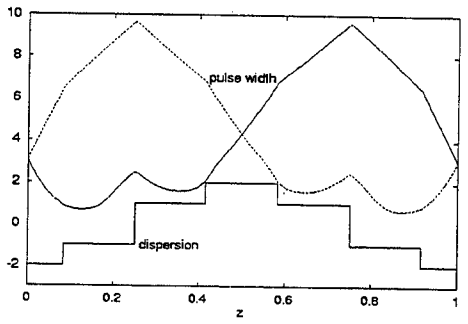


Figure 2. Effect of bistability. Two stable periodic solutions (pulse widths evolution is shown) do exist in the map shown below. In this case the chirp-free points corresponding to the minima of the pulse width are not in the centers of the symmetry.

This paper has shown from an elementary symmetry analysis that in dispersion compensated systems where a "lossless" model is valid, both RZ and NRZ, that nonlinearity requires a chirp free point at the centre of each section.

References.

1. N. J. Smith, F. M. Knox , N. J. Doran, K. J. Blow and I. Bennion, Electron. Lett., 32, 54 (1996).

2. N. J. Smith, N. J. Doran, F. M. Knox and W. Forysiak, Opt. Lett., 26, 1981 (1996).

3. S. K. Turitsyn, E. G. Shapiro and V. K. Mezentsev, Opt. Fiber Techn., 4, 384 (1998).

4. T. Georges and B. Charbonnier, IEEE Photon. Techn. Lett., 9, 127 (1997).

5. T. S. Yang, W. L. Kath and S. K. Turitsyn, Opt. Lett. 23, 597 (1998).

Cross phase induced pulse splitting - the optical axe

Lukas Helczynski, Bjorn Hall, Dan Anderson and Mietek Lisak
Department of Electrodynamics, Chalmers University of Technology, S-412 96 Göteborg, Sweden
bjorn.hall@elmagn.chalmers.se
Anders Berntson
Ericsson Telecom AB, S-126 25 Stockholm
Mats Desaix
Department of Engineering Sciences, The University of Boras, Box 874,Boras, Sweden

Introduction Manipulation of optical pulses using cross phase modulation by a control pulse is a well established technique for e.g. compression and switching of optical pulses in time and or frequency. Mostly analysis and applications have been concentrated to situations where the nonlinearity is of the focusing type, c.f. e.g.[1]. However, some interest has also been given to situations involving a defocusing Kerr nonlinearity. In some of the numerical simulations of this situation, it can be seen that for a copropagating pump-probe pair of pulses, the signal pulse tends to change form in the sense that it begins to broaden and start to develop "ears" in the outer parts of the intensity profile, cf e.g. [2].

In the present work we consider in more detail, both analytically and numerically, the effects of cross phase modulation in a situation involving a pump-probe configuration in a nonlinear defocusing Kerr medium. In particular it is shown that the previously observed deformation of the probe pulse is only the first stage of a new pulse splitting phenomenon where the pump pulse splits the probe pulse into two smaller (frequency shifted) pulse fragments which separate - a phenomenon suitably named the optical axe.

The analytical analysis consists of two steps: First a perturbative analysis is made which clearly indicates the initial behaviour of the probe pulse for the cases of focusing and defocusing nonlinearity respectively. For the focusing case the pulse starts to compress as expected and for the defocusing case the pulse first broadens, then starts to develop ears and finally splits down the middle. Numerical simulations confirm the splitting, but also show that the two parts acquire symmetrical frequency shifts and start to separate.

A more elaborate analysis, in terms of the variational approach, is then made to analyze the effect of cross phase modulation of a strong pump pulse on a weak probe pulse. The result of this analysis can be summarized in terms of a two dimensional Hamiltonian system for the variation of the pulse width and (for the defocusing case) the separation of the probe fragments. In the case of a focusing nonlinearity, the pulse does not split and the system reduces to a single equation, which can easily be solved to find the dynamical evolution and in particular the compression ratio of the probe pulse. In the defocusing case and for high pump amplitudes, the major effect is the splitting of the probe pulse rather than the internal dynamics of the separating parts. This implies that again the full Hamiltonian system reduces, but this time into a single equation for the separation dynamics. The corresponding equation can easily be solved to find the asymptotic separation velocity (i.e. also the asymptotic frequency shifts) of the pulse fragments.

Finally a numerical analysis is made of the system of coupled nonlinear Schroedinger equations describing the full cross phase modulation induced interaction of the two pulses. The numerical results are also shown to be in good agreement with the variational predictions.

Analytical analysis In the limit of a strong pump and a weak probe pulse, the coupled nonlinear Schroedinger equations can be decoupled into a single nonlinear Schroedinger equation for the pump and a linear Schroedinger equation (including an "external" potential generated by the pump) for the probe. In conventional normalized coordinates, the equation for the slowly varying envelope function of the probe can be written

$$i\psi_x + \frac{1}{2}\psi_{\tau\tau} + U(x,\tau)\psi = 0$$

where the potential $U(x,\tau)$ is proportional to the pump intensity and the sign of U is determined by the relative sign of the linear dispersion and the nonlinear refractive index change. For a focusing medium $U > 0$ whereas for a defocusing medium $U < 0$. We will consider the pump and probe pulses to be Gaussian in time, which implies that a suitable choice of trial function to be used in the variational approach is

$$\psi(x,\tau) = A(x)\exp\{-\frac{[\tau - M(x)]^2}{2a^2(x)} + i[D(x) + C(x)(\tau - M(x) + E(x)(\tau - M(x))^2]\}$$

where the evolution of the pulse is determined by the evolution of the parameter functions, a, A, C, D, E and M. This ansatz function is flexible enough to describe the phenomena which we want to analyze. For the focusing case, M = 0, and the ansatz describes the focusing and subsequent defocusing of the whole probe pulse whereas in the defocusing case we will assume a symmetric situation and the ansatz describes one of the symmetrically separating pulses.

Going through the conventional steps in the variational approach we find that the variational equations with respect to the parameter functions can be reduced to two coupled equations for pulse width, a(x), and pulse separation, M(x) viz.

$$a_{xx} + \frac{\partial \pi}{\partial a} = 0 \qquad \text{and} \qquad 2M_{xx} + \frac{\partial \pi}{\partial M} = 0$$

We will here, for simplicity, concentrate on the case when the pump dynamics and walk-off effects can be neglected, which implies that, without loss of generality, we can write $U = N\exp(-\tau^2)$, where the sign of N is determined by the relative sign of dispersion and nonlinearity and the potential function $\pi = \pi(a, M)$ is given by

$$\pi(a) = \frac{1}{2a^2} - \frac{2N}{\sqrt{1+a^2}}\exp(-\frac{M^2}{1+a^2})$$

Two limiting cases are particularly interesting:

(i) The focusing case (N>0). In this case, no pulse splitting or pulse displacement occurs and we can assume M = 0. The corresponding equation for a(x) can then easily be integrated once and the compressed pulse width can be found in terms of N (assuming $a_x(0)=0$). For strong compression we find

$$a_m \approx \frac{1}{2\sqrt{N}} \frac{1}{\sqrt{1 - \frac{1}{\sqrt{1+a_0^2}}}}$$

where a_o and a_m denote the initial and minimum pulse widths respectively.

(ii) The defocusing case (N<0). In this case, the main dynamics will be a splitting of the pulse into two fragment pulse which are shot out of the interaction region without much "internal" dynamics. Thus this situation is complementary to the first situation in the sense that the internal pulse dynamics involving changes in amplitude and width are less important than the separating motion of the pulses. We can then consider the pulse width, a, as approximately constant, which reduces the system into a single equation for M. This equation is trivially integrated once to yield the asymptotic separation velocity M_x as follows

$$M_x = \sqrt{2\,|N|} \qquad as \quad x \to \infty$$

Numerical simulations The full set of coupled nonlinear Schroedinger equations for the pump and probe has been solved without any simplifying assumptions about the relative amplitudes of the pulses and the results have also been copmpared with the theoretical predictions. Two examples of the numerical results are given in figures 1 and 2. Figure 1 shows the action of the optical axe as it splits the probe pulse into two separating pulses which travel out of the interaction region and then settle into straight line trajectories in (x,τ) space. Fig.2 shows a comparison between the numerical results and the variational predictions for the asymptotic separation velocity. The agreement is seen to be good.

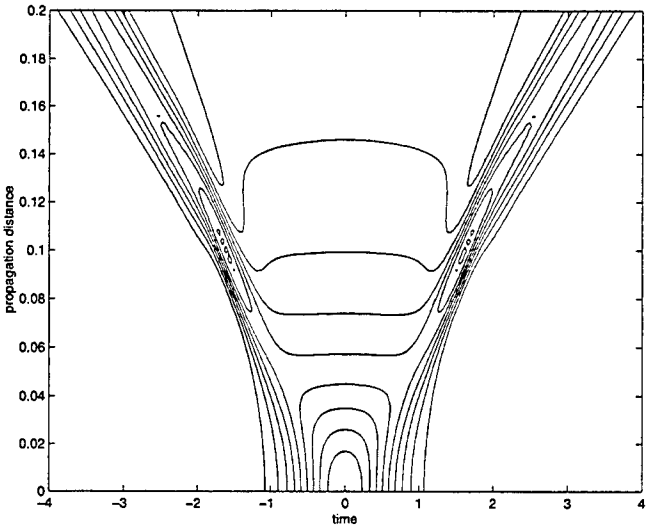


Fig. 1: Numerical simulation result showing the splitting action of the optical axe..

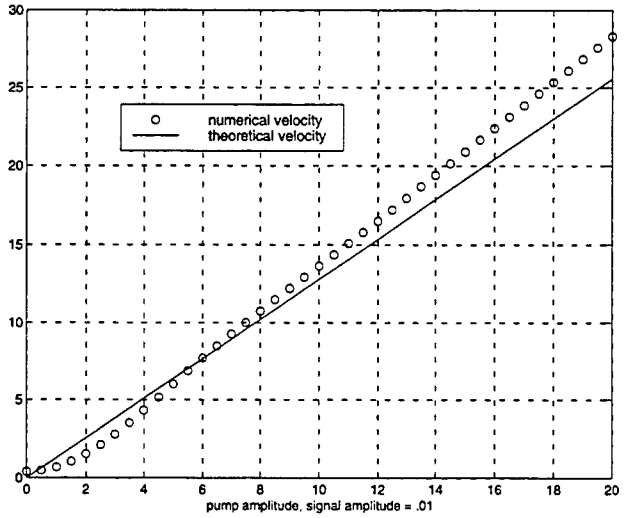


Fig. 2: Comparison between numerical results and variational predictions for the asymptotic separation velocity of the pulse fragments

References

[1] G.P. Agrawal, P.L. Baldeck and R.R. Alfano, Phys.Rev.A 40(1989),5063
[2] J.M.Hickman,A.S.L. Gomes and C.B deArau'jo Phys.Rev.Lett. 68(1992) 3547
[3] D.Anderson, Phys.Rev.27(1983)3135

Modulation Instability in long amplified fiber links with dispersion compensation

Ernesto CIARAMELLA, Mario TAMBURRINI
Fondazione Ugo Bordoni, Via B. Castiglione, 59, 00142 Roma (Italy)
Phone: +39 06 5480 2212; Fax: +39 06 5480 4402; e-mail: eciaramella@fub.it

Introduction. In long amplified links, high bit rate optical NRZ signals may suffer from the Modulation Instabilty (MI) effect, as it enhances noise impairments if fiber dispersion is anomalous [1]. We refer to MI as to spontaneous amplification of a small modulation superimposed to a signal wave, mathematically described by linear expansion of the Nonlinear Schrödinger Equation (NLSE) for a slight perturbation with a CW pump signal [2]. When dispersion is uniform, this analysis shows that MI originates two gain bands in the frequency domain, that are symmetric with respect to the signal carrier and can be characterized by the peak gain G_{MI} and peak frequency detuning $\Delta\nu_{MI}$ [3,4]. Noteworthy $\Delta\nu_{MI}$ depends on the dispersion coefficient D, but G_{MI} is just determined by the Kerr coefficient γ and the pump power P.
Today, most of the installed links use conventional Single Mode Fibers (SMFs), exhibiting a large chromatic dispersion coefficient D in the operating Optical Fiber Amplifier (OFA) bandwidth: to support high bit rate signals (≥10 Gbit/s), those SMF links will most likely use passive components for chromatic Dispersion Compensation (DC) at each amplifier site. Hence, as compensator spacing L_{DC} coincides with OFA spacing L_A, interplay between periodic amplification and dispersion variations will not be negligible, and a lossless approximation can not be applied [5]. In that case it is not yet clear how MI features would be affected: although nonlinear propagation would still occur just in each SMF section, DC may alter phase matching conditions between consecutive spans.
Here we present a detailed analysis of MI in long amplified links with amplifiers and DC, obtained by means of the analytical solution of the exact governing equations. When a typical compensation scheme is used, MI is much different than in uniform fibers, and it produces far lower system impairments. This can have high potential impact on system design.

Results. We considered N span links with $L_{DC}=L_A$ as in Fig.1. In each SMF section the evolution of the field $U(z,t)$ is described by the well known NLSE [2]:

$$i\frac{\partial U}{\partial z}=\frac{1}{2}\beta_2\frac{\partial^2 U}{\partial t^2}-\gamma|U|^2U-i\alpha U \qquad (1)$$

where β_2 is the chromatic dispersion in ps^2/km and α is the fiber loss coefficient. On the other hand, the linear propagation in each lumped compensator and OFA at $z=nL_A$ ($n=1, 2,...N$) is given in the frequency domain by:

$$U(nL_A+,\omega)=G\,e^{-iB\omega^2/2}U(nL_A-,\omega) \qquad (2)$$

where the OFA gain exactly compensates for fiber loss $G=exp(\alpha L_A)$, and B is the compensator dispersion. We studied MI assuming an input ($z=0$) signal consisting of a CW pump with a small perturbation given by a single tone at $\omega=2\pi\nu$ from the carrier:

$$U(0,t)=\sqrt{P}\left(1+a_+^0e^{i\omega t}\right) \qquad (3)$$

In this case Eqn. 1 is linearized and then can be solved using generalized Bessel functions [4]. MI evolution is obtained by iterating N times this solution and that of Eqn. 2. However the overall solution for long links is too involved to be put into an analytical form. We thus implemented a software tool that numerically computes the field solution (this also contains the conjugate spectral component at $-\omega$):

$$U(NL_A,t)=\sqrt{P}\left(1+a_+e^{i\omega t}+a_-e^{-i\omega t}\right) \qquad (4).$$

The results agree very well with those of usual split step simulations, but are obtained in a much shorter (about 3 orders of magnitude less) computing time and are almost free from numerical noise.
We first investigated the MI dependence on the DC amount. To this aim we denoted by fractional residual dispersion δ, the fraction of the SMF dispersion which is not fully compensated for ($\delta=1-B/\beta_2L_{DC}$).

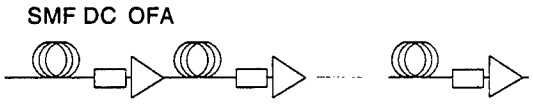


Fig. 1. Link scheme. Each span consists of a 100 km long SMF, a linear dispersion compensator (DC) and an optical amplifier (OFA).

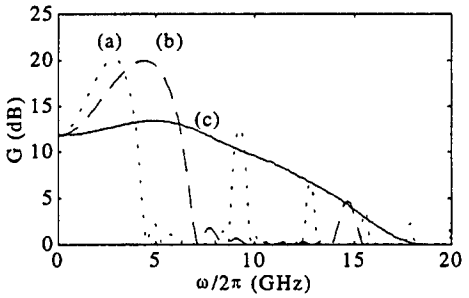


Fig. 2. DC effect on MI band in N=8 span links with input power P=10 mW. Curves a, b, and c, indicate respectively δ=1 (no DC), δ=0.4, and δ=0.05.

In Fig. 2 we report three examples of one side of the symmetric spectral gain curves, showing the power gain experienced by the seed ($G=|a_+|^2/|a_+^0|^2$) versus $\omega/2\pi$ Results were obtained for input power $P=10$ mW in a $N=8$ span link without compensation ($\delta=1$, curve a), with significant DC ($\delta=0.4$, curve b) and with almost complete DC ($\delta=0.05$, curve c). Typical parameters were assumed for the SMF ($\gamma=1.7$ (W km)$^{-1}$, 0.22 dB/km loss coefficient, $D=16$ ps/nm/km). As is also obtained by split-step simulations, besides the usual MI band, other instability peaks arise because of the periodic structure of the link [6].
Noteworthy, for moderate compensation, MI is essentially determined by the average span dispersion. This can be seen in curve b, obtained for $\delta=0.4$: here compensation does increase the $\Delta\nu_{MI}$ value compared to curve a, but the gain spectrum is almost the same we obtain for an equivalent link with uniform dispersion coefficient δD. As also typical for uniform dispersion fibers, G_{MI} value is not much affected. On the other hand, as δ approaches zero, MI deviates from this average behavior: as illustrated in curve c, the peak frequency for $\delta=0.05$ does not increase further; moreover, the peak gain is quite lowered. Clearly in this case phase matching variations are so strong that MI is no more just sensitive to the average dispersion, and therefore originates gain bands exhibiting quite different features.
We give a simple criterion to explain when MI in dispersion compensated links behaves according to the "average dispersion". MI peak position and gain could be estimated by using an average model if no significant phase matching variation occurred over a fiber effective length ($L_{eff}\cong$20 km for previous parameters). For a seed at the MI peak frequency detuning, this gives the condition:

$$\frac{1}{2}|\beta_2|(2\pi\Delta\nu_{MI})^2 L_{eff} < 1 \qquad (5)$$

where β_2 is the chromatic dispersion coefficient in ps^2/km (-20.5 ps^2/km, in this case) [2]. If an average dispersion behavior held, $\Delta\nu_{MI} = 1/2\pi\sqrt{2\gamma P/(-\delta\beta_2)}$ (to this estimate level we neglect its dependence on fiber loss [3]), thus the condition to consistently apply an average dispersion regime will be:

$$\delta > \gamma P L_{eff} \qquad (6)$$

In the previous case this gives $\delta>0.35$, in good agreement with the obtained results.
It has to be noted that in typical transmission systems almost complete DC will take place: as an example, to get 1 ps/nm/km average residual dispersion, we would have $\delta\cong$0.06. Much higher δ values are quite unlikely. In this condition, we find that other MI features are indeed quite peculiar, and could be of relevant interest for system applications. In uniform fibers it is indeed well established that MI originates essentially a mixed Amplitude (AM) and Phase Modulation (PM), whose modulation depths are given by $|a_+ + a_-^*|$ and $|a_+ - a_-^*|$, respectively [1]: the relative amounts of AM and PM vary in the spectral band, as they depend on the ω value of the injected seed and, particularly, at the MI peak they are almost balanced [1]. This behavior is still obtained for quite limited DC amounts: in Fig. 3 (a) we report MI gains for the AM noise (continuous line) and PM noise (dashed line) calculated after N=4, 8, 16 and 32 spans in a link with $\delta=0.4$ (other parameters are the same as in the previous case), here the asymptotic behavior is almost reached after 8 spans, and is clearly composed of the usual mixed AM-PM modulation [1].

Noteworthy, when strong DC is applied, different results are obtained, as MI tends to generate a modulation that is essentially composed of PM, with quite lower AM noise. This is shown in Fig. 3 (b), where we report the evolution of the AM and PM gain for δ=*0.05* (average dispersion: *0.8 ps/nm/km*). We note that in a realistic condition ($N \leq 8$) the asymptotic features of AM and PM are not yet established, moreover in this case the AM noise could be depleted as it experiences a negative gain (in dB). This has an high potential impact on system design, as in the conventional IM-DD systems much lower MI impairments would arise [1]. It might be noted that the negative AM gain is not an asymptotic feature, indeed for low δ values the longitudinal dynamics of MI bands is much slower, so that the asymptotic behavior is obtained after a much larger number of spans. In this case, there is a positive gain for AM, but the PM component still dominates. We point out that the number of spans in real system is typically limited to lower values, thus for system applications the analysis of transients behavior will have much greater implications than the asymptotic treatment.

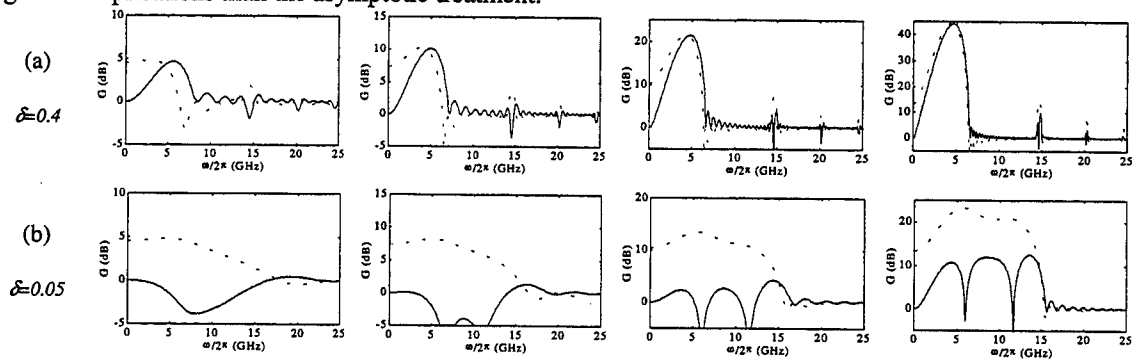


Fig. 3. AM (solid) and PM (dashed line) gain after N=4, 8, 16, 32 spans, with limited DC (δ=0.4) and almost complete DC (δ=0.05). Each amplified span contains a 100 km SMF plus a compensator.

Conclusions. MI bands are investigated in long amplified links made of conventional single mode fibers with periodic linear Dispersion Compensation (DC) and optical amplification. If DC is limited to a moderate percentage, MI bands are essentially determined by the average residual span dispersion. Noteworthy, in the highly realistic assumption that DC is almost complete, peak value and shape of MI bands are much more different, and evolve along the link according to a complex dynamics. In that case, MI essentially affects PM noise, so that the actual amplification of the AM noise is much lower. Moreover, for usual link features, the AM noise can even be attenuated.

Acknowledgements. This work was carried out in the framework of the agreement between Fondazione Ugo Bordoni and Telecom Italia.

References

[1] K. Kikuchi "Enhancement of optical amplifier noise by nonlinear refractive index and group velocity dispersion of optical fibers", *Photonics Technol. Letters*, **5**, 221-223 (1993).

[2] G. P. Agrawal, *Nonlinear fiber optics*, Academic Press (1995).

[3] D. Anderson, M. Lisak, "Modulational Instability of coherent optical fiber transmission signals", *Opt. Lett.* **9**, 468-470 (1984).

[4] M. Karlsson, "Modulation instability in lossy optical fibers'', *J.Opt.Soc.Am.B*, **12,** 2071-2077(1995).

[5] N.J. Smith, N.J. Doran "Modulation Instabilities in fibers with periodic dispersion management", *Optics Lett.*,**21**, 570-572 (1996).

[6] F. Matera, A. Mecozzi, M. Romagnoli, M. Settembre, "Signal propagation in the presence of side-band instability in long fiber links", *Optics Lett.*, **15**, 1499-1501 (1993).

Dynamics of dispersion-managed solitons in optical communication lines with random parameters

F.Kh. Abdullaev , B.B. Baizakov
Physical-Technical Institute of the Uzbek Academy of Sciences,
G. Mavlyanov str. 2-b, 700084, Tashkent, Uzbekistan
Tel: 899 (371) 133-12-71, Fax: 899 (3712) 35-42-91, e-mail: baizakov@physic.uzsci.net

Since the discovery of a new type of solitary waves in optical fiber links with a stepwise dispersion map [1], so called dispersion-managed (DM) solitons, there has been significant advance in understanding their basic properties. DM solitons turned out to be less susceptible to Gordon-Haus timing jitter, provide more dense packing in optical transmission lines and demonstrate extremely stable long distance propagation. The advantages of DM solitons come from the fact, that they possess higher pulse energy compared with that of conventional solitons in a uniform fiber with the same path averaged dispersion. Due to these features DM solitons are now being considered as most perspective information bit carriers in long-haul optical communication systems [2].

An optical transmission line, based on the dispersion compensation technique represents a chain of periodically linked pieces of fibers with alternating anomalous and normal group velocity dispersion. It is reasonable to suggest, that in practical situations corresponding fiber pieces will not be identical both with respect to dispersion magnitudes and lengths. Most likely there will be a random distribution of these parameters over certain mean values. As a result of breaking of the periodicity, DM soliton suffers random perturbations along its path, and eventually disintigrates after some propagation distance.

Main objective of this study is the investigation of DM soliton dynamics in optical transmission lines with a random dispersion map (Fig.1). The propagation of DM soliton is governed by the nonlinear Schrödinger equation (NLSE) for a dimensionless envelope of the electric field

$$iu_z + \frac{d(z)}{2}u_{tt} + \mid u \mid^2 u = 0, \tag{1}$$

where $d(z)$ is a stepwise function describing the dispersion map, which in its turn may be represented as consisting of periodic and random parts

$$d(z) = d_0(z) + d_1(z). \tag{2}$$

In the absence of the randomness it would be a periodic function $d_0(z) = d_0(z + z_+ + z_-)$, where z_+ and z_- are the fiber segment lengths. In our study we will be concerned with the Gaussian white noise model for $d_1(z)$, namely

$$< d_1 >= 0, \quad < d_1(z_1)d_2(z_2) >= 2\sigma^2\delta(z_1 - z_2). \tag{3}$$

We employ the variational approach developed by Anderson [3] to reduce the underlying NLSE to a system of ODE's for DM soliton parameters. With this purpose we will search for the solution to eq.(1) as a localized waveform

$$u(z,t) = A(z)F[\frac{t}{a(z)}]\exp\left(i\phi(z) + ib(z)t^2\right), \tag{4}$$

where A, a, b, ϕ are the complex amplitude, width, chirp parameter and phase respectively, $F(z)$ is the localized function. Here the conserving quantity is the "energy"

$$\int_{-\infty}^{\infty} |u|^2 dx = A^2 a = 1. \tag{5}$$

Random dispersion magnitudes *Random span lengths*



Figure 1: *Sketch of the random dispersion map (solid line). Dashed line corresponds to the regular map.*

Performing standard calculations we arrive to the following variational equations, describing the evolution of the soliton parameters

$$a_z = 2d(z)ab, \tag{6}$$

$$b_z = \frac{C_1 d(z)}{a^4} - \frac{C_2}{a^3} - 2d(z)b^2. \tag{7}$$

where

$$C_1 = \frac{\int_{-\infty}^{\infty} |F_t|^2 dt}{\int_{-\infty}^{\infty} t^2 |F|^2 dt}, \; C_2 = \frac{\int_{-\infty}^{\infty} |F|^4 dt}{4 \int_{-\infty}^{\infty} t^2 |F|^2 dt} \tag{8}$$

For the Gaussian ansatz $F(t) = exp(-t^2)$ one obtains $C_1 = 2$, $C_2 = 1/\sqrt{2}$, and for $F(t) = sech(t)$ corresponding values are $C_1 = C_2 = 2/\pi^2$. We performed numerical simulations of the pulse

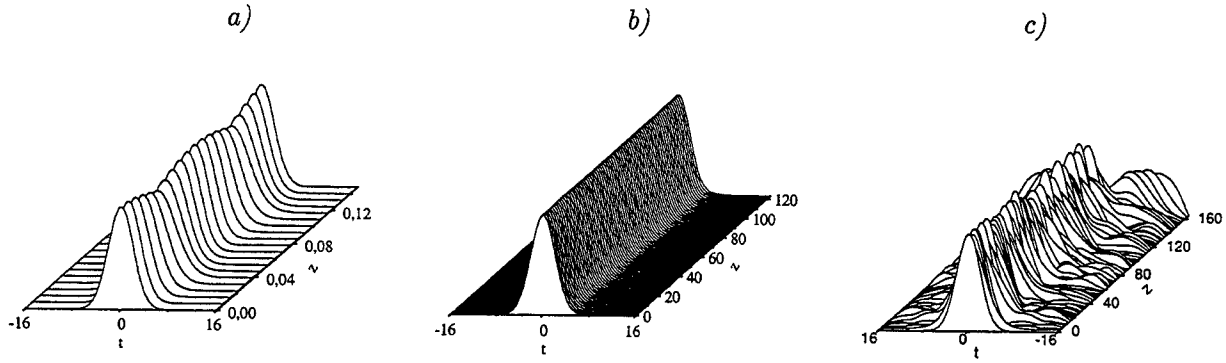


Figure 2: *Pulse shape evolution in optical communication line based on the dispersion-management technique. a) within a unit cell; b) long distance propagation in the case of a regular map; c) pulse disintegration in the case of a random map when dispersion magnitudes are randomly deviated by 8 %. In b) and c) pulse shapes correspond to the beginning of each 15th unit cell. Obtained by numerical solution of the full NLSE.* $d_+ = 30$, $d_- = -28$; $z_+ = z_- = 0.078$; $u(0,t) = 1.52exp(-0.446t^2)$

propagation in optical fiber links with a dispersion map as in Fig.1 using both the full NLS eq.(1) and corresponding variational equations eq.(6), eq.(7). The results are presented in Fig.2 and Fig.3 respectively. As follows from Fig3.a, the random modulation of dispersion magnitudes leads to higher growth rate of the pulse width compared to that of modulation of span lenthgs for the same value of σ. Consequently, in the former case DM soliton disintegrates at shorter distance.

When the dimensionless fiber span lengths are small compared to dispersion magnitudes, the averaged dynamics approach is valid [4]. In this approach a real map with the fiber segments of alternating anomalous and normal dispersions is replaced by a uniform fiber with the path averaged dispersion $\bar{d} = (d_+ z_+ + d_- z_-)/(z_+ + z_-)$. In this formulation the problem can be considered as a particular case of the random Kepler problem in optical solitons context, recently reported in Ref.[5]. In this work an explicit analytical expression has been derived for the mean soliton disintegration time when it propagates in a fiber with randomly varying dispersion.

$$t_d = \frac{1}{\sigma^2}\int_0^\infty \frac{J}{A(J)}dJ \approx \frac{1.68}{\sigma^2}\,, \tag{9}$$

$$A(J) = \frac{J(\pi J+4)(128+448\pi J+448\pi^2 J^2+168\pi^3 J^3+21\pi^4 J^4)}{8\pi^3(\pi J+2)^3}. \tag{10}$$

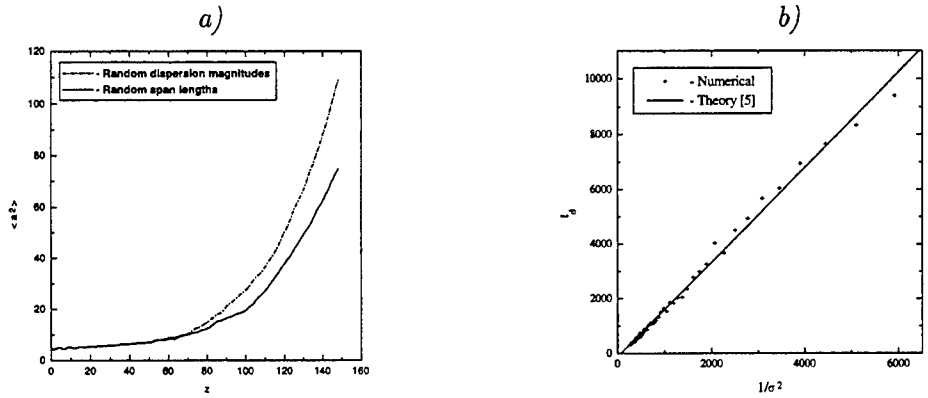


Figure 3: *Growth of the pulse width (a) and the mean decay time (b) for DM soliton according to variational equations. Parameters are the same as in Fig.2. Averaged over 400 realizations.*

Comparison of our numerial simulation results with the prediction of the above theory is shown in Fig.3 (b).

In conclusion, we have performed numerical simulations of the DM solitons propagation in fiber links with randomly varying map parameters. Soliton disintegration due to randomness is shown to occur in such an optical communication line. Numerical calculation results are in good agreement with the theoretical prediction in the averaged dynamics approach.

References

[1] N.J.Smith, F.Knox, N.Doran, K.J.Blow, and I.Bennion, Electr.Lett, **32**, 54, 1996.
[2] "New Trends in Applications of Optical Solitons in Fibers", Ed.A.Hasegawa, Kluwer AP, 1998.
[3] D.Anderson, Phys.Rev, **A27**, 1393, 1983.
[4] J.N.Kutz, P.Holmes, S.G.Evangelidis, and J.P.Gordon, J.Opt.Soc.Am, **15**, 87, 1998.
[5] F.Kh.Abdullaev, J.Bronski, and G.C.Papanicolaou, Physica D, 1998, to be published.

Dispersion-managed solitons and the inverse scattering transform

J. H. B. Nijhof, S. K. Turitsyn and N. J. Doran
Aston University, Photonics Research Group, Aston Triangle B4 7ET, Birmingham, UK
J.H.B.Nijhof@aston.ac.uk

April 28, 1999

The theory of dispersion-managed (DM) solitons is rather well established and is capable of explaining all observed features of the evolution of a single DM pulse [1]. Path-average or variational methods can systematically describe families of DM solitons [1] when the characteristic nonlinear length is much larger than the dispersion compensation period. In the numerical experiments, however, it was observed that DM solitons can exist even for large amplitudes, when the path-average theory formally is not valid. In this paper we apply the inverse scattering transform (IST) method [2] (similar approaches have been considered in [3, 4]), which allows us to describe DM soliton properties beyond the limitations of the path-average theory. We will consider a two-step lossless dispersion map. At the boundary between the fibres we will consider the direct scattering problem in both fibres and we discover the condition which should be satisfied by the scattering data for the potential to be a DM soliton. We will show that the symmetries of the DM soliton imply symmetries in the scattering data.

We begin with a recapitulation of the direct scattering problem, mostly following [2]. Consider the nonlinear Schrödinger equation with piecewise constant coefficients,

$$iu_z - \tfrac{1}{2}\beta'' u_{tt} + \gamma|u|^2 u = 0. \tag{1}$$

Because we are interested in the boundary, where there are two scattering problems to consider (one for the anomalous fibre and one for the normal fibre), we will not normalise (1), since that would probably require a different rescaling of u, z and t for the different fibres. Instead, let $\alpha = \sqrt{|\gamma/\beta''|}$ and $\sigma = \mathrm{sign}(-\gamma/\beta'')$, then (1) is equivalent to the compatibility condition $U_z - V_t + [U,V] = 0$ of the following system:

$$\chi_t = U\chi = \begin{bmatrix} i\lambda & i\sigma\alpha u^* \\ i\alpha u & -i\lambda \end{bmatrix}\chi \quad \text{and} \quad \chi_z = V\chi = \begin{bmatrix} -i\beta''\lambda^2 - \frac{1}{2}i\gamma|u|^2 & \sigma\alpha\beta''(-i\lambda u^* - \frac{1}{2}u_t^*) \\ \alpha\beta''(-i\lambda u + \frac{1}{2}u_t) & i\beta''\lambda^2 + \frac{1}{2}i\gamma|u|^2 \end{bmatrix}\chi. \tag{2}$$

If $\chi(t,\lambda) = [\chi_1,\chi_2]^T$ is a solution of (2), then $\tilde{\chi} \equiv [-\sigma\chi_2^*(t,\lambda^*), \chi_1^*(t,\lambda^*)]^T$ is another solution. Let $\phi(t,\lambda)$ and $\psi(t,\lambda)$ be the solutions that tend to $[0, e^{-i\lambda t}]^T$ for $t \to \infty$ and to $[e^{i\lambda t}, 0]^T$ for $t \to -\infty$ respectively. Then ϕ, $\tilde{\phi}$, ψ and $\tilde{\psi}$ are linearly dependent, and they are related by the scattering coefficients $a(\lambda), b(\lambda)$ via $\phi = a(\lambda)\tilde{\psi} + b(\lambda)\psi$. The field $u(t)$ is completely determined by the scattering data, which consists of a solitonic part $\{\lambda_n, b(\lambda_n)/a'(\lambda_n)\}$ at the zeros of $a(\lambda)$ and a continuous part $\{a(\lambda), b(\lambda)\}$ for $\lambda \in \mathbb{R}$. The evolution over z of $a(\lambda,z)$ and $b(\lambda,z)$ is simple: $a(\lambda,z) = a(\lambda,0)$ and $b(\lambda,z) = b(\lambda,0)\exp -2i\beta'' z\lambda^2$. Via inverse scattering one could now find $u(z,t)$ from the scattering data.

Consider the DM soliton solutions for a two stage dispersion map consisting of an anomalous fibre of length l_a and dispersion $\beta'' = \beta''_a < 0$ and a normal fibre of length l_a and dispersion $\beta'' = \beta''_n > 0$, with equal nonlinear coefficients γ. Choose the origin of the z axis at the midpoint of an anomalous segment, so that $z = l_a/2$ is a boundary. Numerically, dispersion-managed solitons of this map are found to be even in t, $u(z,t) = u(z,-t)$, and totally unchirped in the midpoints of the fibres: in these points, $u(t) = u_0(t)\exp i\theta$ with $u_0(t) \in \mathbb{R}$ for all t. It also seems that the periodic solutions do not have a soliton part (that can be proved if at any z the pulse area is small enough [2]). In the following we assume that there are no solitons in the scattering data, so that u is completely determined by $a(\lambda)$ and $b(\lambda)$ on the real axis.

The above mentioned symmetries of u imply symmetries in $a(\lambda)$ and $b(\lambda)$. If u is even in t, then $S[\chi(t,\lambda)] \equiv [\chi_1(-t,-\lambda), -\chi_2(-t,-\lambda)]^T$ preserves (2). By applying S to ϕ etc., one finds that this symmetry implies that $a(-\lambda) = a^*(\lambda^*)$ and $b(-\lambda) = b(\lambda)$. Similarly, if $u(t) = u_0(t)e^{i\theta}$ with $u_0(t) \in \mathbb{R}$ for all t, we find that $a(-\lambda) = a^*(\lambda^*)$ and $b(-\lambda) = -b^*(\lambda^*)e^{-2i\theta}$. At the midpoints of the fibres u has both symmetries, so there the scattering data must satisfy $a(-\lambda) = a^*(\lambda^*)$ and $b(\lambda) = b(-\lambda) = -b^*(\lambda^*)e^{-2i\theta}$. So for $\lambda \in \mathbb{R}$, the argument of $b(\lambda)$ must be constant modulo π: $b(\lambda) = ie^{-i\theta}b_0(\lambda)$ with $b_0(\lambda) \in \mathbb{R}$.

Now look at the boundary between the fibres at $z = l_a/2$. There, there are two sets of scattering data: $\{a_a(\lambda), b_a(\lambda)\}$ for the anomalous fibre, where $\alpha = \alpha_a = \sqrt{-\gamma/\beta''_a}$, and $\{a_n(\lambda), b_n(\lambda)\}$ for the normal fibre, where $\alpha = \alpha_n = \sqrt{\gamma/\beta''_n}$. $a_{a,n}(\lambda)$ will satisfy $a_{a,n}(-\lambda) = a^*_{a,n}(\lambda^*)$ and $b_{a,n}(\lambda)$ will satisfy

$$b_a(\lambda) = ib_{0a}(\lambda)e^{-i\theta_a - i\beta''_a l_a \lambda^2} \qquad \text{and} \qquad b_n(\lambda) = ib_{0n}(\lambda)e^{-i\theta_n + i\beta''_n l_n \lambda^2} \tag{3}$$

with $b_{0a,n}(\lambda) \in \mathbb{R}$, i.e. $\arg b_{a,n}(\lambda) = \frac{\pi}{2} - \theta_{a,n} + |\beta''_{a,n}| l_{a,n}\lambda^2 \mod \pi$. Conversely, if $u(l_a/2,t)$ is even in t and $u(l_a/2,t)$ is such that b_a and b_n satisfy (3), then $u(z,t)$ is a periodic solutionof (1), for which the nonlinear phase shift over one dispersion map is $2(\theta_n - \theta_a)$.

Given $u(t)$, $a(\lambda)$ and $b(\lambda)$ can be found easily from two coupled integral equations for η_1 and η_2, where $\eta_1(t,\lambda) = \phi_1(t,\lambda)\exp -i\lambda t$ and $\eta_2(t,\lambda) = \phi_2(t,\lambda)\exp i\lambda t$. They are given by

$$\eta_1(t,\lambda) = i\sigma\alpha \int_{-\infty}^{t} u^*(t')e^{-2i\lambda t'}\eta_2(t',\lambda)\,dt' \quad \text{and} \quad \eta_2(t,\lambda) = 1 + i\alpha \int_{-\infty}^{t} u(t')e^{2i\lambda t'}\eta_1(t',\lambda)\,dt' \tag{4}$$

and $b(\lambda) = \eta_1(\infty,\lambda)$ and $a(\lambda) = \eta_2(\infty,\lambda)$. If u (or α) is small, one can "solve" this by Picard iteration (see also [4]): start from $\eta_1(t) = 0$, integrate (4) with this η_1, yielding $\eta_2 = 1$, integrate (4) with this η_2, etc. After integrating each equation once, one finds that

$$b(\lambda) \approx i\sigma\alpha \int_{-\infty}^{\infty} u^*(t)e^{-2i\lambda t}\,dt = i\sigma\alpha\hat{u}^*(2\lambda). \tag{5}$$

So apart from a constant factor, $b^*(\lambda)$ is approximately equal to the Fourier transform of u at frequency $\omega = 2\lambda$. Since we know that at the boundary, the phase of $b(\lambda)$ is quadratic in λ, that implies that the phase of the Fourier transform of u is quadratic in ω. And the coefficient is exactly the one which accumulated linear dispersion would give: $\arg\hat{u}(\omega, l_a/2) = \pi/2 + \theta_a + \frac{1}{2}\beta''_a(l_a/2)\omega^2 \pmod{\pi}$. Note that in the limit of the small amplitudes the Poincare mapping (transform of initial field into the field at the output of the section) found by IST will effectively lead to the same result as obtained by averaging in the spectral domain [5]. Obviously, when the nonlinear phase shift is unequal to zero, or when $|\beta''_a l_a| \neq |\beta''_n l_n|$, the Fourier transform of $\hat{u}^*(2\lambda)$ cannot be equal to both $-ib_a(\lambda)/\alpha_a$ and to $+ib_n(\lambda)/\alpha_n$. If the fibre lengths are the same and the absolute value of the dispersion in both fibres are equal, then obvious next guess is

$$(\hat{u}^*(l_a/2, 2\lambda))^2 \approx b_a(\lambda)b_n(\lambda)/\alpha_a\alpha_n. \tag{6}$$

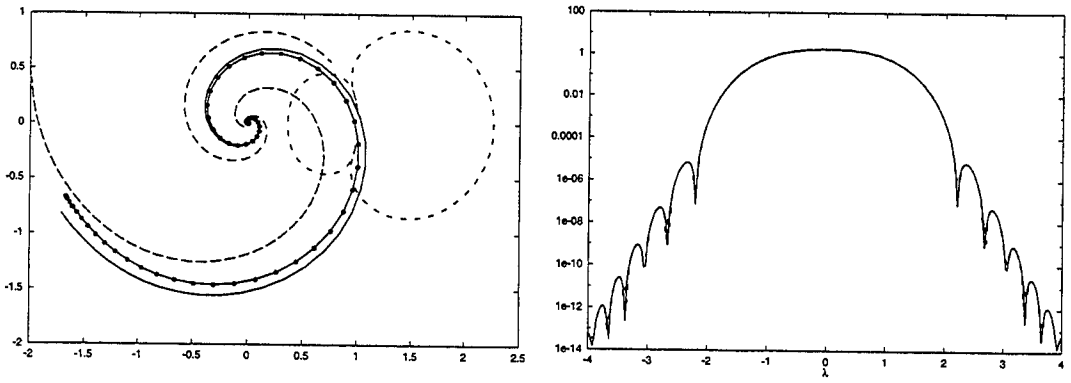


Figure 1: (a) A polar diagram of $\hat{u}^*(2\lambda)^2$ (drawn with dots), $b_a(\lambda)b_n(\lambda)$ (drawn), $a_{a,n}(\lambda)$ (dashed) and $b_{a,n}(\lambda)$ (dotted). (b). $|\hat{u}^*(2\lambda)|^2$ (drawn) and $|b_a(\lambda)b_n(\lambda)|$ (dashed) versus λ. $|\gamma| = |\beta''_{a,n}| = 1$, so $\alpha_a = \alpha_n = 1$; $l_a = l_n = 2$, and the map strength is 5.3. The nonlinear phase shift over one map period is 1.7.

Figure 1 shows a polar diagram for the scattering data and $\hat{u}^*(\lambda)^2$, as well as a comparison between $|b_a(\lambda)b_n(\lambda)|$ and $|\hat{u}(2\lambda)|^2$. Both the amplitude and the phase match very well. Equation (6) must be modified if $\alpha_a \neq \alpha_n$, by weighing the contributions of b_a and b_n; in the extreme case where one of the fibres is linear ($\gamma = \alpha = 0$), in that fibre $b(\lambda)$ is exactly equal to $\hat{u}^*(2\lambda)$, in which case $\hat{u}$ is independent of $b(\lambda)$ in the other fibre.

In conclusion, using symmetries of DM soliton in the two-step lossless map we have found that a necessary and sufficient condition on the scattering data to provide for DM soliton potential is that the phase of the coefficient $b(\lambda)$ has a quadratic dependence on λ in both fibers. We demonstrate that periodic solutions can be constructed beyond the limitations on the soliton amplitude that have been imposed in the previously developed path-average theory. The b coefficients can be related to the spectrum of the pulse, and at the boundary, the pulse is almost exactly linearly chirped, even though the shape of the spectrum might differ considerably between the boundary and the midpoints of the fibres.

References

[1] S. K. Turitsyn, N. J. Doran, J. H. B. Nijhof, V. K. Mezentsev, T. Schäfer, and W. Forysiak. Dispersion-managed solitons. In S. Wabnitz, editor, *Optical Solitons: Theoretical Challenges and Industrial Perspectives*, Les Houches, France, 1998. in press.

[2] S. Novikov, S. V. Manakov, L. P. Pitaevskii, and V. E. Zakharov. *Theory of Solitons — The Inverse Scattering Method.* Consultants Bureau, New York and London, 1984.

[3] G. Luther. report at BRIMS Worskshop on Mathematical Methods in Nonlinear Optics. unpublished, 1996.

[4] A. V. Mikhailov. private communication.

[5] Ildar R. Gabitov and Sergei K. Turitsyn. Averaged pulse dynamics in a cascaded transmission system with passive dispersion compensation. *Opt. Lett.*, 21(5):327–329, March 1996.

Transmission characteristics of optical fiber solitons in a dispersion-slope compensated system

Joji Maeda, Hiromitsu Ogawa, and Nobumitsu Umezawa

Department of Electrical Engineering, Faculty of Science and Technology,
Science University of Tokyo,
2641 Yamazaki, Noda, Chiba 2788510 Japan
TEL: +81-471-24-1501 ext.3705, FAX: +81-471-24-7380

Since the advent of dispersion-slope compensating devices, such as fiber gratings or reversed dispersion-slope fibers [1], techniques of dispersion-slope compensation have been extensively studied in terms of wavelength division multiplexing [2,3].

The effectiveness of dispersion-slope compensation in high speed single channel systems has also been experimentally demonstrated [4,5]. The dispersion-slope, or third order dispersion, destroys the symmetry of transmitted pulses [6]. This results in an increase of bit errors. Dispersion-slope compensation effectively prevents the deformation.

In soliton transmission systems over several tens of Gb/s, the width of the transmitted pulses must be less than 10ps to avoid soliton-soliton interaction. [7] For this range of pulse width, the effect of the dispersion-slope cannot be neglected. Therefore, the effect of dispersion-slope in soliton-based systems is much more serious than that in linear transmission systems of the same bit rate.

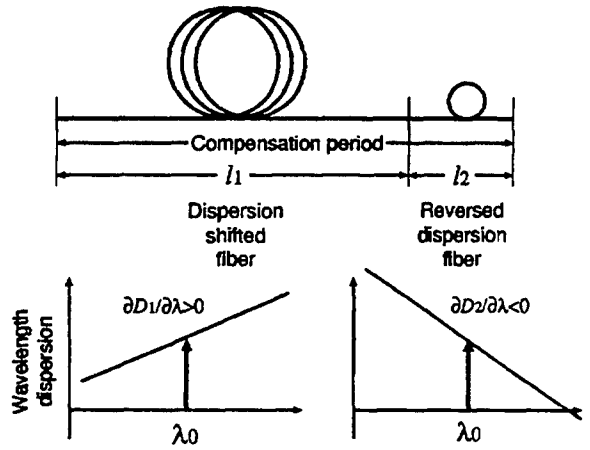


Fig.1. Schematic of dispersion-slope compensation.

In this paper, we numerically study transmission characteristics of a 50Gb/s soliton transmission system using dispersion-slope compensation technique, and show that the technique can drastically improve the maximum transmission distance.

Fig. 1 shows the idea of dispersion-slope compensation using a reversed dispersion-slope fiber (RDF). Total dispersion within a compensation period is flattened by an RDF connected after a dispersion shifted fiber (DSF). The required dispersion-slope of the RDF $\partial D_2/\partial\lambda$ is related to that of the DSF $\partial D_1/\partial\lambda$ and length of DSF l_1 and that of RDF l_2 by

$$\frac{\partial D_2}{\partial\lambda} = -\frac{l_1}{l_2}\frac{\partial D_1}{\partial\lambda}. \tag{1}$$

We numerically solved the following equation using split-step fourier method [6]:

$$i\frac{\partial u(z,t)}{\partial z} + \beta_2\frac{\partial^2 u(z,t)}{\partial t^2} + \beta_3\frac{\partial^3 u(z,t)}{\partial t^3} + \gamma|u(z,t)|^2 u(z,t) = -i\Gamma u(z,t), \tag{2}$$

where $u(z,t)$ is the amplitude of light field in a rotating frame, Γ is fiber loss, β_2 and β_3 are second and third order dispersion, respectively, and γ is the nonlinear coupling constant. The dispersions

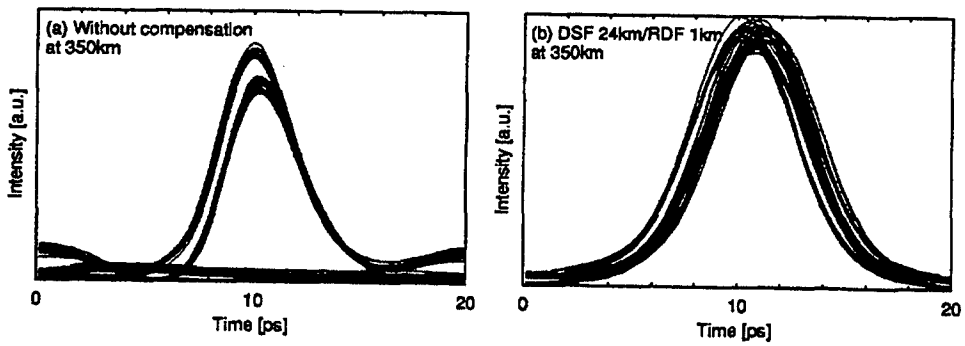


Fig.2. Calculated eye patterns after 350km transmission. (a)without compensation, (b)with compensation (period 25km with reversed dispersion-slope fiber of 1km).

β_2 and β_3 are related with conventional parameters by

$$\beta_2 = -\frac{\lambda^2}{2\pi c} D \tag{3}$$

$$\beta_3 = \frac{\lambda^4}{(2\pi c)^2}\left[\frac{\partial D}{\partial \lambda} - \frac{4\pi c}{\lambda^3}\beta_2\right] \simeq \frac{\lambda^4}{(2\pi c)^2}\frac{\partial D}{\partial \lambda}, \tag{4}$$

where c is light speed in a fiber, λ is the center wavelength of transmitted pulses, and D is the wavelength dispersion. All effects of birefringence, including polarization dispersion, polarization dependent loss, are neglected. Higher order effects other than the dispersion-slope are also neglected.

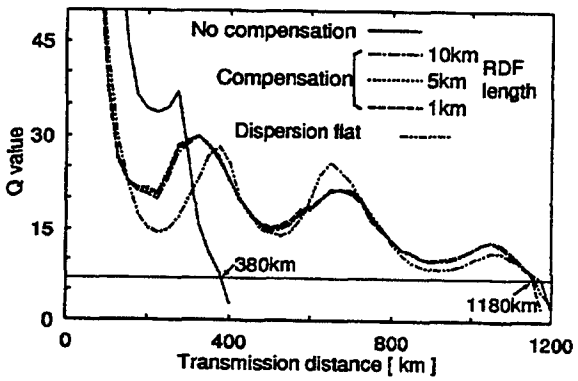


Fig.3. Q values as a function of transmission distance.

We assume a 50Gb/s single channel transmission system, in which ideal sech pulses, whose width is 5ps FWHM, are launching into the transmission line at the transmitter. The center wavelength of the signal is 1552nm, and dispersion and dispersion-slope of fibers at this wavelength are assumed 0.2ps/km/nm, 0.07ps/km/nm, respectively. For these parameters, dispersion length and the third order dispersion length are calculated as 31.6km and 200km, respectively. Fiber loss, amplifier spacing, and nonlinear coupling constant γ are 0.25dB/km, 25km, and 1.73W^{-}1km^{-}1, respectively. Spontaneous emission factor of each amplifier is assumed to be 2, and an optical bandpass filter to reduce ASE noise is inserted at the output of every amplifier. Soliton control schemes such as sliding filters [8–10] or synchronous modulation [11–13] are not considered.

Incident pulse stream is pseudo-random bit stream of 2^6-1, whose eye pattern after transmission are used for calculating Q values. The availability of transmission are determined by Q to be larger than 7 that corresponds to bit error rate of 10^{-12}. The transmitted power is optimized to maximize the transmission distance.

Fig. 2 shows eye patterns of calculated results, where Fig. 2(a) is at 350km without compensation, and Fig. 2(b) is at 350km with compensation, whose compensation period is 25km with a RDF length of 1km. While the eye of the uncompensated system shows a sign of deformation of pulses, that of the compensated system shows no sign of deformation. The jitter of the compensated system is mainly due to the soliton-soliton interaction.

Fig. 3 shows Q values as a function of transmission distance. The compensation period is 25km, and the length of RDFs is varied from 10km to 1km. It is interesting that the length of RDF does not alter the Q values. This can be attributed to relatively short compensation period compared with the third order dispersion length.

Because of high cost of RDFs, long compensation period and short RDF length are preferred. To investigate the longest compensation period, we show in Fig. 4 the change of the maximum transmission distance as a function of the compensation period. To maintain transmission over 1000km, compensation period can be extended to 80km, which is about 0.4 times the third order dispersion length.

In conclusion, we have investigated characteristics of a soliton transmission system employing dispersion-slope compensation. It is revealed that the compensation within 0.4 times the third order dispersion length can effectively improve the system performance. Further improvement would be available by employing soliton control schemes.

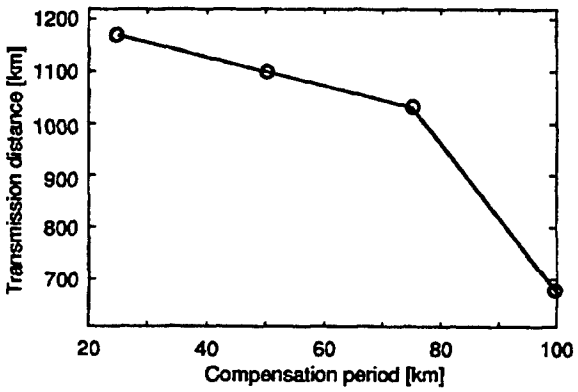


Fig.4. Dependence of the maximum transmission distance on compensation period

References

[1] Y. Akasaka *et al.*, Proc. ECOC '96 **2**, 221–224 (1996).
[2] I. Morita *et al.*, J. Lightwave Technol **17**, 80 (1999).
[3] F. Favre *et al.*, Electron. Lett. **33**, 2135 (1997).
[4] E. Yoshida, T. Yamamoto, A. Sahara, and M. Nakazawa, Electron. Lett. **34**, 1004 (1998).
[5] S. Kawanishi *et al.*, Electron. Lett. **32**, 916 (1996).
[6] G. P. Agrawal, *Nonlinear Fiber Optics* (Academic Press, San Diego, 1989).
[7] A. Hasegawa and Y. Kodama, *Solitons in optical communications* (Oxford University Press, New York, 1995).
[8] L. F. Mollenauer, J. P. Gordon, and S. G. Evangelides, Opt. Lett. **17**, 1575 (1992).
[9] Y. Kodama and S. Wabnitz, Opt. Lett. **19**, 162 (1994).
[10] L. F. Mollenauer, P. V. Mamyshev, and M. J. Neubelt, Opt. Lett. **19**, 704 (1994).
[11] H. Kubota and M. Nakazawa, IEEE J. Quantum Electron. **29**, 2189 (1993).
[12] Y. Kodama, M. Romagnoli, and S. Wabnitz, Electron. Lett. **30**, 261 (1994).
[13] M. Nakazawa, K. Suzuki, H. Kubota, and E. Yamada, Electron. Lett. **32**, 1686 (1996).

Theoretical and numerical methods for dispersion managed solitons

Vincent Cautaerts, Akihiro Maruta and Yuji Kodama

Graduate School of Engineering, Osaka University, 2-1 Yamada-Oka, Suita, Osaka 565-0871, Japan
Phone:+81-6-6879-7728, Fax:+81-6-6879-7774, e-mail:vincent@comf5.comm.eng.osaka-u.ac.jp

1 Introduction

We present here recent results on dispersion management for non-linear return-to-zero pulse propagation in optical fibers. The main purpose of dispersion management is to reduce several effects such as radiation from the pulse due to lumped amplifiers compensating dispersion loss, modulational instability, jitters caused by the collisions between signals in different channels of wavelength-division-multiplexed (WDM) systems, the Gordon-Haus effect resulting from the interaction with noise, and to set a desired average value of dispersion. Additionally, dispersion managed (DM) solitons present a possibility of upgrading installed systems (see for example the UPGRADE project [1]).

The so-called DM soliton can be studied by different methods, which are numerically compared in the present paper. Although they are more general, we applied them to a two-step dispersion map of average dispersion D_{av}, dispersion difference ΔD and of period Z_d. The point $Z = 0$ is fixed at the center of the positive (anomalous) dispersion fiber. Our model equation is $iu_Z + D(Z)u_{TT}/2 + S(Z)|u|^2u = 0$, the nonlinear Schrödinger equation (NLSE). It can incorporate loss and amplification through $S(Z)$ (see for example [2]).

This NLSE admits some conservation laws: three trivial ones being the energy $\int |u|^2 dT$, the moment $i\int uu_T^* dT$ and the "Hamiltonian" $H = 1/2\int[S|u|^4 - D|u_T|^2]dT$, this last one being only valid when both the dispersion and the non-linearities are constants (in which case there are an infinite number of conserved quantities). A test of validity of the different methods exposed here is to see how they conserve, or don't, those quantities.

2 (Numerical) averaging method

Stationary solutions to the propagation problem in a two-step dispersion map have been found numerically [3]. We have found numerically that a pulse *looking like* the stationary solution will emit radiation when propagated to get back to this shape. This process gives the *exact* same pulse shape (to the exception of noise trapped inside the pulse) than the averaging method used in [3] which, by repetitive averaging of the pulse shape, damps the quasi-random phase radiation but doesn't affect the pulse-wide regular phase core solution. Such solutions can be found not only in the positive (anomalous) dispersion region, but also in the negative (normal) dispersion region. For a given dispersion map, they form a correspondance between pulse energy and pulse shape (and hence e.g. RMS width). However this all-numeric process does not provide an explanation of the inner mechanism leading to the existence of this pulse; hence the use of the other developments.

3 Lagrangian theory

Since the short-scale variations of the pulse are essentially linear, with the non-linear effects appearing in the long-scale, we make a change of variable to absorb the former a least partially:

$$u(Z,T) = \sqrt{p(Z)}v(Z,\tau)\exp[iC(Z)\tau^2/2] \qquad \text{with } \tau = p(Z)T. \tag{1}$$

The usual Lagrangian method assumes the function $v(Z,\tau)$ to depend on a finite number of parameters, to get, if the ansatz is properly chosen, a finite dimensional approximate solution of the original problem.

Gaussian ansatz: The simpler ansatz giving interesting results possesses two degrees of freedom, the pulse width $1/p(Z)$ and the chirp $C(Z)$. In addition, the pulse has a third parameter, its phase $\phi(Z)$ as in $v(Z,\tau) = f(\tau)\exp[i\phi(Z)]$, but since it is decoupled from the others, we don't treat it here.

Whatever the localized function $f(\tau)$, the results obtained by the Lagrangian method will be qualitatively the same, up to some scaling factor. A Gaussian ansatz $f(\tau) = \exp[-\tau^2/2]$ is often chosen since the central lobe of the core solution "looks" Gaussian. Since the pulses representable by this ansatz conserve the same shape during propagation, they are called "self-similar" [4].

An unexpected result is that for the case of normal average dispersion a second solution, of lower energy, is present. This solution appears to be unstable, explaining that it is not observed with the averaging method. It is to be noted that such a solution is not just an artifact from our Lagrangian method: the propagation of initially Gaussian pulses of different widths or energies in such a dispersion map shows a longer destruction-free propagation distance in the vicinity of those parameters. A development at small energy gives the critical value of the dispersion difference ΔD_{cr} required to have a solution in the normal average dispersion region (normal dispersion) [5].

The three trivial conservation laws are satisfied locally by the resulting equations, on each segment of constant dispersion fiber.

Extended Hermite-Gaussian ansatz: By allowing more degrees of freedom to the function v, one can get a solution nearer to the exact one. This can be done by interpreting the Gaussian ansatz as the first term in a development in a series of Hermite-Gaussian functions. A second term can be included, and introduces 2 new parameters (amplitude and relative phase of the new component).

The ansatz become $v(\tau,Z) = \exp(i\theta(Z))[A_0(Z)h_0(\tau) + A_4(Z)\exp(i\phi(\tau))h_4(\tau)]\exp(-\tau^2/2)$, where h_i is the i^{th} normalized Hermite function. We considered the h_4 term to be a perturbation, and develop the equations for the case $A_4/A_0 = \alpha \ll 1$. One has to be careful that this introduces a singularity into the $d\phi/dz$ equation, ϕ having no physical meaning when $A_4 = 0$. It is removed by working with the variables $\sigma = \alpha\sin\phi$ and $\kappa = \alpha\cos\phi$.

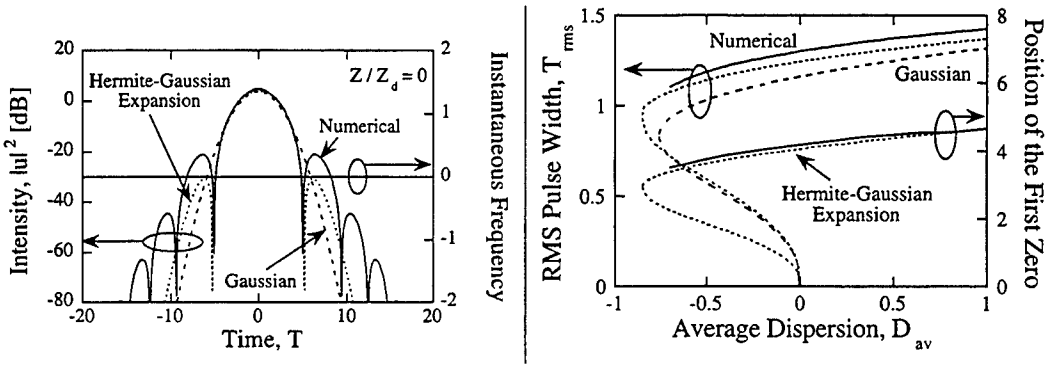


Figure 1: Comparison between the results of the averaging method and Lagrangian methods (Gaussian and Hermite Gaussian) for $Z_d = 1$,$E = 15$ and $\Delta D = 100$ in our reduced units. The left graph represents the pulses at their chirp free point for $D_{av} = 1$. The right graph represents the RMS pulse width as a function of the average dispersion, as well at the position of the first zero in the pulse shape.

Noting $\mathcal{E} := E_0/\sqrt{2\pi}$ where E_0 is the pulse energy, we get

$$\frac{d}{dZ}p = -p^3 DC - \frac{\sqrt{6}p^2 S}{2}\mathcal{E}\sigma \qquad \frac{d}{dZ}\sigma = \frac{-\sqrt{6}pS}{16}\mathcal{E} + \kappa\left[4p^2 D - \frac{233}{128}pS\mathcal{E}\right]$$

$$\frac{d}{dZ}C = p^2 D(1+C^2) - pS\mathcal{E}\left[1 + \frac{\sqrt{6}}{4}(\kappa - 4C\sigma)\right] \qquad \frac{d}{dZ}\kappa = -\sigma\left[4p^2 D - \frac{163}{128}pS\mathcal{E}\right]$$

Figure 1 shows the improvement of the solution, relative to the simpler Gaussian ansatz.

4 Multiscale theory

The *multiscale pulse dynamics* [6] theory is valid for the strong dispersion management case. Its hypotheses are that $Z_d \ll 1$, $\Delta D = O(1/Z_d)$, $D_{av} = O(1)$. A first order development on this base gives a pulse whose (power) spectrum is constant along propagation. This spectrum is given by $\tilde{u}(\omega) = \exp(i\phi(Z,\omega)/2)F(\omega)$ where $\phi(\omega)$ is the phase given by $\omega^2 \int^Z D(s)ds$, as for the linear case, and $F(w)$ is a real function solution of $(\lambda^2 + D_{av}\omega^2)F(\omega) = 2\int\int d\omega_1 d\omega_2 F(\omega+\omega_1)F(\omega+\omega_2)F(\omega+\omega_1+\omega_2)r(\omega_1\omega_2)$. The kernel $r(x)$ is given by a simple *Sinc* function in the case of a two-step dispersion map. ($r(x) = \sin(s\omega_1\omega_2)/(s\omega_1\omega_2)$ where s is the map strength $s = Z_d\Delta D/8$)

More, this method does give results for some region of the parameters where the convergence of the averaging method is extremely poorly.

Figure 2 shows the comparison between the 4 methods of this paper for different settings. The Hermite-Gaussian ansatz appear to be nearer to the true DM soliton, given by the averaging method, than the simpler Gaussian ansatz, for most parameters. Note that the pulse shape, as shown figure 1 is far better, even if the RMS width is not. The multiscale method, mathematically very simple, has a range of applicability much more restricted, but improves as ΔD increases. It does also give the better solution for very small energies when the pulse width is the bigger (and $D_{av} = 1$). In this case, the averaging converge to a sech-like solution, and hence taking a *sech* ansatz in the Lagrangian method should improve the results.

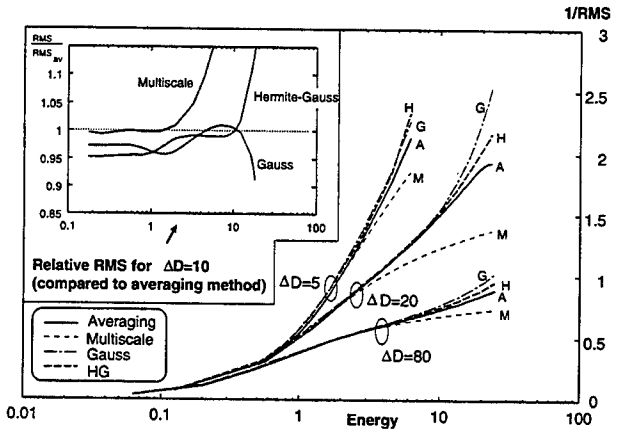


Figure 2: Comparison between the results of the four methods of this paper: averaging (A), multiscale (M), Lagrangian with a Gaussian ansatz (G) and Lagrangian with a Hermite-Gaussian ansatz (H). The main figure is the inverse of the RMS width vs. the energy for different values of ΔD, and the inset represents the ratio between the RMS of the different methods to the one obtained by the averaging technique for a value of $\Delta D = 10$. All curves are for $D_{av} = 1$ and $Z_d = 1$

References

[1] J.J.E.Reid. Soliton transmission in the European network. In A. Hasegawa, editor, *New Trends in Optical Soliton Transmission Systems*. Kluwer Academic Publishers, 1998.

[2] A. Hasegawa and Y. Kodama, *Opt.Lett.*, 16:1385, 1991.

[3] J. Nijhof, N. Doran, W. Forysiak, and F. Knox. *Electronics Letters*, 33(22):1726–1727, 1997.

[4] S.K.Turitsyn *Physical Review E*, 58(2):1256–1259, Aug. 1998.

[5] V. Cautaerts, In *Technical digest CLEO/Europe'98*, 380.

[6] M. J. Ablowitz and G. Biondini. *Optics Letters*, 23(21):1668–1670, Nov. 1998.

Modulational instability in fiber transmission lines with semiconductor optical amplifiers

M. Gölles, S. Darmanyan, G. Onishchukov, A. Shipulin, V. Lokhnygin, and F. Lederer

Friedrich-Schiller-Universität Jena, Institute of Solid State Theory and Theoretical Optics,
Max-Wien-Platz 1, D-07743 Jena, Germany, Tel:+49 3641 9 47174 Fax:+49 3641 9 47162

Signal transmission with semiconductor optical amplifiers (SOA) in 1300 nm fiber communication systems is one opportunity for upgrading the European standard fiber network. Recently experimental progress was reported [1,2]. However, the performance of RZ transmission is essentially constrained by such SOA features as low saturation energy, strong nonlinear phase modulation, and gain recovery time comparable with the bit period. An alternative modulation format could consist in a phase modulated continuous wave (CW) where the above mentioned problems are expected to be relaxed due to the constant power level. We studied the transmission characteristic of this modulation format experimentally. To this end we used a recirculating fiber loop set up [2]. It consisted of a 25 km standard optical fiber and a MQW - SOA followed by a 0.7 nm in-line bandpass optical filter. It turned out that a CW signal can propagate without significant degradation up to several thousands kilometers, while being initially phase modulated it quickly develops a detrimental amplitude modulation (AM). To study this effect a phase modulated ' 010101...'-pattern at 10 GHz was used as the worst case. The operation wavelength was close to 1306.4 nm - the zero dispersion wavelength (ZDW) of the fiber.

The AM frequency amounted to twice the phase modulation frequency. The modulation depth was found to be only slightly intensity-dependent, but nevertheless AM increased with signal power (up to 15 mW). It was also experimentally found, that AM depends strongly on the in-line filter detuning and its bandwidth, i.e. an improved system performance (lower AM depth) was achieved with a 3 nm in-line filter.

However, even in this case it was necessary to adjust the filter very carefully. The use of an in-line optical filter is unavoidable because usually the amplifier peak gain wavelength does not coincide with the operation wavelength and the necessity to cut the power of broadband amplified spontaneous emission. Deviations of the carrier wavelength from the ZDW also led to a considerable system performance degradation in the experiment.

These particular features can be understood in studying the corresponding evolution equation for the averaged field envelope $A(z,t)$

$$i\frac{\partial A}{\partial z}+\left(\frac{\beta_1}{2}-i\beta_2\right)\frac{\partial^2 A}{\partial t^2}+\chi|A|^2 A = i\delta A-\rho(\alpha+i)A\int_{-\infty}^{t}|A(z,t')|^2\exp\left[-\frac{t-t'}{t_r}\right]dt' \quad (1)$$

where β_1, $\beta_2=2\ln[2]/(t_0\Delta\omega_F)^2$, χ, $\delta = h_0/2 - \gamma z_a$, $\rho = a_0^2 P_0 t_0/(2E_{sat})$, t_r, α are coefficients related to fiber dispersion, inverse filter bandwidth, fiber nonlinearity, net gain, saturated amplification, gain recovery time and linewidth enhancement factor, respectively.

Equation (1) was normalized by using normalizing quantities typical for our experiment, i.e., the amplifier/filter spacing z_a=25 km, the time t_0=3.73 ps and the power P_0=12.9 mW. Then the parameters in (1) are $\beta_1=\pm 1$ at wavelengths shifted $\pm$ 5 nm from the zero-dispersion wavelength, respectively, and the Kerr coefficient is χ=1. The filter bandwidth $\Delta\omega_F$ corresponds to 0.7 nm so that β_2=0.163. The saturation energy of SOA were assumed to be E_{sat} = 2 pJ so that the saturation coefficient becomes $\rho = 0.0308$ where the power enhancement factor $a_0^2 = 2\gamma z_a/(1-\exp[-2\gamma z_a]) = 2.56$ was taken into account (fiber loss γ=0.046 km^{-1}).

The CW solution to (1) is $A(z,t)=A_0\exp[i(\Gamma z-\omega t)]$ with the dispersion relation $\Gamma = \beta_1\omega^2/2 + (\chi+\rho\alpha t_r)A_0^2$ and the energy balance $\delta=\beta_2\omega^2 + \rho t_r A_0^2$. $\omega=\omega_0-\omega_F$ designates the deviation of the carrier frequency ω_0 from the central filter frequency ω_F. A phase modulation $A(0,t) = A_0\exp[i(\Phi(t)-\omega t)]$ at input causes changes in the field evolution $A(z,t)$. In first order approximation we found at ZDW ($\beta_1 = 0$) that the phase modulated signal, $\Phi(t)=\varepsilon_m\sin[\omega_M t]$, evokes an amplitude modulation with frequency $2\omega_M$. Within this approximation the modulation depth reads as

$|A_{max}/A_{min}|^2 \approx 1+2\,\beta_2 z\,(|\varepsilon_m\omega_M|+|\omega|)^2$. The comparison between experimental data, direct numerical calculations and first order approximation shows a good agreement.

However, to obtain a general picture of the stability of a CW solution against small complex-valued modulations in the above system we perform a linear stability analysis. Modulational instability (MI) is a well-investigated phenomenon in fibers exhibiting a Kerr nonlinearity [3] but was not addressed up to now in fiber systems with SOAs and filters. We show that depending on the dispersion regime stable periodical patterns as well as CW solutions may emerge. In particular, it will turn out that narrow in-line filters evoke MI.

Inserting the perturbed solution $A(z,t) = (A_0 + \varepsilon(z,t))\exp[i(\Gamma z-\omega t)]$ into (1) and linearizing it in $\varepsilon(z,t)$ one obtains

$$i\frac{\partial\varepsilon}{\partial z}+\left(\frac{\beta_1}{2}-i\beta_2\right)\left(\frac{\partial^2\varepsilon}{\partial t^2}-2i\omega\frac{\partial\varepsilon}{\partial t}\right) +\chi A_0^2\left(\varepsilon+\varepsilon^*\right)+\rho(\alpha+i)A_0^2\times \quad (2)$$
$$\times\int_{-\infty}^{t}\left(\varepsilon(z,t')+\varepsilon^*(z,t')\right)\exp\left[-\frac{t-t'}{t_r}\right]dt'=0$$

Separating real and imaginary parts as $\varepsilon = v + iw$ we found the increment λ of spectral components $\bar{v},\bar{w} \sim \exp[\lambda z]$ from $\det[L]=0$ where

$$L=\begin{pmatrix}\lambda+a+\dfrac{2\rho A_0^2 t_r}{1-2i\omega_M t_r} & b\\ -b-2\chi A_0^2-\dfrac{2\rho\alpha A_0^2 t_r}{1-i\omega_M t_r} & \lambda+a\end{pmatrix} \quad (3)$$

with $a=i\beta_1\omega\omega_M+\beta_2\omega_M^2$ and $b=-\beta_1\omega_M^2/2+2i\beta_2\omega\omega_M$. Consequently, λ is obtained from

$$(\lambda+a)^2+\frac{2\rho A_0^2 t_r(\lambda+a)}{1-i\omega_M t_r} +b\left(b+2\chi A_0^2+\frac{2\rho\alpha A_0^2 t_r}{1-i\omega_M t_r}\right)=0 \quad (4)$$

Eq. (4) exhibits conventional MI [3] for $\chi=\beta_1=1$ or -1 and $\rho=0$, $\delta=0$, $\beta_2=0$. Our primary concern is to identify the role that play the SOA and the filter with respect to MI, so we set the fiber nonlinearity and the fiber dispersion to zero for a moment. It is evident from (4) that the CW solution is stable if the carrier frequency is identical to the center frequency of the filter ($\omega=0$). However depending on the filter offset ($|\omega| > 0$) there are modulationally unstable domains $\Re[\lambda]>0$ in ω-ω_M-parameter space as shown in Fig.1, where the displayed range $\Omega=\omega t_0$ corresponds to a wavelength detuning of ± 0.2 nm. Without SOA the instability may start at very small filter detuning and should arise for modulational frequencies $2\omega \geq \omega_M \geq 0$. The maximum MI gain occurs at $\omega=\omega_M$ because that sideband is located at the filter transmission maximum. However, the SOA modifies the situation. The gap $\omega_c < \omega < 0$ appearing between both regions increases with the CW power. The stable region at the red filter edge is more pronounced than the region at the blue edge. This is due to the increasing MI gain caused by the AM induced red shift of SOA.

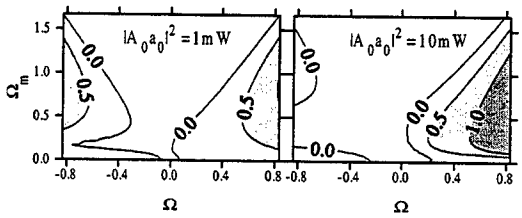


Fig.1: MI gain in dB/(25 km) at ZDW without Kerr nonlinearity for $\beta_2=0.163$, $\rho=0.0308$, $\alpha=5$, $t_r=53.7$.

Accounting also for Kerr nonlinearity and fiber dispersion additional effects may appear due to conventional MI [3]. Fig. 2 shows how the situation changes in the normal and anomalous dispersion regime as well as at ZDW for two different values of the input power (1 mW and 10 mW).

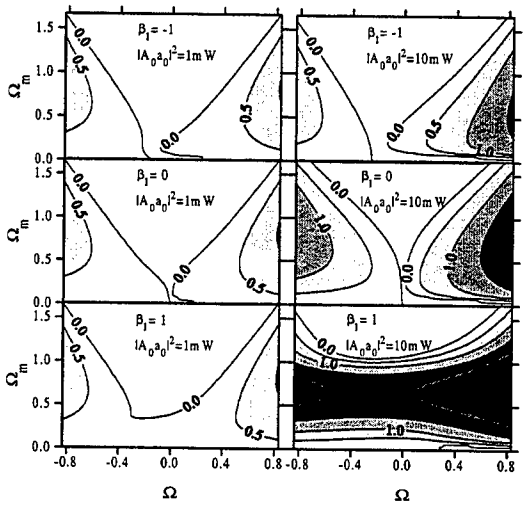


Fig.2: MI gain as in Fig.1, but with Kerr-nonlinearity at normal dispersion ($\beta_1=-1$), ZDW ($\beta_1=0$) and anomalous dispersion ($\beta_1=1$) for input power 1 mW and 10 mW.

In the anomalous dispersion regime conventional MI dominates for large input powers. At normal dispersion as well as at ZDW MI is mainly evoked by the filter when the input

power is small. A higher input power changes the characteristic due to a combined action of Kerr and SOA nonlinearity (see Fig. 2).
However, the location of the gap at the red filter edge in the normal dispersion regime depends on the power which might be important in experiments. Increasing the power stable domains can become unstable (compare the two plots on top of Fig.2). In the case under consideration this happens, e.g., for a 0.03 nm red shifted input signal at about 4 mW.
Using a beam propagation method we performed a numerical experiment with $A(0,t) = A_0 [1 + 0.05 \cos(\omega_M t)] \exp(-i\omega t)$ where the modulational frequency ω_M corresponds to the maximum of the increment $\Re[\lambda(\omega,\omega_M)]$. These numerical calculations show that the spectral evolution is primarily governed by an interplay of a finite number of harmonic waves caused by four-wave-mixing and dispersion. They are separated by the modulational frequency ω_M so that we assume $A(z,t)=\Sigma_j c_j(z) \exp[-i\, j\, \omega_M\, t]$. We obtain from (1) the evolution of the spectral amplitudes as

$$0 = i\frac{dc_m}{dz} - \left(i\delta + \left(\frac{\beta_1}{2} - i\beta_2 \right) (m\omega_M)^2 \right) c_m + \sum_{\substack{j,k,l: \\ m=j-k+l}} \left(\chi + \frac{\rho(\alpha+i)t_r}{1-i(m-j)\omega_M t_r} \right) c_j c_k^* c_l \qquad (5)$$

It is evident that the solution of (5) is much easier than that of (1). An obvious consequence of (5) is that for $\omega_M t_r >> 1$ the effective nonlinearity depends only marginally on the linewidth enhancement factor α. We compared the BPM calculations with the solution of (5) and obtained a good agreement provided that the high frequency components are sufficiently small.
Fig. 3 shows the evolution of a modulated CW solution at anomalous dispersion for $\Omega = 0$ and $\Omega_M \approx 0.7$ for small (a) and high peak power (b). For small powers the initial modulation is washed out whereas if the power increases an instability is induced - the modulation increases and a stationary periodic field distribution appears. Because of this instability the CW solution $A = A_0 \exp[i(\Gamma z - \omega_M t)]$ where gain balance holds is not attained. An interesting behavior can be observed in the normal dispersion domain. Selecting a modulation frequency and a power that apply to an unstable region but are close to the boundary of instability the instability manifests itself in the formation of a stable pattern (see Fig.4a). Increasing the power the solution moves into the stable region. Because it is close to the boundary of instability the modulation is only weakly damped. So, a new sideband with a frequency being located in the unstable region can be generated and a pattern at frequency $2\omega_M$ is created (see Fig.4b).
We studied the influence of third-order dispersion ($i\beta_3 \partial^3 A/\partial t^3$) on MI. We found a purely imaginary shift of the increment $\lambda + a \rightarrow \lambda + a - i\beta_3\omega_M(\omega_M^2+3\omega^2)$ and a correction for the effective dispersion in $b \rightarrow b + 3\beta_3\omega(\omega_M)^2$ in equations (3) and (4). However we observed only a minor influence on $\Re[\lambda]$.

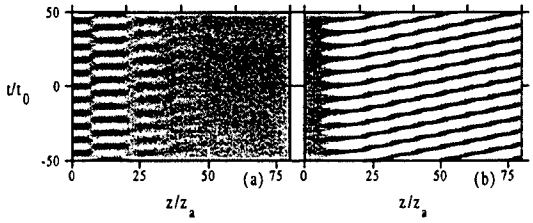


Fig.3. Propagation of AM CW-signal at anomalous dispersion, $\omega = 0$, $\omega_M/(2\pi) = 30$ GHz for input power $|A_0 a_0|^2 = 1$ mW (a) and $|A_0 a_0|^2 = 10$ mW (b)

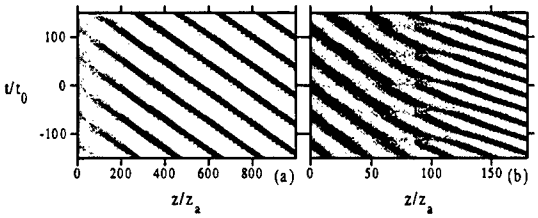


Fig.4. Propagation of AM CW-signal at normal dispersion, $\omega = 0$, $\omega_M/(2\pi) = 4.5$ GHz for fiber input power $|A_0 a_0|^2 = 1$ mW (a) and $|A_0 a_0|^2 = 10$ mW (b)

In conclusion, we analyzed the MI of CW solutions in transmission lines with SOA and filters. A stable region in the anomalous dispersion domain could be identified. Transitions to amplitude modulated structures were observed both numerically and experimentally.

[1] J.J.E. Reid, L. Cucala, M. Ferreira, M. Settembre, H. Haunstein, and R.C.J. Smets, *in Technical Digest of ECOC*, 1998, paper WdD01, pp. 567
[2] G. Onishchukov, V. Lokhnygin, A. Shipulin, P. Riedel, Electron. Lett. **34** (1998), 1597
[3] A. Hasegawa, W.F. Brinkman, IEEE J. Quantum Electron., **QE-16** (1980), 694.

Propagation and break-up of pre-chirped N-soliton pulses in anomalous optical fibers

D. Krylov, L. Leng, and K. Bergman
Department of Electrical Engineering, Princeton University J303, E-Quad, Olden Street, Princeton, New Jersey 08544
krylov@ee.princeton.edu, lleng@ee.princeton.edu, bergman@ee.princeton.edu

J. C. Bronski
Department of Mathematics, University of Illinois Urbana, Illinois 61801

J. N. Kutz
Department of Applied Mathematics, University of Washington, Seattle, Washington 98105

With the advent of disperion-managed communications systems, the practice of pre-chirping pulses is becoming increasingly commonplace. The dynamics of chirped pulses is much richer than the unchirped case and leads to new and unexpected behaviors. Understanding how pre-chirping affects pulse propagation in fiber optic systems is of significant theoretical and practical importance. Recent analytic [2], computational [3], and experimental [4] evidence suggests that a strongly chirped N-soliton pulse which is injected into an anomalous optical fiber will break-up into a train of fundamental ($N = 1$) solitons which are ordered by height and propagate away from the initial chirped pulse shape in such a way that the taller ejected fundamental solitons move faster than those of smaller amplitude. Previous findings [5, 6] have shown N-soliton breakup due to asymmetric perturbations such as third order dispersion, Raman effect, filtering, and asymmetric pre-chirp. The effect we describe is more subtle, occuring even for symmetric pre-chirp, and is an example of symmetry breaking. Thus it has the possibility of fundamentally limiting systems which rely on chirped pulse propagation.

The propagation of the electric field envelope in an anomalous dispersion fiber in the presence of the Kerr nonlinearity is given by the normalized nonlinear Schrödinger equation:

$$i\epsilon\frac{\partial Q}{\partial Z} + \frac{\epsilon^2}{2}\frac{\partial^2 Q}{\partial T^2} + |Q|^2 Q = 0 \tag{1}$$

where for our purposes $\epsilon \ll 1$. Here Q represents the electric field envelope normalized by the initial peak field power $|E_0|^2$, T represents the physical time normalized by $T_0/1.76$ where T_0 is the FWHM of the pulse, and the variable Z is the physical distance multiplied by the parameter ϵ and divided by the nonlinear length $Z_{NL} = (\lambda_0 A_{\text{eff}})/(2\pi n_2 |E_0|^2)$. The parameters n_2=2.6×10^{-16} cm^2/W, A_{eff}, λ_0, and c correspond to the nonlinear index coefficient, effective cross-section area, free-space wavelength and speed of light respectively. Epsilon is a nondimensional parameter which measures the relative strength of the nonlinearity versus dispersion and is given by:

$$\epsilon^2 = [\lambda_0^3 D A_{\text{eff}}]/[4\pi^2 c n_2 |E_0|^2 (T_0/1.76)^2] \tag{2}$$

where D is the chromatic dispersion (in ps/(km-nm)) in the optical fiber. We note that the condition $\epsilon \ll 1$ can be met by propagating in a low dispersion fiber with high intensities since $\epsilon \propto D/|E_0|^2$. Numerical simulations begin at $Z = 0$ with the strongly chirped, symmetric pulse profile:

$$Q(0, T) = \text{sech}(T) \exp\left(2i \,\text{sech}(T)/\epsilon\right) . \tag{3}$$

We note that in the absence of chirp the solution will, in general, consist of an N-soliton bound state. A typical realization of the pulse dynamics is presented in Fig. 1 where we depict the dynamic evolution of the pulse breakup with an initial strong chirp and $\epsilon = 0.1$. The evolution is as predicted from theory: pairs of fundamental solitons are ejected symmetrically away from the middle region

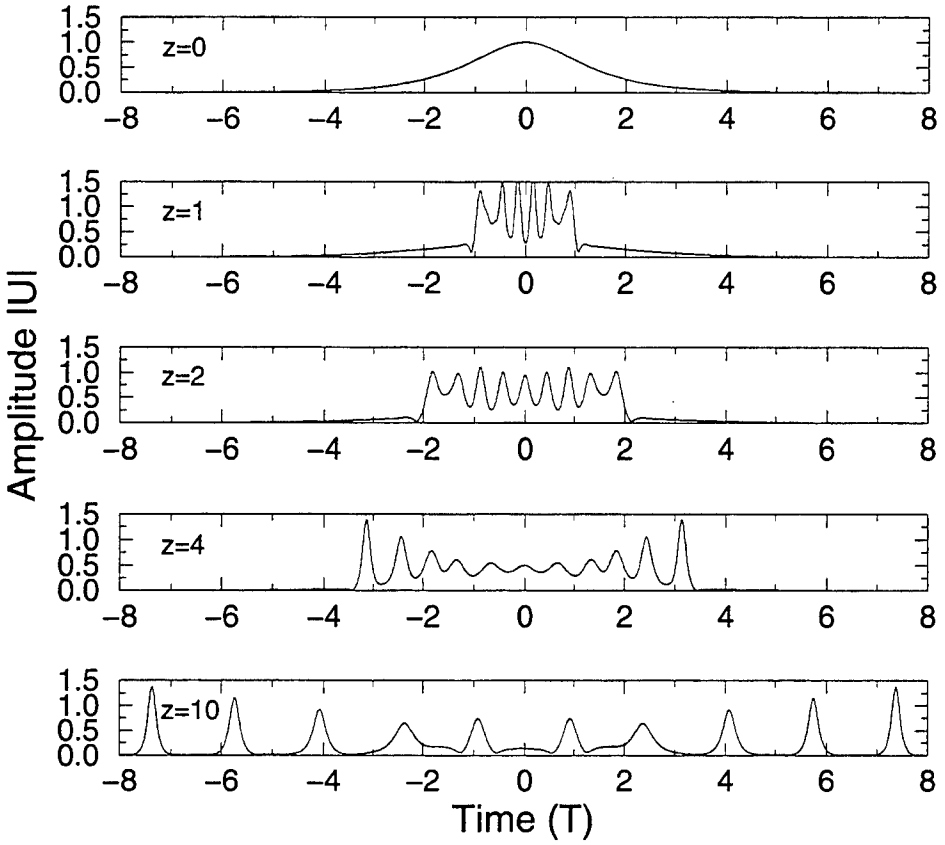


Figure 1: Numerical simulation showing ejection of solitons from an initial, strongly pre-chirped soliton pulse of the hyperbolic secant form.

with their pulse speeds being determined by their amplitude [2, 3]. After an initially ($Z = 4$) strong oscillatory structure develops, an ordered ejection of fundamental soliton pulses occurs. By $Z = 10$, the fundamental solitons are well-separated, distinct and continue to move away from $T = 0$.

We verify the theoretical and numerical predictions by performing experiments (see Fig. 2) in which strongly pre-chirped pulses are propagated in anomalous dispersion fiber. A Spectra-Physics Opal optical parametric oscillator (OPO) provides a train of 160-fs (FWHM) transform limited optical pulses at a repetition rate of 82MHz and centered at a wavelength of λ_0=1550nm. The light is coupled into an erbium-doped amplifier (EDFA) that is 20m long and has a normal dispersion parameter D =–25ps/(nm-km). By starting with low average powers of several milliWatts and then amplifying the signal in the EDFA, we are able to keep the spectral width of the pulses essentially unchanged while providing significant chirp. The EDFA used saturates near 70mW, giving an adequate range of powers to perform the experiment. The optical pulses that emerge from the amplifier have a temporal width of 6ps (FWHM) and a spectral (3dB) bandwidth of 20nm, indicating that they are strongly chirped with the linear chirp parameter C on the order of 35 [7]. The pulses are then sent to a 400m section of Corning LEAF dispersion-shifted fiber (DSF) which has a dispersion zero at 1520nm (D=3.0 ps/(nm-km) at 1550nm) and a core of 10μm.

Since the breakup produces ultra-short pulses, the time-domain behavior is measured via an auto-correlation. In Fig. 3, we depict the experimental results for input powers of 8, 11, and 14 mW. As the power is increased, we see the break-up into M=2, 3, and 4 pulses respectively since the auto-correlator produces (2M-1) peaks. This demonstrates clearly the phenomena of the pulse break-up due to chirp. It is the dominant effect in the pulse propagation. Of course, once the break-up

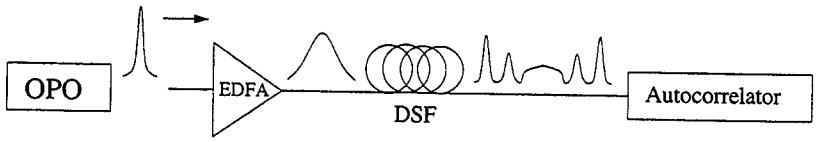


Figure 2: Schematic of experimental configuration which includes an optical parametric oscillator (OPO), Erbium-doped fiber amplifier (EDFA), and dispersion-shifted fiber (DSF).

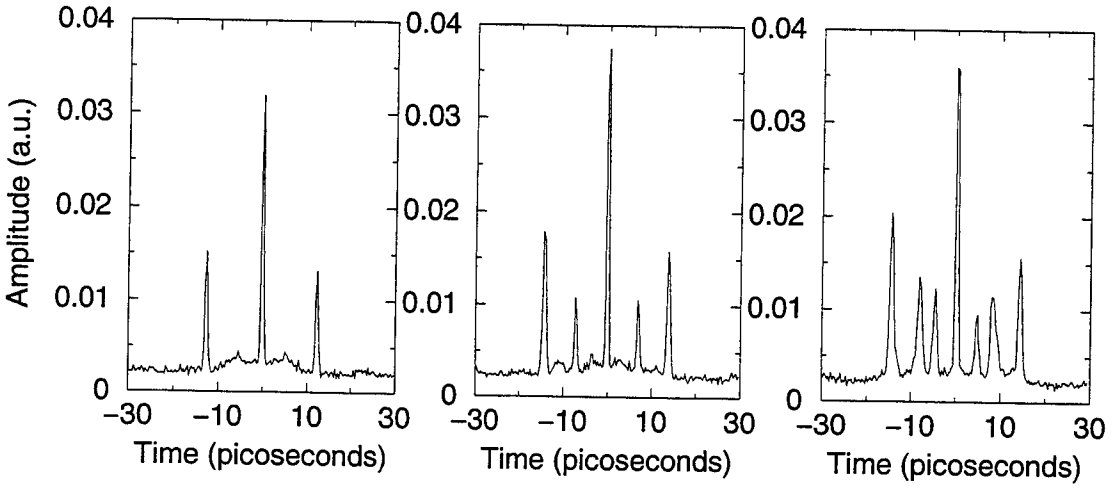


Figure 3: Autocorrelations demonstrating pulse break-up into two (left), three (center), and four (right) pulses. The corresponding input powers are 8, 11, and 14mW respectively.

and ejection have occurred, we expect that the effects due to third-order dispersion and the Raman self-frequency shift will act to modify the pulse shapes. However, the basic phenomena of the pulse breakup in the N-soliton limit remains unaffected and dominated by pre-chirp.

This behavior has important consequences for optical fiber applications since it implies that an intense, strongly chirped pulse which is inserted into a low-dispersion, anomalous fiber will begin breaking up over a fairly short distance. This is demonstrated both numerically (Fig. 1) and experimentally (Fig. 3) and implies that pre-chirped, N-soliton pulses undergo an irreversible pulse breakup where a number of fundamental solitons are symmetrically ejected away from the pulse with the tallest solitons moving faster than the smaller ones. This phenomena can occur over hundreds of meters of fiber and should be avoided in implementations of dispersion-managed transmission systems which rely on chirped solitons [1].

References

[1] see, for example, *New Trends in Optical Soliton Transmission Systems*, Ed. A. Hasegawa (Kluwer Academic, Dordrecht, Netherlands, 1998)

[2] J. C. Bronski, Physica D **97**, 376 (1996).

[3] J.C. Bronski and J.N. Kutz, Phys. Lett. A **254**, 325 (1999).

[4] D. Krylov, L. Leng, K. Bergman, J. N. Kutz, J. C. Bronski, in *Ultrafast Electronics and Optoelectronics*, OSA Tech. Dig. 74 (OSA, Washington, DC, 1999)

[5] S. R. Friberg and K. W. DeLong, Opt. Lett. **17**, 979 (1992).

[6] Y. Kodama and A. Hasegawa, IEEE J. of Quantum Electronics, **QE-23**, 510 (1987).

[7] G. P. Agrawal, *Nonlinear Fiber Optics*, (Academic, San Diego, 1989).

10 Gbit/s OTDM to 4 x 2.5 Gbit/s WDM conversion using an SOA-NOLM, Bragg gratings and a supercontinuum pulse source

D. M. Ryan and N. J. Doran

Photonics Research Group,

School of Engineering and Applied Science,

Aston University, Aston Triangle,

Birmingham B4 7ET, United Kingdom

ryandm@aston.ac.uk, n.j.doran@aston.ac.uk

Near future optical networks are likely to exploit both time and wavelength division multiplexing (TDM and WDM) of data. These networks will require a number of basic functional features to effect both add/drop multiplexing and the demultiplexing of all TDM channels simultaneously. A number of techniques have been used to effect the simultaneous isolation of all TDM channels [1,2]. Perhaps one of the more elegant approaches was by Uchiyama *et al* [1] who used a linearly chirped clock pulse and an all-fibre nonlinear loop mirror (NOLM) to demultiplex 10 Gbit/s channels from a 100 Gbit/s TDM datastream.

Here we use an SOA-NOLM (nonlinear loop mirror which uses a semiconductor optical amplifier as the switching nonlinearity) [3]. The clock pulses are obtained by spectrally slicing supercontinuum pulses using Bragg gratings. The experimental set-up is used to simultaneously demultiplex four 2.5 Gbit/s channels (each output at a different wavelength) from a 10 Gbit/s TDM datastream.

The experimental set-up is shown in Figure 1 below. The supercontinuum pulses are generated by propagating narrow high power pulses (~2 ps FWHM and ~12 dBm average power) at a wavelength of 1548 nm through 16 km of dispersion shifted fibre (λ_0=1548 nm). These pulses are spectrally sliced to yield four wavelengths between 1550 and 1554 nm with 100 GHz channel spacing using the four serial Bragg gratings. Each Bragg grating reflects one specified wavelength and transmits all other wavelengths. The gratings are physically spaced so that reflections from successive gratings are temporally spaced by 100 ps and each temporal slot contains a different wavelength. The 10 Gbit/s TDM (four channels) control data is at a wavelength of 1534 nm and switches all four channels to four different wavelengths simultaneously.

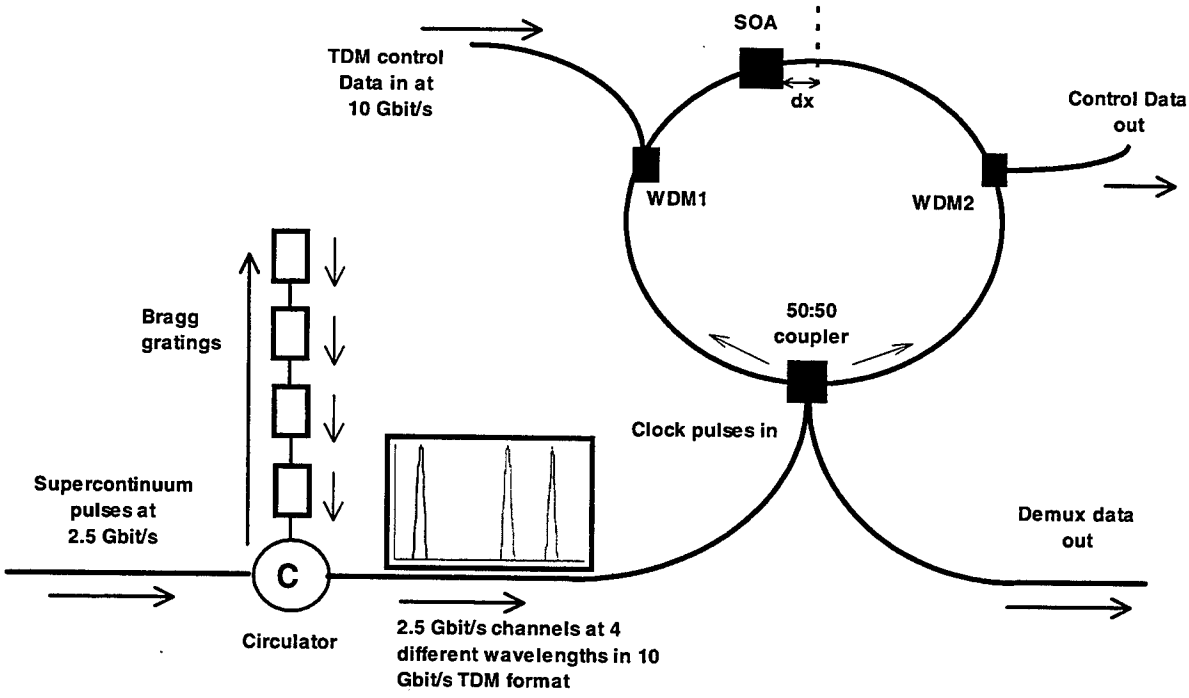


Figure 1: Experimental set-up for TDM-WDM interface

Each demultiplexed channel is isolated at output using a narrow bandpass filter and bit error rates (BER) measured. The bit error rates are also measured for the cases when only one of the four channels is demultiplexed. These results are compared and overall power penalty determined.

The switching rate of the SOA-NOLM is limited by the gain recovery time of the semiconductor amplifier. The amplifier used in the current set-up has a recovery time of 100 ps which restricts the operation to demultiplexing a 2.5 Gbit/s channel from a 10 Gbit/s TDM datastream. Amplifiers with shorter gain recovery times could be used to increase the switching rate of the SOA-NOLM. The above set-up could then be used to either demultiplex more channels or a four channels at higher bitrates.

[1] Uchiyama K., Takara H., Morioka T., Kawanishi S. and Saruwatari M.: '100 Gbit/s multiple-channel output all-optical demultiplexing based on TDM-WDM conversion in a nonlinear optical loop mirror', *Electron. Lett.*, **32**, pp. 1989-1991 (1996)

[2] Duelk M., Fischer St., Gamper E., Vogt W., Gini E., Melchior H., Hunziker W., Puleo M. and Girardi R.: 'Full 40 Gbit/s OTDM to WDM conversion: Simultaneous four channel 40:10 Gbit/s all-optical demultiplexing and wavelength conversion to individual wavelengths', *Tech. Dig. Optical Fiber Communication Conference* (OFC'99), paper PD17-1

[3] Sokoloff J.P., Prucnal P.R., Glesk I. and Kane M.: 'A terahertz optical asymmetric demultiplexer (TOAD)', *IEEE Phot. Tech. Lett.*, **5**, pp. 787-790 (1993)

Photorefractive grating assisted directional coupler

Ewa Weinert-Rączka and Robert Iwanow
Institute of Electronics and Informatics, Technical University of Szczecin
Al.Piastów 17, 70-310 Szczecin, Poland, Tel +(48)-91-494466, Fax +(48)-91-342113
e-mail: ewar@arcadia.tuniv.szczecin.pl

1. Introduction

Transfer of light between different waveguides is one of the crucial functions of the integrated optics systems. The power exchange between waveguides, placed in a closed proximity to form a directional coupler, is efficient when the light propagates in them with the same velocity. In case of different propagation constants the coupling can be obtained by means of a diffraction grating formed by periodic changes of the refractive index along the propagation direction [1-3]. The grating constant $K=2\pi/\Lambda$ (where Λ is the length of the grating period) should be equal to the difference between propagation constants of coupled modes ($K=\beta_A-\beta_B$). Such systems, called Grating Assisted Couplers (GACs) are used as narrow frequency filters and demultiplexing elements. The grating in the traditional GAC has constant, immutable parameters, what limits the operation of the coupler to one, strictly defined frequency. A tuneable coupler can be realised when the grating is created by two external beams interfering in a nonlinear medium [4]. Parameters of such a grating depend on the external waves properties and can be tuned during the work of the device.

Here we propose a new type of the directional coupler which is controlled by the photorefractive grating. The grating is created by a short pulse of the external waves and lasts until the arrival of the next pulse which can amplify or erase it. Guided modes being the subject of switching have lower frequencies and their influence on the grating can be neglected.

2. Performance of the coupler

The coupler consists of two different channel waveguides parallel to the z-axis of the co-ordinate system. Parameters of the channels differ enough to avoid power exchange between them. The grating required to mediate coupling, is created by two external waves forming an interference pattern along the z axis.

$$I = I_0(x,z,t)\exp(-\alpha_{ex}y)\,[1 + m\cos(Kz)]$$

where I_0 denotes the intensity of the external beams at the surface of the coupler, α_{ex} describes the absorption coefficient, m is the modulation depth and K the grating constant. For strongly absorbed external waves the interference pattern is created only in a thin surface layer of a depth about $1/\alpha_{ex}$. A high frequency light excites free carriers and by the photorefractive effect leads to the modulation of refractive index. Coupling between two different modes in the presence of the grating are described by equations [4,5]:

$$i\,dA_1/dz = G_{12}A_2\exp[\,i(\beta_1-\beta_2)z]\exp(-iKz)$$

$$i\,dA_2/dz = G_{21}A_1\exp[-i(\beta_1-\beta_2)z]\exp(iKz),$$

where β_ν are propagation constants and A_ν amplitudes of modes. The coupling coefficients for TE modes $G_{\mu\nu} = (\omega\varepsilon/N)\iint \Delta\varepsilon_G\, E_\mu E_\nu^* dxdy$, with $N=(N_\mu N_\nu)^{1/2}$ and $N_\nu=(2\beta_\nu/\omega\mu_0)\iint E_\nu E_\nu^* dxdy$

$\Delta\varepsilon_G$ describes the amplitude of the dielectric constant changes within the grating and E_ν is a transverse distribution of the νth mode electric field. The amplitude of the refractive index grating necessary to obtain transfer of light can be estimated from the relation $G_{\mu\nu} = \pi/2L$, where L denotes the length of the coupler [1].

3. Photorefractive material

As a photorefractive material we chose semi-insulating multiple quantum wells (MQW) structure operated with an external electric field which is applied parallely to the layer planes and to the K vector of the grating [6]. The detail calculations were performed for the coupler with a guiding slab consisting of 75Å GaAs wells and 100Å $Al_{0.3}Ga_{0.7}As$ barriers. The MQW structure, in accordance with previous studies [7,8] was simulated by a strongly anisotropic homogeneous semiconductor with the parallel mobilities of the

carriers much higher then the perpendicular ones. An efficient operation of the coupler is possible with high frequency external waves writing the grating and lower frequency guided modes reading it. The wavelengths (λ_{ex} = 630 nm and λ_g = 845nm) were chosen from the spectral dependence of the absorption and electro-refraction coefficients presented in Fig.1. Absorption curves consist from Gaussian peaks for light hole and heavy hole absorption and continuum contributions from absorption to free electron-hole pairs [9,10] ($\alpha_E(\lambda)$ – in the presence of an external electric field and $\alpha_0(\lambda)$ – without the field). The change of the refractive index, $\Delta n_E(\lambda)$, due to the absorption changes caused by the quantum confined Franz-Keldysh effect was calculated using Kramers-Krönig relations [11]. The parameters of the approximation were taken from the paper of Wang et al. [12].

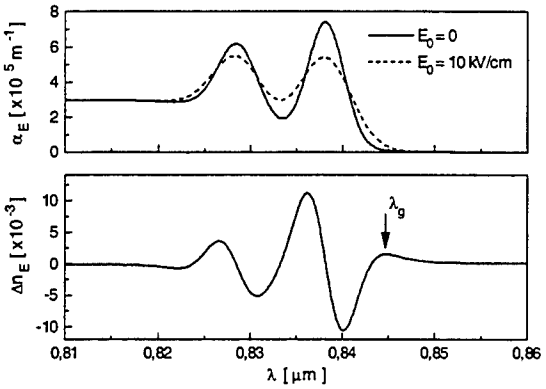


Fig.1. Spectral dependence of absorption and electro-refraction.

The propagation constants and field profiles of the modes for the chosen λ_g were determined using the effective index method and the transfer matrix approach [5]. The resulting grating amplitude and fringes spacing necessary for transfer signals between the waveguides in the designed coupler (consisting of two 0.4 μm high rib $Al_{0.5}Ga_{0.5}As$ waveguides of widths 0.4 μm and 0.7 μm separated by 0.6 μm strip of AlAs and placed on MQW layer) are $\Delta n = 2.25 \times 10^{-4}$ per 1 cm of the device length and Λ = 84.5 μm.

4. Dynamics of the grating.

For high frequency external waves the main photorefractive mechanism in MQW layer relays on the interband excitation of electrons and holes, their movement due to the drift and diffusion and finally a recombination to the donor traps. The resulting space-charge electric field causes the change of the refractive index due to the electro-optic effect. Such a model leads to the following equations based on a classical Kukhtarev-Vinetskii model [7]:

$$\frac{\partial n_e}{\partial t} = \frac{\alpha}{h\nu} I - \gamma_e n_e N_D^+ + \frac{1}{e}\frac{\partial j_e}{\partial z}$$

$$\frac{\partial n_h}{\partial t} = \frac{\alpha}{h\nu} I - \gamma_h n_h (N_D - N_D^+) - \frac{1}{e}\frac{\partial j_h}{\partial z}$$

$$j_e = e\mu_e n_e E + \mu_e k_B T \frac{\partial n_e}{\partial z}$$

$$j_h = e\mu_h n_h E - \mu_h k_B T \frac{\partial n_h}{\partial z}$$

$$\frac{\partial N_D^+}{\partial t} = \gamma_h n_h (N_D - N_D^+) - \gamma_e n_e N_D^+$$

$$\frac{\partial E}{\partial z} = \frac{e}{\varepsilon\varepsilon_0}(N_D^+ + n_h - n_e - N_A)$$

The symbols in above equations are: n_e - the free electron and n_h - the free hole concentrations, N_D - donors, N_D^+ - ionised donors and N_A - acceptors concentrations, j_e - the electronic and j_h - the hole current densities, E - the total electric field ($E=E_0 + E_{sc}$, where E_{sc} is a space-charge fields and E_0 is an external field), I - the light intensity, γ_e and γ_h - the constants describing recombination of electrons and holes, μ_e - electron and μ_h - hole mobilities along the quantum wells, ε_0 - the permittivity of the vacuum, ε - the effective dielectric constant of MQW structure, e - the absolute value of the elementary charge, k_B - the Boltzmann constant and T - the absolute temperature. Thermal excitation of the carriers and transverse carrier mobility are not included in the above set of equations. The later condition is fulfilled due to the high difference between longitudinal and transverse carrier mobilities.

The set of equations was solved numerically for the initial conditions $E_0 = 10^6$ V/m and $N_D^+(0) = N_A = N_D/2$, trap density $N_D = 10^{23}$ m^{-3}, absorption coefficient $\alpha_{ex} = 10^5$ m^{-1} and other parameters as in [7]. The time evolution of the space-charge field presented in Fig.2 exhibits the same saturation value for different light

intensities and a strong influence of intensity on the response time of the device .

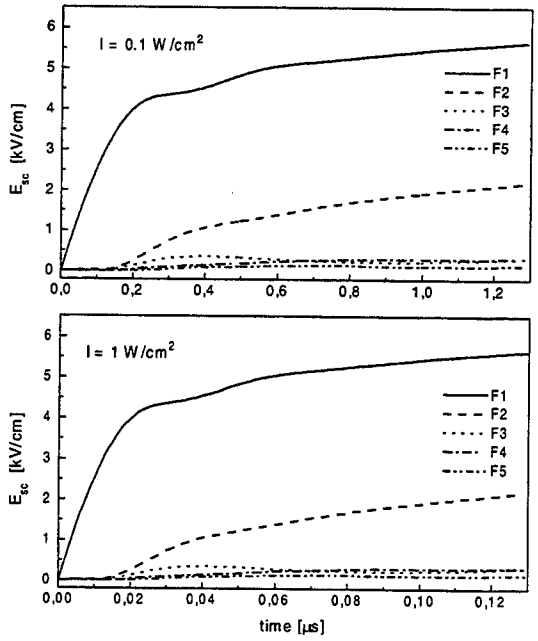


Fig.2. Time evolution of the first five Fourier components of space-charge field for different external waves intensities.

The evolution of the space-charge field generated by the short pulse of light is presented in Fig.3.

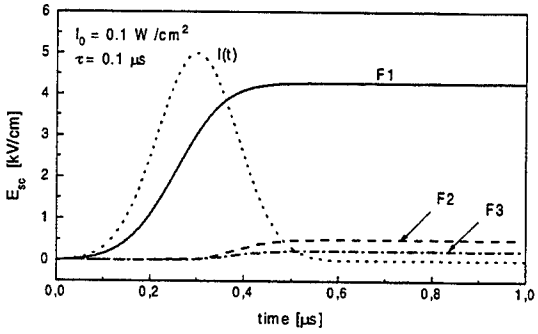


Fig.3. The time evolution of the first three Fourier components of the space-charge field for $I = I_0 \exp(-(t-t_0)^2/2\tau^2)$.

The grating life-time depends mainly on the materials dark conductivity and in the absence of free carriers which is assumed here can be very long.

The refractive index changes in the semi-insulating MQW structures $\Delta n(E) = (-1/2)\, n_0^3\, sE^2$, where s is a quadratic electrooptic coefficient [6]. According to our calculations s coefficient due to the Franz-Keldysh effect for λ_g=845 nm is in the range of 7×10^{-13} cm^2/V^2. Hence the achieved electric field causes index change about 3×10^{-4} and can provide switching in 0.8 cm long device.

5. Conclusions

It has been shown that a thin photorefractive grating in semi-insulating MQW material can be used to control an asymmetric directional coupler. A choice of the output guide and the wavelength of the switched signals depends on the grating parameters and can be varied during the work of the device. The grating does not require a permanent presence of the external waves. Pump pulses are necessary only for writing, refreshing or erasing of the grating. Signal waves at low frequency do not destroy the grating which makes a potential application of the system as an all-optical switching element with memory possible. The switching time of the coupler depends on the intensity of the external waves and can be below 0.1 μs what allows potential applications for routing groups of signals.

6. References

[1] C. Elachi, C. Yeh, Opt. Commun. **7**, 201 (1973).
[2] W.P.Huang, H.A.Haus, J.Lightwave Techn. **LT-7**, 920 (1989).
[3] R. R. A. Syms, J. Opt. Soc. Am. **A8**, 1062 (1991).
[4] E. Weinert-Rączka, J. Opt. Soc. Am. **B11**, 2340 (1994)
[5] E.Weinert-Rączka, W.Biehlig and F. Lederer, J. Opt. Soc. Am. **B14**, 3232 (1997).
[6] A.M.Glass, D.D.Nolte, H.D.Olson, G.E.Doran, D.S.Chemla and W.H.Knox, Opt.Lett. **15**, 264 (1990).
[7] L. F. Magaña, F. Agulló-López and M. Carrascosa, J. Opt. Soc. Am. **B11**, 1651 (1994).
[8] M. Aguilar, M. Carrascosa and F. Agulló-López, J. Opt. Soc. Am. **B 13**, 2630 (1996).
[9] D. S. Chemla, D. A. B. Miller, P. W. Smith, A. C. Gossard, W. Wiegmann, IEEEE J. Quantum. Electron. **20**, 265 (1984).
[10] D.D. Nolte, D.H. Olson, G.E.Doran, W.H.Knox, A. M. Glass, J.Opt. Soc. Am. **B7**, 2217 (1990).
[11] D. C. Hutchings, M. Sheik-Bahae, D. J. Hagan, E.W.Van Stryland, Opt.Quantum.Electron.**24**, 1 (1992).
[12] Q. Wang, R. M. Brubaker, D. D. Nolte and M. R. Melloch, J. Opt. Soc. Am. **B9**, 1626 (1992).

Engineering competing quadratic and qubic nonlinearities

Ole Bang, Carl Balslev Clausen, and Peter L. Christiansen
Department of Mathematical Modelling, Technical University of Denmark, Building 305, DK-2800 Lyngby, Denmark
Tel.: (+45) 45 25 30 92; Fax: (+45) 45 93 12 35; E-mail: plc@imm.dtu.dk

Lluis Torner
Laboratory of Photonics, Department of Signal Theory and Communications,
Universitat Politecnica de Catalunya, Gran Capitan UPC-D3, Barcelona, ES 08034, Spain
Tel: 34 93 401 6527; Fax: 34 93 401 7232; E-mail: torner@tsc.upc.es

Quasi-phase-matching (QPM) is now a well-established technique for achieving walk-off free broadband phase-matching at room temperature in any material, and thus allow efficient second-harmonic-generation (SHG) (see [1] for a review). In particular, QPM through photolithographically controlled electric-field poling in ferro-electric materials, such as $LiNbO_3$, is promising due to the possibilities of engineering the mask, and thus the QPM grating [2,3].

Lately interest has thus turned towards engineering the QPM grating. Changing the grating in the direction of propagation one can achieve SHG at several wavelength [4], compressing optical pulses without introducing phase distortions [5,3], or enhancing the cascaded phase shift of the fundamental [6]. A fan-out design (i.e. change in the transverse direction) can be used to obtain broad spectral coverage of the SHG phase-matching wavelength [2,7]

It has also been shown that solitons can exist in QPM quadratic nonlinear media [8,9], even under the influence of a random domain length [10,9]. Introducing a weak chirp of the domain length in the propagation direction allows for adiabatic shaping of solitons [11]. With lateral paterning the profile of the solitons can be engineered [12] and with local distortions such as steps and impurities [13] or tilts and dislocations [14], the solitons can be steered in the transverse direction.

In all these works the nonlinearity was always purely quadratic. However, it was recently shown that QPM induces cubic nonlinear terms, such as self- and cross-phase modulation (SPM and XPM), in the equations describing the evolution of the averaged fields [8]. This induced cubic nonlinarity affects the amplitude and phase modulation of cw waves [15], while still supporting solitons [8], and thus it offers the possibility of enginering the properties of QPM quadratic (or $\chi^{(2)}$) nonlinear materials.

The induced Kerr nonlinearity, which is an unavoidable result of incoherent or non phase-matched coupling between modes [17], is of a fundamentally different nature than the inherent material Kerr nonlinearity. Consequently, its effect can be significantly different from the known results for competing $\chi^{(2)}$ and inherent $\chi^{(3)}$ nonlinearities, both in the case of SHG [16] and solitons (see [17] for a review). It is interesting that the induced cubic nonlinearity is equivalent to the additional nonlinearity experienced by the guided center soliton in dispersion managed optical fibre systems.

As we will show, the induced cubic nonlinearity in a typical QPM $LiNbO_3$ crystal is more than an order of magnitude weaker than the inherent material cubic nonlinearity. This leaves an important question if we want to make use of the induced cubic nonlinearity: Can the QPM grating be engineered to make the induced SPM coefficient comparable to the inherent material one, and if so, what effect does this have on the $\chi^{(2)}$ nonlinearity? In this letter we try to answer this question.

We consider a linearly polarized electric field $\vec{E} = \hat{e}[E_1(z)\exp(ik_1z - i\omega t) + E_2(z)\exp(ik_2z - i2\omega t) + c.c.]/2$, propagating in a lossless QPM $\chi^{(2)}$ medium, where only the nonlinear susceptibility is modulated. When both frequencies ω and 2ω are far from material resonances, the dynamical equations take the form

$$i\partial_z E_1 + G(z)\chi_1 E_1^* E_2 e^{-i\Delta kz} = 0, \quad (1)$$
$$i\partial_z E_2 + G(z)\chi_2 E_1^2 e^{i\Delta kz} = 0, \quad (2)$$

where $\partial_z \equiv d/dz$, $\chi_j = \omega d_{\text{eff}}/(n_j c)$, $E_1(z)$ is the slowly varying envelope of the fundamental wave (FW) with frequency ω and wavevector k_1, and $E_2(z)$ is the corresponding second harmonic (SH) with wavevector k_2. The effective nonlinearity coeffient $d_{\text{eff}} = |\chi^{(2)}|/2$ is given in MKS units, and $\Delta k = 2k_1 - k_2 = 2\omega(n_1 - n_2)/c$ is the wavevector mismatch, where $n_j = n(j\omega)$ is the refractive index at the frequency $j\omega$ (j=1,2). The total intensity $I = \eta_0(n_1|E_1|^2 + n_2|E_2|^2)/2$ is conserved, where $\eta_0 = \sqrt{\epsilon_0/\mu_0}$ is the specific admittance of vacuum.

The periodic modulation of the $\chi^{(2)}$ susceptibility is described by the periodic grating function $G(z)$ with amplitude 1. For the most efficient first order QPM with the typical square grating with constant domain length $L_0 = \pi/\kappa_0$, the dynamical equations for the average amplitudes $w = \langle E_1 \rangle$ and $v = i\langle E_2 \rangle$,

$$i\partial_z w + \eta_1 w^* v e^{-i\beta_0 z} + (\gamma_2|w|^2 - \gamma_1|v|^2)w = 0, \quad (3)$$
$$i\partial_z v + \eta_2 w^2 e^{-i\beta_0 z} - 2\gamma_2|w|^2 v = 0, \quad (4)$$

were derived in [8] assuming that the domain length is much shorter than the length L of the crystal, $L_0 \ll L$,

and close to the coherence length $L_c=\pi/\Delta k$, corresponding to a small residual mismatch, $\beta_0 = \Delta k - \kappa_0 \ll \kappa_0$. Here $\eta_j=2\chi_j/\pi$ and $\gamma_j=\chi_1\chi_j(1-8/\pi^2)/\kappa_0$. The system (3-4) is easily extended to incorporate higher order QPM and diffraction in the transverse x and/or y direction [8].

Consider $LiNbO_3$ and a fundamental wavelength of λ_1=1.064μm, for which d_{33}=32pm/V. The nonlinear refractive index has been measured to $n_{\rm ref}=48\cdot 10^{-14}$esu, for n_1=2.2 and n_2=2.23 [18], giving the SPM coefficient $\gamma_{\rm spm}=n_{\rm ref}\omega/c$=0.04pm/V^2. In comparison, for perfect matching, $L_0=L_c=\lambda_1/4(n_2-n_1)\approx 9\mu$m, the induced Kerr nonlinearity is an order of magnitude lower, $\gamma_2=4(\pi^2-8)d_{\rm eff}^2 L_0/(\pi n_1 n_2\lambda^2)$=0.004pm/V^2. Generally the coherence length is shorter than 9μm and thus the cubic nonlinearity induced by single period QPM will be even weaker.

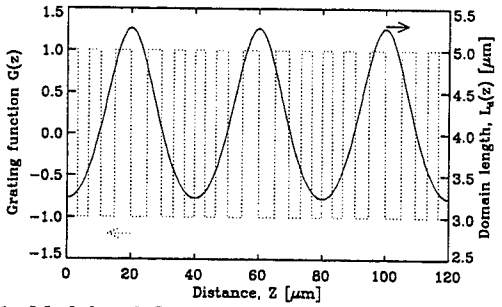


FIG. 1. Modulated QPM grating function $G(z)$ (left, dotted) with the corresponding domain length $L_d(z)$ (right, solid) for $L_2=10L_0=40\mu$m and ϵ_2=1.2.

Let us instead consider weakly modulated QPM gratings with Fourier series of the form

$$G(z)=\sum_n g_n \exp[inf(z)], \qquad (5)$$

where g_n=0 for n even and $g_n=2/(i\pi n)$ for n odd, are the coefficients of the unperturbed square grating. Unless otherwise indicated the sum is from $n=-\infty$ to $n=\infty$. We take $f(z)=\kappa_0 z+\epsilon_2\sin(\kappa_2 z)$, where the modulation period $L_2=2\pi/\kappa_2$ is long compared to the unperturbed domain length, $L_0 \ll L_2$. This corresponds to a square grating with a slowly varying domain length given by

$$L_d(z)\approx \pi/\partial_z f=\pi/[\kappa_0+\epsilon_2\kappa_2\cos(\kappa_2 z)], \qquad (6)$$

in the limit when the domain length is much shorter than the crystal length, $L_d \ll L$. The modulation is illustrated in Fig. 1 for a typical unperturbed domain length of L_0=4μm, with ϵ_2=1.2 and L_2/L_0=10. The ratio is here chosen to be relatively small in order to be able to see the modulation of $G(z)$ with the eye.

First we assume a first order QPM with a slow variation of the short domain length, i.e., $L_0 \sim L_c \ll L$ and $L_0 \ll L_2$. Then we expand $E_j(z)$ in Fourier series of harmonics of the wavenumber κ_0, $E_1=\sum_n w_n(z)\exp(in\kappa_0 z)$ and $E_2=\sum_n v_n(z)\exp(in\kappa_0 z)$, where the coefficients are slowly varying compared with the domain length L_0, i.e., $|\partial_z w_n| \ll |\kappa_0 w_n|$ and $|\partial_z v_n| \ll |\kappa_0 v_n|$. Following the approach outlined in [8] we obtain the equations for the average fields $\tilde w=w_0$ and $\tilde v=iv_0$ on the L_0-scale

$$i\partial_z\tilde w+\eta_1 D_1\tilde w^*\tilde v e^{-i\beta_0 z}+(\gamma_2|\tilde w|^2-\gamma_1|\tilde v|^2)\tilde w=0, \qquad (7)$$
$$i\partial_z\tilde v+\eta_2 D_{-1}\tilde w^2 e^{-i\beta_0 z}-2\gamma_2|\tilde w|^2\tilde v=0. \qquad (8)$$

where the quadratic nonlinearity now is multiplied by the periodic function $D_\pm=D_\pm(z)=\exp[\pm i\epsilon_2\sin(\kappa_2 z)]$, compared to Eqs. (3-4). Since $D_\pm(z)$ is periodic it can be expanded in a Fourier series,

$$D_\pm(z)=\sum_n d_{\pm n}\exp(in\kappa_2 z),\ d_n=J_n(\epsilon_2), \qquad (9)$$

where $J_n(\epsilon_2)$ is the Bessel function of the first kind of order n. Thus $d_{-n}=(-1)^n d_n$.

There are two different cases in which an analytical treatment is possible: In the adiabatic limit when $D_\pm(z)$ varies much slower than $\tilde w(z)$ and $\tilde v(z)$ the field can be assumed to adiabatically follow the variation of $D_\pm(z)$. This was studied theoretically (using the undepleted pump approximation) [5] and later observed experimentally [3] for pulses in aperiodic chirped QPM gratings in $LiNbO_3$. In similar weakly chirped QPM gratings it has been shown theoretically that spatial solitons adiabatically adjust their shape to the local domain length through a slowly varying phase-mismatch [11].

Here we consider the opposite case when the modulation period is short compared to the length of the crystal, $L_2 \ll L$. The spectrum of $G(z)$ for such a grating with $L_2=20L_0=100\mu$m and ϵ_2=1.2 is shown in Fig. 2. The blocks of peaks around the κ_0 and $3\kappa_0$ peaks of the unperturbed grating are clearly distinguishable.

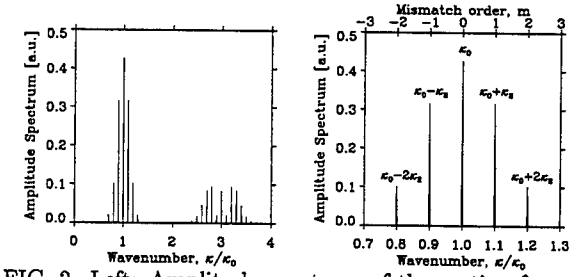


FIG. 2. Left: Amplitude spectrum of the grating function $G(z)$ for $L_2=20L_0=100\mu$m and ϵ_2=1.2. Right: The detailed structure around the first order peak at $\kappa=\kappa_0$ with indication of the order m of the effective mismatch β_m.

We now expand $\tilde w(z)$ and $\tilde v(z)$ in a Fourier series o f harmonics of the wavenumber κ_2, $\tilde w=\sum_n \tilde w_n(z)\exp(in\kappa_2 z)$ and $\tilde v=\sum_n \tilde v_n(z)\exp(in\kappa_2 z)$, where the coefficients are slowly varying on the L_2-scale, $|\partial_z\tilde w_n| \ll \kappa_2\tilde w_n$ and $|\partial_z\tilde w_n| \ll \kappa_2\tilde v_n$. Following again the approach of [8] we obtain the equations for the average fields $w=\tilde w_0$ and $v=\tilde v_0$

$$i\partial_z w+\eta_{1m} w^* v e^{-i\beta_m z}+(\gamma_{2m}|w|^2-\gamma_{1m}|v|^2)w=0, \qquad (10)$$
$$i\partial_z v+\eta_{2m} w^2 e^{-i\beta_m z}-2\gamma_{2m}|w|^2 v=0, \qquad (11)$$

where $\beta_m=\beta_0 - m\kappa_2=\Delta k - \kappa_0 - m\kappa_2 \ll \kappa_2$ is the effective mismatch for matching to the mth peak next to the κ_0 peak, as illustrated in the close-up in Fig. 2. The nonlinearity coefficients are given by

$$\eta_{jm} = \chi_j[2J_m(\epsilon_2)/\pi], \tag{12}$$

$$\gamma_{jm} = \chi_1\chi_j[(\pi^2-8)/\kappa_0 - 4S_m(\epsilon_2)/\kappa_2]/\pi^2, \tag{13}$$

where $S_m=-S_{-m}=\sum_{n\neq 0} J^2_{n+m}/n$. For $m=0$ we obtain $S_0=0$ and thus $\gamma_{j0}=\gamma_j$ of the unperturbed grating, as it should be. Using the well-known recurrence and addition formulas for Bessel functions we calculate $S_1=-2J_0(\epsilon_2)J_1(\epsilon_2)/\epsilon_2$. Closed form analytical expressions for S_m becomes progressively more difficult to obtain for higher orders $m \geq 2$.

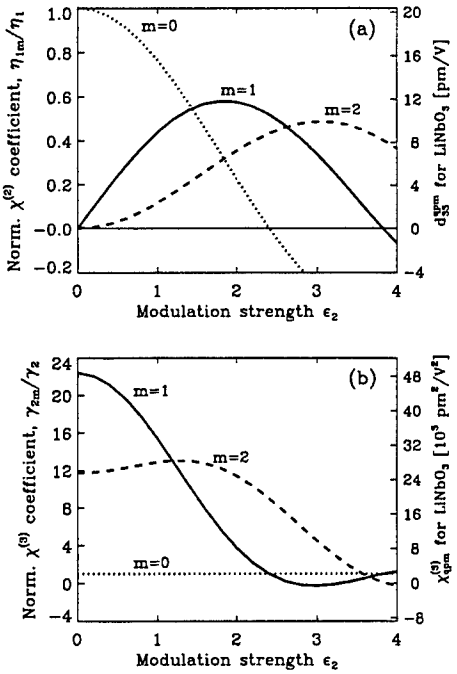


FIG. 3. Normalized effective quadratic nonlinearity η_{1m}/η_1 (a) and induced cubic nonlinearity γ_{2m}/γ_2 (b) versus the modulation strength ϵ_2 for $L_2=20L_0=100\mu m$. The right ordinate axis shows the actual strength for a bulk $LiNbO_3$ crystal.

In Fig. 3 we show the normalized average QPM nonlinearity coefficients η_{1m}/η_1 and γ_{2m}/γ_2 versus the modulation strength ϵ_2 for different orders of phase matching. The grating is the same as in Fig. 2 with $L_2=20L_0=100\mu m$. On the right ordinate are the corresponding values for bulk $LiNbO_3$ of the effective quadratic nonlinearity d^{qpm}_{33}, defined as $\eta_{1m}=\omega d^{qpm}_{33}/(n_1 c)$, and the effective cubic nonlinearity $\chi^{(3)}_{qpm}$, defined as $\chi^{(3)}_{qpm}=8n_1 c\gamma_{2m}/(3\omega)$. From Fig. 3 we see that by matching to for example the $m=1$ peak we can increase the strength of the induced cubic nonlinearity by a factor of 23 (to $48\cdot 10^3$ pm^2/V^2 in $LiNbO_3$) by choosing a sufficiently weak modulation ($\epsilon_2 \ll 1$). In comparison, the inherent material cubic nonlineaity in bulk $LiNbO_3$ is $40\cdot 10^3$ pm^2/V^2, and thus the induced cubic nonlinearity can actually be made dominant by the modulation. However, for weak modulations the effective quadratic nonlinearity is reduced to nearly zero for $m \geq 1$. Choosing the right modulation is thus a matter of optimization. For example, considering again the $m=1$ peak, the optimum value would be around $\epsilon_2=1$, which gives a factor of 18 increase of the induced cubic nonlinearity, while only reducing the quadratic nonlinearity by a factor of 0.4.

The induced cubic nonlinearity could be important for control and shaping of solitons [8]. An important issue is that the modulation allows to achieve phase matching at several wavelengths with equidistant separation, thus allowing for wavelength-division-multiplexing (WDM) with solitons in $\chi^{(2)}$ materials. In this case ϵ_2 should be chosen auch as to maximize the effective quadratic nonlinearity at the individual peaks, i.e. choosing ϵ_2 around 1.5, where all the $m=0$, 1, and 2 peaks have approximately the same strength.

In any case, introducing a modulation of the QPM grating, as we have proposed here, allows to engineer the quadratic and cubic nonlinearities and thus to optimize their competition according to predefined wishes.

[1] M.M. Fejer *et al.*, IEEE J. Quantum Electron. **28**, 2631 (1992).
[2] L.E. Myers *et al.*, J. Opt. Soc. Am. B **12**, 2102 (1995).
[3] M.A. Arbore *et al.*, Opt. Lett. **22**, 1341 (1997).
[4] S. Zhu *et al.*, Phys. Rev. Lett. **78**, 2752 (1997).
[5] M.A. Arbore, O. Marco, and M.M. Fejer, Opt. Lett. **22**, 865 (1997).
[6] M. Cha, Opt. Lett. **23**, 250 (1998).
[7] P.E. Powers, T.J. Kulp, and S.E. Bisson, Opt. Lett. **23**, 159 (1998).
[8] C. Balslev Clausen, O. Bang, and Y.S. Kivshar, Phys. Rev. Lett. **78** (1997) 4749.
[9] L. Torner and G.I. Stegeman, J. Opt. Soc. Am. B **14**, 3127 (1997).
[10] C. Balslev Clausen *et al.*, Opt. Lett. **22**, 271 (1997).
[11] L. Torner, C. Balslev-Clausen, and M.M. Fejer, Opt. Lett. **23**, 903 (1998).
[12] G. Imeshev, M. Proctor, and M.M. Fejer, Opt. Lett. **23**, 673 (1998).
[13] C. Balslev-Clausen and L. Torner, Phys. Rev. Lett. **81**, 790 (1998).
[14] C. Balslev-Clausen and L. Torner, (unpublished).
[15] A. Kobyakov *et al.*, Opt. Lett. **23** (1998) 506.
[16] Y. Zhao, G. Town, M. Sceats, Opt. Comm. **115** (1995) 129. R. Maleck Rassoul *et al.*, Opt. Lett. **22** (1998) 268.
[17] O. Bang *et al.*, Phys. Rev. E **58** (1998) 5057.
[18] R. DeSalvo *et al.*, IEEE J. Quantum Elec. **32** (1996) 1324.

Derivative quadratic nonlinearity and cascaded solitons in quasi-phase-matched waveguide systems

A.M. Kamchatnov
Institute of Spectroscopy, Russian Academy of Sciences, Troitsk, Moscow Reg., 142092, Russia
kamch@isan.troitsk.ru

M. Nevière
Laboratoire d'Optique Electromagnétique, URA CNRS 843, Faculté des Sciences et Techniques de St Jérôme, 13397 Marseille 20, France; Neviere@loe.univ-mrs.fr

A.D. Boardman
Department of Physics, University of Salford, The Crescent, Salford, M5 4WT, UK
A.D.Boardman@physics.salford.ac.uk

V.M. Agranovich
Institute of Spectroscopy, Russian Academy of Sciences, Troitsk, Moscow Reg., 142092, Russia
agran@isan.troitsk.ru

Recently the quasi-phase-matching (QPM) technique has attracted much attention in connection with self-trapping of light in quadratic media[1–4]. The QPM technique is based on the periodic modulation of the nonlinear susceptibility and/or refractive index, by which the additional grating wave vector is introduced. This grating wave vector can be used for compensation of the mismatch between the wave vectors of the fundamental and second harmonic waves. The QPM technique in bulk samples leads to an effective cubic nonlinearity in the form of self- and cross-phase modulation terms[2] which strongly influence on the properties of the cascaded solitons. Here we consider the QPM technique implementation in the waveguide geometry.

As was shown in Ref.[5], the cascaded surface solitons can exist even on the surface of the medium with the bulk inversion symmetry centre due to the contribution of the surface terms with spatial derivatives of the fields to the nonlinear response. Such a surface nonlinearity can be enhanced by the $\chi^{(2)}$ nonlinear film placed on the plane waveguide surface. The effective boundary condition for the electric field $\mathbf{E} = (E_x, 0, E_z)$ of the TM waveguide modes at the surface with thin nonlinear layer placed on it contains the derivative along the direction x of the wave propagation[6]

$$E_x^{>} - E_x^{<} = -\frac{4\pi}{\epsilon}\frac{\partial}{\partial x}\left(\chi E_z^2\right), \tag{1}$$

where ϵ is the dielectric constant just above the nonlinear layer. If the nonlinear susceptibility χ is modulated along the x axis,

$$\chi = \chi(x), \tag{2}$$

we arrive at the waveguide QPM implementation convenient for applications. The corresponding equations governing the evolution of the envelopes A and B of two modes — the fundamental with frequency ω and the second harmonic with frequency 2ω — have the form

$$\begin{aligned} i\left(\frac{\partial A}{\partial x} + k'_\omega \frac{\partial A}{\partial t}\right) - \frac{k''_\omega}{2}\frac{\partial^2 A}{\partial t^2} + \alpha_1 e^{-ik_\omega x}\frac{\partial}{\partial x}\left(A^* B\chi(x) e^{-i(k_\omega - k_{2\omega})x}\right) = 0, \\ i\left(\frac{\partial B}{\partial x} + k'_{2\omega}\frac{\partial B}{\partial t}\right) - \frac{k''_{2\omega}}{2}\frac{\partial^2 B}{\partial t^2} + \alpha_2 e^{-ik_{2\omega}x}\frac{\partial}{\partial x}\left(A^2\chi(x)e^{2ik_\omega x}\right) = 0, \end{aligned} \tag{3}$$

where α_1 and α_2 are the coefficients depending on the dispersion laws of two modes,

$$k_\omega = k_A(\omega), \qquad k_{2\omega} = k_B(2\omega), \tag{4}$$

and t denotes time in the case of temporal solitons or scaled transverse coordinate in the case of spatial solitons.

The periodically modulated nonlinear susceptibility $\chi(x)$ of the layer can be expanded in a Fourier series

$$\chi(x) = \sum_n d_n e^{in\kappa x} \tag{5}$$

with

$$\kappa \simeq 2k_\omega - k_{2\omega}, \tag{6}$$

as well as the amplitudes,

$$A = \sum_n a_n e^{in\kappa x}, \qquad B = e^{i\tilde{\beta}x} \sum_n b_n e^{in\kappa x}, \tag{7}$$

where

$$\tilde{\beta} = 2k_\omega - k_{2\omega} - \kappa \tag{8}$$

is the effective phase-matching parameter ($|\tilde{\beta}| \ll k_\omega, k_{2\omega}, \kappa$) Then the slowly varying Fourier amplitudes a_0 and b_0 obey the average equations

$$\begin{aligned} i\left(\frac{\partial a_0}{\partial x} + k'_\omega \frac{\partial a_0}{\partial t}\right) - \frac{k''_\omega}{2}\frac{\partial^2 a_0}{\partial t^2} + \alpha_1 d_1 \left(ik_\omega a_0^* b_0 + \frac{\partial(a_0^* b_0)}{\partial x}\right) + \left(\gamma|a_0|^2 + \rho|b_0|^2\right) a_0 = 0, \\ i\left(\frac{\partial b_0}{\partial x} + k'_{2\omega} \frac{\partial b_0}{\partial t}\right) - \frac{k''_{2\omega}}{2}\frac{\partial^2 b_0}{\partial t^2} - \tilde{\beta} b_0 + \alpha_2 d_{-1} \left(ik_{2\omega} a_0^2 + \frac{\partial(a_0^2)}{\partial x}\right) + 2\eta|a_0|^2 b_0 = 0 \end{aligned} \tag{9}$$

The effective cubic nonlinearities with coupling constants γ, ρ, η are similar to those in the quadratic bulk media[2]. In addition in the waveguide geometry we obtain new nonlinear terms with derivatives with respect to the propagation coordinate x These derivative nonlinearities can dominate over the cubic nonlinearity and they are the only corrections in the case of sinusoidal grating

$$\chi(x) = 2d_1 \cos(\kappa x), \qquad d_{-1} = d_1, \tag{10}$$

when the cubic terms vanish identically We have investigated the influence of these derivative nonlinearities on the properties of the cascaded $\chi^{(2)}$ solitons in plane waveguides with quasi phase-matched film placed on its surface.

1. L. Torner and G.I. Stegeman, J. Opt. Soc. Am., **B14**, 3127 (1997).
2. C.B. Clausen, O. Bang, and Yu.S. Kivshar, Phys. Rev. Lett. **78**, 4749 (1998).
3. A. Kobyakov, F. Lederer, O. Bang, and Yu.S. Kivshar, Optics Lett. **23**, 506 (1998).
4. C.B. Klausen and L. Torner, Optics Lett. **24**, 7 (1999).
5. V.M. Agranovich, D.M. Basko, A.D. Boardman, A.M. Kamchatnov, and T.A. Leskova, Optics Commun. **160**, 114 (1999).
6. V.M. Agranovich, V.I. Rupasov, and V.Ya. Chernyak, Sov. Phys. Solid State, **24**, 1693 (1983).

KdV Solitons on GaAs Transmission Lines due to the Intrinsic Second Order Nonlinearity

K. Bubke, U. Peschel and D. C. Hutchings
Dept. of Electronics and Electrical Engineering, University of Glasgow, Glasgow G12 8QQ, Scotland, U.K.
Tel: +44-141-330-6008, Fax: +44-141-330-6002, email: k.bubke@elec.gla.ac.uk

I. INTRODUCTION

Nonlinear wave propagation along microwave transmission lines has been previously investigated [1, 2]. The structures under consideration were metal-insulator-semiconductor (MIS) or Schottky contact transmission lines. In this case nonlinearities arise from the voltage dependent depletion layer between metal and semiconductor producing a large nonlinear capacitance. The theoretical models are based on equivalent circuits leading to the well-known KdV equation (or expanded versions). Although pulse compression has been demonstrated in these structures [3], the inherent losses due to free carrier absorption and their slow response make exploitation of these nonlinearities challenging.

In this paper we show that electrical transmission lines on GaAs can exhibit nonlinear pulse propagation without introducing additional nonlinear capacities. The effect we describe here arises from the inherent second order nonlinearity of GaAs, $\chi^{(2)}_{xyz}$, that is the nonlinear polarisation induced by the transverse field distribution of the guided mode. In contrast to the structures mentioned above no additional losses occur. The nonlinearity is instantaneous, so that transition time effects do not limit the pulse width. In the following we derive a KdV equation from Maxwell's equation and investigate possible soliton propagation on a microstrip and a coplanar transmission line.

II. THEORETICAL MODEL

The structures investigated and the underlying coordinate system are sketched in Fig. 1. The z-axis is defined to be parallel to the propagation direction. Since the nonlinearity is weak the induced polarisation does not perturb the transversal mode profile $\vec{E}'(x,y)$ of the guided mode and we can write the electric field in the waveguide as

$$\vec{E}(x,y,z,\omega) = u(\omega,z)\vec{E}'(x,y) \quad . \tag{1}$$

In the following we neglect field components in z-direction. The field evolution in Fourier space under influence of a nonlinear polarisation $\vec{P}$ can be described as [4]

$$\left(\frac{\partial}{\partial z} - j\beta(\omega)\right) u(\omega,z) = \frac{j\omega}{2P_0}\int\int \vec{E}'^{*}\cdot\vec{P}\,dx\,dy \quad , \tag{2}$$

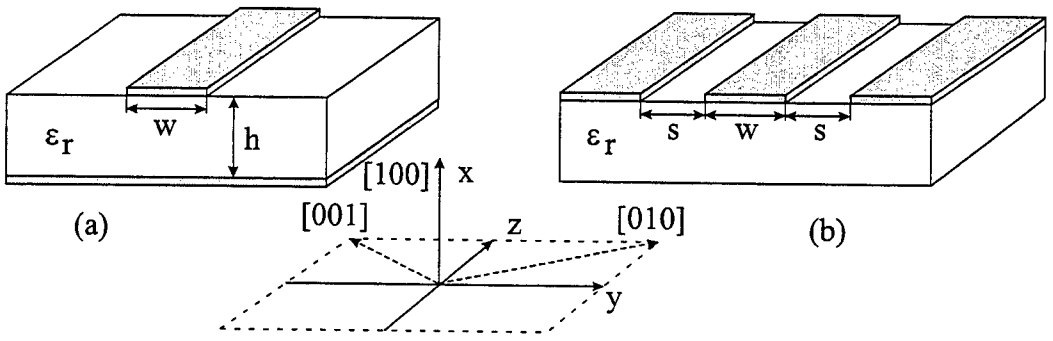


Figure 1: Geometry of the investigated structures: (a) microstrip line and (b) coplanar transmission line. For the examples presented here $w = h = s = 4\mu$m and $\epsilon_r = 12.9$.

where $\beta(\omega)$ and P_0 are the phase constant and the power of the unperturbed mode respectively. For a transformation of the equation into the time domain we expand $\beta(\omega)$ in a Taylor series around zero frequency $\omega = 0$. Taking into account the symmetry property $\beta(-\omega) = -\beta^*(\omega)$ we get

$$\beta(\omega) = j\alpha + \frac{1}{v_0}\omega + j\alpha''\omega^2 + \frac{T_{\mathrm{mic}}}{6}\omega^3 \quad , \tag{3}$$

where v_0 is the group velocity of the microwave, T_{mic} is the third-order dispersion coefficient and α and α'' are the frequency-independent and -dependent loss coefficients respectively. The induced polarisation $\vec{P}$ depends critically on the orientation of the crystal axes in the GaAs substrate. Here we initially examine the case of the usual orientation of transmission lines on GaAs, where growth is parallel to the [100] crystallographic direction and the microstrips are perpendicular to a cleaved facet [011]. However, other orientations are possible (e.g. growth parallel to [111] or [110]) and our model can be easily extended to these cases. The cubic symmetry of GaAs provides only one non-zero tensor element for the second-order susceptibility and we obtain for the nonlinear polarisation

$$\vec{P} = -\epsilon_0 \chi^{(2)} \begin{pmatrix} \frac{1}{2}E_y'^2 \\ E_x' E_y' \\ 0 \end{pmatrix} \quad . \tag{4}$$

After inserting eq. (3) and (4) into eq. (2) and performing the inverse Fourier transform we come up with the following equation, which has the KdV form in the lossless case:

$$\left[\frac{\partial}{\partial z} + \alpha + \left(\frac{1}{v_0} - \chi_{\mathrm{eff}} U(t,z)\right)\frac{\partial}{\partial t} - \alpha''\frac{\partial^2}{\partial t^2} - \frac{T_{\mathrm{mic}}}{6}\frac{\partial^3}{\partial t^3}\right] U(t,z) = 0 \quad . \tag{5}$$

Here we have defined the effective susceptibility χ_{eff} as

$$\chi_{\mathrm{eff}} = \frac{3}{2}\epsilon_0 \frac{1}{P_0^{3/2}} \int\int \chi^{(2)} E_y'^2 E_x' \, dx \, dy \tag{6}$$

and rescaled the amplitude in terms of guided wave power $U(t,z) = u(t,z)/\sqrt{P_0}$. Obviously the overlap integral is different from zero for mixed polarized modes only.

III. RESULTS

The transversal field components $\vec{E}'(x,y)$ were calculated from electrostatics by solving the Laplace equation. As the dimensions of the transmission lines considered are small in

	χ_{eff} in $\mathrm{sm^{-1}W^{-1/2}}$	Δt in ps	P_s in W	V_{mic} in V
microstrip	$5.2 * 10^{-14}$	100	$3.4 * 10^{-2}$	0.834
		10	165	83.4
		1	$1.65 * 10^{6}$	$8.34 * 10^{3}$
coplanar	$3.4 * 10^{-14}$	100	$3.98 * 10^{-2}$	1.45
		10	398	145
		1	$3.98 * 10^{6}$	$14.5 * 10^{3}$

Table 1: Effective susceptibility χ_{eff} for microstrip and coplanar transmission line ($\chi^{(2)}_{GaAs} = 200\mathrm{pmV^{-1}}$ [6]); peak power P_s and voltage V_{mic} for solitons of different FWHM pulse widths Δt.

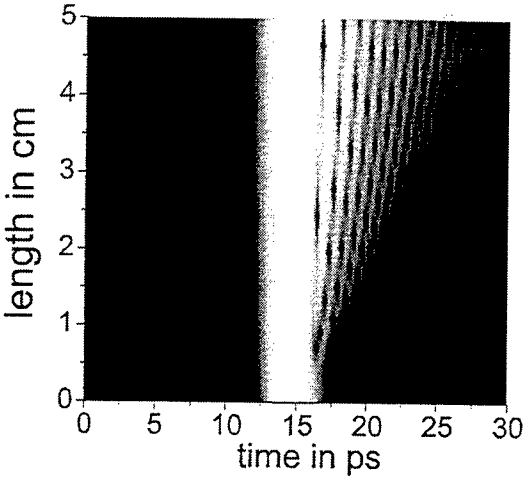


Figure 2: Intensity plot of propagating pulse without nonlinear term along microstrip line; initial pulse width $\Delta t = 1$ ps.

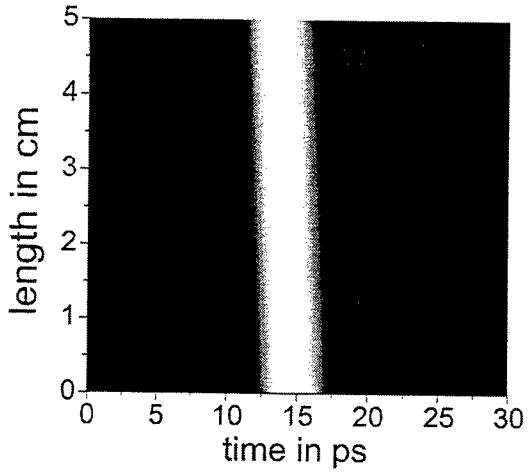


Figure 3: Intensity plot of propagating soliton along microstrip line; pulse width $\Delta t = 1$ ps.

comparison to the wavelength the calculated mode profiles are also a good approximation at higher frequencies. If we neglect losses the soliton solution of eq. (5) is [5]:

$$U(t,z) = A\,\mathrm{sech}^2\left[\left(\frac{\chi_{\mathrm{eff}}A}{2T_{mic}}\right)^{1/2}(t-\eta z)\right] \quad \text{with} \quad \eta = \frac{1}{v_0} - \frac{1}{3}\chi_{\mathrm{eff}}A \quad , \tag{7}$$

where A is an arbitrary amplitude. The effective susceptibilities χ_{eff}, peak power $P_s = A^2$ and voltages V_{mic} for different FWHM pulse widths Δt of a soliton are shown in Table 1. The proportionality $P_s \propto \Delta t^{-4}$ leads to fairly high powers for pulses shorter than 10 ps. However, it should be noted that in the cases considered here mostly fringing fields induce the nonlinear polarisation. This drawback could be overcome by other orientations of the crystal axes leading to higher effective susceptibilies. For example, a [110]-grown sample can provide TE polarisation parallel to [111] crystalline direction and the effective susceptibility only contains the E_y' component. In Fig. 2 and 3 we show intensity plots of pulse propagation with and without induced nonlinearity respectively. Pulse broadening and radiation are clearly shown for linear propagation which are absent in the soliton.

References

[1] D. Jäger , Int. J. Electronics, Vol. **58,** No. 4, pp. 649-669, 1985.

[2] J. M. Arnold and D. F. Parker,"Asymptotic Theory of Nonlinear Pulse Propagation along a Transmission Line on a Semiconductor Substrate", submitted to Radio Science.

[3] M. Case, M. Kamegawa, R. Yu, M. J. W. Rodwell, and J. Franklin, Appl. Phys. Lett., Vol. **58**, No. 2, pp. 173-175, 1991.

[4] M. Börner, R. Müller, R. Schiek and G. Trommer, *Elements of Integrated Optics*, Teubner, Stuttgart, 1990 (in German).

[5] G. B. Whitham , *Linear and nonlinear waves*, Academic Press, 1974.

[6] T. Y. Chang, N. van Tran, C. K. N. Patel, Appl. Phys. Lett., Vol. **13,** No. 10, pp. 357-359, 1968.

Spontaneous formation of symbiotic solitary wave attractors in backward quadratic interaction and parametric oscillators

A. Picozzi,[1] C. Montes,[2] and M. Haelterman [1]

[1] Service d'Optique et d'Acoustique, Université Libre de Bruxelles
50 Avenue F. D. Roosevelt, CP 194/5, B-1050 Brussels, Belgium

[2] CNRS, Laboratoire de Physique de la Matière Condensée
Université de Nice Sophia-Antipolis, Parc Valrose, 06108 Nice Cedex, France

The past few years have witnessed an intense renewal of interest in the concept of optical parametric solitary-wave that was discovered in the early 1970's. Most of the attention in this field of research has been devoted to the class of solitary waves that result from the mutual trapping of two or three-frequency envelopes due to an exact balance between nonlinearity and diffraction (or dispersion) [1]. This class of symbiotic solitary-waves has recently been investigated experimentally both in the spatial and temporal domains. As is well known, another class of symbiotic solitary-waves exists in optical quadratic media that is characterized by a balance between energy exchanges and group-velocity differences between the constituent waves [2–5]. These solitary-waves play a fundamental role in many areas of research [2] such as plasma physics, acoustics, hydrodynamics or nonlinear optics where they have been investigated experimentally in stimulated Raman and Brillouin scattering [6, 7]. Nevertheless, due to their rather complex structures, this class of symbiotic solitary-waves has never been observed in quadratic optical materials.

We show here that new symbiotic solitary-waves of this class can be generated spontaneously in dissipative quadratic media provided that the parametric interaction is quasi-phase matched in a backward configuration [8]. In the parametric amplifier configuration, we show that the velocity of the solitary-wave can be easily controlled by the injected pump intensity and can take any subluminous value, either positive or negative. As a particular case, we show a new mechanism of energy localization through a zero-velocity solitary-wave. Moreover, when the quadratic material is placed inside a singly resonant cavity, the solitary waves are spontaneously generated from noise fluctuations.

We consider a quadratic material in which nondegenerate three-wave interaction takes place through backward quasi-phase matching. The governing equations are given by the following set

$$\frac{1}{v_1}\frac{\partial A_1}{\partial t} - \frac{\partial A_1}{\partial x} + i\rho_1\frac{\partial^2 A_1}{\partial t^2} + \gamma_1 A_1 = \sigma_1 A_3 A_2^* \tag{1a}$$

$$\frac{1}{v_2}\frac{\partial A_2}{\partial t} + \epsilon\frac{\partial A_2}{\partial x} + i\rho_2\frac{\partial^2 A_2}{\partial t^2} + \gamma_2 A_2 = \sigma_2 A_3 A_1^* \tag{1b}$$

$$\frac{1}{v_3}\frac{\partial A_3}{\partial t} + \frac{\partial A_3}{\partial x} + i\rho_3\frac{\partial^2 A_3}{\partial t^2} + \gamma_3 A_3 = -\sigma_3 A_2 A_1 \tag{1c}$$

For definiteness we call A_1, A_2, A_3 the signal, idler and pump waves respectively. σ_i, v_i, γ_i and $\rho_i = (\partial^2 k/\partial\omega^2)_i/2$ are the coupling constants, the velocities, the damping rates and the dispersion coefficients of the crystal at frequency ω_i. The dispersion effect is not at the origin of the new symbiotic solitary waves, however its effect is taken into account in order to verify the robustness of these structures with respect to modulational instabilities.

We first consider the amplifier configuration of the parametric interaction in the case where only the signal wave propagates backward with respect to the pump [$\epsilon = +1$ in Eqs. (1)]. In order to show the

existence of solitary-wave attractors in Eqs. (1), we investigate numerically the basic propagation problem of an initially localized signal in the presence of the counterpropagating continuous pump wave [5].

A typical result is illustrated in Fig. 1 that shows the evolution of the three interacting field envelopes in the signal reference frame defined by ($z = x + vt, \tau = t$). After a complex transient ($t < 70$ps), we observe that the three fields self-structurate in the form of a symbiotic solitary-wave ($t > 0.5$ns) where the signal and the idler components are spatially localized while the pump has a kink shape. The same solitary-wave is reached starting from any profile of the initially localized signal wave allowing to conclude that the three-wave structure is a strong attractor of the backward parametric process in quadratic media.

It is remarkable that the symbiotic solitary-wave does not propagate at the velocity of light in the crystal, but rather with a specific subluminous velocity: the three-wave steady structure drifts to the right in the signal reference frame [Fig. 1]. In a similar way as for stimulated Brillouin scattering [3], we determine analytically the selected velocity through the Kolmogorov-Petrovskii-Piskunov (K.P.P.) conjecture which proved powerful in nonlinear diffusion problems and dynamical pattern selection [9]. The main outcome of this analysis is that the velocity of the solitary-wave can be controlled by the intensity of the injected pump. This is illustrated in Fig. 2 where the selected velocity V^* is plotted versus the continuous pump intensity. The remarkable and unexpected result is that the new symbiotic solitary-wave even exits for zero-velocity $V^* = 0$, a feature that has been verified by direct numerical simulation of Eqs. (1) [5]. The zero-velocity solution makes the new symbiotic solitary-wave attractors interesting for potential applications to all-optical buffers and memories. Besides these applications, this standing solution is also attractive in that it offers a simple way to observe a fundamental phenomenon of nonlinear energy localization.

The pump power required for the experimental observation of the new symbiotic solitary waves is quite large. On the basis of a previous work on Brillouin fiber-resonators, we will show that the same type of symbiotic solitary waves may be also spontaneously generated in the ring-cavity configuration [7]. For this purpose, it is more convenient to consider the parametric configuration where both the signal and idler components propagate backward with respect to the pump [$\epsilon = -1$ in Eqs. (1)], otherwize, no pulse are formed. For the sake of simplicity we investigate here the singly resonant parametric oscillator (SOPO) where only the signal circulates in the cavity [4]. A typical numerical result is illustrated in Fig. 3 that shows the evolution of the three interacting envelopes in the crystal of length $L = 3$ cm, for a pump intensity of 27 kW/cm^2 and a reflection coefficient of $R = 0.99$. After a long transient, the envelopes take the form of the symbiotic solitary wave that is of the same nature as those described above. This result is quite general. It has been observed in a wide parameter range including, in particular, reflection coefficients as small as $R = 0.01$. The generated pulses are in the picosecond range, which makes this SOPO interesting for applications to high-repetition-rate ultrashort pulse train generation.

In summary, a new phenomenon of spontaneous energy localization in the form of a zero-velocity solitary wave has been reported. The advantage of these new solitary-waves with respect to the similar energy localization phenomenon called "gap soliton" in periodic nonlinear media is that they can be generated spontaneously from quantum noise. Moreover, these solitary waves constitute a stable and robust attractor for the three waves interacting inside a singly resonant parametric oscillator.

[1] for a review, see G.I. Stegeman, D.J. Hagan and L. Torner, Opt. Quant. Elect., **28**, 1691 (1996).
[2] D.J. Kaup, A. Reiman and A. Bers, Rev. Mod. Phys., **51**, 275 (1979); S. Trillo, Opt. Lett., **21**, 1111 (1996).
[3] C. Montes, *et al.*, Phys. Rev. E, **55**, 1086 (1997).
[4] A. Picozzi and M. Haelterman, Opt. Lett., **23** 1808 (1998).
[5] A. Picozzi and M. Haelterman, Europhys. Lett., **45**, 463 (1999).
[6] K. Drühl, R.G. Wenzel and J.L. Carlsten, Phys. Rev. Lett., **51**, 1171 (1983).

[7] E. Picholle *et al.*, Phys. Rev. Lett., **66**, 1454 (1991); C. Montes, A. Mamhoud and E. Picholle, Phys. Rev. A, **49**, 1344 (1994); C. Montes, *et al.*, J.Opt. Soc. Am. B (*June, in press*).

[8] G. D'Alessandro, P.St.J. Russel and A.A. Wheeler, Phys. Rev. A, **55**, 3211 (1997) ; J.U. Kang *et al.*, Opt. Lett., **22**, 862 (1997).

[9] V.G. Kolmogorov, I.G. Petrovskii and N.S. Piskunov, Bull. Moscow State University, Math. and Mechanics, **1**, 1 (1937) ; G.Dee and J.S. Langer, Phys. Rev. Lett., **50**, 383 (1983).

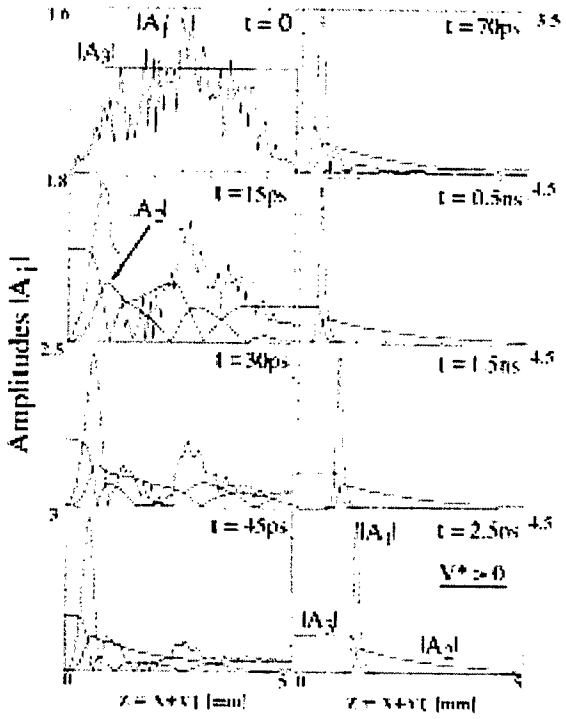


Figure 1: Spontaneous formation of the symbiotic solitary wave attractor: evolution of the three interacting envelopes in the reference frame traveling at the signal velocity v_1.

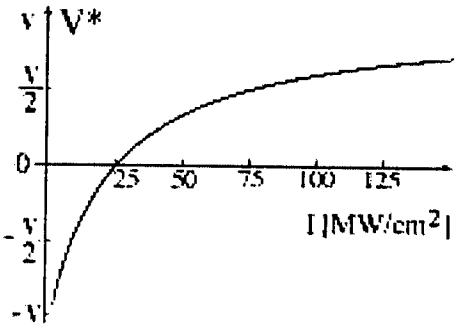


Figure 2: Selected velocity V^* of the symbiotic solitary wave *vs.* the injected pump intensity.

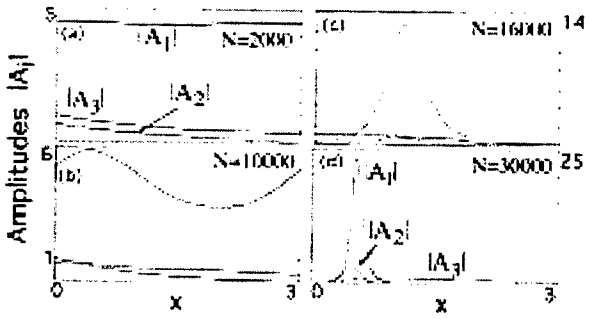


Figure 3: Spatial profiles (at given times) of the three waves interacting in the cavity of length $L =$ 3 cm after N round-trips.

All-optical modulation in second-order nonlinear directional couplers by second-harmonic generation

Uwe Hempelmann
Universität Paderborn, Theoretische Elektrotechnik
Warburger Str. 100, 33098 Paderborn, Germany
Phone: +(49) 5251 60 3013, Fax: +(49) 5251 60 , E-Mail: hempelmann@ieee.org

The application of cascaded second-order nonlinearities for all-optical signal processing has been a field of intense research during the past few years. The potential of cascaded quadratic nonlinearties is based on their ability to mimic third-order nonlinear effects at reduced power, as well as on the direct applicability of the inherent amplitude and phase modulation of the wave mixing (e.g. [1, 2] and references therein). An interesting application belonging to the second alternative is the modulation of a strong pump wave by a weak control signal (all-optical transistor action). Different schemes have been developed for this purpose, which are based on type I, double type I or type II interactions, where also a phase independent control is possible with type II configurations [2, 3]. In this paper, all-optical modulation using a second-order nonlinear directional coupler is shown theoretically by numerical integration of the governing coupled mode equations. The principle of operation is based on the down conversion of a strong second-harmonic (SH) pump wave seeded by a weak control signal at the fundamental frequency (FF), but with no direct SH field being launched at the input.

The directional coupler at hand consists of two parallel waveguides in a second-order nonlinear ferroelectric crystal, which is periodically poled in the region of waveguide "b" as sketched in Fig. 1. Then the effective second-order susceptibility is sign-inverted periodically in $x > 0$, $\chi^{(2)}(\vec{r}) = \hat{\chi}^{(2)} \cdot g(z)$ with the grating function $g(z) = \sum_{i=1}^{\infty} g_i \cos(i\,K\,z)$. The periodic poling is assumed to end at the symmetry plane, so that $\chi^{(2)}(\vec{r}) = \hat{\chi}^{(2)}$ in $x < 0$. Considering type I second-harmonic generation (SHG), the description of the field in terms of the co-propagating lowest-order modes of the single waveguides at both frequencies results in the second-order nonlinear coupled mode equations (1) [2], which imply negligible linear coupling of the SH modes. The guided mode powers are given by $P_{k,\mu}(z) = |C_{k,\mu}(z)|^2$, where $k = a, b$ and $\mu = \omega, 2\omega$, due to proper scaling.

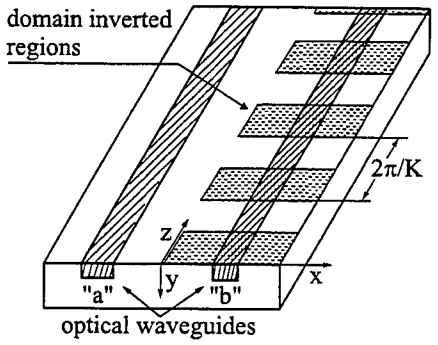


Fig. 1. Directional coupler in a periodically poled second-order nonlinear crystal

$$
\begin{aligned}
j\frac{dC_{a,\omega}}{dz} &= \kappa\, C_{b,\omega}\, e^{+j\delta\beta_\omega z} + \quad \Gamma_a\, C^*_{a,\omega}\, C_{a,2\omega}\, e^{j\Delta\beta_a z} \\
j\frac{dC_{b,\omega}}{dz} &= \kappa\, C_{a,\omega}\, e^{-j\delta\beta_\omega z} + g\,\Gamma_b\, C^*_{b,\omega}\, C_{b,2\omega}\, e^{j\Delta\beta_b z} \\
j\frac{dC_{a,2\omega}}{dz} &= \quad \Gamma_a\, C^2_{a,\omega}\, e^{-j\Delta\beta_a z} \\
j\frac{dC_{b,2\omega}}{dz} &= g\,\Gamma_b\, C^2_{b,\omega}\, e^{-j\Delta\beta_b z}
\end{aligned}
\tag{1}
$$

with the linear mismatch $\delta\beta_\omega = \beta_{a,\omega} - \beta_{b,\omega}$, the wave-vector mismatches in both waveguides $\Delta\beta_\nu = 2\beta_{\nu,\omega} - \beta_{\nu,2\omega}$, $\nu = a, b$, and the coupling coefficients $\Gamma..$ and κ.

Quasi-phase-matching (QPM) of the SHG in waveguide "b" is achieved by a proper choice of the spatial grating frequency K with a single harmonic of K being relevant only, resulting in a small residual mismatch $\delta k_b = \Delta\beta_b - nK$. The nonlinear interaction in channel "a" is still strongly mismatched and, therefore, the conversion efficiency is extremely low. Hence, no SH wave is excited in that waveguide, since there is also no linear coupling to the SH mode in guide "b". If on the other hand the SH-mode in waveguide "a" is excited initially, it is for the reason mentioned above not coupled to the other modes. Therefore, the amplitude $C_{a,2\omega}$ can be neglected in (1), resulting in the reduced coupled mode equations

$$j\frac{dC_{b,\omega}}{dz} = \kappa\, C_{a,\omega}\, e^{-j\delta\beta_\omega z} + \frac{g_n}{2}\,\Gamma_b\, C^*_{b,\omega}\, C_{b,2\omega}\, e^{j\delta k_b z}$$

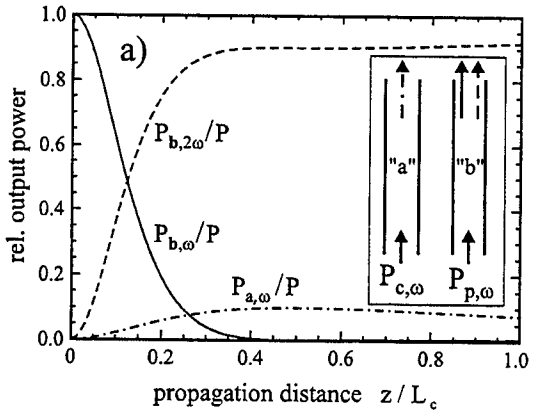
$$j\frac{dC_{a,\omega}}{dz} = \kappa\, C_{b,\omega}\, e^{+j\delta\beta_\omega z} \qquad , \qquad j\frac{dC_{b,2\omega}}{dz} = \frac{g_n}{2}\,\Gamma_b\, C^2_{b,\omega}\, e^{-j\delta k_b z} \tag{2}$$

Except the linear detuning, equ.'s (2) are identical to those for a coupler with waveguide "b" being linear, which has been proposed in [4] for all-optical switching by the total input power. The objective here is the modulation of a strong pump wave by a weak control signal with input fields at the FF only. For this purpose, the device must operate in the vicinity of an unstable eigenmode, which can be perturbed by a weak optical signal. A simple eigenmode of (2) is obviously given by $C_{a,\omega} = C_{b,\omega} = 0$ at an arbitrary $C_{b,2\omega} \neq 0$, which is, due to the vanishing linear directional coupling at 2ω, identical with the respective eigenmode in an isolated waveguide [5, 6]. It is unstable if $|(2\delta k_b)/(g_n\Gamma_b\sqrt{P_{b,2\omega}})| < 2$ [5], which is fulfilled at any power if $\delta k_b \to 0$. Therefore, the desired modulation can be realized via down-conversion of a strong SH pump in channel "b", seeded by a weak signal at ω. The configuration at hand is nearly identical to one of the schemes proposed in [2, 3] in the case when the SH pump is directly excited at input "b", except the linear directional coupling, which can be used to combine SH pump and FF seed.

For the purpose of designing an all-optical device based on the above principle, but with FF input only and without a pre-switched SH generator, the present structure can be viewed as an SH generator integrated together with a beam combiner and a down-converter. This is possible when almost ideal QPM is adjusted in waveguide "b" to realize a strong up-conversion of the FF pump wave launched via input "b", whereas the weak FF control wave is excited at input "a" (see inset of Fig. 2.a). This operation is shown below by the aid of numerical solutions of (1) for the special case of a coupler without linear mismatch ($\delta\beta_\omega = 0$) and with ideal QPM ($\delta k_b = 0$).

Fig. 2.a depicts the evolution of the mode powers when only the pump is launched, $P_{c,\omega} = 0$. The pump power is chosen large enough to cause strong SHG over a propagation distance smaller than the linear half beat length $L_c = \pi/(2\kappa)$. Then the up-conversion is similar to the phase-matched SHG in an isolated waveguide, given by $P_{b,2\omega} = P_{p,\omega}\,\tanh^2(\frac{g_n}{2}\,\Gamma_b\,\sqrt{P_{p,\omega}}\,z)$, and a small fraction of the pump power is coupled to waveguide "a" only. The present parameters are selected to give $\frac{g_n}{2}\,\Gamma_b\,\sqrt{P_{p,\omega}}\,L_c = 7$. If a weak FF control wave is excited at input "a", it is coupled into guide "b", where it serves as a FF seed. This seed reaches significant powers at those propagation distances, at which the pump power in "b" is almost completely up-converted. It thus induces a strong down-conversion as shown in Fig. 2.b and, thereby, the FF output power of guide "b" is switched from zero to 80% of the input power. This down-conversion is sensitive to the power $P_{c,\omega}$ of the control signal as well as to the phase difference between control and pump $\varphi_{c,\omega} - \varphi_{p,\omega}$. It, therefore, permits the power and phase controlled modulation shown in Fig.'s 3.a and 3.b, respectively. The fraction of the pump power, which is coupled to guide "a" (cross-state) is lost for the desired modulation of the FF power in the bar-state. Compared to a scheme with pre-switched SH-generator,

these losses are the price to be paid for the integration of the SH-generator together with the combining and the interaction devices for the SH pump and the FF seed.



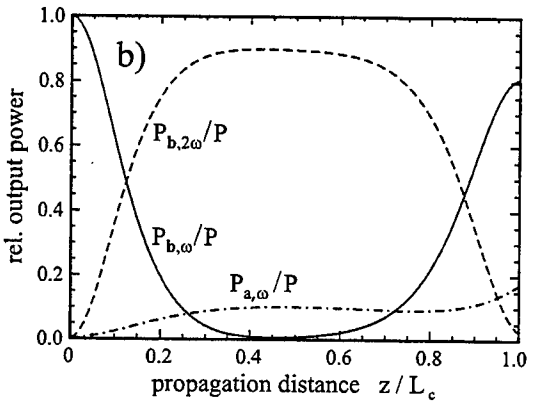
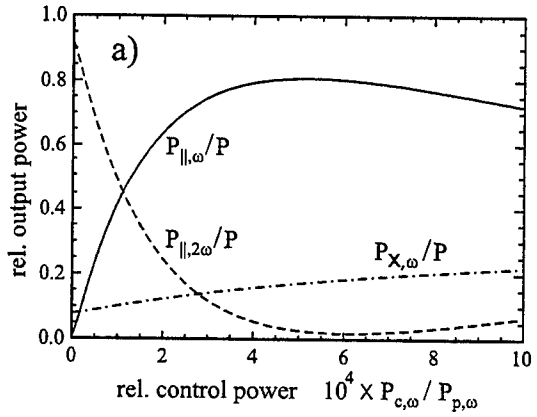


Fig. 2. Mode powers versus propagation distance when a) no control signal is excited and b) a weak control signal with $P_{c,\omega} = 5 \cdot 10^{-4} P_{p,\omega}$ and zero phase difference to the pump is excited



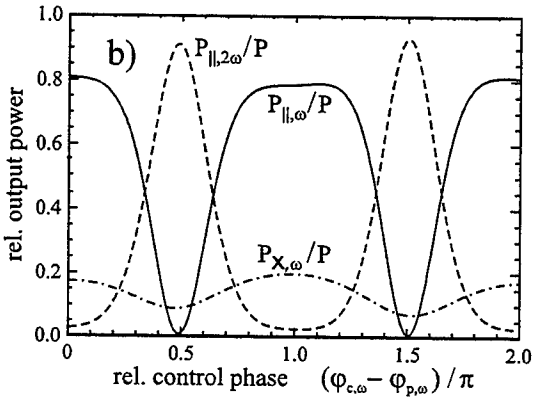


Fig. 3 Modulation of the FF output power $P_{\|,\omega}(L_c)$ in the bar-state of a half beat length coupler controlled a) by the power $P_{c,\omega}$ at zero phase difference and b) by the phase at fixed $P_{c,\omega} = 5 \cdot 10^{-4} P_{p,\omega}$

References

[1] I. Stegeman, D. J. Hagan, and L. Torner, "Cascading phenomena and their applications to all-optical signal processing, mode-locking, pulse compression and solitons," Opt. Quantum Electron. **28**, 1691 (1996)

[2] G. Assanto, "Quadratic cascading: effects and applications", in *Beam shaping and control with nonlinear optics*, F. Kajzar, R. Reinisch, ed.'s, Plenum Press, New York, 341 (1998).

[3] G. Assanto, "Coherent interactions for all-optical signal processing via quadratic nonlinearities", IEEE J. Quantum Electron. **31**, 673 (1995).

[4] G. Assanto, A. Lauretti-Palma, C. Sibilia, and M. Bertolotti, "All-optical switching via second harmonic generation in a nonlinearly asymmetric directional coupler," Opt. Commun. **599** (1994).

[5] S. Trillo, S. Wabnitz, R. Chisari, and G. Cappellini, "Two-wave mixing in quadratic nonlinear medium: bifurcations, spatial instabilities and chaos," Opt. Lett. **17**, 637 (1992).

[6] A. E. Kaplan, "Eigenmodes of $\chi^{(2)}$ wave mixings: cross-induced second-order nonlinear refraction," Opt. Lett. **18**, 1223 (1993).

Modelling the effects of loss and fabrication error for second harmonic generation in semiconductor waveguides

F.A. Katsriku, B.M.A. Rahman and K.T.V. Grattan
City University, Department of Electrical, Electronic and Information Engineering
Northampton Square, London, EC1V 0HB
Tel: +44-171-477-8123 Fax:+44-171-477-8568, e-mail: B.M.A.Rahman@city.ac.uk

Introduction

Compact and robust solid state devices emitting short and coherent wavelengths in the mid infra red are a cost effective way of obtaining new wavelengths which are important in data storage, laser printing, wavelength division multiplexing and all-optical switching applications. Due to the maturity of the fabrication technology, $LiNbO_3$ having a natural birefringence, has proved to be an important material to use in optical systems in the search for new wavelengths. Semiconductor laser in GaAs is a reliable source of high power infrared wavelength, and having a high nonlinear susceptibility tensor and providing good confinement of the waveguide modes and this could also provide a useful source of second harmonic power. However it also suffers from high absorption loss, with the loss factor strongly dependent on wavelength. On the other hand, although GaAlAs has a smaller nonlinear susceptibility value than GaAs, to compensate that it has a much lower loss factor. It also offers the possibility of monolithic device integration involving a high power laser source with the second harmonic generator. In integrated optical semiconductor waveguides the high index difference between the substrate and the core leads to tightly confined modes, which enhances the second harmonic generation. In materials where this happens, because of normal dispersion, the phase matching conditions cannot be satisfied since the refractive index is frequency dependent [1]. It is therefore necessary to correct the phase mismatch at regular intervals. One technique used to achieve this is known as quasi-phase matching (QPM), where the phase difference between the two interacting waves is corrected at regular intervals by means of a structural periodicity built into the nonlinear material at the stage of fabrication [2]. Among the suggested methods for phase matching are domain inversion, domain disordering and wafer bonding. In wafer bonding of GaAs material, wafers grown by organometallic chemical vapour deposition are bonded such that the neighbouring wafers are parallel to each other [2].

The role of numerical simulation in the study, development and evaluation of such GaAs based systems, particularly the effect of material loss, can be immensely valuable for design optimisation. The powerful, accurate and versatile finite element method with the vector $\mathbf{H}$-field [3] has previously been used to find modal solutions for optical waveguides with a diffused index profile and arbitrary guide parameters [4]. It has also proved useful in obtaining the modal fields for modelling of second harmonic generation in $LiNbO_3$ waveguides, and subsequently to study of the evolution of the harmonic field, a finite element-based beam propagation method (BPM) [5,6] has been used. Given the characteristics of these materials, it is important to evaluate numerically the opportunity and scope provided by devices built on such material systems. For such an analysis, a rigorous model is required. In this paper the use of the numerically efficient finite element-based BPM to model second harmonic generation in a waveguide of practical interest is reported. In particular, using this modelling approach, the effect of loss on the overall efficiency of the generated second harmonic power is reported. It is also shown that a better efficiency is achieved by used of $Ga_xAl_{1-x}As$ as the core material rather than GaAs.

Numerical Method

Following from Maxwell's equations, the propagation of an optical field in a given material can be deduced as [5]

$$\nabla^2\phi - p_z\beta^2\phi + qk_o^2\phi = \mathrm{P}_{NL} \qquad (1)$$

Where, P_{NL}, ϕ, β, k_o are the non-linear polarisation, the modal field profile, the propagation constant and wavenumber respectively, and q and p_z relate to the refractive index of the guide. ∇^2 is the Laplacian operator in 3-dimensions. Applying the FEM to equation (1) above will yield the following matrix equation for the propagation model:

$$-j4\beta[\mathrm{B}_{2\omega}]\frac{d\{\phi\}}{dz} + \left([\mathrm{A}_{2\omega}] - 4\beta^2[\mathrm{B}_{2\omega}]\right)\{\phi\} = \{P_{NL}\} \qquad (2)$$

This equation may be solved using a split-step procedure; the propagation step in which the finite difference method is applied within a short interval and the nonlinear step where the effect of the nonlinear term is considered [5].

Results

In the following, a rib waveguide is considered, with an air cladding, where the substrate is made of AlAs and a core of $Ga_xAl_{1-x}As$ is used. The guide dimensions are as follows: guide width, $W = 1.0\mu m$, height of the rib, $h = 1.0\mu m$ and the height of the waveguide slab, $t = 0.2\mu m$. Other guide parameters are as given in the work of Whitbread and Robson [7]. The input power is 20 Watts. In Fig. 1, second harmonic generation in a lossless perfectly quasi phase matched GaAs device is compared with that of $Ga_xAl_{1-x}As$. It can be observed from Fig. 1 that in the absence of

absorption losses, the efficiency of GaAlAs is very high due to its high nonlinear coefficient, thereby implying that it is more suitable material for second harmonic generation than GaAs. It will be shown later that high absorption losses reduce the efficiency of GaAs to such a level that $Ga_xAl_{1-x}As$ based device becomes more efficient.
Next, the effect of material loss has being taken into consideration and a simulated result is shown in Fig. 2 for GaAs. For the purpose of comparison, Fig. 2 shows the simulated results for second harmonic generation in GaAs without loss and without QPM, as a solid line. The broken line shows the curve obtained when the device is simulated without QPM, but taking into consideration the effect of loss. As can be observed, with no QPM, the generated second harmonic power builds up until the first coherence length l_c, slowly dissipates and then settles down to a constant value with a small damped oscillation. The maximum efficiency attained is just about 2.8×10^{-3}% as compared to the lossless case where efficiency of up to about 8.4×10^{-3}% was obtained. The inability to obtain high output power can be attributed entirely to the very high loss of GaAs. The dotted line shows the curve for the power generated when the device is QPM and simulated taking into account the effect of loss. An attempt at introducing QPM does not lead to any appreciable increase in the efficiency of the generated second harmonic power. As can be seen from Fig. 2, the efficiency curve of the generated second harmonic power assumes a periodic nature after the first coherence length. The maximum efficiency obtained is only 4×10^{-3}%. As seen in the figure, without QPM the power generated is attenuated very rapidly. With the introduction of QPM however, some form of periodicity is maintained. This periodicity can be directly attributed to the absorption loss, which effectively nullifies the effect of QPM. In Fig. 3 quasi-phase matched second harmonic generation in a lossy GaAlAs based device is compared with that of the lossless case. The results show that over very short distances, hardly any differences are observed. Provided accurate phase matching can be maintained over the device length, the generated power is shown to be increasing. However, perfectly phase matched domain structures are difficult, if not impossible to fabricate. In a perfectly QPM structure, the sign reversal occurs after a length defined by l_c, the coherence length. Assuming an error $\Delta l_c = l_c - l'_c$ during fabrication, where l'_c is the actual designed value and l_c is the desired value and assuming also that the device is of N domains, then over the entire device length, the accumulated error is given by $N'\Delta l_c$. If the device is sufficiently long, then there comes a point when the accumulated error $N'\Delta l_c = l_c$. Here N' (not equal to N) is an integral number of domain length after which this condition is obtained. At this point, sign reversal is actually offset by the accumulated error and beyond this point a gradual reduction in the generated power will start. This situation is clearly illustrated in Fig. 4. As can be seen, the domain inversion beyond a certain length does not occur after an integer number of coherence lengths. The simulated results for such a waveguide are illustrated in Fig. 5, where two cases are compared to that of the ideal case. As will be observed from the figure, even a 1% error in the fabrication of the domain length could lead to a considerable reduction in the generated second harmonic power. This result is quite informative about the length over which to operate a device. As Fig. 5 also suggests, operating the device at 50 μm could result in nearly zero efficiency if the error in the domain length is just 2%, instead of the predicted 8% efficiency for the ideal case. On the other hand, designing the device to operate at 20 μm will although reduce power, however, the output is reasonably stable with the fabrication error even at 2%. Fig. 6 shows the dependence of the harmonic output on the input power for various assumed fabrication errors. It is well known that increasing the input power could increase the efficiency of the output second harmonic power. The comparison is over a fixed device length of 10 μm. It can be seen that the efficiency is directly proportional to the input power.

Conclusion

An accurate and efficient numerical method has been described for the study of second harmonic generation in semiconductor waveguides. In this paper, numerically simulated results have been presented for second harmonic generation after considering the loss factor. These results show that for the reported values of the nonlinear susceptibility tensor and loss factor, $Ga_{0.2}Al_{0.8}As$ appears to be a better material. Results are also presented for fabrication errors in the domain and if phase matching can be obtained with less than 1% error, appreciable output power can be achieved.

References

[1] A.F. Harvey, *Coherent Light* London: Wiley,1970.
[2] S.J.B. Yoo, R. Bhat, C. Caneau and M.A. Koza, "Quasi-phase-matched second-harmonic generation in AlGaAs waveguide with periodic domain inversion achieved by wafer-bonding", *Appl. Phys. Lett.* **66**, (25), pp.3410-3412, June 1995.
[3] B.M.A. Rahman and J.B. Davies, "Finite-element solution of integrated optical waveguides",*J. Lightwave Technol.*, **LT-2**, pp. 682-688, Oct. 1984.
[4] F.A. Katsriku, B.M.A. Rahman and K.T.V. Grattan, "Finite element analysis of diffused anisotropic optical waveguides", *J. Lightwave Technol.*, **LT-14**, pp. 780-786, May 1996.
[5] F.A. Katsriku, B.M.A. Rahman and K.T.V. Grattan, "Numerical modeling of second harmonic generation in optical waveguides using the finite element method", *IEEE J. Quantum Electron.*, **QE-33**, pp.1727-1733, Oct. 1997.
[6] K.Hayata and M. Koshiba, "Numerical study of guided-wave sum-frequency generation through second-ordernonlinear parametric processes", *J. Opt. Soc. Am., B* **vol. 8**, pp. 449 - 458, Feb. 1991.
[7] N.D. Whitbread and P.N. Robson, "Theoretical analysis of passive visible surface-emitting second harmonic generators", *IEEE J.Quantum Electronic.*, **QE-30**, pp. 139-147, Jan. 1994.

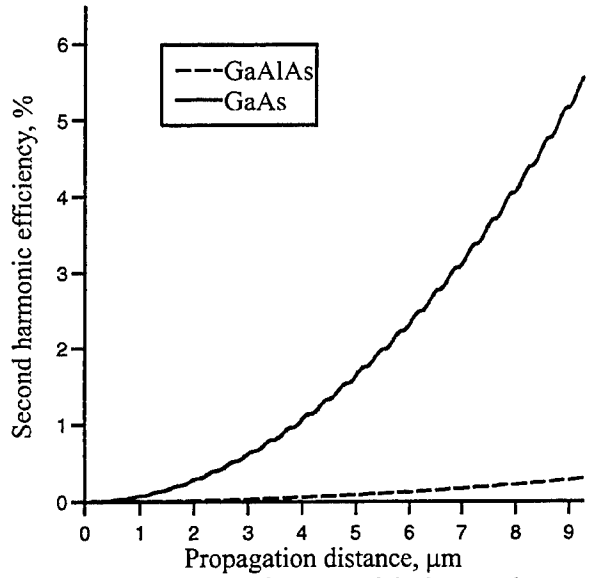


Fig.1 Comparison of QPM SHG in GaAs and GaAlAs,

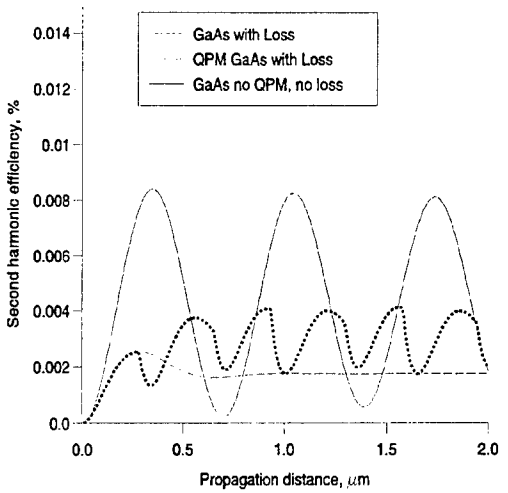


Fig.2 SHG in GaAs taking into consideration the effect of loss

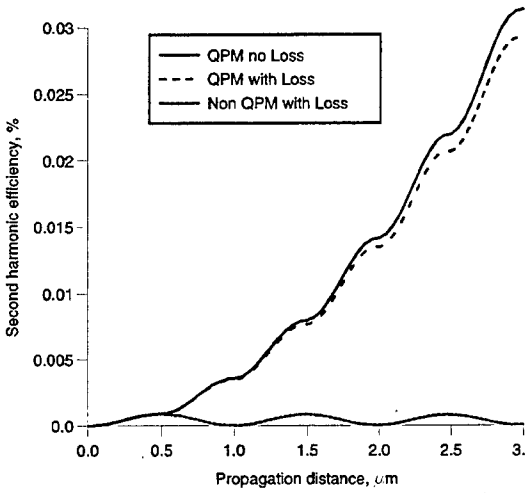


Fig. 3 Comparing SHG in a QPM GaAlAs device, with and without loss.

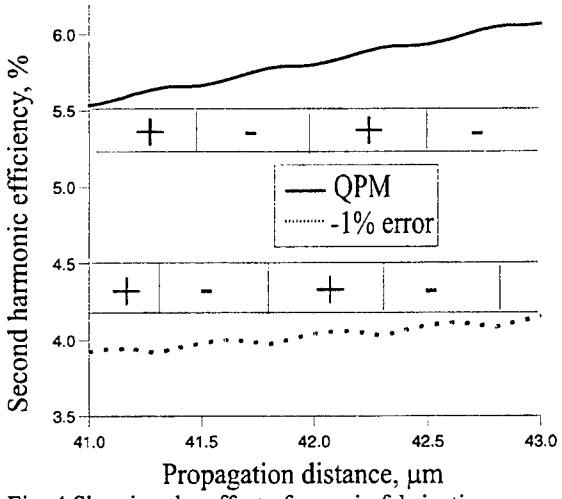


Fig. 4 Showing the effect of error in fabrication on QPM.

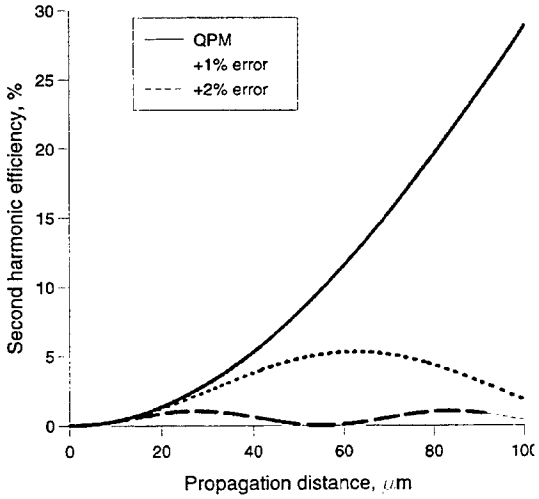


Fig. 5 Comparison of ideal QPM device with error of 1% and 2% in fabrication.

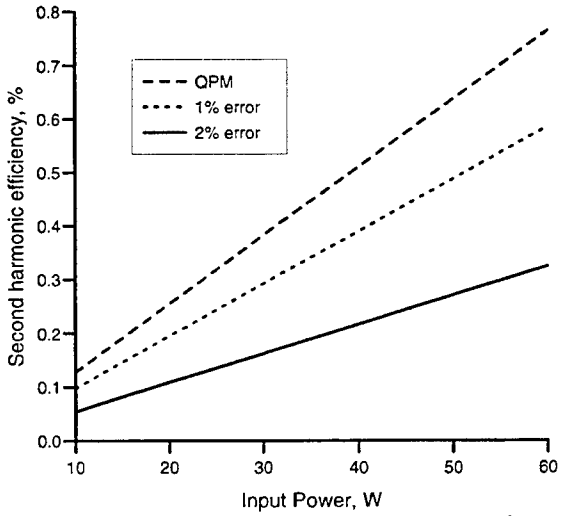


Fig. 6 Dependence of efficiency on input power for ideally matched and 1% and 2% error.

The Study of Nonideal Implementation and Noise Effects on Quasi-Phase-Matched Parametric Interactions in Optical Waveguides

Ching-Fuh Lin, Hsu-Feng Chou, and Yue-Wen Hong

Institute of Electro-Optical Engineering
and
Department of Electrical Engineering
National Taiwan University
Taipei, Taiwan, R.O.C.
Tel: 886-2-23635251 ext. 339
Fax: 886-2-23638247
Email: cflin@cc.ee.ntu.edu.tw

Quasi-phase-matched (QPM) [1], [2] second-order nonlinear effects in optical waveguides have extensive applications because of their versatile and efficient frequency conversion abilities. Recently, QPM devices have been successfully fabricated on many materials such as $LiNbO_3$, $LiTaO_3$, KTP and AlGaAs. Theoretical analyses of the QPM nonlinear effects have also increasing importance for the purpose of understanding the performance of the QPM devices especially when optimal conditions can not be achieved. [3], [4] Precise analytical modeling of those QPM devices is quite difficult when large or irregular geometrical variations exist and the depletion or the noise of the pump wave is not negligible. For a general and accurate analysis, numerical methods are necessary. In this paper, we use the IFD-BPM [5] to investigate the influences of nonideal implementation and pumping noise on the parametric interactions in the optical waveguide.

Fig. 1 shows a schematic of the waveguide configuration for the simulation, where w, n_g, n_c, and Λ are the width of the waveguide, the refractive indices of the waveguide and its neighboring regions, and the period of the modulated $\chi^{(2)}$ grating, respectively. The ideal grating period Λ is chosen as $\Lambda = \frac{2\pi}{|k_p - k_s - k_i|}$, where k_p, k_s, and k_i are the wavevectors of the quasi-phase-matched modes of the pump, the signal, and the idler waves, respectively. The duty cycle of the $\chi^{(2)}$ grating is defined as $\frac{p}{\Lambda}$. The values of those parameters for the simulation are listed in Table 1.

We first simulate the influence of the period variation. The QPM period varies from Λ to 1.05 Λ. The departure of the period from the ideal value results in less efficient energy transfer. Fig. 2 shows the powers of the pump and the signal waves vs. the propagation distance for the period equal to Λ and 1.005 Λ. For the small phase mismatch, e.g., period=1.005Λ, the energy transfer from the pump wave to the signal and the idler waves is delayed to a longer distance, compared to the case of the ideal period. In addition, the peak transfer efficiency decreases from nearly 100 % to only 40 %. As the QPM period increases to be more than 1.01 Λ, the energy transfer becomes oscillatory and the transfer efficiency decreases to less than 0.01 %. The oscillation period from the simulation is different from the

value, $\frac{2\pi}{k_p - k_i - k_s - k_{QPM}}$, calculated from the plane-wave approximation with non-phase-matched components ignored.[2] Because the non-phase-matched terms are ignored in the plane-wave approximation, the oscillation periods predicted by two methods are different. Simulation also shows that the difference of the oscillation period increases as the QPM period variation decreases, indicating that the non-phase-matched components have important influences on the parametric interactions in the QPM condition. These influences are, however, ignored by analytical analyses using the plane-wave approximation.

The influence of duty cycles of the QPM grating is also studied. As the duty cycle is reduced, the energy transfer is delayed, while the peak transfer efficiency remains the same. If the duty cycle continues to decrease to zero, the energy transfer is delayed to a distance approaching infinity. On the other hand, the FWHM distance also expands as the duty cycle is reduced. The FWHM distance is defined as the full width of the distance in which the parametric interaction has its energy transfer beyond half of the maximum. The deviation of the duty cycle from the optimal value of 50% results in a lower effective nonlinear coefficient and so requires a longer device length. However, the FWHM distance is increased, indicating that the smaller duty cycle does not always cause adverse effects. The detail will be further discussed in the presentation.

In addition to the nonideal implementation of the QPM grating structure, the power variation is also found to be influential. For example, the initial power of the pump wave is found to have influences not only on the transfer efficiency, but also on the transfer behavior along the propagation distance. Also, as the initial powers of the signal and the idler waves are reduced simultaneously, the energy transfer is significantly delayed. The peak transfer distance exponentially decreases with the initial signal and idler powers. In addition, the nonzero initial phase of the signal wave is found to cause the energy transfer to be delayed, while the FWHM distance remains the same. The phase influence is significant even when both the initial powers of the signal and the idler waves are simultaneously reduced to only 1 pW. On the other hand, if the signal wave remains at 1 mW, while the power of the idler wave is reduced, the influence of the initial idler power becomes negligible for its power less than 1 μW.

The noise in the pumping wave is also found to have important influence on the parametric interaction. The amplitude and phase noises are studied separately. Noise of sinusoidal modulation on either the amplitude or the phase is simulated. Fig. 3 shows the influence of the amplitude modulation on the power transfer. The pump energy drops faster for the modulation at higher frequencies. The reason is because the higher-frequency noise escapes from the waveguide faster, leading to a fast decrease of the pumping energy. The influence of the phase modulation on the power transfer is shown in Fig. 4. The pump energy also drops faster for the modulation at higher frequencies because of a similar reason.

Detailed discussions of the influences in many aspects will be given in the presentation.

References:

1. S. Somekh and A. Yariv, *Opt. Commun.*, vol. 6, pp. 301-304, 1972.
2. L. E. Myers, R. C. Eckardt, M. M. Fejer, and R. L. Byer, *J. Opt. Soc. Am. B*, vol. 12, pp. 2102-2116, 1995.
3. M. M. Fejer, G. A. Magel, D. H. Jundt, and R. L. Byer, *IEEE J. Quantum Electron.*, vol. 28, pp. 2631-2654, 1992.

4. Wei-Xing Hou, Tow Chong Chong, Hirohiko Kumagai, and Masahiro Hirano, *Jpn. J. Appl. Phys.*, vol. 35, pp. L 5705-L 5710, 1996.
5. Hsu-Feng Chou, Ching-Fuh Lin, and Gin-Chung Wang, "An iterative finite difference beam propagation method for modeling second-order nonlinear effects in optical waveguides," *IEEE J. Lightwave Technol.*, 1998.

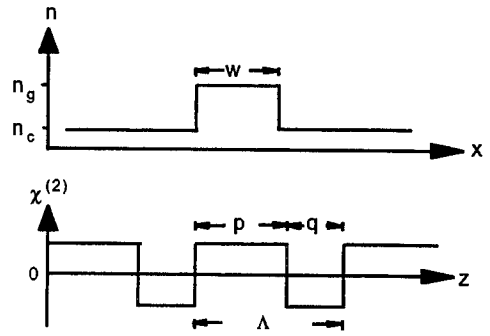


Fig. 1 The index profile along the x-axis and the periodic variation of $\chi^{(2)}$ along the z-direction.

	pump	signal	idler
λ	0.808 um	1.156 um	2.684 um
n_g	2.17703	2.15362	2.10861
n_c	2.17503	2.15162	2.10661
n_{eff}	2.17686	2.15332	2.10774
W	$\chi^{(2)}$	Δx	Δz
12 um	68 pm/V	0.2 um	0.1um

Table 1 The values of parameters used in the simulation.

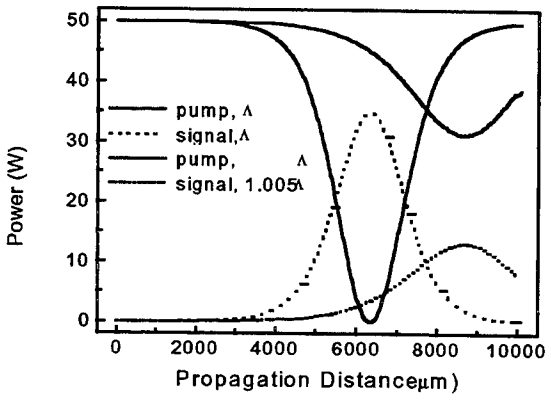


Fig. 2 The simulated power variation along the propagation distance for the period equal to 1.005 Λ.

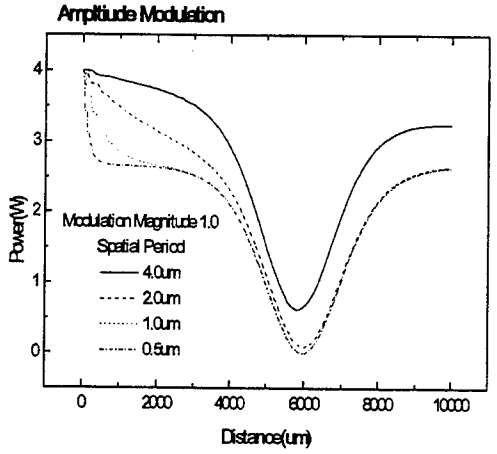


Fig. 3 The influence of the amplitude modulation on the power transfer.

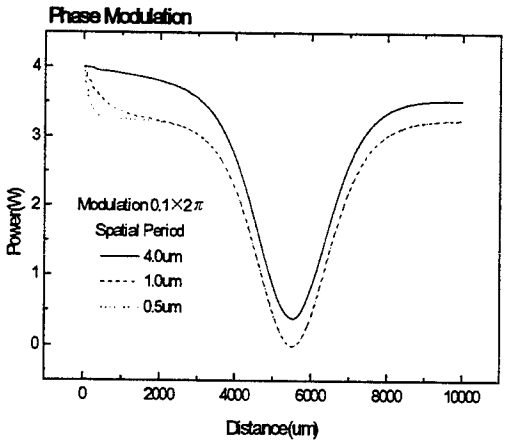


Fig. 4 The influence of the phase modulation on the power transfer.

Finite Difference Beam Propagation Methods for Modeling Quasi-Phase-Matched Second-Order Nonlinear Interaction in Waveguide

Ching-Fuh Lin, Hsu-Feng Chou, and Shing Mou
Institute of Electro-Optical Engineering
and
Department of Electrical Engineering
National Taiwan University
Taipei, Taiwan, R.O.C.
Tel: (02) 23635251 ext. 339 / Fax: (02) 23638247
Email: cflin@cc.ee.ntu.edu.tw

The successful implementation of the quasi-phase-matching (QPM) technique [1] makes second-order nonlinearities have increasing importance in areas such as optical commucation, data storage, spectroscopy, environmental monitoring, and so on. However, exact analytical analyses of these interactions are usually difficult in cases of efficient coversion and waveguide with irregularities. Therefore, numerical techniques based on beam propagation method (BPM) had been proposed by many places to model QPM second-order nonlinear effects. In this work, iterative schemes are proposed and compared with published methods. Without loss of generality, the formulations are given in the second-harmonic generation (SHG) case. The extension to the general three-frequency situation is straightforward.

The wave equation in the presence of nonlinear polarization could be described as follows in the paraxial approximation:

$$2jk_{os}\bar{n}_s\frac{\partial E_s}{\partial z}=\frac{\partial^2 E_s}{\partial x^2}+k_{os}^{\,2}(n_s^{\,2}-\bar{n}_s^{\,2})E_s+\tfrac{1}{2}k_{os}^{\,2}\chi^{(2)}e^{-j\cdot\Delta k\cdot z}E_fE_f$$

$$2jk_{of}\bar{n}_f\frac{\partial E_f}{\partial z}=\frac{\partial^2 E_f}{\partial x^2}+k_{of}^{\,2}(n_f^{\,2}-\bar{n}_f^{\,2})E_f+k_{of}^{\,2}\chi^{(2)}e^{j\cdot\Delta k\cdot z}E_sE_f^{\,*}$$

where $\bar{n}$, k_o, $\chi^{(2)}$ and E are the effective index of the guided mode, the wave vector in free space, the nonlinear coefficient, and the slowly varying envelope of the field, respectively. Subscripts, s and f, represent the second harmonic and the fumdamental waves. $\Delta k_z\equiv 2\bar{n}_f k_{of}-\bar{n}_s k_{os}$. Propagation along the z direction is assumed. For concise purpose of expressions, the following finite difference operators are defined:

$$L_xE_i^{m,s}=\frac{1}{\Delta x^2}(E_i^{m-1,s}-2E_i^{m,s}+E_i^{m+1,s}),\qquad L_{oi}^{\,m,s}=k_{oi}^{\,2}(n_i^{m,s^2}-\bar{n}_i^{\,2}),\quad i=s,f$$

$$F_s^{m,s}=\tfrac{1}{2}k_{os}^{\,2}\chi^{(2)^{m,s}}e^{-j\cdot\Delta k\cdot s\cdot\Delta z},\qquad F_f^{m,s}=k_{of}^{\,2}\chi^{(2)^{m,s}}e^{j\cdot\Delta k\cdot s\cdot\Delta z}$$

Note that $E^{m,s}$ represents the electric field at the point $(x,z)=(m\cdot\Delta x,s\cdot\Delta z)$. With these definitions, the schemes to be compared can be expressed as follows:

EFD-BPM (Explicit Finite Difference Beam Propagation Method) [2]

$$\frac{jk_{os}\bar{n}_s}{\Delta z}(E_s^{m,s+1}-E_s^{m,s-1})=(L_x+L_{os}^{m,s})E_s^{m,s}+F_s^{m,s}E_f^{m,s}E_f^{m,s}$$

$$\frac{jk_{of}\bar{n}_f}{\Delta z}(E_f^{m,s+1}-E_f^{m,s-1})=(L_x+L_{of}^{m,s})E_f^{m,s}+F_f^{m,s}E_s^{m,s}E_f^{m,s^*}$$

IFD-BPM (Iterative Finite Difference Beam Propagation Method) [*this work*]

$$\frac{2jk_{os}\bar{n}_s}{\Delta z}(E_s^{m,s+1^{(t)}} - E_s^{m,s}) = \tfrac{1}{2}\Big[(L_x + L_{os}^{m,s+\frac{1}{2}})(E_s^{m,s} + E_s^{m,s+1^{(t)}}) + (F_s^{m,s}E_f^{m,s}E_f^{m,s} + F_s^{m,s+1}E_f^{m,s+1^{(t-1)}}E_f^{m,s+1^{(t-1)}})\Big]$$

$$\frac{2jk_{of}\bar{n}_f}{\Delta z}(E_f^{m,s+1^{(t)}} - E_f^{m,s}) = \tfrac{1}{2}\Big[(L_x + L_{of}^{m,s+\frac{1}{2}})(E_f^{m,s} + E_f^{m,s+1^{(t)}}) + (F_f^{m,s}E_s^{m,s}E_f^{m,s^*} + F_f^{m,s+1}E_s^{m,s+1^{(t-1)}}E_f^{m,s+1^{(t-1)^*}})\Big]$$

where t is the iteration count and $E^{(t)}$ is the t-th iteration field. $E^{(0)}$ can be derived by various means. In this study, it is obtained by assuming $E^{(-1)} = E^{m,s}$.

SS-BPM (Split-Step Beam Propagation Method) [3]

step 1: $$\frac{2jk_{os}\bar{n}_s}{\Delta z}(E_s^{m,s+1^{(I)}} - E_s^{m,s}) = \tfrac{1}{2}(L_x + L_{os}^{m,s+\frac{1}{2}})(E_s^{m,s} + E_s^{m,s+1^{(I)}})$$

$$\frac{2jk_{of}\bar{n}_f}{\Delta z}(E_f^{m,s+1^{(I)}} - E_f^{m,s}) = \tfrac{1}{2}(L_x + L_{of}^{m,s+\frac{1}{2}})(E_f^{m,s} + E_f^{m,s+1^{(I)}})$$

step 2 : $$E_s^{m,s+1} = \cos(\Delta z \cdot \tfrac{k_{o1}\cdot\chi^{(2)}}{2\cdot\sqrt{\bar{n}_1\bar{n}_2}})E_s^{m,s+1^{(I)}} - j\sqrt{\tfrac{\bar{n}_2}{\bar{n}_1}}e^{-j\cdot\phi}\sin(\Delta z \cdot \tfrac{k_{o1}\cdot\chi^{(2)}}{2\cdot\sqrt{\bar{n}_1\bar{n}_2}})E_s^{m,s+1^{(I)}}$$

$$E_f^{m,s+1} = \cos(\Delta z \cdot \tfrac{k_{o1}\cdot\chi^{(2)}}{2\cdot\sqrt{\bar{n}_1\bar{n}_2}})E_f^{m,s+1^{(I)}} - j\sqrt{\tfrac{\bar{n}_2}{\bar{n}_1}}e^{j\cdot\phi}\sin(\Delta z \cdot \tfrac{k_{o1}\cdot\chi^{(2)}}{2\cdot\sqrt{\bar{n}_1\bar{n}_2}})E_f^{m,s+1^{(I)}}$$

where $e^{j\cdot\phi} = e^{-j\cdot\Delta k\cdot z}E_1/|E_1|$ and $E^{(I)}$ is the intermediate field. In the split-step methods, the linear propagation and the nonlinear couplings are taken into account successively. When dealing with the nonlinear terms, it is assumed in SS-BPM that the coupling between frequencies is constant within each propagation step, which reduces the order of accuracy.

ISS-BPM (Iterative Split-Step Beam Propagation Method) [*this work*]

step 1: exactly the same as in SS-BPM

step 2: $$\frac{2jk_{os}\bar{n}_s}{\Delta z}(E_s^{m,s+1^{(t)}} - E_s^{m,s^{(I)}}) = \tfrac{1}{2}(F_s^{m,s}E_f^{m,s^{(I)}}E_f^{m,s^{(I)}} + F_s^{m,s+1}E_f^{m,s+1^{(t-1)}}E_f^{m,s+1^{(t-1)}})$$

$$\frac{2jk_{of}\bar{n}_f}{\Delta z}(E_f^{m,s+1^{(t)}} - E_f^{m,s^{(I)}}) = \tfrac{1}{2}(F_f^{m,s}E_s^{m,s^{(I)}}E_f^{m,s^{(I)^*}} + F_f^{m,s+1}E_s^{m,s+1^{(t-1)}}E_f^{m,s+1^{(t-1)^*}})$$

The iteration is performed in step 2, which is similar to IFD-BPM but without linear terms.

The QPM-SHG in a $LiNbO_3$ waveguide is considered first. The wavelengths and the refractive indices of the fundamental and the second harmonic waves are 0.808 μm, 0.404 μm, 2.17503, and 2.32679, respectively. The width of the waveguide is 4 μm and $\chi^{(2)}$ is 68.8 pm/V. The initial power levels of the fundamental and the SH waves are 4W/μm and 0. The transverse grid size, Δx, is 0.2 μm. In order to have EFD-BPM stable, Δz is chosen to be 0.08 μm for all schemes. An additional simulation with $\Delta z = 0.01\mu$m is also performed for EFD-BPM. As shown in Fig. 1(a), the power variations obtained by IFD-BPM, SS-BPM and ISS-BPM are identical in the scale used. However, the result obtained by EFD-BPM with $\Delta z = 0.08\mu$m is highly oscillatory and, therefore, only the power variation calculated with $\Delta z = 0.01\mu$m is shown in Fig. 1(b). It is obvious that, even with a much smaller Δz, EFD-BPM still significantly violates the power conversation law after 15000 μm of propagation. Therefore, the convergence of EFD-BPM with respect to the stepsize is much worse than the other schemes.

Next, a birefringently phase-matched SHG is studied to investigate the convergence rate with respect to the stepsize for different schemes. The waveguide geometry is the same as the previous case but the refractive indices are artificially adjusted to meet the phase-matching condition. It is clear in Fig. 2(a) that with $\Delta z = 0.1\mu$m the three schemes agree with each other. When Δz is increased to 15 μm, the power variation obtained by SS-BPM gradually

deviates from the converged result while the one calculated by ISS-BPM departs frenetically at some point. However, the result computed by IFD-BPM is essentially the same as the converged result.

The comparisons indicate that iterative methods are more suitable for the simulation of second-order nonlinearities. This study also indicates that only one iteration is sufficient for good simulations, which assures the efficiency of these iterative schemes. Furthermore, ISS-BPM has better efficiency than IFD-BPM.

In summary, the results of the comparisons among the various BPMs designed to model second-order nonlinearities can be briefly tabled as follows:

	EFD-BPM	IFD-BPM	SS-BPM	ISS-BPM
category	explicit	implicit	partly implicit	implicit
accuracy	second order	second order	first order	first order
time ratio	1	≥ 3 (4)	2.4	≥ 2
convergence	☹	☺☺	😐	☺

Note that the time required by iterative schemes depends on the way $E^{(0)}$ is obtained. If EFD-BPM is used for this purpose, the minimal time ratio is 3 for IFD-BPM.

References:

[1] J. A. Armstrong, N. Blombergen, J. Ducuing, and P. Pershan, *Phys. Rev.*, vols. 127, pp. 1918-1939, 1962

[2] M. Masoudi and J. M. Arnold, *IEEE J. Quantum Electron.*, vol. 31, pp. 2107-2113, 1995

[3] J. M. Krijnen, W. Torruellas, G. I. Stegeman, H. J. W. M. Hoekstra, and P. V. Lambeck, *IEEE J. Quantum Electron.*, vol. 32, pp. 729-738, 1996.

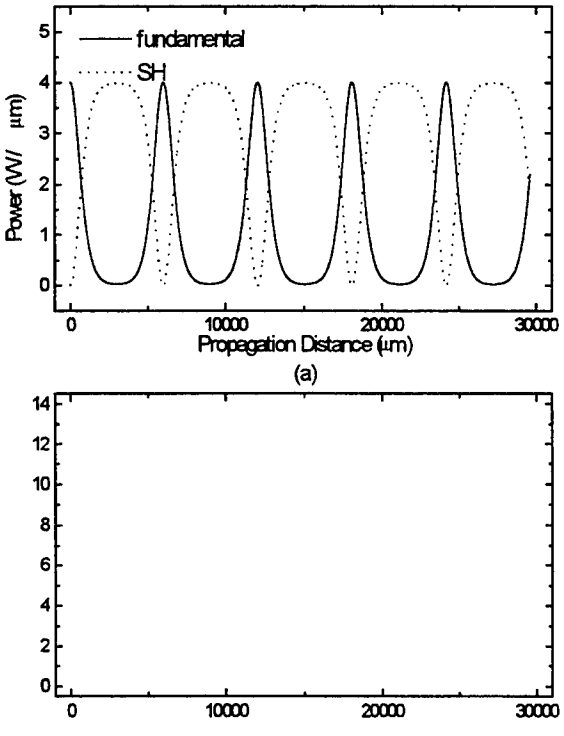


Fig. 1 The power variation along the propagation distance for QPM-SHG simulated by (a) IFD-BPM with one iteration, SS-BPM, ISS-BPM, all calculated with dz=0.08μm. These curves are identical; (b) EFD-BPM with dz=0.01μm

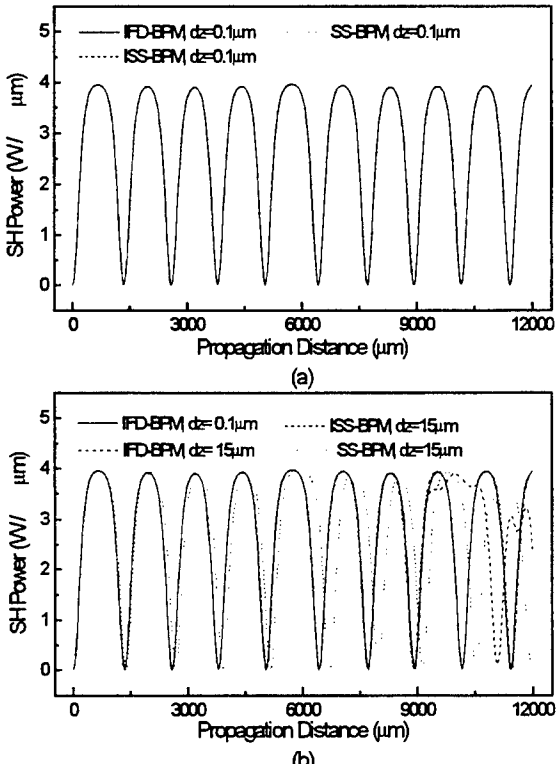


Fig. 2 The simulated SH power variation along the propagati direction in the birefringently phase-matched SHG with (a) dz 0.1μm; (b) dz=15μm; The reslt of IFD-BPM with dz=0.1μ also shown in (b) for reference.

Wavelength conversion from $1.3\,\mu m$ to $1.5\,\mu m$ using Raman-assisted three-wave mixing in a single-mode optical fiber

T. Sylvestre, H. Maillotte, and E. Lantz

Laboratoire d'Optique P.M. Duffieux,
U.M.R CNRS No 6603, Université de Franche-Comté,
25030 Besançon Cedex, France,

P. Tchofo Dinda, and A. B. Moubissi
Laboratoire de Physique de l'Université de Bourgogne, CNRS,
Av. A. Savary , B.P. 47 870, 21078 Dijon Cedex, France

Parametric wave-mixing in dielectric media have been intensively investigated for both its fundamental and applied interests [1]. The areas of application of parametric processes include all-optical wavelength conversion, parametric amplification, or the generation of new optical frequencies [1]. In particular, wavelength conversion between close-spaced channels, by four-wave mixing in a fiber, has been demonstrated for WDM (wavelength division multiplexing) in the spectral band of erbium amplifiers [2]. Besides, for network applications, there is also a strong interest for network operations in wavelength conversion between the two transmission windows of silica fibers, around $1.3\,\mu m$ and $1.5\,\mu m$ [3, 4]. Parametric wave-mixing has been used for such a wide range conversion. For example, a wavelength conversion between $1.3\,\mu m$ and $1.5\,\mu m$ bands using quasi-phase-matched difference-frequency generation was demonstrated in periodically poled $LiNbO_3$ waveguides [5]. On the other hand, it was recently demonstrated that the $1.3\,\mu m \rightarrow 1.5\,\mu m$ wavelength conversion can be achieved by use of the combined effects of Raman scattering and four-wave mixing in an optical fiber [6]. However, the achievement of efficiency for the above mentioned wavelength converters requires the fulfilment of phase-matching conditions, which impose strict limitations in the spectral bandwidth that can be used, and in the operating conditions [5, 6]. Here we theoretically analyse a wavelength conversion from $1.32\,\mu m$ to $1.52\,\mu m$ by means of a Raman-assisted three-wave mixing (RATWM) process in a single-mode optical fiber. This process yields, through the Raman gain, a significant energy transfer from a weak anti-Stokes signal to a Stokes idler (within the Raman gain band), although the TWM that seeds the idler is highly phase-mismatched [7]. The interest here is to overcome the constraints imposed by phase-matching conditions, and to obtain frequency conversion over a large bandwidth, given by the Raman gain curve.

Coupled-mode analysis

Here we consider parametric wave mixing of three collinearly polarised waves with frequencies ω_0, $\omega_1 = \omega_0 - \Omega_c$, and $\omega_2 = \omega_0 + \Omega_c$, which correspond to a pump at wavelength $\lambda_0 = 1.413\,\mu m$, an anti-Stokes signal at $\lambda_2 = 1.32\,\mu m$, and the Stokes idler at $\lambda_1 = 1.52\,\mu m$, respectively, with $\Omega_c = 14.9\,THz$. Note that for pump power levels which are accessible in an optical fiber (less that $1kW$), the TWM interaction under consideration is highly mismatched ($\Omega_c >> \Omega_{pm} \equiv \sqrt{-2\gamma_0 P_0/\beta_2}$, where $\beta_2 = -0.0078\,ps^2/m$ is the group-velocity dispersion of a standard single-mode silica fiber, and $\gamma_0 = 0.28\,W^{-1}km^{-1}$ is the nonlinear coefficient) Consequently, an idler wave can not be generated through this ordinary TWM process, in the absence of any other nonlinear process. This situation is illustrated in Fig. 1 (a), which shows the spatial evolution of the normalised powers obtained from coupled-mode equations[7], $\eta_j(z) - \eta_j(0)$, $\eta_j(z) \equiv P_j(z)/\Sigma P_j(0)$, when the Raman gain is not taken into account. As Fig. 1 (a) shows, a highly mismatched TWM leads to a relatively small periodic power flow between the pump and the two sidebands, which leads to a zero mean power gain for both sidebands. On the other hand, SRS (stimulated Raman scattering) induces a unilateral transfer of energy from higher to lower-frequency waves, which

destroys the spatial periodicity of the parametric energy-exchange process. This Raman effect is clearly visible in Fig. 1 (b), which we obtained by mixing the $1.413\,\mu m$ pump $[P_0(z=0)=60\,W]$ with a $1.32\,\mu m$ signal $[P_2(0)=5\,W]$, though the combined effects of SRS and TWM interaction are not sufficient to generate the idler above the noise level for such pump powers. For higher pump powers, the Raman gain becomes stronger. TWM induces, over each coherence length, a relatively small but non-negligible energy transfer from the pump to the idler, which can ultimately be amplified by the Raman process above the noise level. Fig. 1 (c) demonstrates the generation of the idler, with a strong pump $[P_0=120\,W]$, in a pure SiO_2 fiber. In a GeO_2-doped fiber, the peak Raman gain is several times higher than in a a pure SiO_2 fiber. Figs. 1 (d)–(e) exhibit the same general features as for a pure SiO_2 fiber but with the major difference that the pump power level required to generate the idler is much lower for the GeO_2-doped fiber [compare Fig. 1 (e) with 1 (c)]. It should be noticed that the coupled-mode analysis does not take into account SRS or MI (modulational instability) which may spontaneously grow from quantum noise, and which may alter the wavelength conversion. These nonlinear processes are fully taken into account when solving the nonlinear Schrödinger equations, as we show below.

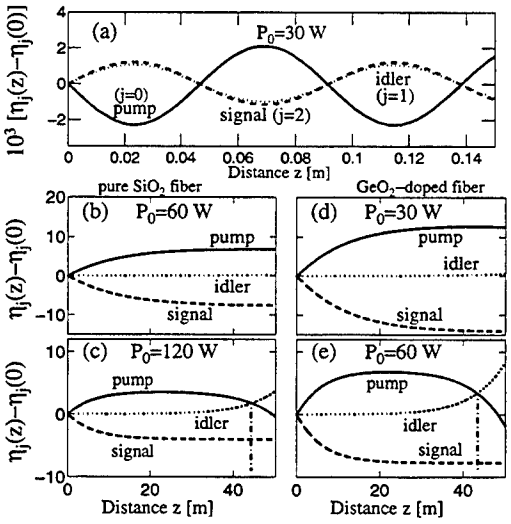


Figure 1: *Normalized powers* $\eta_j(z)-\eta_j(0)$ *versus propagation coordinate* z *for* $P_2(0)=5\,W$ *and different pump powers.* $j=0$ *(pump),* $j=1$ *(idler),* $j=2$ *(signal).*

Nonlinear Schrödinger equation

The amplitude $\mathcal{A}$ of the electric field, in the whole spectral domain, is found to satisfy the following nonlinear Schrödinger equation (NLSE):

$$\frac{\partial \mathcal{A}}{\partial z} = i\frac{\beta_2}{2}\frac{\partial^2 \mathcal{A}}{\partial t^2} + i\,\gamma_0(1-\rho)|\mathcal{A}|^2\mathcal{A} + i\,\gamma_0\,\rho\,\mathcal{A}\int_0^\infty \chi_r(s)\,|\mathcal{A}|^2(t-s)\,ds,, \qquad (1)$$

where we assume hereafter that the parameter ρ (which measures the fractional contribution of the Raman susceptibility to the total nonlinear index) is $\rho=0.18$ for a pure silica fiber, whereas we take $\rho=0.36$ for a fiber with Germania doping. We have performed the full solution of the NLSE (1) with picosecond pulses, by the split-step Fourier method [1]. For each type of fiber, the propagation length was chosen to be approximately the effective walk-off length between the pump and the idler. Figures 2 (a), (b) and (c), which we obtained by mixing a $100\,ps$ pump pulse $[P_0(z=0)=110\,W]$ with a $100\,ps$ signal pulse $[P_2(z=0)=5\,W]$ in a GeO_2-doped fiber,

demonstrate the effectiveness of the $1.32\mu m \rightarrow 1.52\mu m$ wavelength conversion. They also show a spontaneous generation of two MI sidebands, which result from phase-matched TWM interactions in the anomalous dispersion regime. The power imbalance of the two MI sidebands is due to the asymmetric nature of the Raman susceptibility, which amplifies (depletes) the Stokes (anti-Stokes) side of the MI spectrum. Thus, although the wavelength conversion is obtainable in the presence of a spontaneous MI process, Fig 2 (c) shows that MI causes a pump depletion that may increase the power level required for the wavelength conversion in optical fibers with $1.32\,\mu m$ zero-dispersion wavelength. The use of a dispersion-shifted fiber allows to achieve the $1.32\mu m \rightarrow 1.52\mu m$ wavelength conversion in modulationally stable operating conditions, as Fig. 2 (d), (e) and (f) show. An interesting feature is that the conversion efficiency can be high, and even greater than $0\,dB$.

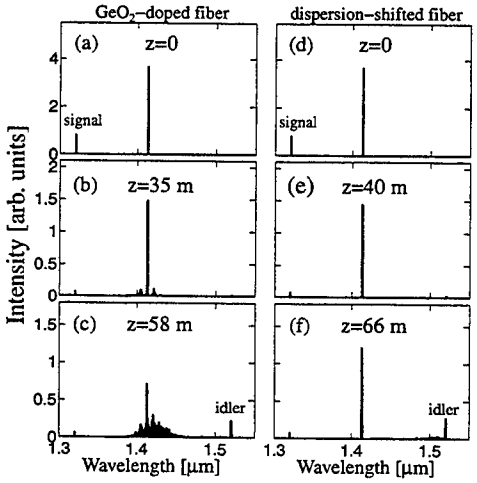


Figure 2: *Numerical solution of the NLSE showing the* $1.3\,\mu m \rightarrow 1.5\,\mu m$ *wavelength conversion.*

In conclusion we have demonstrated, by means of theoretical analysis and numerical simulations, that the combined effects of a highly mismatched TWM interaction and Raman amplification may be exploited for performing all-optical $1.3\,\mu m \rightarrow 1.5\,\mu m$ ultrafast wavelength conversion. Some fiber design considerations, such as the dispersion curves, the type and amount of dopants (GeO_2, P_2O_5), have to be carefully examined for setting up a highly efficient Raman-assisted TWM-based wavelength converter.

References

[1] G.P. AGRAWAL. Nonlinear fiber Optics, 2^{nd} Edition. Academic press Inc, San Diego, 1995.
[2] K. INOUE, T. HASEGAWA, K. ODA, and H. TOBA. *Electron. Lett.*, **29**, 1708, (1993).
[3] P. E. BARNSLEY and J. P. CHIDGEY . *IEEE Photonics Technology Letters*, **4**, 91, (1992).
[4] D. MAHGEREFTEH and M. W. CHBAT . *IEEE Photonics Technology Letters*, **7**, 497, (1995).
[5] C. Q. XU, H. OKAYAMA, and M. KAWAHARA. *Electron. Lett.*, **30**, 2168, (1994).
[6] A. UCHIDA, M. TAKEOKA, and T. NAKATA . *Journal of Lightwave Technology*, **16**, 92, (1998).
[7] T. SYLVESTRE, H. MAILLOTTE, E. LANTZ, and P. TCHOFO DINDA. *"Raman-assisted parametric frequency conversion in a normally dispersive single-mode fiber", (submitted)*, 1999.

Simultaneous second- and third- harmonic generation in layered media and related phenomena.

V. V. Konotop
Department of Physics and Center of Mathematical Sciences, University of Madeira, Praça do Município, Funchal, P-9000, Portugal

V. Kuzmiak
Institute of Radio Engineering and Electronics, Czech Academy of Sciences, Chaberska 57, 182 51 Prague 8, Czech Republic

A considerable activity focused on the study of the phenomena associated with the propagation of electromagnetic waves in periodic nonlinear systems provided bulk of evidence that photonic bandgap (PBG) structures possesing nonlinearity host many interesting and useful phenomena. On the other hand one of the problems traditionally of great interest is the resonant wave interactions, in particular, second (SHG) and third-harmonic (THG) generation. In present communication we report the *simultaneous SHG and THG* in a stratified nonlinear medium .

We illustrate the phenomenon on the example of a multilayer stack which consists of the alternating layers of dielectric materials of thicknesses a and b. The volume filling fraction is therefore $f = a/(a+b)$. By varying both the dielectric constants and FF we demonstrate the possibility of simultaneous SHG and THG i.e. the possibility to satisfy simultaneously the follwing resonant conditions $q_2 = 2q_1 + Q_1$, $\omega_2 = 2\omega_1$, and $q_3 = 3q_1 + Q_2$, $\omega_3 = 3\omega_1$ where $\omega_j \equiv \omega(q_j)$ $(j = 1,2,3)$ is the frequency of the modes with the wave vector q_j and Q_j $(j = 1,2)$ is a vector of the reciprocal lattice. It is important that the layers can possess different nonlinear properties either of $\chi^{(2)}$ or $\chi^{(3)}$ type.

Mathematically the phenomenon is described within the framework of the envelope function approach and the dynamical problem is reduced to the system of equations for slowly varying amplitudes

$$\frac{i}{\omega_1}\frac{dA_1}{dt} + \gamma_3\bar{A}_2A_3 + 2\gamma_1\bar{A}_1A_2 + (\lambda_{1111}|A_1|^2 + \lambda_{1122}|A_2|^2 + \lambda_{1133}|A_3|^2)A_1 + \lambda_{1223}A_2^2\bar{A}_3 + 3\lambda_{1113}\bar{A}_1^2A_3 = 0 \quad (1)$$

$$\frac{i}{\omega_2}\frac{dA_2}{dt} + \gamma_3\bar{A}_1A_3 + \gamma_1A_1^2 + (\lambda_{1122}|A_1|^2 + \lambda_{2222}|A_2|^2 + \lambda_{2233}|A_3|^2)A_2 + 2\lambda_{1223}A_1\bar{A}_2A_3 = 0 \quad (2)$$

$$\frac{i}{\omega_3}\frac{dA_3}{dt} + \gamma_3A_1A_2 + (\lambda_{1133}|A_1|^2 + \lambda_{2233}|A_2|^2 + \lambda_{3333}|A_3|^2)A_3 + \lambda_{1113}A_1^3 + \lambda_{1223}\bar{A}_1A_2^2 = 0 \quad (3)$$

where the coefficients γ and λ depend on physical properties of the layers. This system possess two integrals of motion

$$N = |A_1|^2 + 2\frac{\omega_1}{\omega_2}|A_2|^2 + 3\frac{\omega_1}{\omega_3}|A_3|^2 \quad (4)$$

which can be associated with the energy of the electromagnetic field and

$$H = \gamma_1(A_1^2\bar{A}_2 + \bar{A}_1^2A_2) + \gamma_3(A_1A_2\bar{A}_3 + \bar{A}_1\bar{A}_2A_3) + \lambda_{1113}(\bar{A}_1^3A_3 + A_1^3\bar{A}_3) + \lambda_{1223}(\bar{A}_1A_2^2\bar{A}_3 + A_1\bar{A}_2^2A_3) + \frac{1}{2}(\lambda_{1111}|A_1|^4 + \lambda_{2222}|A_2|^4 + \lambda_{3333}|A_3|^4 + 2\lambda_{1122}|A_1|^2|A_2|^2 + 2\lambda_{1133}|A_1|^2|A_3|^2 + 2\lambda_{2233}|A_2|^2|A_3|^2) \quad (5)$$

which is the energy in terms of the dynamical system characterized by Eqs. (1) - (3). However, in a generic case the system is governed by the Eqs.(1) - (3) seems to be not integrable and we examine its behaviour by using numerical analysis. In order to represent some characteristic features of the problem we have chosen the structure where the slabs a and b are taken to be GaAs and $\beta - BaB_2O_4$ with $f = 0.03$.

We studied the evolution of the intensities $|A_j|^2$ $(j = 1, 2, 3)$ for four particular initial conditions which correspond to various initial distributions of the energy among the individual modes. The evolution of the intensities of the modes reveal two interesting features. Namely, when the energy is distributed to the second harmonic, all amplitudes display nearly harmonic behavior, while in the cases when the input energy into the second harmonic is zero leads to more irregular behaviour of all the modes. Then as a characteristic feature common to all cases considered for the system we observe that there is no total energy transfer from the fundamental mode into the higher harmonics (as it would happen, say, in the case of SHG when the input energy is concentrated in the fundamental mode). Moreover, nonzero energy input of the second or the third harmonic results in decreasing the amount of the energy transferred to the modes. The highest rate of the energy transfer from the fundamental mode to the second and third one is observed in the case when neither second nor third harmonic are initially excited.

In a particular case, when the Kerr nonlinearty is negligible (1)-(3) has an interesting particular solution as follows

$$A_1 = i\alpha_1 \mathrm{sech}(\eta t), \quad A_2 = i\alpha_2 \tanh(\eta t), \quad A_3 = i\mathrm{sech}(\eta t) \tag{6}$$

where $\eta = 3\gamma_1\alpha_1\alpha_2$ and coefficients α_j are expressed through γ_j. This solution describes energy transfer from the first and third harmonic to the second one.

More generally, when all λ are equal to zero we sutudy the stationary points of the respective dynamical system and prove that they exist only at $H = 0$. Such points corresponds to situation where the energy of the electromagnetic field is either distributed among modes or concentrated in one of them and energy exchange among modes does not occur any more. In this case it is possible to arrange the "fractional" frequency conversion $\omega \to \frac{2}{3}\omega$. If $H \neq 0$ the dynamics is characterized by permanent energy exchange among modes.

The solution (6) is a counterpart of the localised wave (soliton) solution which is described by the system of equation

$$\frac{i}{\omega_1}\left(\frac{\partial A_1}{\partial t} + v_1\frac{\partial A_1}{\partial x}\right) + \gamma_3\bar{A}_2A_3 + 2\gamma_1\bar{A}_1A_2 = 0 \tag{7}$$

$$\frac{i}{\omega_2}\left(\frac{\partial A_2}{\partial t} + v_2\frac{\partial A_2}{\partial x}\right) + \gamma_3\bar{A}_1A_3 + \bar{\gamma}_1A_1^2 = 0 \tag{8}$$

$$\frac{i}{\omega_3}\left(\frac{\partial A_3}{\partial t} + v_3\frac{\partial A_3}{\partial x}\right) + \bar{\gamma}_3A_1A_2 = 0 \tag{9}$$

where v_j are the group velocities. This system admits coupled mode solution in a form of coupled bright and dark solliton solution which properties are investigated.

VVK is supported by FEDER and Program PRAXIS XXI, grant N^0 PRAXIS/2/2.1/FIS/176/94. The work has been partially supported by the bilateral agreement JNICT - Czech Academy of Sciences.

A new class of optical solitary waves: *embedded solitons*

Alan R. Champneys
Engineering Mathematics Dept., University of Bristol, Bristol BS8 1TR, UK;
e-mail a.r.champneys@bris.ac.uk; fax +44-117-925-1154 phone +44-117-928-7510

Boris A.Malomed
Interdisciplinary Studies Dept., Faculty of Engineering, Tel Aviv University, Tel Aviv 69978 Israel; e-mail malomed@eng.tau.ac.il; fax +872-3-640-6399; phone +872-3-640-6413

It is commonly held that a necessary condition for the existence of solitons in various nonlinear-Schrödinger-type models is that the soliton's frequency (spatial or temporal) must not fall into the continuous spectrum of radiation modes. The aim of this work is to show that this is not true. We demonstrate that several nonlinear optical models support a new class of *codimension-one* solitons (i.e. existing at isolated frequency values) that are *embedded* into the continuous spectrum. This is possible if the spectrum of the linearized system has (at least) two branches, one corresponding to exponentially localized solutions, and the other to radiation modes. For embedded soliton (ES) the latter component should exactly vanish, at some discrete values of the frequency.

In a recent work [1], the first examples of embedded solitons were found in the generalized Thirring model (GTM) [2] of a nonlinear optical fiber with a Bragg grating, to which second-order spatial dispersion or diffraction terms are added as a *singular perturbation*. Actually, this extended GTM has a broader physical meaning than was assumed in [2]; the second-order terms appear if one derives GTM from Maxwell's equations, taking into account the *wave* terms at next order.

The study of ES carried out in [1] gives rise to several questions. First, can ES be stable? Second, since only quiescent ES were found in [1], can moving ES occur, as these would appear more feasible to observe in practice [3]? Finally, since the nonlinearity in GTM is cubic, can ES be supported by pure *quadratic* ($\chi^{(2)}$) nonlinearities. Very recently [5], the first question was partially answered in a model [4] with competing $\chi^{(2)}/\chi^{(3)}$ nonlinearities. There by an argument applicable to a class of ES-systems, the solitons were found to be *semi-stable* (see below). In this work, we answer positively the second and third questions, by finding moving solitons in GTM, and many distinct ES in a simple three-wave model with pure $\chi^{(2)}$ nonlinearity [6] (note that in [5] no ES were found without cubic terms). These results, along with those in [1] and [5], clearly show the ubiquity of ES in nonlinear-optical models.

We start with the GTM with wave terms (with carrier wavenumber k):

$$iu_t + iu_x + (2k)^{-1}\left(u_{xx} - u_{tt}\right) + \left[(1/2)|u|^2 + |v|^2\right]u + v = 0, \tag{1}$$

$$iv_t - iv_x + (2k)^{-1}\left(v_{xx} - v_{tt}\right) + \left[(1/2)|v|^2 + |u|^2\right]v + u = 0. \tag{2}$$

$u(x,t)/v(x,t)$ are right-/left- traveling waves coupled by resonant reflection on a grating. Eqs. (1),(2) conserve three integrals: a Hamiltonian, and energy and momentum

$$E \equiv \int_{-\infty}^{+\infty}\left[|u(x)|^2 + |v(x)|^2\right]dx \quad \text{and} \quad P \equiv i\int_{-\infty}^{+\infty}\left(u_x^* u + v_x^* v\right)dx\,. \tag{3}$$

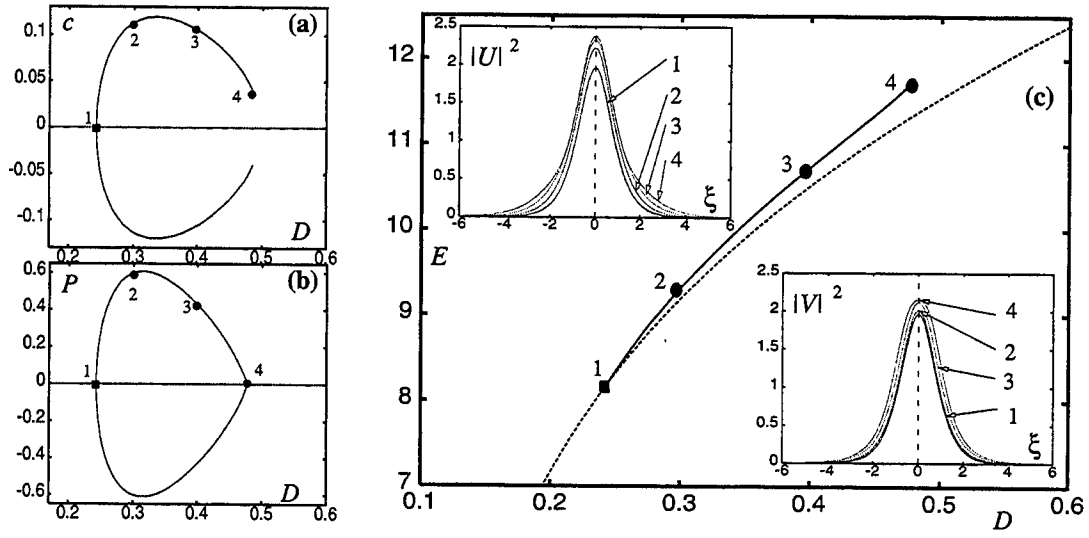


Figure 1: The branch of the moving embedded solitons: the velocity (a), momentum (b), and energy (c) vs. D, with insets showing the shape of the solitons at labeled points. The quiescent-soliton branch from which the moving solitons bifurcate is also shown.

Solitons solutions take the form $u(x,t) = \exp(-i\Delta\omega t)\, U(\xi)$, $v(x,t) = \exp(-i\Delta\omega t)\, V(\xi)$, where $\xi \equiv x - ct$ and c and $\Delta\omega$ are velocity and frequency shift. $U(\xi)$ and $V(\xi)$ satisfy

$$\chi U + i(1-C)U' + DU'' + \left[(1/2)|U|^2 + |V|^2\right] + V = 0, \quad (4)$$

$$\chi V - i(1+C)V' + DV'' + \left[(1/2)|V|^2 + |U|^2\right] V + U = 0, \quad (5)$$

where $\chi \equiv \Delta\omega + (\Delta\omega)^2/2k$, the effective velocity is $C \equiv (1 + \Delta\omega/k)c$, and an effective dispersion coefficient is $D \equiv (1 - c^2)/2k$. The same equations were derived in [1] for: (i) a nonlinear fiber grating including spatial dispersion effects; and (ii) a planar waveguide with a Bragg grating of parallel scores, taking diffraction into regard, and t replaced by a propagation coordinate z.

Quiescent ($c = 0$) ES in the present model were found by numerical continuation in [1]. We present here, for the first time in any model, results on moving ES. Theoretical analysis and numerical solution show that quiescent ES *cannot* be directly continued into moving ones. Nevertheless moving ES exist but they are *codimension-two* solutions, being isolated in both energy and momentum, i.e. described by curves $E(D)$ and $P(D)$ (or $C(D)$ and $\chi(D)$). Out of the three bands of quiescent ES found in [1], only one, corresponding to the smallest values of D gives rise, through a bifurcation, to branches of moving ES. These branches are shown, in various forms, in Fig.1. They terminate where ES pass into the parameter regions of ordinary (non-embedded) solitons. Note that the momentum of the moving ES vanishes at a *nonzero* velocity where the branches terminate.

The energy plays a crucial role in the general analysis of ES stability [5], given that ES exist at isolated values of energy. Hence, any small perturbation which slightly increases energy, is safe, while energy-decreasing perturbations trigger slow (sub-exponential) decay into radiation. In fact ES are semi-stable [5], i.e., stable to linear approximation, but subject to a weakly growing (power-law) *one-sided* instability. Physically this suggests that ES may be observed in experiments, as their existence time/propagation distance is large.

In the light of these stability ideas, one implication from Fig. 1 is that this is, essentially,

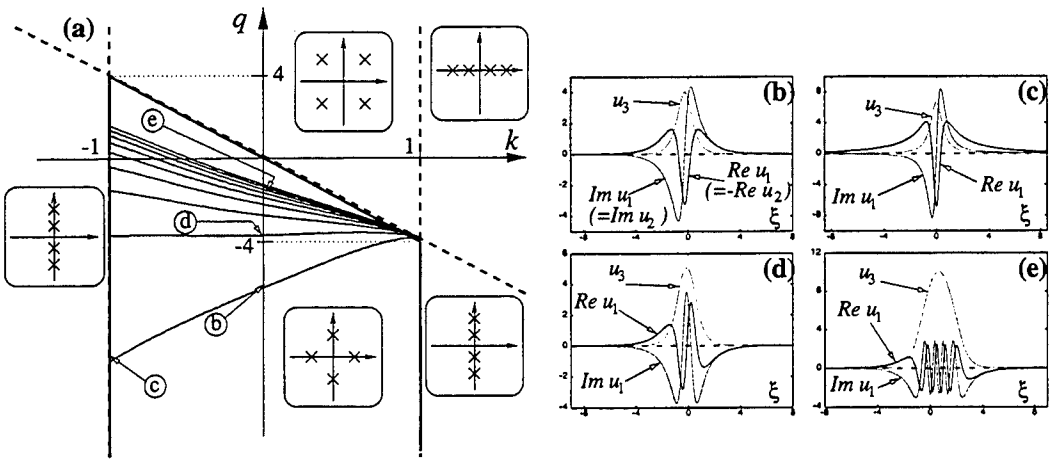


Figure 2: (a) The (k, q) parameter plane of the three-wave model (6),(7) where the linear analysis (summarized in the inset boxes) show that ES can occur only in the region inside the bold lines. The bundle of curves emanating from the point $(k = 1, q = -4)$ are branches of embedded-soliton solutions with $c = 0$. (b)-(e) depict solutions at the labeled points.

a *tri-stable* system, with transitions possible from moving to quiescent ES. Hence the system has potential for use in optical memory. If an incoming ES represents a bit of information, its transition into a quiescent ES implies the incoming bit could be captured and stored in the memory. Estimates of the physical values for experimental observation of these ES in Bragg-grating fibers shows that at carrier wavelength $\lambda \sim 1.5$ μm one needs extremely narrow ~ 10 fs pulses, which can be created in principle. The velocity of the moving ES would be $\lesssim 1/10$ of the normal light speed.

Finally, we report on the easy observation of ES as *spatial solitons* in a planar waveguide model with $\chi^{(2)}$ nonlinearity [6], in which two components of a fundamental harmonic $v_{1,2}$ are coupled by Bragg reflection on a grating of scores parallel to the propagation direction z:

$$i(v_{1,2})_z \pm i(v_{1,2})_x + v_{2,1} + v_3 v_{2,1}^* = 0, \quad (6)$$

$$2i(v_3)_z - qv_3 + D(v_3)_{xx} + v_1 v_2 = 0, \quad (7)$$

Here v_3 is the second-harmonic field, x is the normalized transverse coordinate, q is a mismatch parameter, and D is an effective diffraction coefficient. Solutions to Eqs. (6) and (7) are sought for in the form $v_{1,2}(x,z) = \exp(ikz)\, u_{1,2}(\xi)$, $v_3(x,z) = \exp(2ikz)\, u_3$, with $\xi \equiv x - cz$, c being the slope of the soliton's axis relative to the propagation direction z.

In this model, we have found many ES branches. A bundle of the $c = 0$ branches is displayed in Fig. 2. Solutions with $c \neq 0$ have been found too, and their properties studied in full detail.

[1] A.R. Champneys, B.A. Malomed, and M.J. Friedman, Phys. Rev. Lett. **80**, 4169 (1998).

[2] D.N. Christodoulides and R.I. Joseph, Phys. Rev. Lett. **62**, 1746 (1989); A. Aceves and S. Wabnitz, Phys. Lett. A **141**, 37 (1989).

[3] B.J. Eggleton, R.E. Slusher, C.M. de Sterke, P.A. Krug, and J.E. Sipe, Phys. Rev. Lett. **76**, 1627 (1996).

[4] S. Trillo, A.V. Buryak, and Y.S. Kivshar, Opt. Comm. **122**, 200 (1996).

[5] J. Yang, D.J. Kaup, and B.A. Malomed, "Embedded solitons in second-harmonic-generating systems", preprint.

[6] W.C.K. Mak, B.A. Malomed, and P.L. Chu, Phys. Rev. E **58**, 6708 (1998).

phase-matched second harmonic generation in composite planar waveguide

M. ALSHIKH KHALIL and G. VITRANT
Laboratoire d'Electromagnétisme, Microondes et Optoélectronique, URA CNRS 833, ENSERG,
38 ave des Martyrs, BP 257 , 38016 Grenoble Cedex, France
alshikh@enserg.fr, vitrant@enserg.fr

P. RAIMOND, P.A. CHOLLET and F.KAJZAR
CEA-(LETI-Technologies Avancées) , DEIN/SPE, CEA,-Saclay, 91191 GIF sur YVETTE CEDEX, France

Optical second harmonic generation (SHG) in a waveguide structure has opened the possibility to make compact short wavelength coherent sources. Phase matching in waveguides can be realised by different methods like anomalous dispersion (ADPM)[1], quasi-phase-matching (QPM)[2], counter propagating phase-matching (CPPM), and modal dispersion phase-matching (MDPM)[3]. Here we report on the the preparation and optical characterization of composite waveguides for efficient modal phase-matching. These guides are composed of an ion-exchanged glass substrate top-coated with a layer of nonlinear optical (NLO) polymer. The high-index planar guides are formed by Tl ion-exchange process in KF3 glass substrate. There are two advantages in using Tl ion-exchange: First, the high index variation of the order of $\Delta n \approx 0.05$ which makes the structure relatively insensitive to the fluctuations of the polymer index. Second, these types of waveguides present low propagation losses ($\leq$ 0.1dB/cm). The modes that propagate through the structure have part of their intensity in the polymer and part in the ion exchanged glass substrate. The advantage is to reduce the propagation losses and to maximize the overlap integral. The active layer have been produced with Para-nitroaniline/poly(methyl methacrylate)(PNA-PMMA) side-chain polymer (molar ratio 50:50). The absorption maxima and the cutoff wavelength were measured as 392 nm and 480 nm respectively. Therefore, there is a weak absorption in the short wavelength region, so it is useful for manufacturing a coherent short wavelength source.

A thin film (PNA-PMMA) was deposited by spin coating. The speed of rotation determines the thickness of the polymer. The thickness and the effective indices of the polymer were measured using the m-line technique. Directly following the spinning step the polymer layer is hard-backed in an oven, held at 120 °C for about one hour to eliminate the residual solvent. The glass transition temperature (Tg) of the host polymer is 98°C. The film is poled by a corona discharge just below the Tg of the host polymer to align the dipole moment perpendicularly to the substrate. The high voltage (7 kV) was applied by means of a tungsten needle located at about 1.5 cm from the substrate for 5 minutes. The samples were allowed to cool down to room temperature with the poling field on.
The refractive effective indices of the composite wave-guide were measured with TM polarized light using the prism coupling technique. The refractive index data were fitted with a three term Sellmeier equation.

Modal dispersion phase matching (MDPM) can be realized by adjusting the waveguide thickness and the time of ion-exchange. So, we have

$$n_{eff}^{TM0}(\omega) = n_{eff}^{TM2}(2\omega) \qquad (1)$$

in our case. The efficiency of the harmonic generation process is proportional to the spatial overlap of the fundamental and (SH) waves. This integral is given by:

$$\kappa_{nm}^2 = \frac{\left\{\int_{\text{active layer}} (E_m^{\omega})^2 E_n^{2\omega} dz\right\}^2}{\int_{-\infty}^{\infty} (E_n^{2\omega})^2 dz \left\{\int_{-\infty}^{\infty} (E_m^{\omega})^2 dz\right\}^2} \quad (2)$$

where E_m^{ω} is the electric component of the m^{th} mode at the pump frequency ω. Our numerical calculation of the overlap integral for $TM_0^{\omega} \rightarrow TM_2^{2\omega}$ gives $\kappa_{02}^2 = 0.84 \times 10^4 m^{-1}$.

The refractive index profile and the optical mode profiles in function of Z (Z is the poling axis perpendicular to the direction of propagation) are shown in Figure 2. We see that this structure allows the positive contribution of both fields. This leads to a significant improvement of the overlap integral in Equation (2).

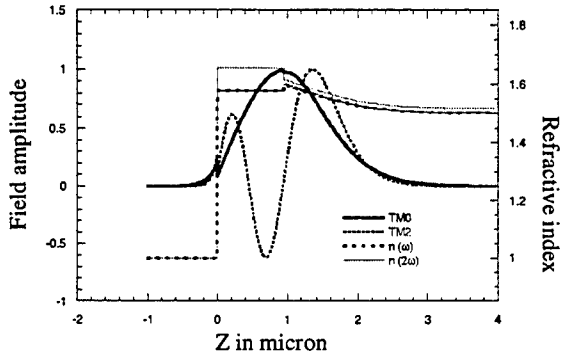


FIG.2. Refractive index profile and normalized electric field profiles of $TM_0^{\omega} - TM_2^{2\omega}$ modes. From 0 to 0.98 μm is the polymer layer. Beginning at Z>0.98 μm: glass substrate and ion-exchange guide.

Frequency doubling was studied by prism coupling the beam delivered by a tunable optical-parametric-oscillator pumped by the third harmonic (355 nm) of Q-switched Nd-YAG laser. This laser has a pulse duration of 10 ns and repetition rate of 10 Hz. The second harmonic power is measured versus the angle of incidence for a given pump wavelength λ=1.018μm. We obtain a peak which occurs for θ=-4.494°. However this maximum does not correspond to phase matching. Indeed, it corresponds to the excitation of the guided mode at the fundamental wavelength, phase-matched excitation of guided mode at harmonic wavelength is only satisfied if the phase matching condition in Eq.(1) is fulfilled. Resonance curves have been shown for different wavelength. The obtained maximum of conversion efficiency is plotted versus the second harmonic wavelength in Figure 3. As a result the maximum which appears in Figure 3. corresponds to the phase matching condition.

The second-harmonic conversion efficiency generated in a waveguide of length L for TM fundamental and TM harmonic is given by

$$\eta = P_{2\omega} / P_{\omega} = \frac{\omega^2}{2\varepsilon_0 c^3} \frac{\chi_{33}^2}{(n_{\text{eff},m}^{\omega})^2 n_{\text{eff},n}^{2\omega}} \times \text{sinc}(\Delta\beta_{m,n} \frac{L}{2}) P_m^{\omega} L^2 \kappa_{nm}^2 \quad (3)$$

where superscripts 2ω and ω correspond to the harmonic and fundamental frequencies, respectively, $n_{\text{eff}} = \beta / k$ is the effective refractive index, χ_{33} is the nonlinear optical coefficient, L is the propagation length, P is the power and $\Delta\beta_{m,n} = \beta_n^{2\omega} - \beta_m^{\omega}$ is the phase mismatch.

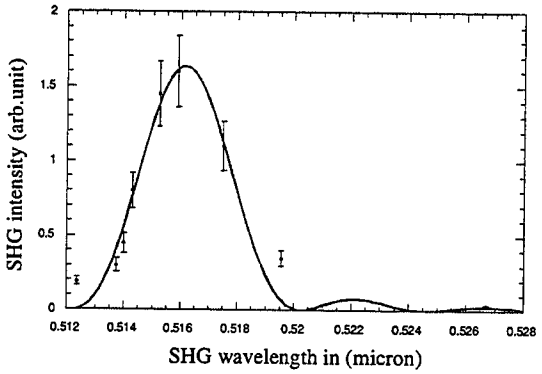


FIG. 3. SHG tuning curves: experimental data and theoretical fitting curves.

Figure 3 displays the experimental points and the theoretical fit according to Eq.(3). It shows phase-matching profile as a function of the SH wavelength. The measured phase-matched SH wavelength is estimated to be 0.516 μm. The measured polymer thickness is equal to 0.98 μm. The measured value of phase matching n_{eff} is 1.5642. These values are in close agreement with the numerical simulation. The propagating mode of the harmonic wave in this nonlinear waveguide was confirmed to be TM2, whereas that of the fundamental was TM0.

The spot size of the incident beam is 0.73mm(H)×1.1mm(V). We have obtained a conversion efficiency of 0.45% for an incident average power of 4 kW. This value is in close agreement with the one calculated from Eq.(2), if we assume $\chi_{33} = 3\text{pm} / \text{V}$ for the polymeric film.

In conclusion, we have presented a new method for efficient second harmonic generation. The conversion efficiency was $\eta = 4.5 \times 10^{-3}$. Larger conversion efficiencies can be obtained by confining light into a composite channel guide. In theses guides, the light is confined almost entirely into the polymer layer, allowing the most efficient use of the optical nonlinearity. Therefore, we can quite easily increase the efficiency by a factor of 1000. Using more efficient nonlinear polymers with higher nonlinearities could further increase the efficiency. The most important feature is that we can monitor the SH wavelength by adjusting the parameters of the ion exchange and the thickness of the polymer layer.

1. T.C. Kowalczyk, K.D. Singer, and P.A. Cahill, Proceeding of SPIE Vol.**2527**, 49 (1995).
2. G. Khanarian, R. A. Norwood, D. Haas, B. Feuer, and D. Karim, Appl. Phys. Lett. **57**, pp. 977-979, 1990.
3. M. Jäger, G.I. Stegeman, S. Yilmaz, W. Wirges, W.Brinker, S. Bauer, M. Ahlheim, M. Stähelin, B. Zysset, F. Lehr, M. Diemeer, and M. C. Flipse, J. Opt. Soc. Am. B **15**, 781 (1998).

Photochromic properties of PMMA-DR1 functionalized polymer films : Evidence of reversible trapped molecular states

Guy Vitrant, Amparo Rodriguez, Xavier Grégoire, Nadege Bodin.
LEMO-ENSERG, BP257, 38016 Grenoble, France.
name@enserg.fr

P.A. Chollet and F. Kajzar
DEIN/SPE - CEA/LETI, 91191 Gif sur Yvette, France.

Introduction.

Photosensitive organic polymers have potential wide-range applications in novel high-performance and low-cost optoelectronic devices. These materials present interesting features on the reversible control of the refractive index and the birefringence which can be applied not only for optical storage, dynamic holographic recording [1] but also for optical control of integrated optical devices. One of the major advantages of these photochromic materials are the large refractive index variations wich can been obtained (up to $\Delta n=0.1$) as compared to what is reached by electro-optical Pockels effect.

In this work we report on measurements of photoinduced optical anisotropy in thin-films of poly(methyl methacrylate) (PMMA) functionalized with Disperse Red 1 (DR1). Under uniform ilumination anisotropy is studied both on the refractive index and on the absorption. We have independently measured the time evolution of the two indices, $n_{//}$ and $n_{\perp}$, parallel and perpendicular to pump light polarization. The results of experimental data are in agreement with the ones of ref. [2] where the birefringence was studied as the difference of the two indices, $\Delta n = n_{//} - n_{\perp}$. However, in contradiction with what is usually admitted, we found experimental evidence that molecular orientation is not able to explain all of the observed results and that it is necessary to invoke a strong contribution from trapped molecular states. This property open new possibilities of applications of such molecular systems.

Experimental set-up and procedure.

Refractive index measurements have been carried out from the study of the grating coupler version of the ATR setup [3]. In this configuration, shown on fig. 1, the polymer guiding film (functionalized with DR1 at 35% molar concentration) is deposited by the spin-coating technique on a silica substrate in which a grating has been previously etched. The grating of period $\Lambda=0.7\mu m$ and of depth $0.15\mu m$ allows the guided mode excitation on the first order. The film is thick enough ($e = 0.635\mu m$) to support two TE and two TM modes at the probe wavelength. From the measurements of the effective indices of these 4 modes, it is possible to deduce the refractive indices n_x, n_y, n_z of the polymer film as well as its thickness e.

The four effective indices are recorded using the experimental set-up shown on fig. 2. A probe beam, coming from a low intensity cw He-Ne laser ($10\mu w$) at the wavelength of $\lambda_s=632.8$ nm, is focused on the sample with the correct angle of incidence to excite guided modes. Birefringence is photo-induced by a pump beam emitted from the green line ($\lambda_p=514$nm) of an argon laser linearly polarized along y which is normally to the sample. The emergent resonance dark lines associated with the excited modes are automatically recorded as a function of the incident intensity and of the angle of incidence with a computer-controlled CCD acquisition system wich allows us to monitor polymer film refractive indices variations.

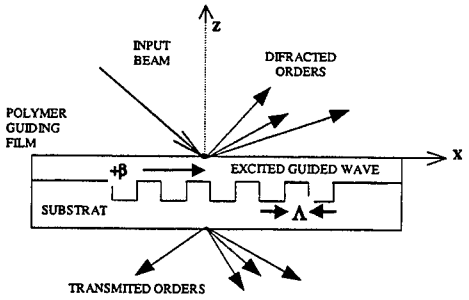


Fig. 1. Schematic representation of the grating coupler configuration.

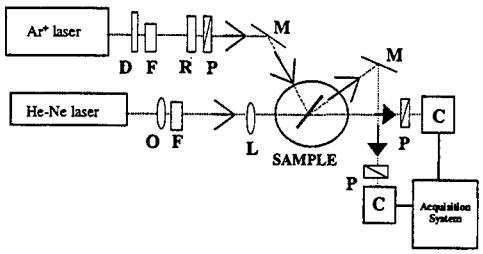


Fig. 2. Experimental set up used for the measurement of the effective indices in the PMMA/ DR1 sample. M1,M2: mirrors; F: filters; L: lens; P: linear polarizers; R: quarter-wave plate; C: CCD camera; D: dispersive plate; O: objective.

Experimental results and analysis.

The results presented on figure 3 were obtained using a y-polarized incident pump beam which is sent for 300s approximately, starting at t=0. with an incident irradiance of 20.1 mW/cm^2. Variations of n_y and n_x are respectively plotted on left and right graphs. During pump illumination, we observe a strong decrease ($\Delta n \approx -0.04$) of the refractive index n_y along the pump polarization. At the same time the refractive index along the axis perpendicular to the pump polarization is only decreased by 0.002. After pumping, the refractive index relaxes to a stationary level and does not return to its initial state even after a long stay in dark period. As a result, a memory effect is obtained.

After relaxation, the average refractive index $\overline{n} = (n_x + n_y + n_z)/3 = (n_y + 2n_x)/3$ does not return to its initial value. A net variation $\Delta\overline{n} \approx -0.025$ is observed.

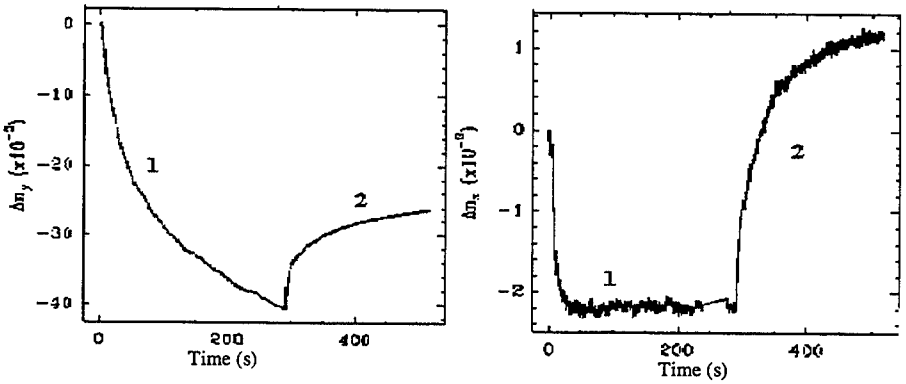


Fig. 3. Evolution of the photoinduced birefringence in a polymeric thin film, PMMA/DR1at 35% molar concentration of thickness e=0,635 μm: (1) under the pump-on period, (2) under relaxation period. (a) photoinduced birefringence along the pump beam polarization .(b) photoinduced birefringence along the axis perpendicular to the pump beam polarization.

The long term stability of the refractive index change has been tested over 24 hours after pumping. On figure 4, starting at point (A), n_y decreases till (B) during parallel pumping. Then stopping the pump in (C), it quickly recovers at the beginning with a characteristic time of the order of 30s and reaches after several minutes a quasi-stationary state which represents 57% of the maximum refractive index change. At the end of this 24 hour period, the material is far from recovered its initial state, and a strong birefringence remains (39% of the maximum refractive index change) as well as a strong decrease of $\overline{n}$ is noticed.

Based on the observed experimental results, we assume that during the pump-on period, the photoinduced birefringence is principally caused by the angular hole burning. Even after the pump-on period the molecular reorientation seems not to play an important role. Currently admitted model assume that all optically excited molecules rapidly relaxes to the fundamental "trans" state [4]. According to this model, molecular reorientation should be the only physical mechanism at the origin of photo-induced birefringence. But, molecular rotation can not modify the average index of the material and in this case $\bar{n}$ should return to its initial value. So, this is in contradiction with what we observe experimentally. As result, we prove that a permanent change of molecular state is the main phenomenon at the origin of the observed photo-induced birefringence. However, we can not exclude that some molecular reorientation process may exist in addition to permanent molecular modification.

Birefringence measurementes were confirmed by absorption spectrums that were recorded under parallel and perpendicular polarization of the probe and pump beams. As in the case of photoinduced birefringence, the anisotropy in polarization dichroism remains after a long stay of the device in darkness. Both refractive index and absorption anisotropies have been found in good agreement through Kramers-Krönig relations.

The persistent induced anisotropy does not correspond to an irreversible bleaching of the sample. This is proved by the experimental results presented on figure 5. This plot shows the change of optical absorption of a probe linearly polarized along y. The record shows the response to a sequence of 13 pumping conditions, alternatively "relax" (darkness) and y/z pumping polarizations. The change of absorption is fully reversible and no molecular destruction or permanent irreversible change is noticed.

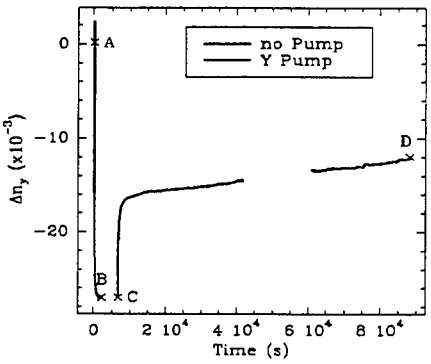


Fig. 4.Stability of the photoinduced birefringence.

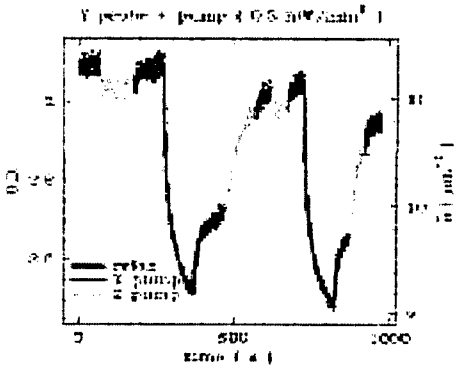


Fig. 5. Reversal of the photoinduced anisotropy in a spin-coated polymeric film: (Y) pump beam parallel to the probe beam. (Z) pump beam perpendicular to the probe beam.

Conclusions.

We have reported the photoinduced memory effect in polymeric thin-films of PMMA functionalized with DRI. We have showed the stability and the reversibility of the induced anisotropy.

The experimental results allows us to derive new results which give a new insight on the underlying physical mechanisms responsible for photo-induced anisotropy. In particular, according to the results shown in this paper, we can predict that a circularly polarized pump erases birefringence as already observed but should induce a decrease of both n_x and n_y.

References

[1] V.P. Pham, T. Galstyan, A. Granger and R.A. Lessard 1997 Jpn. J. Appl. Phys. **36** 429-438.
[2] P. Rochon, J. Gosselin, A. Natansohn and S. Xie 1992 Appl. Phys. Lett. **60** 4.
[3] G.Vitrant et al 1994 Nonlinear Optics: **8** 251-262.
[4] M. Dumont, G. Froc et S. Hosotte 1995 Nonlinear Opt. **9** 327

Chalcogenide glass films for nonlinear optics

S. Spälter, G. Lenz, H.Y. Hwang, J. Zimmermann, S-W. Cheong, T. Katsufuji, M.E. Lines, and R.E. Slusher

Lucent Technologies, 700 Mountain Ave., Murray Hill, New Jersey 07974, USA
Phone: (908) 582 2661, Fax: (908) 582 3260, E-MAIL: sspalter@lucent.com

All-optical switching is considered one of the key technologies for future high-speed optical communication networks. Many different schemes for all-optical switching have been demonstrated in silica fibers exploiting the fiber Kerr nonlinearity. Since the nonlinear refractive index being is small ($n_2 \approx 2.8\times10^{-16}$ cm^2/W in silica), either high power levels or long device lengths are required for switching applications. Compact and low-threshold nonlinear photonic circuits will require novel nonlinear materials combining low losses with ultrafast Kerr nonlinearities at least several hundred times that of silica at the communication wavelength λ=1.55 μm.

Promising candidates for novel switching materials are chalcogenide glasses. Nonlinear refractive indices up to 80 times higher than in silica glass have been reported in chalcogenide glasses[1]. Bandgap engineering is expected to yield even higher values in n_2, while keeping two photon absorption and the corresponding figure of merit (which is defined as $n_2/(\beta\lambda)$ where β is the two-photon absorption coefficient) at acceptable levels[2]. When the optical bandgap energy is tuned to twice the photon energy (1.6 eV for an operation wavelength at 1.55 mm) the nonlinear refractive index is expected to be maximized while two photon absorption is minimized yielding a large figure of merit. Beside high Kerr nonlinearities, chalcogenide glasses offer high optical transparency in the 1-10 μm wavelength region. High quality thin films are easily formed by pulsed laser deposition. Furthermore, chalcogenide glasses exhibit significant photodarkening when exposed to wavelengths corresponding to energies above the bandgap energy[3]. Photodarkening is a photo-induced redshift of the optical absorption edge and is accompanied by an increase in the linear index of refraction in the transparent spectral range. This latter property makes them attractive for patterning of photonic integrated circuits into thin chalcogenide films[4].

Here we report on linear and nonlinear optical properties of three different compounds in the $Ge_{0.25}Se_{0.75-x}Te_x$ system (x = 0, 0.02, 0.08) as well as the demonstration of singlemode waveguides in one of these compounds.

Initially experiments were carried out on polished bulk samples typically 1-2 mm thick. Linear absorption measurements of a 1 mm thick sample $Ge_{.25}Se_{.75}$ showed the typical exponential Urbach edge with a slope of $dE/d(\ln \alpha) = 11.5$ eV^{-1}, down to a level of a few cm^{-1}. At a wavelength of 1.55 μm the absorption was determined to be less than 1 cm^{-1} (limited by dynamic range of the measurement). Next we performed Z-scan measurements to determine the Kerr nonlinearity and the two-photon absorption. Using a femtosecond, high-energy, tunable source measurements were performed at wavelengths 1.2 – 1.55 μm. At 1.55 μm the nonlinear refractive index was found to be ~ 100 times that of silica with a corresponding figure of merit of ~ 2, making it an attractive material for ultrafast all-optical switching. At 1.2 μm close to

the half-gap of this material the Kerr nonlinearity was approximately 400 times that of silica with a slightly larger figure of merit. This indicates that Te can be used to vary the bandgap to a wavelength range that will result in a larger nonlinearity and reasonable figure of merit. We are currently investigating whether the absorption edge can be modified and impurities reduced in order to improve the figure of merit (presumably these mechanisms contribute significantly to the two-photon absorption).

Thin films of thickness 0.5-1 μm were deposited by pulsed laser deposition (PLD) on microscope slides, Hipox silica glass and 10 μm wide silica rib waveguides spaced by 10 μm from targets of bulk $Ge_{0.25}Se_{0.75-x}Te_x$ glass. By AFM measurements, the surface roughness of the chalcogenide films was determined to be as small as 4 nm (rms) for the Hipox silica as well as the rib waveguide substrates. After rapid thermal annealing of the films at 230°C, the optical absorption was measured using a Perkin-Elmer UV-VIS spectrophotometer. Fig. 1 shows the absorption for the three different investigated compositions. The data are represented in the so-called Tauc-form [5] $(h\nu\ \alpha_0)^{1/2} \propto h\nu\text{-}E_g$ such that the value of the optical bandgap is given by the intercept with the $\alpha_0 = 0$ axis. Clearly, the bandgap shifts to lower bandgap energies by increasing the Te concentration in the compounds demonstrating the ability of bandgap engineering in this particular chalcogenide system.

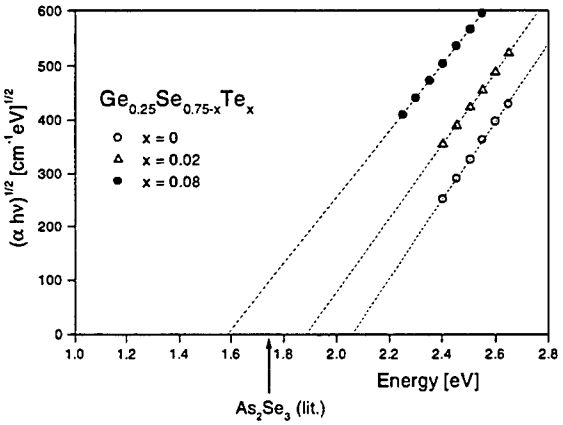


Fig. 1: Absorption of thin chalcogenide films after rapid thermal annealing. The optical bandgap energy corresponds to the intersection with the x-axis.

Next, photodarkening of the films was investigated as a function of exposure time. The results are displayed in Fig. 2. With an exposure wavelength of 532 nm, a bandgap shift of more than 1 % was observed for $Ge_{0.25}Se_{0.67}Te_{0.08}$ while for $Ge_{0.25}Se_{0.75}$ the shift was 3.5%. A slightly higher bandgap shift was found, when the $Ge_{0.25}Se_{0.67}Te_{0.08}$ sample was exposed to 647 nm radiation (although the intensity was lower by a factor of about 2). The better efficiency for exposure with 647 nm is expected since about 10% of the light is transmitted through the 1 μm thin film in contrast to less than 0.1% in the case of exposure with 532 nm radiation.

In agreement with numerical simulations, the 1 μm thin chalcogenide films deposited on top of silica glass rib waveguides exihibit multimode behaviour at a wavelength of 1.55 μm. The index shift corresponding to the photodarkening-induced bandgap shift was used to write singlemode channel waveguides into a planar chalcogenide film. The film was exposed for 210 min at 647 nm through an amplitude mask with 3 μm wide open channels. Sub-picosecond pulses centered at 1.55 μm were coupled into one of the waveguides

and the waveguide output facet was imaged onto a vidicon camera. The intensity profile of the mode is shown in Fig. 3. The well guided mode demonstrates the high quality of the waveguides.

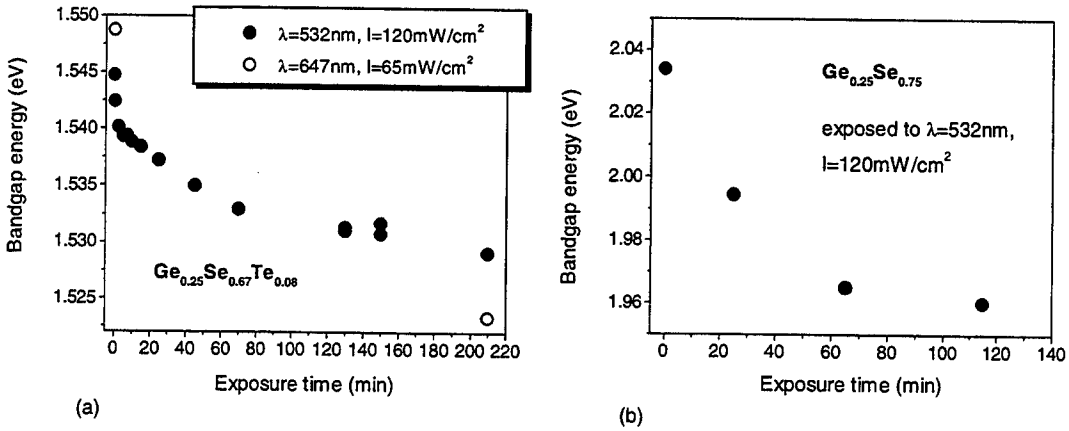


Fig. 2: Shift of the bandgap energy as a function of exposure time for 1 μm thin films of (a) $Ge_{0.25}Se_{0.67}Te_{0.08}$ and (b) $Ge_{0.25}Se_{0.75}$.

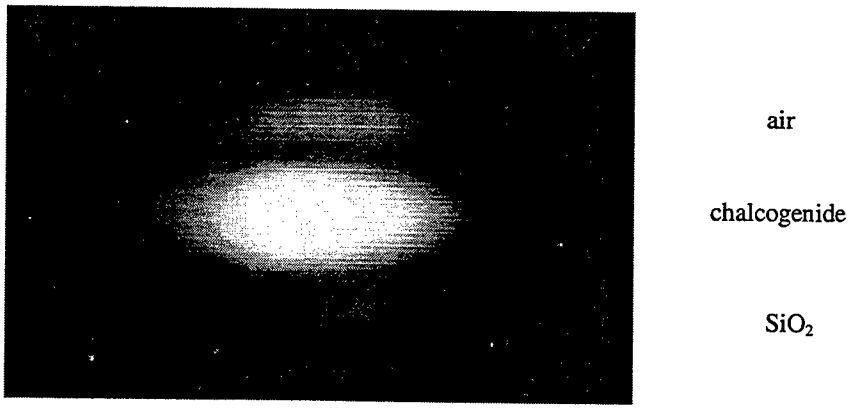


Fig. 3: Single mode pattern at the output facet of a 5 μm × 1 μm waveguide.

Investigations of nonlinear pulse propagation in the photodarkened channels are currently under way. Future directions include the fabrication of Bragg gratings in singlemode chalcogenide waveguides.

[1] M. Asobe, H. Itoh, T. Miyazawa, and T. Kanamori, Electron. Lett. 29, 1966 (1993).
[2] M.E. Lines, J. Appl. Phys. 69, 6876 (1991).
[3] H. Nishihara, M. Haruna, and T. Suhara, *Optical Integrated Circuits*, Opt. and Electro-Opt. Eng. Series, eds.: R.E. Fisher and W.E. Smith (McGraw-Hill, New York, 1989).
[4] S. Ramachandran and S.G. Bishop, Apl. Phys. Lett. 74, 13 (1999).
[5] J. Tauc, Amorphous and Liquid Semiconductors, ed.: J. Tauc (Plenum London, 1974)

WAVEGUIDE WRITING IN As_2S_3 GLASSES BY A TRAIN OF FEMTOSECOND LASER PULSES

T. Cardinal
Institut de le Chimie de la Matière Condensée de Bordeaux, UPR 9048, CNRS, Université Bordeaux I, 33608 Pessac cédex, France, Ph : (33) 5 57 96 25 43, Fax : (33) 5 56 84 27 61
cardinal@icmcb.u-bordeaux.fr

O. M. Efimov, L. B. Glebov, K. A. Richardson, E. Van Stryland, G. I. Stegeman,
Center for Research and Education in Optics and Lasers, University of Central Florida, Orlando, FL 32816 USA

S. H. Park
Yonsei University, Department of Physics, Seoul, Department of Physics, Seoul 120-749, Korea

M. Couzi, J. L. Brunéel
Laboratoire de Physico-Chimie Moléculaire, Université Bordeaux I, UMR 5803, CNRS 33405 Talence cédex, France

Summary

Photoinduced effects in glasses have been widely studied for fabrication of Bragg grating and three-dimensional optical data storage. Recent publications have pointed out the possibility of refractive index change by femtosecond laser exposure of glasses in the transparent spectral region [1, 2]. Controlled writing of waveguide in condensed media based on modification of the optical material properties by laser irradiation may have important implications for example in optical interconnects for high data-rate optical communications systems and integrated optical elements. The ability to arbitrary write permanent waveguides into bulk structure could be very promising in terms of fabrication of integrated optical devices and three-dimensional architecture of such devices.

Chalcogenide glasses are well known to exhibit reversible photo-induced effects to band gap light and sub band gap exposure [3, 4, 5, 6]. The low optical band gap of chalcogenide glasses make them highly sensitive to visible exposure. An exposition to band gap wavelength induces in As_2S_3 glasses a photodarkening, a reduction of the glass band gap, which is, according to Kramers-Kroenig relation, related to the refraction index change in the exposed region. A correlation between reversible photo-induced effects and structural change has been discussed by different authors [7, 8, 9] for bulk and well annealed thin film materials. The increase of As-As homopolar bonds has been demonstrated for an exposure at wavelengths below the band gap.

We report permanent waveguide writing in As_2S_3 bulk glasses by train of femtosecond laser pulses. The diameter of the waveguides was determined not only by the spot size of the focused beam and the energy, but also by the speed of the sample motion during writing. Waveguide with diameters from 1 μm up to 40 μm were written. In Figure 1 are reported micrographs of

waveguide observed by optical microscope. The laser could be used in a stable CW mode with the same average power but in this condition of operation, the waveguide recording ceased even when the average power was increased to nearly 1 Watt.
Indeed the photoinduced structure disappears after a thermal treatment of 2 hours at 25°C below the glass transition temperature, the channel were no longer visible by the optical microscope. The determination of the aperture angle for guiding allowed us to estimate the variation of index Δn between the waveguide and the cladding about 10^{-3}.
A photodarkening of the exposed area was demonstrated. The transmission spectra corresponding to the core of a waveguide (exposed region) of 10 μm diameter and to the cladding (unexposed region) are reported on the figure 2. The measurement indicate a red shift of 15 nm of the band gap that should corresponds to the refraction index variation observed.
Using micro-Raman spectroscopy we propose a description of the chemical mechanism responsible for the index variation and the photodarkening by breakage of As-S chemical bonds and formation of As-As and S-S bonds. The figure 3 shows the increase of the normalized intensity of the vibration band characteristic of As-As chemical bonds (centered at 236 cm^{-1}) on the section of a photo-induced waveguide.
On the basis of these results a two photon absorption origin has been proposed. Similarities between band gap exposure and high intensity sub band gap exposure has been shown. The chemical change produced is very promising for the control and the optimization of the waveguide writing procedure.

References

1- E. N. Glezer, M. Milosavljevic, L. Huang, R. J. Finlay, T. H. Her, J. P. Callan, E. Mazur, Optics Letters, vol 21, N 24, (1996), p2023.
2- K. Miura, Jianrong Qiu, H. Inouye, T. Mitsuyu, Appl. Phys. Lett., 71, 23, (1997), p3329.
3- S. R. Elliott, J. of Non-Cryst. Solids, 81, (1987), p71.
4- S. Ramachandran, S. G. Bishop, J. P. Guo, D. J. Brady, IEEE Phot. Tech. LETT., vol 8, N8, (1996),
5- A. Zakery, P. J. S. Owen, A. E. Owen, J. Non-Cryst. Solids, 198-200, (1996), p769.
6- T. V. glastian, J. F. Viens, A. Villeneuve, M. A. Duguay, K. Richardson, J. Lightwave Tech., vol15, N8, (1997), p1343.
7- M. Frumar, M. Vleck, Z. Cernosek, Z. Plak, T. Wagner, J. Non-Cryst. Solids, 213-214 (1997), p215.
8- J. F. Viens, C. Meneghini, A. Villeneuve, T. Galstian, E. J. Knystautas, M. A. Duguay, K. A. Richardson, T. Cardinal, Submitted to J. Lightwave Technology.
9- K. Tanaka, Solid State Communications, vol 15, (1974), p 1521.

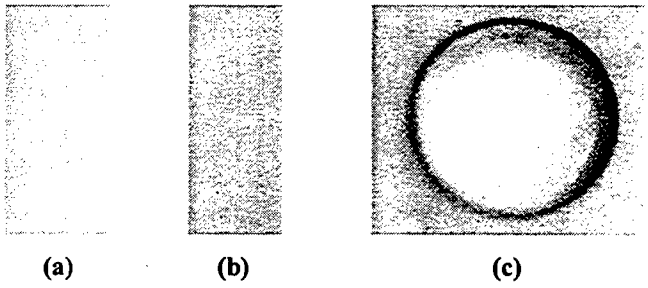


Fig1 Micrographs of the waveguide structure, (a) lateral view of waveguide, diameter ~ 32 μm; (b) lateral view of waveguide, diameter ~ 9 μm; (c) front view of waveguide, diameter ~ 32 μm.

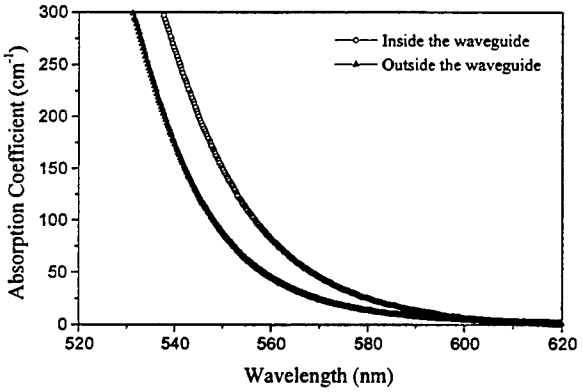


Fig2 Absorption coefficient of the $As_{40}S_{60}$ of the core of the waveguide (exposed region) and of the cladding (unexposed region)

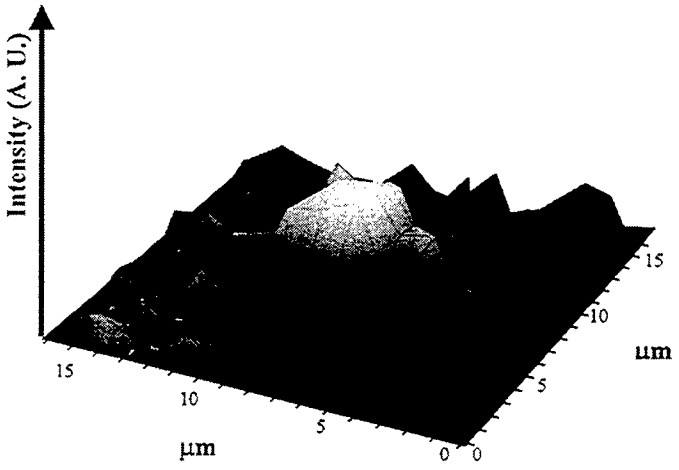


Fig3 Cartography of the evolution of the bands characteristic of As-As chemical bonds (centered at 236 cm^{-1}) of the section of a 5 μm diameter waveguide.

EVIDENCE OF STRUCTURAL ORIENTATIONS IN POLED NIOBIUM BOROPHOSPHATE BULK GLASS

V. Nazabal, E. Fargin, G. Le Flem
I.C.M.C.B, UPR CNRS 9048, Chateau Brivazac, Avenue du Dr Schweitzer, 33608 Pessac cedex, France, Ph : (33) 5 56 84 84 33, Fax : (33) 5 56 84 27 61
Nazabal@icmcb.u-bordeaux.fr

T. Buffeteau, B. Desbat
L. P. C. M., Université de Bordeaux I, UMR 5803 CNRS, 33405, Talence cedex, France

Summary

Non-linear optical properties of transparent materials are the focus of growing interest for elaboration of all-optical devices, such as photonic modulators, optical data storage and telecommunication, or for the spectral extension of laser sources. Basically, the nonlinear optical properties of materials under an electromagnetic field E result from the generation of a polarisation P, which can be expressed as a power series in E:

$$P = \chi^{(1)} + \chi^{(2)} E.E + \chi^{(3)} E.E.E + ...$$

where $\chi^{(1)}$, $\chi^{(2)}$ and $\chi^{(3)}$ respectively are the linear, second and third order nonlinear susceptibilities. As $\chi^{(2)} = 0$ in glasses, Second Harmonic Generation (SHG) is naturally forbidden. Nevertheless, (SHG) was observed in bulk glasses submitted to a thermal poling treatment [1]. The materials reportedly involved are mainly SiO_2- and TeO_2- based bulk oxide glasses. According to Myers et al. two different mechanisms can account for the induced second order susceptibility [1-2]. The first one is due to the coupling between the residual electric field after poling and the glass third-order nonlinearity. The second one is the macroscopic second-order nonlinearity resulting from preferential orientations of polar bonds during poling.

Oxide glasses have been widely investigated for their flexibility of composition, high damage threshold and large transparency regions in the context of high nonlinear indices devices realization [3]. We previously reported a large enhancement of the nonlinear index or $\chi^{(3)}$ susceptibility when introducing large proportions of niobium oxide in a borophosphate glass matrix [4, 5]. According to the first mechanism proposed by Myers et al., glasses with comparable compositions could be good candidates for SHG after poling.

We report on the SHG efficiency and structural characterization of the poled oxide glass of composition 0.7 [0.9 $Ca(PO_3)_2$, 0.1 CaB_4O_7] 0.3 Nb_2O_5. The 2 mm thick glass plate was heated at 300 °C while applying a dc bias of 3 kV during one hour [5]. The homogeneity and intensity of the SHG signal after poling was then controlled by the use of a Q switched (10Hz repetition rate, 10 ns FWHM, 30 mj) Nd:YAG laser pulses at 1064 nm. A lens (50cm focal length) focused on the anodic surface the pump laser beam polarised in the plane of incidence. The angle of incidence was chosen to be equal to 45°. The SHG signal was measured in transmission through the poled glasses [6]. A 1064 nm high reflector, coloured glass filter and a monochromator removed the fundamental radiation. The SHG signal was

Table1-Linear index*, nonlinear $\chi^{(3)}$ susceptibilities* and SHG efficiency

Glasses(mol.%)	n_0* at 1.5μ	$\chi^{(3)*}$ (V^2/m^2) 10^{-21} at 1.5μ	SHG (a. u.) at 1.064μ
Vitreosil SiO_2 glass	1.42±0.03	0.046±0.005	12±1
$0.7[0.9Ca(PO_3)_2,0.1CaB_4O_7]0.3NbO_5$	1.72±0.03	0.91±0.09	1±0.1

**Measurements have been described in ref. 7; $\chi^{(3)}$ values are given here in reference to a standard value of $2.82.10^{-21} V^2/m^2$ for the commercial SF59 glass.*

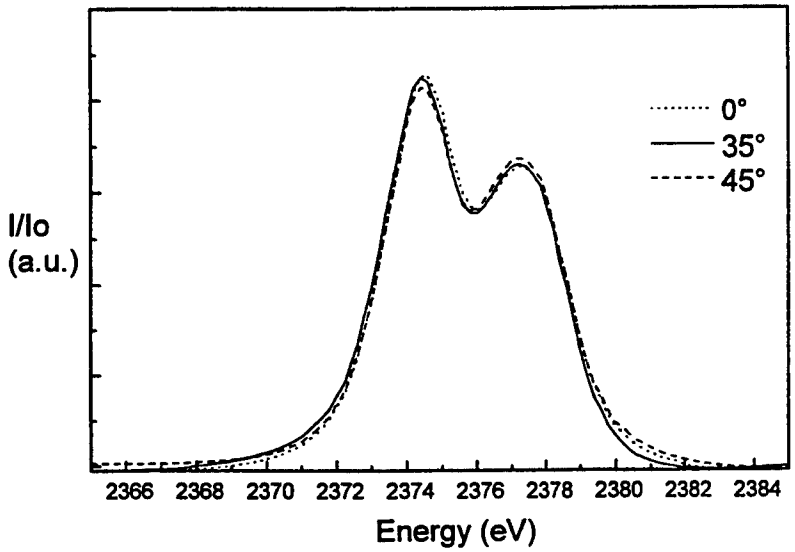


Fig. 1 LIII Nb-edge spectra of the niobium borophosphate glass achieved on the anodic surface

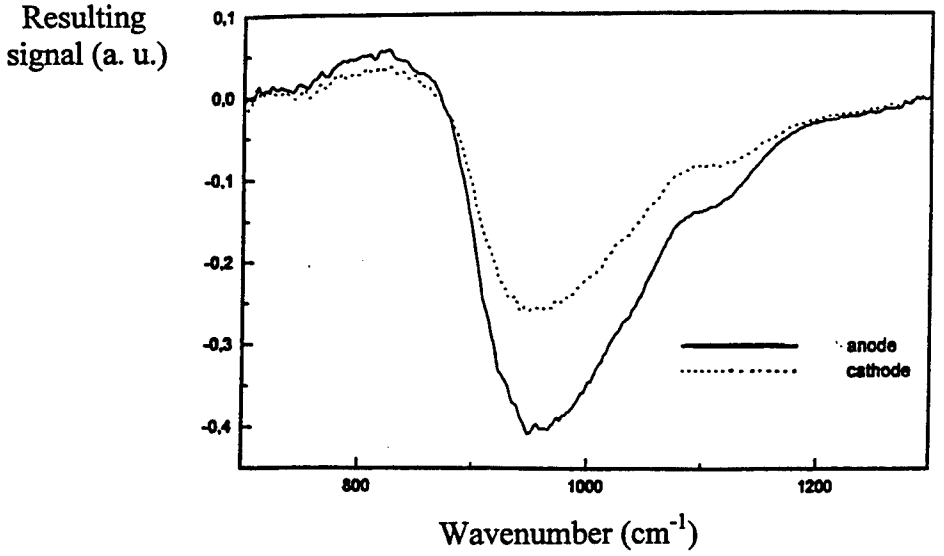


Fig 2 Substraction of the IR reflectance signal of poled anode or cathode surface from the corresponding unpoled surface signal for the niobium borophosphate glass.

recorded with a photomultiplier coupled to a photon counting system. A Vitreosil silica glass reference which was poled under the same experimental conditions was simultaneously measured for comparison. As previously published, the SHG signal was localized close to the surfaces in contact with the electrodes during poling [5]. Measured linear indices, second and third order susceptibilities are given in table1.

Unexpectedly, SHG measurements do not demonstrate a larger efficiency for the borophosphate glass when compared to the silica glass, though a larger $\chi^{(3)}$ value. Nevertheless, experimental conditions of poling have not yet been optimized for the borophosphate glass. They are effectively depending on electrical conduction properties of the glass which are highly correlated with the structure of the glass network.

Structural modifications in the poled glass network near the poled borophosphate glass surfaces were studied by Nb LIII-edge XANES and IR reflectance spectroscopies.

XANES measurements for different angles of the incident polarized beam light with the anode surface of the material are presented on figure 1. Spectra were recorded at LURE (Orsay, France) using the 300mA positron injection current in the SUPERACO storage ring operating at 800MeV. No difference for various angles are observed indicating that no preferential orientation of the niobium oxygenated sites can be evidenced on the anode surface of this glass [6].

IR reflectance experiments were performed using an external reflection attachment (Grosegy, Specoc) at an angle of incidence of 12°. The extinction coefficient can be calculated from the reflectance spectra by the Kramers-Kronig analysis. Structural modifications after poling can be evidenced by calculating the substraction between the poled anode or cathode face reflectance signal and the corresponding unpoled face signal(figure 2). A slight but significant difference appear between 960 and 1150cm^{-1}. The corresponding transitions are attributed to symmetrical and antisymmetrical vibration modes of terminal [PO_3^-] groups on phosphate chains constituting the glass network. The decrease of the signal in this domain can be explained by an orientation of these groups perpendicularly to the anodic surface if the glass.

On the basis of these results, the breakdown of isotropy induced by poling is evidenced. Whether such alterations can account for the measured SHG efficiency in niobium borophosphate glasses needs to be clarified. Ab-initio calculations under investigation could provide promising information.

References

1- R.A. Myers, N. Mukherjee, S.R.J. Brueck, Optics Letters, **16** (1991) 1732-1734.

2- N. Mukherjee, R.A. Myers, S.R.J. Brueck, JOSA B, **11** (1994) 665-669.

3- E. M. Vogel, S. G. Kosinski, D. M. Krol, J. L. Jackel, S. R. Friberg, M. K. Oliver, J. D. Powers, J. of Non-Cryst. Solids, 107 (1989) 244

4- V. Nazabal, E. Fargin, J.J. Videau, G. Le Flem, A. Le Calvez, S. Montant, E. Freysz, A.Ducasse, M. Couzi, J. Of Solid State Chem , **133** (1997) 529-535.

5- T. Cardinal, E. Fargin, G. Le Flem, M. Couzi, L. Canioni, P. Segonds, L. Sarger, A. Ducasse, F. Adamietz, Eur. J. Solid State Inorg. Chem., **33** (1996) 597-605

6- V. Nazabal, E. Fargin, C. Labrugère, G. Le Flem, submitted to J. of Non-Cryst. Solids

7- B. Jeansannetas, S. Blanchandin, P. Thomas, P. Marchet, J.C. Champarnaud-Mesjard, T. Merle-Méjean, B. Frit, V. Nazabal, E. Fargin, G. Le Flem, M. O. Martin, B. Bousquet, L. Canioni, S. Le Boiteux, P. Segonds, L. Sarger, accepted to J. of Solid State Chem.

Optimizing the Conversion Efficiency for the Cerenkov Second Harmonic Generation in Planar Optical Waveguides

Libor Kotacka
Lightwave Device Group, University of Twente, P. O. Box 217, 7500 AE Enschede, Netherlands
Institute of Radio Engineering and Electronics, Chaberska 57, 182 51 Prague, Czech Republic
and
Institute of Physical Engineering, Technical University of Brno, Technicka 2, 616 69 Brno, Czech Republic
kotacka@fyzika.fme.vutbr.cz

Jiri Ctyroky
Institute of Radio Engineering and Electronics, Chaberska 57, 182 51 Prague, Czech Republic
ctyroky@ure.cas.cz

Hugo J. W. M. Hoekstra
Lightwave Device Group, University of Twente, P. O. Box 217, 7500 AE Enschede, Netherlands
h.j.w.m.hoekstra@tn.utwente.nl

The behavior of compact coherent light sources lasing at wavelengths from 600 nm down to green or blue light has already been extensively investigated since 1970s (see e.g. [1,2,3,4]). In this contribution, the coupled mode analysis of second harmonic generation in Cerenkov Regime is presented and the fundamental properties of the SHG conversion efficiency are pointed out. Only $TE^{\omega} - TE^{2\omega}$ conversion is considered, because the results relating to *TM* modes may be deduced similarly as the corresponding results for *TE* modes.

The second harmonic power $P_{2\omega}$ generated in the Cerenkov SHG regime may be written under a non-depleted pump approximation as follows [5]

$$P_{2\omega} = \eta L P_{\omega}^2, \tag{1}$$

where η [1/W] is the normalized SHG conversion efficiency, L is the interaction length and P_{ω} is the power of the fundamental (pump) radiation. The conversion efficiency η obeys the following expression [5,6]

$$\eta = 2\pi\varepsilon_0^2\omega^2 \frac{\beta_{2\omega}}{\rho} d_{33}^2 |I|^2, \tag{2}$$

where d_{33} is the nonlinear coefficient in the substrate (the only substrate is assumed to be nonlinear), $\beta_{2\omega}$ is the propagation constant of the second harmonic radiation and ρ is defined as

$$\rho = 2k\sqrt{n_{s,2\omega}^2 - N^2} \tag{3}$$

where $n_{s,2\omega}$ is the refractive index of substrate at the frequency 2ω, $k = 2\pi/\lambda$, and N is the effective index of the guided mode at the frequency ω. The quantity I is known as an overlap integral defined as

$$I = \int_{-\infty}^{-h} E_{y,\omega}^2 E_{y,2\omega} dx, \tag{4}$$

where $E_{y,\Omega}$ $(\Omega = \omega, 2\omega)$ is the normalized y-component of the electric field of the modes. Since the substrate only is considered to be nonlinear, the integration is carried out over the interval $(-\infty, -h)$; h is the thickness of the guiding layer [7]. It was shown [6,8,9], that the conversion efficiency exhibits a

sharp maximum. The detailed study reveals, that the position of the maximum can be determined as follows. The conversion efficiency maximum occurs if $\rho \to 0$, i.e. when $n_{s,2\omega} = N$. But, assuming $\rho \to 0$, the overlap integral gives a nonzero value under the validity of [8]

$$\sigma \sin(\sigma h) - \Delta \cos(\sigma h) = 0, \tag{5}$$

with $\sigma = 2k\sqrt{n_{g,2\omega}^2 - n_{s,2\omega}^2}$, $\Delta = 2k\sqrt{n_{s,2\omega}^2 - n_{c,2\omega}^2}$, where $n_{g,2\omega}$ is the refractive index of the guiding layer, and $n_{c,2\omega}$ is the refractive index of the cladding, both at the frequency 2ω. The condition (5) results from the normalization constant of the radiation mode at 2ω which appears in overlap integral (4). This normalization constant may be written of the form (according to [7])

$$A_r(\rho) = \left\{ \frac{4\omega\mu_0}{\pi\beta} \left(\frac{\left[\sigma\cos(\sigma h) + \Delta \sin(\sigma h)\right]^2}{\sigma^2} + \frac{\left[\sigma \sin(\sigma h) - \Delta \cos(\sigma h)\right]^2}{\rho^2} \right)^{-1} \right\}^{1/2} \tag{6}$$

It can be seen that for $\rho \to 0$ also $A_r \to 0$ except for cases close to that obeying (5). An inspection of the behavior of $A_r(\rho)$ shows that the value of this normalization constant also continuously differs from zero at a very close vicinity of the values which obey Eq. (5). This fact causes the existence of a very sharp peak of the conversion efficiency (see also [9]). On the other hand from (5), if the thickness of the guiding layer obeys the expression

$$h = \frac{\arctan(\Delta / \sigma) + \pi}{\sigma} \tag{7}$$

(π appears in (6) due to the ambiguity of the function arctan), the position of the peak obeys the modified dispersion equation

$$\frac{\arctan(\delta / \kappa) + \arctan(\gamma / \kappa)}{\kappa} - \frac{\pi + \arctan(\Delta / \sigma)}{\sigma} = 0, \tag{8}$$

where, $\kappa = k\sqrt{n_{g,\omega}^2 - n_{s,2\omega}^2}$, $\delta = k\sqrt{n_{s,2\omega}^2 - n_{c,\omega}^2}$ and $\gamma = k\sqrt{n_{s,2\omega}^2 - n_{s,\omega}^2}$ (according to [7] and putting $N = n_{s,2\omega}$). The subscripts *g, s, c* describe guiding layer, substrate and clad, respectively. Solving this equation one can find that there is only one suitable wavelength which can be converted with the highest conversion efficiency for given indices. This can be done only for a particular thickness of the guiding layer, i.e.

$$h = \frac{\arctan(\delta / \kappa) + \arctan(\gamma / \kappa)}{\kappa}. \tag{9}$$

A detailed study shows [6] that the position of the peak is just at the transition between Cerenkov SHG type and guided-guided SHG type. Therefore the position of the peak can be understood as the cut-off of the $TE_0^{\omega} - TE_1^{2\omega}$ guided SHG.

Fig. 1 depicts the position of the peak of the conversion efficiency for two waveguide configurations as a function of the pump wavelength and the thickness of the guiding layer. The set of points on the left side relates the structure KTP/Ta_2O_5/"cladding" whilst the points on the right represents the structure KTP/Si_3N_4/"clad" (approximately $n_{TaO} \approx 2.1$ and $n_{SiN} \approx 2$; actually, the refractive indices were determined exactly using Sellmeir's relation). It is seen from Fig. 1 that the pair *substrate-guiding layer* determines the region (in Fig. 1 in the wavelength-thickness plane) of the efficient conversion. It can be said that the higher the refractive index of the guiding layer is, the shorter wavelength is efficiently converted and the thinner guiding layer is needed. Further, the cladding has proved to be very important

for the position of the peak. The digits in the Fig. 1 describe the assumed cladding; namely 1 - air, 2 - SiO_2 ($n \approx 1.46$), and 3 - SiON ($n \approx 1.7$). The line connecting the points (1-3) exhibits nearly linear dependence between the wavelength and the thickness. Thus, having any cladding of arbitrary refractive index from the required interval, one can design a device efficiently converting any wavelength within the region determined by the lowest and the highest refractive index of the cladding (between 1 and 3), respectively. An analogous analysis can be performed for the guiding layer except that only particular values of the refractive indices are technically available. This problem can be solved by a suitable combination of two materials for the cladding when one of these materials is assumed to be a "new" cladding. Changing the thickness of the second cladding, so-called *idler*, the peak can be moved *continuously* along the line connecting those two sets of points (within 1-3). Moreover, the refractive index of the idler may be higher than N. Utilizing this, one can easily convert wavelength out of reach for any three-layered waveguide (see points "4a-d" for which $n_{idler} \approx 1.92$). Of course, Eqs. (5), (7), (8) and (9) must be accordingly rewritten for a four-layered system.

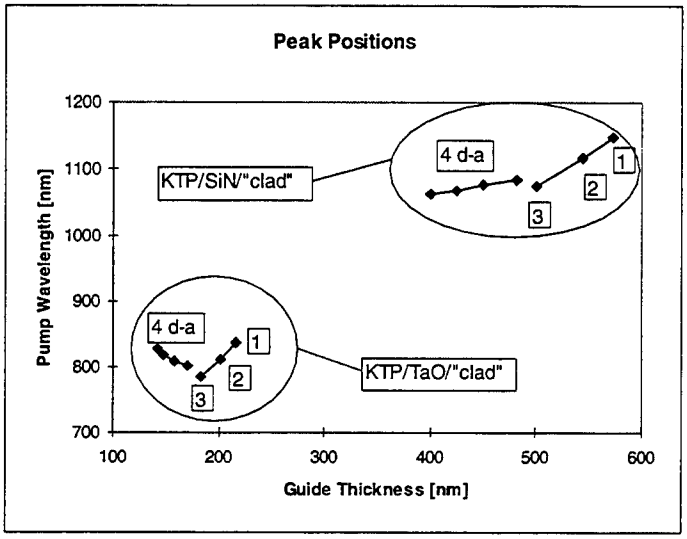


Fig. 1: The peak positions of several waveguide configurations. The digits 1-3 refer to the 3-layered waveguide (see text). The peaks described by 4d-a are relating to the *idler* configuration KTP/"guide"/Y_2O_3/SiO_2. The thickness of the idler is given as follows a - 50 nm, b - 100 nm, c - 150 nm, d - 200 nm.

This work was made within the framework of the EU Project INCO COPERNICUS 96 0194.

References:

[1] M. A. Haase, J. Qiu, J. M. DePuydt and H. Cheng, *Appl. Phys. Lett.* **59**, 1272-1274 (1991).
[2] D. Eger, M. Oron, M. Katz and A Zussman, *Appl. Phys. Lett.* **64**, 3208-3209 (1994).
[3] E. J. Lim, M. M. Fejer, R. L. Byer and W. J. Kozlowsky, *Ell. Lett.* **25**, 731-732 (1989).
[4] H. Yamamoto, T. Sugiyama, J. Jung, T. Kinoshita and K. Sasaki, *J. Opt. Soc. Am. B* **14**, 1831-1837 (1997).
[5] H. Tamada, *IEEE J. Quantum Electron.* **27**, 502-508 (1991).
[6] N. Asai, H. Tamada, I. Fujiwara and J. Seto, *J. Appl. Phys.* **72**, 4521-4528 (1992).
[7] D. Marcuse, *Theory of Optical Dielectric Waveguides.* Academic Press, New York 1974.
[8] R. S. Chang, S. Y. Shaw, *J. Modern Optics* **45**, 103-115 (1998).
[9] J. Ctyroky, H. J. W. M. Hoekstra, L. Kotacka and P. Tobiska , *Proceedings ECIO'99*, Torino Italy, April 13-16, 357-360 (1999).
[10] T. Doumuki, H. Tamada, M. Saitoh, *Appl. Phys. Lett.* **64**, 3533-3535 (1994).

Asynchronous Optical Logic

K.J.Blow, Aston University, Aston Triangle, Birmingham, B4 7ET, UK

A.J.Poustie and R.J.Manning, BT Labs, Martlesham Heath, Ipswich, IP5 3RE, UK

Email: k.j.blow@aston.ac.uk
Tel: +44 (0)121 359 3611 x5278
Fax: +44 (0)121 359 0156

In recent years all-optical logic has been successfully demonstrated in a regenerative mode. The data is synchronous with a local clock and the result of the optical logic is always transferred to the clock. In this way, regeneration is achieved at every optical switch and this gives the system a great deal of stability. A regenerative optical memory [1] can be made which is stable for many hours. We have also demonstrated an all-optical pseudo-random number generator [2] capable of generating sequences with repeat periods longer than the age of the universe and of pipelining multiple copies of shorter tapped shift registers which can be checked using standard electronic bit error rate test sets. Although the use of regenerative logic has many benefits it also incurs the cost of providing sources which can be distributed to each logic gate. Here we will show that, in principle, it is possible to process bit serial data streams asynchronously by which we mean that no local clock is required. The logic architecture will be bit serial so that the bit rate of the data must be matched, within certain limits determined by the length of the packet and the switching window, to the delays in the optical circuits. The regeneration function can then be performed more sparsely with the consequent saving in optical sources.

To be specific, we consider an incoming optical packet where the first bit is defined to be always a 'one'. Marking packets in this way has been considered before e.g. [3] where the first pulse is distinguished through some physical property such as polarisation, intensity or wavelength. In our case this is not necessary and the first pulse will be the same as all the others in the packet thus reducing the transmitter complexity. The simplest function we would want is to produce a single marker pulse that signals the arrival of a packet and can be used to provide subsequent timing information. In figure 1 we show such a circuit.

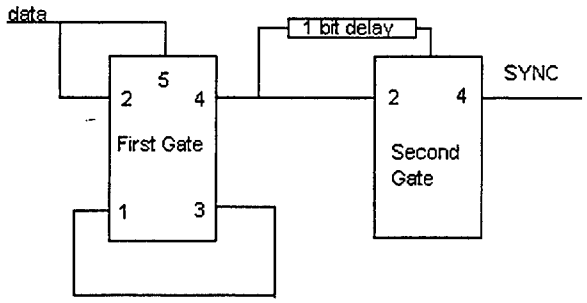


Figure 1

The input packet is split into two and one is used as the switching input (port 5) to the optical gate and the other is supplied as the data to input port 2. In the absence of a switching pulse the gate is configured to be in the bar state and changes to the cross state when a switching pulse arrives. Thus the first 'one' switches a copy of itself into the recirculating loop connecting output 3 to input 1. In each successive time slot either a 'zero' or a 'one' is present. If a 'zero' is applied to the switching input then the gate is left in the bar state and the 'one' in the memory loop continues to circulate. If a 'one' is applied to the switching gate then a one is also applied to input 1. All that happens in this case is that the 'one' initially in the memory loop is exchanged for the 'one' from the data steam. In either case the memory loop remains at a logical 'one' irrespective of the subsequent contents of the packet. Thus output 4 of the first gate goes high on the arrival of the first 'one' and remains in that state. We will discuss the resetting of this circuit later.

The second half of the circuit in Figure 1 detects the transition from 'zero' to 'one'. The output from the first gate is again split into two but now a single time slot delay is introduced between the two copies. The delayed copy is supplied as the switching pulse to input 5 to the second gate and the undelayed copy is supplied to input 2 of the second gate. When the first pulse arrives at input 2 there is nothing at the switching input and the pulse passes to the output at 4. In subsequent time slots a pulse arrives simultaneously at input 2 and the switching input 5 which directs the pulse to output 3 (not shown). Thus

only the first pulse to arrive at the second gate appears at output 4 and this constitutes the synchronisation pulse labelled SYNC in figure 1.

The final question remaining is how to rest the circuit so that the next packet can be recognised. We define our packets to be a fixed number of bits N. The sync pulse can be delayed by N+1 time slots and returned to the switching input of the first gate. Since the packet is of length N time slots the SYNC pulse will arrive after the packet has passed through gate 1 and when the gate changes to the cross state the memory will unload the single 'one' it contains thus resetting the circuit to its initial state.

The major problem with this approach is the use of the recirculating loop around the first gate. The lack of regeneration will lead to cumulative pulse degradation that will place an upper limit on the packet length N. Also, the loop will have to run with less than unity gain in order to avoid lasing. In figure 2 we show the number of consecutive zeros between two pulses which can be tolerated for an amplifier without gain saturation. A relatively small amount of line coding would be required to avoid this possibility.

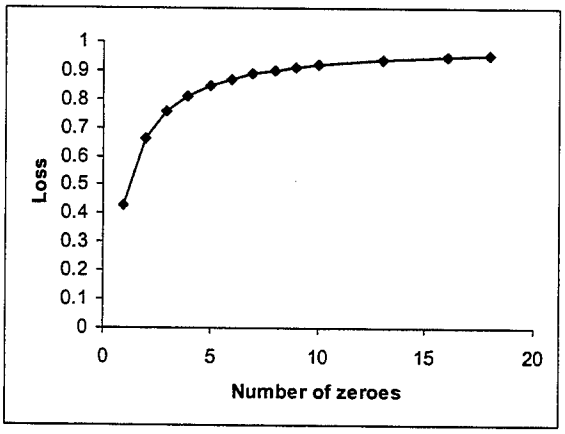


Figure 2

1 A.J.Poustie, K.J.Blow and R.J.Manning, Optics Communications, **140** 184 (1997)

2 A.J.Poustie, K.J.Blow, R.J.Manning and A.E.Kelly, Optics Communications **159** 208 (1999)

3 D.Cotter, M.C.Tatham, J.K.Lucek, M.Shabeer, K.Smith, D.Nesset, D.C.Rogers and P.Gunning, in: G.Prati (Ed.), Photonic Networks and Technologies, Springer-Verlag, Berlin, 401-413, (1997)

A Simple Approach for Estimating Absorption Loss in Organic Thin Solid Films

Shen Yuquan, Li Zhao, Zhao Yuxia, Zhai Jianfeng,
Zhou Jiayun, Qiu Ling,Wang Jianhone
The Institute of Photographic Chemistry, Academia Sinica, Beijing,100101,China

Chen Yingli, Chao Zhuangqi
Department of Applied Physics, Jiaotong University, Shanghai, 200240,China

Edwin YB Pun, Po S Chung
City University of Hong Kong, Tat Chee Avenue, Kowloon, Hong Kong

Summary

Optical loss (OL) is a fundamental and essential parameter of optical materials. It is defined as 10 times the logarithm of light transmittance I/I_0, i.e.,

$$OL = 10 \text{ Log } \frac{I}{I_0} \text{ (dB)} \quad \text{.....(1)}$$

where I_0 and I are the intensities of the incident and transmitted light.

In general, OL includes coupling loss (loss that occurs between the butt-joining of waveguide and optical fiber) and propagation (waveguide) loss. Absorption loss is the primary propagation loss, and is mainly a material intrinsic property.

There are several optical methods for measuring OL, for example, image streak analysis method (ISA or WLS)[1], photothermal deflection spectroscopy(PDS) method [2,3], and so on. However, various light sources are needed in these measurements,. In addition, the technique and the equipment required are usually not familiar to or available for organic material scientists. In order to facilitate the selection of optimal polymer-chromophore systems among vast amount of possibilities, it would be very helpful for material scientists if they could have an approach for OL determination where the techniques and equipment involved are familiar and available to them.

Equation (1) for evaluating absorption related OL can be written as :

$$OL \text{ (dB / cm)} = -10E = -10\varepsilon C \quad \text{.....(2)}$$

Where E and ε, c are the optical absorption (optical density), the molar extinction coefficient, and the molar concentration of the solute, respectively. Eq. (2) indicates that the absorptive OL equals ten times that of the absorption of the system. It is important to mention that for OL determination in solid film, the "E" value in Eq. (2) is the absorption in the transverse direction along the film surface. However, it is not suitable to get a perpendicular absorption value directly from a film and then convert to a value corresponding to the thickness of 1.0 cm, i.e., the E value cannot simply be extrapolated from a few micrometers to a centimeter. This is due to the error in extrapolation and the complexity related with surface effect in thin solid film. However, as Eq. (2) indicates, when ε and C are known, OL is measurable. It is known that ε is a material intrinsic property, and can be determined in UV cell and does not necessary be measured in film form. The molar concentration of a chromophore in polymer film can also be determined by spectroscopic method before the

coating procedure of polymer film. In this paper, we report the details of a simple approach for the determination of OL in solid film by UV-VIS-IR method and its comparison with conventional optical method.

The OL values for the two polyimide polymers determined by the UV-VIS-IR and ISA methods and related experimental data are shown in Table 1.

Table 1 The OL values and related data*

No of the film sample	The "m" value	Chromophore concentration in the polymer(Mol/L)	OL (dB/cm) at λ (nm) =			
			By UV-VIS-IR method		By ISA method	
			750 nm	1300 nm	750 nm	1300 nm
1	0.4	0.65	10.60	1.95	8.0	(1.47)
2	0.7	1.08	17.60	3.24	16	(2.95)

* $\varepsilon_{750nm} = 1.63$ and $\varepsilon_{1300\,nm} = 0.30$

As shown in Table 1, the OL values at 750 nm were calibrated by ISA optical measurements. The values in the parentheses in Table 1 were obtained from OL values at 750 nm by multiplying a ratio of $\varepsilon_{1300nm} / \varepsilon_{750\,nm}$.

As indicated in Table 1, the OL values obtained by the UV-VIS-Near-IR method are consistent with the corresponding data determined by conventional optical measurements.

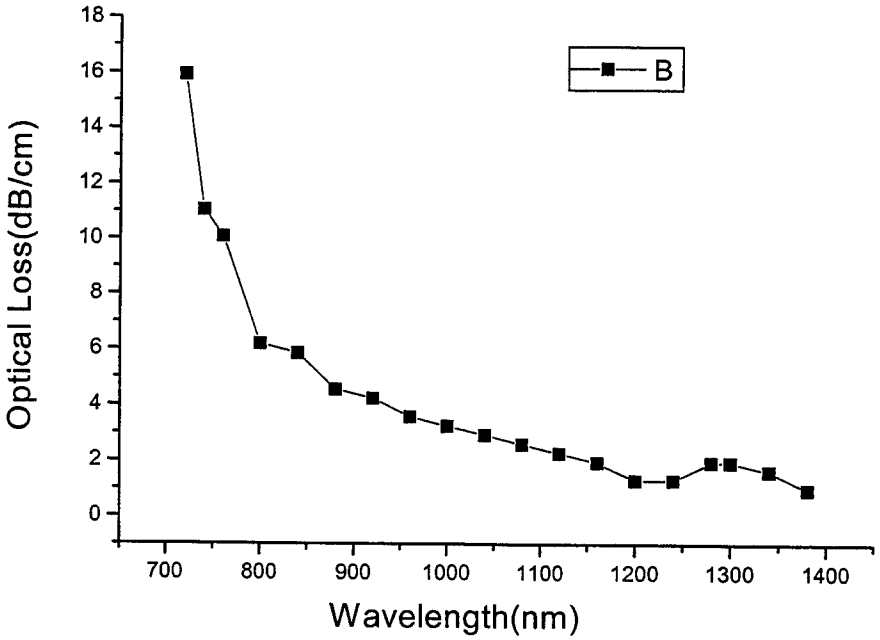


Fig.1 Wavelength dependence of optical loss for a solid film (Sample 2)made from polyimide polymer

According to Eq.(2), OL value at any wavelength can be obtained, as long as the ε value at corresponding wavelength is known. Fig.1 is a plot of a set of OL values at different

wavelengths for a polyimide polymer film.

In conclusion, a simple approach for measuring absorption loss in organic thin solid films has been proposed and demonstrated. The method is applicable to other active or passivity polymer systems. This approach is convenient to material scientists and greatly simplifies the procedure of OL determination, particularly for evaluation OL dispersion performance.

Acknowledgment
The National Natural Science Foundation of China and Chinese National 863 Program Office sponsored this research project

References

1. T.C.Kowalczyk, T.Kosc, and Singer, J.Appl.Phys., 76(4), 2505-2508. 97/75
2. Skumanich,A.,Jurich,M.,and Swalen,J.D., Appl.Phys.Lett., 62,446,1993. 97/75-Ref.18
3. J.T.Yardley, L. Eldada, K.M.T.Stengel, L.W.Shacklette, R.A.Norwood,C.Xu,and C.Wu, SPIE Vol., 3005,155-162. 100/9

Spinning light bullets in second-harmonic-generating media

Yefim Bakman
School of Education, Tel Aviv University, Tel Aviv 69978, Israel; e-mail bakman@ccsg.tau.ac.il; fax +972-3-640-7752

Boris Malomed
Department of Interdisciplinary Studies, Faculty of Engineering, Tel Aviv University, Tel Aviv 69978, Israel; e-mail malomed@eng.tau.ac.il; phone +972-3-640-6413; fax +972-3-640-6399

A theorem guaranteeing the existence of stable "light bullets", i.e., fully localized spatiotemporal solitons, in two- and three-dimensional (2D and 3D) second-harmonic-generation (SHG) media, was proved long ago [1]. However, detailed studies of these solitons have started only recently [2,3]. A variational approximation (VA) for an analytical description of the bullet was developed in [2], and direct simulations have confirmed that stable solitons, close in their shape to the VA prediction, exist indeed [2,3].

In the works [1-3], only nonspinning "bullets" were considered. Spinning spatiotemporal solitons in the 3D SHG medium is a subject of this work. Note that (2+1)D spatial cylindrical solitons with an internal vorticity (which are *not* equivalent to spinning bullets) were recently considered, and it has been found theoretically [4] and experimentally [5] that they are subject to a strong azimuthal instability, exploding into several zero-vorticity solitons. However, cylindrical solitons of the same type with spin 1 were numerically found to be *stable* in a model with the cubic-quintic nonlinearity [6].

The starting point is the system of equations for the fundamental- and second-harmonic (FH and SH) amplitudes u and v [2],

$$iu_z + u_{\tau\tau} + \nabla_\perp^2 u - u + vu^* = 0,\ 2iu_z + \delta u_{\tau\tau} + \nabla_\perp^2 u - \gamma u + (1/2)v^2 = 0, \tag{1}$$

where z and τ are the propagation distance and reduced time, the 2D Laplacian $\nabla_\perp^2$ acts in the transverse plane, $\delta \leq 1$ is a relative SH/FH dispersion coefficient, and γ is the phase-velocity mismatch. Spinning-bullet solutions are looked for in the form

$$u = U(r,\tau,z)\,\exp\left(im\theta\right),\ v = V(r,\tau,z)\,\exp\left(2im\theta\right), \tag{2}$$

where r and θ are polar coordinates in the transverse plane, and m is an integer spin. This transforms Eqs. (1) into

$$iU_z + U_{\tau\tau} + U_{rr} + r^{-1}U_r - \left(1 + m^2 r^{-2}\right)U + VU^* = 0,$$

$$2iV_z + \delta V_{\tau\tau} + V_{rr} + r^{-1}V_r - \left(\gamma + 4m^2 r^{-2}\right)V + (1/2)U^2 = 0. \tag{3}$$

The nonspinning bullets studied in [2,3] correspond to $m = 0$. We will concentrate on the case $m = 1$, as the bullets with $m > 1$ can scarcely be stable. Note that a specific spatiotemporal isotropy, existing in the particular case $\delta = 1$ (identical FH and SH dispersions) for the $m = 0$ bullets [2], does *not* hold in the case $m \neq 0$.

The first objective is to find stationary solutions to Eqs. (3), which are real and z-independent. To get an initial approximation to the solutions, we apply VA based on the Gaussian *ansatz*

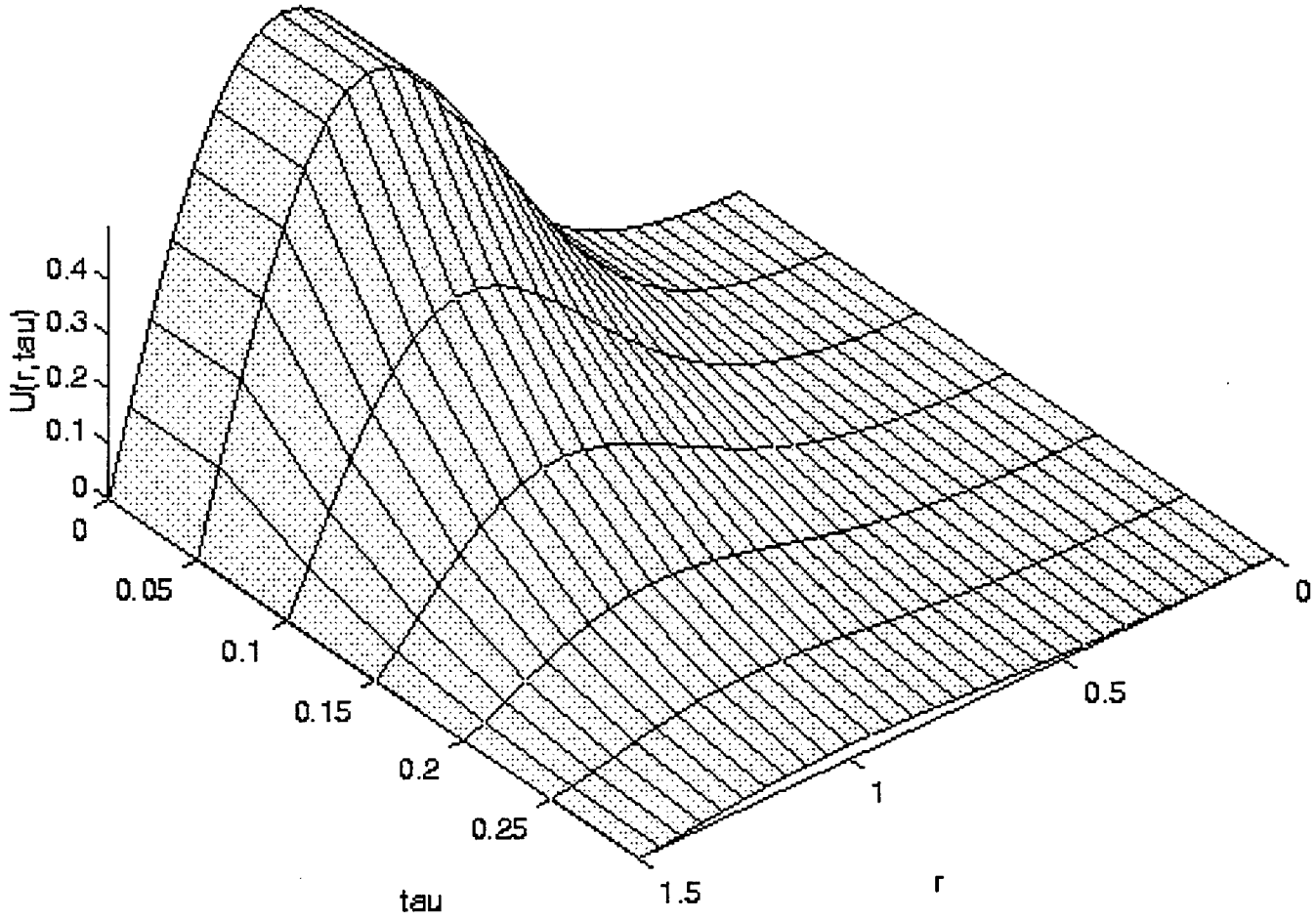


Figure 1: The stationary shape of an $m = 1$ spinning "bullet" at $\gamma = \delta = 1$.

$U(r,\tau) = Ar\exp\left(-ar^2 - \alpha\tau^2\right)$, $V(r,\tau) = Br^2\exp\left(-ar^2 - \beta\tau^2\right)$, with the variational parameters A, B, α, β, and a (the previous results for $m = 0$ [2] suggest to take a single spatial-width parameter a for FH and SH). The substitution of the *ansatz* into the Lagrangian of Eqs. (3) and performing the variation yield an algebraic system, that was solved numerically in the general case, although an explicit analytical solution is sometimes available too. For instance, in a physically interesting case $\delta = 0$, when SH is at the zero-dispersion point, we obtain (for $m = 1$) $\beta = 2\alpha = (2/3)(1+4a)$, $a = (1/36)(4+\gamma)(\sqrt{36/(4+\gamma)} - 1)$. In all the cases considered (in the intervals $0 \leq \gamma \leq 10$, $0 \leq \delta \leq 1$, and even for $m = 2$), VA produces exactly one physical solution.

The next step was to solve numerically Eqs. (3) which yield the shape of the stationary bullet. The numerical solution used, as an initial guess, the VA-predicted shape. It was found that, in accord with the VA prediction, there always exists *exactly one* solution which vanishes at $r = 0$ and $r = \infty$. Generally, the numerically found soliton's shape was quite close to the variational result, except for the fact that the Gaussian ansatz chops off the (exponentially decaying) tails of the soliton at $r \to \infty$ and $|\tau| \to \infty$. An example of the numerical solution is shown in Fig. 1 (only the FH component $U(r,\tau)$ is shown, the shape of the SH one being quite similar).

The second step is to analyze the stability of the bullets. This is crucially important, especially in view of the above-mentioned instability of the spinning cylindrical solitons [4]. A relatively simple part of the analysis is to test the stability against perturbations that do not break the simple θ-dependence postulated in Eqs. (2). We solved the corresponding z-dependent Eqs. (3) for the

complex functions U and V, by means of the 4th-order Runge-Kutta method and using the stationary solution as an initial configuration. The result is that the bullet appears to be stable, at least for moderate values of z for which the simulations were run. Note that the stability of this type (not involving azimuthal perturbations) can be tested too by means of the known Vakhitov-Kolokolov criterion [7]. The criterion has not detected any instability.

The most important part of the stability analysis is to consider azimuthal perturbations, which break the θ-dependence postulated in (2). Direct simulations of Eqs. (1) with four independent variables are to be completed. However, another approach is possible, based on the numerical solution of the linearized version of Eqs. (1), looking for possible unstable perturbation eigenmodes (cf. a similar approach adopted in [4]). To this end, assuming the unperturbed solution (u_0,v_0) in the form obtained above with $m = 1$, one can look for a general eigenmode as

$$u(r,\tau,z,\theta) - u_0 = [U_{11}(r,\tau)\,\exp(in\theta) + U_{12}(r,\tau)\,\exp(i(2-n)\theta)]\,\exp(\lambda z),$$

$$v(r,\tau,z,\theta) - v_0 = [V_{11}(r,\tau)\,\exp(i(n+1)\theta) + U_{12}(r,\tau)\,\exp(i(3-n)\theta)]\,\exp(\lambda z), \qquad (4)$$

where n is an arbitrary integer azimuthal "quantum number" of the perturbation, λ is the instability growth rate sought for, and the functions U_{11} through V_{12} are, generally, complex. It is easy to see that the substitution (4) indeed provides for a closed-form eigenmode.

The eigenvalues λ, determined by the condition that the eigenmode must be everywhere nonsingular, were looked for on a discrete set of parameter values, $\delta = 0$ and 1 (these two opposite cases are most interesting ones), and $\gamma = 0, 1$, and 2. The perturbation azimuthal numbers $n = 0, -1, \pm 2$, and ± 3 were considered (the value $n = +1$ is trivial), as it is unlikely to get an instability at $|n| > 3$ (note that the instability of the $m = 1$ spinning cylindrical soliton was numerically found at $|n| = 3$ [4]).

First, an instability accounted for by purely real positive eigenvalues λ in (4) was searched for. Assuming λ real, a finite result was that it was always imaginary (neutrally stable). Thus, this type of the instability does not occur in the cases considered.

It is more technically difficult to look for complex eigenvalues with $\lambda > 0$. This possibility was investigated in detail at a few points, e.g., $\delta = \gamma = 1$, admitting the same values of n as above. The eigenvalue was sought for, treating $\mathrm{Im}\lambda/\mathrm{Re}\lambda$ as an independent parameter that was given values 2^N, with $N = 0, \pm 1, \pm 2, ..., \pm 10$. No unstable eigenvalue has been found this way. Thus, the conclusion is that, at least at some values of the parameters, the $m = 1$ spinning 3D soliton has a chance to be stable in the SHG medium.

[1] A.A. Kanashov and A.M. Rubenchik, Physica D **4**, 122 (1981).
[2] B.A. Malomed, P. Drummond, H. He, A. Berntson, D. Anderson, and M. Lisak, Phys. Rev. E **56**, 4725 (1997).
[3] H. He and P.D. Drummond, Phys. Rev. **E 54**, 5025 (1998); D. Mihalache, D. Mazilu, J. Dörring, and L. Torner, Opt. Comm. **159**, 129 (1999).
[4] D. Skryabin, W.J. Firth, Phys. Rev. Lett. **79**, 2450 (1997); D.V. Petrov and L. Torner, Opt. Quant. Electr. **29**, 1037 (1997).
[5] D.V. Petrov *et al.*, Opt. Lett. **23**, 1444 (1998).
[6] M. Quiroga-Teixeiro and H. Michinel, J. Opt. Soc. Am. B **14**, 2004 (1997).
[7] M.G. Vakhitov and A.A. Kolokolov, Sov. J. Radiophys. Quantum Electr. **16**, 783 (1973).

Stable solitons in quadratic waveguides with losses and gain

Lucian-Cornel Crasovan, Dumitru Mihalache, Dumitru Mazilu
Department of Theoretical PhysicsΓNational Institute of Physics and Nuclear EngineeringΓPOB MG-6ΓBucharestΓRomania; e-mail mihalake@theor1.theory.nipne.ro; phone/fax +40-1-423-17-01

Boris Malomed
Department of Interdisciplinary StudiesΓFaculty of EngineeringΓTel Aviv UniversityΓTel Aviv 69978ΓIsrael; e-mail malomed@eng.tau.ac.il; phone +972-3-640-6413; fax +972-3-640-6399

Falk Lederer
Institute of Solid State Theory and Theoretical OpticsΓFriedrich-Schiller-Universität JenaΓ Max-Wien-Platz 1ΓD-07743ΓGermany; e-mail pfl@uni-jena.de; phone +49-3641-947170; fax +49-3641-947177

Temporal solitons in a $\chi^{(2)}$ medium have been recently observed for the first time [1]. They were extremely narrow (58 fs)Γwhich made it possible to observe them in a small sample of BBO crystal. The use of the solitons in applications will require to place the crystal into a cavity [2]. For so narrow solitons circulating in the cavityΓthe filtering losses are important. In this workΓ we introduce a realistic $\chi^{(2)}$ model including the losses and compensating gainΓthat gives rise to*stable* temporal solitons (the action of losses [3] and amplification [4] on the $\chi^{(2)}$ solitons was earlier considered in a straightforward way).

It is natural to assume that losses are dominating at the second harmonic (SH)Γwhile *bandwidth-limited* amplification (that we assume to be integrated into the nonlinear crystal as in [5]) operates at the fundamental harmonic (FH). Solitons in models of this type are unstable because the linear gain makes their background unstable. A general way to suppress the background instability was proposed in [6]: the waveguide has to be linearly coupled to a parallel lossy core. In the present contextΓit is sufficient to take into regard only the coupling in the FH component. ThenΓthe stabilized model (whichΓin factΓis a version of a system of Ginzburg-Landau equations for the $\chi^{(2)}$ medium [7]) takes the form:

$$iA_z + (1/2)A_{\tau\tau} + A^* B = i\gamma_0 A + i\gamma_1 A_{\tau\tau} + A', \quad (1)$$

$$iB_z + (\sigma/2)B_{\tau\tau} - \beta B + 2A^2 = -i\Gamma_0 B + i\Gamma_1 B_{\tau\tau}, \quad (2)$$

$$iqA'_z + (i\,\alpha + \nu)A' = A. \quad (3)$$

Here AΓBΓand A' areΓrespectivelyΓthe FH and SH amplitudes in the main core and the FH amplitude in the added lossy oneΓz and τ are the propagation distance and reduced timeΓσ is the relative SH/FH dispersion coefficientΓβ is the phase-velocity mismatchΓγ_0 is the FH gainΓγ_1 accounts for the finite size of the gain bandΓΓΓ_0 and Γ_1 control the losses at SHΓνΓqΓand α being the mismatchΓpropagationΓand loss constants in the added core. The FH (anomalous) dispersion and coupling coefficients are set to be $\equiv 1$; σ and β may have any signΓwhile the parameters on r.h.s. are positive (Γ_1 may be zero). The model assumes that the dispersion and nonlinearity in the added core are much weaker than the losses. We also neglect the group-velocity difference c between FH and SH and mismatch $\Delta\omega$ between the FH gain maximum and SH loss minimum. An estimate shows thatΓin the real case [1]Γthey are negligible if $|c| \ll 500$ km/s and $\Delta\omega \ll 10$ THz.

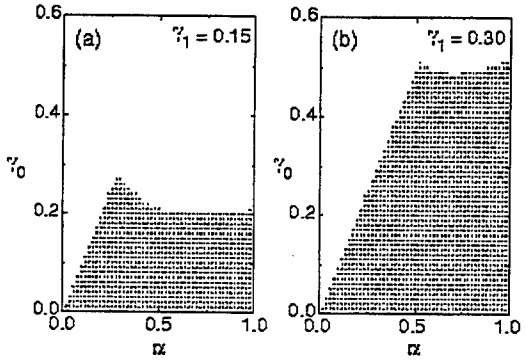


Figure 1: The stable-background domain for $q = 1\Gamma\sigma = 2\Gamma\Gamma_0 = 0.2\Gamma\Gamma_1 = 0.1\Gamma$and $\gamma_1 = 0.15$ (a)Γ or $\gamma_1 = 0.3$ (b).

Nontrivial solitons in a dual-core system may exist if the corresponding coupling length is comparable to the soliton's dispersion length. In the experiment [1]$\Gamma$the latter was few mm$\Gamma$and it is easy to fabricate a dual-core waveguide whose coupling length is a few mm.

The first condition necessary for stability of solitons is the stability of their background$\Gamma A = B = A' = 0$. A corresponding algebraic condition can be easily derived from the linearized equations and analyzed numerically. Typical resultsΓviz.$\Gamma$the background-stability region on the parametric plane $(\alpha\Gamma\gamma_0)$ at fixed values of the other parameters$\Gamma$are shown in Fig. 1. A corollary of the stability condition is $\alpha > \gamma_0\Gamma$i.e.$\Gamma$the loss in the added core must be stronger than the gain in the main one.

Eqs. (1)-(3) admit particular *exact* solitary-pulse solutions in a form which follows the pattern of the recently found exact solutions to a system of stabilized complex Ginzburg-Landau equations with a cubic nonlinearity in the main component [6] (see also [7]):

$$A = a\,[\mathrm{sech}(\lambda\tau)]^{2+i\mu}\,e^{ikz},\ B = b\,[\mathrm{sech}(\lambda\tau)]^{2+2i\mu}\,e^{2ikz},\ A' = a'\,[\mathrm{sech}(\lambda\tau)]^{2+i\mu}\,e^{ikz}. \qquad (4)$$

Here$\Gamma$the inverse width $\lambda\Gamma$chirp $\mu\Gamma$and wavenumber shift k are realΓwhile the amplitudes $a\Gamma a'$ and b may be complex. Substituting (4) into Eqs. (1)-(3)Γone eventually arrives at ten real equations for eight real unknowns. ObviouslyΓa solution may exist if two constraints are imposed on the eight real parameters of the model. We have studied the exact soliton solutions (4) in detail.

Because the background stability is not sufficient for the full dynamical stability of the solitary pulsesΓwe have numerically tested the stability of the exact solitons. The results are *drastically different* from those for the similar model with the cubic nonlinearity obtained in [6]: the exact (4) solitons are unstable in all the cases consideredΓbut other *stable* localized pulses exist in all the casesΓincluding those when the exact solution is not available (recall it is not generic). In particularΓwe observed in the simulations that the unstable exact pulse did not decayΓbutΓ insteadΓalways reshaped itself into a new stable pulse. The same stable pulse can also be generated usingΓinstead of the exact solutionΓan input in the form of sufficiently arbitrary Gaussians: $A = a_0 \exp(-\lambda_0^2\tau^2)\Gamma B = b_0 \exp(-\lambda_0^2\tau^2)\Gamma$and $A' = a_0' \exp(-\lambda_0^2\tau^2)\Gamma$with some $a_0\Gamma b_0\Gamma a_0'$ and λ_0. ThusΓwe conclude that the stable pulsesΓwhose analytical form is unknown$\Gamma$are very robust *attractors*. It is noteworthy that the rearrangement of the initial Gaussian into the stable pulse is much more violent than in the case of the exact initial solitonΓi.e.$\Gamma$the exact solitonΓalthough being unstable$\Gamma$is quite close in shape to the stable pulse.

Thus$\Gamma$the present model is bistableΓits two coexisting attractors being the nontrivial pulse and the stable trivial solution. According to the general principlesΓa *separatrix*Γin the form of an

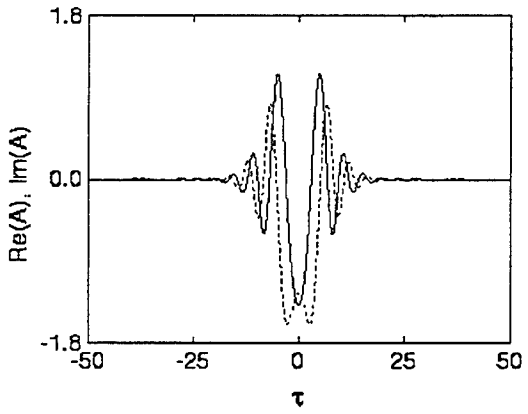


Figure 2: The real and imaginary parts (full and dashed lines) of the stable-pulse solution. Only FH is shown.

unstable stationary solutionΓmust exist between two attractors. It is obvious that the unstable exact soliton is exactly the separatrix.

We have studied in detail the structure of the nontrivial stable pulseΓlooking for it as a numerical stationary solution to Eqs. (1)Γ(2) and (3). As well as in the case of the exact unstable pulseΓit is an even functions of τΓand it is strongly chirpedΓsee a typical example in Fig. 2.

We have performed another series of numerical experimentsΓwhich clearly show that the stable pulse can also be generated by initially seeding a Gaussian solely in the FH componentΓtwo other ones being empty. Because of the bistabilityΓthere is a threshold to generate the stable pulse this wayΓin terms of the intensity of the initial seed. Exactly the same stable pulse is generated with very different initial intensitiesΓprovided that they are above the threshold. On the other handΓ with an insufficient initial intensityΓi.e.Γbelow the thresholdΓthe input Gaussian quickly decays into the trivial solution. The remarkable robustness of the stable pulse and its insensitivity to details of the input make it attractive for the experiment and applications.

[1] P. DiTrapani *et al.*ΓPhys. Rev. Lett. **81**Γ570 (1998).
[2] P.S. Jian *et al.*ΓOpt. Lett. **24**Γ400 (1999).
[3] L. Torner *et al.*ΓOpt. Lett. **20**Γ2183 (1995); B.A. Malomed *et al.*ΓPure Appl. Optics **5**Γ941 (1996).
[4] L. TornerΓOptics Commun. **154**Γ59 (1998).
[5] R. Brinkmann *et al.*ΓIEEE J. Quantum Electron. **QE-30**Γ2356 (1994).
[6] B.A. Malomed and H.G. WinfulΓPhys. Rev. E **53**Γ5365 (1996); J. Atai and B.A. MalomedΓ Phys. Lett. A **244**Γ412 (1998).
[7] L.-C. CrasovanΓD. MihalacheΓB. MalomedΓand F. LedererΓPhys. Rev. EΓin press.

Nonlinear Guided Waves and Their Applications

Vectoral Solitons and Incoherent Solitons

Thursday, 2 September 1999

Yuri Kivshar, Australian National University, Australia
Presider

ThE
16.30-18.45
Salle Morey—St-Denis

New Physics and Applications of Kerr Spatial Solitons in AlGaAs Waveguides

George I. Stegeman* and Lars Friedrich
CREOL School of Optics, University of Central Florida, Orlando, FL, U.S.A.

Patsy Millar and J. Stewart Aitchison
Dept. of Electronics and Electrical Engineering, University of Glasgow, Glasgow, U.K.

Nail N. Akhmediev
Optical Sciences Centre, Australian National University, Canberra, Australia

AlGaAs waveguides have proven to be ideal testing grounds for new concepts in Kerr spatial solitons. They exhibit a combination of a high nonlinear refractive index (n_2=1.5x10^{-13} cm^2/W) and low linear (waveguide losses 0.1-0.15cm^{-1}) and nonlinear loss in the 1.55μm communications band, together with the possibility to integrate optical and electronic devices and a mature growth and processing technology. Here we report two new experiments, one dealing with basic soliton physics and the second an application to reconfigurable interconnects. In the first, solitons were used as steerable waveguides in order to realize a 1x4 reconfigurable interconnect. In the second project we studied the evolution of the polarization state of vector solitons with power and found evidence for the existence of a bifurcation, predicted earlier by numerical simulations.[1]

The idea to use solitons as steerable waveguides in optical routing and switching devices is intriguing as this reconfigurable optical circuitry offers solutions to many problems (such as optical cross- and interconnects) with a simple architecture, potentially low crosstalk and high switching speed. [2,3]

A schematic of the soliton steering sample used in the presented experiments is given in fig.1. The sample consisted of an AlGaAs slab waveguide with a 1μm thick core region (n=3.336), sandwiched between 1.5μm of upper cladding (n=3.29) and 4.0μm of lower cladding (n=3.22) on top of a GaAs substrate. The upper cladding was, except for a 0.5μm layer directly adjacent to the core, p-doped, whereas the lower cladding was n-doped (again with the exception of the 0.5μm next to the core). The waveguide core was undoped. Thus the device could be used as a PIN diode in the direction perpendicular to the waveguiding film. On top of the device a heavily p-doped layer of 0.1μm thickness was formed and photolithographically processed so that only wedge-shaped regions of it remained. By contacting these electrode regions and injecting carriers in the forward-bias regime of the above mentioned diode, the index of the AlGaAs was lowered, thus creating a low index prism in the material.

The soliton is launched so that it passes underneath the wedge-shaped electrode. The resulting spatially anisotropic phase change causes the soliton to be deflected. In the case where the whole width of the soliton is experiencing the phase change, the deflection is correctly predicted by Snell's law. [4] Because the index change in the material is proportional to the injected current, the soliton can be steered dynamically by simply adjusting the current.

---

*full address: 4000 Central Florida Blvd., P. O. Box 162700, Orlando FL 32816, U.S.A.
ph. 1 (407) 823 6915, fax 1 (407) 823 6955, email george@mail.creol.ucf.edu

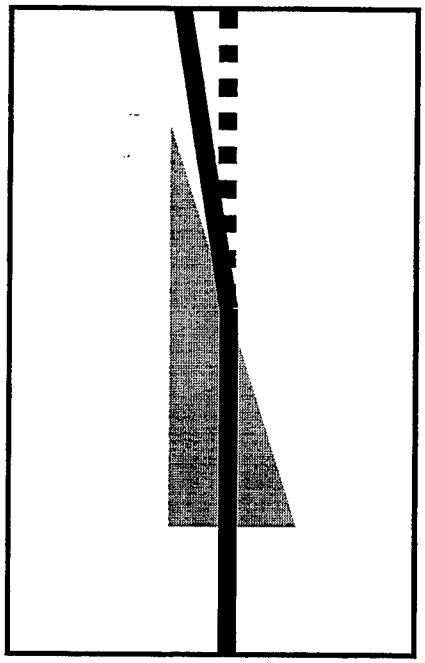


Fig. 1: Schematic of the steering electrode (gray) and the soliton with steering current on (solid line) and off (dashed line).

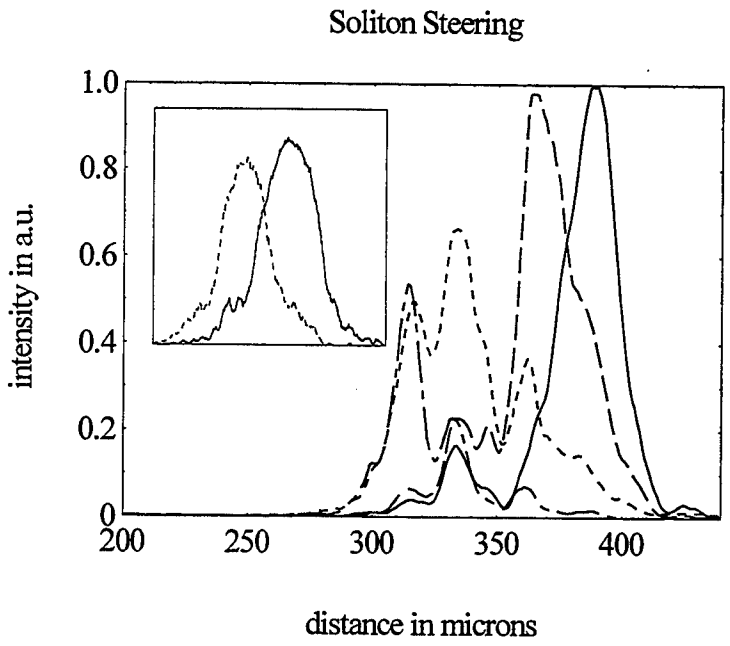


Fig. 2: Linescan image of the end face of the soliton steering sample with soliton deviation sufficient for a 1x4 interconnect. The inset shows an example of soliton steering for a sample with near perfect end faces.

An additively pulse modelocked color center laser operating at a wavelength of 1.55μm, a pulsewidth of 500fs and a repetition rate of 76MHz was used for the experiments. The laser beam was shaped to an elliptical spot using a cylindrical telescope. This allowed efficient coupling to the waveguide while simultaneously reducing diffraction in the unconfined dimension, thus reducing the power required for soliton formation. The $1/e^2$-halfwidth of the in-coupling spot in the plane of the waveguide where diffraction occurred was 20μm, the sample was 2.5 diffraction lengths long. This results in a cw soliton power of about 300W. Soliton beam deflection was achieved by injecting a current via the top electrodes in the forward biased regime. The current consumption of a single device was on the order of 15mA. The soliton remained intact while being deflected as verified by monitoring the beam shape at the output facet. A maximum lateral deflection of about 100μm was obtained at the output face for the current sample design, which corresponds to a deflection angle of 0.3° and an index change of $-3x10^{-4}$ in the prism and provides enough separation for a 1x4 interconnect. A weak signal beam (power ratio signal/soliton=0.03) of the opposite polarization (i.e. TM) but the same wavelength was guided and deflected within the soliton. As it can be seen from Fig. 2, the transmission drops for increased injection current due to free carrier absorption. This mechanism eventually limits the maximal achievable steering angle. Due to imperfections of the end faces of this particular sample, significant scattering occurred, resulting in higher cross-talk between channels than possible with perfect end faces. The inset in Fig. 2 shows the intensity profile for a soliton generated and steered in another sample without end face imperfections.

We also investigated the results of bifurcation in the soliton dispersion with increasing intensity. In vector solitons, the two polarization components are coupled by four-wave mixing (FWM) and cross-

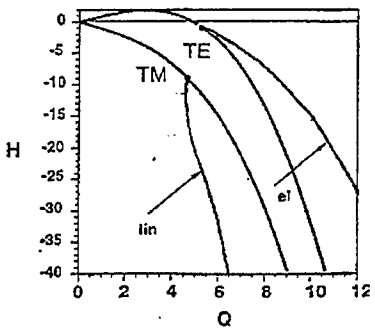


Fig. 3: Hamiltonian H vs. power Q for TE and TM vector solitons in AlGaAs (from [1])

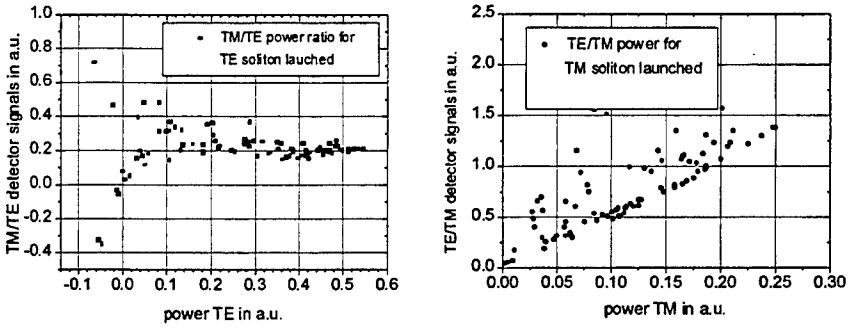


Fig. 4 a) and b): Evolution of the orthogonal polarization component with total soliton power for TE (a) and TM (b) solitons for power levels well above the critical power for bifurcation.

phase modulation (XPM) and can exchange energy with propagation distance via the FWM effect. As shown in fig. 3, at low powers TE and TM solitons are both stable eigensolutions of the system. At high powers, when the waveguide birefringence and the effects of FWM and XPM become comparable, it has been predicted theoretically that a bifurcation occurs in both polarizations. Only the one having the lower value of the Hamiltonian for a given power is stable for a given branch. [1] Hence only TE polarized solitons are stable where-as a pure TM soliton is unstable and the stable part of that branch consists of a linearly polarized vector soliton with both TE and TM polarizations. These predictions were tested.

Experimentally, above the bifurcation point a TE soliton should stay TE-polarized during propagation, whereas a TM soliton should acquire a TE component as the stable branch of the solution is linearly polarized, but not purely TM. As the critical power for the bifurcation scales as the inverse of the birefringence, we measured the birefringence of the AlGaAs waveguide and found $\Delta n=(5.5\pm1.0)\times10^{-4}$, resulting in a critical power of about 1300W and a beat length of 2mm (sample length was 25mm).

The experiments were performed using an OPG/OPA system at a wavelength of 1.57μm, with 10Hz repetition rate and 20ps pulse duration. Solitons were launched with an elliptical beam similar to that described earlier. Maximum power levels were well above the critical power. As shown in fig. 4 a), a TE soliton exhibited a constant portion of TM-polarized light with increasing intensity, mainly due to polarizer imperfections. For a TM soliton, however, the portion of TE light increased with power, i.e. the soliton was linearly polarized, but not purely TM, thus confirming the result of the simulations.

In conclusion, we have carried out experiments that demonstrated the dynamic steering of spatial solitons by electronically induced index changes with sufficient separation for a 1x4 switch. We also investigated the polarization behavior of vector solitons and found evidence for the existence of a bifurcation of the TM branch, causing the polarization state of the soliton to rotate with power.

References:

1. E.A.Ostrovskaja et al., *J. Opt. Soc. Am. B*, **vol. 14**, no.4, (1997), pp. 880-887
2. G.I. Stegeman et al, *Proc. SPIE*, **vol. 2481**, (1995), pp. 270
3. A.W. Snyder et al., *Optics and Photonics News*, **vol. 10**, no. 2, (1999), pp. 35
4. J.U. Kang et al., *Appl. Phys. Lett.*, **vol. 70**, (1997), pp. 1363

Four-Wave Mixing of Vector Solitons

C. Anastassiou, M. Segev, J. A. Giordmaine, and S. Lan
Department of Electrical Engineering, Princeton University, Princeton, NJ 08544
Anastass@ee.princeton.edu, segev@ee.princeton.edu, joeg@ee.princeton.edu, slan@ee.princeton.edu.

K. Stieglitz
Department of Computer Science, Princeton University, Princeton, NJ 08544
ken@cs.princeton.edu

M. Mitchell
Lucent Technologies, Holmdel, NJ 07733
mlm10@lucent.com

M. F. Shih
Department Of Physics, National Taiwan University, Taipei, Taiwan 10764
Mshih@ee.princeton.edu

Interactions between two vector solitons can be described by two coupled nonlinear wave eqs :

$$i\frac{\partial A}{\partial z}+\frac{1}{2}\frac{\partial^2 A}{\partial x^2}+\Delta n(I)A=0 \qquad (1a)$$

$$i\frac{\partial B}{\partial z}+\frac{1}{2}\frac{\partial^2 B}{\partial x^2}+\Delta n(I)B=0 \qquad (1b)$$

where A and B are the two optical fields and Δn is the change in the index of refraction [1]. Consider two generic types of nonlinearity: the Kerr: $\Delta n=(|A|^2+|B|^2)$, and the saturable (which occurs, e.g., in photorefractives): $\Delta n=1/(|A|^2+|B|^2)$. In the Kerr case eqs (1) constitute an integrable system and when two such solitons collide they conserve their total intensity and shape. On the other hand, the saturable system is no longer integrable and the colliding solitons can undergo fusion and fission, and radiate small amounts of energy. Another way to understand collisions is from a waveguide analogy [2]. A Kerr soliton induces a $\mathrm{sech}^2(x)$ waveguide which can guide only a single mode, and it has a (complementary) critical angle of zero (the angle with the propagation axis below which total internal reflection occurs is zero). Therefore, two interacting Kerr solitons at non-zero collision angle can never couple light into each other's induced waveguide, and each one of them conserves its energy and linear momentum. In the saturable case the critical angle is nonzero but at large collision angles the solitons remain unaffected after the collision, as in the Kerr regime [3].

Here we demonstrate, theoretically and experimentally, **energy exchange between vector solitons** takes place at large angles for both the Saturable and the Kerr regimes [4, 5]: an interaction which is unique to vector solitons and does not exist for scalar solitons. Consider collisions between two vector solitons, in which one soliton (soliton 1) initially (at $z=0$) has two field components (A_1 and B_1) and the other soliton (soliton 2) starts with one field component only (A_2), i.e., $B_2=0$. The total intensity for each soliton, remains constant as shown in Fig. 1a, but the components that make up that soliton exchange energy. In Fig. 1b, the B-field initially (at the input) has only a B_1 component but after the collision it gives half of its energy to B_2. An equal amount of energy is given from A_2 to A_1.

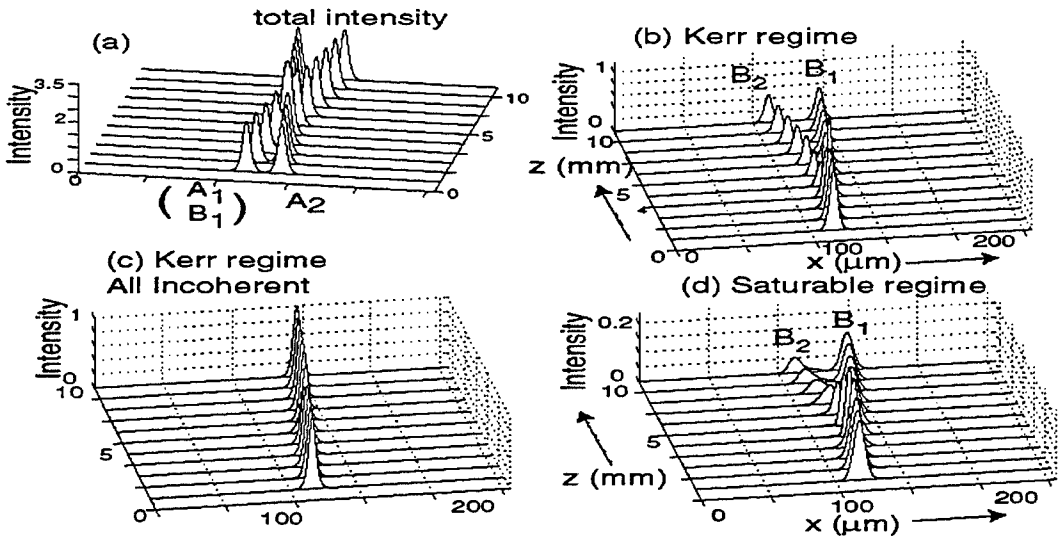


Fig.1. (a) Soliton 1 and 2 maintain their total energy. B-field as a result of collision for three cases: In the Kerr regime with A_1, A_2 coherent (b), A_1 and A_2 are incoherent (c), and for the saturable regime and A_1, A_2 being coherent.

To understand this, we draw on a direct analogy between vector soliton collision and the four-wave-mixing in nonlinear optics: A_1 and A_2 form an interference grating, which is translated (via the nonlinearity) into a periodic index modulation with a grating vector $\mathbf{K} = \mathbf{k}_1 - \mathbf{k}_2$, $\mathbf{k}_1$ and $\mathbf{k}_2$ corresponding to the propagation directions of A_1 and A_2. If the third input beam, B_1, travels in the $\mathbf{k}_1$ direction (as it does, because A_1 and B_1 form soliton 1), then it should Bragg-diffract in the $\mathbf{k}_2$ direction and form a non-zero B_2. But $\mathbf{k}_2$ is the direction of A_2, so B_2 and A_2 together form soliton 2.

Based on this intuition, if A_1 and A_2 are made incoherent with one another, the optical interference pattern phase-fluctuates (due to the mutual incoherence) much faster than the response time of the nonlinearity, and thus does not give rise to the index grating. As a result, no energy exchange takes place, as shown in Fig. 1c [figure 1c simulates eqs. similar to eqs. 1, but with 3 fully independent field components]. The Saturable (photorefractive) nonlinearity gives similar results as the Kerr, showing coupling in Fig. 1d. Again, no energy is coupled if A_1 is made incoherent with A_2.

We performed our experiment in SBN for angles at which scalar solitons do not interact. B_1 is made incoherent with A_1 and A_2 by having the optical length difference (1 m) exceeding the coherence length of the laser (10 cm) [3]. Since the phase of B_1 is varying much faster than the response time of the crystal ($\tau_d \approx 1$ sec), the A and B fields are incoherent with each other with respect to the crystal [5]. The input and output faces of the crystal are imaged on a CCD camera. The slow response of the crystal enables us to view each beam individually by blocking one beam (with a mechanical shutter) and sampling the other within a time interval (~1 msec) shorter than τ_d.

We launch 15 μm FWHM solitons colliding at an angle of 0.7° [inside the crystal] with a total intensity ratio of 2 (normalized to the background intensity) for each soliton, $|A_1|^2 = 3|B_1|^2$, and



Fig. 2. B Field Output after collision. Energy exchange takes place if A_1 and A_2 are coherent (a), but not if they are incoherent (b). (c)When the A field remains blocked then the coupling shown in (a) disappears after a few seconds.

$|B_2|^2 = 0$. In Fig. 2a we see the B field at the output exhibits two peaks which correspond to B_1 and B_2: clearly showing the expected energy switching. When we make A_1 incoherent with A_2 and repeat the experiment, as expected, there is no coupling of energy as shown in Fig. 2b. For energy switching to take place, it is necessary to have A_1 coherent with A_2, and both of them present so as to form the index grating that drives the interaction. For example, if we block the A field long enough, the energy exchange shown in (a) decays (because the index grating decays), and after a time longer than the response time of the nonlinearity the grating is washed out and the energy exchange disappears, as shown in (c).

We then increase the collision angle to 0.9°. As expected from our simulations, at larger angles the energy switching decrease, as shown in Fig. 3(a)

Finally, recalling the analogy with four-wave mixing, we realize that the modulation depth of the grating is proportional to the visibility of the interference, that is, to $A_1 A_2^* / I$ where I is the total intensity. Therefore, keeping the total intensity fixed, the visibility (and thus the energy switching efficiency) should depend on the ratio $|A_1|^2 / |B_1|^2$. We investigate this by comparing results with collision angle of 0.55 ° and two different ratios: $|A_1|^2 = 5|B_1|^2$ and $5|A_1|^2 = |B_1|^2$, shown in Fig. 3(b) and 3(c) respectively. Comparing (b) to (c) we notice that indeed the energy switching is much larger when A_1 is stronger than B, because the visibility is much larger.

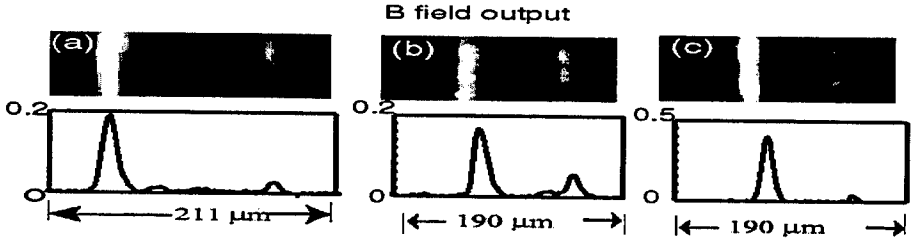


Fig. 3. B-field after collision (a) At a collision angle of 0.9° B shows less coupling. (b), (c) Same as (a) at an angle of 0.55°, and different ratios $|A_1|^2=5|B_1|^2$ and $5|A_1|^2 = |B_1|^2$, respectively, while the total intensity is kept constant.
We see more coupling when A_1 is stronger than B_1.

In conclusion, we have demonstrated, four-wave-mixing interaction of vector solitons which is a unique interaction property of vector solitons and cannot exist for scalar solitons. In this vein, this work suggests the possibility of generating phase-conjugation of solitons, by having the field B_1 propagating counter to A_1. This leads to many other ideas, but we would like to end with just one: this four-wave-mixing interaction of vector solitons lays the experimental foundations for computation with solitons [4]

References

(1) S. V. Manakov, Sov. Phys. JETP 38, 248 (1974).
(2) A. W. Snyder, D. J. Mitchell and Y. S. Kivshar, Mod. Phys. Lett. B 9, 1479 (1995).
(3) M. Shih et al., Appl. Phys. Lett. 69, 4151 (1996).
(4) M. H. Jakubowski, K. Steiglitz and R. Squier, Phys. Rev. E 58, 6752 (1998).
(5) R. Radhakrishnan, M. Lakshmanan and J. Hietarinta, Phys. Rev. E 56, 2213 (1997).

Applied Magnetooptic Soliton Dynamics Based upon TM and TE-TM-Driven Systems

A D Boardman and M Xie

Photonics and Nonlinear Science Group,

Joule Physics Laboratory, School of Sciences, University of Salford, Salford, M5 4WT, UK

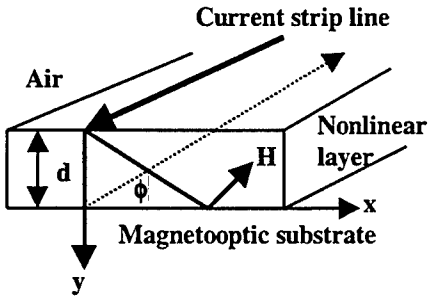
Telephone: +44-161-295-5054, Fax: +44-161-295-5197, e-mail: a.d.boardman@physics.salford.ac.uk

The expected outcome of the use of magnetooptics is the introduction of a new degree of freedom into the kind of guided-wave processes now used routinely in integrated optics [1-5]. In view of this possibility, it is particularly exciting to investigate integrated optical device possibilities that use not only magnetooptic interactions but spatial solitons as well [4,5]. The key issues in promoting the success of this approach are

- the selection of magnetooptic materials
- the creation of optimised magnetooptic waveguides
- the choice of nonlinear process
- the prospect of the soliton dynamics being used to engage in switching, or other forms of soliton channel manipulation.

Two possibilities are considered in this report. The first involves the propagation of TM waves in the structure sketched in fig.1.

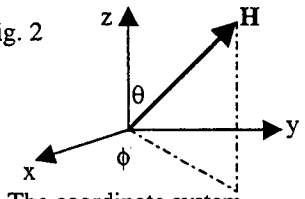
Fig. 1



Here a magnetic field **H** is created by a current I flowing in a stripline along the surface of the device. There is a component of **H** perpendicular to the propagation direction z and the magnetic material, which could be Bi-doped YIG, or a material like lutetium. I is ~60mA, producing H~400e, which is enough to saturate the magnetisation.

The second application concerns TE-TM coupling in the so-called longitudinal configuration. For the arbitrary magnetic field direction, shown in fig. 2, there are general magnetooptic contributions to the dielectric tensor **ε**.

Fig. 2



The coordinate system

$$\underline{\varepsilon} = n^2 \begin{pmatrix} 1 & -iQ\cos\theta & iQ\sin\theta\sin\phi \\ iQ\cos\theta & 1 & -iQ\sin\theta\cos\phi \\ -iQ\sin\theta\sin\phi & iQ\sin\theta\cos\phi & 1 \end{pmatrix}$$

Taking the simplest Kerr nonlinearity permits coupled equations for the amplitudes of the TE and TM waves to be derived in a tractable form. For example, writing the electric field components as

$$A_1 \xi_x \exp\left(-i\frac{\omega}{c}\beta_1 z\right), A_2 \xi_y \exp\left(-i\frac{\omega}{c}\beta_2 z\right), A_2 \xi_z \exp\left(-i\frac{\omega}{c}\beta_2 z\right)\exp(i\omega t)$$

This means that the parabolic equation for A_2 is

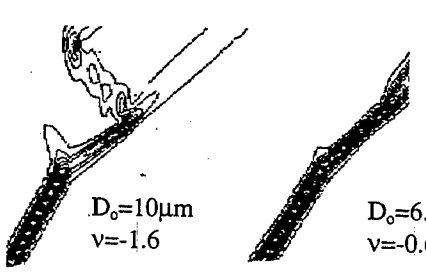
$$2i\frac{c}{\omega}\frac{\partial A_2}{\partial z} = \frac{c^2}{\omega^2\beta_2}\frac{\partial^2 A_2}{\partial x^2} - i(\bar{\varepsilon}_{xy} - i\bar{\varepsilon}_{xz})\exp\left(i\frac{\omega}{c}\gamma z\right)A_1 + 2\bar{\varepsilon}_{yz}A_2 - i\bar{\alpha}A_2 + \bar{\chi}\left[A_1|A_1|^2 + A_2|A_2|^2\right]$$

and similarly for A_1. $\bar{\varepsilon}_{ij}$ are the elements of the magnetooptic tensor displayed in fig.2, $\bar{\alpha}$ is an absorption coefficient, $\bar{\chi}$ is a nonlinear susceptibility. All these quantities are averaged over the selected waveguide, which here is of the form given by fig.1 [with or without the current stripline].

The phase mismatch between the TE and TM waves is $\gamma = \beta_{TE} - \beta_{TM}$, where β_{TE} and β_{TM} are effective indices. For TE-TM coupling there is clearly a need to deal with the $\exp\left(i\frac{\omega}{c}\gamma z\right)$ factor to prevent it from averaging to zero along z. Hence the structure needs to be optimised, if a magnetooptic influence is to be apparent in this application. Returning to the first application $\bar{\varepsilon}_{xy}=0$, $\bar{\varepsilon}_{xz}=0$, leaving only $\bar{\varepsilon}_{yz}$ and so no phase problem exists for this case. Indeed, if $\bar{\varepsilon}_{yz}$ is constant it causes only a simple phase shift. Here, however, $\bar{\varepsilon}_{yz} = \bar{\varepsilon}_{yz}(x)$ and this creates a current-driven potential well that may capture a soliton. Only the ideal case, in which the current line is infinitely thin will be discussed here. This case is very instructive but the consequences of using a finite width stripline will be outlined during the presentation. For a soliton beam width D_o, it is a parameter $\nu = 2\beta_{TM}\frac{\omega^2}{c^2}D_o^2\bar{\varepsilon}_{yz}$ that really determines the well characteristics and a simple Lagrangian analysis will be used to reveal all the properties of the well that are required to make an application. This analysis yields the simple well shape

$$U(x_o) = \nu_o\left[\tanh\left(\frac{p}{2} - x_o\right) + \tanh\left(\frac{p}{2} + x_o\right)\right]$$

where ν is now (realistically) approximated to $\nu = 0$ [$x > \frac{p}{2}$ or $< -\frac{p}{2}$] and $= -\nu_o$ for $-\frac{p}{2} < x < \frac{p}{2}$. p is a measure of the well width determined from a detailed calculation of the magnetic field distribution. x_o is the initial position of the soliton on the x-axis. The application is beautifully simple but powerful. The current I creates an x-dependent magnetic field distribution and a potential barrier, or well, is created depending upon the current flow direction or soliton propagation direction.. Solitons with large angles of incidence to the barrier, and a small kinetic energy, are reflected. The total power is $(c/\omega D_o)^2(4\, D_o/\beta_2\, \bar{\chi})$ so both power P and the magnetooptic parameter change as D_o changes. In fact, $D_o\uparrow \Rightarrow \nu\uparrow$, $P\downarrow$ and $D_o\downarrow \Rightarrow \nu\downarrow$, $P\uparrow$. The effects can be seen in fig.3.



TM SOLITONS IN
CURRENT-CREATED WELL

Fig. 3

Also the sketch in fig.4 shows that the soliton can now be routed to make a soliton circulator. This and other applications will be discussed in some depth.

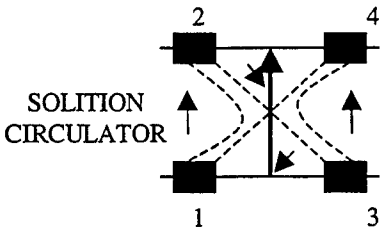


Fig. 4

For the longitudinal case Eq.(1) can be transformed to

$$\gamma\psi_1 + 2i\frac{c}{\omega}\frac{\partial\psi_1}{\partial z} = \frac{c^2}{\omega^2\beta_o}\frac{\partial^2\psi_1}{\partial z^2} + i\bar{\varepsilon}_{xy}\psi_2 + \bar{\chi}\left[\psi_1|\psi_2|^2 + \psi_1|\psi_2|^2\right]$$

where $\psi_{1,2}$ is related to $A_{1,2}$ in such a way as to bring the phase factor, γ onto the line.

If the phase mismatch $\gamma >> \bar{\varepsilon}_{xy}$ then magnetooptic effects will be suppressed, so it is important to be able to optimise the structure. This optimisation will be discussed in detail but the general principle is to seek refractive a index variation through Bi-doping of iron garnet layers and also to vary the quantities averaged over the guiding structure by changing the guide thickness. This will achieve both a reduction in γ and remarkable enhancements of both the magnetooptical and the nonlinear effects. Fig.5 shows a TE polarised spatial soliton in a planar waveguide structure (like AlGaAs) before and after enhancement and it is clear that energy transfer from TE to the TM wave (and vice-versa) is achieved. D is optimised to 1.3 μm and $Lu_{3-x}\,Bi_x\,Fe_{5-y}\,Ga_y\,O_{12}$ is used at x=1.4, y=1.5. The diffraction length is ~ mm so absorption is not a problem. Power levels are a function of the nonlinear material but in this application are ~100W.

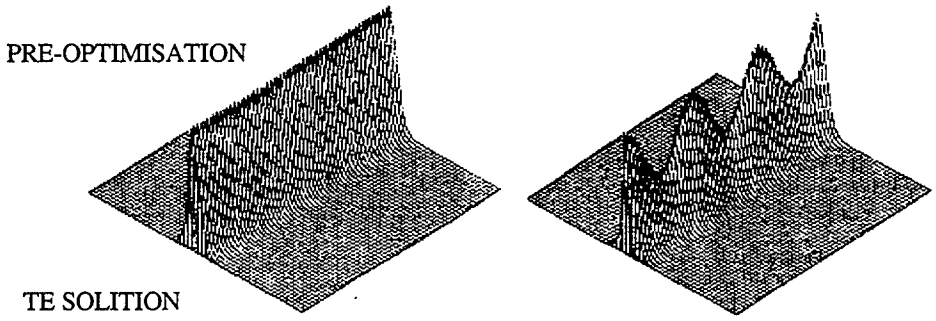


Fig. 5

These applications and other more complex interactions will be presented together with an assessment of currently available magnetooptic materials and the prospects for (2+1) solitons.

References

1. M Wallenhorst, M Niemöller, H Dötsch, P Hertel, R Gerhardt and B Gather, J.App.Phys. **77**. 2902 (1995).

3. O Kamada, J.App.Phys **79**. 5976 (1996).

4. R Gerhardt, S Sare, H Dötsch, T Linewitz and W Toksdorf, Opt.Comm. **102**, 31 (1993).

5. A D Boardman and K Xie, Phys.Rev.Lett. **75**. 4591 (1995).

6. A D Boardman and K Xie, J.Opt.Soc.Am. B **14**, 3102 (1997).

Incoherent Solitons - Properties and Collisions

N. Akhmediev, A. Ankiewicz, A. Snyder
Australian Photonics CRC, Optical Science Centre, Research School of Physical Sciences and Engineering, Australian National University, Canberra ACT 0200, Australia
nna124@rsphysse.anu.edu.au, ana124@rsphysse.anu.edu.au, aws124@rsphysse.anu.edu.au

W. Królikowski, G. McCarthy, B. Luther-Davies
Australian Photonics CRC, Laser Physics Centre, Research School of Physical Sciences and Engineering, The Australian National University, Canberra ACT 0200, Australia
wzk111@rsphysse.anu.edu.au, bld111@rsphysse.anu.edu.au

Solitons have been studied extensively in the last few years [1–3]. Recently, it has been shown experimentally that partially coherent beams can propagate as spatial solitons [4]. A partially coherent beam diverges more rapidly than the corresponding coherent beam of the same transversal extent, with the divergence becoming greater as the coherence becomes weaker. In addition, the nonuniformity of the beam phase causes the intensity of the beam to exhibit speckle structure. In order to form a spatial soliton, the medium has to respond on a time scale which is slower than that of the fast variation of beam phase. Under such circumstances, the medium will "see" a time-averaged light intensity which is a smooth function of spatial coordinates. Then, the beam will be trapped and will propagate in the form of a superposition of many spatial modes. Interestingly, instead of using an incoherent light source, one can generate a partially coherent soliton by superimposing mutually incoherent cw wave packets in such a way that they represent different modes of the self-induced waveguide.

As far as the theoretical description of spatial partially coherent solitons (PCS) is concerned, there are a few possible approaches. The most natural one involves the use of a mutual coherence function [5]. However, this leads to an analytically intractable problem which can only be solved numerically. A theoretical description of spatial incoherent solitons based on the so-called 'coherent density approach', where the partially coherent beam is represented as a superposition of mutually incoherent components, has been developed in [6,7]. The description of a partially coherent soliton as a multimode self-induced waveguide [8] has been especially fruitful. The idea comes from the concept of a vector soliton as multimoded waveguide which is self-induced by its linear modes [9]. Stationary soliton propagation is obtained by using the correct proportions of various mutually incoherent linear modes of the self-induced waveguide. Incoherent solitons can also be treated in the diffractionless ray optics limit [10]. In terms of a multimode waveguide, this limit is valid when the number of modes goes to infinity, so that the soliton becomes completely incoherent.

If the number of modes is finite, then accurate analysis can be done using N coupled nonlinear Schrödinger equations [11]. It has been shown that propagation of partially coherent wave packets in a nonlinear Kerr medium with a slow nonlinear response can be represented by the following set of equations [7]:

$$i\frac{\partial \psi_i}{\partial z} + \frac{1}{2}\frac{\partial^2 \psi_i}{\partial x^2} + \alpha\, \delta n(I)\psi_i = 0, \qquad (1)$$

where ψ_i denotes the amplitude of the i-th component of the beam, α is a coefficient representing the strength of the nonlinearity, x is the transverse co-ordinate, z is the co-ordinate along the direction of propagation, and $\delta n(I) = \sum_{i=1}^{N} |\psi_i|^2$ is the change in refractive index profile created by all the incoherent components of the light beam.

Stationary solutions of Eq.(1) are given by $\psi_i(x,z) = \frac{1}{\sqrt{\alpha}}\, u_i(x) \exp\left(i\frac{\lambda_i^2}{2}z\right)$, with real functions $u_i(x)$ and real eigenvalues λ_i^2. Then the set of Eqs.(1) reduces to the set of ODEs:

$$\frac{\partial^2 u_j}{\partial x^2} + 2\left[\sum_{i=1}^{N} u_i^2\right] u_j = \lambda_j^2 u_j. \qquad (2)$$

This set of equations is also completely integrable for an arbitrary set of real nondegenerate λ_j. Using the results of [13], it can be shown that its solutions can be found from the set of algebraic equations:

$$\sum_{i=1}^{N} \frac{\exp[\lambda_i \bar{x}]\ \exp[\lambda_j \bar{x}]}{\lambda_j + \lambda_i}\, u_i(x) + u_j(x) = -\exp[\lambda_j \bar{x}],$$

where $\bar{x} = x - x_i$ and x_i is a parameter giving the spatial shift of each soliton component.

The analysis gives us N propagation constants λ_j providing the eigenvalues of the problem. These are parameters which nontrivially contribute to the shape of the PCS. Moreover, the solution is actually a $(2N-1)$ - parameter family. It contains N soliton parameters, λ_i, as well as N relative shifts x_i. Admitting translational symmetry of the solution as a whole, we can define all shifts relative to one of them, so that the total solution then contains $2N-1$ free parameters.

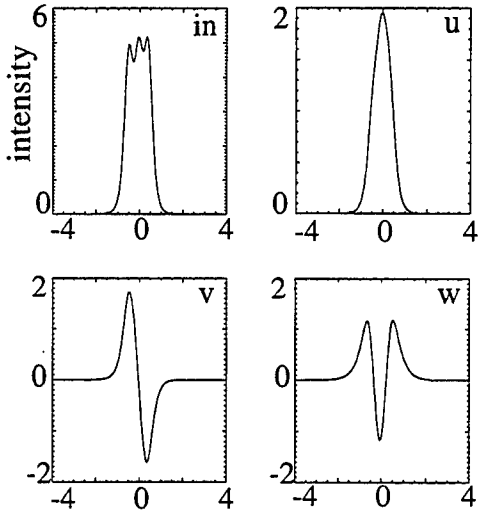


FIG. 1. *(a) The intensity profile of a 3-mode incoherent soliton and the amplitude profiles of its three linear components: (a) zero-th, (b) first, and (c) second.*

The constants λ_j have a dual physical meaning. First, the incoherent soliton can be considered as a nonlinear superposition of N fundamental solitons. Then the λ_j are the amplitudes of the partial fundamental solitons in the multisoliton complex. Secondly, if we consider the sum of the mode intensities as a given self-induced refractive index change, then each λ_j gives an eigenvalue (propagation constant) relating to a certain mode of this waveguide.

The abovementioned $(2N-1)$ parameters give a wide variety of PCS shapes which, in general, are asymmetric and can have either a single or multipeak structure. In Fig.1 we give an example of a partially coherent soliton consisting of three incoherent components ($N = 3$). The intensity profile of these solitons is in general asymmetric (see Fig.1a). It is also clear that the components u, v, w correspond to the fundamental, first and second modes of the waveguide self-induced by the soliton. As the number of constituent components increases, the possible range of profiles of the partially coherent soliton also increases. In the limit of an infinite number of components, the profile of the soliton can be arbitrary.

If the ability of partially coherent solitons to assume a variety of profiles is an unusual novel feature in itself, then the collision properties of these solitons are even more amazing. In Fig.2 we show the collision of two partially coherent solitons consisting of six mutually incoherent modes of a self-induced waveguide. It is clear that the collision induces a dramatic change in the shape of the solitons. After the collision, each beam remains a soliton but then has an intensity profile different from the initial one. In the example in Fig.2, collision leads to the formation of a six-peak structure of the soliton.

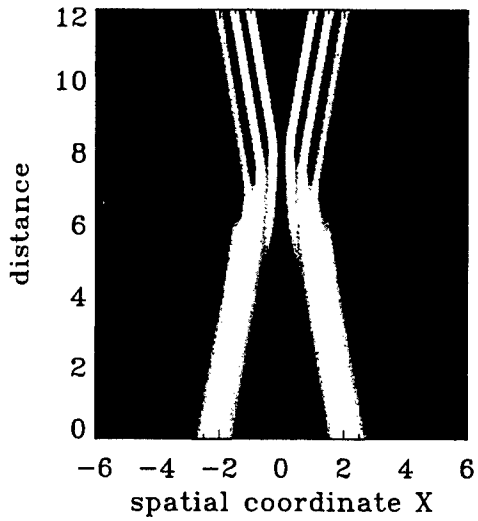


FIG. 2. *Collision of two slightly asymmetric PCS, each consisting of six linear modes. Parameters chosen in this simulation are* $\lambda_1 = 6.0$, $\lambda_2 = 5.0$, $\lambda_3 = 4.0$, $\lambda_4 = 3.0$, $\lambda_5 = 2.0$, $\lambda_6 = 1.0$, $\Delta x_{12} = 0$, $\Delta x_{13} = -0.2$, $\Delta x_{14} = -0.1$, $\Delta x_{15} = -0.3$, $\Delta x_{16} = -0.1$ *and the angle of collision* θ, *is chosen such that* $\tan\theta = 0.3$.

This reshaping can be explained by viewing each incoherent soliton as a multisoliton complex. It is well-known that a soliton collision leads to lateral shift for fundamental solitons. During the collision, each soliton component experiences a lateral shift which depends on the λ_j and on the relative angles of incidence. For an incoherent soliton, each component experiences multiple pair-wise collisions. This leads to assorted lateral shifts and

consequently to a change in the soliton profile.

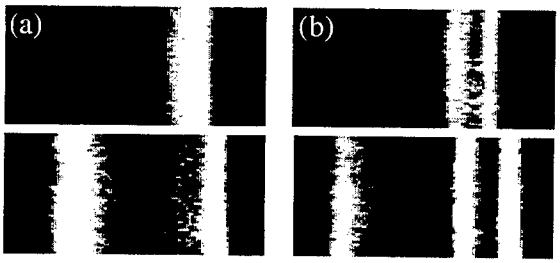


FIG. 3. *Experimental observation of the collision of two-component PCS with a fundamental soliton.*

On the other hand, the reshaping phenomenon can be also understood as mutual refraction of PCS on the self-induced waveguides. Since each constituent mode of the PCS have different phase velocity, each one experiences a different rate of refraction in the impact area of the collision. Self-consistent reassembling of modes after the collision results in a stationary output beam with a modified shape.

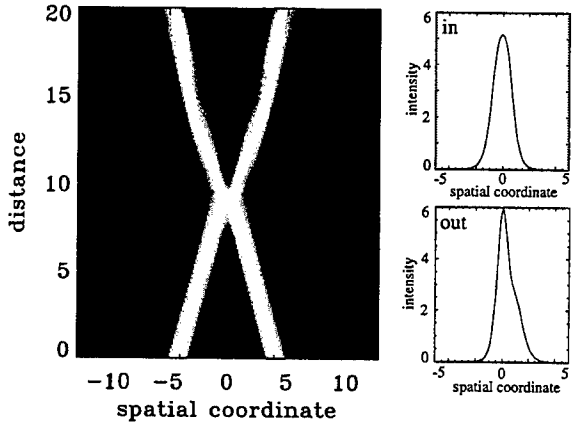


FIG. 4. *Numerical simulation of collision of two-component PCS solitons in a saturable nonlinear medium with the nonlinearity* $\Delta n \propto I/(1+0.05I)$. *The input and output profiles are shown on the r.h.s.*

The collision of partially coherent spatial solitons has been studied experimentally with screening solitons formed in a photorefractive strontium barium niobate crystal biased with high DC field (3kV/cm) [14]. We produced the PCS by copropagating two mutually incoherent 1D beams (stripes) simulating the fundamental and first-order guided modes of the self-induced waveguide, respectively. This composite beam can form a partially coherent soliton when propagating in the biased photorefractive crystal.

We then collided it with another soliton formed by launching an additional single-component beam. Two examples of the collision are shown in Fig.3. The top row shows the output intensity distribution of each PCS during individual propagation while the bottom row illustrates the results of the collisions. In the first instance (Fig.3(a)) the partially coherent soliton forms a single peaked structure. It is quite clear that after the collision it becomes strongly asymmetric; this is an indication of the partial separation of its constituent modes. In the second example (b), the composite soliton exhibits a clear double-peaked structure with the separation between the peaks being 24 microns (Fig.3(b)). When it collides with the fundamental soliton, the two-peaked structure becomes even more pronounced and the separation between peaks increases to 34 microns.

It is worth noting that the photorefractive nonlinearity is not, strictly speaking, of Kerr-type. Therefore, collisions of PCSs transform them into solutions which are not stationary. As a result, solitons exhibit oscillatory dynamics after the collision (see Fig.4).

[1] M. Segev and G. Stegeman, Physics Today, No 8, 42-48 (1998).

[2] A. W. Snyder and F. Ladouceur, Optics and Photonics News, 35 - 39, February 1999.

[3] N. Akhmediev and A. Ankiewicz, *Solitons, nonlinear pulses and beams*, Chapman & Hall, 1997.

[4] M. Mitchell, *et al.*, Phys. Rev. Lett., **77**, 490 (1996); M.Mitchell, and M.Segev, Nature (London), **387**, 880 (1997).

[5] G. A. Pasmanik, Sov. Phys. JETP, **39**, 234 (1974).

[6] D. N. Christodoulides, T. H. Coskun, R. I. Joseph, Opt. Lett., **22**, 1080 (1997).

[7] D. N. Christodoulides *et al.*, Phys. Rev. Lett., **78**, 646 (1997).

[8] M. Mitchell, *et al.*, Phys. Rev. Lett., **79**, 4990 (1997); V. Kutuzov *et al.*, Phys. Rev. E **57**, 6056 (1998); D. N. Christodoulides *et al.*, Phys. Rev. Lett., **80**, 2310 (1998).

[9] A. Snyder, S. J. Hewlett, and D. J. Mitchell, Phys. Rev. Lett., **72**, 1012 (1994).

[10] A. W. Snyder, D. J. Mitchell, Phys. Rev. Lett., **80**, 1422 (1998).

[11] A. Ankiewicz, W. Królikowski, N. N. Akhmediev Phys. Rev. E, **59**, (1999).

[12] N. Akhmediev, W. Królikowski and A. W. Snyder, Phys. Rev. Lett., **81**, 4632 (1998).

[13] Y. Nogami and C. S. Warke, Physics Letters, **59A**, 251 (1976).

[14] W. Królikowski, N. Akhmediev and B. Luther-Davies, Phys. Rev. E, **59**, (1999).

"Cooling" of spatially incoherent light beams using interactions with incoherent and coherent solitons

Tamer H. Coskun*, Alexandra G. Grandpierre and Demetrios N. Christodoulides
Department of Electrical Engineering and Computer Science
Lehigh University, Bethlehem, Pennsylvania 18015
dnc0@lehigh.edu

Mordechai Segev
Physics Department, Technion-Israel Institute of Technology,
and Electrical Engineering Department,
Princeton University, Princeton, New Jersey, 08544

Manipulating the spatial or temporal coherence properties of an optical beam has always been a topic of great interest [1,2]. Along these lines, active processes such as two-wave-mixing [1] as well as spatial filtering [2] (based on the pinhole principle) have been used in order to improve the spatial coherence of an optical beam. Thus far, all the methods for shaping the coherence function employed components (or systems) which do not conserve the total energy borne upon the beam: some involve gain (e.g., a laser) and some involve loss (pinhole), but none was passive. Certainly, it is highly desirable to identify a passive scheme capable of enhancing at-will the spatial correlation length (spatial coherence) at an arbitrarily-chosen point upon a partially incoherent optical beam. Recent theoretical studies [3,4] have shown that the fluctuation statistics of partially spatially-incoherent light can be greatly affected in a nonlinear self-focusing (or defocusing) environment such as biased photorefractives. For example, the coherence length is known to increase within the gray notch of an incoherent dark soliton [3] after its formation. Similarly, the coherence increases at the sides of an incoherent bright soliton [4].

Here we show that the spatial coherence length of a bright partially coherent signal beam can be greatly affected through its interaction with an incoherent/coherent dark spatial soliton. We show that during this interaction, part of the incoherent bright beam is trapped within the dark/gray notch of the controlling dark soliton thus forming a sharp intensity spike. Moreover, while propagating, its correlation length dramatically increases by at least two orders of magnitude. Thus incoherent light can be effectively "cooled" (its entropy being reduced) at any arbitrarily chosen point upon a partially incoherent wavefront using either a coherent or an incoherent dark spatial soliton.

To demonstrate the principle, let us consider a biased Strontium Barium Niobate (SBN) crystal in a standard soliton arrangement. The crystal is used in reversed bias (self-defocusing nonlinearity). Let us assume that a broad partially incoherent bright signal beam interacts incoherently with a partially incoherent/coherent dark soliton during propagation. In that case, these two beams evolve according to the following two integro-differential equations [3]:

$$i\left(\frac{\partial f}{\partial z}+\theta\frac{\partial f}{\partial x}\right)+\frac{\partial^2 f}{\partial x^2}+\frac{k_0}{2}n_e{}^3 r_{33}|E_0|(1+\rho)\frac{f}{1+I_N(x,z)}=0 \tag{1}$$

$$i\left(\frac{\partial g}{\partial z}+\theta\frac{\partial g}{\partial x}\right)+\frac{\partial^2 g}{\partial x^2}+\frac{k_0}{2}n_e{}^3 r_{33}|E_0|(1+\rho)\frac{g}{1+I_N(x,z)}=0 \tag{2}$$

$$I_N(x,z) = I_{NB} + I_{ND} = \int_{-\infty}^{\infty} \left(|f(x,z,\theta)|^2 + |g(x,z,\theta)|^2 \right) d\theta \tag{3}$$

where at the origin $f(z=0,x,\theta) = r^{1/2} G_{NB}{}^{1/2}(\theta)\phi_{0B}(x)$ and $g(z=0,x,\theta) = \rho^{1/2} G_{ND}{}^{1/2}(\theta)\phi_{0D}(x)$. In the above equations, f and g represent coherent densities [3] for bright and dark beams respectively. r_{33} is the electrooptic coefficient of the SBN crystal and E_0 is the bias field strength. r and ρ are the normalized peak intensities of the bright and dark beams and G_{NB} and G_{ND} their normalized angular spectra [3]. Finally ϕ_{0B} and ϕ_{0D} represent their spatial modulation functions at the origin. The coherence properties of the bright beam are manifested in its correlation length [3]:

$$l_c(x) = \int_{-\infty}^{\infty} \left| \frac{\int_{-\infty}^{+\infty} f(x,z,\theta) f^*(x',z,\theta) \exp[ik\theta(x-x')] d\theta}{\sqrt{I_{NB}(x,z) I_{NB}(x',z)}} \right|^2 dx' \tag{4}$$

As an example let us consider a bright incoherent beam with an intensity FWHM of 30 μm. The initial correlation length of this beam is 9 μm ($\theta_0 = 0.55^o$), and it is the same anywhere across the beam [3]. The beam propagates in SBN:75 crystal with $r_{33} = 1022 pm/V$. This beam co-propagates with a dark spatial soliton whose initial intensity FWHM is 7 μm and its maximum normalized intensity is $\rho = 40$. On the other hand the maximum intensity ratio of the incoherent bright beam is $r = 3$, i.e., weaker than the dark one. The wavelength of both beams is 488 nm.

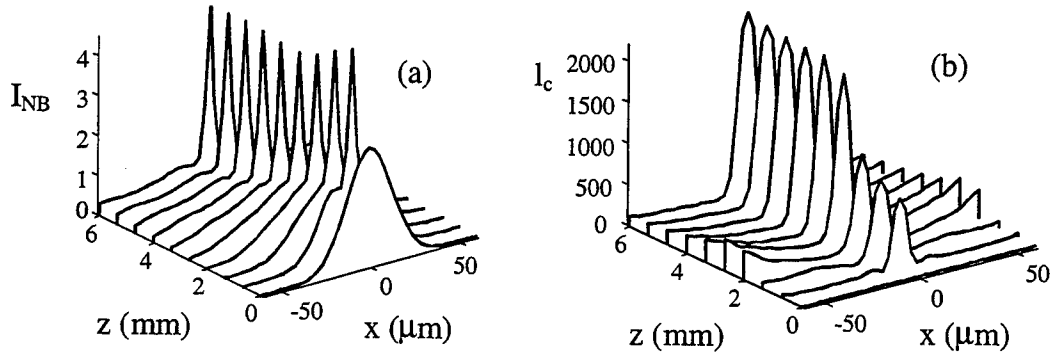


Fig. 1 (a) Evolution of the intensity profile of a bright beam and (b) its correlation length when it co-propagates with a dark coherent spatial soliton.

Figure 1 shows the evolution of the intensity profile of the bright beam as well as its correlation length as function of distance. In this case the dark soliton was assumed to be fully coherent. In our simulations, the angular spectrum G_{ND} collapsed to a delta function and thus Eq.(2) took the form of a standard nonlinear Schroedinger equation. It is clear from Fig.1(a) that part of the incoherent bright beam was captured in the waveguide induced by the dark soliton, whereas the rest of the beam undergoes diffraction. What is very interesting is the fact that coherence of this sharp spike has also increased dramatically. Fig 1(b) shows that the correlation length at the center has increased from 9 μm to 2200 μm, i.e., more than

240 times after 6 *mm* of propagation. Note that this enhancement or "cooling" has been carried out entirely passively, that is without any power transfer between the two beams. **This process is reminiscent of Bose-Einstein condensation**. One can intuitively understand this enhancement by considering the modal properties of dark soliton induced waveguides. As previously shown [5], these waveguides are single-moded even in saturable media. As result, in the absence of any modal competition, the spatial coherence of the trapped light is expected to increase.

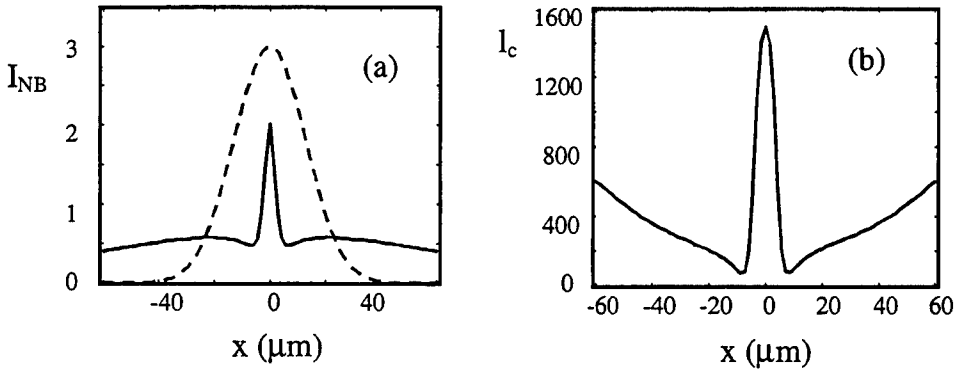


Fig. 2 (a) The input (dashed curve) and output at z = 6 mm (solid curve) intensities of an incoherent bright beam and (b) its coherence length in μm after 6 mm of propagation when it is co-propagating with an incoherent dark soliton.

Even more importantly, "cooling" can be accomplished using a dark incoherent soliton [3,6]. Figure 2 depicts the intensity profile and the correlation length of the bright incoherent beam after $6\,mm$. All the parameters are the same as in Fig. 1, but this time the initial correlation length of the dark **incoherent soliton beam** is $9\ \mu m$ ($\theta_0 = 0.55^o$), i.e., the incoherent beam being "cooled" and the "cooling beam" have the same correlation length. Yet in spite of the fact that the guiding dark beam itself is incoherent, the correlation of the bright signal beam has increased from $9\,\mu m$ to $1500\ \mu m$. This can be intuitively explained by recalling that in a large range of parameters (for first-order incoherent dark solitons [3]) the waveguide induced by an incoherent dark soliton is single-moded: not very different from the waveguide induced by a coherent dark soliton at the same wavelength. In this case the increase in coherence is somewhat lower since at 6 *mm* the dark incoherent soliton has not yet formed: the beam still evolves into its stationary (solitonic) form.

This work was supported by AFOSR, ARO, and NSF
* Permanent address, Pamukkale University, Electronics Engineering Department, Denizli, Turkey.

References

[1] N. V. Bogodaev, L. I. Ivleva, A. S. Korshunov, N. M. Polozkov, and V. V. Shkunov, J. Opt. Soc. Am. B 10, 2287 (1993); M. Cronin-Golomb, H. Kong, and W. Krolikowski, J. Opt. Soc. Am. B 19, 1698 (1992).
[2] P. W. Milloni and J. H. Eberly, *Lasers*, (John Wiley and Sons, New York, 1988).
[3] T. H. Coskun, D. N. Christodoulides, M. Mitchell, Z. Chen, and M. Segev, Opt. Lett. 23, 418 (1998); D. N. Christodoulides, T. H. Coskun, M. Mitchell, Z. Chen, and M. Segev, Phys. Rev. Lett. 80, 5113 (1998).
[4] M. Mitchell, M. Segev, T. H. Coskun, and D. N. Christodoulides, Phys. Rev. Lett. 79, 4990 (1997).
[5] M. F. Shih, Z. Chen, M. Mitchell, M. Segev, H. Lee, R. S. Feigelson, J. P. Wilde, J. Opt. Soc. Am. B 14, 3091 (1997).
[6] Z. Chen, M. Mitchell, M. Segev, T. H. Coskun, and D. N. Christodoulides, Science 280, 889 (1998).

Two-dimensional incoherent light beams in Kerr media

Ole Bang
Department of Mathematical Modelling, Technical University of Denmark, DK-2800 Lyngby, Denmark.
Tel.: (+45) 45 25 30 92; Fax: (+45) 45 93 12 35; email: oba124@rsphysse.anu.edu.au / ob@imm.dtu.dk

Darren Edmundson
Optical Sciences Centre, Research School of Physical Sciences and Engineering,
Australian National University, Canberra ACT 0200, Australia.
Tel.: (+61-2) 6249 3789; Fax: (+61-2) 6249 5184; email: dee124@rsphysse.anu.edu.au

Wieslaw Krolikowski
Australian Photonics Cooperative Research Centre, Laser Physics Centre, Research School of Physical Sciences and Engineering, Australian National University, Canberra ACT 0200, Australia.
Tel.: (+61-2) 6249 3752; Fax: (+61-2) 6249 0029; email: wzk111@rsphysse.anu.edu.au

It was recently demonstrated that a slow self-focusing nonlinear medium can support partially coherent solitons [1,2]. The necessary condition for soliton formation is that the nonlinear response is slow compared to the fast and random fluctuations of the phase front of the incident optical beam. In this case the medium cannot follow the random speckle structure of the beam and responds only to its time-averaged intensity, which is a smooth function of the spatial variables. Following the experiments in photorefractive media [1,2] Christodoulides *et al.* used the so-called coherent density function theory to describe the spatially partially coherent beams [3,4]. In case of the specific logarithmic nonlinearity the stationary soliton solution was found analytically [4].

Spatially partially coherent beams in inertial Kerr media was discussed more than 20 years ago. For instance, Pasmanik [5] analyzed the nonlinear equation for the cross-correlation function to describe self-focusing of incoherent beams. This aberration-free approach indicated collapse, but lead to the incorrect conclusion that the threshold power above which collapse occurs is the same as for coherent beams. Aleshkevich *et al.* [6] later used the mutual coherence function in a more rigorous numerical study, in which fitting to the numerical results gave an empirical formula for the effect of the partial coherence of the beam on the collapse threshold power.

Here we use the coherent density function approach to study the propagation of partially coherent beams in inertial Kerr media. We find the first analytical formula for the collapse threshold power, which shows how the deterioration of spatial coherence tends to suppress self-focusing. Furthermore, we present the results of the first fully 2+1 dimensional numerical propagation of spatially incoherent beams described by the discrete Christodoulides model of coupled nonlinear Schrödinger (NLS) equations [3], which displays an intricate dynamical interplay between the components.

We consider the dynamical equations for incoherent light beams propagating in a bulk Kerr medium [3]

$$i\partial_z f + i\,\vec{\theta}\cdot\nabla f + \nabla^2 f + \gamma I f = 0, \tag{1}$$

where $f=f(\vec{r},z,\vec{\theta})$ is the coherent density function, which is parametrized by the walk-off angle $\vec{\theta}=(\theta_x,\theta_y)$. Since we consider a bulk medium with two transverse dimensions (2D) $\vec{r}=(x,y)$, $\vec{\nabla}=(\partial_x,\partial_y)$, and $\nabla^2=\partial_x^2+\partial_y^2$. The total intensity is represented by f in the following way:

$$I(\vec{r},z)=\int |f(\vec{r},z,\vec{\theta})|^2 d\vec{\theta}, \tag{2}$$

where $\int d\vec{\theta}\equiv\int_{-\infty}^{\infty}\int_{-\infty}^{\infty} d\theta_x d\theta_y$.

Equations (1) can be written in a simpler form without walk-off by applying the unitary transformation

$$f(\vec{r},z,\vec{\theta})=F(\vec{r},z,\theta)\exp(i\theta^2 z/4 - i\vec{\theta}\cdot\vec{r}/2), \tag{3}$$

where $\theta^2=|\vec{\theta}|^2=\theta_x^2+\theta_y^2$. In terms of $F(\vec{r},z,\vec{\theta})$ the dynamical equations become

$$i\partial_z F + \nabla^2 F + \gamma I F = 0. \tag{4}$$

The model (4) conserve the power $P_\theta(\vec{\theta})$ in each angular component and the Hamiltonian H,

$$P_\theta(\vec{\theta})=\int |F(\vec{r},z,\vec{\theta})|^2 d\vec{r}, \tag{5}$$

$$H=\int\int (|\nabla F|^2 - \gamma I|F|^2/2) d\vec{r}d\vec{\theta}, \tag{6}$$

as well as the momentum in the x and y direction, $M_{x,y}=\int\int 2\mathrm{Im}\{F^*\partial_{x,y}F\}d\vec{r}d\vec{\theta}$. Here $\int d\vec{r} \equiv \int_{-\infty}^{\infty}\int_{-\infty}^{\infty} dxdy$. The total power $P=\int P_\theta(\vec{\theta})d\vec{\theta}$ and the total momentum $\vec{M}=\hat{x}M_x+\hat{y}M_y$, are also conserved.

To study Eq. (4) (and thus (1)) analytically we define the effective beam width (i.e. the width of the intensity profile) or so-called virial, $V(z)=P^{-1}\int R^2 I d\vec{r}$, where

$\vec{R}=\vec{r}-\langle\vec{r}\rangle$ and $R=|\vec{R}|$ is the distance from the center of mass $\langle\vec{r}\rangle=P^{-1}\int\vec{r}I(\vec{r},z)d\vec{r}$. The dynamics can then be analyzed from the acceleration of the width, d^2V/dz^2, for which we can derive a simple expression in terms of conserved quantities, the virial relation:

$$\frac{d^2V}{dz^2}=\frac{8}{P}\left(H-\frac{M^2}{4P}\right), \tag{7}$$

where $M^2=|\vec{M}|^2$. If the right hand side of (7) is negative the beam width $V(z)$ will continuously decrease and a collapse, defined as $V(z)\to 0$, will inevitably occur at a finite distance. Thus $H-M^2/(4P)<0$ is a *sufficient condition* for collapse. Importantly, such a collapse of the total wavefunction implies also a collapse of each angular component, $V_\theta(\vec{\theta},z)=P^{-1}\int R^2|F(\vec{r},z,\vec{\theta})|^2d\vec{r}\to 0$. If the right hand side of (7) is positive, $H-M^2/(4P)>0$, we have to do further analysis to determine whether a collapse can occur or not. For example, if the beam is given a sufficiently strong focusing at the input ($dV(0)/dz<0$) a collapse could in principle develop despite the second derivative of the virial being constant and positive.

We will now assume that the profiles of the intensity and the angular power spectrum, are both radially symmetric and Gaussian at the input ($z=0$), i.e.

$$f(\vec{r},z=0,\vec{\theta})=\sqrt{\frac{I_0}{\pi\sigma^2}}\exp(-\frac{\theta^2}{2\sigma^2}-\frac{r^2}{2\Delta^2}), \tag{8}$$

where I_0 is the peak intensity ($I(\vec{r},z=0)=I_0\exp(-r^2/\Delta^2)$. In logarithmic media the beam will maintain its Gaussian statistics during propagation and one can apply the Gaussian Schell-model to describe partially coherent light as in [4]. In inertial Kerr media this is not so.

Transforming this initial condition according to Eq. (3), the total power and the Hamiltonian become

$$P=\pi\Delta^2 I_0,\quad H=\pi I_0+\pi\Delta^2\sigma^2 I_0/4-\pi\gamma\Delta^2 I_0^2/4,$$

with the momentum being zero, $M=0$, due to symmetry. From Eq. (7) we then obtain that the beam will collapse if the total power is above the threshold

$$P_{\rm th}=P_{\rm th}^{\rm nls}(1+\beta), \tag{9}$$

where $\beta=\Delta^2\sigma^2/4$ is the number of speckles inside the beam cross section, and $P_{\rm th}^{\rm nls}=4\pi/\gamma$ is the well-known threshold for collapse of Gaussian beams in the NLS equation. Furthermore, the virial and its derivative are initially $V(0)=\Delta^2$ and $dV(0)/dz=0$, respectively. Therefore, for this initial condition, $P>P_{\rm th}$ is both a *necessary and sufficient* condition for a total collapse in the sense that the total beam width goes to zero, $V(z)\to 0$.

As we would expect the power threshold for collapse, which is depicted in Fig. 1 (solid curve), increases with the degree of of incoherence β. In other words, the more incoherent the beam is the stronger is the tendency to diffract, and the more power is required for collapse to occur. The threshold (9) represents the first analytical prediction of the influence of the degree of incoherence on the self-focusing of partially incoherent beams in inertial Kerr media and fits well with the numerical result $P_{\rm th}=P_{\rm th}^{\rm nls}(1+0.6\beta)$ obtained by Aleshkevich *et al.* [6]. Note that in the *coherent limit* when $\sigma\to 0$ and the angular spectrum becomes a delta-function, the power threshold reduces to the NLS threshold $P_{\rm th}^{\rm nls}$, as it should.

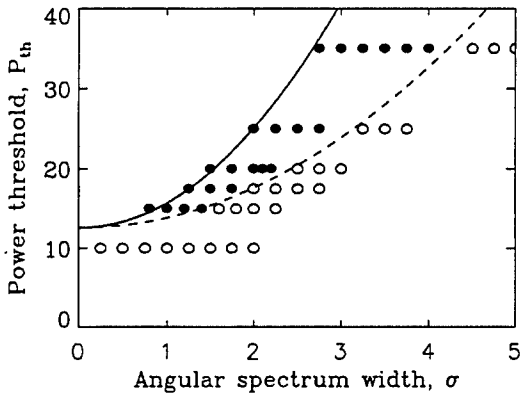


FIG. 1. Theoretically predicted collapse threshold power $P_{\rm th}^{\rm nls}(1+\beta)$ (solid) and the best numerical fit $P_{\rm th}^{\rm nls}(1+0.4\beta)$ (dashed) versus the angular spectrum width σ for $\gamma=\Delta=1$. Filled (open) circles indicates numerical results, in which collapse (diffraction) was observed.

To study the beam propagation numerically we discretize the walk-off space into a center component ($n=1$) at $\theta_x=\theta_y=0$ and $N_{\rm r}$ rings with each $N_{\rm s}$ equidistant spokes or components on them. This gives the discrete equations

$$i\frac{dF_n}{dz}+\nabla^2F_n+\gamma IF_n=0,\quad I=\sum_{n=1}^{N}\Omega_n|F_n|^2, \tag{10}$$

where Ω_n is the solid angle or area around the nth component and $N=N_{\rm r}N_{\rm s}+1$ is the total number of components. The discrete model (10) was first used by Christodoulides *et al.* to study partially incoherent 1+1D solitons in photorefractive media [4].

The numerical results are summarized in Fig. 1, with $P_{\rm th}=P_{\rm th}^{\rm nls}(1+0.4\beta)$ representing the best fit to the collapse threshold power. This lies below both the analytical prediction (9) and the $P_{\rm th}^{\rm nls}(1+0.6\beta)$ found numerically by Aleshkevich *et al.* [6]. The discrepancy between the analytical and numerical results, i.e. the saturation of the numerically found threshold, is an artifact of discreteness, as observed for the simpler two component case [7]. Clearly, with a finite θ-resolution, the power in the central component can be sufficiently high to ensure that a collapse will always occur, disregarding the power in the other components. Furthermore, the nearest components may walk-off and collapse away from the center, thereby created multiple hot spots. We are currently investigating this effect.

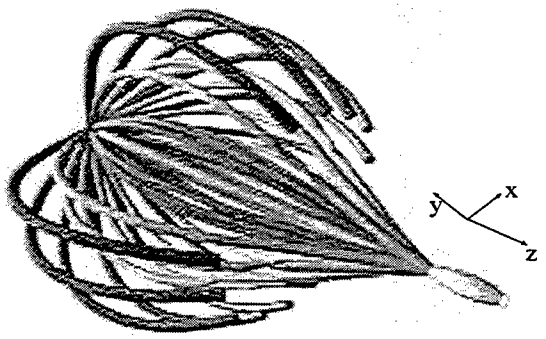


FIG. 2. Evolution of the position of the maximum amplitude of the individual components, represented as tubes, during a collapse for Δ=1, σ=1.75, and P=20. The number of rings and spokes is N_r=N_s=16, and shown is the central component and spoke 1-14 on rings 2, 5, and 7. The corresponding walk-off is θ=0, 0.54, 1.34, and 1.88.

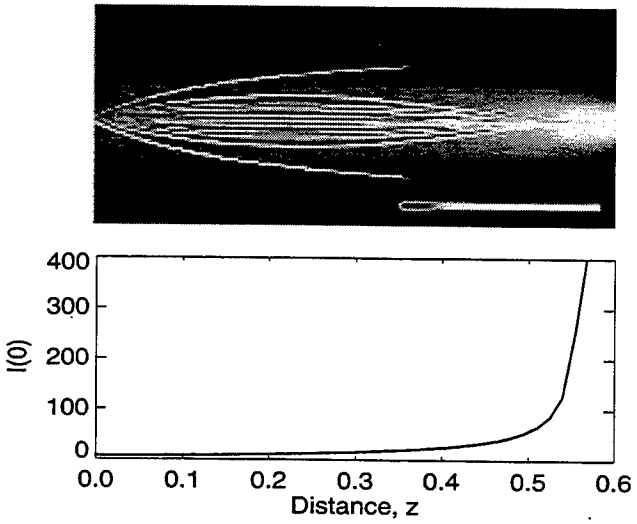


FIG. 3. Top: slice in the y=0 plane of Fig. 2 overlayed the total intensity in grey scale with white being the most intense. Bottom: Evolution of the maximum (center) intensity.

In general each component always starts to walk-off of at an angle Atan(θ), corresponding to simple linear walk-off. Depending on the value of θ for the particular component a certain portion escapes the attractive potential (or waveguide) of the total intensity and continues to walk off, while another portion is captured by this potential and reflected back towards the center. If enough power is reflected back a collapse can occur with the intensity going to infinity at the center r=0. In Figs. 2 and 3 we show the dynamics of such a typical collapse. A few components on each ring have been left out in the 3D picture in order to see the central component.

If the power captured at the center is not enough to initiate a collapse, then all components will diffract and the total beam will spread out, as shown in Figs. 4 and 5. Still some of the components are captured by the potential or waveguide of the total intensity.

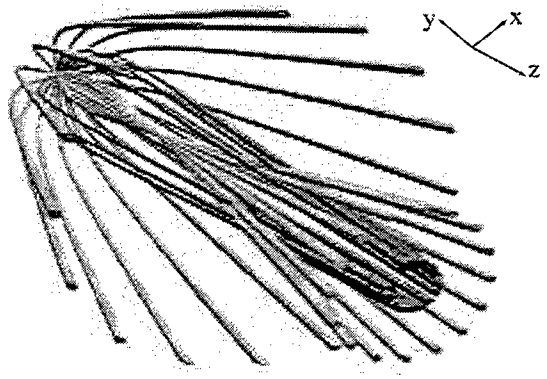


FIG. 4. Evolution of the position of the center of mass of the individual components, represented as tubes, during diffraction for Δ=1, σ=2.75, and P=20. The number of rings and spokes is N_r=N_s=16, and shown is spoke 1-16 on rings 2, 1-14 on ring 5, and 1-16 on ring 7. The corresponding walk-off is θ=0, 0.84, 2.11, and 2.94.

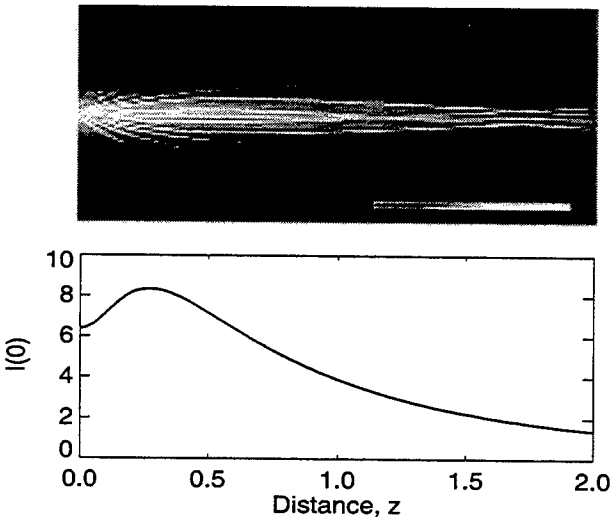


FIG. 5. Top: slice in the y=0 plane of Fig. 4 overlayed the total intensity in grey scale with white being the most intense. Bottom: Evolution of the maximum (center) intensity.

[1] M. Mitchell *et al.*, Phys. Rev. Lett. **77**, 490 (1996).
[2] M. Mitchell and M. Segev, Nature **387**, 880 (1997).
[3] D.N. Christodoulides, T.H. Coskun, M. Mitchell, and M. Segev, Phys. Rev. Lett. **78**, 646 (1997).
[4] Christodoulides *et al.*, Opt. Lett. **22**, 1080 (1997).
[5] G.A. Pasmanik, Sov. Phys. JETP **39**, 234 (1974).
[6] V.A. Aleshkevich, S.S. Lebedev, and A.N. Matveev, Sov. J. Quant. Electron. **11**, 647 (1981).
[7] L. Berge, O. Bang, W. Krolikowski, unpublished.

"Phase memory" effects and incoherent dark Y-soliton splitting

Tamer H. Coskun* and Demetrios N. Christodoulides
Department of Electrical Engineering and Computer Science
Lehigh University, Bethlehem, Pennsylvania 18015
dnc0@lehigh.edu

Zhigang Chen
Department of Physics and Astronomy
San Francisco State University, San Francisco, CA 94132

Mordechai Segev
Physics Department, Technion-Israel Institute of Technology,
and Electrical Engineering Department,
Princeton University, Princeton, New Jersey, 08544

Recent experimental and theoretical studies have shown that incoherent dark solitons are fundamentally different from their coherent counterparts [1-3]. For example, unlike a coherent gray soliton, an incoherent dark soliton does not exhibit a transverse velocity in spite of its grayness [1,3]. On the other hand, as in the case of coherent dark beam [4], an initial π-phase flip at the center of the beam leads to a fundamental dark incoherent soliton, whereas a uniform phase causes the beam to split into a Y-junction incoherent soliton [1].

Here, we show that , in spite of random phase fluctuations which tend to wash out the phase memory, a dark incoherent soliton remembers its initial phase imposed at the center. We compare the higher-order behavior of incoherent and coherent dark solitons under the same initial conditions. Surprisingly, we find that over a wide range of parameters, the Y-splitting is approximately the same irrespective of coherence. Experiments carried out in SBN:60 photorefractive crystal confirm our theoretical predictions.

Let us first discuss the diffraction behavior of coherent and incoherent dark beams under odd and even initial conditions. Diffraction of coherent and incoherent dark beams is analyzed by using the coherent density approach as done in Ref. [1]. The electrooptic coefficient of the crystal is $250\,pm/V$ and its extraordinary refractive index is 2.3.

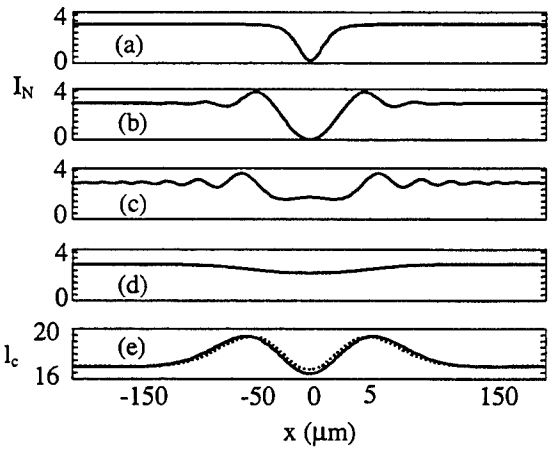


Fig. 1 (a) Intensity profile of an odd or even dark beam at the input. Diffraction of an (b) odd and (c) even coherent dark beam, and (d) an incoherent odd or even dark beam after 12 *mm* of propagation. (e) The coherence length curve in μm as a function of x for the odd (dashed curve) and the even (solid curve) diffracted incoherent dark beam.

The wavelength of the beam is $\lambda_0 = 514\,nm$. The input intensity FWHM of the even and odd dark beams is taken here to be $25\,\mu m$ as shown in Fig.1(a). Moreover, the normalized background intensity is $\rho = 3$. Figs. 1(b) and (c) show the

diffracted intensity profiles of coherent odd and even dark beams respectively after $12\,mm$ of propagation. In this case, the intensity FWHM of the odd dark beam at the output is $42\,\mu m$ whereas that of the even is $76\,\mu m$. It is important to note that after diffraction, the intensity of the odd coherent beam is always zero at the center whereas that of the even is gray-like. Fig. 1(d), on the other hand, demonstrates how an odd or even incoherent dark beam will diffract after 12 mm of propagation when at the input the correlation length, l_c, of the beam is $17\,\mu m$. This latter figure shows that, the intensity profiles of the odd and even incoherent dark beams are almost identical with an output FWHM of $100\,\mu m$. Simulations suggest that the same also applies for the coherence length curves corresponding to these two cases as shown in Fig. 1(e). Thus, from diffraction data alone, it is extremely difficult to distinguish an odd dark beam from an even one. In other words, the randomly changing speckled structure of an incoherent beam leads to a loss of phase memory. Therefore, as a result of this phase washing effect, a sufficiently incoherent dark beam diffracts approximately the same way regardless of the phase information initially imposed on it. An important distinction between diffraction of a coherent and an incoherent dark beam comes from the structure of their background. Figure 1 clearly demonstrates that a diffracted coherent dark beam exhibits intensity ripples on its background. These oscillations tend to disappear in the case of an incoherent beam as a result of its speckled structure.

When on the other hand the nonlinearity is activated, the dynamics of these incoherent beams depend on initial phase information. As previously shown, generation of a single incoherent dark (which is in reality gray) beam or a higher-order triplet requires a π-phase shift [1-3]. Conversely, starting from even initial conditions, an incoherent gray soliton pair or Y-soliton splitting can be obtained [1,2]. In other words, in the presence of nonlinearity, an incoherent dark beam tends to remember its origins and identity, i.e. a "phase-memory" effect is established. Thus, the beam starts to behave in a quasi-coherent fashion [4].

For comparison, experiments with an amplitude notch (even initial conditions) are performed by using both coherent and spatially incoherent light sources. Details regarding the coherent dark soliton experiments can be found in Ref. [4]. For the incoherent case, a rotating diffuser is employed to provide random phase fluctuations across the beam [2]. In this case, we generate a dark notch on a broad partially spatially incoherent beam with controllable degree of coherence. The experimental arrangement is the same as that in Ref. [2], except that the phase mask is now replaced by an amplitude mask.

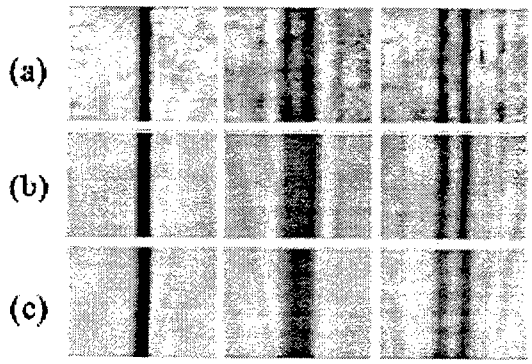


Fig. 2 Experimental observation of coherent and incoherent Y-splitting: (a) coherent dark beam; (b) (c) incoherent dark beam with an average speckle size of $30\,\mu m$ and $15\,\mu m$ respectively. The first column depicts the input intensity, the second one diffraction data, and the third one Y-splitting at –350 V.

Incoherent Y-junction solitons are generated and then compared with the coherent ones. Fig. 2 shows typical experimental results. When the dark beam is coherent and in the absence of nonlinearity, it diffracts from a FWHM of 25 μm (left) to about 58 μm after 12 mm of propagation (middle). Note that, with the exception of the dark notch FWHM (which from simulations is expected to be 76 μm), its intensity structure is in agreement with Fig. 1(c). The discrepancy in FWHM is attributed to the fact that the reflection from the metallic wire introduces a quadratic phase [4] which is not accounted in our simulations.

After applying a voltage of –350 V (negative relative to the c-axis), the dark amplitude notch evolves into a pair of gray solitons (right). The second and third rows of this figure depict the same data when the dark beam is incoherent. The right column of the figure was obtained at –350 V and with an input FWHM of 25 μm. As seen in Fig. 2, the grayness of the soliton pair increases as the coherence of the beam decreases. Nevertheless, the spacing of these two solitons at the crystal output face is about the same for a varying degree of coherence.

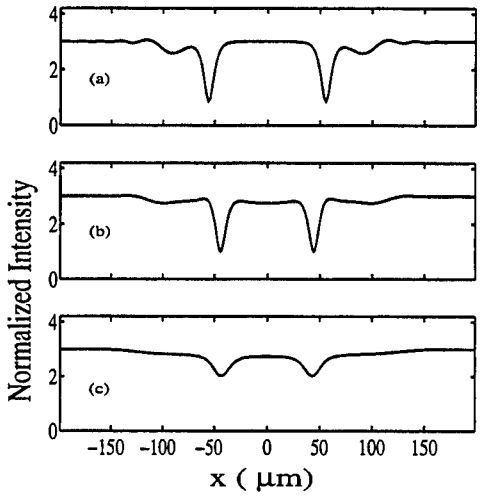


Fig. 3 Intensity profile of a soliton doublet at $z = 12$ *mm* when the external bias is –450 V and the beam is (a) coherent or (b) incoherent with $l_c = 25\mu m$ and (c) $l_c = 17\mu m$.

These experimental results are now compared with numerical simulations. By keeping in mind that in the experiment, the input speckle size of the incoherent beams is $30\mu m$ for Fig. 2(b) and $15\mu m$ for Fig. 2(c) and by considering their diffraction behavior, we estimate that the width of the angular power spectrum in these two cases is 3.5 *mrads* and 5.2 *mrads* respectively. The simulation shown in Fig. 3(a) demonstrates how a coherent soliton doublet forms from a 25 μm even dark beam after 12 *mm* of propagation when the bias voltage is –450 V. For the same bias voltage and initial beam width, the intensity profile of an incoherent doublet after 12 *mm* of propagation is shown in Fig. 3(b) when $l_c = 25\mu m$. Fig. 3(c) depicts similar data when $l_c = 17\mu m$ and again the bias is –450 V. Here, again coherent density is used in obtaining these results. In agreement with the experiment, Fig. 3 demonstrates that the doublet becomes grayer as the incoherency increases. Surprisingly, for this range of parameters, both theory (Fig. 3) and experiment (Fig. 2) suggest that the Y-splitting angle or the doublet separation does not depend strongly on the degree of coherence. Thus, the evolution of incoherent dark solitons in non-instantaneous nonlinear media is associated with strong "phase-memory" effects which are otherwise absent in the linear regime.

This work was supported by AFOSR, ARO, and NSF.
* Permanent address, Pamukkale University, Electronics Engineering Department, Denizli, Turkey.

References

[1] T. H. Coskun, D. N. Christodoulides, M. Mitchell, Z. Chen, and M. Segev, Opt. Lett. 23, 418 (1998).

[2] Z. Chen, M. Mitchell, M. Segev, T. H. Coskun, and D. N. Christodoulides, Science 280, 889 (1998).

[3] D. N. Christodoulides, T. H. Coskun, M. Mitchell, and M. Segev, Phys. Rev. Lett. 80, 5113 (1998).

[4] Z. Chen, M. Segev, S. R. Singh, T. H. Coskun, and D. N. Christodoulides, J. Opt. Soc. Am. B 14, 1407 (1997).

Fixing Solitonic Waveguides in Photorefractive Strontium Barium Niobate

Matthew Klotz, Mike Crosser, Gregory J. Salamo
Physics Department. University of Arkansas, Fayetteville, AR 72701
(501) 575-2506
salamo@comp.uark.edu

Mordechai Segev
Department of Electrical Engineering and Center for Photonics and Opto-Electronic Materials (POEM), Princeton University, Princeton, New Jersey 08544
segev@ee.princeton.edu

Optical spatial solitons[1] in photorefractive crystals[2] have shown potential to form graded index waveguides which can guide other beams[3,4]. A soliton forms when a photoinduced index change in the material exactly compensates for the diffraction of the beam; i.e. the beam creates its own waveguide. In photorefractive materials, a screening soliton is formed by the screening of an externally applied electric field through the transport of photoinduced carries[5]. However, these induced waveguides disappear if the applied field is removed from the material. In this paper we report on the use of soliton formation to create permanent waveguides by selectively reorienting ferroelectric domains within the propagating light beam.

For the experiment, the output of an argon-ion laser is collimated and focused to a spot size of 12 μm on the front face of a 1 cm cubic SBN:75 crystal. When a 3 kV/cm electric field is applied to the crystal along the direction of the spontaneous polarization, the beam self focuses to its input diameter. The external field is then removed and a uniform background beam that fills the crystal is switched on. The space charge field due to photoinduced screening charges is larger than the coercive field of the ferroelectric domains and causes the domains in the area of the incident beam to reverse their orientation. At equilibrium, a new space charge field, due to the bound charge at the domain boundaries is locked in place. This new field increases the index of refraction in only the area of the original soliton, so that a waveguide is formed. The waveguides are observed to have the same size as the original soliton, exhibit single mode behavior and last indefinitely.

In addition to fixing single and multiple solitons (FIG.1), a coherent collision of two solitons was used to fixed several y-junctions in the crystal (FIG.2). Two mutually coherent, in phase beams were focused on the entrance face of the crystal with a peak to peak separation of 33 μm. As the applied electric field was increased, the two beams fused into one output beam, forming a y-junction. Following the procedure outlined above, several y-junctions were fixed in the crystal. The output intensity was observed to be dependent on the relative phase of the input beams. For beams with no phase difference, the output was maximized while with a relative π phase difference, no output was observed. To verify that the y-junction was bidirectional, a HeNe laser was coupled into the 'output' of the y-junction. It was observed that the intensity was evenly divided into two outputs, with a peak to peak separation equal to the original separation of the Argon ion beams. In addition, we also demonstated a technique to form a fixed wave guide which propagated unpolarized light

References

1. R.Y. Chiao, E. Garmire, and C.H. Townes, Phys. Rev. Lett **13**, 479 (1964).
2. M. Segev, B. Crosignani, A. Yariv, and B. Fischer, Phys. Rev. Lett. **68**, 923 (1992).
3. M. Morin, G. Duree, G. Salamo and M. Segev Opt. Lett. 20, 2066 (1995).
4. M. Segev, G.C. Valley, B. Crosignani, P. DiPorto, and A. Yariv, Phys. Rev. Lett. **73**, 3211 (1994).
5. M. Segev, M. Shih, and G. C. Valley, J. Opt. Soc. Am. B **12**, 1628, (1995).

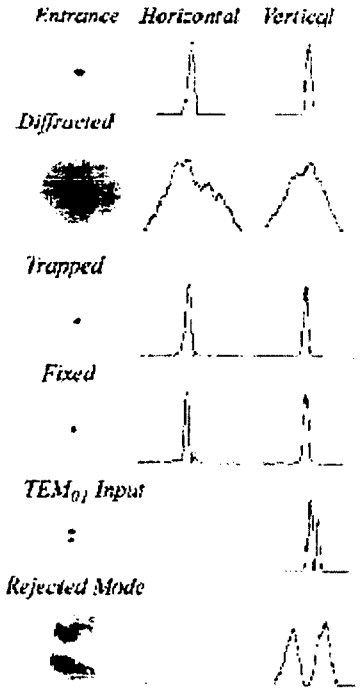


Fig.1 Intensity profiles for a single guided wave, showing the input at the entrance face, the diffracted output at the exit face, the trapped soliton at the exit face and the fixed waveguide output at the exit face. A TEM_{01} input at the entrance face and its rejected output at the exit face are also shown.

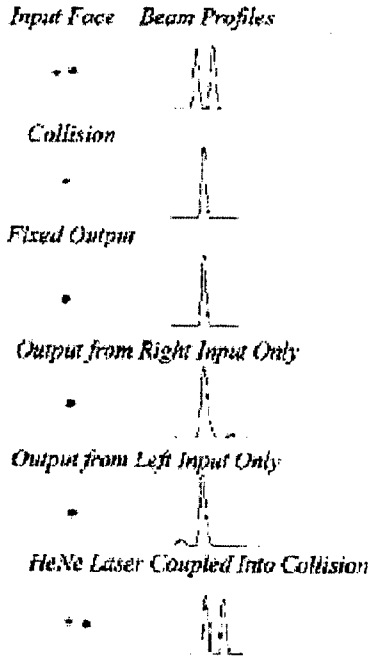


Fig.2 Intensity profiles for a coherent collision, showing the input at the entrance face, the collision at the exit face, and the fixed y junction output at the exit face when excited by both or only one input beam. The output of a HeNe laser coupled into the collision is also shown.

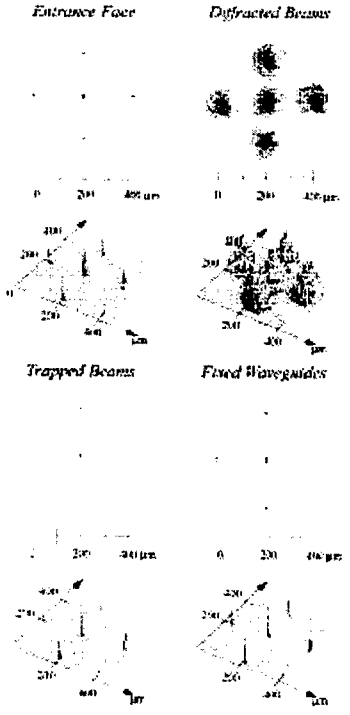


Fig.3 Three dimensional plot of of several fixed soliton waveguides.

Nonlinear Guided Waves and Their Applications

Materials and Characterization

Friday, 3 September 1999

J. Stewart Aitchison, University of Glasgow, UK
Presider

FA
08.00-10.00
Salle Morey—St-Denis

Frequency conversion and parametric processes in form-birefringent semiconductor heterostructures (Invited talk)

V. Berger[1], G. Leo[2]

[1]THOMSON CSF Laboratoire Central de Recherches,
Domaine de Corbeville, 91400 ORSAY, FRANCE.
[2]Dipartimento di Ingegneria Elettronica, Università "Roma Tre",
00146 ROMA, ITALY
e-mail: vincent.berger@lcr.thomson-csf.com

In this talk we discuss the feasibility of a parametric oscillator integrated on a GaAs chip, after reviewing the recent frequency conversion experiments using form birefringence in GaAs/oxidized-AlAs waveguides.

Since bulk GaAs is an optically isotropic semiconductor, birefringence phase-matching is impossible. In spite of this problem, GaAs is a very attractive material for nonlinear optics, for several reasons. Its large $\chi^{(2)}$ ($\simeq$ 100 to 250 pm/V) gives about one order of magnitude greater intrinsic efficiency than the commonly used nonlinear materials. Second, the mature know-how in growth and technology of AlGaAs /InGaAs/GaAs materials provides multiple tools that can be used in a frequency conversion scheme: technological processes enable the design of various optical heterostructures (such as microcavities or quantum wells (QWs)). Furthermore, the possibility of integrating a nonlinear converter with the most efficient laser sources that are QWs is highly attractive, opening the way to complete nonlinear systems (as optical parametric oscillators) on a GaAs chip. Recently, phase-matching has been demonstrated in a GaAs-based waveguide, using form birefringence in multilayer heterostructures GaAs/oxidized AlAs (Alox) [1].

This concept was first demonstrated in a difference frequency generation (DFG) experiment, and details can be found in [1, 2]. Form birefringences n(TE)$-n$(TM) from 0.15 to 0.2 have been measured for different GaAs/Alox waveguides, which is sufficient to phase match mid-infrared generation between 3 μm and 10 μm by DFG from two near-infrared beams. Note that by increasing the width of Alox layers, much higher birefringences up to 0.65 could be achieved, in principle.

Typical mid-IR output powers of 120 nW were obtained at 4.8 μm (TE polarisation) for 0.4 mW and 17 mW of Nd:YAG at 1.32 μm (TE polarisation) and Ti:Sa at 1.035 μm (TM polarisation) pump powers, respectively [2]. By increasing pump powers and reducing scattering losses originating from processing [2], this result can easily be pushed into the μW range, which is an interesting power level for mid-infrared spectroscopic applications. We also demonstrated the general feasability of form birefringence for nonlinear optics phase matching with a SHG experiment at 1.6 μm.

A second step towards the realization of an OPO was the observation of parametric fluorescence. Parametric fluorescence was measured at 2.1 μm in an oxidized AlGaAs form-irefringent waveguide [4]. The signal level measured is around 15 pW, over the range 1.9–2.5 μm, for

typical injection levels of 10 mW. The sample consists of a high-index, strongly birefringent guiding core made of a GaAs-Alox stack, embedded in an AlGaAs cladding, similarly to the sample used for our previous demonstration of DFG.

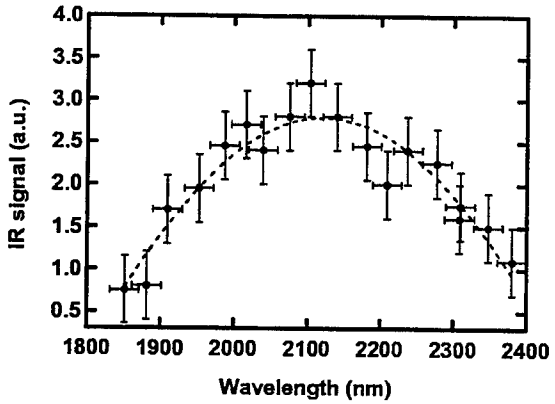


Figure 1: Observed TE spectrum near the half-harmonic frequency of the TM pump at 1.064 μm.

This power level, which is comparable to the first observation of parametric fluorescence at 1.3 μm in $LiNbO_3$ waveguides [5], makes difficult to use a monochromator for the spectroscopy of the generated radiation in the wavelength range of interest here. To this aim we therefore resorted to a set of six narrow-band (40 nm) interferential filters, tunable with the angle of incidence. The spectrum of the TE-polarized output component is shown in Fig.1, where IR generation appears to peak at about 2.1 μm.

One of the most exciting perspectives opened with this new type of nonlinear material is the realization of an OPO on a GaAs chip. To this aim, minimization of losses is the most crucial point. Using the expressions from ref [6], the OPO threshold was calculated and plotted in figure 2 as a function of losses, supposed to be equal at pump, signal and idler frequencies. A typical value of this threshold is less than 100 mW (in the guide) for 1 cm^{-1} losses, and with 90% reflection coefficients. The level of losses is now of the order of 2 cm^{-1}; which implies the need for an improvement of the waveguide fabrication process. After a further decrease of the losses it will be worth to invest in the optimization of broad-band multidielectric mirrors. Note by the way that reflection coefficients up to 90% are currently obtained with high-reflecting mirrors for semiconductor lasers.

Other perspectives of form birefringent semiconductor waveguides will be discussed:

- *Simultaneous frequency conversions:* Form birefringence is an example of building an artificial structure with the desired optical properties, that is an illustration of refractive index engineering. It is obvious that the large number of degrees of freedom in the design of the structures enables to design waveguides with several simultaneous constraints. For instance it is possible to design a guide in which the doubling process $\omega + \omega \rightarrow 2\omega$ and the sum frequency (SFG) process $\omega + 2\omega \rightarrow 3\omega$ are simultaneously phase matched. The three waves ω, 2ω and 3ω obey to a new system of nonlinear coupled equations and interact simultaneously.

- *Use of QWs as nonlinear material:* Form birefringence phase matching has been demonstrated using bulk GaAs as nonlinear material. In principle, the huge nonlinear susceptibilities related to intersubband transitions in quantum wells [7] is readily feasible by growing asymmetric GaAs/AlGaAs quantum wells in the core of a GaAs/Alox structure.

- *Non-critical phase matching:* Another consequence of the large number of degrees of freedom in the design of the structures is the possibility to choose, among all the possible phase-

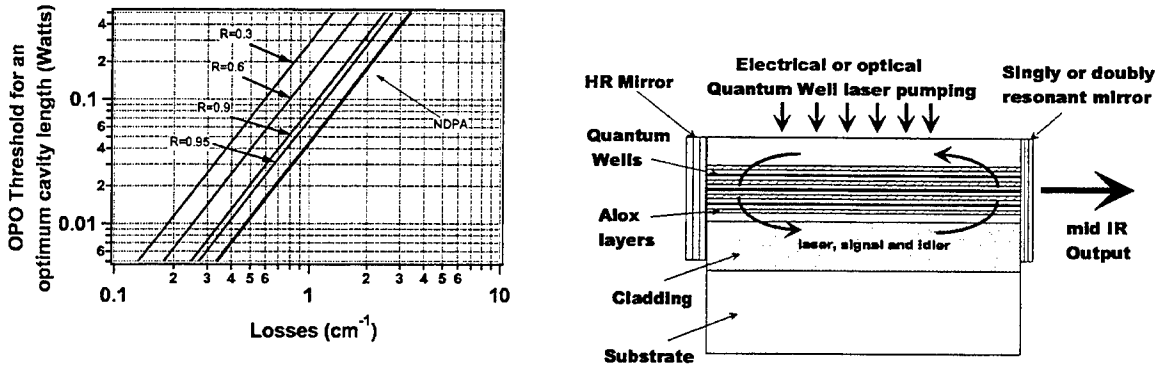


Figure 2: Left: OPO threshold power (coupled inside the waveguide) as a function of waveguide losses, for several reflection coefficients for signal and idler waves. The curve NDPA is the limit of a non-depleted pump approximation. Right: General scheme of an integrated OPO. The semiconductor QWs give the gain for laser action, and the Alox layers give the form birefringence necessary for parametric fluorescence and optical parametric oscillation in the mid IR.

matched structures, the one with the widest phase matching resonance.

- *Self-pumped optical parametric oscillator (QW laser OPO):* The introduction of inverted QWs in the nonlinear structure would be of great interest if the optical gain could be pushed above lasing threshold. In such case, the structure would be basically a semiconductor laser, with intracavity phase-matched parametric fluorescence. If losses at the parametric frequencies are lower than the parametric gain, such a structure, which is schematically represented in Fig. 2, is an OPO which provides its own pump internally. The full OPO system, including laser pump, nonlinear material and cavity, would be integrated in the same cavity on a semiconductor chip. This would represent the smallest OPO system ever realized, and also an alternative way to extend the range of room temperature semiconductor lasers in spectral regions where they are not yet available (*e.g.* around 4 μm). Several problems need to be solved, however, before the realization of such a device: 1) again, losses have to be reduced (this is a processing issue); 2) since the lowest wavelength in the nonlinear interaction must be TM polarized, the QWs have to lase in the TM polarization, which is possible but not usual.

This work was supported by the European Community under the IT "OFCORSEII" program.

References

[1] A. Fiore, V. Berger, E. Rosencher, P. Bravetti, and J. Nagle, Nature **391,** 463 (1998).

[2] P. Bravetti, A. Fiore, V. Berger, E. Rosencher, J. Nagle, O. Gauthier-Lafaye, Opt. Lett. **23,** 331 (1998).

[3] A. Fiore, *et al.* Appl. Phys. Lett. **72,** 2942 (1998).

[4] G. Leo, V. Berger, C. Ow Yang, J. Nagle, submitted to J. Opt. Soc. Am. B (1999).

[5] P. Baldi *et al.*, IEEE J. Quantum Elec. **31**, 997 (1995).

[6] G. P. Bava, I. Montrosset, W. Sohler, and H. Suche, IEEE J. Quantum Electron. **QE-23**, 42 (1987).

[7] For a review of this topics, see V. Berger, p. 345-374, in "Advanced Photonics with Second-Order Optically Nonlinear processes", A. Boardman, ed., Kluwer Accademic Publishers (1999).

Determination of nonresonant optical nonlinearities in undisordered and disordered semiconductor superlattices

D. C. Hutchings
Dept. of Electronics and Electrical Engineering, University of Glasgow, Glasgow G12 8QQ, Scotland, U.K.
Tel: +44-141-330-6026, Fax: +44-141-330-6002, e-mail: dch@elec.gla.ac.uk

Introduction

Direct-gap semiconductors have found numerous applications as diode lasers, light-emitting diodes and optical amplifiers. There is also an emergence of semiconductors as nonlinear optical elements. For example the nonlinear refractive coefficient n_2 at 1.55 μm in AlGaAs is around 10^3 times larger than in silica. The second-order coefficient for optical frequency conversion is similarly enhanced over conventional materials, for example, $\chi^{(2)}_{xyz}$ has a value around 300 pmV^{-1} for GaAs in the near-IR[1] which is 1–2 orders of magnitude larger than conventional ferroelectric crystals. The current limitation on the exploitation of semiconductors as wavelength conversion elements is the development of novel phase-matching techniques, particularly as cubic semiconductors lack an intrinsic material birefringence. One of the emerging technologies for the control of nonlinear optical coefficients is quantum well disordering,[2] opening up the possibility of integrated (with diode laser pump) semiconductor optical parametric oscillators, for example.

A key requirement is a predictive capability for nonlinear optical coefficients in semiconductor heterostructures and their modification under disordering. It has previously been established that induced second-order coefficients are maximised by (1) increasing the number of quantum wells per unit thickness (increasing the density-of-states) and (2) increasing the inter-subband separation.[3] Both of these requirements indicate short-period, deep-well superlattice are desired.

Disordered Superlattice Bandstructure Algorithm

Prediction and optimisation of the linear and nonlinear optical properties requires knowledge of (1) the energies of the electronic states of the material and (2) the optical matrix elements between them (obtainable from the electronic wavefunctions). That is a suitable bandstructure algorithm must lie at the core of any calculation. Here an algorithm is developed for calculating the bandstructure in semiconductor superlattices based on the $\mathbf{k}\cdot\mathbf{p}$ method. The basis functions for this algorithm are the topmost valence band triplet (Γ^{v}_{15}), the lowest conduction singlet (Γ^{c}_{1}) and the higher triplet (Γ^{c}_{15}) states[4] and hence the model is anisotropic and non-centrosymmetric. These higher bands are necessary for obtaining a non-zero second-order nonlinearity[5] and for predicting the substantial anisotropy of third-order nonlinearities in the vicinity of the half-bandgap[6] in bulk semiconductors.

The dynamics of quantum well disordering are most commonly described by Fick's Second Law. This attributes the change in alloy concentration $\phi(z,t)$ under the disordering process to a diffusion equation. On examining the solution of the diffusion equation in Fourier space, the Fourier coefficients of an initial square-wave profile are modified by a Gaussian factor,

$$\phi_n(T) = \begin{cases} \left[(L_p - L_z)\phi_b + L_z\phi_w\right]/L_p & n = 0 \\ -\frac{1}{n\pi}(\phi_b - \phi_w)\sin n\pi\frac{L_z}{L_p}\exp-\left(n\pi\frac{L_d}{L_p}\right)^2 & n \neq 0 \end{cases} \quad (1)$$

where ϕ_w and ϕ_b represent the alloy concentrations for the well and barrier regions respectively, L_z is the well-width, L_p the superlattice period and L_d the diffusion length which characterises the extent of the disordering process. In addition to investigation of disordered profiles, this also allows the Gibbs phenomenon to be circumvented by incorporating a small, nonzero degree of disordering and therefore provides a more satisfactory representation of alloy profiles in the Fourier domain.

The solution of the 14×14 electronic Hamiltonian[4] is also sought in the Fourier domain. Multiplications in real space are replaced with discrete convolutions in Fourier space and the Hamiltonian matrix is transformed from a set of coupled differential equations to a set of $14(2N+1)$ algebraic equations (truncating the Fourier series at the Nth order). This matrix is then diagonalised using standard numerical libraries. An additional advantage of solving the electronic

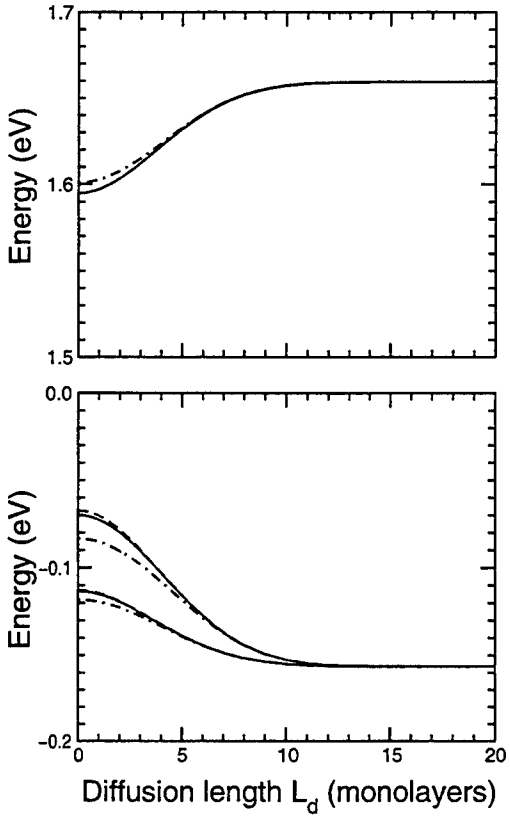


Figure 1: Shift of the lowest conduction state and highest valence band states (k_x, k_y, k_z=0) with disordering diffusion length L_d. The maximum order of the Fourier coefficients taken are 1 (chain), 2 (dashed), 4, 8, 16, 32 (all solid).

Hamiltonian for superlattices is that there is that there is no distinction made between bound and continuum states in contrast to conventional heterostructure solvers.

The example symmetric superlattice structure examined here consists of 10 monolayers of GaAs and 14 monolayers of $Al_{0.5}Ga_{0.5}As$. Fig. 1 shows, as an example, the shift with increasing diffusion length L_d of the lowest conduction and uppermost valence sub-band edges (located at k_x, k_y, $k_z = 0$) taking the maximum order of the Fourier series as indicated. The disordering process causes a blue-shift of the band-edge and restores the heavy-hole/light-hole degeneracy and is effectively complete around $L_d/L_p \sim 1/2$. Note that for this superlattice structure, very few Fourier orders are required for an adequate simulation, with the dominant effect being due to the reduction in amplitude of the first-order Fourier coefficient for the potential profile.

Determination of Nonlinear Optical Coefficients

For the second-order nonlinearity, the heterostructure breaks the degeneracy between the $\chi^{(2)}_{xyz}$ and $\chi^{(2)}_{zxy}$ tensor elements. It is anticipated that the blue-shift of the band-edge on disordering leads to a reduction in the magnitude of the second-order nonlinearity through the resonant denominators. In Fig. 2 the calculated dispersion of $\chi^{(2)}_{zxy}$ is shown for the example AlGaAs superlattice structure described above for the undisordered ($L_d = 0$) and disordered ($L_d = 12$ monolayers) cases. The calculation is based on the three-level $\mathbf{A} \cdot \mathbf{p}$ expressions for the second-order susceptibility derived in Ref. 3 which also incorporate virtual inter-valence transitions. As the bandstructure basis states are taken at the Γ-point, the states at the Brillouin zone edges are not adequately accounted for. Hence the calculated values for the second-order susceptibility contain an unphysical divergent term ($\sim \omega^{-2}$) which is discarded and a constant background value which is underestimated here. However the resonant features are accurately represented and it is these which give rise to the modulation on disordering. For this particular example there is only a modest reduction observed in the value of nonlinear susceptibility (10–20 pmV^{-1}) just beneath the original half-bandgap. The reason for this small modulation

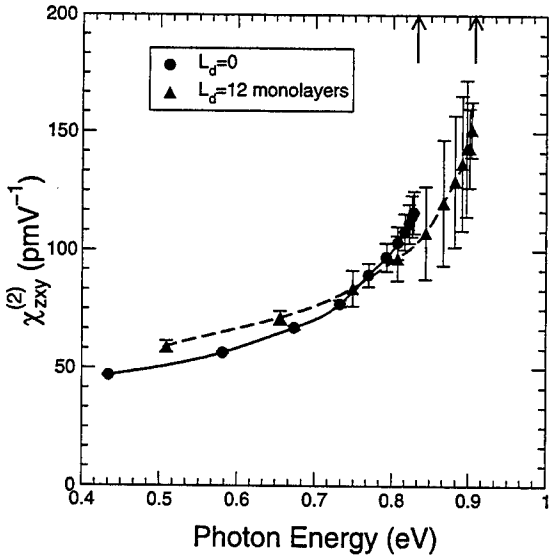


Figure 2: Calculated dispersion of $\chi^{(2)}_{zxy}$ in the AlGaAs superlattice example for $L_d = 0$ and 12 monolayers. The maximum Fourier order was taken to be 8 and the integration limit taken as $k_{\|}(\max) = 0.6$ (eV)$^{1/2}$ (about halfway to the Brillioun zone edge). As the integration takes place over three dimensions in k-space, convergence is relatively slow and the upper bounds on the magnitude of the numerical error after a maximum of 2000 evaluations are also shown. The arrows indicate half the band-edge in both the undisordered and disordered cases.

in the second-order susceptibility is that the increase in bandgap of the "well" regions is compensated by the decrease in bandgap of the "barrier" regions, i.e. the resonance in the second-order susceptibility is enhanced in the disordered case.

An alternative method for controlling the modulation of the second-order susceptibility is to employ asymmetric heterostructures where additional non-zero tensor elements are induced: $\chi^{(2)}_{xzx}$, $\chi^{(2)}_{zxx}$ and $\chi^{(2)}_{zzz}$. These coefficients revert to zero on disordering as the heterostructure is symmetricised. These induced coefficients are small for typical MQW[3,7,8] but should be substantially enhanced in short-period superlattices.

In the case of third-order nonlinearities (nonlinear refraction or two-photon absorption), the heterostructure also causes a breaking of the tensor element degeneracies, providing 8 independent non-zero tensor elements in comparison to 3 for bulk semiconductors. An example of the consequences of this is that cross-phase-modulation between the two orthogonal polarisation components in a semiconductor waveguide is degenerate in bulk but not in heterostructures.

References

[1] M. M. Choy and R. L. Byer, Phys. Rev. B **14**, 1693 (1976).

[2] J. S. Aitchison, M. W. Street, N. D. Whitbread, D. C. Hutchings, J. H. Marsh, G. T. Kennedy and W. Sibbett, IEEE J. Sel. Topics Quantum Electron. **4**, 695 (1998).

[3] D. C. Hutchings and J. M. Arnold, Phys. Rev. B **56**, 4056 (1997).

[4] P. Pfeffer and W. Zawadzki, Phys. Rev. B **41**, 1561 (1990); **53**, 12813 (1996).

[5] M. I. Bell, in *Electronic Density of States*, ed. L. H. Bennett, Natl. Bur. Std. (US) Spec. Publ. **323**, 757 (1971).

[6] D. C. Hutchings and B. S. Wherrett, Phys. Rev. B **52**, 8150 (1995).

[7] S. Janz, F. Chatenoud and R. Normandin, Opt. Lett. **19**, 622 (1994).

[8] A. Fiore, E. Rosencher, V. Berger and J. Nagle, Appl. Phys. Lett. **67**, 3765 (1995).

Ultrafast excitonic saturable absorption at 1.55 µm in heavy-ion irradiated quantum well vertical cavity

J. Mangeney, J. L. Oudar, J. C. Harmand, C. Mériadec, G. Patriarche, G. Aubin
France Telecom - CNET/DTD/CDP, 196 avenue Henri Ravera, 92220 Bagneux, France
tel: +33 1 4231 7258 - fax: +33 1 4253 4930 - jeanlouis.oudar@cnet.francetelecom.fr

N. Stelmakh, J. M. Lourtioz
Institut d'Electronique Fondamentale, CNRS URA 022, Bat. 220, Université Paris-Sud, 91405 Orsay Cedex, France - tel: +33 1 6915 4015 - Nikolai.Stelmakh@ief.u-psud.fr

For the processing of high bit rate optical data transmitted in broadband fiber optic networks, the development of efficient all-optical active devices is of crucial importance, as in many instances one would like to avoid the complexity of using high speed electronics. A specific application in optical data transmission (e. g. soliton [1] or RZ transmission), is that of data regeneration, which can be a complex task, especially in a WDM context. In data regenerators one needs to compensate for the signal distorsions and S/N degradations introduced at the various data processing stages[2]. In particular, amplified spontaneous emission (ASE) due to optical amplifiers introduces a noise in the "zeros" of return-to-zero optical data streams, which must be suppressed when one plans to perform a large number of transformations (such as switching, demultiplexing...) on the data.

Semiconductors are the most promising materials because they offer the possibility of achieving compact devices. Saturable absorbers allow the practical realization of all-optical switches, such as demultiplexing switches[3] based on excitonic absorption in InGaAlAs/InAlAs multiple quantum wells. They can operate at potentially very high repetition rates (>100 Gbit/s), provided that the carrier lifetime is drastically reduced through the introduction of recombination centers during or after the crystal growth[3-5]. In these quantum wells, absorption saturation recovery times shorter than 2 ps have been obtained[3,4], however the reported experiments have been performed at repetition rates below 100 MHz, or at best with short pulse trains simulating a high repetition rate. This leaves as an open question the actual behaviour of the devices under true high repetition rate conditions.

The problems that may be anticipated at high repetition rates are of two kinds: an excessive temperature rise if the dissipated power density is too high, and a recombination bottleneck if the carrier traps that mediate the absorption recovery cannot be cycled fast enough to accomodate for a high average carrier generation rate. The thermal problem can be minimized through a reduction of the switching energy, and the recombination bottleneck can be avoided by the introduction of efficient recombination centers. It has recently been shown that irradiation with high energy heavy ions is a promising way to obtain these two features[4,6]. The excitonic absorption lines of the InGaAs quantum wells were preserved for a nonlinear absorption recovery time as low as 1.7ps, which is favorable to achieve a small switching energy, and subpicosecond recovery time was demonstrated (in bulk GaAs) without any relaxation up to excitation densities as high as 1.6 mJ/cm^2. This rather unique combination of desirable features is due to the fact that irradiation with high energy heavy ions produces clusters of point defects[6]. These clusters should have a high number of electronic states which open up a large number of recombination channels, while their areal density can be kept small enough for the excitonic features to be preserved. In addition, the use of microcavity effects can enhance the effective nonlinearity, and contribute to the reduction of the switching energy[7]. The present devices incorporate a combination of these advantages.

A reflection mode vertical cavity geometry at normal incidence was adopted, because it is intrinsically polarization insensitive, and it allows to play with interferometric effects to cancel the reflection coefficient at low intensity, thereby allowing a high on/off switching ratio. The device structure is shown on Figure 1. The MBE-grown absorber consists of 6 groups of an 7 period MQW InGaAs/InAlAs structure, with the MQW groups separated by InAlAs spacers, and located at the antinodes of the intracavity intensity. This design, with a resonant periodic absorber, ensures a stronger and more uniform coupling of the saturable absorber quantum wells with the optical signal. The samples were irradiated by 12 MeV Ni^+ ions, with an irradiation dose up to 3 10^{12} cm^{-2}. The ions have a high enough energy to go completely through the quantum well structure, leaving only trails of defects along their trajectory, until they are finally stopped in the InP substrate. After irradiation, the cavity was formed by deposition of an Ag film, top-down mounting of the structure, and a final chemical etching to remove the InP substrate. Hence the ions used to create the defects are no longer present in the structure.

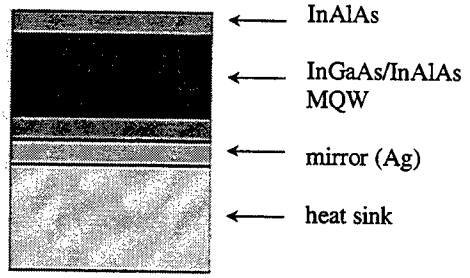


Figure 1: Device structure

The nonlinear response of the devices was measured with a reflection mode pump-probe set-up, using single short pulses generated by a mode-locked fiber laser at 1.55 μm. Two series of measurements were performed, one with a passively mode-locked source generating 1 ps pulses at 20 MHz repetition rate, and the other with an actively mode-locked source generating 5 ps pulses at 10 GHz.

The pump-probe measurements displayed on Figure 2, obtained with the 1 ps, 20MHz laser source, show the reduction of relaxation time that is obtained at increased implantation doses. The relaxation time values deduced from these curves are displayed in Table 1. The evaluation of the relative efficiency of the various samples indicates that the saturation energy is essentially constant (within the experimental accuracy) up to an irradiation dose of 10^{12} cm^{-2}, while there is a noticeable increase of this parameter at

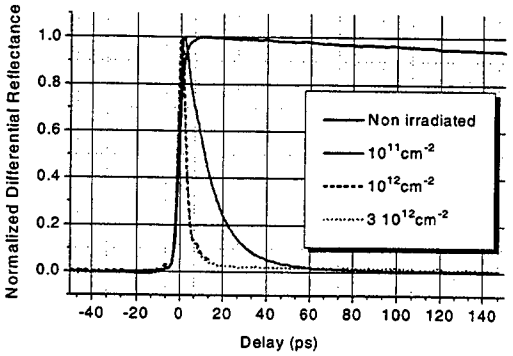


Figure 2: Differential reflectance *vs* probe delay

Irradiation dose	Relaxation time
(non irradiated)	>1 ns
10^{11} cm^{-2}	12.0 ps
10^{12} cm^{-2}	3.2 ps
3 10^{12} cm^{-2}	2.4 ps

Table 1: Relaxation time of the samples at various irradiation doses

the 3 10^{12} cm^{-2} irradiation dose. This is to due to the persistence of the quantum well excitons up to the 10^{12} cm^{-2} dose. For the 10^{11} cm^{-2} irradiated sample, the relaxation time was found constant within the ± 1% experimental accuracy, when measured with pump energies varying from 10 to 30 pJ. The low intensity reflectance R_0 varied somewhat on the sample surface, due to the non-ideal surface uniformity,

with values below 0.04 at the cavity resonance. In that case the contrast ratio R_1/R_0 between the reflectance at high (>10 pJ) and low (<1 pJ) pulse energies could be as high as 3.5:1, and the best measured absolute differential reflectance $\Delta R=R_1-R_0$ was 0.20, which shows the good switching capability of this device. The measurements performed at 10 GHz did not show any degradation of the switching speed at high repetition rate (see Figure 3). The relaxation time measured on the 10^{11} cm^{-2} irradiated sample was 12ps, i.e. exactly the same as the value measured at 20 MHz. For the two faster samples the differential reflectance signal essentially followed the ~5ps pump pulse, indicating that the relaxation time is shorter than the pulse duration.

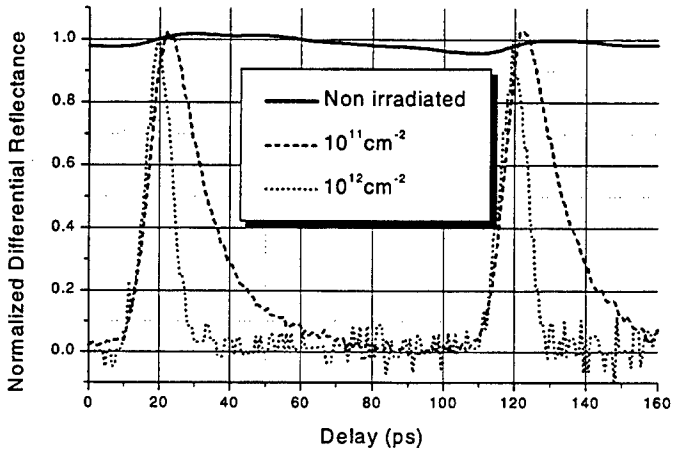


Figure 3: Differential reflectance measured at 10 GHz repetition rate

In conclusion, these results show that heavy-ion irradiated quantum wells can provide the basis for efficient compact optical switching devices, operating at optical communication wavelengths. The reflection mode vertical cavity device structure is advantageous in many respects, including an increased design flexibility, good thermal properties, and polarization insensitivity.

This work was partially supported by the french Telecom Research Network (RNRT - ASTRE project).

References

1. O. Audoin, E. Pallise, E. Desurvire, and E. Maunand, IEEE Photonics Technol. Lett., **10**, 828 (1998)

2. J. C. Simon et al., "All-optical regeneration", Proceedings of ECOC'98 p. 467 (Sept 98), Madrid

3. R. Takahashi, Nonlinear Guided Waves and their Applications, OSA 1998 Techn. Digest Series Vol 5

4. E. Lugagne-Delpon, J. L. Oudar, N. Bouché, R. Raj, A. Shen, N. Stelmakh, and J. M. Lourtioz, Appl. Phys. Lett. **72**, 759 (1998)

5. S. Benjamin, H. Loka, A. Othonos, and P. W. Smith, Appl. Phys. Lett. **68**, 2544(1996)

6. N. Stelmakh, J. Mangeney, A. Alexandrou, and E. L. Portnoi, Appl. Phys. Lett. **73**, 3715 (1998)

7. J. L. Oudar, R. Kuszelewicz, B. Sfez, J. C. Michel, and R. Planel, Opt. and Quant. Electron. **24**, S193 (1992).

DISPERSION-SCAN METHOD FOR THE MEASUREMENT OF NONLINEAR REFRACTION AND ABSORPTION OF WAVEGUIDES

• E. Lopez-Lago, F. Louradour and A. Barthélémy
Institut de Recherche en Communications Microondes et Optiques, UMR n°6615 du CNRS,
Faculté des Sciences, 123 ave. A. Thomas, 87060 Limoges, France.

We propose a new technique for the measurement of the nonlinear refractive index and two photon absorption coefficients of waveguides and bulk nonlinear materials, The presented method, that was named "D-scan[1]", is nothing but the temporal analogue of the Z-scan[2] technique which is based on spatial distortion of gaussian beam. The converging or diverging input beams in the Z-scan are replaced here by up-chirped or down-chirped pulses, the intensity induced wavefront curvature is replaced by intensity induced temporal phaseshift, and finally the far field detection is replaced by a spectral analysis. The D-scan is applicable to waveguides as well as to bulk nonlinear materials, isotropic or anisotropic. This method is principally sensitive to fast (electronic) contribution to the intensity dependent refractive index change and permits to avoid the influence of long time response contribution like the one due to thermal effect. It requires only a single beam delivered by a femtosecond laser source, which avoids the problems of alignment, collinearity and polarisation associated to method based on pump-probe beams.

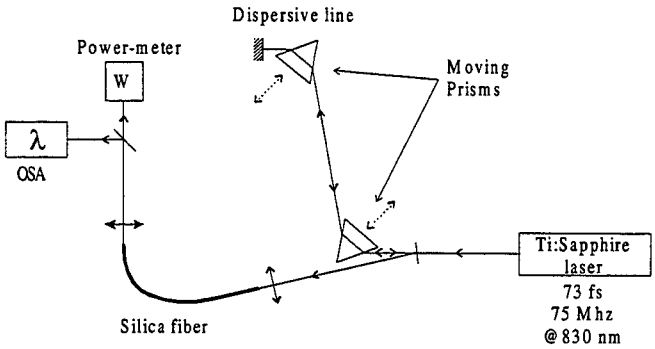


Fig1.

The experimental set-up is depicted on Figure 1 and the operation principle is described in the following. Ultrashort pulses emitted by a femtosecond laser are send in a tunable dispersive line before propagation across the nonlinear material. Dispersion is modified by moving the prisms so that the path of the pulses across the glass is increased or decreased without deviation of the output beam. At the output of the dispersive line, the pulse is broadened and exhibits a parabolic temporal phase profile whose sign depends on the sign of the dispersion introduced, ϕ''. For the particular case of Gaussian pulses described as $E(t)=E_0\exp-(at)^2$, where a is related to the inverse of the characteristic temporal size T_0 ($a=2\mathrm{Ln}2/T_0^2$), at the exit of the dispersive line the chirped pulse is given by: $E_d(t)=\frac{E_0}{\left|\sqrt{1-i2a^2\phi''}\right|}\exp-\left(\frac{a^2-i2a^4\phi''}{1+4a^4\phi''^2}t^2\right)$

The light exiting the dispersive device is then coupled into the sample (a nonlinear waveguide or a bulk material) which is kept fixed. The injected optical power is chosen so as to introduce only moderate nonlinear distortions. After their propagation in the sample the output pulses are analysed by an Optical Spectrum Analyzer (OSA). When the parabolic temporal phase shift experienced by the pulse after its passage through the dispersive line adds with the self phase modulation (SPM) in the sample the output spectrum is broader than in the linear case. On the contrary when the dispersion is of opposite sign with respect to the SPM the combination of the two effects can lead to a spectral narrowing. When the input dispersion is large, whatever its sign, the pulse broadening decreases so much the peak intensity that the propagation across the sample gives a negligible nonlinear contribution.

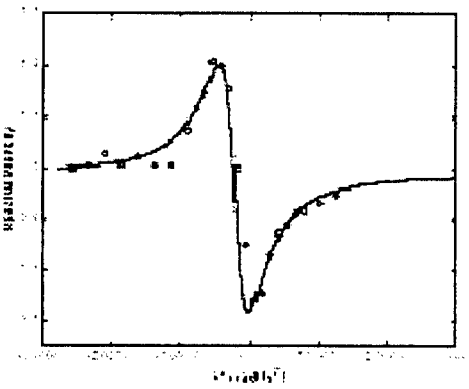


Fig. 2

In a preliminary experiment we have characterized a short sample of single mode silica fiber of 53.5mm length with the 73fs pulses provided by a Ti:Sapphire laser source operating at 830nm. We have plot on Figure 2 the peak spectral intensity versus the dispersion coefficient, ϕ", introduced by the dispersive line, for a peak nonlinear phaseshift, $\Delta\phi_0=2*\pi*n_2*I_0/\lambda=1.15$ radians, (I_0 being the peak intensity of the pulse). The experimental data are shown as open circles, for discrete values of the dispersion. The continuous line corresponds to the result of a numerical simulation assuming a Kerr coefficient $n_2=3.2\ 10^{-11}m^2/GW$. This value deduced from the fitting agrees with the published values for silica fibers in this range of wavelengths[3,4]. We must stress that a negative nonlinearity would give rise to an inversion of the curve, so that the sign of the nonlinearity is clearly identified. The peak to valley deviation of the peak spectral intensity with respect to the linear value, $\Delta I_{p\text{-}v}$, depends on the SPM amplitude and permits to measure the real part of the third order nonlinearity. Calculations indicate that the dependence of the spectral intensity change, $\Delta I_{p\text{-}v}$, on the resolution of the spectrum analyzer can be approximated by $\Delta I_{p\text{-}v}=0.44\{\exp-(0.5(r/r_a)^2\}^{0.25}$. r being the OSA spectral resolution, and r_a the spectral width of the input pulse (FWHMI). For a given spectral resolution of 5nm, $\Delta I_{p\text{-}v}$ varies linearly with the peak nonlinear phaseshift according to the relationship $\Delta I_{p\text{-}v} = 0.418\ \Delta\phi_0$. The imaginary part of the nonlinearity can be deduced from the evolution of the total average transmitted power versus the input dispersion. In Figure 3 we plot typical theoretical evolution of the spectrum peak intensity together with the transmitted average power versus dispersion

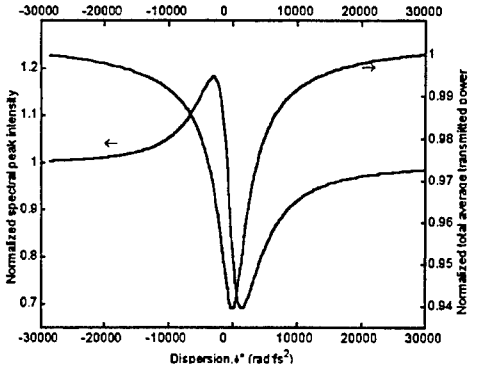


Fig.3

To some extent the D-scan technique is also able to identify the time response, τ, of the nonlinearity. The time dependent refractive index change has been considered in the simulation as the convolution product of the optical pulse intensity with a single exponential decay for the material response[5]. For the particular case of a Gaussian pulse the nonlinear response can be described by:

$$\Delta n(t) = \frac{1}{2\tau} n_2 I_0' \sqrt{\frac{\pi}{A}} \exp\left(\frac{1}{4A\tau^2} - \frac{t}{\tau}\right) Erfc\left(\sqrt{A}t - \frac{1}{2\tau\sqrt{A}}\right)$$

where $I_0'=E_0^2/|(1-2ia\phi")|$ and $A=2a^2/(1+4a^4\phi"^2)$. From the above expression we can see that a non instantaneous nonlinearity shifts the maximum of the phase and introduces a temporal asymmetry on the phase whose magnitude depends on τ, T_0 and ϕ". These effects lead to a frequency shift of the spectrum maximum and an asymmetry in the spectral profile. At the same time the peak spectral intensity variation

versus dispersion decreases, producing the same effect as a lower nonlinearity in the D-scan curves. In Figure 4 we show the frequency shift of the spectral peak versus dispersion assuming τ=30fs, T_0=73fs and $\Delta\phi_0$=1.15 radians. The highest shift is here of about 2.5nm and may be easily detected using standard OSA with 0.1nm resolution. The strongest spectral deviation is reached at ϕ''=0, which corresponds to the narrowest pulse profile at the input. The sensitivity of the method to refractive index change time response (see Figure 5) is limited, on one side, to time response shorter than the pulse duration T_0, and on the other side by the resolution of the spectral analyser. In practice, using pulses of about 70fs duration and an OSA with 0.1nm resolution, time response in the range 5 to 70 fs seems measurable.

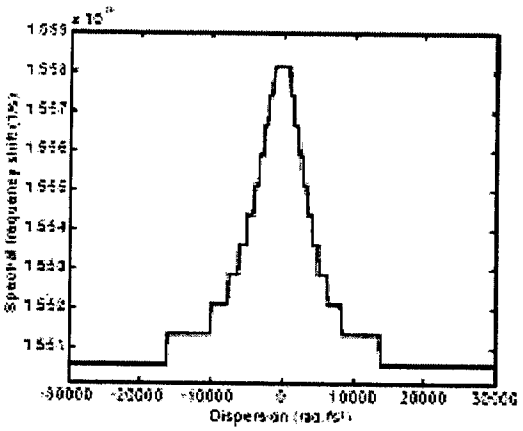


Fig 4

In conclusion, we have presented a simple technique for measuring the fast part of the complex third order nonlinearity of bulk materials and waveguides. To some extent the method is also able to provide the time of response of this fast contribution to the refractive index change. The sensitivity is limited by the OSA performance and was estimated in our set up to be λ/900. The sensitivity can be improved by recording the spectral variations in the pedestal of the spectrum instead of its peak, in a way similar to the "eclipsing" Z-scan technique[6]. Preliminary computations have shown that one order of magnitude increase in the sensitivity can be obtained by shifting the frequency corresponding to the measurement point by one spectral width (FWHMI). Although the experiment reported has been carried at a wavelength of 830nm, this method can be used at other wavelengths.

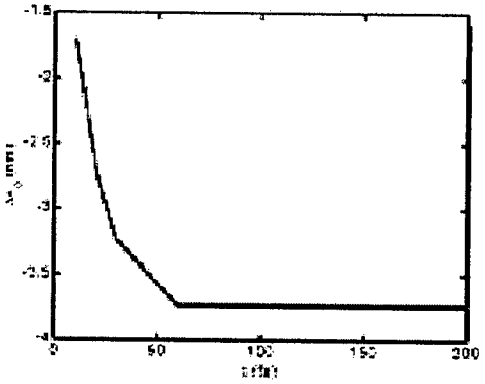


Fig. 5

The authors aknowledge the financial support of the french CNRS program MATERIAU and E. Lopez-Lago thanks the European Commission for the payment of her fellowship.

References

1. F.Louradour, E.Lopez Lago, V.Couderc, A. Barthelemy, L.Mouradian, Proc. ECIO'99, 103, 1999.
2. M. Sheik-Bahae, A.A. Said, T.H. Wei, D.J.Hagan, E.W.Stryland, IEEE J. Quantum Electron QE26, 760,1989.
3. G.P. Agrawal. Nonlinear Fiber Optics, CAT&T, Academic, New York, 1989.
4. E.T.J. Nibbering, et al., Opt. Communications, 119,479,1995.
5. R.H. Stolen, J. P. Gordon, W.J. Tomlinson, H.A. Haus, J. Opt. Soc. Am. B, 6, 1159, 1989.
6. T. Xia, DJ Hagan, M. Sheik- Bahae, E.W.Stryland, Opt. Lett. 19,317, 1994.

Wide bandwidth 1.5 μm and 1.3 μm wavelength conversion in periodically-poled waveguides

M.-H. Chou, K. Parameswaran, and M. M. Fejer
E. L. Ginzton Laboratory, Stanford University, Stanford, CA 94305
fejer@leland.stanford.edu

I. Brener
Bell Labs, Optical Physics Research, 600 Mountain Ave. Murray Hill, NJ 07974-0636
igal@lucent.com

Over the past decade, improvements in nonlinear materials and new methods such as quasi-phasematching, in combination with guided-wave geometries, have led to dramatic increases in the conversion efficiency of three-wave mixing devices. These devices can operate efficiently at CW powers below 100 mW.[1] In recent years, such highly efficient mixers have also been used in signal processing applications analogous to those of RF mixers, but operating at optical frequencies.[2] Examples include wavelength converters for WDM systems, and spectral inversion for dispersion correction. In this presentation, fabrication of quasi-phasematched frequency mixers with mixing efficiencies approaching 1%/mW in periodically-poled lithium niobate waveguides will be briefly reviewed. Applications to various communications functions, including dispersion compensation of 4x10 Gbit/s signals over a 150 km span, will be described.

In a difference frequency mixer, inputs at frequencies ω_p and ω_s generate an output at frequency $\omega_{out} = \omega_p - \omega_s$. (Fig. 1a). The output power P_{out} of such a mixer is related to the pump power P_p and the signal power P_s by $P_{out} = \eta P_p P_s$, where η[W^{-1}] is the nonlinear efficiency. It is convenient to write η as $\eta = \eta_0 L^2$, where the length of the device is L. The normalized efficiency η_0 [W^{-1} cm^{-2}], which depends on the nonlinear susceptibility and the overlap of the modal fields at the pump, signal, and output wavelengths, is useful for comparing different device designs. The best devices operating around 1.5 μm wavelengths today have normalized efficiencies in the range of 0.5 – 1 W^{-1} cm^{-2}, so that in 4 cm long devices efficiencies in the range of 10 W^{-1} are obtained. Note that for a fixed pump power of about 100 mW, such a device has an output linear in the signal power, with conversion loss approaching 0 dB. The output electric field E_{out} is proportional to complex conjugate of the signal field, E_s*, so the device also operates as a phase conjugator or spectral inverter.

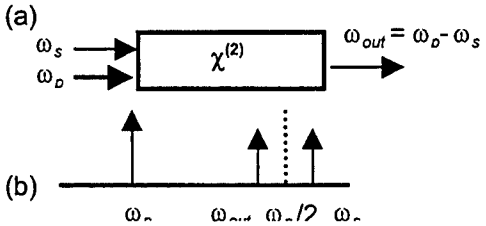


Fig. 1: Schematic description of a difference frequency mixing between a strong pump at ω_P and signal at ω_s

For communications applications, operation is typically near degeneracy, i.e. the signal and output wavelengths are in the 1.5 μm band, and the pump is around 0.78 μm. For an input $\omega_s = \omega_p/2 + \Delta$, the output is $\omega_p/2 - \Delta$, that is the output spectrum is the input spectrum mirrored around half the pump

frequency (Fig. 1b). A practical problem in this scheme is that a waveguide that supports a single mode at the signal wave is highly multimoded at the pump wavelength, significantly complicating stable launching of the pump into the desired (fundamental) mode. An adiabatic waveguide taper can be used to couple an input region single-moded at the pump wavelength into a waveguide that supports a single mode at the signal wavelength, thereby enabling stable launching of the fundamental pump mode into the mixing waveguide.[3] However, the input region is then cutoff for the signal wavelength, requiring launching the signal into a separate waveguide and combining with the pump in the mixing waveguide after the taper, using a wavelength selective directional coupler. Figure 2 shows a complete device of this type. The tapered input regions also provide the freedom to tailor the ellipticity and size of the mode at the input independent of the size and ellipticity in the mixing region. This degree of freedom simultaneously enables large input modes for efficient coupling to single-mode fiber, and tight confinement in the mixing region for high mixing efficiency. Devices 5 cm in length with fiber-to-fiber passive losses below 3 dB and mixing efficiencies of 10 W^{-1} have been constructed in this way.[4]

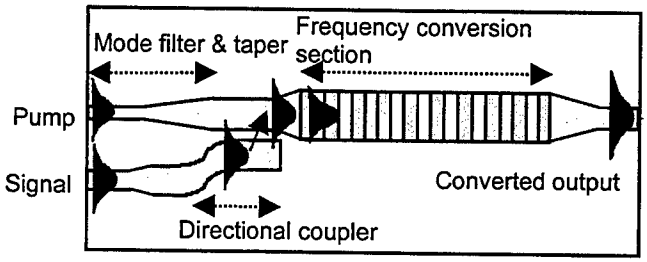


Fig. 2: Schematic of integrated nonlinear frequency mixers. An adiabatic taper transforms the pump radiation into the fundamental mode of the conversion section for mixing with the signal radiation, coupled by a directional coupler.

The signal bandwidth near degeneracy depends only on the square root of the length of the device, so the bandwidth is large even with devices as long as 5 cm, for which 3 dB bandwidths of 60 nm are obtained (Fig. 3). In this device, with 90 mW of 780 nm pump power, the conversion loss was 4 dB. As the only noise source is parametric fluorescence, and the only saturation mechanism is gain compression due to pump depletion, these devices also have a large dynamic range. We have observed 50 dB dynamic range, from –54 dBm to – 4 dBm, limited by measurement equipment rather than the mixing device itself (Fig. 4). The absence of cross-talk mechanisms other than pump depletion also allows simultaneous conversion of multiple input channels without interference. Unlike SOA-based devices, three-wave mixers can convert

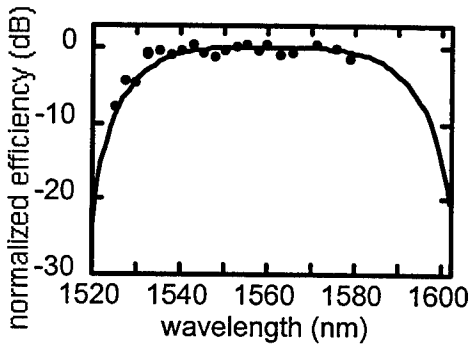


Fig. 3: Normalized efficiency vs. input signal wavelength for a 4 cm long wavelength converter.

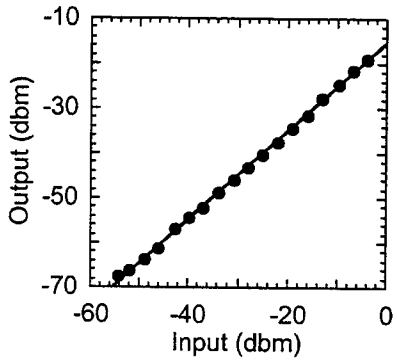


Fig. 4: Mixed output power vs signal input power showing > 50 dB dynamic range.

symmetrically from the 1.3 μm band to 1.5 μm band and from 1.5 μm to 1.3 μm. Bidirectional conversion loss of 9 dB with 40 mW pump power has been demonstrated in these devices.[5]

An alternative to pumping with 780 nm radiation is the use of a cascaded interaction, in which a strong 1560 nm pump is frequency doubled to provide the pump for the frequency mixing process (Fig. 5).[6] Because of the narrow SHG acceptance bandwidth, these two interactions can be carried out simultaneously in the same waveguide without introducing significant interference between multiple input wavelengths. Four input channels were simultaneously converted with 7 dB fiber-to-fiber conversion loss in such a cascaded device. [7]

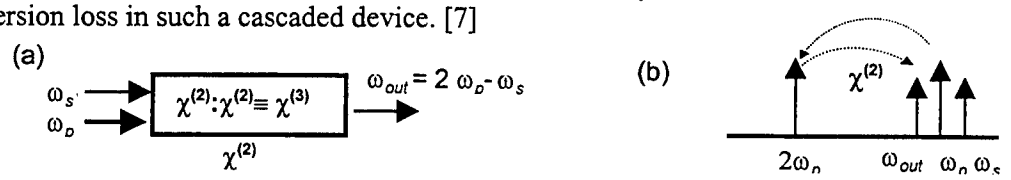


Fig. 5: Schematic description of a cascaded $\chi^{(2)}$ process between a strong pump at ω_p and signal at ω_s. Second harmonic of strong pump mixes with signal to produce output.

This same device was used as spectral inverter to correct for dispersion in a 150 km link operated at 4x10 Gbit/s. Fig. 5 shows the eye diagram for one signal channel with and without spectral inversion at the 75 km mid-span point. It can be seen that the eye diagram is completely open with the mid-span spectral inversion; BER tests indicate only ~1 dB penalty attributable to the mixer after 150 km.[8]

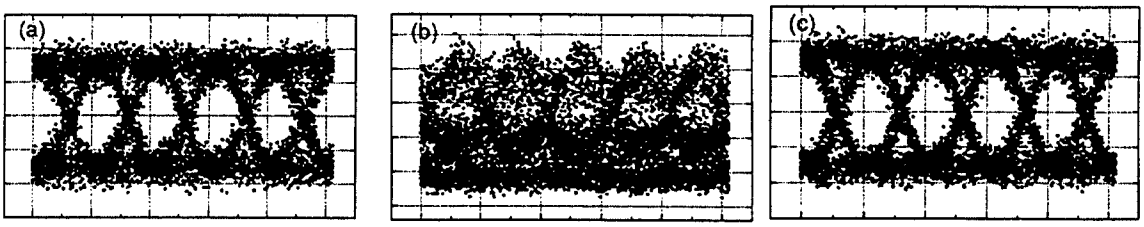


Fig. 6: Eye diagrams for one of the 4 10 Gbit/s channels (a) back to back; (b) unconverted after 150 km of SMF; (c) after mid-span spectral inversion and 150 km of SMF. 100 ps/div

Fabrication methods, additional device and system results, progress in polarization independent operation, and new materials systems promising better performance, such as all-epitaxially patterned twinning of GaAs films will also be presented.[9]

REFERENCE

[1] M. H. Chou, J. Hauden, M. A. Arbore, and M. M. Fejer, *Opt. Lett.* 23, 1004 (1998).

[2] S. J. B. Yoo, J. Lightwave Technol. 14, 955 (1996).

[3] M. H. Chou, M A. Arbore, and M. M. Fejer, *Opt. Lett.* 21, 794 (1996).

[4] M. H. Chou, I. Brener, K. Parameswaran, and M. M. Fejer, CLEO'99, paper CWB8.

[5] M. H. Chou, K. R. Parameswaran, M. A. Arbore, J. Hauden, and M. M. Fejer, in *Conf. on Laser and Electro-Optics*, Vol. **6** of 1998 OSA Tech. Dig. Ser., paper CThZ2.

[6] C. G. Trevino-Palacios, G. I. Stegeman, P. Baldi, and M. P. De Micheli, Electron. Lett. 34, 2157 (1998).

[7] M. H. Chou, I. Brener, M. M. Fejer, E. E. Chaban, and S. B. Christman, *Photonics Technol. Lett.*, **11** 653 (1999).

[8] I. Brener, M. H. Chou, G. Lenz, R. Scotti, E. E. Chaban, J. Shmulovich, D. Philen, K. R. Parameswaran, and M. M. Fejer, *Submitted to ECOC'99.*

[9] L. A. Eyres, C. B. Ebert, M. M. Fejer, J. S. Harris, in *Conf. on Laser and Electro-Optics*, Vol. **6** of 1998 OSA Tech. Dig. Ser., paper CWH4.

Giant two wave mixing in a photorefractive planar waveguide fabricated with He^+ implanted $BaTiO_3$

Pierre Mathey*, Alexandre Dazzi, Pierre Lompré, Pierre Jullien
Laboratoire de Physique de l'Université de Bourgogne, Matériaux Photoréfractifs et Applications
Centre National de la Recherche Scientifique, Unité Propre de Recherche de l'Enseignement Supérieur 5027
9 Avenue Alain Savary, B.P. 47870, 21078 Dijon Cedex, France
* : E-mail : pmathey@u-bourgogne.fr Fax number : 33 3 80 39 59 61

Paul Moretti
Laboratoire de Physico Chimie des Matériaux Luminescents, Unité Mixte de Recherche 5620
Centre National de la Recherche Scientifique, Université Claude Bernard Lyon 1
43 boulevard du 11 Novembre, 69622 Villeurbanne, France

Daniel Rytz
Forschunginstitut für mineralische und metallische Werkstoffe, Edelsteine/Edelmetalle GmbH
Struthstrasse 2, Wackenmühle, 55743 Idar-Oberstein, Germany

1. Introduction

Measurements of the photorefractive gain in a planar waveguide versus parameters like the orientation of the grating vector written by two TE modes, the total incident intensity are presented. Up to now, the results already published about the two wave mixing in $BaTiO_3$ waveguides concern one well defined orientation of the grating vector and waveguide realized by proton mono implantation [1,2]. Our previous studies revealed that H^+ implantation in $BaTiO_3$ results in a poor optical barrier width so that the light confinement in the guide is low [3]. For this reason, we make a guide with a $BaTiO_3$ substrate implanted with He^+ ions. The study of the losses of the fundamental TE mode versus the direction of its propagation in respect with the optical axis is conducted. Then the photorefractive gain induced by the interaction of two TE_0 modes is investigated versus the orientation of the grating vector. It is shown that taking into account the losses, the measured gain values do well agree with the theoretical predictions. The optimized value of the gain is $58\ cm^{-1}$ that is the highest ever reached in a $BaTiO_3$ waveguide. The response time is three orders of magnitude below that in the bulk crystal for the same intensity.

2. Waveguide fabrication and characteristics

The substrate is a nominally undoped $BaTiO_3$ crystal grown at FEE by the TSSG method. It is cut along the crystallographic axis with a size of $6\times5\times3\ mm^3$. The optical axis is along the greatest length and the direction of implantation is along the smallest length. In a previous work, it has been shown that some implantation conditions must be fulfilled to obtain a $BaTiO_3$ waveguide with negligible energy leaks through the optical barrier [3]. In particular, the width and the depth of the implantation barrier must be great enough to correctly confine the guided light. We conclude that He^+ implantation lead to better results than H^+ implantation. Small doses of implantation are also sufficient to 1) obtain a guiding layer with losses as low as possible 2) keep the monodomain structure of the sample . To obtain a sufficient width of index barrier we choose the multi-implantation process with He^+ ion energies of $2,\ 1.9,\ 1.8\ MeV$ each at a dose of $2\ 10^{15}\ ions / cm^2$. M-lines measurements at $\lambda = 514.5\ nm$ revealed that this sample supports three TE guided modes if the wave is ordinarily polarized and one mode for an extraordinarily polarized wave. Fig.2 depicts the evolution of the TE_0 mode loss κ (per unit length) versus the angle α defined in fig.1. There is a minimum ($\kappa \approx 4\ cm^{-1}$) for $\alpha \approx 7°$. The increasing of the loss is probably related to the decrease of the index variation created by the implantation resulting in non negligible energy leaks.

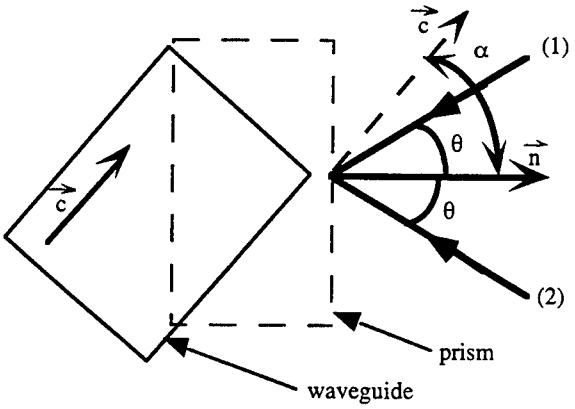


fig.1 : Relative arrangement of the waveguide and the input prism that injects two modes (beam 1 and beam 2). $\vec{c}$ is the optical axis of the guide, $\vec{n}$ is the normal of the entrance face of the prism, $\pm\theta$ are the incident angles of the beams (1) and (2) on the prism.

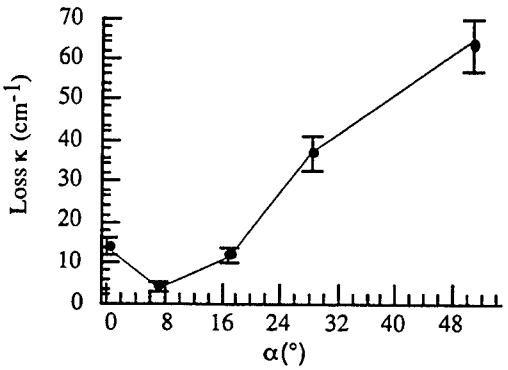


fig.2 : Loss of the TE_0 mode versus the angle α.

3. Photorefractive wave mixing

The interaction of two coherent beams in photorefractive media results in an energy transfer from one strong beam of light (the pump) to a weak beam (the probe). In the bulk, the theoretical expression for the amplification coefficient γ at stationary state has been established to be [4] :

$$\gamma = \frac{1+r}{1+re^{-\Gamma L_{eff}}} \qquad (1)$$

where Γ is the gain, r is the ratio between the pump and probe intensity, L_{eff} is the effective interaction length between the pump and probe beams.
If $r >> 1$ and taking into account the losses, expression (1) simplifies as :

$$\gamma = e^{\Gamma_{eff} L_{eff}} \qquad (2)$$

where $\Gamma_{eff} = \Gamma - \kappa$, κ being the loss of the considered mode.

We use a prism setup to investigate the two wave mixing at $\lambda = 514.5\ nm$ inside the waveguide. This arrangement is a suitable mean to prospect all the angular configurations of the incident beams in respect with the optical axis of the guide and so to determine the optimum disposition for wave mixing. The prism coupling technique also avoids the multimode interaction that can arise if the injection of light is made with microscope objectives. The experimental conditions are : a total incident intensity of $10\ W/cm^2$ in the guide, a pump-probe ratio $r = 500$, $2\theta = 34°$. With our setup, guided waves are mixed in a range for the angle α that is not limited by the cut of the faces of the $BaTiO_3$ substrate. This is not the case in an 0°-cut crystal since the maximum refraction angle due to the index of $BaTiO_3$ is 23°. To correctly compare the experimental and theoretical gains versus α, we take into account the loss κ and we normalize all the gain curves (fig.3). It is clear that the variations of the effective gain (filled circles) is similar to the theoretical gain (dashed curve). In particular, the maximum of the corrected gain is closer to the calculated value ($\alpha \approx 40°$). It is important to underline that the mode losses is the restrictive quantity and can not be neglected. This results in an optimal configuration of the two wave mixing inside the guide that is different from the one in the bulk.
The gain values for the bulk are measured under the same conditions for two values of α : $\Gamma(0°) = 0.5\ cm^{-1}$, $\Gamma(15°) = 12.3\ cm^{-1}$. Considering that the value for $\Gamma(15°)$ represents 80% of

the maximum gain, the maximum expectable gain Γ in the bulk is about $15\ cm^{-1}$. This difference between bulk and waveguide may come from a higher trap density in the waveguide. Another peculiarity of the wave mixing in the guide is that the direction of the energy transfer is reversed compared with that in the bulk medium. The transfer direction being linked to the charge carriers nature and considering that they are holes in a nominally undoped $BaTiO_3$, this seems to indicate that the implantation has changed the nature of the dominant charge species (from holes to electrons).

Figure 4 represents the evolution of the response time τ versus the intensity in the guiding layer and shows that the response time τ in the waveguide is three orders of magnitude lower than the response time in the bulk. This property is in agreement with the hypothesis that the dominant charge carriers in the guide are electrons. The straight lines (fig.4) are numerical fits of the experimental data according to a law of the form I^{-x} . The exponents are $x = 0.18$ for the waveguide and $x = 0.71$ for the bulk. Once again, the property of the guide is different from that of the bulk.

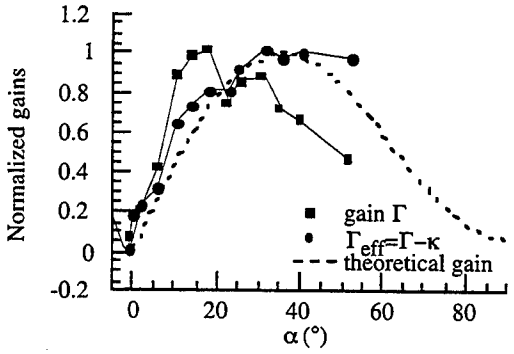


fig.3 : Normalized gain curves versus the angle a. The dashed line represents the theoretical gain in a bulk $BaTiO_3$ sample. The straight lines that join the experimental points are guides for the eyes.

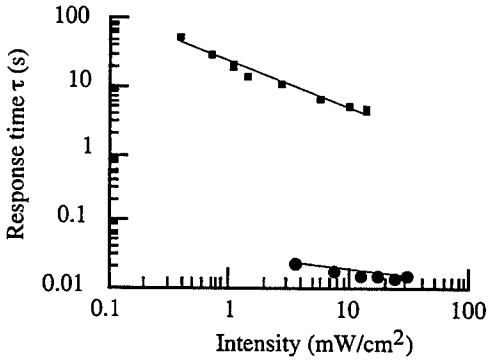


fig.4 : Response time τ versus the light intensity inside the waveguide (●) and inside the bulk crystal (■). The straight line are numerical adjustments of the experimental data according to power laws I^{-x}.

4. Conclusion

Photorefractive effects in a $BaTiO_3$ waveguide realized by He^+ implantation have been demonstrated via two wave mixing experiments. We showed that the prism coupling device is a useful setup to analyze precisely the two wave mixing in waveguides. We have measured the gain and the losses for several angular configurations and deduce the optimal disposition of the beams in respect with the optical axis. The role of the mode losses on the exact value of the gain has been emphasized. The waveguide properties appear to be different from those in the bulk sample. The gain is greater, the response time is shorter (about 1000 times). So that it is necessary to study the waveguide as a new medium with its own properties. The exact role on the photorefractive properties of the dose and temperature during the implantation process are not yet quite understood.

References

[1] K.E. Youden, S.W. James, R.W. Eason, P.J. Chandler, L. Zhang, P.D. Townsend, Optics Lett. **17**, 1509-1511 (1992).

[2] F. Ito, K. Kitayama, Appl. Phys. Lett. **59**, 1933-1934 (1991).

[3] A. Dazzi, P. Mathey, P. Lompré, P. Jullien, Optics Comm. **149**, 135-142 (1998).

[4] P. Yeh, *Introduction to Photorefractive Nonlinear Optics* (Wiley-Interscience Publication, 1993).

Nonlinear Guided Waves and Their Applications

Parametric Effects

Friday, 3 September 1999

L. Lugiato, University of Milan, Italy
Presider

FB
10.30-12.00
Salle Morey—St-Denis

Competition between convection and chromatic dispersion in an all-fiber synchronously driven bistable ring resonator

Stéphane Coen, Philippe Emplit, and Marc Haelterman
Service d'Optique et d'Acoustique, Université Libre de Bruxelles, CP 194/5
50 Av. F. D. Roosevelt, B-1050 Brussels, Belgium
Tel : +32-2-650.28.01, Fax : +32-2-650.44.96, e-mail : Stephane.Coen@ulb.ac.be

Mustapha Tlidi
Optique non linéaire théorique, Université Libre de Bruxelles, Campus Plaine, CP 231
Boulevard du Triomphe, B-1050 Brussels, Belgium
Tel : +32-2-650.59.05, Fax : +32-2-650.58.24, e-mail : mtlidi@ulb.ac.be

Synchronously driven passive fiber resonators constitute a class of devices of growing interest from both fundamental and applied points of view. They can be found in practice as the basic elements of a large number of fiber based-devices such as APM lasers, fiber raman lasers or fiber loop memories. From a more fundamental point of view, a passive nonlinear fiber resonator is structurally so simple and exhibits such a broad spectrum of complex behaviors that it is considered as the paradigm of an optical system prone to instabilities and chaos. In this context, several authors have performed experimental studies of fiber cavities with the aim of demonstrating various phenomena such as optical bistability, period-doubling cascades, or intracavity modulational instability [1, 2]. Because of the weakness of the silica fiber Kerr nonlinearity, most of these experiments have been performed with a pulsed input beam, i.e., the cavity was synchronously pumped. In this configuration, the feedback is achieved by adjusting the cavity length to the pump laser repetition rate so as to superimpose the intracavity pulses with the external pump pulses in the input coupler. Little attention has however been paid to the cavity behavior in presence of a small synchronization mismatch due to unavoidable inaccuracies in the cavity length. In our communication, we show analytically and experimentally through the study of optical bistability that the convective transport mechanism induced by a cavity synchronization mismatch can drastically alter the usual nonlinear cavity properties even when the round-trip time mismatch is much smaller than the pump pulse width. Moreover, our study allows us to demonstrate that the very existence of optical bistability in synchronously driven fiber resonators is intimately linked to a competition between convection and chromatic dispersion.

The competition mechanism between convection and dispersion can be understood as follows [3]. In the absence of dispersion, the feedback is achieved only under perfect synchronization conditions so that, round-trip after round-trip, each point in the intracavity pulse envelope is superimposed to the same point of the input pulse envelope. If the synchronization is not perfect as is always the case in practice, the intracavity pulses undergo a drift with respect to the pump pulses so that the point-to-point superposition no longer takes place and the feedback disappears. Dispersion is able to restore the feedback through the introduction of a non-locality in the pulse envelopes. Indeed, owing to dispersion, the amplitude at a given time τ of the intracavity pulse at the beginning of the cavity round-trip influences, after propagation in the cavity, the amplitude distribution of the pulse in a whole region surrounding time τ. This region of influence may be large enough to compensate for the synchronization mismatch ΔT so as to restore the feedback and hence bistability.

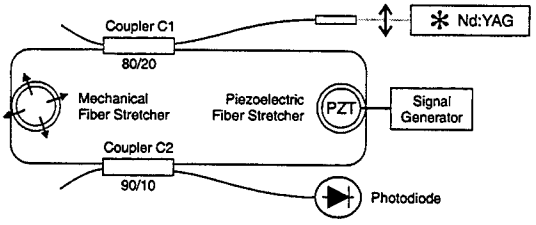


Figure 1: Experimental setup.

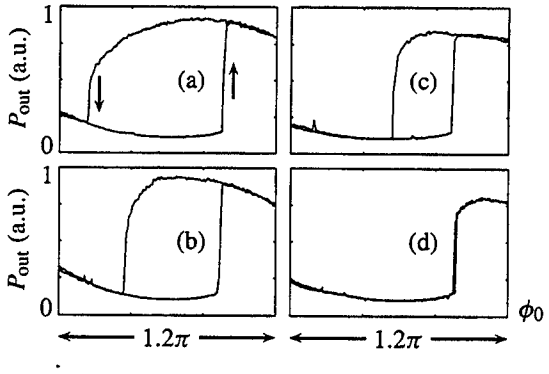


Figure 2: Bistable cycles for (a) a perfect synchronization, and with a synchronization mismatch of (b) 150 fs, (c) 300 fs, and (d) 600 fs. The mean input power was set to 2.8 W.

We have studied experimentally this fundamental competition mechanism between dispersion and convection. In our experiment (see Fig. 1), we use a 7.4 m long all-fiber ring cavity. The cavity is synchronously pumped by a mode-locked Nd:YAG laser emitting 180 ps (FWHM) pulses at 1064 nm with a repetition rate of 82 MHz. The cavity length is precisely controlled by means of a mechanical fiber stretcher [2] that allows for synchronization tuning with a resolution of $\sim$ 50 fs. During our measurements of the bistable cycles, the input power was kept constant while the cavity detuning ϕ_0 was varied by applying a triangular signal to a piezo-electric fiber stretcher. Our results are illustrated in Fig. 2 that shows the bistable cycles obtained with several values of the synchronization mismatch for a mean input power of 2.8 W. These results reveal quite remarkably that a synchronization mismatch as small as $\Delta T = 600$ fs (i.e., only 0.3 % of the pump pulse duration) is sufficient to make bistability disappear.

In order to develop an analytical description of this phenomenon, we have studied with more details the nonlinear intracavity wave dynamics in the presence of convection. In the pulsed regime, the multivalued response of the cavity is associated with the existence, in the profile of the intracavity pulse, of switching waves (SW's) that link adjacent temporal domains in which the system is respectively on the upper and lower states of the bistable cycle [4]. In a cw pumped cavity the SW's consist of steady-state fronts that propagate at a speed determined by the input pump amplitude. For a given cavity detuning, only one value of the pump amplitude S, say S^*, gives rise to a stationary SW. In the pulsed regime in the absence of convection, the SW's in the steady state intracavity pulse profile are located at a time τ corresponding to the critical value of pump amplitude, S^*. Therefore when decreasing the pump pulse amplitude, i.e., when going closer to down switching, the SW's move closer together. This feature is illustrated in Fig. 3(a) that shows several experimental pulse profiles measured at the cavity output by a streak camera in the conditions of Fig. 2(a).

With a non-zero synchronization mismatch, convection is responsible for a drift motion of the SW's at the velocity $d = [2/(|\beta_2|L\alpha)]^{1/2}\Delta T$ where β_2 is the fiber dispersion coefficient, L is the cavity length, α is the overall cavity loss and ΔT is the synchronization mismatch, i.e., the difference between the laser repetition time and the cavity round-trip time. This eventually leads to an asymmetric pulse profile [see Fig. 3(b)] in which SW's are positioned such that their natural velocity counteracts the effect of convection. However, if the convection velocity d is larger than the maximum value of the natural velocity of the SW, there is no mean to compensate for the fast convective motion of the up-stream SW so that the upper state domain is washed away. In this situation bistability is inhibited by convection. Accordingly, the maximum

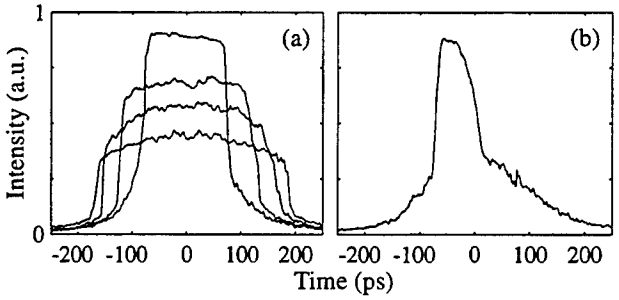


Figure 3: (a) Pulse profiles at zero synchronization mismatch. When approaching down-switching, the SW's go closer together. (b) Asymmetric pulse shape observed with a small cavity mismatch near down-switching.

value of the synchronization mismatch compatible with the bistable operation of the device, say, $\Delta T_{\max}$ is such that the drift velocity d equals the maximum SW velocity $v_{\max}$. For the experimental results presented on Fig. 2, this simple model yields $\Delta T_{\max} \simeq 640$ fs in good agreement with the experimental observation.

To get a better picture of the process described above, we have developed an analytical model of the SW's dynamics. By restricting our analysis to nascent bistability, we have reduced the complex mean field model describing the fiber cavity dynamics to a real Fisher-Kolmogorov equation [5] whose SW solutions are known exactly. This provides us with the approximate value $\Delta T_{\max} = (|\beta_2| L\alpha(\Delta - \sqrt{3})/4)^{1/2}$ where Δ is the normalized cavity detuning. This expression illustrates in particular the competition mechanism between convection and chromatic dispersion discussed above since it shows indeed that a small dispersion leads to a high sensitivity to convection. We have checked the validity of our analytical model by comparing it with the exact SW solution of the mean-field model. Even far from nascent bistability, our model provides a good qualitative agreement for both the SW profile and the SW velocity.

In conclusion, by means of a simple all-fiber resonator, we have experimentally demonstrated that dispersion can efficiently overcome the inhibiting effect of convection in optical bistability. This effect has been described in terms of switching-wave dynamics for which we have developed an analytical model based on a Fisher-Kolmogorov equation. Finally, it should be stressed that the phenomenology described here is very general. We can therefore expect similar phenomena to be observed in other kinds of nonlinear resonators.

[1] H. Nakatsuka, D. Grischkowsky, and A. Balant, Physical Review Letters **47**, 910 (1981).
[2] S. Coen, M. Haelterman, Ph. Emplit, L. Delage, L. M. Simohamed, and F. Reynaud, Journal of the Optical Society of America B **15**, 2283 (1998).
[3] M. Haelterman, G. Vitrant, and R. Reinisch, Journal of the Optical Society of America B **7**, 1309 (1990).
[4] N. N. Rozanov, V. E. Semenov, and G. V. Khodova, Kvantovaya Elektronika (Moskva) **9**, 354 (1982), [Soviet Journal of Quantum Electronics **12**, 193 (1982)].
[5] A. N. Kolmogorov, I. G. Petrovskiĭ, and N. S. Piskunov, Bjul. Moskovskovo Gos. Univ. **17**, 1 (1937).

Dynamical Quadratic Cavity Solitons

D. Michaelis, C. Etrich, U. Peschel, and F. Lederer

Friedrich-Schiller-Universität Jena,
Institut für Festkörpertheorie und Theoretische Optik,
Max-Wien-Platz 1
07743 Jena, Germany
Tel.: 49 3641 947176, Fax: 49 3641 947177, E-mail: dirk@pinet.uni-jena.de

There is constantly growing interest in optical solitons because of their robustness and potential applications in information transmission, processing and storage schemes. Recently resting solitons were identified in scalar [1] as well as vectorial [2,3] intracavity second-harmonic generation. Until now it was common believe that for normal incidence any motion of a localized structure in an externally driven cavity is damped because the momentum is not conserved. As far as expanding structures are concerned growing stripes were found in quadratic as well as in semiconductor cavities [1,4]. In this communication we show that, based on a spatial symmetry breaking of a polarization front (PF) where the two fundamental components are no longer the mirror image of each other, moving 1D cavity solitons may emerge. Moreover, in a 2D configuration a filamentation occurs leading to stable propagating stripes that carry radially symmetric solitons. Another interesting feature of the present configuration is the existence of breathing solitons.

The configuration we are looking at is a high finesse Fabry-Pérot resonator with a $\chi^{(2)}$–cavity. The normalized equations of the two orthogonally polarized fundamental fields FH1 (A_1) and FH2 (A_2) and the second harmonic SH (B) are

$$\left[\mathrm{i}\frac{\partial}{\partial T}+\frac{\partial^2}{\partial X^2}+\frac{\partial^2}{\partial Y^2}+\Delta_\mathrm{A}+\mathrm{i}\right]A_j+A_{3-j}^{*}B=E_j,\quad j=1,2$$

$$\left[\mathrm{i}\frac{\partial}{\partial T}+\frac{1}{2}\left(\frac{\partial^2}{\partial X^2}+\frac{\partial^2}{\partial Y^2}\right)+\Delta_\mathrm{B}+\mathrm{i}\gamma\right]B+A_1A_2=0, \tag{1}$$

where $E_{1/2}$ are the FH input fields, Δ_A and Δ_B are the detunings from the FH and SH resonances. γ describes the ratio of the photon lifetimes. Here we assume negative detunings.

For a symmetric FH input $E_1 = E_2$ a symmetry breaking of the plane wave solutions occurs (Fig.1a). PFs can be formed by connecting the two asymmetric FH branches of different polarization (Fig.1a). If $|\Delta_A|$ is small the PFs are stable and at rest because the FHs are mirror-symmetric to each other (Fig.1b). Increasing $|\Delta_A|$ each stationary PF develops a pronounced peak with a linear internal mode of the PF being localized there. This bound state passes through the trivial translation mode at a certain detuning Δ_A. The stationary PF destabilizes and bifurcates into two PFs where the FH components loose the mirror symmetry and move with opposite velocities. An example of such a moving asymmetric PF is shown in Fig.1c. For the PF with the opposite velocity the shape of the FH fields are interchanged, i.e. now the FH2 exhibits the pronounced peak at the edge of the PF.

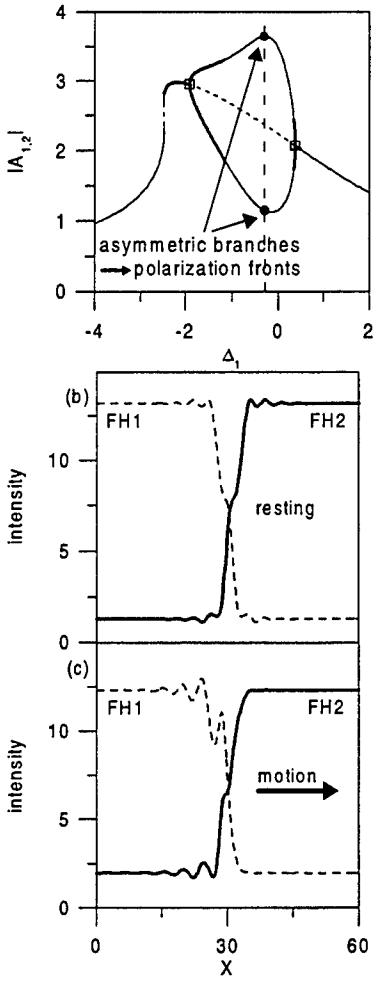


Fig.1 (a) Symmetry breaking of stationary plane wave solutions, thin solid (dashed) lines: stable (unstable), bold solid lines: modulationally unstable, $\Delta_B = -4$, $E = 3.8$, $\gamma = 0.5$.
(b) stable resting polarization front, (c) moving polarization front due to a spatial symmetry breaking

All PFs exhibit conspicuous spatially oscillating tails which form a periodic effective potential and may capture a second PF. As a consequence the interaction of resting PFs (Fig.1b) entails the formation of stationary cavity solitons of different order (Fig.2a). Two asymmetric moving PFs can be combined in two different ways. If PFs with opposite velocities are excited (symmetric excitation) a breathing but resting cavity soliton is formed (Fig.2b). The breathing originates from the interplay of the motion of the individual PFs and the binding force due to the oscillating tails of the constituents of such a cavity soliton. Mathematically it can be considered as a nonlinear coupling of the two unstable eigenmodes of the stationary PFs.

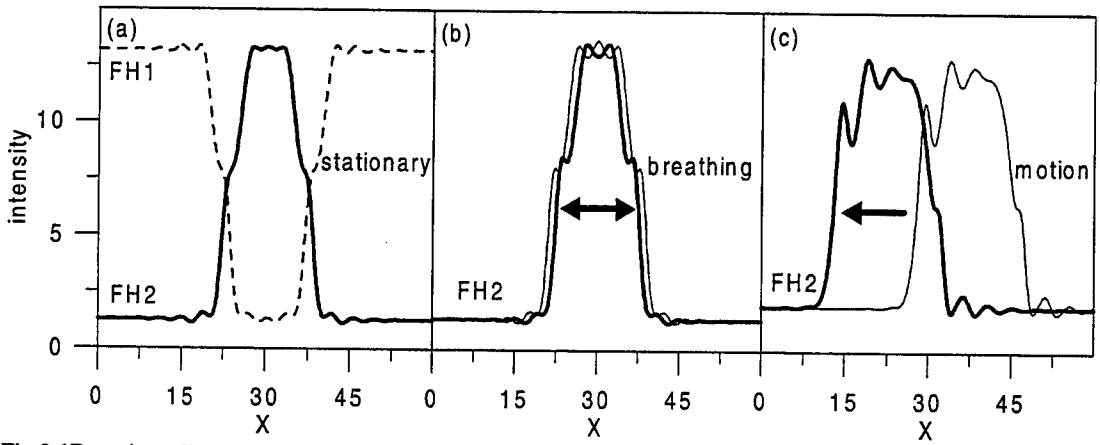


Fig.2 1D cavity solitons (a) stable, stationary, $\Delta_A = -0.2$, (b) oscillating, $\Delta_A = -0.322$, (c) running, $\Delta_A = -0.7$

Combining two PFs with equal velocity (asymmetric excitation) a moving localized structure is created (Fig.2c). Because the soliton consists of two different PFs its shape is asymmetric.

In a 2D configuration this running soliton is modulationally unstable. Though still moving it finally transforms into radially symmetric solitons sitting on the propagating stripe (Fig. 3). Because the whole object has to be asymmetric each stripe edge carries its individual kind of radial filaments.

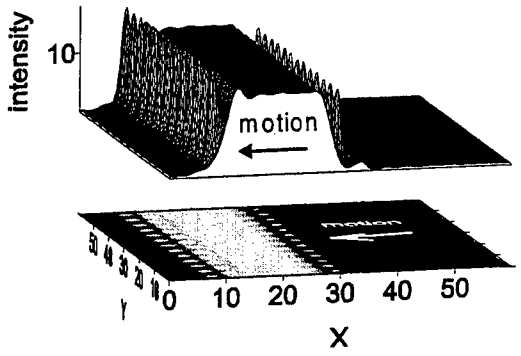


Fig.3 Stable propagating stripe carrying radially symmetric solitons, $\Delta_A = -0.32$

[1] C. Etrich, U. Peschel, and F. Lederer, Phys. Rev. Lett. 79, 2454 (1997)

[2] U.Peschel, D.Michaelis, C. Etrich, and F. Lederer, Phys. Rev. E **58**, R2745 (1998).

[3] S.Longhi, Opt. Lett. **23**, 346 (1998)

[4] L.Spinelli, G.Tissoni, M.Brambilla, F. Prati, and L.Lugiato, Phys. Rev. A **58**, 2542 (1998)

Raman-assisted parametric generation of non phase-matched waves in normally dispersive optical fibers

E. Seve, G. Millot, and P. Tchofo-Dinda
Laboratoire de Physique de l'Université de Bourgogne,
avenue Alain Savary , B.P. 47 870, 21078 Dijon Cedex, France
Fax : (33) 3 80 39 59 71, phone : (33) 3 80 39 59 77, e-mail :seve@jupiter.u-bourgogne.fr

T. Sylvestre, H. Maillotte, and E. Lantz
Laboratoire d'Optique P.M. Duffieux,
U.M.R CNRS, Université de Franche-Comté No 6603,
25030 Besançon Cedex, France,
Fax : (33) 3 81 66 64 23, phone : (33) 3 81 66 64 25, e-mail : herve.maillotte@univ-fcomte.fr

An ordinary three-wave mixing (TWM) process in standard or birefringent single-mode fibers commonly refers to the interaction of a central-frequency wave at frequency ω_0, with a pair of upshifted (anti-Stokes) and downshifted (Stokes) sidebands at frequencies $\omega_2 = \omega_0 + \Omega$ and $\omega_1 = \omega_0 - \Omega$, respectively [1, 2]. Two distinct types of interactions are usually considered, as shown in Fig. 1, namely: *scalar interaction*[1], in which the two sidebands are polarised parallel to the pump, and *vector interactions*[2], in which the sidebands are orthogonally polarised with respect to the pump. However, efficient generation of new optical frequencies requires the fulfilment of phase-matching conditions which impose strict limitations in the Ω - frequency domain. A highly mismatched TWM interaction is characterised by a perfectly periodic energy-exchange process between the three waves, with a very short coherence length (several mm or cm) compared with practical fiber lengths. As a result of the short periodicity of the process, non-phase matched waves cannot be generated and amplified through an ordinary TWM process. To overcome these limitations, we choose to make the stimulated Raman scattering (SRS) enter into play in the TWM-induced energy-exchange processes. The SRS is a well-known nonlinear effect which occurs whenever high-power light beams propagate in optical fibers [3]. SRS induces a unilateral transfer of energy from higher to lower-frequency waves, which destroys the spatial periodicity of the parametric energy-exchange process. As a result, the generation and amplification of a non phase-matched Stokes wave idler is achieved by mixing a strong pump with an anti-Stokes signal.

In this research we present experiments showing the generation and amplification of non-phase matched idler waves through scalar TWM interactions of collinearly polarised waves in a polarisation-maintaining fiber, and through vector interactions of a pump, which is polarised along the slow axis of a weakly birefringent fiber, with a pair of sidebands that are both polarised along the fast axis. Note here that the pump is polarised along the slow axis in order to prevent from any de-polarisation of the pump. On the other hand, it is worth noting also that the phase-matched TWM interaction which takes place in a low-birefringence fiber is the polarization modulational instability [4] which occurs in the following frequency detuning region : $0 < \Omega < 3THz$ (for $P_0 = 300W$) and $0 < \Omega < 4.5THz$ (for $P_0 = 700W$). Consequently, for vector interactions, we consider systematically frequency detunings which are outside those frequency regions. Scalar interactions are not phase matched in the normal dispersion regime, whatever the frequency detuning Ω. The theoretical demonstration of those frequency generation processes by Raman-assisted three-wave mixing (RATWM) is straightforward when using a three-wave model which includes the Raman susceptibility [5]. Figures 2, which we obtained from a coupled mode analysis, represent the evolution of the normalized power of each modes : $\eta_j(z) \equiv P_j(z)/\sum_j P_j(0)$, $j = 0$ (pump), $j = 1$ (Stokes idler) and $j = 2$ (anti-Stokes signal), for different frequency detunings. For each frequency detuning Ω, th pump input peak power was chosen such that the global power gain of the idler wave exceeds

the pump power gain (which results from the RATWM-induced energy transfer from the signal to the pump), for a signal power $P_2(0) = 5W$. As Figs. 2 show, whenever Ω falls in the Raman-gain bandwidth, the parametrically seeded ilder wave is then continuously amplified through Raman gain, and may after several coherence lengths grow up above the noise level. It is important to note that in scalar interactions, the Raman gain is induced by the parallel component of the Raman susceptibility (see Fig. 1a), whereas in vector interactions the Raman amplification results from the combined effects of the parallel and orthogonal components of the Raman susceptibility (see Fig. 1b). The orthogonal component induces an energy transfer from the anti-Stokes to the pump, and a transfer from the pump to the Stokes sideband, whereas the parallel component induces a direct energy transfer from the anti-Stokes to the Stokes sideband. As a result, for scalar interactions, the maximum efficiency of idler generation is obtained for $\Omega = 13.2THz$ (see Fig. 2b), which coincides with the peak parallel Raman gain, whereas for vector interactions the maximum efficiency is obtained for $\Omega = 3.5THz$ (see Fig. 2c), which corresponds to the peak orthogonal Raman gain.

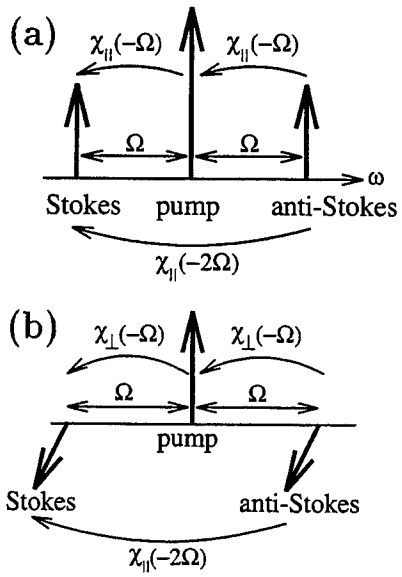


Fig. 1 *Schematic diagram of a scalar (a) and vector (b) TWM interaction.*

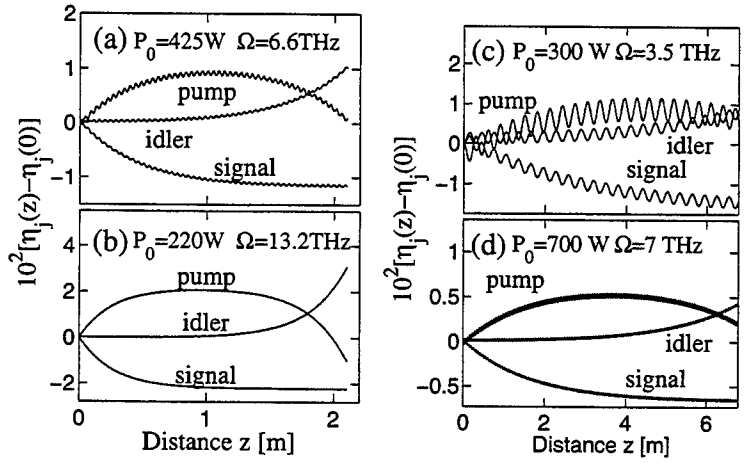


Fig. 2 *Normalized powers $\eta_j(z) - \eta_j(0)$ versus propagation coordinate z for the scalar (a)-(b) and vector (c)-(d) interaction. $j = 0$ (pump), $j = 1$ (idler), $j = 2$ (signal).*

To observe the generation of a non-phase matched idler wave through RATWM, we have implemented different experiments for scalar and vector interactions. In the scalar case, the signal beam was a 40-ps stretched pulse produced by a tunable optical parametric generator/amplifier pumped by the third harmonic of a pulsed mode-locked Nd:YAG laser operating at $1.064\,\mu m$ at a rate of 10 Hz. The same laser source was used to produce the frequency-doubled pump beam, a 35-ps pump pulse. The two beams were launched synchronously along the fast axis of a single-mode high-birefringence fiber. The fiber length was $L = 3\,m$. The output light was spectrally analysed with a littrow grating spectrometer and we obtained spectra shown in Fig. 3(a) and (b), for $P_2(0) = 0.5\,W$ and different frequency detuning. The idler generation is clearly shown, even below the usual SRS threshold when $\Omega \approx 13.2THz$ (see Fig. 3(b)). For this frequency detuning we measured a conversion efficiency as large as $10 \pm 2dB$ for the 0.5 W signal.

In the case of vector interactions, the pump beam was obtained from a cw tunable ring dye laser, pumped by a 4 W Argon laser, and subsequently amplified by a three-stage dye cell. The dye

amplifier was, in turn, pumped by a frequency-doubled, injection-seeded and Q-switched Nd:YAG laser (operating at $\lambda = 532.26$ nm). The pump wavelength was adjusted by tuning the dye laser around $\lambda_p = 580$ nm. The signal pulses were obtained by frequency-shifting the same Nd:YAG laser by self-SRS in a cell filled with CO_2. This frequency shift was necessary to obtain several THz frequency detunings. The signal wavelength was fixed at the value $\lambda_2 = 574.746$ nm. The fiber was initially a non-birefringent fiber in which a weak linear birefringence ($B \approx 10^{-7}$) was introduced by winding the fiber onto a spool with a 14.5 cm diameter. The output light was analysed by a 50 cm spectrometer with a resolution better than 0.04 nm. We obtained a set of spectra shown in Figs. 4(a) and (b), measured for pump peak powers of approximatively 220 W and different frequency detunings Ω. In Figs. 4(a) and (b), ones clearly identifies the MI sidebands, as well as the ordinary Raman Stokes radiation. A noticeable feature in the case of vector interactions is that a relatively strong signal beam is required to generate the idler wave because of the presence of spontaneous PMI and SRS processes which cause a strong pump depletion. In conclusion, the spectra in Figs. 3 and 4 demonstrate that non-phase matched idler waves can be generated by mixing the pump with an anti-Stokes signal beam in a relatively large range of frequency detunings that fall within the Raman gain bandwidth. The main advantage of this Raman-assisted TWM technique is that it offers the possibility of generating new optical frequencies for a relatively large frequency-detuning bandwidth, without having to go through the strict limitations imposed by the phase-matching conditions of ordinary parametric processes.

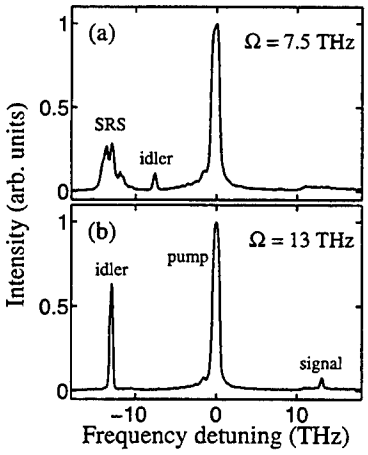


Fig. 3 *Experimental output spectra of scalar interactions. (a)* $\Omega = 7.5THz$, $P_0(0) = 415W$, *and* $P_2(0) = 0.5W$ *(b)* $\Omega = 13THz$, $P_0(0) = 370W$, *and* $P_2(0) = 0.5W$.

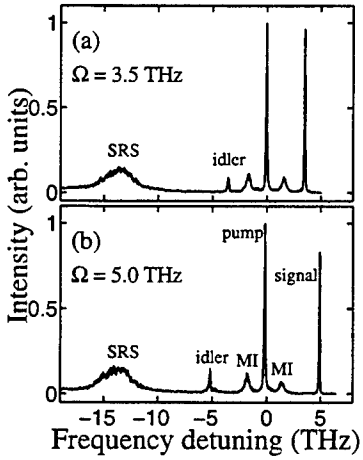


Fig. 4 *Experimental output spectra of vector interactions. (a)* $\Omega = 3.5THz$, $P_0(0) = 210W$, *and* $P_2(0) = 106W$ *(b)* $\Omega = 7THz$, $P_0(0) = 224W$, *and* $P_2(0) = 101W$.

References

[1] K.O. Hill D.C. Johnson B.S Kawasaki and R.I. MacDonald. *J. Appl. Phys.*, **49**, 5098 (1978).

[2] R.K. Jain and K. Stenersen. *Appl. Phys. B*, **35**, 49, (1984).

[3] R.H. Stolen.*Phys. Chem. Glasses*, **11**, 83, (1970).

[4] S. Wabnitz. *Phys. Rev. A.*, **38**, 2018, 1988.

[5] P. Tchofo-Dinda, E. Seve, G. Millot, T. Sylvestre, H. Maillotte, and E. Lantz. *submitted for publication*

Second-Harmonic Generation and Localized Modes in Multilayered Structures

Andrey A. Sukhorukov[1], Yuri S. Kivshar[1], and Ole Bang[2]

[1] *Australian Photonics Cooperative Research Centre, Research School of Physical Sciences and Engineering Optical Sciences Centre, Australian National University, Canberra ACT 0200, Australia*
Phone: (61) 6249 2430, Fax: (61) 6249 5184, E-mail: ans124@rsphysse.anu.edu.au
[2] *Department of Mathematical Modelling, Technical University of Denmark, DK-2800 Lyngby, Denmark*
Phone: (45) 4525 3096, Fax: (45) 4593 1235, E-mail: ob@imm.dtu.dk

Cascaded nonlinearities of noncentrosymmetric optical materials have become an active topic of research due to their potential applications in all-optical switching devices [1]. Parametric interactions are known also to support solitary waves, in particular two-frequency *spatial quadratic solitons* [2]. Usually, solitary waves are considered for homogeneous media where spatial localization is induced by self-focusing and self-trapping effects. However, localized modes can exist even in a linear medium at defects or interfaces. The properties of *nonlinear defect modes* are usually analyzed for non-resonant Kerr-type nonlinearities [3]. Here we consider a qualitatively different situation and introduce a novel type of nonlinear defect mode: a *two-frequency (or two-color) localized photonic mode*, where the energy is localized due to the parametric wave mixing induced by an interface between two linear optical media or a thin layer with a quadratic (or $\chi^{(2)}$) nonlinearity embedded in a linear bulk medium.

First, we notice that there exists a strong experimental evidence of SHG in localized photonic modes. For example, recent experimental results [4] reported SHG in a one-dimensional periodic photonic band-gap structure, in which a nonlinear defect layer was embedded. An enhancement of the parametric interaction in the vicinity of the defect was observed, suggesting that SHG occurs in local modes, being suppressed for propagating modes.

To introduce an analytically solvable model for SHG in localized waves, we consider a fundamental frequency (FF) wave propagating along the Z-direction in a linear slab waveguide. We assume that an interface (or a defect layer) possesses a quadratic nonlinear response, so that the FF wave can parametrically couple to its second harmonic (SH). The coupled-mode equations for the complex envelope functions $E_j(x,Z)$ (j=1,2) can be written in the form,

$$\begin{aligned} i\frac{\partial E_1}{\partial Z} + D_1\frac{\partial^2 E_1}{\partial x^2} + n_1(x)E_1 + \Gamma_1(x)E_1^* E_2 = 0, \\ i\frac{\partial E_2}{\partial Z} + D_2\frac{\partial^2 E_2}{\partial x^2} + n_2(x)E_2 + \Gamma_2(x)E_1^2 = 0, \end{aligned} \tag{1}$$

where D_j are diffraction coefficients ($D_j > 0$). In the approximation of infinitely thin interface layer (valid when the width of each layer is much smaller than the FF wavelength), we take $n_j(x) = n_{0j}(x) + \sum_n \kappa_j \delta(x - x_n)$ and $\Gamma_j(x) = \gamma_j \delta(x - x_n)$, where γ_j are the nonlinearity coefficients, $n_{0j}(x)$ and κ_j account for the phase velocity differences in bulk and interface materials.

Single nonlinear layer. We start our analysis considering a single nonlinear layer ($x_n \equiv 0$) with uniform linear media on both sides of it. In order to reduce the number of parameters, we normalize Eqs. (1) as follows: $E_1(Z) = u(z)/\sqrt{\gamma_1\gamma_2}$, $E_2(Z) = v(z)/\gamma_1$, $\sigma = D_2/D_1$, $\alpha_1 = \kappa_1/D_1$, and $\alpha_2 = \kappa_2/D_1$, where $z = Z/D_1$ is measured in units of D_1. Then the coupled equations are

$$\begin{aligned} i\frac{\partial u}{\partial z} + \frac{\partial^2 u}{\partial x^2} + \nu_1(x)\,u + \delta(x)\,(\alpha_1 u + u^* v) = 0, \\ i\frac{\partial v}{\partial z} + \sigma\frac{\partial^2 v}{\partial x^2} + \nu_2(x)\,v + \delta(x)\,(\alpha_2 v + u^2) = 0, \end{aligned} \tag{2}$$

where $\nu_j(x) = \nu_j^+$, for $x > 0$, and $\nu_j(x) = \nu_j^-$, for $x < 0$. If the mismatch $2\nu_1^\pm - \nu_2^\pm$ is small, then σ=1/2 is a good approximation, that we use below in the numerics. System (2) conserves the total power $P = \int_{-\infty}^{+\infty}(|u|^2 + |v|^2)\,dx$ for spatially localized or periodic solutions.

First, we consider the scattering problem for a plane FF wave at the nonlinear layer. Using the fact that Eqs. (2) are linear for $x \neq 0$, the total field is taken as a superposition of plane waves,

$$u(x,z) = \begin{cases} a_1 e^{-i\lambda_1 z + iq_1^- x} + b_1 e^{-i\lambda_1 z - iq_1^- x}; & x < 0, \\ c_1 e^{-i\lambda_1 z + iq_1^+ x}; & x > 0, \end{cases}$$

$$v(x,z) = \begin{cases} b_2 e^{-i\lambda_2 z - iq_2^- x}; & x < 0, \\ c_2 e^{-i\lambda_2 z + iq_2^+ x}; & x > 0, \end{cases}$$

where a_1, b_1, and c_1 are the amplitudes of the incident, reflected, and transmitted FF waves, respectively. Correspondingly, b_2 and c_2 are the amplitudes of the generated SH waves on both sides of the interface.

In order to illustrate the characteristic physical properties of the system, we assume that the linear media 1 and 2 on each side of the interface are *identical*, i.e. $\nu_j^\pm = \nu_j$ and $q_j^\pm = q_j$. The SH transverse wave number can be found from the phase-matching condition $2\lambda_1 = \lambda_2$, which is a general requirement for stationary propagation of FF and SH without energy exchange: $q_2 = \sqrt{[2q_1^2 - \beta]/\sigma}$, where $\beta = 2\nu_1 - \nu_2$. The q_2 can be either real or imaginary, corresponding to plane waves

and waves that are spatially localized at the interface, respectively (see Fig 1) Note that localization does not depend on the wave amplitudes

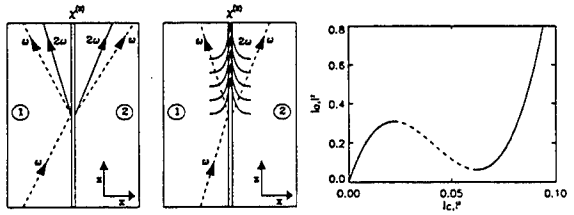


FIG. 1. Left: Scattering of a plane FF wave (dashed) on a $\chi^{(2)}$-interface between two linear media 1 and 2. The generated SH (solid) can be either propagating or localized. Right: Dependence of incident FF intensity $|a_1|^2$ on FF intensity at the layer $|c_1|^2$, illustrating existence of multistability.

Then, using the continuity conditions at the layer, the characteristic equation for the FF wave intensity $|c_1|^2$ at the interface can be obtained,

$$|c_1^6| - 2|c_1^4|\mathrm{Re}(\widetilde{\alpha}_1\widetilde{\alpha}_2) + |c_1^2|\,|\widetilde{\alpha}_1\widetilde{\alpha}_2|^2 = 4|a_1|^2|q_1^-\widetilde{\alpha}_2|^2, \quad (3)$$

where $\widetilde{\alpha}_1 = \alpha_1 + 2iq_1$ and $\widetilde{\alpha}_2 = \alpha_2 + 2i\sigma q_2$. Equation (3) is cubic in $|c_1|^2$, and thus *three different roots* may exist for a given input intensity $|a_1|^2$, corresponding to three different values of the amplitudes at the interface, as shown in Fig. 1. As the SH amplitude is related to the FF intensity, $c_2 = -c_1^2/\widetilde{\alpha}_2$, this describes a *multistable* SHG process. For fixed material parameters the multistable SHG regime can only be observed in certain regions of the input parameters q_1 and $|a_1|^2$. Stability analysis revealed that the growth rate for non-oscillatory instability modes is positive on the branch with negative slope (dashed, Fig. 1), meaning that the corresponding solutions are unstable.

Transmitted FF and generated SH waves can be either propagating or localized. However, the situation when all the FF and SH waves are localized is also possible. This corresponds to *two-frequency nonlinear localized modes.* To find stationary localized solutions for these modes we assume the following conditions in the general scattering problem: (i) no incident plane wave, i.e. a_1=0, and (ii) all transverse wave numbers are imaginary, $q_j = i\mu_j$, where μ_j are real and positive (as the wave amplitudes should vanish at infinity). Such localized states can exist for any combination of material parameters, an example of mode profile is presented in Fig. 2(a). The amplitudes at the interface are $|c_1|^2 = \widetilde{\alpha}_1\widetilde{\alpha}_2$ and $c_2 = -\widetilde{\alpha}_1$. As only one wave number is arbitrary, the solutions constitute a one-parameter family. Analysis shows that the power dependence $P(\mu_1)$ has always, for any values of the material parameters, a branch with positive slope. Under certain conditions a second branch with negative slope may appear, and it corresponds to smaller values of μ_1. We may conclude that for two bistable states the one with lower μ_1 is unstable. We perform numerical simulations and observe switching from a perturbed unstable mode to a stable one.

Such interface mode can be generated by launching a localized FF wave at the interface. This problem can be solved analytically in the undepleted pump approximation, and the analysis reveals that the amplitude of the generated SH exhibits oscillations as the solution approaches asymptotically a stationary two-color localized state. We have performed a number of numerical simulations with Gaussian initial profiles of the FF wave and found that, in the general case, the formation of localized modes is accompanied by the same kind of transitional oscillations, see Fig. 2(b).

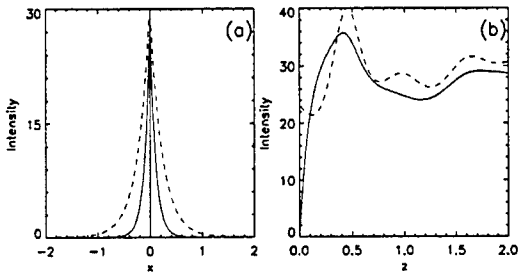


FIG. 2. (a) Intensity profiles of the stable localized state with power P=20 at $\alpha_1 = \alpha_2 = -1$, $\beta = 2$. (b) Generation of a two-color localized mode (FF – dashed, SH – solid). The input power is $P \simeq 28$ and the final state is close to (a).

Multilayer structures. As the next step, we consider an infinite layered structure, consisting of linear slices separated with thin nonlinear layers. We assume that nonlinear layers are uniformly spaced, $x_n = nh$, and bulk medium refractive index is periodic, $n_{0j}(x + nh) \equiv n_{0j}(x)$.

Similar to a single nonlinear interface we would also expect to observe localized stationary solution in multilayered structures. As the first step in this study, it is convenient to reduce the system (1) with periodic coefficients to a set of discrete equations. Indeed, in the stationary case the field in a bulk linear medium is composed of noninteracting counter-propagating FF and SH waves. Regardless to the internal structure of a linear slice between nonlinear interfaces, the wave amplitudes at its edges are related by the transmission matrix:

$$\begin{pmatrix} a_j^{(n+1,-)} \\ b_j^{(n+1,-)} \end{pmatrix} = T^{(j)}(\lambda_j) \begin{pmatrix} a_j^{(n,+)} \\ b_j^{(n,+)} \end{pmatrix}. \quad (4)$$

Here $j = 1, 2$ correspond to FF and SH, and $\pm$ indices denote the waves on the right and the left of the nonlinear layer. Note that the matrix elements depend on the propagation constants, which in turn are related through the phase matching condition $\lambda_2 = 2\lambda_1$.

Equation (4) allows us to describe the field in terms of the amplitudes at the layers, $c_j^{(n)} = a_j^{(n,\pm)} + b_j^{(n,\pm)}$. It is then straightforward to write continuity conditions at the

layers, in the same wave as for a single interface. Finally, we obtain the following system of discrete equations:

$$\begin{aligned} &\eta_1 U_n + (U_{n-1} + U_{n+1}) + \chi_1 U_n^* V_n = 0, \\ &\eta_2 V_n + (V_{n-1} + V_{n+1}) + \chi_2 U_n^2 = 0, \end{aligned} \tag{5}$$

where U_n and V_n are the normalized FF and SH amplitudes at the n-th nonlinear layer. Parameters $\chi_j = \pm 1$ and η_j are defined by the matrix elements.

Now we can use Eqs. (5) to search stationary localized solutions, or *bright gap solitons*. Such a problem was earlier analyzed in [5]. Approximate solutions were found in the limit of highly localized FF component, and the analysis revealed that solitary waves can have different topologies. These results were confirmed by numerical simulations. However, with the analytical method which was used to find approximate solutions, it was impossible to adequately describe FF component, and deviation between the approximate and exact SH profiles was quite large. Thus, a more rigorous analytical description is needed to better understand the properties of discrete localized modes. In order to find approximate localized solutions, we use here the variational method. First, we have to choose trial functions. This is a very important step, as only appropriate class of functions would provide an accurate approximation. As we are searching for localized solutions, it can be assumed that the tails are decaying exponentially. Finally, we introduce two sets of trial functions to account for different topologies [5]: *odd modes*, when the center of symmetry is at a layer,

$$U_n = U_0 e^{-(\rho_1 + i\varphi_1)|n|}, \; V_n = V_0 e^{-(\rho_2 + i\varphi_2)|n|}, \tag{6}$$

and *even modes*, when the center of symmetry is between two neighboring layers,

$$\begin{aligned} U_n &= \begin{cases} U_0 e^{-(\rho_1 + i\varphi_1)|n|}, & n \geq 0, \\ U_0 s_1 e^{-(\rho_1 + i\varphi_1)|n+1|}, & n < 0, \end{cases} \\ V_n &= \begin{cases} V_0 e^{-(\rho_2 + i\varphi_2)|n|}, & n \geq 0, \\ V_0 s_2 e^{-(\rho_2 + i\varphi_2)|n+1|}, & n < 0. \end{cases} \end{aligned} \tag{7}$$

Here the parameters $\varphi_j = 0, \pi$ and $s_j = \pm 1$ are introduced to describe *unstaggered* and *staggered* modes. Unknown values U_0, V_0, ρ_j are determined by minimizing the Lagrangian corresponding to Eqs. (5).

As the system possesses the symmetry $\chi_1 \to -\chi_1$ and $\cos(\varphi_1) \to -\cos(\varphi_1)$, we consider $\chi_1 \chi_2 = 1$ without a lack of generality. The analysis shows that solutions exist only if $s_1 = \cos(\varphi_1)$, $s_2 = 1$, and $\eta_1 \cos(\varphi_1) < -2$. The latter condition means that the FF component is unstaggered for $\eta_1 > 2$, and staggered, otherwise. Similarly, we consider only the case $|\eta_2| > 2$, as for other values the localized solutions are unstable due to resonant interaction with linear waves [5]. The SH is staggered for $2 < \eta_2 < \eta_{22}$, and unstaggered for other parameter values. Here, for odd modes $\sqrt{\eta_{22}} + 1/\sqrt{\eta_{22}} = |\eta_1|$, and for even $\sqrt{\eta_{22} + 1} + 1/\sqrt{\eta_{22} + 1} = |\eta_1|$. The topology doesn't change sharply as the parameter η_2 crosses the curve $\eta_{22}(\eta_1)$, but numerical calculations confirm that the transition occurs in a narrow region close to the separation line. Normalized relative differences between the variational and numerical solutions, and examples of odd modes, are presented in Fig. 3. We see that approximate solutions are much better for larger values of η_j, i.e. when the profiles are highly localized. The results for even modes (not shown) are similar.

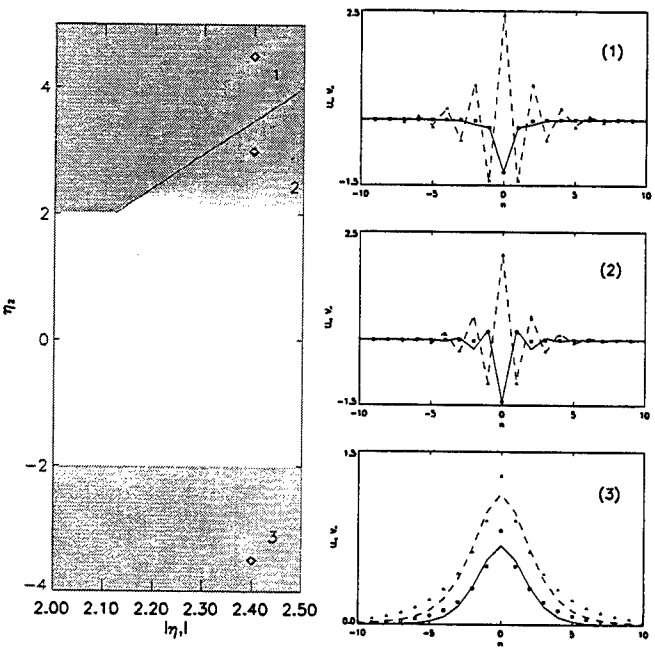


FIG. 3. Left: Color-map in $(|\eta_1|, \eta_2)$ plane showing relative differences between the variational and exact solutions with the odd symmetry. Darker areas correspond to smaller deviations. Right: Mode topologies corresponding to different regions on the left plot (variational solution: FF – triangles, SH – squares; exact profiles: FF – dashed line, SH – solid). (1) staggered FF and unstaggered SH, (2) both components staggered, (3) both unstaggered.

[1] For an overview, see G. Stegeman, D.J. Hagan, and L. Torner, Opt. Quantum Electron. **28**, 1691 (1996).

[2] Yu.N. Karamzin and A.P. Sukhorukov, Zh. Eksp. Teor. Fiz. **68**, 834 (1975); A.V. Buryak and Yu.S. Kivshar, Phys. Lett. A **197**, 407 (1995).

[3] For a general overview, see O.M. Braun and Yu.S. Kivshar, Phys. Rep. **306**, 1 (1998), and references therein.

[4] J. Trull, R. Vilaseca, J. Martorell, and R. Corbalán, Opt. Lett. **20**, 1746 (1995).

[5] T. Peschel, U. Peschel, and F. Lederer, Phys. Rev. E **57**, 1127 (1998).

Generation and characterization of 0.6 THz polarization domain wall trains in a spun fiber

F. Gutty, S. Pitois, P. Grelu, and G. Millot
LPUB, CNRS, 9 Av. A. Savary, BP 47 870, 21078 Dijon, France
gutty@jupiter.u-bourgogne.fr, pitois@jupiter.u-bourgogne.fr, grelu@jupiter.u-bourgogne.fr, millot@jupiter.u-bourgogne.fr

M. D. Thomson
Physikalisches Institut, Johann Wolfgang Goethe Universitaet, 60054 Frankfurt, Germany
thomson@physik.uni-frankfurt.de

J. M. Dudley
Department of Physics, University of Auckland, Private Bag 92019 Auckland, New Zealand
j.dudley@auckland.ac.nz

The instabilities that arise from electromagnetic wave propagation in optical fibers have been the subject of extensive study in recent years. In particular, modulational instability (MI) is a well-known effect where weak periodic perturbations of an intense CW wave experience exponential gain. In the context of optical fiber propagation, MI leads to the amplitude modulation of an initially CW wave, often interpreted as a quasi-degenerate stimulated four-wave mixing effect. In the anomalous dispersion regime, MI can be observed with the propagation of a single incident wave, and this scalar form of MI is associated with the fundamental bright soliton of the nonlinear Schrödinger (NLS) equation [1]. When the additional degree of freedom represented by the state of polarization of the incident light is considered, light propagation in isotropic fibers is described by two incoherently coupled NLS equations, and MI can be extended to the normal dispersion regime [2]. This vector MI has been termed polarization modulational instability (PMI), and Haelterman and Sheppard have shown how PMI is associated with a vector dark soliton which can be viewed as a polarization domain wall (PDW) [3]. The PDW soliton is a localized structure across which the state of polarization of light switches between two counter-rotating circular polarizations (CP's). PDW solitons are of significant fundamental interest as an example of a dynamic soliton structure, and may also be important for applications in high-capacity telecommunications systems [3].

Due to the difficulties inherent in controlling the polarization state of an incident wave in standard optical fiber, the PDW soliton has not previously been experimentally observed. In this paper we report what is to our knowledge the first experimental generation of periodic PDW pulse trains, through the adiabatic reshaping of an injected beating signal in an ultralow birefringence spun fiber. The initial beating signal is obtained by the simultaneous injection of two nanosecond pulses of different frequencies with orthogonal polarisations and equal peak power. Numerical simulations of the two incoherently coupled NLS equations show that the propagation of such a beating signal in an isotropic fiber leads to the formation of PDW structures of counter-rotating CP states. Figure 1 presents typical simulation results showing computed intensity profiles of the CP components after propagation through 1.2 meter of isotropic fiber for two incident fields of peak power 135 W and frequency separation 0.6 THz. It is clear that the computed envelopes form two interlaced periodic trains of domain-wall structures separating uniform domains of counter-rotating CP's. Note that this PDW generation is similar to the process of generation of dark and bright soliton trains by adiabatic reshaping of a scalar beating signal in a fiber with amplification or nonuniform parameters [4].

Figure 2 shows the experimental set-up used to generate and characterise PDW structures. The input beating signal was obtained using two synchronised laser sources producing nanosecond pulses at a

repetition rate of 25 Hz. One beam at a wavelength λ_1=574.06 nm was delivered by a tunable dye laser pumped by a frequency-doubled, Q-switched Nd:YAG laser. The second beam at λ_2=574.72 nm (frequency shifted by 0.6 THz) was obtained by Raman frequency conversion of an additional beam from the Nd:YAG laser. The two beams with orthogonal linear polarizations were focused in an ultra-low birefringence spun fiber (LB600 Fibercore) of length 1.2 m. The isotropy of the spun fiber was carefully verified by checking that any input polarization state was unchanged upon propagation. Since the PDW structures occur in the basis of CP states, a quarter-wave plate and a polarizer was used at the fiber output to select one CP state after propagation. This state was then characterized using a visible spectrometer, a background-free second-harmonic generation (SHG) autocorrelator, and a frequency-resolved optical gating (FROG) measurement set-up based on the spectral analysis of the SHG autocorrelation signal using a UV spectrometer [5]. The spectral, autocorrelation and SHG-FROG signals were sampled and averaged by means of a boxcar integrator.

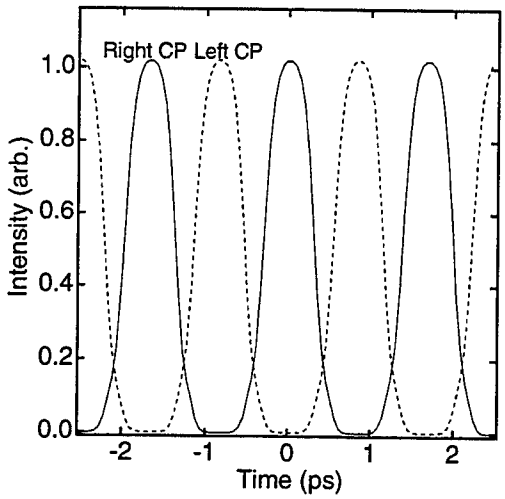


Fig. 1. Intensity profiles of the CP components forming the PDW train.

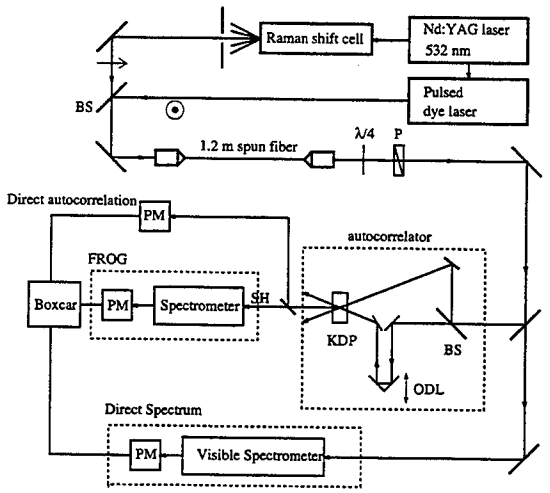


Fig. 2. Schematic of the experimental setup. P, polarizer; λ/4, quarter-wave plate; BS's, beam splitters; PM's, photomultipliers; ODL, optical delay line.

We note that the use of FROG to characterise the output pulse train in these experiments represents a significant advantage over previous experimental studies of MI processes in fibers, since it allows the direct observation of the intensity and phase of the output pulse train. Although FROG has previously only been applied to the characterisation of ultrashort laser pulses of picosecond and femtosecond duration, we have adpated the FROG retrieval algorithm to the characterisation of periodic pulse trains imposed on a CW background. In our experiments, the expected modulation period of the periodic PDW structure is T = 1/0.6 THz = 1.67 ps, more than three orders of magnitude shorter than the input pulse durations so that the approximation of a CW background is well satisfied.

The fundamental output spectrum in these experiments consists of the two input frequencies used to generate the initial beating signal, as well as higher-order sidebands characteristic of the reshaping of the input signal. Fig. 3 shows a typical SHG-FROG trace for experimental parameters corresponding to those used in the numerical simulations shown in Fig.1. The measured SHG-FROG trace shows spectral components at each of the SHG frequencies corresponding to each sideband in the output pulse spectrum, as well as spectral bands at frequencies corresponding to sum frequency mixing. It is clear from the figure that the interference between the different sideband pairs leads to a complex periodic modulation in the FROG trace. The intensity and phase retrieved from this measured FROG trace are shown as the open circles in Fig. 4. The pulse retrieval error was G ≈ 0.013, which synthetic

data tests indicate, is an acceptable error for this form of periodic FROG trace in the presence of noise. Indeed, the visual agreement between the measured and retrieved FROG trace was good, and the spectrum and autocorrelation derived from the retrieved pulse train were in good agreement with independent experimental measurements.

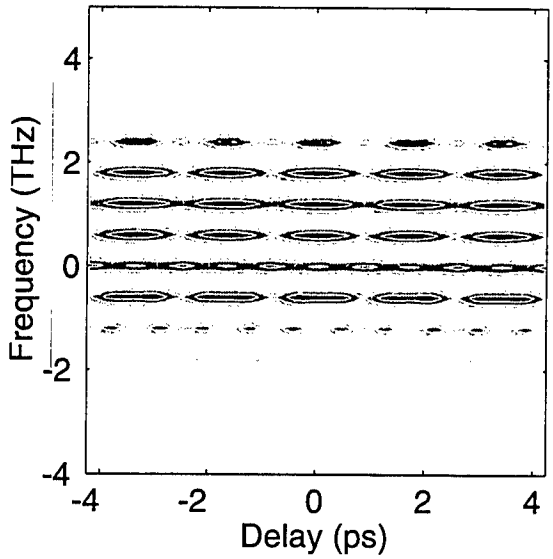


Fig. 3. Experimental SHG-FROG trace of one of the CP components. Zero frequency corresponds to the SHG frequency of the input wavelength λ_2.

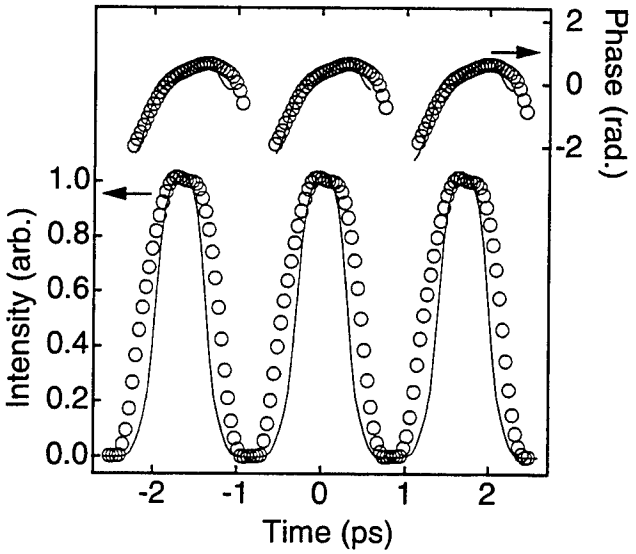


Fig. 4. The circles show the retrieved intensity (left axis) and phase (right axis). The solid lines show the corresponding simulation results.

These experimental measurements show the expected characteristics of PDW pulse trains. In particular, we note that the shape of the retrieved intensity deviates significantly from a simple sinusoid, showing flattened extrema as a result of temporal reshaping during propagation. It is also important to note the observed 100% modulation in the retrieved intensity which indicates the complete switching between the two CP states as expected for the PDW structure. Fig. 4 also shows the corresponding results from numerical simulations for direct comparison with these experimental results, showing very good qualitative agreement in both intensity and phase characteristics. The differences in pulse width between experiment and simulation is attributed to the residual effect of noise in the pulse retrieval process, and uncertainty in the fiber parameters used in the numerical simulations.

In conclusion a complete characterization of the reshaping of a beating signal in a spun fiber has been carried out using spectral, autocorrelation and SHG-FROG measurements. Our experimental results demonstrate that polarization domain walls are generated in the spun fiber.

References

[1] K. Tai, A. Hasegawa, and A.Tomita, Phys. Rev. Lett. **56**, 135 (1986).
[2] A.L. Berkhoer and V.E. Zakharov, Sov. Phys. JETP **31**, 486 (1970).
[3] M. Haelterman and A.P. Sheppard, Phys. Rev. E **49**, 3389 (1994).
[4] E.M. Dianov, P.V. Mamyshev, A.M. Prokhorov, and S.V. Chernikov, Opt. Lett. **14**, 1008 (1989); P.V. Mamyshev, S.V. Chernikov, and E.M. Dianov, IEEE J. Quantum Electron. **27**, 2347 (1991).
[5] R. Trebino and D.J. Kane, J. Opt. Soc. Am. A **10**, 1101 (1993).

Surface emitting THz difference frequency generation in GaAs-based waveguides

Yuri H. Avetisyan

Microwave Engineering Dept., Yerevan State University, 1 Alek Manoogian Str., Yerevan 375049, Armenia
E-mail: gerbarcr@ysu.am

1. Introduction

During past ten years the optical methods have been developed for generation of ultra-short [1] and nanosecond [2] pulses of THz-wave. At the same time, compact mid-power CW sources are also necessary in practice. Since the first observation of CW THz difference frequency generation (DFG) [3], the new configurations of second harmonic generation (SHG) as surface-emitted [4] and backward [5] geometry have been created. In recent paper [6] we reported the possibility of periodically poled lithium niobate (PPLN) to emit THz-wave DFG in surface-emitting geometry (SEG). The main advantage of SEG is a significant increase of generation efficiency due to the possibility of application of resonant cavities both at a pumping and at a difference frequency. The SEG allows the separate optimization of both optical (nonlinear) and THz cavities. This is important taking into consideration the requirements, which are pointed in [7]. For all that, the absorption of emitted wave in SEG is determined by the thickness of nonlinear waveguide, which is usually much less than its length. Unfortunately, the PPLN has so large absorption that resonant enhancement is not more that a few units. It is interesting to investigate other material application in the scheme of SEG. The GaAs is the most suitable material for efficient generation of THz-wave due to its large nonlinear coefficient and its transparent characteristics. The purpose of this paper is to develop a simple theoretical model for cavity enhanced THz-wave DFG in SEG in GaAs-based waveguide.

2. Theory

Let us consider two waves with the frequencies ω_1 and $\omega_2=\omega_1-\omega_3$, which propagate in the same direction into a core of planar GaAs-based waveguide as lowest order TM and TE-modes. The nonlinear mixing of propagating waves will induce a nonlinear polarization P_{NL} at the difference frequency ω_3 with propagation constant:

$$\beta_s = \beta_{TM}(\omega_1) - \beta_{TE}(\omega_2), \tag{1}$$

where $\beta_{TM}(\omega_1)$ and $\beta_{TE}(\omega_2)$ are propagation constants of interacting optical waves.
When $\beta_s = 0$, the nonlinear polarization P_{NL} will create wave in the direction normal to the surface of slab [6,8]. For THz-wave DFG the frequency $\omega_3 << \omega_2, \omega_1$ and condition $\beta_s = 0$ can be written as

$$\omega_3 = \omega_2 \, \Delta n / n_g , \tag{2}$$

where

$$n_g = n_{TM}(\omega_2) + \omega_2 \left(dn_{TM} / d\omega\right)_{\omega 2} \tag{3}$$

is the refractive index of group velocity of TM mode at ω_2 frequency, $\Delta n = n_{TE}(\omega_2) - n_{TM}(\omega_2)$ is the birefringence of optical waveguide, $n_{TE}(\omega_2)$ and $n_{TM}(\omega_2)$ are the refractive indexes of TE and TM modes.

In modern GaAs-based waveguide the value of Δn is 0.01 - 0.22 [8, 9]. The group velocity of light in waveguide depends on many factors. For rough estimation of ω_3 in Eq. (2) we assume $n_g = 4$. Using $\omega_2 = 2.1\ 10^{15}$ cycles/s ($\lambda \approx 0.9\mu$) we obtain $\omega_3/2\pi$ = (0.84 – 18,4) THz. Therefore, the SEG THz-wave DFG can be obtained by birefringence of GaAs-based waveguide.

Let us now evaluate the power P_3 of DFG, taking into consideration the enhancement caused by resonance at both THz and optical frequencies. Using the approximation of slowly varying envelope [10], for configuration presented on Fig. 1, we obtain

$$P_3 = \frac{2^7 \pi^2 d_{eff}^2 W_0 L \cdot F_\Omega F_{\omega 1} F_{\omega 2}}{n^2 n_3 \lambda^2 b} \cdot P_1 P_2, \tag{3}$$

where

$$F_\Omega = \frac{4T_{1\Omega}}{(T_{1\Omega} + \delta_\Omega)^2}, \tag{4}$$

The Eq. (3) was obtained using the conditions that the thickness of waveguide core, a is much less than the distance between two mirrors of THz-wave resonator, $h = m\lambda/2n_3$, where λ is the length of the emitted wave, n_3 is the refractive index of GaAs at ω_3 frequency. We also assume for simplicity that exciting modes of waveguide have very high confinement and $n_{TM} \approx n_{TE} = n$. In Eq. (3,4) we use definitions: d_{eff} is the effective nonlinear coefficient, P_1 and P_2 are the powers of exciting modes, W_0 is the impedance of a free space, $\delta_\Omega = 2\alpha_\Omega h + T_{2\Omega}$, $T_{j\Omega} = 1 - R_{j\Omega}$, $R_{j\Omega}$ (j=1,2) is the reflectivity of mirrors, α_Ω is a power attenuation coefficient and $F_{\omega 1}$, $F_{\omega 2}$ are determined by Eq. (6), which is written now for frequencies ω_1 and ω_2.

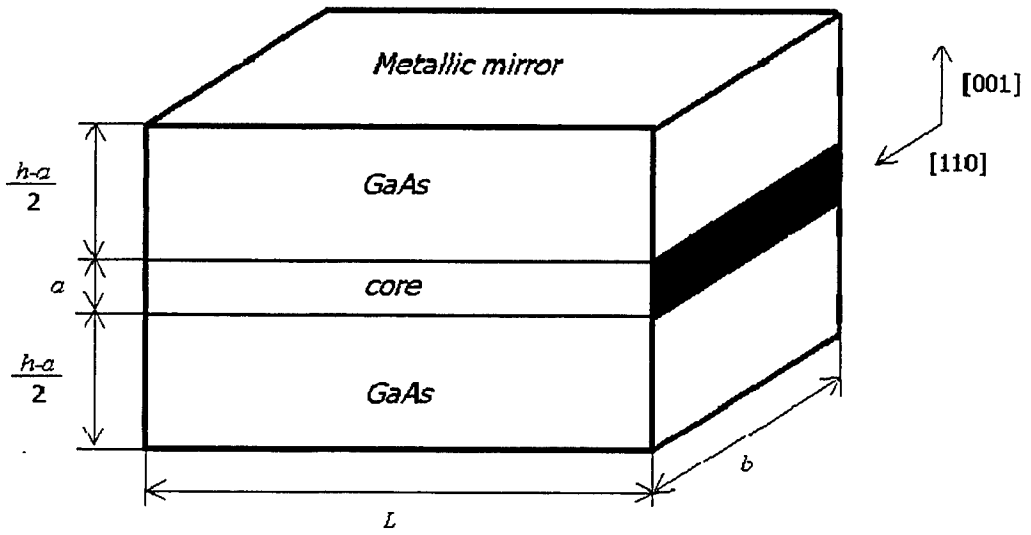


Fig.1. Configuration for cavity-enhanced DFG in surface-emitting geometry

3. Discussion

The Eq. (3) is similar to the expression for the power of SHG, which has been obtained using different method: a coupled mode formalism [11]. In contrast to SHG, the value of overlap integral equals approximately 1 due to the condition that the thickness of waveguide core is much less than the distance between two mirrors of THz-wave resonator. For evaluation of gain due to resonance at THz-wave we substitute in (4) the value h= 83.3μ (for which we have resonance at λ=200μ , n_3=3.6). The maximal gain is about 60 for optimal coupling given as $T_{2\Omega} \approx 0$ and $T_{1\Omega} = 2\alpha_\Omega h = 0.017$, (where $\alpha_\Omega \approx 1\text{cm}^{-1}$ [12] have been used). This value is more than ten times greater that for PPLN case.

For the evaluation of the efficiency of frequency conversion, $\eta = P_3 / P_1 P_2$, substituting in Eq. (3) the values $F_\Omega = 60$, $d_{\text{eff}} = d_{14} = 83$ pm /V [13], λ=200μ, $L = b$ =3mm, and using optimal coupling condition $T_{1\omega j} = \delta_{\omega j} = 0.01$ (j=1,2) we obtain $\eta = 10^{-3}\text{W}^{-1}$. For a pumping power nearly 1W, that is available with modern diode lasers, one will get the output power $P_3 \approx$ 1mW at the wavelength 200μ. This value of power of DFG corresponds to quantum efficiency 20%, taking in account the ratio $\omega_3/\omega_1 \approx 5\ 10^{-3}$. The lack of compact THz-waves generators makes such DFG source useful in many practical applications.

4. Conclusion

It was shown that THz-wave DFG emitted by the GaAs-based planar waveguide can propagates in the normal direction to the surface of a waveguide due to its birefringence. The general expression for DFG in vertical cavity was obtained. It was shown that the double resonant cavity-enhanced surface-emitting DFG enables the design of compact solid-state source of THz waves with the output power sufficient for the practical applications. The use of GaAs as nonlinear medium gives a hope to integrate mixer with pump sources and will create very compact device.

References

1. W.M. Robertson "*Optoelectronic techniques for microwave and millimeter wave engineering*" (Artech House, Norwood , 1995)
2. K. Kawase, M. Sato, T. Taiuchi, H. Ito, Appl. Phys. Lett., 68, 2483-2485 (1996).
3. R.L., Aggarwal, B. Lax, Fetterman H.R., Tannenwald, Clifton B.J., Appl. Phys., 1974, **45**, pp.3972-3974
4. R. Normandin, R. Williams, and F. Chatenoud, Electron. Lett., **26**, 2088-2090 (1990).
5. Y.J Ding, J.B., Khurgin, Opt. Lett., **21**, 1445-1447 (1996).
6. Yu. H. Avetisyan, K. N. Kocharyan, in *Conference on Laser and Elecro-Optics*, paper CThG2, 1999.
7. V. Berger, J. Opt. Soc. Am. B, **14**, 1351-1360 (1997).
8. A. Fiore, V. Berger, E. Rosencher, S. Crouzy, N. Laurent and J. Nagle, Appl. Phys. Lett., **71**, 2587-2589 (1997).
9. S. Khalfalah, R. Legros, A. Munoz-Yague, IEEE Photonics Tech. Lett., **8**, 233-235 (1996).
10. Y. R. Shen "*The principles of nonlinear optics*," (Wiley, New York, 1984).
11. R. Lodenkamper, M. M. Fejer, J. S. Harris, Electron. Lett., **27**, 1882-1884 (1991).
12. R. H. Stolen, Appl. Phys. Lett., **15**, 74-75 (1969).
13. D. Zheng, L. A. Gordon, Y. Wu, R.S. Fiegelson, M.M. Fejer, K.L. Vodopyanov and R.L. Byer, Opt. Lett., **23**, 1010-1012 (1998)

Nonlinear Guided Waves and Their Applications

Frequency Conversion in Glasses versus Crystals

Friday, 3 September 1999

P.G. Kazansky, University of Southampton, UK
Presider

FC
13.30-15.00
Salle Morey—St-Denis

Quasi-Phase-Matched Parametric Fluorescence in Poled Silica Fibres

G. Bonfrate, V. Pruneri, P.G. Kazansky

Optoelectronics Research Centre, Southampton University, Southampton SO17 1BJ, UK

Tel: +44 - 1703 - 593172, Fax: +44 - 1703 - 593149
e-mail: gb@orc.soton.ac.uk

P.R. Tapster and J. G. Rarity

DERA Malvern - Worcestershire - UK.

Summary

Recently the demonstration of highly efficient Second-Harmonic Generation (SHG) in periodically poled silica fibres (PPSF) [1], has opened new prospects for the realisation of second-order nonlinear optical processes in all-fibre devices . In particular the achieved high SHG efficiencies, show PPSF are now mature for the implementation of Parametric Fluorescence (PF), a special case of Difference Frequency Generation (DFG). PF is at the heart of optical parametric oscillators and represents a unique source of correlated photon pairs, whose peculiar characteristics make them extremely useful for the study of quantum interference [2], quantum cryptography [3] and for metrology applications (e.g. absolute measurement of the quantum efficiency of photon counting detectors [4]).

The fabrication of the PPSF samples is fully described in [5]. The period of the patterned aluminium anode, $\Lambda = 56.5$ μm, prodeuced QPM-SHG around 1532 nm, with a conversion efficiency $\eta_{SH} \simeq 4 \cdot 10^{-3}$ %/W (see Ref.1).

The setup for the parametric fluorescence generation is illustrated in Fig.1. Up to 300 mW of pump power were coupled into the sample in the fundamental mode, without exciting higher orders. For the coincidence measurement two InGaAs APDs operated in photon counting mode, were spliced to a 3 dB fibre splitter into which we launched the output from the sample.

The coincidence curve was collected with a Modulation Domain Analyser (MDA) attached to Nuclear Instrumentation Module (NIM) discriminators connected to the APDs.

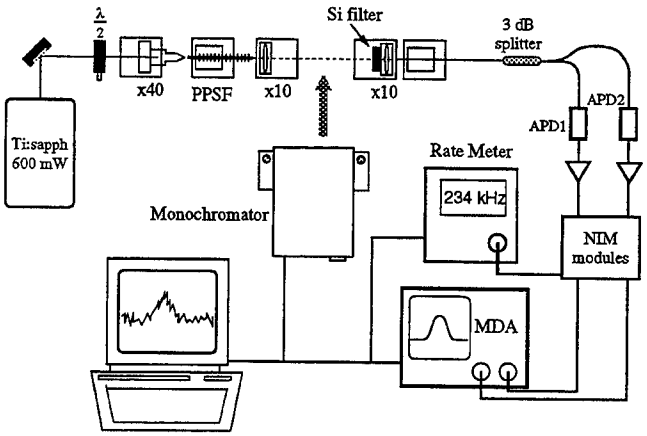


Fig. 1: Setup for parametric fluorescence generation and coincidence measurement. APD: Avalanche Photodiode, PPSF: Periodically Poled Silica Fibre, MDA: Modulation Domain Analyser, NIM: Nuclear Instrumentation Module.

The QPM curve was collected detecting with a single APD the output from the fibre, passed through a monochromator.

Fig.2 illustrates the coincidence curves for vertical (top) and horizontal (bottom) polarisation of the pump, its wavelength being 766 nm. The large background in is due to the high dark counts rate ($\sim$ 200 kHz) of the detectors. The larger signal for vertical pump is due both to the tensorial nature of the nonlinear coefficient and the fibre birefringence.

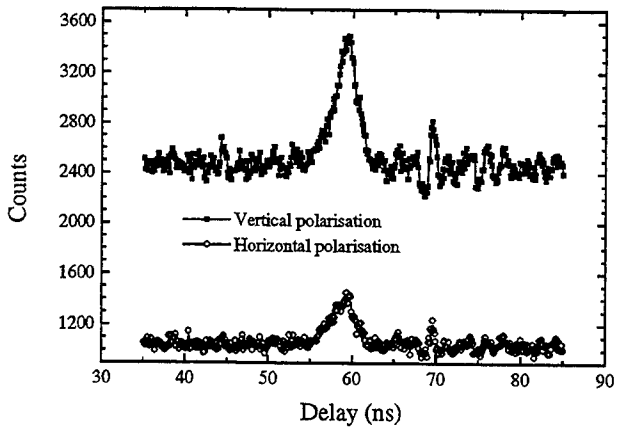


Fig. 2: Coincidence curves for vertical (top) and horizontal (bottom) pump polarisation. Each point corresponds to 0.09 ns interval

Given the coincidence rate $\sim$ 500 Hz, we estimated the quantum efficiencies of the two APDs to

be $1.4 \pm 0.4\%$ and $1.7 \pm 0.4\%$, and the photon pairs production rate to be ~ 150 MHz, in good agreement with the expected 156 MHz.

Fig.3 shows the collected QPM tuning curve. We measured the signal branch, while, due to the roll-off in the detector sensitivity and the significant losses for long wavelengths in the sample, only three idler points could be identified experimentally. The bars correspond to the bandwidth for the process.

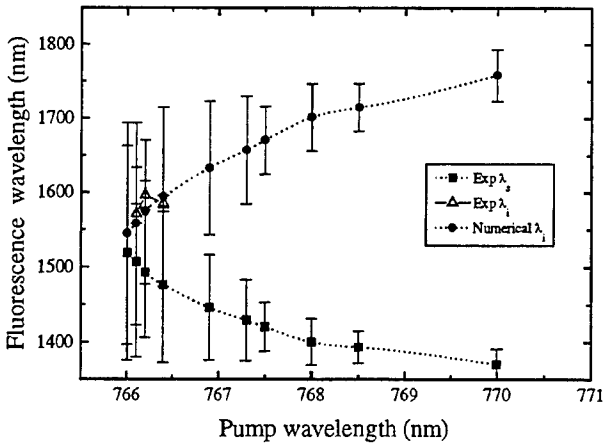


Fig. 3: QPM tuning curve. The bars show the measured signal bandwidth.

We have reported on the observation of quasi-phase matched parametric fluorescence from periodically poled silica fibres. The photon pair production resulted in 150 MHz for 300 mW of pump power at 766 nm. These results clearly show the large potential of periodically poled silica fibres as nonlinear media in all-fibre single photon sources, which are going to play a major role in the future for the implementation of quantum cryptography systems and as absolute metrology standards.

References

[1] V. Pruneri, G. Bonfrate, P. G. Kazansky, D. J. Richardson, N. G. Broderick, J. P. DeSandro, C. Simonneau, P. Vidakovic and J. A. Levenson, Opt. Lett. **24**, 208(1999)

[2] P. R. Tapster, J. G. Rarity and P.C.M.Owens, Phys. Rev. Letts. **73**, 1923 (1994).

[3] A K Ekert, J G Rarity, P R Tapster and M Palma, Phys. Rev. Letts. **69**, 1293 (1992).

[4] J. G. Rarity, K. D. Ridley and P. R. Tapster, Appl. Opt. **26**, 4616(1987)

[5] V. Pruneri and P. G. Kazansky, El. Lett. **33**, 318(1997)

Parametric Mid-Infrared Generation in Periodically Poled Ti:$LiNbO_3$ Waveguides

D. Hofmann, H. Herrmann, G. Schreiber, C. Haase, W. Grundkötter, R. Ricken, W. Sohler
Universität Paderborn, Angewandte Physik, Warburger Str. 100, 33098 Paderborn, Germany
d.hofmann@physik.uni-paderborn.de

Introduction

Integrated optical parametric devices in $LiNbO_3$ have been identified as most attractive tunable nonlinear frequency converters [1] with many applications mainly in environmental sensing and process monitoring. Using periodically poled waveguides and exploiting quasi-phase matching devices of high efficiency can be developed even for mid-infrared- (MIR-) operation allowing optical pumping with diode lasers.
In this contribution, we report quasi-phase matched difference-frequency generation (DFG), optical parametric fluorescence, and optical parametric oscillation of high efficiency in Ti:$LiNbO_3$ waveguides. They have been fabricated in a Z-cut $LiNbO_3$ substrate with lengths up to 90 mm, widths between 15 and 30 µm, and with losses as low as 0.03 dB/cm. By electric field poling periodic domain structures with periodicities of 31.2 to 32.2 µm have been realized up to a length of 80 mm. The corresponding fabrication parameters are given in [2].

Difference-Frequency Generation

To perform the DFG experiments a tunable external cavity laser was used as pump and a He-Ne laser (λ_S = 3391 nm) as signal source [2]. The pump radiation was amplified by an erbium doped fibre amplifier up to 11 mW in the 1520 to 1580 nm spectral range. The transmitted pump power was blocked by a Ge filter. Due to the chopped pump radiation, only the amplified part of signal power was measured together with the generated idler power using an ac-coupled PbS or PbSe photoconductive detector and a lock-in amplifier.
The highest device conversion efficiency was η = 105 %W^{-1} (λ_P = 1568 nm, λ_I = 2917 nm). This figure is more than one order of magnitude higher than previous reported conversion efficiencies [3], [4], [5].

Optical Parametric Fluorescence

Due to the high parametric gain, possible in these waveguides at higher pump power levels, an investigation of spontaneous and stimulated parametric fluorescence in the MIR becomes possible. In this case an external signal source as used for DFG is not necessary.
The experimental set-up is sketched in Fig. 1. A Q-switched Ti:Er:$LiNbO_3$ waveguide laser (λ = 1562 nm, repetition rate R = 2 kHz, $\Delta\lambda$ = 5 nm, P_{Peak} = 500 W) was used as pump laser [6]. On the output side of the periodically poled waveguide the transmitted pump was blocked by a Ge filter. Signal and idler wavelengths were measured using a monochromator and a PbS photoconductive detector.

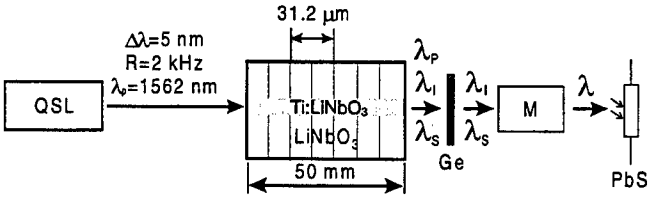


Fig. 1: Experimental set-up: QSL (Q-switched Ti:Er:$LiNbO_3$ waveguide laser), Ge (germanium filter), M (monochromator), PbS (lead sulfide photoconductive detector)

According to the tuning characeristic, spontaneous and stimulated parametric fluorescence is observed at λ_S = 3297 nm (signal) and at λ_I = 2938 nm (idler). As an example, a preliminary result is shown in Fig. 2. The evident difference between signal and idler power levels is due to the power instability of the pump

laser. During the wavelength scan the pump power fell from about 500 W to about 300 W resulting in a much stronger decrease of the signal fluorescence due to its strong pump dependence (see inset of Fig. 2). The broad spectral width of the lines is determined by the low resolution of the monochromator enabling the measurement.

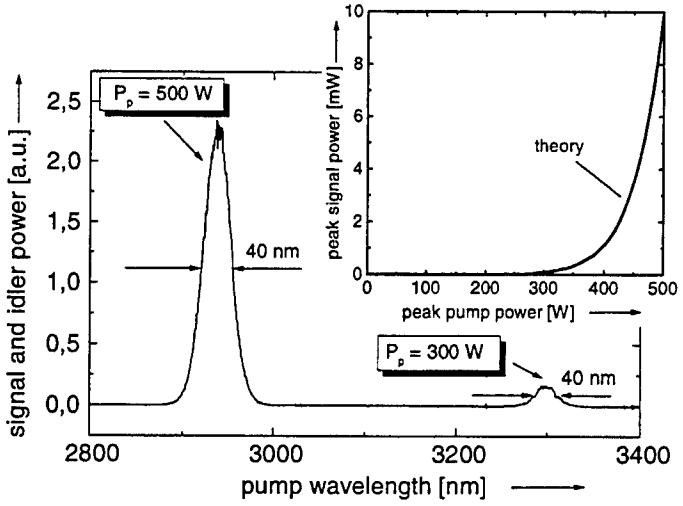


Fig. 2: Measured parametric fluorescence spectrum; inset: calculated signal peak power versus pump peak power

Optical Parametric Oscillation

The low losses of the periodically poled Ti:$LiNbO_3$ waveguides of long effective interaction length (up to 68 mm) enable the development of optical parametric oscillators of very low threshold [7]. Fig. 3 presents calculated results for the pump threshold as function of the reflectivity of the resonator mirrors for a single- (SP-) and double- (DP-) pump pass configuration of a doubly resonant oscillator (DRO).

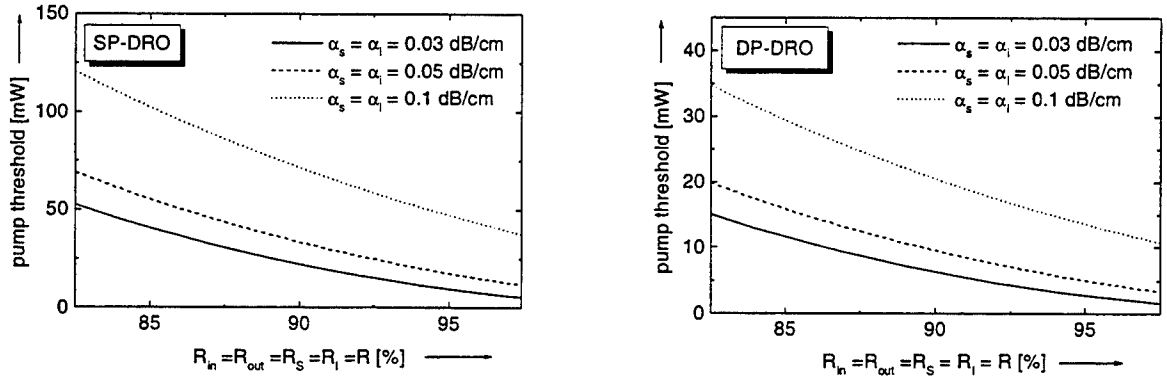


Fig. 3: Pump thresholds of continuous-wave mid-infrared single-pass (SP) and double-pass (DP) doubly resonant integrated optical parametric oscillators as function of mirror reflectivity; different waveguide losses used as parameters

To confirm these results experimentally an integrated optical parametric oscillator (IOPO) was set-up with 90 mm long Ti:$LiNbO_3$ waveguides (80 mm periodically poled with periodicities around 31 μm) in a 0.5 mm thick and 12 mm wide Z-cut, X-propagation $LiNbO_3$ substrate and of external dielectric mirrors in contact with the waveguide end faces. To achieve doubly resonant optical parametric oscillation we used mirrors optimized for high signal (λ_S) and idler (λ_I) reflectivity (≈ 95 % in the 2800 to 3400 nm spectral range) and high pump transmission (80..92 % in the 1500 to 1580 nm spectral range). The IOPO was pumped by a tunable, single-frequency external cavity semiconductor laser (1500 nm < λ_P < 1580 nm) in combination with a high power (up to 27 dBm) fibre amplifier.

The power characteristic of an IOPO with 20 μm wide waveguide is shown in Fig. 4 as signal and idler power versus external pump power together with the power-dependent pump transmission (depletion) at λ_P = 1541.49 nm (degeneracy point: λ_P ≈ 1556 nm). Optical parametric oscillation started at 14 mW; the

corresponding transmitted pump power was only 6.5 mW due to a waveguide coupling efficiency of about 70 %. With rising pump power level also signal and idler power increased up to 6.5 mW at 300 mW pump power. At even higher levels the MIR-ouput saturates at about 7.8 mW. The measured threshold agrees well with modelling results. However, the calculated characteristic has a much steeper slope than the experimental one. Furthermore, the measured pump transmission (depletion) falls with increasing pump power much weaker than theoretically expected. Both discrepancies will be investigated in the near future.

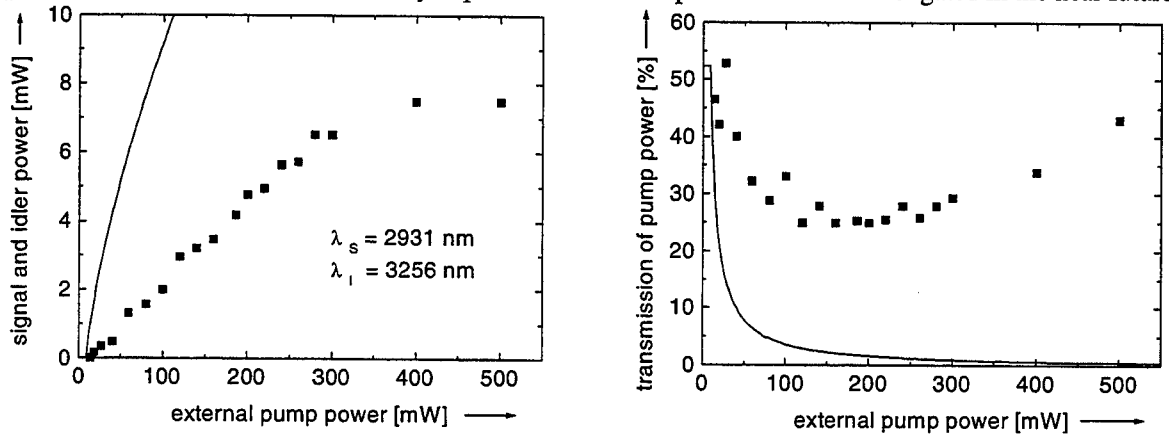


Fig. 4: Power characteristics: Signal and idler power (left) and pump transmission (depletion) (right) as function of external pump power at λ_P = 1541.49 nm; Λ = 31.6 µm; w = 20 µm. Full lines correspond to calculated results with about 70 % estimated waveguide coupling efficiency.

Conclusions

Mid-infrared radiation was generated by difference-frequency generation, optical parametric fluorescence and optical parametric oscillation with very high conversion efficiencies. A continuous-wave integrated optical parametric oscillator of very low threshold was demonstrated, more than two orders of magnitude lower than those of previously reported NIR-devices [8], [9].

This work was supported by the Bundesministerium für Bildung und Forschung (BMBF) under project number 13 N 7024.

References

[1] H. Suche, W. Sohler, "Integrated optical parametric oscillators", Optoelectronics - Devices and Technologies - **4**, 1-20 (1989)

[2] D. Hofmann, G. Schreiber, C. Haase, H. Herrmann, R. Ricken, W. Sohler, Proc. ECIO'99, Torino, Italy, Apr. 14-16, paper FrD3, 505-8

[3] D. J. Bamford, K. P. Petrov, A. T. Ryan, T. L. Patterson, L. Huang, S. J. Field, 1998 OSA Annual Meeting, Baltimore, USA, Oct. 4-9, paper ThVV3

[4] M. A. Arbore, M. H. Chou, M. M. Fejer, CLEO Technical Digest Series **9**, 120 (1996)

[5] M. H. Chou, M. A. Arbore, J. Hauden, M. M. Fejer, paper A.4, Annual Report 1995-96, Center for Nonlinear Optical Materials, Stanford University, Stanford, USA

[6] H. Suche, T. Oesselke, J. Pandavenes, R. Ricken, K. Rochhausen, W. Sohler, S. Balsamo, I. Montrosset, K. K. Wong, Electron. Lett. **34**, 1228-9 (1998)

[7] D. Hofmann, H. Herrmann, G. Schreiber, W. Grundkötter, R. Ricken, W. Sohler, Proc. ECIO'99, Torino, Italy, Apr. 14-16, paper FrE3

[8] M. L. Bortz, M. A. Arbore, M. M. Fejer, Opt. Lett. **20**, 49-51 (1995)

[9] M. A. Arbore, M. M. Fejer, Opt. Lett. **22**, 151-3 (1997)

Near-Infrared Cascaded Difference Frequency Generation in Periodically Poled Ti:$LiNbO_3$ Waveguides

G. SCHREIBER, D. HOFMANN, W. GRUNDKÖTTER, R. RICKEN, AND W. SOHLER

Angewandte Physik, Universität Paderborn
Warburger Str. 100, D-33098 Paderborn, Germany
Tel: +49-5251-60-2295, Fax: +49-5251-60-3422
E-Mail: g.schreiber@physik.uni-paderborn.de

With 155 mW coupled pump power (λ_p = 1.556 μm) a DFG efficiency of -14 dB has been achieved in a 80 mm long periodically poled Ti:$LiNbO_3$ for signals in the 1.5 μm telecommunication band

Introduction

Recently Brener et al. [1] demonstrated highly efficient difference frequency generation in the 1.5 μm telecommunication band by using a cascaded second order nonlinear process in a periodically poled, proton exchanged waveguide in $LiNbO_3$. In such a $\chi^{(2)} : \chi^{(2)}$ based wavelength converter a strong fundamental wave in the 1.5 μm band is used to generate a pump wave at $\omega_p = 2\omega_f$ which interacts with a signal wave at ω_s to generate an idler wave at $\omega_i = \omega_f - \omega_s$. The major advantage of using a cascaded process in comparison with a conventional DFG with a pump of about 780 nm wavelength is that no selective mode excitation is necessary. The idler output power in a $\chi^{(2)} : \chi^{(2)}$ process can be written as $P_i \propto L^4 P_f^2 P_s$ (low fundamental power regime). As it scales with fourth power of the interaction length it is a great challange to develop low loss nonlinear converters of maximum length. Periodically poled Ti:$LiNbO_3$ waveguides are ideal candidates. Based on equations from [2] we calculated the efficiency of an cascaded difference frequency generator for an ideal and lossless periodically poled Ti:$LiNbO_3$ waveguide of 80 mm length. Fig. 1 shows the results for two different nonlinear coefficients $d_{33} = 27$ pmV^{-1} and $d_{33} = 18.7$ pmV^{-1}, both taken from literature [3]. In this contribution we demonstrate for the first time an efficient near infrared "cascaded" DFG wavelength converter using a periodically poled Ti:$LiNbO_3$ waveguide.

Device Fabrication and Experiment

The periodically poled waveguide was fabricated by indiffusion (1060°C, 7.5h) of 7 μm wide and 98 nm high Ti-stripes into the (-Z)-face of a 0.5 mm thick $LiNbO_3$ substrate. A subsequent electric field poling was not possible due to a shallow domain inverted layer on the (+Z)-face. Therefore, we had to remove that layer by careful grinding. As domain inversion always starts on the (+Z)-face it is advantageous to have the waveguides on the preferred side of the sample. Taking these considerations into account we performed as next fabrication step a homogeneous polarisation reversal of the whole sample. Thereafter, the periodic microdomain structure ($\Lambda = 17\mu$m) was fabricated by using the electric field poling method with the structured photoresist on the (+Z)-side. The length of the periodically poled waveguide was 80 mm. Due to inhomogeneities of the waveguides the effective nonlinear interaction length - measured by SHG - was reduced to 50 mm. The corresponding conversion efficiency was 200 %W^{-1} considerably lower than previously observed in other waveguides [4]

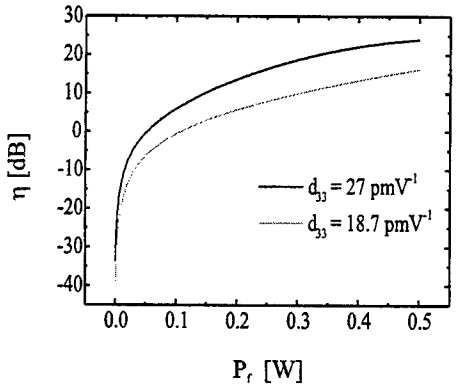


Figure 1: Calculated device efficiency for an ideal, lossless periodically poled Ti:$LiNbO_3$ waveguide of 80 mm length and two different values for d_{33}.

Figure 2. shows the experimental setup to investigate "cascaded" DFG. A high power erbium doped fibre amplifier (up to 27 dBm) was used to amplify the output two tunable external cavity lasers. One was used as the fundamental source to generate by SHG the pump for DFG; the other one was the signal source. Both waves were polarisation controlled and launched into the waveguide by butt-coupling. The coupled fundamental power was 155 mW and the coupled signal power was 54 mW. The generated idler radiation was measured using an optical spectrum analyzer. Fig. 3 shows on the left a corresponding result with an idler power of 2.1 mW. Therefore, the conversion efficiency was -14 dB. By tuning the signal wavelength we measured the conversion bandwidth in the low power regime. The measured figure (see Fig 3. on the right) of 55 nm agrees exactly with the bandwidth calculated for a 50 mm long device.

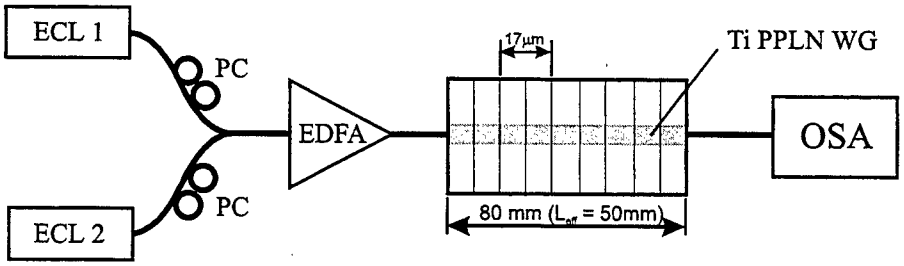


Figure 2: Experimental setup to investigate "cascaded" difference frequency generation; ECL: external cavity laser; PC polarisation controller; EDFA: erbium doped fibre amplifier; OSA: optical spectrum analyzer.

Conclusion and Outlook

We demonstrated "cascaded" difference frequency generation in 80 mm long periodically poled Ti:$LiNbO_3$ waveguides. The maximum efficiency was -14 dB achieved with 155 mW coupled

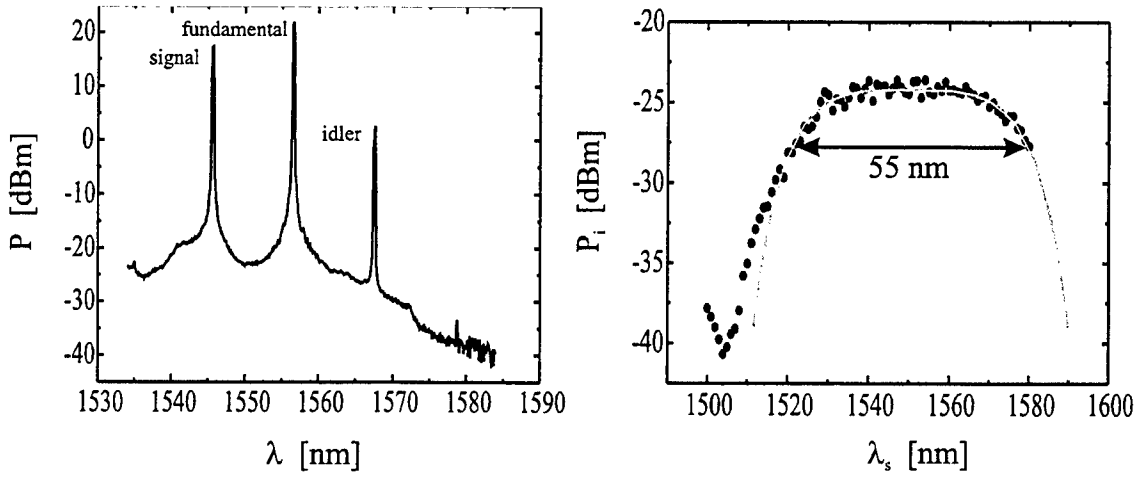


Figure 3: Left: Transmitted optical power of fundamental, signal and idler versus wavelength measured with a spectral resolution of 0.1 nm. The coupled fundamental power was 155 mW. Right: Measured (dots) and calculated (solid line) (spectral resolution 0.1 nm) idler power versus signal wavelength in the low power regime.

pump power. The device efficiency was mainly limited by the effective nonlinear interaction length. It is expected that by further improvements of our waveguide fabrication technology a device of 0 dB conversion efficiency at fundamental power levels of about 100 mW can be developed.

Acknowledgement

This work was supported by the Bundesministerium für Bildung, Wissenschaft, Forschung und Technologie under contract 13N7024.

References

[1] I. Brener, M. H. Chou, and M. M. Fejer, "Efficient wideband wavelength conversion using cascaded second-order nonlinearities in $LiNbO_3$ waveguides", OFC'99 paper FB6-1.

[2] K. Gallo, G. Assanto, and G. I. Stegeman, "Efficient wavelength shifting over the erbium amplifier bandwidth via cascaded second order processes in lithium niobate waveguides", Appl. Phys. Lett. **71**, 1020 (1997).

[3] I. Shoji, T. Kondo, A. Kitamoto, M. Shirane, and R. Ito, "Asolute scale of second-order nonlinear-optical coefficients", J. Opt. Soc. Am. B **14**, 2268 (1997).

[4] G. Schreiber, R. Ricken, and W. Sohler, "Near-Infrared second harmonic and difference frequency generation in peridically poled Ti:$LiNbO_3$ waveguides", ECIO'99 paper WeD1.

Blue upconversion in Tm^{3+}-Yb^{3+}-phosphosilicate rib waveguide generated by a CW pump at 980 nm

M.V.D. Vermelho and J. S. Aitchison

Department of Electronics and Electrical Engineering - University of Glasgow

Glasgow G12 8QQ - Scotland UK

e-mail: m.vermelho@elec.gla.ac.uk

There is considerable interest in materials with high upconversion efficiencies for converting infrared pump wavelengths to the shorter, blue-violet wavelength region. So far, the highest upconversion efficiencies are obtained in fluoride, rather than oxide, hosts because of their lower phonon energies which decrease the multiphonon relaxation rates of rare-earth excited states. In this paper we report an efficient upconversion blue light generation in phosphosilicate glass fabricated by Flame Hydrolysis Deposition (FHD). Sample cores were made of SiO_2-P_2O_5 glass, doped using an aerosol doping technique [1] with Tm-Yb-Na chlorides (0.1-1.0-0.1M respectively).

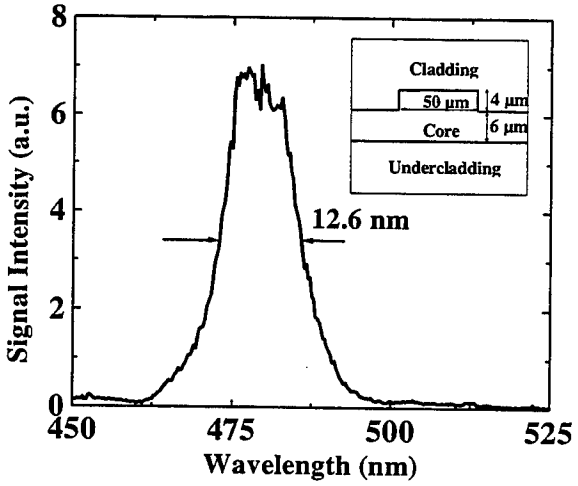


Figure 1: - Power spectrum of the upconverted signal from a 5.5 cm long channel waveguide, pumped by a CW 200 mW

Figure 1 shows a typical power spectrum of the upconverted signal at 476 nm, generated in a 5.5 cm long rib waveguide. For a fundamental CW pump of 200 mW at the absorption peak of Yb^{3+} ions at 975 nm. The spectral bandwidth of 12.6 nm is characteristic of a fluorescent mechanism due to the transition $^1G_4 \rightarrow {}^3H_6$ of the Tm^{3+} ions. Signal power of 130 nW was generated from 150 mW of infrared pump power at 975 nm. Considering that the injected power into the waveguide corresponds to 30% of the delivered power, the calculated process efficiency is 2×10^{-4} %. Similar conversion efficiency was obtained in a Tm^{3+} single doped (0.2M) waveguide pumped by a mode-locked Nd:YAG laser only with high pump power [1]. The low conversion efficiency of the present process is attributed mainly to the unfavourable waveguide geometry. As depicted in the insert of figure 1, the waveguide is highly multimode at the pump and signal wavelength, and has a poor optical confinement due to this rib configuration.

The upconverted signal intensity as a function of the fundamental pump power was analysed and the results are depicted in figure 2. As reported in the literature, the expected result is

of the sort of $P_{blue} \propto P^3_{pump}$ however, measurements repeatedly presented the same quadratic dependence as can be inferred from log-log insert plot of figure 2. This could imply that the upconversion process is saturated in at least one step. Considering reasonable energy transfer probability, moderate level of excitation in the ytterbium population would be suffice to pump the majority of the thulium ions to the first excited state, depleting the ground state and causing saturation.

The efficient energy transfer was confirmed when preliminary results have shown upconvertion blue light for pumping at 800 nm. This process is also under investigation and it can be explained as follow: single Tm^{3+} doped sample pumped at 800 nm did not show blue light generation. This upconversion process should be possible only if the $^3H_5$ level is highly populated due to the $^3F_4 \rightarrow {}^3H_5$ photons decay, which is not possible because the $^3F_4 \rightarrow {}^3H_5$ lifetime is much longer (~10×) than the ground state relaxation from the same level. This upconversion process become possible in the Tm^{3+}/Yb^{3+} doped sample because Yb^{3+} ions creates an efficient route to populate the $^3H_5$ level via energy transfer from Tm^{3+} to Yb^{3+} ($^3F_4 \rightarrow {}^2F_{5/2}$) [3,4], and energy back transfer from Yb^{3+} to Tm^{3+} ($^2F_{5/2} \rightarrow {}^3H_5$).

Previous workers have found that a large ratio of Yb^{3+} to Tm^{3+} ions, close to 100:1, is needed to achieve high upconversion efficiencies [2]. Where as in our sample this ratio is only one order of magnitude different.

The influence of Na^+ in this glass system is also under investigation. Previous measurements in phosphosilicate glass have shown an increase in the Er^{3+} laser lifetime (at 1535 nm) due to the presence of Na^+ ions. Reported second-order nonlinearity in poled silica glass [5] have shown enhancement due to influence of Na^+ as well.

In summary, we have shown two possibilities of efficient CW upconversion blue light generation in phosphosilicate Tm/Yb/Na doped glass (in silica-on-silicon fabricated by FHD). The commercial availability of powerfull diode lasers at the single pump wavelength used (at 800 nm or 980 nm), and the facility of integrate them on the same substrate of the doped waveguides, increase the prospect to produce compact and robust devices to generate blue light.

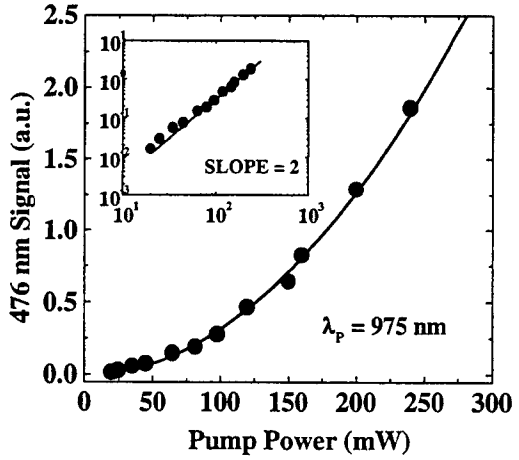


Figure 2 - 476 nm signal intensity as a function of CW fundamental pump power at 975 nm. Insert is a log-log plot of data showing the slope 2.

Acknowledgement

M.V.D. Vermelho would like to thank the Brazilian Agency CNPq (Conselho Nacional de Desenvolvimento Científico e Tecnológico) for his graduate studentship sponsoring.

References

[1] J.R. Bonar, M.V.D. Vermelho, A.J. McLaughlin, P.V.S. Marques, J.S. Aitchison, J.F. MartinsFilho, A.G. Bezerra Jr, A.S.L. Gomes, C.B. deAraujo, "Blue light emission in thulium doped silica-on-silicon waveguides", *Opt. Commun.* **141**, 137 (1997).

[2] Z. Hao, X. Chen, G. Zhang, F. Song, Yan-bing Hou, "Blue upconvertion with excitation at 970 nm in $Yb_{0.18}$-doped $Tm_{0.03}LaP_5O_{14}/Tm_{0.1}LaP_5O_{14}$", *SPIE* **2897**, 275 (1996).

[3] X. Zou, T. Izumitami, "Fluorescence mechanism and dynamics of Tm^{3+} single doped and Yb^{3+}, Tm^{3+} doubly doped glasses, sensitized by Yb^{3+}", *J. of Non-Cryst. Solids* **162**, 58 (1993).

[4] R.H. Page, K.I. Schaffers, P.A. Waide, J.B. Tassano, S.A. Payne, W.E. Krupke, W.K. Bischel, "Upconversion-pumped luminescence efficiency of rare-earth-doped hosts sensitized with trivalent ytterbium", *J. Opt. Soc. A,. B* **15**, 996 (1998).

[5] H. Imai, S. Horinouchi, N. Asakuma, K. Fukao, D. Matsuki, H. Hirashima, and K. Sasaki, "Effects of introduction of sodium and water on second-order nonlinearity in poled synthetic silica glass", *J. Appl. Phys.* **84**, 5415 (1998).

Nonlinear Guided Waves and Their Applications

Dispersion Management 2

Friday, 3 September 1999

Wladek Forysick, Aston University, UK
Presider

FD
15.30-17.00
Salle Morey—St-Denis

Distributed Amplification of Optical Solitons

G. P. Agrawal, Z. M. Liao, and T. Lakoba
The Institute of Optics and Rochester Theory Center
University of Rochester, Rochester, New York 14627 USA

Summary

Optical solitons are reaching the commercial stage for lightwave transmission because they offer the possibility of dynamic balance between group-velocity dispersion (GVD) and self-phase modulation (SPM), the two effects that severely limit the performance of non-soliton systems [1]. Most system experiments employ the technique of lumped amplification and place fiber amplifiers periodically along the transmission line for compensating the fiber loss. However, lumped amplification introduces large peak-power variations, which limit the amplifier spacing L_A to a fraction of the dispersion length L_D [2].

The limitation on the amplifier spacing imposed by lumped amplification can be overcome by using distributed amplification, a technique that was pioneered during the decade of 1980s [3]. It was abandoned after the advent of erbium-doped fiber amplifiers although not completely [4], [5]. In one implementation of this scheme, the transmission fiber itself is lightly doped with erbium ions and is pumped periodically, creating sufficient gain for compensating the fiber loss. Since the gain is distributed throughout the fiber link and compensates losses locally all along the fiber, soliton peak-power variations can be made much smaller compared with the lumped amplification scheme. Although one expects the pump-station spacing L_A to become comparable and even exceed L_D in the case of distributed amplification, a systematic comparison of the lumped and distributed amplification schemes has not been made. Here we report the results of such a systematic study and show that distributed amplification can provide better performance at high bit rates.

Our approach is based on solving numerically the generalized nonlinear Schrödinger equation

$$i\frac{\partial A}{\partial z} - \frac{1}{2}\beta_2(z)\frac{\partial^2 A}{\partial t^2} + \gamma|A|^2 A = \frac{i}{2}[g(z) - \alpha]A + T_R A\frac{\partial |A|^2}{\partial t}, \tag{1}$$

where T_R is the Raman constant and other parameters have their usual meaning [6]. Distributed amplification of solitons is included through the gain $g(z)$. To avoid excessive generation of dispersive waves, we optimize the the dopant density such that $g(z) - \alpha$ deviates from zero as little as possible. For this purpose, we solve the three-level rate equations governing the dynamics of erbium dopants for the case of bidirectional pumping at 1480 nm.

We first demonstrate the advantages offered by distributed amplification for a 20 Gb/s system having 100-km pump-station spacing, uniform dispersion with $\beta_2 = -0.5$ ps^2/km, $\gamma = 3.36$ W^{-1}/km, $T_R = 3$ fs and $\alpha = 0.23$ dB/km. We choose $A(0,t) = \sqrt{P_0}\,\mathrm{sech}(t/T_0)$ with $T_0 = 5$ ps ($T_{\mathrm{FWHM}} = 8.8$ ps). The dispersion length is 50 km for such a system while $L_A = 100$ km. Figure 1 compares soliton evolution for the cases of lumped and distributed amplification. Since $L_A/L_D = 2$ in the case of lumped amplification, the soliton radiates its energy through dispersive waves and is distorted significantly after a few amplification

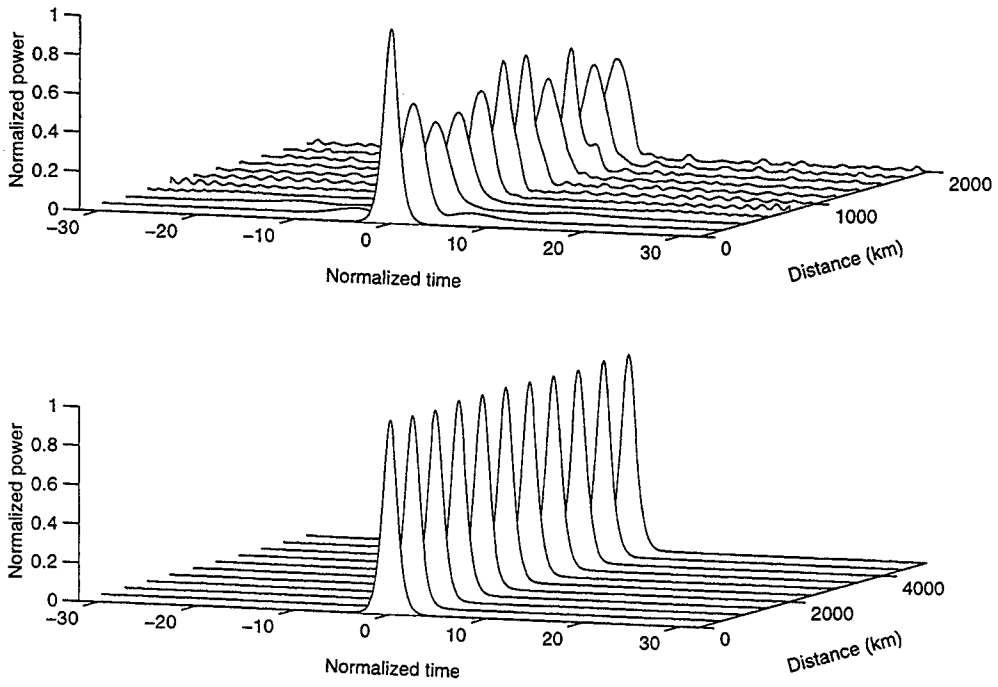


Figure 1: Comparison of lumped (top) and distributed (bottom) amplification schemes for the case of a 20-Gb/s system designed with 100-km amplifier spacing.

stages. Such a system cannot transmit the 20-Gb/s signal over more than 500 km. In contrast, the soliton shows no degradation even after 5000 km when distributed amplification is used. A logarithmic plot shows the contribution of residual dispersive waves to remain below the 10^{-5} level even after 5000 km.

For a bit rate of 40 Gb/s, it was necessary to use $T_0 = 2.5$ ps ($T_{\mathrm{FWHM}} = 4.4$ ps), resulting in a dispersion length of only 12.5 km. Such a system is affected both by soliton self-frequency shift (SSFS) and by soliton interaction. To include soliton interaction, we use a 64-bit pseudorandom sequence in numerical simulations and compare the system performance using two-bit-wide "eye diagrams." Figure 2 (top) shows the combined effects of SSFS and soliton interaction for lumped amplification at a distance of 1000 km. Clearly such a system is inoperable in practice. We have found that both the SSFS and the soliton interaction problems can be solved by combining distributed amplification with dispersion management. Figure 2 (bottom) shows the eye diagram after 5000 km for a dispersion-managed (DM) system under identical operating conditions. The dispersion map consisted of two 50-km fibers with GVD of 0.3 ps^2/km and -0.38 ps^2/km, resulting in an average dispersion of -0.04 ps^2/km and a map strength $|\beta_{21}L_1 - \beta_{22}L_2|/T^2_{\mathrm{FWHM}} = 1.75$. As seen in the bottom part of Figure 2, solitons barely move out of their time slot when distributed amplification is used with DM. We also studied the case of lumped amplifiers with DM and found that both SSFS and soliton interaction are reduced in this case as well (middle part of Fig. 2) although the system performance is better in the case of distributed amplification.

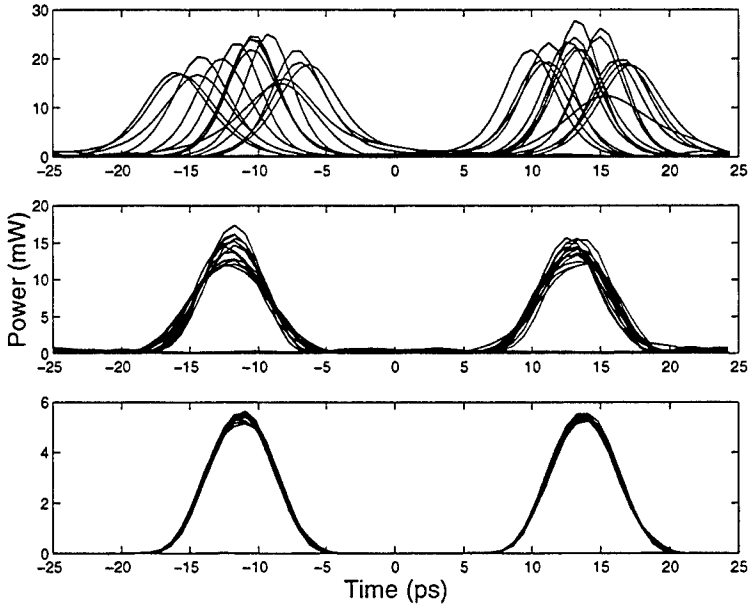


Figure 2: Eye diagrams for a 40-Gb/s system in three different operating conditions: after 1000 km without DM (top); after 5000 km with lumped amplification and DM (middle); after 5000 km with distributed amplification and DM (bottom).

We plan to present a detailed comparison of lumped and distributed amplification schemes for dispersion-managed systems by considering several different dispersion maps and taking into account various sources of performance impairment such as Gordon–Haus timing jitter, soliton interaction, and Raman-induced frequency shift.

References

[1] G. P. Agrawal, *Fiber-Optic Communication Systems*, 2nd ed., New York, Wiley, 1997.

[2] A. Hasegawa and Y. Kodama, *Solitons in Optical Communications*, Clarendon Press, Oxford, 1995.

[3] L. F. Mollenauer, J. P. Gordon, and M. N. Islam, "Soliton propagation in long fibers with periodically compensated loss," *IEEE J. of Quan. Electron.*, vol. 22, pp. 157-173, 1986.

[4] K. Rottwitt, J. H. Povlsen, and A. Bajarklev, "Long-distance transmission through distributed erbium-doped fibers," *J. Lightwave Technol.*, vol. 11, pp. 2105-2115, 1993.

[5] A. Altuncu et. al., "40 Gbit/s error-free transmission over 68 km distributed-erbium doped fibre amplifier," *Electron. Lett.*, vol. 32, pp. 233-234, 1996.

[6] Govind P. Agrawal, *Nonlinear Fiber Optics*, 2nd ed., Academic Press, San Diego, 1995.

Experimental investigation of soliton transmission over high strength dispersion managed transmission lines

S.B. Alleston, P. Harper, D. Govan, I. Bennion, N. J. Doran
Photonics Research Group, Aston University, Aston triangle, Birmingham, B4 7ET, UK
Tel.: +44 121 359 3611 x4949 Fax: +44 121 359 0156 e-mail: s.b.alleston@aston.ac.uk

At present there is much interest in the transmission of 40Gbit/s data as a means of upgrading existing terrestrial networks. These legacy networks consist almost entirely of high average dispersion standard fibre, which severely limits transmission distances due to polarisation mode and chromatic dispersion. One promising technique at 10 Gbit/s is the use of dispersion managed (DM) solitons[1], and there is evidence that DM solitons may be an appropriate approach at 40Gbit/s[2]. At this data rate the bit interval is 25ps, so to ensure a good mark space ratio short (<6ps) pulses will need to be used. The map strength in its usual definition (from [3]) is defined by the difference in dispersion and length of the two alternating sections of fibre and the inverse of the pulsewidth squared, and determines amongst other things the degree of energy enhancement and the amount of pulse breathing within the map. With the pulse width decreasing, the map strength soon becomes intolerably large, making transmission in the usual regime difficult due to the constraints (be they regulatory or practical) of EDFA power availability. However, we have identified a new quasi-linear regime at a much lower average power than predicted in recirculating loop experiments. This appears to work well at high data rates, providing a record transmission distance of 1009km at 40Gbit/s over standard fibre that is twice that of competing technologies[4]. In this paper we present results that seek to clarify certain aspects of this regime and determine the limiting factors for successful transmission.

Experiments were carried out using a recirculating loop as shown in figure 1. The commercially available (Pritel UOC-3) modelocked fibre laser source provided 2ps pulses with a time-bandwidth product of 0.45 at the operating wavelength of 1558nm. A 10Gbit/s 2^{31}-1 PRBS data pattern was imposed on the pulse stream by a lithium niobate amplitude modulator (AM), and this bit stream was multiplexed up to 40Gbit/s using a fibre delay line multiplexer (MUX) in a now standard configuration. The transmission experiments were carried out using a single span recirculating loop containing of two erbium doped fibre amplifiers (EDFA) separated by a length of DCF and a 2.3 nm optical bandpass filter.

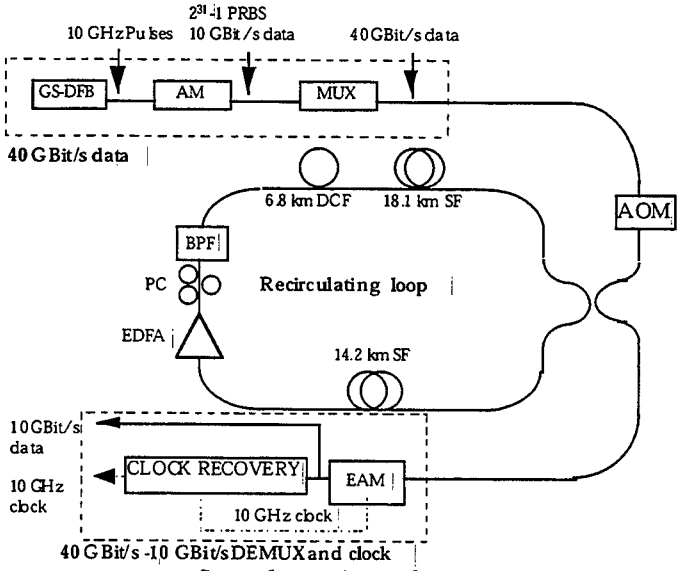


figure 1 experimental set up

The loop consisted of 75km of standard fibre (SF), in section lengths of 32km before and 43km after the EDFAs/DCF respectively, with an average dispersion of +16ps/(nm km) and 14.9km of dispersion compensating fibre (DCF) with a total dispersion of -1200ps/(nm km). The average dispersion zero wavelength was 1556nm and the overall average dispersion at the operating wavelength was +0.04ps/(nm km), the DCF also providing partial slope compensation resulting in a value of +0.02ps/(nm^2 km) for the fibre combination. In figure 2 results are presented showing the total propagation distance for a 40Gbit/s data stream using this map. Included for reference are results using a 5ps pulse and a similar map with the fibre lengths scaled to give a 32km amplifier span for reference. In this case the map strengths were 750 and 51 respectively, with the corresponding dispersion lengths in the standard fibre and the DCF being 200m and 40m.

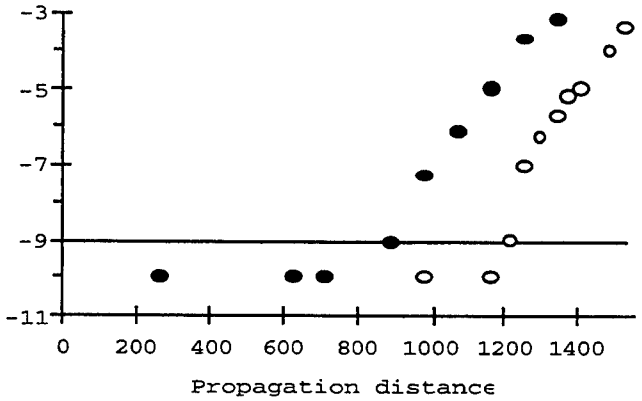


figure 2 BER as a function of distance for 75km span (closed circles) and 32km span(open circles) for demultiplexed 40Gbit/s data

In order to investigate this further, 10Gbit/s transmission experiments were carried out by removing the MUX and DEMUX stages from the experiment and using the same dispersion map and 2ps pulsewidth. At this data rate error free propagation was achieved over 1900km. In figure 3 eye diagrams taken at distances between 0 and 1980km are presented. As can be seen from these, there is little build up in noise in the zeros, whilst the degradation appears to be due to timing jitter. As the Gordon-Haus limit is far in excess of this (~20,000km), the cause of the jitter is most probably due to interactions.

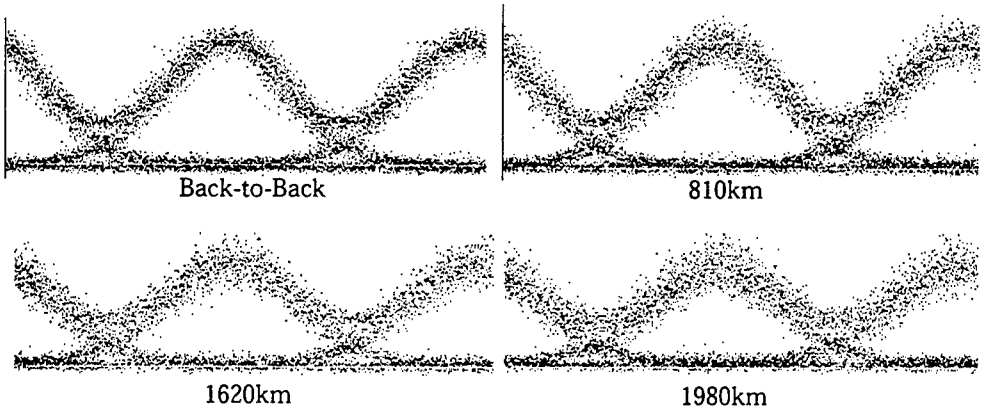


figure 3 eye diagrams at several transmission distances between 0 and 1980km for 10Gbit/s data

The transmission distance was then fixed at 895km, and the average power was varied. Results are presented in figure 4 show eye diagrams at powers between 0.02mW and 0.532mW, which indicate severe degradation at higher powers.

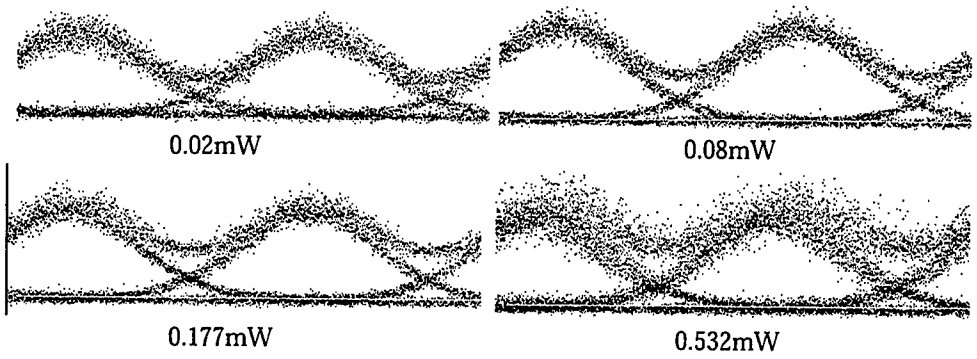


figure 4 Eye diagrams taken at a transmission distance of 895km using different average powers

Furthermore, a fixed data pattern was transmitted to look at interactions, and results are presented in figure 5. These patterns indicate clearly the magnitude of the interactions, as the adjacent pulses quickly become degraded, whilst the separated pulses remain intact.

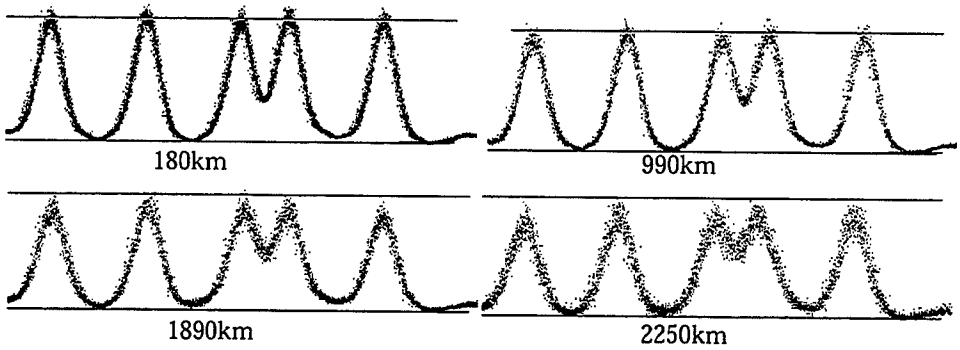


figure 5. Transmitted pulses at various distances indicating degradation due to pulse-pulse interactions

Several other features became apparent during the course of this work. Unlike the 'classical' DM soliton is the reduced energy enhancement. For this map the predicted energy enhancement should be 526 giving an average power of 6.6pJ but the optimum energy was found to be only 25fJ, an enhancement of 2. This would seem to indicate linearity of the transmission regime, but it was also found both experimentally and theoretically that the launch point within the map was critical for successful transmission, indicating that non-linearity remains important for this system.

In conclusion, we have investigated transmission utilising a new quasi-linear regime that looks promising for high data rate transmission over standard fibre. The limiting factor in such a regime was determined to be interaction induced timing jitter, and several features such as a reduced energy enhancement and pulsewidth independence were observed which distinguish this regime from the better understood DM soliton regime.

References.

1)N.J. Smith, F.M. Knox, N.J. Doran, K.J. Blow and I. Bennion. Electron Lett. 1996, **32**, (1), pp54-55.
2) J.H.B. Nijhof, N.J. Doran, W. Forysiak and A. Berntson. Electron. Lett. 1997, **34**, (5) pp481-482.
3) D.S. Govan, W. Forysiak and N.J. Doran:, Opt. Lett, 1998, **23** (19), pp. 1523-1525.
4) S.B. Alleston, P.Harper, I.S. Penketh, I. Bennion, N.J. Doran and A.D. Ellis, OFC '99 paper PD3.

Reduced interaction between π-shifted dispersion-managed solitons

C. Paré, P.A. Bélanger and S. Larochelle

Centre d'Optique, Photonique et Laser (COPL)
Université Laval, Département de Physique
Ste-Foy, Québec, Canada G1K 7P4
FAX: (418) 656-2623
cpare@phy.ulaval.ca, pabelang@phy.ulaval.ca, larochel@gel.ulaval.ca

Although the dynamics of the mutual interaction between the neighboring pulses of a given channel of a dispersion-managed (DM) system can be quite different from what is observed with conventional solitons, pulse interaction still represents an important factor that can limit the bit rate [1-3]. Among the differences in behavior, the quasi independence of the interaction on the relative phase between the pulses in a system with strong dispersion management is noteworthy. As noticed elsewhere [1-2], the reason behind this can be traced back to the fact that the large local dispersion tends to average out the phase-dependent terms of the interaction. The self- and cross-phase modulation terms that remain in the coupled governing equations when dropping the other four-wave mixing contributions leave the interaction phase-independent. Variational models [2-3] that do not include these four-wave mixing terms have indeed been found to be accurate enough when compared with direct numerical simulations. This agreement prevails as long as the pulses remain sufficiently far apart. And, *a priori*, this is the regime of interest for communication purposes as one wants the pulses to be easily distinguishable.

This work is concerned with a different regime where the pulses are brought closer to each other. The evolution of the total field $\Psi = \Psi_1 + \Psi_2$ is then more appropriately described by a single NLS equation:

$$i\Psi_z + \frac{1}{2} D_{1,2} \Psi_{\tau\tau} + |\Psi|^2 \Psi = 0 \quad ,$$

where $D_i \equiv \beta_{2i} / <\beta_2>$, with β_{2i} ($i = 1,2$) representing the dispersion parameter of each fiber segment of length L_i of a two-step dispersion map and $<\beta_2>$ is the path-averaged dispersion. The time $\tau = t/T_o$ is in units of a reference time T_o and the propagation distance z is expressed in terms of the average-dispersion length $d = T_o^2 / |<\beta_2>|$. We mostly rely on numerical simulations for analyzing the interaction between closely spaced DM solitons that are here approximated by Gaussian pulses:

$$\Psi(z=0,t) = \Psi_{01} \exp[-((t+\delta)/T_1)^2] + \Psi_{02} \exp[-((t-\delta)/T_2)^2 + i\theta]$$

where the relative phase θ is introduced. The system parameters considered in the simulations reported below are the following: $L_1 = L_2 = 100$ km, $\beta_{21} = -3.06$ ps^2/km , $\beta_{22} = +2.86$ ps^2/km and $T_1 = T_2 \equiv T_{12} = 13.5$ ps. The amplitude parameters are: $\Psi_{01} = \Psi_{02} = 2.7$. Figure 1 first compares, in terms of contour lines of the pulse profile at the midpoint of the anomalous fiber, the long-haul evolution (200 map periods) of in-phase (a) and π–shifted (b) interacting pulses initially spaced by $2\delta = 6.0\ T_{12}$.

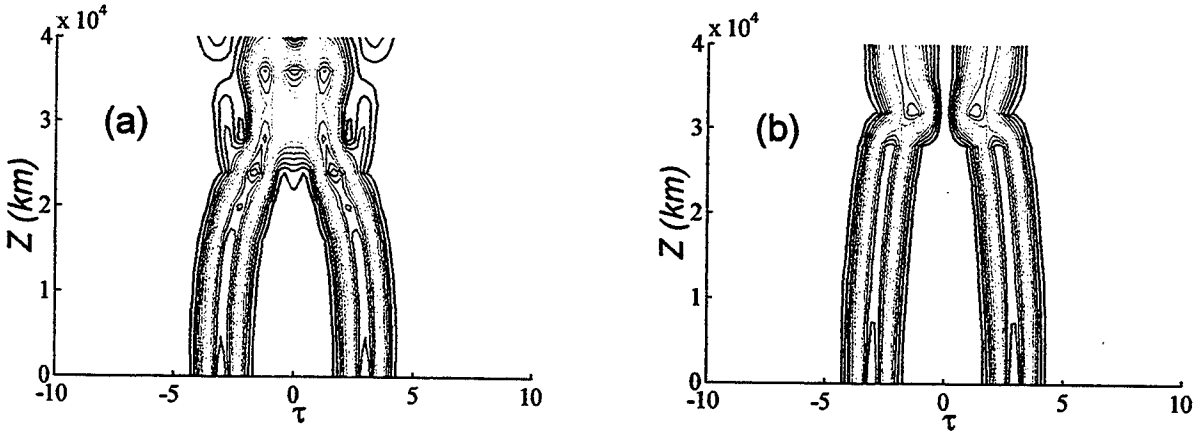


Figure 1. Contour map of the evolution of two interacting DM solitons. a) $\theta = 0$; b) $\theta = \pi$.

Whereas the initial behavior looks similar in both cases, the long term evolution is quite different. In particular, in contrast with the pulse coalescence observed in Fig. 1a, the π–shifted pulses tend to preserve their individuality (Fig. 1b). Figure 2, where the initial separation between the π–shifted pulses is reduced to $2\delta = 2.0\ T_{12}$, is even more contrasting as it shows a quasi steady state. (In the in-phase case, one can hardly talk in terms of *two* pulses as they are too close to each other.)

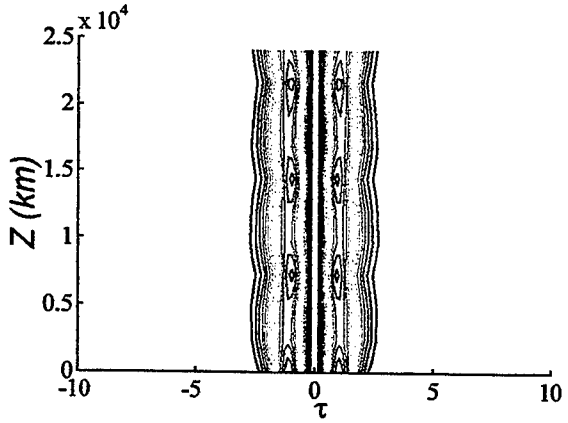


Figure 2. Evolution of two closely spaced π-shifted solitons. The input separation is $2\delta = 2.0\ T_{12}$.

We interpret this behavior as being due to the existence of an *antisymmetric* DM soliton which was discussed elsewhere [4]. Figure 3, which compares the launched π–shifted Gaussians of Fig. 2 with a DM soliton of odd parity having the same peak power as the combined pulses, confirms the validity of this interpretation.

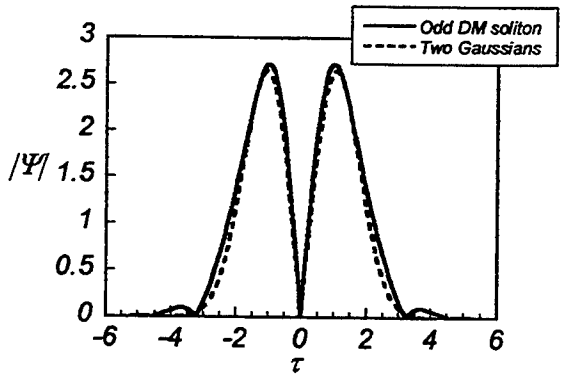


Figure 3. Comparison between an antisymmetric DM soliton and the two π-shifted Gaussian pulses of Fig. 2.

To be of practical interest for communication systems, this behavior should be robust enough to sustain various perturbations. According to our simulations, the most important one appears to be a breaking of the perfect antisymmetry in the launched pulse. Although the subsequent evolution depends, of course, on the importance of this perturbation, we have found that the interacting pulses can preserve sufficiently well their integrity to remain clearly distinguishable even after a few thousands of kilometers. This will be discussed in further detail.

References

[1] T. Yu, A. Golovchenko, A.N. Pilipetskii and C.R. Menyuk, *Opt. Lett.* **22**, 793 (1997).
[2] M. Matsumoto, *IEEE Photon. Technol. Lett.* **10**, 373 (1998).
[3] T. Georges, *J. Opt. Soc. Am.* **B15**, 1553 (1998).
[4] C. Paré and P.-A. Bélanger, *Proc. Nonlinear Guided Waves and Their Applications Tech. Dig.*, Optic. Soc. Amer., Victoria, B.C. Canada, 1998, pp. 39-41.

Energy, frequency and time fluctuations reduction of DMS through Synchronous Amplitude Modulation only

Fabien Merlaud
France Telecom CNET/DTD/RTO, 2 av. Pierre Marzin 22307 Lannion Cedex, France
fabien.merlaud@cnet.francetelecom.fr

Thierry Georges
Algety Telecom, 15 rue Fulgance Bienvenue, 22300 Lannion, France
thierry.georges@algety.com

Introduction

In the scope of high rate submarine long haul transmissions, different kind of in line control systems are investigated. Synchronous amplitude modulation is know to be the most powerful of them : with synchronous modulation 70 000 km of soliton propagation were achieved at 40 Gbit/s in [1] or 8×20 Gbit/s over 10 000 km in [2]. Its benefits on classical path averaged soliton have been demonstrated since several years If this technique limits continuum generation and timing jitter, it causes modulational instability which is usually limited by in line filtering.

The aim of this communication is to show that proprieties of the spectral dependence of the DMS on its energy, which are penalizing for fixed filtering [3], can nonetheless be exploited to reduce in the same time energy, time and frequency fluctuations with in-line synchronous amplitude modulation only.

Modeling

The propagation of a pulse in a non-linear line can be modeled by the normalized Schrödinger equation

$$i\frac{\partial q}{\partial z}+\frac{1}{2}D(z)\frac{\partial^2 q}{\partial t^2}+a(z)|q|^2 q=0 \qquad (2.1)$$

where D is the normalized dispersion of the fiber and $a(z)$ is the relative energy at position z. The evolution of $a(z)$ is driven by fiber loss and amplifier gain. In the following, its value is chosen to be equal to 1 at amplifier output.

The lumped amplitude modulator function can be approximated by its 2nd order taylor expansion

$$T(t)=1-\kappa_2(t-\mu)^2 \qquad (2.2)$$

where μ is the time when the transparency maximum of the amplitude modulator is reached.

Perturbation theory [4] is applied through a Lagrangian formalism on a gaussian pulse $q(z,t)=\sqrt{B}\exp\left(-(1+ib)\frac{(t-\alpha)^2}{2W^2}+i\Phi-i\Omega t\right)$ to the perturbation deriving from an excess gain δ and modulation.

The reference energy is $E=\sqrt{\pi}BW$ and the pulse energy along the line is $E_{line}=aE$. In absence of perturbation $E(z)$ remains constant.Other parameters are defined : $\gamma=\frac{1+b^2}{W^2}$ related to the square of the quadratic bandwidth of q, $\overline{\Omega}^2=\gamma/2$ and $C=-\frac{b}{\gamma}$ the cumulated dispersion with linear and non linear contributions.

The effects of the amplitude modulation on the pulse characteristics are the following:

$$\Delta E=-\kappa_2 E\left[2(\alpha-\mu)^2+\left(W^2-W_0^2\right)\right]\delta(z-z_m) \qquad (2.3)$$

$$\Delta\alpha=-2(\alpha-\mu)W^2\kappa_2\delta(z-z_m) \qquad (2.4)$$

$$\Delta\Omega=2\gamma C(\alpha-\mu)\kappa_2\delta(z-z_m) \qquad (2.5)$$

The excess gain δ appears in eq. (2.3) through $\delta = W_0^2 \kappa_2 / 2$.
When C=0, equation (2.4) is analog to the effects of amplitude modulation on PAS. Nonetheless, as W is enlarged by the chirp which is not present in PAS, the effects of amplitude modulation can be stronger on DMS.
Eq. (2.3) is also analog to the effects of amplitude modulation on PAS. Whereas W is well know to decrease with E for PAS which makes fluctuations amplified trough eq. (2.3), the existence of energy domains where W increases as E increases for DMS allows the reduction of energy fluctuations with amplitude modulators. Actually, making the assumption of an adiabatical variation of W (i.e the pulsewidth for steady propagation at modulator location only depends on the pulse energy), one obtains
$W_E^{'} = 1/W \cdot \left(0.5\left(C^2 - 1/\gamma^2\right)\gamma_E^{'} + \gamma C C_E^{'}\right)$
For the particular case where C is close to zero at the modulator position and if the pulse is not shifted temporally, the distributed energy evolution is driven by $E_z^{'} = \xi k_m (E - E_0)$ with the modulation strength $k_m = 2\kappa_2 W_m^2 / z_{step}$ and $\xi = 0.5\gamma_E^{'} E_0 / \gamma$ where z_{step} is the amplitude modulation spacing. ξ is a correction factor brought by dispersion management (subscript *m* designs the pulse characteristics at modulator position). It has been shown in [4,5] that parameter ξ can be negative for high energy pulses.
Hence, energy fluctuations can be reduce by amplitude modulation if the pulse energy is judiciously chosen.
With DMS, chirp induces a coupling between time shift and frequency. Amplitude modulation has the same effects as a phase modulation. The sign of the product cumulated dispersion times averaged dispersion $\overline{D}C_m$ appears to be important. If this sign is positive, the coupling between time and frequency fluctuations induces a return strength in frequency and an increased efficiency of the time fluctuation reduction.

Influence of amplitude modulation on steady propagation
Let's consider the line sketched in figure 1

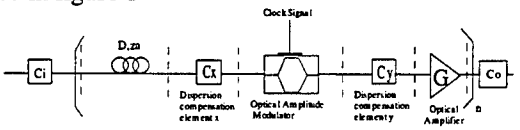


Fig.1 : Implementation of synchronous amplitude modulation in a dispersion-managed link.

Each cell of the line consists of a fiber of length z_a and dispersion *D*, two lumped dispersion compensators c_x and c_y, an amplifier whose gain *G* compensates for the fiber loss. The excess gain for the amplitude modulator loss is included in the modulation characteristic. A prechirp c_i and a postchirp c_0 are also included. The dispersion compensation ratio is then $\rho = \frac{-(c_x + c_y)}{D z_a}$.

Steady propagation can be achieved if c_i and γ at pulse emission are judiciously chosen for a given pulse energy.
In the following, the parameters will be taken as follows : G=100, z_a=0.2, D=100, c_x=-18.4, c_y=-1.4.
Numerical simulations are now performed in order to confirm analytical results.
Numerically the amplitude modulator is considered to achieve a gaussian profile.

Energy evolution
The energy chosen for numerical simulation is E_0=300. The steady point parameters are c_i=-0.99, γ_0=0.72 (so that C_m=0.41) and κ_2=0.0194 is chosen to have k_m=0.3. Figure 2 shows that the numerically the strength is found around 0.11 whereas analytically its value is 0.098. Parameter ξ is then close to –0.33.

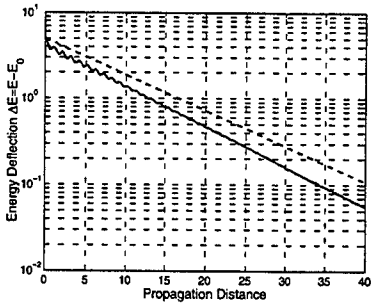


Fig. 2 : Numerical(solid line) and analytical (dashed line) energy evolution of a pulse of energy E=305 in a line whose steady propagation occurs for E=300

Time and frequency fluctuations

It appears that through the linear dispersion and in-line modulation, frequency and time jitter are coupled. If the chirp at modulator location is judiciously chosen, the coupling matrix between $d\alpha$ and $d\omega$, time shift and frequency shift at modulator position, has eigenvalues which are not real, but which real part is negative. The time jitter and frequency fluctuation are then reduced even if timing jitter is translated into frequency fluctuations (see figure 3). As the time references are given by a clock recovery, the frequency fluctuation reduction does not prevent against an uniform frequency shift.

In the case of figure 3, the real part of the coupling matrix eigenvalues is found to be –0.153 analytically and –0.156 numerically which confirms the good agreement between analytical and numerical simulations. This value is close to the theoretical real part $-k_m/2-\overline{D}\gamma_m C_m \kappa_2$ of the coupling eigenvalues.

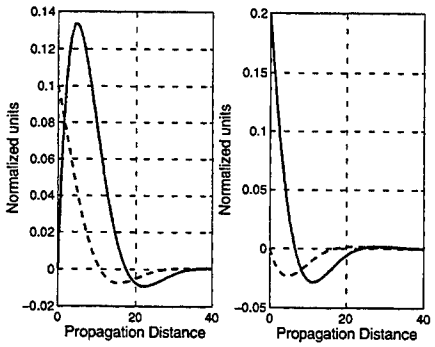


Fig. 3 : Numerical frequency (dashed line) and time (solid line) evolution after a frequency perturbation $\Delta\Omega$=0.1(left) and time perturbation $\Delta\alpha$=0.2 (right)

Conclusion

Singular spectrum proprieties of Dispersion Managed Soliton have been investigated to show the theoretical possibility of the use of in-line synchronous amplitude modulators only to achieve fluctuation control in energy, time and frequency domains. This application requires high energy Dispersion Managed Soliton and does not prevent from a general frequency shift of a pulse train.

References :

[1] K. Susuki et al., Electr. Lett. Vol. 34, n°1, pp 98-100 (1998)
[2] M. Nakazawa et al., Electr. Lett. Vol 34 n°1, pp103-104 (1998)
[3] F. Merlaud et al. paper WdB22, ECOC'98
[4] T. Georges et al., IEICE Trans. Electron., E81-C, 226-231 (1998)
[5] M. Matsumoto, Optics Letters Vol. 23, No 24 (1998)

Tuning of inline filter position for dispersion-managed soliton transmission

A. Tonello, A. D. Capobianco
Istituto Nazionale per la Fisica della Materia,
Dipartimento di Elettronica ed Informatica, Università di Padova,
via Gradenigo 6/A I-35131 ITALY, ph: +39 049 8277723,
fax: +39 049 8277699, e-mail: atonello@dei.unipd.it
S. Wabnitz
Laboratoire de Physique, Université de Bourgogne,
Avenue A. Savary 9, 21011 Dijon, France
S. K. Turitsyn
Photonics Research Group, School of Eng. & Applied Science,
Aston University, Birmingham B4 7ET, UK

Growing demand for high-bit-rate data transmission stimulates intensive research of new fiber communication technologies. Promising way to realize high capacity long-distance and terrestrial fiber communication systems is to exploit dispersion managed (DM) soliton or general return-to-zero (RZ) data formats. Recent experiments of wavelength-division-multiplexed (WDM) RZ signal transmissions with DM showed that the inclusion of in-line filters improves the transmission performance [1]. Indeed, it is well known that guiding filters are important for the control of conventional soliton propagation in fibers [2]. In the case of DM pulses, earlier theoretical studies pointed out that filters are effective in reducing both frequency and energy fluctuations arising from noise [3], interactions [4] and WDM collisions [5]. However, the ability of filters to control energy fluctuations is, in general, strongly reduced in DM systems [3,6]. In striking contrast to the case of guiding center Schrödinger solitons, where the dynamic evolution of the soliton parameters is slow as compared with the amplifier spacing, so that the filtering action may be well described as effectively distributed along the line, the internal dynamics of RZ-DM pulses within a map is critical in determining the stabilizing action of filters [7]. Optimization of the performance of DM transmission systems involves many parameters such as, for instance, strength of the map, average dispersion, initial chirping, strength of the filter, locations of the amplifiers and filters along the dispersion map and so on. In the particular relevant situation when the amplifier spacing coincides or is comparable with the dispersion management period, it is essential to take into account the lumped nature of the filters and the influence of loss on the DM pulse dynamics [4]. Previous analyses basically considered filters placed at the junction between opposite dispersion fibers. In this work we study the effect of the position of a filter anywhere in a lossy dispersion map, and find the optimal points for the stabilization of both energy fluctuations and pulse-to-pulse interactions.

Let us consider a practical dispersion management scheme like that of Figure 1, which represents an upgrade of a link with standard single mode fiber (SMF) by means of dispersion-compensating fibers (DCF). In physical units, dispersion changes from $D1 = 17\text{ps}/(\text{km}\cdot\text{nm})$ to $D2 = -68\text{ps}/(\text{km}\cdot\text{nm})$; The total amplifier span or dispersion map length is $L = 112.5\text{km}$. Fiber loss (0.22 dB/km) is compensated by lumped amplification at the end of each map. Whereas the position of the filter is allowed to slide anywhere within the map. The Gaussian filter transfer function reads (in dimensionless units) as $H(\Omega) = G\exp\{-\beta\Omega^2\}$, where β is the filter strength G is the excess gain; the propagation of a pulse within a map is described by the equation

$$i\frac{\partial q}{\partial z} + \frac{D(z)}{2}\frac{\partial^2 q}{\partial t^2} + a(z)^2|q|^2 q = 0 \qquad (1)$$

where $a(z)$ and $D(z)$ represent the periodic loss and dispersion. It has been shown already that the Gaussian zero-mode approximation in the DM soliton expansion into the Gauss-Hermite functions [8], reducing Eq.1 to a set of ordinary differential equations (ODEs) on the pulse characteristics, works rather well in a range of system parameters. By restricting our attention to the evolution of the Gaussian zero-mode in this expansion [8]: $q(z,t) = a_0 A\exp(-p^2(t-T)^2 + iC(t-T)^2 -$

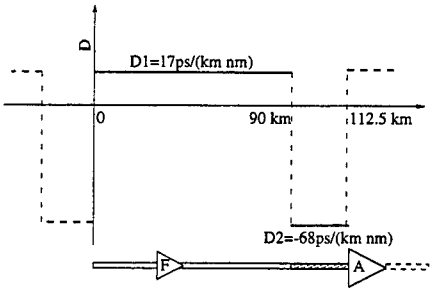


Figure 1: Schematic of the dispersion map.

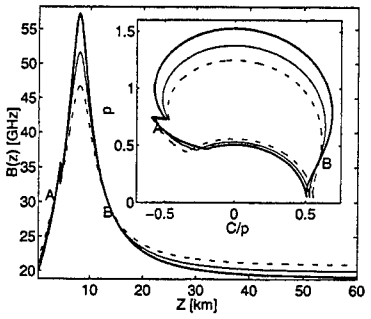


Figure 2: Bandwidth evolution for pulse energies of 7.67 pJ (solid thick curve), 6.86 pJ (solid thin curve), and 6 pJ (dashed curve)

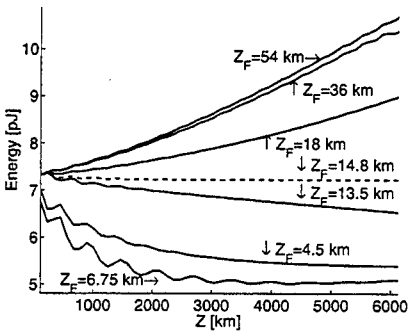


Figure 3: Pulse energy versus propagation distance for different filter positions

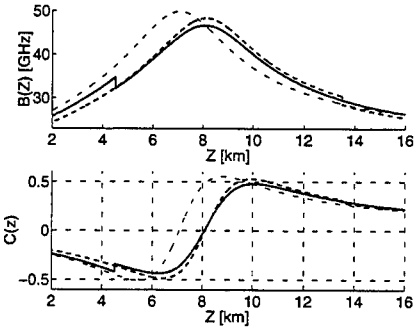


Figure 4: Evolution of bandwidth and chirp with: no filter (dashed thin curve); filter at Z_F = 4.5km (dashed curve); filter at Z_F = 13.5km (solid curve).

$i\kappa(t-T)+i\phi$) (a_0 is the input power enhancement factor), we obtain ODEs governing evolution of the pulse inverse width $p(z)$, chirp $C(z)$ frequency $\kappa(z)$ and temporal shift $T(z)$; the action of the lumped filter on the Gaussian pulse parameters may then be analytically evaluated [3]. We use this approximate approach to explore system properties and then will verify the results by direct simulations of Eq.1. In what follows, we define the spectral bandwidth of the pulse as $B(z) = (1/\pi)\sqrt{2ln(2)[p(z)^2 + C(z)^2/p(z)^2]}$. Figure 2 shows the evolution of the pulse bandwidth along the dispersion map for three different values of the average pulse energy. Here the filter is placed at z = 4.5km, where it introduces a small bandwidth drop. Note in the inset the phase plane trajectory that corresponds to the three periodic solutions or fixed points of the map. Figure 2 shows that, at points between A and B, the bandwidth of the solution grows larger as the energy increases, which leads to a negative feedback or stabilizing action of the filters [6].

In Figure 3, we compare the evolution of the DM pulse energy for different filter positions Z_F in the case of small (10%) amplitude fluctuations at the input. Here we fix $\beta = 0.05$. As can be seen, by placing the filters in the positive feedback region (where the bandwidth drops as the energy increases, e.g., with Z_F = 18km, Z_F = 36km, Z_F = 54km), we observe a continuous growth of the pulse energy with distance. Note that in these situations the pulse bandwidth, and consequently the filter-induced spectral losses, are lower than in the stable cases (Z_F = 4.5km, Z_F = 6.75km, Z_F = 13.5km). As can be seen, greater stability of the pulse energy is achieved whenever the filter is placed near the point B of Figure 2, that is at the end of the negative feedback section. In detail there is an optimal filter position (Z_F = 14.8km in the considered example) for which the energy evolution is a separatrix between growth (Z_F = 18km, Z_F = 36km, Z_F = 54km) and decay (Z_F = 13.5km, Z_F = 6.75km, Z_F = 4.5km). Note that sliding the position of filters in the map

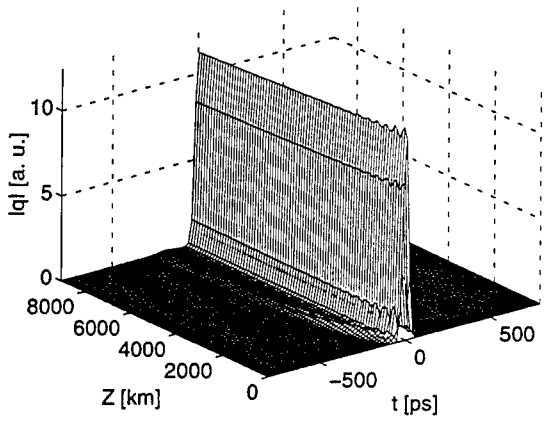


Figure 5: Pulse evolution with negative feedback

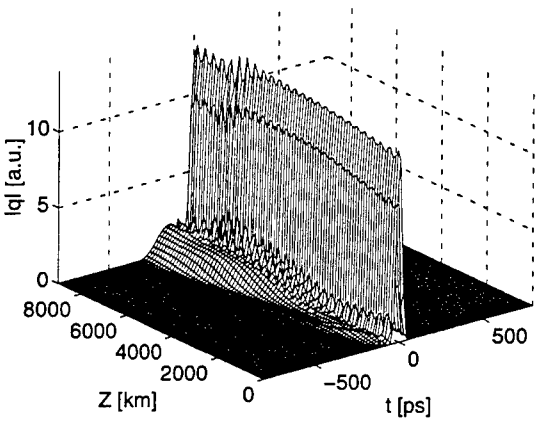


Figure 6: Pulse evolution with positive feedback

shifts both the bandwidth and chirp evolution, as seen in Figure 4. Moreover, besides the instability of the pulse energy, setting a filter in the positive feedback region also enhances the creation of wings in the pulse, which are detrimental for the interaction with nearby bits, as shown in Figure 5 (negative feedback case) and 6 (positive feedback case). Indeed, the control of soliton interactions requires an additional fine tuning of the filter position within the negative feedback section of the SMF. As shown in Figure 7, observe that, by placing the filter near the initial part of the stable domain (point A), i.e., with $Z_F = 4.5$km, the interaction-induced timing shifts in a pseudorandom sequence are strongly reduced. The stabilizing action is seen to be stronger by tuning the filter near point A rather than point B; moreover we observed interference with dispersive radiation near the middle of the negative feedback region. A reasonable trade off between energy and interactions stabilization leads to a best filter position nearby point A, while filters placed at point B have optimal features whenever the pulse energy control has priority over intersymbol interactions.

In summary, we have shown that by tuning the position of a filter within a dispersion-managed map one may substantially increase the energy-stabilization action of the filters, and counteract the timing jitter induced by interactions. This work was partially sponsored by a contract between the University of Bourgogne and the CNET-France Telecom.

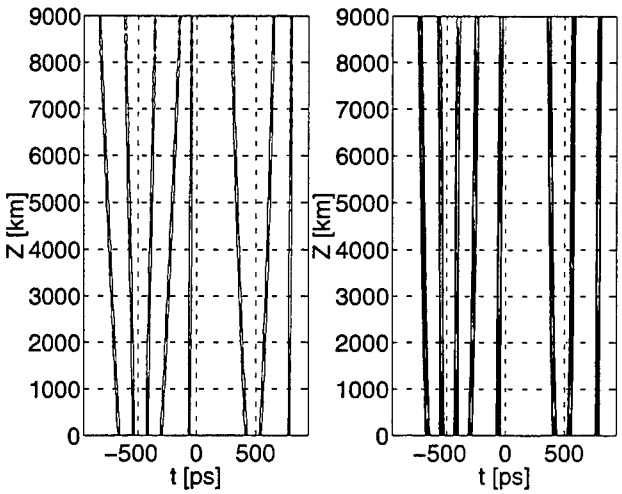


Figure 7: Soliton interaction without (left) with filter control (right); filters near point A

References:

[1] K. Tanaka et al., *Electron. Lett.*, **34**, p. 2257, (1998).

[2] Y. Kodama and A. Hasegawa, *Opt. Lett.* , **17**, p. 31, (1992).
L. F. Mollenauer, P. V. Mamyshev, *IEEE Journ. of Q.E.*, **34**, p. 2089, (1998).

[3] M. Matsumoto, *Electron. Lett.*, **33**, p. 1718, (1997);
F. Merlaud, T. Georges, *ECOC'98 20-24 Sept. 1998*, Madrid Spain, p. 497

[4] M. Matsumoto et al., *Opt. Commun.*, **155**, p. 28, (1998).

[5] S. Wabnitz, *Opt. Lett.*, **21**, p. 638, (1995).

[6] T. Hirooka, S. Wabnitz, *Electron. Lett.*, **35**,p. 665 (1999).

[7] M. Matsumoto, *Opt. Lett.*, **23**, p. 1901, (1998).

[8] S. K. Turitsyn et al., *Opt. Fiber Tech.* , **4**, p. 384, (1998).

Key to Authors and Presiders

Abdullaev, F. Kh. ■ WB3, ThD17
Ackemann, T. ■ WC1, WC4
Aggarwal, I.D. ■ ThB4
Agranovich, V.M. ■ ThD26
Agrawal, Govind P. ■ WA, WD5, FD1
Aitchison, J. Stewart ■ WA2, WA7, WD2, WD13, WE5, ThB3, ThE1, FA, FC4
Akasaka, Y. ■ WB6
Akhmediev, Nail N. ■ WD5, WD8, WD43, WD44, ThE1, ThE4
Alexander, Tristram J. ■ WD27
Alfimov, E. ■ WD35
Alleston, S.B. ■ ThD12, FD2
Anastassiou, Charalambos ■ WE3, ThE2
Anderson, Dan ■ WB2, ThD9, ThD15
Ankiewicz, A. ■ ThE4
Arbel, D. ■ WD42
Assanto, Gaetano ■ WD40, WD45
Aubin, G. ■ FA3
Avetisyan, Yuri H. ■ FB6

Baizakov, B.B. ■ ThD17
Bajdeki, Waldemark ■ WD23
Bakman, Yefim ■ ThD44
Balakin, A.V. ■ ThB5
Balle, S. ■ WC4
Balslev Clausen, Carl ■ WD18, WD24, ThD25
Banfi, G.P. ■ ThC3
Bang, Ole ■ WD18, WD19, WD21, ThD25,ThE6, FB4
Barille, R. ■ WD17
Barland, S. ■ WC4
Barry, L.P. ■ WB4
Barthélémy, A. ■ WE2, FA4
Belanger, Nicolas ■ WA2
Bélanger, P.A. ■ ThD8, FD3
Bennion, I. ■ FD2
Bergé, Luc ■ WD21
Berger, V. ■ FA1
Bergman, K. ■ WD43, WE4, ThD22
Berntson, Anders ■ Wb2, ThD9, ThD10, ThD15
Berzanskis, A. ■ WA6
Blow, K.J. ■ ThD42
Boardman, A.D. ■ WD20, WD28, ThD26, ThE3
Bodin, Nadege ■ ThD37
Bonfrate, G. ■ FC1
Bongrand, Isabelle ■ WB1
Bontemps, P. ■ WD20
Boucher, D. ■ ThB5
Boucherez, E. ■ ThA6
Bouchoule, S. ■ ThA6
Bourdin, J.P. ■ WD17
Bourliaguet, B. ■ WE2
Boyer, Gilbert ■ WB2
Brambilla, M. ■ WD31
Brener, I ■ FA5
Brindel, P. ■ ThA6, ThD2
Broderick, Neil G. ■ ThB, ThB3
Bronski, J.C. ■ ThD22
Brunéel, J.L. ■ ThD39
Bubke, K. ■ WA7, ThD27
Buffeteau, T. ■ ThD40
Buryak, Alexander V. ■ WD1, WD3, WD4
Bushuev, V.A. ■ ThB5

Capobianco, A.D. ■ FD5
Cara, M. ■ WC4
Cardinal, T. ■ ThD39
Castillo, M.D. Iturbe ■ WA5
Cautaerts, Vincent ■ ThD20
Champneys, Alan R ■ ThD35
Chávez-Cerda, S. ■ WA5
Chen, Zhigang ■ WD12, WE3, ThE7
Cheong, S.W. ■ ThD38
Chiang, K.S. ■ ThD7
Chinaglia, W. ■ WA6
Chollet, P. ■ ThD36, ThD37
Chou, Hsu-Feng ■ ThD31, ThD32
Chou, M.-H. ■ FA5
Christiansen, Peter L. ■ WD18, WD24, ThD25
Christodoulides, Demetrios N. ■ WD12, ThE5, ThE7
Chuprakov, Dmitry A. ■ WD14
Ciaramella, E. ■ ThD16
Coen, Stephane ■ FB1
Colet, P. ■ WC2
Collings, B. C. ■ WD43
Conti, Claudio ■ WD40, WD45
Coppo, G. ■ WA6
Coskun, Tamer H. ■ ThE5, ThE7
Couderc, V. ■ WE2
Couzi, M. ■ ThD39
Crasovan, L. ■ WD10, ThD45
Cristiani, I. ■ ThC3
Crosser, Mike ■ ThE8
Ctyroky, Jiri –ThD41
Cundiff, S.T. ■ WD43

Dany, Bruno ■ ThA6, ThD2
Darmanyan, S. ■ WD10, WE6, ThD21
Dazzi, Alexandre ■ FA6
De Angelis, C. ■ WE2
De La Rue, R. ■ ThB3
De Sario, Michele ■ WD40
Degiorgio, V. ■ ThC3
DelRe, Eugenio ■ WA4
Denz, Cornelia ■ WD16
Desaix, Mats ■ ThD15
Desbat, B. ■ ThD40
Desurvire, Emmanuel ■ ThA6, ThD2
Di Trapani, P. ■ WA6
Domanski, Andrzej W. ■ WD23
Doran, Nick J. ■ ThD4, ThD12, ThD14, ThD18, ThD23, FD2
Duchet, C. ■ ThA6
Dudley, J.M. ■ WB4, ThD13, FB5
Dumais, Patrick ■ WD13

Edmundson, D. ■ WD19, ThE6
Efimov, O.M. ■ ThD39
Eggleton, B.J. ■ ThB4
Eisenberg, Hagai ■ WD2, WE5
Emplit, Philippe ■ FB1
Erneux, T. ■ WD38
Etrich, C. ■ WD34, FB2

Fargin, E. ■ ThD40
Feigelson, Robert S. ■ WD12
Fejer, M. ■ FA5
Feldmann, M. ■ WC1
Firth, William J. ■ WA3, WC3, WD6
Forysiak, W. ■ ThD4, FD
Friedrich, Lars ■ WD13, ThE1
Fuerst, Russell A. ■ WD13

Gaididei, Yu. B. ■ WD24
Gallego, R. ■ WC2
Ganne, I. ■ WD29
Garnier, J. ■ WB3
Georges, Thierry ■ FD4
Giordmaine, J.A. ■ WE3, ThE2
Giudici, M. ■ WC4
Glebov, Leonid B ■ ThD39
Gölles, Michael ■ ThD5, ThD21
Govan, D.S. ■ ThD12, FD2
Grégoire, Xavier ■ ThD37
Grandpierre, Alexandra G. ■ ThE5
Grattan, K.T.V. ■ ThD30
Grelu, P. ■ ThD13, FB5
Gross, Y. ■ WD30
Grundkötter, W. ■ FC2, FC3
Gutty, F. ■ ThD13, FB5

Haase, C. ■ FC2
Haelterman, Marc ■ WB5, WD25, WD38, ThD28, FB1
Hall, Bjorn ■ WB2, ThD15
Hanna, D.C. ■ WE2
Harmand, J.C. ■ FA3
Harper, P. ■ ThD12, FD2
Harvey, J.D. ■ WB4
Hasegawa, A. ■ ThA2
Helczynski, Lukas ■ ThD15
Helmfrid, S. ■ ThD1
Hempelmann, Uwe ■ ThD29
Herrmann, H. ■ FC2
Hernandez-Garcia, E. ■ WC2
Hirooka, Toshihiko ■ ThA2

Ho, M.C. ■ WB6
Hoekstra, J.W.M ■ ThD41
Hofmann, D. ■ FC2, FC3
Hong, Yue-Wen ■ ThD31
Hoyuelos, M. ■ WC2
Hutchings, D.C. ■ WA7, ThD27, FA2
Hwang, H.Y. ■ ThD38

Iizuka, Takeshi ■ WD41
Iliew, Rumen ■ WD32
Iwanow, Robert ■ ThD24

Jagadish, C. ■ WD44
Jakubowski, Mariusz ■ WD26
Jian, Pey-Schuan ■ WD32
John, Sajeev ■ ThB1
Jullien, Pierre ■ FA6

Kajzar, Francois ■ ThD36, ThD37
Kamchatnov, A.M. ■ ThD26
Karlsson, Magnus ■ WB2
Karpierz, Miroslaw A. ■ WD23
Kath, William L. ■ ThA3
Katsriku, F.A. ■ ThD30
Katsufuji, T. ■ ThD38
Kazansky, Peter G. ■ FC, FC1
Kazovsky, L.G. ■ WB6
Khalil, M. Alshikh ■ ThD36
Kivshar, Yuri ■ WD4, WD6, WD9, WD18, WD22, WD27, WD41, ThE, FB4
Klotz, Matthew J ■ ThE8
Knöll, Christian ■ ThD5
Knox, W.H. ■ WD43
Kobyakov, A. ■ WE6
Kockaert, Pascal ■ WB5
Kodama, Yuji ■ ThD20
Kolossovski, Kazimir Y. ■ WD1
Konotop, V.V. ■ WD35, ThD34
Koroteev, N.I. ■ ThB5
Kotacka, Libor ■ ThD41
Krauss, T. ■ ThB3
Królikowski, Wieslaw ■ WD5, WD19, WD21, ThE4, ThE6
Krylov, D. ■ WE4, ThD22
Kuszelewicz, R. ■ WD29
Kutz, J. N. ■ WD38, ThD22
Kuwatsuka, H ■ ThC2
Kuzmiak, V. ■ ThD34

Lakoba, T. ■ FD1
Lan, Song ■ WE3, ThE2
Lange, W. ■ WC1
Lantz, Eric ■ ThD33, FB3
Larionov, Yury ■ WD37
Larochelle, S. ■ FD3
Le Flem, G. ■ ThD40
Leclerc, Oliver ■ ThA5, ThA6, ThD2
Lederer, Falk ■ WD10, WD32, WD34, WE, WE6, ThD6, ThD21, ThD45, FB2
Lederer, Max Josef ■ WD44
Leng, L. ■ ThD22
Lenz, Gadi ■ ThB4, ThD38
Leo, G. ■ FA1
Lesage, F. ■ ThD8
Liang, A. ■ ThA2
Liao, Z.M. ■ FD1
Lin, Ching-Fuh ■ ThD31, ThD32
Lines, M.E. ■ ThB4, ThD38
Lisak, Mietek ■ WB2, ThD9, ThD15
Liseev, D.V. ■ WD28
Litchinitser, Natalia M. ■ WD5, ThB4
Liu, X. ■ WA1, ThC4
Lokhnygin, V. ■ ThD21
Lompré, Pierre ■ FA6
Lopez-Lago, E. ■ FA4
Lor, K.P. ■ ThD7
Louradour, F. ■ FA4
Lourtioz, J.M. ■ FA3
Lu, Xin ■ WD14
Lugiato, L. ■ WD31, FB
Luther-Davies, B. ■ WD44, ThE4

Maeda, Joji ■ ThD19
Maggipinto, T. ■ WD31
Maillotte, Herve ■ ThD33, FB3
Malomed, Boris A. ■ WD3, ThD9, ThD10, ThD35, ThD44, ThD45
Mamyshev, P.V. ■ ThA1
Mamysheva, N.A. ■ ThA1
Mangeney, J. ■ FA3
Manning, R.J. ■ ThD42
Mantsyzov, Boris I. ■ ThB2, ThB5
Marhic, M.E. ■ WB6
Marks, Brian S. ■ ThA3
Martin, John ■ WE3
Martorell, Jordi ■ WE1
Maruta, Akihiro ■ ThA4, ThD3, ThD20
Masselin, P. ■ ThB5
Mathey, Pierre ■ FA6
Mathieu, P. ■ ThD8
Mavlayanov, G. ■ WB3
McCarthy, G. ■ ThE4
Mendez-Otero, M.M. ■ WA5
Mériadec, C. ■ FA3
Merlaud, Fabien ■ FD4
Mezentsev, V.K. ■ ThD14
Michaelis, D. ■ WD34, FB2
Mihalache, Dumitru ■ ThD45
Millar, P. ■ ThB3, ThE1
Millot, Guy ■ ThC1, ThD13, FB3, FB5
Minardi, S. ■ WA6
Mitchell, M. ■ ThE2
Mitschke, Fedor ■ WD36
Mizell, Greg ■ WE3
Mizilu, D. ■ ThD45
Molina, G. ■ WE1
Montes, Carlos ■ WB1, ThD28
Morandotti, Roberto ■ WD2, WE5
Moretti, Paul ■ FA6
Mou, Shing ■ ThD32
Moubissi, A.B. ■ ThD33
Musslimani, Z. H. ■ WD22

Nakada, T. ■ ThA2
Nazabal, V. ■ ThD40
Neddam, Frederic ■ ThA5
Nepomnyashchy, A. ■ WD22
Neviére, Michel ■ ThD26
Niculae, A.M. ■ ThD4
Nijhof, J.H.B. ■ ThD14, ThD18

Ogawa, Hiromitsu ■ ThD19
Onishchukov, G. ■ ThD21
Oppo, G.-L. ■ WC2
Orenstein, Meir ■ WD30, WD42
Ostrovskaya, Elena A. ■ WD6
Oudar, J.-L. ■ FA3
Ozheredov, I.A. ■ ThB5

Parameswaran, K. ■ FA5
Pare, Claude ■ ThD8, FD3
Park, S.H. ■ ThD39
Patriarche, G. ■ FA3
Perrini, I. ■ WD31
Pertsch, Thomas ■ WE6
Peschel, U. ■ WA7, WD2, WE1, WE5, ThD27, FB2
Petrov, D.V. ■ WE1
Petter, Jurgen ■ WD16
Picholle, Eric ■ WB1
Picozzi, Antonio ■ WB1, WD25, ThD28
Pincemin, Erwan ■ ThA5, ThA6
Pitois, S. ■ ThD13, FB5
Polyakov, Sergey V. ■ WD39
Poustie, A.J. ■ ThD42
Pruneri, V. ■ FC1
Pun, Edward Y.B. ■ ThD43

Qian, L.J. ■ WA1, ThC4

Rahman, B. M. A. ■ ThD30
Raimond, P. ■ ThD36
Rarity, J G. ■ FC1
Rasmussen, J. Juul ■ WD21
Richardson, D.J. ■ ThB3
Richardson, David J. ■ WB
Richardson, K.A. ■ ThD39
Ricken, R. ■ FC2, FC3
Rini, M. ■ ThC3
Rivoire, G. ■ WD17
Rodriguez, Amparo ■ ThD37
Rosanov, N.N. ■ WD15, WD28
Ross, G.W. ■ WE2
Rouvillain, D. ■ ThA6
Roy, V. ■ ThD8
Rutz, Soeren ■ WD36
Ryan, D.M. ■ ThD23
Rytz, Daniel ■ FA6

Saadeh, Shihadeh ■ ThD6
Sagnes, I. ■ WD29
Saher-Helmy, A. ■ WD13
Salamo, Gregory J. ■ ThD6, ThE8
Saltiel, Solomon ■ WD9, WD27
Sammut, Rowland A. ■ WD1, WD3, WD4
San Miguel, M. ■ WC2
Sanghera, J. S ■ ThB4
Santagiustina, M. ■ WC2
Sapone, S. ■ WA6
Sarkisov, Sergey ■ WD11
Schaepers, B. ■ WC1
Scheuer, J. ■ WD30, WD42
Schreiber, G. ■ FC2, FC3

Sears, Suzanne M. ■ WD7, WD26, WE4
Segev, Mordechai ■ WA4, WD7, WD12, WD22, WD26, WE3, WE4, ThE2, ThE5, ThE7, ThE8
Semenov, V. E ■ WD15
Seve, E. ■ WB3, ThC1, FB3
Shandarov, Stanislav ■ WD37
Shandarov, Vladymir ■ WD37
Shen, Yu ■ ThD43
Shih, Ming-Feng ■ WE3, ThE2
Shipulin, A ■ ThD21
Shkurinov, A.P. ■ ThB5
Sierakowski, Marek ■ WD23
Silberberg, Yaron ■ WD2, WE5
Skryabin, Dmitry V. ■ WA3, WC3, WD6, WD33, ThD11
Slekys, G. ■ WD29
Slusher, R.E. ■ ThB4, ThD38
Smith, P.G.R. ■ WE2
Snyder, A ■ ThE4
Sohler, W ■ FC2, FC3
Soljacic, Marin ■ WD7, WD26, WE4
Soto-Crespo, J.M. ■ WD43, WD44, WE1
Spälter, Stefan ■ ThD38
Spinelli, L. ■ WD31
Squier, Richard ■ WD26
Staliunas, K. ■ WA6
Steblina, Victoria V. ■ WD4
Stegeman, George I ■ WD13, ThD39, ThE1
Steiglitz, K. ■ WD26, ThE2
Stelmakh, N. ■ FA3
Sugahara, Hiroto ■ ThA4
Sukhorukov, Anatoly P. ■ WD39
Sukhorukov, Anatoly P. ■ WD14
Sukhorukov, Andrey A. ■ WD8, WD9, FB4
Sylvestre, Thibaut ■ ThD33, FB3

Tamburrini, M. ■ ThD16
Tan, H.H. ■ WD44
Tapster, P.R. ■ FC1
Tartara, L. ■ ThC3
Tchofo-Dinda, P. ■ ThD33, FB3
Thomsen, B.C. ■ WB4
Thomson, M.D. ■ ThD13, FB5
Tissoni, G. ■ WD31
Tlidi, Mustapha ■ FB1
Tonello, A. ■ FD5
Torner, Lluís ■ WD24, WE1, ThD25
Torres, J.P. ■ WE1
Torruellas, William E ■ WD32
Towers, Isaac ■ WD3
Tredicce, J.R. ■ WC
Trillo, Stefano ■ WA4, WD38, WD45, ThC1
Turitsyn, Sergei K. ■ ThA3, ThD14, ThD18, FD5

Umezawa, Nobumitsu ■ ThD19

Valiulis, G. ■ WA6
Vanin, E.V. ■ ThD1
VanStryland, Eric ■ ThD39
Vermelho, M.V.D. ■ FC4
Vilaseca, Ramon ■ WE1
Villeneuve, Alain ■ WA2, WD13, ThC
Vitrant, Guy ■ ThD36, ThD37
Vyssotina, N.V. ■ WD15

Wabnitz, S. ■ WB3, ThA, ThC1, FD5
Weilnau, Carsten ■ WD16
Weinert-Raczka, Ewa ■ ThD24
Wilkosz, Aaron ■ WD11
Wise, F.W. ■ WA1, ThC4
Wolinski, Tomasz R. ■ WD23

Xie, M. ■ WD28, ThE3

Yadin, Y. ■ WD30
Yang, F.S. ■ WB6
Yang, Tian-Shiang ■ ThA3
Yingli, Chen ■ ThD43
Yuquan, Shen ■ ThD43

Zhuangqi, Cao ■ ThD43
Zimmermann, J. ■ ThD38

Nonlinear Guided Waves and Their Applications

Postdeadline Paper Session

Friday, 3 September 1999

PD
19.00-20.30
Salle Morey-St.-Denis

Nonlinear Guided Waves and Their Applications Topical Meeting
POSTDEADLINE PAPER PRESENTATIONS
Friday, 3 September 1999 • 19.00 – 20.30
Salle Morey-St-Denis

19.00
PD1 HeXLN: A 2-dimensional nonlinear photonic crystal, N.G.R. Broderick, G.W. Ross, D.J. Richardson, D.J. Hanna, *Optoelectronics Res. Ctr., Univ. of Southampton, UK.* The fabrication of a two dimensional hexagonally poled lithium niobate (HeXLN) crystal is reported. 2nd harmonic conversion efficiencies > 60% were measured with picosecond pulses. The 2nd harmonic light is phase matched by multiple reciprocal lattice vectors, resulting in multiple coherent beams being generated.

19.15
PD2 Continuous-wave operation of a modulational instability laser, Stéphane Coen, Marc Haelterman, *Service d'Optique et d'Acoustique, Univ. Libre de Bruxelles, Belgium.* Thanks to a passive all-fiber cavity, we succeed, for the first time, in observing modulational instability in the continuous wave regime.

19.30
PD3 Modulation instability of incoherent beams in non-instantaneous nonlinear media, Marin Soljacic[1], Mordechai Segev[2,3], Tamer Coskum[4], Demetrios N. Christodoulides[4], Ashvin Vishwanath[1], Zhigang Chen[5], *[1]Physics Department, Princeton Univ., USA, [2]Physics Department, Technion – Israel Inst. of Tech., Israel, [3]Electrical Engineering Dept., Princeton Univ., USA, [4]Dept. of Electrical Engineering and Computer Science, Lehigh Univ., USA, [5]Dept. of Physics and Astronomy, San Francisco State Univ., USA.* We show that modulation instability can exist with partially spatially incoherent light beams in a non-instantaneous nonlinear environment. For such incoherent modulation instability to occur, the value of the nonlinearity has to exceed a threshold imposed by the degree of spatial coherence.

19.45
PD4 Observation of quadratic vortex solitons, Paolo Di Trapani, Walter Chinaglia, Stefano Minardi, *Univ. of Insubria, Italy,* Gintaras Valiulis, *Vilnius Univ., Lithuania.* Optical vortex solitons in quadratic nonlinear material have never been observed to date, due to the well known modulation instability of the intense background, which breaks up the beam in many bright solitons before the achievement of vortex soliton regime. In this work we provide experimental evidence, supported by numerical calculations, of the achievement of the vortex-soliton regime by operating in regime of large (self-defocusing) phase mismatch and large walkoff, the walkoff having the role of quenching the instability by moving the spikes out of the embedding beam.

20.00
PD5 Kerr spatio-temporal focusing in a planar glass waveguide, Hagai Eisenberg, Roberto Morandotti, Yaron Silberberg, *Dept. of Physics of Complex Systems, Weizmann Inst. of Science, Israel,* Orit Potashnik, Shimshon Bar-Ad, *School of Physics and Astronomy, Tel-Aviv Univ., Israel,* Duncan Ross, Ulf Peschel, J. Stewart Aitchison, *Dept. of Electronics and Electrical Engineering, Univ. of Glasgow, UK.* We demonstrate, for the first time, simultaneous focusing in space and time due to Kerr nonlinearity. Our results may suggest the possibility of stable light-bullets.

20.15
PD6 Nonlinear pulse dynamics in planar Chalcogenide glass waveguides, S. Spälter, G. Lenz, H.Y. Hwang, J. Zimmermann, S-W. Cheong, T. Katsufuji, R.E. Slusher, *Lucent Tech., Bell Labs., USA.* Record nonlinear phase shifts of up to 3.5 π are accumulated in pulse propagation along singlemode chalcogenide glass planar waveguides with high Kerr nonlinearity.

HeXLN: A 2-Dimensional nonlinear photonic crystal

N. G. R. Broderick, G. W. Ross, D. J. Richardson and D. C. Hanna
Optoelectronics Research Centre, University of Southampton, Southampton, SO17 1BJ, UK.
Phone: +44 (0)1703 593144, Fax: +44 (0)1703 593142,
email: ngb@orc.soton.ac.uk

In one dimension, the concept of quasi-phase matching nonlinear processes by periodically changing the sign of the nonlinearity is well known. The advantages of materials such as periodically poled lithium niobate (PPLN) lies in their engineerability – nonlinear processes over a wide wavelength range can be phase-matched by writing the appropriate nonlinear grating. In these crystals nonlinear processes are efficient when the momentum (phase) mismatch between the interacting waves equals one of the reciprocal lattice vectors (RLV) of the 1-D periodic crystal. Clearly this can only occur in either the co- or counter-propagating direction. Furthermore, for a strictly periodic lattice quasi-phase matching can only occur over a narrow wavelength range since the RLVs are discrete and periodically spaced in momentum space. In order to obtain broader bandwidths densely spaced RLVs are needed. Recently broadband phase-matching was obtained by using a Fibonacci lattice[1]. Fibonacci lattices are an example of 1-D quasi-crystals[2] and as such have a dense spectrum in momentum space. Fibonacci lattices can be thought of as being the 1-D projection of a regular 2-D crystal.

Recently the idea of quasi-phase matching was extended to two-dimensions and the notion of a 2-D "nonlinear photonic crystal" was introduced[3]. In such a 2-D photonic crystal the nonlinear susceptibility changes periodically across the plane while the linear refractive index is constant. Such crystals would have many advantages over a 1-D periodically poled crystal, such as being angle rather than temperature tuned and being able to phase-match multiple wavelengths simultaneously. We report here what is to the best of our knowledge both the first example of hexagonally poled lithium niobate (HeXLN) and the first 2-D nonlinear photonic crystal to be fabricated.

A thin layer of photoresist was first deposited onto the -z face of a 0.3mm thick, z-cut wafer, of $LiNbO_3$, and then photolithographically patterned with the hexagonal array. The x-y orientation of the hexagonal structure was carefully aligned to coincide with the crystal's natural preferred domain wall orientation : $LiNbO_3$ itself has a hexagonal atomic symmetry and shows a tendency for domain walls to form parallel to the y-axis and at +/-60 . Poling was accomplished by applying an electric field via liquid electrodes on the +/- z faces. The short period of the hexagonal array was 18.05 μm, designed for quasi-phase-matched frequency-doubling of 1536nm at a temperature of 160 C. After poling, the sample was lightly etched in acid to reveal the domain profile. The hexagonal pattern was found to be uniform across the sample dimensions of 14 × 7mm (x-y). Fig. 1 shows a magnified section of the HeXLN sample showing clearly the hexagonal honeycomb structure. Each hexagon is a region of domain inverted material - the total inverted area comprises 25% of the overall sample area. Lastly we polished two opposite sides of the HeXLN crystal allowing a propagation length of 14mm through the crystal.

To investigate the properties of the HeXLN crystal we proceeded as follows. The HeXLN crystal was placed in an oven and mounted on a rotational stage which could be rotated by ±10 degrees while still allowing the light to enter. It was pumped by 4ps, 200kW pulses obtained from a high power all-fibre chirped pulse amplification system[4] operating at 20kHz. The output from the CPA system was focussed onto the HeXLN crystal using a 12cm focal length lens. At low input powers the output was as shown in Fig. 2 and consisted of multiple output beams of different colours emerging from the crystal at different angles. In particular two 2nd harmonic beams emerged from the crystal at identical angles of $1.1° \pm 0.1°$ degrees from the remaining fundamental which was, as expected, undeflected by the crystal. Then at slightly wider angles were two green beams (third harmonic of the pump) and at an even wider angle was a blue beam (the fourth harmonic). There was also a third green beam copropagating with the fundamental. As the input power increased the 2nd harmonic spots remained in the same positions while the green light appeared to be emitted over an almost continuous range of angles rather than the discrete angles observed at low powers.

The two 2nd harmonic beams can be understood by referring to the reciprocal lattice (RL) of a hexagonal lattice. The RL of a 2-D hexagonal lattice is another hexagonal lattice[5] only rotated by $\pi/2$. Fig. 2 shows the first Brillouin zone for our crystal. Due to our setup the pump beam propagated along the ΓK direction while the closest reciprocal lattice vectors (RLV) are in the ΓM directions

and it is these RLVs that account for the 2nd harmonic light[3]. Using Eq. (6) of Berger[3] the angle between the fundamental and 2nd harmonic should be 1.07° degrees which agrees well with our measured values. The shortest RLV in the direction of propagation is $\sqrt{3}$ longer and this RLV accounts for the sum frequency generation between the fundamental and the 2nd harmonic. If the crystal were to be rotated by 30 degrees then the propagation angle would be along the ΓM direction and hence we would expect to see efficient 2nd harmonic generation in the co-propagation direction (however at present this is not possible due to the geometry of the oven and the size of the HeXLN crystal).

After filtering out the other wavelengths the 2nd harmonic (from both beams) was directed onto a power meter and the efficiency and temperature tuning characteristics were measured. These results are shown in Fig. 3. Note that the maximum external conversion efficiency is greater than 60% and this is constant over a wide range of input powers. Taking into account the Fresnel reflections from the front and rear faces of the crystal this implies a maximum internal conversion efficiency of 82% – ~ 40% in each beam. Note that, due to nonlinearity in the CPA system the pump bandwidth increased as the pump power increased limiting the conversion efficiency at higher powers. In addition, as the 2nd harmonic power increases the amount of back conversion increases which limits the efficiency as is seen in Fig. 3(c).

In the 1-D case the temperature tuning curve of a length of periodically poled material is expected to have a $sinc(T)$ shape and to be quite narrow – 4.66° degrees for a 1-D PPLN crystal with the same length and period as the HeXLN crystal used here. However, as can be from Fig. 3(b), the temperature tuning curve is much broader with a FWHM of ~ 25° degrees and it exhibits considerable structure. To obtain the temperature tuning curve we collected the 2nd harmonic light from all angles and focussed it onto a silicon head detector. We believe that the increased bandwidth is is due to the multiple reciprocal lattice vectors that are available for quasi-phase matching with each RLV producing a beam in a slightly different direction. Thus the graph in Fig. 3(b) should be considered as the sum of multiple $sinc(T)$ shaped curves. Due to the limitations of the oven we were not able to raise the temperature about 205° degrees and hence could not completely measure the tail of the temperature tuning curve. At temperatures below 120° degrees the conversion efficiency is limited by photorefractive effects. Note that temperature tuning is equivalent to wavelength tuning of the pump pulse and hence it should be possible to obtain efficient phase-matching over a wide wavelength range at a fixed temperature as suggested by the efficient conversion of the broadband pump pulses.

Lastly we measured at the spectra of the light produced however due to space constraints only the fundamental is shown in Fig. 3(c). Fig. 3(c) shows the spectrum near 1533nm for horizontally (solid line) and vertically (dashed) polarised input light. As the phase matching only works for the vertically polarised light the horizontally polarised spectrum is identical to that of the input beam and when compared with the other trace (dashed line) shows the effect of pump depletion and of back-conversion. Note that for the vertically polarised light the amount of back-converted light is almost equal to the residue pump which is as expected given the large conversion efficiency. Fig. 3(c) shows ~ 8dB (85%) of pump depletion which agrees well with the measured value for the internal efficiency calculated using the average power.

In conclusion we have fabricated what we believe to be the first example of a two dimensional nonlinear photonic crystal in Lithium Niobate. Due to the hexagonal structure of the crystal quasi-phase matching is obtained for multiple directions of propagation with conversion efficiencies > 70%. Such HeXLN crystals could find many applications in optics where simultaneous conversion of multiple wavelengths is required. Alternatively a HeXLN crystal could be used as an efficient monolithic optical parametric oscillator. In the near future we will measure the angular dependence of the HeXLN crystal as well as the correlation properties of the two 2nd harmonic beams.

References

[1] S. N. Zhu, *et al.*, Phys. Rev. Lett. **78,** 2752–2755 (1997).

[2] C. Janot, *Quasicrystals: a primer, Monographs on the physics and chemistry of materials; 48* (Clarendon Press, Oxford, 1992).

[3] V. Berger, Phys. Rev. Lett. **81,** 4136–4139 (1998).

[4] N. G. R. Broderick, *et al.*, Opt. Lett **24,** 566–568 (1999).

[5] J. D. Joannopoulos, R. D. Meade, and J. N. Winn, *Photonic Crystals* (Princeton University Press, Princeton, New Jersey, 1995).

[6] P. E. Britton, *et al.*, Opt. Lett. **23,** 1588–1590 (1988).

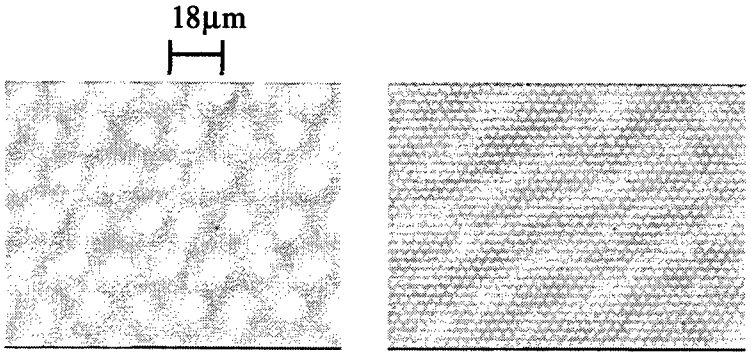


Figure 1: Pictures of the HeXLN crystal on both the large and small scales. The large scales pictures shows the excellent uniformity over the crystal while the fine detail can be seen in the small scale.

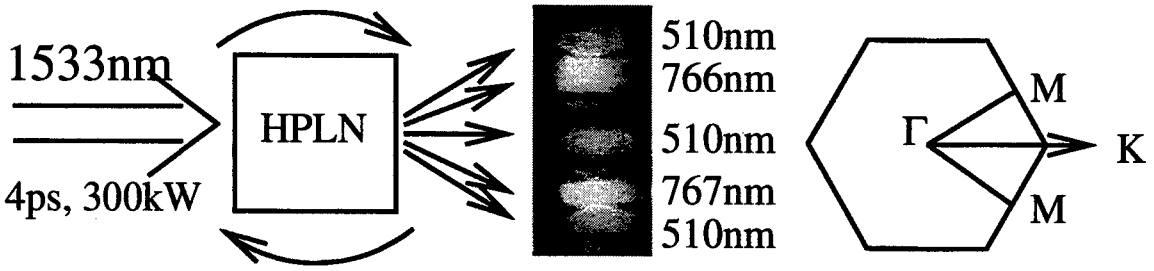


Figure 2: Schematic of the experimental setup, the output beam pattern and a diagram of the first Brillouin zone. For our geometry the pump propagates along the ΓM direction while phase-matching is achieved by RLV in the ΓK directions.

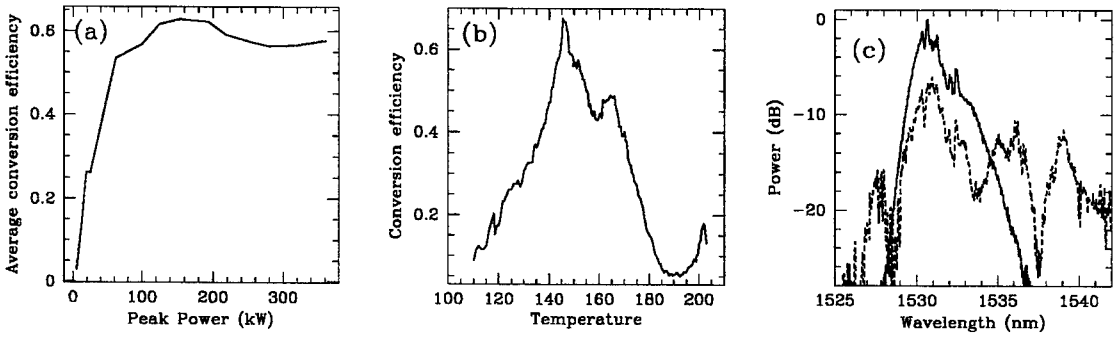


Figure 3: Efficiency and temperature tuning of the HeXLN crystal. Note that the maximum efficiency is > 60% and is limited by pulse walk-off and down conversion. The temperature tuning curve is much broader than a comparable 1-D PPLN crystal and posses multiple features due to the large number of reciprocal lattice vectors available. The last graph shows the pump for both horizontally (solid line) and vertically (dashed line) polarised inputs. Note that the effect of pump depletion and back conversion can be clearly seen.

Continuous-wave operation of a modulational instability laser

Stéphane Coen and Marc Haelterman
Service d'Optique et d'Acoustique, Université Libre de Bruxelles, CP 194/5
50 Av. F. D. Roosevelt, B-1050 Brussels, Belgium
Tel : +32-2-650.28.01, Fax : +32-2-650.44.96, e-mail : Stephane.Coen@ulb.ac.be

Modulational instability (MI) in an optical fiber leads to the spontaneous break-up of a continuous wave (cw) excitation into a periodic train of ultrashort pulses, provided that the dispersion of the fiber is anomalous and the cw input power sufficiently high [1, 2]. Owing to the simplicity of this ultrashort pulse formation process, the exploitation of MI has been considered in many studies for the realization of laser sources adapted to ultrahigh bit-rate optical transmissions. However, despite its simplicity, the MI process in fibers is difficult to control and presents, in this respect, some important drawbacks. For instance : - The generated pulse train repetition rate depends on the incident power level and is therefore subject to fluctuations. - cw operation cannot be achieved due to the low threshold of the competing stimulated Brillouin scattering (SBS) process. - The pulses generated by MI are superimposed on a complex background field, which is detrimental to their subsequent propagation in fiber.

The first step towards the control of MI in fibers has been realized by Hasegawa who suggested in 1984 a configuration in which MI is induced by an initial amplitude modulation [3]. As confirmed in a beautiful experiment [4], the amplitude modulation frequency determines the generated pulse train repetition rate which no longer depends on the incident power level. The use of a passive fiber resonator has then been suggested by Nakazawa *et al* [5]. In this configuration, a cw beam is injected into a fiber ring cavity. During the first round-trips in the cavity, sideband waves grow from noise due to MI gain. If the MI gain is larger than the cavity loss, oscillation of the MI sidebands can be sustained and steady-state pulse trains are generated. Once the pulse train is established, pump fluctuations cannot modify its repetition rate, since the pulse train itself acts as a seed for the next round-trip. Owing to this principle of operation, this simple device has been called MI laser. The steady-state patterns formed in the MI laser consist of dissipative structures that, from a theoretical point of view, are robust attractors of the corresponding infinite-dimensional nonlinear dynamical system. With respect to conservative MI, the MI laser is therefore advantageous in that it potentially offers a better control of the generated pulse trains. Note that this configuration of the MI laser fundamentally differs from the active cavity configuration described in Ref. [6]. As a matter of fact, the device described therein should not be called MI laser since the multiple spectral components emitted by this device are not generated by MI but are simply the result of the multimode nature of the laser. In this case, four-wave-mixing combined with the cavity losses only acts as a mode-locking mechanism in a process that is not related to MI [7].

Experiments on the MI laser have only been performed with low finesse cavities. Under these conditions, relatively high power is required to get MI oscillations and cw operation is not possible. However, it has been shown theoretically that the use of a high finesse cavity allows for low power operation with short fiber lengths [8]. cw operation can then in principle be achieved by means of an intracavity isolator to suppress SBS. The drawback of the high finesse cavities is that the dynamics of MI are strongly sensitive to interference effects between the pump and the cavity fields. On the other hand, this sensitivity to interference effects makes the system much richer. In particular, MI was shown to be possible in the normal dispersion regime [8] and the background field on which the generated pulse train is superimposed can be suppressed by destructive interferences [9].

In our communication, we present the first experimental realization of a cw pumped MI laser. We have used for this purpose a 115 m-long all-fiber passive ring cavity made up of standard telecommunication fiber (see Fig. 1). The cavity is pumped by a DFB fiber laser that emits a cw beam at $\lambda = 1555$ nm. The pump beam is amplified up to 120 mW before being coupled into the cavity through a fused fiber coupler. The same coupler is used to extract the MI laser output signal that therefore interferes with the reflected part of the cw pump beam so as to cancel the background field on which the MI pulse train is superimposed. The input/output fiber coupler has a high intensity reflectivity coefficient of 90 % so that the cavity finesse can be made relatively high, $\mathcal{F} \simeq 25$. This improves the cavity field confinement effect and the effective nonlinearity of the device. However, while a high cavity finesse and a long cavity length both contribute to lower the MI threshold, it imposes stringent conditions on the coherence of the pump laser that must have a linewidth smaller than the cavity resonance width, $(c/(nL))/\mathcal{F} \simeq 70$ kHz (L is the cavity length and n is the group index of the fiber). The DFB fiber laser used in our experiment easily meets this goal since it exhibits a linewidth of 1 kHz. An integrated fiber isolator is incorporated into the cavity. It rejects the backward travelling Stokes wave generated through SBS and prevents the cavity from operating as a Brillouin laser. In practice, the 40 dB isolation provided by our isolator has turned out to be insufficient. To completely suppress SBS in our cavity, we have then slightly phase-modulated the cw pump beam at a harmonic of the cavity free-spectral-range larger than the Brillouin gain bandwidth. Finally, an optical path piezoelectric modulator is used to control the cavity length interferometrically so as to maintain the cavity on resonance. Path fluctuations resulting from external mechanical and thermal perturbations are compensated by a servo-controller whose input signal is the intensity of the first MI sideband lobe that is measured by spectrally resolving the MI laser output signal on a diffraction grating. The operating point is selected by comparing this intensity with an adjustable reference level in such a way that the cavity detuning can be fixed and controlled. The inclusion of this servo-controller is one of the key ingredients that has allowed us to operate the MI laser under steady-state conditions for indefinite periods of time. It demonstrates that simple low frequency electronics is sufficient to control the interferometric nature of the intracavity processes and to generate ultra-high repetition rate cw pulse trains.

Under these conditions, we were able to comfortably investigate the cw MI laser. In terms of the power at the cavity input, the oscillation threshold has been observed to be as low as 80 mW. This corresponds to an intracavity power of 510 mW when the cavity is on-resonance. Typical results are shown in Fig. 2 : (a) shows the spectrum and (b) the intensity auto-correlation trace measured at the

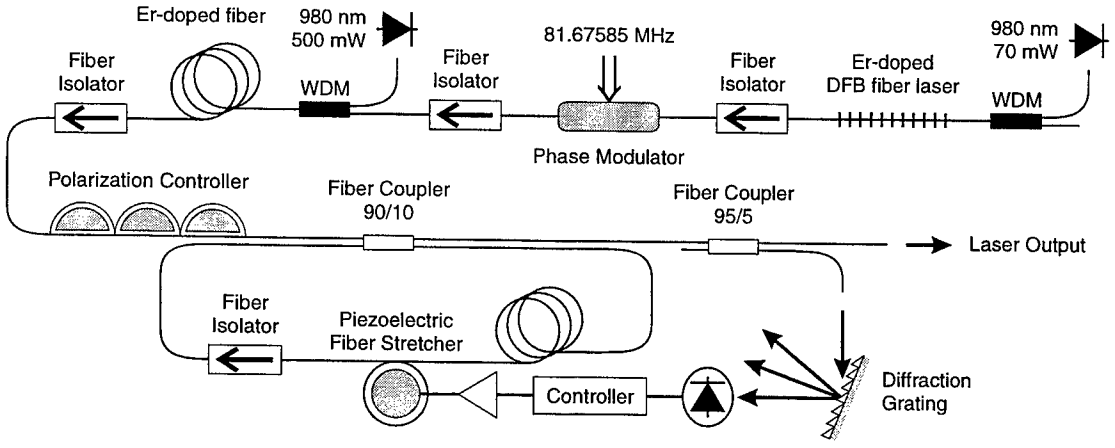


Figure 1: Experimental setup.

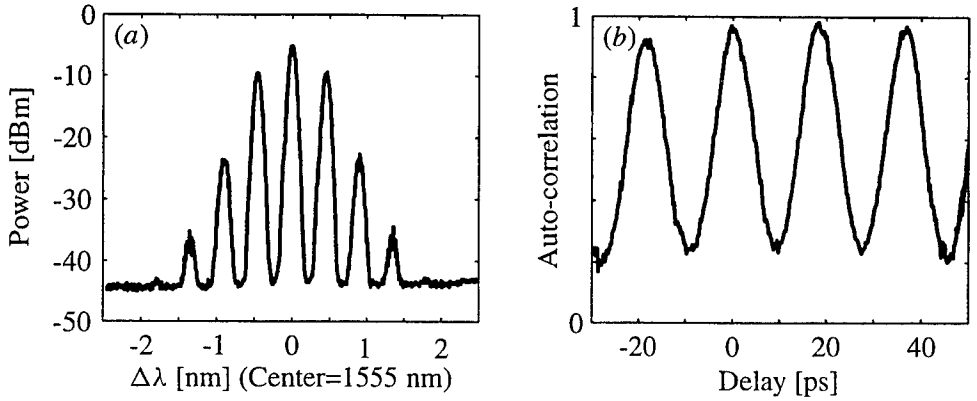


Figure 2: Output of the MI laser. (a) is the optical spectrum while (b) is the auto-correlation trace.

output of the MI laser for a pump power of 100 mW. The optical spectrum exhibits a series of peaks separated by 0.46 nm corresponding to a repetition rate of 58 GHz. Let us notice that the harmonics are visible up to the fourth order despite the remarkably moderate pump power we used. The repetition rate of the laser was observed to be stable on a high resolution Fabry-Perot spectrum analyzer. The auto-correlation trace (b) confirms the generation of a deeply modulated pulse train at 58 GHz. The large modulation depth of the signal is due to the use of a high finesse cavity to host the MI process contrary to what was considered in the earlier experiment of Nakazawa *et al* [5]. As a matter of fact, numerical simulations performed with the experimental parameters show that the background of the output pulse train should be very close to zero and that the limited auto-correlation contrast seen in Fig. 2(b) only comes from the relatively poor mark-to-space ratio of the generated pulse train. Note finally that the theory of intracavity MI [8] shows that the repetition rate of the MI laser scales as $(|\beta_2|L\mathcal{F})^{-1/2}$ where β_2 is the dispersion coefficient of the fiber. This scaling explains the relatively low repetition rate of 58 GHz observed in our experiment. The repetition rate can however be easily increased up to several hundreds of GHz by shortening the cavity and by taking advantage of the low dispersion coefficient of dispersion-shifted-fibers.

In summary, by means of a high finesse fiber resonator, we have, for the first time, successfully operated a MI laser in the cw regime. Our experiment constitutes the first demonstration of MI in the cw regime and reveals that the MI process in fibers can be totally controlled. In particular, since the MI laser is in essence a quadruply resonant optical parametric oscillator, our experiment demonstrates that simple low frequency electronics can efficiently overcome the high phase-sensitivity of such devices so as to allow for low power operation. This opens up new possibilities for the application of MI to the realization of laser sources adapted to ultrahigh bit-rate optical transmissions.

[1] A. Hasegawa and W. F. Brinkman, IEEE Journal of Quantum Electronics **16**, 694 (1980).
[2] K. Tai, A. Hasegawa, and A. Tomita, Physical Review Letters **56**, 135 (1986).
[3] A. Hasegawa, Optics Letters **9**, 288 (1984).
[4] K. Tai, A. Tomita, J. L. Jewell, and A. Hasegawa, Applied Physics Letters **49**, 236 (1986).
[5] M. Nakazawa, K. Suzuki, and H. A. Haus, Physical Review A **38**, 5193 (1988).
[6] E. Yoshida and M. Nakazawa, Optics Letters **22**, 1409 (1997).
[7] M. Quiroga-Teixeiro *et al*, Journal of the Optical Society of America B **15**, 1315 (1998).
[8] M. Haelterman, S. Trillo, and S. Wabnitz, Optics Letters **17**, 745 (1992).
[9] S. Coen and M. Haelterman, Optics Communications **146**, 339 (1998).

Modulation Instability of Incoherent Beams in Non-Instantaneous Nonlinear Media

M. Soljacic, M. Segev, T. Coskun, D. N. Christodoulides, A. Vishwanath, and Z. Chen

Modulation Instability (MI) is a fairly common phenomenon in non-linear wave systems; it can typically be observed on top of a pulse that is very smooth compared to the other characteristic length scales of the physical system. Small noise perturbations grow on top of the pulse as the pulse propagates, draining energy from large wavelengths into smaller wavelengths. Eventually, the pulse disintegrates. This phenomenon has been observed in very many non-linear coherent wave systems. MI phenomena can be regarded as a precursor for existence of solitons. The recent demonstration of existence of incoherent solitons [4] led us to wander whether MI can be observed for incoherent waves also. In this article, we demonstrate analytically and numerically, [1] that MI can exist in systems of incoherent waves also. It exists in non-instantaneous nonlinear media, when the average phase fluctuation time across the beam (or between modal constituents) is much shorter than the response time of the medium. In this case, the nonlinear change in the refractive index depends only on the time average of the light intensity. Incoherent MI occurs when the value of the nonlinearity exceeds a threshold imposed by the degree of spatial coherence. We use analytical and numerical methods to study the properties of incoherent MI in a general self-focusing non-instantaneous medium. We solve the incoherent MI problem in closed form for input beams with Lorentzian angular power spectra, and arbitrary forms of nonlinearities. Then, we confirm our results with numerical simulations, and further study general cases of input beams along with propagation-evolution effects.

The incoherent light we analyze is propagating in the z-direction, with its spatial coherence length being significantly smaller than its temporal coherence length; i.e., the beam is a partially-spatially-incoherent and quasi-monochromatic (the wavelength of light λ is much smaller than each of these coherence lengths). The nonlinear material is non-instantaneous, that is, the nonlinear index change is a function of the optical intensity, time-averaged over the response time of the medium, τ, which is much longer than the coherence time of the light, t_c. Assuming the light is linearly polarized and $E(r,z,t)$ represents its slowly varying amplitude, we define $B(r_1,r_2,z)=<E^*(r_2,z,t)E(r_1,z,t)>$ where the brackets denote the time average (taken over τ). The equation for B, as derived from paraxial nonlinear wave equation, is [3]:

$$\frac{\partial B}{\partial z}-\frac{i}{k}\frac{\partial^2 B}{\partial r\partial\rho}=\frac{in_0}{k}\left(\frac{\omega}{c}\right)^2\left\{\delta n(r_1,z)-\delta n(r_2,z)\right\}B, \tag{1}$$

where ω is the carrier frequency, k is the carrier wave-vector, n_0 is the background refractive index, δn is the tiny nonlinear modification to the refractive index, $r=(r_1+r_2)/2$ is the middle point coordinate, and $\rho=r_1-r_2$ is the difference coordinate. $B(r,\rho,z)$ is known as the spatial correlation function, and $I(r,z)=B(r,\rho=0,z)$ is the time-averaged light intensity. Clearly, from the definition of B, we have the constraint $B(r,\rho,z)=B^*(r,-\rho,z)$.

To study MI, we assume the incident light to have a uniform intensity, except for small intensity perturbations that also depend on r and z. Thus, B can be written as: $B(r,\rho,z)=B_0(\rho)+B_1(r,\rho,z)$, where $B_1<<B_0$, $B_0(\rho)$ representing the uniform background, so the uniform background intensity is given by $I_0=B_0(\rho=0)$. The dependence of δn on r comes from B_1, so to the lowest order in B_1, $\{\delta n(r_1,z)-\delta n(r_2,z)\}=\kappa\{B_1(r_1,\rho=0,z)-B_1(r_2,\rho=0,z)\}$, where $\kappa=d[\delta n(I)]/dI$ evaluated at I_0 is the marginal nonlinear index. In the Kerr case ($\delta n=\gamma I$), so $\kappa=\gamma$. Note that, because of time-averaging properties of the material, any random time-dependent perturbation, no matter how large, if it occurs on a time scale shorter than τ, averages to zero; only time-independent perturbations lead to MI in our system. Therefore, linearizing Eq.(1) in B_1 produces:

$$\frac{\partial B_1}{\partial z}-\frac{i}{k}\frac{\partial^2 B_1}{\partial r\partial\rho}=\frac{in_0}{k}\left(\frac{\omega}{c}\right)^2\kappa\left\{B_1(r+\frac{\rho}{2},\rho=0,z)-B_1(r-\frac{\rho}{2},\rho=0,z)\right\}B_0(\rho). \tag{2}$$

Up to this point, the discussion is general and applies for any correlation function $B_0(\rho)$. In what follows, we assume that $B_0(\rho)$ has a Lorentzian-shaped k-spectrum, because in this case, one can obtain closed-form analytical results. That is, we assume $\hat{B}_0(k_x)=A/[k_x^2+k_{x0}^2]$, where for any $F(\rho)$, $\hat{F}(k_x)=\frac{1}{2\pi}\int_{-\infty}^{\infty}d\rho F(\rho)e^{ik_x\rho}$ is the Fourier transform of $F(\rho)$. In this case the normalized angular power spectrum of the source is also Lorentzian (i.e., $G_N(\theta)=(\theta_0/\pi)(\theta^2+\theta_0^2)^{-1}$ where the angle $\theta=k_x/k$ is measured in radians). The background uniform intensity is then $I_0=\pi A/k_{x0}$. The physically acceptable

eigenmodes of the Eq.(2) can be written as $B_1(r,\rho,z)=\exp(gz)\exp[i(\alpha r+\phi)]L(\rho)+\exp(g^*z)\exp[-i(\alpha r+\phi)]L^*(-\rho)$, where ϕ is an arbitrary real phase that carries no physical significance, α is real and g is associated with the MI gain. These modes automatically satisfy $B_1(r,\rho,z)=B_1^*(r,-\rho,z)$. For each α one can obtain a set of modes $L(\rho)$ needed to describe any perturbation B_1. We look for the modes that grow: those with g that is not pure imaginary. By assuming a Lorentzian k-spectrum $\hat{B}_0(k_x)=A/[k_x^2+k_{x0}^2]$ in Eq.(2), after a few lines of algebra [1] we get the following result for the mode that grows, if g is bigger than zero:

$$\frac{g}{k}=-(k_{x0}/k)(|\alpha|/k)+(|\alpha|/k)\sqrt{\frac{\kappa I_0}{n_0}-\left(\frac{\alpha}{2k}\right)^2}, \qquad (3)$$

where in the above expression κ represents the marginal nonlinear index change because of the constant background intensity, and as previously noted $k_{x0}/k=\theta_0$. The result of Eq.(3) clearly demonstrates that the MI growth rate is substantially affected by the coherence of the source. Moreover, in the limit $k_{x0}\to 0$, it correctly reduces to the well known result of coherent MI. Even more importantly, Eq.(3) indicates that for a given degree of coherence, MI occurs only when the quantity κI_0 exceeds a specific threshold. More specifically, incoherent MI exists **only if** $\kappa I_0/n_0>\theta_0^2$, whereas when $\kappa I_0/n_0<\theta_0^2$, MI is ***entirely eliminated***. In other words, the more incoherent a source is, the larger κI_0 (marginal index change) that is required to induce MI. Computer simulations suggest that this trend **is *universal* and is independent of the angular power**. Having found $g(\alpha)$, one can then easily determine the intensity of the perturbation $I_1(r,z)=B_1(r,\rho=0,z)$.

To apply the result of Eq.(3) for Kerr nonlinearity $\delta n(r)=\gamma I$, we set $\kappa=\gamma$; to illustrate this result, we present it graphically in Fig.1. In this case, $\kappa I_0=\delta n$, so the larger the non-linear index change, the stronger MI.

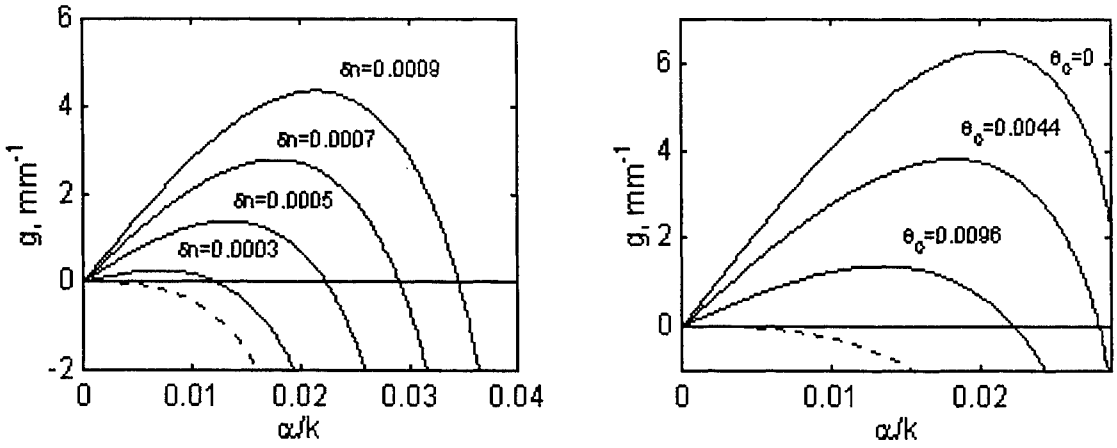


Figure 1: Incoherent MI for Kerr nonlinearity: growth rate of perturbations vs the perturbation transverse wavelength. λ=500nm in vacuum, and n_0=2.3. The background uniform intensity has a Lorentzian angular power spectrum of width θ_0. The nonlinear index change due to the background is given by δn. In the left plot, we show gain curves for a few δn's, with a fixed θ_0=0.0096 rads; the dashed line in the plot has δn marginally small enough so that MI just disappears. In the right plot, we show gain curves for a few θ_0's, with a fixed δn=0.0005; the dashed line in the plot has θ_0 marginally large enough so that MI just disappears.

To verify our analytical findings and to further explore incoherent MI, we use computer simulations. In particular, the intensity/correlation MI dynamics of Eq.(1) are investigated by means of the coherent density approach [2]. The power Fourier spectrum of the intensity fluctuations growing on top of the constant incoherent background is used to identify the spatial frequencies that exhibit maximum gain. Figure 2 shows the evolution of the power spectra of the intensity fluctuation

when the angular power spectrum of the source is Lorentzian, and the nonlinearity is Kerr type. In this example, θ_0=9.6mrads, γI_0=5*10^{-4}, $n_0 = 2.3$, and λ=500nm. These results indicate that maximum MI gain is attained at a normalized spatial frequency $\alpha / k \approx 0.0135$, with a peak value of g=1.37mm^{-1}, both in an excellent agreement with that predicted from Eq. (3) as also depicted in Fig.1 for the same set of parameters. Note that in this case the spatial frequency where maximum MI gain occurs remains invariant during propagation. After a certain distance (in this example after 9 mm) additional sub-bands emerge as in the case of coherent MI. Physically, this effects is "secondary" MI: modulation instability for which the first amplified instability peak acts as a "pump" and plays the role of B_0. Numerical simulations also confirm another prediction of the analytic result: **the existence of a threshold for incoherent MI**. The numerical study can also provide information about the evolution of incoherent MI from input beam of angular power spectra different than the Lorentzian shape.

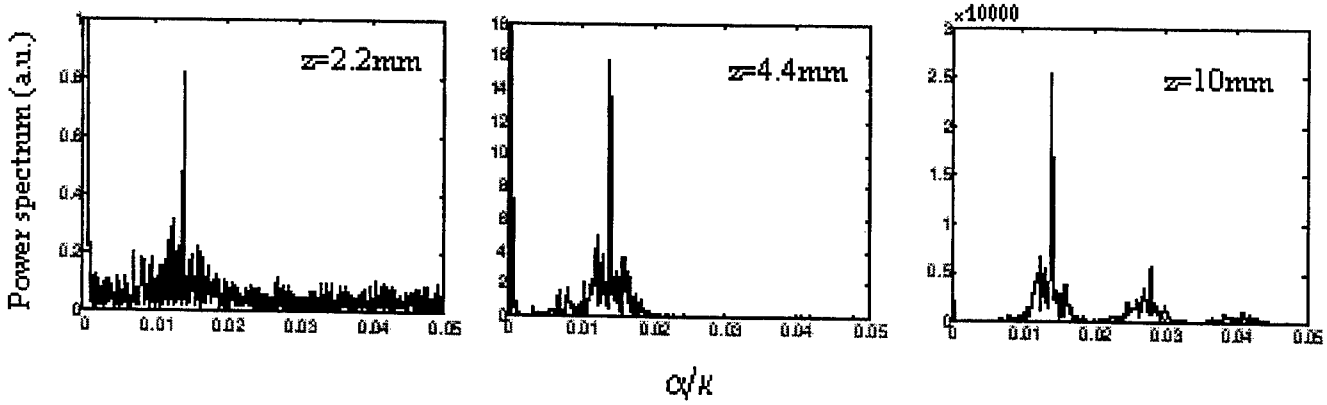


Figure 2: Power spectrum of an incoherent beam during propagation in Kerr nonlinearity when the source power spectrum is Lorentzian with θ_0=0.0096rads and δn=0.0005.

As described in [1], our analytical approach can be used to obtain analytical understanding of MI with an arbitrarily shaped angular power spectrum, but some of the integrals involved typically have to be solved numerically; for the Lorentzian case, one can obtain closed-form solutions as we did. For example, when we apply this idea for input beams with Gaussian power spectra, we also obtain an excellent agreement between our analytical approach, and our numerics. The analytic expansion here also captures the fact that there always exists a threshold κI_0 for incoherent MI to occur.

To conclude, we have shown that modulation instability exists in partially incoherent systems, and that its existence requires the marginal nonlinear index change times the background intensity, κI_0 to be above a well-defined threshold. There is no similar threshold in the coherent MI case! The κI_0 is determined by the spatial degree of coherence (angular power spectrum). To emphasize the fundamental importance of this result, we note that partially incoherent light is a system in which the "quasi-particles" are only weakly phase-correlated (with the extreme case being a fully incoherent system in which the "quasi-particles" are fully non-correlated). Yet this weakly-correlated system exhibits features characteristic of a phase-transition: above a well-defined threshold, it collapses and forms "clusters" (filaments). From this view point, the threshold value plays the role of the Curie temperature, and, like in any phase transition effects, small fluctuations grow rapidly. What we have done here is to identify MI in an incoherent system, which is fundamentally a system in which repulsion forces are much weaker than the attraction forces. Since nature is full of nonlinear systems in which incoherent wave-packets exist (e.g. optics, and plasma physics), we expect that these systems will exhibit MI as well. We therefore believe that this work lays the foundations for instabilities and pattern formation in any nonlinear incoherent system in nature. From all of these arguments, one thing is obvious: there are many more new and exciting features that are intimately related to incoherent modulation instability, and are yet unraveled and call for future research. **Finally, we want to note that we have very recently obtained first preliminary experimental proof for existence of threshold incoherence in systems involving incoherent MI.**

References

(1) M. Soljacic et al; submitted to Phys. Rev. Lett. (July 1999).

(2) D. N. Christodoulides, T. H. Coskun, M. Mitchell and M. Segev, Phys. Rev. Lett. **78**, 646 (1997); ibid **80**, 2310 (1998).

(3) V. V. Shkunov and D. Z. Anderson, Phys. Rev. Lett. **81**, 2683 (1998).

(4) M. Mitchell and M. Segev, Nature (London) **387**, 880 (1997).

Observation of quadratic vortex solitons

Paolo Di Trapani, Walter Chinaglia, and Stefano Minardi,
University of Insubria, Como, Italy, Ditrapan@fis.unico.it

Gintaras Valiulis
Vilnius University, Vilnius, Lithuania, Gintaras.Valiulis@ff.vu.lt

Spatial solitary waves in quadratic nonlinear media are currently attracting the attention of many researchers, both for their beauty and unique potential of performing ultrafast, digital-like, all-optical signal processing. Since their discovery in 1994,[1] however, all the experimental observations have been limited to the lowest-order case of the bright solitons, while no data are available for the higher-order or vortex solitary waves (VS). Actually, the bright soliton can be considered as a quite common event, since this is the final state toward which any beam sufficiently focused and intense should spontaneously evolve under parametric interaction. On the contrary, quadratic VS are supposed to be very rare objects to be found because of the well known modulation instability of the background embedding the core, instability which breaks up the beam into bright solitons[2] thus preventing the achievement of the diffraction-free dark-core propagation (VS regime). Rare but precious, especially for the possibility of performing algebraic operations at THz rate by suitably playing with their "quantized" topological charge.[3] This justify the efforts of many researchers to find out the way to beat this instability. One possible solution recently proposed is that of adopting a weak self-defocusing Kerr contribution to the nonlinear interaction[4]. We are not aware of any experiment done in this direction.

In this work we propose a different approach for achieving the background stabilization and the VS regime, based on the effect of the transverse walkoff in phase-mismatched second-harmonic (SH) generation. In fact, at large positive Δk the $X^{(2)}$ cascading mimics the Kerr self-defocusing nonlinearity, which is known to support VS formation.[5] The peculiarity of the $X^{(2)}$ case comes from the weak SH field, which actually controls the growth of the modulation instability. In the case of walkoff, the spikes which are formed tend to propagate at the walkoff direction, due to their large SH energy content. For sufficiently small beams, they will soon move out of the beam. This spike expulsion should work as a self-quenching mechanism for the modulation instability itself (see the discussion below).

In the experiment, the nonlinear crystal which we selected for the VS formation is a 30mm LBO cut at θ=90° ϕ=15° and operated in type I phase matching. This cut was chosen in order to have the suitable walkoff angle (ρ□0.5°, close to normal incidence) for the background stabilization. At the selected temperature of 130° and at the chosen FH wavelength of 970 nm the self-defocusing and self-focusing interaction occurred for ϕ angles smaller and bigger than 14.4°, respectively.

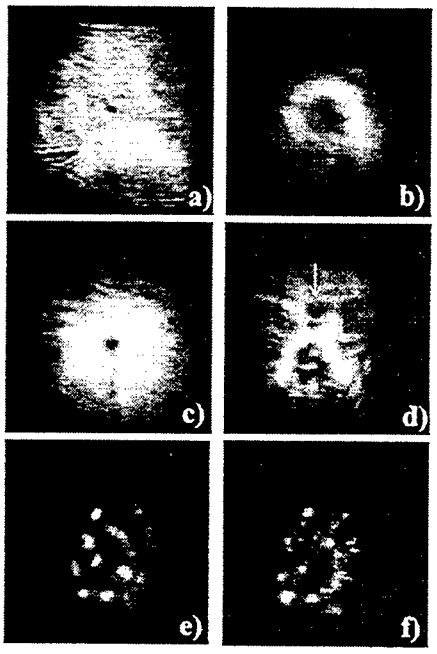


Fig. 1. a): input vortex; b): linear output; c-d): nonlinear output in self defocusing., FH and SH e-f): nonlinear output in self focusing., FH and SH

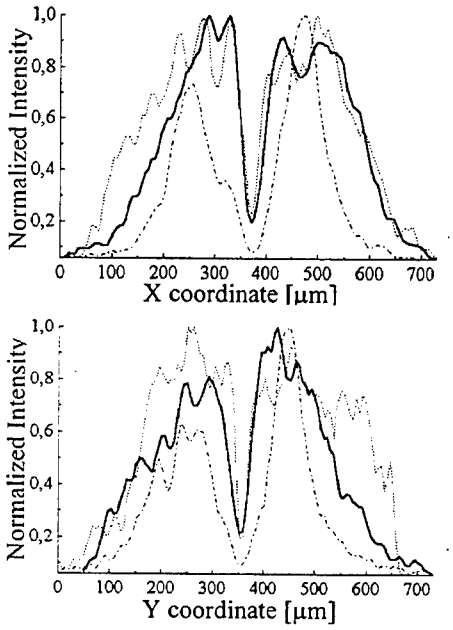


Fig. 2. Transverse x and y profiles. Dotted: input; dashed-dotted: output linear; full: output nonlinear.

Fig. 2. Transverse x and y profiles. Dotted: input; dashed-dotted: output linear; full: output nonlinear.

The most of the work has concerned the generation of the suitable vortex beam for the VS excitation, that means sufficiently large, flat-top, intense, with a very narrow-core singularity and finally at a wavelength which unfortunately can not be that directly available from our Nd:glass laser systems (or harmonics). This charge-1 vortex was than obtained by single-pass parametric amplification of a weak vortex beam, this one being generated by a fork hologram diffracting the tunable radiation from a commercial 3-pass parametric quantum-noise amplifier. All the amplifiers are pumped by different portions of the same 1ps green pulses from a frequency doubled, CPM Nd:glass laser. The final parametric amplification of the vortex was performed in a walkoff-free type II LBO (tuning range limited to 960-980 nm), the walkoff absence being needed for the amplification of a vortex with a sufficiently small core (in non soliton regime) and the type II operation to narrow the gain bandwidth and to prevent undesired cascading effects due to close-to-degeneracy operation.

In the first part of this report we provide the experimental results supporting the claim of the achievement of the VS regime. **Fig. 1a** is a snapshot of the input FH vortex beam, as it appears at the entrance face of the SH-generator LBO crystal. The corresponding x and y transverse-coordinate profiles are given by the dotted lines in **Fig. 2** top and bottom, respectively. The input dark-core singularity has a slightly elliptical shape with FWHM diameters d_x=34μm and d_y=31μm; the embedding beam is about 0.45mm wide, with a pulse-energy content of 40 μJ (average intensity of about 30 GW/cm^2). The effect of the linear propagation of the vortex inside the crystal, whose length is 10 times larger than the Rayleigh range of the input core, is shown by the low-intensity profile in **Fig. 1b**, taken at the crystal output face (dashed-dotted profiles in **Fig. 2**), whose core diameter are d_x=200μm and d_y=210μm. The achievement of the diffraction-free propagation of the core (VS regime) is evident from the high-intensity output profile in **Fig 1c** (full lines in **Fig. 2**), exhibiting a perfectly round core of FWHM diameters d_x= d_y=52μm. This results is obtained for self-defocusing cascading $X^{(2)}$ effect, at Δk =+20cm^{-1} and ρ=0.47°. The corresponding SH field is given in **Fig. 1d**. The arrow indicates the position of the VS singularity, and its direction that of the transverse walkoff. The conversion efficiency is here below 3%. The process of VS formation appeared to be a very stable phenomenon, being the results quite insensitive to small changes in intensity or Δk. A completely different behavior is observed at the self-focusing side of the tuning, characterized by beam breakup into several solitary waves. Typical examples are the FH and SH output profiles shown in **Figs. 1e** and **1f**, respectively, obtained at Δk = -20cm^{-1} and for an input intensity twice lower than in the self-defocusing case.

In order to verify the impact otf the walkoff we have repeated the measurements for the case of a walkoff-free 30mm type I LBO SH generator (cut at θ=90° ϕ=0°), for similar input conditions except for the wavelength, here set to 1055nm. For all Δk's in the 0-150cm^{-1} range we always observed beam break-up without any significant reduction in output core diameter (respect to the linear case). What we have obtained is consistent with the result recently presented by Petrov *et Al.*[2] In fact, they have observed bthe bright soliton formation using a KTP crystal, whose walkoff is very weak. These results thus confirm the strategic role of the walkoff to achieve VS formation.

In the second part of this work we investigate the stability of the achieved VS regome. To this end we report our preliminary numerical results addressing the features of the beam-profile evolutions at larger distances than those achievable in our experiments. Calculations were done in the monochromatic approximation and neglecting the Kerr nonlinearity and the internal scattering inside the crystal. The input conditions and parameters (Δk=100cm^{-1}, Intensity=100 GW/cm^2, ρ=0.6°) are close to those in the experiment, if proper rescaling is performed. **Figs. 3a** and **3b** show the FH vortex-beam dynamics in the absence and in the presence of walkoff, respectively. Without walkoff, a number of solitary-wave spikes keep growing close to the core region (due to larger input intensity), severely distorting the beam and preventing the VS formation. With walkoff, on the contrary, a longer distance is needed for the spikes to grow. Moreover, they appear already far form the center and move soon outside the beam, where their growth is quenched due to the absence of energy refilling. In this case the spikes do not appreciably interfere with the core-region dynamics and the VS regime is well maintained. **Fig. 3c** shows the evolution of the FWHM core diameter for the linear case and for the nonlinear with and without walkoff. **Fig. 3d** show the different transverse velocities of the VS core and of the (largest) spike in the beam, due to the different SH energy content.

In our experiment, we were able to obtain the formations of the spikes within our 30 mm crystal only by operating it at very small (positive) Δk, for the given intensity. By suitably optimizing wavelength, temperature and angle in order to achieve the maximum walkoff (ρ=0.6°) we obtained the FH output profile shown in **Fig. 4**, which exhibits a VS formation (output core diameters d_x=33μm d_y= 46μm) with a single spike exiting the beam. We like to mention that the spikes tend to be formed on the bottom side of the two bright stripes evident in the SH profile shown in Fig. 1d .

In the last part we investigated the impact that the finite size of the external beam has on the vortex dynamics. To this end we repeated the experiment with a vortex with the same core size, but with an embedding beam 4-5 times smaller in diameter. For self-defocusing phase mismatch we were not able to see any VS formation, due to the fast beam diffraction. On

changes in intensity or Δk, since the beam tend to break up in several lobes. These result, which we obtained also in numerical experiment, has to be probably attributed to the effect of the self focusing on the whole beam, whose intensity gradient is comparable to that of the core.

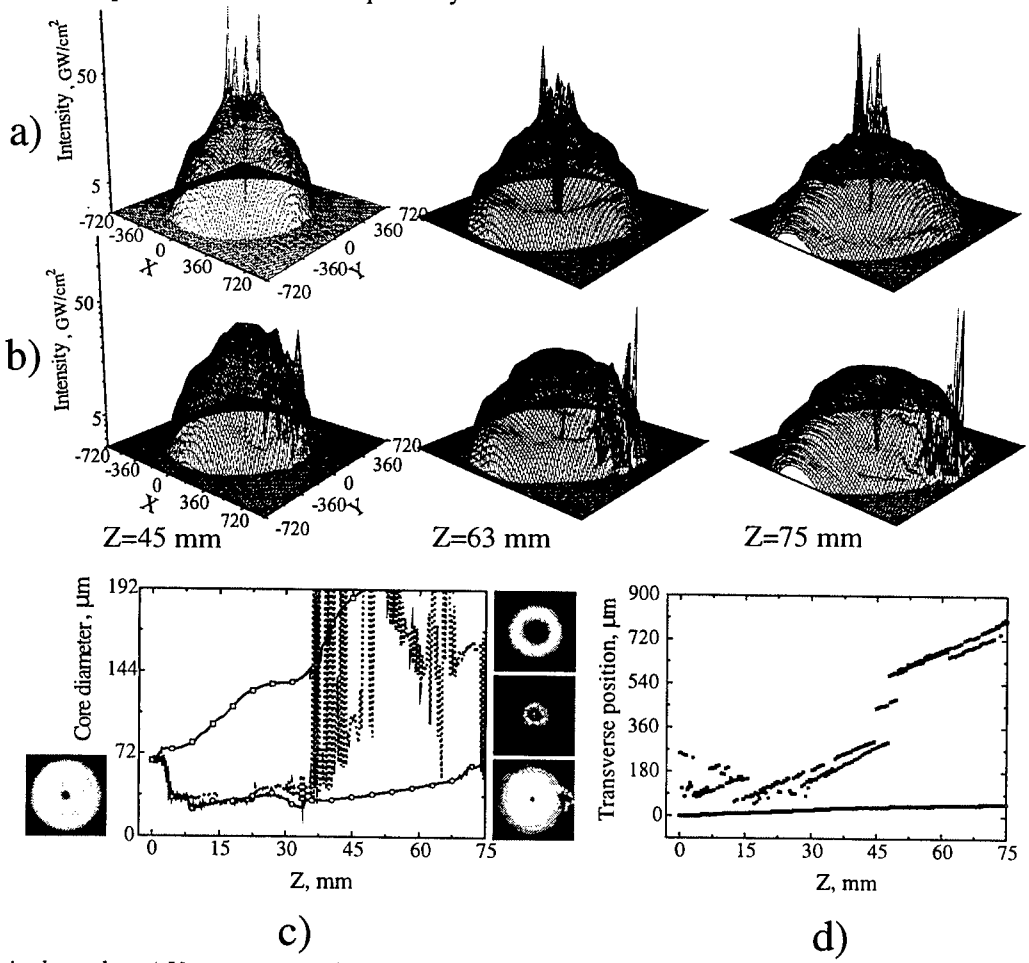


Fig. 3. Numerical results. a) Vortex-profile dynamics at large distances without walkoff; b) with walkoff ρ=0.7°. c) Core diameters for linear (squares), nonlinear without walkoff (dotts) and nonlinear with walkoff (circles) dynamics. Left: input-beam profile; right, from top to bottom: output-beam profile linear propagation, nonlinear without walkoff, nonlinear with walkoff. d)Transverse positions of the VS core (empty squares) and the largest spike (filled squares) in the case of walkoff.

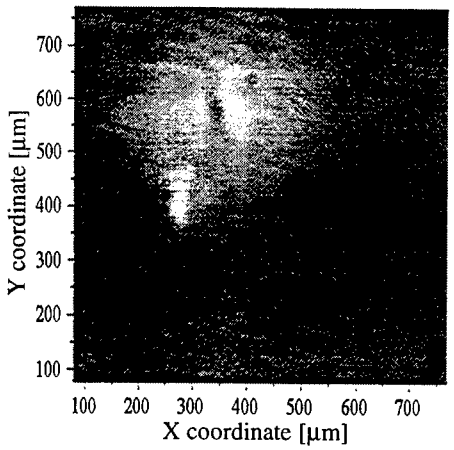


Fig. 4. Vortex soliton formation in consitions of large walkoff and small phase mismatch, with a single spike exiting the beam.

P. Di Trapani like to thank dr. Hao He for charming discussions on VS, fronting the Pacific Ocean waves.

References

[1] W.E. Toruellas, Z. Wang, D.J. Hagan, E.W. Van Stryland, GI. Stegeman, L. Torner, and C.R. Menyuk, Phys. Rev. Lett. **74**, 5036 (1995)

[2] D.V. Petrov, L. Torner, J. Martorell, R. Vilaseca, J.P. Torres, and C. Cojocarn, Opt. Lett. **23,** 1444 (1998)

[3] I.V. Basistiy, V.Y. Bazhenov, M.S. Soskin, and M.V. Vasnetsov, Opt. Comm. **103,** 422 (1993)

[4] J.A. Tristam, A.V. Buryak, and Y.S. Kivshar, Opt. Lett. **23,** 670 (1998)

[5] G.A. Swartzlander, and C.T. Law, Phys. Rev. Lett. **69,** 2503 (1992)

Kerr Spatio-Temporal Focusing in a Planar Glass Waveguide

Hagai Eisenberg, Roberto Morandotti and Yaron Silberberg
Department of Physics of Complex Systems
Weizmann Institute of Science, Rehovot 76100, Israel
feisen@wis.weizmann.ac.il, feyaron@wis.weizmann.ac.il

Orit Potashnik and Shimshon Bar-Ad
School of Physics and Astronomy, Tel-Aviv University,
Ramat Aviv 69978, Tel-Aviv, Israel

Duncan Ross, Ulf Peschel* and J. Stewart Aitchison
Department of Electronics and Electrical Engineering
University of Glasgow, Glasgow G128QQ, Scotland

Optical solitons can be formed in the presence of the optical Kerr effect. They were demonstrated both in the time domain as stable light pulses [1], and in the space domain as self-guided beams in a slab waveguide [2]. Whenever a light beam or pulse are permitted to diffract or disperse in more than one transverse direction, they are expected, according to a slowly varying amplitude analysis, to be unstable. Focusing of a beam in a bulk medium above a certain power threshold may not stop until damage to the medium occurs. A light pulse propagating in an anomalously dispersing planar waveguide is another case where light has two dimensions to diffract in. Such a pulse should exhibit spatio-temporal collapse [3]. Slowly varying amplitude analysis suggest catastrophic collapse, however full wave calculations show that phase defects which are produced can arrest the collapse [4].

It has been proposed that focusing of such light pulses may be balanced due to their hybrid spatio-temporal nature and form stable *light-bullets* [3]. Such stable light bullets were suggested to result from a few mechanisms. Some examples are saturation of the Kerr nonlinear refractive index, nonlinear absorption or inclusion of non-paraxial corrections to the slowly varying amplitude approximation. Recently, stable spatio-temporal pulses have been demonstrated in a material with cascading of quadratic nonlinearity [5]. The stability in this case is a result of the saturation nature of the nonlinearity. The propagation of spatio-temporal pulses in a Kerr medium has been demonstrated, but only in the case of normal group velocity dispersion where solitons and light bullets are not supported [6].

We report here the results of the first experiment of propagation of light pulses in a planar waveguide in the anomalous dispersion wavelength regime. Our source pulses are 60fs long at a wavelength of 1.52μm with a repetition rate of 1kHz. The maximum in-coupled peak power is about 10MW although for our experiment we use much less power. The waveguide is a single-mode step planar Silica waveguide, 5cm long and 1cm wide with no significant linear losses. We control the input beam profile by using cylindrical optics. The output facet is imaged onto an infrared camera and sampled and analyzed in a computer. The output pulse length is measured by using an auto-correlator in a non-collinear setup.

The important parameters in this experiment are the diffraction and dispersion lengths. They are defined as $L_{DF} = k_0 W_0^2$ and $L_{DS} = T_0^2 / \beta_2$ respectively, where W_0 and T_0 are the spatial and temporal widths.

---

* Permanent Address: IFTO, Fsu-Jena, Jena, Germany

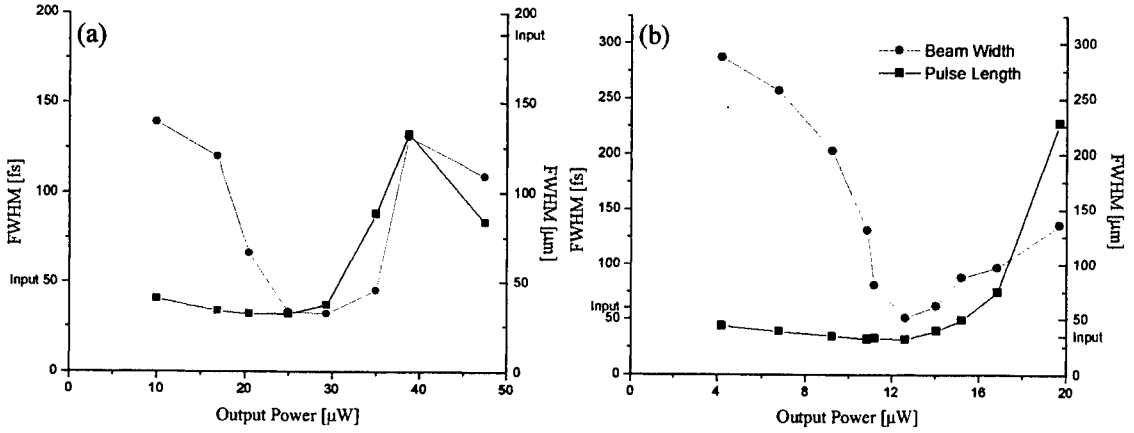


Fig. 1: Spatial and temporal widths of the (a) symmetric and (b) asymmetric pulses as a function of the in-coupled power.

The input pulse length of 50-60fs corresponds to a dispersion length of about 12cm. In order to achieve a similar diffraction length, the spatial width should be about 175μm.We used two beam sizes in our experiments, one 190μm wide, having lengths ratio close to 1:1 and a narrower beam, about 30μm wide, with a ratio of about 1:6 between the dispersion and diffraction lengths. The relatively short waveguide, only about a half dispersion length, is not a limitation in this experiment, because the dominant distance is the nonlinear length, which is about 0.5mm for the typical power used. We find the pulse to contract during propagation, while reducing its dispersion length considerably.

The output pulse length and beam width, for the two input beam sizes, as a function of the in-coupled power are presented in Fig. 1. Apparently, the pulse shrinks with increasing power in both directions until reaching a minimum value, and then it starts to expand. For the asymmetric case (1:6 ratio), in the spatial direction, contraction is fast and expansion is slow whilst it is the opposite in the temporal dimension. In the case of the symmetric pulse (1:1 ratio), contraction and expansion in both dimensions look more uniform. In the symmetric case, a pulse of 190μmX50fs is compressed to 30μmX30fs.

While we do observe temporal contraction of the pulses, the symmetric case is expected to contract symmetrically in both directions. We suspect that our temporal measurements are limited by the setup. This is suggested by the shallow and flat minimum of the temporal width data. Spectral measurements of the light emerging from the sample suggest that the pulses focus temporally to about 15fs whilst our shortest temporal measurement is 30fs. In Fig. 2 we present a comparison between the spectra main features of the two kinds of input pulses. The data is re-scaled to the power where the minimal widths are achieved. Fig. 2a shows the Raman shift of the pulse spectrum center and Fig. 2b shows the spectrum broadening due to self-phase-modulation (SPM). These two nonlinear effects suggest that the nonlinear action is much stronger in the focusing of the symmetric pulse. Therefore, we can assume that a symmetric pulse contracts in time more than a 1:6 ratio pulse. The actual spectrum of the output light beyond the minimal width power (not shown here) expands on a linear power scale over more than 600nm.

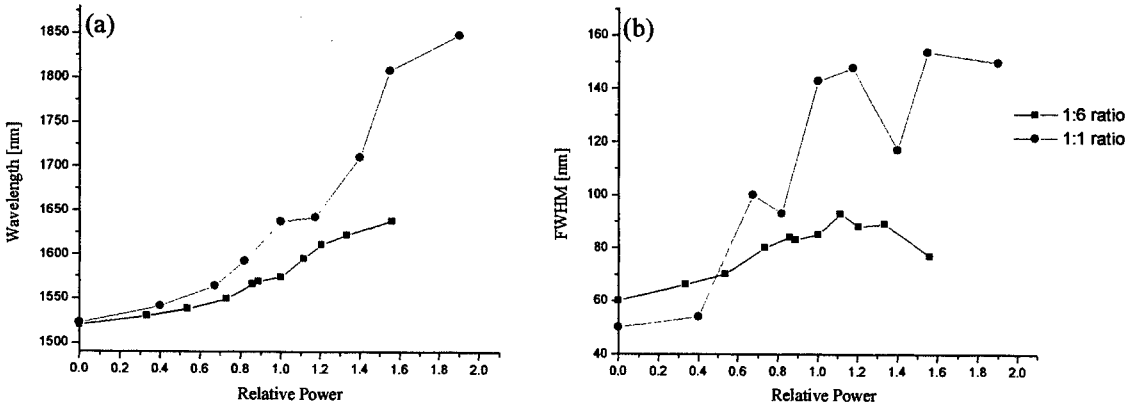


Fig. 2: (a) Raman shift of the central wavelength and (b) Self-phase-modulation induced broadening on the pulse spectra as a function of power for the two kinds of pulses. The power is re-scaled such that a unit value corresponds to the maximal pulse compression.

We note that along the range of 25-30μW of average power for the symmetric case, the pulse dimensions remain almost unchanged. We do not know whether this is due to the above mentioned limitations in our set-up. However, also the Raman shift and SPM broadening are rather constant in this range.

These results suggest that there is a stable regime where light bullets may exist. Above the stability range, the pulses start to expand rather than to collapse as predicted by the slowly varying amplitude theory. A simple explanation can be that the pulse is self-focusing and the focal point is moving backward when the power is increased, until it reaches the output facet. When the power is further increased, the focus enters the waveguide. For a range of intensities the pulse retains its shape, but beyond this range, it expands. We know that no damage was done to the waveguide because these results were reproducible in consequent experiments.

In conclusion, we observed for the first time a simultaneous contraction of light pulses in time and space as the result of Kerr nonlinearity action. Although we have difficulties in measuring pulses of such an ultra short duration (about 3 optical cycles in this wavelength), the contraction is evident, and probably reaches the size of about 30μmX15fs in the symmetric case. Due to the fast increase in peak power of the focusing pulses, we observed strong effects on their spectrum. At high power, the spectrum expands over more than 600nm on a linear power scale.

References

[1] L.F. Mollenauer, R.H. Stolen and J.P. Gordon, Phys. Rev. Lett. **45**, 1095 (1980).

[2] A. Barthelemy, S. Maneuf and C. Froehly, Opt. Commun. **55**, 201 (1985). J.S. Aitchison, Y. Silberberg, A.M. Weiner, D.E. Leaird, M.K. Oliver, J.L. Jackel, E.M. Vogel and P.W.E. Smith, J. Opt. Soc. Am. B **8**, 1290 (1990). J.S. Aitchison, K. Al-Hemyari, C.N. Ironside, R.S. Grant and W. Sibbett, Electron. Lett. **28**, 1879 (1992).

[3] Y. Silberberg, Opt. Lett. **15**, 1282 (1990).

[4] H.S. Eisenberg, Y. Silberberg, Phys. Rev. Lett. **83**, 540 (1999).

[5] X. Liu, L.J. Qian and F.W. Wise, Phys. Rev. Lett. **82**, 4631 (1999).

[6] J.K. Ranka, R.W. Schirmer and A.L. Gaeta, Phys. Rev. Lett. 77, 3783 (1996).

Nonlinear pulse dynamics in planar Chalcogenide glass waveguides

S. Spälter, G. Lenz, H.Y. Hwang, J. Zimmermann, S-W. Cheong, T. Katsufuji, and R.E. Slusher

Lucent Technologies, Bell Labs, 700 Mountain Ave., Murray Hill, New Jersey 07974, USA
Phone: (908) 582 2661, Fax: (908) 582 3260, E-MAIL: sspalter@lucent.com

High speed optical communication systems require ultrafast all-optical switching and processing. These functions are going to be implemented by controlling optical signal pulses by optical control pulses. The interaction of signal and control pulses is mediated by optical nonlinearities. Because of its fast response time, a preferred nonlinearity is the optical Kerr effect. All-optical switching has been demonstrated with the Kerr nonlinearity in silica glass fibers for many different schemes. However, the Kerr nonlinearity in silica fibers is relatively small ($n_2 \approx 2.8\times10^{-16}$ cm^2/W), making it inefficient for compact and low-threshold integrated photonic circuits. Therefore, novel nonlinear materials are required that combine a strong Kerr nonlinearity with low linear and nonlinear losses at the 1.55 μm communication wavelength. From an application point of view, glasses are particularily attractive allowing for a relatively simple, low-cost fabrication of integrated all-optical circuits.

Chalcogenide glasses are among the most promising candidates for use as a high Kerr-nonlinear switching material. Nonlinear refractive indices up to 80 times higher than in silica glass have been reported in chalcogenide glass [1]. Bandgap engineering is expected to yield even higher values in n_2, while keeping two photon absorption and the corresponding figure of merit (FOM) at acceptable levels.[2,3] While all-optical switching has been shown in 1 m long chalcogenide glass fibers [1], in planar chalcogenide waveguides, nonlinear phase shifts only up to $\pi/2$ have been demonstrated.[4]

In this paper, we present experimental results for large nonlinear phase shifts, well above π, using ultrashort pulses propagating along singlemode waveguides. The guides are written in chalcogenide glass films by photodarkening.[3] All results shown are based on the chalcogenide glass compound $Ge_{0.25}Se_{0.75}$. Recently, its Tauc bandgap was measured at 2.06 eV.[3] The linear refractive index was determined to be at $n_0 = 2.4$ at 1.55 μm by ellipsometry. From a bulk $Ge_{0.25}Se_{0.75}$ glass, a 1.9 μm thin film was deposited by pulsed laser deposition on a SiO_2/Si substrate. After rapid thermal annealing of the film at 220°C, singlemode channel waveguides were written into the chalcogenide film by photodarkening through an amplitude mask with 3 μm wide open channels.[3] The film was exposed for one hour to 100 mW/cm^2 of laser radiation at

532 nm. Finally, both ends of the guides were carefully cleaved resulting in 2.8 cm long waveguides. A schematic of one photodarkened chalcogenide waveguide is shown in Fig. 1.

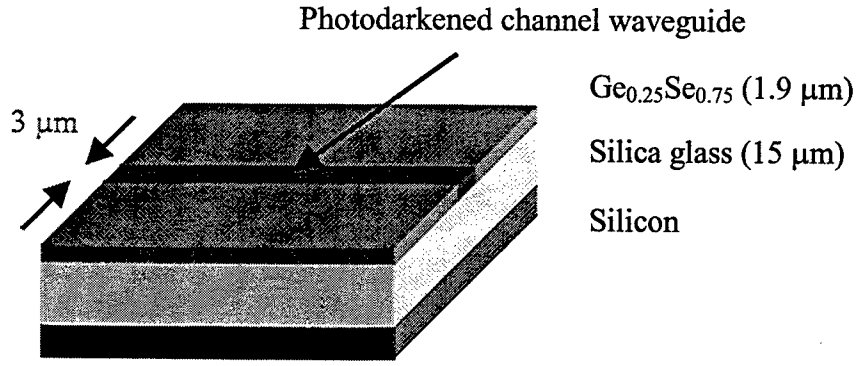
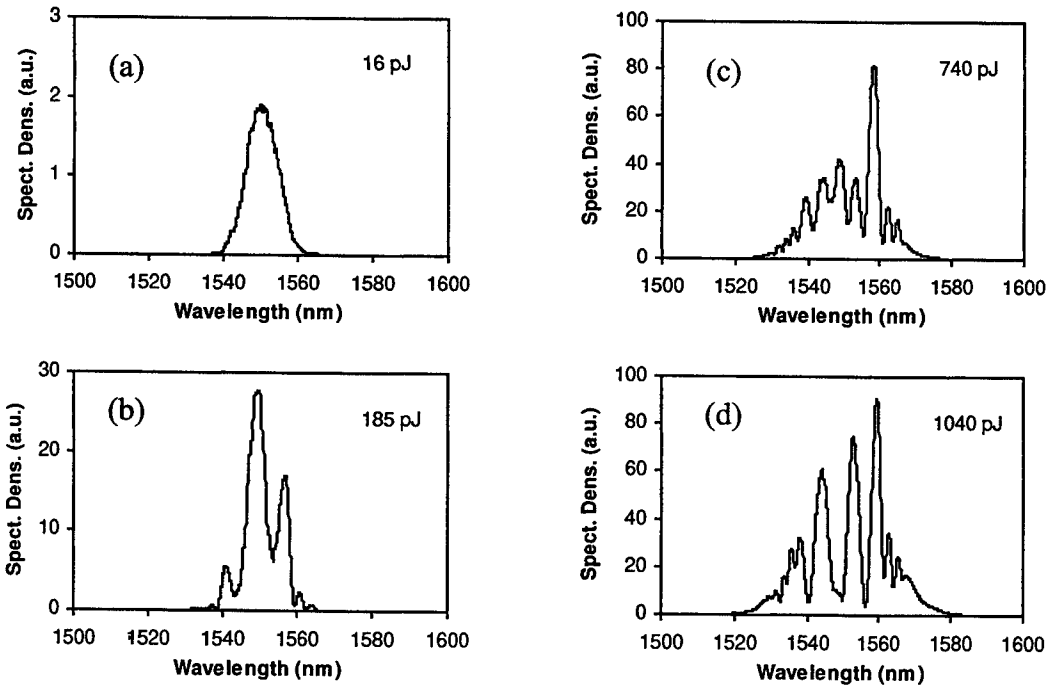


Fig. 1: Schematic of one of the photodarkened waveguides.

In order to investigate nonlinear pulse dynamics in one of the channel waveguides, nearly transform limited 270-fs pulses were coupled into the guide using a 40x microscope objective. Pulse energies ranged up to 1.04 nJ in front of the input facet at a repetition rate of 13.5 MHz. The overall input-to-output transmission was at 13%, including a 19% coupling efficiency and 31% Fresnel losses at the two interfaces. Waveguide intrinsic absorption and scattering losses are small garanteeing a nearly uniform pulse energy along the waveguides.



Figs. 2(a)-(d): Spectra measured at the waveguide output for different launched pulse energy.

Figs. 2(a), (b), (c), and (d) show the pulse spectra after propagation along the 2.8 cm waveguides for incident pulse energies of 16, 185, 740, and 1040 pJ respectively. A high aperture optical fiber was placed at the waveguide output so that it captured only a small portion of the transmitted light. Its spectrum was subsequently measured using an optical spectrum analyzer.

The output spectrum of the low energy pulses (Fig. 2(a)) corresponds to the input spectrum centered at the wavelength λ = 1550 nm with a spectral width of 9.3 nm (FWHM) assuming a sech-shaped spectral envelope. Increasing the energy results in significant spectral broadening as well as in an oscillatory structure as expected from self phase modulation.[5] Spectral asymmetries with respect to the center wavelength may be attributed to intrapulse Raman processes.[6] The Raman gain is expected to scale with n_2 compared to silica glass.[7] Due to the small pulse width used in our experiment intrapulse Raman scattering is likely to be observed. By comparison to numerical simulations, the maximum nonlinear phase shift at the pulse peak intensity is estimated to be at 3.5 π in Fig. 2(d). Assuming an effective area of 8 μm^2 in accordance to mode field calculations, we obtain an approximate value for the nonlinear index of $n_2 = 1.5 \times 10^{-14}$ cm^2/W corresponding to about 54 $\times$ $n_2(SiO_2)$. This value is within the same order of magnitude as previous Z-scan measurements on $Ge_{0.25}Se_{0.75}$ bulk samples[3] and also agrees with theoretical estimates.[2]

In order to assess the impact of nonlinear absorption, we recorded the output energy as a function of the input energy. As shown in Fig. 3, the high-energy transmission deviates only slightly from a linear fit obtained from the low energy data. If we are modelling the deviation as a two-photon absorption (TPA) process, the TPA coefficient is extracted to be $\alpha_2=5.3\times10^{-12}$ cm/W where a Gaussian spatial and temporal profile of the pulses has been taken into account.[8] Defining a figure of merit FOM=$n_2/(\alpha_2\lambda)$, with all-optical switching possible for FOM>1, we obtain FOM=18. This high figure of merit clearly demonstrates the potential of the planar chalcogenide waveguides for all-optical switching devices. We are exploring other chalcogenide compounds with the bandgap adjusted slightly above twice the photon energy, hence promising an order of magnitude improvement in n_2.

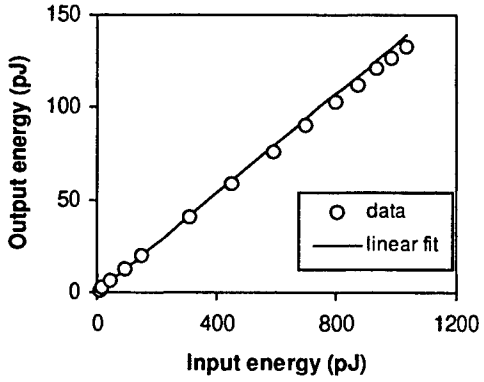


Fig. 3: Output energy versus input energy.

[1] M. Asobe, H. Itoh, T. Miyazawa, and T. Kanamori, Electron. Lett. **29**, 1966 (1993).
[2] M.E. Lines, J. Appl. Phys. **69**, 6876 (1991).
[3] S. Spälter, G. Lenz, H.Y. Hwang, J. Zimmermann, S-W. Cheong, T. Katsufuji, M.E. Lines, and R.E. Slusher, *Nonlinear Guided Waves and their Applications Topical Meeting,* (Optical Society of America, Washington, DC 1999), paper ThD38.
[4] K. A. Cerqua-Richardson, J.M. McKinley, B. Lawrence, S. Joshi, and A. Villeneuve, Opt. Mat. **10**, 155 (1998).
[5] G. P. Agrawal, *Nonlinear fiber optics*, (Academic Press, San Diego, 1995).
[6] F.M. Mitschke and L.F. Mollenauer, Opt. Lett. **11**, 659 (1986).
[7] M. Asobe, T. Kanamori, K. Naganuma, H. Itoh, and T. Kaino, J. Appl. Phys. **77**, 5518 (1995).
[8] W.L. Smith, *CRC Handbook of Laser Science and Technology*, M.J. Weber, ed. (CRC Press, Cleveland, Ohio, 1986), Vol. 3, Pt. 1.

Nonlinear Guided Waves and Their Applications Topical Meeting
KEY TO AUTHORS

Aitchison, J. Stewart, PD5

Bar-Ad, Shimshon, PD5
Broderick, N.G.R., PD1

Chen, Zhigang, PD3
Cheong, S-W., PD6
Chinaglia, Walter, PD4
Christodoulides, Demetrios N., PD3
Coen, Stéphane, PD2
Coskum, Tamer, PD3

Di Trapani, Paolo, PD4

Eisenberg, Hagai, PD5

Haelterman, Marc, PD2
Hanna, D.J., PD1
Hwang, H.Y., PD6

Katsufuji, T., PD6

Lenz, G., PD6

Minardi, Stefano, PD4
Morandotti, Roberto, PD5

Peschel, Ulf, PD5
Potashnik, Orit, PD5

Richardson, D.J., PD1
Ross, Duncan, PD5
Ross, G.W., PD1

Segev, Mordechai, PD3
Silberberg, Yaron, PD5
Slusher, R.E., PD6
Soljacic, Marin, PD3
Spälter, S., PD6

Valiulis, Gintaras, PD4
Vishwanath, Ashvin, PD3

Zimmermann, J., PD6

Nonlinear Guided Waves and Their Applications
Technical Program Committee

General Chairs:
David J. Richardson, *Univ. of Southampton, UK*
Stefan Wabnitz, *Univ. de la Bourgogne, Dijon, France*

Program Chairs:
J. Stewart Aitchison, *Univ. of Glasgow, UK*
Falk Lederer, *Univ. of Jena, Germany*
Mordechai Segev, *Princeton Univ., USA*

Category 1: Nonlinear Fiber Effects and Temporal Solitons
Y. Kodama, *Ohio State Univ., Columbus, USA, Chair*
G. Agrawal, *Univ. of Rochester, USA*
P. Mamyshev, *Tyco Submarine Systems, USA*
T. Georges, *CNET, Lannion, France*
W. Forysiak, *Aston Univ., UK*

Category 2: Spatial Solitons and Transverse Effects
Yu. Kivshar, *Australian National Univ., Canberra, Australia, Chair*
Y. Silberberg, *Weizmann Inst., Rehovot, Israel*
L. Torner, *Universität Polit. Catalunya, Barcelona, Spain*
W. Torruellas, *Washington State Univ., Pullman, USA*

Category 3: Nonlinear Periodic Structures and Cavities
L. Lugiato, *Univ. of Milan, Italy, Chair*
S. Trillo, *Univ. of Ferrara, Italy*
J. R. Tredicce, *Univ. of Nice, France*
M. de Sterke, *Univ. of Sydney, Australia*
P. St. J. Russell, *Univ. of Bath, UK*

Category 4: Frequency Conversion and Switching
A. Barthélémy, *Univ. of Limoges, France, Chair*
M. Asobe, *NTT, Japan*
P.G. Kazansky, *Univ. of Southampton, UK*
P. Di Trapani, *Univ. of Milan, Italy*

Category 5: Materials and Fabrication
A. Villeneuve, *Univ. of Laval, Quebec, Canada, Chair*
W. Sohler, *Univ. Paderborn, Germany*
T. Kaino, *Tohoku Univ., Japan*
F. Laurell, *Royal Inst. of Tech., Sweden*
P. LiKamWa, *Univ. of Central Florida, USA*

***Gregory Magel,** *Texas Instruments Inc., USA*

**OSA Technical Council Representative*